

The 12th International Workshop on
Nonlinear Dynamics of Electronic Systems

NDES 2004
Évora, Portugal
May 9-13

Published by
Centro de Geofísica de Évora
Universidade de Évora, Portugal

Cover: Historical street of Évora

Title: Proceedings of the 12th International Workshop on
Nonlinear **D**ynamics of **E**lectronic **S**ystems (**NDES 2004**)

Editors: Jason A. C. Gallas, Mourad Bezzeghoud, Pedro G. Lind, João Corte Real

Editor's address: Universidade de Évora and Centro de Geofísica de Évora
Colégio Luis Verney, Rua Romão Ramalho, 59
7002-554 Évora, Portugal
<http://www.cge.uevora.pt>
<http://www.uevora.pt>

Print: Serviço de Reprografia e Publicação da Universidade de Évora
Largo dos Colegiais 2, 7000-803, Évora, Portugal

Printing of the cover: Gráfica Eborensis

Number of copies: 165

Legal Deposit: 211317/04
ISBN: 972-778-073-3
April, 2004

Proceedings of the
12th International Workshop on
Nonlinear Dynamics of Electronic Systems
NDES 2004

Centro de Geofísica de Évora,
Universidade de Évora,
Portugal, May 9-13, 2004

Edited by:
Jason A. C. Gallas
Mourad Bezzeghoud
Pedro G. Lind
João Corte Real

Published by
Centro de Geofísica de Évora
Universidade de Évora
Largo dos Colegiais 2, 7000-803, Portugal

Conference Location and Organization
Universidade de Évora and Centro de Geofísica de Évora

Organizing Committee

JASON GALLAS	<i>Chair, Univ.Federal, RGS, Porto Alegre, Brazil & CGE, Évora, Portugal</i>
JOÃO CORTE REAL	<i>Universidade de Évora & CGE, Évora, Portugal</i>
MOURAD BEZZEGHOUD	<i>Universidade de Évora & CGE, Évora, Portugal</i>
PEDRO LIND	<i>CGE, Évora, Portugal</i>
RUI NAMORADO ROSA	<i>Universidade de Évora & CGE, Évora, Portugal</i>
ANDREIA DIONÍSIO	<i>Universidade de Évora, Évora, Portugal</i>
ARMANDO PIRES	<i>Universidade de Évora, Évora, Portugal</i>
ANA MARIA SILVA	<i>Universidade de Évora & CGE, Évora, Portugal</i>
DAVID BERRY	<i>Universidade de Évora & CGE, Évora, Portugal</i>
RUI VILELA MENDES	<i>Instituto Superior Técnico, Lisboa, Portugal</i>
JOÃO COSTA FREIRE	<i>Instituto Superior Técnico, Lisboa, Portugal & IEEE Portugal</i>

International Scientific Committee

RICARDO CHACÓN	<i>School of Industrial Engineering, Badajoz, Spain</i>
ANTHONY DAVIES	<i>King's College London, England</i>
ALEXANDER DMITRIEV	<i>Russian Academy of Sciences, Moscow, Russia</i>
JASON GALLAS	<i>Universidade Federal do RGS, Porto Alegre, Brazil & CGE</i>
MARIA HAASE	<i>ICA-2, Universität Stuttgart, Germany</i>
MARTIN HASLER	<i>EPFL, Lausanne, Switzerland</i>
BERT KAPPEN	<i>University of Nijmegen, The Netherlands</i>
GÉZA KOLUMBÁN	<i>Technical University, Budapest, Hungary</i>
ERIK LINDBERG	<i>Technical University, Kopenhagen, Denmark</i>
HANS-ANDREA LOELIGER	<i>ETH Zurich, Switzerland</i>
WOLFGANG MATHIS	<i>Universität Hannover, Germany</i>
MANUEL MATIAS	<i>IMEDEA, Palma de Mallorca, Spain</i>
GILLES MILLERIOUX	<i>Université Henri Poincaré, Nancy, France</i>
FRED NEERHOFF	<i>University of Technology, Delft, Netherlands</i>
MACIEJ OGORZALEK	<i>Univ. of Mining & Metallurgy, Krakow, Poland</i>
ALBERTO PINTO	<i>Universidade de Porto, Porto, Portugal</i>
JOSÉ SOUSA RAMOS	<i>Instituto Superior Técnico, Lisboa, Portugal</i>
TOSHIMICHI SAITO	<i>HOSEI University, Tokyo, Japan</i>
ACAR SAVACI	<i>Institute of Technology, Izmir, Turkey)</i>
WOLFGANG SCHWARZ	<i>Technical University of Dresden, Germany</i>
GIANLUCA SETTI	<i>University of Ferrara, Italy</i>
RICARDO SEVERINO	<i>Universidade do Minho, Braga, Portugal</i>
WILLI-HANS STEEB	<i>Rand Afrikaans University, South Africa</i>
RUEDI STOOP	<i>ETH Zurich, Switzerland</i>

Sponsors

Fundação Eugénio de Almeida
Fundação Calouste Gulbenkian
Fundação para a Ciência e a Tecnologia
Câmara Municipal de Évora
Banco Espírito Santo
CARMIM – Reguengos de Monsaraz
Universidade de Évora
Centro de Geofísica de Évora

NDES 2004 had the support of IEEE

Preface

NONLINEAR DYNAMICS OF ELECTRONIC SYSTEMS 2004 (NDES 2004) is the twelfth in a series of international specialist workshops on Nonlinear Dynamics of Electronics Systems, since 1993, when the first NDES workshop took place in Dresden. Since then, the NDES has steadily increased its impact in the scientific community, becoming a truly international event, the largest of its kind in Europe.

In 2004, the workshop brought together specialists in engineering and applied sciences, in physics and geophysics and in mathematics, in order to provide an opportunity to meet in a low-cost informal setting to address new theoretical and practical results, novel analysis and design methods in nonlinear dynamic systems and circuits and to discuss open problems in nonlinear science in general.

NDES2004 has been organized and hosted by the *Centro de Geofísica de Évora* (Centre of Geophysics of Évora) of the *University of Évora*, Portugal. *Évora* is, since 1986, a UNESCO World Heritage Site.

This book of proceedings contains all accepted papers, distributed among the following subjects: Circuit systems, Chaos, Stability and Control, Nonlinear Time Series Analysis, Chaos in Earth Sciences, Econophysics and Econometrics, Biological Systems and Synchronization.

We are very grateful to the following sponsors: *Fundação Eugénio de Almeida, Fundação Calouste Gulbenkian, Fundação para a Ciência e a Tecnologia, Câmara Municipal de Évora, Banco Espírito Santo, CARMIM – Reguengos de Monsaraz and Universidade de Évora.*

We are also very grateful to the invited speakers for contributing to NDES2004 and for meeting our deadlines.

We express our warm thanks to all the technicians that enthusiastically collaborated to make this event a pleasant reality; in particular we would like to mention the contribution of Luis Almas (University of Évora).

Finally we also thank all participants for their contributions and for coming. We wish all a very productive and enjoyable stay in Évora!

Évora, April 15, 2004
The Editors

Contents

I Invited Speakers	1
<i>Synchronization and pattern recognition in pulse-coupled neural networks,</i> HERMANN HAKEN	3
<i>Pattern formation of dunes,</i> HANS JURGEN HERRMANN	9
<i>Synchronization analysis of coupled noncoherent oscillators,</i> JURGEN KURTHS, Mamen Romano, Marco Thiel	17
<i>Network dynamics: tools and examples,</i> RUI VILELA MENDES	22
<i>Ideal turbulence,</i> ALEXANDER SHARKOSVSKY	34
<i>Economic fluctuations and statistical physics: the puzzle of large fluctuations,</i> HARRY EUGENE STANLEY, Xavier Gabaix, Parameswaran Gopikrishnan, and Vasiliki Plerou	42
II Contributed Papers	53
<i>Nonparametric embedding of dynamical systems,</i> M. Abel and K. Ahnert	55
<i>Nonlinear forecasting of earthquakes: a decade of results and future work,</i> E. Ivo Alves	59
<i>Innovation systems by nonlinear networks,</i> P. Andriani, F. Conti, L. Fortuna, M. Frasca, G. Passiante, and A. Rizzo	63
<i>Autocorrelation function and power spectrum of spiral chaos in dynamical systems,</i> V.S. Anishchenko, T.E. Vadivasova, G.I. Strelkova, and G.A. Okrokvetskikh	67
<i>A MOS circuit for the Lotka- Volterra chaotic oscillator,</i> Tetsuya Asai, Yusuke Kanazawa, Masayuki Ikebe, and Yoshihito Amemiya	71
<i>Chaotic third-order log-domain filter,</i> Alon Ascoli, Orla Feely, and Paul Curran	75
<i>A Generalized modulation law for generating constant- envelope spread-spectrum signals via frequency modulation,</i> Michele Balestra, Stefano Santi, Riccardo Rovatti and Gianluca Setti	79

<i>A new phenomenon: parametric chaos,</i> A.L. Baranovski and A.J. Lawrance	83
<i>Synchronization of chaotic colpitts oscillators with parameter mismatch,</i> Antanas Baziliauskas, Romanas Krivickas, and Arunas Tamasevicius	87
<i>Oscillations in the first-order recursive digital filters with magnitude truncation,</i> Yuriy Bryuhanov	91
<i>Clustering and nonlinear forecast for electronic devices market demand,</i> M. Bucolo, F. Caizzone, L. Fortuna, and G. Tomarchio	95
<i>Hardware prototype of the two-stage chaotic Colpitts oscillator for the UHF range,</i> S. Bumeliene, A. Tamasevicius, G. Mykolaitis, A. Baziliauskas, and E. Lindberg	99
<i>Comparison between Perturbation and Volterra methods,</i> Antonio Buonomo and A. Lo Schiavo	103
<i>Bifurcation analysis and chaotic behavior in boost converters: experimental results,</i> Donato Cafagna and Giuseppe Grassi	107
<i>Generation of chaotic beats in a modified Chua circuit - Part I: dynamic behaviour,</i> Donato Cafagna and Giuseppe Grassi	111
<i>Generation of chaotic beats in a modified Chua circuit - Part II: Circuit design,</i> Donato Cafagna and Giuseppe Grassi	115
<i>Electromagnetic synchronization of slip,</i> T. Chelidze, T. Matcharashvili, and O. Lursmanashvili	119
<i>Analysis of weight time series of patients with eating disorders,</i> F. Cuadros and M.I. Parra	122
<i>Homoclinic chaos in coupled Chua's oscillator,</i> S.K. Dana, S. Chakraborty, and G. Ananthakrishna	126
<i>Entropy-based independence test,</i> Andreia Dionisio, Rui Menezes, and Diana A. Mendes	130
<i>Syntesis of single-transistor chaotic oscillators,</i> Alexander S. Dmitriev, Elena V. Efremova, and Alexander D. Khilinsky	133
<i>Amplitude modulation and demodulation of chaotic carriers,</i> Alexander S. Dmitriev, Lev V. Kuzmin, and Anton M. Laktushkin	138
<i>Bifurcation associated with the Fitzhugh-Nagumo Systems,</i> Jorge Duarte, Luis Silva, and J. Sousa Ramos	142
<i>Application of State-Space Transformations to the Noise Analysis of Oscillators,</i> Thomas Falk and Wolfgang Schwarz	146
<i>Conductance: from electrical networks, through graphs, to dynamical systems,</i> Sara Fernandes and Jose Sousa Ramos	150

<i>Effects of sequence-dependent elastic properties in tandemly repeated DNA,</i> Alexandre F. da Fonseca, C.P. Malta, and M.A.M. de Aguiar	154
<i>A chaotic circuit with ferroelectric nonlinearity,</i> Luigi Fortuna, Mattia Frasca, Salvatore Graziani, and Salvatore Reddiconto	158
<i>Spatio-temporal dynamics towards self-synchronization index,</i> Luigi Fortuna, M. La Rosa, D. Nicolosi, and G. Sicurella	162
<i>Storing binary patterns in two-dimensional networks of nonlinear systems,</i> Zbigniew Galias and Maciej Ogorzalek	166
<i>The first eigenvalue of the Laplacian and the ground flow of a compact surface,</i> Clara Grácio and J. Sousa Ramos	170
<i>Circuit model of the atmospheric response function,</i> L. Hevesi, I.M. Janosi, A. Kiraly	174
<i>Emergent oscillations in a system of coupled nonlinear elements with broken symmetry,</i> V. In, A. Kho, A.R. Bulsara, J. Neff, B. Meadows, A. Palacios, P. Longhini, B. Ando, and S. Baglio	178
<i>Study of electronic master-slave MFHN neurons,</i> Sabir Jacquir, S.Binczak, J.M.Bilbault, V.B.Kasantsev, and V.I.Nekorkin	182
<i>Application of nonlinear dynamical systems to image encryption,</i> Kristina Kelber	186
<i>Nonlinear dynamics of cochlear information processing,</i> A. Kern and R. Stoop	190
<i>Synchronized firing of Fitzhugh-Nagumo neurons by noise,</i> H. Kitajima and T. Hattori	194
<i>A simple chaotic circuit with impulsive switch depending on time and state,</i> Yoshifumi Kobayashi, Hidehiro Nakano, and Toshimichi Saito	198
<i>Abelian Differential Equations Define Chaos Generator,</i> Tohru Kohda and Aya Katoh	202
<i>Numerical experiments with ground on AED theory: Investigation of Energetic Processes in Disordered Systems,</i> Aliaksei Konash, Paval Buka and Sergej Bagnich	206
<i>Rich synchronization of simple spiking oscillators,</i> Yoshio Kon'no, Toshimichi Saito, and Hiroyuki Torikai	210
<i>Cascaded return map models a nonperiodically clocked CPM boost converter,</i> Joerg Krupar and Wolfgang Schwarz	214
<i>Non-authorized access to the chaotic communication channel based on the partial approach to the inverse problem of non-linear dynamics,</i> V.N. Kuleshov and M.V. Tomashevskaya	219

<i>Two-stage impulsive control for the synchronization of chaotic systems,</i> K. Li, Y.C. Soh, and Z.G. Li	223
<i>On the Mechanisms behind Chaos,</i> Erik Lindberg	227
<i>General mechanism for suppression of homoclinic chaos,</i> Alexander Loskutov and Arsen Janoev	231
<i>On the existence of periodic solutions to the equation of a forced nonlinear oscillator,</i> Oleg Makarenkov	235
<i>Synchronizability of power-law and fractally coupled dynamical networks,</i> Mate Marodi	238
<i>Excitation-reshaping-induced chaotic escape from a potential well,</i> J.A. Martfnez and R. Chacon	242
<i>Coupled piecewise linear maps: from coherence to clustering,</i> Iryna Matskiv and Yuri Maistrenko	246
<i>Co-movements and threshold adjustment for the Portuguese and U.S. stock market volatility,</i> Rui Menezes and Nuno B. Ferreira	250
<i>Performances of unknown input observers for chaotic LPV maps in a stochastic context,</i> Gilles Millerieux and Jamal Daafouz	255
<i>Quantitative methods for the characterization of complex surface structures,</i> Alejandro Mora and Maria Haase	259
<i>Image processing with a cellular nonlinear network,</i> S. Morfu, P. Marqui, and J.M. Bilbault	263
<i>Schemes of Polynomial Equations that Characterize the Variational Behaviour,</i> F.L. Neerhoff and P. van der Kloet	267
<i>Identification of Bifurcation Parameters in Boost PFC Circuit,</i> Mohamed Orabi and Tamotsu Ninomiya	271
<i>On the start-up behavior of singularly perturbed harmonic oscillators,</i> Marcus Prochaska and Wolfgang Mathis	276
<i>Reconstruction of driven and coupled time-delay systems from time series,</i> M.D. Prokhorov, A.S. Karavaev, and V.I. Ponomarenko	280
<i>Conductance and noncommutative dynamical systems,</i> Carlos Correia Ramos, Nuno Martins, and Jose Sousa Ramos	284
<i>Antiphase to in-phase synchronization in coupled Chua's oscillators,</i> P.K. Roy and S.K. Dana	288

<i>Limit cycles in autonomous two-dimensional first order recursive digital filters with nonlinear adder without quantization,</i> D.V. Rudykh, M.V. Lebedev, and A.L. Priorov	292
<i>Complex Dynamics of a Two-cavity Klystron Oscillator with Delayed Feedback,</i> N.M. Ryskin and A.M. Shigaev	296
<i>D/A converters and iterated function systems,</i> Toshimichi Saito, Junya Shimakawa, and Hiroyuki Torikai	300
<i>The time-series modelling and circuit implementation from time-frequency domain specifications,</i> F. Acar Savaci and Nalan Ozkurt	304
<i>Collapse and Coexistence of Duck Solution in a Circuit Driven by an Extremely Small Periodic Force,</i> Munehisa Sekikawa, Naohiko Inaba, Tetsuya Yoshinaga, and Hiroshi Kawakami	308
<i>Topological invariants in a model of a time-delayed Chua's circuit,</i> R. Severino, A. Sharkovsky, J. Sousa Ramos and S. Vinagre	312
<i>Fractal analysis of X-ray chest images,</i> Maciej H. Slomczynski and Bozena Swidzinska	316
<i>Sympatric specification in an age-structured population living on a lattice,</i> Adriano O. Sousa	320
<i>Complexity measures for nonlinear electronic systems: Comment on the Shiner-Davison-Landsberg measure,</i> R. Stoop, N. Stoop, A. Kern, and W. H. Steeb	324
<i>VHF and UHF chaotic Colpitts oscillators,</i> A. Tamasevicius, G. Mykolaitis, S. Bumeliene, R. Krivickas, and E. Lindberg	328
<i>Variability of interburst intervals in 2D slow-fast maps for neural responses,</i> Gouhei Tanaka and Kazuyuki Aihara	332
<i>Controlling the chaotic colpitts oscillator by altering its oscillation energy,</i> V. Tereshko, R. Chacdn, and J. Carballar	336
<i>Spurious structures in recurrence plots induced by embedding,</i> M. Thiel, M.C. Romano, and J. Kurths	340
<i>Fractal properties of chaotic dynamical systems in reverse time and its application for data encryption,</i> A.I. Tomashevskiy and M.V. Kapranov	344
<i>Bifurcation in current coupled BVP oscillators,</i> Shigeki Tsuji, Tetsushi Ueta, and Hiroshi Kawakami	348
<i>An Aspect of Oscillatory Conditions in Linear Systems and Hopf Bifurcations in Nonlinear Systems,</i> Tetsushi Ueta and H. Kawakami	352

<i>Floquet Numbers and Dynamic Eigenvalues,</i> P. van der Kloet and F.L. Neerhoff	356
<i>Synchronization in models of discrete phase oscillators,</i> Anna Vasylenko, Yu. Maistrenko, M. Hasler	360
<i>Application of fractal analysis in detection of bone structure changes,</i> Michal Wroblewski and Bozena Swidzinska	364
<i>An Extended Bernoulli Map Driven by Dynamic Thresholding,</i> Kenji Yano and Kiyoshi Tanaka	368
<i>Optimal multi-user chaos-shift-keying communication systems,</i> Ji Yao	372
<i>Heart Tissue as a Dynamical System,</i> E. Zhuchkova and A. Loskutov	376
<i>A Model for The ‘Chaotic’ Oscillations of Congenital Nystagmus</i> Christopher M. Harris and David L. Berry	380
Index by authors	385

Part I
Invited Speakers

Synchronization and Pattern Recognition in Pulse-Coupled Neural Networks

H. Haken

Institute for Theoretical Physics I
 Center of Synergetics
 University of Stuttgart
 70550 Stuttgart
 Germany

e-mail: haken@theo1.physik.uni-stuttgart.de
 WWW: <http://www.theo1.physik.uni-stuttgart.de/>

Abstract - *This paper establishes and studies equations of a network that is composed of neurons with their dendrites and axons. The pulse generation in the axon is described by means of phase oscillators, whereas the dendritic currents are described by linear damping equations with source terms as which the incoming pulses act. The equations take into account delays and noise. In the case of phase-locking the equations have been solved previously by the author. The main objective of the present paper is to study in how far these equations may serve for pattern recognition. It is shown that either a random phase approximation for the stored patterns or a triple interaction term suffice to treat pattern recognition. It is pointed out how then recognized patterns can be either encoded as completed prototype patterns or as phase-locked states. It is suggested that to understand pattern recognition it is not only necessary to consider the whole network instead of “grandmother” cells but equally well the whole intermediate steps.*

rate is a measure of intensities. These spikes serve as a universal “language” in the brain. More recently it has been found that under specific experimental conditions spike trains stemming from different neurons can synchronize. This is occasionally invoked as a solution to the so-called binding problem, namely our sensory inputs are processed by different parts of the brain but in spite of that eventually an object with its different properties is identified as such.

I. INTRODUCTION

Nature impresses us again and again by its ingenious solutions of problems that are also of high technological interest to us. Thus it is surely worthwhile to study the functioning of our brain from such a point of view. In my contribution I take as a starting point neuro-physiological data combined with some experimental data, though surely there still will be a large gap between the real functioning of our brain and our models. The brain is composed of about one hundred billion neurons that communicate via electrical spikes by means of some kind of pulse-code modulation, i.e. the spike

II. BASIC EQUATIONS. PHASE-LOCKING

Let me consider an individual neuron that is the building block of the neural net (Fig. 1)

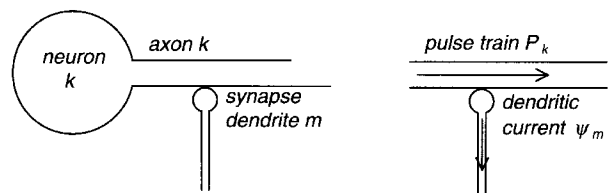


Fig. 1: Scheme of a neuron

It receives inputs from other neurons via its dendrites and gives its output to other neurons by its axon that then branches. The connection between the axonic tree on the one hand and the dendritic trees of the other neurons on the other hand is done in general by chemical synapses. The signals are emitted in form of pulses along the axon, whereas the signals received by the dendrites from the synapses are transported as d. c. electric currents. Thus I am introducing two kinds of variables, namely the pulses on the one hand and the electric

currents on the other hand [1]. The pulse generation is taken care of by the model of a phase oscillator in analogy to the rotating beam of a lighthouse. Whenever the phase-angle ϕ (of the beam) reaches a specific value, a pulse is emitted. Quite often the coupling between phase oscillators is taken care of by a sinusoidal coupling $\sin(\phi_j - \phi_k)$. Here, however, I want to take care of such a coupling by means of the pulses. The model I am treating can be considered as a generalized integrate and fire model. The equation for the current Ψ_m of the dendrite with label m reads

$$\left(\frac{d}{dt} + \gamma\right)^\alpha \Psi_m(t) = \sum_k a_{mk} P_k(t - \tau_{km}) + F_{\Psi_m}(t). \quad (1)$$

In it γ is a damping constant of the dendritic current. The exponent α can be 1 or 2 or even a non-integer. The coefficients a_{mk} are proportional to the synaptic strengths. P_k describes the pulses or spikes stemming from neuron k , τ_{km} are delay times and F_{Ψ_m} is a fluctuating force (noise source). We represent the pulses in the form

$$P(t) = f(\phi(t)) \quad (2)$$

with

$$f(\phi(t)) = \dot{\phi} \sum_n \delta(\phi - 2\pi n), \quad (3)$$

which can also be written in the form

$$= \tilde{f}(t) = \sum_n \delta(t - t_n) \quad (4)$$

where the times t_n are defined by

$$t_n: \phi(t_n) = 2\pi n, \quad n \text{ integer}. \quad (5)$$

This corresponds to what I have called the lighthouse model in a similar context. The phases of the neurons are described by the phase oscillator equation

$$\begin{aligned} & \dot{\phi}_j(t) + \gamma' \phi_j(t) \bmod 2\pi \\ & = S_j \left(\sum_m c_{jm} \Psi_m(t - \tau'_{mj}) + p_{ext,j} \right) + F_{\phi,j}(t), \end{aligned} \quad (6)$$

where γ' is a damping constant. The prescription $\bmod 2\pi$ means that ϕ is to be reduced by an integer multiple of 2π until it has reached a size between 0 and 2π . On the r. h. s. S_j is a nonlinear function that we will specify below, c_{jm} are coefficients, τ'_{mj} are delay times, $p_{ext,j}$ is an external signal impinging on neuron j and $F_{\phi,j}$ are fluctuating forces. $S(X)$ will be used in the form

$$S(X) = \frac{rX}{1 + aX^2}. \quad (7)$$

Its discussion must be postponed to a subsequent paper. In order to eliminate the dendritic currents from equations (1) and (6), we write equation (1) in the form

$$\left(\frac{d}{dt} + \gamma\right)^\alpha \Psi(t) = g(t) \quad (8)$$

and note that it can be solved by means of the Green's function

$$\begin{aligned} K_\alpha(t - \sigma) &= (t - \sigma)^{\alpha-1} e^{-\gamma(t-\sigma)}, \quad \text{for } t \geq \sigma \\ &= 0 \quad \text{for } t \leq \sigma \end{aligned} \quad (9)$$

in the form

$$\Psi(t) = \int_0^t K_\alpha(t - \sigma) g(\sigma) d\sigma. \quad (10)$$

Inserting the result (10) into (6) with the corresponding indices and the explicit form of g , we find a closed set of equations for the phases ϕ_j . We do not write down the rather lengthy result here but rather mention that this case has been studied under rather general conditions in my book "Brain Dynamics" [1] under the assumption that $p_{ext,j}$ is independent of j and the coefficients a and c fulfil some requirements. Furthermore it was assumed that S (7) can be approximated by its numerator. The equations are nevertheless highly nonlinear because of (3). As I have demonstrated in my book, there exists a *stable phase-locked solution* whose pulse intervals have been calculated there. In the present paper I want to study in how far this kind of equations can also represent an algorithm for pattern recognition. To this end I want to write down just

one specific example where no time-delays are considered and the fluctuations have been dropped. Taking into account the nonlinear terms of S , the corresponding equation reads

$$\dot{\phi}_j(t) + \gamma' \phi_j(t) \bmod 2\pi = h_j X_j - k_j X_j^3 \quad (11)$$

where h_j and k_j are some constant coefficients that stem from S and will be chosen appropriately below. The variables X_j are defined by

$$X_j = \sum_l A_{jl} \int_0^t K_\alpha(t-\sigma) P_l(\sigma) d\sigma + p_{ext,j}, \quad (12)$$

where on the r. h. s. the coefficients A_{jl} are combinations of the original coefficients a and c .

III. PATTERN RECOGNITION

I briefly remind the reader of what we understand by pattern recognition. When an incomplete pattern is offered to the system this pattern should be completed by the action of what is called an associative memory. In order to treat the system (11), I evaluate (12) under the assumption of dense pulses. In such a case I may use an approximation of the integral in (12) so that it is split into the pulse rate of neuron l , ω_l and the remaining integral over K . I use the abbreviations

$$\bar{K} = \frac{1}{2T} \int_0^T K(\sigma) d\sigma \quad (13)$$

and

$$\int_0^t K(t-\sigma) d\sigma = \hat{K}(t) \approx const \text{ for } t > 1/\gamma. \quad (14)$$

In order to obtain handy equations. I form the difference between equation (11) at times $t+T$ and $t-T$, where the resulting l. h. s. can be interpreted according to

$$\frac{1}{2T} (\dot{\phi}_j(t+T) - \dot{\phi}_j(t-T)) = \frac{d\omega_j}{dt}. \quad (15)$$

I thus obtain (with $p_{ext,j} = 0$)

$$\frac{d\omega_j}{dt} = \sum_l A_{jl} \omega_l \bar{K} - 3 \sum_l A_{jl} \omega_l \bar{K} \left(\sum_l A_{jl} \omega_l \hat{K} \right)^2. \quad (16)$$

We now turn to the problem of pattern recognition in more detail. Precisely speaking, the patterns are conveyed to the neural net by means of the inhomogeneous terms $p_{ext,j}$. In the following, I make the replacement

$$p_{ext,j} \rightarrow p_j. \quad (17)$$

The linear term on the r. h. s. of (16) then occurs in the form of

$$\sum_l A_{jl} \omega_l \bar{K} \rightarrow \sum_l A_{jl} \omega_l \bar{K} + \frac{1}{2T} (p_j(t+T) - p_j(t-T)). \quad (18)$$

In the following we want to treat pattern recognition as an initial value problem. We must postpone the detailed justification of this procedure to a later paper. In other words, we assume the external signal in the form

$$p_j(t) = p_j \delta(t-t_o). \quad (19)$$

In confining our analysis to short times, we can cast (16) using (18) and (19) into the form

$$\frac{d\omega_j}{dt} = \sum_l A_{jl} \omega_l \bar{K} + p_j \delta(t). \quad (20)$$

This implies that we may solve the equations (16) as an initial value problem where the initial value is given by

$$\omega_j(+0) = p_j. \quad (21)$$

In order to make contact with an approach to pattern recognition by means of the synergetic computer that I developed some years ago [2], I introduce the eigenvectors v^k to the equation

$$\sum_l A_{jl} v_l^k = \lambda_k v_j^k, \quad (22)$$

where A can be considered as a synaptic matrix. I make the replacement

$$\omega_j \rightarrow q_j \quad (23)$$

in this way introducing the new variables q_j that I decompose according to

$$q_j = \sum_k \xi_k v_j^k. \quad (24)$$

Introducing (24) into (16) and projecting on the vectors v^k , I obtain equations of the form

$$\dot{\xi}_k = \lambda \xi_k - \sum_{k'k''} C_{kk'k''} \xi_{k'} \xi_{k''}, \quad (25)$$

where for simplicity I have assumed that all eigenvalues of (22) are equal. The coefficients C are defined by

$$\sum_j \tilde{k}_j v_j^{k+} v_j^{k'} v_j^{k''} = C_{kk'k''}. \quad (26)$$

(25) is not yet the form of the synergetic computer equation. However, one can make the following consideration: Let us assume that one is allowed to make a random phase approximation with respect to the v s. That would imply that C is vanishing only if

$$k = k' = k'' = k''' \quad 1 \text{ possibility} \quad (27)$$

or if

$$\left. \begin{array}{l} k = k' \quad k'' = k''' \\ k = k'' \quad k' = k''' \\ k = k''' \quad k' = k'' \end{array} \right\} 3 \text{ possibilities}$$

is fulfilled. In the former case there is only one possibility, whereas in the latter case there are three possibilities. Thus we may conclude that the averaged equation (25) can be cast into the form

$$\dot{\xi}_k = \lambda \xi_k - E \sum_{k' \neq k} \xi_{k'}^2 - C \xi_k^3, \quad C < E \quad (29)$$

with the initial condition

$$\xi_k(0) = (\tilde{v}^{k+} q(0)). \quad (30)$$

This is precisely the form of the equations of the synergetic computer that allow pattern recognition

provided that the initial values are given by (30), (21), (23). At this moment a typical difficulty arises when one wants to correlate mathematical models with neuro-physiological data. I must admit that for the time being I do not know how to realize this random phase average. Thus I have considered another neural network configuration which leads precisely to the same basic synergetic computer equation (29). The corresponding equations read with (12) and $p_j = 0$,

$$\dot{q}_j = X_j (1 - \sum_{j'} X_{j'}^2) + \sum_{jj''j'''} G_{jj''j'''} X_{j'} X_{j''} X_{j'''} \quad (31)$$

The first term can be easily interpreted as a saturation term in which the saturation of a specific neuron is achieved by a global saturation, namely by means of

$$S(X) = \frac{X}{1+X^2} \approx X(1-\overline{X^2}) \quad (32)$$

The last term in (31) will require further studies because it implies that three neurons are coupled to a fourth one. It implies so-to-speak higher correlations between neurons. Actually, it appears that such higher order relations are needed in order to explain some psycho-physical experiments but this must be left to a later study. The coefficients G are defined by

$$G_{jj''j'''} = \sum_k v_j^k v_{j'}^{k'+} v_{j''}^{k''+} v_{j'''}^{k'''+} \quad (33)$$

Invoking the results on the synergetic computer, I may discuss the outcome of this analysis as follows: Provided that a specific pattern, even incomplete, is shown to this network by means of p_j eventually a fixed point is reached that is connected with the specific pattern of the pulse rates $\omega_j \equiv q_j$ at each neuron. Fig. 2 shows an example of the recognition process:



Fig. 2: The synergetic computer can restore the whole pattern

Because of the nonlinear dynamics, the fixed points ($\xi_k \neq 0, \xi_{k'} = 0$ for $k' \neq k$) are normalized, e.g.

$$\xi_k = 1. \quad (34)$$

Thus the fixed points q_j^k are normalized also, since

$$q_j^k = v_j^k \xi_k = v_j^k \quad (35)$$

and

$$\sum_j (q_j^k)^2 = \sum_j (v_j^k)^2 = 1. \quad (36)$$

We assume as usual that the prototype patterns (v_j^k) are normalized according to (36) and are orthogonal on their adjoint vectors.

$$\sum_j v_j^{k+} v_j^{k'} = \delta_{kk'}. \quad (37)$$

We introduce a projection from layer 1 with outputs q_j on layer 2 with inputs $p_j^{(2)}$ according to

$$p_j^{(2)} = \sum_{j'} B_{jj'} q_{j'} \quad (38)$$

where

$$\sum_k \Omega_k v_j^{k+} = B_j. \quad (39)$$

If pattern k_0 has been recognized, i.e.,

$$q_j = q_j^{k_0} = v_j^{k_0}, \quad (40)$$

we obtain because of (37)

$$p_j^{(2)} = \sum_k \Omega_k \delta_{kk_0} = \Omega_{k_0}. \quad (41)$$

Layer 2 may now undergo a coherent (synchronized) spike dynamics of phases $\phi_j^{(2)}$

$$p_j^{(2)} \rightarrow \phi_j^{(2)} \quad (42)$$

which may indicate that pattern k_0 has been recognized. Layer 2 may then serve as an initial layer for further information processing.

Clearly, the projection (38) can be generalized so that a pattern v is transformed to another one u , where

$$p_j^{(2)} = \sum_{j'} B_{jj'} q_{j'} \quad (43)$$

and

$$B_{jj'} = \sum_k u_j^k v_j^{k+}. \quad (44)$$

IV. CONCLUDING REMARKS. THE JOURNEY IS THE REWARD

In my contribution I started from model equations that seem to take import traits of real neurons into account. In order to treat pattern recognition, I did two steps: I had to introduce an additional neuronal coupling and to perform the analysis on dense pulses. From this, at least two tasks for further research result:

Are the additional couplings realized in brains? Or are there other couplings with a similar effect? This is, of course, a question for neurophysiologists.

How can one treat the basic equations without resorting to the case of dense pulses?

In conclusion, I want to make a general remark on pattern recognition by humans. In the beginning, a number of researchers in the field of neuroscience suggested that patterns are recognized by “grandmother” cells. Now there is a rather general consensus that this is done by a whole network. It is, however, assumed that hereby attractor states (in the sense of dynamic systems theory) are reached. I want to suggest that pattern recognition is more than that. It is a process going on at several levels and has no “terminal”. What I suggested above on the relation between layer 1 and 2 may be just a small section (or interlude) in which even a number of feedback loops are involved.

References

- [1] H. Haken: Brain Dynamics, Springer, Berlin (2002)
- [2] H. Haken: Synergetic Computers and Cognition, Springer, Berlin (1991), second edition 2004

Further detailed references can be found there.

PATTERN FORMATION OF DUNES

H.J. Herrmann^{1,2}

¹ Institute for Computer Applications 1,
University of Stuttgart,
Pfaffenwaldring 27,
70569 Stuttgart, Germany

² Universidade Federal do Ceará,
60020-181 Fortaleza, Brazil

e-mail: hans@ica1.uni-stuttgart.de

WWW: <http://www.ica1.uni-stuttgart.de>

Abstract—*Dunes are aerodynamic instabilities of a mobile ground. Only recently the equations of motion of a free granular surface born by air and gravity have been established. I will present the equations and analyse their stability. A numerical solution gives very good quantitative agreement with field measurements. As function of wind velocity and the amount of sand various patterns are reproduced. I will discuss in particular Barchan dunes that under certain conditions behave like solitons and can in other cases breed offspring. Also practical applications like protection against desertification will be discussed.*

the wide range of length and time scales to be covered — from the dynamics of single sand grains, the formation of ripples, to the genesis and migration of dune fields, the time and length scales span over more than seven orders of magnitude — the derivation of the model will not be given here. We will instead after reviewing our experimental measurements present the basic elements of the model and finally compare the two.

The simplest and best known type of dune is the barchan dune shown in Fig. 1, shaped in a crescent, which occurs if the wind comes steadily from the same direction throughout the year and if there is not enough sand to cover the entire surface. Barchan dunes move proportionally to the wind velocity and inversely proportionally to their height. They are encountered for instance in Peru [4], [5], [6], [7], in Namibia [8] and Morocco [9]. On these dune fields, hundreds of barchans can be found, generally all of the same size. The dunes have heights between 1.5 and 10 m, while their bases are typically 40 to 150 m long and 30 to 100 m wide. The windward or stoss-side of the dune has typical slopes between 8° and 20° and is limited by a sharp edge, called the brink. The brink coincides in many cases with the crest of the dune and separates the slip face from the dune's windward side. Roughly speaking, its section is a parabola-like curve reaching from the tip of one horn to the point of maximum slip face height and back to the tip of the other horn. Despite the fact that for more than 50 years geologists and geographers have been measuring dunes in the field and have obtained data on height, width, length, volume and dune velocity, very little is yet known [10], [11] about the exact quantitative shape of barchans. From a mathematical point of view, the barchan dune is a symmetrical object in the wind direction, but in nature there are many

I. INTRODUCTION

Everybody knows the majestic wave-like shapes of dunes in the desert. Sand dunes develop wherever loose sand is driven by a fluid (air, water ...) that lifts grains from the ground and entrains them into a surface flow. The diverse conditions of wind and sand supply in different regions on Earth give rise to a large variety of different shapes of aeolian dunes [1], [2], [3]. Moreover, dunes have been found on the sea-bottom and even on Mars. Despite the long history of the subject, the underlying physical mechanisms of dune formation are still not very well understood. How are aerodynamics (hydrodynamics) and the particular properties of granular matter acting together to create dunes? How is the shape of a dune maintained when it grows and moves? What determines the size of dunes? Due to the fact that neither now nor in the near future we will be able to simulate dunes on the grain scale (an average barchan comprises 10^{15} grains), we concentrate in the following on an effective continuum model that can be applied to sand dunes or other geomorphological problems on a large scale. Due to the highly complicated physical processes involved (saltation, turbulent wind) and



Fig. 1. Barchan dunes near Laâyoune, Morocco. The dune in the front, on the left side was measured in detail during our field trip in May 1999, see [14].

factors, like non-steady winds or inclined ground surfaces leading to asymmetrical shapes. Numerical simulations to predict the evolution of barchan dunes and their exact shape have been performed by [12], [13].

II. EXPERIMENTAL MEASUREMENTS OF A BARCHAN DUNE

A. Dune Morphology

Qualitatively the crescent-like shape of the barchan is well known. The first measurements concerning barchan dunes and their morphologic relationships were performed by Coursin (1964) [15] in Mauritania and Finkel (1959) [4] in the Pampa de La Joya in southern Peru. Hastenrath (1967,1987) [5], [6] analysed barchans in the same area and revisited the site 20 years later. Additional investigations in the same field were undertaken by Lettau and Lettau (1969). [7] Slattery (1990) [8] measured barchan dunes in Namibia. However, they did not measure the entire shape of the dune, but only the typical lengths. Our own field measurements [14] were performed in a dune field in the Sahara desert, located in southern Morocco (former Spanish Sahara) near the city of Laâyoune.

We define for each horn, the lengths L_a, L_b and the widths W_a, W_b independently, as did Finkel (1959) [4]. The orientation of the measuring axis is chosen according to the wind direction, which coincides with the symmetry line for a totally symmetric dune. Furthermore, we introduce the length of the slip face L_s and the length L_0 from the dune's toe on the windward side to the brink. Finally, the height of the slip face H is defined at the highest point of the brink, which is the intersection of the brink and the longitudinal centerline of the dune.

The relationship between the width of the horns $W = W_a + W_b$ and the height H of the slip face has been studied many times. An overview can be found by Hesp and Hastings (1998). [10] A linear relationship was found between the height H and the width

of the horns W .

$$W = a_W H + b_W \quad (1)$$

For the management of dune movement the volume V of a dune is one of the most interesting features, apart from the rate of movement v_d . Together they determine the bulk flux Q_b of sand transported by the dunes.

$$Q_b = \rho_{sand} v_d V \quad (2)$$

To obtain the total flux Q_t , in addition to the bulk flux the inter-dune-flux Q_i , has to be taken into account.

$$Q_t = Q_b + Q_i \quad (3)$$

A study of these fluxes has been performed by Sarnthein and Walger (1974) [16]. In the following we concentrate on the bulk flux and the dune volume.

According to Oulehri (1992) [9], the rate of movement of the dunes in the area of Laâyoune is 32 m yr^{-1} for a dune of 9 m height. The bulk density of the dune sand is 1670 kg m^{-3} , on average. Using these data and the calculated volume of $23\,000 \text{ m}^3$ for dune 7, we obtain a flux of $1.2 \text{ million t m}^{-1} \text{ yr}^{-1}$ or $736\,000 \text{ m}^4 \text{ yr}^{-1}$. Lettau and Lettau (1969) [7] estimated a bulk flux of $20\,550 \text{ m}^4 \text{ yr}^{-1}$ for an average barchan of the Pampa de La Joya whose height was 3 m. A large barchan with a height of 5.2 m gave a bulk flux of $60\,000 \text{ m}^4 \text{ yr}^{-1}$.

The overall length L of a barchan is the sum of the length L_0 from the windward foot of the dune to its crest, the length of the slip face L_s , and the average of the horn lengths $L_h = (L_a + L_b)/2$

$$L = L_0 + L_s + \frac{L_a + L_b}{2} \quad (4)$$

This definition uses four lengths, of which only the length of the slip face L_s has an obvious dependence on the height H ,

$$L_s = \frac{H}{\tan \Theta}, \Theta \quad (5)$$

where Θ is the angle of repose with typical values between 31° and 35° . This angle is an intrinsic property of the sand and is therefore independent on the aeolian processes.

Finkel [4] reported for the horn length.

$$L_x = a_x H + b_x \quad (6)$$

Further the ratio of the horn length L_h to the stoss-side length L_0 also depends on the dune's height. This shows clearly that the relative position of the slip

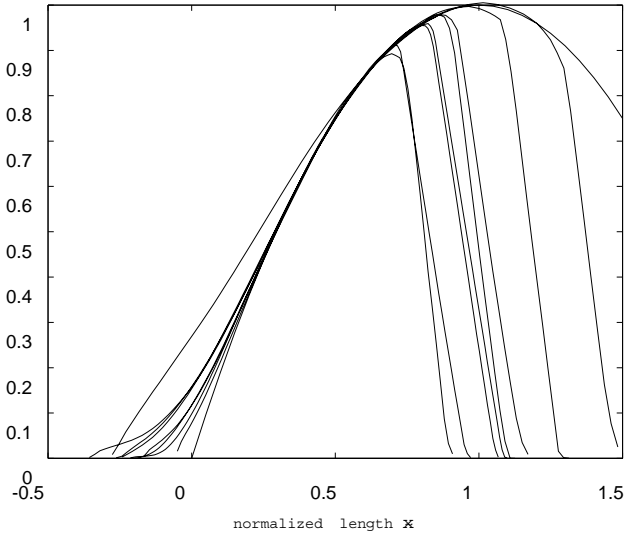


Fig. 2. Profile along the symmetry plane of the dunes (thin lines) using normalized variables and the standard parabola (thick line) from [14].

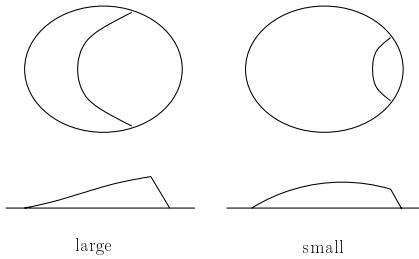


Fig. 3. Sketch of a small and a large dune.

face within the whole dune varies from small to large dunes and that the ratio of horn length to total length increases with the height as shown in Fig. 3. This disproves scaling invariance of barchan dunes. The size scaling of Barchans can be used to put them all on top of each other by rescaling the axis for each dune and using dimensionless variables. This is done for the longitudinal cross section in Fig. 2. We see that on the windward part the shape is a paraboloid and the brink position b_o moves to the right for larger dunes. In fact b_o is a linear function of the height. Therefore we have a deviation from perfect size scaling as shown in Fig. 3. Looking from the top, the brink line has also the shape of a parabola.

B. Wind velocity and sand flux

Correlated measurements of the wind velocity v and the sand flux q have been performed [17] on a large barchan dune near the beach of Jericoacoara (see Fig. 4) during the first week of December 2000, at the end of the dry season. The dune has approximately



Fig. 4. Aerial photography of the coastal dune field near Jericoacoara.

34 m in height, a width of 600 m, and the length of its windward side is 200 m. When a fully turbulent atmospheric boundary layer develops over a flat surface it gives rise to a logarithmic velocity profile $v(z)$ [18],

$$v(z) = \frac{u_*}{\kappa} \ln \frac{z}{z_0}, \quad (7)$$

where u_* denotes the shear velocity, z_0 the roughness length of the surface, and $\kappa = 0.4$ the von Kármán constant. The shear velocity u_* has dimensions of velocity but is defined in terms of the shear stress $\tau = \rho_{\text{air}} u_*^2$ and density ρ_{air} of the air. According to Hunt et al. [19] the height l of the shear stress layer can be obtained implicitly through

$$l = \frac{2\kappa^2 L}{\ln l/z_0}, \quad (8)$$

where L is the characteristic length of the dune which is measured from the half height of the windward side to the crest, according to the definition of [19]. From Eq. (8), we obtain for $L = 100$ m and a roughness length $z_0 = 10^{-4}$ m, a height of this layer of $l \approx 3.2$ m ($l \approx 4$ m for $z_0 = 10^{-3}$ m). Hence, we placed the anemometers at a height of 1 m that is well inside the shear stress layer. One should note that it is very difficult to measure the wind velocity with standard anemometers within this layer for small dunes. This is the main reason for choosing a large dune. A reference anemometer has been placed approximately 300 m upwind of the dune's foot and has been kept there during all the measurements. With a second

anemometer, we measured the average velocity v_i every 24 m on the central profile during 10 minutes. Finally, we normalized the average velocity $\langle v_i \rangle$ by the average velocity in the same period obtained from the reference anemometer, $\langle v_{r,i} \rangle$. By doing so, we could get rid of the long term (> 10 minutes) variations in the wind speed time series throughout the day and obtain the shear velocity $u_{*,i}$ through

$$1 + \hat{u}_{*,i} = \frac{u_{*,i}}{u_{*0}} = \frac{\langle v_i \rangle}{\langle v_{r,i} \rangle}, \quad (9)$$

where $\hat{u}_{*,i}$ is the dimensionless shear velocity perturbation of the air caused by the dune and u_{*0} is the undisturbed shear velocity far upwind of the dune. u_{*0} can be calculated assuming a typical logarithmic profile from turbulent flow Eq. (7). During our measurements, the wind was blowing quite constantly and had an average value of 7.5 m s^{-1} at the reference station. Assuming a roughness length $z_0 = 2.5 \times 10^{-4} \text{ m}$, we obtain from Eq. (7) the undisturbed shear velocity over the plane $u_{*0} = 0.36 \text{ m s}^{-1}$. The averaged and normalized measured shear velocities are plotted in Fig. 5.

We also measured the sand flux on the central slice of the dune using cylindrical traps with a diameter of 5 cm and an opening of 1 cm at the front. The back-side of the traps have an opening of 2 cm covered by a fabric with pores smaller than the grain diameter. The traps were placed at the same positions where the wind speed has been measured. From the mass m of the collected sand, the collection time T , and the width w of the opening, we calculated the sand flux $q = m/(T w)$. The measured sand fluxes are shown in Fig. 6.

III. THE MODEL

Since we are interested in the formation and movement of dunes, the important time scale of our problem is defined by the erosion and deposition processes that changes the surface. A significant change of the surface happens within some hours or even days. In contrast to this, the time scale of the wind and the saltation process is of the order of seconds and therefore several orders of magnitude faster. Hence, we will use in the following stationary solutions for the wind field and the sand flux. Similarly we neglect the finite life time of avalanches (a few seconds) and consider them as instantaneous compared to the movement of the dunes. The separation of the different time scales and the resulting approximations lead to an enormous simplification, because it decouples

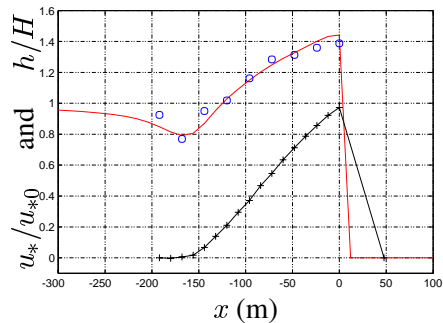


Fig. 5. The circles show the measured shear velocity u_* and wind speed $v(z = 1\text{m})$ normalized by their reference values u_{*0} and $v_0(z = 1\text{m})$, respectively. The solid line depicts the prediction of Eq. (11) using the measured height profile $h(x)$ shown in the bottom curve (crosses). The depression at the dune's foot is about 0.8 and the maximum speed-up at the brink is approximately 1.4 from [17].

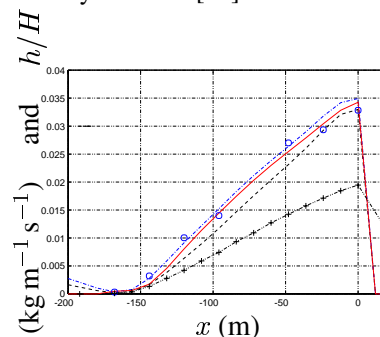


Fig. 6. Measured and calculated sand flux onto the central slice of a barchan dune. The circles denote measurements and the solid line the prediction of the non-equilibrium sand flux model, Eq. (13) (solid line). The two dashed lines correspond to the classical empirical relation for saturated flux: ref. [19] and ref. [27] is depicted. Yet, these saturated sand flux relations cannot correctly predict the sand flux near the dune's foot and show clearly that the assumption of saturation breaks down from ref. [17].

the different physical processes. The entire model can be thought of as four (almost) independent parts: the stationary wind field over a complex terrain, the stationary aeolian sand transport, the time evolution of the surface due to erosion, and avalanches.

A. The wind shear stress

The fully turbulent atmospheric boundary layer develops over a flat surface the logarithmic velocity profile $v(z)$ of eq. 7 [18]. A perturbation of the ground $h(x)$ such as a dune or hill gives rise to a non-local perturbation $\hat{\tau}(x)$ of the undisturbed air shear stress τ_0 ,

$$\tau(x) = \tau_0 [1 + \hat{\tau}(x)]. \quad (10)$$

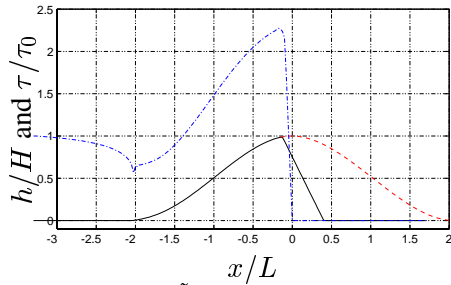


Fig. 7. The envelope $\tilde{h}(x)$ of the windward profile of a dune $h(x)$ (solid line) and the separating streamline $s(x)$ (dashed line) form together a smooth object which is used to calculate the air shear stress $\tau(x)$ (dash-dotted line) on the windward side. In the region of recirculation the air shear stress τ is set to zero.

The functional dependence of the air shear stress perturbation is crucial for the understanding of the stability of dunes and to predict the sand flux onto the windward side of a dune. Analytical calculations of the flow over a gentle hill yield an analytical expression for the shear stress perturbation $\hat{\tau}(x)$ [?], [20], [21]. We performed further simplifications in order to obtain a minimal expression that captures the crucial features (and only those) and is applicable for sand dunes [22]. The resulting formula for the air shear stress perturbation $\hat{\tau}$ is,

$$\hat{\tau}(x) = A \left(\frac{1}{\pi} \int_{-\infty}^{\infty} \frac{h'}{x - \xi} d\xi + Bh' \right), \quad (11)$$

where h' denotes the spatial derivative of the dune's profile $h(x)$ in wind direction. The coefficients $A(L/z_0)$ and $B(L/z_0)$ depend only logarithmically on the ratio between the characteristic length L of the dune and the roughness length z_0 of the surface. For a dune with a length and width ratio $W/L \approx 1$ and $L/z_0 = 4.0 \cdot 10^5$ we obtain $A \approx 3.2$ and $B \approx 0.3$ from Ref. [14], [22]. Equation (11) has several features that are important for dune formation. First, the air shear stress is completely scale invariant and leads to the same speed-up for small and large dunes. This is expected in the fully turbulent regime where no characteristic length exists. Secondly, the shear stress perturbation $\hat{\tau}(x)$, Equation (11), scales with the height H and inversely with the characteristic length L of the dune and thus with the average slope of the dune's windward side, $\hat{\tau} \propto H/L$. Thirdly, a depression of $\tau(x)$ in front of the hill occurs as a consequence of the strongly non-local contribution in Equation (11). Finally, the shear stress perturbation $\hat{\tau}(x)$ for the windward side of the dune is calculated using Eq. (11), the profile $h(x)$ on the windward side, and the separating streamline $s(x)$ on the lee side. The result is shown in

Fig. 5 together with the measured mean values (averages over 10 minutes intervals) normalized according to Eq. 9. The agreement between model results and measurements is good. From this, we can conclude that the heuristic model of the separation bubble combined with the analytic expression, Eq. (11), provide a reasonable approximation for the wind field above the dune. This strategy enormously reduces the computational effort, compared to the numerical solution of turbulence models and the averaged three dimensional Navier–Stokes equation.

Equation (11) is based on a perturbation theory and can only be applied to smooth hills. Jackson and Hunt [20] assumed $H/L < 0.05$, whereas Carruthers et al. [23] showed that mean slopes up to $H/L \approx 0.3$ give reasonable results. The windward side of a barchan dune is always below the latter value and the formula should be applicable. However, flow separation occurs at the brink, which is out of the scope of the linear perturbation theory. A heuristic solution to solve this problem has been suggested by Zeman and Jensen [24]. They introduced a separation bubble that comprises the recirculating flow (the large eddy in the wake of the dune), which reaches from the brink (the point of detachment) to the bottom (to the point of reattachment) see fig III-A. We model the separating streamline by a third order polynomial that is a smooth continuation of the profile $h(x)$ at the brink x_{brink} and at the reattachment point $x_{brink} + L_r$, i.e. $h(x_{brink}) = s(0)$, $h'(x_{brink}) = s'(0)$, $s(L_r) = 0$, $s'(L_r) = 0$, where $L_r \approx 6H$ is the downwind distance of the reattachment point from the brink. The shear stress perturbation $\hat{\tau}(x)$ for the windward side of the dune is finally calculated using equation (10), the profile $h(x)$ on the windward side, and the separating streamline $s(x)$ on the lee side. An example is depicted in fig. III-A.

B. The Sand flux

Sand transport has been studied already by Bagnold [25] and it was also him who proposed the first phenomenological law that predicted the sand transport from the shear stress of the air. Improved laws have been proposed by several authors in the meantime [26], [7], [27]. However, all these relations assume that the sand flux q is in equilibrium and can be written as a function of the shear stress τ , $q(\tau(x))$. Temporal or spatial transients are completely neglected. In the following we will call such a relation *saturated*, because it predicts the amount of sand that can be maintained in the saltation layer at a

certain air shear stress τ .

This condition is hardly fulfilled at the windward foot of an isolated dune [21], e.g. a barchan, where the bed changes rapidly from bedrock or vegetation to sand. Besides the particular conditions at the dune’s foot, the sand flux may never reach saturation [28] on the entire windward side, where the shear velocity increases gradually from the foot to the crest. Wind tunnel measurements indicate that the typical time to reach saturation in saltation is approximately two seconds [29], which corresponds to a saturation length of the order of 10 m. This length is of the order of the dune size and can not be neglected if the sand flux on the entire windward side is significant. Furthermore, it has been observed that the time to reach saturation increases for shear velocities close to the threshold [29]. In this situation, the sand flux may never reach saturation on the entire windward side and should increase exponentially with distance from the dune’s foot [28]. In recent years, several models to calculate the wind field have been developed, from analytic boundary layer approximations to numerical solutions of the Navier–Stokes equation with an enormous computational effort. Although some previous studies have discussed the limits of the saturation approximation in detail [21], much less effort has been dedicated to the development of sand flux relations that effectively incorporate non–saturation effects [30].

For the saturated flux many different functional forms of these sand transport laws exist and have been used in the past. For high shear stresses, however, they all converge to the simple relation proposed by [1],

$$q_s \propto \tau^{3/2}. \quad (12)$$

All other more elaborate relations add higher order corrections to the Bagnold formula that become important close to the air shear stress threshold. To overcome the limitation of saturation and to obtain information about the dynamics of the saltation process, numerical simulations on the grain scale have been performed in the last years [31], [32], [33]. Still, concerning the modeling of dune formation, both approaches had to be discarded. The microscopic models are computationally too expensive and the equilibrium assumption that is inherent in the simple flux relations does not hold on the entire windward side of a dune [11], [12], [14], [21], [34]. Since both known approaches cannot be used to model dune formation we developed a new phenomenological continuum saltation model that is computationally very efficient on the one side and on the other side incorporates the dy-

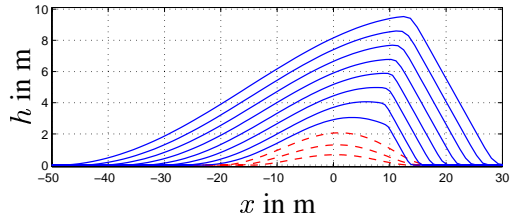


Fig. 8. The solutions for large volumes — above a critical height — are dunes including a slip face, whereas for small volumes heaps develop. An important fact is that the steepest lee side of a heap (dashed lines) is approximately 15° , which is well below the angle of repose of 34° .

namics of the saltation layer and thus allows for saturation transients [34]. In this model the sand flux is defined by a differential equation of the form

$$\frac{\partial}{\partial x} q = \frac{1}{l_s} q \left(1 - \frac{q}{q_s} \right), \quad (13)$$

where $q_s(\tau)$ is the saturated sand flux and $l_s(\tau)$ the characteristic length of the saturation transients, called saturation length. The saturation length $l_s(\tau)$ depends on the air shear stress, but converges towards a constant value for $\tau \gg \tau_t$ [34]. A comparison between the saturated sand flux, our model, Equation (13), and the field measurements from Jericoacuara can be seen in Figure 6. One observes that Equation (13) gives the right behaviour at the foot of the Barchan while the neglect of the transient gives an unphysical dip.

C. The surface evolution

A spatial change in sand flux implies that erosion or deposition takes place and the surface changes in height. The time evolution of the surface can be calculated from the conservation of mass,

$$\frac{\partial h}{\partial t} = \frac{1}{\rho_{\text{sand}}} \frac{\partial q}{\partial x}, \quad (14)$$

where ρ_{sand} is the bulk density of dune sand. Finally, we note that Equation (14) is the only remaining time dependent equation and thus defines the time scale of the model.

The full dune model can be sketched as follows. An initial surface h is used to start the time evolution. If flow separation has to be modeled the separating streamline $s(x)$ is calculated. Next, the air shear stress $\tau(x)$ onto the given surface h (or h and s) is calculated using Equation (10). From the air shear stress $\tau(x)$ the sand flux can be determined using Equation (13). Then, the integration forward in time of the surface is

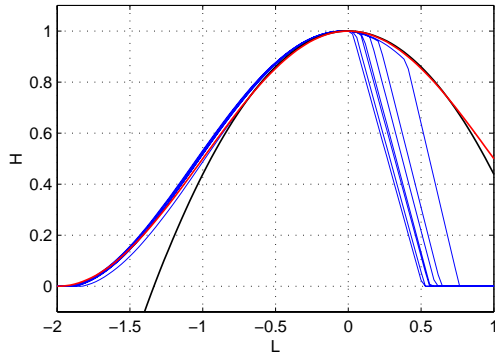


Fig. 9. Profiles along the symmetry plane of 3d Barchans of different size normalized on a single height as obtained from the model (from [35]).

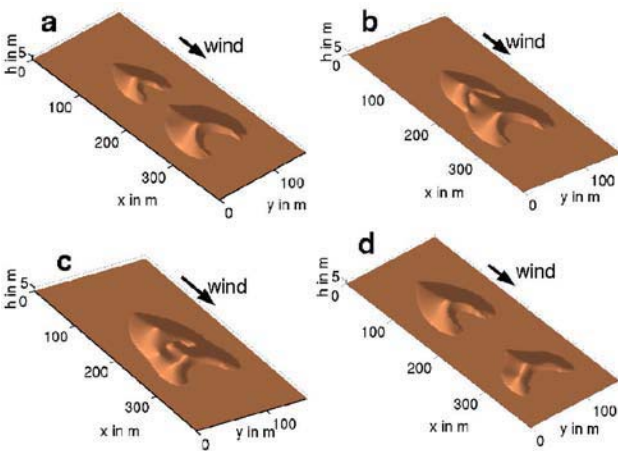


Fig. 10. Four snapshots of the solitary wave behavior of two Barchan dunes placed behind each other. The parameters are $h_2 = 7.5\text{m}$ and $\delta h/h_2 = 0.9$. **a** the two Barchans reached their steady form. In **b**, 0.48 years after **a**, the smaller Barchan bumps into the larger. **c** shows the hybrid state 0.63 years after **a**. In **d** the two dunes left the hybrid state (1.42 years after **a**) from [36].

calculated from the mass conservation, Equation (14). Finally, sand is eroded and transported downhill if the local angle $\partial_x h$ exceeds the angle of repose. This redistribution of mass (avalanches) is performed until the surface slope has relaxed below the critical angle. The time integration is calculated until the final shape-invariantly moving solution is obtained.

IV. THE SHAPE OF THE DUNE AND OUTLOOK

In order to analyze the properties of the shape-invariantly moving solution of our model, we performed a series of calculations varying the volumes of the Gaussian hills that have been used as initial configuration. The final shape invariantly moving solutions are displayed in Fig. 8. For small volumes we

obtained heaps without a slip face, whereas for large volumes dunes with a slip face developed. Hence, there is a minimal height for dune formation or, more precisely, a minimal height for the formation of a slip face. Empirically, this was observed many times in nature.

The simulation also showed that the Barchan shape is a steady state solution. Starting from different initial configurations having the same volume, one always obtains after a certain transient the same crescent shape dune. This dune moves with constant velocity inversely proportional to its height and quantitatively agrees with the ones measured in the field for corresponding volume.

Simulating 3d Barchans by starting from an initial Gaussian heap can be done under essentially two boundary conditions: an absorbing bedrock [$q = 0$] for coastal dunes or a finite influx and $q \neq 0$ on the bedrock for desert dune fields. In Fig. 9 we see longitudinal profiles along the symmetry plane of desert Barchans for different initial volumes of dunes, normalized such that their heights fall on top of each other. One observes that the measured profiles from Fig. 2 agree very well with this prediction. The numerical study of Fig. 9 also shows that the tail on the windward side is not parabolic but rather logarithmic.

One can also using our programme construct virtual dunes and produce virtual desert landscapes. One example is shown in Fig. 10 where one sees four images of the time evolution of two dunes. The one in front was a little larger than the one behind and therefore also slower. When the two dunes approach each other, their relative velocity decreases and becomes zero shortly before they touch. The larger dune in front starts to loose sand to the dune behind until the dune behind is the larger one and the dune in front, being now the smaller one, can leave the scene since it is now faster. Eventually the two dunes will have the same size and shape before and after the collision and only that their role has been inverted. Therefore they have survived the collision without change and effectively crossed each other. One says they behaved like solitons. If the dune behind is even smaller, it will be swallowed by the larger one, but it might eventually eject baby Barchans at the horns. This phenomena we call breeding. If the dune behind is even smaller, it will completely be swallowed by the dune in front which we call coalescence. A morphological diagram for the three cases was obtained in ref. [36].

Starting from measured topographies one can predict the future evolution and therefore planify in ad-

vance to protect cities and fields against moving sand masses in the Sahara. Another perspective of the use of our equations of motion is the possibility to study techniques used to stop or destroy dunes, like Bofix, as introduced by Meunier in Nouakchott. Here low fences are placed strategically on the dune in order to deviate the wind in such a way that digs through eddies and currents virtually channels in the sand effectively splitting the dune in pieces.

V. ACKNOWLEDGEMENT

We want to thank our collaborators P. Rognon, J.S. de Andrade, A. Poliakov, L.P. Maia, K. Kroy and V. Schwämmle.

REFERENCES

- [1] Bagnold R. A. *The physics of blown sand and desert dunes*. Methuen, London, 1941.
- [2] Pye K. and Tsoar H. *Aeolian sand and sand dunes*. Unwin Hyman, London, 1990.
- [3] Lancaster N. *Geomorphology of desert dunes*. Routledge, London, 1995.
- [4] Finkel H. J. The Barchans of Southern Peru. *Journal of Geology* 67, 614–647 (1959)
- [5] Hastenrath S. The Barchans of the Arequipa Region, Southern Peru, (1967).
- [6] Hastenrath, S. The barchan dunes of Southern Peru revisited. *Zeitschrift für Geomorphologie* 31-2, 167–178 (1987)
- [7] Lettau, K., Lettau, H. Bulk transport of sand by the barchans of the Pampa de La Joya in Southern Peru. *Zeitschrift für Geomorphologie N.F.* 13-2, 182–195 (1969)
- [8] Slattery, M. C. Barchan migration on the Kuiseb river delta, Namibia. *South African Geographical Journal* 72, 5–10 (1990).
- [9] Oulehri, T. Etude géodynamique des migrations de sables éoliens dans la région de Laâyoune (Nord du Sahara marocain). Ph.D. thesis, l'Université Paris 6, Paris. no. 92-12 (1992)
- [10] Hesp, P. A., Hastings, K. Width, height and slope relationships and aerodynamic maintenance of barchans. *Geomorphology* 22, 193–204 (1998).
- [11] Wiggs, G. F. S., Livingstone, I., Warren, A. The role of streamline curvature in sand dune dynamics: evidence from field and wind tunnel measurements. *Geomorphology* 17, 29–46 (1996).
- [12] Wippermann, F. K., Gross, G. The wind-induced shaping and migration of an isolated dune: A numerical experiment. *Boundary Layer Meteorology* 36, 319–334 (1986).
- [13] Howard, A. D., Morton, J. B. Sand transport model of barchan dune equilibrium. *Sedimentology* 25, 307–338 (1978).
- [14] Sauer mann G., Rognon P., Poliakov A., Herrmann H.J. The shape of the barchan dunes of Southern Morocco. *Geomorphology* 36, 47–62 (2001).
- [15] Coursin, A. Observations et expériences faites en avril et mai 1956 sur les barchans du Souehel el Abiodh (région est de Port-Étienne). *Bulletin de l' I. F. A. N.* 22A, no. 3, 989–1022 (1964).
- [16] Sarnthein, M., Walger, E. Der äolische Sandstrom aus der W-Sahara zur Atlantikküste. *Geologische Rundschau* 63, 1065–1087 (1974).
- [17] Sauer mann, G., Andrade Jr., J.S., Maia, L.P., Costa, U.M.S., Araújo, A.D., Herrmann, H.J. Wind Velocity and Sand Transport on a Barchan Dune (2001).
- [18] Landau and Lifshitz. *Fluid Mechanics*, volume 6 of *Course of Theoretical Physics*. Pergamon Press, London, 1963.
- [19] Hunt, J.C.R., Leibovich S., Richards K.J. Turbulent wind flow over smooth hills. *Q.J.R. Meteorol. Soc.* 114, 1435–1470 (1988).
- [20] Jackson, P.S., Hunt J.C.R. Turbulent wind flow over a low hill. *Q.J.R. Meteorol. Soc.* 101, 929 (1975)
- [21] Weng, W.S., Hunt J.C.R., Carruthers, D.J., Warren A., Wiggs, G.F.S., Livingstone, I., Castro, I. An experimental study of Froud number effect on wind-tunnel saltation. *Acta Mechanica Suppl.* 1, 145-157 (1991).
- [22] Kroy K., Sauer mann G., Herrmann H.J. A minimal model for sand dunes, *Phys. Rev. Lett.*, 88:054301, 2002. Preprint cond-mat/0203040.
- [23] Carruthers, D.J., Hunt J.C.R. Atmospheric Processes over Complex Terrain. Vol. 23, Chapter Fluid Mechanics of Airflow over Hills: Turbulence, Fluxes, and Waves in the Boundary Layer. *Am. Meteorological Soc.*
- [24] Zeman, O., Jensen N.O. Progress report on modeling permanent form sand dunes. *Risø National Laboratory M-2738* (1988).
- [25] Bagnold R.A. The movement of desert sand. *Proc. R. Soc. London, Ser. A*, 157:594–620, 1936.
- [26] Owen P.R. Saltation of uniformed sand grains in air. *J. Fluid. Mech.*, 20:225–242, 1964.
- [27] Sørensen M. An analytic model of wind-blown sand transport. *Acta Mechanica (Suppl.)* 1, 67-81 (1991).
- [28] Lancaster, N., Nickling W.G., McKenna Neumann C.K., Wyatt V.E. Sediment flux and airflow on the stoss slope of a barchan dune. *Geomorphology* 17, 55-62 (1996).
- [29] Butterfield, G.R. Sand transport response to fluctuating wind velocity. In N.J. Clifford, J.R. French, and J. Hardisty (eds.) *Turbulence: Perspectives on Flow and Sediment Transport*, Chapter 13, 305-335, John Wiley & Sons Ltd. (1993).
- [30] van Dijk, P.M., Arens, S.M., van Boxel J.H. Aeolian processes across transverse dunes ii: Modelling the sediment transport and profile development. *Earth Surf. Process. Landforms* 24, 319-333 (1999).
- [31] Robert S. Anderson and Peter K. Haff. Simulation of eolian saltation. *Science*, 241:820, 1988.
- [32] R. S. Anderson. Wind modification and bed response during saltation of sand in air. *Acta Mechanica (Suppl.)*, 1:21–51, 1991.
- [33] I. K. McEwan and B. B. Willetts. Numerical model of the saltation cloud. *Acta Mechanica (Suppl.)*, 1:53–66, 1991.
- [34] Gerd Sauer mann, Klaus Kroy, and Hans J. Herrmann. A phenomenological dynamic saltation model for dune formation. *Phys.Rev.E*, 64:31305, 2001.
- [35] Gerd Sauer mann. Modeling of wind blown sand and desert dunes. Universität Stuttgart, 2001. PhD Thesis.
- [36] V. Schwämmle and H. J. Herrmann. *Nature*, 426:619–620, 2003.

SYNCHRONIZATION ANALYSIS OF COUPLED NONCOHERENT OSCILLATORS

J. Kurths, M.C. Romano, M. Thiel

Institute of Physics, Universität Potsdam,
14469 Potsdam, Germany
e-mail: juergen@agnld.uni-potsdam.de

G.V. Osipov, M.V. Ivanchenko

Department of Radiophysics,
Nizhny Novgorod University, 23, Gagarin Avenue,
603950 Nizhny Novgorod, Russia

Abstract—We present two different approaches to detect and quantify phase synchronization in the case of coupled non-phase coherent oscillators. The first one is based on the general idea of the curvature of an arbitrary curve. The second one is based on recurrences of the trajectory in phase space. We illustrate both methods in the paradigmatic example of the Rössler system in the funnel regime. We show that the second method is applicable even in the case of noisy data.

I. INTRODUCTION

Phase synchronization has been studied extensively during the last years [1], as this phenomenon has found numerous applications in natural [2] and engineering systems [3]. Two systems are said to be phase synchronized when their respective frequencies and phases are locked. Till now chaotic phase synchronization (CPS) has been mainly observed for chaotic attractors with rather coherent phase dynamics. These attractors have a relatively simple topology of oscillations and a well-pronounced peak in the power spectrum, which allows to introduce the phase and the characteristic frequency of motions. However, some difficulties appear dealing with non-coherent attractors with a rather broad band power spectra. Then it might not be straightforward to define a phase of the oscillations, and in general no single characteristic time scale exists. In contrast to phase coherent attractors, it is quite unclear whether some phase synchronized state can be achieved.

To treat this problem, we propose in this paper two different approaches: i) we present a method that defines the phase more generally and allows to study CPS in systems of coupled chaotic oscillators with

even strongly noncoherent phase properties and ii) we propose a method based on recurrences in phase space, that allows to quantify indirectly CPS, which even works in the case of noisy noncoherent oscillators.

We demonstrate the applicability of both methods for the paradigmatic system of two coupled nonidentical Rössler oscillators:

$$\begin{aligned} \dot{x}_{1,2} &= -\omega_{1,2}y_{1,2} - z_{1,2}, \\ \dot{y}_{1,2} &= \omega_{1,2}x_{1,2} + ay_{1,2} + \mu(y_{2,1} - y_{1,2}), \\ \dot{z}_{1,2} &= 0.1 + z_{1,2}(x_{1,2} - 8.5), \end{aligned} \quad (1)$$

where μ is the coupling strength. $\omega_{1,2}$ determine the mean frequency of the oscillators in the case of phase coherent attractors. In our simulations we take $\omega_1 = 0.98$ and $\omega_2 = 1.02$. The parameter $a \in [0.15 : 0.3]$ governs the topology of the chaotic attractor. When a is below a critical value a_c ($a_c \approx 0.186$ for $\omega_1 = 0.98$ and $a_c \approx 0.195$ for $\omega_2 = 1.02$), the chaotic trajectories always cycle around the unstable fixed point $(x_0, y_0) \approx (0, 0)$ in the (x, y) subspace, i.e., $\max(y) > y_0$ (Fig. 1a). In this case, the rotation angle

$$\phi = \arctan \frac{y}{x} \quad (2)$$

can be defined as the phase, which increases almost uniformly, i.e., the oscillator has a coherent phase dynamics. Beyond the critical value a_c , the trajectories no longer always completely cycle around (x_0, y_0) , and some $\max(y) < y_0$ occur, which are associated with faster returns of the orbits; the attractor becomes a funnel one. Such earlier returns in the funnel attractor happen more frequently with increasing a (Fig. 1b). It is clear that for the funnel attractors, usual (and rather simple) definitions of phase, such as Eq. (2) [1], are no longer applicable.

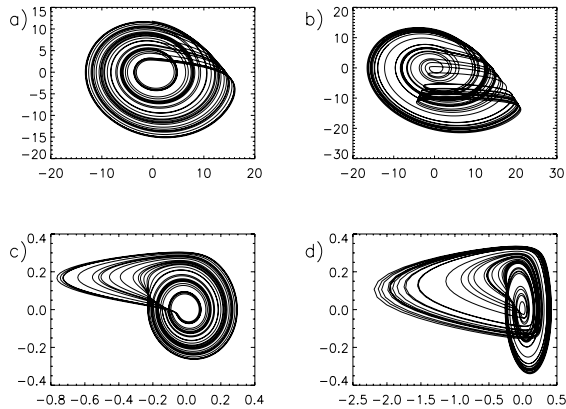


Fig. 1. Upper panel (a),(b): projections of the attractors of the Rössler systems (1) onto the plane (x, y) ; lower panel (c),(d): projections onto (\dot{x}, \dot{y}) . The parameters are $\omega = 1.02$ and $a = 0.16$ (a),(c), resp. $a = 0.2925$ (b),(d).

II. PHASE CALCULATION BASING ON CURVATURE

In order to overcome the problem of the definition of the phase in the case of noncoherent oscillators, we firstly propose another approach which is based on the general idea of the curvature of an arbitrary curve [4]. For any two-dimensional curve $\vec{r}_1 = (u, v)$ the angle velocity at each point is $\nu = \frac{ds}{dt}/R$, where $ds/dt = \sqrt{\dot{u}^2 + \dot{v}^2}$ is the speed along the curve and $R = (\dot{u}^2 + \dot{v}^2)^{3/2}/[\dot{v}\ddot{u} - \dot{u}\ddot{v}]$ is the radius of the curvature. If $R > 0$ at each point, then $\nu = \frac{d\phi}{dt} = \frac{\dot{v}\ddot{u} - \dot{u}\ddot{v}}{\dot{u}^2 + \dot{v}^2}$ is always positive and therefore the variable ϕ defined as $\phi = \int \nu dt = \arctan \frac{\dot{v}}{\dot{u}}$, is a monotonically growing angle function of time and can be considered as a phase of the oscillations. Geometrically it means that the projection $\vec{r}_2 = (\dot{u}, \dot{v})$ is a curve cycling monotonically around a certain point.

These definitions of ϕ and ν hold in general for any dynamical system if the projection of the phase trajectory on some plane is a curve with a positive curvature. We find that it is applicable to a large variety of chaotic oscillators, such as Lorenz system [5], Chua circuit [6] or the model of an ideal four-level laser with periodic pump modulation [7].

This is clear for phase-coherent as well as funnel attractors in the Rössler oscillator. Here projections of chaotic trajectories on the plane (\dot{x}, \dot{y}) always rotate around the origin (Fig. 1, c, d) and the phase can be defined as

$$\phi = \arctan \frac{\dot{y}}{\dot{x}}. \quad (3)$$

We have to note that for the funnel chaotic attractors the coupling may change their topology. As a conse-

quence the strong cyclic structure of orbits projection in the (\dot{x}, \dot{y}) -plane may be destroyed and the phase measurement Eq. (3) fails occasionally for intermediate values of coupling. But for small coupling and for coupling near the transition to CPS, the phase is well-defined by Eq. (3) [8].

We use two criteria to detect the existence of CPS: locking of the mean frequencies $\Omega_1 = \langle \nu_1 \rangle = \Omega_2 = \langle \nu_2 \rangle$, and locking of the phase $|\phi_2(t) - \phi_1(t)| \leq const$ (we consider here only 1:1 synchronization). Applying the new definition of the phase Eq. (3) to the system of Eq. (1) for $a = 0.2925$ (strongly noncoherent) and $\mu = 0.179$, we obtain the phase difference represented in Fig. 2. We find two large plateaus in the

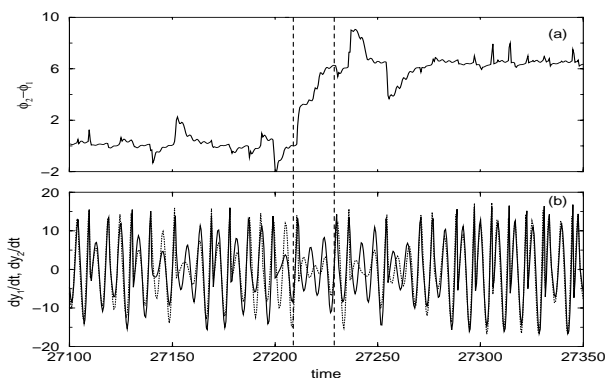


Fig. 2. (a) Time evolution of phase difference of the system of Eq. (1). (b) Variables $y_{1,2}$ in system (1) for $a = 0.2925$ and $\mu = 0.179$. Solid and dotted lines correspond to the first and the second oscillator, respectively. In the time interval between dashed lines the first oscillator produces 4 rotations in the (\dot{x}_1, \dot{y}_1) -plane around the origin, but the second one generates only 3 rotations, which leads to a phase slip in (a).

evolution of the difference of the phases with time, i.e. we detect CPS, but we also find a phase slip associated to a different number of oscillations in the two oscillators in the represented period of time. This means, we observe the seldom occurrence of phase slips. It is interesting to note that in this system CPS occurs after one of the positive Lyapunov exponents passes to negative values, i.e. it is also a transition to generalized chaotic synchronization (GCS).

Although this approach works well in noncoherent model systems, we have to consider that one is often confronted with the computation of the phase in experimental time series, which are usually corrupted by noise. In this case, some difficulties may appear in computing the phase by Eq. (3), because derivatives are involved in its definition. We will address this problem in the next section.

III. PHASE SYNCHRONIZATION BY MEANS OF RECURRENCES

Here, we propose a rather different approach based on recurrences in phase space to detect and quantify CPS. The concept of recurrence in dynamical systems goes back to Poincaré [9], when he proved that after a sufficiently long time interval, the trajectory of a chaotic system will return arbitrarily close to each former point of its route.

We define a recurrence of the trajectory of a dynamical system $\{\vec{x}_i\}_{i=1}^N$ in the following way: we say that the trajectory has returned at $t = j\delta t$ to the former state at $t = i\delta t$ if

$$R_{i,j}^{(\varepsilon)} = \Theta(\varepsilon - \|\vec{x}_i - \vec{x}_j\|) = 1, \quad (4)$$

where ε is a pre-defined threshold, $\Theta(\cdot)$ is the Heaviside function and δt is the sampling rate [10]. Based on this definition of recurrence, it is straightforward to estimate the probability $P^{(\varepsilon)}(\tau)$ that the system returns to the neighborhood of a former point \vec{x}_i of the trajectory (the neighborhood is defined as a box of size ε centered at \vec{x}_i , as we use the maximum norm) after τ time steps

$$\begin{aligned} \hat{P}^{(\varepsilon)}(\tau) &= \frac{1}{N-\tau} \sum_{i=1}^{N-\tau} \Theta(\varepsilon - \|\vec{x}_i - \vec{x}_{i+\tau}\|) \\ &= \frac{1}{N-\tau} \sum_{i=1}^{N-\tau} R_{i,i+\tau}^{(\varepsilon)}. \end{aligned} \quad (5)$$

This function can be considered as a generalized autocorrelation function, as it also describes higher order correlations between the points of the trajectory in dependence on the time delay τ . A further advantage with respect to the linear autocorrelation function is that $\hat{P}^{(\varepsilon)}(\tau)$ is determined for a trajectory in phase space and not only for a single observable of the system's trajectory. Further, we have recently shown that it is possible to reconstruct the attractor by only considering the recurrences of single components of the system [11]. Because of this, it is also possible to estimate dynamical invariants of the system (e.g. entropies and dimensions) by means of recurrences in phase space even without embedding [12], i.e. the recurrences of the system in phase space contain information about higher order dependencies within the components of the system. This method has been successfully applied to experimental flow [12] and geophysical data [13].

For a periodic system in a 2-dimensional phase space,

it can be easily shown that

$$P(\tau) = \lim_{\varepsilon \rightarrow 0} \hat{P}^{(\varepsilon)}(\tau) = \begin{cases} 1 & : \tau = T \\ 0 & : \text{otherwise} \end{cases}$$

For coherent chaotic oscillators, such as Eq. 1 for $a = 0.16$, $\hat{P}^{(\varepsilon)}(\tau)$ has local maxima at multiples of the mean period, but the probability of recurrence after one or more rotations around the fixed point is less than one.

Analyzing the probability of recurrence, it is possible to detect CPS for noncoherent oscillators. This approach is based on the following idea: Originally, a phase ϕ is assigned to a periodic trajectory \vec{x} in phase space, by projecting the trajectory onto a plane and choosing an origin, around which the whole trajectory oscillates. Then an increment of 2π is assigned to ϕ , when the point of the trajectory has returned to its starting position, i.e. when $\vec{y}(t+T) - \vec{y}(t) = \vec{0}$. Analogously to the case of a periodic system, we can refer an increment of 2π to ϕ to a complex non-periodic trajectory $\vec{x}(t)$, when $|\vec{x}(t+T) - \vec{x}(t)| \sim 0$, or equivalently when $|\vec{x}(t+T) - \vec{x}(t)| < \varepsilon$, where ε is a pre-defined threshold. That means, a recurrence $R_{t,t+\tau}^{(\varepsilon)} = 1$ can be interpreted as an increment of 2π of the phase in the time interval τ .

$\hat{P}^{(\varepsilon)}(\tau)$ can be viewed as a statistical measure on how often ϕ in the original phase space has increased by 2π or multiples of 2π within the time interval τ . If two systems are in PS, in the mean, the phases of both systems increase by $k \cdot 2\pi$, with k a natural number, within the same time interval τ . Hence, looking at the coincidence of the positions of the maxima of $\hat{P}^{(\varepsilon)}(\tau)$ for both systems, we can quantitatively identify PS (from now on, we omit (ε) and $\hat{\cdot}$ in $\hat{P}^{(\varepsilon)}(\tau)$ to simplify the notation). The proposed algorithm consists of two steps:

- Compute $P_{1,2}(\tau)$ of both systems based on Eq. (5).
- Compute the cross-correlation coefficient between $P_1(\tau)$ and $P_2(\tau)$

$$CX^{1,2} = \frac{\langle \bar{P}_1(\tau) \bar{P}_2(\tau) \rangle}{\sigma_1 \sigma_2}, \quad (6)$$

where $\bar{P}_{1,2}$ means that the mean value has been subtracted and σ_1 and σ_2 are the standard deviations of $P_1(\tau)$ resp. $P_2(\tau)$.

If both systems are in PS, the probability of recurrence is maximal at the same time and $CX^{1,2} \sim 1$. In contrast, if the systems are not in PS, the maxima of the probability of recurrence do not occur simultaneously. Then we observe a drift (Fig. 3b) and expect low values of $CX^{1,2}$.

Now we exemplify this algorithm for two topologically different regimes of the Rössler system (Eq. 1): the phase coherent ($a = 0.16$) and the noncoherent one, namely the funnel attractor ($a = 0.2925$). First, we consider the phase coherent regime, where for $\mu = 0.05$ both systems are in PS [14]. If we compute $P(\tau)$ for both systems in PS, we observe that the local maxima occur at $\tau = n \cdot T$, where T is the mean period of both Rössler systems (Fig. 3a). The

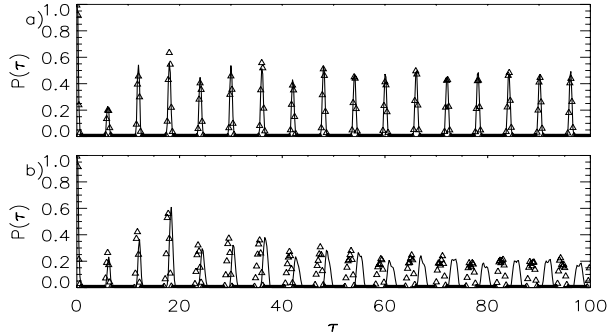


Fig. 3. $P(\tau)$ for the two mutually coupled coherent Rössler systems with $a = 0.16$ for coupling strength $\mu = 0.05$ (a) and for $\mu = 0.02$ (b). Solid line: system 1, triangles: system 2. .

heights of the local maxima are in general different for both systems if they are only in PS and not fully synchronized, but the positions of the local maxima of $P(\tau)$ are the same. Thus a recurrence to a former neighborhood after τ time steps does not occur with the same probability for the two systems, but the conditional probability that a recurrence in the second system occurs given that the first system has not returned yet, is almost 0. For $\mu = 0.02$ the systems are not in PS and the positions of the maxima of $P(\tau)$ do not coincide anymore (Fig. 3b), clearly indicating that the frequencies are not locked. In addition, we observe that the peaks of $P(\tau)$ become broader, as the phase coherence of the oscillators decreases when they are not in PS. We obtain $CX^{1,2} = 0.0139$ for the coupling strength $\mu = 0.02$ and $CX^{1,2} = 0.998$ for $\mu = 0.05$. Hence applying this criterion, we confirm that for $\mu = 0.05$ the oscillators are in PS and for $\mu = 0.02$ they are not in PS, in accordance with [14]. Now we regard the more complex case of two Rössler systems in the noncoherent funnel regime ($a = 0.2925$) with added observational noise. Our aim is to show, that also in more complicated cases, where also noise is present, the recurrence approach is able to detect CPS. We again consider two values of the coupling strength: $\mu = 0.05$, where the oscillators are

not in PS and $\mu = 0.2$, where the oscillators are in PS, according to [14]. We add 20% of independent noise to each component of both oscillators and perform the recurrence analysis (see Fig. 4). We observe that the structure of $P(\tau)$ in the funnel regime (Fig. 4a and b) is rather different from the one in the Rössler system with standard parameters (Fig. 3a and b). The peaks in $P(\tau)$ are not as well pronounced as in the coherent regime, reflecting the different time scales that come into play or the broad band power spectrum in the funnel system. However, we see that for $\mu = 0.2$ the locations of the local maxima coincide for both oscillators (Fig. 4a), whereas for $\mu = 0.05$ the positions of the local maxima do not coincide anymore (Fig. 4b). We

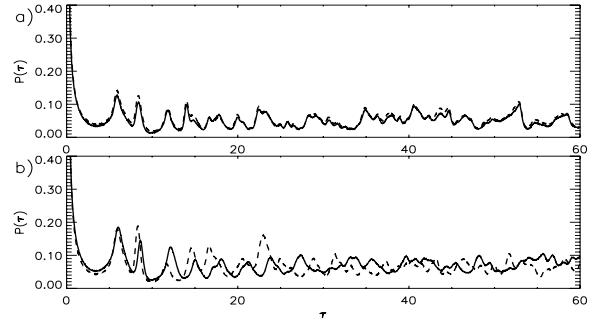


Fig. 4. $P(\tau)$ for the two mutually coupled Rössler systems with $a = 0.2925$ for coupling strength $\mu = 0.2$ (a) and for $\mu = 0.05$ (b). Solid line: system 1, dashed line: system 2. 20% of observational independent noise was added to each component of both noncoherent oscillators.

obtain $X^{1,2} = 0.9701$ for coupling strength $\mu = 0.2$ and $X^{1,2} = 0.2095$ for $\mu = 0.05$, confirming that both oscillators are in PS in the first case but are not in the second one [14].

Next, we show that our algorithm is also valid for the detection of PS in chains of weakly coupled oscillators. This extension to N oscillators is straightforward: we compute $P_j(\tau)$ for each oscillator j (Eq. 5) and their respectively local maxima τ_j^i according to

$$\frac{dP_j(\tau^i)}{d\tau^i} \simeq 0.$$

Then we choose the set of times of local maxima τ_r^i of an arbitrary oscillator r as reference and compute $\Delta\tau_j^i = \tau_j^i - \tau_r^i$ for each oscillator j . Now even clusters of oscillators in PS are easily recognized, as the mean slope of $\Delta\tau_j^i$ versus i is equal for all oscillators j belonging to the same cluster.

We apply this algorithm to a chain of coupled non-

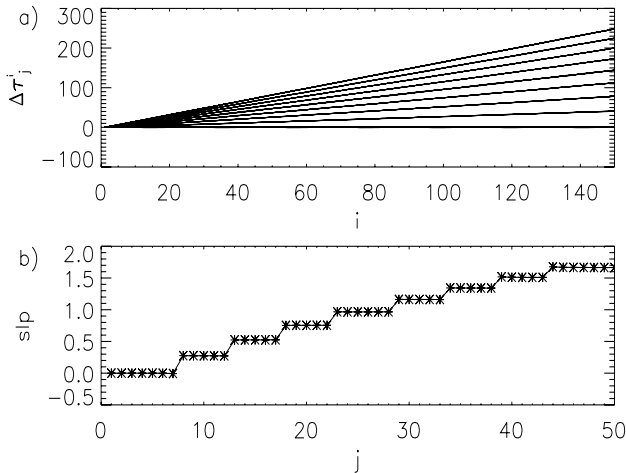


Fig. 5. a) Difference between the local maxima of the probability of recurrence for a chain of 50 Rössler oscillators diffusively coupled for $\mu = 0.18$ and $\delta = 9 \times 10^{-3}$. b) Slope of $\Delta\tau_j^i$ versus i for $j = 1, \dots, 50$ with $\mu = 0.18$ and $\delta = 9 \times 10^{-3}$

identical Rössler oscillators with a nearest-neighbor diffusive coupling

$$\begin{aligned} \dot{x}_j &= -\omega_j y_j - z_j, \\ \dot{y}_j &= \omega_j x_j + a y_j + \mu(y_{j+1} - 2y_j + y_{j-1}), \\ \dot{z}_j &= 0.4 + z_j(x_j - 8.5), \end{aligned} \quad (7)$$

where the index $j = 1, \dots, N$ denotes the position of an oscillator in the chain, μ is the coupling coefficient and ω_j corresponds to the natural frequency of each individual oscillator [15]. We consider a linear distribution of natural frequencies $\omega_j = \omega_1 + \delta(j - 1)$, where δ is the frequency mismatch between neighboring systems. For the coupling strength $\mu = 0.18$ and $\delta = 9 \times 10^{-3}$ we compute $P_j(\tau)$ for $j = 1, \dots, 50$ and the positions of the local maxima τ_j^i for each oscillator. We choose the oscillator $j = 1$ as reference and compute $\Delta\tau_j^i$ for $j = 1, \dots, 50$ (Fig. 5a). Furthermore, we represent the slope of $\Delta\tau_j^i$ versus i given by a linear regression for $j = 1, \dots, 50$ in Fig. 5b. We detect 9 clusters of oscillators in PS, in accordance with [15]. We have also analyzed this chain of Rössler oscillators with other values of the coupling strength and we obtain the same results as in [15]. Also the computation of the matrix $CX^{i,j}$ of the cross-correlation coefficients between $(P_i(\tau), P_j(\tau))$ yields the same results as in [15].

IV. CONCLUSIONS

In this paper we have presented two different approaches to overcome the problem of defining the phase in the case of noncoherent oscillators. The first one is based on the general idea of curvature of an arbitrary curve, and yields a new definition of the phase, that is applicable to a broad class of oscillators, not only to coherent ones. The second approach that we have presented, is an indirect one. It does not compute the phase explicitly, but it detects CPS by means of the joint probability of recurrence in phase space. This method can be also applied to detect CPS in noncoherent oscillators and it is additionally very robust against noise and can be easily implemented. Further, it also allows the detection of clusters of phase synchronized oscillators in distributed systems.

REFERENCES

- [1] M. Rosenblum, A. Pikovsky, and J. Kurths, Phys. Rev. Lett. **76**, 1804 (1996); A. Pikovsky, M. Rosenblum, G. Osipov, and J. Kurths, Physica D **104**, 219 (1997); A. Pikovsky, M. Rosenblum, and J. Kurths, *Synchronization* (Cambridge Nonlinear Science Series 12, 2001); S. Boccaletti, J. Kurths, G.V. Osipov, D. Valladares, and C. Zhou, Phys. Rep. **366**, 1, (2002).
- [2] R.C.Elson *et al.*, Phys. Rev. Lett., **81**, 5692 (1998); P.Tass *et al.*, *ibid.* **81**, 3291 (1998); C.M.Ticos *et al.*, *ibid.* **85**, 2929 (2000); V.Makarenko and R.Llinas, Proc. Natl. Acad. Sci. USA, **95**, 15474 (1998); B.Blasius, A.Huppert, and L.Stone, Nature, **399**, 354 (1999); C.Schäfer *et al.*, Nature, **392**, 239 (1998).
- [3] D.J.DeShazer *et al.*, Phys. Rev. Lett., **87**, 044101 (2001); S.Boccaletti *et al.*, *ibid.* **89**, 194101 (2002); I.Kiss and J.Hudson, Phys. Rev. E, **64**, 046215 (2001).
- [4] G.Fisher, *Plane algebraic curves*, AMS, 2001.
- [5] C.Sparrow, *The Lorenz Equations: Bifurcations, Chaos, and Strange Attractors*, Springer-Verlag, Berlin, 1982.
- [6] R.N.Madan, *Chua circuit: A paradigm for chaos*, World Scientific, Singapore, 1993.
- [7] W.Lauterborn, T.Kurz, and M.Wiesenfeldt, *Coherent Optics. Fundamentals and Applications*, Springer-Verlag, Berlin, Heidelberg, New York, 1993.
- [8] J.Y.Chen *et al.*, Phys. Rev. E **64**, 016212 (2001).
- [9] H. Poincaré, Acta Math. **13**, 1 (1890).
- [10] J. -P. Eckmann, S. O. Kamphorst, and D. Ruelle, Europhys. Lett. **4**, 973 (1987).
- [11] M. Thiel, M.C. Romano, and J. Kurths, to appear in Phys. Lett. A, (2004).
- [12] M. Thiel, M.C. Romano, P. Read, and J. Kurths, Chaos **14** (2), 234-243 (2004).
- [13] N. Marwan, M.H. Trauth, M. Vuille, J. Kurths, Climate Dynamics 21(3-4), 317-326 (2003).
- [14] G. V. Osipov, B. Hu, C. Zhou, M. V. Ivanchenko, and J. Kurths, Phys. Rev. Lett. **91**, 024101 (2003).
- [15] G. V. Osipov, A. Pikovsky, M. Rosenblum, and J. Kurths, Phys. Rev. E **55**, 2353 (1997).

Network dynamics: tools and examples

R. Vilela Mendes

Universidade Técnica de Lisboa and Grupo de Física Matemática,
Complexo Interdisciplinar, Av. Gama Pinto 2, 1649-003 Lisboa, Portugal

Abstract—*Some mathematical tools and results are presented which may be used to study the dynamics of agents living on a network as well as the networks themselves as evolving dynamical systems. They include decomposition of differential dynamics, ergodic techniques, estimates of invariant measures, etc. Some examples are discussed as an application of the dynamical tools.*

I. INTRODUCTION

The network concept appears quite often in the description of extended dynamical systems. The metabolic processes of living beings are a network with the substrates as nodes, linked together whenever they participate in the same biochemical reaction. Protein-protein as well as gene expression and regulation are also networks. Social, economic and political networks are the backbone of human society, the internet is a network, etc.[1] [2]. Most studies deal with networks as statistical objects, with extensive use of the tools of statistical mechanics [3]. Much less attention has been paid to the dynamical phenomena taking place in the networks or to the behavior of the evolving networks as dynamical systems.

The main purpose of this paper is to describe some tools for the treatment of networks (both regular and irregular) as dynamical systems. Results from differential dynamics and ergodic theory will be presented. For other useful tools, namely, conditions for multistability, computational mechanics and logical approaches, refer to [4].

II. DIFFERENTIAL DYNAMICS TOOLS

A. Describing dynamics by global functions

The node dynamics in many networks may be modelled by ordinary differential equations of the form

$$\frac{dx_i}{dt} = X_i(x) = \alpha_i + \sum_{j \neq i} W_{ij} f(x_j) - \gamma_i x_i \quad (1)$$

For a neural network, the x_i 's might be firing rates and the W_{ij} 's synaptic intensities [5], for a genetic regulatory system [6] [7] the variables x_i would code for the concentrations of RNA, proteins or other metabolic components and W_{ij} for the production constants (measuring the strength of j on i), $f(\cdot)$ being the regulation function and $-\gamma_i x_i$ a degradation term, etc.

A.1 Symmetric systems

Eq.(1) is a particular case of the Cohen-Grossberg form [8], used by these authors to describe continuous-time neu-

ral networks,

$$\frac{dx_i}{dt} = a_i(x_i) \left\{ b_i(x_i) - \sum_{j=1}^n W_{ij} f_j(x_j) \right\} \quad (2)$$

Cohen and Grossberg proved that, for the symmetric case ($W_{ij} = W_{ji}$), the following function

$$V(x_i) = - \sum_{i=1}^n \int^{x_i} b_i(\xi_i) f'_i(\xi_i) d\xi_i + \frac{1}{2} \sum_{j,k=1}^n W_{jk} f_j(x_j) f_k(x_k) \quad (3)$$

is a Lyapunov function, that is

$$\frac{d}{dt} V(x_i) \leq 0 \quad (4)$$

along the orbits if $a_i(x_i) f'_i(x_i) > 0$. Hopfield's[9] "energy" function is a particular case of this result.

The existence of a Lyapunov function is a useful device to characterize the asymptotically stable states of the network or for the synthesis of networks with a desired number of stable asymptotic solutions[10].

In the case of symmetric connections the continuous-time result of Cohen and Grossberg has been extended to a class of discrete-time systems ([11] and references therein). For non-symmetric connections of particular form, namely

$$\mu_j W_{ij} = \mu_i W_{ji} \quad (5)$$

$\mu_i > 0$, and time evolution of the connection strengths of Hebbian type

$$\frac{d}{dt} W_{ij} = -\gamma_{ij} W_{ij} + f_i(x_i) f_j(x_j) \quad (6)$$

in [12] or $W_{ij} W_{ji} > 0$ and $\prod_C W_{ij} = \prod_C W_{ji}$ along every cycle in [13], Lyapunov functions may also be constructed.

A.2 General systems

The Cohen-Grossberg result has been generalized for arbitrary w'_{ij} s in Ref.[14], namely given

$$\begin{aligned} W_{ij} &= W_{ij}^{(S)} + W_{ij}^{(A)} \\ W_{ij}^{(S)} &= \frac{1}{2} (W_{ij} + W_{ji}) \\ W_{ij}^{(A)} &= \frac{1}{2} (W_{ij} - W_{ji}) \\ V^{(S)} &= - \sum_{i=1}^n \int^{x_i} b_i(\xi_i) f'_i(\xi_i) d\xi_i \\ &\quad + \frac{1}{2} \sum_{j,k=1}^n W_{jk}^{(S)} f_j(x_j) f_k(x_k) \\ H &= \sum_{i=1}^n \int^{x_i} \frac{f_i(\xi_i)}{a_i(\xi_i)} d\xi_i \end{aligned} \quad (7)$$

Supported by Fundação para a Ciência e Tecnologia
e-mail: vilela@cii.ful.pt

one has the following

Theorem [14] If $a_i(x_i)/f_i'(x_i) > 0 \forall x, i$ and the matrix $W_{ij}^{(A)}$ has an inverse, the vector field \dot{x}_i in Eq.(2) decomposes into one gradient and one Hamiltonian component, $\dot{x}_i = \dot{x}_i^{(G)} + \dot{x}_i^{(H)}$, with

$$\begin{aligned} \dot{x}_i^{(G)} &= -\frac{a_i(x_i)}{f_i'(x_i)} \frac{\partial V^{(S)}}{\partial x_i} = -\sum_j g_{ij}(x) \frac{\partial V^{(S)}}{\partial x_j} \\ \dot{x}_i^{(H)} &= -\sum_j a_i(x_i) w_{ij}^{(A)}(x) a_j(x_j) \frac{\partial H}{\partial x_j} \\ &= \sum_j \Gamma_{ij}(x) \frac{\partial H}{\partial x_j} \end{aligned} \quad (8)$$

and

$$\begin{aligned} g_{ij}(x) &= \frac{a_i(x_i)}{f_i'(x_i)} \delta_{ij} \\ w_{ij}(x) &= -a_i(x_i)^{-1} (W^{(A)})^{-1}_{ij}(x) a_j(x_j)^{-1} \end{aligned} \quad (9)$$

$(\sum_j \Gamma_{ij} \omega_{jk} = \delta_{ik})$. $g_{ij}(x)$ and $\omega_{jk}(x)$ are the components of the Riemannian metric and the symplectic form.

The conditions on $a_i(x_i)$, $f_i'(x_i)$ and $w_{ij}^{(A)}$ insure that g is a well defined metric and that ω is non-degenerate.

The decomposition (8) is useful, for example, on the design of oscillatory networks and on the study of gated learning rules[15]. The nature of the dynamics in the network will depend on the relative strength of the gradient and the Hamiltonian components. Howse, Abdallah and Heileman[15] propose to measure this relative strength by comparing $\frac{dV^{(S)}}{dt}$ with $\frac{dH}{dt}$. However, these quantities vary in space and time and it is the compensation of the two effects that in particular regions of phase space lead to the attractors of the dynamics, for example to limit cycles (see below).

The identification, in the differential system (2), of just one gradient and one Hamiltonian component, with explicitly known potential and Hamiltonian functions, is a considerable simplification as compared to a generic dynamical system. For a general dynamical system a representation by one or two functions is possible only locally[16] and explicit forms for the functions are not easy to obtain[17] [18]. Global decomposition for general dynamical systems require one gradient and $n - 1$ Hamiltonian components[16], namely

$$\dot{x}_i = -\sum_j g_{ij}(x) \frac{\partial V}{\partial x_j} + \sum_{k=1}^{n-1} \sum_{j=1}^n (\omega_{(k)}^{-1}(x))_{ij} \frac{\partial H^{(k)}}{\partial x_j} \quad (10)$$

$\{\omega_{(k)}(x)\}$ being a set of canonical symplectic forms adapted to each Hamiltonian component. This result is a generalization to n dimensions of the 2-dimensional result of Roels[19]. The first term in (10) is the dissipative component and the second one corresponds to a volume-preserving dynamical system.

The above results lead to a convenient characterization of dynamical systems of type (1) or (2). For the symmetric case the existence of a Lyapunov function guarantees global asymptotic stability of the dynamics. However

not all vector fields with a Lyapunov function are differentially equivalent to a gradient field. Therefore the fact that a gradient vector is actually obtained gives additional information, namely about structural stability of the model. A necessary condition for structural stability of the gradient vector field is the non-degeneracy of the critical points of $V^{(S)}$, namely $\det \left\| \frac{\partial^2 V^{(S)}}{\partial x_i \partial x_j} \right\| \neq 0$ at the points where $\frac{\partial V^{(S)}}{\partial x_i} = 0$. In a gradient flow all orbits approach the critical points as $t \rightarrow \infty$. If the critical points are non-degenerate, the gradient flow satisfies the conditions defining a Morse-Smale field, except perhaps the transversality conditions for stable and unstable manifolds of the critical points. However because Morse-Smale fields are open and dense in the set of gradient vector fields, any gradient flow with non-degenerate critical points may always be C^1 -approximated by a (structurally stable) Morse-Smale gradient field. Therefore given a symmetric model of the type (2), the identification of its gradient nature provides a easy way to check its robustness as a physical model.

Although Lyapunov functions may in some cases be constructed for discrete-time systems [11], the natural functional representation of maps is through generating functions. This is well known for canonical maps of symplectic manifolds[20] and has been generalized in [21] for non-canonical maps.

The representation of network dynamics by global function applies to neural networks of several types [5], to more general networks [22] [23] and, in view of an established correspondence [24], to a large range of connectionistic systems.

B. Cycles

Existence of limit cycle oscillations in networks is an important issue [25] [26] [27]. The decomposition theorems provide a tool to look for candidate orbits with limit cycle properties. Many years ago Pontryagin [28], studying small perturbations of Hamiltonian fields on the plane

$$\dot{x} = \frac{\partial H}{\partial y} + \varepsilon A(x, y, \varepsilon), \quad \dot{y} = -\frac{\partial H}{\partial x} + \varepsilon B(x, y, \varepsilon) \quad (11)$$

introduced the notion of *generating cycle* $\gamma(c)$, lying on a level curve $H = c$, when the perturbed equation has a cycle that depends continuously on ε , for small $|\varepsilon|$, and tends to $\gamma(c)$ when $\varepsilon \rightarrow 0$. Pontryagin's result states that if $\gamma(c)$ is a generating cycle, then

$$I(c) = \int_{\gamma(c)} (Bdx - Ady) = 0 \quad (12)$$

the integration being along $\gamma(c)$ at $\varepsilon = 0$.

Further results on the existence of cycles were later proved both for weakly coupled oscillators and for more general systems with parametrized families of solutions (see [29], chapter 9 and references therein). A generalization of Pontryagin's result to dynamical systems with constants of motion [30], leads to a necessary condition for

the existence of a cycle using the decomposition in (10), namely

$$\int \left\{ \left(\nabla H^{(i)} \cdot \nabla V \right) + \sum_{k \neq i} \omega_{(k)} \left(\nabla H^{(i)} \cdot \nabla H^{(k)} \right) \right\} d\gamma_i = 0 \quad (13)$$

the integration being along a closed level curve γ_i of H_i .

A similar result holds for discrete-time maps which belong to a differentiable arc with constants of motion [31]. A *constant of motion* for a map f defined on a manifold M is a differentiable function $\Phi : M \rightarrow \mathbb{R}$ such that for some orbit γ , $\Phi \circ \gamma = \text{constant}$. It generalizes the notion of first integral which would require this to hold for all orbits. A family of maps f_ε is called a *differentiable arc with constants of motion* if (i) each f_ε has a constant of motion Φ_ε for some orbit γ_ε ; (ii) The constant of motion Φ_0 of f_0 is a first integral in a neighborhood of γ_0 ; (iii) the maps $\varepsilon \rightarrow f_\varepsilon, \varepsilon \rightarrow \gamma_\varepsilon, \varepsilon \rightarrow \Phi_\varepsilon$ are differentiable. Then

$$\sum_{n=0}^{N_0-1} D\Phi_0(\gamma_0(n+1)) | f'(\gamma_0(n)) = 0 \quad (14)$$

N_0 being the period of the orbit γ_0 .

Both (13) and (14) give only necessary equations for the existence of limit cycles in the composite dynamics. Nevertheless they are useful tools to identify limit cycle candidates. Sufficient conditions may also be obtained in particular low-dimensional cases [32] [33].

In the same way as the Hamiltonian components of the dynamics provide a tool to look for limit cycles, the stationary points of the gradient potential provide information on the multistability of the dynamics and the nature of their basins of attraction. It is also a tool for the construction of the invariant measures of the dynamics (see below).

C. Network examples

C.1 A gene regulation network

The p53 gene was one of the first tumour-suppressor genes to be identified, its protein acting as an inhibitor of uncontrolled cell growth. The p53 protein has been found not to be acting properly in most human cancers, due either to mutations in the gene or inactivation by viral proteins or inhibiting interactions with other cell products. Although apparently not required for normal growth and development, p53 is critical in the prevention of tumour development, contributing to DNA repair, inhibiting angiogenesis and growth of abnormal or stressed cells [34]-[38]. In addition to its beneficial anticancer activities it may also have some detrimental effects in human aging [39].

The p53 gene does not act by itself, but through a very complex network of interactions[40]. Here I will discuss a simplified network, which although not being accurate in biological detail, tends to capture the essential features of the p53 network as it is known today. In particular, several different products and biological mechanisms are lumped together into a single node when their function is identical.

The network is depicted in Fig.1. The arrows and signs denote the excitatory or inhibitory action of each node on the others and the letters b, g, c, r, p, m, a denote their intensities (or concentrations).

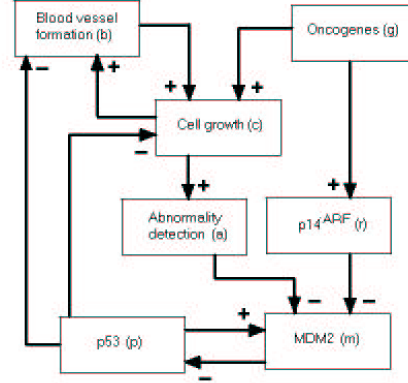


Fig. 1. A simplified p53 network model

The p53 protein is assumed to be produced at a fixed rate (k_p) and to be degraded after ubiquitin labelling. The MDM2 protein being one of the main enzymes involved in ubiquitin labelling, the inhibitory node (m) is denoted MDM2. There is a positive feedback loop from p53 to MDM2, because the p53 protein, binding to the regulatory region of the MDM2 gene, stimulates the transcription of this gene into mRNA.

Under normal circumstances the network is “off” or operates at a low level. The main activation pathways are the detection of cell anomalies (a), like DNA damage, or aberrant growth signals, such as those resulting from the expression of several oncogenes (the p14^{ARF} pathway, r). They inhibit the degradation of the p53 protein, which may then reach a high level. There are several distinct activation pathways. For example, in some cases phosphorylation of the p53 protein blocks its interaction with MDM2 and in others it is a protein that binds to MDM2 and inhibits its action. However, the end result being a decrease in the MDM2 efficiency, they may both be described as inhibitory inputs to the MDM2 node.

The p53 protein controls cell growth and proliferation, either by blocking the cell division cycle, or activating apoptosis or inhibiting the blood-vessel formation (b) that is stimulated by several tumors. In our simplified p53 network all these effects are coded on the following set of equations

$$\begin{aligned} \frac{dp}{dt} &= k_p - W_{pm} f_m(m) \\ \frac{dm}{dt} &= W_{mp} f_p(p) - W_{mr} f_r(r) - W_{ma} a - \gamma'_m m \\ \frac{db}{dt} &= W_{bc} f_c(c) - W_{bp} f_p(p) \\ \frac{dc}{dt} &= W_{cg} g + W_{cb} f_b(b) - W_{cp} f_p(p) \\ \frac{dr}{dt} &= W_{rg} g - \gamma_r r \end{aligned} \quad (15)$$

One should note that an increased level of cellular p53 is not by itself sufficient for it to become a transcriptional activator controlling cell growth. Conformational changes of the protein are also needed which are stimulated by the activation pathways or may be therapeutically induced. Also some viruses produce proteins that inactivate p53. All this means that in reality some of the coupling constants in Eqs.(15), (for example W_{cp}) may also be dynamical variables.

The regulation functions $f(\cdot)$ are positive nonlinear functions with a threshold and a saturation level. By shifting variables to compensate for thresholds and rescaling the coupling constants they may be normalized by the coefficient of the linear part, that is

$$f_i(x_i) = x_i + \dots \quad (16)$$

With a rescaling of p, m, b, c, r and redefinition of the constants we may consider

$$k_p = W_{mp} = W_{bc} = W_{cg} = W_{rg} = 1 \quad (17)$$

Furthermore, from the last equation in (15)

$$r(t) = \frac{1}{\gamma_r} g + \left(r(0) - \frac{g}{\gamma_r} \right) e^{-\gamma_r r} \quad (18)$$

Replacing r by its steady state value g/γ_r , and rescaling W_{mr} we are left with

$$\begin{aligned} \frac{dp}{dt} &= 1 - W_{pm} f_m(m) \\ \frac{dm}{dt} &= f_p(p) - W_{mr} g - W_{ma} a - \gamma_m m \\ \frac{db}{dt} &= f_c(c) - W_{bp} f_p(p) \\ \frac{dc}{dt} &= g + W_{cb} f_b(b) - W_{cp} f_p(p) \end{aligned} \quad (19)$$

a system of four dynamical variables and two control parameters g and a .

Using the dynamics decomposition discussed before one obtains

$$\begin{aligned} V^{(S)} &= - \int^p f'_p(\xi) d\xi - \int^c f'_c(\xi) d\xi \\ &\quad + \int^m (W_{mr} g + W_{ma} a + \gamma_m \xi) f'_m(\xi) d\xi \\ &\quad + \frac{1}{2} \sum_{x_i=p,m,b,c} W_{ij}^{(S)} f_i(x_i) f_j(x_j) \\ H &= \sum_{x_i=p,m,b,c} \int^{x_i} f_i(\xi) d\xi \end{aligned} \quad (20)$$

$$g_{ij} = \frac{1}{f'_i(x_i)} \delta_{ij} \quad \Gamma_{ij} = -W_{ij}^{(A)} \quad (21)$$

(i, j)	$W_{ij}^{(S)}$	$W_{ij}^{(A)}$
pm	$\frac{1}{2} (W_{pm} - 1)$	$\frac{1}{2} (W_{pm} + 1)$
pb	$\frac{1}{2} W_{bp}$	$-\frac{1}{2} W_{bp}$
pc	$\frac{1}{2} W_{cp}$	$-\frac{1}{2} W_{cp}$
mb	0	0
mc	0	0
bc	$-\frac{1}{2} (W_{cb} + 1)$	$\frac{1}{2} (W_{cb} - 1)$

The reaction of m and c to external stimuli (g and a) and the production rate of p are coded on the first three terms

of the potential function $V^{(S)}$. For coupling constants of order unit, one sees from (22) the existence of a damped Hamiltonian oscillation for the $p-m$ system, and a dangerous runaway behavior of $b-c$ arising from its dominantly gradient dynamics. The action of p on b and c is of mixed gradient-Hamiltonian type. Hence, from inspection of the nature of the global functions describing the dynamics, one concludes that (at least in this model) the controlling action of p53 may only be effective in particular circumstances. That is, it will depend on the initial conditions. This conclusion is now checked by a detailed study of the solutions.

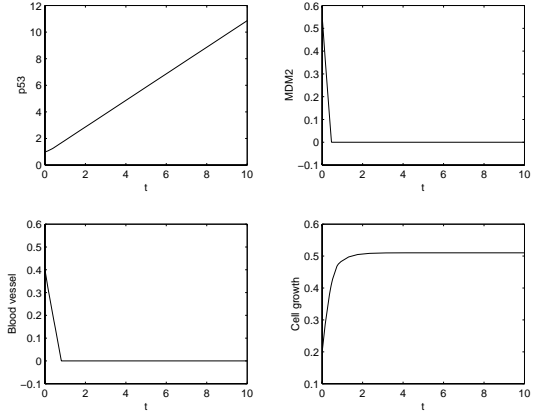


Fig. 2. Time evolution of the network (19)

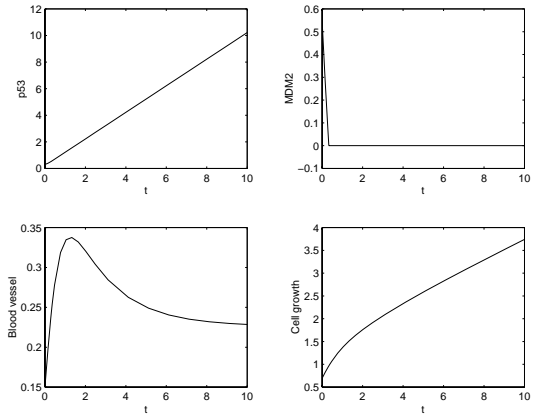


Fig. 3. Same as Fig.2 with different initial conditions

Consider first the linear approximation to the system. The solutions are, for the $p-m$ system

$$\begin{aligned} p(t) &= \bar{p} + p'(t) \\ m(t) &= \bar{m} + m'(t) \end{aligned} \quad (23)$$

with

$$\begin{aligned} \bar{p} &= W_{mr} g + W_{ma} a + \frac{\gamma_m}{W_{pm}} \\ \bar{m} &= \frac{1}{W_{pm}} \end{aligned} \quad (24)$$

$$\begin{aligned}
 p'(t) &= e^{-\gamma_m/2} \left\{ \left(p(0) - \bar{p} \right) \cos \alpha t \right. \\
 &\quad \left. + \frac{1}{\alpha} \left[\frac{\gamma_m}{2} \left(p(0) - \bar{p} \right) \right. \right. \\
 &\quad \left. \left. - W_{pm} \left(m(0) - \frac{1}{W_{pm}} \right) \right] \sin \alpha t \right\} \\
 m'(t) &= e^{-\gamma_m/2} \left\{ \left(m(0) - \frac{1}{W_{pm}} \right) \cos \alpha t \right. \\
 &\quad \left. + \frac{1}{\alpha} \left(p(0) - \bar{p} - \frac{\gamma_m}{2} \left(m(0) - \frac{1}{W_{pm}} \right) \right) \sin \alpha t \right\}
 \end{aligned} \tag{25}$$

and $\alpha = \sqrt{W_{pm} - \gamma_m^2/4}$.

As expected, one sees a damped oscillatory behavior of the $p-m$ system and, in the absence of stimuli ($a = g = 0$) the p level is small and controlled by the degradation of m .

For b and c one now obtains

$$\begin{pmatrix} b(t) \\ c(t) \end{pmatrix} = \begin{pmatrix} W_{bp} \bar{p} \\ \frac{W_{cp} \bar{p} - g}{W_{cb}} \end{pmatrix} - \int_0^t e^{A(t-\tau)} \begin{pmatrix} W_{bp} p'(\tau) \\ W_{cp} p'(\tau) \end{pmatrix} d\tau + e^{At} \begin{pmatrix} c(0) - W_{bp} \bar{p} \\ b(0) - \frac{W_{cp} \bar{p} - g}{W_{cb}} \end{pmatrix} \tag{26}$$

where A is the matrix

$$A = \begin{pmatrix} 0 & 1 \\ W_{cb} & 0 \end{pmatrix} \tag{27}$$

This matrix has eigenvalues $\pm \sqrt{W_{cb}}$ implying that $b(t)$ and $c(t)$ are going to have terms proportional to $\exp(t\sqrt{W_{cb}})$ and $\exp(-t\sqrt{W_{cb}})$. Hence p (p53) will only have a controlling effect on cell proliferation if the coefficient of the exponentially growing terms becomes negative. Multiplying (26) on the left by the matrix $\frac{1}{2} \begin{pmatrix} \sqrt{W_{cb}} & 1 \\ -\sqrt{W_{cb}} & 0 \end{pmatrix}$ that diagonalizes A one obtains the coefficient of the exponentially growing term

$$\begin{aligned}
 B(t) &= e^{t\sqrt{W_{cb}}} \left\{ \frac{\sqrt{W_{cb}}}{2} \left(c(0) - W_{bp} \bar{p} \right) \right. \\
 &\quad \left. + \frac{1}{2} \left(b(0) - \frac{W_{cp} \bar{p} - g}{W_{cb}} \right) \right\} \\
 &\quad - \int_0^t e^{(t-\tau)\sqrt{W_{cb}}} \left(\frac{\sqrt{W_{cb}}}{2} W_{bp} + \frac{1}{2} W_{cp} \right) p'(\tau) d\tau
 \end{aligned} \tag{28}$$

The conclusion is that control of cell proliferation is obtained only if $\exists t$ such that $B(t) < 0$. Therefore it depends strongly on the initial conditions. This conclusion, inferred both from the dynamical decomposition and the linear approximation is borne out by simulation of the non-linear problem. Figs.2 and 3 show two time evolutions of the equations (15) with $f(x) = \tanh(x)$, $W_{pm} = W_{mr} = W_{ma} = W_{bp} = W_{cb} = W_{cp} = 1$, $\gamma_m = 0.01$, $g = a = 1$ and the vector field $\dot{x}_i = F_i$ truncated to $\dot{x}_i = F_i \cdot \text{OR}(\text{sign}(x_i), \text{sign}(F_i))$, because concentrations cannot become negative. The behavior depends strongly on the value of the initial conditions. In conclusion, the

implication (of the model) is that unless p53 starts acting⁵ soon enough its action is useless and other means have to be used to control cell proliferation.

D. Evolving networks

In many networks found in Nature, as important as the structure of the network, is the path that the network took to reach that final state. Social or economic networks, industrial, transportation and communication networks, ecological webs, biological networks, all are examples of evolving networks. In many cases their complex structure is a simple consequence of the principles of their growth. Several network growth schemes have been studied (see [1], [2] and [3] for reviews).

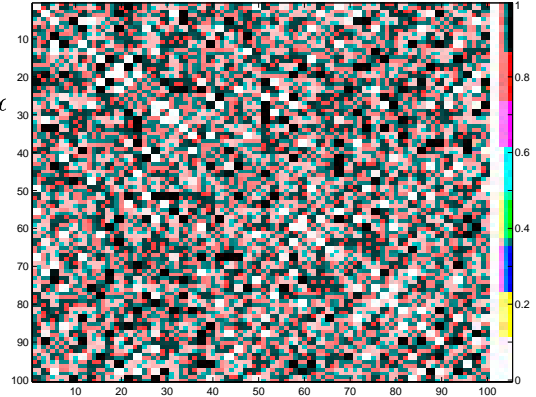


Fig. 4. Typical equilibrium configuration of network connections evolved according to Eqs. (29)-(30) ($\alpha = 1, \beta = 0$)

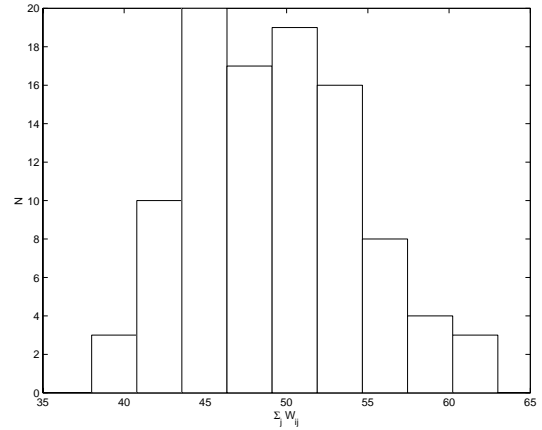


Fig. 5. Degree distribution of the network in Fig.4

Network evolution occurs either by the addition or elimination of interactions between existing nodes or by the addition of new nodes. In both cases, network evolution may be looked at as a dynamical system in the space of network connections. In the case of growing networks, this dynamical point of view may also be used by considering the evolution from zero of previously vanishing connections.

This dynamical approach will be explored here. Using the global function description, discussed in Section 2.1, two types of evolving networks will be considered. The

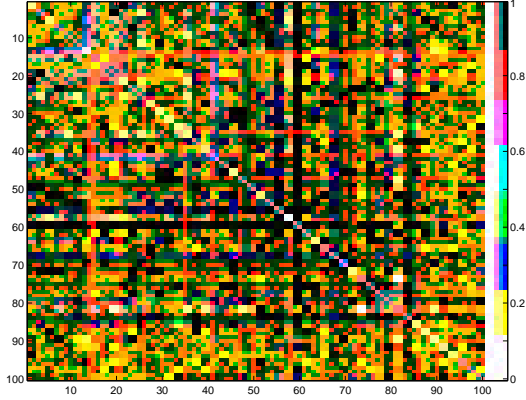


Fig. 6. Same as in Fig.4 with $\alpha = 1$ and $\beta = 0.003$

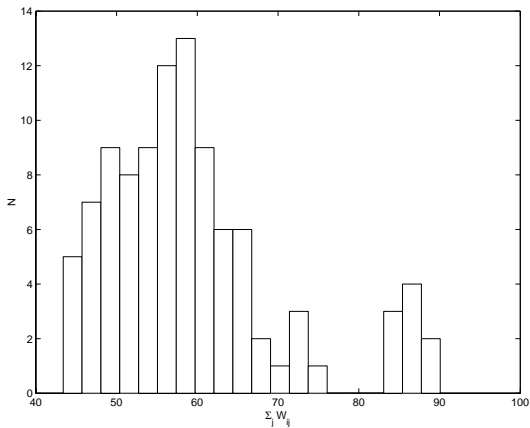


Fig. 7. Degree distribution of the network in Fig.6

simplest situation occurs when the dynamics of the connections is derived from a potential. In this case, exact expressions for mean values and invariant measures may be obtained.

Consider

$$V_1(\{W\}) = \alpha \sum_{i < j} W_{ij}^2 (W_{ij} - 1)^2 + \beta \sum_{i \neq j \neq l} (W_{ij} - 1)^2 W_{jl}^2 \quad (29)$$

with the network evolving according to

$$\frac{dW_{ij}}{dt} = -\frac{\partial V_1}{\partial W_{ij}} \quad (30)$$

When $\alpha \neq 0$ and $\beta = 0$, the connections evolve either to zero or to one, depending on the initial conditions. Therefore the network (with N nodes), as a dynamical system, is a multistable system with $2^{N(N-1)/2}$ different equilibrium points. A typical configuration, obtained from random initial conditions, is shown in Fig.4 ($N = 100$) to which corresponds the degree distribution shown in Fig.5.

When $\beta \neq 0$ the behavior is quite different, as shown in the typical configuration of Fig.6 and degree distribution Fig.7. The degree K_i of a node i is defined to be

$$K_i = \sum_j W_{ij} \quad (31)$$

holding for all intermediate values of W_{ij} .

One sees that for $\beta \neq 0$ some nodes are more connected than others. $V_1(\{W\})$ with $\beta \neq 0$ is a model for preferential attachment.

It is not practical to obtain mean values and distributions directly from simulations. This being a multistable system many different simulations with well distributed initial conditions would be required to obtain accurate values. However, in this case, exact expressions may be obtained from the unique invariant measure for the system with small random perturbations, as discussed in Section 3.2

$$\rho^\epsilon \sim \exp(-2\epsilon^{-2} V_1(\{W\})) \quad (32)$$

As a second example consider

$$V_2(\{W\}) = \alpha \sum_{i < j} W_{ij}^2 (W_{ij} - 1)^2 + \beta \sum_{i < j} \sum_{k \neq i, j} \frac{1}{|i-j|} (W_{ik}^2 + W_{jk}^2) ((W_{ik} - 1)^2 + (W_{jk} - 1)^2) \quad (33)$$

For $\beta \neq 0$ a typical configuration is shown in Fig.8. The main feature is the correlation between node connections. For $\alpha = 1, \beta = 0.05$ and $N = 100$ the sum of correlations between the node connections is around 20 whereas for $\alpha = 1, \beta = 0$ it is ≈ 4.5 . In conclusion, $V_2(\{W\})$ is a model for (approximate) node replication.

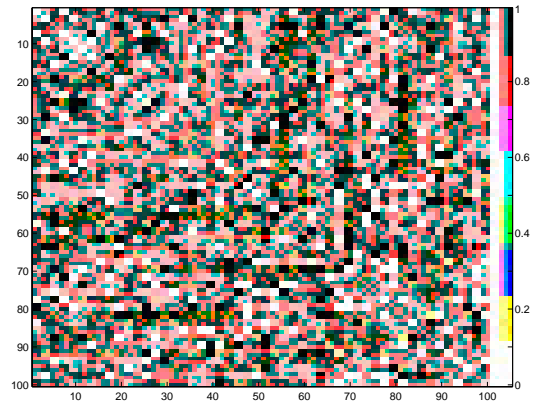


Fig. 8. Typical equilibrium configuration of network connections evolved by the potential $V_2(\{W\})$ ($\alpha = 1, \beta = 0.05$)

III. ERGODIC TOOLS

Topological and differential notions provide useful characterizations of the overall structure of phase space. However, what is more important for the applications is the dynamics in the phase space regions most frequently visited by the system. This is provided by the ergodic theory, in particular by the classification of invariant measures and their characterization by *ergodic parameters*.

Let a dynamical system evolve on the support of a measure μ which is left invariant by the dynamics. An *ergodic parameter* $I_F(\mu)$, characterizing the measure, is obtained

whenever the following limit

$$I_F(\mu) = \lim_{T \rightarrow \infty} \frac{1}{T} \sum_{n=1}^T F(f^n x_0) \quad (34)$$

exists for μ -almost every x_0 . For continuous-time dynamics f denotes the time-one map.

A. Lyapunov and conditional exponents

Lyapunov exponents are the most widely used ergodic parameters. More recently *conditional exponents* have also been proposed as an useful characterization of the dynamics.

Let $f : M \rightarrow M$, with $M \subset R^m$, μ a measure invariant under f and Σ a splitting of M induced by $R^k \times R^{m-k}$. The *conditional exponents* are the eigenvalues $\xi_i^{(k)}$ and $\xi_i^{(m-k)}$ of the limits

$$\begin{aligned} \lim_{n \rightarrow \infty} (D_k f^{n*}(x) D_k f^n(x))^{\frac{1}{2n}} \\ \lim_{n \rightarrow \infty} (D_{m-k} f^{n*}(x) D_{m-k} f^n(x))^{\frac{1}{2n}} \end{aligned} \quad (35)$$

where $D_k f^n$ and $D_{m-k} f^n$ are the $k \times k$ and $m-k \times m-k$ diagonal blocks of the full Jacobian. For $k = m$, $\xi_i^{(m)} = \lambda_i$ are the *Lyapunov exponents*.

Proposed by Pecora and Carroll [41] to characterize synchronization in chaotic systems, rigorous conditions for the existence of these limits have been proven in [42]. Existence μ -almost everywhere of both Lyapunov and conditional exponents is guaranteed by the conditions of Oseledec's multiplicative ergodic theorem, in particular the integrability condition,

$$\int \mu(dx) \log^+ \|T(x)\| < \infty \quad (36)$$

T being either the Jacobian or its $k \times k$ and $m-k \times m-k$ diagonal blocks. The set of points where the limit is defined has full measure and

$$\lim_{n \rightarrow \infty} \frac{1}{n} \log \|D_k f^n(x) u\| = \xi_i^{(k)} \quad (37)$$

with $0 \neq u \in E_x^i / E_x^{i+1}$, E_x^i being the subspace of R^k spanned by eigenstates corresponding to eigenvalues $\leq \exp(\xi_i^{(k)})$.

Based on the spectra of Lyapunov and conditional exponents, several global quantities have been defined to characterize self-organization and creation of structures in networks of multiagent systems with arbitrary connection structures. I list here the definitions and refer to Refs. [43] and [44] for proofs and examples.

A.1 Structure index related to the Lyapunov spectrum

A structure (in a collective system) is a phenomenon with a characteristic scale very different from the scale of the elementary units in the system. In a multi-agent system, a structure in space is a feature at a length scale larger than the characteristic size of the agents and a structure in

time is a phenomenon with a time scale larger than the cycle time of the individual agent dynamics. A (temporal) *structure index* may then be defined by

$$S = \frac{1}{N} \sum_{i=1}^{N_s} \frac{T_i - T}{T} \quad (38)$$

where N is the total number of components (agents) in the coupled system, N_s is the number of structures, T_i is the characteristic time of the structure i and T is the cycle time of the isolated agents (or, alternatively the characteristic time of the fastest structure). A similar definition applies for a *spatial structure index*, by replacing characteristic times by characteristic lengths.

Structures are collective motions of the system. Therefore their characteristic times are the characteristic times of the separation dynamics, that is, the inverse of the positive Lyapunov exponents. Hence, for the *temporal structure index*, one may write

$$S = \frac{1}{N} \sum_{i=1}^{N_+} \left(\frac{\lambda_0}{\lambda_i} - 1 \right) \quad (39)$$

the sum being over the positive Lyapunov exponents λ_i . λ_0 is the largest Lyapunov exponent of an isolated component or some other reference value.

The temporal structure index diverges whenever a Lyapunov exponent approaches zero from above. Therefore the structure index diverges at the points where long time correlations develop. Also, when in a multiagent network the coupling between the agents increases, the positive part of the Lyapunov spectrum contracts leading to an effective dimension reduction and to partial synchronization effects[45].

A.2 Exponent entropies and dynamical selforganization

Self-organization in a system concerns the dynamical relation of the whole to its parts. The conditional Lyapunov exponents, being quantities that separate the intrinsic dynamics of each component from the influence of the other parts in the system, provide a *measure of dynamical selforganization* $I_\Sigma(\mu)$

$$I_\Sigma(\mu) = \sum_{k=1}^N \{h_k(\mu) + h_{m-k}(\mu) - h(\mu)\} \quad (40)$$

the sum being over all relevant partitions $\Sigma_k = R^k \times R^{m-k}$ and

$$\begin{aligned} h_k(\mu) &= \sum_{\xi_i^{(k)} > 0} \xi_i^{(k)}; h_{m-k}(\mu) \\ &= \sum_{\xi_i^{(m-k)} > 0} \xi_i^{(m-k)}; h(\mu) = \sum_{\lambda_i > 0} \lambda_i \end{aligned}$$

are the *exponent entropies*, that is, the sums over positive conditional and Lyapunov exponents.

$I_\Sigma(\mu)$ may also be given the following dynamical interpretation: Lyapunov exponents measure the rate of information production or, equivalently, they define the dynamical freedom of the system, in the sense that they control

the amount of change that is needed today to have an effect on the future. In this sense the larger a Lyapunov exponent is, the freer the system is in that particular direction, because a very small change in the present state will induce a large change in the future. The conditional exponents have a similar interpretation concerning the dynamics as seen from the point of view of each agent and his neighborhood [43]. However the actual information production rate is given by the sum of the positive Lyapunov exponents, not by the sum of the conditional exponents. Therefore, $I_\Sigma(\mu)$ is a measure of apparent dynamical freedom (or apparent rate of information production).

Being constructed as functions of well defined ergodic limits, both $I_\Sigma(\mu)$ and S are also well defined ergodic parameters. They characterize the dynamics of multiagent networks and, in addition, also provide some insight on the relation between dynamics and the topology of the network [46].

B. Construction of invariant measures

In general a deterministic system has a multitude of invariant measures. However, some of them have little practical interest, because they are not stable for small random perturbations. Because systems in Nature are subjected to perturbations, only the stable measures are *physical measures*. In some cases it is possible to use the properties of the deterministic system to identify the physical measures. For example, in Axiom A systems a unique physical measure may be identified with the Sinai-Bowen-Ruelle (SBR) measure, a measure absolutely continuous along unstable manifolds. However in most cases, for example in the multistable systems so frequent in natural networks, the SBR characterization is useless. Instead, it is better to study the stochastic differential equation that is obtained from (1) by addition of a small noise term

$$dx_i = X_i(x) dt + \varepsilon \sigma(X) dW_t \quad (41)$$

W_t being a Wiener process and $\sigma(X)$ a X -dependent diffusion coefficient. A great deal of information on the invariant measure for this process may be obtained using the theory of small random perturbations of dynamical systems [47] [48] [49].

If, in the decomposition (8), $X(x)$ has only a gradient component, an explicit form for the invariant measure may be obtained. If

$$X(x) = -\nabla_{(g)} V(x) \quad (42)$$

$\nabla_{(g)}$ being the gradient in the metric

$$ds^2 = \sum a_{ij}(x) dx_i dx_j \quad (43)$$

with $\sigma(x)$ in (41) chosen such that

$$a_{ij}(x) = (\sigma(x) \sigma^*(x))_{ij}^{-1} = g_{ij}(x) \quad (44)$$

then, the density of the invariant measure is

$$\rho^\varepsilon(x) = C_\varepsilon \exp(-2\varepsilon^{-2} V(x)) \quad (45)$$

as may be easily checked from the forward Kolmogorov equation. In this case, finding the stable minima and level sets of $V(x)$ one characterizes the multistability of the network, their basins of attraction and, from the values of $V(x)$ in these sets, the relative occurrence probability of each attractor.

For general $X(x)$, small ε estimates of the invariant measure for (41) are also possible. Here the crucial role is played by the functional

$$S_{0T}(\varphi) = \int_0^T \sum_{ij} \frac{a_{ij}(\varphi_t)}{2} \left(\dot{\varphi}_t^i - X^i(\varphi_t) \right) \left(\dot{\varphi}_t^j - X^j(\varphi_t) \right) dt \quad (46)$$

and the infimum

$$U(x, y) = \inf \{ S_{0T}(\varphi) : \varphi_0 = x, \varphi_T = y, t \in [0, T] \} \quad (47)$$

taken over intervals $[0, T]$ of arbitrary length.

An equivalence relation is established between points in the domain by $x \sim y$ if $U(x, y) = U(y, x) = 0$. Let the domain be partitioned into a number of compacta $\{K_i\}$ with each ω -limit set of the deterministic dynamics contained entirely in one compactum and $x \sim y$ inside each compactum. Then, the (small ε) asymptotics of the invariant measure is obtained from the invariant measure of the Markov chain of transitions between the compacta. For sufficiently small ε the measure of each compactum is approximated by

$$\exp \left\{ -\varepsilon^{-2} \left(W(K_i) - \min_i W(K_i) \right) \right\} \quad (48)$$

where

$$W(K_i) = \min_{g \in G(i)} \sum_{(m \rightarrow n) \in g} V(K_m, K_n) \quad (49)$$

$V(K_m, K_n)$ is the minimum of the function (47) between points in compacta K_m and K_n and the sum runs over graphs that have exactly one closed cycle and this cycle contains the compactum K_i . For proofs I refer to [47].

C. A family of ergodic parameters

Ergodic parameters like the Lyapunov and the conditional exponents, are global functions of the invariant measure. However, the invariant measure itself contains more information. Ergodic parameters being defined by infinite-time limits, these quantities will fluctuate and, in general, fluctuations will not be Gaussian. The quantity describing the fluctuations is again an ergodic parameter and the same reasoning applies in turn to its fluctuations, etc.[50]. Therefore, to characterize the measure, a larger set of parameters is needed. To construct this larger set from the fluctuations is not very practical and a different approach will be followed here, namely a variational approach.

In a restricted sense, a variational principle states that the equations of motion may be written in the form $\delta S = 0$, where S is a functional of the dynamical variables and δ

is the Gateaux derivative. Only a limited set of dynamical systems may be described by a variational principle in this restricted sense. However, if one only requires that $\delta S = 0$ and the equations of motion possess the same set of solutions, essentially all differential equation problems admit a variational formulation[51]. Let

$$\dot{x}_i = X_i(x) \quad (50)$$

be a differentiable continuous-time dynamical system and S be the functional

$$S = \int \int_0^T dt d\tau \sum_i \left\{ \dot{x}_i(t) - X_i(x(t)) \right\} g(t, \tau) \left\{ \dot{x}_i(\tau) - X_i(x(\tau)) \right\} \quad (51)$$

where $g(t, \tau)$ is a symmetric kernel ($g(t, \tau) = g(\tau, t)$). Let us compute the Gateaux derivative for variations in space restricted by the boundary conditions

$$u(0) = u(T) = 0 \quad (52)$$

From

$$\delta_u S = - \int \int_0^T dt d\tau \sum_{i,k} u_k(t) \left\{ \delta_{ki} \frac{dg(t, \tau)}{dt} - \partial_k X_i(x(t)) g(t, \tau) \right\} \left\{ \dot{x}_i(\tau) - X_i(x(\tau)) \right\} \quad (53)$$

we have

Lemma: The equations of motion (50) and the critical points of the functional ($\delta_u S = 0$) have the same set of solutions if

$$K(t, \tau) = \delta_{ki} \frac{dg(t, \tau)}{dt} - \partial_k X_i(x(t)) g(t, \tau) \quad (54)$$

is invertible.

Remarks:

a) If $K(t, \tau)$ is not invertible, the solutions of the equations of motion are still critical points of the functional, but this one might have other solutions.

b) A variational principle, with only $u(0) = 0$ being required, may also be obtained by choosing a kernel such that $g(t, T) = 0$.

The critical points of the S functional contain the same information as the equations of motion. Therefore the dynamics may be characterized by the properties of the critical points, in particular by their Hessian matrix. Computing the second Gateaux derivative on the orbits one obtains

$$\delta_{u,v}^2 S|_{\delta S=0} = \int \int_0^T dt d\tau \sum_{i,j} u_i(t) v_j(\tau) H_{ij}(t, \tau) \quad (55)$$

with

$$H_{ij}(t, \tau) = \sum_k \left\{ \frac{dg(t, \tau)}{dt} \partial_j X_i(x(\tau)) - \partial_i X_k(x(t)) g(t, \tau) \partial_j X_k(x(\tau)) + \frac{d^2 g(t, \tau)}{dt d\tau} \delta_{ij} + \partial_i X_j(x(t)) \frac{dg(t, \tau)}{d\tau} \right\} \quad (56)$$

Now assume that the symmetric kernel $g(t, \tau)$ is a function of finite support of $t - \tau$

$$g(t, \tau) = g(t - \tau) = 0 \quad \text{for} \quad |t - \tau| > r \quad (57)$$

Define

$$J_{0,T}^{(n)} = \int \int_0^T Tr(H^n(t, \tau)) dt d\tau \quad (58)$$

as well as

$$J_{0,T}^{(n)'} = J_{0,T}^{(n)} + \int \int_{T-r}^{T+r} |Tr(H^n(t, \tau))| dt d\tau + \int \int_{-r}^r |Tr(H^n(t, \tau))| dt d\tau$$

Then

$$J_{0,T_1+T_2}^{(n)'} \leq J_{0,T_1}^{(n)'} + J_{T_1,T_2}^{(n)'}$$

and we are in the conditions of Kingman's sub-additive ergodic theorem. Taking limits, if both X_i and $\partial_i X_k$ are bounded $J_{0,T}^{(n)'}$ and $J_{0,T}^{(n)}$ differ only by a finite quantity and one concludes:

Theorem: If μ is an invariant measure of the dynamics in (50), X_i and $\partial_i X_k$ are bounded and there is $M \geq 0$ such that $J_{0,T}^{(n)} \geq -M$ for sufficiently large T , then the limit

$$I_n(\mu) = \lim_{T \rightarrow \infty} \frac{1}{T} J_{0,T}^{(n)} \quad (59)$$

exists and

$$\int \lim_{T \rightarrow \infty} \frac{1}{T} J_{0,T}^{(n)} d\mu = \lim_{T \rightarrow \infty} \frac{1}{T} \int J_{0,T}^{(n)} d\mu$$

$I_n(\mu)$ for $n = 1, 2, \dots$ is a family of ergodic parameters for the μ -measure preserving dynamics.

A similar construction for discrete-time maps may be found in [52] [53].

D. Synchronization, mode-locking and dynamical correlations

The onset of correlated motions in coupled many-agent systems is a phenomenon of widespread occurrence in many scientific fields. The most dramatic effect is the synchronization of assemblies of coupled dynamical systems which, when in isolation, may have quite different rhythms [54]. Examples are biological rhythms [55] like the pacemaker cells in the heart[56], neural systems[57], synchronous metabolism [58], flashing fireflies[59], laser arrays[60], even fads and social trends may be interpreted as synchronization of distinct agent dynamics. The study of the correlated behavior of many-agent dynamics is also closely related to the problem of control in extended dynamical systems.

I will consider both the coupled behavior of non-chaotic systems (oscillators with distinct individual frequencies) and of systems with isolated chaotic dynamics. In both cases one may distinguish between globally coupled systems and systems where each agent has a limited range or number of interacting partners.

For systems of oscillators the canonical example is the Kuramoto model [61] [62],

$$\frac{d\theta_i}{dt} = \omega_i + \frac{K}{N-1} \sum_{j=1}^N \sin(\theta_j - \theta_i) \quad (60)$$

with $K > 0$ and the frequencies ω_i randomly distributed around a central value ω_0 with the shifted Cauchy distribution

$$p(\omega) = \frac{\gamma}{\pi [\gamma^2 + (\omega - \omega_0)^2]} \quad (61)$$

A great deal of work has been done on this model (for a review see [63]). The existence of a synchronized cluster is characterized by the order parameter

$$r(t) = \left| \frac{1}{N} \sum_{j=1}^N e^{i\theta_j(t)} \right| \quad (62)$$

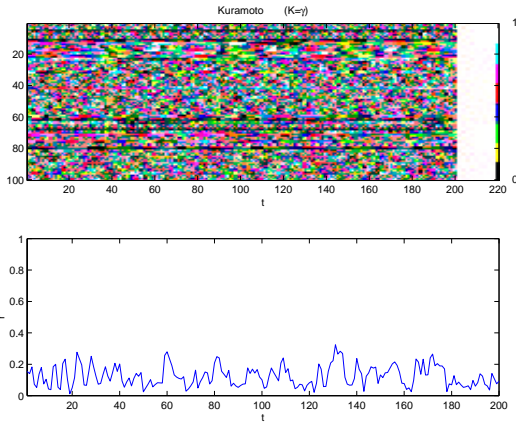


Fig. 9. A Kuramoto system below threshold

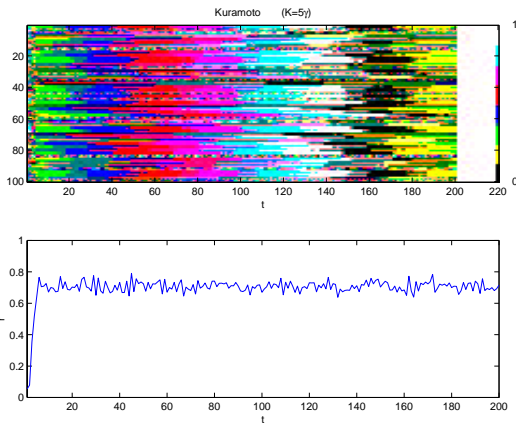


Fig. 10. A Kuramoto system above threshold

It is found that in the $N \rightarrow \infty$ and $t \rightarrow \infty$ limit, $r = 0$ for $K < 2\gamma$ and $r = \sqrt{1 - (2\gamma/K)^2}$ for $K \geq 2\gamma$. That is, there is a coupling threshold above which part of the

oscillators starts to synchronize. Figs.9 and 10 show the nonsynchronized (at $K = \gamma$) and the synchronized (at $K = 5\gamma$) behavior for 100 oscillators. The upper plot displays the color-coded values of the oscillator variables at the end of each unit time interval. The lower plots show the time evolution of the order parameter. Fig.11 compares the numerically computed Lyapunov spectrum in the synchronized and non-synchronized situations. One sees that even below the synchronization threshold ($K = 2\gamma$), part of the Lyapunov exponents becomes negative, meaning that there are many contracting directions, implying an effective dimension-reduction of the asymptotic behavior of the system. This clearly suggests that synchronization is not the whole story and that even before synchronization strong correlations must develop between the dynamics of the individual oscillators.

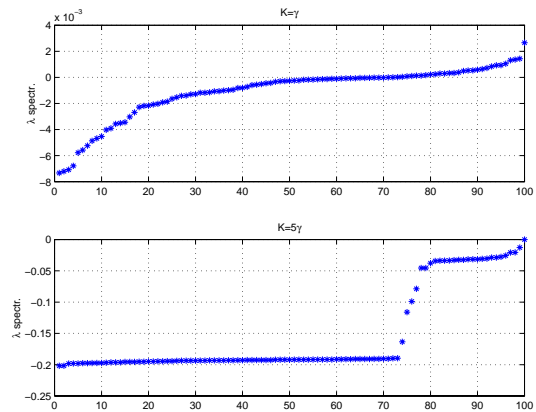


Fig. 11. Lyapunov spectrum below and above threshold for the Kuramoto system

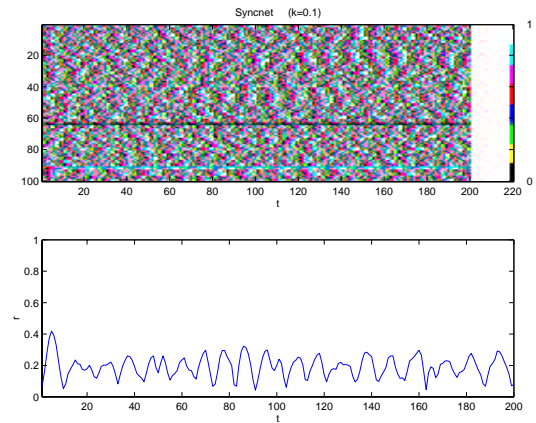


Fig. 12. Non-synchronized behavior of the discrete-time oscillators (Eq.63)

A type of correlation, of which synchronization is a limiting case is *mode-locking*. Mode-locking is the entrainment of some integer combination of the frequencies to zero. It also plays an important role in the dynamics of coupled oscillators [64]. However even if all the effective frequencies are incommensurable, the existence of negative Lyapunov directions, implies the existence of dynamical

correlations between the oscillators. What is important is the dimension of the invariant measure and the correlations may be characterized by the eigenvectors of the Lyapunov spectrum. These notions are better clarified in a simple model with exactly computable Lyapunov spectrum. Let the dynamics of an assembly of discrete-time oscillators be

$$x_i(t + 1) = x_i(t) + \omega_i + \frac{k}{N - 1} \sum_{j=1}^N f_\alpha(x_j - x_i) \tag{63}$$

with $x_i \in [0, 1]$ and $f_\alpha(x_j - x_i) = \alpha(x_j - x_i) \pmod{1}$ and the ω_i 's distributed according to $p(\omega)$, as above.

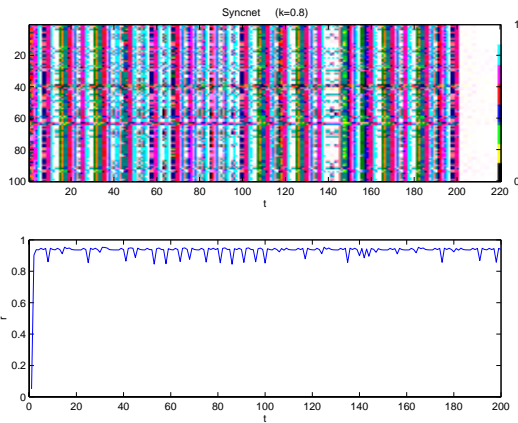


Fig. 13. Synchronized behavior of the discrete-time oscillators (Eq.63)

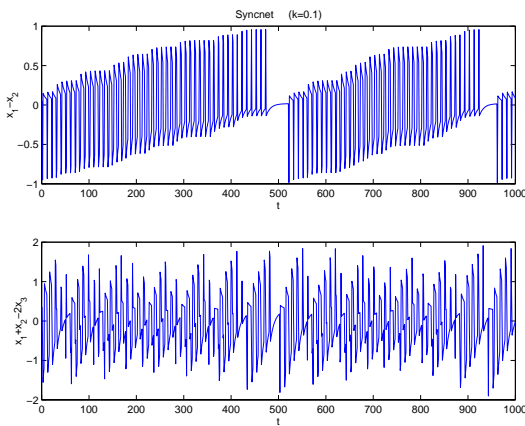


Fig. 14. Correlations in the discrete-time oscillators system.

The Lyapunov spectrum is composed of one isolated zero and $\log\left(1 - \frac{N}{N-1}\alpha k\right)$ $(N - 1)$ -times. However, although (for all $k > 0$) $N - 1$ contracting directions are always present, it is only for sufficiently large k that synchronization effects emerge as shown in Figs.12 and 13. Nevertheless dynamical correlations do exist for all k , no matter how small and the Lyapunov dimension is always one. In this case, the eigenvectors of the Lyapunov spectrum may be exactly computed and the correlations explicitly identified. This is illustrated in Fig.14.

So far I have dealt with coupled oscillators, that is, with systems which have individual nonchaotic dynamics. Another important field with many practical applications refers to the case where the individual node dynamics is chaotic. Synchronization of chaotic systems has been extensively studied (for a review see [65]) and is still a field of current research [66]. However, as in the oscillators, for networks of chaotic elements the interesting phenomena go beyond synchronization effects. Correlations and self-organization effects may be characterized by ergodic parameters. I refer to [43] and [45] for illustrative examples of networks of chaotic elements both globally connected and with a limited range of interactions. The Lyapunov spectrum and the entropies associated to the conditional exponents provide a characterization of the emergent phenomena. It should be noticed that dynamical correlations play an important role in the organization of the dynamics even when there is no reduction of the Lyapunov dimension [45]. As before these correlations are associated to the eigenvectors of the Lyapunov spectrum.

REFERENCES

- [1] R. Albert and A.-L. Barabási; *Statistical mechanics of complex networks*, Rev. Mod. Phys. 74 (2002) 47-97.
- [2] S. N. Dorogovtsev and J. F. Mendes; *Evolution of networks: From biological nets to the internet and WWW*, Oxford Univ. Press, Oxford 2003.
- [3] R. Pastor-Satorras, M. Rubi and A. Diaz-Guilera (Eds.); *Statistical mechanics of complex networks*, Springer, Berlin 2003.
- [4] R. Vilela Mendes; *Tools for network dynamics*, to appear in Int. Journal of Bifurcation and Chaos.
- [5] S. Grossberg; *Nonlinear neural networks: Principles, mechanisms and architectures*, Neural Networks 1 (1988) 17-61.
- [6] J. J. Tyson and H. G. Ohtmer; *The dynamics of feedback control circuits in biochemical pathways*, Progress in Theor. Biology 5 (1978) 1-62.
- [7] H de Jong; *Modeling and simulations of genetic regulatory systems: A literature review*, J. Comp. Biology 9 (2002) 67-103.
- [8] M. A. Cohen, S. Grossberg ; *Absolute stability of global pattern formation and parallel memory storage by competitive neural networks*, IEEE Transactions on Syst., Man and Cybern., 13 (1983) 815-826.
- [9] J. J. Hopfield; *Neurons with graded response have collective properties like those of two-state neurons*, Proc. Nat. Acad. Sciences USA 81 (1984) 3088-3092.
- [10] M. A. Cohen; *The construction of arbitrary stable dynamics in nonlinear neural networks*, Neural Networks 5 (1992) 83-103.
- [11] F. Fogelman Soulié, C. Mejia, E. Goles and S. Martinez; *Energy functions in neural networks with continuous local functions*, Complex Systems 3 (1989) 269-293.
- [12] B. Schürmann; *Stability and adaptation in artificial neural systems*, Phys. Rev. A40 (1989) 2681-2688.
- [13] B. Fiedler and T. Gedeon; *A class of convergent neural network dynamics*, Physica D111 (1998) 288-294.
- [14] R. Vilela Mendes and J. T. Duarte; *Vector fields and neural networks*, Complex Systems 6 (1992) 21-30.
- [15] J. W. Howse, C. T. Abdallah and G. L. Heileman; *Gradient and Hamiltonian dynamics applied to learning in neural networks*, in Advances in Neural Information Processing Systems 8, MIT Press 1996.
- [16] R. Vilela Mendes and J. T. Duarte ; *Decomposition of vector fields and mixed dynamics*, J. Math. Phys. 22 (1981) 1420-1422.
- [17] H. D. I. Abarbanel and A. Rouhi; *Hamiltonian structures for smooth vector fields*, Phys. Lett. A124 (1987) 281-286.
- [18] P. Crehan; *On the local Hamiltonian structure of vector fields*, Mod. Phys. Lett. A9 (1994) 1399-1405.
- [19] J. Roels; *On the local decomposition of a vector field on a symplectic surface as the sum of a gradient and a Hamiltonian field*, Comptes Rendus Acad. Sci. Paris 278 SerA. (1974) 29-31.
- [20] J.-P. Amiet and P. Huguenin; *Generating functions of canonical maps*, Helvetica Physica Acta 53 (1980) 377-397.

- [21] R. Vilela Mendes; *Generating functions for noncanonical maps*, Lett. Math. Phys. 11 (1986) 289-292.
- [22] L. O. Chua and L. Yang; *Cellular neural networks: Theory*, IEEE Trans. Circuits Syst. 35 (1988) 1257-1272.
- [23] L. O. Chua and L. Yang; *Cellular neural networks: Applications*, IEEE Trans. Circuits Syst. 35 (1988) 1273-1290.
- [24] J. Dooyne Farmer ; *A Rosetta stone for connectionism*, Physica D 42 (1990) 153-187.
- [25] J.-L. Gouzé; *Positive and negative circuits in dynamical systems*, J. of Biological Systems 6 (1998) 11-15.
- [26] E. Plahte, T. Mestl and S. W. Omholt; *Stationary states in food web models with threshold relationships*, J. of Biological Systems 3 (1995) 569-577.
- [27] E. H. Snoussi; *Necessary conditions for multistationarity and stable periodicity*, J. of Biological Systems 6 (1998) 3-9.
- [28] L. S. Pontryagin; *On dynamical systems close to Hamiltonian systems* (Russian), Zh. Eksp. Teor. Fiz. 4 (1934) 234-238.
- [29] F. C. Hoppensteadt and E. M. Izhikevich; *Weakly coupled neural networks*, Springer, NY 1997.
- [30] J. T. Duarte and R. Vilela Mendes; *Deformation of Hamiltonian dynamics and constants of motion in dissipative systems*, J. Math. Phys. 24 (1983) 1772-1778.
- [31] R. Vilela Mendes and J. T. Duarte; *Arcs of discrete dynamics and constants of motion*, Lett. Math. Phys. 6 (1982) 249-252.
- [32] R. Vilela Mendes; *Deformation stability of periodic and quasiperiodic motion in dissipative systems*, in *Deformation theory of algebras and structures and applications*, M. Hazewinkel and M. Gerstenhaber (Eds.), Kluwer Acad. Pub., Dordrecht 1988.
- [33] R. Vilela Mendes; *Multistability in dynamical systems*, in "Dynamical systems: From crystal to chaos", J.-M. Gambaudo, P. Hubert, P. Tisseur and S. Vaienti (Eds.), pp. 105-113, World Scientific 2000.
- [34] P. May and E. May; *Twenty years of p53 research: Structural and functional aspects of the p53 protein*, Oncogene 18 (1999) 7621-7636.
- [35] B. Vogelstein, D. Lane and A. J. Levine; *Surfing the p53 network*, Nature 408 (2000) 307-310.
- [36] D. B. Woods and K. H. Vousden; *Regulation of p53 function*, Exp. Cell Reserach 264 (2001) 56-66.
- [37] W. R. Taylor et al.; *Mechanisms of G2 arrest in response to overexpression of p53*, Mol. Biol. of the Cell 10 (1999) 3607-3622.
- [38] K. H. Vousden; *p53: Death star*, Cell 103 (2000) 691-694.
- [39] N. E. Sharpless and R. A. DePinho; *p53: Good cop/Bad cop*, Cell 110 (2002) 9-12.
- [40] K. W. Kohn; *Molecular interaction map of the mammalian cell cycle control and DNA repair systems*, Molecular Biol. of the Cell 10 (1999) 2703-2734.
- [41] L. M. Pecora and T. L. Carroll; *Synchronization in chaotic systems*, Phys. Rev. Lett. 64 (1990) 821-824; *Driving systems with chaotic signals*, Phys. Rev. A44 (1991) 2374-2383.
- [42] R. Vilela Mendes; *Conditional exponents, entropies and a measure of dynamical self-organization*, Phys. Lett. A248 (1998) 167 - 171.
- [43] R. Vilela Mendes; *Characterizing self-organization and coevolution by ergodic invariants*, Physica A276 (2000) 550-571.
- [44] R. Vilela Mendes; *Structure generating mechanisms in agent-based models*, Physica A 295 (2001) 537-561.
- [45] R. Vilela Mendes; *Clustering and synchronization with positive Lyapunov exponents*, Phys. Lett. A257 (1999) 132-138.
- [46] T. Araújo, R. Vilela Mendes and J. Seixas; *A dynamical characterization of the small-world phase*, Phys. Lett. A319 (2003) 285-289.
- [47] M. I. Freidlin and A. D. Wentzell; *Random perturbations of dynamical systems*, Springer-Verlag, New York 1984.
- [48] M. I. Freidlin and A. D. Wentzell; *Random perturbations of Hamiltonian systems*, Memoirs of the American Mathematical Society no. 523, 1994.
- [49] Yu. I. Kifer; *On small random perturbations of some smooth dynamical systems*, Mat. USSR-Izv. 8 (1974) 1083-1107.
- [50] D. Ruelle; *Theory and experiment in the ergodic study of chaos and strange attractors*, in Proc. VIII Int. Congress on Mathematical Physics, pgs. 273-282, M. Mebkhout and R. Sénéor (Eds.), World Scientific, Singapore 1987.
- [51] E. Tonti; *Variational formulation for every nonlinear equation*, Trieste ICTP report SMR/92-20 and references therein.
- [52] R. Vilela Mendes; *A variational formulation for dissipative maps*, Phys. Lett. A104 (1984) 391-395.
- [53] A. Carreira, M. O. Hongler and R. Vilela Mendes; *Variational formulation and ergodic invariants*, Phys. Lett. A155 (1991) 388-396.
- [54] A. Pikovsky, M. Rosenblum and J. Kurths; *Synchronization. A universal concept in nonlinear sciences*, Cambridge Univ. Press 2001.
- [55] A. T. Winfree; *Biological rhythms and the behavior of populations of coupled oscillators*, J. Theor. Bio. 16 (1967) 15-42.
- [56] C. S. Peskin; *Mathematical Aspects of Heart Physiology*, Courant Inst. Math. Sciences, New York 1975.
- [57] D. Golomb and D. Hansel; *The number of synaptic inputs and the synchrony of large sparse neuronal networks*, Neural Comput. 12 (2000) 1095-1139.
- [58] J. Aldridge and E. K. Pye; *Cell density dependence of oscillatory mechanisms*, Nature 259 (1976) 670-671.
- [59] J. Buck; *Synchronous rhythmic flashing of fireflies*, Quart. Rev. Bio. 63 (1988) 265-289.
- [60] Z. Jiang and M. McCall; *Numerical simulation of a large number of coupled lasers*, J. Opt. Soc. Am. 10 (1993) 155.
- [61] Y. Kuramoto; *Chemical Oscillations, Waves and Turbulence*, Springer, Berlin 1984.
- [62] Y. Kuramoto; *Collective synchronization of pulse-coupled oscillators and excitable units*, Physica D 50 (1991) 15-30.
- [63] S. H. Strogatz; *From Kuramoto to Crawford: exploring the onset of synchronization in populations of coupled oscillators*, Physica D143 (2000) 1-20.
- [64] R. S. MacKay; *Mode-locking and rotational chaos in networks of oscillators: A mathematical framework*, J. Nonlinear Sci. 4 (1994) 301-314.
- [65] L. M. Pecora, T. L. Carroll and J. F. Heagy; *Synchronization in chaotic systems, Concepts and applications in Handbook of Chaos Control*, ch. 10, H. G. Schuster (Ed.), Wiley-VCH, Weinheim 1999.
- [66] G. W. Wei, M. Zhan and C.-H. Lai; *Tayloring wavelets for chaos control*, Phys. Rev. Lett. 89 (2002) 284103.

IDEAL TURBULENCE

Alexander Sharkovsky

Institute of Mathematics
National Academy of Science of Ukraine
Kiev, Ukraine
e-mail: asharkov@imath.kiev.ua

Abstract—*Ideal turbulence is a mathematical phenomenon which occurs in certain infinite-dimensional deterministic dynamical systems and implies that the attractor of a system lies off the phase space and among the attractor points there are fractal or even random functions. A mathematically rigorous definition of ideal turbulence is based on standard notions of dynamical systems theory and chaos theory.*

Ideal turbulence is observed in various idealized models of real distributed systems of electrodynamics, acoustics, radiophysics, etc. In systems without internal resistance, cascade processes are capable to birth structures of arbitrarily small scale and even to cause stochastization of the systems. Just these phenomena are inherent in ideal turbulence and they help to understand the mathematical scenarios for many features of real turbulence.

I. INTRODUCTION

The term *turbulence* in the wide sense is used when describing spatial-temporal chaos in parameters distributed systems. Many effects of turbulence can be observed in deterministic infinitely-dimensional dynamical systems, induced, in particular, by boundary value problems (BVP) for partial differential equations (PDE).

The distinguishing features of turbulence are cascade processes of emergence of structures of decreasing scales and chaotic mixing. In real distributed systems, processes of reducing structures to smaller and smaller size cannot go indefinitely because of their internal resistance. In idealized systems, cascade processes may produce structures of arbitrarily small scale and even lead to stochastization of the systems (when their long-term behavior should be described in terms of probabilistic theory). These effects are realizable in mathematical models through certain idealizations of real distributed systems.

Effective study of such models has become possible only in the last 20-30 years due to development the theory of difference equations with continuous time

based on the theory of dynamical systems given by one-dimensional maps.

We present an original approach to modelling turbulent processes, which was developed in our research on chaotic dynamics in infinite-dimensional dynamical systems and in boundary value problems for partial differential equations [1-32]. These investigations have led to the fixation of the term *ideal turbulence* as a mathematical phenomenon, and now this term is represented, in particular, in the “Encyclopedia of Nonlinear Science” which is prepared to publication (see, <http://www.routledge-ny.com/nonlinsci>).

This talk follows to our recent talks [29-31].

II. SPATIAL-TEMPORAL CHAOS IN BOUNDARY VALUE PROBLEMS

We begin with several simple examples. Let us consider the simplest BVP

$$w_t - w_x = 0, \quad x \in [0, 1], \quad t \in \mathbb{R}^+, \quad (1)$$

$$w(1, t) = f(w(0, t)), \quad (2)$$

where f is a C^1 -smooth function. On substituting the general solution of (1) $w(x, t) = u(x + t)$, where u is an arbitrary C^1 -smooth function, into the boundary condition (2) we obtain the *difference equation* (DE) with continuous argument

$$u(\tau + 1) = f(u(\tau)), \quad \tau \in \mathbb{R}^+. \quad (3)$$

Any initial condition for this BVP

$$w(x, 0) = \varphi(x), \quad x \in [0, 1],$$

with φ being a C^1 -smooth function, gives the initial condition

$$u(\tau) = \varphi(\tau), \quad \tau \in [0, 1], \quad (4)$$

for the DE (3). Here it should be noted that both the solution of the BVP, generated by the initial data φ , and the corresponding solution of the DE (3) will be C^1 -smooth if, and only if $\varphi(1) = f(\varphi(0))$ and

$\varphi(1) = f(\varphi(0))\varphi(0)$, that is a usual assumption in BVP theory, so-called the C^1 -smooth consistency conditions.

The solution $u(\tau)$ of the DE (3) with the initial condition (4) can be written in the form

$$u(\tau) = f^n(\varphi(\{\tau\})), \quad n \leq \tau < n + 1, \quad n = 0, 1, \dots, \quad (5)$$

where f^n is the n -th iteration of f (i.e., $f^n = f \circ f^{n-1}$ and $f^0(x) \equiv x$), and hence the corresponding solution of the BVP can be written in the form

$$w(x, t) = f^{[t+x]}(\varphi(\{t+x\})), \quad t \in \mathbb{R}^+, \quad (6)$$

where $[\cdot]$ and $\{\cdot\}$ are the integral and fractional parts of a number; in particular,

$$w(x, n) = f^n(\varphi(x)).$$

Thus, the properties of solutions of both the BVP (1), (2) and the DE (3) should be closely connected to the properties of the difference equation with discrete time

$$u_{n+1} = f(u_n), \quad n \in \mathbb{Z}^+, \quad (7)$$

or, what amounts to the same thing – to the properties of the dynamical system given by the map

$$u \mapsto f(u). \quad (8)$$

Every solution u_n , $n \in \mathbb{Z}^+$, of the equation (7) is determined uniquely by the value $u_0 \in R$: $u_n = f^n(u_0)$. Every solution $u(\tau)$, $\tau \in \mathbb{R}^+$, of the DE (3) is determined by its values on the interval $[0, 1)$: $u_\varphi(\tau) = f^{[\tau]}(\varphi(\{\tau\}))$, $\tau \geq 0$. Thus, every solution of the DE (3) consists of a continual family of solutions of (7). The dynamics of solution of the DE (3) can be treated as dynamics of continuum of uncoupled oscillators: at every point $\tau \in [0, 1)$, there is disposed the same oscillator $u \mapsto f(u)$; its oscillations are independent of oscillations at other points from the interval $[0, 1)$, and therefore, if the map f possesses so-called sensitive dependence on initial data, the states of oscillators that were very close in an initial moment, can be very different with time.

Typical evolution of a solution of the BVP (1), (2) is shown on Fig. 1.

If it is necessary to investigate asymptotic behavior of solutions of a BVP, it is usually convenient to transfer to a dynamical system (DS) generated by shifts along solutions of the BVP on the space of its initial states. The BVP (1), (2) induces, on the space of its initial states, dynamical systems of shifts

$$S^t : \varphi(x) \mapsto f^{[t+x]}(\varphi(\{t+x\})), \quad t \in \mathbb{R}^+, \quad (9)$$

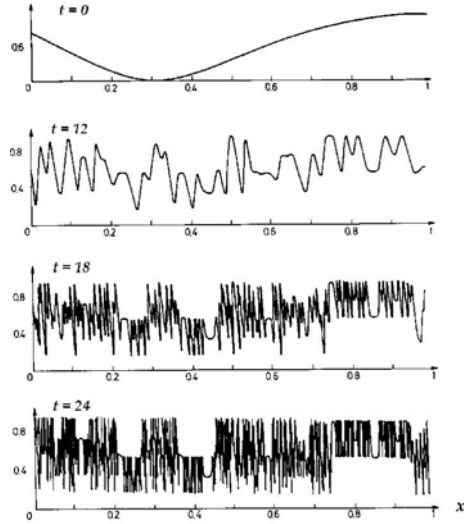


Fig. 1. Typical behaviour of solutions of the BVP (1), (2) if the corresponding one-dimensional map f has an attracting cycle of the period $\neq 2^i$, $i \geq 0$.

in particular, $S[\varphi] = f \circ \varphi$.

An analogous investigation may be realized for BVPs for the wave equation and related ones. A representative example is the BVP

$$w_{tt} - w_{xx} = 0, \quad x \in [0, 1], \quad (10)$$

$$w(0, t) = 0, \quad w_t(1, t) = h(w_x(1, t)), \quad (11)$$

with h being a C^1 -smooth function on the real line R . The initial conditions

$$w(x, 0) = \varphi(x), \quad w_t(x, 0) = \psi(x) \quad (12)$$

specify the phase space for the DS of shifts, associated with the BVP. Starting from the general solution for the equation (10)

$$w(x, t) = u(t+x) + v(t-x),$$

with u, v being arbitrary functions, and the boundary conditions (11), one can obtain the representation of S^t in terms of the iterations of some one-dimensional map (as, for example, in [13]), but the corresponding formulas are too unwieldy to be given here. Note only, that this map, labeled $f : z_n \mapsto z_{n+1}$, is defined implicitly by

$$z_{n+1} - z_n = h(z_n + z_{n+1}).$$

When (11) is replaced with $w(0, t) = 0$, $w_x(1, t) = h(w_x(0, t))$, there arise a two-dimensional map defined by $z_{n+1} - z_{n-1} = z(u_n)$.

There are many other one- and many-dimensional BVPs whose dynamics is represented by one- and

low-dimensional maps. For these BVPs, we come across a situation similar to that considered in the above examples. The turbulent properties of solutions are displayed mostly impressively in case of two spatial variables (Fig. 2).

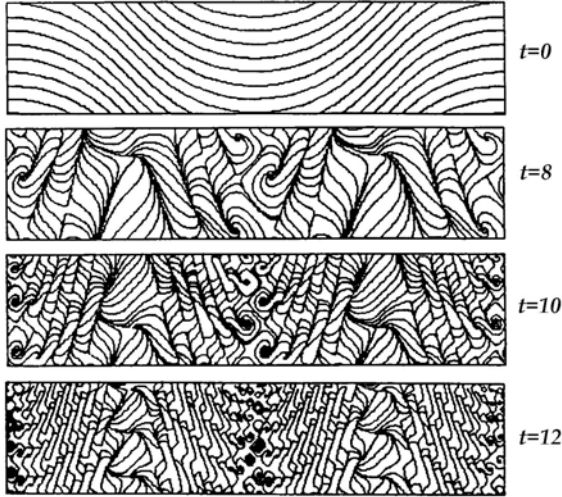


Fig. 2. Evolution of flow lines for the vector field (w^1, w^2) given by $w_t^1 = -w_x^1 - w_y^1$, $w_t^2 = w_x^2 + w_y^2$, $0 \leq x \leq 1, -\infty < y < +\infty$, and $w^2(0, t) = w^1(0, t)$, $w^2(1, t) = f(w^1(1, t))$ with $f(z) = 2(1 - z^2) - 1$.

Evolutionary BVP for PDE generally induce infinite-dimensional dynamical systems on their spaces of initial states. For parabolic PDE (such as Navier-Stokes equation), the attractor of the associated DS is in many cases a finite-dimensional subset of the phase space. Another situation occurs in problems for hyperbolic equations which we just consider here: the phase space of the associated DS (which consists of smooth functions), as a rule, does not contain its attractor. Therefore, when analyzing evolutions given by our BVP, we need to involve classes of functions, which are wider than the class of smooth functions, and to use special metrics in order to complete the phase space of the original DS and to describe by this means the asymptotic behavior of trajectories and, in particular, to construct the attractor of the DS.

For a description of the asymptotic behavior of trajectories it is expediently to use (as is accepted in the theory of dynamical systems) the concept of the ω -limit set of a trajectory. We use also a standard notion of attractor but here we have to consider not only the original space C^k but also a new space \mathcal{C} obtained via the completion of the space C^k , for example, by the use some right metric ρ .

By the attractor \mathcal{A} we mean the smallest closed

set in a phase space \mathcal{C} which has the property that $\omega[\varphi] \subset \mathcal{A}$ for all $\varphi \in C^k$ outside of a set of first Baire category (with respect to C^k -topology).

For many DE and BVP, the attractor will consist of discontinuous multivalent functions, which could result on a very complicated long-time behavior of (smooth) solutions. In this case, we typically observe self-structuring phenomena, whose description calls for the notions of self-excited structures, cascade process of appearance of structures, self-similarity, fractal structures and etc. Moreover, for these problems, there may occur self-stochasticity phenomena, which lie in the fact that the attractor of a deterministic DS contains random functions.

III. IDEAL TURBULENCE: DEFININIONS

A mathematical definition of turbulence can be given for dynamical systems on spaces of smooth or piecewise smooth functions. Spatial-temporal chaoticization in a DS is perceived as an evolution of such functions which leads to that their behavior becomes more and more intricate and the limit states of the DS cannot be described with smooth functions (see Fig. 1). The attractor of the DS is not contained entirely in the phase space, and the DS needs to be extended on a wider functional space so that this new space contains ω -limit sets of all or almost all trajectories. The spaces of fractal and random functions are particularly appealing for use as such wider space. By a fractal function is meant a function whose graph is a fractal (in the wide sense).

A. Spaces and Metrics

Let $\{C^k(D, E), T, S^t\}$ be an infinite-dimensional dynamical system with $C^k(D, E)$ being the space of C^k -functions $\varphi : D \rightarrow E$, $D \subset \mathbb{R}^l$, $E \subset \mathbb{R}^m$ ($k, l, m \geq 1$), $T = \mathbb{R}^+$ or \mathbb{Z}^+ . The phase space C^k equipped a priori with the “ordinary” C^k -metric is noncompact. Therefore, for some or even for almost all trajectories $S^t[\varphi]$, $\varphi \in C^k$, the corresponding ω -limit sets $\omega[\varphi]$ may be found empty.

To operate with the extended phase spaces, it is, of course, necessary to use metrics which should satisfy to certain physical considerations. If, for example, we investigate asymptotic behavior of the function $S^t[\varphi](x)$ as $t \rightarrow \infty$ in the presence of large gradients in both x and t and, in particular, we have to analyse the values of the function at some point $x = x$, we should consider the values of this function at some ε -neighborhood of x too; if we have to analyse this function at all $x \in D$ then we should choose, by de-

creasing ε , an “optimal resolving power” – small but finite ε – depending on “objects” studied.

For a space containing fractal functions we take the space of multivalent functions $\zeta : D \rightarrow E$, whose graphs are closed sets (such functions are called upper semicontinuous), and a metric is taken as follows

$$\rho^\Delta(\zeta_1, \zeta_2) = \sup_{\varepsilon > 0} \min \left\{ \varepsilon, \sup_x d_H(V_{\zeta_1}^\varepsilon(x), V_{\zeta_2}^\varepsilon(x)) \right\},$$

where $d_H(\cdot, \cdot)$ is the Hausdorff distance between sets, $V_\zeta^\varepsilon(x) = \zeta(V_\varepsilon(x))$, and $V_\varepsilon(\cdot)$ is the ε -neighborhood of a point. The metric ρ^Δ is equivalent to that given by the Hausdorff distance between the graphs of functions.

A function $\xi : D \rightarrow E$, deterministic or random, can be interpreted as a collection of all its finite-dimensional distributions. Whereas the metric ρ^Δ allows for the sets of values taken on by functions in the vicinity of points from D , a metric in the space, containing random functions along with deterministic ones, should allow for the distributions of these values. Consequently, to obtain a desired metric starting from ρ^Δ , the set $\zeta(V_\varepsilon(x))$ should be replaced with the distributions of ξ on $V_\varepsilon(x)$. Thus we obtain the metric

$$\rho^\#(\xi_1, \xi_2) = \sup_{\varepsilon > 0} \min \left\{ \varepsilon, \sum_{r=1}^{\infty} \frac{1}{2^r} \sup_x d(\varepsilon, \xi_1, \xi_2) \right\},$$

where

$$d(\varepsilon, \xi_1, \xi_2) = \frac{1}{\text{mes } E^r} \int_{E^r} |F_{\xi_1}^\varepsilon(x, z) - F_{\xi_2}^\varepsilon(x, z)| dz,$$

D^r and E^r are the direct products of r copies D and E respectively, and $F_\xi^\varepsilon(x, z)$, $x \in D^r$, $z \in E^r$, is the averaging of the r -dimensional distributions of ξ over ε -neighborhood of a point $x \in D^r$. For a deterministic function $\xi : D \rightarrow E$, all its distributions are defined uniquely by its distribution function $F_\xi(x, z) = \chi_{(-, z)}(\xi(x))$, $x \in D$, with $\chi_A(\cdot)$ being the indicator of the set A .

B. Definitions

Let $C^\Delta = C^\Delta(D, E)$ be the completion of the phase space $C^k(D, E)$ via the metric ρ^Δ with upper semicontinuous functions and $C^\# = C^\#(D, E)$ be the completion of the phase space $C^k(D, E)$ via the metric $\rho^\#$ with random and deterministic functions.

For an initial state $\varphi : D \rightarrow E$, denote by $\omega_\Delta[\varphi]$ the set of the limit points of the trajectory $S^t[\varphi]$ in the space C^Δ and by $\omega_\#[\varphi]$ the set of the limit points of $S^t[\varphi]$ in the space $C^\#$.

The initial state φ is said to generate *ideal turbulence* (IT) if the set $\omega_\Delta[\varphi]$ contains at least one “point” that is a fractal function.

Along similar line, the initial state φ is said to generate *stochastic turbulence* (SIT) if the set $\omega_\#[\varphi]$ contains at least one “point” that is a random function.

If there is a great deal of initial states which generate IT or respectively SIT, then IT or respectively SIT is said to occur in the DS.

This classification of turbulence can of course be extended. For instance, let $\zeta \in C^\Delta$ and $\mathcal{M}(\zeta) = \{x \in D : \zeta(x) \text{ consists of more than one point}\}$. The initial state φ is said to generate *weak ideal turbulence* (WIT) if φ does not generate IT but there exists at least one function $\zeta \in \omega_\Delta[\varphi]$ such that the set $\mathcal{M}(\zeta)$ is infinite.

If we consider a BVP it is natural to say that *IT, or WIT, or SIT arises in a BVP* if such a turbulence occurs in the corresponding DS.

C. Simplest model for ideal turbulence

A simple example of DSs with turbulence is the discrete DS acting on the space of smooth functions $\varphi : D \rightarrow E$ according to the rule

$$S : \varphi \mapsto f \circ \varphi, \tag{13}$$

where $f : E \rightarrow E$ is a smooth function and the symbol \circ is for the composition of functions. The trajectory through a “point” φ can be written in the form

$$S^n[\varphi] = f^n \circ \varphi \text{ or } S^n[\varphi](x) = f^n(\varphi(x)), \quad n \in \mathbb{Z}^+,$$

herein the superscript n denotes the n -th iteration. The last formula implies that the dynamics of almost every trajectory $S^n[\varphi]$, $n \in \mathbb{Z}^+$, can be treated as the dynamics of continuum of uncoupled oscillators: at every point $x \in D$ there is a “pendulum” which oscillates by the law $z_n \mapsto z_{n+1} = f(z_n)$ with $z_0 = \varphi(x)$; its oscillations are independent of the “pendulums” at other points of D . Just the independence of the oscillators causes IT in the DS (13). Moreover, when f has the property of sensitive dependence on initial data on some open set $E \subset E$, those φ such that $\varphi(D) \cap E \neq \emptyset$ often generates SIT. In more general situations, which just occur in applied problems, the oscillation law depends on an initial data φ and/or a point $x \in D$, and, finally, it can be time-dependent.

A description of long-term properties for the DS (13) is most advantageous when f is a one-dimensional map and D and E are intervals. In this case, one has the following criterion (*):

I. In the DS (13), there occurs

(1) weak ideal turbulence, if the map f has periodic trajectories of periods 2^i , $0 \leq i \leq l$, with some $l > 1$, and no other periodic trajectories;

(2) ideal turbulence, if the map f has a periodic trajectory of period $\neq 2^i$, $i = 0, 1, \dots$

II. In the DS (13), there occurs stochastic turbulence, if the map f possesses a smooth (i.e., absolutely continuous with respect to the Lebesgue measure) ergodic invariant measure.

For quadratic and so-called quadratic-like maps f , criterion (*) can be sharpened. Namely, both the assertions I and II remain valid when the words "for every φ from some open set of initial data" are replaced with the words "for almost every φ " ("almost every" is meant in a topological sense).

Let f in the DS (13) be the parameter-dependent map $f_\lambda : z \mapsto \lambda z(1 - z)$, $z \in [0, 1]$, $0 < \lambda \leq 4$. If the parameter λ varies in the interval $(1 + \sqrt{6}, \lambda)$ with $\lambda \approx 3.57$ being the limit value for the period-doubling bifurcation values of λ , there occurs WIT and the progression of ideal turbulence follows the period-doubling pattern. Where $\lambda > \lambda$, the map f_λ has a cycle with a period differing from the powers of 2 and there occurs IT in the DS. Finally, there is a set of positive Lebesgue measure $\Lambda \subset (\lambda, 4]$ such that the map f_λ with $\lambda \in \Lambda$ has an ergodic smooth invariant measure and hence SIT in the DS is a non-exclusive phenomenon. In particular, when $\lambda = 4$, the map $z \mapsto 4z(1 - z)$ has an invariant measure with the density $p(z) = 1 / \pi \sqrt{z(1 - z)}$ and the support $[0, 1]$. Then for almost every φ , the set $\omega_\#[\varphi]$ consists of a single point which is the pure random function with x -independent distribution $F(x, z) = \int_0^z p(z) dz = (2/\pi) \arcsin \sqrt{z}$ and the attractor of the DS consists of just this one point.

Generally, functions that make up ω -limit sets may appear to be deterministic on one subset of D and random on the other. Such may take place where the map f possesses several attractors and the initial values interval $\varphi(D)$ "clings to" the basins of at least two attractors.

It makes sense to note that the topological entropy of the DS (13) is equal to 0 in case WIT and is equal to ∞ in case IT.

IV. MATHEMATICAL FUNDAMENTALS OF IDEAL TURBULENCE

If a BVP induces an infinite-dimensional DS whose dynamics is specified by some interval map, then the theory of one-dimensional maps allows one to un-

derstand why and how turbulence occurs in the BVP and to present scenarios for *self-structuring and self-stochasticity phenomena*. This is best demonstrated by the BVP (1), (2) with quadratic map $f : I \rightarrow I$.

For *ideal turbulence*, the main factor is the complex topological structure of the set $\mathcal{D}(f)$ of points of unstable trajectories of f , in particular, the local self-similarity of $\mathcal{D}(f)$ at the points of repelling cycles and at their preimages.

If the map f has a cycle whose period is different from a power of 2, the Hausdorff dimension of $\mathcal{D}(f)$ is positive and hence the graph of every solution $w_\varphi(x, t)$, remaining a smooth surface, becomes as $t \rightarrow \infty$ more and more close to a certain fractal surface of Hausdorff dimension > 2 .

The cascade process of appearance of structures in the solutions of the BVP is directly related to the intricate topological and dynamical organization of the basins of attracting cycles of f . As a rule such a basin is of the form $\cup_{i=0} B_i$, where $B_i = f^{-1}(B_{i-1})$, $i > 1$, $B_1 = f^{-1}(B_0) \setminus B_0$ with B_0 being the domain of immediate attraction of the corresponding cycle, therewith the boundary points of the basin belong to the set $\mathcal{D}(f)$. It is obvious that $B_{i'} \cap B_{i''} = \emptyset$ if $i \neq i'$, every B_i consists of open (nonintersecting) intervals (possible, $B_i = \emptyset$ for i greater than some $i_0 > 0$).

Let $m(B_i)$ be the number of intervals B_{ij} which are components of B_i . If m is the period of the cycle, then $m(B_0) = m$. Let $B_{i'j'}$ and $B_{i''j''}$, $i < i'$, be intervals such that $f^{i'}(B_{i'j'}) = f^{i''}(B_{i''j''})$ (and, in addition, $f^{i'}|_{B_{i'j'}}$, $f^{i''}|_{B_{i''j''}}$ are one-to-one maps), and let an initial state $\varphi(x)$ be such that $\varphi(D) \supset B_{i'j'} \cup B_{i''j''}$. Then whatever $\bar{t} > 0$, the solution $w_\varphi(x, t)$ "draws" the same "picture" (structure) on the set $D_{i'j'} = \varphi^{-1}(B_{i'j'})$ at the moment $t = \bar{t} + i$ and on the set $D_{i''j''} = \varphi^{-1}(B_{i''j''})$ at the moment $t = \bar{t} + i'$. In this case, one can say that the solution $w_\varphi(x, t)$ produces coherent structures on the sets $D_{i'j'}, D_{i''j''} \subset D$. Since $\text{diam } B_{ij} \rightarrow 0$ as $i \rightarrow \infty$, the scale of structures produced at a moment t decreases ad infinitum as $t \rightarrow \infty$.

If $m \neq 2^i$, between any two intervals $B_{i'j'}$ and $B_{i''j''}$, $i \neq i'$, there is an interval $B_{i_*j_*}$ with $i > i_*, i_*$. The process of structures production by the solution is cascade and, moreover, the rate of structures production during the cascade process is specified by $c_i = m(B_{i+1})/m(B_i)$, therewith $\log c_i \rightarrow \text{ent } f$ as $i \rightarrow \infty$, where $\text{ent } f$ is the topological entropy of f .

For *stochastic turbulence*, of fundamental importance is both the occurrence of a smooth ergodic in-

variant measure (s.e.i.m.) for the map f and the fact that for interval maps, the availability of s.e.i.m. is not extraordinary point (for wide classes of parameter-dependent maps, the parameter values which result in the map possessing s.e.i.m., form a set of positive Lebesgue measure). Where the quadratic map $f : I \rightarrow I$ possesses s.e.i.m., it has the property of sensitive dependence on initial data on the support of s.e.i.m. and, moreover, almost every trajectory $f^n(z)$, $n \in \mathbb{Z}^+$, restores s.e.i.m. (that is, the residence time of the trajectory in a set $A \subset I$ is equal to the measure of A). In view of (9), such *temporal stochasticity* of trajectories of f transforms into *spatial-temporal stochastization* of solutions for the BVP and causes SIT via cascade processes of “birth and crushing” structures up to infinitely small sizes.

V. VISUALISATION OF IDEAL TURBULENCE, AND COMPUTER TURBULENCE

The visualisation of IT is connected with certain difficulties in computing. These difficulties arise due to the fact that IT is accompanied by cascade processes of birth of structures of infinitely decreasing scales. This raises the question of what one should do with the precision of calculations. If mathematical models involving IT describe a real physical object then decreasing the diameters of structures to zero conflicts with the discrete nature of the physical object. Thus these models can describe adequately real processes only within certain space-time scales.

The discreteness brought in the models by calculation algorithms leads to that the results of numerical investigation of these models may be found more close (in certain sense) to the reality than exact solutions (not in spite of “incorrect” calculations but owing to these). When IT occurs in a BVP, sometimes exact solutions “dictate”, nevertheless, laminar dynamics and only their space-time discretization results in just turbulent dynamics. In such cases, we say that “computer turbulence” takes place [21,26,28].

VI. A EXAMPLE: A TIME-DELAYED CHUA’S CIRCUIT

We consider the BVP for a lossless transmission line with tunnel diode (Fig.3)

$$v_x = -Li_t, \quad i_x = -Cv_t, \quad 0 \leq x \leq l, \quad t \in \mathbb{R}^+, \quad (14)$$

$$v(0, t) = 0, \quad i(l, t) = G(v(l, t) - E - Ri(l, t)), \quad (15)$$

under the assumption $C_1 = 0$. Here $v(x, t)$ and $i(x, t)$ are the voltage and the current along the line, L and C denote the inductance and capacitance per unit length,

and the function G specifies a $v - i$ characteristic of the diode:

$$G(u) = \begin{cases} m_0 u, & |u| \leq 1, \\ m_1 u - (m_1 - m_0)\text{sgn } u, & |u| \leq 1. \end{cases}$$

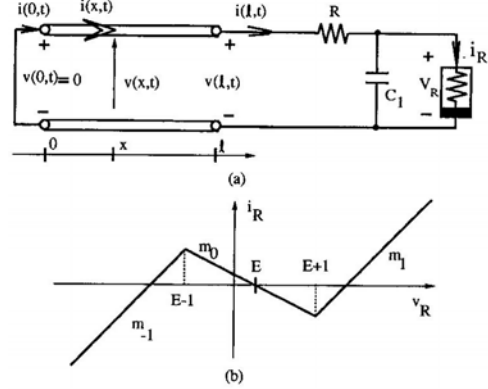


Fig. 3. (a) The time-delayed Chua’s circuit. (b) The $v_R - i_R$ characteristic of Chua’s diode.

Solution (10) under the condition $v(0, t) = 0$ is of the form

$$\begin{aligned} v(x, t) &= \alpha(t - x/\nu) - \alpha(t + x/\nu), \\ i(x, t) &= (1/Z)[\alpha(t - x/\nu) + \alpha(t + x/\nu)], \end{aligned} \quad (16)$$

where $\nu = \sqrt{1/LC}$, $Z = \sqrt{L/C}$, and α is an arbitrary function. With the new variables $\tau = (\nu t/l - 1)/2$, $z(\tau) = \alpha(2l\tau/\nu)$, combining (16) and the second boundary condition (15) gives the continuous argument difference equation

$$\begin{aligned} z(\tau + 1) + z(\tau) &= \\ F(z(\tau) - z(\tau + 1)), \quad \tau \geq -1. \end{aligned} \quad (17)$$

Thus, the behavior of solutions of the BVP is determined by the one-dimensional map $f : z_n \rightarrow z_{n+1}$, which is defined implicitly by $z_{n+1} + z_n = F(z_n - z_{n+1})$. In case of particular function G and particular parameters, conditions to the occurrence of IT can be formulated (Fig. 4, as given in [13]).

The shift operator S^t specifying a dynamical system associated with the BVP can be expressed in terms of the map f by reference to (16).

If G is a piecewise linear function, as in case of Chua’s diode, then there usually exists a parameter region where the map f has an invariant interval into which f is equivalent to the map

$$\begin{aligned} g(z) &= \begin{cases} p(z - a) + 1, & [0, a], \\ q(1 - z), & (a, 1], \end{cases} \\ p > 0, \quad q > 1, \quad a &= 1 - 1/q. \end{aligned} \quad (18)$$

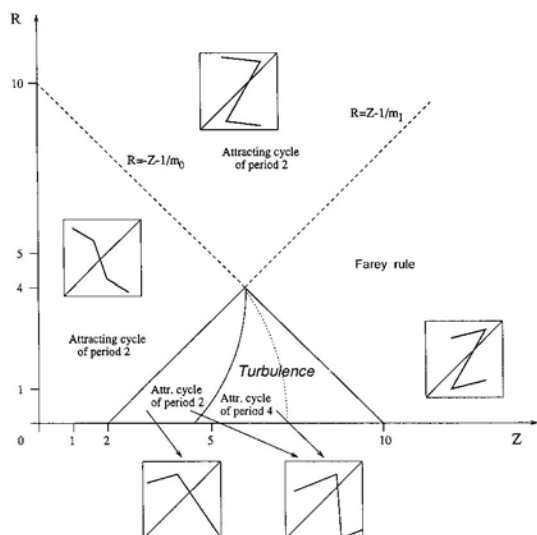


Fig. 4. Partition of R - Z parameter plane according to asymptotic behavior of the one-dimensional map for $E < 1 + Rm_0$ when $m_0 = -\frac{1}{10}$ and $m_1 = \frac{1}{2}$. Representative maps in each region where simple behavior occurs are shown.

For any integer $m > 1$, the map g has an attracting cycle of period m if and only if $\sum_{i=0}^{m-2} p^{-i} \leq q < p^{-m+1}$. For other values of parameters (p, q) from the domain $0 < p < 1$, the map g has a “smooth” invari-

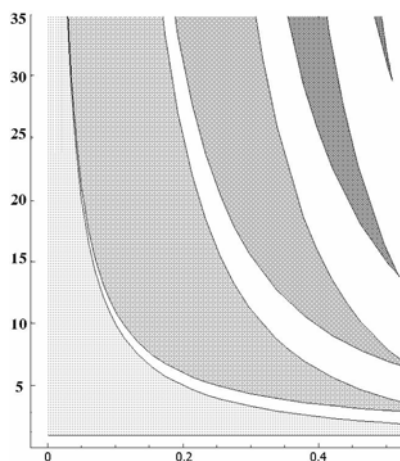


Fig. 5. Bifurcation diagram for the family (18) in the plane (p, q) . Parameter values from the “white” region result in SIT, and these from the “grey” regions result in IT without stochastization.

ant measure (see Fig. 5 and Fig. 6), which means that SIT appears in the BVP just when the parameters of the BVP are reduced to this part of the domain $0 < p < 1$. In case the map g has an attracting cycle with period $m > 2$ (in the domain $0 < p < 1$) the

BVP generates IT only (without stochastization).

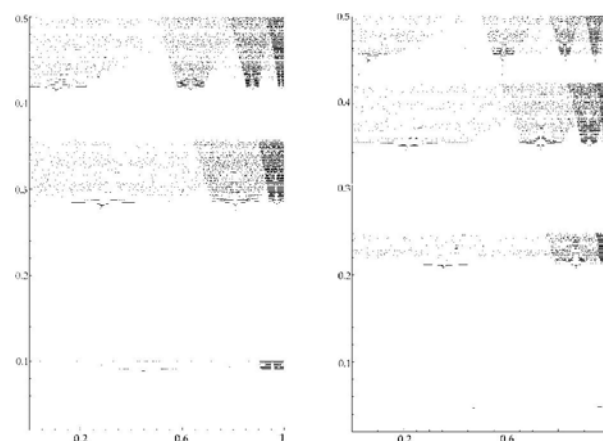


Fig. 6. Bifurcation diagram for the family (18) in the plane (z, p) with $q = 10$ (left) and $q = 20$ (right).

* * *

In conclusion, it should be noted that the creation of a perturbation theory which will allow to analyse not only idealized models but also non-idealized ones, is not only important but also very difficult mathematical problem.

Acknowledgements

This work is supported by the Ministry of Education and Science of Ukraine, State Fund of Fundamental Investigations, project No 01.07/00081.

REFERENCES

- [1] Sharkovsky, A.N., *On oscillations whose description is given by autonomous difference and differential-difference equations*, in *Proc. VIII ICNO (1978)*, **2**, Academia, Prague, pp. 1073-1078, 1979.
- [2] Sharkovsky, A.N., “Dry” turbulence, in *Short Comm. of Intern. Congress Mathematicians, Warszawa, 1983*, 10 (12), 4, Warszawa 1983.
- [3] Sharkovsky, A.N., “Dry” turbulence, in *Proc. Conf. “Non-linear and Turbulent Processes in Physics”* (ed. by Sagdeev, R.Z.), Gordon and Breach, **3**, pp. 1621-1626, 1984.
- [4] Sharkovsky, A.N., Maistrenko, Yu.L., and Romanenko, E.Yu., *Difference Equations and Their Applications*, Kluwer Academic Publisher, 1993.
- [5] Maistrenko, Yu.L., Romanenko, E.Yu., and Sharkovsky, A.N., *Attractors of difference equations and turbulence*, in *Proc. Intern. Workshop “Plasma theory and nonlinear and turbulent processes in physics” (Kiev, 1987)*, World Sci. Publ., Singapore, pp. 520-536, 1988.
- [6] Lukin, K.A., Maistrenko, Yu.L., Sharkovsky, A.N., Shestopalov, V.P., *One-dimensional initial-boundary value problems of the electrodynamics with nonlinear boundary conditions*, Preprint 87.39, Inst.Math. of NAS of Ukraine, Kiev, 1987, 15p. (in Russian).

- [7] Romanenko, E.Yu., and Sharkovsky, A.N., *Formation of structures and autostochasticity in distributive systems*, in *Proc. IV Intern. Workshop "Nonlinear and turbulent processes in Physics"* (Kiev, 1989), **2**, Naukova Dumka, Kiev, pp. 416-419, 1989.
- [8] Lukin, K.A., Maistrenko, Yu.L., Sharkovsky, A.N., Shestopalov, V.P., *A difference equations method in a resonator problem with the nonlinear reflection*, Reports of Acad.Sci. USSR, **309**, n2, 1989 (in Russian).
- [9] Sharkovsky, A.N., and Romanenko, E.Yu., *Ideal turbulence: Attractors of deterministic systems may lie in the space of random fields*, Intern. J. Bifurcation and Chaos, **2**, n1, pp. 31-36, 1992.
- [10] Sharkovsky, A.N., Romanenko, E.Yu., *Problems of turbulence theory and iteration theory*, in *Proceedings of ECIT-91*, World Scientific, Singapore, pp. 241-252, 1992.
- [11] Sharkovsky, A.N., *Chaos from a time-delayed Chua's circuit*, IEEE Transactions on Circuits and Systems.I., **40**, n10, pp. 781-783, 1993.
- [12] Sharkovsky, A.N., Maistrenko, Yu.L., Deregel, Ph., and Chua, L.O., *Dry turbulence from a time delayed Chua's circuit*, J. Circuits, Systems and Computers, **3**, n2, pp. 645-668, 1993.
- [13] Sharkovsky, A.N., *Ideal turbulence in an idealized time-delayed Chua's circuit*, Intern. J. Bifurcation and Chaos, **4**, n2, pp. 303-309, 1994.
- [14] Sharkovsky, A.N. and Sivak, A.G., *Universal phenomena in solution bifurcations of some boundary value problems*, Nonlinear Math. Physics, **1**, pp. 147-157, 1994.
- [15] Maistrenko, Yu.L., Maistrenko, V.L., Vikul, S.I., and Chua, L.O., *Bifurcations of attracting cycles from time-delayed Chua's circuit*, Intern. J. Bifurcation and Chaos, **5**, n3, pp. 653-671, 1995.
- [16] Romanenko, E.Yu., Sharkovsky, A.N., and Vereikina, M.B., *Self-structuring and self-similarity in boundary value problems*, Intern. J. Bifurcation and Chaos, **5**, n5, pp. 145-156, 1995.
- [17] Sharkovsky, A.N., Deregel, Ph., and Chua, L.O., *Dry turbulence and period-adding phenomena from a 1-D map*, Intern. J. Bifurcation and Chaos, **5**, n5, pp. 1283-1302, 1995.
- [18] Sharkovsky, A.N., *Universal phenomena in some infinite-dimensional dynamical systems*, Intern. J. Bifurcation and Chaos, **5**, n5, pp. 1419-1425, 1995.
- [19] Romanenko, E.Yu., Sharkovsky, A.N., *From one-dimensional to infinite-dimensional dynamical systems: Ideal turbulence*, Ukrain. Math. J., **48** (12), pp. 1604-1627 (in Ukrainian), pp. 1817-1842, 1996.
- [20] Romanenko, E.Yu., Sharkovsky, A.N., and Vereikina, M.B., *Structural turbulence in boundary value problems*, in *Proc. 1st Intern. Conf. "Control of Oscillations and Chaos"*, St.Petersburg, v.3, pp. 492-497, 1997.
- [21] Sharkovsky, A.N., Berezovsky, S.A., *Computer Turbulence*, in *Proc. Intern. Conf. "Self-similar systems"* (Dubna, 1998), Joint Inst. Nuclear Reseach, Dubna, Russia, pp. 251-259, 1999.
- [22] Sharkovsky, A.N., Romanenko, E.Yu., and Vereikina, M.B., *Self-structuring and self-stochasticity in difference equations and some boundary value problems*, in *Proc. Intern. Conf. "Self-similar systems"* (Dubna, 1998), Joint Inst. Nuclear Reseach, Dubna, Russia, pp. 237-250, 1999.
- [23] Romanenko, E.Yu., Sharkovsky, A.N., and Vereikina, M.B., *Self-stochasticity in deterministic boundary value problems*, Nonlinear Boundary Value Problems, **9**, Inst. Appl. Math. and Mech., NAS of Ukraine, Donetsk, pp. 174-184, 1999.
- [24] Sharkovsky, A.N., *Iteration of continuous functions and dynamics of solutions for some boundary value problems* (*Proc. ECIT-98*), Ann. Math. Silesianae, **13**, pp. 243-255, 1999.
- [25] Romanenko, E.Yu., Sharkovsky, A.N., *From boundary value problems to difference equations: A method of investigation of chaotic vibrations*, Intern. J. Bifurcation and Chaos, **9**, n7, pp. 1285-1306, 1999.
- [26] Sharkovsky, A.N., Berezovsky, S.A., *Transitions of "correct-incorrect" numerical calculations for solutions of some problems. "Phase transitions" in computer turbulence*, in *Proc. 2nd Intern. Conf. "Control of Oscillations and Chaos"* (COC'2000), St.Petersburg, Russia, **1**, pp. 6-9, 2000.
- [27] Sharkovsky, O.M., *Dynamical systems generated by boundary value problems. Ideal turbulence. Computer turbulence*, in *Proc. Ukrainian Math. Congress*, **12**, Kiev, pp. 125-129, 2003 (in Ukrainian).
- [28] Sharkovsky, A.N., Berezovsky, S.A., *Phase transitions in correct-incorrect calculations for some evolution problems*, Intern. J. Bifurcation and Chaos, **13**, pp. 1811-1821, 2003.
- [29] Sharkovsky, A.N., Romanenko, E.Yu., Berezovsky, S.A., *Ideal Turbulence: Definition and Models*, in *Proc. Intern. Conf. "Physics and Control"* (20-22 August, 2003), **1**, Petersburg, Russia, pp. 23-30, 2003.
- [30] Sharkovsky, A.N., *Difference equations and boundary value problems*, in *New Progress in Difference Equations, Proc. ICDEA'2001*, Taylor & Francis, pp. 3-22, 2004.
- [31] Sharkovsky, A.N., *Ideal Turbulence: Definition*, in *Proc. ECIT'02*, 2004 (in press).
- [32] Sharkovsky, A.N., Romanenko, E.Yu., *Difference equations and dynamical systems generated by some classes of boundary value problems*, in *Proc. Steklov Math.Inst.*, Moscow, 2004.

ECONOMIC FLUCTUATIONS AND STATISTICAL PHYSICS: THE PUZZLE OF LARGE FLUCTUATIONS

H. Eugene Stanley,¹ Xavier Gabaix,² Parameswaran Gopikrishnan,¹ and Vasiliki Plerou¹

¹Center for Polymer Studies and Department of Physics

Boston University, Boston, MA 02215 USA

²Department of Economics, MIT, Cambridge, MA 02142
and National Bureau of Economic Research, Cambridge, MA 02138

Abstract—*We present an overview of recent research applying ideas of statistical physics to try to better understand puzzles regarding economic fluctuations. One of these puzzles is how to describe outliers, phenomena that lie outside of patterns of statistical regularity. We review evidence consistent with the possibility that such outliers may not exist. This possibility is supported by recent analysis by Plerou et al. of a database containing the bid, ask, and sale price of each trade of every stock. Further, the data support the picture of economic fluctuations, due to Plerou et al., in which a financial market alternates between being in an “equilibrium phase” where market behavior is split roughly equally between buying and selling, and an “out-of-equilibrium phase” where the market is mainly either buying or selling.*

fail for a few outliers, but that there occur similar outliers of every possible size. In fact, if one analyzes only a small data set (say 10^4 data points), then outliers appear to occur as “rare events.” However, when orders of magnitude more data (10^8 data points) are analyzed, one finds orders of magnitude more outliers—so ignoring them is not a responsible option, and studying their properties becomes a realistic goal. One finds that the statistical properties of these “outliers” are identical to the statistical properties of everyday fluctuations. For example, a histogram giving the number of fluctuations of a given magnitude x for fluctuations ranging in magnitude from everyday fluctuations to extremely rare fluctuations (“financial earthquakes”) that occur with a probability of only 10^{-8} is a perfect straight line in a double-log plot.

I. INTRODUCTION

Interactions between economists and physicists have begun to make progress in answering significant questions. In particular, these collaborations have the potential to change the paradigm for understanding economic fluctuations. Until relatively recently, theories of economic fluctuations invoked the label of “outlier” (bubbles and crashes) to describe fluctuations that do not agree with existing theory. These outliers are of interest, as they correspond to extremely large and unpredictable changes of sufficient magnitude to wreak havoc.

The paradigm of “statistical regularity plus outliers” does not exist in the physical sciences. Indeed, if events occur that do not conform to predictions of the appropriate theory, then that theory is immediately relegated to the dust bin and new theories are sought. An example are the “outliers” that led to the demise of classical mechanics, eventually replaced by the theory of relativity.

Traditional economic theory does not predict outliers, but recent analysis of truly huge quantities of empirical data suggests that classic theories not only

An analogy with earthquake research is perhaps not entirely inappropriate. If one studies limited data sets, a paradigm arises in which there are everyday (unnoticeable except by sensitive seismometer) “tremors,” punctuated from time to time by rare events (“earthquakes”). Thanks to the empirical work, we now know that the partition of shocks into “tremors” and “earthquakes” is not valid. Rather, if one examines enough data, one sees that the shocks occur for all possible magnitudes. The law named after Gutenberg and Richter refers to a statistical formula that gives all the data from the smallest tremors to the “big ones.” This law is that the histogram giving the number of shocks of a given size is a straight line in a log-log plot [1], [2], [3]—there are no outliers.

Thus, an inappropriate paradigm can arise when a limited quantity of data are considered in which data are partitioned into everyday events (often describable by one statistical law) and rare events which, since they are not described by the law are terms outliers. Has an inappropriate paradigm arisen in economic research? In economic research, there are fluctuations in stock prices, number of shares trading hands, and total number of fluctuations. Recent empirical studies calculating histograms for all three quantities are lin-

ear on log-log plots (albeit with different slopes). In mathematical language, the occurrence probability of such quantity's fluctuations appear to be described by a power law.

In economics, neither the existence of power laws nor the exact exponents has any accepted theoretical basis. Professionally, empirical laws such as the aforementioned power laws are called “stylized facts,” a term that to my ear always sounds dismissive. Accordingly, some theoretical understanding is urgently needed or else these laws will continue to be largely irrelevant. Of course facts, even facts without any interpretation, may have practical value. For example, the Gutenberg-Richter law enables one to calculate the risk of a shock (tremor or earthquake) of a given magnitude, and hence informs the building codes of Los Angeles and Tokyo. Similarly, the empirical laws governing economic fluctuations enable one to calculate the risk of an economic shock of a given magnitude.

The lack of a coherent theory is unfortunate, especially in economics where facts without theoretical foundation is considered a deplorable situation. Accordingly, my collaborators and I have been seeking to develop a theoretical framework within which to interpret these new empirical facts, and recently some progress is beginning to occur [4], [5]. This work is potentially significant since it provides a theoretical framework within which to interpret the new empirical laws. Specifically, the model fulfills these requirements for such a basic “microscopic” model of the stock market. It is founded on realistic features of the stock market, and reflects the view that market participants have of the functioning of the market, as well as the main determinants of their trading behavior.

II. FIRST DISCOVERY OF SCALING AND UNIVERSALITY

That at least *some* economic phenomena are described by power law tails has been recognized for over 100 years since Pareto investigated the statistical character of the wealth of individuals by modeling them using the *scale-invariant* distribution

$$f(x) \sim x^{-\alpha}, \tag{1}$$

where $f(x)$ denotes the number of people having income x or greater than x , and α is an exponent that Pareto estimated to be 1.5 [6], [7]. Pareto noticed that his result was *universal* in the sense that it applied to nations “*as different as those of England, of Ireland, of Germany, of the Italian cities, and even of Peru*”.

A physicist would say that the universality class of the scaling law (1) includes all the aforementioned countries as well as Italian cities, since by definition two systems belong to the same universality class if they are characterized by the same exponents.

In the century following Pareto's discovery, the twin concepts of scaling and universality have proved to be important in a number of scientific fields [8], [9], [10]. A striking example was the elucidation of the puzzling behavior of systems near their critical points. Over the past few decades it has come to be appreciated that the scale-free nature of fluctuations near critical points also characterizes a huge number of diverse systems also characterized by strong fluctuations. This set of systems includes examples that at first sight are as far removed from physics as is economics. For example, consider the percolation problem, which in its simplest form consists of placing pixels on a fraction p of randomly-chosen plaquettes of a computer screen. A remarkable fact is that the largest connected component of pixels magically spans the screen at a threshold value p_c . This purely geometrical problem has nothing to do, at first sight, with critical point phenomena. Nonetheless, the fluctuations that occur near $p = p_c$ are scale free and functions describing various aspects of the incipient spanning cluster that appears at $p = p_c$ are described by power laws characterized by exponent values that are universal in the sense that they are independent of the details of the computer screen's lattice (square, triangle, honeycomb). Nowadays, the concepts of scaling and universality provide the conceptual framework for understanding the geometric problem of percolation.

It is becoming clear that almost any system comprised of a large number of interacting units has the potential of displaying power law behavior. Since economic systems are in fact comprised of a large number of interacting units has the potential of displaying power law behavior, it is perhaps not unreasonable to examine economic phenomena within the conceptual framework of scaling and universality [8], [9], [10], [11], [12], [13], [14], [15], [16], [17], [18], [19]. We will discuss this topic in detail below.

III. INVERSE CUBIC LAW OF STOCK AND COMMODITY PRICE FLUCTUATIONS

So having embarked on a path guided by these two theoretical concepts, what does one do? Initially, critical phenomena research—guided by the Pareto principles of scaling and universality—was focused finding which systems display scaling phenomena, and

on discovering the actual values of the relevant exponents. This initial empirical phase of critical phenomena research proved vital, for only by carefully obtaining empirical values of exponents such as α could scientists learn which systems have the same exponents (and hence belong to the same *universality class*). The fashion in which physical systems partition into disjoint universality classes proved essential to later theoretical developments such as the renormalization group [10]—which offered some insight into the reasons why scaling and universality seem to hold; ultimately it led to a better understanding of the critical point.

Similarly, our group’s initial research in economics—guided by the Pareto principles—has largely been concerned with establishing which systems display scaling phenomena, and with measuring the numerical values of the exponents with sufficient accuracy that one can begin to identify universality classes if they exist. Economics systems differ from often-studied physical systems in that the number of subunits are considerably smaller in contrast to macroscopic samples in physical systems that contain a huge number of interacting subunits, as many as Avogadro’s number 6×10^{23} . In contrast, in an economic system, one initial work was limited to analyzing time series comprising of order of magnitude 10^3 terms, and nowadays with high frequency data the standard, one may have 10^8 terms. Scaling laws of the form of (1) are found that hold over a range of a factor of $\approx 10^6$ on the x -axis [20], [21], [22], [23], [24]. Moreover, these scaling laws appear to be universal in that they, like the Pareto scaling law, hold for different countries [25], for other social organizations [26], [27], [28], and even for bird populations [29].

Recent attempts to make models that reproduce the empirical scaling relationships suggest that significant progress on understanding firm growth may be well underway [30], [31], [32], [33], leading to the hope of ultimately developing a clear and coherent “theory of the firm.” One utility of the recent empirical work is that now any acceptable theory must respect the fact that power laws hold over typically six orders of magnitude; as Axtell put the matter rather graphically: “*the power law distribution is an unambiguous target that any empirically accurate theory of the firm must hit*” [20].

With this background on power laws and scale invariance in geometry and in economics, we turn now to the well-studied problem of finance fluctuations, where a consistent set of empirical facts is

beginning to emerge. One fact that has been confirmed by numerous, mostly independent, studies is that stock price fluctuations are characterized by a scale-invariant cumulative distribution function of the power law form (1) with $\alpha \approx 3$ [34], [35], [36]. This result is also universal, in the sense that this inverse cubic law exponent is within the error bars of results for different segments of the economy, different time periods, and different countries—and is the same for stock averages as different as the S&P and the Hang Seng [37].

This “inverse cubic law” disagrees with the classic work of Ref. [8] on price fluctuations of cotton, which appear to have display scale free behavior (“no outliers”) but with much fatter tails characterized by $\alpha \approx 1.7$; this work is of interest because if $\alpha < 2$, then the distribution is of the Lévy form. To understand this discrepancy, Matia and collaborators have wondered if the reason for the fatter tails of cotton is that cotton is a commodity, and commodities exist in limited supply so that when a commodity is needed one must sometimes pay exorbitant prices (e.g., electricity in California). Accordingly, they analyzed a large number of commodities, but they found that these commodities have tails described not by $\alpha < 2$ but rather by $\alpha \approx 3$ [38], [39]. Another possible reason is that Mandelbrot analyzed three data sets, each containing only about 2000 points, while the results on stocks typically contain about 40,000 points per stock (and 1000 stocks, or 40,000,000 total data points). This possibility was tested by choosing randomly 2000 points to analyze, but again one cannot obtain $\alpha < 2$. A third possible explanation of this discrepancy is that the cotton market was “out of equilibrium”, and that such out-of-equilibrium markets have fatter tails—a possibility consistent with recent analysis of stock price fluctuations [40], [41]. A fourth possible explanation is that at the time period in which the cotton data were collected, commodities were intrinsically different than they are today when the Matia data were collected, as today commodities are traded in ways not entirely dissimilar to the way that stocks are traded. Still another possibility is that the cotton distribution has $\alpha < 2$ in the central region analyzed in 1963, but ultimately crosses over to power law in the distant tails (not analyzed in 1963). This disagreement led to the development of a class of mathematical processes called *truncated Lévy* distributions—which has attracted the attention of a number of mathematicians and is actually taught in Columbia University’s graduate school of finance [42], [43], [44], [45],

[46], [47], [48], [49]. In any case, one of the challenges of econophysics is to resolve current results with the classic 1963 analysis of Mandelbrot.

Newcomers to the field of scale invariance often ask why a power law does not extend “forever” as it would for a mathematical power law of the form $f(x) = x^{-\alpha}$. This legitimate concern is put to rest by reflecting on the fact that power laws for natural phenomena are not equalities, but rather are asymptotic relations of the form $f(x) \sim x^{-\alpha}$. Here the tilde denotes *asymptotic equality*. Thus $f(x)$ is not “approximately equal to” a power law so the notation $f(x) \approx x^{-\alpha}$ is inappropriate. Similarly, $f(x)$ is not proportional to a power law, so the notation $f(x) \propto x^{-\alpha}$ is also inappropriate. Rather, asymptotic equality means that $f(x)$ becomes increasingly like a power law as $x \rightarrow \infty$. Moreover, crossovers abound in financial data, such as the crossover from power law behavior to simple Gaussian behavior as the time horizon Δt over which fluctuations are calculated increases beyond about a year (i.e., the power law behavior holds for time horizons up to a month or even a year, but for horizons exceeding a year there is a distinct crossover to Gaussian behavior. Such crossovers are characteristic also of other scale-free phenomena in the physical sciences [9], [10], where the Yule distribution often proves quite useful.

For reasons of this sort, standard statistical fits to data are inappropriate, and often give distinctly erroneous values of the exponent α . Rather, one reliable way of estimating the exponent α is to form successive slopes of pairs of points on a log-log plot, since these successive slopes will be monotonic and converge to the true asymptotic exponent α . One finds that successive slopes for the empirical data converge rapidly to a value $\alpha \approx 3$ while successive slopes for the model diverge. While it is clear that a simple three-factor model [50] cannot generate power law behavior, it is less clear why the empirical data analyzed appear at first glance to be well approximated by the model. The first fact is that the region of linearity of the data is not so large as in typical modern studies because the total quantity of data analyzed is not that large, since only a low-frequency time series comprising daily data is used. Only 28,094 records are analyzed [50] (not 4×10^7 as in recent studies [36], [37]) and the model simulations are presented for limited sample size. The second fact is that when one superposes a curved line (the model) on a straight line (the data), the untrained eye is easily tempted to find agreement where none exists—and closer inspec-

tion of Figs. 2–5 of Ref. [50] reveals actually a rather poor agreement between model and data due to the pronounced downward curvature of the model’s predictions [51].

IV. OTHER SCALE-INVARIANT QUANTITIES DESCRIBING ECONOMIC FLUCTUATIONS

Other quantities characterizing stock movements (such as the volatility, share volume traded, and number of trades) also display a range of power law behavior over a range of typically $\approx 10^2$ [52], [53], [54], [55]. The exponents characterizing the power law decays are different for different quantities; it is tempting to conjecture that in finance there may exist a set of relations among the power law exponents found, just as there exist relations among the exponents characterizing different quantities near the critical point. Finally, it is well-known that while the autocorrelation function of price returns decays rapidly, the autocorrelation function of the absolute values of price returns is power-law correlated in time (see [52] and extensive earlier work cited therein).

Consider, for example, the volatility. There are several possible definitions of this quantity, all of which seem to give the same scale invariant properties. But why care about volatility at all? On the cover of the 15 May 2000 issue of Forbes magazine is a large photograph of Henk Paulson, CEO of Goldman Sachs, and the headline quotation “*Volatility is Our Friend.*” Why is this the case? Because it is known that volatility clusters, i.e., there are time correlations in this quantity. Our group has attempted to quantify these correlations, and found evidence of power law behavior [52], [56], [57], [58]. If we plot an economic earthquake such as Black Monday (19 October 1987) on which date most worldwide stock indices dropped 30–50 percent, and then plot and compare the volatility (the absolute value of the fluctuations), we see a big peak in the volatility curve on Black Monday. But even prior to Black Monday the value of the volatility on our graph seems to be particularly unstable; there is some precursor to Black Monday evident in its behavior. One can imagine a computer program that would monitor volatility, not necessarily for the entire market but certainly for an individual stock, and the volatility calculation would need to be updated in real time.

There are correlations in the stock price change, but those correlations have a very short range—on the order of a few minutes—and they decay exponentially in time. Our group calculated the autocorrelation func-

tion of stock-price changes and plotted the logarithm of the function linearly in time; since the logarithm of e^{-x} is $-x$, we get a straight line. In contrast, for the volatility we find that the autocorrelation function is linear on log-log paper, meaning that the correlations in the volatility are power-law in nature. That, in turn, translates to mean they are much, much longer-range in time.

In order to quantify long-range power law volatility correlations, we developed a method of analyzing a non-stationary time series. The volatility of a financial market is non-stationary: there are days when the volatility is quiet and days when it is active. The statistical properties of a volatility time series are changing in time. The standard deviation of that time series is fluctuating wildly on every scale, which is the reason conventional methods are not effective. The method our group has been developing—detrended fluctuation analysis (DFA)—gets rid of trends in the raw data [59], [60], [61], [62]. We take a graph of the volatility expressed in absolute values (i.e., it is always positive) in which we see the peaks that indicate it is a very “noisy” or non-stationary time series, we integrate this time series, and we subtract the mean. This produces an up-and-down “landscape.” We then look for correlations in this landscape. We do this by partitioning the landscape into “windowboxes” of a fixed size, e.g., 200—does the regression fit to the fluctuations in that windowbox? We then calculate for each box the RMS fluctuation around the regression line. Finally, we average the RMS fluctuation for all 40,000 windowboxes of the entire series. With that many windowboxes, we get a very accurate measurement. We call the quantity f . We repeat the entire calculation for windowboxes one-half as big (size 100). Obviously, the smaller the windowbox, the less the fluctuation. This give us the circle for size 100. We repeat this a number of times. When that fluctuation is plotted as a function of windowbox size we find, contrary to what we might expect—that in almost all correlated signals the fluctuations increase as the square root of the windowbox size—the fluctuations instead increase more rapidly than that. That means there is some positive correlation in the signal. This analysis method produces results with very little noise. The data fall very close to the straight line, and the exponent can be obtained with a high degree of accuracy. All this allows us to analyze quantitatively the behavior of the volatility as a function of time and elucidate its correlations. This could be very useful information for people actually working in financial markets.

The distribution of volatility fluctuations has also been the object of extensive study. It was at one time believed by many that the volatility follows a log-normal distribution—i.e., the number of times the volatility has a certain value follows not a Gaussian but a log-normal distribution, i.e., one has $e^{-(\log x)^2}$ not e^{-x^2} . But until our group’s work, no one had studied *all* the data: *every* trade [52]. Our doing it meant we could study relatively rare events, those occurring much less frequently than everyday events. What we find is that the log-normal part of the curve—the middle—though true for the middle, does not describe the tails. The huge volatilities in the tails are described by a different exponent μ . We also see that volatility clusters—i.e., that volatility is correlated in time.

V. CROSS-CORRELATIONS AMONG FLUCTUATIONS OF DIFFERENT STOCKS

Another capability of such a software package could be the ability to determine how the fluctuations of one stock price correlate with those of another. This question of cross-correlation is one we have been studying [63], [64], [65], [66], [67], [68], [69], [70]. To quantify cross-correlations, we draw a circle corresponding to the stock price x and draw a second circle corresponding to the stock price x , say, five minutes later. If we make the difference in the radii proportional to G , the stock price change, then we can think of the market as thousands of circles, each growing and shrinking—a kind of pulsation that is a function of time. The key is that these correlations change in time. Car sales by Ford and GM may be anti-correlated during some time periods and positively correlated during others.

The standard approach to this problem is to calculate, by brute force, a huge square matrix that has as many rows as there are companies in the database. Each element of the matrix is the correlation between the price change of company i and the price change of company j , but to find a genuine correlation we have to be able to distinguish between correlations from coincidences. In order to do that we draw on something developed by Wigner in his work in nuclear physics—random matrix theory. Random matrix theory compares the matrix calculated by brute force from stock market data with a random matrix that also has 1000 rows and 1000 columns—but with every number generated randomly. Somewhere hidden in the huge matrix calculated by brute force from stock market data are the true correlations. To uncover them, we first diagonalize the matrix in order to determine its eigen-

values, and then make a histogram that gives the number of times each given eigenvalue is found. The histogram curve of a random matrix, unlike this one from real data, can be predicted exactly. For a random matrix there is never an eigenvalue > 2.0 . The histogram of the empirical stock price data, on the other hand, contains a significant number of eigenvalues > 2.0 . Some are as big as 5.0. These eigenvalues of necessity must correspond to genuine correlations.

The eigenvalue of a matrix has a corresponding eigenvector—a column matrix of 1000 elements—each element of which is a different weight from each of the 1000 stocks. So we can look at the column vectors that correspond to these deviating, genuinely-correlated eigenvalues and ask: what kind of stocks entered into each of these eigenvectors? What we found, fortunately, has implications for portfolios. If we restart the graph at 2.0—removing the distortions of the random values—and look at the 20 eigenvalues > 2.0 , we see that the stocks that make up most of the weights in the corresponding eigenvectors are almost entirely transportation stocks in the first case, almost entirely paper in the second, almost entirely pharmaceuticals in the third, and so on. In other words, the market *automatically* partitions itself into separate business sectors [69], [70], [71]. Thus a physicist who know nothing about the stock market can mathematically partition the economy into separate business sectors!

The sectors and the quantitative degree to which each constituent firm conforms to the sector can be monitored and updated as a function of time, e.g., every 15 minutes. Firms that belong to the same business sector can be monitored in a kind of rainbow spectrum. The “good” firms sticking to the business sector are assigned to the “violet” end of the spectrum, and the “bad” firms deviating from the sector are assigned to the “red.” When a firm first starts to move to the red end of the spectrum start to deviate, this alerts the trader to consider action.

VI. EQUILBRIUM VS. OUT-OF-EQUILIBRIUM MARKET PHASES

Before concluding, we ask what sort of understanding could eventually develop if one takes seriously the power laws that appear to characterize finance fluctuations. It is tempting to imagine that there might be analogies between finance and known physical processes displaying similar scale-invariant fluctuations. One initially promising analogy was with turbulence: In turbulence, one adds energy at a large scale and this

energy is dissipated at smaller and smaller scales in a scale-invariant fashion. Similarly, if external news is added at a large scale, then this news is dissipated by traders at smaller and smaller scales in a scale-invariant fashion. Despite some initial claims [72], these similarities are not borne out by quantitative analysis—although one finds non-Gaussian statistics, and intermittency, for both turbulence fluctuations and stock price fluctuations, the time evolution of the second moment and the shape of the probability density functions are different for turbulence and for stock market dynamics [73], [74].

More recent work pursues a rather different analogy, phase transitions in spin systems. It is not new to say that the set of all firm fluctuations is like a set of subunit fluctuations in a physics system such as a spin glass. Each fluctuation can be up or down, or any magnitude, and fluctuations interact with one another via interactions that are certainly long-range and of both signs. Further, the interactions change with time. A given subunit fluctuation is influenced (a) by other fluctuations (so the exchange interactions among spins is somewhat like the “herd effect”), and (b) by forces external to the system (so the external field is somewhat like “news” which plays a role in determining the sign and magnitude of fluctuations).

If this crude analogy were to hold even approximately, then a first step should perhaps be to seek to identify the analogs for the price fluctuation problem of field and temperature in the magnetic problem. Stock prices respond to demand, just as the magnetization of an interacting spin system responds to the magnetic field. Periods with large number of market participants buying the stock imply mainly positive changes in price, analogous to a magnetic field causing spins in a magnet to align. Recent work [75] quantifies the relations between price change and demand fluctuations, and finds results reminiscent of phase transitions in spin systems, where the divergent behavior of the response function at the critical point (zero magnetic field) leads to large fluctuations [9]. More precisely, buying and selling behavior in complex financial markets are driven by demand, which can be quantified by the imbalance in the number of shares transacted by buyers and sellers over a time interval Δt .

If demand is the analog of magnetic field, then what is the analog of temperature? To answer this question, Plerou et al. [40], [41] analyze the probability distribution of demand, conditioned on its local noise intensity Σ , and find the surprising existence of a crit-

ical threshold Σ_c separating two market phases. Their findings for the financial market problem are identical to what is known to occur in all phase transition phenomena, wherein the behavior of a system undergoes a qualitative change at a critical threshold K_c of some control parameter K . Plerou et al interpret these two market phases as corresponding to two distinct conditions of the financial market: (a) The “ $\Sigma < \Sigma_c$ market phase”, where the distribution of demand is single peaked with the most probable value being zero, they interpret to be the market *equilibrium phase*, since the price of the stock is such that the probability of a transaction being buyer initiated is equal to the probability of a transaction being seller initiated, and (b) the “ $\Sigma > \Sigma_c$ market phase”, where the distribution of demand is bimodal, they interpret to be the *out-of-equilibrium phase*, since the price of the stock is such that there is an excess of either buyers or of sellers and there is a non-zero net demand for the stock.

It should be possible to design a software package that could be on every trader’s desk allowing instant access to data on any firm in which time is partitioned into two different phases: equilibrium and out-of-equilibrium. Qualitatively and informally many people use those terms in reference to the stock market, but in this case we would be actually *quantifying* the extent to which the market is in or out of equilibrium. If we graph the price-change of a particular stock as a function of time for a sequence of 15-minute intervals and use two different symbols for data points when the market is in equilibrium and for those for when it is out of equilibrium, we notice that in general a stock price is not changing when the market is in equilibrium and is changing when the market is out of equilibrium. This could be useful in that it could be an indicator of the relative stability of an individual stock. When the market is out of equilibrium, the probability that a stock price is going to change is higher than when the market is in equilibrium.

VII. DISCUSSION

Since the evidence for an analogy between stock price fluctuations and magnetization fluctuations near a critical point is backed up by quantitative analysis of finance data, it is legitimate to demand a theoretical reason for this analogy. To this end, we discuss briefly one possible theoretical understanding for the origin of scaling and universality in economic systems. As mentioned above, economic systems consist of interacting units just as critical point systems consist of interacting units. Two units are correlated in what

might seem a hopelessly complex fashion—consider, e.g., two spins on a lattice, which are correlated regardless of how far apart they are. The correlation between two given spins on a finite lattice can be partitioned into the set of all possible topologically linear paths connecting these two spins—indeed this is the starting point of one of the solutions of the two-dimensional Ising model (see Appendix B of [9]). Since correlations decay exponentially along a one-dimensional path, the correlation between two spins would at first glance seem to decay exponentially. Now it is a mathematical fact that the total number of such paths grows exponentially with the distance between the two spins—to be very precise, the number of paths is given by a function which is a product of an exponential and a power law. The constant of the exponential *decay* depends on temperature while the constant for the exponential *growth* depends only on geometric properties of the system [9]. Hence by tuning temperature it is possible to achieve a threshold temperature where these two “warring exponentials” just balance each other, and a previously negligible power law factor that enters into the expression for the number of paths will dominate. Thus power law scale invariance emerges as a result of canceling exponentials, and universality emerges from the fact that the interaction paths depend not on the interactions but rather on the connectivity. Similarly, in economics, two units are correlated through a myriad of different correlation paths; “everything depends on everything else” is the adage expressing the intuitive fact that when one firm changes, it influences other firms. A more careful discussion of this argument is presented, not for the economy but for the critical phenomena problem, in Ref. [10].

VIII. SUMMARY

In summary, physicists are finding this emerging field fascinating. For a long time, physicists did relatively little in economics. A major reason for this is that, until recently, the amount of data routinely recorded concerning financial transactions was insufficient to be useful to physicists. That fact is no longer true. Now every trade is recorded, along with bid-ask quotes for every trade, and these data are made available.

Part of the reason for the invention of the neologism “econophysics” (in the tradition of the neologisms “biophysics,” “astrophysics,” “geophysics”...) was to enable our physics students to persuade the departmental administrators that their dissertation re-

search topics actually belonged in the physics department. The neologism seems to have caught on, and there are now several conferences each year with the word “econophysics” in the title.

Finally, a word of humility with respect to our esteemed economics colleagues is perhaps not inappropriate. Physicists may care passionately if there are analogies between physics systems they understand (like critical point phenomena) and economics systems they do not understand. But why should anyone else care? One reason is that scientific understanding of earthquakes moved ahead after it was recognized [1], [2] that extremely rare events—previously regarded as statistical outliers requiring for their interpretation a theory quite distinct from the theories that explain everyday shocks—in fact possess the identical statistical properties as everyday events; e.g., all earthquakes fall on the same straight line on an appropriate log-log plot. Since economic phenomena possess the analogous property, the challenge is to develop a coherent understanding of financial fluctuations that incorporates not only everyday fluctuations but also those extremely rare “financial earthquakes”.

Acknowledgments

We thank NSF for financial support and we thank our collaborators: L. A. N. Amaral, S. V. Buldyrev, D. Canning, P. Cizeau, S. Havlin, Y. Lee, Y. Liu, P. Maass, R. N. Mantegna, K. Matia, M. Meyer, B. Rosenow, M. A. Salinger, and M. H. R. Stanley.

REFERENCES

[1] B. Gutenberg and C. F. Richter, *Seismicity of the Earth and Associated Phenomenon, 2nd Edition* (Princeton University Press, Princeton, 1954)

[2] D. L. Turcotte, *Fractals and Chaos in Geology and Geophysics* (Cambridge University Press, Cambridge, 1992)

[3] J. B. Rundle, D. L. Turcotte, and W. Klein, *Reduction and Predictability of Natural Disasters* (Addison-Wesley, Reading MA, 1996).

[4] X. Gabaix, P. Gopikrishnan, V. Plerou, and H. E. Stanley, “A Theory of Power-Law Distributions in Financial Market Fluctuations,” *Nature* **423** (2003) 267–270.

[5] X. Gabaix, P. Gopikrishnan, V. Plerou, and H. E. Stanley, “A Simple Theory of Asset Market Fluctuations, Motivated by the Cubic and Half Cubic Laws of Trading Activity in the Stock Market,” *Quarterly Journal of Economics* (submitted).

[6] V. Pareto, *Cours d’Economie Politique* (Lausanne, Paris, 1897)

[7] S. Solomon and P. Richmond, “Stable power laws in variable economies; Lotka-Volterra implies Pareto-Zipf” *Eur Phys J B* **27** (2002) 257-261.

[8] B. B. Mandelbrot, “The Variation of Certain Speculative Prices,” *J. Business* **36** (1963) 394–419.

[9] H. E. Stanley, *Introduction to Phase Transitions and Critical Phenomena* (Oxford University Press, Oxford, 1971).

[10] H. E. Stanley, “Scaling, Universality, and Renormalization: Three Pillars of Modern Critical Phenomena,” *Rev. Mod. Phys.* **71** (1999) S358–S366.

[11] H. Takayasu, ed., *Empirical Science of Financial Fluctuations: The Advent of Econophysics* (Springer, Berlin, 2002).

[12] R. N. Mantegna and H. E. Stanley, *An Introduction to Econophysics: Correlations and Complexity in Finance* (Cambridge University Press, Cambridge, 2000)

[13] J.-P. Bouchaud, “Power Laws in Economics and Finance: Some Ideas from Physics,” *Quantitative Finance* **1** (2001) 105–112.

[14] J. P. Bouchaud and M. Potters, *Theory of Financial Risk* (Cambridge University Press, Cambridge, 2000).

[15] H. Levy, M. Levy and S. Solomon, *Microscopic Simulation of Financial Markets* (Academic Press, New York, 2000)

[16] B. M. Roehner, *Hidden Collective Factors in Speculative Trading* (Springer, Berlin, 2001).

[17] B. M. Roehner, *Patterns of Speculation* (Cambridge Univ Press, Cambridge, 2002).

[18] W. Paul and A. Baschnagel, *Stochastic processes from physics to finance* (Springer, Berlin, 1999).

[19] J. Voit, *The Statistical Mechanics of Financial Markets* (Springer, Berlin, 2001).

[20] R. L. Axtell, “Zipf Distribution of US Firm Sizes” *Science* **293** (2001) 1818–1821.

[21] M. H. R. Stanley, S. V. Buldyrev, S. Havlin, R. Mantegna, M. A. Salinger, and H. E. Stanley, “Zipf Plots and the Size Distribution of Firms,” *Econ. Lett.* **49** (1996) 453–457

[22] M. H. R. Stanley, L. A. N. Amaral, S. V. Buldyrev, S. Havlin, H. Leschhorn, P. Maass, M. A. Salinger, and H. E. Stanley, “Scaling Behavior in the Growth of Companies,” *Nature* **379** (1996) 804–806.

[23] L. A. N. Amaral, S. V. Buldyrev, S. Havlin, H. Leschhorn, P. Maass, M. A. Salinger, H. E. Stanley, and M. H. R. Stanley, “Scaling Behavior in Economics: I. Empirical Results for Company Growth,” *J. Phys. I France* **7** (1997) 621–633.

[24] S. V. Buldyrev, L. A. N. Amaral, S. Havlin, H. Leschhorn, P. Maass, M. A. Salinger, H. E. Stanley, and M. H. R. Stanley, “Scaling Behavior in Economics: II. Modeling of Company Growth,” *J. Phys. I France* **7** (1997) 635–650.

[25] H. Takayasu and K. Okuyama, “Country Dependence on Company Size Distributions and a Numerical Model Based on Competition and Cooperation,” *Fractals* **6** (1998) 67–79.

[26] V. Plerou, L. A. N. Amaral, P. Gopikrishnan, M. Meyer, and H. E. Stanley, “Similarities between the Growth Dynamics of University Research and of Competitive Economic Activities” *Nature* **400** (1999) 433–437.

[27] D. Canning, L. A. N. Amaral, Y. Lee, M. Meyer, and H. E. Stanley, “A Power Law for Scaling the Volatility of GDP Growth Rates with Country Size,” *Econ. Lett.* **60** (1998) 335–341.

[28] Y. Lee, L. A. N. Amaral, D. Canning, M. Meyer, and H. E. Stanley, “Universal features in the growth dynamics of complex organizations” *Phys. Rev. Letters* **81** (1998) 3275–3278.

[29] T. Keitt and H. E. Stanley, “Scaling in the Dynamics of North American Breeding-Bird Populations,” *Nature* **393** (1998) 257.

[30] L. A. N. Amaral, S. V. Buldyrev, S. Havlin, M. A. Salinger,

- and H. E. Stanley, "Power Law Scaling for a System of Interacting Units with Complex Internal Structure," *Phys. Rev. Lett.* **80** (1998) 1385–1388.
- [31] J. Sutton, "The Variance of Firm Growth Rates: The Scaling Puzzle," *Physica A* **312** (2002) 577.
- [32] F. Cecconi, M. Marsili, J. R. Banavar, and A. Maritan, "Diffusion, Peer Pressure, and Tailed Distributions," *Phys. Rev. Lett.* **89** (2002) 088102.
- [33] M. Wyart and J.-P. Bouchaud, "Statistical Models for Company Growth," cond-mat/0210479 (October 2002).
- [34] T. Lux, "The Stable Paretian Hypothesis and the Frequency of Large Returns: An Examination of Major German Stocks," *Appl. Finan. Econ.* **6** (1996) 463–475.
- [35] P. Gopikrishnan, M. Meyer, L. A. N. Amaral, and H. E. Stanley, "Inverse Cubic Law for the Distribution of Stock Price Variations," *Eur. Phys. J. B* **3** (1998) 139–140.
- [36] V. Plerou, P. Gopikrishnan, L. A. N. Amaral, M. Meyer, and H. E. Stanley, "Scaling of the Distribution of Price Fluctuations of Individual Companies," *Phys. Rev. E* **60** (1999) 6519–6529.
- [37] P. Gopikrishnan, V. Plerou, L. A. N. Amaral, M. Meyer, and H. E. Stanley, "Scaling of the Distributions of Fluctuations of Financial Market Indices," *Phys. Rev. E* **60** (1999) 5305–5316.
- [38] K. Matia, L. A. N. Amaral, S. Goodwin, and H. E. Stanley, "Non-Lévy Distribution of Commodity Price Fluctuations" *Phys. Rev. E: Rapid Communications* **66** (2002) 045103. cond-mat/0202028.
- [39] K. Matia, Y. Ashkenazy, and H. E. Stanley, "Multifractal Properties of Price Fluctuations of Stocks and Commodities," *Europhys. Lett.* **61** (2003) 422–428.
- [40] V. Plerou, P. Gopikrishnan, and H. E. Stanley, "Two-Phase Behaviour of Financial Markets," *Nature* **421**, 130 (2003). cond-mat/0111349.
- [41] V. Plerou, P. Gopikrishnan, and H. E. Stanley, "Symmetry Breaking in Stock Demand", *Phys. Rev. E* (submitted) cond-mat/0111349.
- [42] R. N. Mantegna and H. E. Stanley "Stochastic Process with Ultraslow Convergence to a Gaussian: the Truncated Lévy Flight," *Phys. Rev. Lett.* **73** (1994) 2946–2949.
- [43] R. N. Mantegna and H. E. Stanley, "Scaling Behavior in the Dynamics of an Economic Index" *Nature* **376** (1995) 46–49.
- [44] B. Podobnik, P. Ch. Ivanov, Y. Lee, A. Chessa, and H. E. Stanley, "Systems with correlations in the variance: Generating power law tails in probability distributions" *Europhysics Letters* **50** (2000) 711-717
- [45] R. N. Mantegna and H. E. Stanley, "Ultra-Slow Convergence to a Gaussian: The Truncated Lévy Flight" in *Lévy Flights and Related Topics in Physics* [Proc. 1994 International Conf. on Lévy Flights], edited by M. F. Shlesinger, G. M. Zaslavsky, and U. Frisch (Springer, Berlin, 1995), pp. 300–312.
- [46] R. N. Mantegna and H. E. Stanley, "Modeling of Financial Data: Comparison of the Truncated Lévy Flight and the ARCH(1) and GARCH(1,1) Processes" [Proc. Int'l IUPAP Conf. on Statistical Physics, Taipei], *Physica A* **254** (1998) 77–84.
- [47] B. Podobnik, P. Ch. Ivanov, Y. Lee, and H. E. Stanley, "Scale-invariant Truncated Lévy Process," *Europhysics Letters* **52** (2000) 491–497.
- [48] P. Ch. Ivanov, B. Podobnik, Y. Lee, and H. E. Stanley (2001), "Truncated Lévy Process with Scale-Invariant Behavior" [Proc. NATO Advanced Research Workshop on Application of Physics in Economic Modeling, Prague], *Physica A* **299**, 154–160.
- [49] J. A. Skjeltorp (2001), "Scaling in the Norwegian Stock Market," *Physica* **283**, 486–528.
- [50] B. LeBaron, "Stochastic Volatility as a Simple Generator of Financial Power Laws and Long Memory," *Quantitative Finance* **2** (2001) 621–631.
- [51] H. E. Stanley and V. Plerou, "Scaling and Universality in Economics: Empirical results and Theoretical Interpretation" *Quantitative Finance* **1** (2001) 563–567.
- [52] Y. Liu, P. Gopikrishnan, P. Cizeau, M. Meyer, C.-K. Peng and H. E. Stanley, "The Statistical Properties of the Volatility of Price Fluctuations," *Phys. Rev. E* **60** (1999) 1390–1400.
- [53] V. Plerou, P. Gopikrishnan, L. A. N. Amaral, X. Gabaix, and H. E. Stanley, "Diffusion and Economic Fluctuations," *Phys. Rev. E (Rapid Communications)* **62** (2000) 3023–3026.
- [54] P. Gopikrishnan, V. Plerou, X. Gabaix, and H. E. Stanley, "Statistical Properties of Share Volume Traded in Financial Markets," *Phys. Rev. E (Rapid Communications)* **62** 4493–4496
- [55] V. Plerou, P. Gopikrishnan, X. Gabaix, L. A. N. Amaral, and H. E. Stanley, "Price Fluctuations, Market Activity, and Trading Volume" [Proc. 2000 Santa Fe Econophysics Conference], *Quantitative Finance* **1** (2001) 262–269.
- [56] Y. Liu, P. Cizeau, M. Meyer, C.-K. Peng, and H. E. Stanley, "Quantification of Correlations in Economic Time Series" *Physica A* **245** (1997) 437–440.
- [57] P. Cizeau, Y. Liu, M. Meyer, C.-K. Peng, and H. E. Stanley, "Volatility distribution in the S&P500 Stock Index" *Physica A* **245** (1997) 441–445.
- [58] B. Podobnik, K. Matia, A. Chessa, P. Ch. Ivanov, Y. Lee, and H. E. Stanley, "Time Evolution of Stochastic Processes with Correlations in the Variance: Stability in Power-Law Tails of Distributions" *Physica A* **300** (2001) 300-309.
- [59] C.-K. Peng, S. V. Buldyrev, S. Havlin, M. Simons, H. E. Stanley, and A. L. Goldberger, "On the Mosaic Organization of DNA Sequences," *Phys. Rev. E* **49** (1994) 1691–1695.
- [60] K. Hu, Z. Chen, P. Ch. Ivanov, P. Carpena, and H. E. Stanley, "Effect of Trends on Detrended Fluctuation Analysis" *Phys. Rev. E* **64** (2001) 011114-1 physics/0103018.
- [61] Z. Chen, P. Ch. Ivanov, K. Hu, and H. E. Stanley, "Effect of Nonstationarities on Detrended Fluctuation Analysis" *Phys. Rev. E* **65** (2002) 041107-1 physics/0111103.
- [62] J. W. Kantelhardt, S. Zschiegner, E. Koscielny-Bunde, S. Havlin, A. Bunde, and H. E. Stanley, "Multifractal Detrended Fluctuation Analysis of Nonstationary Time Series," *Physica A* **316** (2002) 87
- [63] T. Guhr, A. Müller-Groeling, and H. A. Weidenmüller, "Random-Matrix Theories in Quantum Physics: Common Concepts," *Phys. Reports* **299** (1998) 189–425.
- [64] M. L. Mehta and F. J. Dyson, "Statistical Theory of the Energy Levels of Complex Systems. V," *J. Math. Phys.* **4** (1963) 713–719.
- [65] F. J. Dyson, "The Distribution of Singular Values of Certain Random Matrices," *Revista Mexicana de Física* **20** (1971) 231.
- [66] A. M. Sengupta and P. P. Mitra, "Distributions of Singular Values for Some Random Matrices," *Phys. Rev. E* **60** (1999) 3389–3392.
- [67] L. Laloux, P. Cizeau, J.-P. Bouchaud and M. Potters, "Noise

- Dressing of Financial Correlation Matrices,” *Phys. Rev. Lett.* **83** (1999) 1469–1482.
- [68] V. Plerou, P. Gopikrishnan, B. Rosenow, L. A. N. Amaral, and H. E. Stanley, “Universal and Nonuniversal Properties of Financial Cross-Correlation Matrices,” *Phys. Rev. Lett.* **83** (1999) 1471–1475.
- [69] P. Gopikrishnan, B. Rosenow, V. Plerou, and H. E. Stanley, “Quantifying and Interpreting Collective Behavior in Financial Markets,” *Phys. Rev. E: Rapid Communications* **64** (2001) 035106.
- [70] V. Plerou, P. Gopikrishnan, B. Rosenow, L. A. N. Amaral, T. Guhr, and H. E. Stanley, “A Random Matrix approach to Financial Cross-Correlations” *Phys. Rev. E* **65** (2002) 066126 cond-mat/0108023.
- [71] B. Rosenow, V. Plerou, P. Gopikrishnan, and H. E. Stanley, “Portfolio Optimization and the Random Magnet Problem,” *Europhys. Lett.* **59** (2002) 500–506 cond-mat/0111537.
- [72] S. Ghashgaie, W. Breymann, J. Peinke, P. Talkner, and Y. Dodge, “Turbulent Cascades in Foreign Exchange Markets,” *Nature* **381** (1996) 767–770.
- [73] R. N. Mantegna and H. E. Stanley, “Turbulence and Exchange Markets,” *Nature* **383** (1996) 587–588.
- [74] R. N. Mantegna and H. E. Stanley, “Stock Market Dynamics and Turbulence: Parallel Analysis of Fluctuation Phenomena” [Proc. International Conference on Pattern Formation in Fluids and Materials], *Physica A* **239** (1997) 255–266.
- [75] V. Plerou, P. Gopikrishnan, X. Gabaix, and H. E. Stanley, “Quantifying Stock Price Response to Demand Fluctuations,” *Phys. Rev. E* **66** (2002) 027104 cond-mat/0106657.

Part II
Contributed Papers

Nonparametric embedding of dynamical systems

M. Abel and K. Ahnert

Institute of Physics, University of Potsdam,
Potsdam, Germany

e-mail: markus@stat.physik.uni-potsdam.de

WWW: <http://www.stat.physik.uni-potsdam.de/~markus>

Abstract—*We present first results using nonparametric functions for embedding. The method works using an iterative nonparametric regression procedure to estimate functional dependencies; it is robust against noise. A quantitative measure for the importance of terms is given by the individual correlation of terms with their residuals. We illustrate the functioning by the well-known example of the Lorenz-system numerically. This way we work out the basis for the application to experimental data.*

I. INTRODUCTION

In time-series analysis, one of the main question is the construction of a model in embedding space, minimal in mathematical complexity but maximal in its ability to reproduce the dynamics of a measured system. In experimental analysis the information about the process dynamics is usually obtained by measuring of one dynamical variable at discrete times. From these measurements, the dynamics of the system can in principle be reconstructed from a scalar time series using time-delayed coordinates [1]. The set of equations in embedding space can be estimated and approximated. In this paper we present an estimation procedure of the dynamical system in phase space by an additive functional structure of state variables. We show first results concerning functional dependencies in reconstruction space. Ongoing work [7] includes a full nonlinear analysis of the reconstructed dynamical system (stability, Lyapunov-exponents, etc.). The nonparametric estimation has been developed in statistical sciences [3] and it is robust against noise. Basically, a multidimensional function relation is mapped to a sum of nonlinear functions. The motivation for such modeling is that many chaotic systems which are described by ODE(s) possess an additive structure. We give an outline of the method by means of numerically simulated data from the Lorenz system as a standard example.

Many of the results shown are in the first stage of research. We decided to present them anyway to spark

a scientific discussion about the possible use of statistical approaches in nonlinear dynamics. To our opinion the joint application of statistical and nonlinear dynamical methods bears much potential to find very general descriptions of dynamical systems with data analysis.

II. MODELING IN EMBEDDING SPACE

There exist several excellent reviews and books to the topic [2], [1]. Therefore, we only briefly repeat some basics which are necessary below. Hereafter we consider an attractor A of a dynamical system with dimension r . An embedding is a smooth diffeomorphism from A to some space R^m ; thus the differential structure of A is preserved under transformation. In real experiments, the state space variables are accessed by a measurement function; we will not treat this issue here, since our aim is to check the general functioning of our method for the best-possible case. So, we perform numerical simulations for a model system to obtain time series of various variables in “continuous” time. We then discard all but one variables and construct a dynamical system in embedding space.

The goal of many research groups is the identification of geometrical and dynamical system properties, as fractal dimensions of any kind, information, Lyapunov exponents, fixed points, stable and unstable manifolds etc.. We will show first steps towards a modeling by nonparametric additive embedding [3].

We consider a system governed by a set of ODE’s:

$$\dot{\vec{x}} = \vec{F}(\vec{x}), \quad (1)$$

where $x \in R^n$, $F : R^n \mapsto R^n$. This set of equations defines the flow F_t in phase space. We assume that there exists an attractor $A \subset R^n$ with box-counting dimension d , $k \leq n$. In [1] it has been shown that almost every smooth map $\Psi : R^k \mapsto R^m$, $m > 2d$, is an embedding, i.e. a smooth diffeomorphism from A onto its image $\Psi(A)$.

Due to differentiability, the whole dynamics is mapped and the trajectory $\xi(t) = \Psi(x(t))$ obeys an

ODE in embedding space:

$$\dot{\vec{\xi}} = \vec{\Phi}(\vec{\xi}), \quad (2)$$

with $\xi \in R^m$, $F : R^m \mapsto R^m$. In this article, we focus on *additive* models for Φ_i and show how to obtain them by numerical analysis.

The standard embedding uses the delay-coordinate map $H(f, \tau)$ with f a smooth function on $M \subset R^k \mapsto R$, and $\tau \in R$ some real number [1]. One obtains

$$H(f, \tau) = (f(x), f(F_{-\tau}(x)), f(F_{-2\tau}(x)), \dots, f(F_{-(m-1)\tau}(x))) . \quad (3)$$

The particular case of f the identity is included (which is used below). We identify above the embedding map Ψ with H , the coordinates in embedding space are then $\xi_0 = f(x)$, $\xi_1 = f(F_{-\tau}(x))$, etc. . We test our ideas about nonparametric, additive embedding by means of the delay-coordinate embedding on the well understood Lorenz-system.

III. NONPARAMETRIC EMBEDDING

To find a dynamical system in embedding space, several approaches exist. [2]. The probably most general one is the concept of locally linear fits, parametric procedures use polynomial fits or neural networks. The problem with local linear fitting is that one cannot find a general analytic expression nor is it possible to visualize the results in dimensions $D > 2$. Polynomial ansatzes tend to involve too many terms for accurate reproduction and analytical treatment; for neural networks a physical interpretation is very hard.

Let us assume the time derivatives $\dot{\xi}$ in embedding space as given. Assuming ergodicity, each measurement in time can be considered as a different realization of the flow. The best estimator in the least-square sense [2], [4] is:

$$\Phi_i = E \left[\dot{\xi}_i \mid \xi_0, \dots, \xi_m \right], \quad (4)$$

with $E[\]$ the expectation value operator. This is the basis for local linear fitting and other nearest neighbor methods. The neighbors of the point x are used for an estimate of the above expectation value. In an additive model (AM)

$$\Phi_i = \sum_{j=1}^m \phi_{ij}(\xi_j) + \epsilon_i, \quad (5)$$

the functions ϕ_{ij} are given in general, nonparametric form, ϵ_i is the modeling error. An estimate for the

constituents ϕ_{ij} is found using the iterative backfitting procedure, where the expectation value operator is applied alternately on each variable to obtain a better estimate for the next iteration step [3]. For the application of this statistical approach to spatio-temporal data analysis, see [5], [4]. We have implemented a moving average and the more convenient smoothing spline procedure, the functions are given in numerical form accordingly. The results below are obtained by spline smoothing [8].

Equivalent to the minimization of the least-square error is the maximization of the correlation between rhs and lhs in Eq. 5. The correlation C_{ij} between the j th term in the sum (5) with sum of the remaining terms gives an indication of its significance for the model, e.g. for $j = 1$, calculate $C_{i1} = C \left[\phi_{i1} ; \Phi_i - \sum_{j=2}^m \phi_{ij} \right]$. If the correlation is close to one the model is good, for correlation close to zero the model is not capable to approximate the dynamics, for intermediate values it can be suitable to estimate a stochastic model using the residual error ϵ .

The additive model approximates best the hypersurface in phase space defined by the flow Φ in a statistical sense. The dynamical and geometrical properties can be checked by a nonlinear analysis of the model. Predictions are possible on the basis of the obtained model.

One drawback of the method is that the functions ϕ_{ij} are given in purely numerical form. Asymptotic properties and errors due to missing data have to be treated with great care. If one fits analytical functions to the estimated ϕ_{ij} after the backfitting procedure, one can arrive at useful dynamical equations in embedding space, where the ϕ_{ij} can be visualized directly. Consider, e.g., a function like $\exp(\xi)$ which is badly represented by a polynomial, but rather recognizable in a 2D graph - fitting a 1D function is much easier than fitting in higher dimensions.

A natural criticism to an additive model is the absence of "mixing" terms like products $\xi_i \dot{\xi}_j$. In principle it is not excluded that a transformation exists which transforms products to a pure additive structure, as e.g. the logarithmic transform. Problems seem to arise if products and sums are mixed like in $\xi_i \dot{\xi}_j + \xi_k$. We find that functions with two arguments approximate well the geometry in embedding space, this coincides with observations from neural networks [6] (a two-layer perceptron seems to suffice to approximate the dynamics), we consequently do not go beyond.

IV. RESULTS

As many others, we use the Lorenz system

$$\dot{x} = -\sigma(y - x) \tag{6}$$

$$\dot{y} = -xz - rx - y \tag{7}$$

$$\dot{z} = xy - bz \tag{8}$$

with $\sigma = 10$, $b = 8/3$, $r = 28$. With these parameters, the attractor of the system has box-counting dimension $d = 2.01$ and to almost certainly find an embedding, one should use $m = 5$. At this point we recall that already mappings with $m \leq 2d$ can be an embedding. We present results for $m = 3$ and discuss some for $m = 4$, a detailed presentation is given elsewhere [7].

The data have been generated by fourth order Runge–Kutta integration with time step $t = 0.01$. The first variable is used for the delay-coordinate map with the standard value $\tau = 0.18$. Using different delays in each delay coordinate, did not change results substantially. Since we are given the derivative \dot{x} , we automatically have the derivative of the embedding coordinates – in real experiments derivatives have to be calculated from data [4]. We have assembled $N = 150000$ data points, including transients. The latter can be used for the estimation since they contain information about the system, too. A dependence of the results on N is not discussed here, the main change for fewer data is seen in the tails of the functions with higher error bars.

First, an estimate for the embedding dimension is determined using the correlations of local linear estimation (this corresponds to a crude approximation of the correlation dimension). So, the general model $\dot{\xi}_i = F(\vec{\xi}_i)$ is estimated yielding an almost perfect correlation $C = 0.998$ and $C = 0.9995$ for embedding dimension three and four, respectively. In a statistical sense, we consequently do not expect much better modeling in four dimensions, dynamically it may well be the case that the fourth dimension is crucial; a detailed inspection is subject of current research. Below, we illustrate the method showing results for the probably imperfect three dimensional case.

A straightforward application of backfitting to a three-dimensional delay coordinate vector plus derivatives yields for the first embedding equation $\dot{\xi}_i = \sum_{j=1}^m \phi_{ij}(\xi_j)$ the functions displayed in Fig. 1. The correlation $C_0 = C[\dot{\xi}_1; \sum_{j=1}^4 \Phi_j(\xi_j)] = 0.998$ indicating a very good model, the same holds for the second coordinate. In contrast to this, we ob-

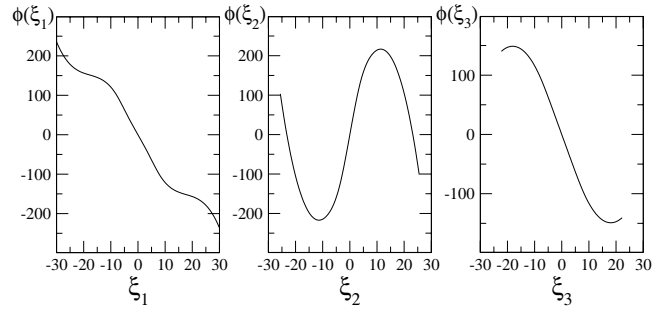


Fig. 1. Typical result for nonparametric, nonlinear functions obtained by the backfitting algorithm using smoothing splines, the three functions for the first component ξ_1 , $\phi_{11}(\xi_1)$, $\phi_{12}(\xi_2)$, and $\phi_{13}(\xi_3)$ are shown. Note the strongly nonlinear form of the functions.

tain $C_0 = 0.92$ for the third coordinate showing that some dynamics is missing. To obtain better correlations, one can generalize the model to functions depending on two variables [8]: there exist three possibilities, e.g. for ξ_1 : $\dot{\xi}_1 = \phi_{12}(\xi_1, \xi_2) + \phi_{13}(\xi_1, \xi_3)$, $\dot{\xi}_2 = \phi_{23}(\xi_2, \xi_3) + \phi_{21}(\xi_1)$. For each combination the correlations are calculated and the resulting functions are inspected. On this basis one finds the best correlation for the model $\dot{\xi}_3 = \phi_1(\xi_1) + \phi_{23}(\xi_2, \xi_3)$ (Fig. 2). For a prediction of the

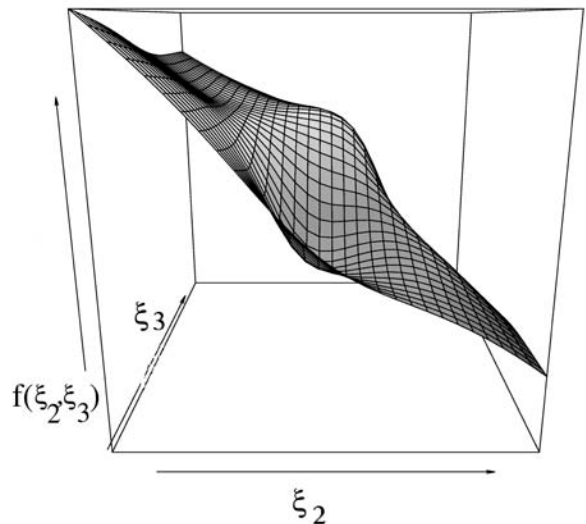


Fig. 2. Thin-plate spline estimate for the function $\phi_{23}(\xi_2, \xi_3)$ for the third component in embedding space. An approximation with polynomials is difficult.

dynamics, one has to integrate the dynamics with the found functions, as given in terms of splines. We did

so for the additive model (5). As a basic test, we analyzed the fixed points to successfully recover the fixed points as found by simply plotting the delay coordinate vector. The integration with a Runge-Kutta 4th order scheme yield for a three dimensional embedding two limit cycles about the elliptic fixed points. That means that either the dynamical system is not complete and one has to go to higher embedding dimensions or the fitting procedure is not very good. Indeed, for embedding dimension five, we find in the projection to the first 3 coordinates a set of limit cycles lying on the orbits of the embedded chaotic attractor, see Fig. 3. For higher dimensions, no chaos is found either. The reason probably lies in the restriction one imposes by the additive structure of the model. The consequences a given structure of a dynamical system has on the topology of the attractor are an open research field. It seems that at least for the procedure we use, the structure of a low dimensional dynamical system in embedding space has to be similar to the original one. Consequently, the next step

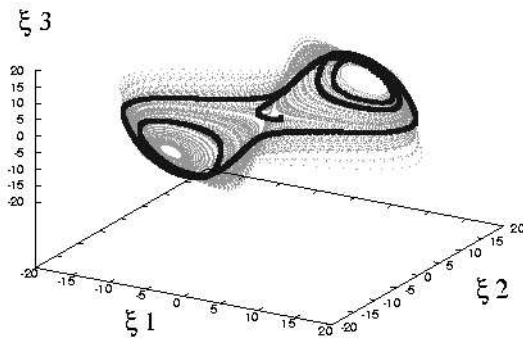


Fig. 3. Plot of a set of trajectories in embedding space on top of the embedded attractor (grey dots, $\xi_i = x(t - (i - 1) * \tau)$). The evolution for 19 different initial conditions is shown (filled squares).

is to integrate functions of two arguments, as shown above, this work is ongoing. A quick fit with analytical expressions did not yield satisfying results, the integrated system was globally unstable.

V. CONCLUSIONS

We have presented a consequent approach to find numerical and analytical model systems in embedding space. The basic idea is to reduce the multi-dimensional local linear model to an additive one. This is achieved by projection of the embedding variables onto some 1 or two dimensional subspaces

where we can estimate the involved nonlinear functions numerically in a nonparametric way. This nonparametric approach has the major advantage that one does not need to choose beforehand a certain basis in which the functions are given (like, e.g., polynomials). Thus combinations of, e.g., polynomials, exponentials, and trigonometric functions are possible to be estimated *a posteriori*.

The method has been applied to the Lorenz-system with standard parameters. Transients can be used and are even useful to cover the whole space investigated, leading to a more homogeneous data base. The reconstruction of the time-continuous system yields promising results: the fixed point structure has been recovered almost perfectly; the *local* topology of the embedded system could be reproduced in a low dimensional space. Global quantities, like Lyapunov exponents, are not yet determined correctly. One could interpret the findings as an “effective” Lorenz system with smaller parameter r . Ongoing research concerns the analysis of functions dependent on two variables and the general problem of the topology of dynamical systems. Future investigations will concern stability analysis and Lyapunov exponents in embedding space for a full and quantitative characterization of the found dynamical systems. We think that the development and the application of such a kind of analysis can guide towards a systematic procedure to identify dynamical systems of simple structure and analytical value in embedding space.

REFERENCES

- [1] T. Sauer, J. Yorke, and M. Casdagli. Embeddology. *J. Stat. Phys.*, 65(3/4):579–615, 1991.
- [2] H. Kantz and T. Schreiber. *Nonlinear time series analysis*. Cambridge University Press, 1997.
- [3] T.J. Hastie and R.J. Tibshirani. *Generalized Additive Models*. Chapman and Hall, London, 1990.
- [4] M. Abel. Nonparametric modeling and spatio-temporal data analysis. *Int. J. Bif. Chaos*, 14(6), 2004.
- [5] H. U. Voss, M. Buenner, and M. Abel. Identification of continuous spatio-temporal systems. *Phys. Rev. E*, 57(3):2820–2823, 1998; H. U. Voss, P. Kolodner, M. Abel, and J. Kurths. Amplitude equations from spatio-temporal binary-fluid convection data. *Phys. Rev. Lett.*, 83(17):3422–3425, 1999.
- [6] A. Priel and I. Kanter. Time series generation by recurrent neural networks. *Ann. Math. Art. Int.*, 39(3):315–332, 2003.
- [7] M. Abel, K. Ahnert, S. Mandelj and J. Kurths. in preparation
- [8] 1D functions are obtained by own software, 2D ones by using the libraries of the R-project: <http://www.r-project.org>.

NONLINEAR FORECASTING OF EARTHQUAKES: A DECADE OF RESULTS AND FUTURE WORK

E. Ivo Alves

Centro de Geofísica da Universidade de Coimbra,
Av. Dias da Silva, 3000-134 Coimbra, Portugal
e-mail: livo@ci.uc.pt

Abstract—*In 1994, a new earthquake forecasting method was developed, that integrated in a neural network several forecasting tools that had been originally developed for financial analysis. This method was tested with the seismicity of the Azores, predicting the July, 1998, and the January, 2004, earthquakes, albeit within very wide time and location windows. Work is beginning to integrate physical precursors in the neural network, in order to narrow the forecasting windows.*

I. INTRODUCTION

When looking for analytical tools designed to forecast time-series, it was found that the practical domain in which they are most commonly used is financial forecasting – especially for the prediction of trends in the stocks, bonds, commodities and currencies markets [1] – where these tools take the name “financial oscillators”.

Time-series of earthquake parameters are also of a chaotic nature, often with comparable fractal dimensions, and testing the financial oscillators on seismicity was a natural step.

The transposition of scenery appears to be fairly straightforward. Instead of analysing a series of quotes in order to predict the next quote, one has to analyse a series of seismic quiescences (periods of time between observed earthquakes), effects and epicentral locations in order to predict the next quiescence, effects and local.

A natural doubt can arise by now: if a predictive model must be related to the process it tries to predict, and there is no relationship between the fluctuation mechanisms of markets and seismic mechanisms, why and how should this approach work?

Indeed, there is an important relationship because both are deterministic non-periodic processes - chaotic processes.

But there is still a more important reason for using these "financial" tools: they reduce the degree of chaos in the analysed sequence, making it more predictable.

The fractal dimension of a system is a measure of

its degree of chaoticity. The movement of a particle in the real plane can take dimensions between 1 (completely deterministic) and 2, in the case of Brownian movement (completely random). We expect that a sequence of, say, earthquake magnitudes, will have a fractal dimension between 1 and 2. If we calculate that dimension and then the dimension of the sequence of moving averages (the simplest oscillator, in which most others are based) we find such a reduction of fractal dimension - a reduction of chaos [2].

The evaluation of the effects of an earthquake can be made resorting to seismic magnitudes or intensities. The first one has the natural advantage of being quantitative and directly proportional to the liberated energy but has a serious shortcoming: the available data-series only begin in the 20th century. If one is to forecast damaging earthquakes, one needs to study very long time series – historical seismicity – hence resort to semi-quantitative intensity data.

This, and the need to predict those earthquakes that are effectively damaging, led us to work with Modified Mercalli Intensities and to try and find a method that would deal with semi-quantitative data.

II. THE OSCILLATORS

Since these are intended to be periodic functions, one must first choose a time-sequence

$x_i, i = 1, 2, \dots, n$ (events), and a period P .

The following formulas intend to represent the developed computational algorithms, rather than being a rigorous mathematical description of each function [1]. The chosen oscillators were:

A. Moving Averages (MA)

$$MA(P)_i = (x_i + x_{i-1} + \dots + x_{i-P+1}) / P$$

B. MA Convergence-Divergence (MACD)

Let there be two MA's of different periods, P and Q , such that $P > Q$. Then,

$$MACD(P, Q)_i = MA(P)_i - MA(Q)_i$$

C. Relative Strength Index (RSI)

Let u be the average of positive variations in the considered period P and let d be that of negative variations. Then,

$$RSI(P) = 100 - (100 / (1 + (u / d))).$$

D. Real-Modulated Index (RM)

$$RM(P)_i = x_i / MMP_i$$

E. Optimised Decision Index (ODI)

$$ODI(P)_i = [RM(P)_i + RM(P)_{i-1} + \dots + RM(P)_{i-P+1}] / P$$

F. Stochastic Oscillator (SO)

Let m be the minimum and M the maximum of x_i in the considered period P . Then,

$$SO(P)_i = (x_i - m) / (M - m).$$

G. Momentum (MOM)

$$MOM(P)_i = x_i - x_{i-P+1}$$

H. Pattern matching.

This was another very simple analytical tool was added to the six "financial" oscillators, to calculate the minimal algebraic difference pattern-matching with the last sequence of 20 values.

Let there be a sequence $x_i ; i = 1, 2, \dots, n$, we intend to find the most probable value for x_{n+1} .

Take the vector of the last 20 values,

$$[x_n, x_{n-1}, x_{n-2}, \dots, x_{n-19}]$$

and the immediately previous one,

$$[x_{n-1}, x_{n-2}, x_{n-3}, \dots, x_{n-20}]$$

and add their absolute termwise differences:

$$S_1 = |x_n - x_{n-1}| + |x_{n-1} - x_{n-2}| + \dots + |x_{n-19} - x_{n-20}|.$$

Iterate the process,

$$S_2 = |x_n - x_{n-2}| + |x_{n-1} - x_{n-3}| + \dots + |x_{n-19} - x_{n-21}|$$

...

$$S_{n-20} = |x_n - x_{20}| + |x_{n-1} - x_{19}| + \dots + |x_{n-19} - x_1|.$$

The most similar vector will be the one for which that sum is minimal, for instance

$$S_m = |x_n - x_{n-m}| + |x_{n-1} - x_{n-m-1}| + \dots + |x_{n-19} - x_{n-m-19}|$$

and so the next most likely value will be

$$x_{n+1} = x_{n-m+1}.$$

As was demonstrated elsewhere [3] there are periods P which yield optimal results in the analysis of seismic sequences. These are of 4 occurrences for RSI and RM, 7 for SO, 21 for ODI and 28 for MOM.

Since the computational algorithm for ODI21 implies the calculation of RM21, and the calculation of RM21 that of MA21, we have to calculate in all nine oscillators, namely, MA4, MA21, MACD21-4, RSI4, RM4, RM21, ODI21, SO7 and MOM28. Of these, only RSI4, RM4, MACD21-4, SO7, ODI21 and MOM28 will be used as input to the neural net. Tests showed that the extended training time is not compensated by a better accuracy if one was to use all the computed oscillators.

The first applications of these tools for seismic prediction, though encouraging, had two shortcomings: first, their outputs are qualitative, since the oscillators only indicate if a trend is rising, declining or stable ("buy", "sell" or "hold"); then, when we apply several oscillators to the same sequence the results are not always consistent.

Both quantitative output and consistency were achieved by integrating the oscillators in an artificial neural network (ANN).

III. THE NEURAL NETWORK.

ANN's are software emulators of the nervous system and seemed adequate because of their mathematical universality, fault-tolerance, and ability to deal with semi-quantitative data such as the modified Mercalli intensity (MMI).

In [4] it was shown that a neural network can behave as a model for the seismic process. That, together with the extensive use of neural nets in prediction tasks – mainly, again, in finance – indicated that these tools could be successful in integrating the oscillators to produce quantitative results.

Neural networks are distributed parallel processing systems (software programs) that emulate the behaviour of natural neurones in the animal nervous system.

Figure 1 illustrates the particular kind of neurodes (artificial neurones) chosen for this task, of the many available – Rosenblatt's perceptron [5].

The input of a neurode is the sum S of the products of the outputs of other neurodes x_i by the so-called connection-weights, w_i :

$$S = \sum_{i=1}^N w_i x_i$$

The output of a neurode is a function $f(S)$ of that sum; in this case, the sigmoid function was chosen:

$$f(S) = \frac{1}{1 + e^{-S}}$$

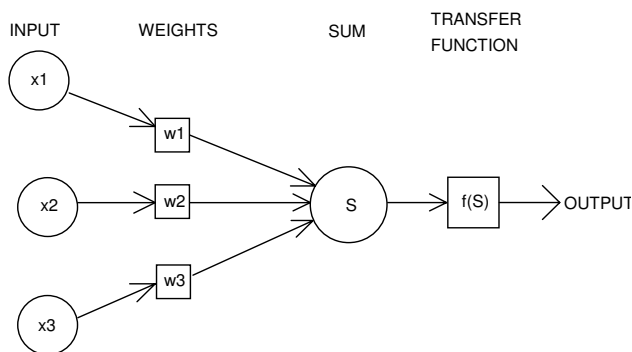


Figure 1 – Rosenblatt’s perceptron.

The complete neural network is a set of neurodes, arranged in layers, three in this case: an input layer (IL), a middle or hidden layer (HL) and an output layer (OL).

Neurodes are arranged in such a way that the ones in the same layer are not connected among themselves, but are connected to all the neurodes in the previous and next layers - the network is said, thus, to be partially connected.

The learning process is quite simple. The network is fed with an array of three columns (time, intensity and location) and as many lines as there are registered seismic occurrences.

The input layer neurodes are the input data: the oscillators. Since we intend to predict three variables (time, intensity and location), we shall have seven oscillators times three, twenty-one, input neurodes.

The best hidden layer's size was found to be four neurodes.

The output layer will have as many neurodes as the variables we try to predict: three.

Then we have in all $(21 \times 4) + (4 \times 3) = 96$ connections. This architecture is illustrated in figure 2.

The program calculates the oscillators for each variable until the 29th occurrence (remember that one oscillator, MOM28, only yields results from the 29th value onwards) and, beginning with random weights, propagates the weighed sums to the hidden layer and from there to the output layer, where the output values are compared with the real values for the next (30th) occurrence.

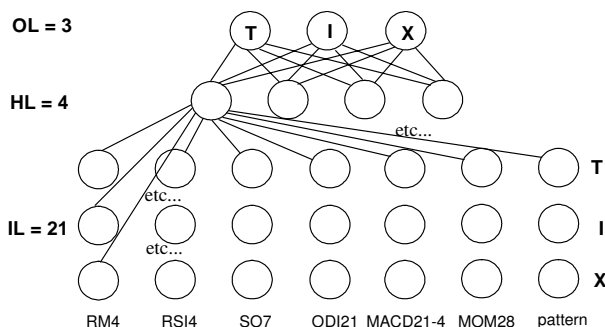


Figure 2 – Architecture of the neural network. IL: input layer. HL: hidden layer. OL: output layer. T: times of pause. I: intensities. X: locations. Abbreviations for the oscillators are in the text.

Using the algorithm of backpropagation of errors [6], the error is used to adjust the weights OL-HL and then HL-IL. The process is repeated for all the data and that concludes what is called one training epoch. Then, all these steps are repeated for as many epochs as are necessary to obtain an acceptable minimum training error - in our case, 2% - when the net is considered to be trained. (The training algorithm was adapted from [7].)

The net being trained, we can use the last set of connection weights - the one that yields minimal errors - and the oscillators that were calculated for the last observation, and propagate the weighed sums from IL to HL and from there to OL where we get the prediction of the time, intensity and location of the next, unknown occurrence.

IV. RESULTS

A computer program was built that calculates the oscillators, trains the neural network and predicts the next occurrences using the calculated connection-weights [3].

Since it would probably not be realistic to try and predict the exact geographical co-ordinates of the next epicentres, these were divided in major groups of one-degree latitude, between 24° W and 31° W.

In order to optimise both characteristics of neural networks, memory and generalisation, training sets with 100 examples were used. This number was chosen to be roughly equal to the number of connections, so that the network would be neither strongly overdetermined nor strongly underdetermined.

The ANN was trained with historical and instrumental seismic data from the Azores, between 1912 and 1993, for earthquakes with $MMI \geq V$. It forecasted an earthquake to be felt in the Azores Central Group with $VI \leq MMI \leq VII$ in February 1998 \pm 5

months [8].

In July 9, 1998, an earthquake struck the Azores, being mostly destructive in the island of Faial, in the Central Group (MMI=VII).

When this last earthquake was included in the ANN training set, the net forecasted an earthquake to be felt in the Azores Central Group with $VI \leq \text{MMI} \leq VII$ in February 2004 \pm 6 months [9].

Between December 2003 and February 2004 the Azores have been experiencing an earthquake swarm. The maximum intensity (MMI=V) was felt in the island of Graciosa, Central Group, on January 28, 2004 [10], the strongest since 1998.

These results are encouraging, but more needs to be done.

V. FUTURE WORK

Historically, there have been two major approaches to seismic forecasting. The approach that was followed in the preceding paragraphs is based on a mathematical analysis of earthquake catalogues. The other one is based upon the understanding of earthquake-triggering mechanisms and on the monitoring of well-known earthquake physical precursors [for example 11, 12, 13].

Now, a research group is beginning work on project *DESIRE* (*Dynamic Evaluation of Seismic Risk*).

In this project, three permanent stations will be deployed in Coimbra, Porto and Vila Real, continuously monitoring seismic waves, water piezometry, ground self-potential and EM piezoelectric emissions. Periodically, profiles of the anomaly of magnetic susceptibility will be made across the relevant seismogenic structures in Northern Portugal.

These data, recognised seismic precursors, will be added as input nodes to a similar ANN to the one that was described above, together with the pre-processed catalogue data as in the previous strictly mathematical method. The much more complete catalogue in Continental Portugal, as compared to that of the Azores, will allow us to work this time with seismic magnitudes.

We expect that this mixed approach will succeed in narrowing the time forecast window – that is, to achieve the goal of mid- to short-term prediction.

REFERENCES

- [1] S. B. Achelis. *Technical Analysis from A To Z*, McGraw-Hill, 1995.
- [2] E. I. Alves. Notice on the Predictability of Earthquake Occurrences, *Memórias e Notícias*, 117, pp. 51-61, 1994.
- [3] E. I. Alves. *Uma Abordagem Conexcionista ao Problema da Previsão Sísmica*. Ph.D. Thesis (in Portuguese), Univ. Coimbra, 1995.
- [4] E. I. Alves. A simple seismic computational model. *Memórias e Notícias*, 120, pp. 37-42, 1995.
- [5] F. Rosenblatt. *Principles of Neurodynamics: Perceptrons and the Theory of Brain Mechanisms*, Spartan Books, New York, 1962.
- [6] D. E. Rumelhart *et al.* Learning Internal Representations by Error Propagation. In: *Parallel Distributed Processing*, eds. D. E. Rumelhart, J. L. McClelland and the PDP Research Group, vol. 1, pp 318-362, MIT Press, Cambridge, Mass., 1986.
- [7] E. Rich and K. Knight. *Artificial Intelligence*. McGraw-Hill, Singapore, 1991.
- [8] E. I. Alves. *Techniques for Predicting Natural Disasters*. 1st Cycle of Conferences on Engineering Geology, guest lecture. Institute for Water Research, Coimbra, October 8, 1996.
- [9] E. I. Alves. Earthquake Prediction in the Azores: First Results and Forecasts. *J. Conf. Abs.* 4, 1, 544, 1999.
- [10] Azores Regional Civil Protection and Firemen Service. Communiqué 11/2004.
- [11] M. A. Sadowski *et al.* The Processes Preceding Strong Earthquakes in Some Regions of Middle Asia. *Tectonophysics*, 14, 3/4, pp. 295-308, 1972.
- [12] M. J. S. Johnston and G. E. Mortensen. Tilt Precursors Before Earthquakes on the San Andreas Fault. *Science*, 186, pp. 1031-1033, 1974.
- [13] J. Latoussakis *et al.* Temporal Characteristics of Some Earthquake Sequences in Greece. *Tectonophysics*, 193, 4, pp. 299-310, 1991.

This work was funded by project DESIRE, POCTI.

INNOVATION SYSTEMS BY NONLINEAR NETWORKS

*P. Andriani***, F. Conti*, L. Fortuna*, M. Frasca*, G. Passiante****, A. Rizzo***

* Dipartimento di Ingegneria Elettrica, Elettronica e dei Sistemi,
Università degli Studi di Catania, Viale A. Doria 6,

**Dipartimento di Elettrotecnica ed Elettronica,
Politecnico di Bari, Via Re David 200

*** Durham University Business School Mill Hill Lane Durham,
City DH1 3LB United Kingdom

**** Department of Innovation Engineering, University of Lecce, Italy
e-mail: [fconti, lfortuna, mfrasca]@diees.unict.it

Abstract—*Cellular Neural Networks (CNNs) constitute a powerful paradigm for modelling complex systems. Innovation systems are complex systems in which small and medium enterprises play the role of simple units interacting each other. In this paper innovation systems based on CNN are investigated. It is shown how a model based on CNN can reproduce the main features of innovation systems and how this model can be generalized to include different aspects of the actors of the financial market.*

I. INTRODUCTION

Complex systems are often defined as systems made of elementary units interacting with simple laws and able to allow the emergence of an holistic global behavior. Recently the theory of complex systems, intended as systems that intrinsically retain the possibility to respond to the environment in different ways, has been applied to innovation systems [7].

The key point is that industrial network have to be adaptive to respond to the complex unpredictable behavior of the market and that innovation plays a fundamental role to achieve adaptability. Survival and success are possible if the elements of the network are able to learn and change.

In this work Cellular Neural Networks (CNNs) [3], [4], [5] modelling innovation systems are introduced. CNNs have been already used to model complex nonlinear phenomena in spatially distributed systems. In fact an n-dimensional CNN may represent any complex system in which interactions among the elements of the system are ruled by local connections and where the main features of the basic unit are reflected by the model assumed for the elementary CNN cell.

The main idea of the approach here presented is to use each layer of a multi-layer CNN to model a particular variable of the financial system. Complexity

can be added by adding further layer in the model, i.e. increasing the dimension of the basic cell.

In particular this paper focuses on a very simple model of innovation in systems of interconnected agents. As introduced before this can be extended to account for other characteristics of the elementary agent by adding other CNN layers.

The model for innovation examined in this paper is based on the simple rules discussed in a recent paper by Watts [8]. This model accounts for the presence (and the absence under certain conditions) of global cascades in networks of agents.

Global cascades represent the spread of the innovation along the whole network and are common in many social and economic phenomena. For example it accounts for the fact that some books, movies or songs become very popular despite their initial small marketing budgets [1].

This is an example of what often happens in economic and social systems in which the knowledge of the problem or the ability to process the available information are limited and the decision makers have to pay attention to each other [2].

In the example of a popular hit recommendations of friends and neighbors can play a fundamental role in the choice of a movie, a book or a song. This phenomenon in economics is known as information cascade: individuals make decision on the basis of the action of other individuals of the population, thus allowing the possibility that the whole system exhibits a herd-like behavior.

The model proposed by Watts [8] and here implemented by the CNN paradigm provides a possible explanation for this phenomenon in terms of a binary-state decision random network.

This model is detailed in Section 2. Section 3 deals with the CNN model, while Section 4 presents the re-

sults of the simulation of the CNN model, showing how the CNN model can reproduce the main features of the innovation model. Section 5 draws the conclusions of the paper.

II. CELLULAR AUTOMATA MODEL

In this Section the model for innovation proposed by Watts [8] is briefly reviewed. This model extends the model introduced by the sociologist Granovetter [9], which illustrated his results on the brink of rioting and assumed that each person's decision is dependent on what everyone else is doing.

This model described a population of agents which must decide between two actions: adopt or not a new technology. Watts used a model based on a cellular automaton (CA)[6] to model this system.

Individuals are represented by binary variables that can adopt or not the innovation. If the individual adopt the innovation the cell state of the cellular automata is 0, if don't adopt the innovation the state of the cellular automata state is 1. Connections among individuals are assumed random.

Each individual is characterized by a threshold. In fact, each individual adopts the innovation if the percentage of connected individuals that has already adopted the innovation is greater than its threshold. The threshold is different for each agent and represents the attitude to innovation of the given agent.

This simple model is able to account for the emergence of global cascades, in which innovation spread in the whole network. However global cascades are possible only under particular conditions.

The main result is that the presence of cascades depends on the average number of connections between individuals. When the number of connections is too small there is no room for cascades. When the number of connections increases, the attitude to innovation increases until global cascades become possible. However if the network is very connected global cascades become rare events.

The reason of this behavior is that each individual makes its decision on the basis on a percentage of the individuals with which he is connected and that adopted innovation. Thus increasing the connectivity level two bifurcation points are evident: cascades are therefore possible only if connectivity is neither small or too large.

More in detail some simulation results are here discussed. The number of initial innovators is kept constant (as in Fig. 1), and the behavior with respect to different average numbers of connections is investi-

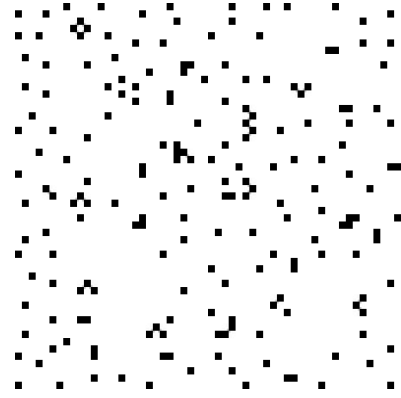


Fig. 1. The initial condition of the CA model represents the initial innovators (black pixel indicate that the cell status is 1, thus the individual is an innovator).

gated.

There is no cascade if the number of connections is too small: in this case innovation does not spread (Fig. 2(a) shows an example).

If the connection is increased, cascade propagation becomes possible, innovation does spread in the whole network. Fig. 2(b) shows an example of this behavior. If the number of connections is too high, the attitude to innovation of the network decreases, since each agent is connected with many other individuals and so needs many innovators to be convinced. Fig. 2(c) is an example of this last case.

The results highlight the presence of two phase transitions when the mean number of connections is increased.

III. INNOVATION MODELS BASED ON CNNS

The simple model of cascade propagation is an example of how CNN can be used for modelling complex financial systems.

In this Section we show how CNN can be used to reproduce the main features of the CA model introduced by Watts. Moreover they allow the generalization of the random network to a generic grid of connected units and the extension of the discrete time model to a continuous one.

Different grids can therefore be studied and connections can be assumed local or mostly local leading to the possibility of studying innovation propagation in different topologies.

In the following a regular grid (shown in Fig. 3) is taken into account and standard 1-layer templates are used. In fact each innovator can be modelled by the state of a cell of a 1-layer CNN. Now the decision to adopt or not the innovation takes place as a continuous process. The saturation points +1 and -1 represent the

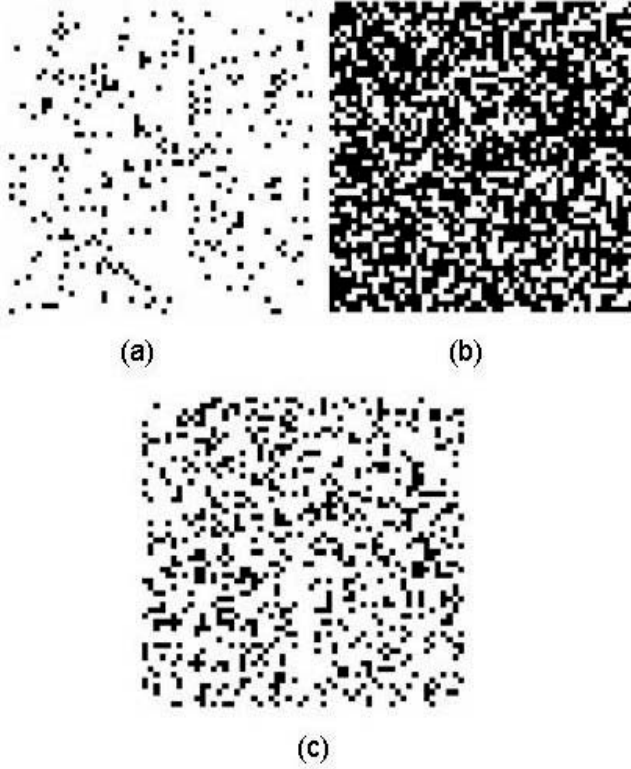


Fig. 2. Innovation propagation in a random network with respect to different connectivity levels, the mean number of connections is: 5 (a), 30 (b) and 50 (c). Cascade propagation is possible only in case (b).

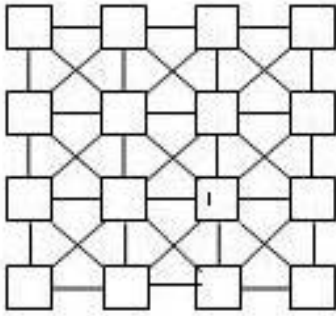


Fig. 3. Scheme of a CNN.

decision to adopt the innovation or not, respectively.

The state equation of the cell $C(i,j)$ is the following [4], [5]:

$$\dot{x} = -\frac{x_{ij}}{R_{ij}} + i_1 + \sum (A_{ij:kl}y_{kl} + B_{ij:kl}u_{kl}) \quad (1)$$

where:

$$N_r(i, j) = C(k, l) : \max(|k - i|, |l - j| < r) \quad (2)$$

r is the size of the neighborhood, A and B are the feedback and control template, respectively, and:

$$i = 1..N, j = 1..M \quad (3)$$

To completely specify the model templates have to be designed in order to reproduce the features of the decision maker unit. This step implies a sort of translation between CA rules and CNN templates.

Recently great advances have been done in the direction of an analytical universal method to accomplish this step [11], but until now this step still requires trial and error.

However in this case this step can be accomplished by adapting templates already known. The behavior of each cell depends on the neighbor states in such a way that if the percentage of neighbor innovators is greater than a threshold the cell itself should become an innovator.

This resembles the rules for game of life, and therefore similar templates have been adopted [10]. In particular the bias value has to be changed to account for the condition on the threshold. In fact it is the bias that mimics the threshold of the individual.

Finally the neighborhood radius r has to be chosen. Since we want to study the effects of different connectivity levels, three different neighborhood radius have been chosen: $r=1$, $r=2$ and $r=3$.

The A and B templates remain qualitatively the same in the three cases, but the bias has to be properly scaled in order to represent a percentage threshold. In particular the bias has been chosen so that it represents a percentage threshold equals to 44 in all the three cases discussed in the following.

In particular, for example in the case of $r=1$ the templates that we considered are:

$$A = \begin{bmatrix} 0 & 0 & 0 \\ 0 & 1 & 0 \\ 0 & 0 & 0 \end{bmatrix}; B = \begin{bmatrix} 1 & 1 & 1 \\ 1 & 1 & 1 \\ 1 & 1 & 1 \end{bmatrix} \quad (4)$$

and the bias is $I=4$. For $r=3$ the A template is a 7×7 matrix with only the central element different from zero, the B template is a 7×7 matrix with all unitary elements and the bias is $I=22$.

The final output of the CNN model for innovation is the logic OR between the result of the processing of these templates and the input representing the initial state of innovators.

IV. SIMULATION RESULTS

As initial distribution of innovators the same initial condition of the CA model represented in Figure 1 has been considered.

The simulation results shown in Fig. 4 confirm that, even in the case of regular grids, cascade propagation

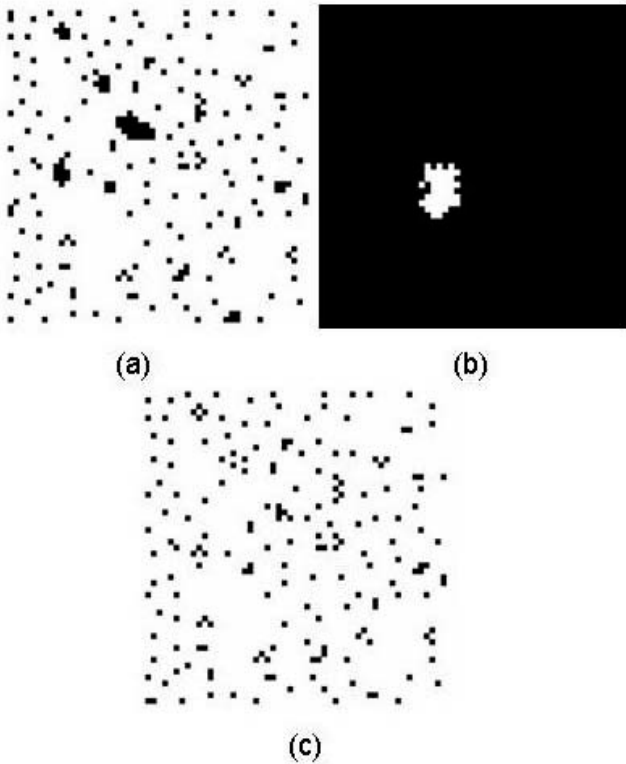


Fig. 4. Simulation result of a CNN with: (a) $r=1$, (b) $r=2$ and (c) $r=3$.

does not depend on the number of initial innovators, but on the mean number of the connections.

In particular Fig. 4 shows simulation results for a CNN with $r=1$, $r=2$ and $r=3$.

The same scenario depicted by Watts appears, there are two phase transitions: when the connectivity is low ($r=1$) there are no global cascades; for $r=2$ global cascades are possible, and for $r=3$ global cascades occurs rarely.

Similar results can be obtained with different initial conditions. This allows us to conclude that cascade propagation does not depend on the number of initial innovators but on individual thresholds and connectivity levels.

V. CONCLUSIONS

In this paper it is shown how CNNs can be used to model complex system models arising in the field of financial and innovation systems. In particular a suitable CNN implementation of a simple model of innovation [8] has been illustrated.

The use of CNN allows to consider continuous time instead of discrete time models and provides a generalization of the paradigm of connectivity.

In fact by using CNNs different kinds of connections (either regular or almost locally connected sys-

tems) can be studied.

Moreover, CNN models can be easily simulated on parallel hardware, thus allowing real-time simulation of complex financial systems.

Another methodological aspect of the CNN approach is the possibility of adding complexity to the basic cell model by adding new CNN layers modeling other interest variables of the elementary agent.

The CNN model for innovation presented as a case study shows the effectiveness of the approach confirming the presence of two phase transitions in the model of innovation.

If the network is poorly connected no global cascade may occur, if the network is too largely connected global cascades become rare events.

ACKNOWLEDGMENTS

This was been supported by the Italian "Ministero dell'istruzione, dell'Universit  e della Ricerca (MIUR) under the Firb project RBNE01CW3M.

REFERENCES

- [1] Gladwell, M., *The Tipping Point: How Little Things Can Make a Big Difference*, Little Brown New York, 2000.
- [2] S. Bikhchandani, D. Hirshleifer and I. Welch, *J. Pol. Econ.*, 100(5), 992-1026, 1992.
- [3] L. O. Chua and T. Roska, *CNN: The paradigm*, IEEE Transactions on Circuits and Systems I, vol. 35, 147-156, 1993.
- [4] L.O. Chua and L. Yang, *Cellular Neural Network: Teory*, IEEE Transactions on Circuits and System I, vol. 35, 1257-1272, 1988.
- [5] L.O. Chua, L. Yang and T. Roska, *Cellular Neural Network: applications*, IEEE Transactions on Circuits and System I, vol. 35, 1273-1290, 1988.
- [6] S. Wolfram, *Theory and application of cellular automata*, World Scientific, 1986.
- [7] P. Allen, *A Complex systems approach to learning in adaptive networks*, Int. J. of Innovation Management, vol. 5, no. 2, 149-180, 2001.
- [8] D. J. Watts, *A simple model of global cascades on random networks*, Proc. Natl. Acad. Sci. 99, 5766-5771, 2002.
- [9] S. H. Strogatz, *Sync: The Emerging Science of Spontaneous Order*, Hyperion Press, 2003.
- [10] K. R. Crouse, E. L. Fung and L. O. Chua, *Efficient implementation of neighbourhood logic for cellular automata via the cellular neural network universal machine*, IEEE Transactions on Circuits and System I, vol. 44, no.4, 1997.
- [11] L. O. Chua, S. Yoon, R. Dogaru, "A Nonlinear Dynamics Perspective of Wolfram's New Kind of Science. Part I: Threshold of Complexity", Int. J. Bifurcation and Chaos, vol. 12, no. 12, pp. 2655-2766, 2002.

AUTOCORRELATION FUNCTION AND POWER SPECTRUM OF SPIRAL CHAOS IN DYNAMICAL SYSTEMS

V.S. Anishchenko, T.E. Vadivasova, G.I. Strelkova and G.A. Okrokvertskhov

Institute of Nonlinear Dynamics,
Saratov State University,
Saratov, Russia

e-mail: galya@chaos.ssu.runnet.ru
WWW: http://chaos.ssu.runnet.ru

Abstract *We study numerically and experimentally the behavior of the autocorrelation function and the power spectrum of spiral attractors without and in the presence of noise*

I. INTRODUCTION

The problem of decay of autocorrelation functions (ACF) in continuous dynamical systems with dimension $N \geq 3$ is one of the fundamental and still unsolved tasks of the theory of chaos. For two-dimensional discrete systems that satisfy the Smale axiom-A it has been only proven that the ACF can be bounded from above by an exponentially decreasing function [1], [2], [3], [4]. In certain cases the ACF decays exponentially with the exponent that is defined by the inverse of the Kolmogorov entropy $h = \lambda^+$, where λ^+ is the positive Lyapunov exponent [3]. In a common case, such statements are not fulfilled for even hyperbolic maps. Regularities of the ACF decay in differential systems with chaotic attractors of both hyperbolic and nonhyperbolic types are even more complicated from a viewpoint of their theoretical description. As was shown in [5], [6], [7], the rate of the ACF decay in differential systems depends essentially on the structure of an attractor and on the influence of noise. Moreover, the positive Lyapunov exponent does not define the regularities of decay of autocorrelations [6], [7]. In the present paper we substantiate numerically and experimentally that for typical nonhyperbolic attractors of the spiral type in R^3 , the autocorrelations decay exponentially. With this, two time scales can be distinguished, i.e., $\tau \leq \tau_{\text{cor}}$ and $\tau > \tau_{\text{cor}}$. In the first case the exponential decay is defined by fluctuations of the instantaneous amplitude and in the second case it depends on the effective diffusion coefficient B_{eff} . The power spectrum of spiral or phase-coherent chaos exhibits a pronounced peak at the basic (average) frequency and, consequently, the envelope of the ACF decreases relatively slow [8],

[9], [10], [11]. Spiral attractors can be observed in such well-known systems as the Rossler oscillator, the Anishchenko Astakhov oscillator [10], or the Chua circuit [12]. The self-sustained oscillations in these systems can remind the dynamics of noisy periodic oscillators of a Van der Pol oscillator type [13], [14], [15], [16], [17].

From the classical theory we know the analytic solution for the ACF of oscillations which represent a narrow-band random process $x(t) = A(t)[\cos \omega_0 t + \phi(t)]$:

$$\begin{aligned} \Psi_x(\tau) &= \langle x(t)x(t+\tau) \rangle - \langle x(t) \rangle^2 \\ &= \frac{1}{2}[\Psi_A(\tau) + A_0^2] \exp(-B\tau) \cos \omega_0 \tau, \end{aligned} \quad (1)$$

where $\Psi_A(\tau)$ is the ACF of amplitude fluctuations, $A_0 = \langle A(t) \rangle$, and B is the instantaneous phase diffusion coefficient. $A(t)$ and $\phi(t)$ are assumed to be the slow random functions of time, and the phase dynamics can be described by a Wiener process:

$$\dot{\phi}(t) = 2B\xi(t), \quad B = \frac{\omega_0 \sqrt{2D}}{2A_0}, \quad (2)$$

where $\xi(t)$ is the white noise with intensity D .

As seen from expression (1), the ACF is represented as a sum of two terms. The first one is determined by the ACF of the amplitude fluctuations and the second term depends on the phase fluctuations. According to the Wiener-Khinchin theorem the power spectrum will consist of two terms too, namely, a broad-band noise pedestal $S_1(\omega)$ stipulated by a small correlation time of $\Psi_A(\tau)$ and a Lorentzian:

$$S(\omega) = S_1(\omega) + \frac{B}{B^2 + (\omega - \omega_0)^2}. \quad (3)$$

As we have shown in [18], the expressions (1) and (3) hold not for the stochastic dynamics of the Van der Pol oscillator only. They appear to be valid in a

more general case when the process of stochastic oscillations can be described in the form of harmonic noise $x(t) = A(t) \cos[\omega_0 t + \phi(t)]$ with slowly varying amplitude and phase. Now we use this concept to characterize the spiral chaos.

II. NUMERICAL AND EXPERIMENTAL RESULTS

Let us consider the well-known Rossler system:

$$\begin{aligned} \dot{x} &= -y - z + \sqrt{2D}\xi(t), & \dot{y} &= x + \alpha y, \\ \dot{z} &= \beta + z(x - \mu), \end{aligned} \quad (4)$$

where $\xi(t)$ is the normalized Gaussian source of δ -correlated noise with zero mean and D is the noise intensity. We $x \alpha = \beta = 0.2$ and $\mu = 6.5$. Let us introduce the change of variables

$$x(t) = A(t) \cos \Phi(t), \quad y(t) = A(t) \sin \Phi(t), \quad (5)$$

which determines the amplitude $A(t)$ and the full phase $\Phi(t)$ of the chaotic oscillations. Substituting (5) Eqs. (4) can be re-written as follows:

$$\begin{aligned} \dot{A} &= \frac{1}{2}\alpha A(1 - \cos 2\Phi) - z \cos \Phi + \sqrt{2D}\xi(t) \cos \Phi, \\ \dot{\Phi} &= 1 + \frac{1}{2}\alpha \sin 2\Phi + \frac{1}{A}z \sin \Phi - \frac{\sqrt{2D}}{A}\xi(t) \sin \Phi, \\ \dot{z} &= \beta + z(A \cos \Phi - \mu). \end{aligned}$$

In our numerical calculations we use both systems (4) and (6).

In [7] it has been recently shown that for spiral chaos in the Rossler system the variance $\sigma_\phi^2(t)$ of the instantaneous phase grows linearly in time both without noise ($D = 0$) and when $D \neq 0$. The variance of the total phase is equal to the variance of its non-regular component $\phi(t) = \Phi(t) - \bar{\omega}t$, where $\bar{\omega} = \langle \dot{\Phi}(t) \rangle$ is the mean frequency of the chaotic oscillations. This linear dependence of variance $\sigma_\phi^2(t)$ on time allows us to introduce the effective phase diffusion coefficient

$$B_{\text{eff}} = \left\langle \frac{1}{2} \frac{d\sigma_\phi^2(t)}{dt} \right\rangle. \quad (7)$$

In our numerical simulation of system (4) we calculate the normalized ACF of chaotic oscillations $\Psi_x(\tau) = \psi_x(\tau)/\psi_x(0)$. Using Eqs. (6) we compute the ACF $\Psi_A(\tau)$ and the effective phase diffusion coefficient B_{eff} . We use the time-averaging procedure for calculating $\Psi_x(\tau)$ and $\Psi_A(\tau)$. The coefficient B_{eff} is computed by averaging over an ensemble of realizations [7]. Figure 1 shows the calculation results

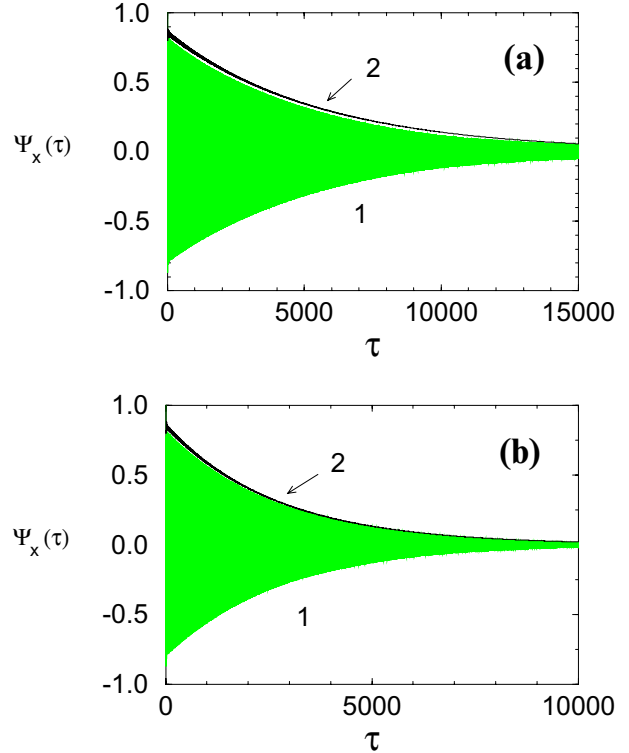


Fig. 1. Calculation results for the Rossler system (4) with $\alpha = \beta = 0.2$ and $\mu = 6.5$. Normalized ACF $\Psi_x(\tau)$ (curve 1) and the approximation of its envelope (8) (curve 2) for (a) $D = 0$, $B_{\text{eff}} = 0.00019$ and (b) $D = 0.001$, $B_{\text{eff}} = 0.00032$

(6) for $\Psi_x(\tau)$ in system (4). The ACF decays almost exponentially both without noise (Fig. 1(a)) and in the presence of noise (Fig. 1(b)). For $\tau < 20$ there is an interval on which the correlations decrease much faster.

Using Eq. (1) we can approximate the envelope of the calculated ACF $\Psi_x(\tau)$. To do this, we substitute the numerically computed characteristics $\Psi_A(\tau)$ and $B = B_{\text{eff}}$ into an expression for the normalized envelope $\Gamma(\tau)$:

$$\Gamma(\tau) = \frac{1}{2} \frac{[\Psi_A(\tau) + A_0^2]}{[\Psi_A(0) + A_0^2]} \exp(-B|\tau|). \quad (8)$$

The calculation results for $\Gamma(\tau)$ are shown in Fig. 1(a,b) by black dots (curves 2). It is seen that the behavior of the envelope of $\Psi_x(\tau)$ is described well by Eq. (8).

As can be seen from Fig. 1, for small correlation time $\tau \geq 0$ the ACF $\Psi_x(\tau)$ demonstrates a sharp decrease and then decays exponentially. This fact can be explained by calculating $\Psi_A(\tau)$ that is shown in Fig. 2. As seen from the graph, the nonnormalized ACF $\Psi_A(\tau)$ decreases abruptly in time resembling a δ -function. As follows from expression (1), this decrease will form the behavior of $\Psi_x(\tau)$ near zero.

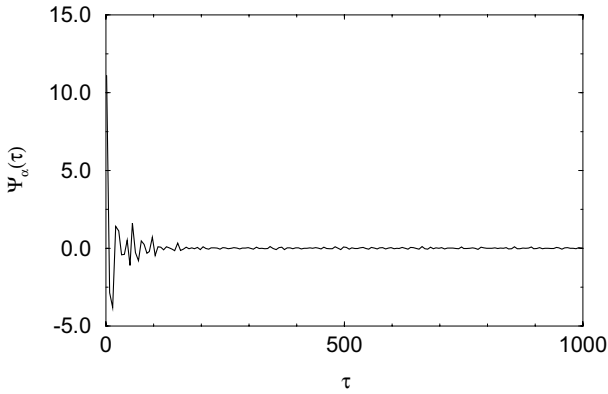


Fig. 2. The autocorrelation function $\Psi_A(\tau)$ of amplitude uctuations for the Rossler system (4) with $\alpha = \beta = 0.2$ and $\mu = 6.5$

Now we compare the numerical results with experimental data obtained for an analog model of the Rossler oscillator, that corresponds to Eqs. (4) and the control parameter values as in Fig. 1. Figures 3 5 show the experimental results that con rm completely the ndings of numeric simulation. As seen from Fig. 3, variance $\sigma_\phi^2(t)$ grows practically linearly in time. In this case we can estimate experimentally the value of the effective phase diffusion coef cient B_{eff} as the tangent of the slope angle of the approximating straight line $B_{\text{eff}} = 0.015 \text{ rad}^2/\text{sec}$. Figure 4 represents ACF $\Psi_x(\tau)$ calculated on experimental realization $x(t)$ of the analog model of the system (4). There-in we also plot envelope $\Gamma(\tau)$ that is determined from (8) by using the calculation data of $\Psi_A(\tau)$ (Fig. 2) and B_{eff} (Fig. 3). As seen from Fig. 4, the experimental results are in a very good agreement with the numerical ndings presented in Fig. 1. Figure 5 illustrates the measurement results for the power spectrum of spiral chaos. The spectrum exhibits a well-pronounced peak whose shape is well approximated by Lorentzian (3) with the spectral linewidth de ned by the diffusion coef cient $B_{\text{eff}} = 0.015 \text{ rad}^2/\text{sec}$.

III. CONCLUSIONS

It has been experimentally established that in the regime of spiral chaos the instantaneous phase variance of chaotic oscillations grows, on average, linearly with the diffusion coef cient B_{eff} . Without noise this coef cient is de ned by the chaotic dynamics of the system. In the presence of noise the growth of the phase variance is also linear but the B_{eff} value increases. The ACF of the spiral chaos decays in time according to the exponential law $\exp(-B_{\text{eff}}\tau)$. The spectral linewidth of oscillations at the basic frequency is de ned by the effective phase diffusion coef cient from the expression (3).

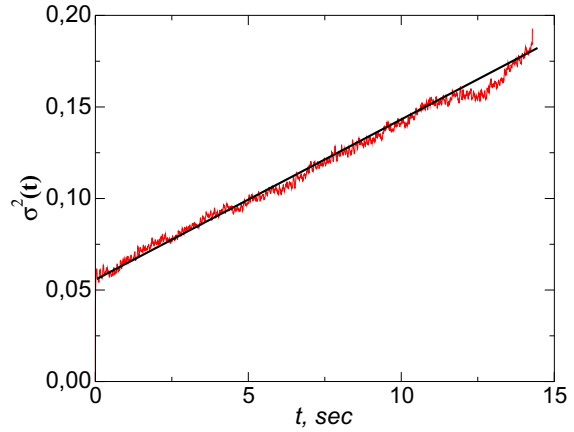


Fig. 3. The experimental temporal dependence of the variance for the Rossler system with $\alpha = \beta = 0.2$ and $\mu = 6.5$

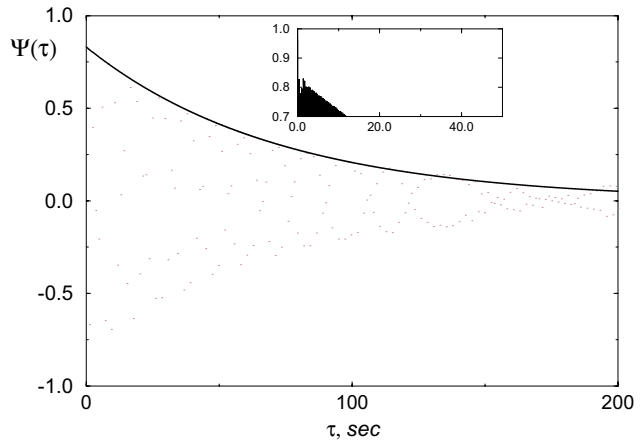


Fig. 4. The experimental ACF $\Psi_x(\tau)$ of spiral chaos in the Rossler system and its envelope (thick line)

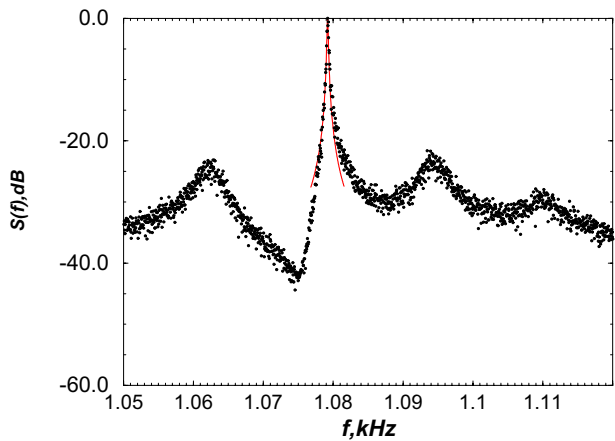


Fig. 5. The experimental power spectrum for the Rossler system and its approximation by the Lorentzian (thin line)

ACKNOWLEDGEMENTS

This work was partially supported by Award No. SR-006-X1 of the U.S. Civilian Research and Development Foundation and by the grant of RF Ministry of Education (No. E02-3.2-345). G.I.S. acknowl-

edges support from INTAS (grant No. YSF 2002-3 Renewal) and the President grant (MK-2833.2004.2). G.A.O. acknowledges support from the Russian Ministry of Education (No. A03-2.9-334).

REFERENCES

- [1] D. Ruelle, Thermodynamic Formalism , *Encyclopedia of Mathematics and its Applications*, vol. 5, Addison-Wesley Reading, Massachusetts, 1978.
- [2] M. Pollicott, On the rate of mixing of Axiom A flows , *J. Invent. Math.*, vol. 81, p. 413–426, 1985.
- [3] G.M. Zaslavsky, R.Z. Sagdeev, D.A. Usikov, and A.A. Chernikov, *Weak Chaos and Quasi-Regular Patterns* , Cambridge Univ. Press, 1991.
- [4] M.L. Blank, *Stability and Localization in Chaotic Dynamics* , Moscow Center for Continuous Math. Education, Moscow, 2001 (in Russian).
- [5] D. Ruelle, Flots qui ne melangent pas exponentiellement , *C. R. Acad. Sci., Paris, Ser. A*, vol. 296, pp. 191–193, 1983.
- [6] V.S. Anishchenko, T.E. Vadivasova, A.S. Kopeikin, J. Kurths, and G.I. Strelkova, Effect of noise on the relaxation to an invariant probability measure of nonhyperbolic chaotic attractors , *Phys. Rev. Lett.*, vol. 87, 054101, 2001.
- [7] V.S. Anishchenko, T.E. Vadivasova, A.S. Kopeikin, J. Kurths, and G.I. Strelkova, Peculiarities of the relaxation to an invariant probability measure of nonhyperbolic chaotic attractors in the presence of noise , *Phys. Rev. E*, vol. 65, 036206, 2002.
- [8] J. Crutchfield et al., Power spectral analysis of a dynamical system , *Phys. Lett. A*, vol. 76, pp. 1–4, 1980.
- [9] A. Arneodo, P. Collet, C. Tresser, Possible new strange attractors with spiral structure , *Commun. Math. Phys.*, vol. 79, pp. 573–579, 1981.
- [10] V.S. Anishchenko, *Dynamical Chaos Models and Experiments* , World Scientific, Singapore, 1995.
- [11] L.P. Shilnikov, Mathematical problems of nonlinear dynamics: a tutorial , *Int. J. Bifurcation Chaos*, vol. 7, pp. 1953–2001, 1997.
- [12] R.N. Madan (Ed.), *Chua's circuit: A paradigm for chaos* , World Scientific, Singapore, 1993.
- [13] V.S. Anishchenko, T.E. Vadivasova, D.E. Postnov, and M.A. Safonova, Synchronization of chaos , *Int. J. Bifurcation Chaos*, vol. 2, pp. 633–644, 1992.
- [14] V.S. Anishchenko, T.E. Vadivasova, D.E. Postnov, O.V. Sosnovtseva, S.W. Wu, L.O. Chua, Dynamics of the nonautonomous Chua's circuit , *Int. J. Bifurcation Chaos*, vol. 5, pp. 1525–1540, 1995.
- [15] V.S. Anishchenko, V.V. Astakhov, T.E. Vadivasova, O.V. Sosnovtseva, C.W. Wu, and L.O. Chua, Dynamics of two coupled Chua's circuits , *Int. J. Bifurcation Chaos*, vol. 5, pp. 1677–1699, 1995.
- [16] M.G. Rosenblum, A.S. Pikovsky, J. Kurths, Phase synchronization of chaotic oscillations , *Phys. Rev. Lett.*, vol. 76, pp. 1804–1807, 1996.
- [17] A.S. Pikovsky, M.G. Rosenblum, G.V. Osipov, and J. Kurths, Phase synchronization of chaotic oscillators by external driving , *Physica D*, vol. 104, pp. 219–238, 1997.
- [18] V.S. Anishchenko, T.E. Vadivasova, G.A. Okrokvertskhov, G.I. Strelkova, Correlation Analysis of Dynamical Chaos, *Physica A*, vol. 325, pp. 199–212, 2003.

A MOS CIRCUIT FOR THE LOTKA-VOLTERRA CHAOTIC OSCILLATOR

Tetsuya Asai, Yusuke Kanazawa, Masayuki Ikebe, and Yoshihito Amemiya

Department of Electrical Engineering, Hokkaido University,

Kita 13, Nishi 8, Kita-ku, Sapporo 060-8628, Japan

e-mail: asai@sapiens-ei.eng.hokudai.ac.jp

Abstract— *This paper presents an analog integrated circuit (IC) that implements the Lotka-Volterra (LV) chaotic oscillator. The LV system describes periodic or chaotic behaviors in prey-predator systems with a simple mathematical form. The proposed circuit consists of a small number of metal-oxide-semiconductor field-effect transistors (MOS FETs) operating in their subthreshold region, which is very suitable for large-scale IC implementation. A general method for implementing the LV system on analog ICs is also presented.*

I. INTRODUCTION

The design of chaotic oscillators has been a subject of increasing interest during the past few years [1]. Indeed, analog integrated circuits that implement chaotic oscillatory systems provide us important cues for exploring and discovering novel forms of information processing. Many designs of chaotic oscillators were introduced starting from the use of a coil in Chua's circuit to the use of large blocks such as operational amplifiers. In both cases, the fabrication area was very large. These designs were also dependent on the use of floating capacitors, the use of high supply voltage and high power dissipation, which is not preferred in fabrication due to the demanding need for portable devices in our world today. In this paper, we propose micropower analog MOS circuits that exhibit chaotic behaviors with very simple circuit construction.

II. ANALOG MOS CIRCUITS FOR THE LOTKA-VOLTERRA MODEL

The Lotka-Volterra (LV) model is one of the earliest predator-prey models to be based on sound mathematical principles. It forms the basis of many models used today in the analysis of population dynamics. We here employ a LV model that describes interactions between three species in an ecosystem, i.e.; one predator and two preys [2]. In addition to the predation of the preys, the two preys compete with each other for

their feeding ground. The dynamics are given by

$$\tau \dot{x}_1 = (1 - x_1 - x_2 - k y)x_1, \quad (1)$$

$$\tau \dot{x}_2 = (a - b x_1 - c x_2 - y)x_2, \quad (2)$$

$$\tau \dot{y} = (-r + \alpha k x_1 + \beta x_2)y, \quad (3)$$

where x_1 and x_2 represent the prey population, y the predator population, τ the time constant, the rests (k , a , b , c , r , α and β) are control parameters.

By introducing three new variables:

$$X_1 = \ln x_1, \quad X_2 = \ln x_2, \quad Y = \ln y, \quad (4)$$

Eqs. (1), (2) and (3) can be transformed into:

$$\tau \dot{X}_1 = 1 - \exp(X_1) - \exp(X_2) - k \exp(Y), \quad (5)$$

$$\tau \dot{X}_2 = a - b \exp(X_1) - c \exp(X_2) - \exp(Y), \quad (6)$$

$$\tau \dot{Y} = -r + \alpha k \exp(X_1) + \beta \exp(X_2). \quad (7)$$

This transformation has two merit for analog MOS implementation: i) the resultant equations [(5), (6) and (7)] do not have multiplying terms of system variables and are described by linear combination of exponential functions, which enables us to design the circuit without any analog multiplier; ii) the exponential nonlinearity is essential characteristics of semiconductor devices, which enables us to design a circuit based on the intrinsic characteristics of semiconductors. We here use the exponential current-voltage characteristics of subthreshold MOS FETs [3].

In the subthreshold region of operation without body effect, the drain-source current of a saturated n-type MOS FET is given by

$$I_{ds} = I_0 \exp\left(\frac{\kappa}{V_T} V_{gs}\right) \quad (8)$$

where I_{ds} represents the drain-source current, V_{gs} the gate-source voltage ($\geq 4V_T$ for saturation), κ the effectiveness of the gate potential, and $V_T \equiv kT/q \approx 26$ mV at room temperature (k is Boltzmann's constant, T the temperature, and q the electron charge), and I_0 the fabrication parameter. Typical parameter values for minimum-size devices fabricated in a standard 1.5- μ m n-well process are $I_0 = 0.5 \times 10^{-15}$ A

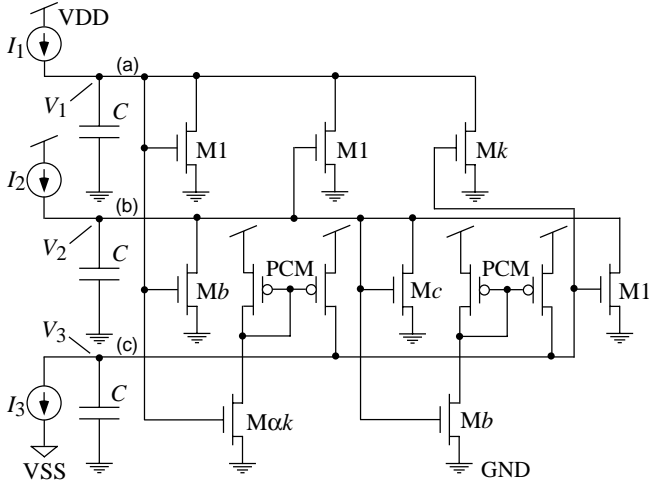


Fig. 1. Construction of LV circuit.

and $\kappa = 0.6$. Note that Eq. (8) is valid only when the MOS FET is saturated; i.e., $V_{gs} \geq 4V_T$.

Figure 1 shows construction of the LV circuit. Applying KCL at node (a) and (b) in Fig. 1, we obtain

$$C\dot{V}_1 = I_1 - I_0^{(M1)} \exp\left(\frac{\kappa}{V_T} V_1\right) - I_0^{(M1)} \exp\left(\frac{\kappa}{V_T} V_2\right) - I_0^{(Mk)} \exp\left(\frac{\kappa}{V_T} V_3\right) \quad (9)$$

$$C\dot{V}_2 = I_2 - I_0^{(Mb)} \exp\left(\frac{\kappa}{V_T} V_1\right) - I_0^{(Mc)} \exp\left(\frac{\kappa}{V_T} V_2\right) - I_0^{(M1)} \exp\left(\frac{\kappa}{V_T} V_3\right) \quad (10)$$

where $I_0^{(M)}$ the fabrication parameter. The node voltages V_1 and V_2 are also given to the gates of MOS FETs $M\alpha k$ and $M\beta$, respectively. Because the currents of $M\alpha k$ and $M\beta$ are copied to node (c) by two pMOS current mirrors (PCMs in Fig. 1), the node equation is represented by

$$C\dot{V}_3 = -I_3 + I_0^{(M\alpha k)} \exp\left(\frac{\kappa}{V_T} V_1\right) + I_0^{(M\beta)} \exp\left(\frac{\kappa}{V_T} V_2\right). \quad (11)$$

Equations (9) to (11) become equivalent to Eqs. (5) to (7), respectively, when

$$V_i = \frac{V_T}{\kappa} X_i, \quad (i = 1, 2, 3), \quad \tau = \frac{CV_T}{i_0 \kappa}, \quad (12)$$

$$\frac{I_1}{i_0} = 1, \quad \frac{I_2}{i_0} = a, \quad \frac{I_3}{i_0} = r, \quad (13)$$

$$\frac{I_0^{(M1)}}{i_0} = 1, \quad \frac{I_0^{(Mk)}}{i_0} = k, \quad \frac{I_0^{(Mb)}}{i_0} = b, \quad (14)$$

$$\frac{I_0^{(Mc)}}{i_0} = c, \quad \frac{I_0^{(M\alpha k)}}{i_0} = \alpha k, \quad \frac{I_0^{(M\beta)}}{i_0} = \beta, \quad (15)$$

where i_0 represents the normalized current.

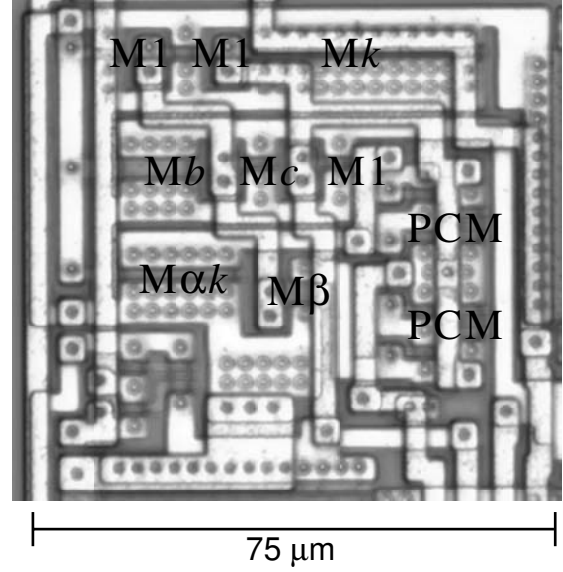


Fig. 2. Chip micrograph of a fabricated LV circuit (MOSIS, vendor: AMIS, n -well single-poly double-metal CMOS process, feature size: $1.5 \mu\text{m}$, total area: $75 \mu\text{m} \times 40 \mu\text{m}$).

MOS FET	W (μm)	L (μm)
M1	4	1.6
Mb	12	3.2
Mc	4	1.6
Mk	40	1.6
$M\alpha k$	20	1.6
$M\beta$	4	3.2

TABLE I
SIZE OF NMOS FETs ON LV CHIP.

III. EXPERIMENTAL RESULTS

We fabricated a prototype circuit using a $1.6\text{-}\mu\text{m}$ scalable complementary-MOS (CMOS) rule (MOSIS, vendor: AMIS, n -well single-poly double-metal CMOS process, $\lambda = 0.8 \mu\text{m}$, feature size: $1.5 \mu\text{m}$). Figure 2 shows a micrograph of the LV circuit. We employed the same parameter set of the LV system ($k = 10$, $b = 1.5$, $c = 1$, $\alpha k = 5$, $\beta = 0.5$) as in [2] where a stable focus bifurcates into chaotic oscillation via stable period- n cycles. The resultant size of nMOS FETs are listed in Tab. 1. The pMOS current mirrors (PCM) were designed with a dimension of $W/L = 4 \mu\text{m} / 1.6 \mu\text{m}$. The circuit took up a total area of $75 \mu\text{m} \times 40 \mu\text{m}$.

In the following experiments, we added external capacitors ($C = 0.1 \mu\text{F}$) out of the chip due to the time resolution of our measurement systems. We used Ag-

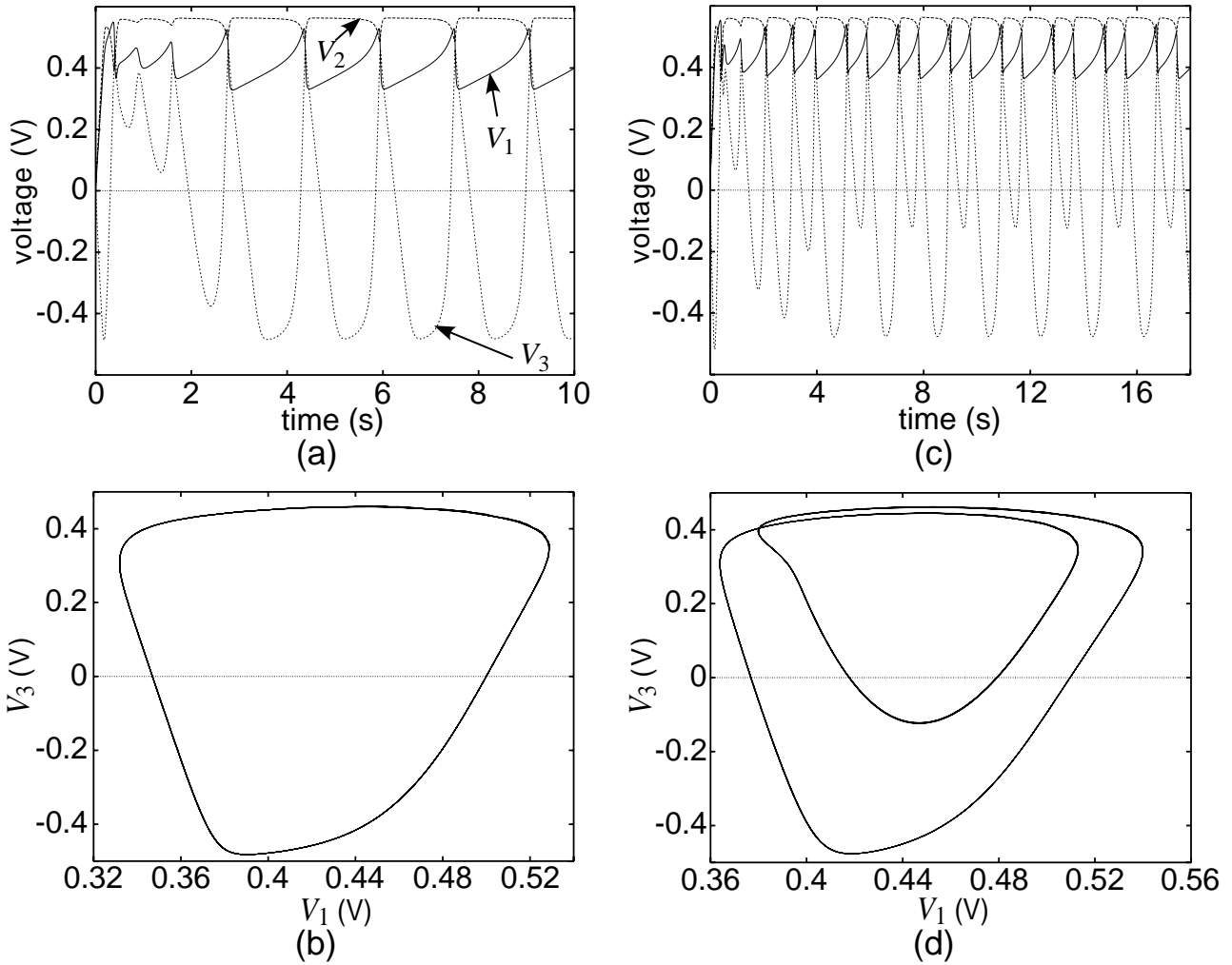


Fig. 3. Experimental results of fabricated LV circuit. (a) and (c) show time course of system variables (V_1 , V_2 and V_3). (b) and (d) show trajectories on a V_1 - V_3 plane. (a) and (b) represent results for $I_3 = 320$ nA, while (c) and (d) results for $I_3 = 360$ nA.

ilent 4156B as external current sources for the input. Time courses of V_1 , V_2 and V_3 were sampled simultaneously by Agilent 4156B. The supply voltage (VDD) was set at 2.5 V. The input currents (I_1, I_2) were fixed at (250, 287) nA. We examined dynamic behaviors of the fabricated LV circuit by changing the rest input current I_3 that corresponds to the control parameter r in (3).

Figure 3 shows the measurement results. Figures 3(a) and 3(b) show the time course of the system variable (V_1 , V_2 and V_3) and trajectories on a V_1 - V_3 plane, respectively. In this experiment, I_3 was set at 320 nA. The LV circuit exhibited stable oscillation with period-1 cycles. In Figs. 3(c) and 3(d), which represent the time course of the system variable and trajectories on a V_1 - V_3 plane, respectively, I_3 was set at 360 nA. The LV circuit exhibited stable oscillation with period-2 cycles. Figures 4(a) and 4(b) show the time

course of the system variable and trajectories on a V_1 - V_3 plane, respectively. In this experiment, I_3 was set at 420 nA. The maximum value of the Lyapunov exponents was 10.1, which indicated that the LV circuit exhibited chaotic oscillation.

We confirmed whether the qualitative behavior of the circuit is consistent with the theoretical analysis. According to [2], as the value of the control parameter r increases from r_1 to r_2 , the Hopf bifurcation occurs at $r \equiv r_\alpha$ and $r \equiv r_\beta$ where the stable focus bifurcates ($r_1 < r < r_\alpha$) to the unstable focus with enclosing limit cycle ($r_\alpha < r < r_\beta$). Then the unstable focus bifurcates to the stable focus ($r_\beta < r < r_2$). We confirmed this transition (stable focus \rightarrow unstable focus with enclosing limit cycle \rightarrow stable focus) in the LV circuit during the increase of I_3 ($\sim r$). Figure 5 shows the bifurcation diagram obtained from the LV circuit. The diagram was created as follows: 1) when

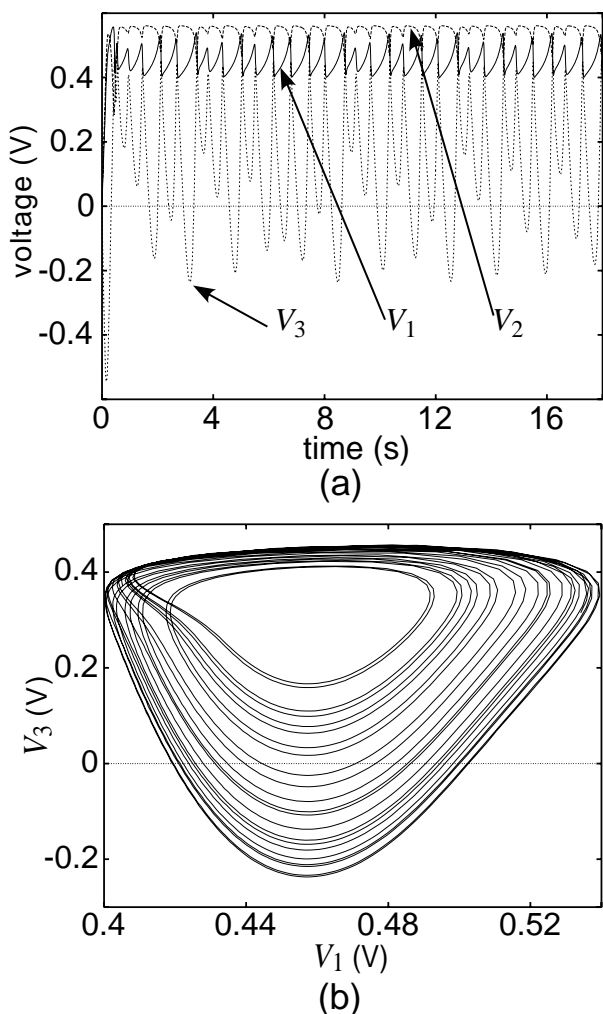


Fig. 4. Experimental results of fabricated LV circuit. (a) and (b) show time course of system variables (V_1 , V_2 and V_3) trajectories on a V_1 - V_3 plane, respectively, when $I_3 = 420$ nA.

the circuit had stable focus with a given I_3 , the stable value of V_3 was plotted, 2) when the circuit oscillated with a given I_3 , the value of V_3 at which $\dot{V}_3 = 0$ was plotted. When $I_3 < 182$ nA, the LV circuit did not oscillate (stable focus). The stable focus bifurcated at $I_3 \approx 182$ nA to stable period-1 cycles. Increasing the value of I_3 , further bifurcations to period-2 cycles, period-4 cycles, chaotic cycles occurred around 370 nA $< I_3 < 450$ nA. Finally, the unstable focus bifurcated to a stable focus again at $I_3 \approx 580$ nA.

The results in Fig. 5 indicates two important properties of the proposed LV circuit: 1) although we used practical subthreshold MOS FETs, the bifurcation property is qualitatively consistent with the result of theoretical analysis; 2) the LV circuit exhibits stable oscillation with period- n and chaotic cycles over a wide range of I_3 ; i.e., 182 nA $< I_3 < 580$ nA,

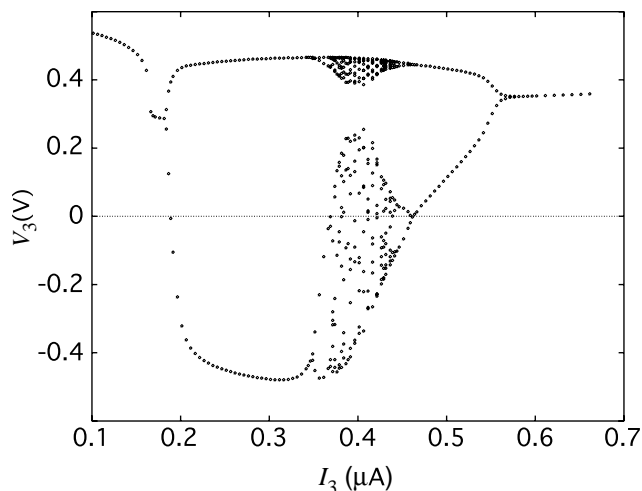


Fig. 5. Bifurcation diagram of LV circuit.

which allows the LV circuit to keep stable oscillation under noisy environment, even though the subthreshold MOS FETs were used in the circuit.

IV. SUMMARY

We proposed an analog integrated circuit (IC) that implements the Lotka-Volterra (LV) chaotic oscillator. We designed very simple (just 12 transistors) circuit for the LV oscillator where all transistors operated in their subthreshold region. The LV oscillator was fabricated using a $1.6\text{-}\mu\text{m}$ scalable rule (MOSIS, vendor: AMIS, n -well single-poly double-metal process, $\lambda = 0.8$ μm , feature size: 1.5 μm). The circuit took up a total area of 75 $\mu\text{m} \times 40$ μm . Although the quantitative results of the fabricated circuit were inconsistent with the theoretical analysis, the qualitative behavior (bifurcation property) agreed well with the result of theoretical analysis. Furthermore, the LV circuit exhibited stable oscillation with period- n and chaotic cycles over a wide range of control current, which enables us to design a stable oscillator that can operate under noisy environment, even though the subthreshold MOS FETs were used in the circuit.

REFERENCES

- [1] G. Chen and T. Ueta, Eds., *Chaos in Circuits and Systems*. World Scientific, New Jersey, 2002.
- [2] M. Mimura and Y. Kan-on, "Predation-mediated coexistence and segregation structures," in *Patterns and Waves*, North Holland, 1986, pp. 129-155.
- [3] A. G. Andreou, K. A. Boahen, P. O. Pouliquen, A. Pavasović, R. E. Jenkins, and K. Strohhenn, "Current-mode subthreshold MOS circuits for analog VLSI neural systems," *IEEE Trans. Neural Networks*, vol. 2, pp. 205-213, 1991.

CHAOTIC THIRD-ORDER LOG-DOMAIN FILTER

Alon Ascoli, Orla Feely and Paul Curran

Department of Electronic and Electrical Engineering
University College Dublin
Dublin 4, Ireland
e-mail: alon.ascoli@ucd.ie

Abstract—Operation of log-domain filters revolves around the large-signal exponential current-voltage relationship of the bipolar junction transistor (BJT), which is used to map the input currents to the logarithmic domain, where the analog processing takes place, and to convert the resulting filtered voltage waveforms back to the linear domain. Sometimes, the inherent internal nonlinearity of such circuits is the cause of unwanted externally-nonlinear effects. In this paper a differential third-order log-domain Chebychev low-pass filter is designed by applying the method of operational simulation of doubly-terminated LC ladders. When the six grounded shunt capacitors of this filter are properly replaced with three half-sized floating capacitors, as is common practice in internally-linear fully-differential capacitively-loaded circuits, under particular conditions the resulting system exhibits limit-cycle oscillations, period-doubling bifurcations and chaotic behaviour for zero-input. The presence of chaos is confirmed by extracting the spectrum of Lyapunov exponents of the system from the time series of the output voltage.

I. INTRODUCTION

The large-signal exponential relationship between the collector current and the base-emitter voltage of the BJT is used in log-domain filters [1]-[2] to logarithmically compress the input currents before any analog processing is applied to them. The resulting nonlinear voltages are then appropriately filtered and finally converted to output currents using the exponential mapping once again. Due to the compressing and expanding actions, log-domain filters are less sensitive to noise, show lower levels of distortion and exhibit higher dynamic range than conventional analog electronic circuits. For the same reason low-power and high-speed operation are key features of such circuits.

Ideally the output currents of log-domain filters are linearly filtered versions of the input currents.

However, the intrinsic internal nonlinearity of such circuits is sometimes responsible for the appearance of unexpected externally-nonlinear behaviour.

Application of the method of operational simulation of doubly-terminated LC ladders [2] allows us to design a differential third-order log-domain Chebychev low-pass filter (section II).

A common practice in internally-linear fully-differential capacitively-loaded circuits is to replace each pair of equal-value shunt capacitors, connected between two output nodes and ground, with a half-sized floating capacitor placed between those nodes. However, application of such technique to internally-nonlinear circuits, such as log-domain filters, may result in the loss of external linearity [3].

Section III describes the main results of this paper. The differential third-order log-domain Chebychev LC ladder low-pass filter designed in section II is stable. On the other hand, when the six grounded shunt capacitors of this filter are appropriately replaced with three half-sized floating capacitors, for zero input and under special conditions limit-cycle oscillations, period-doubling bifurcations and chaotic behaviour are observed at the output of the resulting circuit. The occurrence of chaos in this third-order autonomous system is confirmed by computing the corresponding spectrum of Lyapunov exponents, extracted from the time series of the output voltage using the algorithm presented in [4].

Finally conclusions are drawn in section IV.

II. BALANCED 3RD-ORDER LOW-PASS FILTER

This section presents the log-domain filter which shows the nonlinear behaviour described in section III. We first apply the method of operational simulation of doubly-terminated LC ladders [2] to design a single-ended third-order log-domain Chebychev low-pass filter with a pass-band ripple of 1 dB and a cut-off frequency of 1 MHz. The LC ladder passive prototype implementing a third-order Chebychev low-pass filter is shown in Fig. 1. The

values of the passive components are first chosen to obtain a pass-band ripple of 1 dB and a cut-off frequency of 1 rad/sec. The frequency scaling transformation is then applied to the values of the inductor and of the capacitors so that the cut-off frequency of the passive low-pass filter is 1 MHz.

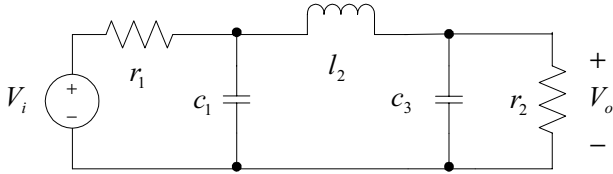


Fig. 1 LC ladder passive prototype of a third-order Chebyshev low-pass filter. The input and output voltages are V_i and V_o respectively.

Table 1 shows the values of the parameters of the passive prototype satisfying the given specifications.

Name	r_1 [Ω]	c_1 [μF]	l_2 [μH]	c_3 [μF]	r_2 [Ω]
Value	1	0.32	0.16	0.32	1

Table 1 Names and values of the circuit elements of the LC ladder passive low-pass filter of Fig. 1 for a passband ripple of 1 dB and a cut-off frequency of 1 MHz.

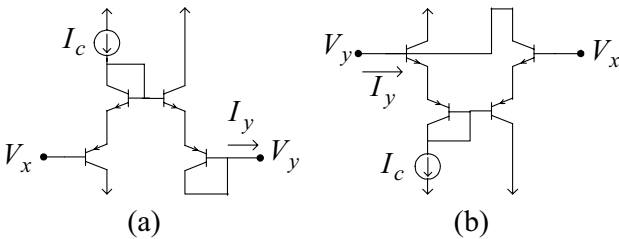


Fig. 2 Log-domain cells with opposite polarities: a) positive cell and b) negative cell. For each cell V_x and V_y represent the input and output voltages respectively, I_y is the output current and I_c a constant current source.

Application of the technique of operational simulation of doubly-terminated LC ladders [2] to the passive prototype of Fig. 1 allows us to derive the nodal equations for the log-domain counterpart:

$$\begin{aligned}
 C_1 \frac{dV_1}{dt} &= (I_o + I_{in}) e^{-\frac{V_1}{2V_T}} - I_o - I_o e^{\frac{V_2 - V_1}{2V_T}} + I_o e^{\frac{V_1}{2V_T}} \\
 C_2 \frac{dV_2}{dt} &= I_o e^{\frac{V_1 - V_2}{2V_T}} - I_o e^{\frac{V_3 - V_2}{2V_T}} \\
 C_3 \frac{dV_3}{dt} &= I_o e^{\frac{V_2 - V_3}{2V_T}} - I_o
 \end{aligned} \tag{1}$$

where $\{C_1, C_2, C_3\} = I_o (2V_T)^{-1} \{c_1, l_2, c_3\}$ denote the shunt capacitors connected between nodes at voltages V_i ($i = 1, 2, 3$) and ground, V_T is the thermal voltage of the BJTs, I_{in} the input current and I_o a constant current source.

The log-domain positive and negative cells shown in Fig. 2 [2] are used to implement each term in the right-hand sides of eqns. (1). Applying the Translinear Principle [2] to each log-domain cell of Fig. 2, the expression of the corresponding output current is found to be:

$$I_y = I_c e^{\frac{V_x - V_y}{2V_T}} \tag{3}$$

Then, adding to the resulting circuit a compressing stage at the input and an expanding block at the output, as shown in Fig. 3, where

$$V_x = 2V_T \ln\left(\frac{I_c + I_x}{I_c}\right) = LOG(I_x) \tag{4}$$

$$I_y = I_c e^{\frac{V_y}{2V_T}} - I_c = EXP(V_y)$$

we obtain the circuit shown in Fig. 4, which implements a single-ended third-order log-domain Chebyshev LC ladder low-pass filter with a pass-band ripple of 1 dB and a 3-dB cut-off frequency of 1 MHz, as confirmed by a PSpice AC analysis.

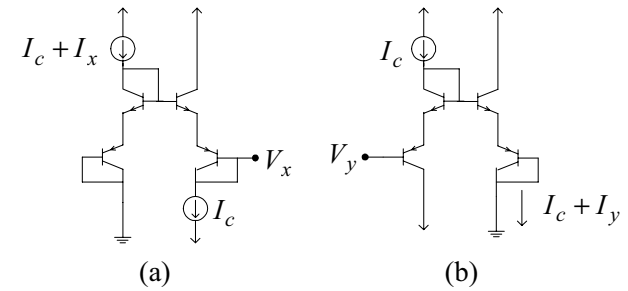


Fig. 3 Signal companding blocks: a) input LOG stage and b) output EXP stage. I_c is a constant current source, V_x the compressed version of input current I_x and I_y , the expanded form of output voltage V_y .

In all the PSpice simulations described in this paper the supply voltages are set to $\pm 1.5 V$, the values of the circuit elements in Fig. 4 are given in Table 2 and the devices modeling the npn and pnp BJTs are perfectly matched with parameter values as those of device 2N3904 except for the forward-current gain, which is set to the typical value of 100.

A balanced version of the low-pass filter of Fig. 4

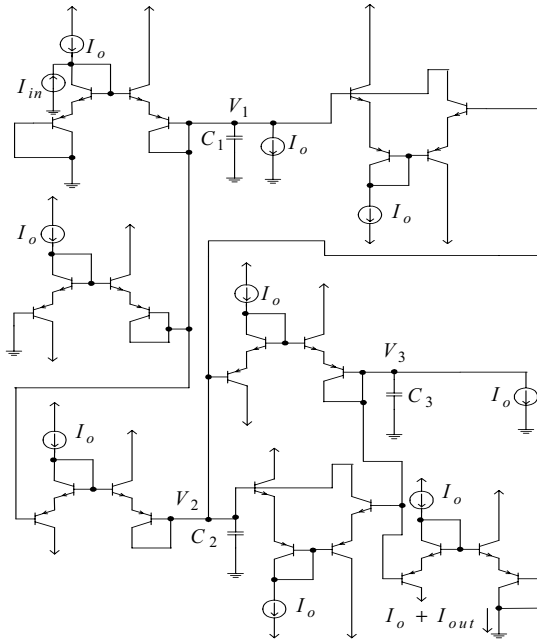


Fig. 4 Single-ended third-order log-domain Chebyshev LC ladder low-pass filter.

Name	I_o [μA]	C_1 [nF]	C_2 [nF]	C_3 [nF]
Value	100	0.62	0.31	0.62

Table 2 Names and values of the circuit elements of the circuit of Fig. 4.

is synthesized by adopting a procedure similar to that used in [2] to derive the differential log-domain integrator from the single-ended one.

The resulting filter is shown in Fig. 5, where V_{opi} and V_{oni} ($i = 1, 2, 3$) denote the voltages across the six grounded shunt capacitors (that need to be two times larger than those of the single-ended low-pass filter with the same cut-off frequency), I_{ip} and I_{in} are the positive and negative input currents, while I_{op} and I_{on} the positive and negative output currents respectively. Again, a PSpice AC analysis of the circuit confirms that the design requirements, earlier specified, are indeed satisfied.

III. CHAOS IN FLOATING-CAPACITOR FILTER

The total circuit capacitance is reduced by a factor of 4 if we properly replace the six grounded shunt capacitors in the circuit of Fig. 5 with three half-sized floating capacitors. However, the resulting circuit topology loses external linearity: a brief perturbation of the floating-capacitor filter with zero input can give rise to sustained nonlinear oscillations.

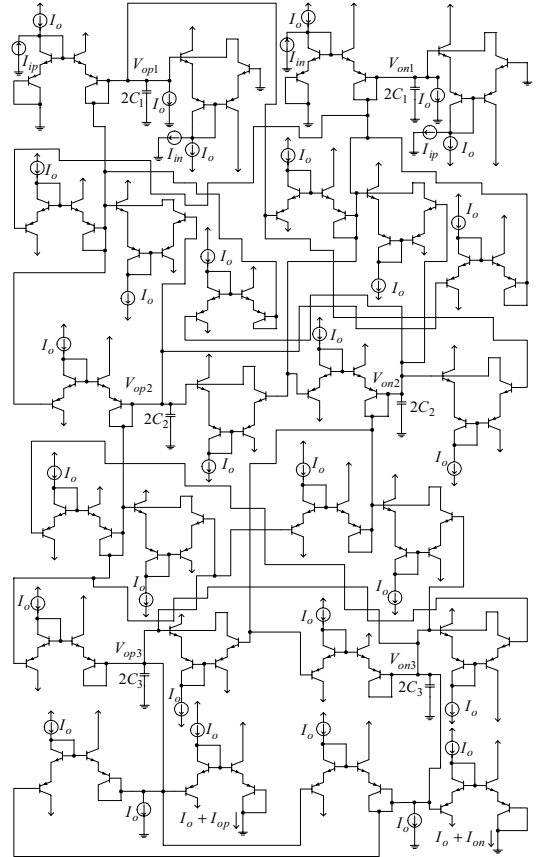


Fig. 5 Differential version of the third-order log-domain Chebyshev LC ladder low-pass filter of Fig. 4.

Interesting nonlinear behaviour is observed if the values of floating-capacitors C_2 and C_3 are set to $0.1 nF$ and $0.2 nF$ respectively and that of C_1 is adjusted in small steps. The state variables of this autonomous third-order system are defined as the voltages across the three floating capacitors: $V_{Ci} = V_{opi} - V_{oni}$ ($i = 1, 2, 3$). A period-two limit cycle is detected for C_1 equal to $0.55 nF$. Fig. 6 shows the projection of this cycle on the $V_{C3} - V_{C2}$ plane. Increasing the value of C_1 further, when this floating-capacitor equals $0.59 nF$ a period-doubling bifurcation takes place: the period-two limit cycle becomes unstable and a period-four limit-cycle is born. This is clear from Fig. 7. Further increases in the value of C_1 do not cause any change in the attractor of the system until a chaotic attractor appears for $C_1 = 0.6 nF$ (Fig.8). Use of the algorithm presented in [4] allows us to extract the Lyapunov exponents ($\lambda_1 \approx 0.01$, $\lambda_2 \approx 0$ and $\lambda_3 \approx -0.015$) from the time series of output voltage V_{C3} . The robustness of this computation is clear from Fig. 9, that shows the fluctuation in the values of the Lyapunov exponents as the time delay is varied in the phase space reconstruction technique of delays [4].

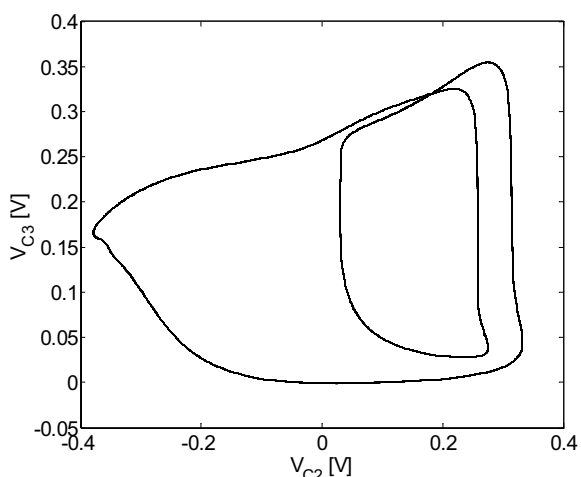


Fig. 6 Projection of the period-two limit cycle on the $V_{C3} - V_{C2}$ plane. Capacitor C_1 is set to 0.55 nF .

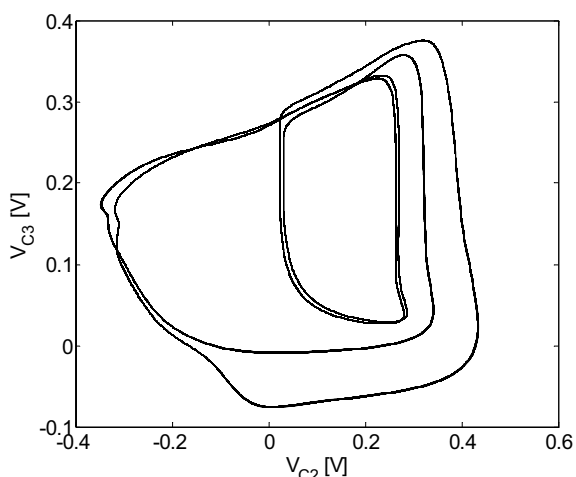


Fig. 7 Projection of the period-four limit cycle on the $V_{C3} - V_{C2}$ plane. Capacitor C_1 equals 0.59 nF .

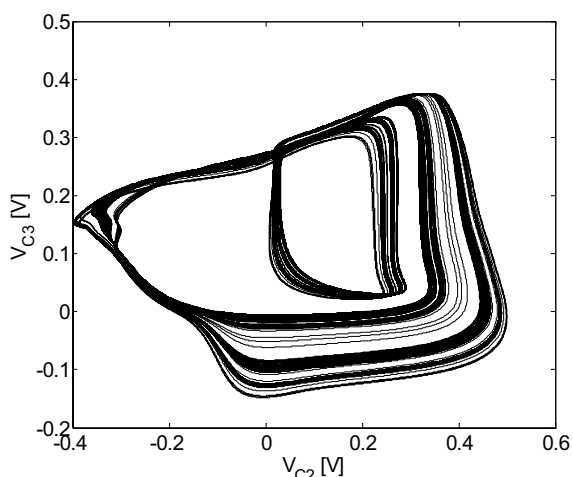


Fig. 8 Projection of the chaotic attractor on the $V_{C3} - V_{C2}$ plane. The value of capacitor C_1 is 0.6 nF .

It is worthy to note that for each value of the time delay in Fig. 9 the largest Lyapunov exponent λ_1 is

positive and the sum of λ_1 , λ_2 and λ_3 is negative. At this point we are neither able to detect the period-one limit-cycle nor other period-doubling bifurcations before the occurrence of chaos. Future work will aim at understanding whether or not this is a new route to chaos.

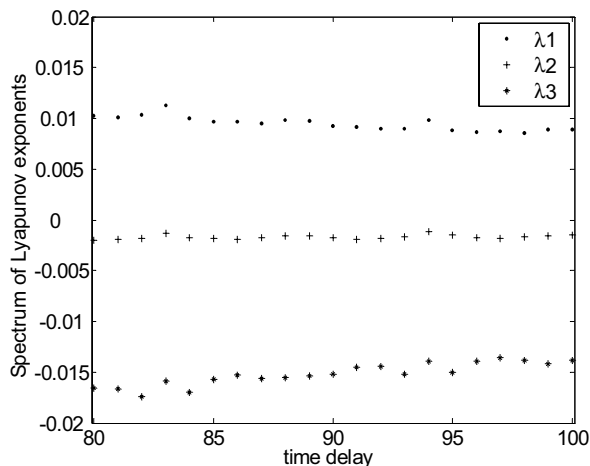


Fig. 9 Variation of the spectrum of Lyapunov exponents with respect to the time delay.

IV. CONCLUSIONS

The internal nonlinearity of log-domain filters is sometimes responsible for the occurrence of undesired externally-nonlinear behaviour. In this paper we apply a standard linear design technique to a differential third-order log-domain Chebychev LC ladder low-pass filter and we show the instability of the resulting circuit. In particular we detect limit-cycle oscillations, period-doubling bifurcations and chaotic behaviour for special choices of capacitors. It is the first time a simple third-order log-domain filter is found to behave chaotically.

REFERENCES

- [1] D. R. Frey: "Log-domain filtering: an approach to current-mode filtering", *IEE Proc.-G*, vol. 140, no. 6, pp. 406-416, Dec. 1993
- [2] G. W. Roberts and V. W. Leung: "Design and analysis of integrator-based log-domain filter circuits" (Kluwer Academic Publishers, Norwell, Massachusetts, 2000)
- [3] A. Ascoli, A. Mahon and O. Feely: "Nonlinear dynamics of first-order log-domain circuits", *Proc. Conf. Nonlinear Dynamics Elec. Syst. (NDES 2003)*, vol. I, pp. 17-20, May 2003
- [4] R. Hegger, H. Kantz and T. Schreiber: "Practical implementation of nonlinear time series methods: The TISEAN package", *CHAOS* 9, 413-435 (1999)

A GENERALIZED MODULATION LAW FOR GENERATING CONSTANT-ENVELOPE SPREAD-SPECTRUM SIGNALS VIA FREQUENCY MODULATION

M. Balestra, S. Santi, R. Rovatti, G. Setti

DI University of Ferrara, Italy

ARCES, DEIS University of Bologna, Italy

e-mail: mbalestra, gsetti@ing.unife.it, rrovatti, ssanti@deis.unibo.it

Abstract—*In this paper we generalize the calculus of the Power Density Spectrum (PDS) of a Constant-Envelope Spread-Spectrum (CE-SS) signal obtained by means of a frequency modulation (FM) using a random Pulse Amplitude Modulated (PAM) signal as the modulation law made by a generic pulse function. We choose two possible profile of such pulses aiming to approximate those generated by the analog circuit implementing the chaotic map and we present both analytical and numerical results that show how the pulse shape affect the PDS shape of the modulated signal.*

I. INTRODUCTION

Spread-spectrum signal processing techniques are encountering a growing interest as they pair or outclass the performance of conventional approaches; for instance, most of the next generation communication systems based on spread-spectrum schemes can achieve both good robustness to noise and low co-channel interference.

Furthermore, the ability to operate with low electromagnetic interference to narrowband neighbour equipment is appealing in designing systems like DC-DC converters, power actuators, clock-signals, etc. Indeed, as the emitted energy is dangerous because it is very concentrated in spectrum [1], some spread-spectrum techniques were proposed to redistribute the power over a wide frequency range [1] [2] [3] [4]. In fact, as Federal Communication Commission (FCC) regulations constrain peak power density spectrum of all signals in the electronic equipment [5], the key idea is to shape time-switching function to spread its power density spectrum to reduce the corresponding peak value, thus providing a more Electromagnetic Compliant (EMC) equipment, without compromising the proper operation of the circuit.

Among the several techniques proposed so far which relies on this principle, in this paper, we deal with Constant Envelope Spread-Spectrum (CE-SS)

signals constructed via frequency modulation, using a random PAM waveform as the driving signal and we propose a generalization of the mathematical tool provided in [11] for the PDS estimation, by generalizing the frequency modulation law by means of a generic pulse.

We then apply such analytical result in modelling non-ideal behavior of circuit that produces the modulation law sequence, aiming to determine the impact on the PDS of such non-ideal pulses.

This study can be of interest for example in EMC applications, where altering the modulation law may result in a significant loss of performances (in terms of PDS peak reduction). Although the pulse imperfection cannot be corrected or compensated in hardware, knowing how such irregularities act on the PDS, should lead to a different choice of the modulation parameters aiming at restore the performances of the ideal modulation scheme.

In section II we present a mathematical tool to deal with the PDS of signal generated via the frequency modulation of random sequences forming the modulation law by means of a generic pulse. This is an extension of the mathematical results provided in [11].

In section III we apply the analytical result using an approximation of the PAM pulse by means of simple functions. We approximate two usual behavior of such a pulse in real applications and we estimate the PDS of a particular spread spectrum FM waveform which shows high EMC performances when an ideal PAM driving signals is used [6]. We then compare the analytical results with those obtained by simulation and derive some conclusions.

II. POWER DENSITY SPECTRUM GENERALIZATION

Let us consider a frequency modulated (FM) sinusoidal carrier $s(t)$ which is formally described as:

$$s(t) = \cos \left[2\pi \left(f_0 t + \Delta f \int_{-\infty}^t \xi(\tau) d\tau \right) \right] \quad (1)$$

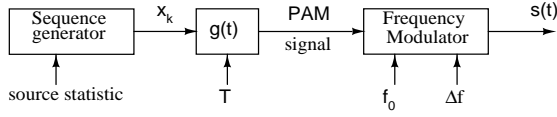


Fig. 1. Modulation scheme.

where f_0 is the carrier frequency, Δf is the frequency deviation and $\xi(t)$ is the modulation law. In the following, we shall indicate the PDS of $s(t)$ as $\Phi_{ss}(f)$. In our discussion we follow [10][11] and we assume that the structure of $\xi(t)$ is defined on a sequence of discrete-time symbols $\{x_k\}$ as sketched in figure 1.

More formally we have $\xi(t) = \sum_{k=-\infty}^{\infty} x_k g(t - kT)$, where T is the symbol update period and $g(\cdot)$ is a generic function that can assume non-null values only in $]0, T]$. Notice that is possible that $|g(t)| > 1$ thus violating the Δf constraint for the frequency modulation. However, we restrict ourselves to functions that represent a good approximations of feasible non-ideal behaviors of the analog circuit that produces $\xi(t)$.

To better express the modulation characteristics let us introduce a modulation index $m = \Delta f T$ and consider the low pass equivalent $\tilde{s}(t) = e^{i[2\pi\Delta f \int_{-\infty}^t \xi(\tau) d\tau]}$ of the signal $s(t)$.

If we assume that the symbols $\{x_k\}$ are generated by an ergodic process, then $\tilde{s}(t)$ is cyclo-stationary [7][8] and Power Density Spectrum $\Phi_{ss}(f)$ of the signal $s(t)$ is well defined. The relation among $\Phi_{ss}(f)$ and $\Phi_{\tilde{s}\tilde{s}}(f)$ is given by[7]:

$$\Phi_{ss}(f) = \frac{1}{2} [\Phi_{\tilde{s}\tilde{s}}(f - f_0) + \Phi_{\tilde{s}\tilde{s}}(-f - f_0)]$$

which, considering only positive frequencies, can be approximated by

$$\Phi_{ss}(f) \approx \Phi_{\tilde{s}\tilde{s}}(f - f_0)$$

From the PDS definition:

$$\Phi_{\tilde{s}\tilde{s}}(f) = \lim_{M \rightarrow \infty} \frac{1}{2MT} E \left[|\tilde{S}_M(f)|^2 \right] \quad (2)$$

where

$$\tilde{S}_M(f) = \int_0^{MT} \tilde{s}(\tau) e^{-i2\pi f \tau} d\tau$$

and $E[\cdot]$ indicates the expectation with respect to the process generating the modulating sequence.

By defining

$$\tilde{\sigma}_n(f) = e^{-i2\pi f n T} \int_0^T \tilde{s}(\xi + nT) e^{-i2\pi f \xi} d\xi$$

we can write $\tilde{S}_M(f) = \sum_{n=0}^{M-1} \tilde{\sigma}_n(f)$, and so we obtain[9]:

$$|\tilde{S}_M(f)|^2 = \sum_{k=0}^{M-1} \sum_{n=0}^{M-k-1} \tilde{\sigma}_{n+k}(f) \tilde{\sigma}_n^*(f) = \quad (3)$$

$$\sum_{n=0}^{M-1} \tilde{\sigma}_n(f) \tilde{\sigma}_n^*(f) + 2\text{Re} \left\{ \sum_{k=1}^{M-1} \sum_{n=0}^{M-k-1} \tilde{\sigma}_{n+k}(f) \tilde{\sigma}_n^*(f) \right\}$$

where $*$ denotes complex conjugation operation. With this, (2) can be written as

$$\Phi_{\tilde{s}\tilde{s}}(f) = K_1(f) + 2\text{Re}\{K_2(f)\} \quad (4)$$

By defining

$$H(x_n, f) = \int_0^T e^{i2\pi\Delta f x_n \mathcal{G}(\xi)} e^{-i2\pi f \xi} d\xi \quad (5)$$

where

$$\mathcal{G}(\xi) = \int_0^\xi g(\tau) d\tau \quad (6)$$

we have

$$\tilde{\sigma}_n(f) \tilde{\sigma}_n^*(f) = |H(x_n, f)|^2$$

From now on, we assume the $\{x_k\}$ as a sequence generated by a process of independent random symbols; taking the expectation of the first term of (3) we can write:

$$K_1(f) = \frac{1}{2T} E_x [|H(x, f)|^2] \quad (7)$$

With the assumption of independence of the symbols we can write, for $k > 0$:

$$E_x [\tilde{\sigma}_n(f) \tilde{\sigma}_{n+k}^*(f)] = E_x \left[e^{-i2\pi(fT - \Delta f Gx)} \right]^{k-1} \cdot E_x \left[e^{-i2\pi(fT - \Delta f Gx)} H^*(x_n, f) \right] E_x [H(x_n, f)] \quad (8)$$

where $G = \mathcal{G}(T)$. Thus, if $(fT - \Delta f Gx) \neq 0$ and assuming $|E [e^{-i2\pi(fT - \Delta f Gx)}]| < 1$ we easily get

$$K_2(f) = \frac{E_x [e^{-i2\pi(fT - \Delta f Gx)} H^*(x, f)] E_x [H(x, f)]}{2T(1 - E_x [e^{-i2\pi(fT - \Delta f Gx)}])} \quad (9)$$

Notice that by replacing $g(t)$ with a function which is 1 in $]0, T]$ and 0 elsewhere in (5)-(9), (4) reduces to the formulas (9)-(10) in [11].

III. PDS ESTIMATION

Evaluation of equations (4) (7) and (9) for a generic function $g(t)$ could be a hard task. We then approximate $g(t)$ by means of N simple functions of amplitude a_n , such as $g(t) = \sum_{n=0}^{N-1} a_n \chi(t - n\Delta T)$ where $\Delta T = T/N$ and $\chi(\cdot)$ is 1 in $]0, \Delta T]$ and 0 elsewhere. Furthermore, we consider a binary process for $\{x_k\}$ such as we constrain the sequence x_k to assume only two values with the same probability (Binary modulation) (i.e. $x_k \in \{-1, +1\}$). For such modulation the value of the index modulation that gives the lower PDS peak is $m \cong 0.318$ [6], which is one of the lowest achievable by FM modulation schemes when dealing with sinusoidal carriers [6].

With this assumption, equation (7) and (9) can be calculate as follow:

$$K_1(f) = \frac{\Delta T^2}{2T} \sum_{l=1}^N \sum_{h=1}^N e^{-i2\pi f T(l-h)} \sum_{p=0}^1 A_{l,p}(f) A_{h,p}(f) \quad (10)$$

$$K_2(f) = \frac{\Delta T^2 B(f)}{4T} \sum_{l=1}^N \sum_{h=1}^N e^{-i2\pi f \Delta T(l-h)} \cdot \sum_{p=0}^1 \sum_{q=0}^1 A_{l,p}(f) A_{h,q}(f) \quad (11)$$

where

$$A_{k,r}(f) = e^{(-1)^r i\pi \Delta f \Delta T (2 \sum_{j=1}^{k-1} a_j + a_k)} \cdot \text{sinc}(\pi \Delta T (f + (-1)^{r+1} a_k \Delta f)) \quad (12)$$

$$B(f) = \frac{1}{e^{i2\pi f T} - \cos(2\pi G \Delta f \Delta T)} \quad (13)$$

and $\text{sinc}(x) = \sin(x)/x$, $G = \Delta T \sum_{j=0}^{N-1} a_j$.

In this simple case, we can evaluate the spectrum even when $|E[e^{-i2\pi(fT - \Delta f G x)}]| = 1$. For this purpose, we are interested in the behavior of the power series

$$R(f) = \sum_{k=1}^{+\infty} e^{-i2\pi f k T} \cos^k(2\pi \Delta f G) \quad (14)$$

It is clear that, when the condition $\cos(2\pi \Delta f G) < 1$ holds, (14) may be written in the close form

$$R(f) = \frac{1}{e^{i2\pi f T} + \cos(2\pi \Delta f G)} \quad (15)$$

On the other hand, when $\cos(2\pi \Delta f G) = 1$, the series $R(f)$ fails to converge in the space of the continuous functions over the real axis. So, a different

kind of convergence has to be considered. First of all, it is convenient to split real and imaginary part of (14) according to Euler formula. We obtain

$$R(f) = \sum_{k=1}^{+\infty} \{\cos(2\pi f k T) + i \sin(2\pi f k T)\} \quad (16)$$

We separately consider the real and the imaginary part. For the real part, notice that

$$1 + 2 \sum_{k=1}^{+\infty} \cos(2\pi f k T) = \sum_{k=-\infty}^{\infty} e^{i2\pi k f T} = \frac{1}{T} \sum_{k=-\infty}^{\infty} \delta\left(f - \frac{k}{T}\right) \quad (17)$$

where $\delta(\cdot)$ is the Dirac Delta distribution. With this, we obtain

$$\sum_{k=1}^{+\infty} \cos(2\pi f k T) = \frac{1}{2} \left\{ -1 + \frac{1}{T} \sum_{k=-\infty}^{\infty} \delta\left(f - \frac{k}{T}\right) \right\} \quad (18)$$

For the imaginary part, we consider the series

$$\sum_{k=1}^{+\infty} \sin(2\pi f k T) = \cot(\pi f T) \quad (19)$$

where the equality can be verified taking the Fourier series of $\cot(\cdot)$ function.

So, in this case, equation (11) holds with $B(f) = \hat{B}(f)$ where

$$\hat{B}(f) = \left(\left\{ -\frac{1}{2} + \frac{1}{2T} \sum_{k=-\infty}^{\infty} \delta\left(f - \frac{k}{T}\right) \right\} + i \cot(\pi f T) \right)$$

To study the impact on the PDS of a modulation law $\xi(t)$ constructed by means of a non ideal pulse behavior, we consider $g(t)$ to be the step-response of a system with one or two poles. For the two-poles system, we here consider a conceivable underdamped second-order response with damping coefficient of $\zeta = 0.2$. Poles of both one-pole and two-poles systems has the same real part for comparison purposes. We assume these systems to be a good approximation of non-ideality in real modulation systems.

The approximation by means of simple functions of the two step-response are shown in figure 2, where $N = 40$. If the modulation law $\xi(t)$ is made by means of this pulses, equations (4), (10), (11) and (12) permit to compute the analytical PDS on both cases as shown in figure 3. Exploiting normalization, these results matches those obtained via simulations (shown in figure 4).

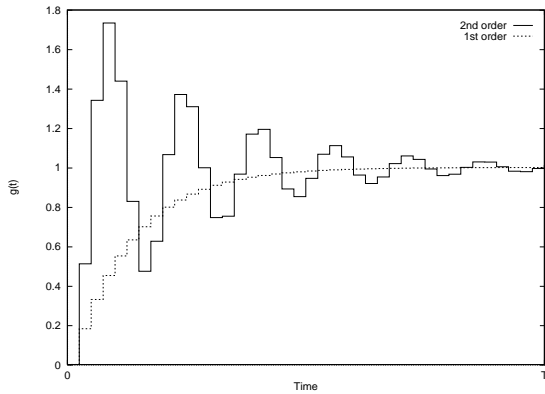


Fig. 2. Approximation of $g(t)$ step response pulses.

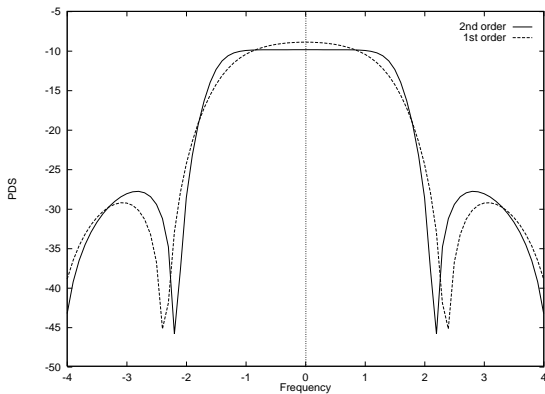


Fig. 3. Analytical PDS of the signal modulated by means of non-ideal pulses (normalized parameters).

The PDS obtained with a 2nd order step-response pulse has almost no difference from the one obtain with an ideal unity pulse, while the spectrum achieved with a 1st order step-response pulse present a different profile with consequent greater power peak. Although this slightly loss of performance for example in the EMC environment, can be reduced by increasing the value of the modulation index m , this result shows that the profile of the pulse $g(t)$ might have a non negligible impact on the PDS and should be taken in account while designing the modulation system.

IV. CONCLUSIONS

In this paper we have generalized the calculation of the PDS of a frequency modulated carrier presented in [11], by considering a generic pulse by which to construct the modulation law. Although the analytical solution of equations (4) (7) and (9) is not easy to derive for a generic pulse function $g(t)$, we can obtain a mathematical expression for the PDS by considering an approximation by means of simple functions of the pulse itself. We showed that the impact of the non-ideality of $g(t)$ should be consider in the design phase since the impact of the pulse shape on the PDS

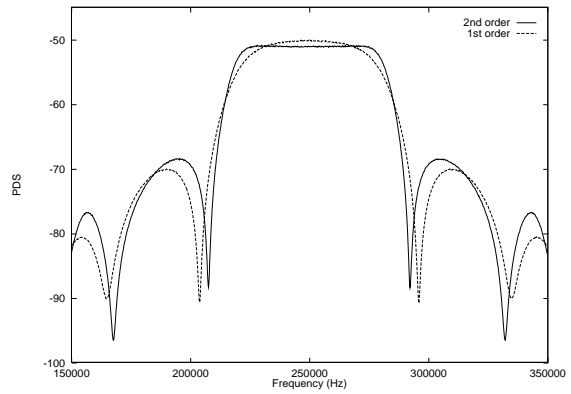


Fig. 4. PDS of the signal modulated by means of non-ideal pulses via simulations ($f_0 = 250\text{kHz}$, $\Delta f = 20\text{kHz}$, $m = 0.318$).

could be compensated by acting on the others degrees of freedom of the system, such as the modulation index m or the statistics of the symbols $\{x_k\}$ [11].

REFERENCES

- [1] K.B. Hardin, J.T. Fessler and D. R. Bush. Spread spectrum clock generation for the reduction of radiated emissions. In *Proceedings of the International Symposium on Electromagnetic Compatibility*, pp. 227–231, 1994.
- [2] J. Krupar, W. Schwartz. Reducing the EMI of Mixed Signal Circuits by Nonperiodic Clocking. In *International Workshop NDES 2002*, Izmir, Turkey, 2002.
- [3] A.M. Stankovic, H. Lev-Ari. Randomized modulation in power electronic converters. In *Proceedings IEEE*, vol. 90, pp. 782-799, May 2002.
- [4] R. Rovatti, G. Setti, and S. Graffi. Chaos based FM of clock signals for EMI reduction. In *Proceedings of ECCTD'99*, vol.1, (Stresa),pp. 373–376, Sept. 1999.
- [5] Federal Communication Commission. FCC methods of mesurement of radio noise emissions from computing devices. *FCC/OST MP-4*, July 1987.
- [6] M. Balestra, R. Rovatti, G. Setti. Power Spectrum Density Tuning In Random and Chaos-Based Timing Signal Modulation Techniques With Improved EMC. In *Proceedings of NDES2003*, Scuol, Switzerland, 2003.
- [7] J. G. Proakis. *Digital Communications*. McGraw-Hill, 4th ed., 2000.
- [8] G. Mazzini, R. Rovatti and G. Setti. Spectrum of randomly frequency modulated signals. In *Proceedings of NDES2000*, (Catania),pp. 146–150, May 2000.
- [9] W.R. Bennett, S.O. Rice. Spectral Density and Autocorrelation Functions Associated with Binary Frequency-Shift Keying. In *The Bell System Technical Journal*, Sept. 1963.
- [10] S. Callegari, R. Rovatti, and G. Setti. On the spectrum of signals obtained by driving FM modulators with chaotic sequences. In *Proceedings of ECCTD2001*, vol. II, (Helsinki), pp. 189192, 2001.
- [11] S. Callegari, R. Rovatti, and G. Setti. Generation of constant-envelope spread-spectrum signals via chaos-based FM: Theory and simulation results. In *IEEE Transactions on Circuits and Systems, Part I*, 2003.

A NEW PHENOMENON: PARAMETER CHAOS

A. L. Baranovski and A. J. Lawrance

Institute for Fundamentals of Electrical Engineering and Electronics
 Dresden University of Technology
 D-01062 Dresden, Germany
 e-mail: baranovs@iee1.et.tu-dresden.de
 &
 School of Mathematics and Statistics
 University of Birmingham
 Birmingham B15 2TT, UK
 e-mail: A.J.Lawrance@bham.ac.uk

Abstract—This paper is principally concerned with the effect of splitting and permuting the branches of a fully stretching piecewise linear map, with particular regard to the effect on the autocorrelation of the associated chaotic sequence. The autocorrelation function is shown to be a chaotic function of the shift parameter of the map. The implication is that slight variations in this parameter lead to very different statistical dependency properties of the map, maybe of considerable practical importance. This sensitivity is conceptually distinct from the well known sensitivity concerned with initial conditions and traditionally a signature of chaos. The present notion is one of parameter sensitivity, being termed here parameter chaos and apparently not explored previously and indeed is not evident with many types of parameters. This suggests speculatively that the sensitivity is associated with the shift operation and the slopes of the map’s branches being preserved. The paper presents both analytical and computational studies of the phenomena.

is explored in the paper, both analytically and computationally.

The paper draws on two works [4,5].

Consider the class Φ of fully stretching 1-dimensional m -branch piece-wise linear maps $\phi: X \rightarrow X$ given by

$$\Phi(x) \equiv \phi_i(x) = a_i x + b_i, x \in C_i \quad (1)$$

where $\{C_i =]c_{i-1}, c_i], i = 1, 2, \dots, m\}$ is a mutually exclusive and exhaustive partition of the interval $X = (c_0 = -1, c_m = 1)$ into m sub-intervals. Each element of the partition is mapped by ϕ on to X .

This class of maps is illustrated in Figure 1. In Section 2 they will be transformed by a permutation and division operation to be described.

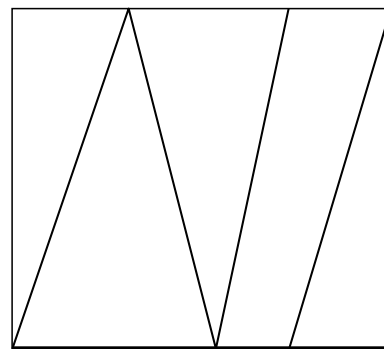


Figure 1 Illustration of a 4-branch piecewise linear fully stretching map

I. AIMS AND BASIS

We explore a class of maps which is produced by a special type of permutation and division transformation of piece-wise linear fully stretching chaotic maps; the class of maps produced is itself piece-wise linear but not fully stretching. We explore the chaotic structure and the statistical properties of the new class, both generally and through exemplification with well-known maps. A key feature revealed is that the autocorrelation function is extremely sensitive to a parameter involved in the division process and this new effect thereby suggests a notion of *parameter chaos* which

The natural invariant probability density function $f_X(x)$ of the map $\Phi(x)$ follows from the standard Perron–Frobenius equation in the form

$$f_X(x) = \sum_{i=1}^m f_X\{\phi_i^{-1}(x)\} |\phi_i^{-1}(x)| \quad (2)$$

where the pre-image functions of $\Phi(x)$ are denoted as $\phi_i^{-1}(x)$ with derivative function $\phi_i^{-\prime}(x)$; they satisfy the equation $\Phi(\phi_i^{-1}(x)) = x$. Since

$$\phi_i^{-\prime}(x) = (x - b_i)/a_i, |\phi_i^{-\prime}(x)| = 1/|a_i|, \text{ and}$$

hence that the uniform distribution over $(-1, +1)$ is the required solution.

The Lyapunov exponent of a map, measuring its chaotic divergence behaviour, is given by

$$\lambda = E \{ \ln |\Phi'(X)| \} \quad (3)$$

and for the class Φ of maps is given by

$$0 < \lambda = -\frac{1}{2} \sum_{i=1}^m (c_i - c_{i-1}) \ln \frac{c_i - c_{i-1}}{2}. \quad (4)$$

From this it may be seen how the number and positions of the branches affect the chaotic behaviour of the map and that λ is upper bounded by $\ln(m)$ which occurs for equi-spaced branches.

The autocorrelation function of fully stretching piece-wise linear maps, as given by [1,2] is

$$C_\Phi(n) = \{C_\Phi(1)\}^n, \quad C_\Phi(1) = \sum_{i=1}^m \frac{1}{|a_i| \cdot a_i}. \quad (5)$$

One focus of the present paper is the effect of permuting and splitting the branches of such maps and its effect on the autocorrelation function (5).

II. A DIVISION AND PERMUTATION TRANSFORMATION CLASS OF MAPS

Imagine the class Φ of maps in m strips according to its branches defined by the intervals C_1, C_2, \dots, C_m . Now imagine that the i^{th} branch is further sub-divided into $n_i (\geq 1)$ vertical strips at the arbitrary ordered points $c_{i1} < c_{i2} < \dots < c_{in_i}, i = 1, 2, \dots, m$ creating the intervals $C_{i1}, C_{i2}, \dots, C_{in_i}, i = 1, 2, \dots, m$. Thus the new map can be thought of as having $n = n_1 + \dots + n_m$ sub-branches over the intervals

$$C_{i1}, \dots, C_{in_i}, C_{21}, \dots, C_{2n_2}, \dots, C_{m1}, \dots, C_{mn_m}. \quad (6)$$

The new class of maps $K(\Phi)$, called the *split-shift class*, consists of those maps formed by permuting the locations of the n sub-branches of (6) and so gives a piece-wise linear but not fully stretching map of n branches. It is clear that there can be $2^n n!$ such maps since each branch can have positive or

negative slope and there are $n!$ permutations. A smaller class of maps, $K_1(\Phi)$, is produced when all $n_i = 1$ and hence the original branches are permuted undivided; this class has $2^m m!$ members. Important mathematical aspects of these maps are the simple forms of their invariant distributions and Lyapunov exponents. The class is illustrated in Figure 2 by permutation and division applied to the map in Figure 1.

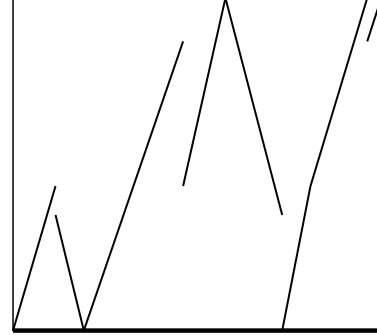


Figure 2 A map from the $K(\Phi)$ -class

Invariant Distribution of the $K(\Phi)$ -Class. After permutation, the value of the slope of the C_{ij}^{th} branch remains the same but its intercept depends on its position. This implies via the argument after (2) which does not depend on intercept terms, that the uniform distribution over $(-1, +1)$ is still the invariant distribution, essentially from a permutation of the terms in this equation with $m \equiv n$.

Lyapunov Exponent of the $K(\Phi)$ -Class. From the result (3), it is first clear that for members of the Φ -class which involve only permutation of the original branches, the Lyapunov exponent remains the same. However, this is actually true for the division members as well since the lengths of intervals associated with given constant slope values do not change, only their locations, and so the Lyapunov integral expression remains constant.

Statistical Dependency of the $K(\Phi)$ -Class. Statistical dependency behaviour is not maintained between corresponding maps in the class when splitting is involved. However, for permutation only, the result (5) indicates that the class $K_1(\Phi)$ does maintain autocorrelation.

It can be also shown that an arbitrary piece-wise linear map with an invariant measure is topologically conjugated with a map from an

extended class $K(\Phi)$. This extended class is structured as a chain of square bricks lying on a diagonal from left top to right bottom, each of them containing a map from $K(\Phi)$.

A. Sub-class of the Split-Shift Class of Maps

A particular sub-class $K_S(\Phi)$ of $K(\Phi)$ is obtained by splitting only the *last* branch of Φ into two at a point δ ($0 < \delta < 1 - c_{m-1}$) from its end and then permuting the second half-branch to be the first branch of the new map; δ is called the *shift parameter* in this case, and $K_S(\Phi)$ will be called the *split-shift* class. An illustration is given by Figure 3 for a Bernoulli map where $\delta = 0.75$. In general, the branch boundaries for the split-shift class are thus at the points $q_0 \equiv c_0, q_1 = c_0 + \delta, \dots,$

$$q_m = c_{m-1} + \delta, q_{m+1} \equiv c_m$$

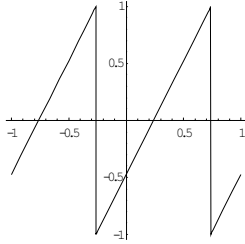


Figure 3 The split-shift Bernoulli map

which define intervals $Q_i =]q_{i-1}, q_i], i = 1, \dots, m + 1$. The corresponding map slopes over these intervals are $(a_m, a_1, \dots, a_{m-1}, a_m)$ where (a_0, a_1, \dots, a_m) are defined in terms of c_0, c_1, \dots, c_m .

The *split-shift* maps of the class $K_S(\Phi)$ thus take the form

$$\Gamma(x) \equiv \begin{cases} \gamma_1(x) = \phi_m \{x - (\delta - 2)\} & x \in Q_1 \\ \gamma_i(x) = \phi_{i-1}(x - \delta) & x \in Q_i \end{cases} \quad (7)$$

Maps in this class have the property $\Gamma(-1) = \Gamma(+1)$ which follows from the division of the last interval of a map in class Φ and its shift to be the first interval.

Maps in class $K_S(\Phi)$ have the same invariant distribution as those in Φ and the same Lyapunov exponent as the maps in Φ .

Maps in $K_S(\Phi)$ are also ergodic except when Φ is the tent or skew tent map [1].

The difference in capacities of the introduced classes is in the order $K(\Phi) \supset K_S(\Phi) \supset \Phi$.

II. AUTOCORRELATION OF THE SPLIT-SHIFT CLASS OF MAPS

Considering a general ergodic map Γ over X with uniform invariant distribution of mean zero and variance σ^2 , a general expression for its autocorrelation at lag n given by

$$C_\Gamma(n) = \frac{1}{2\sigma^2} \int_{y=-1}^{+1} y\Gamma^n(y)dy \quad (8)$$

where $\Gamma^n(\cdot)$ is the n -fold convolution of the map function Γ , $\sigma^2 = 1/3$ and $C_\Gamma(0) = 1$.

The integral (8) can be evaluated analytically by sub-dividing its range over each branch of the map and applying the pre-image transformation $y = \gamma_i^{-1}(z)$ appropriate to each branch. This is effectively a Perron-Frobenius operation, as set out in [3] for the calculation of dependency.

The resulting expression can be written in simply structured form

$$C_\Gamma(n) = C_\Phi(1)C_\Gamma(n-1) + \frac{1}{\sigma^2 a_m} I_{n-1}(\beta), \quad (9)$$

where $C_\Phi(1)$ has been defined at (5) and

$$\beta \equiv \gamma_1(q_0) = 1 - \delta a_m,$$

$$I_{n-1}(\beta) \equiv \int_{-1}^{\beta} \Gamma^{n-1}(z) dz = -\frac{1}{a_m} I_{n-2}(\beta) +$$

$$\begin{cases} \frac{1}{a_m} I_{n-2} \{ \Gamma(\beta) \} & \beta \in Q_1 \\ \frac{1}{a_{i-1}} I_{n-2} \{ \Gamma(\beta) \} & \beta \in Q_i, i = 2, \dots, m + 1. \end{cases} \quad (10)$$

The initial function $I_0(\beta)$ enabling (10) to be solved explicitly is

$$I_0(\beta) = \frac{1}{2}(\beta^2 - 1).$$

The important implications of (9)-(10) will be developed in the rest of the paper, focussing on the sensitivity which it implies of the split-shift map's autocorrelation function to the value of its shift-parameter δ . Note, however, if β was a fixed point of the map $\Gamma(\cdot)$, as it is in the tent map case of Φ , there would be no sensitivity, except perhaps computational.

A. Autocorrelation of the Split-Shift Bernoulli Map

To exemplify the sensitivity result, the Bernoulli map is taken as the initial map in class Φ as was illustrated in Figure 3 for $\delta = 0.75$. Then the first n iterations of (9)-(10) lead to the explicit result for the autocorrelation function of the split-shift Bernoulli map

$$C_{\Gamma}(n) = 2^{-n-1} \left(\sum_{j=1}^n d_{n,j+1} \beta_j^2 - 1 \right), \quad n = 1, 2, \dots \quad (11)$$

where $d_{i,1} = 1, d_{i,2} = \begin{cases} 3 & i \text{ odd} \\ 0 & i \text{ even} \end{cases};$

$$d_{i+1,j+1} = d_{i,j} - d_{i,j+1}, \quad i \geq 6, \quad j \geq 2;$$

$$\beta_j = \Gamma(\beta_{j-1}), \quad j = 1, 2, \dots, n-1, \quad \beta_1 = \beta. \quad (12)$$

Two illustrations of this autocorrelation function are displayed in Figure 4.

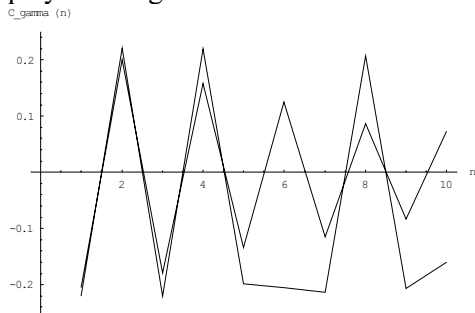


Figure 4 The autocorrelation function of the split-shift Bernoulli map illustrated by the two cases of the shift parameter $\delta = 1/3$ and $\delta = 1/3 + 0.001$

To appreciate the chaotic nature of the autocorrelations, first note from (12) that the sequence of iterations $\{\beta_1, \beta_2, \dots\}$ evolves via the chaotic Bernoulli split-shift map function itself. More over it starts with $\beta_1 = 1 - 2\delta$ which is linearly related to the map's shift parameter δ and must therefore be extremely sensitive to δ . This is not quite the usual meaning of sensitive dependence on initial value because the map parameter itself is involved and not fixed. A consequent chaotic aspect of the autocorrelations follows from the equations (11) showing that $C_{\Gamma}(n)$ depends on the chaotic sequence $\{\beta_1, \beta_2, \dots, \beta_n\}$, $n = 1, 2, \dots$. Thus, the sense in which the autocorrelations are chaotic is that they are extremely sensitive to the value of the map parameter δ , as tentatively illustrated in Figure 4. This will be termed *parameter chaos*. There are

possible serious implications to computational robustness here, particularly in engineering applications of chaos. The actual chaotic process of $\{C_{\Gamma}(n), n = 1, 2, \dots\}$ is too high dimensional to specify autonomously, but a useful basic description in relation to δ is given by their individual and stationary marginal density functions: in a sense, this is parallel to the uniform invariant distribution for the sequence $\{\beta_1, \beta_2, \dots\}$. We show [4,5] that there is fast convergence as n becomes large of the distribution of $C_{\Gamma}(n)$ to Gaussian form, although it should be noted that it is not an invariant distribution of $C_{\Gamma}(n)$ in the usual sense.

III. CONCLUSIONS

The paper has identified and explored the notion of *parameter chaos*, where by an important dynamical or statistical aspect of a map is very sensitive to the value taken by a parameter. Although it seems plausible that the effect arises from the shift operation on the branches, investigation of the generality of the effect is currently being continued. What is known is that for most piecewise linear and not necessarily fully stretching maps, the autocorrelation function varies smoothly with parameters. When it does not, as here, there will be computational lack of robustness with possibly unwelcome effects in applications. This makes the topic an important one to peruse further.

REFERENCES

[1] A. L. Baranovski and D. Daems. Design of 1-Dchaotic maps with prescribed statistical properties. *Int. Journal of Bifurcations and Chaos*, 5, N 6, 1585-1598, 1995.
 [2] A. L. Baranovski, "Design of deterministic dynamical systems forming chaotic oscillations with controlled probabilistic characteristics," PhD thesis, Tomsk State University, USSR, 1989. Available at: <http://www.konsultant.de/baranovski/PhDthesis>
 [3] A. J. Lawrance and N. Balakrishna. Statistical aspects of chaotic maps with negative dependency in a communications setting. *J. R. Statistic. Soc. B*, 63, 2001.
 [4] A. L. Baranovski and A. J. Lawrance. Piece-wise linear maps and parameter chaos. Accepted for *Russian Physics Journal*, Kluwer Press, 2004.
 [5] A. L. Baranovski and A. J. Lawrance. Is there chaos in statistical characteristics of chaos? A talk at the Seminar on statistical aspects of nonlinear systems. Dresden, September 2003.

SYNCHRONIZATION OF CHAOTIC COLPITTS OSCILLATORS WITH PARAMETER MISMATCH

*Antanas Baziliauskas, Romanas Krivickas, Arūnas Tamaševičius**

Department of Signal Processing, Faculty of Telecommunications and Electronics,
Kaunas University of Technology, Studentų 50, LT-3031, Kaunas, Lithuania
e-mail: Antanas.Baziliauskas@stud.ktu.lt, Romanas.Krivickas@ktu.lt

WWW: <http://www.ktu.lt/en/>

*Plasma Phenomena Laboratory, Semiconductor Physics Institute,
A. Goštauto 11, Vilnius, LT-2600, Lithuania

e-mail: tamasev@pfi.lt

WWW:http://www.pfi.lt/index_e

Abstract — *The method of linear difference signal has been applied to investigate the effect of synchronization between coupled chaotic Colpitts oscillators. Two different configurations: (1) coupled collector nodes, and (2) coupled emitter nodes have been considered. The influence of the parameter mismatch, namely the mismatch of the transistors has been studied. Results of numerical also hardware investigations are presented.*

studied by means of the PSpice simulations only [3]. No experimental evidence was given. In the present work we make use of the explicit state-space equations and investigate two chaotic Colpitts oscillators either coupled via the collector nodes (C–C configuration), similarly to [3], or coupled via the emitter nodes (E–E configuration). In addition to fully identical oscillators the case of mismatched oscillators has been studied. Moreover, experiments with hardware prototypes have been carried out.

I. INTRODUCTION

Classical oscillators such as Colpitts, RC phase shift and Wien-bridge are commonly used to generate periodic nearly sinusoidal waveforms. However with particular sets of circuit parameters, the oscillators can produce chaotic waveforms as well. In the Colpitts oscillator, chaos has been demonstrated by means of PSpice simulations and hardware experiments [1].

An important feature of chaotic systems is the fact that even fully identical oscillators generate asynchronous waveforms due to their extreme sensitivity on the initial conditions. In numerical simulations one can set the same initial conditions for each system and get the same chaotic waveforms at the outputs. Meanwhile in real physical systems this is not possible. Synchronous behaviour can be achieved by means of coupling of the oscillators. The possible application of chaotic synchronization, e.g. to communication has been discussed in [2]. However, in practice the parameters of the systems are inherently somewhat different. Therefore, synchronization between mismatched oscillators is of particular interest. Synchronization of chaotic Colpitts oscillators to our best knowledge was

II. CHAOTIC COLPITTS OSCILLATOR

In this section we introduce the circuit under investigation (Fig. 1) and define the corresponding state-space equations using a piece-wise linear approximation for forward-active mode nonlinear current-voltage relationship of the bipolar junction transistor (BJT).

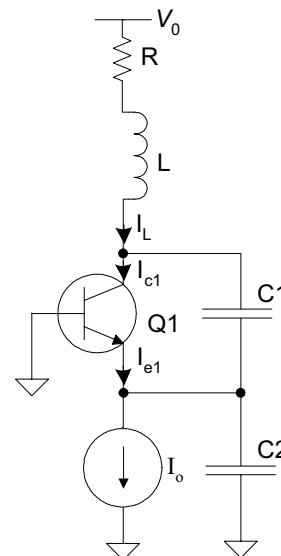


Fig. 1. Circuit diagram of the Colpitts oscillator.

The oscillator consists of a single BJT, biased in the forward-active region by means of the dc voltage and current sources, V_0 and I_0 , respectively. The feedback network consists of an inductor L , a series loss resistor R , and a capacitive divider C_1 – C_2 .

The fundamental frequency of the Colpitts oscillator can be estimated from the formula:

$$f^* = \frac{1}{2\pi} \sqrt{(C_1 + C_2) / LC_1 C_2} .$$

The dynamics of the Colpitts oscillator is described by a system of three autonomous state-space equations:

$$\begin{cases} \dot{x} = y - F(a, z), \\ \dot{y} = -x - z - by, \\ \dot{z} = \varepsilon(y - 1). \end{cases} \quad (1)$$

Here the state variables are defined as

$$x = \frac{V_{C1}}{V^*}, \quad y = \frac{\rho I_L}{V^*}, \quad z = \frac{V_{C2}}{V^*}, \quad V^* = \rho I_0.$$

Two linear segments are used to approximate the nonlinear current-voltage characteristic of the base-emitter junction of a BJT in a forward-active mode. As a result, the piece-wise linear function F is given by:

$$F(a, z) = \begin{cases} 1 - az, & az < 1, \\ 0, & az \geq 1. \end{cases}$$

All the other parameters in Eq. (1) are defined as

$$\tau = \sqrt{LC_1}, \quad \rho = \sqrt{\frac{L}{C_1}}, \quad \varepsilon = \frac{C_1}{C_2},$$

$$a = \frac{\rho}{r}, \quad b = \frac{R}{\rho}.$$

Here r is the differential resistance of the base-emitter junction of a BJT in a forward-active mode. In Eq. (1) we have assumed that the collector current I_c is proportional to the emitter current I_e according to the BJT forward-active mode relationship $I_{c1} = \alpha I_{e1}$. Base current has been neglected. As a result, we have set $\alpha=1$. Time is normalized using $t' = t/\tau$. Fig. 2 shows the projection of the phase trajectories of the Colpitts oscillator described by Eq. (1) on the plane z versus $(x+z)$.

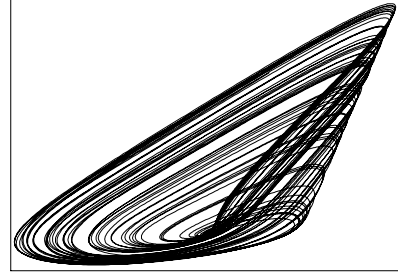


Fig. 2. Phase portrait, z vs. $(x+z)$. $a = 15$, $b = 0.8$, $\varepsilon = 1$.

III. SYNCHRONIZATION OF CHAOTIC COLPITTS OSCILLATORS

This section will focus on synchronization between two chaotic Colpitts oscillators coupled in two different ways. Let us consider two oscillators O1 and O2, coupled via linear resistor R_k (Fig. 3).

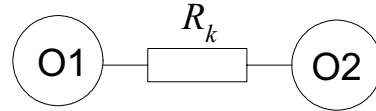


Fig. 3. Coupled oscillators.

The coupling coefficient between the two oscillators is defined as $k = \rho/R_k$. We note, that for very small values of k the system in Fig. 3 exhibits hyperchaotic behaviour described elsewhere [4]. However, the state-space equations presented in [4] correspond to an arbitrary strength of coupling, therefore are valid in the case of synchronization:

$$\begin{cases} \dot{x}_1 = y_1 - F(a, z_1) + k(x_2 + z_2 - x_1 - z_1), \\ \dot{y}_1 = -x_1 - z_1 - by_1, \\ \dot{z}_1 = \varepsilon(y_1 - 1) + k(x_2 + z_2 - x_1 - z_1), \\ \dot{x}_2 = y_2 - F(h, z_2) + k(x_1 + z_1 - x_2 - z_2), \\ \dot{y}_2 = -x_2 - z_2 - by_2, \\ \dot{z}_2 = \varepsilon(y_2 - 1) + k(x_1 + z_1 - x_2 - z_2). \end{cases} \quad (2)$$

Here

$$F(h, z) = \begin{cases} 1 - hz, & hz < 1, \\ 0, & hz \geq 1. \end{cases} \quad h = \frac{\rho}{r_2}.$$

The r_2 is the differential resistance of the BJT of the second oscillator (note, $h=a$ in the matched case).

The state-space equations corresponding to the coupling via the emitter nodes are simpler than in the previous case:

$$\begin{cases} \dot{x}_1 = y_1 - F(a, z_1), \\ \dot{y}_1 = -x_1 - z_1 - by_1, \\ \dot{z}_1 = \varepsilon(y_1 - 1) + k(z_2 - z_1), \\ \dot{x}_2 = y_2 - F(h, z_2), \\ \dot{y}_2 = -x_2 - z_2 - by_2, \\ \dot{z}_2 = \varepsilon(y_2 - 1) + k(z_1 - z_2). \end{cases} \quad (3)$$

We introduce the synchronization threshold k_{th} defining it to be the minimum-coupling coefficient k required for full synchronization of chaotic oscillators at different initial conditions and after the transients. For the C-C configuration numerical integration of Eq. (2) with $a = h = 15$, $b = 0.8$, and $\varepsilon = 1$ gives the value of $k_{th} = 0.15$. In the case of the E-E configuration integration of Eq. (3) yields $k_{th} = 0.09$. In Fig. 4 we show the dynamics of the synchronization process. Note that when the difference in the dynamics of the two oscillators vanishes, the overall system remains chaotic, nevertheless.

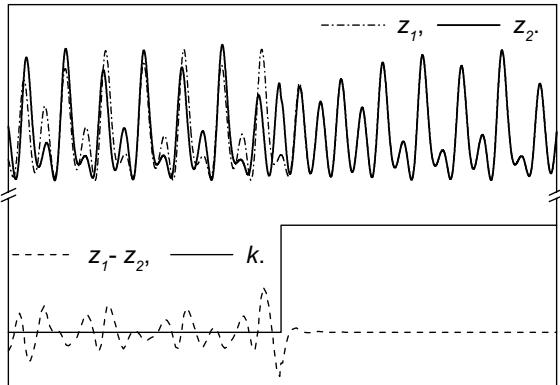


Fig. 4. Waveforms of the variables z_1 and z_2 (dash-dotted and solid lines in the top, respectively). Coupling coefficient $k(t)$ and difference signal $(z_1 - z_2)$ (solid and dashed lines in the bottom, respectively)

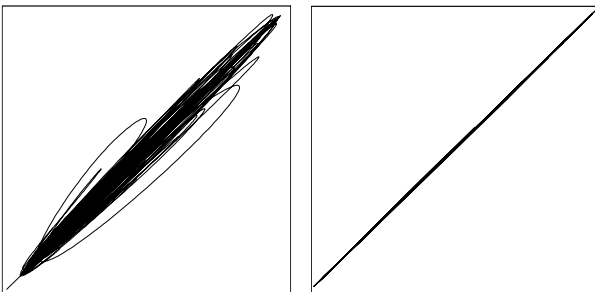


Fig. 5. Phase portraits, z_1 versus z_2 from Eq. (3). Left: nearly full synchronization at $k = 0.08 < k_{th}$. Right: full synchronization at $k = 0.11 > k_{th}$.

Using the coupling coefficient k close to the k_{th} either nearly full (Fig. 5, left) or full synchronization (Fig. 5, right) can be observed.

We have repeated all the computations for the mismatched oscillators. In the mismatched cases k_{th} is defined as the minimum value of k required diminishing the signals $\langle (z_1 - z_2)^2 \rangle^{1/2} / \langle z_1^2 \rangle^{1/2}$ (E-E) or $\langle (x_1 + z_1 - x_2 - z_2)^2 \rangle^{1/2} / \langle (x_1 + z_1)^2 \rangle^{1/2}$ (C-C) to values less than 2%. Table 1 shows the estimated k_{th} for different h for the both coupling configurations. As the mismatch level $\Delta = (h - a)/a$ increases, the synchronization threshold increases as well.

$\Delta, \%$	a	h	k_{th} (C-C)	k_{th} (E-E)
0	15	15	0.15	0.09
0.1	15	15.015	0.17	0.11
1	15	15.15	0.41	0.16
5	15	15.75	0.53	0.46

Table 1: Synchronization threshold k_{th} for different mismatch levels and for both coupling configurations.

IV. EXPERIMENT

The experimental circuit (Fig. 6) slightly differs from the one shown in Fig. 1. The emitter current I_0 is set by means of the base divider $R1-R2$ and the series emitter resistor Re . The capacitor $C0$ grounds the base with respect to the ac signals, thus ensuring the common-base configuration of the transistor. The oscillators O1 and O2 have been built using the following values: $L = 0.86$ mH, $C_1 = C_2 = 470$ nF ($f^* \approx 11$ kHz, $\rho = 43 \Omega$), $R = 36 \Omega$, $V_0 = 12$ V, $C_0 = 47 \mu$ F, $R_1 = R_2 = 3$ k Ω , $Re = 510 \Omega$. The transistors used in the experiments are the 2N3904 type ones.

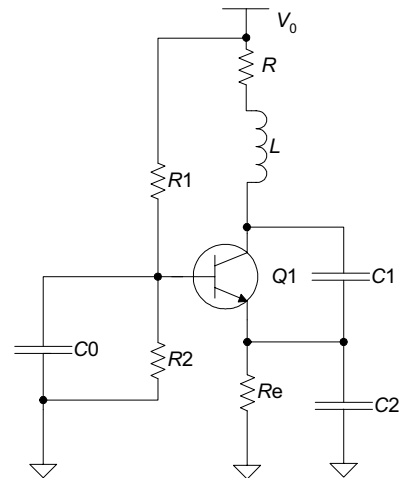


Fig. 6. Circuit diagram of the experimental oscillator.

The experimental illustrations are presented in Fig. 7 and Fig. 8.

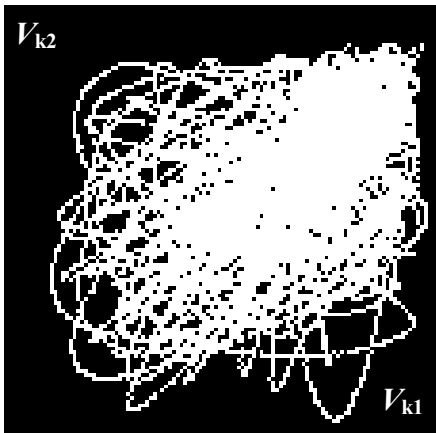


Fig. 7. Phase portrait, collector voltage V_{k2} vs. V_{k1} for unsynchronized oscillators. $R_k > 1 \text{ k}\Omega$ ($k < 0.05$).

In the case of unsynchronized chaotic generators the phase portrait is a very complicated one, indicating “random” mutual phases and amplitudes of the oscillations.

On the other hand the fine diagonal in Fig. 8 proves, that the momentary amplitudes and phases of the oscillations coincide, i.e. the oscillators are fully synchronized for $R_k = 50 \Omega$ (C–C configuration) and $R_k = 200 \Omega$ (E–E configuration) The measured root mean square of the difference signal, that is the synchronization error $SE = \langle (V_{k1} - V_{k2})^2 \rangle^{1/2} / \langle (V_{k1})^2 \rangle^{1/2}$ is less than 1%. The reverse quantity the synchronization quality SQ is higher than 100.

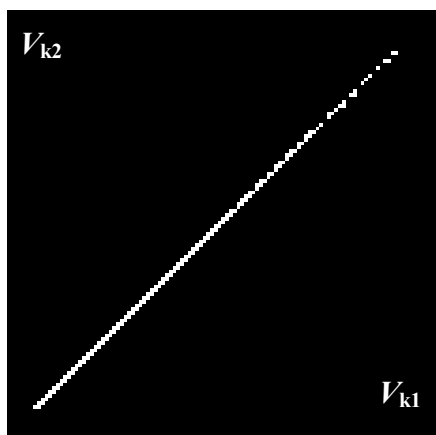


Fig. 8. Phase portrait, collector voltage V_{k2} versus V_{k1} for synchronized oscillators. $R_k = 50 \Omega$ (C–C coupling) and $R_k = 200 \Omega$ (E–E coupling).

V. CONCLUSIONS

In this work the method of linear difference signal was applied to investigate the two-way synchronization between two chaotic Colpitts oscillators. The synchronization threshold, that is the minimum value of the coupling coefficient required to get full or nearly full synchronization was evaluated from the rate equations for matched and mismatched oscillators in both, the C–C and E–E coupling configurations. Experimental measurements agree qualitatively with numerical results.

ACKNOWLEDGEMENTS

Part of this work was carried out at University College Dublin under a Marie Curie Fellowship (A.B.). Two of us (A.B. and A.T.) were partially supported by Lithuanian State Science and Studies Foundation. One of us (A.T.) was partially supported by the EC project “The Center in Processing, Research and Application of Advanced Materials (PRAMA)” under contract No. G5MA-CT-2002-04014.

REFERENCES

- [1] M. P. Kennedy. Chaos in the Colpitts oscillator. *IEEE Trans. Circuits Syst. I*, vol. 41, No. 11, pp. 771-774 (1994).
- [2] T. Yang, and L. O. Chua. Impulsive stabilization for control and synchronization of chaotic systems: Theory and application to secure communication. *IEEE Trans. Circuits Syst. I*, vol. 44, No. 10, pp. 976-988 (1997).
- [3] V. A. Burykin, A. I. Panas. Chaotic synchronization of RF generators. In *Proc. NDES'97*, pp. 548-553, Moscow, Russia, 1997.
- [4] A. Čenys, A. Tamaševičius, A. Baziliauskas, R. Krivickas, E. Lindberg. Hyperchaos in coupled Colpitts oscillators, *Chaos, Solitons & Fractals*, vol. 17, No. 2, pp. 349-353 (2003).

OSCILLATIONS IN THE FIRST-ORDER RECURSIVE DIGITAL FILTERS WITH MAGNITUDE TRUNCATION

Yu.A. Bruhanov

Chair of Dynamics of Electronic Systems, Department of Physics,
Yaroslavl State University,
Sovetskaya 14, Yaroslavl, 150000, Russian Federation
e-mail: bruhanov@uniyar.ac.ru

Abstract—*Oscillations under constant external influence in high-pass and low-pass filters are considered. Numbers represent using the fixed point arithmetic and additional code. The method of one-dimensional point mapping is applied. Dynamic modes are characterized by probability diagrams. Expressions for the most probable oscillations on the filters output are received at any quantity of quantization levels.*

I. INTRODUCTION

Basic difference of the digital filters from analog one's is limited accuracy of performance the arithmetic operations and set of filter's parameters caused by the limited number of used bits. Therefore digital oscillatory system generally is essentially nonlinear, and have the undesirable phenomena named quantization effects [1]. At enough quantity of bits these effects are insignificant and for the analysis of their influence the linear model of system behaviour is used. If the amount of bits is not enough (it is necessary for increase the computational speed), and also under constant or sine influence sampled with frequency, divisible the frequency of a sinusoid, the linear model is inapplicable [2-4]. In work [5] the effects of quantization in the digital first order recursive filter with the rounding off the results of addition and representation of numbers in a direct code are investigated.

Let's consider oscillations under constant external influence A in digital high-pass and low-pass filters realized at the basis of recursive first order circuits at any quantity of bits, i.e. levels of quantization L , in representation of addition results. We assume that numbers represent with fixed point, the filter parameter a is given without an error, quantization is performed with magnitude truncation, variables are represented in the form of numbers with justification to the right (as integer numbers), and the adder has the transfer characteristic with saturation (without regard for quantization effects).

Magnitude truncation is realized for the binary numbers represented in an additional code. Thus the quantity of quantization levels – is the even number, and the adder characteristic in the case of saturation is expressed by function

$$f(\phi) = \begin{cases} [\phi] & \text{by } 0 \leq \phi < N_1, \\ N_1 & \text{by } \phi \geq N_1, \\ [\phi + N] - N & \text{by } -N < \phi < 0, \\ -N & \text{by } \phi \leq -N, \end{cases}$$

where $[\cdot]$ - the integer part of number, $N_1=N-1$, $N=L/2..$ In the case $\phi \geq 0$ segments of the characteristics corresponding to values $[\phi]$, we will designate 0, I, II, ..., N_1 , and for $\phi < 0$ the segments designated -I, -II, ..., $-N$, correspond to values $[\phi + N] - N$.

Oscillations in the filters under investigation are described by the difference equation

$$x(n+1)=f(ax(n)+A).$$

Because using of integer arithmetic the step of quantization is equal to unit, A - integer.

Let us introduce the function $y(n)=x(n+1)$. Processes will be considered on the plane of states (x, y) by the point mapping technique [6]. In this case, the first return function takes the form $y=f(ax+A)$.

We have in view, that because of quantization in system of the first order are probable L conditions. Generally depending on an initial condition $x(0)$ in system the various established movements are possible. Because all L probable initial conditions are independent, equiprobable, let's determine concept of probability P of established movement B as ratio $P(B)=m/L$, where m – the quantity of the initial conditions corresponding to this movement.

The parameter of the filter a gets out from the field of stability without taking into account effects of quantization, i.e. $0 < |a| < 1$.

As well as in [5], let's break the plane of conditions into the areas according to segments of the adder characteristic. We will designate these regions, as well as corresponding segments. The border of areas $[\phi]$, $[\phi]+1$ is expressed by dependence $x = ([\phi]+1 - A)/a$. The border belongs to area $[\phi]+1$.

II. OSCILLATIONS UNDER CONSTANT INFLUENCE

At the presence of constant external influence A , the plot of the first return function intersects the ordinate axis at the point $y=A$; in this case, $\phi = A$. Let's consider the case $A>0$.

Let $a>0$. At $A=1$ for all values $0 < a < 1$ for border of areas I, II we have $x > 1$, therefore the least values of abscissa point of crossing the first return function and bisectrix always equally 1 and the most probable established is movement with period $T=1$ and amplitude $X=1$. Below it is designated $T=1(1)$. We will consider case $A=2$. Lamere diagram for $L=12$, $a=7/11$ is shown on Fig. 1a. Here, the first return function intersects the bisectrix at $x \in \{3, 4, 5\}$. Hence, at start from the points $[x] \in [-6; 3]$ oscillation $T=1(3)$ is established. Therefore the probability of this oscillation is equal $10/12$. Below it is designated $P(3)=10/12$. At start from the points $x \in \{4, 5\}$ we have accordingly movements $T=1(4)$, $T=1(5)$ with probabilities $P(4)=P(5)=1/12$ accordingly. Consideration of movements at $a \in (0, 1)$ allow us to construct bifurcation and probability diagrams. Last is shown on Fig. 2a.

The investigation of oscillations for a number of values L and A makes it possible to ascertain the following relationships for the most probable values of $x=X$. At $A=1$ on the filter's output always we have $T=1(1)$. If external influence satisfies to a condition $1 < A < N_1$ in the low-pass filter the most probable movement $T=1(X)$ where $A \leq X < N_1$ is established if on Lamere diagram points X and $X-1$ belong to the areas X . It means the performance of a condition

$X \leq aX + A < X + 1 \cap X \leq a(X - 1) + A < X + 1$, therefore

$$(X - A)/(X - 1) \leq a < (X + 1 - A)/X .$$

In the case $X=N_1$ it is necessary, that the point $x=N_1-1$ on Lamere diagram belonged to area N_1 .

Using stable condition we receive

$$1 > a \geq (N_1 - A)/(N_1 - 1) ,$$

Notice, that thus movement $T=1(N_1)$ is unique. At $A=N_1$, $a \in (0, 1)$ the filter's output we have unique established oscillation $T=1(N_1)$.

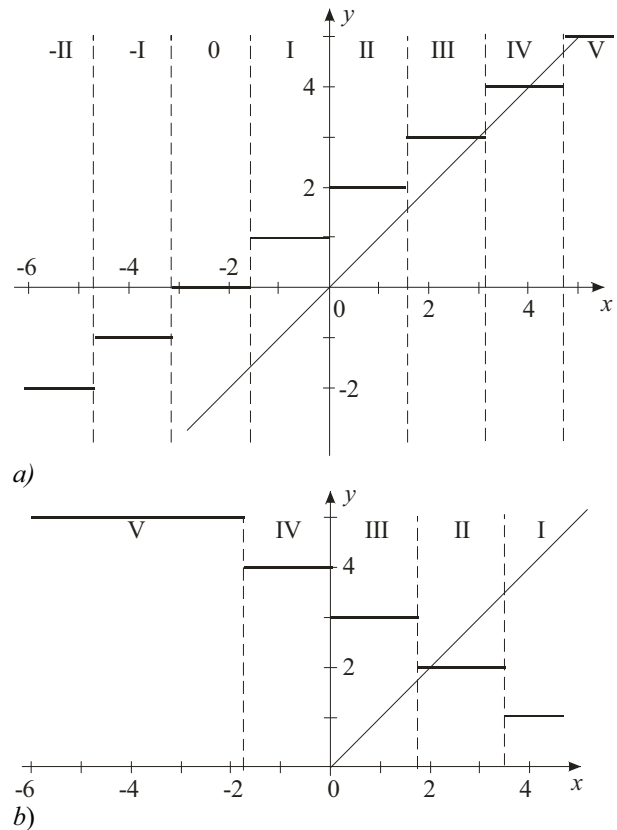


Fig. 1. Lamere diagrams for $L=12$
 a) low-pass filter $A=2$, $a=7/11$;
 b) high-pass filter $A=4$, $a=-4/7$.

The received laws allow us to find dependence $X(a)$ for any L and A .

Let $a<0$. At $A=1$ for all values L and $-1 < a < 0$ plot of first return function is not crossed with the bisectrix, points $x=0$ and $x=1$ on Lamere diagram belong according to areas I and 0, in the filter there are only parasitic oscillations with period $T=2$ and instant values $x \in \{0; 1\}$. Below it is designated $T=2(1/0)$. At $A>1$ picture varies. Let's consider case $A=4$. As an example on Fig. 1b Lamere diagram for $L=12$, $a = -4/7$ is shown. Here the plot of the first return function is crossed with the bisectrix in a unique point at $x=2$. It means, that at start from the points $[x] \in [-6; 5]$ in the filter oscillations $T=1(2)$

are established. At other values of parameter a there can be movement $T=1(3)$, and also parasitic oscillations with period $T=2$ and various instant values. Consideration of movements at $a \in (-1; 0)$ allow us to construct bifurcation and probability diagrams. Last is shown on Fig. 2b.

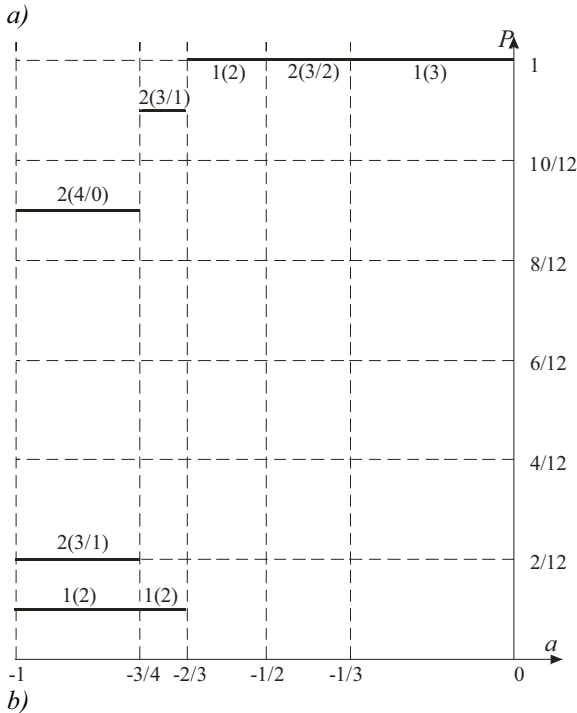
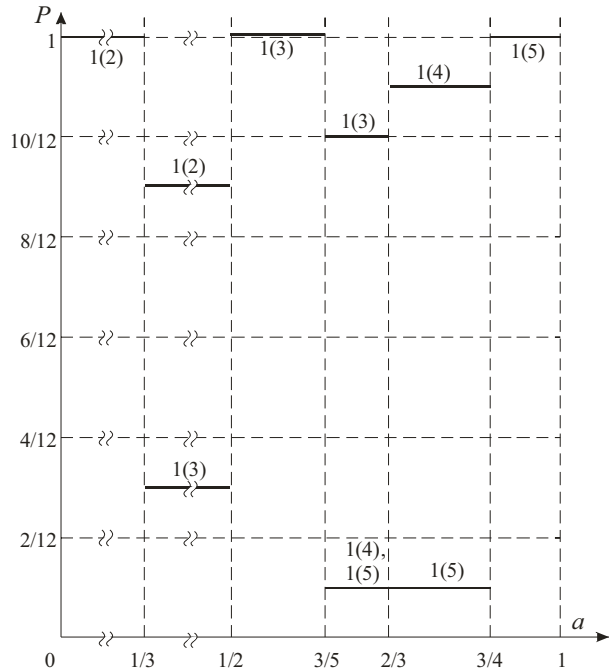


Fig. 2. Probability diagrams for $L=12$
 a) low-pass filter $A=2$;
 b) high-pass filter $A=4$.

The investigation of oscillations for a number of values L and $A > 1$ makes it possible to ascertain the following relationships for the most probable values of X . Generally for any $1 < A \leq N_1$ on the high-pass filter's output we have $T=1(X)$, where $1 < X < A$ if on Lamere diagram point X and $X-1$ or points X and $X+1$ belong to area X . It means the performance of the condition

$$X \leq aX + A < X + 1 \cap X \leq a(X - 1) + A < X + 1$$

or

$$X \leq aX + A < X + 1 \cap X \leq a(X + 1) + A < X + 1.$$

Therefore

$$(X - A) / X \leq a < (X + 1 - A) / (X - 1) \quad (1)$$

or

$$(X - A) / (X + 1) \leq a < (X + 1 - A) / X \quad (2)$$

In the same range of values A on the filter's output we have $T=1(1)$ if (2) is carried out. In comparison to another with determined (1), (2) areas of parameter $a < 0$ there correspond the most probable parasitic oscillations with period $T=2$.

The received laws allow us to establish dependence $X(a)$ for any L and A .

Let's consider the case $A < 0$. Using the technique described above, we receive the following laws for the most probable established oscillations for any L and A .

At $a > 0$, $-N + 1 < A < 0$ on the filter's output we have oscillation $T=1(X)$, where $-N < X < A$ if on Lamere diagram point X and $X+1$ belongs to the area X . It means the performance of the condition

$$X \leq aX + A < X + 1 \cap X \leq a(X + 1) + A < X + 1,$$

therefore

$$(X + 1 - A) / (X + 1) < a \leq (X - A) / X.$$

In the same range of values A in the case $X = -N$ it is necessary, that point $X+1$ belonged to the area $-N$. Using stable condition we receive

$$a > (-N + 1 - A) / (-N + 1),$$

At $A \in \{-N, -N + 1\}$ we have unique established movement $T=1(-N)$.

If $a < 0$, $A = -1$ on the filter's output there is always unique oscillation $T=1(-1)$ since on a plane of conditions for border of areas $-1, 0$ we have $x < -1$ and a unique point of crossing of the first return function and corresponds bisectrix $x = -1$. For $-N \leq A < -1$ in the high-pass filter we have the most probable established oscillation $T=1(X)$, where $A \leq X < -1$ if on Lamere diagram point X and $X-1$ or points X and $X+1$ belong to the area X . Resulting ratio turn out from (1), (2) by only replacement of signs \geq and $<$ on \leq and $>$ accordingly.

Theoretical results were verified by computer simulation. The obtained relationships can be easily extended to cover the case where variables are represented in the form of numbers with justification to the left (that is, in the form of fractional numbers). To do this, it is sufficient to introduce another variable $\bar{x} = xq$, where $q = 1/N$ is the quantization step.

III. CONCLUSIONS

The digital high-pass and low-pass filters realized on the basis of the first order recursive circuit with any quantity of quantization levels with amplitude truncation of addition results when the adder without taking into account effects of quantization has the characteristic with saturation are considered. For the characteristic of nonlinear dynamic modes probability diagrams are offered. By the method of dot mapping oscillations under constant external influence of two signs are investigated. Expressions for calculations of the most probable established modes are received. The results may be used in creating the information transmission systems with digital processing of signals.

ACKNOWLEDGMENT

Work is executed under financial support of Russia Foundation of Basic Research (grant 02-02-17500).

REFERENCES

[1] V. Capellini, A.G. Constantinidis and P. Emiliani. Digital Filters and their Applications. Academic Press, London, 1978.
 [2] T. Bose, D. Brown, "Zero-input limit cycles due to rounding in digital filters", *IEEE Trans. Circuits & Syst.*, vol. 36, pp. 931-933, June 1989.

[3] B.D. Green, L. Turnev, "New limit cycle bounds for digital Filters", *IEEE Trans. Circuits & Syst.*, vol. 35, pp. 365-374, April 1988.
 [4] Tien-Lin Chang, "Suppression of limit cycles in digital filters designed with one magnitude-truncation quantizer", *IEEE Trans. Circuits & Syst.*, vol CAS-28, pp. 107-111, February 1981.
 [5] Bryuhanov Yu.A. Oscillations in the first-order recursive digital filters with truncation. *In Proc. of the 2003 Workshop on Nonlinear Dynamics of Electronic Systems. Scoul/Schuls, Switzerland, 2003. P. 37-40.*
 [6] Butenin N.V., Neimark Y.I., Fufaev N.A. Introduction to the theory of nonlinear oscillations. - M.: Nauka, 1987.

CLUSTERING AND NONLINEAR FORECAST FOR ELECTRONIC DEVICES MARKET DEMAND

M. Bucolo¹, F. Caizzone², L. Fortuna¹, G. Tomarchio^{1,2}

¹ DIEES Universita' di Catania, email mbucolo@diees.unict.it

² STMicroelectronics Catania Site, email giusy.tomarchio@st.com

Abstract - *The purpose of this study is to define a suitable strategy that, based on supervised clustering, allows developing system to forecast the market demand of products of a worldwide semiconductor firm, STMicroelectronics. In based on the results of a clustering phase. The clustering approach allows to group the time series carrying on the same qualitative information; therefore the modelling phase has been performed on classes and not series by series. The final target is to have a single model that can be representative for all the elements of a class.*

I. INTRODUCTION

The aim of this study is to develop a strategy to cluster and to model the market demand of semiconductor devices [3].

The case study is related to the Discrete and Standard Product Group (DSG) of the semiconductor firm STMicroelectronics. The group is managed through 15 product families that cover a wide product portfolio of about 12.000 products; sales are spread world wide on different sales channel.

The considered data set has been described in details in Section II.

The purpose is to develop an effective methodology to reduce the complexity inner the system and to overcome problems arising from the limited number of available points. In this case the demand forecasting is not a pure mathematical exercise because it is strictly related with the economic projection of the problem. For those reasons the strategy has been carried on through two phases: the clustering phase and the modelling one.

The *clustering phase* is described in Section III and is based on a Multivariate Analysis that allowed to group the time series with similar qualitative information like yearly growth evolution, same cyclic behaviour, stochastic or deterministic nature. The multivariate analysis is

particular market demand is related to semiconductor devices belonging to Discrete and Standard Group that covers a wide product portfolio. To face the complexity due to identify each product, the modelling strategy has been based on the composed study of the variables by moving from statistical analysis to signal analysis. In Section IV the *modelling phase*, driven by the results obtained in the clustering phase, is reported; the modelling approach is developed by looking at the class as a whole unit all through its representative element, and not to each element, and then the identified model is applied to all the class elements.

The modelling phase has been carried on through nonlinear NARMA models.

II. DATA SET

Data analysis is related to the Booking Orders for the product families belonging to the DSG group in the period from January 1991 to November 2002; data has been sampled with a monthly frequency; therefore the number of points available is 132. The Booking has been considered in terms of *Book Value*: customer's orders quantity of dollars registered in the observation month.

The 15 product families that, here, have been indicated with the prefixes from T1 to T15 manage the products of DSG group; moreover the prefix T16 is referred to the variable that represents the evolution of the orders for the DSG group.

III CLUSTERING STRATEGY BASED ON MULTIVARIATE ANALYSIS

This clustering strategy has been based on a supervised multivariate analysis. In order to highlight different aspects of information, the data set has been processed by using different techniques. The process flow consists of two main steps. In the first the step multivariate analysis has

been structured by choosing different mathematical techniques, which have allowed to underling particular characteristic of the Book trends. In the second step, all the characteristics that have been extracted from each variable have been compared to each other in order to create a classification. The mathematical methods that have been applied are related to both the statistical analysis and the signal processing analysis.

A Statistical Analysis

The statistical analysis has been performed in order to characterize the evolution of market demand by looking for criteria to evaluate the quantitative growth of the market demand. The parameters that have been computed are the average, the variance, and the ratio variance over average.

As the variables reflect the life of products, the characterization of a family by an average value evaluated during all its lifetime can not give a satisfying information, therefore statistics have not been computed on the total life time of product families but with different time windows: three, six and twelve months. For each product family and for each analysis three curves have been built.

The complete analysis, therefore, have brought to a characterization of this *average trends*, *variance trends* and *variance versus average ratio trends* computed by quarters, half years and years.

All these time windows selected are particularly relevant from an economic point of view.

To realize the classification the adopted criteria have based on range variation of all the obtained curves, for each single type of analysis. Following, for each analysis, the economic meaning and the criteria selected to build classes are reported.

The *Average Trends* allows to remark how the average volume is evolving by compressing the time in fixed window of three, six and twelve months. It has been possible to highlight how the average trend is always growing as group reach more and more business volume.

The *Variance Trends* characterize how the signal changes versus the average. The trend is related, in this case, to the considered window. The last two years that have been characterized by a market contraction, show a greater variance.

The *Variance versus Average ratio Trends* are a way to quantify the volatility of the signals as they measure how much the variance fluctuates around

the average. It is possible to highlight that volatility seems to growth in relation with average growth especially for some product families.

B Signal Analysis

The signal analysis allows to track the qualitative information that time series bring. It is not expected the results have to be always the same. As already pointed out the time series reflect the evolution, in time, of the products market request to the company and it is a function of the complex dynamics among the firm, its environment and the market. The mathematical techniques that have been carried on are the correlation analysis, the frequency analysis and a test to evaluate the determinism of a time series, the Kaplan's test.

The time series have been pre-processed in order to filter spurious and exceptional events trough a moving average filter on 3 months.

Measuring how much time series related to the 15 P&L are correlated to the time series of the group DSG (T16) has performed the Correlation Analysis. The correlation degree with T16 has been analysed under two different points of view, one by taking in account the value of maxim amplitude of the correlation function and the other by considering the time window that allows to obtain this maximum. These two parameters, respectively, allow us to underline the trend similarity of two curves and at which time shift that occurs. To obtain the different classes the criteria adopted are related to the correlation degree; the threshold has been fixed at 0.5.

The aim of the *Frequency Analysis* is to find the characteristic periodicities in the series. The classes have been distinguished trough a set of base frequencies that have been selected in relation to the highest value of the power spectrum; the selected frequencies are 3, 12 and 24 months.

The *Kaplan's Test* [5] is, particularly, suitable for short time series where exceptional events can occur. This test has been applied to investigate about the nature of the system represented by the time series. It allows to characterize if the nature of dynamics under consideration are more close to the deterministic or stochastic behaviour. Time series have been aggregated in function of the results of the test.

C Clustering Results

At this point, the obtained six sets of classes are based on criteria selected ad hoc for each analysis.

In this phase the results coming from each step have been compared in order to find a unique, most meaningful and complete set of classes.

The global set of classes has been identified comparing the results coming both from statistical and signal analysis. Moreover the results have been compared in order to find the classes that are homogeneous in both analyses.

In Table 1 the final set of four classes is reported, for each class the P&L that have been associated are indicated. As it can be noticed the P&L indicated T1, T4, T7, T8, T13 and T14 are not included because through the parameter selected not enough strong similarity with the other families has been found.

In Figs 2-3, respectively, the class 1 and class 2 are shown. It can be considered the qualitative similarity of the trend related to the booking for the product families T2 and T9 included in class 1 and for product families T10 and T11 in class 2.

Table 1: Global set of classes.

Classes	Time Series
Class 1	T2 – T9
Class 2	T5 – T6
Class 3	T10 – T11
Class 4	T12 – T3

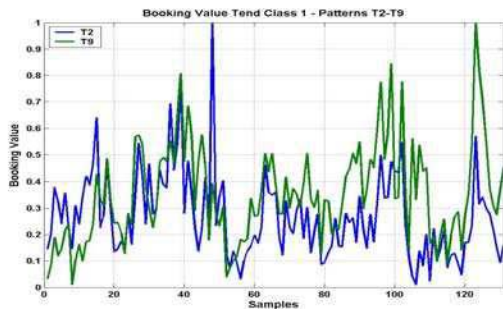


Fig.2: Class 1: T2 (blue) – T9 (green).

VI. MODELING STRATEGY

The purpose of this phase of study is to answer the following question: “it is possible after grouping “homogeneous” elements in class, to model a class be considering the trend of only one element with satisfactory performance”.

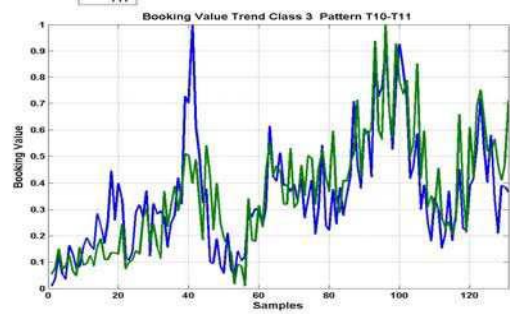


Fig.3: Class 3: T10 (blue) – T11 (green).

To face this task the *modelling phase* has been structured in the following steps:

- to smooth peaks, the data have been normalized with 3 months moving average;
- inside the class, the booking of one element has been chosen as *training pattern*, meanwhile, the trend of the other one has been considered as *test pattern*;
- structure of the model selected is the NARMA model;
- The choice of best model has been evaluated in relation with the minimum RSME on the test pattern.

A Model Structure

The models have been developed with nonlinear NARMA structure as follows:

$$y(t) = f(y(t - 1), y(t - 2), y(t - 3))$$

where f is a nonlinear function, three regression time samples are considered.

NARMA models have been implemented by using MultiLayerPerceptron (MLP) paradigm; the main features of the adopted structure are the following:

- the firing function of the neurons in hidden layers is sigmoid;
- the firing function of the neuron in the input layer is linear;
- the initial conditions for the weights and biases are random variables in the range [0.1, 0.9];
- the learning *Delta Strategy* is single step.

The topology of the network consists of:

- the *number of input neurons* are varying are three;

- the number of *hidden neurons* is chosen in the range [1:6] during the test phase in relation with the minimum value of the performance index selected;
- the *output neuron* is one.

B Modeling Results

The results show, globally, the meaningfulness of the followed approach. For each class it has been proved that the clustering strategy could drive the modelling phase. Moreover the NARMA structure allows to obtain good tolerance of error. Table 2 reports the error measured with RSME index both for the training and test phase. The value of the error is always below $8 * 10^{-3}$.

Classes	RSME Train	RSME Test
Class 1	$7.2 * 10^{-3}$	$5.5 * 10^{-3}$
Class 2	$3.6 * 10^{-3}$	$5.9 * 10^{-3}$
Class 3	$5.0 * 10^{-3}$	$5.4 * 10^{-3}$
Class 4	$3.0 * 10^{-3}$	$7.7 * 10^{-3}$

Table 2: Class modelling, RSME in training and test.

In Figs. 4-5 there are reported, respectively, the results obtained for Class 1 and Class 3. In Fig. 4 the trend of the test pattern (T9) that has been evaluated by the selected model is plotted in green solid line, meanwhile the real value of the variable T9 are in blue solid line. The trend of the variable (T2) chosen as training pattern is reported in a red dot line.

In Fig. 5 the trend of the test pattern (T11) that has been evaluated by the selected model is plotted in green solid line, meanwhile the real value of the variable T11 are in blue solid line. The trend of the variable (T10) chosen as training pattern is reported in a red dot line.

It is, clearly visible how the variable obtained by the model follows the original one, nevertheless the model has been built by using a different variable as training pattern.

V CONCLUSION

The DSG group is managed through 15 product families that cover a wide product portfolio of about 12.000 products. To face with the inner complexity of this system the strategy that has been developed consists in two phases: the clustering phase and the modelling one. It has

been proved that the clustering strategy could drive the modelling phase

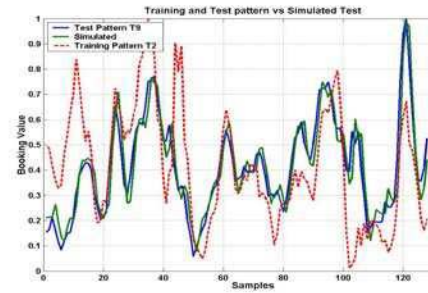


Fig. 4: Class 1 – Evaluated test pattern (Blue), training pattern (T2) and test pattern (T9).

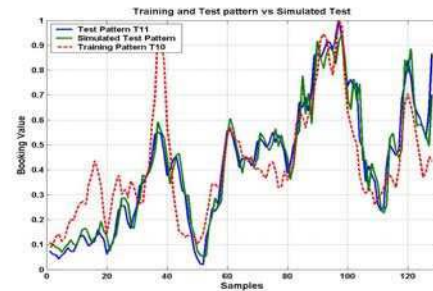


Fig. 5: Class 3 – Evaluated test pattern (Blue) training pattern (T10) and test pattern (T11).

. The obtained results are really satisfactory both in terms of possibility to group the variables and in terms of the possibility to create a unique model that is representative for all the elements of the class.

The long-term objective is to extend this strategy at products level, this will bring a great enhancement to the potentiality of this strategy.

References

[1] S. Makridakis “Forecasting: its role and value for planning and strategy”, *International Journal of Forecasting* (12) Elsevier 1996

[2] M. Bucolo, F. Caizzone, L. Fortuna, G. Tomarchio, ‘Nonlinear Models for Semiconductor Market Forecast’, *Nonlinear Phenomena in Complex Systems- Education and Upbringing Publishers, National Academy of Science Belarus and Belarusian State University.*

[3] M. Bucolo, F. Conti, L. Fortuna, G. Tomarchio, ‘Nonlinear Clustering Strategy to Characterize Financial time Series’, *11th International IEEE Workshop on Nonlinear Dynamics of Electronic Systems (NDES 2003)*, Scuol, May 2003.

[4] H. Gruber “The evolution of market structure in semiconductors: the role of product standards” *Research Policy* Elsevier 2000

[5] D. T. Kaplan, ‘Exceptional events as evidence for determinism’, *Activity Report, Physica D*, vol. 12, 1994

HARDWARE PROTOTYPE OF THE TWO-STAGE CHAOTIC COLPITTS OSCILLATOR FOR THE UHF RANGE

S. Bumelienė¹, A. Tamaševičius¹, G. Mykolaitis^{1,2}, A. Baziliauskas³ and E. Lindberg⁴

¹Plasma Phenomena Laboratory,
Semiconductor Physics Institute,
A. Goštauto 11, Vilnius, LT-2600, Lithuania
e-mail: tamasev@pfi.lt
WWW:http://www.pfi.lt/index_e

²Department of Physics,
Faculty of Fundamental Sciences,
Vilnius Gediminas Technical University,
Saulėtekio 11, Vilnius, LT-2040, Lithuania

³Department of Signal Processing,
Faculty of Telecommunications and Electronics,
Kaunas University of Technology,
Studentų 50, Kaunas, LT-3031, Lithuania
e-mail: Antanas.Baziliauskas@stud.ktu.lt
WWW:<http://www.ktu.lt/en/>

⁴Ørsted•DTU Department,
348 Technical University of Denmark,
Ørsted's Plads, Kgs. Lyngby, DK-2800, Denmark
e-mail: el@oersted.dtu.dk
WWW:<http://www.es.oersted.dtu.dk/~el/>

Abstract—A hardware prototype of the novel two-stage Colpitts oscillator employing the microwave BFG520 transistors with the threshold frequency of 9 GHz is described. The circuit is investigated both numerically and experimentally. Typical phase portraits, positive Lyapunov exponent and broadband continuous power spectra confirm chaotic performance of the oscillator in the ultrahigh frequency range (300 to 1000 MHz). The two-stage chaotic Colpitts oscillator exhibits better spectral characteristics compared to a classical single-stage Colpitts oscillator. The relative bandwidth is either 0.47 or 0.74 at the central frequency of about 500 MHz within the spectral unevenness of either 10 dB or 20 dB, respectively.

I. INTRODUCTION

Chaos in the Colpitts oscillator was first reported at the kilohertz frequencies [1]. Later the circuit was investigated in the high frequency (HF: 3 to 30 MHz) range [2,3]. Chaotic oscillations were demonstrated at the fundamental frequency $f^*=23$ MHz using the 2N2222A [2] also at $f^*=26$ MHz using the 2N3904 [3] bipolar junction transistors, both with approximately the same threshold frequency f_T of 300 MHz. By means of the

PSpice simulations chaos was predicted at $f^*=500$ MHz using the microwave AT41486 type transistor with f_T of 3 GHz [2] and at $f^*=1$ GHz employing the BFG520 transistor with f_T of 9 GHz [3,4]. However these results were not confirmed experimentally at that time. Very recently we demonstrated chaos in a hardware prototype at $f^*=450$ MHz, $f^*=780$ MHz, and $f^*=1060$ MHz using the BFG520 microwave transistor [5]. Analysis shows that in a classical (single-transistor) Colpitts oscillator, chaotic oscillations can be generated up to approximately $f^*\approx 0.1f_T$ [6], that is at $f^*\approx 900$ MHz with the BFG520. Indeed, only weak chaos with 20 to 30 dB height peaks at f^* also at its sub-harmonic and higher harmonic components can be expected for $f^*=1000$ MHz [3,4]. Moreover, the last minute PSpice simulations indicate that chaotic oscillations observed experimentally at $f^*=1060$ MHz [5] are due to the parasitic elements, like wiring inductance and wiring loss resistance that can be important at the ultrahigh frequencies [7]. In the present work we recall to a two-stage Colpitts oscillator introduced several years ago and promising higher fundamental frequencies, up to $f^*\approx 0.3f_T$ [3,4]. We describe an example of a hardware implementation of the modified oscillator and give experimental evidence of its chaotic performance in the ultrahigh frequency (UHF: 300 to 1000 MHz) range.

II. CIRCUITRY

Simplified circuit diagram of the two-stage Colpitts oscillator [3,4] is sketched in Fig. 1, meanwhile its specific hardware implementation is presented in Fig. 2.

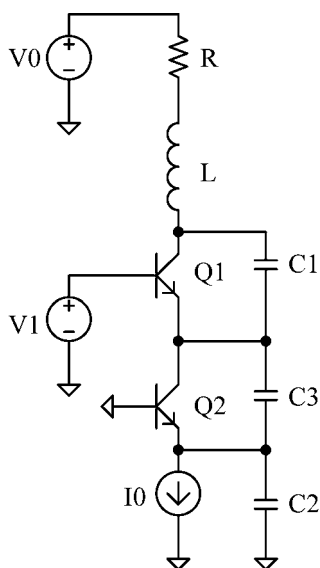


Fig. 1. Two-stage Colpitts oscillator

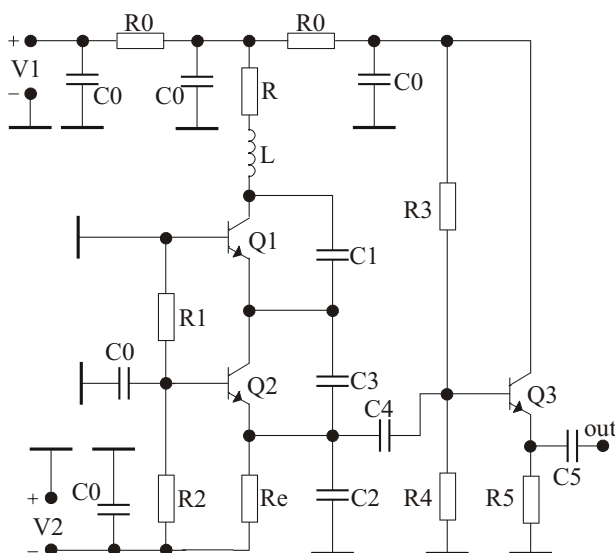


Fig. 2. Full circuit diagram of the two-stage Colpitts oscillator

The Q1-Q2-based stages compose the intrinsic two-stage Colpitts oscillator while the Q3-based one is an emitter follower inserted to buffer the influence of the measuring devices. The resonance tank combines the loss resistor R, the inductor L, and three series capacitors C1, C2, C3. The C4 is a

coupling capacitor. Small auxiliary capacitors of 300 pF (not shown in the circuit diagram) are connected in parallel with the main blocking capacitors C0 to improve filtering at high frequencies. The bias emitter current I_0 can be tuned by varying the voltage source V2.

III. PSCIPICE SIMULATION RESULTS

In the hardware prototypes the circuit parameters were the following: $R_0=100 \Omega$, $R_1=510 \Omega$, $R_2=3 \text{ k}\Omega$, $R_3=5.1 \text{ k}\Omega$, $R_4=3 \text{ k}\Omega$, $R_5=200 \Omega$, $R_e=1.5 \text{ k}\Omega$, $C_0=47 \text{ nH}$, $C_2=C_3=10 \text{ pF}$, $C_4=1 \text{ pF}$, $C_5=270 \text{ pF}$ (other parameters of the tank elements, namely R, L, and C1 depend on the chosen fundamental frequency f^* and are given in the captions to Figs. 4,5). We note, that in a real circuit the total tank inductance L consists of: (1) the L_{ext} controlled by an external inductive element, (2) the parasitic inductance of the loss resistor L_R , and (3) the parasitic inductance L_{C0} of the filter capacitor. Thus, $L=L_{ext}+L_R+L_{C0}$. The two latter values are approximately 2 nH, each. The microwave transistors BFG520 discussed in the Introduction were employed in the circuit. The specific values of the supply voltages V_1 and V_2 were adjusted to achieve the desired chaotic performance of the oscillator. Simulations of the circuit in Fig. 2 were performed by means of the Electronics Workbench Professional simulator, based on the PSpice software. The Gummel-Poon model of the transistors was employed. Chaotic performance of the oscillator is observed in a sufficiently wide range of the control parameters and is illustrated in Fig. 3 with a typical phase portrait. It was simulated using the following resonance tank and supply voltage values: $R=47 \Omega$, $L=16 \text{ nH}$, $C_1=2.4 \text{ pF}$, $V_1=10 \text{ V}$, $V_2=24 \text{ V}$.

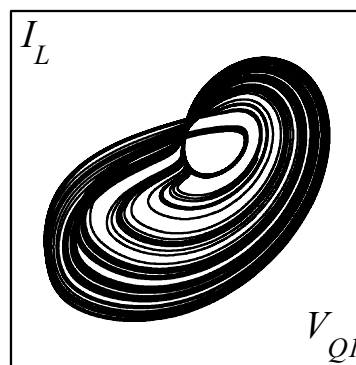


Fig. 3. Typical chaotic phase portrait, current through the inductive element I_L versus collector voltage V_{Q1}

IV. EQUATIONS, LYAPUNOV EXPONENTS

Dynamics of the two-stage oscillator in Fig. 1 is given by the following set of ordinary differential equations:

$$\begin{cases} C_1 \frac{dV_{C1}}{dt} = I_L - I_{EQ1}(r, V_{C2}, V_{C3}), \\ L \frac{dI_L}{dt} = V_0 - V_{C1} - V_{C2} - V_{C3} - RI_L, \\ C_3 \frac{dV_{C3}}{dt} = I_L - I_{EQ2}(r, V_{C2}), \\ C_2 \frac{dV_{C2}}{dt} = I_L - I_0, \end{cases} \quad (1)$$

We note, that by omitting in (1) the third equation for V_{C3} and setting $V_{C3} = 0$ in the other equations one comes to the set describing the classical Colpitts oscillator. In eqn. (1) the forward current gain of the both transistors in the common base configuration is assumed for simplicity to be $\alpha = 1$, that is the base currents are neglected. By introducing the following dimensionless state variables

$$x = \frac{V_{C1}}{\rho I_0}, \quad y = \frac{I_L}{I_0}, \quad z = \frac{V_{C2}}{\rho I_0}, \quad v = \frac{V_{C3}}{\rho I_0}, \quad t = \frac{t}{\tau} \quad (2)$$

and parameters

$$\begin{aligned} \rho &= \sqrt{\frac{L}{C_1}}, \quad \tau = \sqrt{LC_1}, \quad \varepsilon_2 = \frac{C_2}{C_1}, \quad \varepsilon_3 = \frac{C_3}{C_1}, \\ a &= \frac{\rho}{r}, \quad b = \frac{R}{\rho} \end{aligned} \quad (3)$$

eqns. (1) are transformed into the form convenient for numerical integration:

$$\begin{cases} \frac{dx}{dt} = y - F_1(a, z, v), \\ \frac{dy}{dt} = -x - z - v - by, \\ \varepsilon_3 \frac{dv}{dt} = y - F_2(a, z), \\ \varepsilon_2 \frac{dz}{dt} = y - 1, \end{cases} \quad (4)$$

In eqns.(4) the constant term $V_0/\rho I_0$ has been omitted since it does not influence the overall

dynamics of the system. The nonlinear functions F_1 and F_2 describe the current-voltage characteristics of the base-emitter junctions of the Q1 and Q2 transistors, respectively. They can be presented in the form of two-segment piece-wise linear functions:

$$F_1(a, z) = \begin{cases} 1 - a(z + v), & a(z + v) < 1, \\ 0, & a(z + v) \geq 1. \end{cases} \quad (5)$$

$$F_2(a, z) = \begin{cases} 1 - az, & az < 1, \\ 0, & az \geq 1. \end{cases} \quad (6)$$

Parameter a in expressions (5) and (6) depends on r , the differential resistance of the base-emitter junction in the forward-active mode. In this simplified mathematical model the r is considered to be a constant parameter. Meanwhile in experiments it can be controlled by the emitter dc bias current I_0 .

To characterize the two-stage Colpitts oscillator quantitatively we made use of the Matlab Lyapunov Exponent's Toolbox (LET) and estimated the full spectrum of the Lyapunov exponents. The LET requires the Jacobian matrix of the corresponding state-equations. Since eqns. (4) contains two piece-wise linear functions F_1 and F_2 , each two-segments ones, the Jacobian matrix has four different forms. For the specific parameter values $a=10$, $b=0.4$, and $\varepsilon_2=\varepsilon_3=5$ the LET provides the following Lyapunov exponents:

$$\lambda_1 = 0.27, \lambda_2 = 0, \lambda_3 = -0.31, \lambda_4 = -0.57. \quad (7)$$

Though eqns.(4) describe a four-dimensional system it possesses only one positive Lyapunov exponent, $\lambda_1 > 0$. Thus, despite the enlarged dimensionality of the system the two-stage Colpitts oscillator remains simply chaotic one in contrast to a coupled system of two classical Colpitts oscillators that has two positive Lyapunov exponents, therefore exhibits hyperchaotic behaviour [8]. Employing the Kaplan-Yorke conjecture

$$d_L = j + \frac{\sum_{i=1}^j \lambda_i}{|\lambda_{j+1}|}, \quad \sum_{i=1}^j \lambda_i > 0, \quad \sum_{i=1}^{j+1} \lambda_i < 0 \quad (8)$$

we evaluated the Lyapunov dimension $d_L = 2.88$, that is rather close to 3 and is essentially larger than the corresponding measure of the classical single-stage Colpitts oscillator ($d_L = 2.08$) estimated for similar set of the parameter values.

V. EXPERIMENTAL RESULTS

To illustrate the performance of the oscillator experimentally several power spectra were taken at different fundamental frequencies f^* with spectral resolution of 120 kHz. Two of them are presented in Figs. 4,5. The spectra are broadband continuous ones with only rather flat rises at the f^* and near the subharmonics $f^*/2$ (Fig. 4) or the $f^*/3, 2f^*/3$ (Fig. 5).

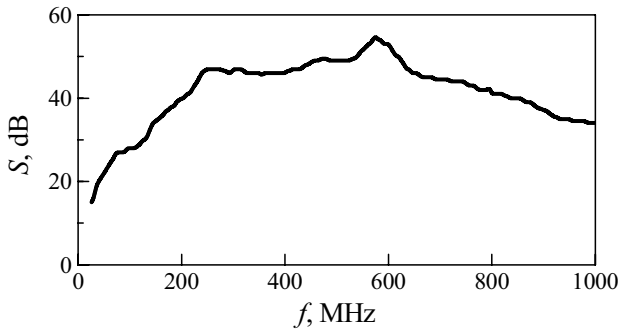


Fig. 4. Experimental power spectra. $f^* \approx 600$ MHz, $R=33 \Omega$, $L_{ext}=12$ nH, $C_1=2$ pF, $V_1=10$ V, $V_2=25$ V

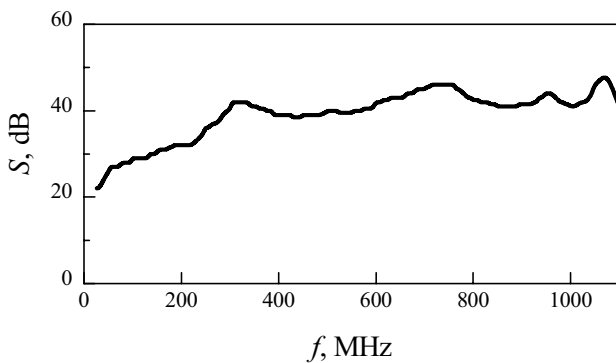


Fig. 5. Experimental power spectra. $f^* \approx 1100$ MHz, $R=17 \Omega$, $L_{ext}=4$ nH, $C_1=1$ pF, $V_1=6.3$ V, $V_2=27$ V

In comparison with a classical single-stage oscillator investigated for this frequency range previously in [5,7] the modified version exhibits essentially better spectral features. For example, in Fig. 4 the lower and upper frequency band limits are $f_1=250$ MHz and $f_2=700$ MHz within the spectral unevenness of 10 dB, while $f_1=150$ MHz and $f_2=1000$ MHz within the unevenness of 20 dB. Thus, for the central frequency $f_c=(f_2+f_1)/2$ of about 500 MHz the relative bandwidth $\Delta=(f_2-f_1)/(f_2+f_1)$ is 0.47 and 0.74, respectively. Moreover, the spectrum shown in Fig. 5 covers the full UHF range (300 to 1000 MHz, $f_c=650$ MHz, $\Delta=0.54$) with the unevenness of less than 6 dB.

VI. CONCLUSIONS

A hardware prototype of the two-stage Colpitts oscillator has been designed for the UHF range and described in details. It has been demonstrated numerically and experimentally to generate broadband chaotic oscillations. The two-stage chaotic Colpitts oscillator has better spectral characteristics than the classical single-transistor oscillator.

ACKNOWLEDGMENTS

This work was supported in part by Lithuanian State Science and Studies Foundation. One of us (A.T.) was partially supported by the EC project "The Center in Processing, Research and Application of Advanced Materials (PRAMA)" under contract No. G5MA-CT-2002-04014.

REFERENCES

- [1] M. P. Kennedy. Chaos in the Colpitts oscillator. *IEEE Trans. Circuits Syst. I.*, vol. 41, No. 11, pp. 771-774 (1994).
- [2] C. Wegener and M. P. Kennedy. RF Chaotic Colpitts oscillator. In *Proc. NDES'95*, pp. 255-258, Dublin, Ireland, 1995.
- [3] G. Mykolaitis, A. Tamaševičius, S. Bumelienė, G. Lasienė, A. Čenys, A. N. Anagnostopoulos and E. Lindberg. Towards microwave chaos with two-stage Colpitts oscillator. In *Proc. NDES'01*, pp. 97-100, Delft, The Netherlands, 2001.
- [4] A. Tamaševičius, G. Mykolaitis, S. Bumelienė, A. Čenys, A. N. Anagnostopoulos and E. Lindberg. Two-stage chaotic Colpitts oscillator. *Electron. Lett.*, vol. 37, No. 9, pp. 549-551 (2001).
- [5] G. Mykolaitis, A. Tamaševičius and S. Bumelienė. Experimental demonstration of chaos from the Colpitts oscillator in the VHF and the UHF ranges. *Electron. Lett.*, vol. 40, (2004).
- [6] A. Tamaševičius, S. Bumelienė and G. Mykolaitis. Evaluation of bipolar transistors for application to RF chaotic Colpitts oscillator. *Scientific Proceedings of Riga Technical University. Ser. 7. Telecommunications and Electronics*, vol. 1, pp. 53-54 (2001).
- [7] A. Tamaševičius, G. Mykolaitis, S. Bumelienė, A. Baziliauskas, R. Krivickas and E. Lindberg. VHF and UHF chaotic Colpitts oscillators. In *Proc. NDES'04*, Évora, Portugal, 2004.
- [8] A. Čenys, A. Tamaševičius, A. Baziliauskas, R. Krivickas, E. Lindberg. Hyperchaos in coupled Colpitts oscillators, *Chaos, Solitons & Fractals*, vol. 17, No. 2, pp. 349-353 (2003).

COMPARISON BETWEEN PERTURBATION AND VOLTERRA METHODS

A. Buonomo and A. Lo Schiavo

Dipartimento di Ingegneria dell'Informazione,
Seconda Università di Napoli,
Via Roma, 29 – 81031 Aversa (CE), Italy
e-mail: antonio.buonomo@unina2.it, loschiavo@ieee.org
WWW: <http://www.dii.unina2.it>

Abstract—*The perturbation method is compared with the methods of Volterra series and of Picard's simple iteration when applied for predicting the distortion in nonlinear analog circuits. Exact relationships among them are established showing that they lead to asymptotically equivalent series solutions of circuit equations and provide very similar approximants to the solution.*

I. INTRODUCTION

The analysis of nonlinear harmonic distortion in analog integrated circuits involves the calculation of the steady-state response to a periodic signal in a nonlinear time-invariant circuit. This can be found using a variety of numerical methods or, when it is possible, through analytical methods. Obviously, the latter are generally preferred as they allow symbolic expressions for the harmonics to be derived, providing a better understanding of the distortion-generating mechanism.

The Volterra series method is a powerful analytical method for the analysis of nonlinear systems, both autonomous [1] and forced [2]-[3], and it is frequently used for predicting the nonlinear distortion in a variety of circuits. This method, which is suitable for weakly nonlinear circuits, enables a periodic solution to be determined in the form of a series, in principle, to any order of accuracy. However, the calculation of higher-order kernels rapidly becomes too complicated, especially for nonlinearities of non-polynomial type.

As an alternative, a method relying on the classical theory of regular perturbation was presented for analyzing nonlinear oscillators [4] and for predicting the distortion in nonlinear analog circuits [5]. Since in the cases where the prediction of harmonic distortion is of interest the actual response slightly differs from the linear

approximation, it is natural to view the former as a small perturbation of the latter, and thus to formulate the problem of determining the periodic response in analog circuits as a regular perturbation problem. Consequently, the response is sought in the form of a power series in a perturbation parameter through a procedure of successive approximations. As in [4], the method presented in [5] combines the classical method of perturbation and the Harmonic Balance, allowing the coefficients of series to be determined by recurrent formulae, thus providing the periodic response in a closed analytical form to any approximation order.

Here, we present a rigorous comparison between the Volterra series method and the perturbation method, as well as with the Picard iteration method [6], showing that these methods lead to the same series solution of the describing equation of a circuit with a polynomial nonlinearity, and evolve very similar approximants to the solution. Consequently, the perturbation method is a valid alternative to the Volterra series method, as already observed in [5] through a numerical investigation.

II. PERTURBATION METHOD

We describe the perturbation method presented in [5] in order to make easier the comparison with other methods. Let us consider a circuit with an excitation $u(t)$, T -periodic in time t , and a single nonlinearity $z = g(x)$, representing a nonlinear two-terminal or a nonlinear controlled source. The nonlinearity $z = g(x)$ can represent the current-voltage characteristic of a nonlinear resistor, the charge-voltage characteristic of a nonlinear capacitor, the flux-current characteristic of a nonlinear inductor, or the input-output characteristic of a nonlinear two-terminal. We consider the

controlling variable of the nonlinearity, $x(t)$, as the unknown variable and, thus, the periodic nonlinear problem is solved when this variable is determined. Once the controlling variable is known, any other circuit variable can be obtained by linear transformation.

The circuit equation can be put in the operator form

$$x = \mathcal{S}u + \mathcal{Y}g(x) \quad (1)$$

where the symbols \mathcal{S} and \mathcal{Y} denote linear operators. Decomposing the nonlinearity into its linear and nonlinear part, that is setting $g(x) = \alpha x + \beta f(x)$, where $f^{(1)}(0) = 0$, the equation describing the behavior of the circuit, can be written in the form

$$x = \mathcal{G}u + \beta(1 - \mathcal{Y}\alpha)^{-1}\mathcal{Y}f(x) \quad (2)$$

where $\mathcal{G} = (1 - \mathcal{Y}\alpha)^{-1}\mathcal{S}$. The last term of (2) accounts for the effect of the nonlinearity on the circuit response and is neglected when the method of equivalent linearization is used.

As analog circuits are usually designed minimizing the nonlinear distortion, the last term in (2) must be small as compared to the previous terms and, consequently, (2) can be seen as a perturbation of the linear equation $x = \mathcal{G}u$. Thus, we can put (2) in the perturbation form

$$x = \mathcal{G}u + \varepsilon \mathcal{M}f(x) \quad (3)$$

where ε is a normalization parameter, such that $\varepsilon \mathcal{M} = \beta(1 - \mathcal{Y}\alpha)^{-1}\mathcal{Y}$. The parameter ε assumes the meaning of a perturbation parameter, as its value determines the nearness of the nonlinear equation to its linear approximation. Observe that the entity of ε is not meaningful, being significant the smallness of the perturbation entity only, here represented by $\varepsilon \mathcal{M}f(x)$. Equation (3) is formulated as a regular perturbation problem and, for ε tending to zero, reduces to the equation describing the circuit when its nonlinearity is neglected, that is $x = \mathcal{G}u$. Accordingly, we write the solution of (3) as a perturbation of the linear solution $x_0 = \mathcal{G}u$, in the form $x(t, \varepsilon) = x_0(t) + \varepsilon h(t, \varepsilon)$, where $\varepsilon h(t, \varepsilon)$ is the remaining part of the solution $x(t, \varepsilon)$ accounting for the effect of the nonlinearity.

Assuming the analyticity of $f(x)$, we calculate the periodic solution $x(t, \varepsilon)$ of (3), of which we admit the existence, in the form of power series of ε

$$x(t, \varepsilon) = x_0(t) + x_1(t)\varepsilon + x_2(t)\varepsilon^2 + \dots \quad (4)$$

In order to calculate the periodic coefficients $x_k(t)$, we substitute (4) in both sides of (3) and expand $f[x(t, \varepsilon)]$ in a power series of ε at $\varepsilon = 0$. Thus, we get

$$x_0 + x_1\varepsilon + x_2\varepsilon^2 + \dots = \mathcal{G}u + \varepsilon \mathcal{M}(f_0 + f_1\varepsilon + \dots) \quad (5)$$

where the Taylor-series coefficients $f_k(t)$, $k = 0, 1, \dots$, are calculated by

$$\begin{aligned} f_0 &= f(x_0) \\ f_k &= f^{(1)}(x_0)z_1 + f^{(2)}(x_0)z_2 + \dots + f^{(k)}(x_0)z_k \quad (6) \end{aligned}$$

Here, $f^{(n)}(x_0)$ denotes the n th derivative of $f(x)$ evaluated at $x = x_0$, and the z_n 's are given by

$$z_n = \frac{1}{n!} \sum_{\substack{l_1 + \dots + l_n = k \\ l_j \geq 1}} x_{l_1} \dots x_{l_n} \quad (7)$$

Then, balancing the coefficients of the same powers of ε in (5), the coefficients $x_k(t)$ are recursively determined in an explicit form through the recurrent formulae

$$x_0 = \mathcal{G}u \quad (8a)$$

$$x_1 = \mathcal{M}f_0 = \mathcal{M}f(x_0) \quad (8b)$$

$$x_2 = \mathcal{M}f_1 = \mathcal{M}f^{(1)}(x_0)x_1 \quad (8c)$$

$$x_3 = \mathcal{M}f_2 = \mathcal{M}\left(f^{(1)}(x_0)x_2 + f^{(2)}(x_0)x_1^2/2\right) \quad (8d)$$

$$x_k = \mathcal{M}f_{k-1} = \mathcal{M}\left(f^{(1)}(x_0)z_1 + \dots + f^{(k-1)}(x_0)z_{k-1}\right) \quad (8e)$$

allowing us to construct the successive approximations to the solution $x(t, \varepsilon)$ with the desired accuracy. Let $x^{(0)} = x_0$ be the zero-order

approximation in ε to the solution, the successive approximations are determined by the iteration procedure

$$x^{(k)} = x_0 + x_1\varepsilon + \dots + x_k\varepsilon^k \quad (9)$$

$$x^{(k)} = x^{(k-1)} + x_k\varepsilon^k \quad (10)$$

whereby the solution can be constructed by repetitively calculating x_k through (8e), that is the response of a linear circuit described by the linear operator \mathcal{M} , subject to a time-domain forcing signal f_{k-1} . This calculation can be easily carried out in the frequency-domain, as shown in [5].

Like the Volterra series method, the perturbation method can be applied only for mildly nonlinear circuits or for limited signal amplitudes. Differently from the Volterra series method, the formulae are based on the usual transfer functions of linear analysis and the method can be practically used for non-polynomial nonlinearities too, as well as for obtaining harmonics higher than the third.

III. CONNECTION WITH VOLTERRA AND PICARD METHODS

Now, we investigate the connection between the perturbation method and the well-known methods of the simple iteration (Picard method) and of the Volterra series. To this end, we first show a property of the solution achieved through the proposed method.

The solution of the linearized problem corresponding to (3), i.e. x_0 , is the *generating solution* of the constructive method (9), meaning that all x_k 's are calculated through (8e), starting from x_0 . Assuming that $f(x)$ is a polynomial nonlinearity, $f(x) = c_2x^2 + c_3x^3 + \dots$, and putting x_0 into (8b), terms of type $c_k\mathcal{M}x_0^k$ results in x_1 . Then, putting x_1 into (8c), it follows that x_2 includes the terms $2c_2^2\mathcal{M}x_0\mathcal{M}x_0^2$, $3c_2c_3\mathcal{M}x_0^2\mathcal{M}x_0^2$, $2c_2c_3\mathcal{M}x_0\mathcal{M}x_0^3, \dots$. As terms of the general type $\mathcal{M}x_0^i(\mathcal{M}x_0^j)^q$ arise in x_k , we define as the order of a term in x_k the number m of times values of x_0 multiplied together. It is easy to verify that x_0 is a term of order $m=1$, x_1 includes terms of order $m \geq 2$ and x_2 includes terms of order $m \geq 3$.

Generalizing, we show the following:

Theorem 1. The coefficient x_k in (8e) contains terms of order $m \geq (k+1)$.

Proof. By virtue of (7), f_{k-1} can be rewritten in the expanded form

$$f_{k-1} = f^{(1)}(x_0) x_{k-1} + f^{(2)}(x_0)(x_1x_{k-2} + x_2x_{k-3} + \dots + x_{k-2}x_1) + \dots + \frac{f^{(k-1)}(x_0)}{(k-1)!} x_1^{k-1} \quad (11)$$

As $f^{(1)}(x_0)$ has terms of order greater or equal to 1 and x_{k-1} has terms of order greater or equal to k , it follows that $f^{(1)}(x_0)x_{k-1}$ generates terms of order $m \geq (k+1)$. All other terms in (11), $f^{(n)}(x_0)x_{l_1}x_{l_2}\dots x_{l_n}$, with $2 \leq n \leq (k-1)$ and $l_1 + \dots + l_n = k-1$, contain n factors x_{l_j} each of order greater or equal to (l_j+1) , which together have order greater or equal to $(l_1 + \dots + l_n + n)$. Thus, all remaining terms in (11) generate terms of order $m \geq (k-1+n)$ and, hence, of order $m \geq (k+1)$.

From Theorem 1 and (9), we deduce that $x^{(k)}$ and $x^{(k-1)}$ have the same terms of order $m \leq k$, as well as all higher-approximations $x^{(k+j)}$, $j \geq 1$. Further, if we write $x^{(k)}$ in the form

$$x^{(k)} = \mathcal{X}_{1,k}(t) + \mathcal{X}_{2,k}(t) + \dots + \mathcal{X}_{m,k}(t) + \dots, \quad (12)$$

where $\mathcal{X}_{m,k}$ denotes the sum of terms with the same order m at the k th approximation, we can conclude that all terms of order $m \leq k$ of (12) are definitively determined at the $(k-1)$ th approximation, and higher approximation add higher-order terms only.

Applying the Picard method to the integral equation (3) and assuming x_0 as an initial guess solution, the construction of the solution $x(t, \varepsilon)$ proceeds following the iteration procedure

$$\begin{aligned} x_p^{(0)} &= x_0 \\ x_p^{(k)} &= x_0 + \varepsilon \mathcal{M} f(x_p^{(k-1)}) \end{aligned} \quad (13)$$

The first approximation to the solution,

$x_p^{(1)} = x_0 + \varepsilon \mathcal{M}f(x_0)$, is equal to that achieved through the perturbation method, by virtue of (8b). The second approximation is $x_p^{(2)} = x_0 + \varepsilon \mathcal{M}f(x_0 + \varepsilon x_1)$. Developing $f(x)$ in a Taylor series of ε and taking into account (8b), we get

$$x_p^{(2)} = x_0 + x_1\varepsilon + x_2\varepsilon^2 + \mathcal{M}g_1(\varepsilon, x_0, x_1)\varepsilon^3 \quad (14)$$

where x_2 is given by (8c) and $g_1(\varepsilon, x_0, x_1)\varepsilon^2$ represents the complementary term. Proceeding in the same way, the k th approximation can be written in the form

$$x_p^{(k)} = x_0 + x_1\varepsilon + \dots + x_k\varepsilon^k + \mathcal{M}g_{k-1}(\varepsilon, x_0, \dots, x_{k-1})\varepsilon^{k+1} \quad (15)$$

where x_k is given by (8e) and $g_{k-1}\varepsilon^k$ is the complementary term. Comparing (15) with (9), we deduce that the regular perturbation method and the Picard method give rise to different approximations, for $k > 1$. However, they lead to solutions which are asymptotically equivalent, that is obtained summing equivalent power series.

Let us now write the k th approximation to the solution of the Picard's iteration method, $x_p^{(k)}$, and that of the Volterra series method, $x_V^{(k)}$, as

$$x_p^{(k)} = \gamma_{1,k} + \gamma_{2,k} + \dots + \gamma_{m,k} + \dots \quad (16)$$

$$x_V^{(k)} = \beta_{1,k} + \beta_{2,k} + \dots + \beta_{m,k} + \dots \quad (17)$$

where $\gamma_{m,k}(t)$ and $\beta_{m,k}(t)$ denote the sum of terms having the same order m , in the sense outlined above. A straightforward generation of the Volterra series in the time domain was derived in [6], who showed that $\gamma_{m,k} = \beta_{m,k}$, for $m \leq k$.

Theorem 2. The perturbation method, the Picard method and the Volterra series method give the same terms of order m at the k th approximation to the solution of the integral equation (3), for $m \leq k$. Further, they lead to the same series solution.

Proof. As, by virtue of Theorem 1, we have $\chi_{m,k} = \gamma_{m,k}$ for $m \leq k$, and $\gamma_{m,k} = \beta_{m,k}$ for $m \leq k$ [6], we deduce that $\chi_{m,k} = \beta_{m,k}$ for $m \leq k$. The k th

approximations provided by the three methods are thus identical in the terms of order less or equal to k . From this, we deduce that the series solutions achieved by the three methods are asymptotically equivalent.

It follows, from the above results, that we can deduce the same conclusions as in [6] and extend them to the perturbation method.

IV. CONCLUSIONS

The perturbation procedure and the Volterra series evolve very similar k th approximations to the solution, as they contain the same terms of order less or equal to k . However, the k th approximation of the Volterra series contains no higher-order terms, whereas the perturbation method does. A frequency domain formulation of the perturbation procedure (8),(9) which is simple and straightforward to apply, is based on the usual transfer function of linear dynamic systems, avoiding the calculation of frequency domain Volterra kernels. In addition, the perturbation procedure allows us to formally handle nonlinearities of non-polynomial type, as the transistor exponential nonlinearities.

REFERENCES

- [1] L.O. Chua and Y.S. Tang, "Nonlinear oscillation via Volterra series," IEEE Trans. Circuits Syst., vol. 29, pp. 150-168, 1982.
- [2] P. Wambacq and W. Sansen, Distortion analysis of analog integrated circuits, Norwell, MA: Kluwer, 1998.
- [3] P. Wambacq, G.E. Gielen, P.R. Kinget and Sansen W, "High-frequency distortion analysis of analog integrated circuits," IEEE Trans. on Circuits Syst.-II, vol. 46, no.3, pp. 335-345, 1999.
- [4] A. Buonomo and C. Di Bello, "Asymptotic formulas in nearly sinusoidal nonlinear oscillators," IEEE Trans. on Circuits Syst.- I, vol. 43, pp. 953-963, 1996
- [5] A. Buonomo, A. Lo Schiavo, "Perturbation analysis of weakly nonlinear forced circuits", Proc. of NDES 2003, Scuol, Switzerland, May 18-21, 2003, pp.45-48.
- [6] B.J. Leon and D.J. Schaeffer, "Volterra series and Picard iteration for nonlinear circuits and systems," IEEE Trans. on Circuits and Syst., vol. 25, no. 9, pp. 789-793, 1978.

BIFURCATION ANALYSIS AND CHAOTIC BEHAVIOR IN BOOST CONVERTERS: EXPERIMENTAL RESULTS

D. Cafagna and G. Grassi

Dipartimento di Ingegneria dell'Innovazione,
Università degli Studi di Lecce, Lecce, ITALY
{donato.cafagna; giuseppe.grassi}@unile.it

Abstract – This paper presents an experimental set-up for investigating some dynamic phenomena that can occur in DC-DC boost converters. To this purpose, the paper illustrates bifurcation analyses and possible pathways through which the converter may enter chaos. In particular, based on experimental measurements, it is shown that variations of supply voltage and inductance generate interesting bifurcations and novel routes to chaos.

I. INTRODUCTION

In recent years it has been observed that a large number of power electronic circuits can exhibit deterministic chaos [1]-[5]. Referring to power DC-DC converters, it has been demonstrated that buck and boost converters are prone to subharmonic behavior and chaos [5]-[6]. Even though the approaches in [2]-[3] are very interesting, further experimental analysis is required on the parameter domains in which chaotic behavior may occur. Therefore, the aim of this paper is to experimentally investigate some dynamic phenomena that can occur in DC-DC boost converters. In particular, the paper presents an experimental set-up for obtaining bifurcations and possible pathways through which the boost converter may enter chaos. The paper is organized as follows. In Section 2 the state equations of the current-programmed boost converter are reported. In Section 3 the circuit implementation of the proposed converter is illustrated. In Section 4 it is experimentally shown that the variations of the supply voltage and inductance lead to new bifurcation paths and routes to chaos. These results are illustrated by means of the measured time waveforms of the inductor current and the PSpice phase portraits.

II. EQUATIONS OF THE BOOST CONVERTER

The current-programmed boost converter includes an inductor L , a diode D , a DC source V_{in} , a resistance R , a capacitor C and a feedback path that consists of a flip-flop and a comparator (Fig.1). The converter is assumed to operate in continuous mode [6]. Namely, the inductance L and the switching period T are chosen so that the inductor current $i(t)$ never falls to zero. Hence, there are two switch states: i) switch S ON and diode D OFF; ii) switch S OFF and diode D ON. Therefore, the state equations of the boost converter are [4]:

$$\begin{bmatrix} \frac{dv}{dt} \\ \frac{di}{dt} \end{bmatrix} = \begin{bmatrix} -1/RC & 0 \\ 0 & 0 \end{bmatrix} \begin{bmatrix} v \\ i \end{bmatrix} + \begin{bmatrix} 0 \\ 1/L \end{bmatrix} V_{in} \quad (1)$$

$$\text{for } nT \leq t < (n+d)T;$$

$$\begin{bmatrix} \frac{dv}{dt} \\ \frac{di}{dt} \end{bmatrix} = \begin{bmatrix} -1/RC & 1/C \\ -1/L & 0 \end{bmatrix} \begin{bmatrix} v \\ i \end{bmatrix} + \begin{bmatrix} 0 \\ 1/L \end{bmatrix} V_{in} \quad (2)$$

$$\text{for } (n+d)T \leq t < (n+1)T;$$

where $v(t)$ is the voltage across the capacitor C , n is an integer and d is the duty cycle. The current $i(t)$ is chosen as the programming variable, which generates the ON-OFF driving signal for the switch S after the comparison with a reference current I_{ref} . While S is ON, $i(t)$ increases until reaches the value of I_{ref} . Then, S is turned OFF and remains OFF until the next cycle begins.

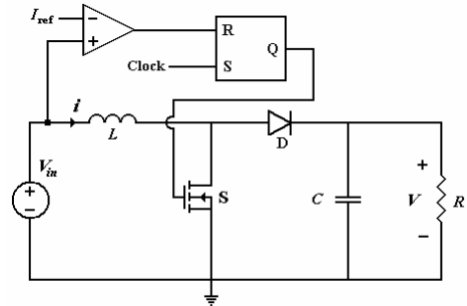


Fig.1. Current-programmed boost converter.

III. CIRCUIT IMPLEMENTATION

This Section illustrates the PSpice design of the implemented boost converter (Fig.2). The switch S is realized using a MOSFET. Its control circuitry is based on the OpAmp LM339 used as a comparator. In particular, the LM339 compares the reference voltage V_{ref} with the voltage across the resistance R_3 in series with the drain of the MOSFET. Note that this voltage is proportional to the current $i(t)$ through the inductor L when the MOSFET is turned ON. Therefore, the output of the comparator is high when the inductor current reaches the value $I_{ref} = V_{ref} / R_3$, whereas it is low when the inductor current is less than I_{ref} . Now the generation of the clock signal is described. At first, the integrated device NE555C is considered in order to generate a square wave with duty cycle $d = 0.9$. By making the derivative of the rising edge of the square wave, it is possible to obtain an impulsive signal that represents the SET input of the SR latch. Additionally, by making the derivative of the falling edge, the signal able to control the duty cycle is obtained. Referring to the latch, its output signal is high (i.e., the MOSFET is ON) when an impulsive signal arrives at the SET input. On the other hand, its output signal is low (i.e., the MOSFET is OFF) when a proper impulsive signal arrives at the RESET input.

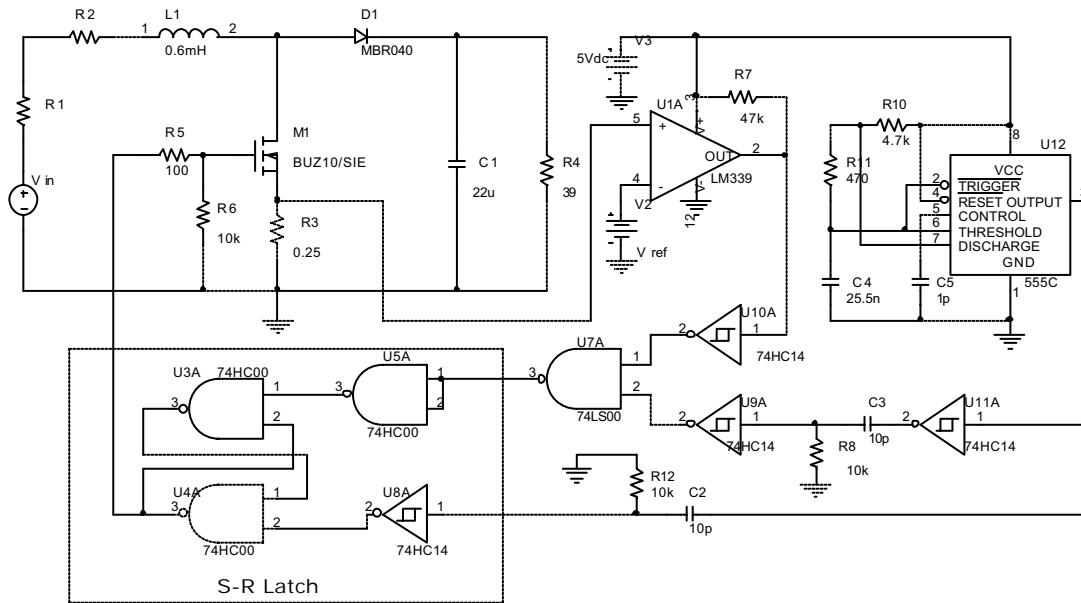


Fig.2. Circuit diagram of the experimental current-programmed boost converter.

Such RESET signal, by means of an OR gate, can be either the output of the comparator or the signal able to control the duty cycle.

IV. BIFURCATIONS AND CHAOS: EXPERIMENTAL RESULTS

In this Section the way the boost converter changes its behavior is experimentally analyzed by varying some parameters, while keeping fixed the current I_{ref} . The considered oscilloscope is the HP184A.

A. Route to chaos by varying parameter V_{in}

Herein the behavior of the boost converter is analyzed by varying the supply voltage V_{in} , whereas the following circuit parameter values have been fixed:

$$R = 39\Omega, C = 22\mu F, L = 0.6mH, I_{ref} = 1.05A, f = 1/T = 10kHz.$$

At first the value of the supply voltage is chosen as $V_{in} = 10V$. Fig.3(a) shows the measured inductance current of the implemented converter under a fundamental periodic operation. The vertical scale is 200mA/div and the horizontal scale is 0.1ms/div. The PSpice phase portrait, corresponding to Fig.3(a), is shown in Fig.3(b).

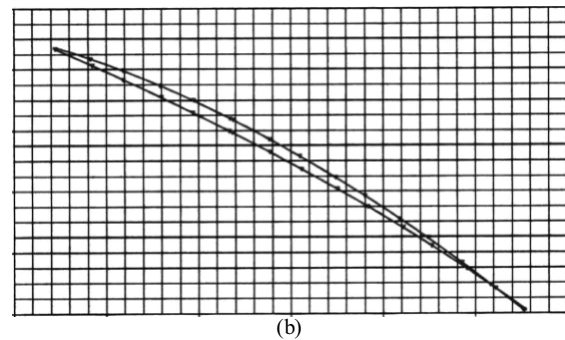
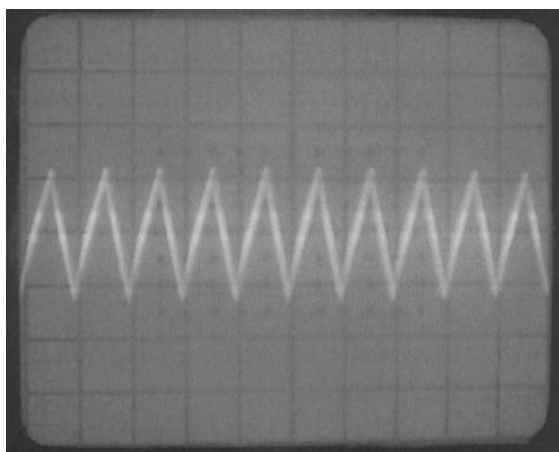
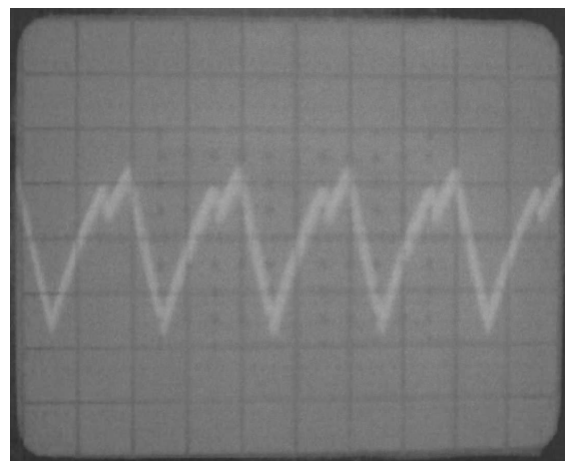


Fig.3. Fundamental periodic operation: (a) experimental time waveform of the inductor current (time-scale: 9ms-10ms; current-scale: 0.5A-1.1A); (b) (i, v) -phase portrait using PSpice (current-scale: 0.5A-1.1A; voltage-scale: 12V-13V).

When the voltage V_{in} is decreased, many other operating regimes are possible. For example Fig.4(a) shows the experimental time waveform of the current $i(t)$ for a period-two subharmonic operation ($V_{in} = 8V$). The corresponding PSpice phase portrait is shown in Fig.4(b).



(a)



(a)

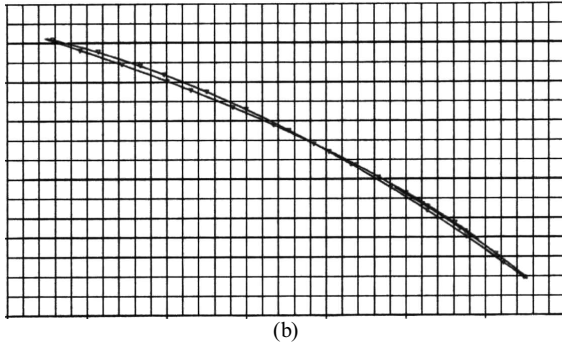


Fig.4. $2T$ subharmonic operation: (a) experimental waveform of the inductor current (time: 9ms–10ms, 0.1 ms/div; current: 0.4A–1.2A, 200mA/div); (b) (i, v) -phase portrait using PSpice (current: 0.4A–1.1A; voltage: 8.8V–10.4V).

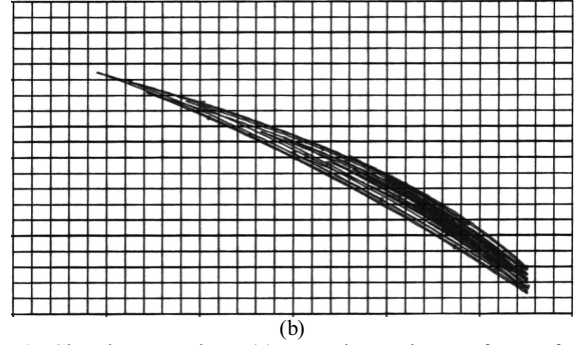


Fig.6. Chaotic operation: (a) experimental waveform of the inductor current (time: 9ms–10ms, 0.1ms/div; current: 0.5A–1.1A, 200mA/div); (b) (i, v) -phase portrait using PSpice (current: 0.5A–1.1A; voltage: 6.5V–8.5V).

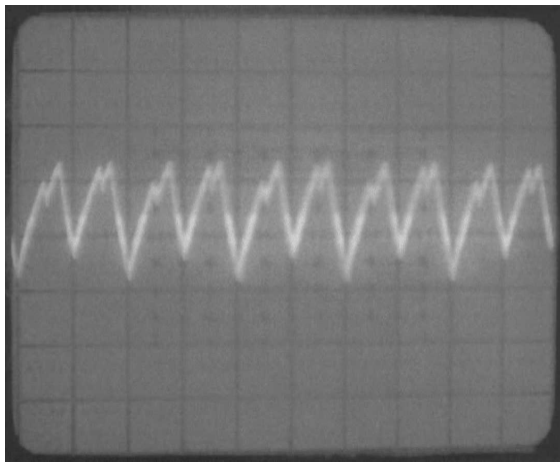
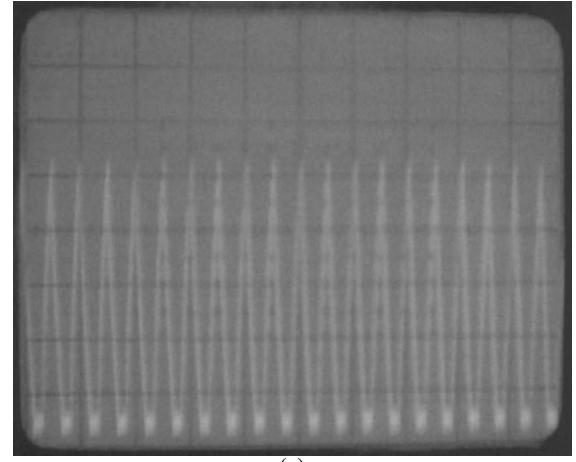
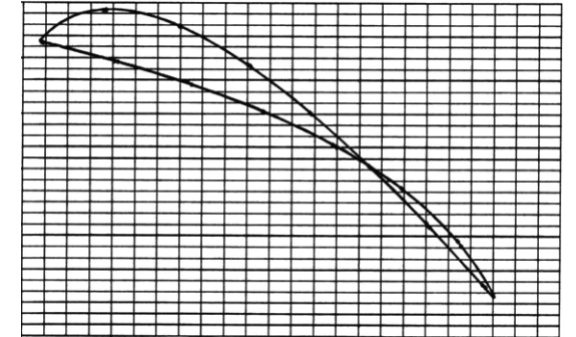


Fig.5. Quasi- $4T$ subharmonic operation: experimental waveform of the inductor current (time: 8ms–10ms, 0.2ms/div; current: 0.5A–1.1A, 200mA/div).

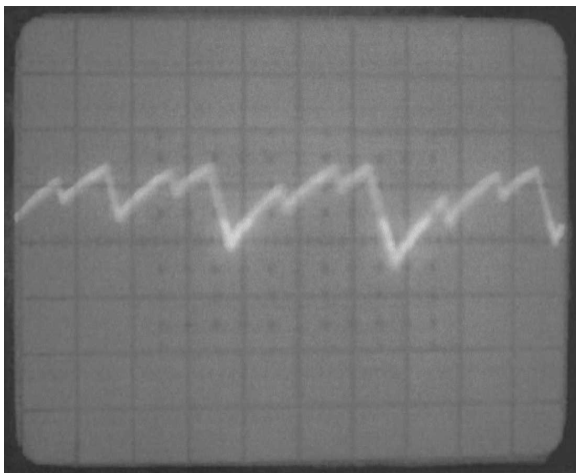


(a)



(b)
Fig.7. Fundamental periodic operation: (a) experimental waveform of the inductor current (time: 8ms–10ms, 0.2ms/div; current: 0.0A–1.2A, 200mA/div); (b) (i, v) -phase portrait using PSpice (current: 0.0A–1.2A; voltage: 7.0V–7.6V).

Additionally, by taking $V_{in} = 7.2V$, it is possible to obtain a quasi-periodic operation. Fig.5 shows the experimental quasi- $4T$ periodic waveform of the inductance current. Finally, when the value of the supply voltage V_{in} is further decreased, the chaotic operating regime appears. The experimental current waveform and the PSpice phase portrait for the circuit operating in the chaotic regime ($V_{in} = 7V$) are shown in Fig.6(a) and Fig.6(b), respectively.



(a)

B. Route to chaos by varying parameter L

Herein the behavior of the boost converter is analyzed by varying the inductance L , whereas the following circuit parameter values have been fixed:

$R = 39\Omega$, $C = 22\mu F$, $V_{in} = 7V$, $I_{ref} = 1.05A$, $f = 1/T = 10KHz$. At first the inductance is chosen as $L = 0.15mH$. Fig.7(a) and Fig.7(b) show the measured inductance current waveform and the corresponding PSpice phase portrait, respectively, under periodic operation of period T .

When the inductance L is increased, many other operating regimes are possible. For example Fig.8(a) shows the experimental time waveform of the inductance

current for a period-two subharmonic operation ($L = 0.3\text{mH}$). The corresponding PSpice phase portrait is shown in Fig.8(b). Additionally, for $L = 0.53\text{mH}$, a quasi-periodic operation is obtained. Fig.9 shows the experimental result for the quasi-4T periodic operation. Finally, when L is further increased, the circuit behavior goes toward chaotic regimes. For example, for $L = 0.6\text{mH}$, the measured current and the PSpice phase portrait for the chaotic regime are shown in Fig.10(a) and Fig.10(b), respectively.

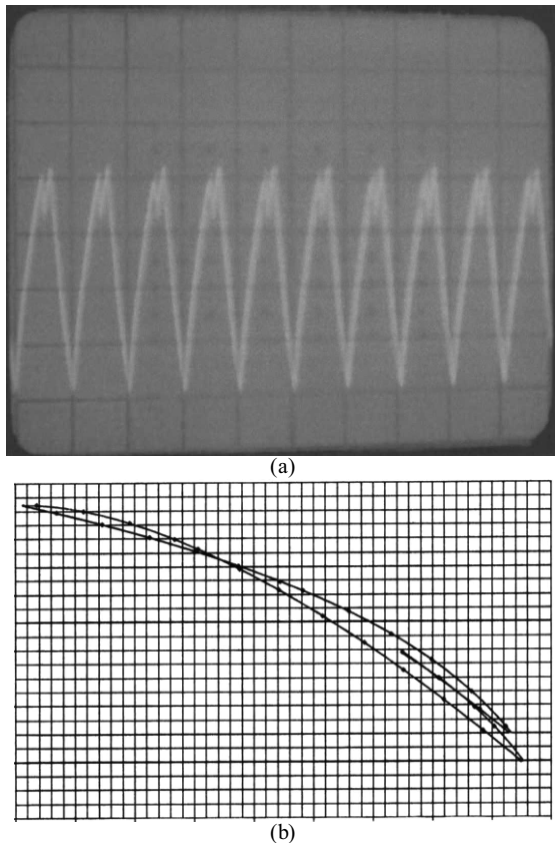


Fig.8. 2T subharmonic operation: (a) experimental waveform of the inductor current (time: 8ms–10ms, 0.2ms/div; current: 0.2A–1.2A, 200mA/div); (b) ξ, ν -phase portrait using PSpice (current: 0.2A–1.1A; voltage: 7.0V–8.2V).

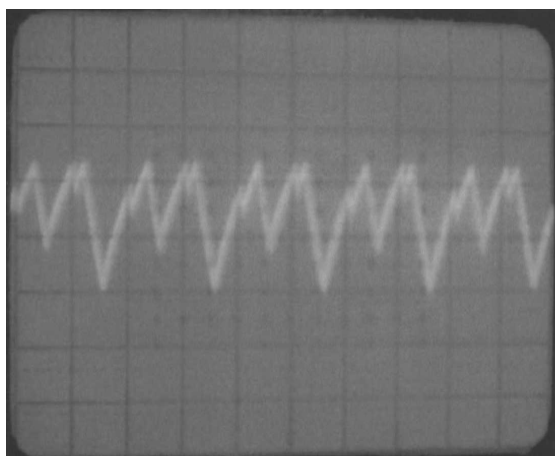


Fig.9. Quasi-4T subharmonic operation: experimental time waveform of the inductor current (time-scale: 8ms–10ms, 0.2ms/div; current-scale: 0.5A–1.1A, 200mA/div).

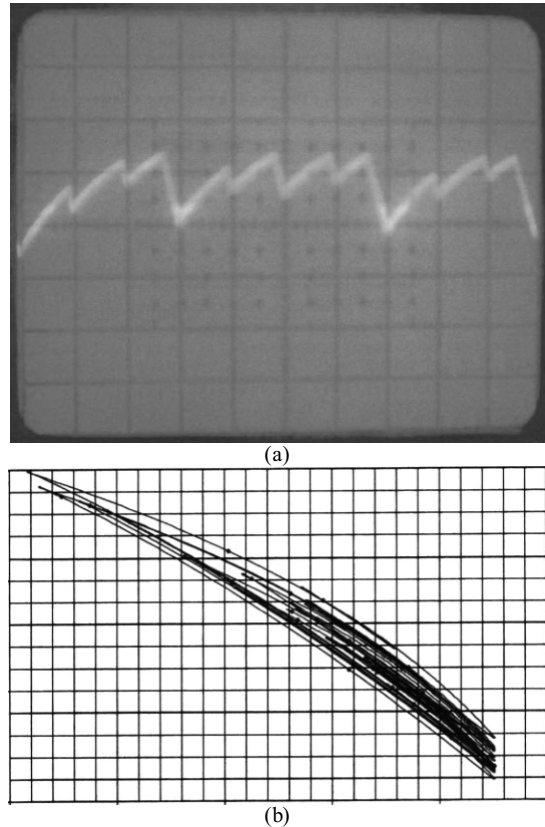


Fig.10. Chaotic operation: (a) experimental waveform of the inductor current (time: 9ms–10ms, 0.1ms/div; current: 0.5A–1.1A, 200mA/div); (b) ξ, ν -phase portrait using PSpice (current: 0.5A–1.1A; voltage: 6.5V–8.0V).

V. CONCLUSION

This paper has experimentally analysed some dynamic phenomena that can occur in current-programmed DC-DC boost converters. Namely, bifurcation analyses as well as possible pathways through which the converter may enter chaos have been shown. In particular, an experimental set-up has been implemented to show how variations of supply voltage and inductance may lead to interesting bifurcation paths and novel routes to chaos.

REFERENCES

- [1] S. Parui, S. Banerjee. Bifurcations due to transition from continuous conduction mode to discontinuous conduction mode in the boost converter. *IEEE Trans. On Circuits and Systems - I*, vol.50, no.11, 2003, pp.1464-1469.
- [2] J. Deane, D. Hamill. Instability, Subharmonics and Chaos in Power Electronic Systems. *IEEE Trans. Power Electronics*, vol.5, no.3, 1990, pp.260-267.
- [3] J. Deane. Chaos in a Current-Mode Controlled Boost dc-dc Converter. *IEEE Trans. On Circuits and Systems - I*, vol.39, no.8, 1992, pp.680-683.
- [4] W.C. Chan, Chi K. Tse. Study of Bifurcations in Current-Programmed DC/DC Boost Converters: From Quasi-Periodicity to Period-Doubling. *IEEE Trans. On Circuits and Systems - I*, vol.44, no.12, 1997, pp.1129-1142.
- [5] H.C. Iu, Chi K. Tse. Study of Low-Frequency Bifurcation Phenomena of a Parallel-Connected Boost Converter System via Simple Averaged Models. *IEEE Trans. On Circuits and Systems - I*, vol.50, no.5, 2003, pp.679-686.
- [6] S. Banerjee, G.C. Verghese, Eds. Nonlinear phenomena in Power Electronics. *IEEE Press*, 2001.

GENERATION OF CHAOTIC BEATS IN A MODIFIED CHUA'S CIRCUIT PART I: DYNAMIC BEHAVIOUR

D. Cafagna and G. Grassi

Dipartimento di Ingegneria dell'Innovazione,
Università degli Studi di Lecce, Lecce, ITALY
{donato.cafagna; giuseppe.grassi}@unile.it

Abstract – *This paper and the companion one [1] illustrate the new phenomenon of chaotic beats in a modified version of the Chua's circuit, driven by two sinusoidal inputs with slightly different frequencies. In particular, in this paper the behaviour of the proposed circuit is analyzed both in time-domain and state-space, confirming the chaotic nature of the phenomenon and the effectiveness of the design.*

I. INTRODUCTION

In the field of chaotic systems, different complicated behaviors such as period-adding sequences, generation of multi-scroll attractors, synchronization phenomena and intermittency properties have been widely studied [2]-[4]. Very recently, a fascinating phenomenon has been investigated in [5], where the behaviors of Kerr and Duffing nonlinear oscillators driven by two sinusoidal inputs with slightly different frequencies have been analyzed. In particular, the authors of ref. [5] started by considering that in linear systems the interaction of two sinusoidal signals is the well-known phenomenon called *beats* [6]. Namely, when two waves with slightly different frequencies interfere, the frequency of the resulting waveform is the average of the frequencies of the two waves, whereas its amplitude is modulated by an envelope, the frequency of which is the difference between the frequencies of the two waves (see Fig.1). This concept has been generalized in [5], where the generation of chaotic beats in coupled nonlinear systems with very small nonlinearities has been studied.

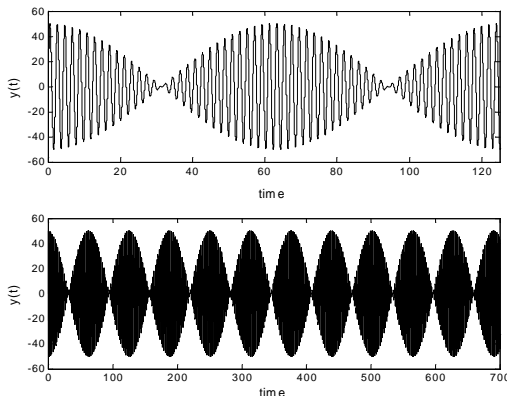


Fig. 1. Beats in linear systems: the combination of $25 \sin(3.0*t)$ and $25 \sin(3.1*t)$ generates a waveform with amplitude 50, fundamental frequency 3.05 and envelope frequency 0.1.

Based on these considerations and on the results reported in [7], this paper and the companion one [1] aim

to investigate the generation of chaotic beats in a novel modified version of the Chua's circuit.

The paper is organized as follows. In Section 2 the equations of the proposed non-autonomous circuit are reported. It consists in a modified version of the autonomous Chua's circuit, where two sinusoidal inputs characterized by slightly different frequencies have been added. In Section 3 numerical integrations of dimensionless equations get a first insight into the generation of chaotic beats. By exploiting PSpice simulator, Section 4 illustrates the phenomenon in the circuit implemented in the companion paper [1]. The study of the beat phenomenon concludes with the analysis of the behaviour of the proposed circuit driven by two sinusoidal signals with equal frequencies.

II. THE PROPOSED CIRCUIT

The state equations of the proposed non-autonomous circuit (Fig.2), constituted by two capacitors, an inductor, a linear resistor, the Chua's diode and two external periodic excitations, are:

$$\begin{aligned} C_1 \frac{dv_{C_1}}{dt} &= \frac{v_{C_2} - v_{C_1}}{R} - g(v_{C_1}) + A_1 \sin(2\pi f_1 t) \\ C_2 \frac{dv_{C_2}}{dt} &= \frac{v_{C_1} - v_{C_2}}{R} + i_L \\ L \frac{di_L}{dt} &= -v_{C_2} + A_2 \sin(2\pi f_2 t) \end{aligned} \quad (1)$$

where A_1 and A_2 are the amplitudes of the periodic excitations, f_1 and f_2 are their frequencies whereas

$$g(v_{C_1}) = G_b v_{C_1} + 0.5(G_a - G_b)(|v_{C_1} + B_p| - |v_{C_1} - B_p|) \quad (2)$$

is the characteristic of the Chua's diode [3].

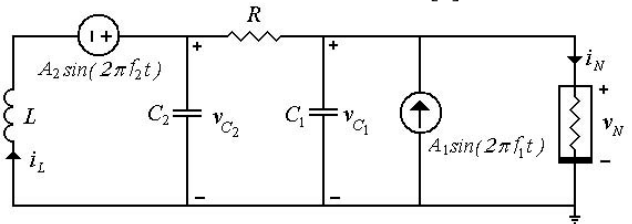


Fig. 2. The proposed modified Chua's circuit.

The dynamics of (1) depend on a set of eleven circuit parameters: $C_1, C_2, L, R, G_a, G_b, B_p, A_1, A_2, f_1, f_2$. The number of parameters is reduced by normalizing the equation of the nonlinear resistor, so that its breakpoints are at ± 1 instead of $\pm B_p$. By introducing dimensionless variables x_1, x_2, x_3 and τ :

$$v_{C_1} = x_1 B_p, \quad v_{C_2} = x_2 B_p, \quad i_L = x_3 \frac{B_p}{R}, \quad t = \tau RC_2,$$

and redefining τ as t , the following equations are obtained:

$$\begin{aligned} \frac{dx_1}{dt} &= \alpha[x_2 - x_1 - g(x_1)] + \alpha A_1^d \sin(2\pi f_1^d t) \\ \frac{dx_2}{dt} &= x_1 - x_2 + x_3 \\ \frac{dx_3}{dt} &= -\beta x_2 + A_2^d \sin(2\pi f_2^d t) \end{aligned} \quad (3)$$

with

$$g(x_1) = bx_1 + 0.5(a - b)(|x_1 + 1| - |x_1 - 1|) \quad (4)$$

where $\alpha = \frac{C_2}{C_1}$, $\beta = \frac{R^2 C_2}{L}$, $a = RG_a$, $b = RG_b$,

$A_1^d = \frac{A_1 R}{B_p}$, $A_2^d = \frac{A_2 \beta}{B_p}$, $f_1^d = RC_2 f_1$ and $f_2^d = RC_2 f_2$ (the superscript d means "dimensionless"). Thus, the set of eleven circuit parameters turns into the set of eight dimensionless parameters $\{\alpha, \beta, a, b, A_1^d, A_2^d, f_1^d, f_2^d\}$.

III. NUMERICAL INTEGRATIONS

In this Section the phenomenon of beats in the dimensionless system (3) is investigated.

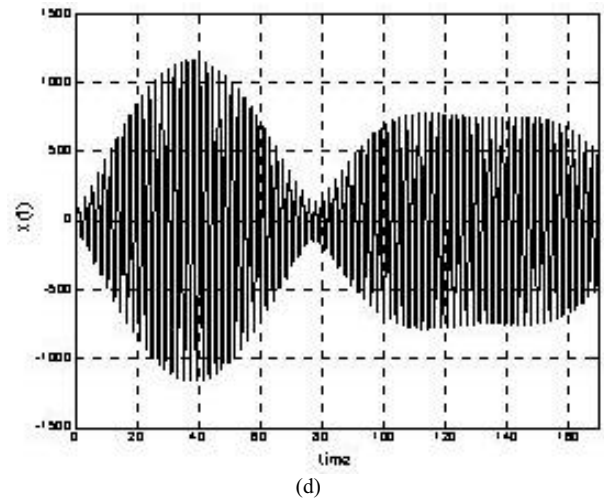
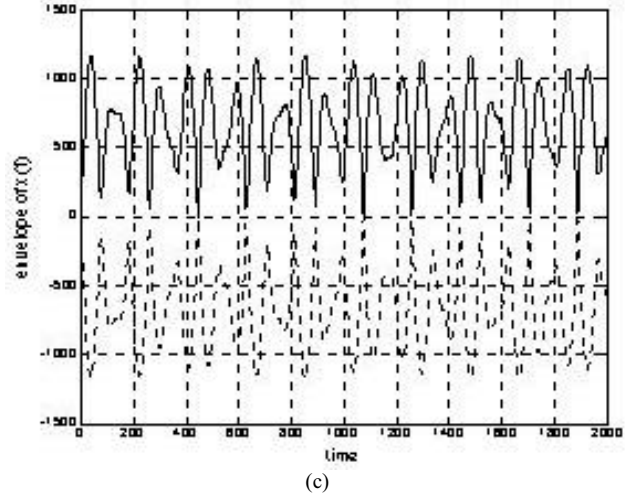
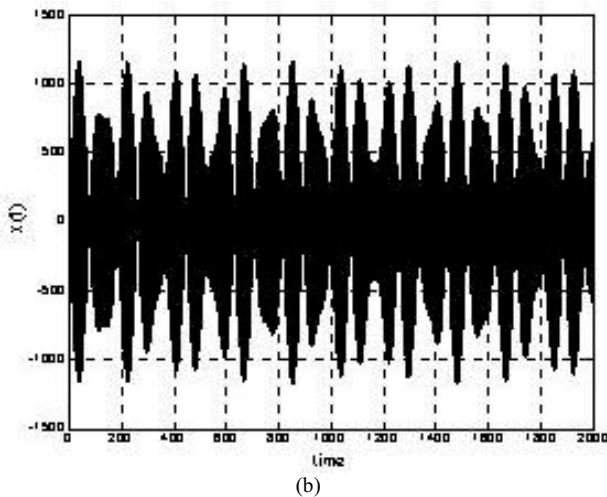
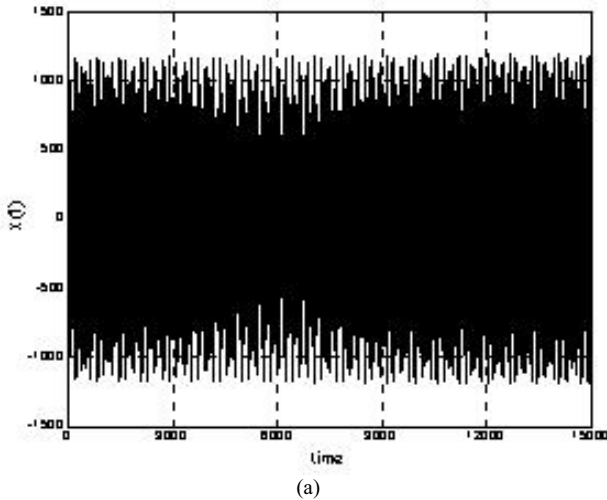


Fig. 3. Behaviors of the variable x_1 for different time-scales; (a): $t \in [0, 15000]$; (b): $t \in [0, 2000]$; (c): envelope of x_1 for $t \in [0, 2000]$; (d): $t \in [0, 170]$.

By varying the parameters $\{\alpha, \beta, a, b, A_1^d, A_2^d, f_1^d, f_2^d\}$, several numerical integrations of equations (3)-(4) have been carried out. After a first round of integrations, the complexity has been reduced by selecting the values $a = -1.1429$, $b = -0.7143$ and $\beta = 14.283$. Successively, extensive integrations have been carried out for several values of the parameters α, A_1^d, A_2^d and slightly different values of the frequencies f_1^d and f_2^d . In particular, it is interesting to analyze the system behavior for $\alpha = 6.799$, $A_1^d = A_2^d = 25$, $\omega_1^d = 2\pi f_1^d = 3.0$ and $\omega_2^d = 2\pi f_2^d = 3.1$. To this purpose, Fig.3 shows the time behaviors of the state variable x_1 for different resolutions of the time scale. More precisely, Fig.3(a) makes perceive the chaotic nature of the signal x_1 , whereas Fig.3(b) highlights the occurrence of chaotic beats generated by its envelope (Fig.3(c)). Moreover, Fig. 3(d) reveals in the signal x_1 both an amplitude modulation due to the chaotic envelope and the presence of a fundamental frequency. Further analysis, related to the power spectral density (Fig.4),

confirms the chaotic nature of signal x_1 as well as the presence of a fundamental frequency $f^* = 0.48828$ (i.e., $\omega^* = 3.0679$).

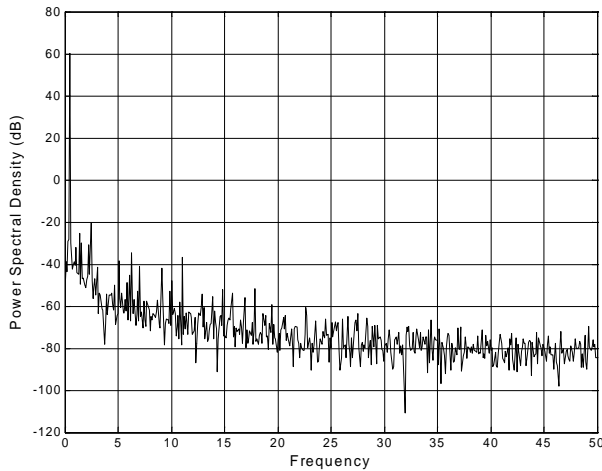


Fig. 4. Broadband spectral density of the signal x_1 (fundamental frequency at $f^* = 0.48828$).

Finally, referring to the chaotic nature of the signal x_1 , the Lyapunov exponents of system (3) are calculated. By considering each sinusoidal forcing term as parameter, a null exponent is obtained. Namely, the calculated Lyapunov exponents are:

$$\lambda_1 = 0.00043, \lambda_2 = 0.00000, \lambda_3 = -0.03805, \lambda_4 = -4322.4.$$

Notice the presence of one positive Lyapunov exponent, which confirms the chaotic dynamics of system (3).

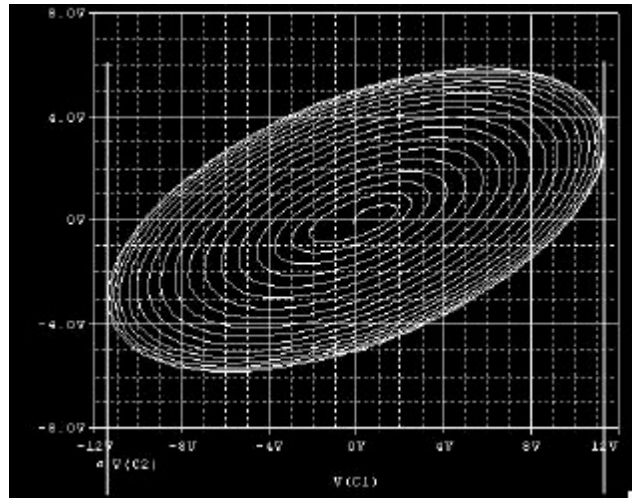
IV. PSpice SIMULATIONS

Since numerical integrations of the dimensionless system (3) have shown the occurrence of chaotic beats, the aim of this Section is to investigate the beat phenomenon in the circuit, which has been designed in the companion paper [1]. In particular, based on the dimensionless parameter values reported in the previous Section, the design procedure has led to the following dimensional parameter values (see details in [1]):

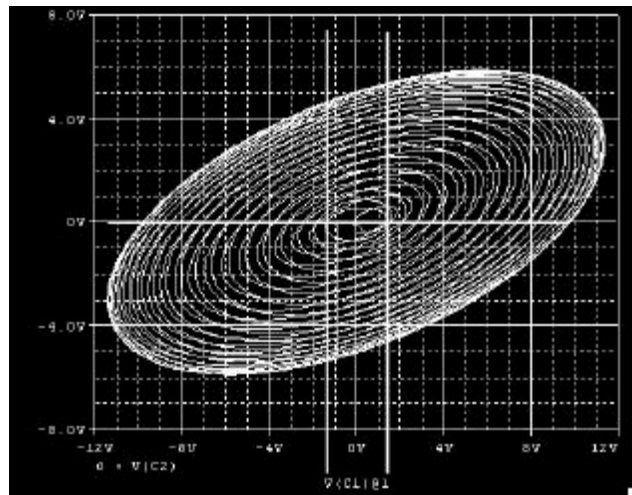
$$R = 1000 \Omega, C_1 = 10 \text{ nF}, C_2 = 67.99 \text{ nF}, L = 4.76 \text{ mH}, \\ B_p = 0.01 \text{ V}, G_a = -1.1428 \text{ m}\Omega^{-1}, G_b = -0.7142 \text{ m}\Omega^{-1}, \\ A_1 = 0.25 \text{ A}, A_2 = 17.49 \text{ V}, f_1 = 7022.57 \text{ Hz}, f_2 = 7256.66 \text{ Hz}.$$

By exploiting (5), PSpice simulator is used to describe the chaotic amplitude modulation of the beats in the proposed circuit. In particular, several phase portraits are carried out in the (v_{C1}, v_{C2}) -state space, at different time units. The results are reported in Fig.5(a)-(d), where in each figure the evolution of the trajectory with respect to the previous illustration has been highlighted. In particular, Fig.5(a) shows that the circuit dynamics start from the origin and expand until v_{C1} approximately reaches the values $\pm 11.4\text{V}$. Then, Fig.5(b) illustrates that the trajectory of variable v_{C1} shrinks back until the values $\pm 1.4\text{V}$ are approximately reached. In Fig.5(c) the

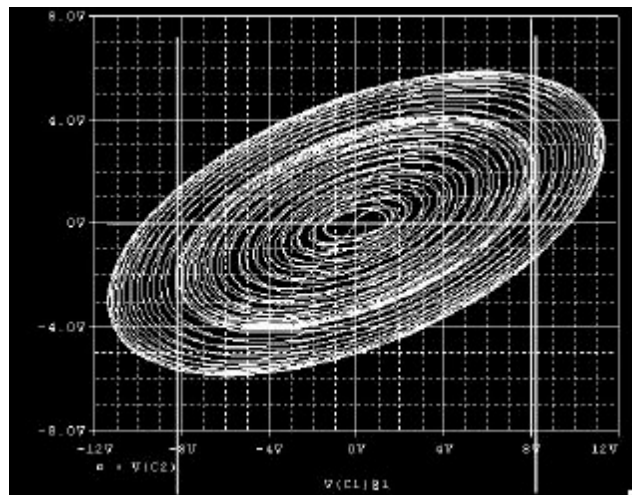
dynamics expand again until they reach the values $\pm 8.15\text{V}$. Successively, in Fig.5(d) the values $\pm 11.25\text{V}$ are approximately reached. These expanding and contracting behaviors go on *chaotically* for increasing times until the “final” attractor is obtained (see also [1]).



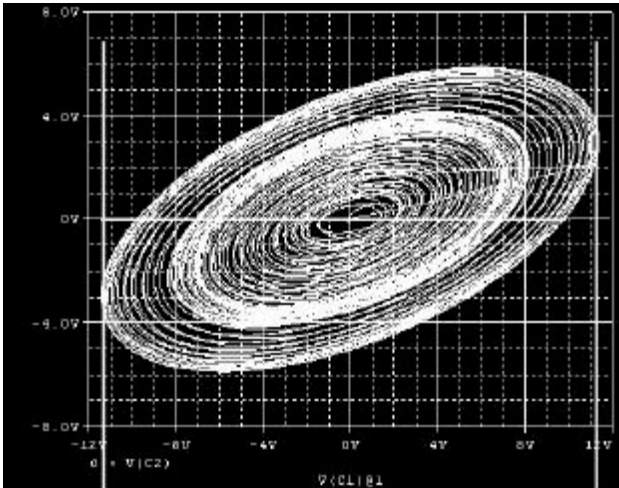
(a)



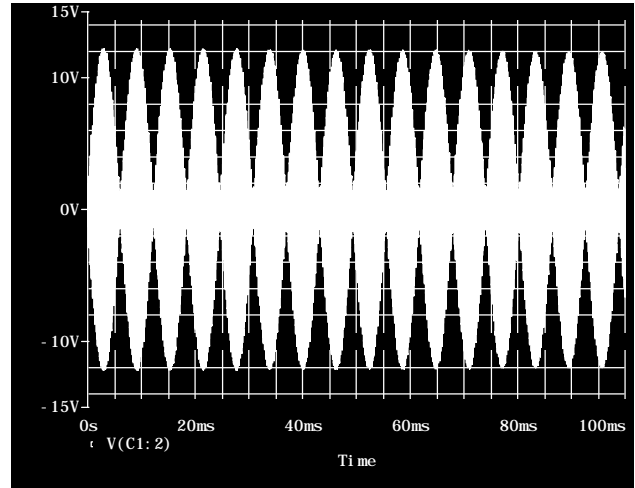
(b)



(c)



(d)



(a)

Fig. 5. Phase portraits at different time units using Pspice. (a): $t = 2.5\text{ms}$; (b): $t = 5.2\text{ms}$; (c): $t = 7.5\text{ms}$; (d): $t = 15\text{ms}$.

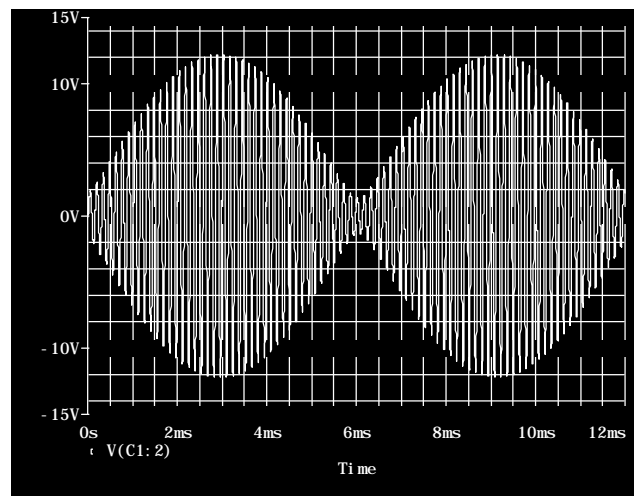
V. DISCUSSION

In order to better understand the formation of the chaotic beats, the circuit dynamics are analyzed by taking the circuit parameters (5) but equal frequencies $f_1 = f_2 = 7022.57\text{ Hz}$. The resulting time waveforms of the variable v_{C1} are reported in Fig.6(a)-(b) for two different resolutions of the time scale. Figure 6 clearly highlights that in this case the expanding and contracting behavior goes on *periodically* for increasing times. More precisely, Fig.6(a) highlights the presence of beats due to a *periodic* envelope, whereas Fig.6(b) reveals the presence of a fundamental frequency. Based on these considerations, it can be argued that for equal frequencies $f_1 = f_2 = 7022.57\text{ Hz}$ the proposed non-autonomous circuit is not able to generate chaotic beats. However, notice that in this case the circuit exhibits *periodic* amplitude modulated signals, which are very similar to the beats obtained in *linear* systems.

We would point out that further investigation is required for better understanding the chaotic beats phenomenon. In particular, observations for other sets of parameters should be carried out, along with further analysis related to the conditions assuring the existence of the phenomenon.

VI. CONCLUSIONS

This paper and the companion one [1] have focused on a modified version of the Chua’s circuit, characterized by two sinusoidal inputs with slightly different frequencies. In particular, in this paper the new phenomenon of chaotic beats has been analyzed both in time-domain and state-space, confirming the effectiveness of the design approach developed in [1].



(b)

Fig. 6. Behaviors of v_{C1} for different time-scales using PSpice; (a): $t \in [0, 100\text{ms}]$; (b): $t \in [0, 12\text{ms}]$.

REFERENCES

- [1] D. Cafagna, G. Grassi. Generation of chaotic beats in a modified Chua’s circuit – Part II: Circuit Design. Submitted to *12th International IEEE Workshop on Nonlinear Dynamics of Electronic Systems (NDES 2004)*, Evora, Portugal, 9-13 May 2004.
- [2] G. Chen, T. Ueta. *Chaos in circuits and systems*. World Scientific Series on Nonlinear Science, Singapore, 2002.
- [3] L. Chua. Chua’s circuit 10 years later. *Int. Journal of Circuit Theory and Applications*, vol. 22, pp. 279-305, 1994.
- [4] G. Grassi, D.A. Miller. Theory and experimental realization of observer-based discrete-time hyperchaos synchronization. *IEEE Trans. Circuits Systems – Part I*, vol. 49, no. 3, pp. 373-378, 2002.
- [5] K. Grygiel, P. Szlachetka. Generation of chaotic beats. *Int. Journal of Bifurcations and Chaos*, vol. 12, no.3, pp. 635-644, 2002.
- [6] C.R.Wylie. *Differential equations*. McGraw-Hill, NY, 1979.
- [7] D.Cafagna, G.Grassi. Generating chaotic beats in coupled non-autonomous Chua’s circuits, *Proc. of 16th European Conference on Circuit Theory and Design (ECCTD 2003)*, Krakow, Poland, 1-4 Sept. 2003.

GENERATION OF CHAOTIC BEATS IN A MODIFIED CHUA'S CIRCUIT PART II: CIRCUIT DESIGN

D. Cafagna and G. Grassi

Dipartimento di Ingegneria dell'Innovazione,
Università degli Studi di Lecce, Lecce, ITALY
{donato.cafagna; giuseppe.grassi}@unile.it

Abstract – *This paper and the companion one [1] illustrate the new phenomenon of chaotic beats in a modified version of the Chua's circuit, driven by two sinusoidal inputs with slightly different frequencies. In particular, in order to satisfy the constraints imposed by the beats dynamics studied in [1], this paper presents a novel implementation of the voltage-controlled characteristic of the Chua diode. Moreover, by exploiting Pspice simulator, the beats phenomenon generated by the designed circuit is investigated in detail.*

I. INTRODUCTION

Very recently, a new fascinating phenomenon has been investigated in [1]-[2], where the behavior of nonlinear systems in the presence of sinusoidal excitations has been analyzed. In particular, reference [1] illustrates the phenomenon of chaotic beats in a modified version of the Chua's circuit, driven by two sinusoidal inputs with slightly different frequencies. More precisely, in [1] the behaviour of the circuit is numerically analyzed both in time-domain and state-space, confirming the chaotic nature of the beat phenomenon in nonlinear systems. While reference [1] focuses on the dynamics of chaotic beats, the aim of this paper consists in illustrating both the design procedure of the modified Chua's circuit and the corresponding beats generation using Pspice simulator.

The paper is organized as follows. Section 2 illustrates the design of a novel modified version of Chua's circuit. In particular, in order to satisfy the constraints of the beats dynamics found in [1], a new implementation of the characteristic of the Chua diode is proposed. Finally, by exploiting PSpice simulator, Section 3 illustrates the beats phenomenon generated by the designed circuit.

II. CHAOTIC BEATS: CIRCUIT DESIGN

The proposed circuit (see also [1]) is constituted by two external periodic excitations, a linear resistor, an inductor, two capacitors and a nonlinear resistor. The state equations for the voltages v_{C1} , v_{C2} and the current i_L are:

$$\begin{aligned} C_1 \frac{dv_{C1}}{dt} &= \frac{v_{C2} - v_{C1}}{R} - g(v_{C1}) + A_1 \sin(2\pi f_1 t) \\ C_2 \frac{dv_{C2}}{dt} &= \frac{v_{C1} - v_{C2}}{R} + i_L \\ L \frac{di_L}{dt} &= -v_{C2} + A_2 \sin(2\pi f_2 t) \end{aligned} \quad (1)$$

where A_1 and A_2 are the amplitudes of the periodic excitations, f_1 and f_2 are their frequencies whereas

$$g(v_{C1}) = G_b v_{C1} + 0.5(G_a - G_b)(|v_{C1} + B_p| - |v_{C1} - B_p|) \quad (2)$$

represents the characteristic of the Chua's diode [3]. Before designing the circuit, consider its dimensionless equations (3)-(4) reported in ref. [1] and note that the amplitude of the dimensionless variables x_1 , x_2 and x_3 is very large (see [1]). If $B_p = 1$ V, it follows that the dimensional variables $v_{C1} = x_1 B_p$ and $v_{C2} = x_2 B_p$ are characterized by amplitudes in the range of KVolt. In order to carry out a feasible circuit design, it is useful to reduce the value of B_p . To this purpose, by choosing $B_p = 0.01$ V, $R = 1000 \Omega$ and by considering the dimensionless parameters $\{\alpha, \beta, a, b, A_1^d, A_2^d, f_1^d, f_2^d\}$ (the values of which have been found in [1]), it results

$$A_1 = \frac{B_p}{R} A_1^d = 0.25 \text{ A} \quad \text{and} \quad A_2 = \frac{B_p}{\beta} A_2^d = 17.49 \text{ V}.$$

Moreover, by taking $C_1 = 10$ nF, it results $C_2 = \alpha C_1 = 67.99$ nF,

$$L = \frac{R^2 C_2}{\beta} = 4.76 \text{ mH}, \quad G_a = \frac{a}{R} = -1.1428 \text{ m}\Omega^{-1},$$

$$G_b = \frac{b}{R} = -0.7142 \text{ m}\Omega^{-1}, \quad f_1 = \frac{f_1^d}{RC_2} = 7022.57 \text{ Hz} \quad \text{and}$$

$$f_2 = \frac{f_2^d}{RC_2} = 7256.66 \text{ Hz}.$$

Now, the Chua diode is properly implemented by taking into account that B_p is 0.01 V and that the maximum amplitude of the voltage v_{C1} is scaled down to approximately 12V. The adopted configuration is reported in Fig.1, whereas the driving-point (DP) characteristic obtained using Pspice is reported in Fig.2(a). In particular, the Chua diode reported in Fig.1 has been implemented by taking: $R_1 = 2333 \Omega$, $R_2 = R_3 = R_5 = R_6 = 150 \Omega$, $R_4 = 875 \Omega$, two 1N4148 diodes, two 0.01V batteries and four LF411 op amps biased with ± 18 V supplies. Note that the considered LF411 op amp enables an accurate characteristic to be obtained, since it draws negligible input current (by virtue of its JFET input stage) with a maximum input offset voltage of 1.0mV (i.e., one order of magnitude smaller than the 10mV of the breakpoints).

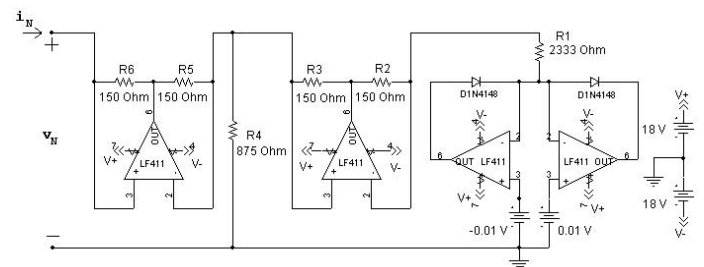
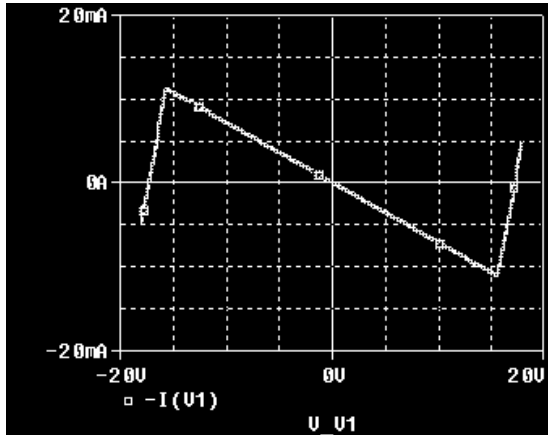
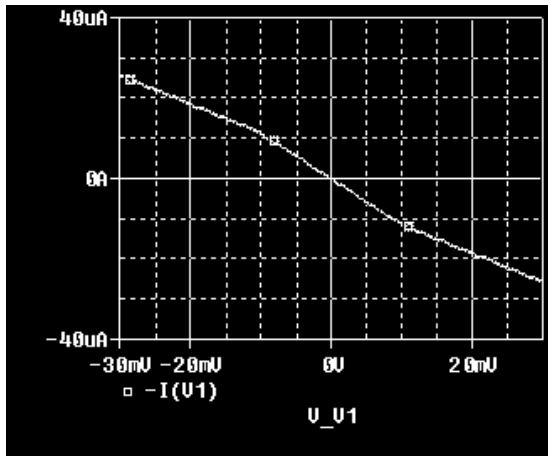


Fig. 1. Implementation of the Chua diode using PSpice.



(a)

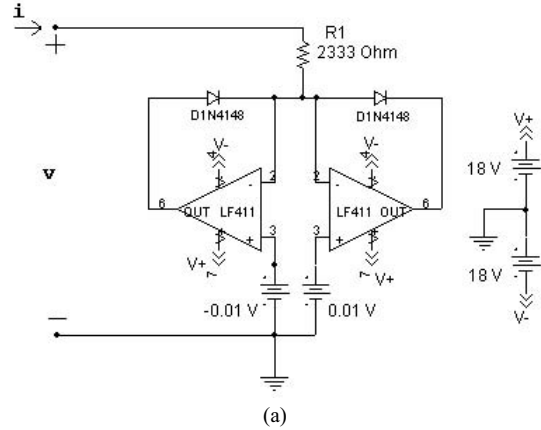


(b)

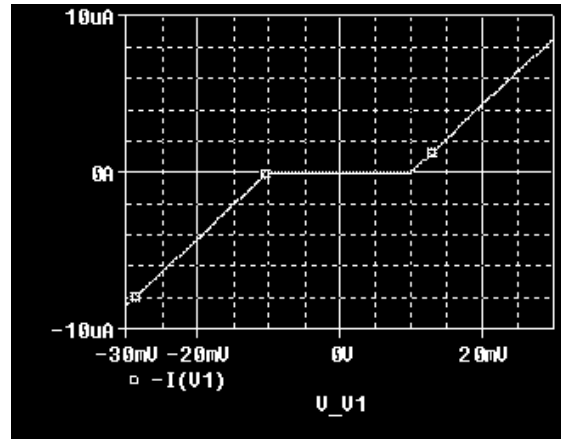
Fig. 2. Characteristic of the diode ($V_{V1} \equiv v_N$ and $-I(V1) \equiv i_N$).
 (a) overall characteristic with outer breakpoints at $\pm 16V$;
 (b) characteristic around the inner breakpoints at $\pm 10mV$.

The voltage-controlled characteristic reported in Fig.2 has been implemented by connecting four devices in parallel, as shown in the following. At first, the two-terminal device reported in Fig.3(a) has been designed, with the aim of obtaining the characteristic reported in Fig.3(b)-(c). In particular, the DP characteristic has zero slope between its breakpoints at $\pm 0.01V$ (obtained using two $0.01V$ batteries) and has slope $|G_b - G_a|$ (obtained using the linear resistor $R_1 = 2333 \Omega$) outside the breakpoints (Fig.3(b)). Note that the three segments and the two breakpoints correspond to linear operation of the op amps [4]-[6]. The second step has consisted in designing the two-terminal device reported in Fig.4(a). In particular, a negative resistance converter [6]-[7] has been added in parallel to the two-terminal device reported in Fig.3(a) in order to obtain the DP characteristic reported in Fig.4(b)-(c). It has zero slope between its breakpoints at $\pm 0.01V$ and has slope $-|G_b - G_a|$ outside the breakpoints (Fig.4(b)). Note that the outer segments in Fig.4(c) are due to the eventual passivity of the negative resistance converter and saturation of the op amps [3]. The third step has consisted in designing the two-terminal device reported in Fig.5(a) where a passive resistor ($R_4 = 875\Omega$)

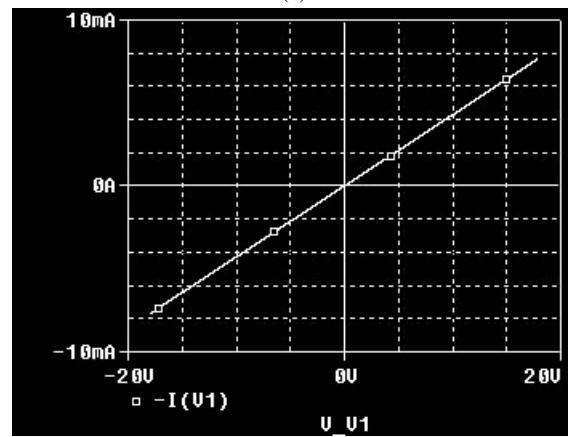
has been added in parallel to the two-terminal device reported in Fig.4(a), so that the DP characteristic reported in Fig.5(b)-(c) is obtained. It has slope $|G_a|$ between its breakpoints at $\pm 0.01V$ and has slope $|G_b|$ outside the breakpoints (Fig.5(b)).



(a)



(b)



(c)

Fig. 3. (a): First stage of the diode ($V_{V1} \equiv v$ and $-I(V1) \equiv i$);
 (b): its characteristic in the range $\pm 30mV$ (with zero slope between the breakpoints at $\pm 10mV$ and slope $|G_b - G_a|$ outside them);
 (c): its characteristic in the range $\pm 20V$.

The final step has consisted in adding a further negative resistance converter (see Fig.1) in parallel to the two-terminal device reported in Fig.5(a), so that the overall

DP characteristic reported in Fig.2(a)-(b) is obtained. As required, it has slope $-|G_a| = -1.1428 \text{ m}\Omega^{-1}$ between its breakpoints at $\pm 0.01\text{V}$ (Fig.2(b)) and has slope $-|G_b| = -0.7142 \text{ m}\Omega^{-1}$ outside them (but within the outer breakpoints at $\pm 16\text{V}$, see Fig.2). Since the maximum amplitude of voltage $v_{C1} \equiv v_N$ has been scaled down to approximately 12V, the positive slope of the two outer dissipative segments ($G_c = 5.8569 \text{ m}\Omega^{-1}$ beyond the breakpoints at $\pm 16\text{V}$, see Fig.2(a)) does not affect the circuit behavior.

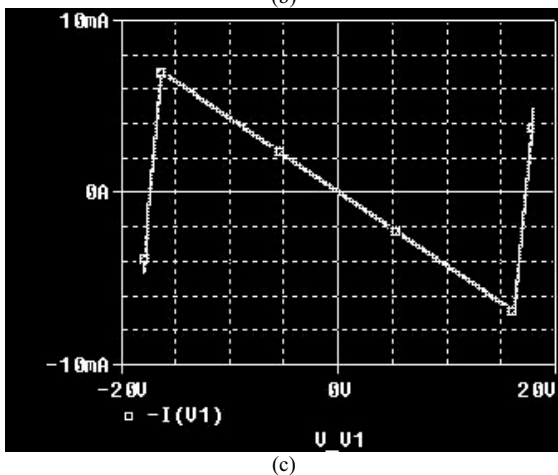
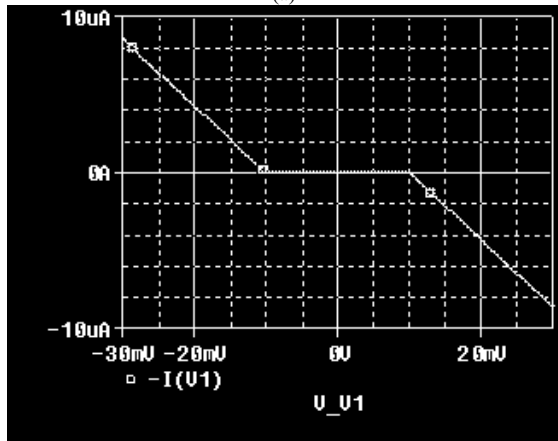
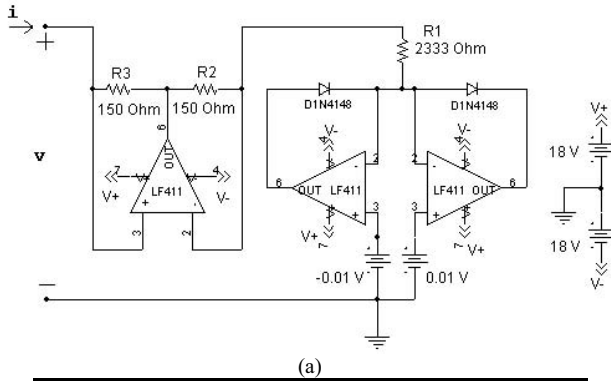


Fig. 4. (a): Second stage of the diode ($V_{V1} \equiv v$ and $-I(V1) \equiv i$); (b): its characteristic in the range $\pm 30\text{mV}$ (with zero slope between the breakpoints at $\pm 10\text{mV}$ and slope $-|G_b - G_a|$ outside them); (c): its characteristic in the range $\pm 20\text{V}$.

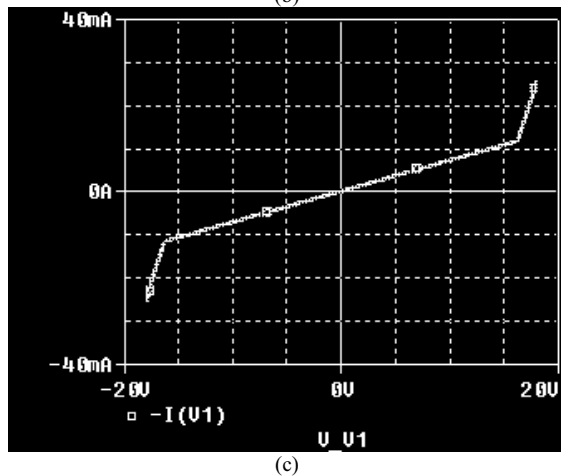
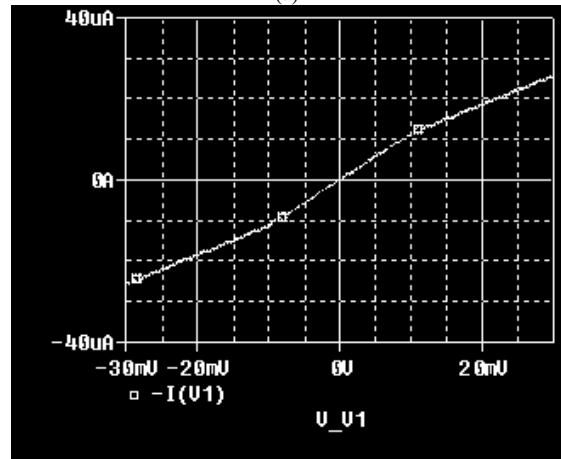
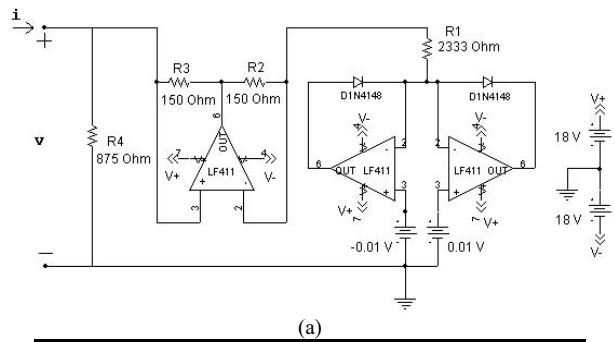


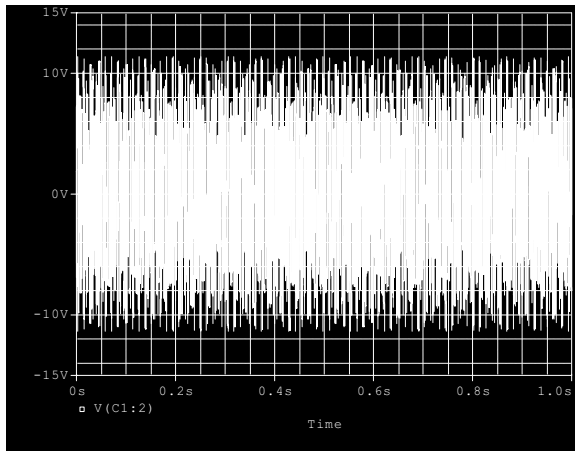
Fig. 5. (a): Third stage of the diode ($V_{V1} \equiv v$ and $-I(V1) \equiv i$); (b): its characteristic in the range $\pm 30\text{mV}$ (with slope $|G_a|$ between the breakpoints at $\pm 10\text{mV}$ and slope $|G_b|$ outside them); (c): its characteristic in the range $\pm 20\text{V}$.

Finally, note that the proposed design approach has two main advantages: i) the slopes and breakpoints of the characteristic can be set independently; ii) the breakpoints $\pm B_p$ are independent of the saturation levels of the op amp output voltage.

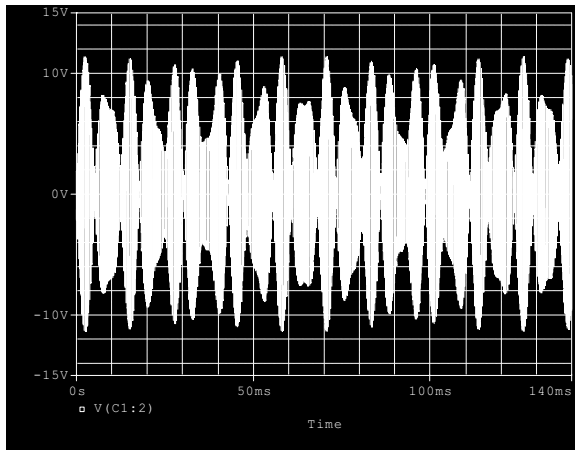
III. CHAOTIC BEATS: PSPICE ANALYSIS

Herein, the aim is to investigate the beats phenomenon in the designed circuit. By using PSpice, the results reported in Fig.6 are obtained, where the time behaviors of the voltage v_{C1} for different resolutions of the time scale are shown. In particular, Fig.6(a)-(b) confirms the

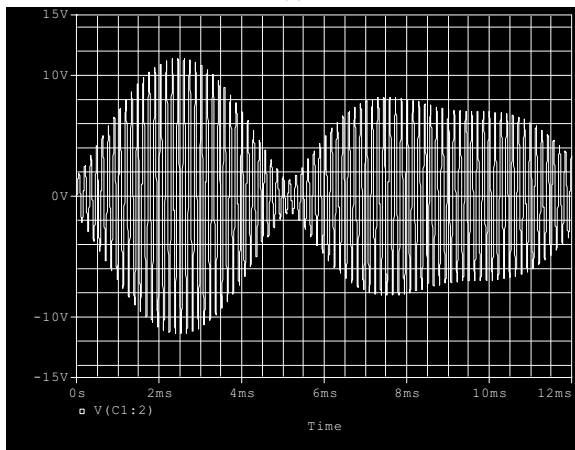
occurrence of the chaotic beats studied in [1], whereas Fig.6(c) confirms the presence of a fundamental frequency as well as an amplitude modulation due to the chaotic envelope (see [1] for details).



(a)



(b)



(c)

Fig. 6. Time behaviors of v_{C1} for different resolutions of the time scale; (a): $t \in [0, 1s]$; (b): $t \in [0, 140ms]$; (d): $t \in [0, 12ms]$.

Finally, Fig.7 shows the time behaviors of the voltage v_{C2} and of the current i_L , confirming the presence of chaotic beats for all the variables of the designed circuit.

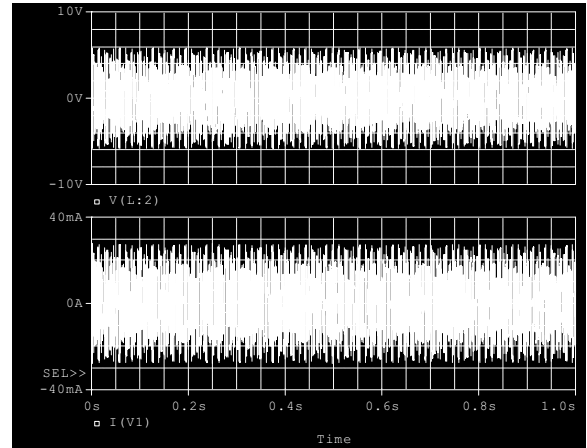


Fig. 7. Time behaviors of $v_{C2} (\equiv V(L:2))$ and of $i_L (\equiv I(V1))$.

IV. CONCLUSIONS

The conclusion of the study (illustrated in this paper and the companion one [1]) is that the recent phenomenon of chaotic beats can be obtained in a modified version of the Chua's circuit, characterized by two sinusoidal inputs with slightly different frequencies. In particular, in order to satisfy the constraints imposed by the beats dynamics [1], this paper has shown a new implementation of the characteristic of the Chua diode, with the following advantages: i) the slopes and breakpoints can be set independently; ii) the breakpoints are independent of the saturation levels of the op amps. PSpice simulations have confirmed the chaotic nature of the phenomenon, along with the effectiveness of the design approach. The next step, on which the authors are currently working, is the hardware implementation of the designed circuit.

REFERENCES

- [1] D.Cafagna, G.Grassi. Generation of chaotic beats in a modified Chua's circuit – Part I: Dynamic Behavior. Submitted to the 12th International IEEE Workshop on Nonlinear Dynamics of Electronic Systems (NDES 2004), Evora, Portugal, 9-13 May 2004.
- [2] K.Grygiel, P.Szlachetka. Generation of chaotic beats. *International Journal of Bifurcations and Chaos*, vol.12, no.3, pp.635-644, 2002.
- [3] M.P.Kennedy. Three steps to chaos-Part II: a Chua's circuit primer. *IEEE Trans. on CAS – Part I*, vol.40, no.10, pp.657-674, 1993.
- [4] L.O.Chua, F.Ayrom. Designing non-linear single op-amp circuits: a cook-book approach. *International Journal of Circuit Theory and Applications*, vol.13, pp.235-268, 1985.
- [5] L.O.Chua, C.W.Wu, G.Q.Zhong, L.F.Liu. Synthesizing arbitrary driving-point and transfer characteristics. *IEEE Trans. on CAS – Part I*, vol.45, no.12, pp.1225-1232, 1998.
- [6] M.P.Kennedy. Synthesis of continuous three-segment voltage-controlled piecewise-linear resistors for Chua's circuit family using operational amplifiers, diodes and linear resistors. *Int. Journal of Circuit Theory and Applications*, vol.21, pp.551-558, 1993.
- [7] K.Soundararajan, K.Ramakrishna. Nonideal negative resistors and capacitors using an operational amplifier. *IEEE Trans. on CAS*, vol.22, no.9, pp.760-763, 1975.

ELECTROMAGNETIC SYNCHRONIZATION OF SLIP

T. Chelidze¹, T. Matcharashvili¹, O. Lursmanashvili²

¹Institute of Geophysics of Georgian Academy of Sciences, 1 Alexidzestr, 380093 Tbilisi, Georgia

²Tbilisi State University, 1, Chavchavadze Ave, 380028, Tbilisi, Georgia

e-mail: chelidze@ig.acnet.ge

Abstract— *Character of changes of slip regimes in experiments on laboratory spring-slider system under external forcing have been investigated. Here we report the experimental evidence of induced by external periodic electromagnetic (EM) influence phase synchronization in slip dynamics.*

I. INTRODUCTION

It is well known that many physical, biological or technical systems often respond in a very original way to external driving signals. One of possible response is synchronization. For the last decade synchronization phenomena of complex dynamical systems has attracted much interest [1]. At present various types of synchronization is known, e.g. complete or identical synchronization, generalized synchronization, lag and phase synchronization [1, 2, 3].

In present study phase synchronization in the experimental spring-slider system is shown.

Recently, in the experiments on laboratory spring-slider system subjected to a constant pull, with weak mechanical or EM periodic forces superimposed on it was shown that the instability (here, slip) of the mechanical system driven close to the critical state can either be initiated or hampered under strong external EM pulses [4, 5]. This observation, together with earlier reports about essential influence of strong external electrical impact on dynamics of seismic systems mechanics [5, 6], points that the EM field can affect and even control the mechanical stability of systems that are close to the critical state.

It was found that variable external periodic EM forcing leads to the clear phase synchronization of slip of spring-slider system.

II. MATERIALS AND METHODS

Experimental setup of our experiments representing itself a system of two plates of roughly finished basalt (with average height of surface asperities of 0.1–0.2 mm), where a

constant pulling force was applied to the upper (sliding) plate [5, 6]. In addition, the same plate was subjected to electric periodic (50 Hz) perturbations with variable amplitude, which was much weaker when compared to the pulling force.

Different regimes of slip were excited depending on the amplitude of applied weak external EM influence (Fig. 1). Slip events, were recorded as acoustic emission bursts.

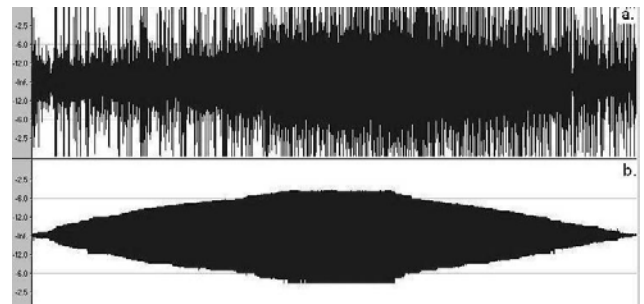


Fig.1.a) Acoustic emission during slip and b) variable external periodical EM influence.

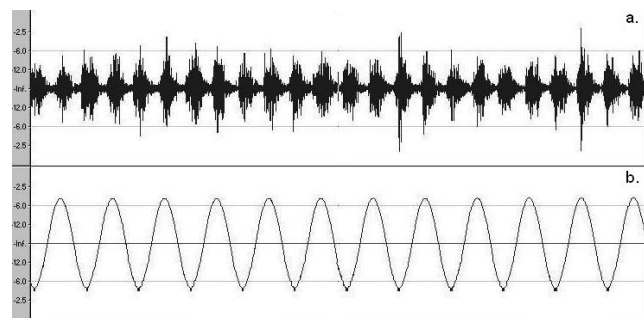


Fig.2.a) Enlarged recording of acoustic emission during slip and b) external periodical EM influence at complete phase synchronization (central part of Fig. 1).

Acoustic emission waveforms as well as sinusoidal EM signal ($f = 50$ Hz) were digitized at 44 kHz.

In order to be able to use easiest approach for estimating of phases we have transformed digitized waveforms in that way to have well pronounced sharp picks as markers. For this purpose, after subtraction of noise, consecutive wave trains from acoustic waveforms were picked up. Then time series of maximums in wave trains were composed (Fig. 3). The same was done for external periodic signal. After all, because our dataset was transformed to a spike train containing distinct markers we have used phase difference determination technique described in Pikovski [1].

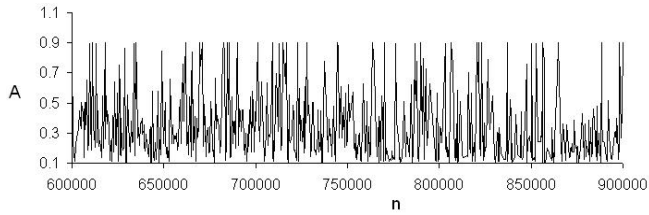


Fig.3. Part of time series of consecutive amplitudes in acoustic signal.

As statistical measure of the quality of synchronization we have calculated the full width at half maximum (FWHM) of probability density distribution of phase differences.

In order to have additional quantitative tests for temporal variation of phase synchronization

Shannon entropy $S = -\sum_{i=1}^N P_i \log(P_i)$, where P_i

is the probability of event to occur within the i box, was calculated for mentioned phase difference sequence. Then in order to evaluate the strength of functional dependence between phase variation of analyzed waveforms and external sinusoidal signal we used a measure of statistical independence between two variables, the averaged mutual information:

$$I(T) = \sum_{i=1}^N P(x(i), x(i+T)) \log_2 \left[\frac{P(x(i), x(i+T))}{P(x(i))P(x(i+T))} \right]$$

[7, 8], where $P(x(i))$ is probability of finding $x(i)$ measurement in time series, $P(x(i), x(i+T))$ is joint probability of finding measurements $x(i)$ and $x(i+T)$ in time series and T is the time lag.

III. RESULTS AND DISCUSSION

The regimes of slip recorded as acoustic emission vary from the perfect synchronization of slip events with the perturbing periodic EM impact, to the complete desynchronization of microslip events and perturbations.

As it follows from our results, in our Experiments on the spring-slider system we deal with phase synchronization of microslip events. Indeed, well defined horizontal part of synchrogram in Fig. 4a, represents time during which the acoustic emission become phase synchronized to the external sinusoidal influence in wide range of their amplitudes.

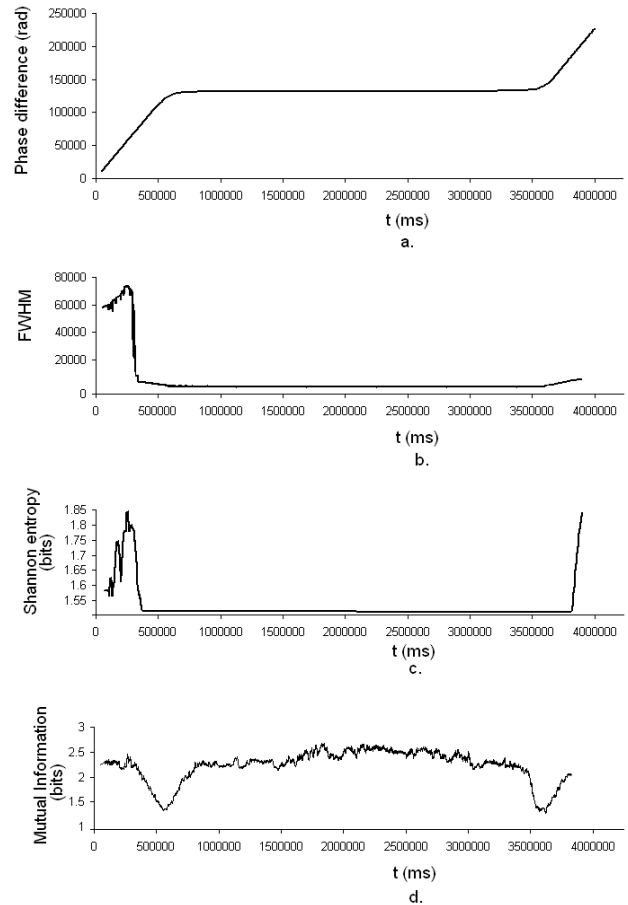


Fig. 4. a) Phase difference between acoustic emission and sinusoidal signal. b) FWHM) of probability density distribution of phase difference, c) Shannon entropy of phase difference, d) Mutual Information variation between phases of acoustic emission and external sinusoidal forcing.

It is known that probability density distribution must be narrower for synchronized signal comparing to non synchronized one. As it follows from Fig. 4 b,

density distribution is indeed much more narrow for the part of Fig. 4a, attributed as synchronized.

Moreover, clear decrease of entropy value indicates that dynamics of acoustic emission becomes much more regular for this part of acoustic emission data set (Fig. 4 c).

It is interesting that there exists some transitional effect before and after phase synchronization in acoustic emission visible as two clear minima in extent of functional interdependence between acoustic emission and EM sinusoidal forcing (Fig. 4, d).

IV. CONCLUSIONS

Influence of external EM field on spring-slider system can significantly affect their mechanical stability. In wide range of amplitudes external periodic forcing lead to clear synchronization of micrislip. The effect of phase synchronization of slip was established.

REFERENCES

- [1] A. Pikovsky, M.G. Rosenblum, J.Kurth. Synchronization: Universal Concept in Nonlinear Science (Cambridge University Prsee, Cambridge, 2001).
- [2] M.G. Rosenblum, A. Pikovsky, J.Kurth. Phase synchronization of chaotic oscillators. *Phys. Rev. Lett.*, 76, 1804-1808, 1996.
- [3] M.G. Rosenblum, A. Pikovsky, J.Kurth. Effect of phase synchronization in driven chaotic oscillators. *IEEE Trans. CAS-I*, 44. 874-881, 1997.
- [4] T. Chelidze, N. Varamashvili, M. Devidze, Z. Tchelidze, V. Chikhladze, T. Matcharashvili.: Laboratory Study of Electromagnetic Initiation of Slip, *Annals of Geophysics*, 45, 587–599, 2002.
- [5] T. Chelidze, V. Lursmanashvili, Electromagnetic and mechanical control of slip: laboratory experiments with slider system, *Nonlinear Processes in Geophysics*, 20, 1–8, 2003.
- [6] T. Chelidze, T., Matcharashvili, Electromagnetic control of earthquakes dynamics? *Computers and Geosciences*, 29. 5. 587-593. 2003
- [7] H. Kantz, T. Schreiber, 1997. *Nonlinear time series analysis*. C. U. P. Cambridge 350pp.
- [8] Cover, T. M., Thomas, J. A. *Elements of Information Theory*. J.W.S, NY, 1991, p. 280.

ANALYSIS OF WEIGHT TIME SERIES OF PATIENTS WITH EATING DISORDERS

F. Cuadros¹ and M.I. Parra²

¹Departamento de Física, ²Departamento de Matemáticas,
 Universidad de Extremadura,
 06071-Badajoz, Spain
 e-mail: ¹cuadros1@unex.es, ²mipa@unex.es

Abstract—*The present work is an approach to a real problem suggested to us by the Psychiatry Unit of the Hospital Complex of Badajoz: eating disorders (EDs). The treatment of these patients is focused on the control of their weight. Since this is an objective measurable variable that is sufficiently representative of the disease, we believe that its analysis may provide interesting results with application in clinical practice.*

An exhaustive analysis of the time series of the daily weights of hospitalized patients compared with those of control subjects and tested against simulated series revealed that linear techniques are insufficient to explain the underlying dynamics. It was more useful to approach the problem within the conceptual framework of the theory of non-linear dynamic systems.

As the principal conclusion drawn from the work, we conjecture that the fractal dimension of the attractor that appears in the phase diagram of the weight allows one to characterize the behaviour of the ED patient.

I. THE PROBLEM

The objective that we set ourselves in beginning this work was to approach real problems that arise in psychiatry with the aim of modeling and characterizing the symptoms of different psychiatric alterations and of evaluating the corresponding therapies, in order to establish objective means of diagnosis and prognosis.

In psychiatry, diagnosis is based fundamentally on the patient's "state", which is the information needed to describe a system, while prognosis tells of the "dynamics", i.e., of the rules that govern how the state of a system changes over time. One could hence think, as in a dynamic system, of a patient whose psychopathological alteration evolves over time.

In particular, the present work centres on a problem that arouses great interest amongst health personnel – eating disorders (EDs). These are problems of great relevance socially and medically because of their sin-

gularity, gravity, and social interest, and their complexity and resulting difficulties in diagnosis and treatment. If not treated early on, they can evolve into situations of extreme gravity [1].

Anorexia nervosa (AN) and bulimia nervosa (BN) are the principal ED diagnoses. They predominantly affect females – the male:female ratio is 1:10. The age of onset is usually around adolescence.

The variable chosen for analysis was the subject's daily weight, measured while still fasted in the morning by the health professional, using a precision scale. This variable was selected because it forms the central axis of treatment.

Working with real data involves a series of limitations that, in the present case, are augmented by the fact that the data are from humans. In general, these time series are short and noisy, and have a non-stationary behaviour. Consequently, one must apply the analytical methods with especial caution.

In so far as possible, we eliminated biases in the results and preconceived ideas by using a double blind technique and a control group for comparison.

II. DESCRIPTION OF THE DATA

The study environment was the Psychiatry Unit of the Hospital Complex of Badajoz. All the patients were diagnosed with some ED according to the criteria of the DSM-IV manual [2] and treated in the same context, receiving the same pharmacological treatment, diet program, and cognitive-behavioural orientation psychotherapy. Table 1 summarizes the main characteristics of the time series analysed:

Number of cases	ED	Feeding
33	AN	Oral
4	AN	NGT
20	Control	Normal
8	Control	Diet
10	Others	
75		

So as to carry out comparative studies, we shall work with the normalized weight, i.e.

$$x_t^i = \frac{w_t^i}{w_1^i} \times 100, \quad t = 1, 2, \dots, N_i, \quad (1)$$

where w_t^i represents the weight recorded for the i -th subject on the t -th day of monitoring, with N_i being the length of the series. We shall then denote by

$$\{x_t^i\}_{t=1}^{N_i}, \quad i = 1, 2, \dots, N_c \quad (2)$$

the normalized time series corresponding to the i -th subject, where N_c is the total number of cases analysed.

Figure 1 plots an example of each of the patterns of behaviour that we found.

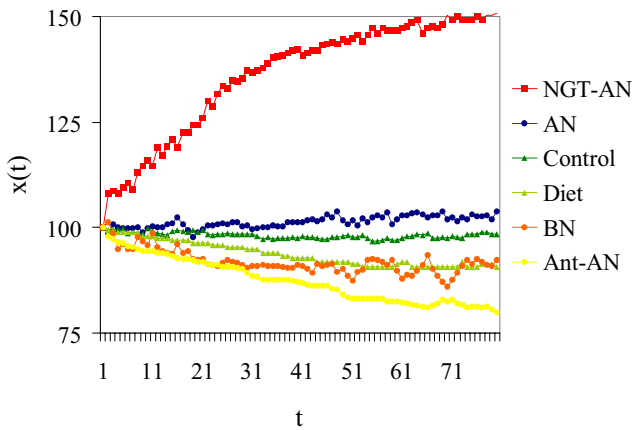


Fig. 1. Examples of the time series analysed. From top to bottom: NGT-fed AN patient, orally-fed AN patient, control subject eating normally, control subject on a strict diet, BN patient, and patient with a history of AN.

One observes in all the series except those of the healthy controls trends that are more marked the greater the control of the treatment – diet or NGT feeding. The fluctuations are greater in the series corresponding to ED patients, especially orally fed anorexia nervosa or bulimia nervosa patients.

III. RESULTS

The linear models that we used as a first approximation suffer from major limitations [3]. Since they interpret all the regular structure of the data as linear correlations, this means that small changes in the system have small effects. This, however, is not the behaviour that is typical of psychiatric patients. In their evolution, a multitude of variables interact with each other such that the outputs are not proportional to the strength of the inputs.

More interesting results were provided by tools corresponding to non-linear dynamic systems.

A. Simulation

Given the limited number of cases available, we designed two algorithms, one based on logical rules and another on the empirical distribution function, to simulate series with patterns of behaviour similar to those of the group that was used for learning. For more details, see [4].

B. The phase space

The phase space representation is a very effective means of displaying in a single plot all of a system's dynamics, since the axes of the phase space contain all the aspects of the system's dynamics. In the present case, the plot in the phase plane of the normalized weight, x_t , versus the variation of the weight, x'_t , shows more clearly the different temporal evolution patterns (Figure 2).

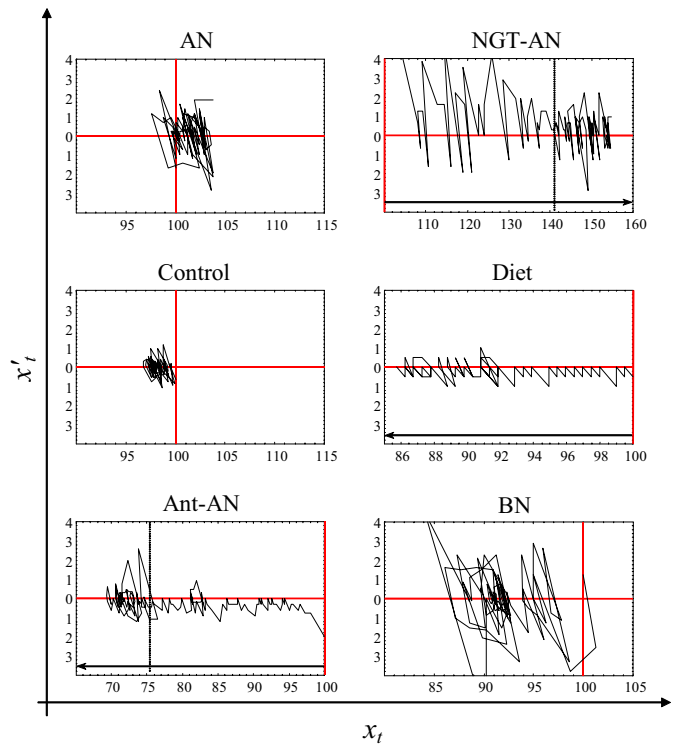


Fig. 2. Two-dimensional phase space representing geometrically the evolution of the time series shown in Figure 1. The variable x_t is the patient's normalized weight, and x'_t is the variation in weight on the t -th day of monitoring. The vertical lines mark significant changes in the feeding of the subject, the horizontal arrows the direction of the evolution of the weight, and the other arrows the direction of the evolution of the trajectories.

There appears a possible attractor in the cases of the

orally-fed ED patients, and the subjects on a strictly controlled diet present an approximately linear behaviour. One observes that the main difference between patients and healthy subjects lies in the space occupied by their corresponding trajectories.

C. Estimate of the dimension

To characterize the different types of temporal evolution, we used the fractal dimension of the attractor that appears in the phase plane, based on the general expression [5]:

$$d^{(q)} = \frac{1}{q-1} \lim_{\varepsilon \rightarrow \infty} \frac{\log \sum_{i=1}^{n(\varepsilon)} p_i^q}{\log \varepsilon} \quad (3)$$

where $n(\varepsilon)$ is the number of boxes of side ε needed to cover the object, and p_i is the probability that the trajectory passes through the i -th box. The particular cases $q = 0, 1, 2$ are equivalent to calculating the capacity, d_C , information, d_I , and correlation d_G , dimensions, respectively.

In view of the limitations of the time series with which we were working, we took certain precautions to ensure the consistency and robustness of the results. Firstly, we estimated the dimension using the different definitions (d_C , d_I , and d_G), finding comparable results. Secondly, we estimated the values over time (i.e., for time series of lengths 1,2, up to N_i) for each case analysed, finding that the behaviour of the ED patients can be characterized by the corresponding fractal dimension for series lengths ≥ 30 . Finally, we estimated the dimension of a good number of series obtained by simulation.

Figure 3 shows the estimates of d_C for the real cases and for the simulated series¹.

The value of the dimension was between 1 and 2 [6] for all the cases studied. At the lower end of the range were the values corresponding to the time series of strictly controlled subjects (either on a diet, or with NGT feeding). The intermediate region corresponded to the orally-fed ED patients. Finally, the upper end of the range corresponded to the control subjects. The values obtained for the simulated series lay within the same range of values as those of the series that were used in the learning stage of the simulation algorithms for both patients and controls.

IV. CONCLUSIONS

We would highlight the following as the most interesting conclusions:

¹The d_I and d_G results were very similar, and are not shown for the sake of simplicity.

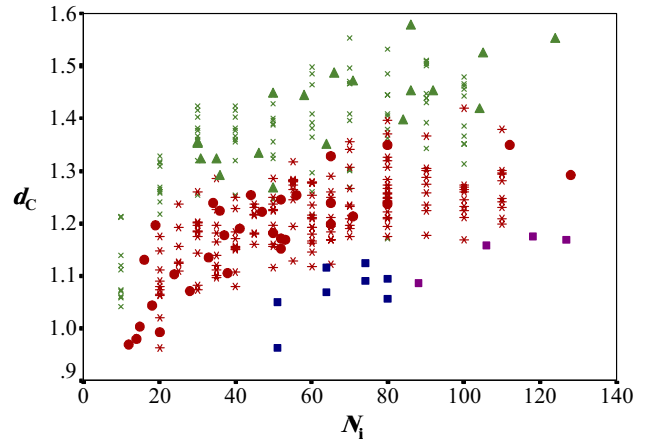


Fig. 3. Estimates of the capacity dimension versus length of the time series. The plots correspond to: AN patients (●) and simulated series trained with AN-patient series (*); control subjects (▲) and simulated series trained with the control-subject series (×); and subjects with some other type of pathology maintained on a strict diet or NGT-fed anorexia nervosa patients (■).

- We studied the phase diagram of the temporal evolution of the weights of ED patients, characterizing this evolution on the basis of the fractal dimension of the attractor.
- To solve the problem of the limited number of time series available of ED patients, we designed a simulation strategy that allows one to obtain a unlimited number of sequences with properties similar to those of the originals. The estimates of the dimension of the simulated time series were comparable to those of the group that was used in the learning stage of the simulation.
- To check the consistency and robustness of the estimates of the fractal dimension, we used different definitions of this dimension, and verified the monotonous nature of the relationship between the length of the series, beyond a certain minimum value, and the estimate of the dimension.
- The estimates of the fractal dimension of the phase diagrams of subjects with strictly controlled feeding were close to unity. Completely the contrary was the case for the healthy subjects, who had no kind of forcing or restriction in their eating: they presented the highest values of the fractal dimension. Finally, the dimensions for the orally-fed ED patients were intermediate in value, being higher the more irregular their behaviour.
- As a result of this study, we conjecture that the box-counting dimension has shown itself to be a measure of great utility in characterizing the evolution of pa-

tients with eating behaviour disorders, since it can assist the therapist in selecting treatment strategies.

The results presented in this report are in reality a starting point. We recognize that many open questions remain into which we would like to go deeper in the future. For example, in which direction should the therapist lead the patient? Towards linear behaviour or towards chaotic behaviour? Nevertheless, we were greatly encouraged by the interest that our results aroused in the clinical personnel with whom we were collaborating, especially in regard to the objective assistance that this could represent in their decisions about treatment, although it can not replace their own criteria.

REFERENCES

- [1] C.G. Fairburn and P.J. Harrison. Eating Disorders. In *The Lancet*, **361**, pp. 1–10, 2003.
- [2] American Psychiatric Association. Diagnostic & Statistical Manual of Mental Disorders DSM-IV-TR. American Psychiatric Press: Washington, 1994.
- [3] M.S. Salcedo, M.I. Parra, F. Cuadros F. and J.R. Gutiérrez. Patrones estadísticos lineales versus no lineales para el estudio de los TCAs. In *Revista de Psiquiatría Infanto-Juvenil*, **3**, pp. 141–147, 2000.
- [4] M.I. Parra, F. Cuadros, M.S. Salcedo and J.R. Gutiérrez. Simulación de series temporales: aplicación al estudio de TCA. In *Proc. 27 Congreso Nacional de Estadística e Investigación Operativa*, pp. 4341–4349, Lleida, Spain, 2003.
- [5] H. Atmanspacher, H. Scheingraber and W. Voges. Global scaling properties of chaotic attractor reconstructed from experimental data. In *Physical Review A*, **34**, pp. 1314–1322, 1988.
- [6] M.I. Parra, F. Cuadros, M.S. Salcedo and J.R. Gutiérrez. Chaotic dynamics of weight time series in anorexic inpatients. In *Proc. XXth IUPAP International Conference on Statistical Physics*, pp. 6, Paris, France, 1998.

HOMOCLINIC CHAOS IN COUPLED CHUA'S OSCILLATORS

Syamal Kumar Dana¹, Satyabrata Chakraborty², G. Ananthakrishna^{3,4}

^{1,2}Instrument Division, Indian Institute of Chemical Biology, Kolkata 700032, India

³Material Research Centre and ⁴Centre for Condensed Matter Physics, Indian Institute of Science, Bangalore 560 012, India

E-mails:¹skdana@iicb.res.in, ²satya_iicb.yahoo.com, ^{3,4}garani@mrc.iisc.ernet.in

Abstract—We report the experimental observation of homoclinic chaos in two Chua's oscillators diffusively coupled in the weak coupling limit. Evidence of homoclinic orbit is found by tuning control parameters when one oscillator is double-scroll chaotic in the period-adding regime while the other oscillator is in excitable state. Near homoclinic chaos, the return time maps show a distribution in the periods characterizing chaos.

1. INTRODUCTION

A homoclinic orbit is biasymptotic to a saddle type equilibrium set. In 3-D, the simplest Shil'nikov's scenerio deals with a saddle focus. It has been shown that in the vicinity of a homoclinic orbit, there are countably infinite number of periodic orbits if it satisfies Shil'nikov criteria [1,2]. The latter is stated in terms of the eigen values of the fixed point ($\sigma \pm j\omega, -\gamma$). When σ and γ are positive, the orbit approaches the saddle focus along the stable eigendirection spiraling away in the unstable manifold corresponding to the complex conjugate eigenvalues. When σ and γ are negative, the orbit spirals-in along the attractive two dimensional plane and exits along the unstable direction. The Shil'nikov condition refers to $|\gamma/\sigma| > 1$. Although, the geometry of the homoclinic chaos appears highly regular, its chaotic behavior is characterized by large variations in the return times of unstable periodic orbits close to the homoclinic point. As the homoclinic orbit is structurally unstable, it is not easy to observe in experiments even though homoclinic chaos has been observed previously in many experiments, such as liquid crystal flow [3], CO₂ laser [4], optically bistable device [5] and others systems.

Homoclinic chaos has striking similarities with spiking train of biological neurons and it is considered as one of the important mechanism for the emergence of spiking and bursting [6,7].

Moreover, recent investigations on CO₂ laser [8-9] also show promise in encoding messages in the interspike intervals of homoclinic chaos for its possible application in secure communication. While the Shil'nikov condition refers to a complete approach to homoclinicity, several studies [10-12] show that incomplete approach is seen in many dynamical systems. In both cases, periodic states of period adding type dominate the bifurcation diagram. Numerical methods [13] are available to obtain both homoclinic and heteroclinic orbits in Chua's circuit, but experimental observation of homoclinic oscillation in unidirectionally coupled Chua's circuits was first reported in our earlier paper [14].

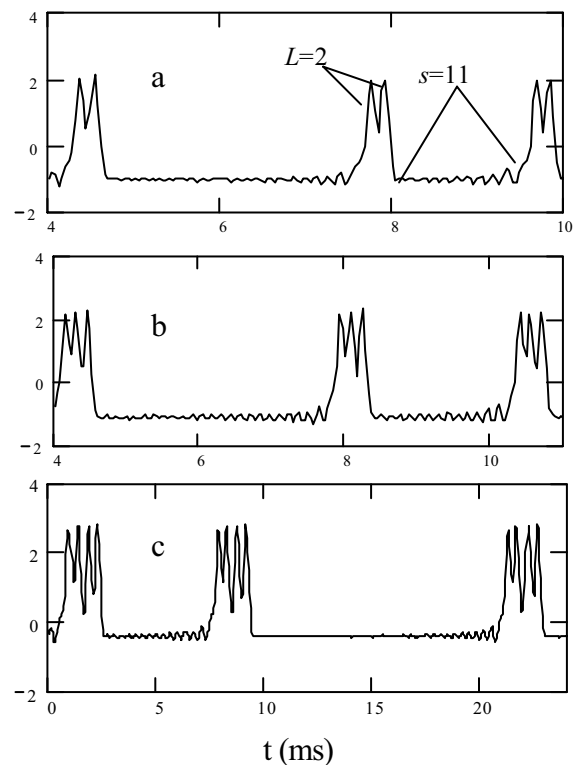


Fig.1. Time series of V_{C1} with $L=2,3,4$ for circuit components (a) $R_1=1386\Omega$, $R_8=1833\Omega$ and $R_C=95\text{ k}\Omega$ (b) $R_1=1427\Omega$, $R_8=1954\Omega$ and $R_C=136.6\text{ k}\Omega$ (c) $R_1=1384\Omega$, $R_8=1833\Omega$ and $R_C=101\text{ k}\Omega$.

Here, we report our experimental observations on homoclinic chaos of the Shil'nikov type using two diffusively coupled Chua's oscillators. The Chua's circuit is well known for its double scroll attractor [15] with three saddle foci, one near the origin and other two in mirror symmetric positions. As can be seen from Fig.1 and Fig.3, homoclinic chaos observed in our experiment has a special feature, namely, the orbit approaches one of the saddle foci along the stable eigenvector and spirals away in the unstable eigenspace, in contrast to the previous experiments [3-5]. This homoclinic structure has particular relevance to the mechanism of emergence of bursting oscillations near a homoclinic bifurcation, in a generic sense, as discussed in [6]. We have also observed bursting type oscillations near homoclinic bifurcation which will be reported elsewhere. The evidence for homoclinic chaos are seen in the form of mixed mode oscillations denoted by L^s where L and s refer to the large and small amplitude loops respectively. In our set up, we have observed $L=2,3$ and 4, the large loops near one saddle focus and smaller loops around the other saddle focus.

In the next sections we describe our circuit scheme with the details of homoclinic chaos and its return map of return time to characterize its chaotic behavior. The last section contains conclusions.

II. HOMOCLINIC CHAOS IN COUPLED CHUA'S OSCILLATORS

For a selected parameter space, the double scroll chaotic trajectory mostly revolves around the mirror symmetric saddle foci but occasionally switches from one to the other. Here we used a double scroll oscillator for selected circuit parameters as our first oscillator. We coupled a second oscillator kept in stable equilibrium state, instead of introducing a slow dynamics as usually proposed to obtain spiking or bursting oscillations for many other systems, biological [6-7] and physical [16]. Effectively, the double scroll trajectory of the first oscillator is pushed close to one of its mirror symmetric saddle foci by the stable node of the second oscillator. Homoclinic chaos is then obtained by adjusting the coupling resistance near the homoclinic bifurcation. The mechanism of how the presence of a stable node of second oscillator induces homoclinic chaos in the first oscillator is yet to be understood properly although it seems to behave like introducing a slow dynamics. The circuit diagram is shown in Fig.2.

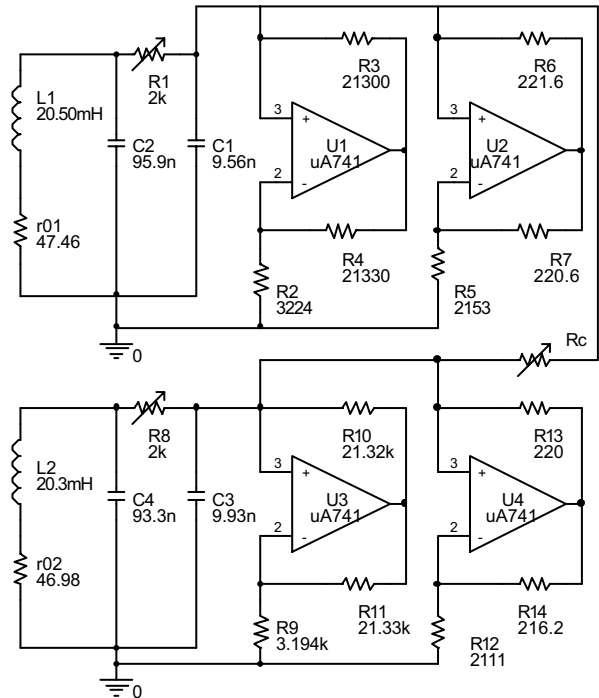


Fig.2. Coupled Chua's Circuit :power supply is $\pm 9V$

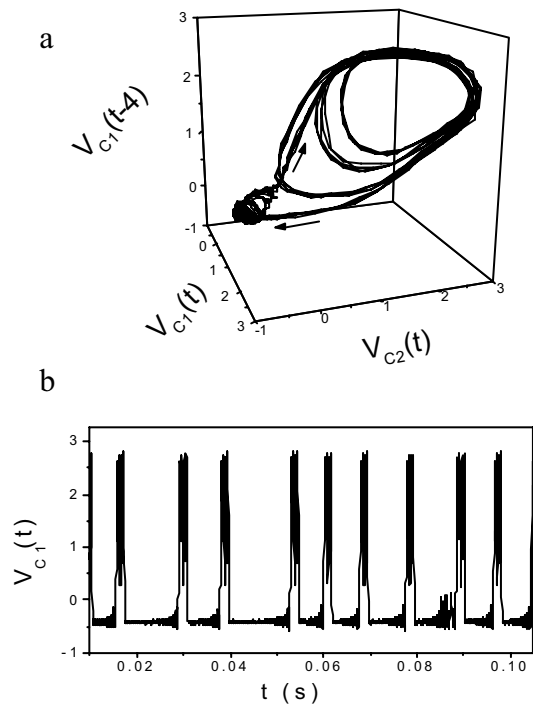


Fig.3. Homoclinic chaos for $L=4$: (a) reconstructed in 3-D space with measured time series of $V_{C1}(t)$, $V_{C2}(t)$ and time delayed $V_{C1}(t-4)$, (b) time series of $V_{C1}(t)$. Arrows indicate direction of the trajectory. $R_1=1384\Omega$, $R_8=1833\Omega$, $R_C=101k\Omega$.

The governing equations of the coupled circuit are given by

$$\begin{aligned}
 \frac{dV_{C1}}{dt} &= \frac{1}{R_1 C_1} [(V_{C2} - V_{C1}) - R_1 f(V_{C1})] + \frac{1}{C_1 R_C} (V_{C3} - V_{C1}) \\
 \frac{dV_{C2}}{dt} &= \frac{1}{R_1 C_2} (V_{C1} - V_{C2} + R_1 I_{L1}) \\
 \frac{dI_{L1}}{dt} &= \frac{1}{L_1} (-V_{C2} - r_{01} I_{L1}) \\
 \frac{dV_{C3}}{dt} &= \frac{1}{R_8 C_3} [(V_{C4} - V_{C3}) - R_8 f(V_{C3})] + \frac{1}{C_3 R_C} (V_{C1} - V_{C3}) \\
 \frac{dV_{C4}}{dt} &= \frac{1}{R_8 C_4} (V_{C3} - V_{C4} + R_8 I_{L2}) \\
 \frac{dI_{L2}}{dt} &= \frac{1}{L_2} (-V_{C4} - r_{02} I_{L2}) \quad (1)
 \end{aligned}$$

where the piecewise linear function $f(V_C)$ is given by

$$f(V_{C_{1,3}}) = \begin{cases} b_{1,2} V_{C_{1,3}} + (b_{1,2} - a_{1,2}) & \text{if } V_{C_{1,3}} < -1 \\ a_{1,2} V_{C_{1,3}} & \text{if } -1 \leq V_{C_{1,3}} \leq 1 \\ b_{1,2} V_{C_{1,3}} + (a_{1,2} - b_{1,2}) & \text{if } V_{C_{1,3}} > 1 \end{cases} \quad (2)$$

The slopes $a_{1,2}$ and $b_{1,2}$ of the piecewise linear function are [17]

$$a_{1,2} = \left(-\frac{1}{R_{2,9}} - \frac{1}{R_{5,12}}\right) R_{1,8}; b_{1,2} = \left(\frac{1}{R_{3,10}} - \frac{1}{R_{5,12}}\right) R_{1,8} \quad (3)$$

The state variables are the voltages $V_{C1,C3}, V_{C2,C4}$ measured at respective capacitor nodes and the inductor current $I_{L1,L2}$. Measured time series of V_{C1} and V_{C2} are recorded using a digital oscilloscope with a sampling rate of $40\mu s$.

The first oscillator is set at double scroll chaotic state in the period-adding regime by R_1 and the second oscillator is set at excitable state (stable equilibrium) by R_8 . Then for a selected coupling resistance R_C chosen as the bifurcation parameter, homoclinic cycles make L large amplitude loops and s small amplitude loops as shown in Fig.3(a). The number of L -loops is entirely controlled by R_1 , while R_C controls the number of s -loops. The latter is seen near the saddle focus between large spikes. Once R_1 is set, the control parameter R_C is adjusted within a narrow range near the homoclinic bifurcation when the number of s -loops varies randomly with large fluctuations in the interspike intervals of quasi-homoclinic orbits. It may be noted that the range of coupling resistance R_C is always set in the weaker limit. The number of s -loops increases as the

trajectory moves closer and closer to the saddle focus. Theoretically, a countable infinity of unstable periodic orbits exists near the homoclinic bifurcation whose fluctuating periods are characterized by a large variation in the numbers of s -loops. In our experiment, we obtain a large variation in the number of s -loops for a limited measurement time. This is also revealed by the large variations in the interspike intervals for a fixed R_C value as shown in the time series in Fig.1 and Fig.3(b). A plot of the period T with the bifurcation parameter R_C is shown in Fig.4. The period here is defined as the estimated mean of interspike intervals at a particular R_C value. As R_C approaches the homoclinic bifurcation parameter $R_C^* \approx 101k\Omega$, T increases exponentially. Although the time period fluctuates for a fixed R_C value, homoclinic chaos has a characteristic mean time period. It reflects the chaotic nature of homoclinic cycles near the bifurcation point.

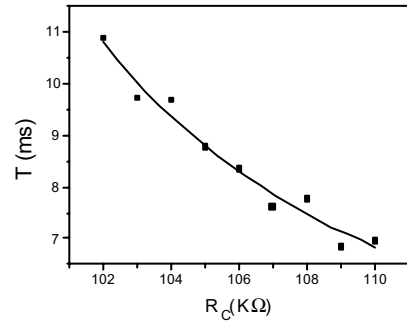


Fig.4. Time period with bifurcation parameter: solid curve is an exponential fitting on experimental data (square). Parameters: $R_1=1384\Omega$, $R_8=1833\Omega$, $R_C^* \approx 101k\Omega$ for $L=4$.

III. RETURN TIME MAP

The return time return map is a very useful tool [4] for the analysis of homoclinic chaos. The global return time of quasi-homoclinic trajectories are obtained from the measured scalar signal. The crossing time of the smaller loops to a voltage level of $V_{C1} = -0.35V$ indicated by the bold horizontal line near saddle focus shown in Fig.5(a) are calculated. The time interval between the successive crossings with $dV_{C1}/dt > 0$ is taken as $t(i)$ for the i th crossing. The return time map in Fig.5(b) shows the multivalued structure indicating chaotic behaviour.

IV. CONCLUSIONS

Multi-loop homoclinic chaos has been generated using two diffusively coupled Chua's oscillators. The

geometry of the homoclinic chaos in experimental circuit has relevance to the emergence of bursting in biological cells. Thus, it could be a useful model for understanding the mechanism of bursting oscillations in general.

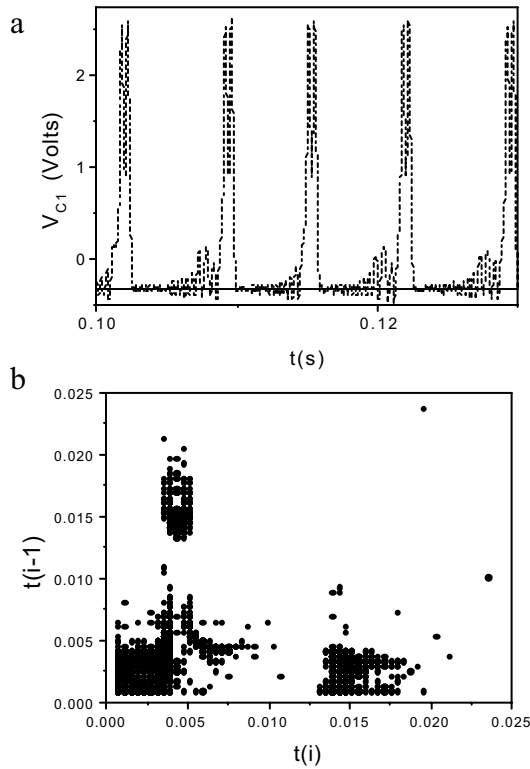


Fig.5. Retrun time map of homoclinic chaos: (a) measured time series of V_{C1} for $L=2$. The crossing is indicated by horizontal bold line at $V_{C1}=-0.35$, (b) $t(i+1)$ versus $t(i)$ plot. All time scales are in sec. $R_1=1389\Omega$, $R_8=1814\Omega$, $R_C=93k\Omega$.

ACKNOWLEDGEMENTS

This work is partially supported by the BRNS, Department of Atomic Energy, Government of India, under Grant no.2000/34/13/BRNS. S.K.D wishes to acknowledge P.G.Vaidya P.K.Roy for their valuable discussions and comments.

REFERENCES

[1] Y.A.Kuznetsov, Elements of Applied Bifurcation Theory, Springer-Verlag, NY, 1995.
 [2] S.Wiggins, Introduction to Applied Nonlinear Dynamical Systems, Springer-verlag, NY, 1990.
 [3] T.Peacock, T.Mullin, Homoclinic bifurcations in a liquid crystal flow, *J.Fluid.Mech.*, vol.432, pp.369-386, 2001.

[4] A.N.Pisarchik, R.Meucci, F.T.Arecchi, Theoretical and experimental study of discrete behaviour of Shil'nikov chaos in a CO₂ laser, *Eur.Phys.J. D*, vol.13, pp.385-391,2001.
 [5] R.Herrero, R.Pons, J.Farjas, F.Pi, G.Orriols, Homoclinic dynamics in experimental Shil'nikov attarctor, *Phy.Rev.E*,vol.53, no.6, 5627-5636, 1996.
 [6] V. N. Belykh, I. V. Belykh, M. Colding-Jorgensen, E. Mosekilde, Homoclinic bifurcations leading to the emergence of bursting oscillations in cell models, *Eur. Phys.J. E*, vol.3, pp.205-219, 2000.
 [7] E.M.Izhikevich, Neural excitability, spiking and bursting,*Int.J.Bifur. Chaos.Appl.Sci.Engg.*, vol.10,no.6, pp.1171-1266, 2000.
 [8] E.Allaria, F.T.Arecchi, A.Di Garbo, M.Meucci, Synchronization of homoclinic chaos, *Phy.Rev.Lett.*, vol.86, vo.5, pp.791-794, 2001.
 [9] I.P.Mariño, E.Allaria, R.Meucci, S.Boccaletti, chaotic systems, *Chaos*, vol.13, no.1, pp. , 2002.
 [10] P.Glendenning, C.Sparrow, Local and global behaviour near homoclinic orbit, *J.Stat.Phy.*, vol.35,pp. 645-696, 1984
 [11] P.Gaspard, R.Kapral, G.Nicolis, Bifurcation phenomena near homoclinic systems: a two parameter analysis, *J.Stat. Phy.*, vol.35, pp.697-727, 1984.
 [12] S.Rajesh, G.Ananthakrishna, Incomplete approach to homoclinicity in a model with bent-slow manifold geometry, *Physica D*, vol.140, pp.193-212, 2000.
 [13] R.O.Medrano-T.M.S.Baptista, I.L.Caldas, Homoclinic orbits in piecewise system and their relation with invariant sets, *Physica D*, vol.186, pp.133-147,2003.
 [14] S.K.Dana, S.Chakraborty, Homoclinic oscillation in coupled Chua's oscillator in weaker of limit of phase synchronization, *Int.J.Bifur. Chaos Appl. Sci.Engg.* (2004,in press)
 [15] L.O.Chua, M.Komuro, T.Matsumoto, The double scroll family, *IEEE Trans.Cir.Systs.*,vol.CAS-33, pp.1072,1986.
 [16] R.Meucci, A.Di garbo, E.Allaria, F.T.Arecchi, Autonomous bursting in a homoclnic system, *Phy.Rev.Lett.*,vol.88, pp.144101, 2002.
 [17] M.P.Kennedy, Three steps to chaso-A Chua's circuit primer, *IEEE Trans.Cir.Systs.-I*, vol.40, no.10, pp.657, 1993.

ENTROPY-BASED INDEPENDENCE TEST

Andreia Dionísio*, Rui Menezes** e Diana A. Mendes**

*Universidade de Évora, Departamento de Gestão de Empresas

Largo dos Colegiais, 2

7000 Évora, Portugal

e-mail: andreia@uevora.pt

**ISCTE, Av. Forças Armadas, 1649-026 Lisboa,

Portugal, rui.menezes@iscte.pt; diana.mendes@iscte.pt

Abstract—This paper investigates the possibility to analyse the structure of unconditional or conditional (and possibly nonlinear) dependence in financial returns without requiring the specification of mean-variance models or a theoretical probability distribution, through an entropy-based test.

I. INTRODUCTION

The most known measure of dependence between two random variables is the coefficient of linear correlation, but its application requires a pure linear relationship, or at least a linear transformed relationship [see e.g. Granger et al., (1994); Maasoumi et al., (2002)], because it is nothing but a normalized covariance and only accounts for linear relationships. However, this statistics may not be helpful in determining serial dependence if there is some kind of nonlinearity in the data. In this context, it seems that a measure of global dependence is required, that is, some measure that captures linear and nonlinear dependencies, without requiring the specification of any kind of model of dependence. Urbach (2000) defends a strong relationship between entropy, dependence and predictability. This relation has been studied by several authors, namely Granger and Lin (1994); Maasoumi and Racine (2002); Darbellay and Wuertz (2000). On the basis of the above arguments we try to find out a rationale to the following question: “Is it possible to inquire about any unconditional, or conditional (and possibly nonlinear) dependence structure in returns without requiring the specification of mean-variance models and theoretical distribution probabilities?”

II. INFORMATION AND PREDICTABILITY

A measure that takes the value 0 when there is total independence and 1 for total dependence is one of the most practical ways to evaluate (in)dependence between two vectors of random variables \vec{X}, \vec{Y} . Let $p_{\vec{X}, \vec{Y}}(A \times B)$ be the joint probability distribution

of (\vec{X}, \vec{Y}) and $p_{\vec{X}}(A)$, $p_{\vec{Y}}(B)$ the underlying marginal probability distributions, where A is a subset of the observation space of \vec{X} and B a subset of a observation space of \vec{Y} , such that we can evaluate the following expression:

$$\ln \frac{p_{\vec{X}, \vec{Y}}(A \times B)}{p_{\vec{X}}(A) p_{\vec{Y}}(B)}. \quad (1)$$

If the two events are independent, then $p_{\vec{X}, \vec{Y}}(A \times B) = p_{\vec{X}}(A) p_{\vec{Y}}(B)$, and so equation (1) will take the value zero.

Granger, Maasoumi and Racine (2002) consider that a good measure of dependence should satisfy the following six “ideal” properties:

1. Must be well defined for both continuous and discrete variables;
2. Must be normalized to zero if \vec{X} and \vec{Y} are independent, and lying between -1 and $+1$, in general;
3. The modulus of the measure should equal 1 if there is an exact nonlinear relationship between the variables;
4. Must be similar or simple related to the linear correlation coefficient in the case of a bivariate normal distribution;
5. Must be metric in the sense that it is a true measure of “distance” and not just a measure of “divergence”;
6. Must be an invariant measure under continuous and strictly increasing transformations.

Consider two vectors of random variables (\vec{X}, \vec{Y}) . Let $p_{\vec{X}}, p_{\vec{Y}}$ and $p_{\vec{X}, \vec{Y}}$ be the probability density function (pdf) of \vec{X}, \vec{Y} and the joint probability distribution of (\vec{X}, \vec{Y}) . Denote by $H(\vec{X})$, $H(\vec{X}, \vec{Y})$ and $H(\vec{Y}|\vec{X})$ the entropy of \vec{X} , the joint entropy of the two arguments (\vec{X}, \vec{Y}) and the conditional entropy of \vec{Y} given \vec{X} . Then, the mutual information can be

defined by the following expression:

$$\begin{aligned}
 I(\vec{X}, \vec{Y}) &= H(\vec{X}, \vec{Y}) - H(\vec{Y}|\vec{X}) \\
 &= H(\vec{X}) + H(\vec{Y}) - H(\vec{X}, \vec{Y}) \quad (2) \\
 &= \int \int p_{\vec{X}, \vec{Y}}(x, y) \log \frac{p_{\vec{X}, \vec{Y}}(x, y)}{p_{\vec{X}}(x)p_{\vec{Y}}(y)} dx dy.
 \end{aligned}$$

Since $H(\vec{Y}) \geq H(\vec{Y}|\vec{X})$, we have $I(\vec{X}, \vec{Y}) \geq 0$, assuming equality iff \vec{X} and \vec{Y} are statistically independent. So, the mutual information between the vectors of random variables \vec{X} and \vec{Y} can be considered a measure of dependence between these variables, or better yet, the statistical correlation of \vec{X} and \vec{Y} .

The statistics defined in equation (2) satisfies some of the desirable properties of a good measure of dependence [see Granger et al., (2002)]. In equation (2), we have $0 \leq I(\vec{X}, \vec{Y}) \leq +\infty$, which difficult comparisons between different samples. In this context Granger and Lin (1994) and Darbellay (1998), among others, use a standard measure for the mutual information, the global correlation coefficient, defined by: $\lambda(\vec{X}, \vec{Y}) = \sqrt{1 - e^{-2I(\vec{X}, \vec{Y})}}$. This measure varies between 0 and 1 being thus directly comparable to the linear correlation coefficient r , based in the relationship between the measures of information theory and variance analysis. The function λ captures the overall dependence, both linear and nonlinear, between \vec{X} and \vec{Y} .

According to properties presented by mutual information, and because independence is one of the most valuable concepts in econometry, we can construct a independence test based on the following hypothesis: $H_0 : p_{X,Y}(x, y) = p_X(x)p_Y(y)$, $H_1 : p_{X,Y}(x, y) \neq p_X(x)p_Y(y)$. If H_0 , then $I(X, Y) = 0$ and the independence between the variables is found. If H_1 then $I(X, Y) > 0$ and we reject the null hypothesis of independence. The above hypothesis can be reformulated in the following way:

$$H_0 : I(X, Y) = 0, \quad H_1 : I(X, Y) > 0.$$

The above hypothesis can be reformulated in the following way: in order to test adequately the independence between variables (or vectors of variables) we will need to calculate the critical values. In our case this is based upon simulated critical values for the null distribution or the percentile approach¹.

¹These values have been found through the simulation of critical values based upon a white noise, for a number of sample sizes. Given that the distribution of mutual information is skewed, we can adopt a percentile approach to obtain critical values.

One of the difficulties for calculate the mutual information from empirical data lies in the fact that the underlying pdf is unknown. There are, essentially, three different methods to estimate mutual information: histogram-based estimators; kernel-based estimators; parametric methods. According to Modde-meijer (1999), histogram-based estimators are divided in two groups: equidistant cells (see e.g. Modde-meijer, 1999) and equiprobable cells, i.e. marginal equiquantisation [see e.g. Darbellay, (1998a)]. The second approach, marginal equiquantisation, presents some advantages, since it allows for a better adequacy to the data and maximizes mutual information [Darbellay, (1998a)].

The definition of mutual information is expressed in an abstract way and it is based on space partitions. To simplify, let us consider a finite dimension Euclidian space, $\mathbb{R} = \mathbb{R}^x \times \mathbb{R}^y$, and let $\Gamma_X = \{A_i\}_{i=1}^{n_1}$ $\Gamma_Y = \{B_j\}_{j=1}^{n_2}$ be two generic partitions of the subspaces \mathbb{R}^x and \mathbb{R}^y . Then the mutual information is a positive number defined as:

$$\begin{aligned}
 I(\vec{X}, \vec{Y}) &\equiv \sup_{\{A_i\}\{B_j\}} \sum_{i,j} P_{\vec{X}, \vec{Y}}(A_i \times B_j) \\
 &\quad \left[\log \frac{P_{\vec{X}, \vec{Y}}(A_i \times B_j)}{P_{\vec{X}}(A_i) P_{\vec{Y}}(B_j)} \right].
 \end{aligned}$$

The supremum is taken over all the finite partitions of \mathbb{R}^x and \mathbb{R}^y . The conventions $0 \ln\left(\frac{0}{z}\right) = 0$ for $z \geq 0$ and $z \ln\left(\frac{z}{0}\right) = +\infty$ are used. Darbellay (1998a) shown that mutual information is finite if and only if the measure $P_{\vec{X}, \vec{Y}}$ is absolutely continuous with respect to the product measure $P_{\vec{X}} \times P_{\vec{Y}}$. The system $\Gamma = \Gamma_X \times \Gamma_Y$ is a partition of $\mathbb{R} = \mathbb{R}^x \times \mathbb{R}^y$ and is the product of two marginal partitions, one of \mathbb{R}^x and another of \mathbb{R}^y . Marginal equiquantisation consists of dividing each edge of a cell into α (normally $\alpha = 2$) intervals with approximately the same number of points. The approximateness of the division has two causes: the number of points in a cell may not be exactly divisible by α , or some X may take repeating values [for more details see for example Darbellay, (1998)].

We applied this approach to measure global (linear and nonlinear) dependence in some financial time

Appendix A lists the 90th, 95th and 99th percentiles of the empirical distribution of the mutual information for the process $y_t = \epsilon_t$ with $\epsilon_t \sim i.i.d.N(0, 1)$, having been made 5000 simulations for each critical value. This methodology was applied as proposed by Granger, Maasoumi and Racine (2002), and according to these authors, the critical values can be used as the base to test for time series serial independence.

series and in the end, we can say that the main advantage of the application of the mutual information in financial time series is the fact that this measure captures the global serial dependence (linear and nonlinear) without any request about some theoretical probability distribution or specific model of dependency. Even if this dependence is not able to refute the efficient market hypothesis, it is important to the investor to know that the rate of returns are not independent and identically distributed.

REFERENCES

- [1] Darbellay, G. (1998). An Adaptative Histogram Estimator for the Mutual Information, UTIA Research Report, n.º 1889, Acad. Sc., Prague.
- [2] Darbellay, G. and Wuertz, D. (2000). *Physica A*, 287, 429-439.
- [3] Fama, E. (1991). *Journal of Finance*, 46, 5, December, 1575-1617.
- [4] Granger, C. and Lin, J. (1994). *Journal of Time Series Analysis*, 15, 4, 371-384.
- [5] Granger, C, Maasoumi, E. and Racine, J. (2002). A Dependence Metric for Possibly Nonlinear Processes, UCSD Working Paper.
- [6] Maasoumi, E. and Racine, J. (2002). *Journal of Econometrics*, 107, 291-312.
- [7] Urbach, R. (2000). *Footprints of Chaos in the Markets - Analysing non-linear time series in financial markets and other real systems*, Prentice Hall, London.

III. APPENDIX A

Critical values tables for testing serial independence through mutual information for $N(0, 1)$ data. 5000 replications were computed.

N=100			
Percentiles			
Lag	90	95	99
1	0.0185	0.0323	0.0679
2	0.1029	0.1232	0.1933
3	0.1059	0.1260	0.1722

N=200			
Percentiles			
Lag	90	95	99
1	0.0092	0.0214	0.0361
2	0.0561	0.0701	0.1080
3	0.0591	0.0918	0.1318

N=500			
Percentiles			
Lag	90	95	99
1	0.0037	0.0070	0.0144
2	0.0222	0.0369	0.0501
3	0.06799	0.0788	0.1128

N=1000			
Percentiles			
Lag	90	95	99
1	0.0019	0.0045	0.0071
2	0.0133	0.0191	0.0311
3	0.0340	0.0399	0.0568

N=1500			
Percentiles			
Lag	90	95	99
1	0.0013	0.0026	0.0045
2	0.0101	0.0133	0.0224
3	0.0222	0.0267	0.0369

N=2000			
Percentiles			
Lag	90	95	99
1	0.0009	0.0019	0.0033
2	0.0061	0.0094	0.0147
3	0.0169	0.0203	0.0278

N=2500			
Percentiles			
Lag	90	95	99
1	0.0008	0.0015	0.0030
2	0.0054	0.0078	0.0129
3	0.0134	0.0171	0.0251

SYNTHESIS OF SINGLE-TRANSISTOR CHAOTIC OSCILLATORS

Alexander S. Dmitriev, Elena V. Efremova, Alexander D. Khilinsky

Institute of RadioEngineering and Electronics, Russian Academy of Sciences,
Mokhovaya St. 11/7, GSP-3, 103907, Moscow, Russia,
E-mail: chaos@mail.cplire.ru

Abstract – *In this report the problem of forming chaotic signals with preassigned spectrum is discussed. An approach to construction of single-transistor chaotic oscillators with preassigned spectrum on the basis of “active component (transistor) – passive quadripole closed in feedback loop” structure is proposed. It is shown that in the oscillator with such structure it is possible to obtain chaotic spectrum which envelope is close to the shape of the amplitude-frequency response of feedback loop of the system.*

I. INTRODUCTION

Use of dynamic chaos in radio communications and radiolocation [1 - 4] requires creation of chaotic sources with prescribed spectral and statistical characteristics.

For practical reasons, the circuitry used in chaotic oscillators must include mainly "classical" electronic components. In particular, it is desirable to employ bipolar and field-effect transistors.

Today the theory of construction of regular oscillators [5], including transistor oscillators, is well developed. From the other hand there is a theory of preassigned chaotic power spectrum formation in the class of ring-structure oscillation systems [6]. In this case, the shape of the power spectrum is determined by collective frequency response of frequency-selective elements in the feedback loop of the system. In this paper we try to use present experience in both areas and develop an approach to the transistor oscillator with preassigned spectrum construction.

II. STRUCTURE OF THE OSCILLATOR ON THE BASIS OF ACTIVE NETWORK AND PASSIVE QUADRIPOLE

From the theory of oscillations it is known what in the structure composed of an active network with nonlinear I-V characteristic and a passive element closed in feedback loop (Fig. 1) in the case when the conditions of phase and amplitude balance are

satisfied regular oscillations are excited. The active network and passive network are the quadripoles.

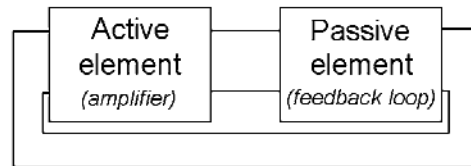


Fig. 1. Structure “active network – passive quadripole closed in feedback loop”.

As an active element a bipolar transistor can be used. As passive quadripole any linear quadripole, with which the conditions of exciting and existence of oscillations can be kept, may be used. It is a common model of transistor oscillator. In particular all three-point circuits are special cases of such structure (Fig. 2).

In such a representation of the transistor oscillator structure it can be seen that it has much in common with ring-structure oscillation systems. The difference between ring oscillators and single-transistor oscillators is the use of active quadripole with no dropping characteristic and absence of buffers between circuit elements in transistor oscillator. A possibility of power spectrum envelope control was shown by means of formation of amplitude-frequency response (AFR) of passive element system in feedback loop in the class of ring oscillators. Due to existence of chaotic dynamics in transistor oscillators with 1.5 degrees of freedom an opportunity of chaotic oscillation power spectrum formation in these systems can be expected by means of a choice of element sequence in the feedback loop circuit.

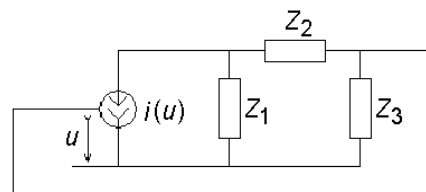


Fig. 2. The structure of three-point circuit. It seems advisable to begin investigations with the

simplest oscillators – oscillators based a single transistor and a minimum number of elements which give a possibility of chaotic oscillations (as is known, it is possible in systems with 1.5 degrees of freedom). Then analyze the process of power spectrum formation in such system after that complicate the system by means of adding new components for creating conditions for more complicated spectrum.

III. FORMATION OF POWER SPECTRUM IN THREE-POINT CIRCUIT

Let us begin with a well-known oscillator with 1.5 degrees of freedom in which chaotic oscillations exist, i.e., capacitive three-point circuit or Colpittz oscillator [7-8], it is shown in Fig. 3.

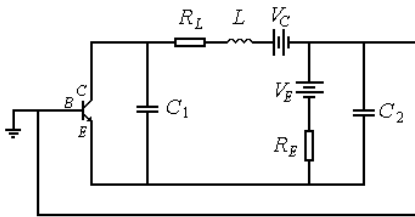


Fig. 3. Schematic diagram of the capacitive three-point circuit.

The oscillator dynamics can be described as follows:

$$\begin{aligned} C_1 \dot{V}_{CE} &= I_L - I_C, \\ C_2 \dot{V}_{BE} &= (V_E - V_{BE})/R_E - I_L - I_B, \\ L \dot{I}_L &= V_C - V_{CE} - R_L I_L + V_{BE}, \end{aligned} \quad (1)$$

where V_{CE} , V_{BE} are collector-emitter and base-emitter voltages, respectively; I_L , I_C , I_B are currents through inductance, collector and base, respectively.

$$\begin{aligned} I_B &= 0, \text{ where } V_{BE} \leq V_T; \\ I_B &= (V_{BE} - V_T)/R_{BE}, \text{ when } V_{BE} > V_T; \\ I_C &= \beta I_B, \end{aligned} \quad (2)$$

where $V_T \approx 0.75$, V_T is barrier potential; R_{BE} is base-emitter resistance; and β is transistor gain factor.

For analysis we use the parameter set: $V_E=2$ V, $V_C=7$ V, $L=30$ μ H, $R_L=40$ Ohm, $R_E=400$ Ohm, $R_{BE}=200$ Ohm, $\beta=300$. Let us analyze the signal power spectrum at the passive network output. In Fig. 4 the power spectrum and AFR of the feedback loop are shown. As can be seen in the figure, the power spectrum envelope is close to the AFR form.

Let us fix the value of parameter at L and investigate the spectrum evolution by variation of parameters C_1 and C_2 . In search for chaotic modes we use a two-parameter diagram of Lyapunov

exponents on the parameter plane (C_1, C_2) (Fig. 5), where the Lyapunov exponent values are denoted by gray scale.

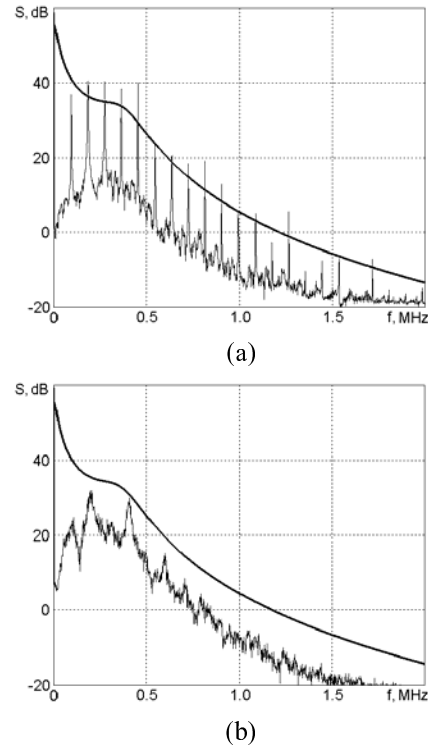


Fig. 4. AFR of feedback loop and signal power spectrum of three-point circuit at the parameters values (a) $C_1=13$ nF, $C_2=9.7$ nF and (b) $C_1=15$ nF, $C_2=9.7$ nF.

Let us choose two modes with close parameter values and different values of Lyapunov exponent. So in the case $C_1=13$ nF, $C_2=9.7$ nF the value of Lyapunov exponent is $\lambda=0.05$ and in the case $C_1=15$ nF, $C_2=9.7$ nF $\lambda=0.13$. In Fig. 4 (a, b) power spectra for these two cases are shown. As can be seen, for two almost identical AFR the power spectra are very different from each other. The more smooth spectra correspond to the larger value of Lyapunov exponent.

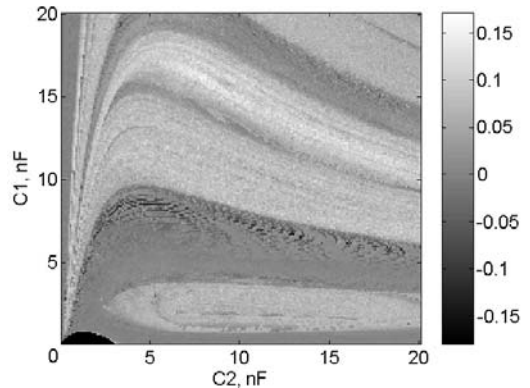


Fig. 5. Two-parameter diagram of Lyapunov exponents in (C_1, C_2) plane.

So, these results confirm that in chaotic oscillators of considered structure it is possible to obtain chaotic power spectrum with the envelope close to the form of AFR of feedback loop. Moreover of two modes with close parameter values the more smooth spectrum corresponds to the larger Lyapunov exponent.

On the basis of this analysis it is possible to formulate the necessary requirements for forming the preassigned power spectrum of transistor oscillator.

1. The oscillator structure must involve active network (transistor) and passive network closed in the feedback loop.
2. In the oscillator chaotic oscillations must exist as a result of collapse of fixed-frequency or two-frequency regular self-oscillating mode.
3. Frequency-selective circuit in the feedback loop must be adjusted so that the amplitude-frequency response of the open loop (magnitude of complex transfer function of feedback loop) agrees with the desired form of power spectrum envelope.
4. To adjust the power spectrum smoothness it is necessary to provide possibility of changing component nominal values in order to find the mode with larger Lyapunov exponent.

IV. CHAOTIC OSCILLATOR WITH 2.5 DEGREES OF FREEDOM

Let us show that the described approach to power spectrum formation and analysis is applicable not only in the case of three-point oscillator but allows to make new chaotic oscillators with preassigned spectrum.

For this aim we add an additional *RLC*-link in the feedback loop that is a low-pass filter. Schematic diagram of this oscillator is shown in Fig. 6.

Dynamic modes of the oscillator are described by the following system of equations:

$$\begin{aligned}
 C_1 \dot{V}_{CE} &= I_L - I_C, \\
 C_3 \dot{V}_{BE} &= I_{L3} - I_B, \\
 L \dot{I}_L &= V_C - V_{CE} - R_L I_L + V_{C2}, \\
 C_2 \dot{V}_{C2} &= (V_E - V_{C2}) / R_E - I_L - I_{L3}, \\
 L_3 \dot{I}_{L3} &= V_{C2} - V_{BE} - R_3 I_{L3},
 \end{aligned} \tag{3}$$

where V_{CE} , V_{BE} are collector-emitter and base-emitter voltages, respectively; V_{C2} is voltage on capacity C_2 and I_L , I_{L3} , I_C , I_B are currents through inductances L , L_3 , collector and base, respectively. As in the case of three-point circuit I-V characteristic is a piecewise-linear function (2).

For analysis we use the parameter set: $V_E=2$ V,

$V_C=7$ V, $L=30$ μ H, $L_3=30$ μ H, $R_L=40$ Ohm, $R_E=400$ Ohm, $R_{BE}=200$ Ohm, $\beta=300$. Let us investigate the dependence of power spectrum form on AFR of feedback loop.

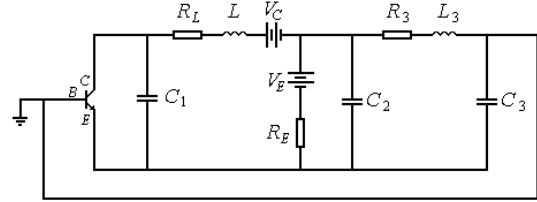


Fig. 6. Schematic diagram of the oscillator with 2.5 degrees of freedom.

In Fig. 7 the AFR of feedback loop and corresponding signal power spectrum of this oscillator are shown. As can be seen the power spectrum envelopes are in good match with AFR of feedback loop both in frequency and in amplitude characteristics.

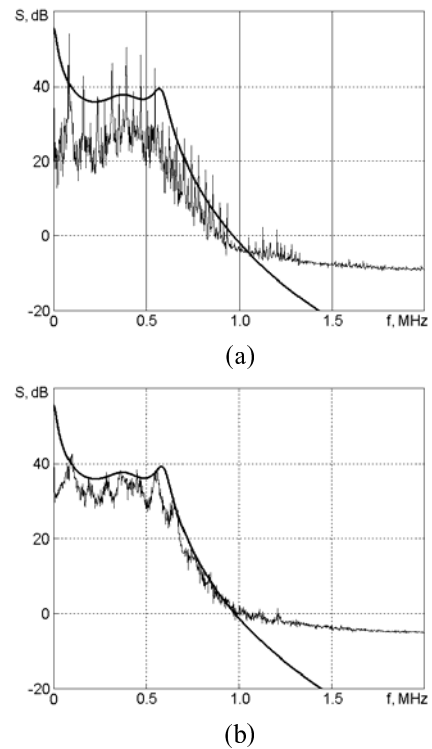


Fig. 7. AFR of feedback loop and signal power spectrum at the parameters values (a) $C_1=7.3$ nF, $C_2=16.4$ nF, $C_3=3.06$ nF, $R_3=10$ Ohm and (b) $C_1= 7.3$ nF, $C_2= 16.4$ nF, $C_3=2.9$ nF, $R_3=10$ Ohm.

To scan for chaotic modes with the most smooth spectrum we use two-parameter diagram of Lyapunov exponent. Two-parameter diagram of Lyapunov exponents in (R_3, C_3) plane is shown in

Fig. 8. Power spectrum of the mode with parameter values $C_1=7.3$ nF, $C_2=16.4$ nF, $C_3=3.06$ nF, $R_3=10$ Ohm is shown in Fig. 7a. Lyapunov exponent for this mode is $\lambda=0.02$. Let us consider a mode with larger Lyapunov exponent value but similar form of the AFR of feedback loop. For the mode with parameters $C_1= 7.3$ nF, $C_2= 16.4$ nF, $C_3=2.9$ nF, $R_3=10$ Ohm (Fig. 7b) $\lambda=0.08$. As can be seen from comparison of Figs. 7a and 7b AFR forms for these two modes are very similar but power spectrum envelope forms are fundamentally different. As in the case of three-point circuit, the value of Lyapunov exponent determines the smoothness of the power spectrum envelope. The larger value of Lyapunov exponent, the more smooth and close to the AFR is the power spectrum envelope of the mode.

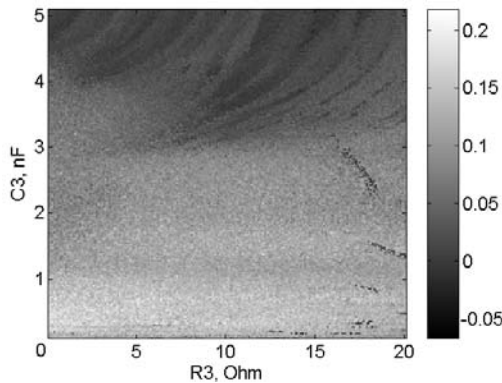


Fig. 8. Two-parameter diagram of Lyapunov exponents in (R_3, C_3) plane on $C_1=7.3$ nF, $C_2=16.4$ nF.

Adding new components increases the number of system control parameters. So in such system greater variety of spectrum forms can be expected.

As can be seen in Figs., the agreement of the power spectrum with AFR form is better in the system with 2.5 degrees of freedom than in the three-point circuit.

This shows that increasing degrees of freedom allows to achieve not only complication of AFR form but also more accurate match between AFR form and power spectrum envelope form.

So, on example of oscillator with 2.5 degrees of freedom a possibility of synthesis of transistor chaotic oscillators with preassigned spectrum is confirmed.

V. CONCLUSIONS

In this paper the problem of preassigned chaotic power spectrum formation in oscillators based on the structure “transistor – passive quadripole closed in

feedback loop” is discussed.

On example of capacitive three-point circuit it is shown that in the oscillators with such structure it is possible to obtain power spectrum close to AFR of feedback loop.

The necessary requirements for forming the preassigned power spectrum in transistor oscillator are formulated.

On example of a model of oscillator with 2.5 degrees of freedom a possibility of synthesis of transistor chaotic oscillators with preassigned spectrum in agreement with described principles is demonstrated. As is shown, in this oscillator the chaotic power spectrum form can be close to the form of AFR of feedback loop. The spectrum smoothness can be controlled by means of varying the system parameter values finding from the two-parameter Lyapunov exponent diagram.

ACKNOWLEDGMENT

This report is supported in part by grants from Russian Foundation for Fundamental Research (No. 02-02-16802, 03-02-16747).

REFERENCES

- [1] Kosarev L., Halle K.S., Eckert K., Chua L. and Parlitz U. “Experimental demonstration of secure communications via chaotic synchronization”, *Int. J. Bifurcation and Chaos*, vol. 2, no. 3, pp. 709-713, 1992.
- [2] Cuomo K. and Oppenheim A. “Circuit implementation of synchronization chaos with applications to communications”, *Phys. Rev. Lett.*, vol. 71, no. 1, pp. 65-68, 1993.
- [3] Bel’skiy Yu.L. and Dmitriyev A.S. “Transmission of information by means of deterministic chaos”, *J. Comm. Technology and Electronics*, vol. 38, no. 15, pp. 1-5, 1993.
- [4] Bauer A., Kiliyas T., Schwarz W. “Chaotic bit stream generators for puls-stream radar application”, *Proc. of NDES-1997*, Moscow, pp. 410-415, 1997.
- [5] Kapranov M.V., Kuleshov V.N., Utkin G.M. “Oscillation theory in radio engineering”, M.: Science, 1984.
- [6] Dmitriev A. S., Panas A. I., Starkov S. O. “Ring oscillating systems and their application to the synthesis of chaos generators”, *Int. J. of Bifurcation and Chaos*. vol. 6, no. 5, pp. 851-865, 1996.
- [7] Kennedy M. “Chaos in Colpitts oscillator”, *IEEE Trans. Circ. Syst.-1*, vol. 41, no. 11, pp. 771-774, 1994.

- [8] Feo O., Maggio G. and Kennedy M. “The Colpitts oscillator: families of periodic solutions and their bifurcations”, *Int. J. Bifurcation and Chaos*, vol. 10, no. 5, pp. 935-958, 2000.

AMPLITUDE MODULATION AND DEMODULATION OF CHAOTIC CARRIERS

Alexander S. Dmitriev, Lev V. Kuzmin, Anton M. Laktushkin

Institute of Radio-Engineering and Electronics, Russian Academy of Sciences,
Mokhovaya St., 11-7, GSP-3, 125009, Moscow, Russia,
e-mail: chaos@mail.cplire.ru
WWW:<http://www.cplire.ru/html/InformChaosLab/index.htm>

Abstract – *In this paper the notion of amplitude modulation of chaotic signals is introduced, similar to amplitude modulation of harmonic signal. Necessary conditions for modulation and demodulation of chaotic carrier are discussed. In particular, the type of chaotic carrier is discussed from the point of view of optimal demodulation. Demodulation accuracy estimates are also presented.*

$[F_1, F_2]$. Next, let's introduce transformation of the chaotic signal $x(t)$, defined by

$$v(t) = m(t)x(t), \quad (1)$$

where $m(t) = m_0 i(t)$ for AM with suppression carrier or $m(t) = m_0 i(t) + 1$ for AM without suppression carrier, m_0 is a constant, and $i(t)$ is an information signal.

I. INTRODUCTION

At present much attention is devoted to application of chaotic signals in communications. In particular, it concerns the use of such signals as information carrier. As an example, the direct chaotic communication systems introduced in [1–3] can be considered. In those systems processes of generation, modulation and demodulation are performed in radio or microwave band. Different modulation schemes are introduced in [1]. In the simplest one, the symbol “1” is represented by chaotic radio pulse at a prescribed position and symbol “0” by void position. In the report a possibility of application of amplitude modulation (AM) [4] in the direct chaotic communication systems is considered. The above mentioned modulation scheme can be regarded as a special case of the amplitude modulation of chaotic signals, where the information signal is a sequence of video pulses.

Further we will see that under appropriate conditions the demodulation of signal $v(t)$ can be achieved. This fact allows us to define transformation (1) as an amplitude modulation of the chaotic carrier $x(t)$, similar to amplitude modulation of harmonic carrier. Moreover, AM of chaotic signal can be divided into AM with carrier suppression and without carrier suppression. Consider the spectral properties of $v(t)$. For that let us apply Fourier transform to (1). This yields the following expression

$$V(f) = M(f) \otimes X(f), \quad (2)$$

where $V(f)$, $M(f)$ and $X(f)$ are Fourier transforms of the signals $v(t)$, $m(t)$ and $x(t)$. Symbol \otimes means convolution.

It is shown in the report that some classical methods of amplitude modulation and demodulation can be applied to modulation and demodulation of the chaotic carriers.

Since the spectrum $X(f)$ of the chaotic signal $x(t)$ occupies frequency band $[-F_2, -F_1] \cup [F_1, F_2]$ and the spectrum $M(f)$ of signal $m(t)$ occupies frequency band $[-W, W]$, the spectrum $V(f)$ of the signal $v(t)$ occupies the frequency band $[-F_2 - W, -F_1 + W] \cup [F_1 - W, F_2 + W]$. Thus the positive frequency band occupied with the spectrum of the signal $v(t)$ can be represented as $[F_1 - W, F_2 + W]$. And the width of this band (ΔF) is represented by expression

III. AMPLITUDE MODULATION OF A CHAOTIC CARRIER

Let $x(t)$ be a passband signal, generated with some chaotic source, and occupy a frequency band

$$\Delta F = (F_2 - F_1) + 2W. \quad (3)$$

IV. DEMODULATION OF THE AMPLITUDE MODULATED CHAOTIC CARRIER

Let us evaluate a possibility of recovering information from the amplitude modulated chaotic signal. First, consider the case, when the receiver possesses an exact copy of the chaotic carrier generated in the transmitter. By analogy with a coherent receiver for amplitude modulated harmonic carrier, let us introduce a coherent receiver for amplitude modulated chaotic signal. This receiver consists of a multiplier and a low pass filter with the cut-off frequency W equal to the baseband width of some modulation signal $m(t)$ (see Fig. 1a).

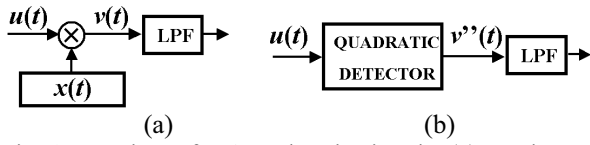


Fig. 1. Receivers for AM chaotic signals: (a) – coherent receiver; (b) – non-coherent receiver.

The multiplier performs multiplication of the modulated chaotic signal $v(t)$ by a copy of the chaotic signal $x(t)$, generated in the transmitter. The signal at the output of the multiplier can be represented as

$$v(t) = m(t)x^2(t) = m(t)[A + y_b(t) + y_p(t)], \quad (4)$$

where A is a constant, $y_b(t)$ is a component of $x^2(t)$ which occupies the frequency band $[-F_2 + F_1]U[F_2 - F_1]$; $y_p(t)$ – is a component of $x^2(t)$ which occupies the frequency band $[-2F_2, -2F_1]U[2F_1, 2F_2]$. Further we will consider the spectrum properties only for positive frequencies. Let us rewrite equation (4) as

$$v'(t) = m(t)A + m(t)y_b(t) + m(t)y_p(t). \quad (5)$$

First term in (5) is a useful signal; the second one is low-frequency disturbance, which occupies frequency band from zero up to $F_2 - F_1 + W$, and, finally the third term is a high-frequency disturbance. The use of low-pass filter after multiplier partially allows to eliminate the disturbances. To completely remove high-frequency disturbance the following condition for the cut-off filter frequency must be satisfied

$$W < F_1. \quad (6)$$

The low-frequency disturbance cannot be completely eliminated in general, but its influence can be adjusted by choosing the chaotic carrier type.

V. NON-COHERENT RECEIVER

A possible structure of non-coherent demodulator of chaotic signal is depicted in Fig. 1b and its structure is similar to the structure of non-coherent demodulator of harmonic carrier. Demodulator consists of an envelope detector (quadratic, for example) and a lowpass filter. If the modulated chaotic carrier (1) is fed to the input of quadratic envelope detector then the signal at the output will be

$$v''(t) = m^2(t)A + m^2(t)y_b(t) + m^2(t)y_p(t), \quad (7)$$

where A , $y_b(t)$, $y_p(t)$ are the same as in expression (4). We can see from (7) that similar to the non-coherent receiver of amplitude modulated harmonic carrier, for non-coherent receiver of amplitude modulated chaotic carrier the modulation must be without suppression of carrier. For modulation without suppression carrier the expression (7) can be rewritten as

$$\begin{aligned} v''(t) = & A + 2m_0Ai(t) + Ai^2(t) + \\ & (m_0^2i^2(t) + 2m_0i(t))y_b(t) + \\ & + (m_0^2i^2(t) + 2m_0i(t))y_p(t) \end{aligned} \quad (8)$$

In (8) the second term is proportional to the original information signal. The last term is the high frequency signal that can be removed by lowpass filter after envelope detector. The last term occupies frequency band (9)

$$[2F_1 - 2W, 2F_2 + 2W]. \quad (9)$$

To remove high-frequency signal, band (9) must not coincide with the low-pass filter frequency band, i.e.,

$$W < 2F_1 - 2W \text{ or } W < \frac{2}{3}F_1. \quad (10)$$

The third and fourth terms in (16) are low-frequency disturbance whose frequency band partially overlaps the frequency band of information signal. This disturbance cannot be eliminated completely by

filtering, so it corrupts information signal at the detector output. However, appropriate choice of chaotic carrier parameters can reduce the level of disturbance. In the next section we will consider the phase chaotic signal as a carrier, and we will show that disturbance can be rather low for such type of carrier.

VI. PHASE-CHAOTIC CARRIER

Let us define a phase-chaotic signal as a signal with chaotic phase $\varphi(t)$ defined by

$$x(t) = \cos(2\pi f_0 t + \alpha\varphi(t)), \quad (11)$$

where f_0 is the center of frequency band of $x(t)$. $\varphi(t)$ is a chaotic signal produced by a chaotic source, α is a constant parameter. It can be seen from (11) that the larger α the larger the amplitude of chaotic signal $\alpha\varphi(t)$, so it yields to spectrum spreading of $x(t)$. Otherwise, with decreasing α the spectrum of $x(t)$ becomes narrower and for $\alpha \Rightarrow 0$ $x(t)$ tends to harmonic signal.

Let for fixed α the spectrum of $x(t)$ occupy the band $[F_1, F_2]$. Consider signal $x^2(t)$:

$$x^2(t) = \frac{1}{2}[1 + \cos(4\pi f_0 t + 2\alpha\varphi(t))]. \quad (12)$$

If one substitutes $x(t)$ in (4) by (12), then $A = 0.5$, $y_b(t) = 0$, $y_p(t) = \frac{1}{2}\cos(4\pi f_0 t + 2\alpha\varphi(t))$. Therefore, for double-sideband amplitude modulation of $x(t)$ and for coherent receiver is zero $y_b(t) = 0$. So, it is possible to recover information (modulating) signal without disturbances by using proper lowpass filter. Consequently, the phase chaotic carrier can be regarded as the optimal carrier among all the chaotic carriers involved.

Let us analyze the signal structure at the output of the quadratic detector (7) for non-coherent demodulation of phase-chaotic carrier. Low-frequency disturbance is zero $y_b(t)=0$, as well as for coherent receiver. High-frequency disturbance $y_p(t)$ can be completely removed by low-pass filter. So, at the receiver output we have the signal

$$v'''(t) = Am^2(t). \quad (13)$$

Taking into account that modulation is without carrier suppression, we have

$$v'''(t) = A(1 + 2m_0 i(t) + m_0^2 i^2(t)). \quad (14)$$

Quadratic signal component occupies frequency band $[0, 2W]$, so we can await that the power of this component will be two times smaller after low-pass filter with cut-off frequency W . Therefore, the power ratio of information signal $P_s \sim \overline{(2mi(t))^2}$ and disturbance quadratic signal $P_d \sim \frac{1}{2}\overline{(m^2 i^2(t))^2}$ is described by

$$10\lg(P_s / P_d) = 10\lg(8m_0^{-2}) \text{ [dB]}, \quad (15)$$

where it is implied that $\overline{i^2(t)} = 1$ and $\overline{i(t)} = 0$. From (15) we can see that the quality of recovered information signal at the receiver output becomes worse with increasing modulation depth m_0 .

VII. NUMERICAL SIMULATION

Numerical simulation of demodulation of phase chaotic carrier has been carried out to evaluate the quality of the recovered information signal at the receiver. The modulating (information) signal is lowpass. Both coherent and non-coherent receivers are considered. For evaluation of signal quality we introduce the signal to disturbance ratio (S/D) defined by

$$S / D = 10\lg(P_s / P_d), \quad (16)$$

where P_s is the power of information signal $i(t)$, P_d is the power of the difference between original information signal $i(t)$ and the evaluated signal $i'(t)$ at the receiver output. All frequencies were scaled to 1 (Nyquist frequency). Numerical simulation consists of two stages.

At the first stage, the double sideband modulation of phase-chaotic carrier with coherent receiver was investigated. Influence of information signal bandwidth W and parameters of phase-chaotic carrier on quality of demodulated signal were analyzed. Spectrums of information signal, chaotic carrier and modulated chaotic carrier and corresponding waveforms are depicted in Fig. 2. It was shown that when frequency bands corresponding to the modulating signal and the chaotic carrier do not overlap, i.e.

when condition (10) is fulfilled, the quality of demodulated signal is rather high ($S/D \approx 77$ dB, Fig. 2). If condition (10) is broken the quality of demodulated signal is rather low ($S/D \approx 15$ dB).

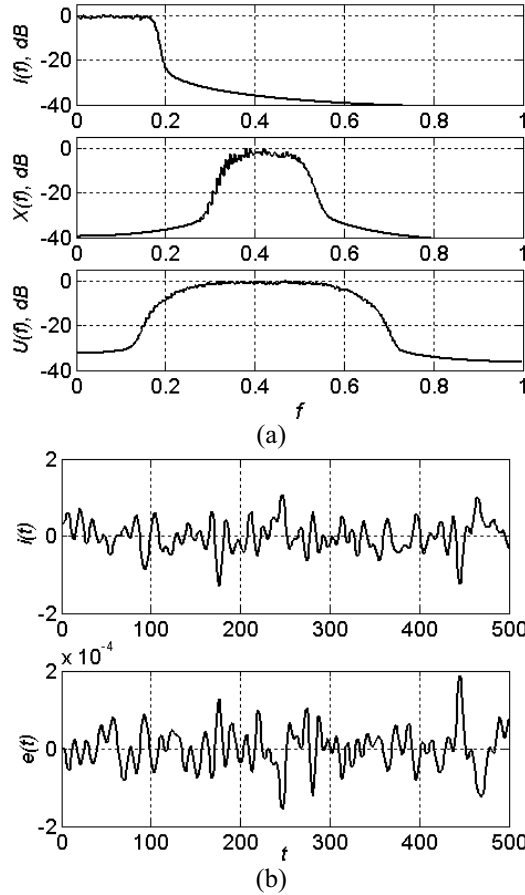


Fig. 2. Simulation results under conditions $W=0.18$, $F_1=0.33$, $F_2=0.53$: (a) – spectrums of information, chaotic and modulated chaotic signal; (b) – original information signal $i(t)$ and error signal $e(t)$.

At the second stage the double sideband modulation with non-coherent receiver was investigated for different modulation depth m_0 and bandwidth W , F_1 , F_2 . Simulation results of the quality of demodulated signal as a function of modulator parameters are depicted in Fig. 3, where the S/D vs bandwidth W for different modulation depth m is plotted. One can see that disturbance of demodulated signal decreases with decreasing modulation depth. This fact qualitatively agrees with expression (15) that also points at increasing quality of demodulated signal out with decreasing modulation depth. However, it is necessary to take into account that the presence of noise does not allow to make the value of modulation depth arbitrarily small because it yields increase of noise power at the output of the receiver, so the

compromise value of modulation depth must be chosen.

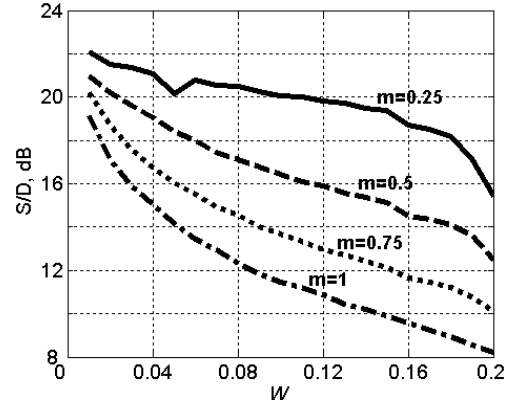


Fig. 3. S/D ratio vs information signal bandwidth W , for different m_0 and $F_1=0.33$, $F_2=0.53$.

VIII. CONCLUSION

The method of amplitude modulation of chaotic carrier is proposed. It was shown that quality of demodulated signal depends on parameters of modulation-demodulation scheme and on type of chaotic carrier. In particular it was shown that the use of phase-chaotic signal and coherent receiver gives rather high quality of demodulated signal. This fact allows us to conclude about potential applicability of amplitude modulation of chaotic carrier for direct chaotic communication systems.

This report is supported by a grant from Russian Foundation for Fundamental Research (No. 02-02-16802). The authors wish to thank Dr. Yu.V. Andreev for many suggestions and comments concerning analysis of the problem.

REFERENCES

- [1] Dmitriev A., Kyarginsky B., Panas A., Starkov S. "Direct chaotic communication scheme at microwave frequencies", *J. of Communications Technology and Electronics*, v. 46, no. 2, pp. 207-214, 2001.
- [2] Dmitriev A., Kyarginsky B., Panas A and Starkov S., "Direct chaotic communication system. Experiment", *Proc. of NDES'2001*, Delft, Netherlands, pp. 157-160, 2001.
- [3] Dmitriev A., Panas A. and Starkov S., "Direct chaotic communication in microwave band", *Electronic Nonlinear Science Preprint*, nlin.CD/0110047.
- [4] Franks L. E., *Signal Theory*, Englewood Cliffs, New Jersey, Prentice-Hall (1969).

BIFURCATIONS ASSOCIATED WITH THE FITZHUGH-NAGUMO SYSTEMS

Jorge Duarte, Luís Silva and J. Sousa Ramos

Departamento de Engenharia Química, Secção de Matemática,
Instituto Superior de Engenharia de Lisboa, Rua Conselheiro Emídio Navarro 1, 1949-014 Lisboa,
Portugal

e-mail: `jduarte@deq.isel.ipl.pt`
Departamento de Matemática, Universidade de Évora
Rua Romão Ramalho, 59, 7000-671 Évora, Portugal
e-mail: `lfs@uevora.pt`

Departamento de Matemática, Instituto Superior Técnico, Av. Rovisco Pais, 1
1049-001 Lisboa, Portugal
e-mail: `sramos@math.ist.utl.pt`

Abstract—*The Fitzhugh-Nagumo-like systems are well-known in physiology and they contributed enormously to the formation of a new field of applied mathematics, the study of excitable systems. Our work provides a study of some bifurcations associated with canonical return maps for a Fitzhugh-Nagumo system. We characterize the dynamics, in particular some routes to chaos, in special regions of the parameter space.*

I. INTRODUCTION

The present paper analyses a piecewise-linear Fitzhugh-Nagumo system depending on three real parameters A , θ and T .

The Fitzhugh-Nagumo model governs the initiation of the nerve impulse and can be derived from a simplified model of the cell membrane. Here the cell consists of three components: a capacitor representing the membrane capacitance, a current-voltage device for the fast current, and a resistor, inductor and battery in series for the recovery current. In the 1960s Nagumo, a Japanese electrical engineer, built this circuit using a tunnel diode ([1]), thereby attaching his name to the system.

The presence of the three parameters leads to a large variety of dynamics, each of them responsible for a specific physiological function. For physiologists it is highly desirable to have a global view of all possible qualitatively distinct responses of the Fitzhugh-Nagumo model for several values of the parameters. This reduces to the knowledge of the bifurcation diagram.

Our goal in this paper is to use the bifurcation theory to characterize the dynamics of a special type of

return maps for a singular system.

II. DESCRIPTION OF THE MODEL

The model is a planar piecewise linear system for which the equations are given by

$$\begin{cases} \epsilon \frac{dv}{dt} = f(v) - w + \psi(t) & \equiv F(v, w, t) \\ \frac{dw}{dt} = v - \delta w & \equiv G(v, w) \end{cases} \quad (1)$$

Here $f : \mathbb{R} \rightarrow \mathbb{R}$ is the continuous, piecewise linear function defined by

$$f(v) = \begin{cases} -\alpha_1 v + \gamma_1 & \text{for } v < v_l \\ \alpha_2 v - \gamma_2 & \text{for } v_l \leq v < v_r \\ -\alpha_3 v + \gamma_3 & \text{for } v \geq v_r \end{cases}$$

where α_i and γ_i , $i = 1, 2, 3$, are fixed positive constants and $0 < v_l < v_r$. Without loss of generality we assume that $\gamma_1 = 0$. The forcing function $\psi : \mathbb{R} \rightarrow \mathbb{R}$ is a piecewise constant periodic function of period T , defined by

$$\psi(t) = \begin{cases} 0 & \text{for } mT \leq t < (m + \theta)T \\ A & \text{for } (m + \theta)T \leq t < (m + 1)T \end{cases} \\ m = 0, \pm 1, \pm 2, \dots$$

where $A > 0$ and $\theta \in [0, 1]$. In the context of biophysical models of excitable membranes, this forcing corresponds to injection of a depolarizing current during a fraction $(1 - \theta)T$ of each cycle. The dynamical variables of the Fitzhugh-Nagumo model are v and w . The variable v represents the voltage and is called the excitation variable, while variable w is called the recovery variable. We assume that ϵ is very small. The assumption $\epsilon \ll 1$ often appear in the literature in the form $\epsilon \rightarrow 0$. Since the small parameter multiplies

the derivative $\frac{dw}{dt}$, the system is called singularly perturbed. Figure 1 shows the nullclines of the system (1).

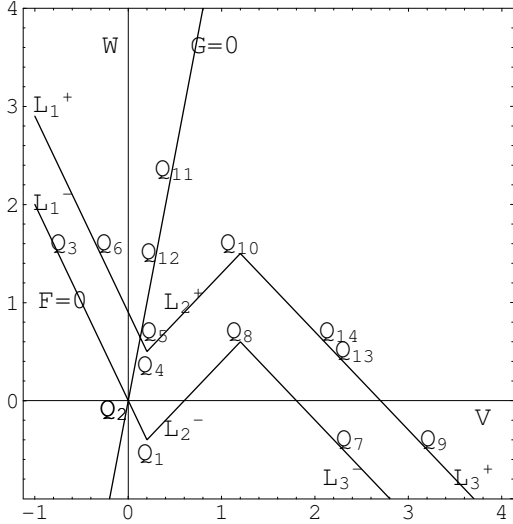


Fig. 1. A schematic of the nullclines of (1). The coordinates for the standard values of the parameters are $\alpha_1 = 2, \alpha_2 = \alpha_3 = 1, \gamma_2 = 0.6$ and $\gamma_3 = 1.8$. For these parameters $A_1 = 0.4, A_2 = 0.8, A_3 = 1.8, v_l = 0.2$ and $v_r = 1.2$.

As Othmer and Watanabe showed in [2], in the singular limit $\epsilon = 0$, the system (1) reduces to

$$\frac{dw}{dt} = \begin{cases} -\lambda_i(w - w_i^*) & , (v, w) \in L_i^- \\ -\lambda_i(w - (w_i^* + A_i^*)) & , (v, w) \in L_i^+ \end{cases} \quad (2)$$

where $w_i^* \equiv \frac{\gamma_i}{1 + \delta\alpha_i}$ and $A_i^* \equiv \frac{A}{1 + \delta\alpha_i}, i = 1, 3$.

The w_i^* (resp., $w_i^* + A_i^*$) are the w -coordinates of the rest points (resp., virtual rest points, i.e., the intersection of the extension of L_i^\pm with $G = 0$). We have $w_1^* = 0, w_1^* + A_1^* = W_5, w_3^* = W_{12}, w_3^* + A_3^* = W_{11}$. Note that solutions are constrained to the lines L_i^\pm when $\epsilon = 0$.

III. DISCRETE DYNAMICS. BIFURCATIONS AND ROUTES TO CHAOS

Maps from an interval to itself provide a simple and helpful context, which allow us to study interesting properties of several dynamical systems. As in [2] and [3], we shall use a map derived from the singular system. In order to facilitate comparison of return maps

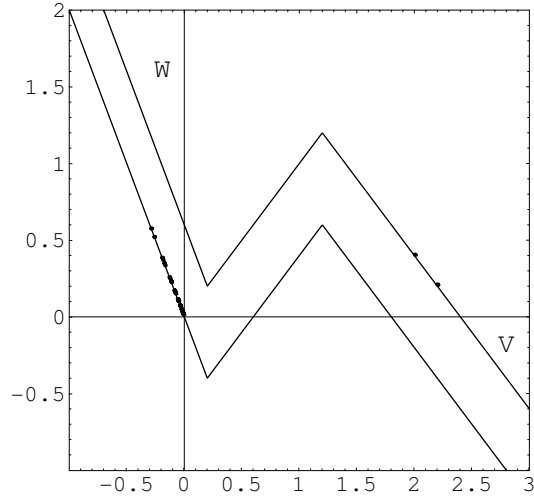


Fig. 2. Solution of (2) in phase plane for $(A, \theta, T) = (0.6, 0.4, 4.0)$.

for different combinations of the parameters A, θ and T , we map the w -coordinate into the unit interval via transformation

$$x_n = \begin{cases} \frac{w}{W_8 + W_{10}} & \text{if } (v, w) \in L_1^-, w \geq 0 \\ 1 - \frac{w}{W_8 + W_{10}} & \text{if } (v, w) \in L_3^-, w \geq 0 \end{cases}$$

The 3-parameters family of return maps are obtained by numerically computing the trajectories of 5000 points in $(0, 1)$ for one period of the forcing. By a period one (or return map) we mean a map from the unit interval to itself that maps a point into its image after time T (one cycle of the forcing). The interval $(0, 1)$ decomposes into a disjoint union of characteristic intervals. (See [2] and [3] for more details). We can gain some qualitative insights by studying representative return maps that arise for several parameters values. If we consider the invariant regions of the return maps for special values of the parameters, we find that we can have one of the following three types of canonical maps which arise when $0.8 < A \leq 1.8$:

- *Type A* maps - this family has three branches and two turning points,
- *Type B* maps - this family has four branches and three turning points,
- *Type C* maps - this family has two branches and one turning point.

In this paper we restricted our attention to *Type A* maps (quoted as $f_{A,\theta,T}$), which have three branches and two turning points (Fig.3).

The maps can display various qualitative types of behavior for different values of the parameters A, θ and T : steady states, periodic cycles of differ-

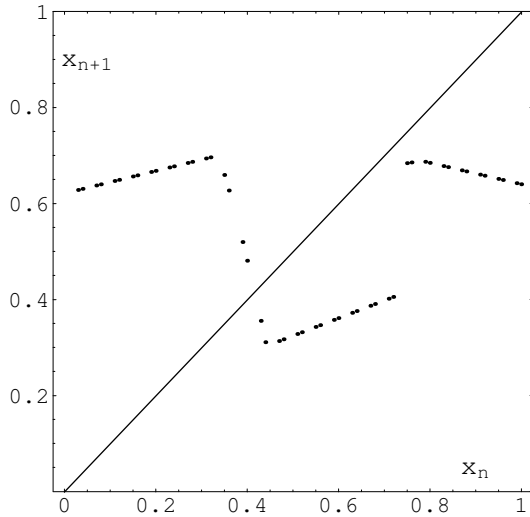


Fig. 3. The computed return map for $(A, \theta, T) = (1.1, 0.1, 1)$

ent lengths and chaos. The changes from one form of qualitative behavior to another as a parameter is changed are called bifurcations, and the parameter values at which they occur are called bifurcation points. An important goal in studying the return maps is to understand the bifurcations that can appear for several values of the parameters. Instead of formulating general statements at this point, we are going to discuss explicit cases, which occur in the model. We consider the dynamics for small fixed θ and variable T . To see the long term behavior for all values of $T \in (0.2, 1.25)$ at once we plot the orbit diagram, which show only the attractive orbits. Figure 4 plots the system's attractor as a function of the period for $A = 1.1$. We fix θ at 0.1 and we iterate the return map from a single point 2000 times and plot the last 100 iterates.

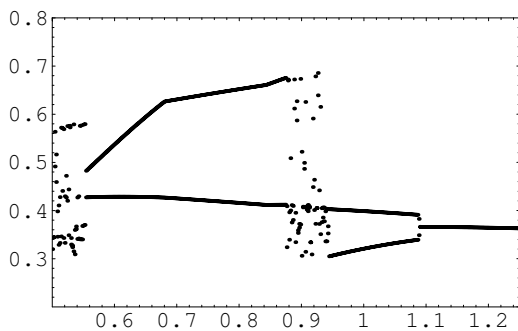


Fig. 4. Images under the return map of the initial point $x_0 = 0.5$ versus the period T for $\theta = 0.1$ and $A = 1.1$. The initial point is iterated 2000 times and the last 100 iterates are plotted for each period in this figure.

When the parameter θ and A are fixed and the period T is increased, the slope of the middle branch becomes steeper while the other two pieces become flatter.

The last numerical results raise many important questions. We attempt to identify types of bifurcations that can occur for several values of the parameters when T decreases from 1.25 to 0.2. Since the family of return maps is obtained by numerically computing the trajectories of a certain number of points in $(0, 1)$, we must rely on graphical and numerical arguments to elucidate the qualitative behavior. The analytical methods don't work in this context.

Firstly, amongst the bifurcations of *Type A* maps, we quote two types of bifurcations that occur when T decreases from 1.25 to 0.2: period-doubling bifurcation (for instance at $T \sim 1.094$) and saddle-node bifurcation, which explains the birth of a periodic cycle at $T \sim 0.874$. These maps don't undergo a succession of period-doubling bifurcations which lead to chaos. We don't have a period-doubling cascade in periodic windows like in the family of quadratic maps $ax(1 - x)$. The *Type A* maps are continuous and piecewise differentiable. (the derivative doesn't exist at the turning points).

In the study of *Type A* maps, we identified bifurcations that don't occur in the bifurcation sequence for the family of quadratic maps. To describe these bifurcations we start our analysis at $T = 1.0$, where the attractor is a period-4 cycle, as indicated by the four branches (Fig. 4) We analyse the stability of a cycle reducing the problem to a question about the stability of a fixed point, as follows. The graph of a fourth-iterate (Fig. 5) map provides sufficient insight about the stability of the period-4 cycle.

The four fixed points at which the slope of the map has absolute value less than 1 corresponds to a stable period-4 cycle. In contrast, the slope exceeds 1 in the remaining fixed points (one period-1 cycle and one period-2 cycle).

Figure 6 shows a partial bifurcation diagram of the *Type A* return maps.

As T decreases, a pair of repulsive orbits are created at $T \sim t_2$. The graph of the fourth-iterate map is helpful to understand the birth of these orbits.

In order to facilitate the analysis about the stability of the fixed points, we present figures 7 and 8 which represent the slopes of the return map at these points when $T \sim t_2$ and $T \sim t_1$, respectively.

Therefore we emphasize the creation of pairs of repulsive orbits at $T \sim t_2$ and the occurrence of a in-

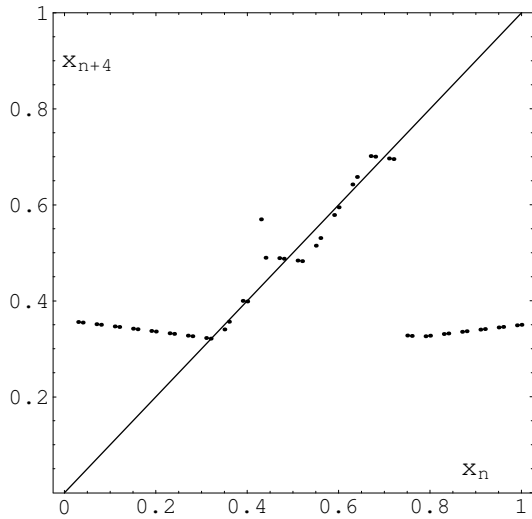


Fig. 5. The fourth-iterate map for $(A, \theta, T) = (1.1, 0.1, 1)$.

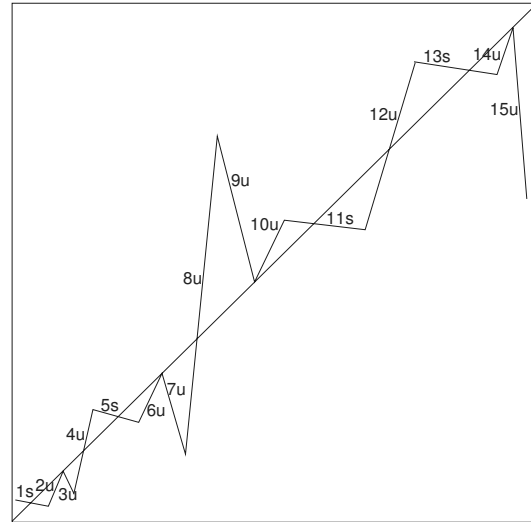


Fig. 7. Representation of the slopes of the fourth-iterate map at the fixed points when $T \sim t_2$.

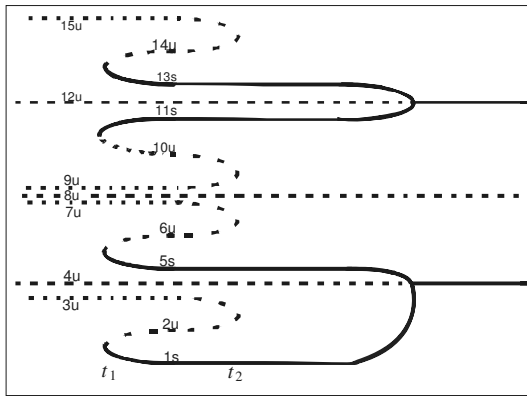


Fig. 6. Sketch (not to scale) of the bifurcation diagram of the *Type A* maps for $A = 1.1, \theta = 0.1$ and $T \in (\sim 0.94, \sim 1.25)$. There are two special values of T , which are $t_1 = 0.942318$ and $t_2 = 0.94883$.

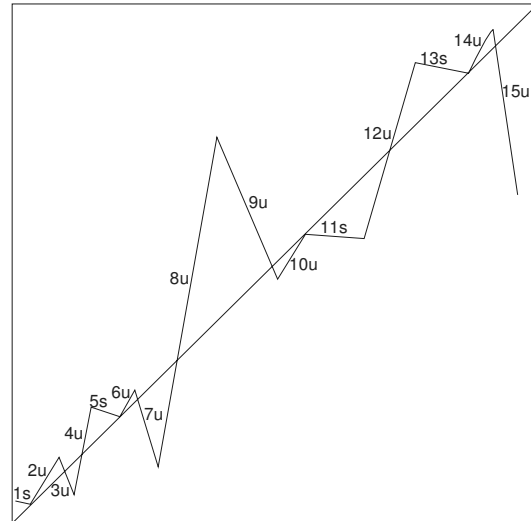


Fig. 8. Representation of the slopes of the fourth-iterate map at the fixed points when $T \sim t_1$.

verted saddle-node bifurcation at $T \sim t_1$, that is, the destruction of pairs stable-unstable orbits. It's interesting to notice that all these types of bifurcations are independent of the parameters. Indeed, they occur when we plot the system's attractor as a function of A and as a function of θ .

Regarding the previous description, we derive our main result

Theorem 1: Let $f_{A,\theta,T}$ be the three parameters family of canonical return maps of Type A. Then we have the occurrence of four types of bifurcations: period doubling bifurcation, saddle-node bifurcation, saddle-node inverted bifurcation and a non standard bifurcation (creation of a pair of unstable orbits).

REFERENCES

- [1] J. Nagumo, S. Arimoto and S. Yoshizawa, An active pulse transmission line simulating nerve axon, *Proc. IRE.50*, pp. 2061-2070, 1964.
- [2] H. G. Othmer and M. Watanabe, Resonance in excitable systems under step function forcing. I Harmonic solutions, *Adv. in Math. and Sci. Applics.* **4**, pp.399-441, 1994.
- [3] H. G. Othmer, M. Watanabe and M. Xie, Resonance in excitable systems under step function forcing. II. Subharmonic solutions and persistence, *Physica D* **98**, 75-110, 1996.
- [4] J. Duarte and J. Sousa Ramos, Topological entropy as a measure of chaos in forced excitable systems, *International Journal of Pure and Applied Mathematics*, Vol. 4, 2, pp. 165-181, 2003.

Application of State-Space Transformations to the Noise Analysis of Oscillators

Thomas Falk, Wolfgang Schwarz

Technical University Dresden, Institute for Basics of Electrical Engineering and Electronics
 Mommsenstr. 13, 01062 Dresden, Germany
 e-mail: falk@iee.et.tu-dresden.de

Abstract — *In this paper we use a state-space transformation to simplify the tangential system of an oscillator. The resulting system consists of two static, time varying maps and a decoupled LTI system. The structure of the transformed system is used to simplify the noise analysis of the oscillator.*

I. INTRODUCTION

Oscillators have a key function for the realisation of modern communication systems. Thus there is still a great interest in the analysis of oscillators. A lot of empirical articles can be found in the literature from the last 50 years (e.g. [8], [6]) and also rigorous analyses leading to numerical algorithms (e.g. [4], [3]).

The analysis of the influence of perturbations on an oscillator can be done by the analysis of its tangential system. Unfortunately most tools for the small signal analysis of nonlinear systems are difficult to apply to oscillators. Although there are generalisations of the transfer functions for LTV systems (e.g.[10]), an approach which would be comparable in ease of use to the algorithms in the analysis of LTI-systems does not exist. Due to this difficulties most of the analyses of oscillators are normally done numerically [7], [4], [3].

In this paper we describe an approach to the analysis of oscillators, which uses Lyapunov transformations to simplify the tangential system of the oscillator. This transformation will lead to an natural definition of phase noise and amplitude noise corresponding to [7] and yields a decomposition of the LTV system into one describing the evolution of the phase deviation of the oscillator and another one for the amplitude deviation. An example will conclude the paper.

II. THE OSCILLATOR AND ITS LTV SYSTEM

A n -dimensional oscillator is described by its state space equations¹

$$\dot{\mathbf{x}} = f(\mathbf{x}) + \boldsymbol{\xi} \quad (1)$$

where \mathbf{x} is the state and $\boldsymbol{\xi}$ describes the perturbation e.g. by noise of the active circuit elements. The system (1) has the homogeneous solution \mathbf{x}_0 for $\boldsymbol{\xi} = 0$ with the period T : $\mathbf{x}_0(t) = \mathbf{x}_0(t + T)$.

A perturbation of the oscillator results into a deviation $\Delta\mathbf{x}$ from the limit cycle \mathbf{x}_0 and a phase shift τ on the limit cycle. Thus an ansatz [7] for the solution of (1) is

$$\mathbf{x}(t) = \mathbf{x}_0(t + \tau(t)) + \Delta\mathbf{x}(t) \quad (2)$$

The behaviour for small signal perturbations by \mathbf{b} is described by the tangential system of (1):

$$\dot{\mathbf{u}} = \mathbf{A}(\mathbf{x}) \mathbf{u} + \boldsymbol{\xi} \quad \text{with} \quad \mathbf{A}(\mathbf{x}) = \frac{\partial f_i(\mathbf{x})}{\partial x_j} \quad (3)$$

For $\boldsymbol{\xi} = 0$ this tangential system has a stationary solution $\mathbf{u}_s(t) = \dot{\mathbf{x}}(t)$, corresponding to the Floquet exponent $\lambda_1 = 0$. All other Floquet exponents λ_i are smaller than zero, if the system (1) has a stable periodic solution \mathbf{x}_0 .

The general homogeneous solution of (3) for $\boldsymbol{\xi} = 0$ has the form:

$$\mathbf{u}(t) = \sum_{i=1}^n c_i \mathbf{u}_i(t) = \sum_{i=1}^n c_i \mathbf{l}_i(t) e^{\lambda_i t} \quad (4)$$

where the $\mathbf{l}(t)$ are periodic functions with the period T , also called Floquet functions. With $\mathbf{u}_n = \mathbf{u}_s = \dot{\mathbf{x}}_0$ this has the form

$$\mathbf{u}(t) = c_n \dot{\mathbf{x}}_0(t) + \sum_{i=1}^{n-1} c_i \mathbf{l}_i(t) e^{\lambda_i t} \quad (5)$$

¹Note that this system is an simplified model. The perturbation process $\boldsymbol{\xi}$ depends in general on \mathbf{x} .

III. TRANSFORMATION OF THE TANGENTIAL SYSTEM

In order to simplify the tangential system (3), it can be transformed by a suitable Lyapunov transformation $\mathbf{T}(t)$ [9]:

$$\mathbf{u} = \mathbf{T}\mathbf{v} \quad \text{and} \quad \mathbf{v} = \mathbf{T}^{-1}\mathbf{u}. \quad (6)$$

The transformed system has then the form

$$\dot{\mathbf{v}} = \mathbf{B}\mathbf{v} + \mathbf{T}^{-1}\boldsymbol{\xi} \quad \text{with} \quad \mathbf{B} = \mathbf{T}^{-1}(\mathbf{A}\mathbf{T} - \dot{\mathbf{T}}) \quad (7)$$

This system has the same stability properties as the original one (3), in the sense that both systems have the same Floquet exponents [1]. Note that the perturbation vector $\boldsymbol{\xi}$ is transformed by the time varying transformation \mathbf{T}^{-1} and thus gets modulated.

A. Transformation to a LTI System

The transformation \mathbf{T} can be chosen freely, as long its inverse \mathbf{T}^{-1} exists. If all the Floquet vectors \mathbf{l} in (4) are known, the transformation \mathbf{T} can be constructed by using the Floquet vectors in the columns of the matrix $\mathbf{T} = (\mathbf{l}_1, \dots, \mathbf{l}_n)$ [5]. The resulting system matrix \mathbf{B} is then a diagonal matrix:

$$\mathbf{B} = \begin{pmatrix} \lambda_1 & \cdots & 0 \\ \vdots & \ddots & \vdots \\ 0 & \cdots & \lambda_n \end{pmatrix} \quad (8)$$

and the system (3) decomposes into n independent one-dimensional differential equations:

$$\dot{v}_i = \lambda_i v_i + \sum_{j=0}^n \mathbf{T}_{ij}^{-1} \boldsymbol{\xi}_j \quad (9)$$

The structure of a transformed system is shown in Fig. 2 for the example discussed in section V.

Unfortunately in general only one vector of the \mathbf{l}_i is known. In this case only an incomplete transformation can be done as described in the following.

B. Incomplete Transformation

The term *incomplete* refers here to the not complete diagonalisation of the tangential system if only the one known vector $\mathbf{l}_n = \dot{\mathbf{x}}_0$ can be used for the transformation.

If for one column of \mathbf{T} the known solution \mathbf{x}_0 of (3) is used and the other ones are chosen arbitrary

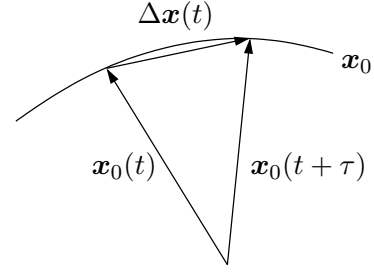


Fig. 1. Relation between the v_n and the phase shift of the oscillator

[5], i.e. $\mathbf{T} = (\mathbf{t}_1, \dots, \mathbf{t}_{n-1}, \mathbf{x}_0)$, the new system matrix \mathbf{B} has the following structure:

$$\mathbf{B} = \begin{pmatrix} b_{1,1} & \cdots & b_{1,n-1} & 0 \\ \vdots & \ddots & \vdots & \vdots \\ b_{n-1,1} & \cdots & b_{n-1,n-1} & 0 \\ b_{n,1} & \cdots & b_{n,n-1} & 0 \end{pmatrix} = \left(\begin{array}{c|c} \mathbf{B}' & 0 \\ \hline \mathbf{b}' & 0 \end{array} \right) \quad (10)$$

and the resulting transformed system is

$$\begin{aligned} \dot{\mathbf{v}}' &= \mathbf{B}'\mathbf{v}' + (\mathbf{T}^{-1})' \boldsymbol{\xi} \\ \dot{v}_n &= \mathbf{b}'\mathbf{v}' + \sum_{i=0}^n \mathbf{T}_{ni}^{-1} \boldsymbol{\xi}_i \end{aligned} \quad (11)$$

where $(\mathbf{T}^{-1})'$ is the matrix \mathbf{T}^{-1} without its last row. Thus evolution of the variables v_1 to v_{n-1} is described by a $n - 1$ -dimensional differential equation system while the variable v_n depends on a weighted sum of the other variables, but it has no feedback to them.

IV. TRANSVERSAL PROCESS AND TANGENTIAL PROCESS OF AN OSCILLATOR

After one of the above transformations the variable v_n relates to the length of a tangential vector in the original system (1). Thus it corresponds to a phase shift τ of the reference trajectory $\mathbf{x}_0(t+\tau)$ (see also Fig. 1):

$$\tau(t) \approx \frac{v_n(t)}{|\dot{\mathbf{x}}_0(t)|} \quad (12)$$

The other variables form a vector describing the transversal deviation from the reference trajectory.

To keep things simple, in the following we will assume that a transformation to a LTI system was possible and that the oscillator is two-dimensional, i.e. $n = 2$. Then the perturbation signal $\boldsymbol{\xi}$ gets transformed by a structure as shown in Fig. 2. There are several points to notice:

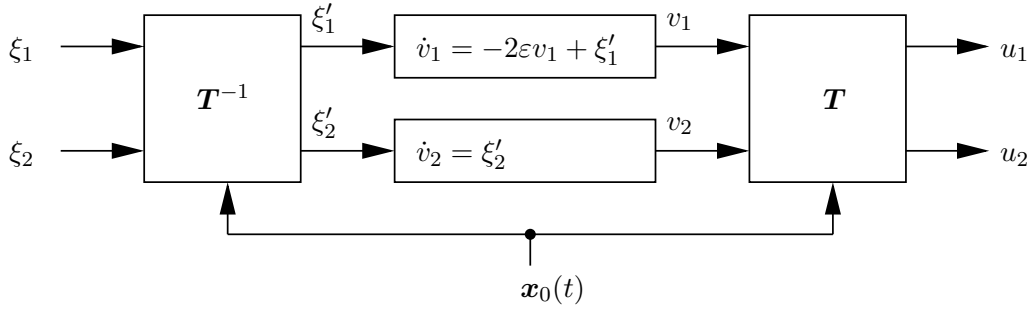


Fig. 2. Transformations and variables in the example

- The noise gets transformed by two time varying maps and one LTI filter.
- The evolution of each state variable v_i is described by a differential equation of first order with a constant coefficient corresponding to the Floquet exponent.
- If there are two oscillators with the same Floquet exponents, their noise behaviour is different only by the transformation \mathbf{T} and its inverse, which modulates the input noise.

This structure allows a step-by-step calculation of the stochastic characteristics at the output. We will give equations for the variance of the processes in the following. It is assumed, that the perturbation process $\boldsymbol{\xi}$ consists of n independent white noise processes with normal distribution.

Even if the input noise $\boldsymbol{\xi}$ is assumed to be a stationary process, the input $\boldsymbol{\xi}'$ to the transformed system is in general an cyclo-stationary process modulated by the transformation:

$$\boldsymbol{\xi}' = \mathbf{T}(t) \boldsymbol{\xi} \quad (13)$$

Its variance $\sigma_{\boldsymbol{\xi}'}^2$ is

$$\sigma_{\boldsymbol{\xi}'}^2 = (\mathbf{T}^{-1})^{(2)} \sigma_{\boldsymbol{\xi}}^2 \quad (14)$$

where $\mathbf{M}^{(2)}$ a matrix with each element squared.

A. Transversal Process

In a two-dimensional oscillator the variable v_1 is a direct measure for the deviation from the limit cycle of the oscillator. Its evolution is according to Eq. (9) determined by a LTI-filter of first order:

$$\dot{v}_1 = \lambda_1 v_1 + \sum_{i=1}^2 \mathbf{T}_{1i}^{-1} \xi_i \quad (15)$$

The variance of v_1 is

$$\sigma_{v_1}^2(t) = e^{-2\epsilon t} \int_0^t \sigma_{\xi'_1}^2(\eta) e^{2\epsilon\eta} d\eta. \quad (16)$$

The value of v_1 corresponds to the length of a deviation vector in the direction of \mathbf{l}_1 . Thus the vector $\Delta\mathbf{x}$ in (2) is

$$\Delta\mathbf{x}(t) = v_1(t)\mathbf{l}_1(t) \quad (17)$$

with the stochastic properties determined by v_1 . This corresponds to an amplitude modulation of the carrier \mathbf{l}_1 by v_1 .

B. Tangential Process

The absolute value v_2 of the tangential deviation results from the integration of the transformed perturbation $\boldsymbol{\xi}'$:

$$\dot{v}_2 = \sum_{i=1}^2 \mathbf{T}_{2i}^{-1} \xi_i. \quad (18)$$

The integration of the cyclo-stationary process $\boldsymbol{\xi}'$ results into a process with monotonic increasing variance:

$$\sigma_{v_2}^2(t) = \int_0^t \sigma_{\xi'_2}^2(\eta) d\eta \quad (19)$$

By (12) v_2 is directly connected with the phase deviation of the oscillator. Thus the reference signal \mathbf{x}_0 gets phase modulated by v_2 or respectively frequency modulated by ξ'_2 .

V. EXAMPLE

In this example we will discuss an oscillator which is given by the differential equation system

$$\begin{aligned} \dot{x}_1 &= x_2 + \epsilon(1 - x_1^2 - x_2^2)x_1 + \xi_1(t) \\ \dot{x}_2 &= -x_1 + \epsilon(1 - x_1^2 - x_2^2)x_2 + \xi_2(t) \end{aligned} \quad (20)$$

This system has the stationary solution \mathbf{x}_0 für $\xi_i(t) = 0$

$$x_{10}(t) = \sin(t) \quad x_{20}(t) = \cos(t). \quad (21)$$

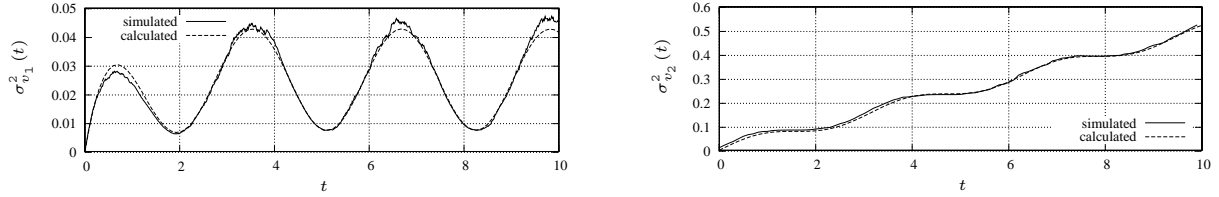


Fig. 3. Evolution of the transversal (left) and the tangential (right) processes variance

independent off the parameter $\varepsilon > 0$. The homogeneous tangential system is

$$\dot{\mathbf{u}} = \left[\begin{pmatrix} -\varepsilon & 1 \\ -1 & -\varepsilon \end{pmatrix} + \varepsilon \begin{pmatrix} \cos(2t) & -\sin(2t) \\ -\sin(2t) & -\cos(2t) \end{pmatrix} \right] \mathbf{u}. \quad (22)$$

The transformation \mathbf{T} has the form

$$\mathbf{T}(t) = \begin{pmatrix} x_1(t) & \dot{x}_1(t) \\ x_2(t) & \dot{x}_2(t) \end{pmatrix} = \begin{pmatrix} \sin(t) & \cos(t) \\ \cos(t) & -\sin(t) \end{pmatrix} \quad (23)$$

and leads to the system

$$\dot{\mathbf{v}} = \begin{pmatrix} -2\varepsilon & 0 \\ 0 & 0 \end{pmatrix} \mathbf{v}. \quad (24)$$

which in this case has a very simple structure. The structure of the system after its transformation is shown in Fig. 2.

The variance of the transversal part converges for large t to

$$\sigma_{v_1}^2(t) = \frac{1}{8\varepsilon} (\sigma_{\xi_1}^2 + \sigma_{\xi_2}^2) + \frac{2\varepsilon \cos(2t) + \sin(2t)}{4(1 + 4\varepsilon^2)} (\sigma_{\xi_2}^2 - \sigma_{\xi_1}^2) \quad (25)$$

and the variance of the tangential part is

$$\sigma_{v_2}^2(t) = \frac{t}{2} (\sigma_{\xi_1}^2 + \sigma_{\xi_2}^2) + \frac{1}{4} \sin(2t) (\sigma_{\xi_1}^2 - \sigma_{\xi_2}^2) \quad (26)$$

as shown in Fig. 3. If the input variances are equal, i.e. $\sigma_{\xi_1}^2 = \sigma_{\xi_2}^2 = \sigma_{\xi}^2$ the terms for the variances reduce to

$$\sigma_{v_1}^2(t) = \frac{\sigma_{\xi}^2}{4\varepsilon} \quad (27)$$

and

$$\sigma_{v_2}^2(t) = \sigma_{\xi}^2 t \quad (28)$$

It can be seen, that the transversal process is (cyclo-)stationary while the tangential process is non-stationary with monotonic increasing variance.

From the corresponding correlation functions the spectra of the oscillator signal $\mathbf{x}(t)$ can be calculated [2].

A similar system has been analysed in [5], which does not decompose into independent LTI differential equations. Thus the analysis is more complicated, but the structure of the decomposition of the tangential system remains the same if the Floquet vectors are used.

VI. CONCLUSIONS

Lyapunov state space transformations have been used for the analysis of the noise behaviour of oscillators. These transformations yield especially in the case of two dimensional oscillators a simple model for understanding the signal transforming in the oscillator leading to phase and amplitude noise.

REFERENCES

- [1] L. Ya. Adrianova. *Introduction to Linear Systems of Differential Equations*. Translation of Mathematical Monographs. American Mathematical Society, 1991.
- [2] Leon W. Couch. *Digital and Analog Communication Systems*. Prentice Hall, 2000.
- [3] Alper Demir, Amit Mehrotra, and Jaijeet Roychowdhury. Phase noise in oscillators: A unifying theory and numerical methods for characterisation. *IEEE Trans.*, 47(5):655–673, May 2000.
- [4] Alper Demir and Alberto Sangiovanni-Vincentelli. *Analysis and Simulation of Noise in nonlinear electronic Circuits and Systems*. Kluwer Academic Publishers, 1998.
- [5] Thomas Falk and Wolfgang Schwarz. An explicit formulation of the sensitivity function of two-dimensional oscillators. In *Proc. NDES 2003*, Scoul, Swiss, 2003.
- [6] A. Hajimiri and T.H. Lee. *The Design of Low Noise Oscillators*. Kluwer Academic, 1999.
- [7] Franz X. Kaertner. Analysis of white and $f^{-\alpha}$ noise in oscillators. *Int. Journal of Circuit Theory and Applications*, 18:485–519, 1990.
- [8] D. B. Leeson. A simple model of feedback oscillator noise spectrum. *Proceedings of the IEEE*, 43:329–330, 1966.
- [9] Pieter van de Kloet. *Modal Solutions for Linear Time Varying Systems*. PhD thesis, TU Delft, 2002.
- [10] Lofti Zadeh. Frequency analysis of variable networks. *IRE Proceedings*, 38:291–299, 1950.

Conductance: from electrical networks, through graphs, to dynamical systems

Sara Fernandes and J. Sousa Ramos

Departamento de Matemática, Universidade de Évora

Rua Romão Ramalho, 59, 7000-671 Évora, Portugal

e-mail: saf@uevora.pt

Departamento de Matemática, Instituto Superior Técnico

Av. Rovisco Pais 1, 1049-001 Lisboa, Portugal

e-mail: sramos@math.ist.utl.pt

Abstract—We introduce the notion of conductance in dynamical systems on iterated maps of the interval. Our starting point is the notion of conductance in the graph theory. We pretend to apply the known results in this new context.

I. INTRODUCTION

The transfer of concepts from one area of knowledge to another has been serving as impulsive force of the development of mathematics. It was so with the entropy, which arrived from the thermodynamic and was brought by Kolmogorov to the dynamical systems. Today, thanks to Sinai, Adler, Konheim, McAndrew, Misiurewicz, Szlenk and others, this concept is commonly used and calculated in this area, see [6].

Our objective with this paper is to introduce the notion of conductance in the discrete dynamical system on the iterated map of the interval. We will use the Markov partition of the interval to define an associated graph. By analogy with the electric circuits, the conductance was defined and is known for a regular graph without orientation. We will extend this definition to a more general setting to include both non-regular and oriented graphs, which are more useful to represent our dynamical systems. Then, we go back, and bring the definition of conductance with us to use in the study of certain families of maps, which cannot be differentiated by the topological entropy.

II. CONDUCTANCE OF A DISCRETE DYNAMICAL SYSTEM

In this section we will introduce formally, the notion of conductance of a dynamical system. First we will introduce this concept in the graph theory, where it has been studied for several years, see [1] for more details.

A. Graphs

An *unordered graph* G is an ordered pair of sets (V, E) , such that E is a subset of $V \times V$ of unordered

pairs of V . We will call V the set of *vertices* and E the set of *edges*. An edge $\{i, j\}$ is said to join the vertices i and j and is denoted by ij . The *order* of G is the number of vertices in G and is denoted by $|G|$. The *degree* of a vertex i is the number of edges in E , which one of the "endpoints" is i , that is, the number of elements of E , for which i is one of the two components. A graph is said *k-regular* if each vertex has degree k , for some k and is said *connected* if there isn't any isolated vertex (every vertex has an edge with him as endpoint). To each unordered, connected k -regular graph G with n vertices $\{1, 2, \dots, n\}$, is associated a *simple random walk* $X = (x_t)_{t=0}^{\infty}$ in its simplest form: starting at x_0 , its next vertex, x_1 , is chosen randomly from the neighbours of x_0 . Next x_2 is chosen among neighbours of x_1 , and so on. Set $p_i(t) = Prob(x_t = i)$. Thus X is the simple random walk (Markov Chain) with initial distribution $p_0 = (p_1^{(0)}, p_2^{(0)}, \dots, p_n^{(0)})$ and $p_t = (p_1^{(t)}, p_2^{(t)}, \dots, p_n^{(t)}) = p_0 P^t$ is the distribution of x_t . We view the distributions as row vectors in \mathbb{R}^V and we call P the transition matrix.

Definition 1: A row vector $\pi \in \mathbb{R}^V$ is a stationary distribution of the chain X with transition matrix P if

- a) $\pi(i) \geq 0$, for all $i \in V$;
- b) $\sum_{i \in V} \pi(i) = 1$;
- c) $\pi = \pi P$

Definition 2: A Markov chain X with transition matrix P is said to be *ergodic* if it has a stationary distribution. Is said to be *irreducible* if for all $i, j \in V$, there is an m such that $(P_{ij})^m > 0$. Is said *aperiodic* iff for all $i \in V$, $\gcd\{m : (P_{ij})^m > 0\} = 1$.

It is known that any finite, irreducible Markov chain is ergodic.

Back to our simple random walk, we have then p_t tends to the stationary distribution, that is, in this case, the vector $\pi = (\frac{1}{n}, \frac{1}{n}, \dots, \frac{1}{n})$. The measure of the speed of convergence $p_t \rightarrow \pi$, is given by the *mixing rate* of the random walks on G

$$\mu = \sup_{p_0} \limsup_{t \rightarrow \infty} \|p_t - \pi\|_{\frac{1}{2}}^{\frac{1}{t}}$$

where the supremum is taken over all initial distributions p_0 . As is pointed out in [1], the mixing rate μ is easily described by the eigenvalues of P . By definition, $P = A/k$, where $A = (a_{ij})_{i,j=1}^n$ is the adjacency matrix of G , defined for $i \neq j$ by the number of edges from i to j (note that an edge from i to j is also an edge from j to i) and for $i = j$, by the number of loops at i . As usual, A is identified with a linear endomorphism of the vector space $C_0(G)$ of all functions from V into \mathbb{C} . The matrix P is hermitian and then it has only real eigenvalues. It is known that $1 = \lambda_1 > \lambda_2 \geq \dots \lambda_n > -1$ and we have that the mixing rate μ is precisely $\lambda = \max\{\lambda_2, |\lambda_n|\}$.

In fact, we shall estimate the speed of convergence to the stationary distribution in terms of the *conductance* Φ_G of a graph. The definition follows.

Definition 3: Let G be an *unordered, connected, k-regular graph*. Define the conductance Φ_G of G by

$$\Phi_G = \min_{U \subset V} \frac{e(U, \bar{U})}{d \min\{|U|, |\bar{U}|\}}$$

where $\bar{U} = V \setminus U$ and $e(U, \bar{U})$ is the number of edges from U to \bar{U} . Note that if $|U| \leq n/2$, as we may assume, then $k|U| = \sum_{u \in U} d(u)$ is the maximal number of edges that may leave U , so $\frac{e(U, \bar{U})}{d|U|}$ is the proportion of edges "leaving" U .

So, for a dynamical system described by an hermitian matrix, we can speak about the conductance introduced in the above definition.

B. Markov Chains

In a general way, to each discrete dynamical system (I, f) defined by the iterates of a map f on the interval I , we associate a Markov matrix, which is representable by a non-regular, oriented graph G_f (the elements of E are now ordered pairs). So we have systems defined by the adjacency matrix $A_f = (a_{ij})$ of G_f , that is, the 0 – 1 matrix where $a_{ij} = 1$ iff ij is an edge. In turn, to each A_f , we associate a probability matrix P_f and an invariant measure (the measure of maximal entropy) π . So we have what is called a random walk in a weighted directed graph, with loops allowed, described by a transition matrix P_f , which is no longer hermitian, but can however represent an ergodic system. We can now establish the notion of conductance of a discrete dynamical system.

Definition 4: Let f be a map on the interval, $P_f = (P_{ij})_{i,j=1}^n$ be the probability matrix associated to f and $\pi_f = (\pi_i)_{i=1}^n$ be the invariant measure. Define con-

ductance of (I, f) by

$$\Phi_f = \min_{\substack{0 < \pi(S) \leq 1/2 \\ S \subset V}} \frac{\sum_{i \in S, j \in \bar{S}} \pi_i P_{ij}}{\sum_{i \in S} \pi_i}$$

Another possible approach to the conductance is through the discrete laplacian of a graph defined next.

Definition 5: Let $A_f = (a_{ij})_{i,j=1}^n$ be the adjacency matrix associated to (I, f) and G_f the Markov graph. Define the diagonal matrix $D_f = (d_{ij})_{i,j=1}^n$, putting in the diagonal d_{ii} the number of edges that incide (in and out) in the vertex i (loops contribute with 2). We will call the matrix

$$\Delta_f = D_f - (A_f + A_f^T)$$

the laplacian matrix of the graph G_f .

As we will see, the smallest non-zero eigenvalue of the laplacian is closely related with the conductance of the system.

III. BIMODAL FAMILY

Lets consider a bimodal family of maps $S_{a,b}$ (cubic like maps, see Figure 1), depending on two parameters a and b . We want one parameter to be related with the topological entropy (defined as the logarithm of the growth number of periodic points) and use the second to distinguish the systems via conductance.

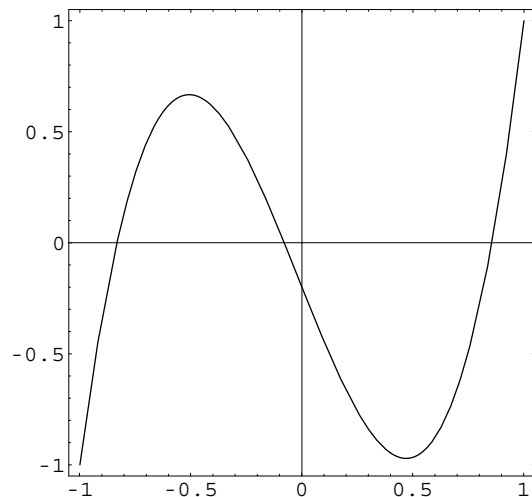


Fig. 1. Cubic like map.

For different values of the parameters a and b we obtain trajectories, which can be symbolically expressed by the itineraries of the two critical points c_1 and c_2 .

If we take a point x in I , we will call the address of x , $A(x)$, one of the symbols L, A, M, B, R according to the following rule:

$$A(x) = \begin{cases} L & \text{if } x < c_1 \\ A & \text{if } x = c_1 \\ M & \text{if } x > c_1 \text{ and } x < c_2 \\ B & \text{if } x = c_2 \\ R & \text{if } x > c_2 \end{cases}$$

The itinerary of $x \in I$ will be then the sequence of symbols $A(x), A(f(x)), A(f(f(x))) \dots$

Using the itinerary of the critical points c_1 and c_2 we obtain a Markov partition of the interval I . There exists an uncountable quantity of different dynamic types. To introduce the study of conductance and discrete laplacian in the maps of the interval we considered 3 families, given by the pair of itineraries of the critical points:

1. $((R^k A)^\infty, (L^k B)^\infty)$, $k = 1, 2, \dots$; with topological entropy $h_t(f) \in [0, \log(3)]$.
2. $((RM^k A)^\infty, (LM^k B)^\infty)$, $k = 1, 2, \dots$; with topological entropy $h_t(f) \in [0, \log(2)]$.
3. $RM^k(BLM^k)^\infty$ and $RL^k(BLL^k)^\infty$, $k = 1, 2, \dots$. Here the trajectory of c_1 falls in the trajectory of c_2 ; with constant topological entropy $h_t(f) = \log(2)$.

After a numerical study, we can state the following result.

Theorem 1: Let $f : I \rightarrow I$ be a piecewise monotone map. The conductance Φ_f and the first non-zero eigenvalue $\lambda_1(\Delta_f)$ of the discrete laplacian Δ_f are functions that decrease when the periods of the critical points increase, converging to a constant depending on the topological entropy of f .

This result can be proved by symbolic dynamic methods and it is illustrated in Figures 2, 3, 4 and 5,

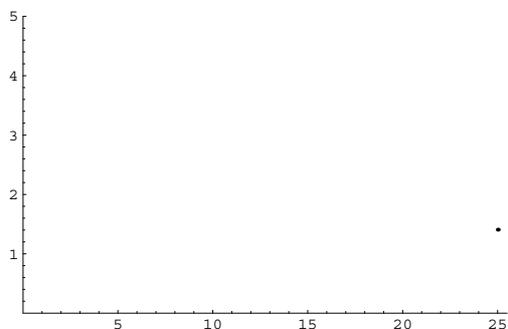


Fig. 2. The first eigenvalue $\lambda_1(\Delta)$ ($\dim A_f$) for the family $((R^k A)^\infty, (L^k B)^\infty)$, with topological entropy $\in [0, \log(3)]$.

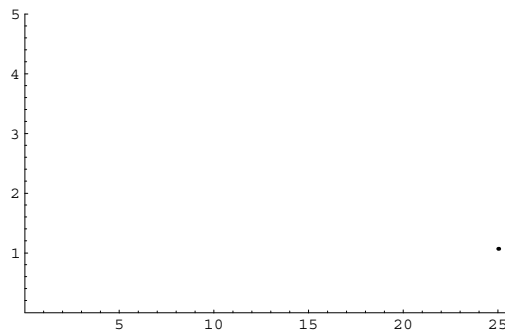


Fig. 3. The first eigenvalue $\lambda_1(\Delta)$ ($\dim A_f$) for the family $((RM^k A)^\infty, (LM^k B)^\infty)$, with topological entropy $\in [0, \log(2)]$.

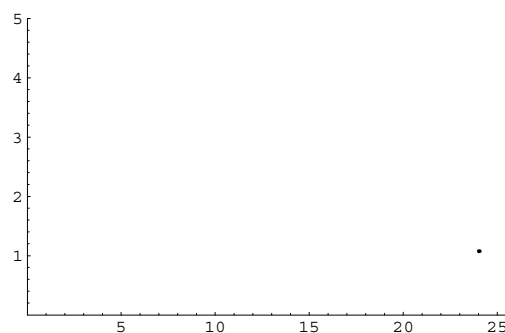


Fig. 4. The first eigenvalue $\lambda_1(\Delta)$ ($\dim A_f$) for the family $RL^k(BLL^k)^\infty$, with constant topological entropy $= \log(2)$.

In the Figure 3 the oscillation in the decreasing of the $\lambda_1(\Delta_f)$ is due to parity of number of M symbols (because the function $f|_M$ has negative slope).

In the Figure 6 and Figure 7 we can see the variation of the modulus of the second eigenvalue $\lambda_2(A_f)$ of the adjacency matrix A_f increasing with the dimension of A_f , see [2] and [3] for the relation with the mixing rate.

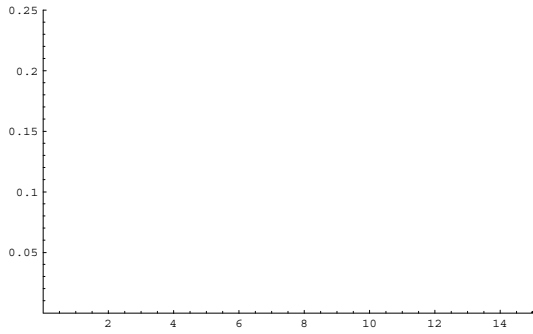


Fig. 5. The conductance $\Phi_f(\dim A_f)$ for the family $RL^k(BLL^k)^\infty$, with constant topological entropy $= \log(2)$.

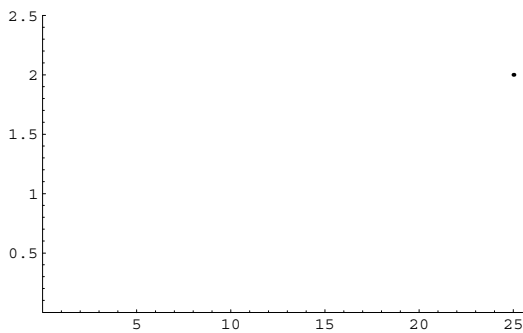


Fig. 6. The second eigenvalue $\lambda_2(A_f)$ ($\dim A_f$) for the family $((RM^k A)^\infty, (LM^k B)^\infty)$, with topological entropy $\in [0, \log(2)]$.

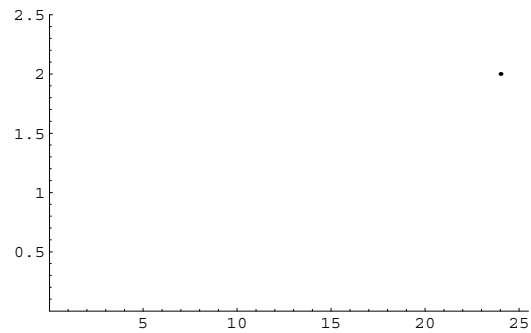


Fig. 7. The second eigenvalue $\lambda_2(A_f)$ ($\dim A_f$) for the family $RM^k(BLM^k)^\infty$, with constant topological entropy $= \log(2)$.

REFERENCES

- [1] B. Bollobás, Modern Graph Theory. *Graduate Texts in Mathematics*, 184, Springer, 1998.
- [2] S. Fernandes, J. Sousa Ramos, *Spectral Invariants of Iterated Maps of the Interval*, To appear in Grazer Math. Ber.
- [3] S. Fernandes, J. Sousa Ramos, *Second Smaller Zero of Kneading*, 8th International Conference on Difference Equations and Applications, July 28 - August 1, 2003, Brno, Czech Republic.
- [4] V. Guruswami, Rapidly Mixing Markov Chains: A Comparison of Techniques (A Survey).
- [5] J. Milnor and W. Thurston, *On Iterated Maps of the Interval*, in: J. C. Alexander (ed.) *Proceedings Univ. Maryland 1986-1987*. Lect. Notes in Math. 1342, 465-563, Springer-Verlag, Berlin–New York, 1988.
- [6] P. Walters, An Introduction to Ergodic Theory, *Graduate Texts in Mathematics*, 79, Springer, 1982.

Effects of Sequence-Dependent Elastic Properties in Tandemly Repeated DNA

Alexandre F. da Fonseca, C. P. Malta and Marcus A. M. de Aguiar

Instituto de Física,
Universidade de São Paulo, USP,
CEP 05508-900, São Paulo, SP, Brazil
e-mail: afonseca@if.usp.br and coraci@if.usp.br

Instituto de Física ‘Gleb Wataghin’,
Universidade Estadual de Campinas, UNICAMP,
CEP 13083-970, Campinas, SP, Brazil
e-mail: aguiar@ifi.unicamp.br
WWW: <http://www.ifi.unicamp.br/~aguiar>

Abstract—*Tandemly repeated sequences of DNA are modeled as nonhomogeneous elastic rods. Using the framework of the Kirchhoff rod model we study the tridimensional conformations of rods with periodically varying Young’s modulus. Using tools of dynamical systems we analyze the effects of the Young’s modulus oscillations in the stroboscopic maps and in the regular (non chaotic) spatial configurations of the filaments. These configurations correspond to local minima of the total elastic energy of the rod. The periodic variations of the filament Young’s modulus lead to deviations from the well known helix solution, and the resulting shape is either a slightly deformed helix or a highly twisted and compacted rod. Deviations from the helix shape are larger near resonance.*

the rod.

A significant fraction of all eukaryotic genomes consist of the so-called tandemly repeated sequences of DNA [12], [13]. They are pieces of repetitive DNA formed by nucleotide sequences of varying length and composition reaching up to 100 megabasepairs of length [12]. We shall assume that the DNA is intrinsically an untwisted straight rod, but we include sequence-dependent stiffness. We consider it as a nonhomogeneous Kirchhoff rod where small periodic variations of the Young’s modulus are considered to model the *tandemly repeated* characteristics of the rod. Since the equilibrium equations can be written in a Hamiltonian formulation, we analyze the effects of this nonhomogeneity in both the stroboscopic maps and the structure of the periodic (non-chaotic) equilibrium solutions. These regular equilibrium solutions correspond to local minima of total elastic energy of the rod. We shall show how the sequence-dependent mechanical properties of filaments deviate their tridimensional structure from the well known uniform solution, namely, the helix.

I. INTRODUCTION

We shall consider here the elastic continuum rod model, which is appropriate for studying the general behavior of very long DNA molecules [1]. Models that take into account the atoms and molecules forming the DNA can be computationally solved only if the total length is not too long. References [1], [2] give a good review.

The Kirchhoff rod model [3] is a good framework to study both the statics and the dynamics of thin elastic filaments [4], [5]. This model has been used to study the elastic behavior of rods in different areas of knowledge, ranging from Engineering [6], [7], [8] to Biology [9], [10], [11].

It is known that the elastic parameters of the DNA are sequence-dependent [2] so, in order to improve the DNA elastic rod model, we consider a filament with nonhomogeneous elastic parameters. We assume that the Young’s modulus depends on the position along

II. THE KIRCHHOFF ROD MODEL

Basically, the equations of the Kirchhoff model result from the applications of the Newton’s laws of mechanics to a thin rod that is assumed to be weakly bent (the radius of curvature at each point of the rod is much larger than the radius of the cross section) [5], [14].

In order to derive a set of equations for the rod we have to define the variables used to describe a thin filament. First, we define a smooth curve \mathbf{x} in the 3D space parametrized by the arclength s that will represent the axis of the rod. Second, a local orthonormal basis (also called *director basis*) $\mathbf{d}_i = \mathbf{d}_i(s, t)$,

$i = 1, 2, 3$, is defined at each point of the curve, with \mathbf{d}_3 chosen as the tangent vector, $\mathbf{d}_3 = \mathbf{x}'$ (the prime denotes derivative with respect to s , and the dot with respect to t). The two orthonormal vectors \mathbf{d}_1 and \mathbf{d}_2 lie in the plane perpendicular to \mathbf{d}_3 . These vectors are chosen such that $\mathbf{d}_1, \mathbf{d}_2, \mathbf{d}_3$ form a right-handed orthonormal basis for all values of s . The evolution in the space and in time of the director basis is given by the so-called *twist* and *spin equations*, respectively,

$$\mathbf{d}_i' = \mathbf{k} \times \mathbf{d}_i, \quad \dot{\mathbf{d}}_i = \boldsymbol{\omega} \times \mathbf{d}_i, \quad i = 1, 2, 3, \quad (1)$$

where the vectors \mathbf{k} and $\boldsymbol{\omega}$ are the twist and spin vectors. Both \mathbf{k} and $\boldsymbol{\omega}$ can be written in the director basis: $\mathbf{k} = \sum_{i=1}^3 k_i \mathbf{d}_i$ and $\boldsymbol{\omega} = \sum_{i=1}^3 \omega_i \mathbf{d}_i$. k_1 and k_2 are the components of the curvature of the rod, and k_3 is the twist density. The solution of the twist and spin vectors determines the vector \mathbf{d}_3 that can be integrated to give the space curve \mathbf{x} .

Let \mathbf{F} and \mathbf{M} be the total force and moment with respect to the axis of the rod. We are interested in the static Kirchhoff equations, given by (in properly scaled units):

$$\mathbf{F}' = 0, \quad (2)$$

$$\mathbf{M}' + \mathbf{d}_3 \times \mathbf{F} = 0, \quad (3)$$

$$\mathbf{M} = E(s)k_1 \mathbf{d}_1 + E(s)k_2 \mathbf{d}_2 + \Gamma_0 k_3 \mathbf{d}_3, \quad (4)$$

where $\Gamma_0 = 2\mu/E_0$ is the average adimensional elastic parameter of the rod and $E(s)$ is a dimensionless function representing the variation of the Young's modulus around the average value E_0 . Γ_0 varies between $2/3$ (incompressible material) and 1 (hyperelastic material). We do not consider shear modulus variation.

III. THE HAMILTONIAN FORMULATION

The main advantage of a Hamiltonian formulation is that the theory of chaotic Hamiltonian systems and stroboscopic maps can be directly applied to understand the spatial behavior of the filament. We shall follow the derivation by Nizette and Goriely [10]. The static Hamilton's equations for the Kirchhoff model are analogous to those of a symmetric spinning top in a gravity field, with the arc length s along the rod playing the role of time.

The equation (2) implies that the tension \mathbf{F} is constant along the rod. We choose the direction of the force as the z -direction (in a fixed Cartesian basis):

$$\mathbf{F} = F \mathbf{e}_z. \quad (5)$$

Substituting equation (5) in equation (3) and projecting along \mathbf{e}_z we have

$$\mathbf{M}' \cdot \mathbf{e}_z \equiv M_z' = 0, \quad (6)$$

which represents a first integral. By projecting the equation (3) along \mathbf{d}_3 we obtain another integral, M_3 :

$$\mathbf{M}' \cdot \mathbf{d}_3 = (\mathbf{M} \cdot \mathbf{d}_3)' \equiv M_3' = 0. \quad (7)$$

If the Young's modulus is a constant along the rod, it is possible to show that the elastic energy per unit arclength,

$$H = \frac{1}{2} \mathbf{M} \cdot \mathbf{k} + \mathbf{F} \cdot \mathbf{d}_3, \quad (8)$$

is also a constant.

The orthonormal Cartesian basis is connected to the director basis through the Euler angles:

$$\mathbf{d}_i = \sum_{j=1}^3 S_{ij} \mathbf{e}_j, \quad (9)$$

where $\mathbf{e}_3 \equiv \mathbf{e}_z$ and S_{ij} can be seen in references [10], [14].

Using the equation (9), the equation (8), in Euler angles, is given by

$$H = \frac{P_\theta^2}{2E(s)} + \frac{P_\phi^2}{2\Gamma_0} + \frac{(P_\psi - P_\phi \cos \theta)^2}{2E(s) \sin^2 \theta} + F \cos \theta, \quad (10)$$

where $E(s)$ is the scaled Young's modulus. It should be remarked that Γ_0 has no influence in the tridimensional shape of the equilibrium solutions. The total elastic energy of the rod can be obtained by integration of the equation (10),

$$E_T = \int_0^L H ds, \quad (11)$$

where L is the total length of the rod. The momenta are defined by

$$\begin{aligned} P_\theta &\equiv E(s)\theta', \\ P_\phi &\equiv \Gamma_0 (\phi' + \psi' \cos \theta), \\ P_\psi &\equiv E(s)\psi' \sin^2 \theta + P_\phi \cos \theta. \end{aligned} \quad (12)$$

It is possible to show that an effective potential $V(\theta)$ related to the Hamiltonian formulation of the homogeneous case has a minimum at θ_0 and the frequency ω_0 of small oscillations around the minimum is given by:

$$\omega_0 = P_\phi^2 + 2V(\theta_0) - 6F \cos \theta_0. \quad (13)$$

The solution $\theta = \theta_0$ related to the minimum of the potential corresponds to a perfect helix.

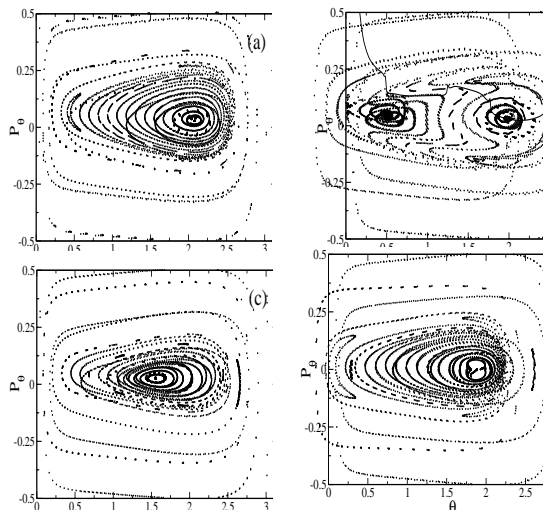


Fig. 1. Stroboscopic maps for $P_\psi = 0.086$, $P_\phi = 0.043$ and $F = 20\text{pN}$. The frequency of the Young's modulus oscillation in each map is: (a) $\omega = 0.60\omega_0$; (b) $\omega = 0.85\omega_0$; (c) $\omega = \omega_0$; (d) $\omega = 2\omega_0$. The map in (b) shows the total elastic energy of the rod (full line) in proper units.

We shall consider the following periodic variation of the scaled Young's modulus

$$E(s) = 1 + \alpha \cos(\omega s), \quad (14)$$

where α is the parameter of perturbation and ω is the frequency of the Young's modulus oscillation. In the case of a homogeneous filament, $E(s) \equiv 1$.

To obtain the equilibrium configurations we first solve Hamilton's equations for θ and P_θ . Then, we solve Eq.(12) for ψ and reconstruct the filament, $\mathbf{x}(s)$, by integrating \mathbf{d}_3 along s . $\mathbf{x}(s)$ is a function of the initial conditions $\theta(s=0) \equiv \theta_0$ and $P_\theta(s=0) \equiv P_0$. Without lack of generality, we can set $P_0 = 0$ so that θ_0 will be a conformation parameter. In solving the equation for ψ we set its initial value $\psi_0 = 0$.

IV. NUMERICAL RESULTS

The numerical calculations have been performed with the following fixed mechanical parameters: $\alpha = 0.1$, $P_\psi = 0.086$, $P_\phi = 0.043$ and $F = 20\text{pN}$. These parameters, excepting the force F , are written in properly scaled units. The value of P_ϕ corresponds to an excess of 5% of the linking number [16] due to thermal fluctuations. The value of the force corresponds to a compressing force consistent with the values in the literature [17], [18].

Fig. 1 shows stroboscopic maps in the $\theta - P_\theta$ plane for $\omega = 0.60\omega_0$ (Fig. 1a), $\omega = 0.85\omega_0$ (Fig. 1b), $\omega = \omega_0$ (Fig. 1c) and $\omega = 2.00\omega_0$ (Fig. 1d). In

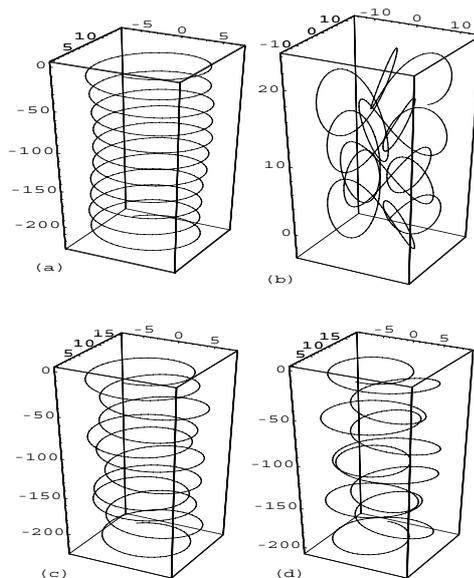


Fig. 2. Tridimensional conformations corresponding to the center of the main islands seen in Fig.1a-c. (a) $\omega = 0.60\omega_0$ (center of the island of Fig.1a); (b) $\omega = 0.85\omega_0$ (center of the left island of Fig.1b); (c) $\omega = 0.85\omega_0$ (center of the right island of Fig.1b); (d) $\omega = \omega_0$ (center of the island of Fig.1c).

Fig. 1 there is a large stability island enclosing the main equilibrium point at $\theta \simeq 2.08\text{rad}$ and $P_\theta = 0$. The stroboscopic map in the Fig. 1b exhibits two different equilibrium points. Fig. 1b displays, in the same frame, the total elastic energy of the rod, E_T , in proper units (full line) (we chose the total length $L = 1000$, in scaled units). We can see that the total elastic energy presents minima centered at the equilibrium points.

The shape of the tridimensional configurations corresponding to the equilibrium points, lying at the center of the islands in the stroboscopic maps of Fig. 1, are obtained by solving the Hamiltonian equations using the values of the equilibrium point for θ and P_θ as initial conditions θ_0 and P_0 and constructed the filament $\mathbf{x}(s)$.

The Fig. 2 shows that the shape of the equilibrium point tridimensional configuration changes as the frequency is varied. We can see in panels (a), (c) and (d) that the tridimensional configurations of the nonhomogeneous rod can present a slightly deformed helix-like shape. The panel (b), related to the equilibrium point at the center of the left island in the stroboscopic map of Fig. 1b, shows a different kind of solution, the rod being very twisted and compacted. We have shown [19] that as the frequency varies, the center of the main islands in the stroboscopic maps moves, and

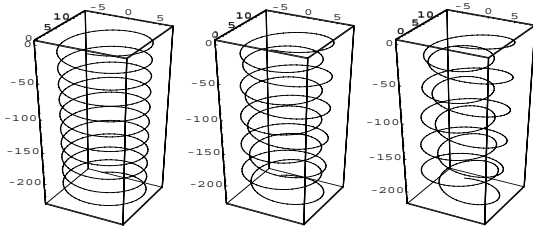


Fig. 3. Tridimensional shape of the configurations corresponding to the center island that appears in the stroboscopic maps for $\omega = \omega_0$ and different α (stroboscopic maps not shown). From left to right, homogeneous case, $\alpha = 0.001$ and $\alpha = 0.01$.

the shape of the corresponding tridimensional configuration changes. Transitions from a helix-like pattern to a twisted and compacted one, and vice-versa, are observed.

The sensitivity of the shape of the nonhomogeneous rod to the amplitude α of the nonhomogeneity can be tested. Fig. 3 shows the helix solution of the homogeneous case $\alpha = 0$ (on the left), the solution for $\alpha = 0.001$ (middle) and $\alpha = 0.01$ (on the right), in the case of the resonance $\omega = \omega_0$. Also, these solutions can be compared to that in the Fig. 2d ($\alpha = 0.1$). We can see that even for small nonhomogeneity α , the tridimensional configuration of the rod is significantly deviated from the helix shape when ω is close to ω_0 (resonance).

V. CONCLUSIONS

The tridimensional structure of a molecule consisting of tandemly repeated sequences has been modeled by the Kirchhoff rod model, using a periodic Young’s modulus to simulate the *tandemly repeated* characteristics of the molecule.

Using the Hamiltonian formulation of the Kirchhoff equations, we calculated stroboscopic maps for different frequencies of the periodic Young’s modulus of the rod (14). We also showed that the equilibrium points in the stroboscopic maps are local minima of the rod total elastic energy.

The main result of this numerical experiment is that the tridimensional conformations of the DNA may be very sensitive to sequence-dependent properties, especially if these are in resonance with other natural periods of the filament. It is well known that various other elements, besides sequence-dependent effects, combine to determine the conformation of DNA molecules, like self-contact, salt concentration, anisotropy and interaction with proteins. Our results

show that sequence-dependent effects alone may have a significant influence on the shape of the DNA. This could be, therefore, a possible mechanical function of the “junk” sequences.

This work was partially supported by the Brazilian agencies FAPESP, CNPq and FINEP.

REFERENCES

[1] T. Schlick, Modeling Superhelical DNA - Recent Analytical and Dynamic Approaches, *Current Opinion in Structural Biology* 5, No. 2, pp. 245–262, 1995.

[2] W. K. Olson, Simulating DNA at Low Resolution, *Current Opinion in Structural Biology* 6, No. 2, pp. 242–256, 1996.

[3] G. Kirchhoff, Über das Gleichgewicht Und Die Bewegung Eines Unendlich Dünnen Elastischen Stabes, *J. Reine Angew. Math.* 56, pp. 285–313, 1859.

[4] E. H. Dill, Kirchhoff Theory of Rods, *Archives of the History of Exact Sciences* 44, No. 1, pp. 1–23, 1992.

[5] A. Goriely and M. Tabor, Nonlinear Dynamics of Filaments I: Dynamical Instabilities, *Physica D* 105, pp. 20–44, 1997.

[6] Y. Sun and J. W. Leonard, Dynamics of Ocean Cables with Local Low-Tension Regions, *Ocean Engineering* 25, No. 6, pp. 443–463, 1997.

[7] M. A. Vaz and M. H. Patel, Three-Dimensional Behavior of Elastic Marine Cables in Sheared Currents, *Applied Ocean Research* 22, No. 1, pp. 45–53, 2000.

[8] E. E. Zajac, Stability of Two Loop Elastics, *J. Applied Mechanics* 29, pp. 136–142, 1962.

[9] A. Goriely and M. Tabor, Spontaneous Helix Hand Reversal and Tendril Perversion in Climbing Plants, *Physical Review Letters* 80, No. 7, pp. 1564–1567, 1998.

[10] M. Nizette and A. Goriely, Towards a Classification of Euler-Kirchhoff Filaments, *J. of Mathematical Physics* 40, No. 6, pp. 2830–2866, 1999.

[11] I. Tobias, D. Swigon and B. D. Coleman, Elastic Stability of DNA Configurations. I: General Theory, *Physical Review E* 61, No. 1, pp. 747–758, 2000.

[12] B. Charlesworth, P. Sniegowski and W. Stephan, The Evolutionary Dynamics of Repetitive DNA in Eukaryotes, *Nature* 371, No. 6494, pp. 215–220, 1994.

[13] J. Hsieh and A. Fire, Recognition and Silencing of Repeated DNA, *Annual Review of Genetics* 34, pp. 187–204, 2000.

[14] A. F. Fonseca and M. A. M. de Aguiar, Near Equilibrium Dynamics of Nonhomogeneous Kirchhoff Filaments in Viscoelastic Medium, *Physical Review E* 63, No. 1, art. no. 016611, 2001.

[15] A. F. da Fonseca and M. A. M. de Aguiar, Solving the Boundary Value Problem for Finite Kirchhoff Rods, *Physica D* 181, pp. 53–69, 2003.

[16] J. F. Marko and E. D. Siggia, Statistical-Mechanics of Supercoiled DNA, *Physical Review E* 52, No. 3, pp. 2912–2938, 1995.

[17] R. B. Macgregor, Effect of Hydrostatic Pressure on Nucleic Acids, *Biopolymers* 48, No. 4, pp. 253–263, 1998.

[18] V. Norris, T. Onoda, H. Pollaert and G. Grehan, The Mechanical Advantages of DNA, *Biosystems* 49, No. 1, pp. 71–78, 1999.

[19] A. F. da Fonseca, C. P. Malta and M. A. M. de Aguiar, Helix-to-helix transitions in nonhomogeneous Kirchhoff filaments, e-print:physics/0201118.

A CHAOTIC CIRCUIT WITH FERROELECTRIC NONLINEARITY

Luigi Fortuna, Mattia Frasca, Salvatore Graziani, Salvatore Reddiconto

Dipartimento di Ingegneria Elettrica Elettronica e dei Sistemi
 Università degli Studi di Catania - Viale A. Doria, 6 - 95100 Catania, Italy
 E-mail: [lfortuna, mfrasca, sgraziani]@diees.unict.it

Abstract—*In this paper the possibility of observing strange attractors in an electronic circuit including a nonlinear ferroelectric component has been investigated. The ferroelectric constitutes the medium interposed between the two plates of a capacitor. A circuit exploiting the nonlinearity of the ferroelectric has been designed, while the parameters have been found by performing numerical integration with respect to different values of them. The circuit has been realized on a discrete components board. Experimental results, showing that for a suitable range of parameters a chaotic attractor emerges, are reported.*

I. INTRODUCTION

Since the seminal work of Edward Lorenz [2] in 1963, chaos has been widely investigated. Decades of efforts have been devoted to discover new mathematical systems showing chaotic attractors. Chaos appears in a lot of different phenomena and soon the interest on chaotic phenomena has fascinated circuit designers. The first chaotic circuit is the well-known Chua's circuit [3]. Then many other chaotic circuits have been designed. Some of them implement the dynamics of the mathematical systems showing chaos, others exploit the fundamental feature of electronic devices to show chaotic behavior.

Only recently the role hysteresis plays in chaotic circuits has been deeply studied. Several chaotic circuits based on hysteresis have been proposed. In particular in [6], [7] four-dimensional circuits are considered. The family of circuits described in these works includes a small parameter. When this parameter is very small it can be assumed that there exist two symmetric three-dimensional circuit connected by hysteretic switching [7]. In these circuits the hysteresis is therefore represented by piece-wise linear elements. Another relevant example of class of chaotic circuits with hysteresis makes use of differential hysteresis comparator [10].

The presence of hysteresis in these circuits allows to achieve higher order chaos from low dimensional circuits. For instance, it is well known that to show

chaos autonomous circuits should have order greater than two. In [4] an autonomous second order circuit with an hysteretic inductor is shown to be able to show chaotic dynamics: this is due to the fact that hysteresis adds a further memory variable to the circuit. An even more interesting phenomenon due to hysteresis is the emergence of hyperchaos in 3D circuits with hysteresis. It is well known that hyperchaotic behavior, characterized by two positive Lyapunov exponents, can be observed in circuits with order higher than three (in fact, one Lyapunov exponent has to be zero and one has to be negative, thus to have two positive Lyapunov exponents the circuit order has to be at least four). The circuit introduced in [5], the so-called Saito oscillator, shows hyperchaotic behavior based on a hysteretic nonlinearity. However, the nonlinearity is realized by means of a piece-wise resistor. In this work we substitute this nonlinearity with a real hysteretic device and successfully investigate the possibility of obtaining chaotic behavior. In fact the aim of the work is to show chaotic behavior in a circuit with a hysteretic device such as a ferroelectric capacitor.

In particular the hysteresis is constituted by a ferroelectric device. The ferroelectrics constitutes the medium interposed between the two plates of a capacitor, and is obtained by successive vapour deposition of Strontium, Tantalum and Bismuth on Platinum substrates in small areas. The device is characterized by a nonlinear hysteretic behavior observed by estimating the output voltage by using a Sawyer-Tower configuration.

The paper is organized as follows: the main characteristics of the ferroelectric device are briefly discussed in Section II, the circuit including the ferroelectric device is described in details in Section III, experimental results showing the chaotic behavior of the circuit are illustrated in Section IV, and Section V draws the conclusions of the paper.

II. THE FERROELECTRIC DEVICE

Even if ferroelectricity has been discovered in the beginning of the XX century, only recently ferroelectric materials are gaining interest since their possible

applications in electronics and communications. For instance non-volatile memories can be realized with ferroelectric devices since ferroelectric materials retain the information when the power is switched off.

Ferroelectric materials are polarized materials having two possible orientations of the spontaneous polarization vector. By applying an electric field is possible to switch the two orientations of the polarization vector. The hysteretic behavior is due to the energy needed to change the polarization of domains of electric polarization.

In our case the ferroelectric device consists of a medium interposed between the two plates of a capacitor, and is obtained by successive vapour deposition of Strontium, Tantalum and Bismuth on Platinum substrates in small areas.

Modelling ferroelectric materials is very difficult. Several approaches, based on the so called state space model [13], viscoelastic model [14], or tanh model [15], have been proposed. The limited predictive capabilities of these models are overcome by the Preisach model [16]. However, the prediction capabilities of this last model are accurate only in the quasi-static domain.

This constitutes a drawback that does not allow the use of this model in the design of chaotic circuits, where the working frequency is usually high. For this reason in the following a very simple model of the ferroelectric hysteresis has been assumed.

III. DESIGN OF THE CIRCUIT

Different circuits showing chaos and based on hysteretic behaviour of the nonlinearities are reported in literature. In particular, in the circuit reported in [5] the nonlinearity consists of a piecewise linear resistor, only the two tracts with positive slope are effectively involved in the dynamics and an hysteretic behavior switching between these two linear segments of the nonlinearity can be addressed as responsible of the emergence of hyperchaos in the circuit.

In particular the dimensionless equations regulating the behavior of the chaotic circuit with hysteresis [5] are the following:

$$\begin{cases} \frac{dx}{dt} = -z - w \\ \frac{dy}{dt} = \gamma(2\delta y + z) \\ \frac{dz}{dt} = \rho(x - y) \\ \varepsilon \frac{dw}{dt} = x - h(w) \end{cases} \quad (1)$$

where the nonlinearity $h(x)$ is the following:

$$h(x) = \begin{cases} w - (1 + \eta) & \text{for } w \geq \eta \\ -\eta^{-1}w & \text{for } |w| < \eta \\ w + (1 + \eta) & \text{for } w \leq -\eta \end{cases} \quad (2)$$

and it is assumed that parameter ε is very small.

We tried to ask the question if it is possible to design a circuit with the same structure of system (1) but including the ferroelectric hysteretic device. As in equations (1) the limit $\varepsilon \rightarrow 0$ allows to consider the variable $w(t)$ in quasi static behavior, we considered the following set of dimensionless equations:

$$\begin{cases} \frac{dx}{dt} = -z - f(x) \\ \frac{dy}{dt} = \gamma(2\delta y + z) \\ \frac{dz}{dt} = \rho(x - y) \end{cases} \quad (3)$$

where $f(x)$ is the functional that models the hysteresis of the ferroelectric capacitor.

As discussed in Section II, several models can be assumed for the complex behavior of the ferroelectric capacitor. Our first approach was to simulate equations (3) by keeping the model of the ferroelectric very simple and searching for chaotic solutions of system (3). Thus the functional $f(x)$ was considered a simple model of the ferroelectric device defined by two functions (the upper curve and the lower curve of the ferroelectric hysteresis). Of course this simple model does not account for the whole complexity of the behavior, but was able to predict chaotic behavior both in simulation and in circuit experiments.

The model based on the upper and lower hysteretic curves was derived from experimental data collected on the ferroelectric. More precisely these were derived by using a Sawyer-Tower circuit [11]. A further parameter is introduced in the system, the ferroelectric characteristics is multiplied by a gain factor.

Chaotic solutions of system (3) were searched for, by performing numerical integration with respect to different values of the parameters. This step was preliminary to the design of the circuit. Simulations showed that exists a suitable range of parameters for which an attractor very similar to that presented in [5] emerges. Fig. 1 shows the chaotic attractor obtained in the simulation step.

The circuit implementing equations (3) has been realized by using an Operational Amplifier board. The electrical scheme of the circuit is shown in Fig. 2.

IV. EXPERIMENTAL RESULTS

Experimental results obtained with the circuit described above show that for a suitable range of parameter a chaotic attractor emerges. In particular Fig. 3

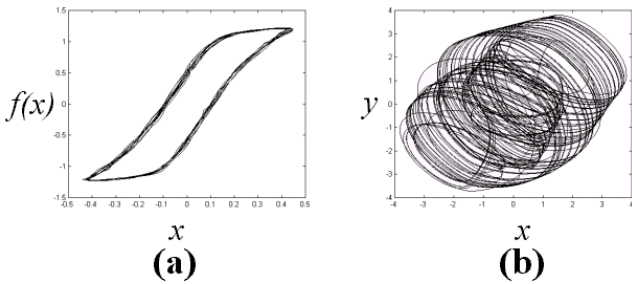


Fig. 1. (a) Characteristics of the ferroelectric device obtained by using a Sawyer-Tower circuit. (b) Simulation results. $x - y$ projection of the chaotic attractor obtained by numerical integration of system (3) for the following values of parameters: $\gamma = 1$, $\delta = 1$, $\rho = 7$ (the gain factor amplifying the ferroelectric characteristics was fixed to 18.79).

shows the projection of the attractor onto the phase plane $x - y$ and Fig. 4 onto the phase plane $x - z$.

These oscilloscope photographs have been recorded by a digital video camera, this technique allowed to highlight the presence of unstable orbits in the chaotic attractor. Fig. 5 shows one of such orbits, this complex unstable limit cycle can be observed just for a few of frames before disappearing.

Further experimental results deal with synchronization of these chaotic attractors. Even if simulation results are good and show the possibility of successfully using several synchronization schemes, experiments do not confirm these results. Two reasons can explain this behavior: first of all the parameters of the non-linearity of the ferroelectric material change from circuit to circuit in a relevant way, then the ferroelectric materials suffer from aging due to the great number of working cycles related to the frequency (relatively high for these materials) of the chaotic attractor generated.

V. CONCLUSIONS

The paper addresses the possibility of exploiting the rich dynamics of ferroelectric hysteresis to obtain new chaotic attractors with low cost circuits. In particular ferroelectric devices are used. These devices show an important hysteretic behavior due to the possibility of having different orientations of the polarization vector.

The starting point for the circuit introduced in this paper is the well-known Saito oscillator [5] based on a piece-wise hysteretic resistor. By keeping the same

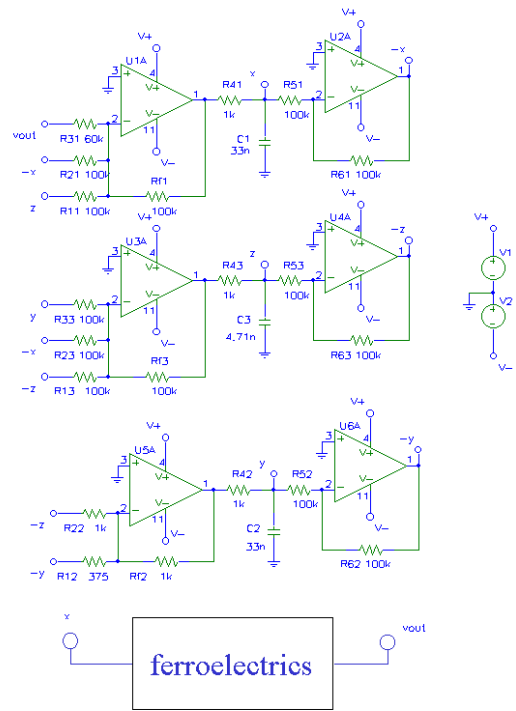


Fig. 2. Electrical scheme of the chaotic circuit with ferroelectric hysteresis.

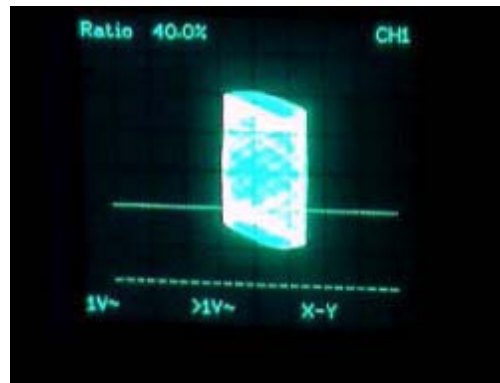


Fig. 3. Projection of the chaotic attractor onto the phase plane $x - y$.

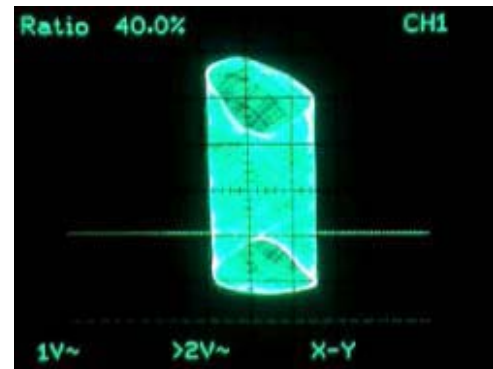


Fig. 4. Projection of the chaotic attractor onto the phase plane $x - z$.

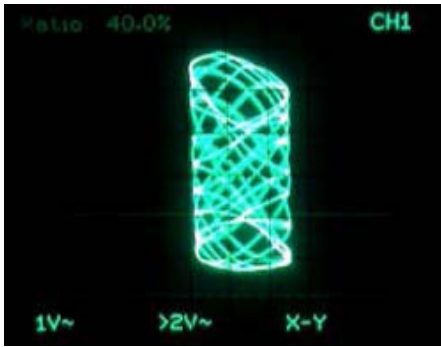


Fig. 5. Projection of the chaotic attractor onto the phase plane $x - z$.

basic structure of the Saito oscillator it is shown how hyperchaos can be generated by a circuit including a ferroelectric hysteresis.

Experimental results have been presented. Synchronization issues of these chaotic attractors have been also discussed.

REFERENCES

- [1] A. B. Somebody. A Very Important Result. In *Proc. NDES'04*, pp. 1–10, Évora, Portugal, 2004.
- [2] E. N. Lorenz, “Deterministic nonperiodic flow”, *J. Atmosph. Sci.*, 20:130–141, 1963.
- [3] R. N. Madan, *Chua's circuit: a paradigm for chaos*, World Scientific Series on Nonlinear Sciences, Series B, Vol. 1 (World Scientific, Singapore), 1993.
- [4] Y. Nishio, S. Mori, “Chaotic phenomena in an LCR oscillator with a hysteresis inductor”, *Circuits and Systems, 1991., IEEE International Symposium on*, pp. 2873 -2876 vol. 5, 1991.
- [5] T. Saito, “An Approach Toward Higher Dimensional Hysteresis Chaos Generator”, *IEEE Trans. on Circuits and Systems I*, vol. 37, no. 3, March 1990.
- [6] T. Saito, “Reality of Chaos in Four-Dimensional Hysteretic Circuits”, *IEEE Trans. on Circuits and Systems I*, vol. 38, no. 12, 1991.
- [7] K. Mitsubori, T. Saito, “A Four-Dimensional Plus Hysteresis Chaos Generator”, *IEEE Trans. on Circuits and Systems I*, vol. 41, no. 12, 1994.
- [8] M.E. Lines, A.M. Glass, *Principles and Applications of Ferroelectrics and Related Materials*, Oxford University Press, 1996.
- [9] P. Arena, S. Baglio, L. Fortuna, G. Manganaro, “Hyperchaos from Cellular Neural Networks”, *IEE Electronics Letters*, vol. 31, no 4, pp. 250-251, 1995.
- [10] J. E. Varrientos, E. Sanchez-Sinencio, “A 4-D Chaotic Oscillator Based on a Differential Hysteresis Comparator”, *IEEE Trans. CAS I*, vol. 45, no. 1, 1998.
- [11] C. Kittel, *Introduction to Solid State Physics*, Wiley, New York, 1986.
- [12] R. Habel, S. Blochwitz, H. Beige, “Controlled chaos in ferroelectric systems”, *Applications of Ferroelectrics, 1994, ISAF '94*, pp. 229 -232, 1994.
- [13] R. Banning, W.L. de Koning, Han J.M.T.A. Adriaens, R.K. Koops, “State-space analysis and identification for a class of hysteretic systems”, *Automatica* 37, pp. 1883-1892, 2001.
- [14] H. Richter, E.A. Misawa, D.A. Lucca, H. Lu, “Modelling nonlinear behavior in a piezoelectric actuator”, *Precision Engineering*, 25, pp. 128-137, 2001.
- [15] B. Jiang, P. Zurcher, R.E. Jones, S.J. Gillespie, J.C. Lee, “Computationally Efficient Ferroelectric Capacitor Model for Circuit Simulation”, *1997 Symposium on VLSI Technology Digest of Technical Papers*, 1997.
- [16] I.D. Mayergoyz, *Mathematical Modelling of Hysteresis*, Springer, New York, 1991.

SPATIO-TEMPORAL DYNAMICS TOWARDS
SELF-SYNCHRONIZATION INDEX

L. Fortuna¹, M. La Rosa^{1,2}, D. Nicolosi², G. Sicurella²

¹Dipartimento di Ingegneria Elettrica Elettronica e dei Sistemi,
Università degli Studi di Catania, Catania, Italia
e-mail: lfortuna@diees.unict.it

²SST group, Corporate R&D,
STMicroelectronics, Catania, Italia
e-mail: [manuela.la-rosa, donata.nicolosi, giovanni.sicurella]@st.com

Abstract— A self-synchronization index is proposed to characterize pattern-oriented systems dynamics. Starting from spatial modes theory, the index has been defined as the number of relevant spatial modes and therefore identifies the system degree of freedom. The proposed strategy is validated adopting it to quantify self-synchronization in two kinds of pattern-oriented systems: 2-D Chua’s circuit arrays and Hindmarsh-Rose neurons lattices. In both cases a close relationship between synchronization performances and adopted measure has been confirmed.

I. INTRODUCTION

The key point of this work is the development of a new strategy to characterize emerging spatio-temporal patterns in distributed systems. There are two main problems to face studying simulated and real-world pattern oriented networks: a huge amount of data distributed both in time and space and the definition of a meaningful index for better understanding the phenomena.

Synergetic theory explains the emergence of patterns by considering complex systems as structures of coupled nonlinear subsystems that exhibit macroscopic behaviors both in time and space [1]. In the following, spatially coherent patterns are investigated by assuming that spatio-temporal systems can be described using a few dominant modes with a spatial distribution [2][3]. The proposed strategy is focused on the definition of an index for evaluating the self-synchronization features of extended complex systems: the freedom degree index f . This index represents the number of relevant degrees of freedom of the system and corresponds to the number of relevant spatial modes describing the spatial patterns temporal evolution. In particular, one of three different dynamics can be characterized: spatio-temporal

chaos, emergence of patterns and self-synchronized behavior. The proposed strategy has been validated investigating the spatio-temporal dynamics in two different cases of study: bidimensional lattices of Chua’s circuits and Hindmarsh-Rose (H-R) neurons. The defined index allowed characterizing and comparing the networks dynamic behaviors towards the system parameter D that represents the connection strength.

II. SPATIAL MODES IN SPATIO-TEMPORAL SYSTEMS

It is well known that a linear superposition of a set of basic patterns, the so-called modes, can be used to represent spatial patterns shown at a certain time t by spatially extended systems [2]. Therefore, spatio-temporal patterns can be modeled by using few spatial modes. Given a time series $X \in \mathfrak{R}^{T \times N}$ of a spatio-temporal system, where T is the number of samples and N the number of subsystems, it can be expanded into a set of orthonormal components s_k each one having a corresponding amplitude $w_k(t)$:

$$X^* t^{\dagger} = \sum_{k=1}^{\hat{A}} w_k(t) s_k \tag{1}$$

where $t=1 \dots T$ is the sample index.

In order to evaluate s_k , the covariance matrix R of the spatio-temporal time series X , is calculated. Since R is symmetric, its eigenvalues η_k and its orthogonal eigenvectors s_k follow the relation:

$$R s_k = \eta_k s_k \tag{2}$$

The eigenvectors are the spatial modes and the eigenvalue η_k represents the contribution of the eigenvector s_k to the whole signal. It is assumed that the eigenvalues are ordered respect to their magnitude and their sum is equal to the unity:

$$\sum_{k=1}^{\hat{A}} \eta_k = 1 \tag{3}$$

The number of spatial modes, which can be up to the number of subsystems N , can be decreased reducing in this way the degrees of freedom of the spatio-temporal system. This can be done, by selecting the spatial modes with the largest eigenvalues in the Singular Value Decomposition (SVD).

In real data analysis, the highest eigenvalues are associated to the spatially coherent dynamics while the smaller ones are related to incoherent dynamics. In pattern-oriented systems, the highest eigenvalues can be associated to the spatial self-synchronized dynamics while the smaller ones can be associated to the spatially unsynchronized chaotic dynamics.

The point corresponding to a gap from the higher to the smaller eigenvalues distribution is adopted as the number of meaningful spatial modes that identify spatially coherent dynamics [4][5].

A. Self-Synchronization index

Starting from the previous considerations, in order to evaluate the self-synchronization degree of a pattern-oriented system, a new index is here introduced. This index, indicated with f , represents the number of freedom degrees of the system and is defined as the minimum value of F , for which the following relation is satisfied:

$$f = \min_k F : \sum_{k=1}^k \lambda_k \geq 0.9 \quad (4)$$

The introduction of a freedom degree index, allows quantifying the self-organization level of an extended network and evaluating its behavior versus structural parameters.

Given the time series X previously defined, three main classes of dynamic behavior can be identified through the evaluation of the index f :

- Spatio-temporal chaos: each unit performs a different behavior characterized by $f = N$.
- Emerging patterns: the units aggregate in synchronized clusters and $1 < f < N$.
- Synchronization: each unit performs the same behavior as a unique system and $f = 1$.

III. SYNCHRONIZATION IN PATTERN ORIENTED NETWORKS

A fundamental parameter in pattern-oriented systems is the diffusion coefficient D that weights the amount of information exchanged between interconnected subsystems.

This parameter has been here characterized by quantifying its effects on the spatio-temporal dynamics of

two types of extended 2-D lattices: Chua's circuits and H-R neurons. Then, to validate the proposed approach, networks synchronization has been characterized by using the index f : the freedom degree index strategy has been applied in order to classify system spatio-temporal behaviors towards D parameter.

A. Two-dimensional lattices of Chua's circuits

A regular lattice has been built by connecting 100 Chua's circuits spatially disposed on a 10x10 matrix. The single unit equations have been modified considering a nearest-neighbor coupling of radius one which behavior is described by the following equations:

$$\begin{aligned} \frac{dx_i}{dt} &= c(y_i - az_i - h(x_i)) \\ \frac{dy_i}{dt} &= x_i - y_i - z_i - D \sum_{j \in \mathcal{N}_i} y_j - C y_i \\ \frac{dz_i}{dt} &= d y_i \\ h(x_i) &= bx_i - 0.5(a/b)(|x_i - 1| + |x_i + 1|) \end{aligned} \quad (5)$$

where $a = -1.27$, $b = -0.68$, $c = 32$, $d = 9$, $C = 8$.

The lattice collective behavior has been investigated by varying the coupling intensity D . Fig. 1 shows the time series of three generic cells of the lattice, while Fig. 2 shows the spatial patterns obtained considering four different time instants for increasing values of D . In this case, a bidimensional 64-color map has been used.

Spatio-temporal chaos is observed for weak coupling strength, $D \in [0.1 \div 1]$: every cell evolves with its own dynamics according to its random initial conditions and the lattice behaves chaotically in time and space; by increasing D the lattice starts exhibiting emerging patterns. Finally, for D values higher than 4, self-organization takes place and the systems conveys to perfect chaotic synchronization.

The self-synchronization index approach has been validated, by evaluating the index f for increasing values of D . Coherently with the previous results, a value of f has been associated to the dynamic evolution of the lattice characterizing then the system synchronization degree versus the coupling D , as is it shown in Fig. 3. The index f decreases as the coupling strength increases: it is maximum for $D = 0$, when all the circuits are disconnected and spatio-temporal chaos is shown. For small values of $D \in [0.1 \div 1]$, the index value becomes smaller and

emerging patterns arise. Then, for values of D greater than 4, the index f becomes equal to 1 and the perfect chaotic synchronization is reached: the system constituted by 100 cells behaves as a whole and only one dynamic evolution can be isolated.

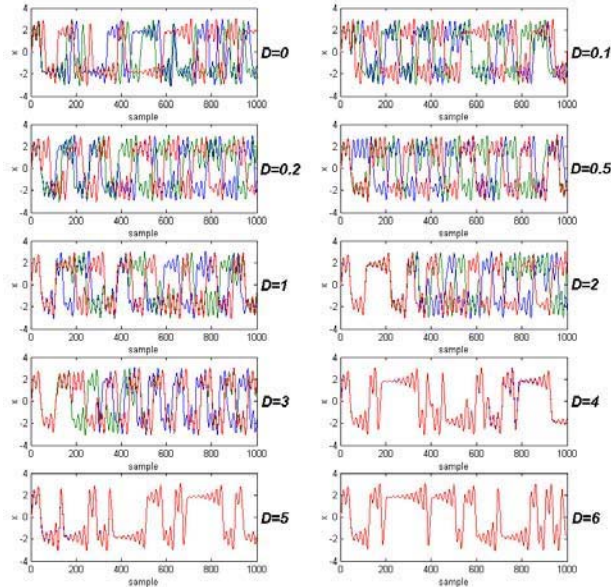


Fig. 1. x variable time series for increasing values of the diffusion coefficient D . Three generic circuits are considered (red line, blue line and green line).

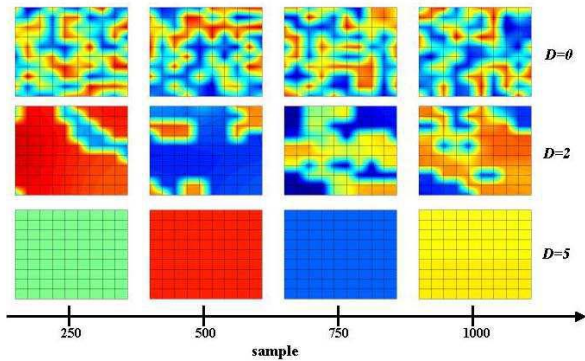


Fig. 2. Two-dimensional maps of 10x10 Chua's circuit lattices for different values of the diffusion coefficient D .

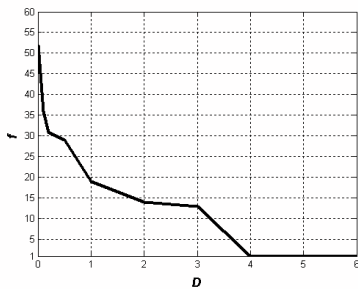


Fig. 3. Freedom degree index f versus diffusion coefficient D in a 10x10 lattices of Chua's circuits.

B. Two-dimensional network of Hindmarsh-Rose neurons

A 2-D network of Hindmarsh-Rose neurons is built by disposing each unit on a 10x10 array with radius one. The lattice dynamics is defined by the following equations:

$$\begin{aligned} \frac{dx_i}{dt} &= y_i - 3x_i^2 + x_i^3 + z_i - I_i - D \sum_{j \in \mathcal{N}_i} x_j + Cx_i \\ \frac{dy_i}{dt} &= 1 - 5x_i^2 - y_i \\ \frac{dz_i}{dt} &= rz_i - rS(x_i - 1.6) \end{aligned} \tag{6}$$

where $C=8$ is the number of connected cells and $i=1 \div 100$, $r=0.0021$, $S=4$, $I=3.281$.

The H-R model is a three state-variables model in which $x(t)$ and $y(t)$ model the fast dynamics while $z(t)$ models the slow one; I represents the synaptic current. In the first differential equation of (6), a term representing the coupling between the i_{th} neuron and its neighbors has been introduced; this term has been opportunely weighted by the coupling strength D . The model parameters have been set in such a way that each isolated neuron is characterized by a chaotic behavior, each of them starting from random initial conditions.

In Fig. 4 and 5 the membrane potentials x of three coupled neurons and the two-dimensional maps of the lattice, respectively, are displayed for increasing values of D . As shown in Fig. 4, the system is characterized by two different regimes, slow and fast, requiring a different and accurate analysis.

In the uncoupled case, when $D=0$, the potentials $x(t)$ evolve independently and the maps, displayed for different time instants, present isolated spots underlining the uncorrelated evolution of each neuron. In case of weak couplings, when $D \in [0.1 \div 2]$, the neurons evolve with slow periodic dynamic and fast unsynchronized spikes; as shown in Fig. 5, spatio-temporal patterns arise. The dynamics changes for stronger couplings, when $D > 3$; in this case, the neurons are chaotically synchronized as shown in Fig. 4 and 5.

When the perfect synchronization is obtained both burst slow activities and spike fast regime become synchronized: the 100 neurons behave as an individual chaotic one and the 64-color maps obtained for fixed time instants have a homogeneous color. The spatio-temporal behavior of the H-R lattice has been then investigated by using the freedom degree index

f. The obtained results confirmed the close relationship between synchronization performances and adopted measure. Starting from weak couplings, the synchronization index is far from 1, as shown in Fig. 6.

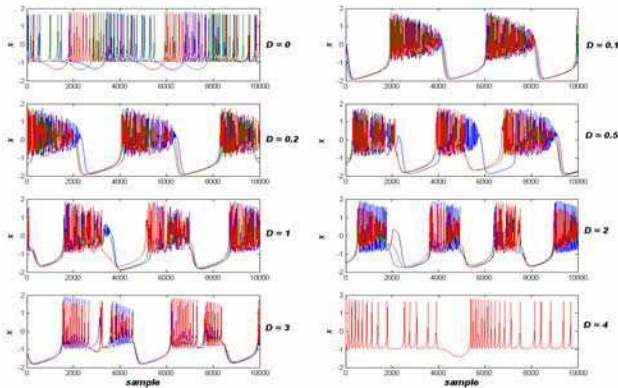


Fig. 4. x variable time-series for different values of the diffusion coefficient D . Three generic neurons are considered (red line, blue line and green line).

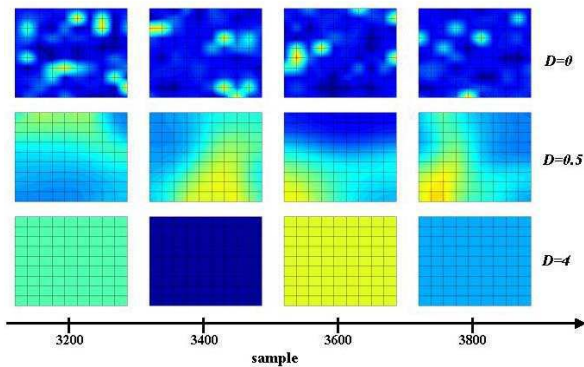


Fig. 5. Two-dimensional maps of 10x10 Hindmarsh-Rose neuron networks for different values of the diffusion coefficient D .

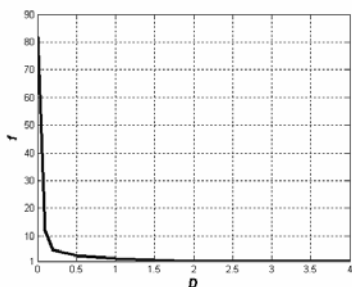


Fig. 6. Freedom degree index f versus diffusion coefficient D in a 10x10 network of neurons.

The freedom degree index curve appears very steep

and decreases suddenly for higher values of the coupling strength D . The network self-organization, quantified according to the perfect synchronization of both slow and fast regimes, respectively burst and spikes dynamics, is obtained for a diffusion coefficient D higher than 3 when $f=1$, as reported in Fig. 6.

IV. CONCLUSIONS

An innovative strategy is proposed in order to characterize self-synchronization in pattern-oriented networks. In particular a self-synchronization index has been defined, identifying the number of degrees of freedom of the system. Two case of study have been considered: a two-dimensional network of Chua's circuits and a second one of H-R neurons. First, the network dynamic behavior has been described both in time and space for different values of the coupling strength D , then, the self-synchronization index strategy has been adopted to characterize the different behaviors found in the previous analysis identifying the network dynamics with a single index.

ACKNOWLEDGEMENTS

The activity has been partially supported by the Italian "Ministero dell'Istruzione, dell'Università e della Ricerca" (MIUR) under the FIRB Project RBNE01CW3M_001.

REFERENCES

- [1] H. Haken. Synergetics. An Introduction, Springer, 1983.
- [2] R. Friedrich, V.K. Jirsa, H. Haken, C. Uhl. Analyzing Spatio-Temporal Patterns of Complex Systems. In *Nonlinear Analysis of Physiological Data*, Springer.
- [3] M. Bucolo, L. Fortuna, M. Frasca, M. La Rosa, D. S. Shannahoff-Khalsa, L. Schult, J.A. Wright. Independent Component Analysis of Magnetoencephalography Data, In *Proc. 23rd EMBC*, Istanbul, Turkey, 2001.
- [4] T. Schreiber, A. Schmitz. Discriminating Power of Measure of Nonlinearity in Time Series. In *Physical Rev. E*, vol. 55, pp. 5543-5547, 1997.
- [5] D. S. Broomhead, G. P. King. Extracting Qualitative Dynamics from Experimental Data. In *Physica D*, vol. 50, pp. 217-236, 1986.
- [6] J. L. Hindmarsh, R. M. Rose. *Proc. R. Soc. London B* 221(1984) 87.

STORING BINARY PATTERNS IN TWO-DIMENSIONAL NETWORKS OF NONLINEAR SYSTEMS

Z. Galias and M. Ogorzałek

Department of Electrical Engineering,
AGH - University of Science and Technology, Kraków, Poland,
e-mail: galias@agh.edu.pl, maciej@agh.edu.pl

Abstract— *In this paper, we investigate synchronization and cluster formation phenomena in two-dimensional arrays of locally interconnected chaotic circuits. We report the existence of an abundance of attractors, for which each cell stores a binary information. We describe a simple method for storing binary patterns in the network. We also address the question which patterns can be successfully stored in the network and discuss problems of pattern stability and influence of parameter mismatch.*

I. INTRODUCTION

One of the theories explaining the functionality of the brain relies on the dynamical representations. Construction of patterns of brain activity constitutes the key to understanding of various phenomena including perception, memory, attention etc. [2]. Many different kinds of artificial neural networks have been proposed to mimic such functionality [1], [3], [4]. Also special types of information processing can be obtained using Cellular Nonlinear Networks [5], [6]. In this paper we combine two aspects - chaotic unit cells and abundance of existing attractors to obtain binary pattern storage.

After introduction of the dynamical array in section III we study the problem of existence of many attractors, corresponding to binary patterns. In section IV we describe how to force the network to store a given binary pattern. We also show examples of patterns, which cannot be stored and attempt to characterize those patterns. In section V we investigate stability of patterns, the size of their basins of attraction and influence of parameters mismatch. Finally in section VI, we show two examples of behavior of larger networks and discuss the influence of network size on the ability of the network to store binary patterns.

This research has been supported in part by the European Community research program “COSYC of SENS”, no. HPRN-CT-2000-00158 and by AGH-UST grant 11.11.120.182

II. DYNAMICS OF THE NETWORK

Let us consider a two-dimensional array composed of simple third-order nonlinear systems (Chua’s circuits). The dynamics of an $n \times m$ array can be described by

$$\begin{aligned} C_2 \dot{x}_{i,j} &= G(z_{i,j} - x_{i,j}) - y_{i,j} + \sum_{(k,l) \in N_{i,j}} G_1(x_{k,l} - x_{i,j}), \\ L \dot{y}_{i,j} &= x_{i,j}, \\ C_1 \dot{z}_{i,j} &= G(x_{i,j} - z_{i,j}) - f(z_{i,j}), \end{aligned} \quad (1)$$

where $i = 0, 1, 2, \dots, n - 1, j = 0, 1, 2, \dots, m - 1$ and f is a five-segment piecewise linear function:

$$f(z) = m_2 z + 0.5 \cdot (m_1 - m_2)(|z + b_2| - |z - b_2|) + 0.5 \cdot (m_0 - m_1)(|z + b_1| - |z - b_1|). \quad (2)$$

$x_{i,j}$ and $z_{i,j}$ denote the voltages across the capacitors C_2 and C_1 respectively, and $y_{i,j}$ is the current through the inductor L in the cell (i, j) (i.e. belonging to the i th column and j th row – see Fig. 1). $N_{i,j}$ de-

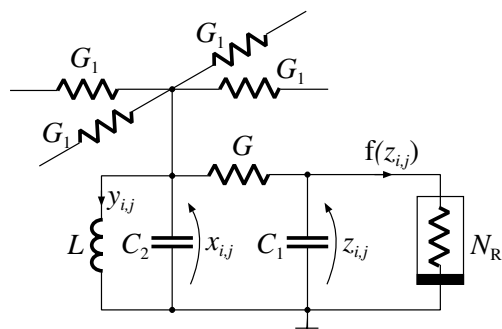


Fig. 1. A third order circuit coupled with its neighbors by means of conductances G_1

notes the neighborhood of the cell (i, j) , i.e. a set of cells directly connected with the cell (i, j) . We consider the case when each cell is connected with its four nearest neighbors (i.e. $N_{i,j} = \{((i + 1) \bmod n, j), ((i - 1) \bmod n, j), (i, (j + 1) \bmod m), (i, (j - 1) \bmod m)\}$) by means of conductances G_1 (here $G_1 = 20$). In our study we use parameter values for

which an isolated circuit generates the “double scroll” chaotic attractor: $C_1 = 1/9, C_2 = 1, L = 1/7, G = 0.7, m_0 = -0.8, m_1 = -0.5, m_2 = 0.8, b_1 = 1, b_2 = 2$.

III. EXISTENCE OF MANY ATTRACTORS

Let us consider the network composed of $n \cdot m = 10 \cdot 10$ cells. To make a classification of steady states of the network we have run a number of simulations starting the network with random initial conditions. Four examples are shown in Figs. 2–5. In each case the network converges to a limit set (steady state). To show the state of the whole network, we plot a snapshot using shades of gray to represent the value of z variable in each cell. We plot also projections of the system trajectory onto chosen sub-spaces. Projection onto the plane $(z_{i,j}, y_{i,j})$ shows a trajectory of a given cell, while the projection onto the plane $(z_{k,l}, z_{i,j})$ indicates the synchronization between two cells.

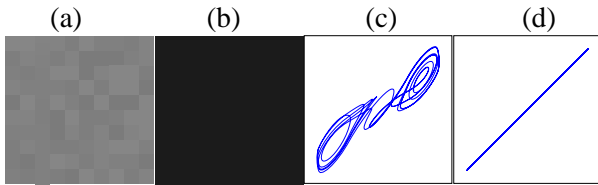


Fig. 2. (a) Initial state ($t = 0$), (b) Steady state ($t = 300$); Plots of variables in the steady state: (c) $y_{0,0}$ versus $z_{0,0}$, (d) $z_{4,6}$ versus $z_{0,0}$.

For the first example snapshots of the initial state and the steady state are shown in Fig. 2(a,b). A uniform coloring for the whole network in Fig. 2(b) indicates that all cells are synchronized. This is confirmed by plotting projection of the trajectory onto the plane $(z_{k,l}, z_{i,j})$ for two distant cells (k, l) and (i, j) (see Fig. 2(d)). Trajectories of individual cells form double-scroll attractors (Fig. 2(c)). Fully synchronized state is observed most frequently when the network is started from random initial conditions, which indicates that its basin of attraction is large.

In the second example, in the steady state there are two clusters of cells oscillating synchronously. This corresponds to groups of light and dark squares in Fig. 3(b). Oscillations generated by cells belonging to different clusters are shown in Fig. 3(c,d). The cells in different clusters operate in distinct regions of the \mathbb{R}^3 space (for cells in one cluster $z > 0$, while for the second one $z < 0$). Very good synchronization between the cells within clusters is shown in Fig. 3(e). In the steady state the behavior of the network is periodic.

Fig. 4 shows an example where one cluster is much smaller than the other. Clusters have sizes 17 and 83, respectively. Another important difference is that the

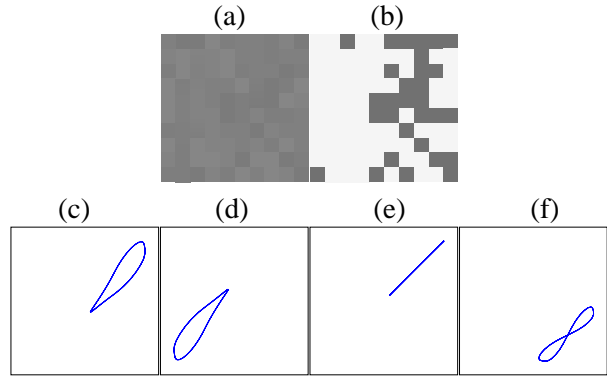


Fig. 3. (a) snapshot at $t = 0$, (b) snapshot at $t = 300$; plots in the steady state: (c) $y_{0,0} - z_{0,0}$, (d) $y_{4,4} - z_{4,4}$, (e) $z_{4,6} - z_{0,0}$, (f) $z_{4,4} - z_{0,0}$.

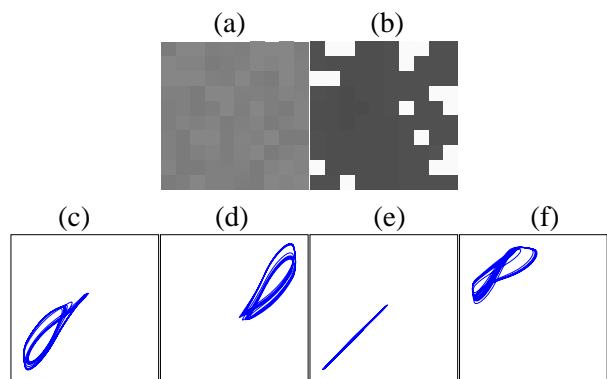


Fig. 4. (a) Initial state ($t = 0$), (b) steady state ($t = 300$); plots in the steady state: (c) $y_{0,0} - z_{0,0}$, (d) $y_{6,0} - z_{6,0}$, (e) $z_{4,4} - z_{0,0}$, (f) $z_{6,0} - z_{0,0}$.

network in the steady state oscillates chaotically (see Fig. 4(c,d)). There is very good synchronization between cells belonging to each cluster (Fig. 4(e)).

The last example shows pattern switching phenomena. The network started with random initial conditions for time $t \in [20, 45]$ displays a pattern with cluster sizes 94 and 6 (Fig. 5(a)). This structure is however not stable. At $t \approx 45$ the pattern changes. Most of the cells from the larger cluster leave the region $z > 0$ and a pattern with clusters of size 13 and 87 emerges (Fig. 5 (b)). This last pattern is stable. After very long integration time is still persists in the network. The cells within a cluster are not fully synchronized. Sometimes small bursts can be seen (Fig. 5(c)), but all the time the cluster pattern is clearly visible.

Among an abundance of observed attractors most frequent is the state of full synchronization. Other attractors are characterized by two clusters of cells operating in distinct regions of the \mathbb{R}^3 space. In some sense this attractors can be regarded as binary patterns. If a cell operates in the region $z > 0$ (or $z < 0$) we say it corresponds to binary “1” (or “0”). In some

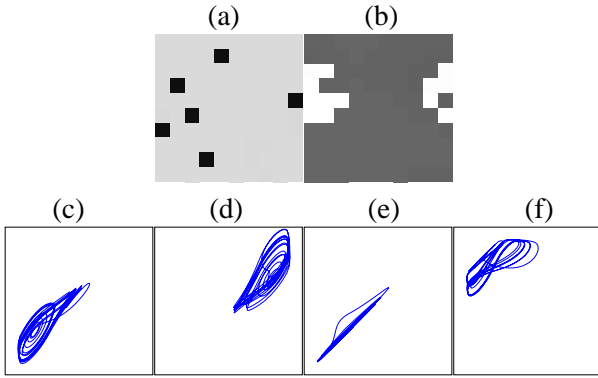


Fig. 5. (a) Initial state ($t = 10.5$) and (b) steady state ($t = 300$); plots in the steady state: (c) $y_{0,0} - z_{0,0}$, (d) $y_{1,5} - z_{1,5}$, (e) $z_{5,5} - z_{0,0}$, (f) $z_{1,5} - z_{0,0}$.

cases patterns are not stable.

IV. STORING PATTERNS

An important question, which arises in this context is how can we force the network to display a given pattern. We test a very simple approach. First, we choose a point (x, y, z) on the double-scroll attractor positioned far from the hyperplane $z = 0$ and satisfying the condition $z > 0$. In cells, which we want to code as binary “1” we set $(x_{i,j}, y_{i,j}, z_{i,j}) = (x, y, z)$ as an initial condition. For other cells we set $(x_{i,j}, y_{i,j}, z_{i,j}) = (-x, -y, -z)$. It appears that in this simple way we can force the network to store a given binary pattern. An example is shown in Fig. 6.

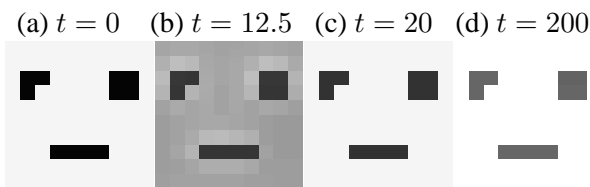


Fig. 6. Storing a pattern

Since the initial state (Fig. 6(a)) does not belong to the attractor corresponding to the binary pattern stored, we observe transient oscillations (see shades of gray in Fig. 6(b)). After some time the network converges to the attractor. Snapshots taken at $t = 20$ and $t = 200$ confirm that in the steady state the cells in each cluster oscillate synchronously.

In Fig. 7, we show four other examples of patterns that were successfully stored in the network.

There are some patterns which are not stable. Two examples are shown in Fig. 7(e,f). If we try to impose these patterns using the method described above the system displays them for some time, but eventually escapes to a stable attractor – in both cases the

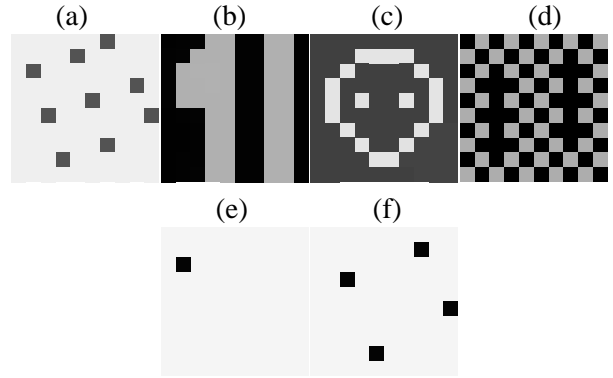


Fig. 7. First row – stored patterns (snapshot at $t = 40$); second row – unstable patterns, impossible to store

trajectory is attracted to the steady state with all cells synchronized. It seems that patterns for which one of the clusters is very small are unstable. Further analysis is necessary to characterize the class of unstable patterns.

V. STABILITY OF PATTERNS

In order to study stability of binary patterns, we carry out two different tests.

In the first test we modify the network parameters. All parameters of cells are disturbed by a random deviation of maximum amplitude 0.01% of nominal value. Two snapshots taken at the steady state are shown in Fig. 8. Initially a binary pattern is formed. Later, the cells within clusters are not fully synchronized (different shades of grey) but still the cluster structure is clearly visible.

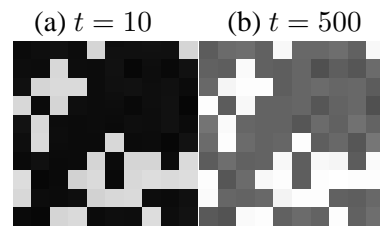


Fig. 8. Behavior of network with nonuniform cells.

In the second test we disturb all variables in the network displaying a binary pattern by adding a random value of a small amplitude. In this way we can test the size of the basin of attraction of the corresponding attractor. Results for the pattern from Fig. 6(d) are shown in Fig. 9. The maximum amplitude of perturbation was 0.5 (Fig. 9(a)) and 1.0 (Fig. 9(c,e)). In two cases the pattern was recovered in a correct way (Fig. 9(b,d)), while in the last case one bit was detected with error (Fig. 9(f)).

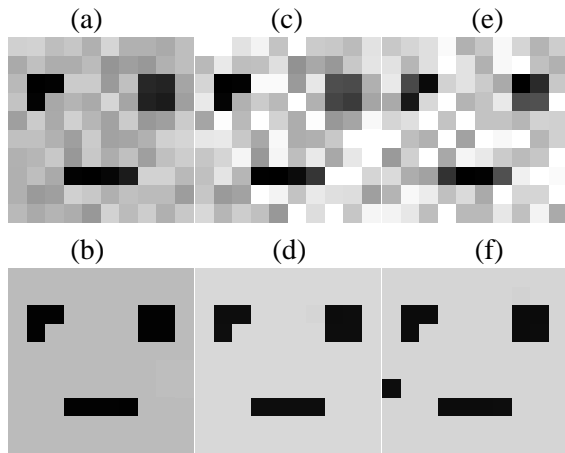


Fig. 9. Stability of patterns, (a), (c), (e) disturbed patterns, (b), (d), (f) recovered patterns

VI. LARGER NETWORKS

Let us now consider two examples of larger networks. The behavior of a 20×20 network started with random initial conditions is shown in Fig. 10. The binary pattern visible in Fig. 10(b) evolves (see Fig. 10(c)) and around $t = 200$ the final pattern emerges (Fig. 10(d)). This pattern persists even for $t \leq 5000$. Although the binary pattern is stable there is no full synchronization between the cells in the clusters – waves traveling through the network are visible as different shades of gray for cells belonging to a given cluster.

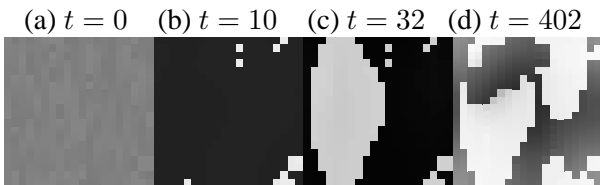


Fig. 10. Dynamics of a network of 20×20 cells

As a last example we show simulations of the network composed of 100×100 cells. In this case the network started from random initial conditions after $t > 4$ displays a binary pattern (Fig. 11(b)). This pattern is however not stable. At $t = 18$ a circular wave appears and the behavior becomes disorganized. Snapshots taken at $t = 100$ and $t = 500$ are shown in Fig. 11(c,d). The mode of pattern variation is typical for large networks.

These two simulations show that the property of storing binary patterns depends on the network size. It seems that the number of stable patterns is smaller for large networks. For very large networks binary patterns are not stable and more complex behavior is observed.

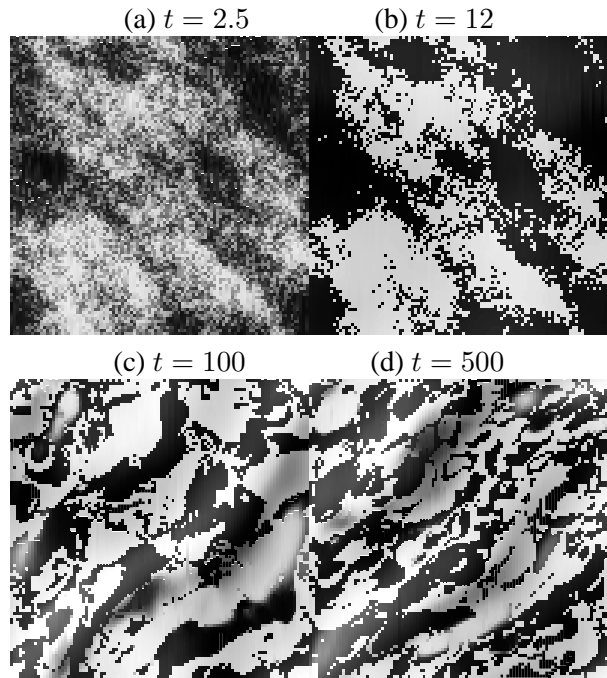


Fig. 11. Behavior of a network of 100×100 cells

VII. CONCLUSIONS

Arrays of locally coupled chaotic circuits show an abundance of pattern formation phenomena. Using position of the attractors in the phase space it is possible to give a binary description to such patterns. We have investigated the formation of binary patterns in arrays of Chua’s circuits coupled via a regular resistive grid. Further we have proposed a simple method for obtaining a desired binary pattern by appropriate choice of initial states of the network. Stability of patterns and influence of non-uniformity and size of the networks have also been addressed.

REFERENCES

- [1] D. Amit, H. Gutfreund, and H. Sompolinsky. Storing infinite numbers of patterns in a spin-glass model of neural networks. *Phys. Rev. Lett.*, 55:1530–1533, 1985.
- [2] W.J. Freeman, "Tutorial on Neurobiology: From Single Neurons to Brain Chaos", *Int. J. Bif. Chaos*, Vol.2, No. 3, pp. 451–482, 1992.
- [3] D.O. Gorodnichy. "Designing High Performance Attractor-based Neural Networks", Ph.D. Dissertation, Academy of Sciences of Ukraine, Kiev, 1997, (in Russian).
- [4] S. Ishii, K. Fukumizu and S. Watanabe. A network of chaotic elements for information processing. *Neural Networks*, 9, pp. 25–40, 1996.
- [5] C. Rekeczky, I. Szatmari, P. Foldesy and T. Roska, "Analogic Cellular PDE Machines", *World Congress Comp. Intel.*, 2002,
- [6] S.-S. Lin, T.-S. Yang, "On The Spatial Entropy and Patterns of Two-Dimensional Cellular Neural Networks", *Int. J. Bif. Chaos*, Vol. 12, No. 1 (2002) 115–128.

The first eigenvalue of the Laplacian and the ground flow of a compact surface

Clara Grácio and J. Sousa Ramos

Departamento de Matemática, Universidade de Évora
 Rua Romão Ramalho, 59, 7000-671 Évora, Portugal
 e-mail: mgracio@uevora.pt

Departamento de Matemática, Instituto Superior Técnico
 Av. Rovisco Pais 1, 1049-001 Lisboa, Portugal
 e-mail: sramos@math.ist.utl.pt

Abstract— *We present some results whose central theme is that the phenomenon of the first eigenvalue of the Laplacian and the ground flow of the compact surface (bitorus). Our main tool is a method for studying how the hyperbolic metric on a Riemann surface behaves under deformation of the surface. With this model, we show that there are variation of the first eigenvalue of the Laplacian and the ground flow with the Fenchel-Nielsen coordinates, that characterize the surface.*

I. INTRODUCTION

The Selberg trace formula has been of great interest to mathematicians for almost 50 years. It was discovered by Selberg, who also defined the Selberg zeta function, by analogy with the Riemann zeta function, to be a product over prime geodesics in a compact Riemann surface.

The Selberg trace formula has been of great interest to mathematicians for almost 50 years. It was discovered by Selberg [13], who also defined the Selberg zeta function, by analogy with the Riemann zeta function, to be a product over prime geodesics in a compact Riemann surface. But the analogue of the Riemann hypothesis is provable for the Selberg zeta function. The trace formula shows that there is a relation between the length spectrum of these prime geodesics and the spectrum of the Laplace operator on the surface.

More recently quantum physicists (specifically those working on quantum chaos theory) have been investigating the Selberg trace formula and its generalizations because it provides a connection between classical and quantum physics. In fact, of late there has been much communication between mathematicians and physicists on this and matters related to the statistics of spectra and zeta zeros.

For the computation of the length geodesic spectrum see [11]

In this note, we announce a collection of results connected to the behavior of the first eigenvalue $\lambda_1(S)$ of a compact Riemann surface S of genus 2, endowed with a metric of constant curvature -1 .

The idea of studying the first eigenvalue of a Riemann surface via the study of eigenvalues of 3-regular graphs comes from the work of Buser [5], [7]. In effect, our approach here is a variation on his idea, where we first study the behavior of λ_1 on finite-area Riemann surfaces connected to 3-regular graphs, and then see how λ_1 changes when we deformed the surface. It is interesting to pass back and forth between the geometric and graph-theoretic pictures. One reason for doing this is that a problem which appears difficult from one point of view may be relatively easy, or even solved, from the other point of view. Another reason is that attitudes towards various results may differ markedly in two areas, and comparing them may be an important source of insight.

Our main analytic tool is a method for studying how the hyperbolic metric of a finite-area Riemann surface behaves under such a deformation.

The first eigenvalue of the Laplacian on a surface can be viewed as a functional on the space of Riemannian metrics of a given area.

Every such surface is represented by a quotient space H^2/Γ of the upper half-plane H^2 by a Fuchsian group Γ which is isomorphic to a fundamental group of \mathcal{M} . The discrete group Γ is identified with the corresponding system of generators. A fundamen-

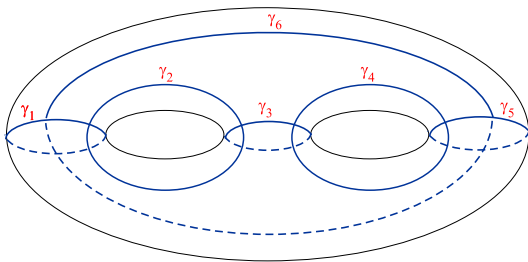


Fig. 1. Bitorus

tal domain \mathcal{F} is defined. The method is to decompose Riemann surface into a set of 2 pairs of pants by simple closed geodesics. Then the Fenchel-Nielsen coordinates are defined by geodesic length functions of three simple closed geodesics and twist angles along these geodesics.

Here we use a real-analytic embedding of the Teichmüller space \mathcal{T} of closed Riemann surfaces of genus 2 onto an explicitly defined region $\mathcal{R} \subset \mathcal{R}'$. The parameters are explicitly defined in terms of the underlying hyperbolic geometry. The parameters are elementary functions of lengths of simple closed geodesics, angles and distances between simple closed geodesics. The embedding is accomplished by writing down four matrices in $PSL(2, \mathbb{R})$, where the entries in these matrices are explicit algebraic functions of the parameters. With explicit constructions and side pairing transformations (see [12]) we define the Fuchsian group Γ representing the closed Riemann surface of genus 2.

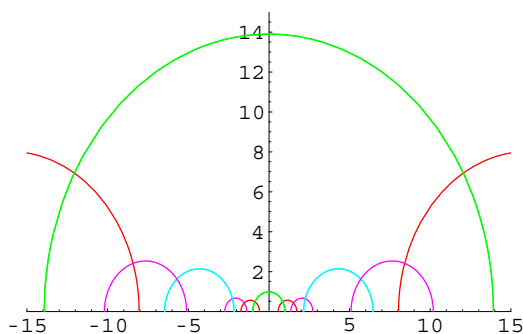


Fig. 2. Hyperbolic plane

Cheeger’s celebrated inequality relates the first non-trivial eigenvalue of a compact manifold to an isoperimetric constant, the Cheeger constant, defined as follows: let S be a closed Riemannian manifold (compact, no boundary) and let X be a hypersurface dividing S into two parts, A and B . Then

$$h(S) = \inf_S \frac{area(X)}{\min(vol(A), vol(B))}$$

where the infimum runs over all such hypersurfaces X . Let λ_1 denote the first nontrivial eigenvalue of S . Cheeger in [8] proved:

Theorem 1: Let S be a closed Riemannian manifold. Then $\lambda_1 \geq \frac{1}{4}h^2$.

This bound is remarkable for its universal character. It is natural to ask whether there is an upper bound for the first eigenvalue in terms of Cheeger’s constant. With an added hypothesis on curvatures, such an up-

per bound was proved by [7]:

Theorem 2: Suppose that S is a smooth Riemannian manifold with $Ricc(S) \geq -c$. Then there are constants c_1 and c_2 depending on c so that $\lambda_1 \leq c_1h + c_2h^2$.(see [7]).

It is not surprising that there are graph-theoretic analogues of these notions and results. As usual, there are different conventions and normalizations which are essentially equivalent. It convenient to stick to the case of k -regular graphs G , and define the Laplacian as

$$\Delta(f)(x) = \frac{1}{k} \sum_{y \sim x} (f(x) - f(y))$$

and the Cheeger constant to be

$$h(G) = \inf_E \frac{\#(X)}{\min(\#(A), \#(B))}$$

where E runs over collections of edges such that $G - E$ decomposes into two pieces A and B , and $\#(A)$ (resp. $\#(B)$) denotes the number of vertices in A (resp. B).

Cheeger’s inequality then becomes:

Theorem 3: $\lambda_1 \geq \frac{1}{2k^2}h^2$,(see [1]).

The analogue of Buser’s inequality is:

Theorem 4: $\lambda_1 \leq 2h$.(see [1]).

The importance of the study of the first eigenvalue of a Riemann surface is fairly well established by now in the literature. But with the introduction of the notion of conductance of a dynamical system, particularly in the graph theory, and with the relationship with the smallest non-zero eigenvalue of the Laplacian this importance get bigger. Another field is beginning.

II. VARIATIONS WITH FENCHEL-NIELSEN COORDINATES

In a general way, to each discrete dynamical system (I, f) defined by the iterates of a map f on the interval I , we associate a Markov matrix, which is representable by a non-regular, oriented graph G_f (the elements of E are now ordered pairs). So we have systems defined by the adjacency matrix $A_f = (a_{ij})$ of G_f , that is, the 0 – 1 matrix where $a_{ij} = 1$ iff ij is an edge. We can now establish the notion of conductance of a discrete dynamical system. For more details see [10].

Definition 1: Let $A_f = (a_{ij})_{i,j=1}^n$ be the adjacency matrix associated to (I, f) and \tilde{G}_f the Markov graph. Define the diagonal matrix $D_f = (d_{ij})_{i,j=1}^n$, putting in the diagonal d_{ii} the number of edges that incide (in and out) in the vertex i (loops contribute with 2). We

will call the matrix

$$\Delta_f = D_f - (A_f + A_f^T)$$

the Laplacian matrix of the graph G_f .

As we will see, the smallest non-zero eigenvalue of the Laplacian is closely related with the conductance of the system. This result can be proved by symbolic dynamic methods.

To explicit construction of a fundamental domain we consider the geodesics in the hyperbolic plane H^2 given the surface $\mathcal{M} = \mathcal{H}^\epsilon / -$, see Fig. 2. When we cut the surface \mathcal{M} along these geodesics then we divide it into four equilateral hexagons. The sides are obtained by the intersection of the axis, they are geodesics segments. These geodesics are the shortest geodesics in the free homotopy class of loops corresponding to some elements h_i ($i = 1, \dots, 6$) of $\Gamma = \pi_1(\mathcal{M})$, the fundamental group of \mathcal{M} . We have the hexagon H_1 whose sides s_i are the arcs of γ_i and these arcs are contained in the axes of the hyperbolic transformations h_i ($i = 1, \dots, 6$). Their translation length in the positive direction along these axis is $2l_i$ where l_i denote the length of $\gamma_i = l(\gamma_i)$. They are four of the parameters. The other parameters are the gluing angles. So:

$$\begin{aligned} c_1 &= l(\gamma_1), c_2 = l(\gamma_2), c_3 = l(\gamma_3), c_4 = l(\gamma_4), \\ \sigma &= |P - P_2|, \tau = \text{arc tanh}(\cos(\theta_2)), \\ \rho &= \text{arc tanh}(\cos(\theta_3)) \end{aligned}$$

But c_4 is determined by the others parameters, so with this parametrization, each point t_i of the Teichmüller space \mathcal{T} is $t_i = t_i(c_1, c_2, c_3, \sigma, \tau, \rho)$. This construction is dependent from the choice of the original geodesics γ_i , the chain, thus the dependence from the parameters $c_i = l(\gamma_i)$.

The sides are labelled s_1, \dots, s_{12} reading counter-clockwise from the zero.

Let H^2/Γ our compact surface of genus $g = 2$. The fundamental domain is a bounded fundamental polygon whose boundary ∂F consists of the 12 geodesics segments s_1, \dots, s_{12} .

Each side s_i of F is identified with s_j , by an element $g \in \Gamma$ and so each $g \in \Gamma$ produces a unique side s , namely, $s = \overline{F} \cap g(\overline{F})$. There is a bijection between the set of the sides of F and the set of elements g in Γ for which $\overline{F} \cap g(\overline{F})$ is a side of F .

We construct a map from the set of the sides of F onto itself, $g : s_i \rightarrow s_j$ where s_i is identified with s_j . This is called a *side-pairing* of F . The *side-pairing* elements of Γ generate Γ .

In this construction we choose the side rule for the pairing

$$\begin{aligned} s_1 &\rightarrow s_7, s_2 \rightarrow s_{12}, s_3 \rightarrow s_5, \\ s_4 &\rightarrow s_{10}, s_6 \rightarrow s_8, s_9 \rightarrow s_{11} \end{aligned}$$

With this choice we explicitly calculate formulas for the side pairing transformations $g_1, \dots, g_6, g_7 = g_1^{-1}, \dots, g_{12} = g_6^{-1}$. This mean that $s_7 = g_1(s_1), \dots, s_9 = g_6(s_{11})$, $s_1 = g_7(s_7), \dots, s_{11} = g_{12}(s_9)$, thus we obtain explicitly the generators $g_i = g_i(c_1, c_2, c_3, \sigma, \tau, \rho)$, $i = 1, \dots, 12$.

With the linear fractional transformations defined above it is possible to obtain the boundary map: $f_\Gamma : \partial F \rightarrow \partial F$, defined by piecewise linear fractional transformations in the partition $\mathcal{P} = \{\mathcal{I}_i = [\sqrt{\rho}, \sqrt{\rho} + \infty), i = 1, \dots, 11, [p_{12}, p_1)\}$, which is orbit equivalent to the action of the fundamental group Γ on ∂F . The boundary map is represented by

$$\begin{aligned} f_\Gamma : \bigcup_{i=1, \dots, 12} I_i &\rightarrow \bigcup_{i=1, \dots, 12} I_i \\ f_\Gamma(x)|_{I_i} &= g_i(x), \quad i = 1, \dots, 12 \end{aligned}$$

We are able to define a map that codifies the expansion of boundary points of F . And we determine the Markov matrix A_Γ associated to Γ . Let be A_Γ the matrix

$$a_{ij} = \begin{cases} 1 & \text{if } J_j \subset f_\Gamma(J_i) \\ 0 & \text{otherwise} \end{cases}$$

In [11] we have introduced a Markov partition for the Bowen-Series boundary map f_Γ associated with the fundamental group Γ and we defined the 24×24 Markov matrix A_Γ . It is known that there are the correspondence between the closed geodesics of the surface and the conjugacy classes of the group so with the list above we identify each closed geodesic. We obtained the length spectrum of the closed geodesics by computing $l(g) = 2 \text{ Arc cos } h[\text{tr}(g)/2]$.

Returning to our original question, we note that a closed surface of genus at least 2 has uncountably many hyperbolic structures up to homotopy relative to the boundary, and these may be parametrized by Fenchel-Nielsen coordinates in Teichmüller space, so they have the remarkable property, known as flexibility. But, in spite of this flexibility, there is the following property, that state the existence of constants, who guarantees a certain boundedness of hyperbolic structures under deformation of a hyperbolic surface.

Theorem 5: Let \mathcal{M} a hyperbolic surface of genus $g = 2$ (bitorus). Then smallest non-zero eigenvalue

of the Laplacian is bounded from above by a constant $c_0 < 1/4$ (see [14]).

In this communication we determine explicitly this constant. First we need to be clear this constant.

Definition 2: Let be a geodesic chain $\gamma_1, \gamma_2, \gamma_3, \gamma_4$ where the four geodesics have equal length and the twist parameters are zero. We call regular domain of the genus $g = 2$ closed Riemann surface \mathcal{M} with this Fenchel-Nielsen coordinates choice.

Here, the Cheeger constant is $h(G_f)$ is the minimum of the conductances on \mathcal{M}_\square where $t = t(c_1, c_2, c_3, \sigma, \tau, \rho)$ is a point of the Teichmüller space \mathcal{T} .

We are able to introduced our main result. We denote by $\Phi(\Delta_f)$ the eigenvector associated to the smallest non-zero eigenvalue of the Laplacian Δ_f , and we designate it by *ground flow eigenvector*.

Theorem 6: Let $\Phi(\Delta_f)$ be the *ground flow eigenvector associated to the compact surface \mathcal{M} , then the total sum of its components is zero.*

Proof: The prove can be obtained using the fact that the Laplacian matrix Δ_f is symmetric. ■

See [9] and [10] for the relation with the mixing rate.

ACKNOWLEDGEMENTS

The authors are (partially) supported by FCT (Portugal) trough the program POCTI/FEDER.

REFERENCES

[1] R. Brooks, *Spectral geometry and the Cheeger constant*, J. Friedman (ed.), Expanding Graphs, Proc. DIMACS Workshop, AMS (1993), 5–19.

[2] R. Brooks, *Platonic surfaces*, Comm. Math. Helv. 74 (1999), 156–170.

[3] R. Brooks and E. Makover, *Riemann surfaces with large first eigenvalue*, to appear.

[4] R. Brooks and E. Makover, *Random construction of Riemann surfaces*, to appear.

[5] P. Buser, *Cubic graphs and the first eigenvalue of a Riemann surface*, Math. Zeit. 162 (1978), 87–99.

[6] P. Buser, *A note on the isoperimetric constant*, Ann. Scient. Éc. Norm. Sup. 15 (1982), 213-230.

[7] P. Buser, *On the bipartition of graphs*, Discrete Appl. Math. 9 (1984), 105–109.

[8] J. Cheeger, *A lower bound for the smallest eigenvalue of the Laplacian*, in: Gunning (ed.), Problems in Analysis, Princeton University Press (1970), pp. 195–199.

[9] S. Fernandes, J. Sousa Ramos, *Spectral Invariants of Iterated Maps of the Interval*, To appear in Grazer Math. Ber.

[10] S. Fernandes, J. Sousa Ramos, *Second Smaller Zero of Kneading*, 8th International Conference on Difference Equations and Applications, July 28 - August 1, 2003, Brno, Czech Republic.

[11] C. Gr´acio, J. Sousa Ramos, *Symbolic dynamics and hyperbolic groups*, Grazer Math. Ber., 339, pgs. 195-206, 1999.

[12] C. Gr´acio, J. Sousa Ramos, *Boundary maps and Fenchel-Nielsen coordinates*, International Jour. Bifurcation and Chaos, 13, 7 (2003) 1949-1958.

[13] A. Selberg, *On the estimation of Fourier coefficients of modular forms*, in: A. L. Whiteman (ed.), Theory of Numbers, Proc. Symp. Pure Math. 8 (1965), pp. 1–15.

[14] P. Schmutz, *New results concerning the number of small eigenvalues on Riemann surfaces*, J. reine angew. Math. 471(1996), 201-220.

CIRCUIT MODEL OF THE ATMOSPHERIC RESPONSE FUNCTION

László Hevesi¹, Imre M. Jánosi² and Andrea Király²

¹Laboratory for Information Technology,
²Department of Physics of Complex Systems,
 Lorand Eötvös University,
 Budapest, Hungary
 e-mail: janos@lecco.elte.hu
 WWW: <http://complex.elte.hu>

Abstract— *The atmospheric response function gives the most probable daily mean-temperature change as a function of temperature anomaly, that is the deviation from long-term average value for a particular calendar day. We demonstrate that this response function is inherently nonlinear and climate specific. The shape of the function can be well fitted by a third order polynomial, and the noise amplitude also depends on the anomaly. An electric circuit realization provides a straight tool for an exhaustive investigation of the pretty large parameter space.*

I. INTRODUCTION

What is the expected average temperature tomorrow? If your estimate is exactly the same as the value today plus/minus 2 Centigrade, your success rate will be well over 60%, at least in temperate climate. The naïve prediction can be improved by considering tendencies on the previous days. Temperature changes at calm weather are expected to follow the seasonal time-course, otherwise, e.g. in midlatitudes, active cyclones and anticyclones determine atmospheric parameters for a couple of days. Nevertheless, warming or cooling trends can not persist forever, there comes an unavoidable turning point.

Intuitively, turning of temperature trends should have an increasing probability, when the state of the atmosphere is shifted farther and farther from the “normal” conditions. Meteorologists define the normal state of atmosphere by means of averages taken over properly chosen time and space domains. For example, the daily mean-temperature on 9 May in Budapest is expected around 14.5 °C based on averaging over several years for the same calendar day. The difference between the actual value and the long-time average is termed as the temperature anomaly $(\Delta T)_i$ for the i th day of the year. Figure 1 shows the probability that the temperature moves back toward the long-time average on the next day, as a function of anomaly. The

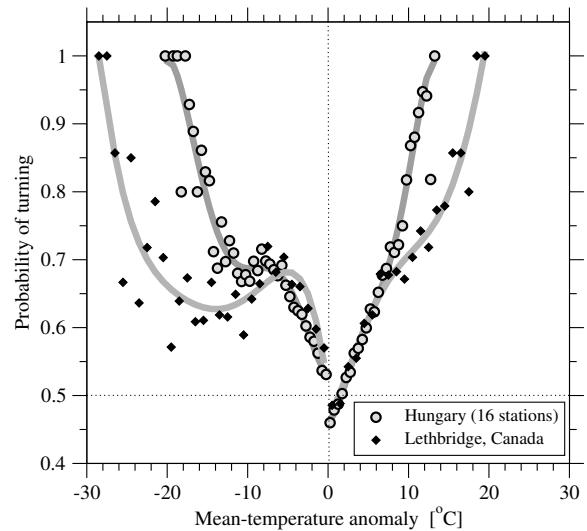


Fig. 1. Turning probability of daily mean-temperature as a function of daily mean-temperature anomaly. Circles: aggregated data for 16 Hungarian weather stations, 38 years each; diamonds: Lethbridge, Canada (49° 38' N, 112° 48' W), 64 years. The gray lines only guide the eyes.

data illustrate well that our anticipation is not too far from reality, however, the analysis of the highly non-trivial curves is beyond the scope of the present work.

The nomenclature (and actually Fig. 1) already suggest that the long-time average value of daily mean-temperatures is somehow associated with a kind of equilibrium state. However, any measured data can be averaged, but the physical meaning of the average value should be always explained. In this work we show that (i) the long-time daily average temperature is an attribute of a stable atmospheric equilibrium state. (ii) The behavior around this equilibrium can be described by a temperature response function, which is climate dependent. (iii) The parameter space is investigated by a simple circuit model of the response function.

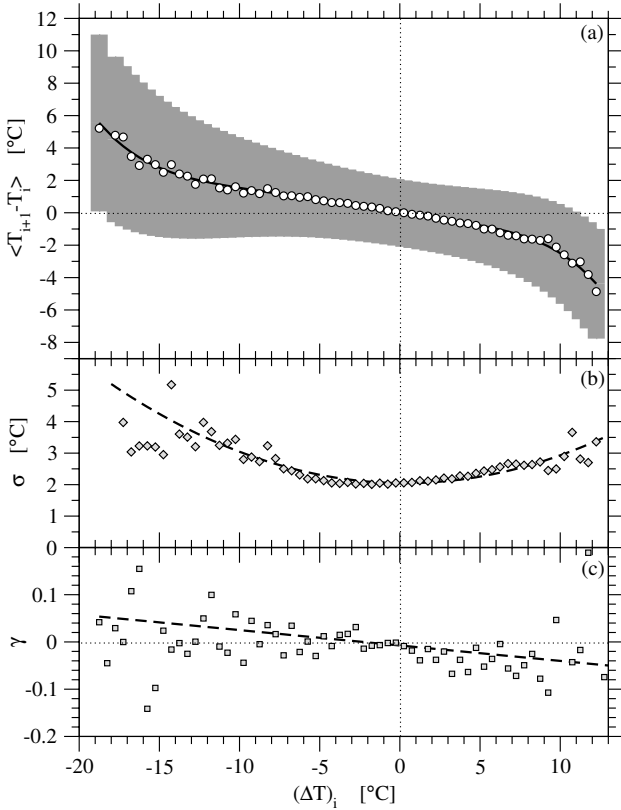


Fig. 2. Empirical atmospheric temperature response function for 16 weather stations in Hungary. **(a)** The average temperature step $\langle T_{i+1} - T_i \rangle$ (circles) as a function of temperature anomaly ΔT_i , the gray band indicates the standard deviation. The solid line is a fifth order polynomial fit. **(b)** The standard deviation σ (diamonds), and **(c)** the skewness γ as a function of temperature anomaly ΔT_i . Dashed line in (b) indicates a parabolic fit.

II. TEMPERATURE RESPONSE FUNCTION

A system is said in stable equilibrium, when its spontaneous motion is restricted to a bounded phase space domain, and the effect of external perturbations decays in finite time. To be more specific for the atmospheric temperature, the first criterion means that its probability distribution is bounded and invariant in time, the second means that large anomalies are followed by backward steps in a couple of days. While histograms of temperature fluctuations are evaluated routinely [1], the "response function" has been introduced only recently [2].

Figure 2 shows the one-day mean-temperature response for Hungary. The data set is described in details in Ref. [3], long-range correlation properties are analyzed in [2], [4]. Records for other geographic locations are obtained from the Global Daily Climatology Network provided by the US National Climatic Data Center [5].

The elements of the response function in Fig. 2 support that the long-time average temperature represents a stable (dynamic) equilibrium state of the lower atmosphere:

- The expected response vanishes at zero anomaly, and finite deviations imply a finite average temperature step of the opposite sign (Fig. 2a).
- Fluctuations are enhanced at larger anomalies in both directions (Fig. 2b).
- The partial probability distributions at around a given anomaly value are skewed "backward", i.e. fluctuations toward the equilibrium have higher probabilities than in the opposite direction (Fig. 2c)

Note that the curve of the average response (Fig. 2a) is asymmetric and strongly nonlinear. The best empirical fit is a fifth order polynomial, however a cubic approximation is acceptable as well [2].

III. RESPONSE FUNCTION CLIMATOLOGY

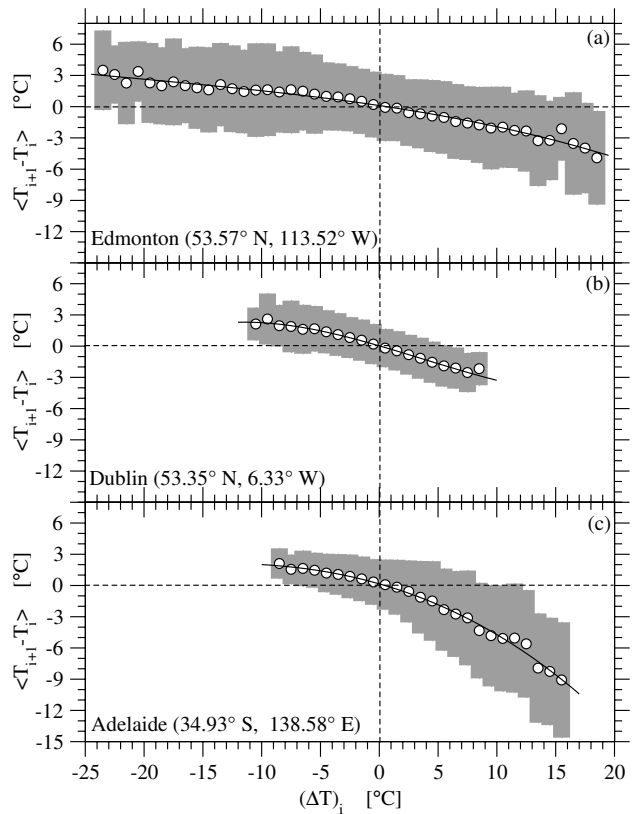


Fig. 3. Empirical atmospheric temperature response function for three weather stations:**(a)** Edmonton (Canada) 64 years, **(b)** Dublin (Ireland) 80 years, and **(c)** Adelaide (Australia) 112 years daily data. The plots are in the same scales. Gray band indicates one standard deviation. Thin lines are cubic fits.

Figure 3 clearly illustrates that the response function is not universal, it depends strongly on the geographic location and local climate. In order to com-

TABLE I
FITTED COEFFICIENTS OF EQ. (1) FOR SEVERAL
WEATHER STATIONS IN DIFFERENT CLIMATES.

	$c_1 \times 10$	$c_2 \times 10^3$	$c_3 \times 10^4$
Adelaide (AUS)	-3.215	-15.143	-1.488
Bamberg (D)	-1.964	-9.029	-3.589
Basel (CH)	-1.495	-7.837	-6.298
Budapest (H)	-1.242	-7.593	-7.965
Darwin (AUS)	-2.924	-18.371	-9.436
De Bilt (NL)	-1.988	-5.699	-2.540
Dublin (IRL)	-3.048	-5.270	-0.000
Edmonton (CAN)	-1.677	-3.041	-0.490
Hamburg (D)	-1.961	-4.981	-2.294
Kremsmünster (A)	-1.384	-7.799	-7.420
La Estan. (URY)	-2.993	-6.054	-0.695
Lethbridge (CAN)	-1.955	-3.555	-0.623
Lugano (CH)	-2.554	-9.517	-2.524
Melbourne (AUS)	-3.569	-13.274	-11.606
Oslo (NOR)	-1.969	-4.020	-1.377
Paris (F)	-1.644	-7.956	-5.223
Potsdam (D)	-1.669	-7.418	-4.118
Säntis (CH)	-1.675	-0.615	-3.039
Sydney (AUS)	-3.807	-30.069	-16.989
Ullungdo (KOR)	-2.685	-10.394	-12.817
Zürich (CH)	-1.591	-7.506	-7.037
Willis Isl. (AUS)	-1.982	-27.334	-160.87

pare different weather stations more quantitatively, we fitted the average response by a third order polynomial:

$$\langle T_{i+1} - T_i \rangle = \sum_{n=1}^3 c_n (\Delta T)_i^n, \quad (1)$$

where $(\Delta T)_i$ is the mean-temperature anomaly on the i th day, $\langle T_{i+1} - T_i \rangle$ denotes the average change of the daily mean-temperature on the next day. The coefficients are given in Table I for a couple of places.

Note that all the signs of the coefficients c_n are negative. This means, first of all, that the atmosphere exhibits a strong negative feedback, large temperature fluctuations are damped. The lack of turning points is a physically plausible requirement, thus the parameter space is restricted by the condition [6]:

$$c_2^2 < 3c_1 * c_3. \quad (2)$$

Furthermore, the data do not coincide with an odd cubic function. When we denote the curve by $y(x) = \sum_{n=1}^3 c_n x^n$, the symmetry centre (x_s, y_s) (point of in-

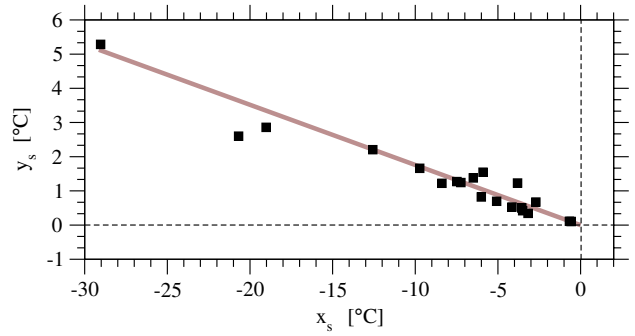


Fig. 4. The shift of the symmetry center Eq. (3) for the stations listed in Table I. [The fits for Adelaide and Dublin do not satisfy condition (2)].

flection) obeys a shift [6]:

$$x_s = -\frac{c_2}{3c_3} \quad y_s = \frac{2c_2^3 - 9c_1 c_2 c_3}{27c_3^2}. \quad (3)$$

It is interesting to see that the shifts are arranged along a line (Fig. 4). The leftmost three stations are La Estanzuela (Uruguay), Lethbridge (Canada), and Edmonton (Canada), the most symmetric curves belong to Willis Island (Australia) and Säntis (Switzerland). Since these locations represent very different climate, an easy explanation is hardly given.

Note finally that the response function (Fig. 2a, Figs. 3a-c) can be approximated by a straight line of negative slope at around zero anomaly. This picture is consistent with the simplest first-order autoregressive (AR1) model of temperature anomaly fluctuations, where a stochastic process is defined as [1], [2]:

$$(\Delta T)_{i+1} = a(\Delta T)_i + \xi_i. \quad (4)$$

Here $a < 1$ is the AR1 coefficient, and ξ is a noise term of appropriate amplitude and correlation properties [2]. Numerical tests confirmed that the relation $a \approx (1 + c_1)$ is fulfilled for each case (note that c_1 is negative), numerical inaccuracies are due to the linear fit of nonlinear curves.

IV. CIRCUIT MODELING

Analog computers are almost extinct, nevertheless several fruitful concepts survived “digitalization” [7]. As for our particular problem, an exhaustive investigation of the parameter space is quite demanding: there are (at least) three parameters for the average response, another three for the parabolic noise function, and there are many possible temporal anomaly courses on different time scales. An attractive solution is to construct an electric circuit model where parameters can be tuned by potentiometers, input is provided

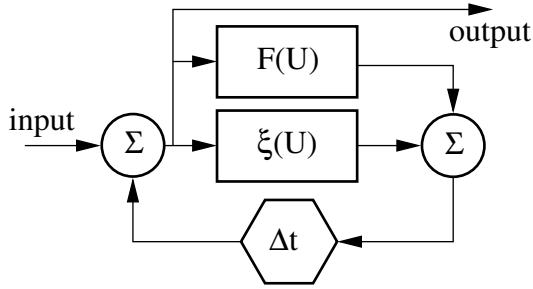


Fig. 5. Conceptual circuit model of the atmospheric response function. $F(U)$ is the polynomial Eq. (1), $\xi(U)$ is the noise generator reproducing Fig. 2b with parabolic coefficients $b_0, b_1,$ and b_2 , Δt is a time-delay unit.

by a signal generator, and the output is readily accessible by means of an oscilloscope (Fig. 5).

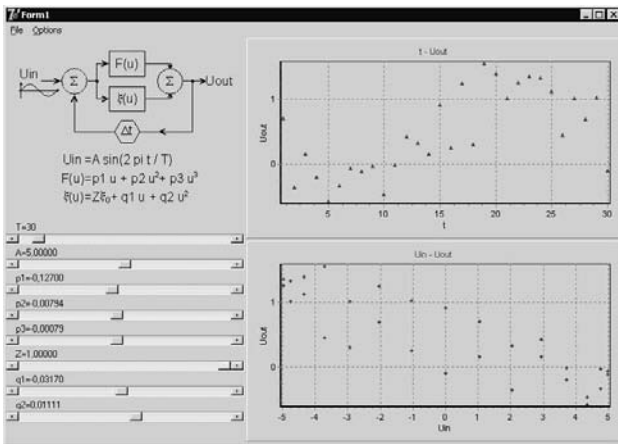


Fig. 6. Graphical user interface for a software realization of the circuit model in Fig. 5. The graphs show the response to a sinusoidal excitation, at parameters for Budapest (see Table I).

Obviously, an electric circuit of similarly low complexity can be easier realized by means of known software tools. The graphical user interface of our test version is shown in Fig. 6. Though the system seems to be simplistic, it is easy to find parameter ranges where the behavior is fairly nontrivial. As an example, we illustrate the consequence of an increased quadratic noise term in Fig. 7. The fitted parabolic function in Fig. 2b (dashed line) is

$$\sigma(\Delta T) = 2.049 - 0.0058\Delta T + 0.0094(\Delta T)^2 \quad (5)$$

If the coefficient of the last term in Eq. (5) is increased by a factor of five, the symmetric sinusoidal signal becomes strongly distorted with an anomalously high maximum (the amplitude of the excitation is 10 units), and a loop appears in the input vs. output function.

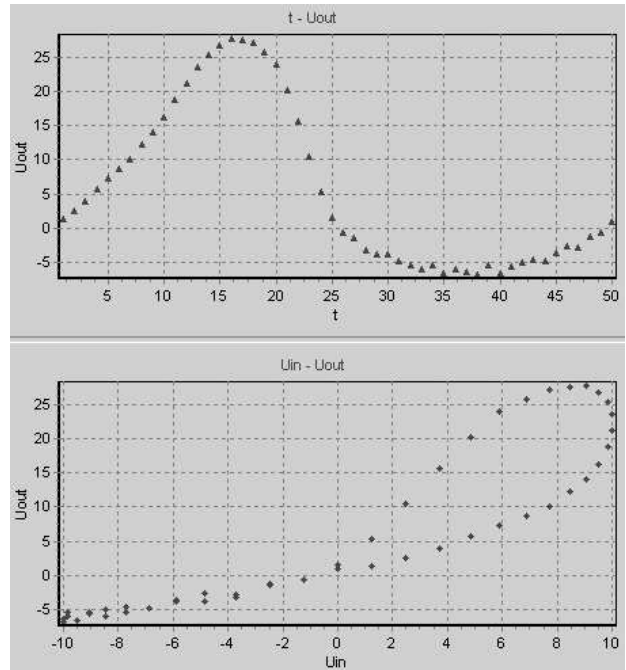


Fig. 7. Anomalous temperature-course for our Budapest-model where the only parameter perturbed is the quadratic term in the noise function (see text).

Note that the extreme heatwaves for summer 2003 gave rise to an intense discussion on the nature and role of temperature variability over the European continent [8].

Of course, we do not expect chaotic behavior for response functions of parameters listed in Table I. Nevertheless, the model can help to explore the surprisingly rich behavior of the “weather-oscillator” described above.

This work was supported by the Hungarian Science Foundation (OTKA) under grant no. T032437.

REFERENCES

- [1] H. von Storch, and F. W. Zwiers. *Statistical Analysis in Climate Research*. (Cambridge Univ. Press, Cambridge, 1999).
- [2] A. Király, and I.M. Jánosi. Stochastic modeling of daily temperature fluctuations. *Phys. Rev. E* **65**, 051102 (2002).
- [3] I.M. Jánosi, and G. Vattay. Soft turbulent state of the atmospheric boundary layer. *Phys. Rev. A* **46**, 6386-6389 (1992).
- [4] A. Király, and I.M. Jánosi. Detrended fluctuation analysis of daily temperature records: Geographic dependence over Australia. *Meteorol. Atmos. Phys.*, accepted (2004).
- [5] <http://www.ncdc.noaa.gov/oa/ncdc.html>
- [6] R. W.D. Nickalls. A new approach to solving the cubic. *Math. Gaz.* **77**, 354-359 (1993).
- [7] R. C. Weyrick. *Fundamentals of analog computers*. (Prentice-Hall, New York, 1969).
- [8] Ch. Schär *et al.* The role of increasing temperature variability in European summer heatwaves. *Nature* **427**, 332 - 336 (2004).

EMERGENT OSCILLATIONS IN A SYSTEM OF COUPLED NONLINEAR ELEMENTS WITH BROKEN SYMMETRY

Visarath In, Andy Kho, Adi R. Bulsara, Joe Neff, Brian Meadows
SPAWAR Systems Center, San Diego, CA 92152-5000, USA

Antonio Palacios, Patrick Longhini

Dept. of Mathematics and Statistics, San Diego State University, San Diego, CA 92182, USA

Bruno Ando, Salvatore Baglio

Dip. Elettrico Elettronico e Sistemistico, Univ. of Catania, 95125 Catania, Italy

Abstract — *Overdamped bistable systems can be described by the generic form $\dot{x} = -\nabla U(x)$, where $U(x)$ is a bistable potential energy function. It is well known that an overdamped system does not oscillate on its own so that, to switch states, the system must be forced by an external periodic signal with large enough amplitude to overcome the potential energy barrier that separates the two stable attractors (minima). However, well-designed coupling schemes, together with the appropriate choice of initial conditions can induce oscillations when a control parameter exceeds a threshold value, thereby eliminating the need for the forcing function. We demonstrate these concepts numerically and experimentally using three “single-domain” fluxgate magnetometers that are coupled unidirectionally in a ring; this configuration is the basis of simple, low-power, and inexpensive magnetometers for weak dc magnetic field detection.*

I. INTRODUCTION

Overdamped bistable dynamics, of the generic form $\dot{x} = -\nabla U(x)$, underpin the behavior of numerous systems in the physical world. The most-studied example is the overdamped Duffing system: the dynamics of a particle in a bistable potential $U(x) = -ax^2 + bx^4$. Bistable systems are also, frequently characterized by a “soft” (to be contrasted with the “hard” Duffing potential which approaches $\pm\infty$ far more steeply) potential consisting of a nonlinear addition to a parabolic component, the latter being, of course, characteristic of linear dynamics. Amongst these systems, the dynamics of a hysteretic ferromagnetic core (treated as a macroscopic single-domain entity) have recently attracted some attention, because they underpin very cheap magnetic field sensors, operated in the time domain [2]. Absent an external forcing term, the state-point $x(t)$ will rapidly

relax to one of two stable attractors, for any choice of initial condition; this behavior is, of course, universal in overdamped dynamical systems.

Recently, we have demonstrated [1], [3] that coupling an *odd* number $N \geq 3$ of overdamped bistable elements in a ring, with uni-directional coupling, and ensuring that at least one of them has an initial state that is different from the others, can lead to oscillatory behavior, when the coupling strength exceeds a critical value. The characteristics of the bifurcation to oscillatory behavior depend on the system dynamics and the manner in which the elements are coupled. Here, we outline the dynamics of uni-directionally coupled single domain ferromagnetic cores, focusing on the dynamics past the critical point, and demonstrate how one may derive the oscillation frequency together with its scaling behavior as a function of the coupling strength which is taken to be our control parameter. This frequency serves as a useful quantifier of a very small (compared to the hysteresis loop width) “target” signal, assumed to be dc throughout this work.

II. COUPLED “SINGLE-DOMAIN” MAGNETIC SYSTEMS

We begin by enunciating some of the results which have already been presented in [1], [3], confining ourselves to the $N = 3$ case (the extension to arbitrary N will become clear later on), thereby setting up the context of the problem at hand. Using the coupled magnetic “fluxgate” magnetometers as an example [1], we start with the system

$$\begin{aligned}\dot{x}_1 &= -x_1 + \tanh(c(x_1 + \lambda x_2 + \epsilon)) \\ \dot{x}_2 &= -x_2 + \tanh(c(x_2 + \lambda x_3 + \epsilon)). \\ \dot{x}_3 &= -x_3 + \tanh(c(x_3 + \lambda x_1 + \epsilon))\end{aligned}\quad (1)$$

where $x_i(t)$ represents the (suitably normalized) magnetic flux at the output (i.e. in the sec-

ondary coil) of each unit, and $\varepsilon \ll U_0$ is an externally applied dc magnetic flux. It is important to note that the oscillatory behavior occurs even for $\varepsilon = 0$, however when $\varepsilon \neq 0$, the oscillation characteristics change. The elements (i.e. magnetometers) in (1) are assumed identical, c being a temperature-dependent nonlinearity parameter (each element is bistable for $c > 1$), and U_0 being the energy barrier height of any of the elements, absent the coupling. Notice that the (uni-directional) coupling term, having strength λ , which is assumed to be equal for all three elements is *inside* the nonlinearity, a direct result of the mean-field nature of the description (in the fluxgate magnetometer, the coupling is through the induction in the primary or “pick up” coil).

A simple numerical integration of (1) (starting with *non-identical* initial conditions) reveals oscillatory behavior for $\lambda < \lambda_c$, where λ_c is a critical (or threshold) value of the coupling strength (as seen in [1], $\lambda_c < 0$, so that $|\lambda| > |\lambda_c|$ in the oscillatory regime). The oscillations are non-sinusoidal, with a frequency that increases as the coupling strength decreases away from λ_c . For $\lambda > \lambda_c$, however, the system quickly settles into one of its steady states, regardless of the initial conditions; the same result ensues if N is even, or if the coupling is bi-directional. As a side-note, we point out that the appearance of oscillations for $\lambda < \lambda_c$ does not violate any conservation laws; in a practical implementation, some onboard power (e.g. to drive the coupling circuit) is always present. The dc target signal ε has the effect of skewing the potential function (for zero coupling) of each element. This has implications for the oscillation frequency as well as the residence times (or, equivalently, the zero-crossings) of individual elements of the connected array, in their stable attractors. This induced asymmetry has been exploited by us [2] in a design for an inexpensive, low-power, and simple to operate fluxgate magnetometer.

Figure 1 shows the oscillations and the summed response $X(t) = \sum_i x_i(t)$ for the system (1), for different values of the coupling strength λ and dc asymmetrizing signal ε . We note that the individual responses $x_i(t)$, while having the same frequency (assuming that the parameters c and λ are the same throughout the dynamics (1)), are offset in phase by $2\pi/N$. Increasing N leads to different frequencies for the individual elements $x_i(t)$, with a concomittant phase difference between

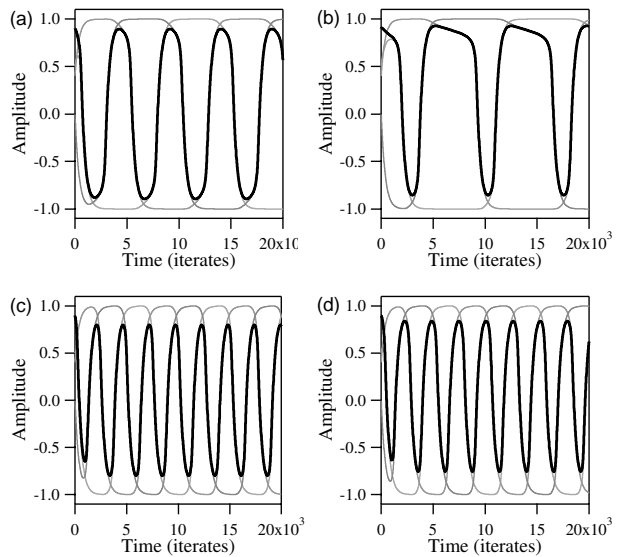


Fig. 1. Emergent oscillatory behavior in the coupled system (1). (a) shows the oscillations near the critical point. Summed response is indicated by thick lines in all panels. Typical of the heteroclinic cycles, the amplitudes are fully grown at the start of the bifurcation and the frequency is low. At the birth of the oscillations, the frequency is zero as predicated by the heteroclinic bifurcation. $\lambda = -0.65, \varepsilon = 0$. (b) shows the oscillations for $\lambda = -0.65, \varepsilon = 0.05$. Notice that the sum signal is greatly offset between the upper state (above zero) and the lower state (below zero). (c) shows the oscillations for a higher coupling strength $\lambda = -0.75$, and $\varepsilon = 0$. Contrasted with figure (a), the frequency increases significantly. The frequency scaling with respect to λ obeys the $1/2$ power law. Figure (d) has the same λ value as in (c) but $\varepsilon = 0.05$. Notice the decrease in frequency when the target signal ε is non-zero.

solutions; however, the summed response has a frequency that is *independent* of N , as long as the other parameters c and λ remain unchanged.

III. DYNAMICS

We now turn to a more detailed description of the dynamics (1), confining ourselves to the immediate neighbourhood of the critical point in the oscillatory regime, i.e., the separation $\lambda_c - \lambda$ is small. We carry out the analysis for $N = 3$ elements, with the generalization to arbitrary N made clear at the end. We refer to figure 1, specifically the top row which corresponds to the case of small separation $\lambda_c - \lambda$. Note that figure 1 was generated using a specific set of initial conditions, however the dynamics evolve independently of this choice, as long as at least one element has

an initial state different from the others.

For small separation $\lambda_c - \lambda$ it is clear that the state-points spend the bulk of their transition times reaching the inflexion points $\pm x_{inf} = \pm \sqrt{(c-1)/c}$, after which the passage to the opposite minimum (at ± 1) is very rapid. One also notes that the elements evolve two at a time, with one element always remaining in its steady state while the others evolve. This behavior, which is most pronounced near the critical point, has been quantified elsewhere [5]. It is also clear (figure 1) that the zero crossing points $t_0 (= 0), t_1, t_2$ etc. of the summed output $X(t)$ also correspond to the crossing points of the individual elements e.g. t_1 corresponds to the zero-crossing of $x_1(t)$, t_2 for $x_3(t)$, etc. Hence, the problem of finding the period T_+ of the summed output, or the individual oscillation periods $T_i \equiv T_3$ (which are all the same; the suffix refers to the $N = 3$ case) reduces to determining the zero-crossing times $t_{1,2}(t)$.

From our discussion above it is evident that, during the dominant part (in figure 1 this corresponds to the half-cycle starting at $x_1 = 1$) of the evolution of $x_1(t)$, the element $x_2(t)$ remains in its steady state $x_+ \approx 1$ (the exact locations of the fixed points can be readily found via simple calculus, as has been done in [2], and for $c > 1$ are very close to ± 1 , due to the tanh function) so that the first of the equations (1) can be simplified to:

$$\dot{x}_1(t) = -x_1 + \tanh c(x_1 + \lambda + \varepsilon), \quad (2)$$

corresponding to simple ‘‘particle-in-potential’’ motion. Formally integrating this equation yields,

$$t_1 = \int_1^0 \frac{dx_1}{\tanh c(x_1 + \lambda + \varepsilon) - x_1}, \quad (3)$$

where t_1 is the time taken (for this choice of initial conditions) by the state-point $x_1(t)$ to evolve from its attractor at $+1$, to 0 (figure 1). This integral cannot be evaluated analytically, in general. Similarly, we see that $x_3(t)$ evolves while $x_1(t) \approx -1$ so that we have

$$\dot{x}_3(t) = -x_3 + \tanh c(x_3 - \lambda + \varepsilon), \quad (4)$$

whence we obtain,

$$t_{12} \equiv t_2 - t_1 = \int_{-1}^0 \frac{dx_3}{\tanh c(x_3 - \lambda + \varepsilon) - x_3}. \quad (5)$$

From these two integrals, we may write down the period T_+ of the summed output as $T_+ = t_{12} + t_1$

by formally summing the above expressions. A little manipulation of the integration limits shows immediately that $T_+ = 2t_1$ for $\varepsilon = 0$, as expected. Having obtained the above expressions, it is easy to see that $t_3 = T_+ + t_1, t_4 = 2T_+, t_5 = 2T_+ + t_1, t_6 = 3T_+$, etc. In particular, we can write down the expression for the individual periods as $T_3 = 3T_+$, and for the phase differences between individual solutions as $t_3 - t_1 = t_5 - t_3$ etc., so that the phase difference is $2\pi/3$. The generalization of the above observations to arbitrary N should now be clear. In this case, the individual periods (and the phase offsets) do change; however, again, only two elements are simultaneously evolving at any given time, the remainder staying in their steady states. Hence, the period of the summed output is always the same, and we obtain, $T_+ = T_i/N$ where T_+ is now the summed output of N (odd) elements, and T_i is the period of the individual oscillations for the $i = N$ case. The phase offset between solutions for arbitrary N is $2\pi/N$.

The integrals in (3) and (5) may be evaluated just past the critical point, where the integrands display sharply peaked behavior. After some algebra we obtain [5] the elegant expression for the sum period T_+ :

$$T_+ = \frac{\pi}{\sqrt{cx_i}} \left[\frac{1}{\sqrt{\lambda_c - \lambda}} + \frac{1}{\sqrt{\lambda_c - \lambda + 2\varepsilon}} \right]. \quad (6)$$

A comparison between the period obtained from this expression and from direct numerical simulations is presented in Fig. 2. We see that the analytical expression captures the dynamics well, especially near the bifurcation threshold, but also well into the oscillating regime. This is attributable to the fact that the peaked nature of the denominators of (3) and (5) persists well into the oscillating regime, even though the peaks get broader as one moves deeper into this regime.

IV. EXPERIMENTS

We show here, preliminary results from an experimental setup involving three coupled PCB fluxgate magnetometers; for details see [5].

The experimentally observed oscillations are quite striking (figure 3). The system readily oscillates in a travelling pattern. Like the model, the system favors this pattern no matter how many times it is restarted. The frequency of oscillations is about 33.5 Hz. Each wave is phase shifted by exactly

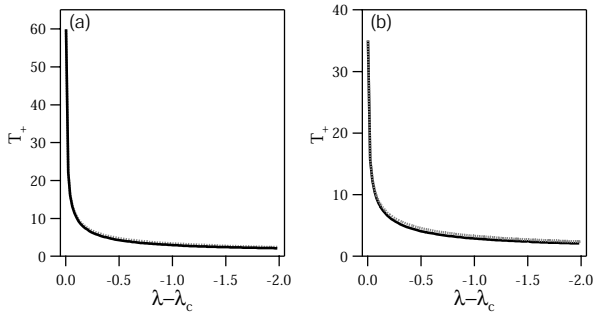


Fig. 2. Period T_+ of the sum signal obtained via numerical simulation of the dynamics (1) (solid curve), and via the expression (6). Left: $c = 4, \epsilon = 0$. Right: $\epsilon = 0.2$. The approximation agrees very well with the numerically obtained period, even for large λ and ϵ .

$\frac{2\pi}{3}$ as predicted by the model. Comparison of the oscillations from the experiment to the numerical results shows good qualitative agreement, but the waveform from the experiment is a mirror image of the waveform from the model. This is probably due to the inversion of the winding of the coils in the construction of the fluxgates. In addition, since we do not know the value of c and the time constant τ in the actual device (we set $\tau = 1$ in the model), we cannot correctly compare the time scales in the model and the experimental observations. The amplitudes of the oscillations in the experiment are also arbitrary compared to the model because the recorded voltages depend on the gains set in the coupling circuit. The magnetic flux in the model saturates between ± 1 , but in the fluxgate devices, this quantity cannot be measured directly.

V. CONCLUSIONS

We reiterate that the oscillatory behavior discussed above does not occur in a single unforced fluxgate magnetometer. Even when coupled, the number of elements, initial conditions, and the type of coupling, are critical for the emergence of this behavior. Our ideas reveal potentially new ways to enhance the utility and sensitivity of other classes of nonlinear dynamic sensors (e.g. ferroelectric detectors for electric-fields, or piezoelectric detectors for acoustic applications) by careful coupling and configuration.

REFERENCES

[1] V. In, A. Bulsara, A. Palacios, P. Longhini, A. Kho, J. Neff, Phys. Rev. **E68**, 045102(R) (2003).

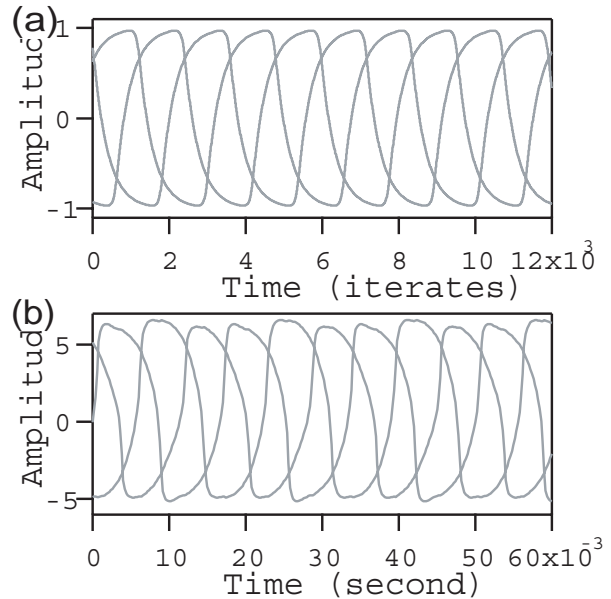


Fig. 3. Top: the numerical data for $c=4, \lambda = -1.55$, and $\epsilon = 0$. Bottom: the experimental data from 3 coupled PCB fluxgate magnetometers. There is very good qualitative agreement between the model and the experimental systems as indicated by the similarity of the waveforms between top and bottom panels. The experimental system lacks a couple of parameters (the device time constant τ and the c value) that are necessary for determining the exact frequency to match with the numerical result. The amplitudes of experimental time-series are also on a different scale because the voltages recorded at the output of the experiment are determined by the overall gains in the circuits used to couple the magnetometers.

[2] A. Bulsara, C. Seberino, L. Gammaitoni, M. Karlsson, B. Lundqvist, J. W. C. Robinson; Phys. Rev. **E67**, 016120 (2003).
 [3] V. In, A. Palacios, P. Longhini, J. Neff, B. Meadows, Phys. Rev. Lett. **91**, 244101 (2003).
 [4] See e.g. H. Stanley, *Introduction to Phase Transitions and Critical Phenomena*, (Oxford Univ. Press, 1971).
 [5] A. Bulsara, V. In, A. Kho, A. Palacios, W. Rappel, J. Acebron, S. Baglio; Phys. Rev. E (2003) submitted.

STUDY OF ELECTRONIC MASTER-SLAVE MFHN NEURONS

S. Jacquir^a, S. Binczak^a, J.M. Bilbault^a, V.B. Kazantsev^b and V.I. Nekorkin^b

^aLaboratoire LE2I, CNRS UMR 5158, Aile des Sciences de l'Ingénieur, Université de Bourgogne, BP 47870, Dijon Cedex, France

^bInstitute of Applied Physics of RAS, 46 Uljanov str., 603950 Nizhny Novgorod, Russia
e-mail: stbinc@u-bourgogne.fr
WWW: http://www.le2i.com

Abstract— *An electrical circuit is proposed to realize an unidirectional coupling between two cells, mimicking chemical synaptic coupling. We show the frequency-doubling and the chaotic dynamics depending on the coupling strength in a master-slave configuration. In all experiments, we stress the influence of the coupling strength on the control of the slave neuron.*

I. INTRODUCTION

Although the differential equations are used to model the nerve membrane, we suggest to describe overall activity of the neuron by one of these models. Moreover, we propose an experimental electronic implementation of it. Indeed in the literature, some electronic neurons have been realized such as the Nagumo's lattice [1] and the Neuristor device [2]. In the first part of this paper, the FitzHugh-Nagumo (FHN) equation with modified excitability has been used to conceive the electronic MFHN neuron [3], [4]. Its experimental bifurcation curves in the dimensionless plane (η, ε) is given. This MFHN circuit leads to complex dynamics of travelling waves [5], [6] emerging from saddle homoclinic loop bifurcations. In the second part, we use the MFHN circuit as a basic cell to realize a master-slave configuration. Two cells are coupled in an unidirectional manner, which would correspond to two neurons coupled synaptically. After the presentation of the electronic circuit giving this coupling, we discuss the experimental conditions for which the master dynamics controls the excitability of the slave neuron leading to a shift of bifurcation curves, a variation of an eigen interspike frequency or a phenomenon of intermittency route to chaos.

II. EXPERIMENTAL DESCRIPTION OF ONE CELL

A. Electrical circuit

The nonlinear circuit, as sketched in Fig. 1, can be described as follows: Part (A) is a parallel association of three different branches, two of them being resistive and commuted by silicium diodes ($Vd = 0.6 V$) while the third one is a negative resistor obtained with an operational amplifier.

Due to diodes' commuting behaviour, the resulting I-V characteristic is nonlinear and can be modelled by a cubic polynomial function for an appropriate set of parameters so that

$$I_{NL} = f(U) = \frac{1}{R_0} \left[U - \frac{\gamma^2 U^3}{3} \right], \quad (1)$$

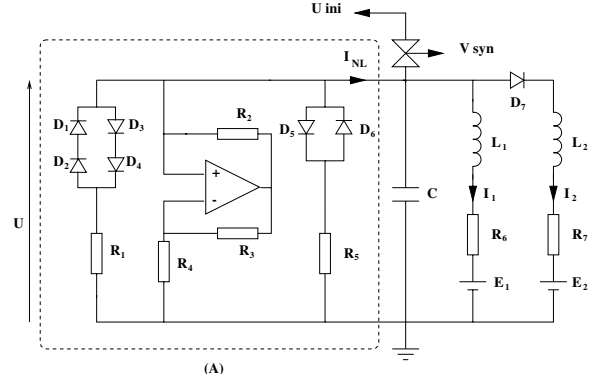


Fig. 1. Diagram of the nonlinear circuit

where U and I_{NL} are respectively the voltage and the corresponding current. The parameters R_0 and γ are obtained by a fitting approximation, e.g. by least mean square's method. We obtain a good match between experimental results and equation (1) by setting $R_0 = 1010 \Omega$ and $\gamma = 1.138 V^{-1}$ [3]. This nonlinear resistor is in parallel with a capacitance and two branches in parallel including inductances, resistances and voltage sources, one of them being commuted by a silicium diode so that setting the conditions $\frac{R_6}{L_1} = \frac{R_7}{L_2}$, $E_2 = -Vd$, and using a piecewise linear I-V description for diode D_7 , $I_2 = 0$ if $U < 0$. Therefore, using Kirchhoff's laws, the system of equations can be expressed in a normalized way by :

$$\begin{cases} \frac{dV}{d\tau} = \left[V - \frac{V^3}{3} \right] - W \\ \frac{dW}{d\tau} = \varepsilon \left[g(V) - W - \eta \right] \end{cases} \quad (2)$$

Where $V = \gamma U$ and $W = \gamma R_0 (I_1 + I_2)$ correspond, in biological terms, to the membrane voltage and the recovery variable; $\tau = \frac{t}{R_0 C}$ is a rescaled time, $\varepsilon = \frac{R_0 R_6 C}{L_1}$ the recovery parameter and $\eta = \gamma \frac{R_0}{R_6} E_1$ a bifurcation parameter. $g(V)$ is a piecewise linear function, $g(V) = \alpha V$ if $V \leq 0$ and $g(V) = \beta V$ if $V > 0$ where $\alpha = \frac{R_0}{R_6}$ and $\beta = \frac{L_1 + L_2}{L_2} \frac{R_0}{R_6}$ control the shape and location of the W-nullcline [3].

B. Experimental bifurcation curves of MFHN circuit

This section presents different dynamics of the MFHN neuron [3]. In the case, $\alpha = \beta = 1$, the system corresponds to the standard FitzHugh-Nagumo equation where nullcline can only intersect at a single equilibrium point leading to Andronov-Hopf bifurcations. In the general case $\alpha \neq \beta$, resolving equation (2), three nullcline points are expected. The phase portrait is very similar to the one occurring from the modified Morris-Lecar equations [7], [8] proposed to model barnacle muscle fibres and pyramidal cells. Considering the case $\alpha = 0.5$ and $\beta = 1.96$, an experimental determination of the bifurcation curves in the parameter plane (η, ε) is proposed in Fig. 2. Several results are to

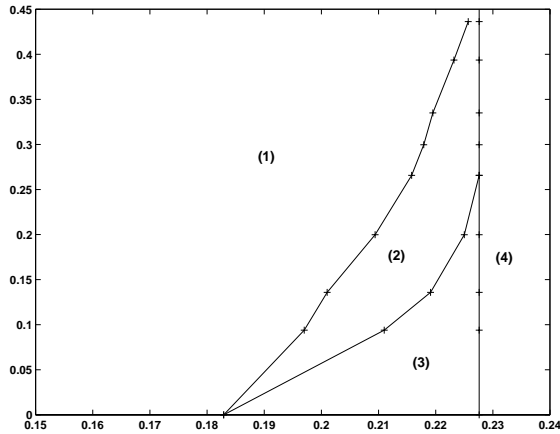


Fig. 2. Experimental bifurcation curves in the dimensionless plane (η, ε) .

be distinguished depending on the location of the nullcline points and on initial conditions. In domain (1), two points are stable and unstable foci, while one point is a saddle, the system responds with an excitation pulse. Domain (2) corresponds to the bistability case characterized by the existence of a stable fixed point and a stable limit cycle that has appeared from a big homoclinic loop bifurcation. Then the model exhibits oscillations if the perturbation is large enough. In domain (3), the fixed point loses stability via a subcritical Andronov-Hopf bifurcation and only oscillations occur in the model, which are similar to the spiking train of pulses. Note that in the region (2), another saddle homoclinic loop bifurcation has taken place leading to a small unstable limit cycle near the fixed point. Experiments have shown that, contrary to standard FHN, arbitrarily long interspike intervals can be found, as the two lower equilibrium points are merging. Finally, in domain (4), a single unstable fixed point exists leading to oscillations, see [3] for more details. The existence of these domains has been confirmed with numerical simulations and stability analysis of equation (2). In the following section, we study a specific case of coupling between two cells.

III. UNIDIRECTIONAL COUPLING OF TWO CELLS

The neurons communicate mainly between them through specialized devices called synapses via chemical messages. The chemical synapse transmits the impulse unidirectionally. Therefore, it is interesting to conceive and to real-

ize an electrical circuit including the same features as the synaptical coupling. We present in Fig. 3 the unidirectional coupling between two cells leading to a master-slave configuration where $N_i (i = 1, 2)$ are described by the circuit of Fig. 1. Let us introduce D the coupling parameter

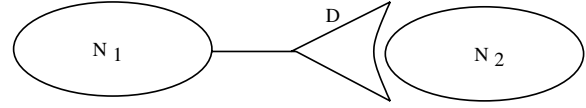


Fig. 3. Coupling between two cells N_1 and N_2 .

(synaptic strength). Its circuit, as illustrated in the Fig. 4, includes an adder-inverter, an inverter and then a follower. U_1 (resp. U_2) is the voltage capacitor of the cell N_1 (resp.

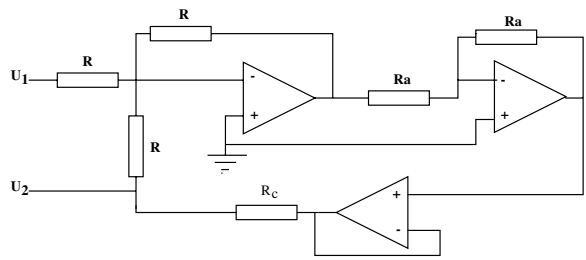


Fig. 4. Unidirectional coupling circuit.

N_2). The value of the resistor R is fixed to $100k\Omega$, which is large compared to the other components so that the current going through $2R$ is negligible, $Ra = 10k\Omega$, while Rc is a detuning parameter which allows to control the coupling parameter value. Note also that the initial condition can be loaded in the neuron via an analogue commutator controlled by V_{syn} . Although it is usual to study a system with normalized variables, it is more convenient to describe electrical circuits with experimental variables. Therefore, we will keep both variables (as normalized V_1 and experimental U_1) in the following of this paper. Using Kirchoff's laws, the normalized equations corresponding to the coupling between two MFHN neurons in a master-slave configuration can be expressed by:

$$\begin{cases} \frac{dV_i}{d\tau} = \left[V_i - \frac{V_i^3}{3} \right] - W_i + DV_1\delta_{2,i} \\ \frac{dW_i}{d\tau} = \varepsilon_i \left[g(V_i) - W_i - \eta_i \right] \end{cases} \quad (3)$$

with $i = \{1, 2\}$, $D = \frac{R_0}{R_c}$, and where $\delta_{2,i}$ is a Kronecker symbol, so that $\delta_{2,1} = 0$ and $\delta_{2,2} = 1$.

Therefore, the two neurons are coupled so that a part of current weighted by D via R , and generated by N_1 is included in N_2 . The two neurons are initially set to voltage U_1ini and U_2ini , due to the analogue commutators controlled by voltage V_{syn} . When the initial conditions are loaded, these commutators are switched off while the two neurons are connected via a third commutator controlled by $\overline{V_{syn}}$. Note that the time delay between the two neurons has not been taken into account in this circuit, a master-slave configuration rendering it unnecessary.

A. The master in a resting state

When the voltage is so that V_1 is constant (the cell N_1 is in a resting state), it is straightforward to show that the variable W_2 and the bifurcation parameter η_2 of the cell N_2 are given by:

$$\begin{cases} \eta_2(V_1) = \eta_2(V_1 = 0) - DV_1 \\ W_2(V_1) = W_2(V_1 = 0) + DV_1 \end{cases} \quad (4)$$

Therefore, it implies a modification of the excitability of the cell N_2 corresponding to a shift in the (η, ε) plane illustrated on Fig. 5. The initial conditions are so that, when $D = 0$, the master neuron N_1 lies in domain (1), while the slave neuron N_2 is in domain (3) and generates a spiking train of pulses. When the unilateral coupling is increased and reaches a critical value, the neuron N_2 ceases to oscillate and stays in the resting state, meaning that the slave neuron has been moved from domain (3) to domain (1) of Fig. 2. This ability of neuron N_1 to inhibit neuron N_2 corresponds to the shift predicted by equation (4): As $V_1 < 0$, increasing D implies to increase $\eta_2(D, V_1)$ and therefore the bifurcation curves of Fig. 2 are translated along abscissa, while the value of η_2 defined by the electrical parameters of neuron N_2 has not been changed. This result suggests that, for a defined activity of a slave neuron, the strength of a unilateral coupling should be above a critical value to give to the master neuron the control on the slave neuron. In Fig. 5, experimental values $(D, \eta[D, V_1])$ corre-

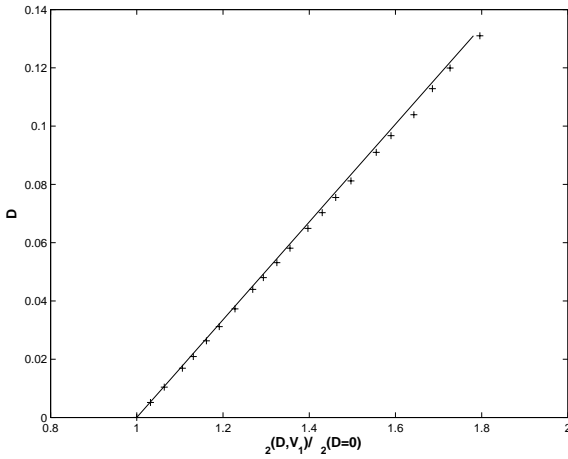


Fig. 5. Shifted bifurcation curve of the slave neuron N_2 between domains (1) and (3). Parameters: Master neuron N_1 : $\alpha_1 = 0.5, \beta_1 = 1.96, \epsilon_1 = 0, \eta_1 = 0.01$ leading to $V_1 = -1.05$ (i.e. $U_1 = -921mV$) Slave neuron N_2 : $\alpha_2 = 0.5, \beta_2 = 1.96, \epsilon_2 = 0$

spond to the shifted bifurcation curve between domains (1) and (3) of the neuron N_2 with $\varepsilon_2 = 0$ and when the master neuron N_1 lies in domain (1) in a resting state so that $V_1 = -1.05$. Comparison shows a good match between experimental results (+) and equation (4) (continuous line), validating the unilateral coupling circuit.

B. The master in a spiking regime

In this section, we present some results when the master is in domain (2) and oscillates. As V_1 is varying in time, we

cannot express a simple relationship between the parameters of neuron N_2 and V_1 , as in equation (4). Nevertheless, oscillations of neurons N_1 let V_1 be alternatively positive and negative, which implies that the bifurcation curves of neurons are translated along the abscissa in the plane (η, ϵ) in a periodic manner (the position of saddle points of the cell N_2 is moved periodically). Thus, the slave neuron N_2 initially situated in the vicinity of a bifurcation curve may be able to cross sometimes this curve and develop a different dynamical behaviour. Therefore we have investigated the unilateral coupling influence on N_2 , in the case when neuron N_1 is initially (i.e. when $D = 0$) in domain (3) and oscillating, while the slave neuron N_2 is in domain (1).

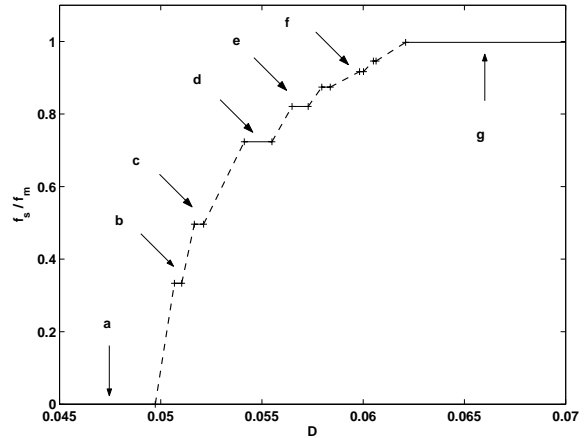


Fig. 6. Normalized eigen interspike slave frequency f_s by interspike master frequency f_m versus D with $C = 0nF, \epsilon_1 = \epsilon_2 = 0, \eta_1 = 0.199$ and $\eta_2 = 0.109$.

According to the value of D , several different dynamical behaviours can be identified, as illustrated in Fig. 6 and 7:

- In case a, the coupling strength is small, leading to sub-threshold oscillations of f_m frequency, which are not taken into account in Fig. 6 but observable in Fig. 7.
- In cases b to f, stable periodic oscillations appear whose eigen interspike frequency follows a devil's staircase-like curve. Only specific values of f_s/f_m are obtainable. Increasing the coupling strength causes the period-doubling in the slave cell, that is the period is multiplied by 2, 4, 8, 16 and so on.
- In case g, N_2 is fully synchronized with N_1 . The slave neuron oscillates in the same manner than the master one.

The slave neuron shows also a chaotic sequence of spikes resulting with variable interspike intervals. This chaotic regime, corresponding to the dot lines in Fig. 6, between the period-doubling plateaus, is so that the interspike slave period is varying during the experiments. When the coupling parameter is gradually increased, we firstly proceed from a periodic spiking regime to a chaotic regime via a sequence of period-doubling bifurcations. Finally, it leads to the reappearance of periodic dynamics inserted in the chaotic zones. The chaotic puffs disturb the periodic spiking regime. This is intermittency, as introduced by [9]. Increasing the coupling parameter causes the increase of the frequency disturbances and then the chaos dominates the regime in the slave cell [10], [11]. An illustration of a

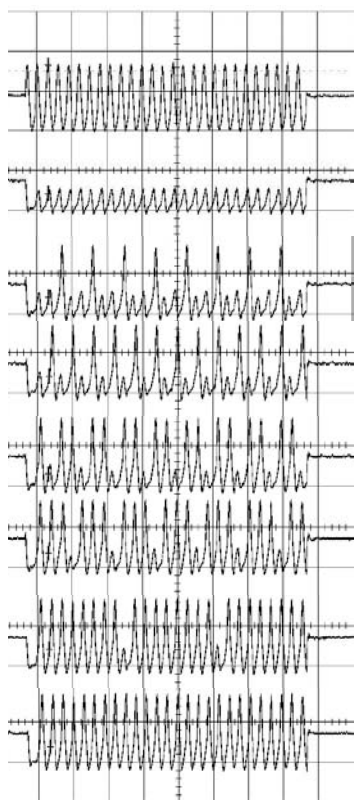


Fig. 7. Temporal evolution of experimental voltage U_2 for different values of D corresponding to cases (a - g) of Fig. 6. Voltage of the master neuron N_1 is shown on top. Abscissa : 0.1ms per division; ordinate : 1 V per division.

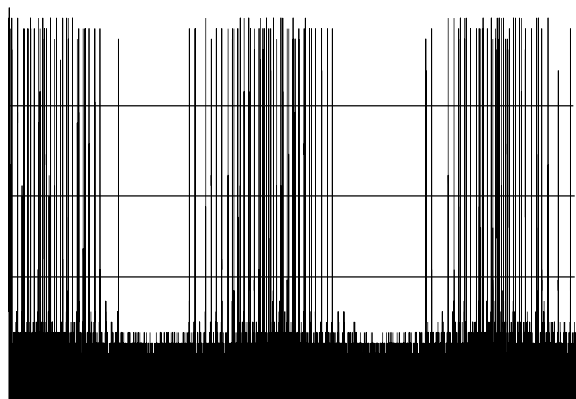


Fig. 8. Chaotic signal in the case where $D = 0.0535$. Abscissa : 5s per division; ordinate : 1 V per division.

chaotic signal is given in Fig. 8 for $D = 0.0535$. The corresponding probability of normalized interspike slave frequency fs/fm is presented on Fig. 9. This figure shows that in a chaotic regime, the interspike frequencies are distributed widely in the range $[0, 0.4fm]$. These experiments show that the unilateral coupling strength controls the slave neuron, from a silent to a chaotic dynamical behaviour.

IV. CONCLUSION

We have introduced an electrical circuit which allowed an unidirectional coupling without delay between two cells,

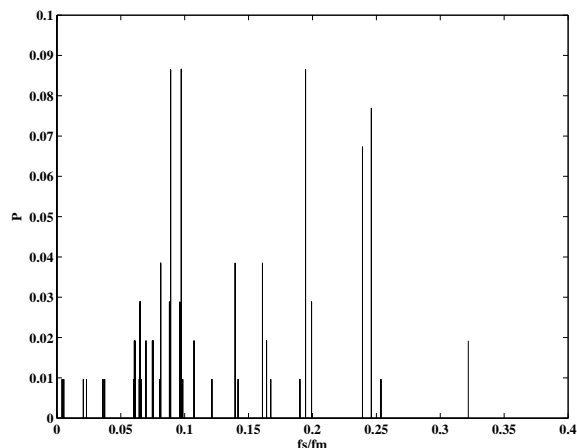


Fig. 9. Normalized distribution of the interspike frequency of N_2 corresponding to the signal in Fig. 8.

in a master-slave configuration. We have showed that the intervals between successive spikes can be chaotic and depends on the coupling strength. We suggest that this study can be helpful in understanding the different dynamics of potential propagation in brain cells. To complete this work, it would be of interest to study the bidirectional coupling, corresponding to the electric synapse case, and the influence of the size of the network on the fractal dimension of the information [4]. This nonlinear electrical circuit cell, gives indeed the opportunity to realize a large scale network.

V. ACKNOWLEDGMENTS

This research has been supported by the Russian-French program of joint research (grant 04610PA), the Russian Foundation for Basic Research (grant 03-02-17135) and INTAS grant (YSF 2001-2/24).

REFERENCES

- [1] J. Nagumo, S. Arimoto and S. Yoshizawa, An active impulse transmission line simulating nerve axon, *Proc. IRE* 50 (1962) 2061-2070.
- [2] A. C. Scott. *Neuroscience: A mathematical primer*, Springer-Verlag, New York, 2002.
- [3] S. Binczak, V. B. Kasantsev, V. I. Nekorkin, J. M. Bilbault, Experimental study of bifurcations in modified FitzHugh-Nagumo cell, *Electronics Letters* 39 (2003) 961-962.
- [4] V. B. Kasantsev, V. I. Nekorkin, S. Binczak, J. M. Bilbault, Spiking patterns emerging from wave instabilities in a one-dimensional neural lattice, *Phys. Rev. E* 68 (2003) 017201,1-4.
- [5] V. B. Kazantsev, Selective communication and information processing by excitable systems, *Phys. Rev. E* 64 (2001) 056210.
- [6] S. P. Dawson, M. V. D'Angelo and J. E. Pearson, Towards a global classification of excitable reaction-diffusion systems, *Phys. Lett. A* 265 (2000) 346-352.
- [7] J. Rinzel and B. B. Ermentrout, Analysis of neural excitability and oscillations, In *Methods in neuronal modeling*, C. Koch and I. Segev editors, second edition, MIT press, Cambridge, Massachusetts (1998) 251-292.
- [8] C. Koch. *Biophysics of computation: Information processing in single neurons*, Oxford University Press, Oxford, 1998.
- [9] Y. Pomeau and P. Manneville, Intermittent transition to turbulence in dissipative dynamical systems, *Comm. Math. Phys.* 74 (1980) 189-197.
- [10] E. Ott, C. Grebogi and J. A. Yorke, *Phys. Rev. Lett.* 64 (1990) 1196-1199.
- [11] A. H. Nayfeh, B. Balachandra, Applied nonlinear dynamics, A Wiley-Interscience Publication.

APPLICATION OF NONLINEAR DYNAMICAL SYSTEMS TO IMAGES ENCRYPTION

Kristina Kelber

Department of Electrical Engineering,
University of Applied Sciences,
Friedrich-List-Platz 1,
D-01069 Dresden, Germany
e-mail: kelber@et.htw-dresden.de

Abstract—*This paper deals with the application of nonlinear dynamical systems to image encryption. Both, classical number theory - based and chaos-based encryption systems are considered from a common nonlinear dynamics point of view. One system of each type is considered in more detail. Finally improvements of a chaos-based system [1] and results of its VHDL modeling are presented.*

I. INTRODUCTION

A large number of chaos-based crypto systems has been suggested and investigated during the past decade (e.g. [1], [2]). These systems have also been compared to conventional number theory-based algorithms ([3], [4]). In this paper number theory-based and chaos-based methods are considered from a common nonlinear dynamics point of view. Applications to image encryption are investigated. Finally a chaos-based system introduced in [1] and its digital realization (VDHL implementation) are discussed in more detail and some improvements to the original system are suggested.

II. REQUIREMENTS FOR IMAGE ENCRYPTION

Classical encryption systems are designed to cipher text messages. Unlike text messages image data possess properties like high redundancy and high bulk data capacity. Furthermore, several applications require consistence of specific image file formats. Security requirements are often not very strict. Thus image encryption systems should possess

- high speed (large amount of data),
- high flexibility (adaptation to security requirements and images formats) and
- required level of security (depending on application)

III. ALGORITHMS BASED ON NUMBER THEORY

In applied cryptography there exist block cipher and stream cipher. Block cipher apply an encryption function E_k to a block of plain text p_i in order to obtain a block of cipher text c_i . Stream cipher operate on continuous bit streams.

A well-known and well-established block cipher algorithm based on number theory is the Data Encryption Standard (DES) [5]. It has been developed in 1976 and is still used very widely. In this paper it is used to demonstrate properties of such systems.

A. Electronic Codebook Mode

DES is a block cipher algorithm which maps 64 bits of plain text p_i to 64 bits of cipher text c_i depending on a key k of 56 bits. The encryption function E_k might be realized as a very large look up table (2^{64} entries) and thus can be considered as a static nonlinearity depending on the encryption key k only. This basic mode of operation is called Electronic Codebook Mode (ECB, Fig. 2A). It is used e.g. for applications requiring direct access to data blocks like data bases.

In ECB identical plain text blocks p_i are mapped to identical cipher text blocks of c_i . For images which are often strongly correlated this leads to encrypted images which still show information of the original image. As an example Fig. 1 shows that the image structure of an bitmap is still visible after encryption using DES in ECB mode (key: 0123456789ABCDEF (hex), using software CrypTool [6]). This is a problem because cipher text must not leak any information of the plain text as already pointed out bei Shannon in [7]. Therefore block ciphers in ECB mode are not suitable for image encryption.

B. Modes of operation including dynamics

To avoid such problems, modes of operation including memory and feedback have been introduced [5]. Most common modes are (Fig. 2B-D)

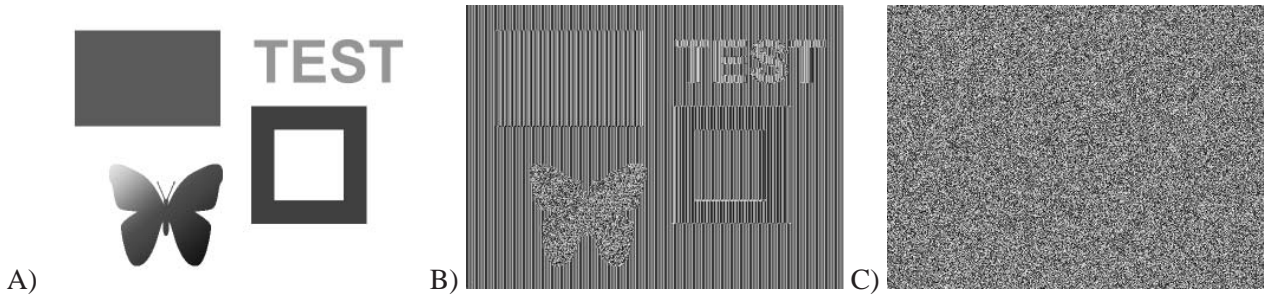


Fig. 1

A) ORIGINAL IMAGE (RGB24), B) DES ECB CODED, C) DES CBC CODED (KEY: 0123456789ABCDEF)

- Cipher Block Chaining (CBC, $c_i = E_k(p_i \oplus c_{i-1})$)
- Output Feedback (OFB, $c_i = p_i \oplus z_i, z_i = E_k(z_{i-1})$)
- Cipher Feedback (CFB, $c_i = p_i \oplus E_k(c_{i-1})$)

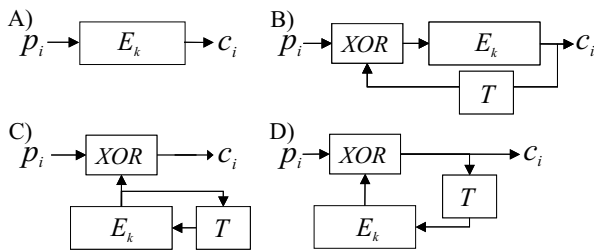


Fig. 2

MODES OF OPERATION: A) ECB, B) CBC, C) OFB, D) CFB

Using one of these modes for DES the structure of the image information is not visible anymore (e.g. DES in CBC mode, Fig. 1C). Choice of a specific mode depends on requirements of the application.

C. Nonlinear dynamics point of view

Considering modes of operation from nonlinear dynamics point of view shows the correspondences:

- ECB = static nonlinear map
- CBC and CFB = inverse system¹
- OFB = pseudo-chaotic masking²

¹with in general low dimension but strong nonlinearity

²for DES key stream is periodic with period $< 2^{64}$

For image encryption systems dynamics is required as shown in Fig. 1. Additional a very complex nonlinearity (E_k) is necessary which has to depend strongly on the encryption key (see algorithm and cryptographic strength of DES [5]). Using a large key space³ is not sufficient if the nonlinearity is weak and can be analyzed easily. This also applies to chaos-based encryption systems as pointed out e.g. in [8].

³possible keys to be checked for extended key search

IV. CHAOS-BASED ALGORITHMS

Now chaos-based algorithms are considered. To encrypt digital images - which are represented by digital data - on digital systems (finite state space machines) chaotic system (infinite state space) have to be discretized.

A. Using static nonlinearities

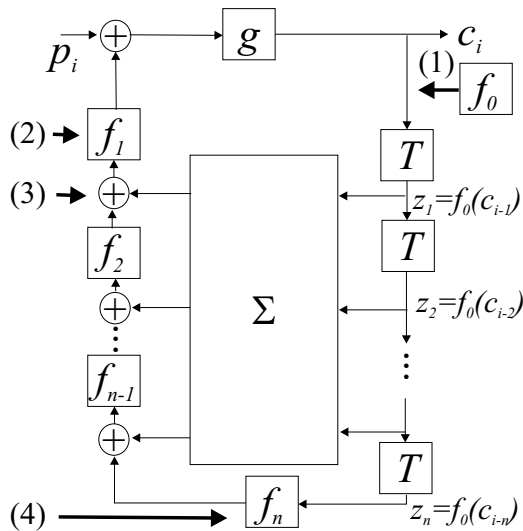
One approach is to construct very complex 2D or 3D chaotic maps the discretization of which leads to bijective maps. In contrast to ECB mode of DES the maps are parametrized to the size of the complete image. Then the static nonlinearity is applied to the complete image all at ones. In this case the ECB mode problem depicted in Fig. 1B is omitted. An example of such a system using 3D baker maps is described in [2]. Ciphering speed of that systems is much higher than that of DES [2].

B. Using dynamics

Using dynamics leads to chaos-based discrete-time inverse systems which are comparable to the cipher feedback mode.

B.1 General encoder structure

A general design approach is the statement of Shannon [7] that the cipher text of a good (binary) cipher should be uniformly distributed in order to prevent successful statistical attacks. This idea has been extended to continuous-value systems and encrypted signals with n -dimensional uniform distribution in [1]. The general encoder structure derived there is depicted in Fig. 3. The system operates on the continuous interval $I = [-1, 1)$ using modulo addition over I (depicted by \oplus). Maps f_i and g need to preserve uniform distribution over I and one of the maps f_i has to be a $m : 1$ -map. Realization of Σ is arbitrary as long as at least two neighboring states z_i and z_{i-1}



(1) to (4) indicate improvements suggested in Sec. IV-B.3.

Fig. 3

GENERAL ENCODER STRUCTURE

influence the key stream. Map g has to be invertible in order to enable decryption.

B.2 Basic realization example

A basic realization of that system is shown in Fig. 4 [1]. Due to the properties of the modulo addition the

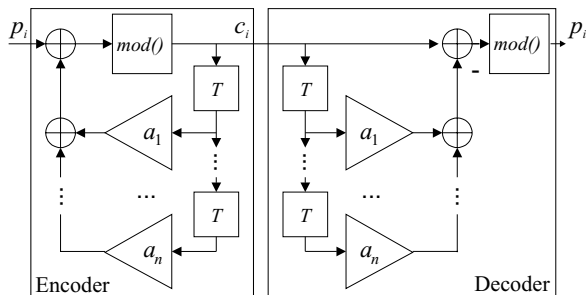


Fig. 4

BASIC REALIZATION OF THE CHAOS-BASED DISCRETE-TIME ENCODER

encoder corresponds to an IIR filter with one single nonlinearity $mod(x) = x - 2 \cdot \lfloor \frac{x+1}{2} \rfloor$, the decoder to a FIR filter with the same nonlinearity. For digital implementations the nonlinearity can be realized by neglecting the overflow bits of the additions. That approximation can be considered linear over $GF(2^w)$ (w = word length). Thus the nonlinearity of the system is very weak and it can be analyzed with fairly low effort as shown in [8]. However, like a binary scrambler it hides image information in an uniformly distributed noise-like signal (Fig. 5). This may be sufficient for some application such as video surveillance.

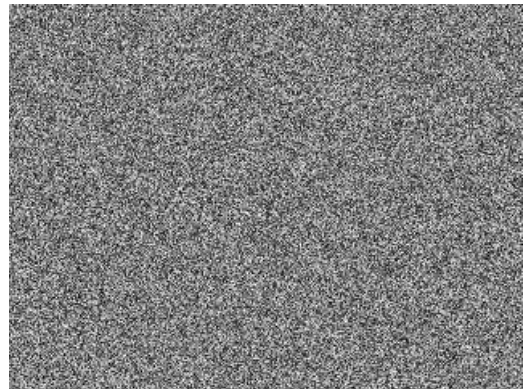


Fig. 5

IMAGE IN FIG. 1A ENCODED BY A 3RD-ORDER SYSTEM USING KEY (123, 45, 67)

B.3 Digital realization and improvements

Analysis of DES has shown that a strong nonlinearity is important for a high level of secrecy. The following suggestions increase the nonlinearity of the basic system (Fig. 4) within the framework of the general encoder structure (Fig. 3) without really increasing computational effort.

(1) **Introduction of a nonlinear function f_0** to omit direct transmission of system states and thus to make successful attacks to the system presented in [8] much more difficult. This map has to preserve uniform distribution.

(2) **Realization of f_i and g .** Maps f_i have to preserve uniform distribution. Such maps can be realized by an l bit left shift of the input (multiplication by 2^l) and subsequent replacement of the l least significant bits of the result by a permutation of the l most significant bits of the input signal. Such maps can be realized by permutation of connections in the VHDL model. Because they are invertible they can be used for g as well.

(3) **Modification of carry-in bit of additions**, either fixed to 1 or depending on bits of the input signals or on the encryption key.

(4) **Replacement of a_n in Fig. 4 by a map f_n according to (2)** saves a $w \times w$ multiplication. It also overcomes the problem of suitable selection of a discrete-value multiplier to meet the requirements specified in [1].

(5) **Selection of nonlinearities f_i** can be either fixed, depending on the key or dynamically depending on the value of signal bits.

(6) **Modification of the values of a_i** depending on signal bits.

(7) **Complex calculation of parameters a_i** from a smaller key (like round key generation in DES) to reduce input pins.

(8) **Replacement of multipliers a_i** by a static or dynamic nonlinear subsystem Σ (comp. Fig. 3 & 4).

This ideas allow adjustment of cipher speed or level of secrecy to the requirements of the application.

B.4 Results of FPGA implementation

For real-time processing of images a high cipher speed is required. Therefore the system in Fig. 4 with suggested improvements (1) to (3) has been modeled in VHDL and synthesized for the FPGA Xilinx-Spartan II having 1200 Slices⁴. Results of the scalable design are presented in detail in [9]. They show that the whole codec (encoder and decoder) with system dimension $n = 3$ fits to one such FPGA chip up to a word length of 24 bits (Tab. I). Approximations of the cipher speed based on timing analysis of the synthesized circuit are shown in Tab. II. They show that for $w \geq 16$ an uncompressed video stream of $270MBit/s = 33.75MByte/s$ can be processed in real-time.

w	8	16	24	32
slices	134	476	1047	1692

TABLE I
NO. OF SLICES VERSUS WORD LENGTH

w	max. clock freq. in MHz		cipher speed in $MByte/s$	
	encoder	decoder	encoder	decoder
8	24.4	128.2	24.4	128.2
16	17.2	91.6	34.4	183.2
24	15.4	65.3	46.2	195.9
32	15.3	69.3	61.2	277.2

TABLE II
CIPHER SPEED OF FPGA REALIZATION DEPENDING ON
WORD LENGTH w

B.5 Application to image encryption

The VHDL model has been used to encrypt RGB24 bitmaps. To achieve image file format consistence and to avoid successful known plain text attack (images headers are well defined) only pixel values have been

encoded. The header remained unchanged. Without using identical fixed or key dependent initial values z_i for encoder and decoder the self-synchronizing property of the system leads to $n \cdot word\ length$ bits at the beginning of the sequence which might be decoded incorrectly.

For fixed file format applications (e.g. RGB24 bitmaps) one can also encode the complete file and replace the beginning of the sequence by the original file header. The decoder can encode the header again using identical initial conditions in order to calculate initial system states z_i for decoding of pixel values.

V. SUMMARY

In this paper different encryption systems have been considered from a common nonlinear dynamics point of view. It turned out that high level of secrecy requires strong nonlinearity. For image encryption at least some dynamics is necessary too.

Furthermore a digital approximation of a chaos-based encryption system has been discussed and improvements of such systems by additional nonlinearities without much additional computational effort have been suggested. A FPGA implementation demonstrated suitability of such systems for encryption of images and allow a realistic performance estimation.

ACKNOWLEDGEMENT

The author is grateful to Alex Gleich for VHDL implementation of the system. She would also like to thank Alex Gleich and Wolfgang Schwarz for stimulating discussions.

REFERENCES

- [1] M. Götz, K. Kelber, W. Schwarz: Discrete-time chaotic encryption systems - Part I: Statistical design approach, *IEEE Trans. Circ. & Syst.-I*, vol. 44(10), pp. 963–969, 1997.
- [2] Y. Mao, G. Chen, S. Lian: A Novel Fast Image Encryption Scheme Based on 3D Chaotic Baker Maps, *Int. J. Bifurcation & Chaos*, June, 2003.
- [3] F. Dachselt, W. Schwarz: Chaos and Cryptography, *IEEE Trans. Circ. & Syst.-I*, vol. 48(12), pp. 1498–1509, 2001.
- [4] L. Kočarev: Chaos-based Cryptography: A Brief Overview, *IEEE Circ. & Syst. Magazine*, Vol. 1(3), pp. 6–21.
- [5] B. Schneier: *Angewandte Kryptographie*, Addison-Wesley, 1996.
- [6] CrypTool Version 1.3.05, <http://www.cryptool.de/>.
- [7] C.E. Shannon: Communication Theory of Secrecy Systems, *Bell System Tech. J.*, vol. 28, pp. 656–715, 1949.
- [8] F. Dachselt, K. Kelber, W. Schwarz: Discrete-time chaotic encryption system - Part III: Cryptographical Analysis, *IEEE Trans. Circ. & Syst.-I*, vol. 45(9), pp. 883–888, 1998.
- [9] A. Gleich, S. Müller: VHDL realisation of an encryption system (in German), student project report, HTW Dresden, 2004.

⁴2 LUT, 2 carry logic units, 2 MANDs and 2 flip flops

NONLINEAR DYNAMICS OF COCHLEAR INFORMATION PROCESSING

A. Kern and R. Stoop

Institute of Neuroinformatics,
Swiss Federal Institute of Technology Zürich,
Zürich, Switzerland
e-mail: albert@ini.phys.ethz.ch
WWW: <http://www.stoop.net/group>

Abstract—*The nonlinear amplification process in the mammalian cochlea gives rise to a variety of phenomena, which manifest as two-tone suppression and combination tone generation. These nonlinear effects show that, besides mere mechanical-to-neural transduction, the cochlea performs significant information processing on a biophysical, pre-neural level. As nonlinear cochlear processing is a precondition for successful feature extraction at higher neural stages, its profound understanding is of interest for the design of intelligent acoustic sensors. In this contribution, we provide a thorough explanation of suppression and combination tone generation, where we rely on Hopf-type cochlear amplifiers. The underlying cochlear model can be implemented as an electronic circuit.*

I. INTRODUCTION

The first theory of the mammalian hearing organ, the fluid-filled cochlea, was put forward by H.L.F. Helmholtz in 1863 [1]. Based on anatomical investigations, Helmholtz proposed that each segment of the basilar membrane (BM), which separates the cochlear fluid, acts as a tuned oscillator. A sound of given frequency thus elicits maximum oscillations at a specific location in the cochlea (characteristic place), so that the cochlea acts as a spatial Fourier analyzer (tonotopic principle). Mechano-sensitive cells on the BM then transduce the mechanical vibrations into neural signals. In 1928, the tonotopic principle has been verified experimentally by von Békésy [2]. In contrast to Helmholtz' original theory, however, the tonotopic principle is correctly deduced from the exponentially decaying transversal BM stiffness $E(x) = E_0 \exp(-\alpha x)$, by applying linear hydrodynamical theory [3], [4]. Cochlear hydrodynamics has also been described in terms of electronic circuit analogs [5].

In the early 1970s, increasing evidence was furnished that the cochlear response is strongly nonlin-

ear [6], which was in stark contrast to the prevalent linear theory. With the detection of otoacoustic emissions [7] it became clear that a nonlinear force-generating mechanism must be present in the cochlea. In 1985, the outer hair cells (OHC), which reside on the BM, have been identified as the source of this mechanical amplification, and as the origin of cochlear nonlinearity [8]. This discovery has triggered intensive research in the following two decades [9]. In particular, it has been shown that a degeneration of OHC causes cochlear hearing loss. In this case, even the use of sophisticated hearing aids often results only in partial improvement of auditory performance; especially the capability for auditory scene analysis frequently remains severely hampered. It thus follows that, in addition to mechano-to-neural transduction, the cochlea performs significant information processing by means of the nonlinear amplification mechanism. Cochlear information processing applies mainly to the frequency domain, while processing of time information is performed on the neural level.

For two nonlinear phenomena – two-tone suppression and combination tone (CT) generation – there exist ample physiological measurements. Both phenomena arise if two tones are applied simultaneously to the ear. In the case of suppression, the BM response to a single tone of frequency f_1 , is reduced (*suppressed*) in the presence of a second tone of frequency f_2 . Evidently, the suppressive effect of the f_1 - and f_2 -tones is mutual. Combination tones (distortion products) with frequencies $f_{CT} = n f_1 + m f_2$ ($n, m \in \mathbb{Z}$) are generated by the nonlinear interaction between the two frequency components. Due to the structural properties of the cochlea, only the frequencies $2f_1 - f_2$ and (to a lesser extent) $f_2 - f_1$ ($f_2 > f_1$) are able to propagate to their respective characteristic places.

In this contribution, we give a detailed explanation for the observed nonlinear phenomena, based

on nonlinear dynamical systems theory. Specifically, the cochlear amplification mechanism is described in terms of oscillators undergoing a Hopf bifurcation (Hopf oscillators). By this approach, the experimental observations can be explained by a variation of the effective Hopf bifurcation parameter in the presence of a second tone.

II. THE HOPF COCHLEA MODEL

Recently, it has been shown [10] that the basic characteristics of hearing can be explained from the mathematical properties of the driven Hopf oscillator,

$$\dot{z} = (\mu + i\omega_0)z - |z|^2z + F(t), \quad z(t) \in \mathbb{C}, \quad (1)$$

where ω_0 is the natural frequency of the oscillation, $\mu \in \mathbb{R}$ denotes the bifurcation parameter, and $F(t) = Fe^{i\omega t}$ is an external periodic forcing with frequency ω . In the absence of external forcing, (1) describes the generic differential equation displaying a Hopf bifurcation. For an input $F(t)$, $z(t)$ can be considered as the amplified signal. The steady-state solution for periodic forcings is obtained by the ansatz $z(t) = Re^{i\omega t + i\phi}$, which leads to a cubic equation in R^2 ,

$$F^2 = R^6 - 2\mu R^4 + [\mu^2 + (\omega - \omega_0)^2]R^2. \quad (2)$$

Assuming $\omega = \omega_0$ and $\mu < 0$, for $F \ll |\mu|^{3/2}$, the response is linear, $R \approx -F/\mu$. If $F \gg |\mu|^{3/2}$, the R^6 -term becomes dominant, and the compressive nonlinear regime is entered, $R \approx F^{1/3}$, with the amplification gain decreasing like $F^{-2/3}$. For $\omega \neq \omega_c$, $R \approx F/\sqrt{\mu^2 + (\omega - \omega_c)^2}$, and the response is always linear. If $\mu > 0$, stable limit-cycles emerge, which explains the generation of otoacoustic emissions.

The fact that the properties of (2) explain the observed characteristics of hearing – linear BM response for weak stimuli ($\lesssim 30$ dB SPL), and a compressive nonlinearity for moderately intense responses – motivated the development of a Hopf-type cochlea model (for details see [11]). From energy-balance arguments [12], the cochlea differential equation,

$$\frac{\partial e(x, \omega)}{\partial x} = -\frac{e(x, \omega)}{v(x, \omega)} \left[\frac{\partial v(x, \omega)}{\partial x} + d(x, \omega) \right] + \frac{a(x, e(x, \omega), \omega)}{v(x, \omega)}, \quad (3)$$

was derived. $e(x, \omega)$ denotes the one-dimensional energy density of the cochlear fluid, $v(x, \omega)$ is the group velocity of the BM traveling wave, $d(x, \omega)$ encompasses viscous losses, and $a(\cdot)$ denotes the nonlinear

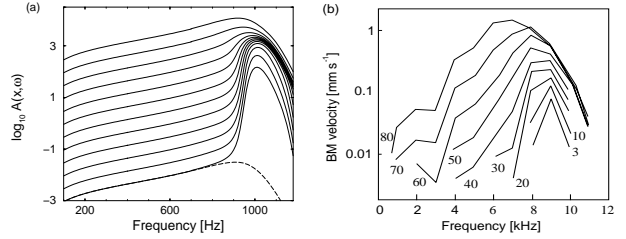


Fig. 1. Frequency response at fixed location on BM. (a) Hopf cochlea model, Eqs. (2-4). (c) Experimental measurements [13].

active amplification by OHC. Based on cochlear biophysics (see [11])

$$a(e, x, \omega) = L(R(\sqrt{\sigma e(x, \omega)}))^2, \quad (4)$$

where L and σ are constants, and $R(\cdot)$ is determined by (2). The connection between the cochlea model and experimentally measured BM response A is given by the relation $A(x, \omega) = (2e(x, \omega)/E(x))^{1/2}$ ($E(x) = E_0 \exp(-\alpha x)$ denotes the BM stiffness).

The frequency response of the cochlea model (measured at fixed location on BM) displays remarkable coincidence with experimental measurements (Fig. 1). Optimal responses are obtained if feedforward couplings between the Hopf amplifiers are taken into account [11]. In the following analysis, however, we use the simpler version of the model (Fig. 1a).

III. NONLINEAR COCHLEAR SIGNAL PROCESSING

In the presence of a tone consisting of two frequencies, the driving term of (1) reads

$$F(t) = F_1 e^{i\omega_1 t + i\psi_2} + F_2 e^{i\omega_2 t + i\psi_1} + F_{CT} e^{i\omega_{CT} t + i\psi_{CT}}, \quad (5)$$

where we allow for phases ψ_k of the two frequency components, $F_k > 0$, and $\omega_k = 2\pi f_k$, $k = \{1, 2\}$. When CT responses at frequency $\omega_{CT} = 2\omega_1 - \omega_2$ ($\omega_2 > \omega_1$) are generated at a certain site on the BM, these constitute a component of the input to Hopf oscillators at neighboring BM locations. For the Hopf cochlea model, the last term in (5) must therefore be considered.

The steady-state solution of (1) is obtained from the Fourier series ansatz

$$z(t) = R_1 e^{i\omega_1 t + i\phi_1} + R_2 e^{i\omega_2 t + i\phi_2} + R_{CT} e^{i\omega_{CT} t + i\phi_{CT}} + \sum_j R_j e^{i\omega_j t + i\phi_j}. \quad (6)$$

The third term denotes the propagating combination tone with frequency $\omega_{CT} = 2\omega_1 - \omega_2$ ($\omega_2 > \omega_1$), and

the sum includes all higher-order contributions $\omega_j = n\omega_1 + m\omega_2$, $\{n, m\} \in \mathbb{Z}^2 \setminus \{2, -1\}$.

After some calculations, the response to frequencies ω_1, ω_2 is obtained as

$$F_k^2 = R_k^6 - 2\mu_{eff,k}R_k^4 + [\mu_{eff,k}^2 + (\omega_k - \omega_0)^2]R_k^2, \quad (7)$$

where $k = \{1, 2\}$ and $j \neq k$. These equations can be interpreted as single Hopf equations with effective bifurcation parameters $\mu_{eff,k} = \mu - 2R_j^2$ (cf. Eq. (2) and note that $\mu < 0$). Since the small-signal gain is given by $1/|\mu_{eff}|$, it becomes evident that the *suppressive effect* in the presence of a second tone is captured by a shift of the effective bifurcation parameter away from the bifurcation point.

The response at ω_{CT} is obtained in the same way,

$$F_{CT}^2 + R_1^4 R_2^2 - 2R_1^2 R_2 F_{CT} \cos(2\phi_1 - \phi_2 + \psi_{CT}) = R_{CT}^6 - 2\mu_{eff,CT}R_{CT}^4 + [\mu_{eff,CT}^2 + (\omega_{CT} - \omega_0)^2]R_{CT}^2. \quad (8)$$

If comparing (8) with (7), three points attract our attention. First, we note from the emergence of an effective bifurcation parameter $\mu_{eff,CT} = \mu - 2(R_1^2 + R_2^2)$, that suppression plays a crucial role in CT generation. Secondly, the term $R_1^4 R_2^2$ expresses CT generation in the absence of external driving, F_{CT} . From the discussion in Sec. II, it is seen that the CT response is given by $R_{CT} \approx R_1^2 R_2 / \mu$, if $R_1^2 R_2 < |\mu|^{3/2}$ (assuming $\omega_{CT} = \omega_0$). If R_2 is kept fixed and R_1 is increased, we thus assume a 2 dB/dB increase of R_{CT} .

As a third point, we observe that the presence of an external driving F_{CT} at frequency ω_{CT} not only gives rise to the term F_{CT}^2 . In addition, a phase-dependent term is induced, where ϕ_k ($k = 1, 2$) denote the phase differences between R_k and the driving force,

$$\phi_k = \arctan \frac{\omega_k - \omega_0}{\mu - R_k(R_k^2 - 2R_j^2)} - \psi_{CT}, \quad j \neq k. \quad (9)$$

For a single Hopf oscillator, the CT response is easily computed from (8) and (9). In the cochlea model, however, the phase ψ_{CT} is determined by the cochlear hydrodynamic wave. The computation of the cos-term in (8) thus becomes difficult, but fortunately, its contribution to CT generation can be neglected for the following arguments. Firstly, if f_1 and f_2 are not too close, either F_{CT} or $R_1^2 R_2$ dominate on the left hand side of (8), so that the cos-term always remains small. This has been verified by numerical simulations for the frequencies used. Secondly, the interaction with the hydrodynamic wave causes rapid changes of ψ_{CT}

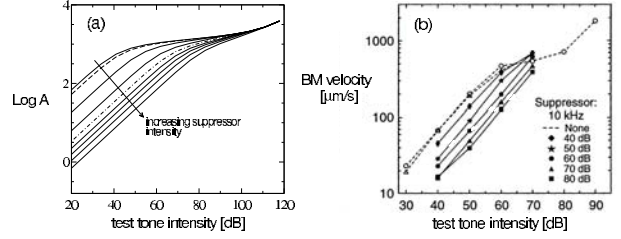


Fig. 2. Two-tone suppression: a) Model response: suppressor intensity increases from 10 dB to 110 dB in steps of 10 dB. The 10, 20, and 30 dB lines coincide. b) Experimental measurements [15].

along the BM, so that the contributions by the phases are effectively averaged out.

The Hopf model response for a two-frequency tone is obtained by resolving a system of three differential equations of the form (3). This provides the energy densities e_k and e_{CT} . As R_k and R_{CT} must be substituted in (4), these equations are coupled by Eqs. (7) and (8) [14].

A. Two-Tone Suppression

In two-tone suppression experiments, the response to one tone (the *test tone*) is measured in the presence of a *suppressor* tone (indexing by t and s). The test-tone input-output function obtained by the Hopf cochlea model, determined for increasing suppressor intensity, shows nearly perfect agreement with experimental measurements (Fig. 2). In this representation, the BM response at characteristic place (the location of maximum BM response, cf. Fig. 1) is plotted as a function of sound intensity. For suppressor levels I_s below 40 dB (top curve in Fig. 2) we recognize the strong compressive nonlinearity which is characteristic for the single-frequency cochlear response. For $I_s \gtrsim 40$ dB (dashed line in Fig. 2a), the small-signal gain of the test tone becomes significantly reduced, with constant separations between the curves. If $I_s > 70$ dB (dashed-dotted line), these are reduced by a factor of about 1/3.

The Hopf cochlea model provides an explanation for these observations. Since the small-signal response of the test tone is given by $R_t = F_t/|\mu_{eff,t}|$, and $\mu_{eff,t} = \mu - 2R_s^2$, we conclude that suppressive effects become appreciable if $\mu_{eff,t}$ deviates significantly from μ , which is the case if $F_s \sim R_s \gtrsim \sqrt{|\mu|}$. The spacing between the curves reflects the compressive nonlinearity of the suppressor response, R_s . For $I_s < 70$ dB, $R_t \sim F_t/R_s^2 \sim F_t/I_t$, which explains the constant spacings between the curves in Fig. 2. If the suppressor enters the compressive non-

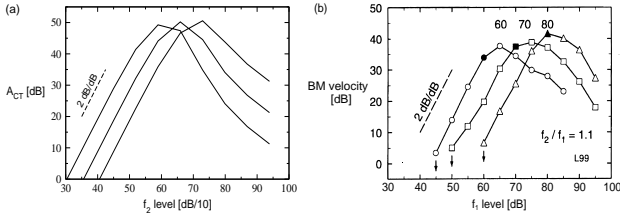


Fig. 3. Combination tone generation: BM response at characteristic place for a tone with frequency $f = 2f_1 - f_2$, as a function of f_1 -intensity. a) Model response (curves for $f_2 = 60, 70, 80$ dB; $f_1 = 930$ Hz, $f_2 = 1000$ Hz, $f_2/f_1 = 1.05$). b) Experimental measurements [16] ($f_2/f_1 = 1.1$).

linear regime, $R_s^2 \sim F_s^{2/3} \sim I_s^{1/3}$ holds, which leads to a reduction of the spacing by 1/3. It is remarkable that the same effect is observed in the experiment.

B. Combination Tones

CT measurements are performed in a variety of experimental settings [16]. We restrict our analysis to the situation where the CT response is measured as a function of the intensity of the f_1 -component, while the level of the f_2 -component is kept fixed (Fig. 3). We observe a close agreement of the model results with the experimental measurements.

An explanation of Fig. 3 is again provided by the Hopf cochlea model. At the increasing branches of the curves, the slope is exactly 2 dB/dB, as was predicted from Eq. (8). The role of suppression is twofold: For low f_1 -levels, suppression of the CT stems exclusively from the f_2 -component. This explains the decrease of the CT response upon increase of the f_2 -level (while f_1 -intensity remains fixed), which is observed when CT responses at different curves are read off for fixed f_1 -intensity. For the same reason, the 2 dB/dB-slope remains unaffected: From Eq. (8) follows $F_{CT} \approx R_2 R_1^2 / \mu_{eff,CT} \sim R_1^2$, as $\mu_{eff,CT}$ is only a function of R_2 for small f_1 -intensities. Since $\mu_{eff,CT} = \mu - 2(R_1^2 + R_2^2)$, the contribution of the f_1 -component to suppression becomes significant if $R_1 \gtrsim R_2$, which is the case when the intensity of the f_1 -component exceeds the f_2 -level. This explains the decrease of the CT response for large f_1 -intensities.

IV. CONCLUSION

In the preceding section we have demonstrated that the Hopf cochlea model provides an successful description of cochlear nonlinear phenomena. The role of suppression in cochlear information processing consists in the reduction of the response to small-amplitude signals (which can be considered as noise).

This leads to a pattern-sharpening effect, analog to the increase in resolution of neural receptive fields, which is achieved by lateral or surround inhibition. The role of combination tones is less clear. Possibly, they may help in signal identification (scene analysis) if several signals of comparable magnitude are present; if the signal intensities differ, the combination tone is readily suppressed. CT generation sometimes plays a role in music – the phenomenon has been described for the first time by the violinist Tartini in 1714,

For the design of intelligent acoustic devices, which perform signal identification and scene analysis tasks, a profound understanding of the nonlinear phenomena in mammalian hearing may provide helpful. For example, if a speech recognition system is endowed with a simple cochlea model as a front end, its performance increases significantly [17]. We therefore expect that the Hopf approach to cochlear modeling will be of great benefit for developing sound-processing devices. Hopf oscillators can be implemented as electronic circuits [18].

REFERENCES

- [1] H.L.F. Helmholtz, *Die Lehre von den Tonempfindungen als physiologische Grundlage für die Theorie der Musik* (Vieweg, Braunschweig, 1863).
- [2] G. von Békésy, *Phys. Z.* **29**, 793 (1928).
- [3] O.F. Ranke, *Die Gleichrichter-Resonanztheorie* (Lehman, München, 1931).
- [4] B.P. Peterson and L.C. Bogert, *J. Acoust. Soc. Am.* **22**, 369 (1950).
- [5] R.L. Wegel and C.E. Lane, *Physical Review* **23**, 266 (1924).
- [6] W.S. Rhode, *J. Acoust. Soc. Am.* **49**, 1218 (1971).
- [7] D.T. Kemp, *J. Acoust. Soc. Am.* **64**, 1386 (1978).
- [8] W.E. Brownell, C.R. Bader, D. Bertrand, and Y. de Ribaupierre, *Science* **227**, 194 (1985).
- [9] W.E. Brownell, A.A. Spector, R.M. Raphael, and A.S. Popel, *Annu. Rev. Biomed. Eng.* **3**, 169 (2001).
- [10] V.M. Eguíluz, M. Ospeck, Y. Choe, A.J. Hudspeth, M.O. Magnasco, *Phys. Rev. Lett.* **84**, 5232 (2000).
- [11] A. Kern and R. Stoop, *Phys. Rev. Lett.* **91**, 128101 (2003).
- [12] G.B. Whitham, *Linear and Nonlinear Waves* (Interscience Publishers, New York, 1999).
- [13] M.A. Ruggero, *Curr. Opin. Neurobiol.* **2**, 449 (1992).
- [14] For the model, it is assumed that the wave propagation along the cochlea can be described by linear hydrodynamic theory. The energy densities associated with the different frequency components (e_1 , e_2 and e_{CT}) are therefore exclusively coupled through the active process (term $a(\cdot)$ in (3)).
- [15] M.A. Ruggero, L. Robles, N.C. Rich, *J. Neurophysiol.* **68**, 1087 (1992).
- [16] L. Robles, M.A. Ruggero, and N.C. Rich, *J. Neurophysiol.* **77**, 2385 (1997).
- [17] J. Tchorz and B. Kollmeier, *J. Acoust. Soc. Am.* **106**, 2040 (1999).
- [18] J.-J. van der Vyver, A. Kern, and R. Stoop, In: *Proc. of the IEEE European Conference on Circuit Theory and Design (ECCTD)* vol. III, 285 (2003).

SYNCHRONIZED FIRING OF FITZHUGH-NAGUMO NEURONS BY NOISE

H. Kitajima and T. Hattori

Faculty of Engineering, Kagawa University, Takamatsu, Kagawa, Japan

e-mail: kitaji@eng.kagawa-u.ac.jp

WWW: <http://www.eng.kagawa-u.ac.jp/~kitaji/>

Abstract— *We investigate the influence of noise on the synchronization between the spiking activities of neurons with external impulsive forces. By choosing the appropriate noise intensity and a number of neurons subject to noise we find that small noise can be a promoter of synchronization phenomena in neural activities.*

I. INTRODUCTION

A neuron, or the fundamental element of the brain, generates various temporal patterns of spikes. Among such firing patterns, synchronous firing of neurons in connection with neural signal processing has attracted much interest(see [1] and references therein). In particular, the influence of noise on the synchronization [2] are studied for several types of neurons:e.g. Hodgkin-Huxley [3–5] and FitzHugh-Nagumo [6,7], because real neurons can operate accurately even in a noisy environment. However, in these studies, to obtain synchronous firing patterns very large noise intensity is needed.

In this paper we consider globally coupled FitzHugh-Nagumo(FHN) neurons with external noise and periodic impulsive forces. By choosing appropriate noise intensity and a number of neurons subject to noise we find that small noise can be a promoter of synchronization phenomena in neural activities.

II. SYSTEM EQUATION

The system equation of electrically (gap junction) coupled FHN neurons is described as

$$\begin{aligned} \frac{dx_i}{dt} &= c \left(x_i - \frac{1}{3}x_i^3 + y_i \right) + h \sum_{k \in \mathbb{Z}} \delta(t - 2k\pi/\omega) \\ &\quad - \frac{w}{N-1} \sum_{j=1, j \neq i}^N (x_i - x_j) + D_i \xi_i(t) \\ \frac{dy_i}{dt} &= -\frac{1}{c}(x_i + by_i + a) \end{aligned} \quad (1)$$

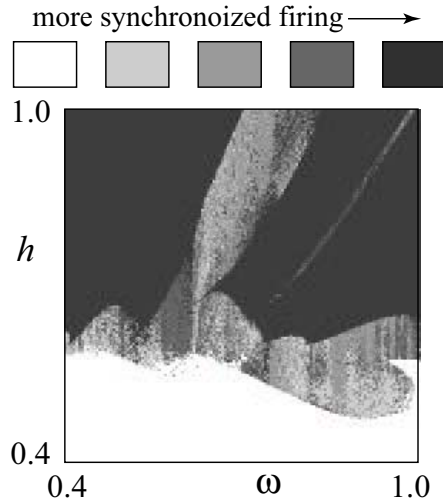


Fig. 1. The parameter region in which synchronous firing is observed. $D_i = 0$.

where i indicates neuron number, $\delta(t)$ is the Dirac's delta function, h and ω are the amplitude and the angular frequency of the impulsive force, respectively, w is the coupling coefficient, $\xi_i(t)$ is the Gaussian white noise with $\langle \xi_i(t) \xi_i(t') \rangle = \delta(t - t')$ and D_i denotes the noise intensity. We use the different noise for each neuron. To generate a random number we use Mersenne Twister method [8]. The values of system parameters are fixed as

$$a = 0.7, b = 0.8, c = 3.0, w = -0.3 \quad (2)$$

for the occurrence of a stable equilibrium point in the system of Eq. (1) with $h = 0$ and $D_i = 0$. Equation (1) is numerically integrated by using stochastic Euler method [9,10] with the time step $\Delta t = 2\pi/1024$.

III. RESULTS

In Fig. 1 we show the results of counting a number of neurons with synchronous firing in the parameter space (ω, h) . In the darker region we observe more synchronous firing. In the white region, coupled neurons never fire, because it is not

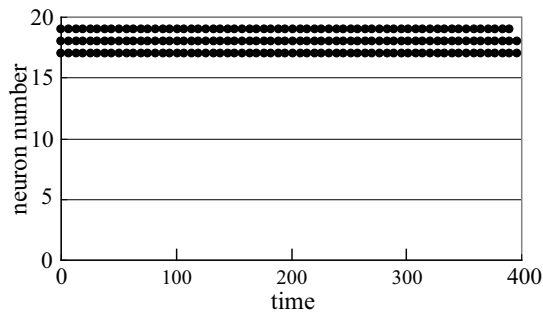


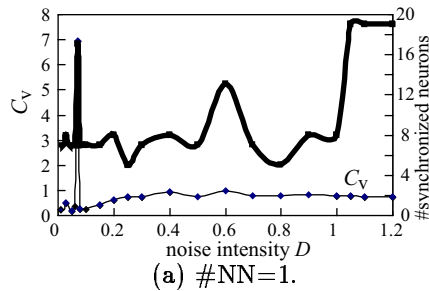
Fig. 2. Time series after the transient time (1024×1000 steps) in Eq. (1) with $D = 0$, $\omega = 0.436$ and $h = 0.592$.

enough impulsive stimulus. In order to obtain more synchronous firing, we inject the noise $\xi_i(t)$ to some FHN neurons in the coupled system. A number of neurons subject to the noise is abbreviated to “#NN”. We choose three parameter sets of ω and h from Fig. 1 for the occurrence of few synchronous firing and after adding the noise we study the effect of the noise on the synchronization.

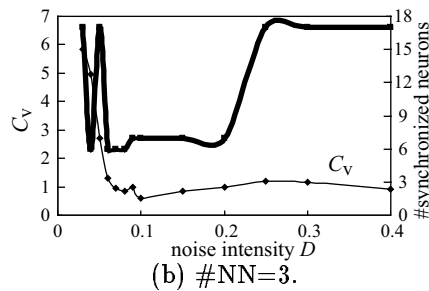
A. Case(1)

We set the values of parameters (ω, h) as (0.436, 0.592). In this parameter setting the raster records of all the firing events in the coupled system without the noise is shown in Fig. 2. From this figure we can see that only three neurons (neuron 17 to 19) generate spikes. After adding the noise we calculate coefficient of variation (C_v) of interspike interval (ISI) for neuron 1 and count a number of neurons with synchronized firing by changing the noise intensity and #NN, see Fig. 3. Thick and thin solid curves indicate the number of neurons with synchronized firing and C_v , respectively.

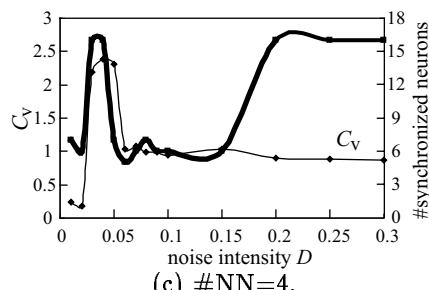
In Fig. 3(a) adding the small intensity noise ($D=0.07$) to only one neuron (neuron 20), complete synchronized firing of 17 neurons is observed. Figure 4(a) shows firing events as time series data at $D=0.07$ and #NN=1. From Fig. 3 we can see that when the noise intensity is less than 0.1, the number of neurons with synchronized firing and C_v are increased simultaneously. On the other hand for large intensity of the noise all neurons except noise-injected neurons produce synchronous firing and C_v converges to about 1 which shows irregular spikes [11, 12]. In Fig. 4(b) we show the temporal firing pattern at $D=0.4$ and #NN=3. At this noise level all neurons



(a) #NN=1.



(b) #NN=3.



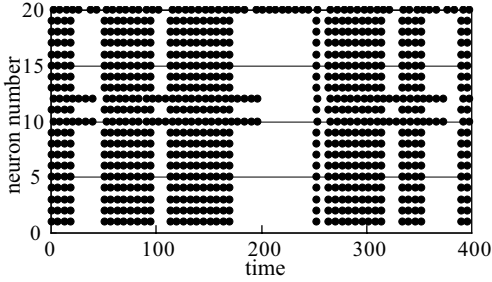
(c) #NN=4.

Fig. 3. Coefficient of variation (C_v) and the number of neurons with synchronized firing as a function of D_i observed in Eq. (1) with $\omega = 0.436$ and $h = 0.592$. After a transient time we calculate them using 40,000 time steps data.

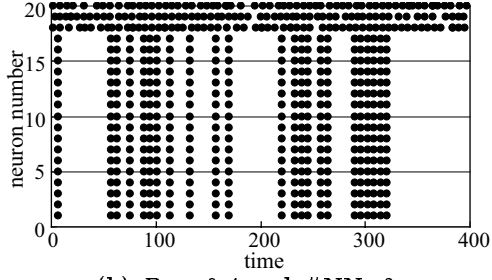
except noise-injected neurons are synchronized. This synchronous firing pattern is robust against adding the small intensity noise ($D_i=0.001$) to these synchronized 17 neurons, see Fig. 4(c).

B. Case(2)

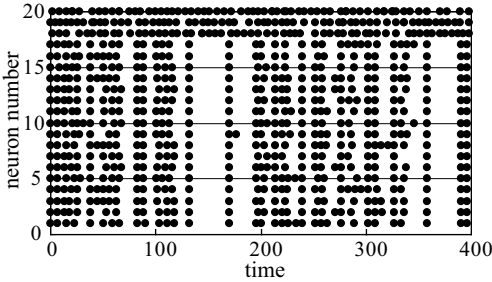
In the second case we set the values of parameters (ω, h) as (0.4, 0.585). Traveling wave is observed when $D=0$ shown in Fig. 5(a). The order of firing is controllable by changing initial conditions of x_i . Figure 6 shows C_v and the number of neurons with synchronous firing. For small value of the noise intensity C_v is almost zero which means regular spikes. In this case also the increase in C_v and the number of neurons with synchronous firing occur at similar values of the noise intensity. An example of complete synchronized neurons due to an appropriate amount of the noise is shown in Fig. 5(b).



(a) $D_i = 0.07$ and $\#NN=1$.



(b) $D_i = 0.4$ and $\#NN=3$.



(c) $D_i=0.001 (i=1, \dots, 17)$ and $D_i=0.4 (i=18, 19, 20)$.

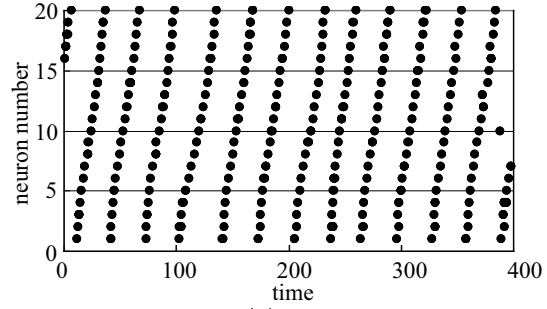
Fig. 4. Temporal firing pattern observed in Eq. (1) with $\omega = 0.436$ and $h = 0.592$ and different noise intensity.

C. Case(3)

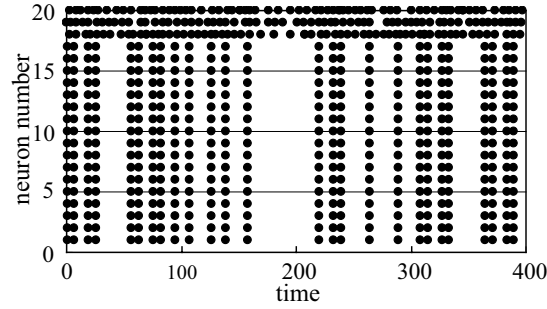
In the third case we set the values of parameters (ω, h) as (0.94, 0.594). Even in the case of the absence of the noise neurons produce irregular spikes, see Fig. 7(a). Figure 8(a) shows that we cannot obtain complete synchronization only by adding the noise to one neuron. By increasing the number of neurons subject to the noise and the noise intensity, complete synchronous firing can be achieved as shown in Fig. 8(b). Although it cannot be achieved, complete synchronous firing is observed in some time interval, see Fig. 7(b).

IV. CONCLUSIONS

We have investigated the influence of noise on synchronous firing in globally coupled FHN neurons with external impulsive force. We decided the three values of the amplitude and the angu-

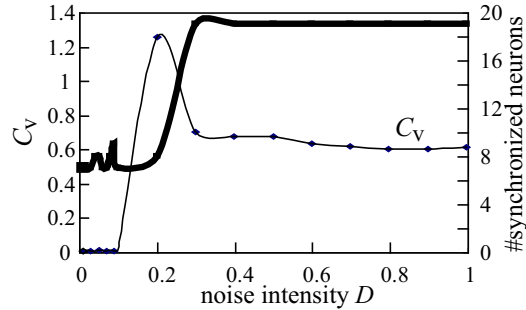


(a) $D = 0.0$.

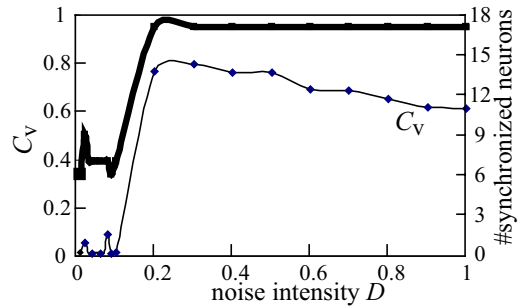


(b) $D = 0.4$ and $\#NN=3$.

Fig. 5. Temporal firing pattern observed in Eq. (1) with $\omega = 0.4$ and $h = 0.585$.



(a) $\#NN=1$.



(b) $\#NN=3$.

Fig. 6. C_v and the number of neurons with synchronous firing as a function of D_i observed in Eq. (1) with $\omega = 0.4$ and $h = 0.585$.

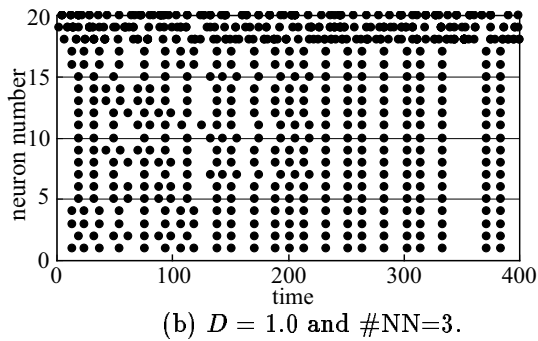
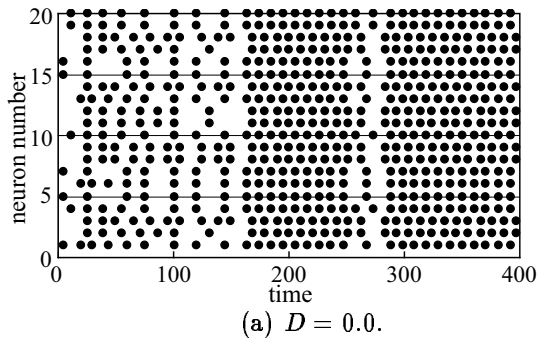


Fig. 7. Temporal firing pattern observed in Eq. (1) with $\omega = 0.94$ and $h = 0.594$.

lar frequency of the impulsive force. In each case an appropriate amount of noise (intensity and the number of neurons subject to the noise) can synchronize firing of neurons. This is extension of noise-induced synchronization [9, 13, 14], because the neurons without the noise are indirectly influenced by the noise through the electrical coupling. We calculated C_v and the number of neurons with synchronous firing as a function of the noise intensity and found that for the small noise intensity they are increased simultaneously. It is an open problem to study a system of synaptically coupled neurons containing a time delay.

REFERENCES

[1] H. Fujii, H. Ito, K. Aihara, N. Ichinose and M. Tsukada, Dynamical cell assembly hypothesis -theoretical possibility of spatio-temporal coding in the cortex, *Neural Networks*, **9**(8), 1303–1350, 1996.
 [2] A. Pikovsky, M. Rosenblum and J. Kurths, *Synchronization: A universal concept in nonlinear sciences*, Cambridge University Press, Cambridge, 2001.
 [3] Y. Wang, D.T.W. Chik and Z.D. Wang, Coherence resonance and noise-induced synchronization in globally coupled Hodgkin-Huxley neurons, *Phys. Rev. E*, **61**, 740, 2000.
 [4] J.N. Casado, Synchronization on two Hodgkin-Huxley neurons due to internal noise, *Phys. Lett. A*, **310**, 400–406, 2003.
 [5] G. Schmid, I. Goychuk and P. Hänggi, Channel noise and synchronization in excitable membranes, *Physica A*, **325**, 165–175, 2003.

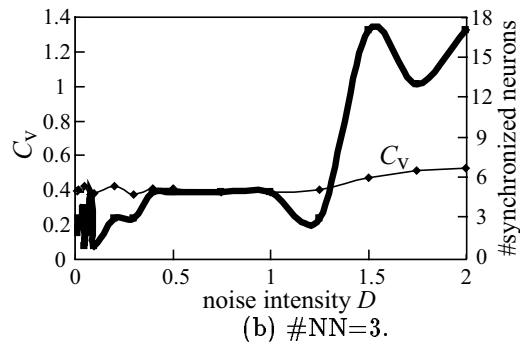
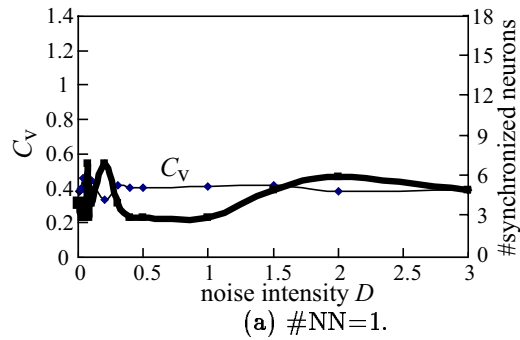


Fig. 8. C_v and the number of neurons with synchronous firing as a function of D_i observed in Eq. (1) with $\omega = 0.94$ and $h = 0.594$.

[6] A.M. Lacasta, F. Sagués and M. Sancho, Coherence and anticoherence resonance tuned by noise, *Phy. Rev. E*, **66**, 045105, 2002.
 [7] M.P. Zorzano and L. Vázquez, Emergence of synchronous oscillations in neural networks excited by noise, *Physica D*, **179**, 105–114, 2003.
 [8] M. Matsumoto and T. Nishimura, Mersenne Twister: A 623-dimensionally equidistributed uniform pseudo-random number generator, *ACM Trans. on Modeling and Computer Simulation*, **8**(1), 3–30, 1998.
 [9] R. Toral, C.R. Mirasso E. Hernández-García and O. Piro, Analytical and numerical studies of noise-induced synchronization of chaotic systems, *Chaos*, vol.11, no.3, pp.665–673, 2001.
 [10] M. San Miguel and R. Toral, *Stochastic Effects in Physical Systems, Instabilities and Nonequilibrium Structures VI*, ed. E. Tirapegui, J. Martínez and R. Tiemann, pp.35–130, Kluwer Academic, Dordrecht, 2000.
 [11] W.R. Softky and C. Koch, The High Irregular Firing of Cortical Cells Is Inconsistent with Temporal Integration of Random EPSPs, *J. of Neurosci.* **13**(1), 334–350, 1993.
 [12] C. Christodoulou and G. Bugmann, Coefficient of variation (CV) vs mean interspike interval (ISI) curves: what do they tell us about brain?, *Neurocomputing*, **38-40**, 1141–1149, 2001.
 [13] D. He, P. Shi and L. Stone, Noise-induced synchronization in realistic models, *Phys. Rev. E*, **67**, 027201, 2003.
 [14] H. Sakaguchi, Noise-induced synchronization for phase turbulence, *Phys. Lett. A*, **318**, 553–557, 2003.

A SIMPLE CHAOTIC CIRCUIT WITH IMPULSIVE SWITCH DEPENDING ON TIME AND STATE

Yoshifumi Kobayashi, Hidehiro Nakano and Toshimichi Saito

EECE Dept., HOSEI Univ., Koganei, Tokyo, 184-8584 Japan

e-mail: tsaito@k.hosei.ac.jp

http://www.nonlinear.k.hosei.ac.jp/

Abstract— This paper presents a simple chaotic circuit consisting of two capacitors, one linear two-port VCCS and one time-state-controlled impulsive switch. The impulsive switch causes rich chaotic and periodic behaviour. The circuit dynamics can be simplified into a one-dimensional return map that is piecewise linear and is piecewise monotone. Using the return map, we clarify parameters conditions for chaotic attractors, periodic attractors and co-existence state of attractors.

I. INTRODUCTION

This paper presents a simple nonautonomous chaotic circuit based on integrate-and-fire dynamics [1]-[4] and dependent switched capacitor circuits [5]-[7]. The circuit consists of two capacitors, one linear two-port voltage-controlled current source (ab. VCCS), and one firing switch. The a capacitor voltage vibrates divergently and the divergence can be suppressed by the firing switch that depends on both time and the capacitor voltage. This time-state-controlled impulsive switch (ab. TSCIS) causes rich chaotic and periodic behaviour. The circuit dynamics can be simplified into a one-dimensional return map that is piecewise linear and is piecewise monotone. Using the return map, we clarify parameters conditions for chaotic attractors, periodic attractors and co-existence state of attractors. In the final version, we will present a simple test circuit with typical laboratory data.

As compared with existing various nonautonomous chaotic circuits (see [6] [8] and references therein), our circuit has some properties including the following. (1) the refractory threshold controls the discontinuity points of the return map and can cause interesting chaotic/periodic behaviour, (2) the TSCIS relates deeply to stretching and folding mechanism to generate chaos and is applicable to wider class of two or more dimensional circuit, and (3) the circuits configuration is simple and is suited for integration. Also, the impulsive switching relates deeply to integrate-and-fire neuron models [1]-[3] and pulse-coupled neural

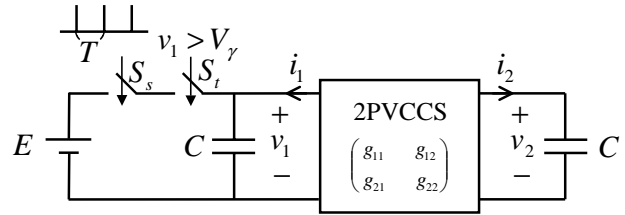


Fig. 1. A circuit model.

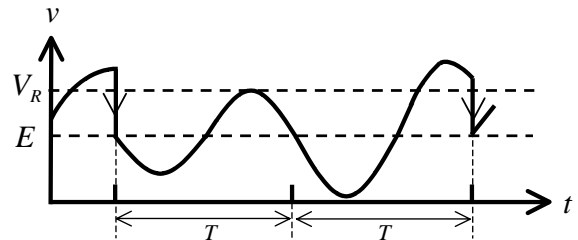


Fig. 2. Time-domain wave-forms.

networks [7] [9]-[11]. These systems can exhibit a variety of synchronous/asynchronous phenomena and have a variety of applications including associative memory [9] [10] and image segmentation [11]. If our TSCIS circuit is developed into a novel PCNN, it may contribute to analysis of rich synchronous phenomena and application to flexible information processing.

II. THE CHAOTIC CIRCUIT

Fig. 1 shows the circuit model. In the figure, a 2-port VCCS and two capacitors construct a linear sub-circuit described by

$$\frac{d}{dt} \begin{bmatrix} C_1 v_1 \\ C_2 v_2 \end{bmatrix} = \begin{bmatrix} g_{11} & g_{12} \\ g_{21} & g_{22} \end{bmatrix} \begin{bmatrix} v_1 \\ v_2 \end{bmatrix} \quad (1)$$

We assume that Equation (1) has unstable complex characteristic roots $\delta\omega \pm j\omega$:

$$\omega^2 = -\frac{g_{12}g_{21}}{C_1 C_2} - \frac{1}{4} \left(\frac{g_{11}}{C_1} - \frac{g_{22}}{C_2} \right)^2 > 0, \quad (2)$$

$$\delta = \frac{1}{2\omega} \left(\frac{g_{11}}{C_1} + \frac{g_{22}}{C_2} \right) > 0.$$

In the figure, series of S_s and S_t constructs the time-state-controlled impulsive switch (ab. TSCIS). If the

TSCIS does not exist, the capacitor voltages diverge with vibration. This dynamics relates to stretching mechanism for chaos generation. The TSCIS suppresses the divergence as shown in Fig. 2: if the first capacitor voltage v_1 exceeds a refractory threshold V_r at time mT , v_1 is reset to the base level E instantaneously holding the continuity of v_2 , where m is a positive integer and T is a basic period of the TSCIS.

$$\begin{bmatrix} v_1(t^+) \\ v_2(t^+) \end{bmatrix} = \begin{bmatrix} E \\ v_2(t) \end{bmatrix} \text{ if } v_1(t) > V_r \text{ and } t = mT. \quad (3)$$

We refer to this switching as compulsory firing (ab. CFR) hereafter. Here we introduce the following dimensionless variables and parameters:

$$\begin{aligned} \tau &= \omega t, \quad x = \frac{v_1}{V_T}, \quad \dot{x} = \frac{dx}{d\tau}, \quad y = \frac{1}{V_T} \left(p v_1 + \frac{g_{12}}{\omega C_1} v_2 \right) \\ d &= \omega T, \quad a = \frac{V_r}{V_T}, \quad p = \frac{1}{2\omega} \left(\frac{g_{11}}{C_1} - \frac{g_{22}}{C_2} \right), \quad q = \frac{E}{V_T} \end{aligned} \quad (4)$$

where V_T is a criterion voltage based on the dynamic range of the VCCS. Using these, Equations (refosc) and (3) are transformed into the following normal form equations.

$$\text{CFR: } (x(\tau^+), y(\tau^+)) = (q, y(\tau) - p(x(\tau) - q)) \text{ if } x(\tau) > a \text{ and } \tau = md$$

$$\begin{bmatrix} \dot{x} \\ \dot{y} \end{bmatrix} = \begin{bmatrix} \delta & 1 \\ -1 & \delta \end{bmatrix} \begin{bmatrix} x \\ y \end{bmatrix} \text{ otherwise} \quad (5)$$

where m is a positive integer. This normalised equation has five parameters: the damping δ , the jumping slope p , the base q , the basic period d and the refractory threshold a . In an interval of switchings, Equation (6) has exact piecewise solution:

$$\begin{bmatrix} x(\tau) \\ y(\tau) \end{bmatrix} = e^{\delta\tau'} \begin{bmatrix} \cos \tau & \sin \tau \\ -\sin \tau & \cos \tau \end{bmatrix} \begin{bmatrix} x(\tau_s) \\ y(\tau_s) \end{bmatrix} \quad (6)$$

where $(x(\tau_s), y(\tau_s))$ denotes a state vector just after the switching at time τ_s and $\tau \equiv \tau - \tau_s$. For simplicity, we select d and a as control parameters and the other three parameters are fixed: $\delta = 0.05$, $p = 0.8$ and $q = -0.5$. Fig. 3 shows typical phenomena calculated using the exact piecewise solution. In order to classify the periodic phenomena, we use ratio of the switching per basic period. For example, Fig. 3(a) shows 1 : 1 periodic orbit where the x resets once during one basic period and Fig. 3(b) shows 2 : 1 periodic orbit where the x resets once during two basic period. In some parameter range, 1 : 1 and 2 : 1 periodic orbits can coexist as shown in Fig. 3(c) and the system exhibit one of them depending on an initial

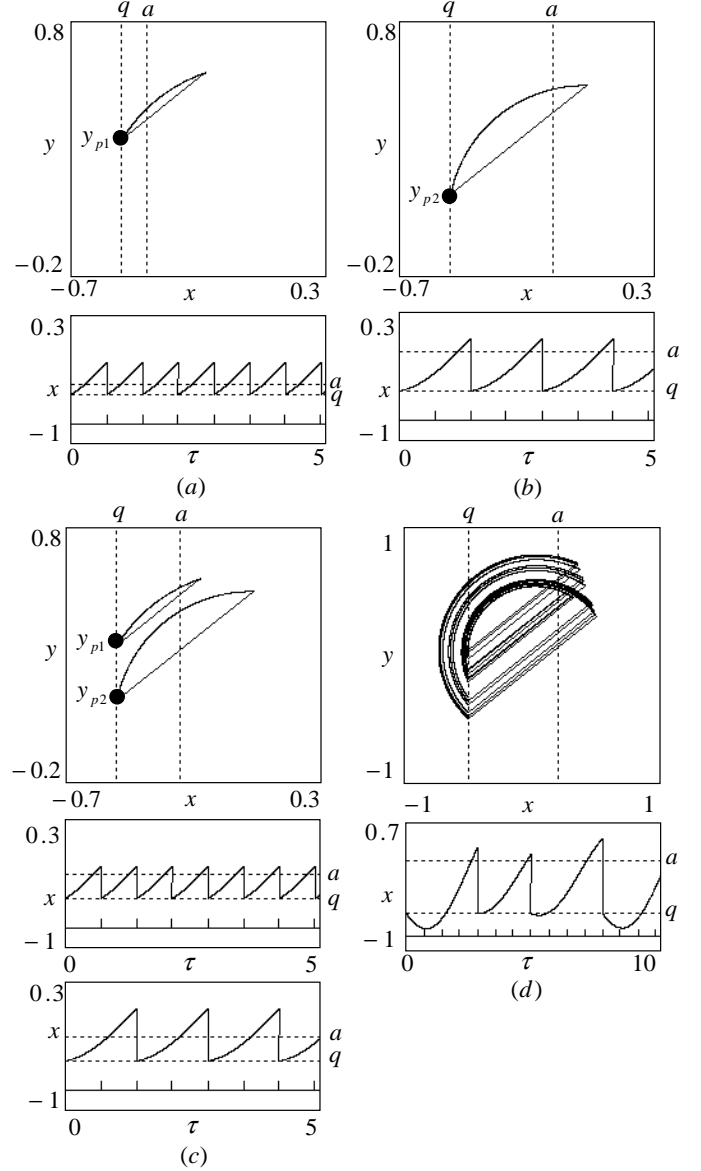


Fig. 3. Typical phenomena ($\delta = 0.05$, $p = 0.8$, $q = -0.5$, $d = 0.7$). (a) 1:1 periodic orbit ($a = -0.4$), (b) 2:1 periodic orbit ($a = -0.1$), (c) Coexistence of 1:1 and 2:1 periodic orbits ($a = -0.25$), (d) Chaotic attractor ($a = 0.2$).

state. This system can also exhibit chaotic attractor as shown in Fig. 3(d).

III. ANALYSIS

In order to analyse the phenomena, we derive a 1-D return map. As illustrated in Fig. 4, a CFR occurs at $\tau = \tau_s$, the trajectory is reset to a point (q, y_0) on the base line $x = q$. The trajectory starting from (q, y_0) rotates divergently around the origin and is reset to a point (q, y_1) when the next CFR occurs. Then we can define the following 1-D return map.

$$f : y_0 \mapsto y_1. \quad (7)$$

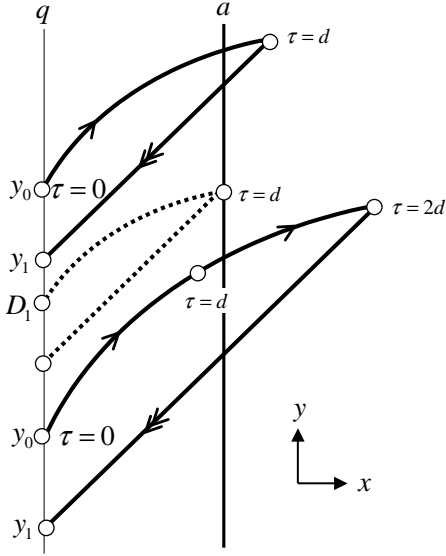


Fig. 4. Phase plane.

Since the system is piecewise linear the map can be calculated analytically:

$$f(y_0) = y(\tau_s + md) - p(x(\tau_s + md) - q), \quad (8)$$

where m is given by $\min_m x(\tau_s + md) \geq a$. This return map is piecewise linear and piecewise monotone. Fig. 5 shows typical 1-D return maps, where (a) and (b) correspond to Figs. 3(c) and (d), respectively. Let B_m be a subset of y_0 such that a trajectory starting from a point $y_0 \in B_m$ exhibits CF at $\tau = \tau_0 + md$. Let D_m be a discontinuity point between B_{m+1} and B_m :

$$D_m = \frac{a - e^{\delta md} \cos(md)}{e^{\delta md} \sin(md)}. \quad (9)$$

In Fig. 5(a), there exist two stable fixed points $y_{p1} \in B_1$ and $y_{p2} \in B_2$ corresponding to 1 : 1 and 2 : 1 periodic orbit, respectively. Fig. 5(b) shows a chaotic attractor where the attractor is on B_3 and B_4 . Fig. 6 shows the bifurcation diagram for the refractory a . Let us consider existence condition for periodic orbits. There exists fixed point $y_{pm} = f(y_{pm})$ corresponding to $m : 1$ periodic orbit if $D_m < y_{pm} \leq D_{m-1}$, where

$$y_{pm} = q \frac{p - e^{\delta md} (\sin(md) + p \cos(md))}{1 + e^{\delta md} (p \sin(md) - \cos(md))}. \quad (10)$$

The fixed point y_{pm} is stable if $|Df(y_{pm})| < 1$, where Df is the derivative of f :

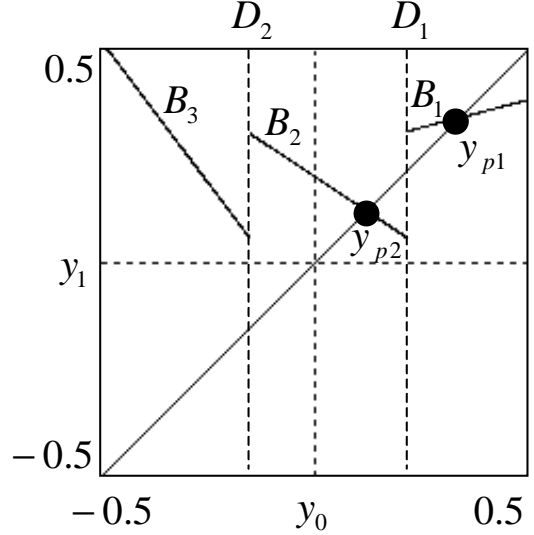
$$Df(y) = e^{\delta md} (-p \sin(md) + \cos(md)) \text{ for } y \in B_m.$$

That is, an $m : 1$ periodic orbit exists if $(d, a) \in P_m$:

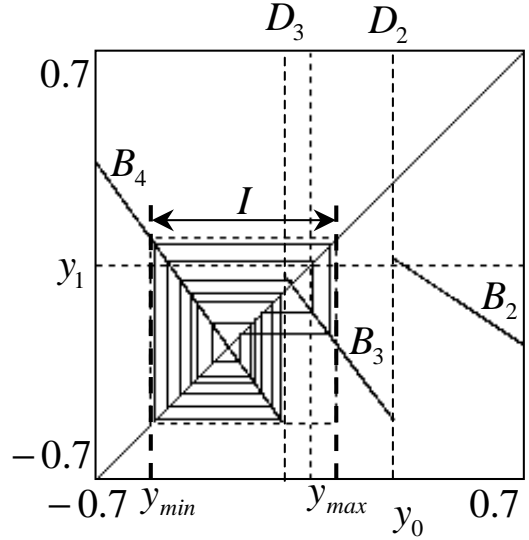
$$P_1 \equiv \{(d, a) | D_1 < y_{p1}, |Df(y_{p1})| < 1\},$$

$$P_m \equiv \{(d, a) | D_m < y_{pm} \leq D_{m-1}, |Df(y_{pm})| < 1\}$$

for $m \geq 2$.



(a)



(b)

Fig. 5. Typical 1-D return maps ($\delta = 0.05$, $p = 0.8$, $q = -0.5$, $d = 0.7$). (a) $a = -0.25$, (b) $a = 0.2$.

Fig. 7 shows an existence region for each periodic orbit. Next, we consider existence condition for chaos attractor. An interval $I \equiv (y_{min}, y_{max})$ is said to an invariant interval if $f(I) \subseteq I$. If y_{max} exists on B_m , y_{min} exists on B_{m+1} and if $|Df(y_0)| > 1$ for $y_0 \in B_m \cup B_{m+1}$, then f generates chaos on I . Fig. 8 shows a existence region for each chaos attractor. f generates chaos and the chaotic orbit behaves on B_m and B_{m+1} for $m \geq 2$ if $(d, a) \in C_{m,m+1}$:

$$C_{m,m+1} = \{(d, a) | D_{m+1} < y_{min} \leq D_m,$$

$$D_m < y_{max} \leq D_{m-1}, |df(y_0)| > 1 \text{ for } y_0 \in I\}.$$

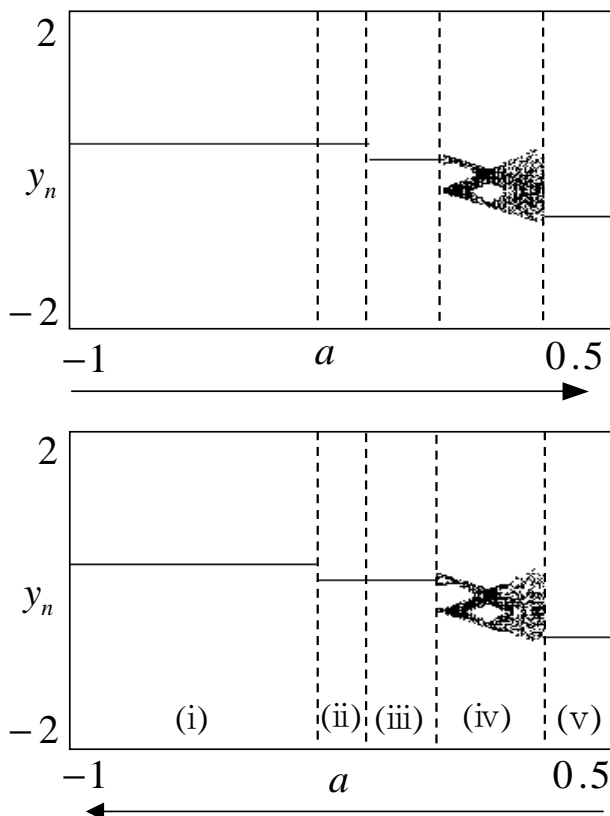


Fig. 6. (a) Bifurcation diagram ($\delta = 0.05, p = 0.8, q = -0.5, d = 0.7$). The i region exhibits 1:1 periodic orbit, the ii region exhibits coexistence of 1:1 and 2:1 periodic orbits, the iii region exhibits 2:1 periodic orbit, the iv region exhibits chaotic attractor, the v region exhibits 5:1 periodic orbit.

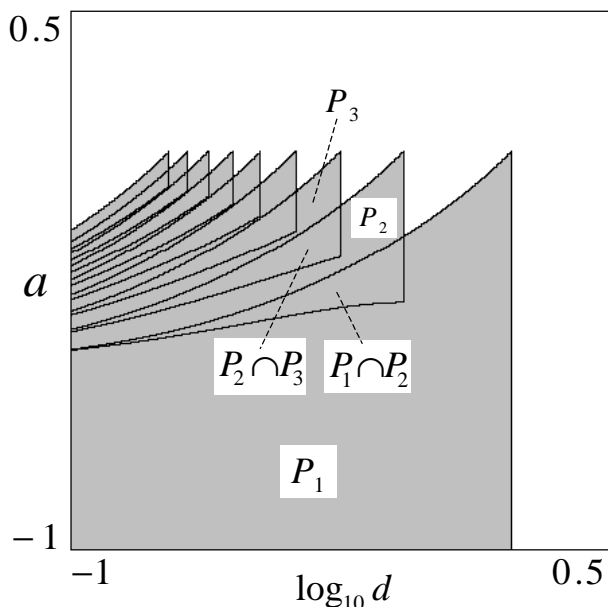


Fig. 7. Existence region for each periodic orbit ($\delta = 0.05, p = 0.8, q = -0.5$). ($1 \leq m \leq 9$).

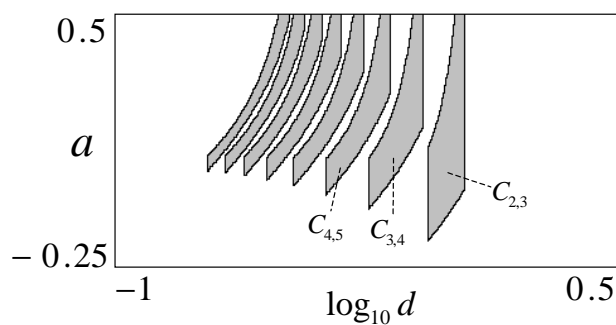


Fig. 8. Existence region for each chaos attractor ($\delta = 0.05, p = 0.8, q = -0.5$). ($2 \leq m \leq 9$).

IV. CONCLUSIONS

We have considered a simple chaotic circuit including TSCIS. The TSCIS causes rich chaotic/periodic phenomena and the phenomena are analysed using one-dimensional piecewise linear (and monotone) return map. Future problems include detailed analysis of bifurcation phenomena and application of the TSCIS to higher dimensional circuits and PCNNs.

REFERENCES

- [1] J. P. Keener, F. C. Hoppensteadt and J. Rinzel, Integrate-and-fire models of nerve membrane response to oscillatory input, *SIAM J. Appl. Math.*, 41, pp. 503-517, 1981.
- [2] R. E. Mirollo and S. H. Strogatz, Synchronization of pulse-coupled biological oscillators, *SIAM J. Appl. Math.*, 50, pp. 1645-1662, 1990.
- [3] E. M. Izhikevich, Resonate-and-fire neurons, *Neural Networks*, vol. 14, pp. 883-894, 2001.
- [4] T. Allen, Complicated, but rational, phase-locking responses of a simple time-base oscillator, *IEEE Trans. Circuits Syst.*, 30, 9, pp. 627-632, 1983.
- [5] K. Mitsubori and T. Saito, Mutually Pulse-coupled Chaotic Circuits by using Dependent Switched Capacitors *IEEE Trans. Circuits Syst. I*, 47, 10, pp. 1469-1478, 2000.
- [6] K. Miyachi, H. Nakano and T. Saito, Response of a simple dependent switched capacitor circuit to a pulse-train input, *IEEE Trans. Circuits Syst. I*, 50, 9, pp. 1180-1187, 2003.
- [7] H. Nakano and T. Saito, Basic dynamics from a pulse-coupled network of autonomous integrate-and-fire chaotic circuits, *IEEE Trans. Neural Networks*, 13, 1, pp. 92-100, 2002.
- [8] Y. S. Tang, A. I. Mess, and L. O. Chua, Synchronization and chaos, *IEEE Trans. Circuits Syst.*, 30, 9, pp.620-626, 1983.
- [9] E. M. Izhikevich, Weakly pulse-coupled oscillators, FM interactions, synchronization, and oscillatory associative memory, *IEEE Trans. Neural Networks*, 10, 3, pp. 508-526, 1999.
- [10] G. Lee and N.H. Farhat, The bifurcating neuron network 1, *Neural Networks*, 14, pp.115-131, 2001.
- [11] S. R. Campbell, D. Wang and C. Jayaprakash, Synchrony and desynchrony in integrate-and-fire oscillators, *Neural Comput.*, 11, pp. 1595-1619, 1999.

ABELIAN DIFFERENTIAL EQUATIONS DEFINE CHAOS GENERATOR

Tohru Kohda and Aya Katoh

Department of Computer Science
and Communication Engineering,
Kyushu University,
Fukuoka, Japan

e-mail: kohda@csce.kyushu-u.ac.jp

Abstract—Bernoulli shift or tent map is a simple example of ergodic maps generating chaos. Several well-known ergodic maps topologically conjugate to the tent map are shown to be governed by Abel’s differential equations. Jacobian elliptic Chebyshev rational map is shown to be induced by a typical elliptic integral in real numbers. It is also shown to generate a sequence of 2-dimensional i.i.d. binary random variables.

I. INTRODUCTION

Bernoulli shift and its associated binary function, called Rademacher function, can produce a sequence of independent and identically distributed (i.i.d.) binary random variables (BRVs) in a sense that they furnish us with a model of independent tosses of a ‘fair’ coin. Tent map, closely related to the Bernoulli map, and its associated binary function can also generate a sequence of i.i.d. BRVs. Ulam and Von Neumann[1] showed that the logistic map is topologically conjugate to the tent map via the homeomorphism $h^{-1}(\omega) = \frac{2}{\pi} \sin^{-1} \sqrt{\omega}$. They also pointed out that the logistic map is a strong candidate for pseudorandom number generation (PRNG) even though it has a non-uniform absolutely continuous invariant (ACI) measure. Motivated by Ulam-Neumann’s sophisticated statement, we have recently shown that a class of ergodic maps with *equidistributivity property* (EDP) can generate a sequence of i.i.d. BRVs if their associated binary functions satisfy *constant summation property* (CSP) [2]–[3]. A chaos-based generator of random bits [4] is known to be a PRNG method without using linear feedback shift register sequences [5].

Let $w = w(z)$ be the algebraic function determined by $F(z, w) = 0$, where $F(z, w)$ is a polynomial in z and w and let $R(z, w)$ be a rational function on a Riemann surface [6],[7]. Integrals of the form $\int R(z, w)dz$ are called Abelian integrals. Bernoulli shift or tent map is a typical example of addition (or

duplication) formula. It is well known that Euler’s (or Abel’s) addition formula can be represented in elliptic integrals.

Several well-known ergodic maps topologically conjugate to the tent map are shown to be governed by Abel’s differential equations in the following sense: (1) inverse function of a homeomorphism defining an ergodic map is represented by an Abelian integral; (2) its derivative with respect to a single parameter gives ACI measure of the map and (3) the map satisfies an Abelian differential equation with respect to the parameter and induces a 2-dimensional map.

Derivative of Jacobian elliptic Chebyshev rational map [8] is shown to induce an elliptic curve [9], defined by an elliptic integral in real numbers. Real-valued orbits on the curve are shown to produce a sequence of 2-dimensional i.i.d. BRVs.

II. INVERSE FUNCTION OF HOMEOMORPHISM AND ELLIPTIC FUNCTION

Consider an ergodic map $\tau : I = [d, e] \rightarrow I$ with its unique ACI measure, denoted by $f(\omega)d\omega$.

Bernoulli map with $f(\omega)d\omega = d\omega$ is defined as

$$\tau_B(\omega) = 2\omega \pmod{1} = \begin{cases} 2\omega, & 0 < \omega < \frac{1}{2}, \\ 2\omega - 1, & \frac{1}{2} \leq \omega < 1. \end{cases} \quad (1)$$

If ω is represented by its binary expansion as $\omega = 0.d_1(\omega)d_2(\omega)\cdots$, then the binary expansion of $\tau_B(\omega)$ is given by $\tau_B(\omega) = 0.d_2(\omega)d_3(\omega)\cdots$. This implies that $\tau_B(\cdot)$ shifts the digits one place to the left. The functions $d_k(\cdot)$, called Rademacher functions, furnish us with a model of independent tosses of a fair coin. A sequence $\{d_k(\omega)\}_{k=0}$ can be regarded as a sequence of i.i.d. BRVs in a sense that for almost every ω , $d_k(\omega)$ can imitate coin tossing. Another map and its associated binary function are as follows. Consider piecewise linear map of p branches with $f(\omega)d\omega = d\omega$, given by [10]

$$N_p(\omega) = (-1)^{p\omega} p\omega \pmod{p}, \quad \omega \in [0, 1]. \quad (2)$$

In particular, $N_2(\omega)$ is referred to as the tent map. In-

introduce its associated BRV defined as

$$a_k = \begin{cases} 0, & \text{for } N_2^k(\omega) \leq \frac{1}{2}, \\ 1, & \text{for } N_2^k(\omega) > \frac{1}{2}. \end{cases} \quad (3)$$

Then for $\omega = 0.d_1(\omega)d_2(\omega)\cdots$, we get

$$a_0(\omega) = d_1(\omega), \quad a_k(\omega) = d_k(\omega) \oplus d_{k+1}(\omega), \quad k \geq 1, \quad (4)$$

where \oplus denotes a modulo 2 addition (or exclusive-or) operation. Hence $N_2(\omega)$ and its associated binary functions $a_k(\cdot)$ can generate a sequence of i.i.d. BRVs. Naturally, the important question arises, that can any other map and its associated binary function generate a sequence of i.i.d. BRVs? We have got an affirmative answer to this question [2]–[3], which is firstly, the map should satisfy EDP and secondly, the binary function should satisfy CSP. EDP and CSP respectively correspond to trivial and non-trivial partition of the interval [3]. Fortunately, EDP is satisfied by many well-known maps. Furthermore, EDP is proven to be invariant under topological conjugation.

Definition 1: (Topological Conjugation) [11] Two transformations $\bar{\tau} : \bar{I} \rightarrow \bar{I}$ and $\tau : I \rightarrow I$ on intervals \bar{I} and I are called *topologically conjugate* if there exists a homeomorphism $h: \bar{I} \xrightarrow{\text{onto}} I$, such that

$$\tau(\omega) = h \circ \bar{\tau} \circ h^{-1}(\omega). \quad (5)$$

Suppose $\tau(\omega)$ and $\bar{\tau}(\bar{\omega})$ have their ACI measures denoted by $f(\omega)d\omega$ and $\bar{f}(\bar{\omega})d\bar{\omega}$ respectively. Then, these ACI measures satisfy the relation

$$f(\omega) = \left| \frac{dh^{-1}(\omega)}{d\omega} \right| \bar{f}(h^{-1}(\omega)). \quad (6)$$

Remark 1: If we take $N_2(\bar{\omega})$ as $\bar{\tau}(\bar{\omega})$, then $f(\omega)$ is simply represented by the derivative of $h^{-1}(\omega)$. Hence, if $h(\bar{\omega})$ can be given in an inverse function form, then its integrand gives an ACI measure within normalization factor. Most famous example of inverse functions is sin function, *i.e.*,

$$\omega = \int_0^{\sin \omega} \frac{du}{\sqrt{1-u^2}}. \quad (7)$$

This remark is a starting point of our study. In fact, Ulam and von Neumann [1] gave the logistic map

$$L_2(\omega) = 4\omega(1-\omega), \quad \omega \in [0, 1] \quad (8)$$

with $f(\omega)d\omega = \frac{d\omega}{\pi\sqrt{\omega(1-\omega)}}$ which is topologically

conjugate to $N_2(\bar{\omega})$ using $h^{-1}(\omega) = \frac{2}{\pi} \sin^{-1} \sqrt{\omega}$.

III. ABEL'S DIFFERENTIAL EQUATIONS

The example mentioned above implies that duplication formula gives chaos. To observe it thoroughly, consider an irreducible algebraic equation [6],[7]

$$F(z, w) = 0, \quad (9)$$

where $F(z, w)$ is a polynomial in z and w that is not representable as a product of two polynomials. The set of all pairs (z, w) satisfying eq.(9) is called an *algebraic curve*. In particular, consider eq.(9) with the form

$$\left. \begin{aligned} w^2 &= A(z - \alpha_1)(z - \alpha_2)\cdots(z - \alpha_{2p+1}), \\ w^2 &= A(z - \alpha_1)(z - \alpha_2)\cdots(z - \alpha_{2p+2}). \end{aligned} \right\} \quad (10)$$

If $p = 1$, we get an *elliptic curve* and for $p > 1$ a *hyperelliptic curve*. Consider a rational function $R(z, w)$ on Riemann surface belonging to eq.(10). Obviously, the expression (7) is an example of an *elliptic integral* $\int R(z, w)dz = \int \frac{dz}{w}$ ¹. Most important elliptic function is the Weierstrass one $\mathcal{P}(u)$, written by

$$w^2 = f = 4z^3 - g_2z - g_3, \quad (11)$$

$$u = \int_{\mathbb{P}} \frac{dz}{\sqrt{f(z)}}, \quad \frac{dz}{du} = \sqrt{f(z)}. \quad (12)$$

Different values of the above integral have the form

$$\pm u + 2m\omega + 2m\omega', \quad (13)$$

where u is one of these values, m and m' are arbitrary integers and ω, ω' are half-periods. Expressions about two variables w, z using a single parameter u such as eqs.(11)–(12) are called *uniformization* [6]. Let

$$z_i = \mathcal{P}(u_i), w_i = \mathcal{P}'(u_i), \text{ for } 1 \leq i \leq 3. \quad (14)$$

Abel's addition theorem states that if

$$u_1 + u_2 + u_3 = 0 \pmod{2\omega, 2\omega'}, \quad (15)$$

then there exist a and b such that

$$w_i = az_i + b, 1 \leq i \leq 3. \quad (16)$$

Such uniformization gives a 2-dimensional chaotic sequence governed by an Abel's differential equation as follows.

(1) logistic map: Transformation $x = \sin^2 \theta$ gives

$$\left(\frac{dx}{d\theta} \right)^2 = 4x(1-x). \quad (17)$$

Let $x_n = \sin^2 \theta_n, \theta_{n+1} = 2\theta_n$. Then we get 2-dimensional sequences $\{(x_n, y_n)\}_{n=0}$, given by

$$x_{n+1} = L_2(x_n) = 4x_n(1-x_n), \quad (18)$$

$$y_{n+1}^2 = \left(\frac{1}{2} \cdot \frac{dL_2(x_n)}{d\theta} \right)^2 = 4L_2(x_n)(1-L_2(x_n)). \quad (19)$$

¹More precisely speaking, if $p = 0$, (z, w) satisfying eq. (10) gives a circular (or hyperbolic) curve and an *elementary integral* $\int R(z, \sqrt{az^2 + bz + c}) dz$.

(2) Chebyshev map of degree 2:

Grossmann and Thomaе [10] observed that Chebyshev polynomial maps of degree p ($p = 2, 3, \dots$) [12]

with $f(\omega)d\omega = \frac{d\omega}{\pi\sqrt{1-\omega^2}}$, written by

$$T_p(\omega) = \cos(p \cos^{-1} \omega), \quad \omega \in [-1, 1] \quad (20)$$

is topologically conjugate to $N_p(\omega)$ via $h(\bar{\omega}) = \cos \pi \bar{\omega}$. Transformation $x = \cos \theta$ gives

$$\left(\frac{dx}{d\theta}\right)^2 = 1 - x^2. \quad (21)$$

Let $x_n = \cos \theta_n$, $\theta_{n+1} = 2\theta_n$. Then we get 2-dimensional sequences $\{(x_n, y_n)\}_{n=0}$, written by

$$x_{n+1} = T_2(x_n) = 2x_n^2 - 1, \quad (22)$$

$$y_{n+1}^2 = \left(\frac{1}{2} \cdot \frac{dT_2(x_n)}{d\theta}\right)^2 = 1 - (T_2(x_n))^2. \quad (23)$$

(3) Katsura map:

Katsura and Fukuda [13] gave a rational function version of $L_2(\omega)$ with parameter k , defined as

$$R_2^{\text{sn}^2}(\omega, k) = \frac{4\omega(1-\omega)(1-k^2\omega)}{(1-k^2\omega^2)^2}, \quad \omega \in [0, 1] \quad (24)$$

with its ACI measure

$$f(\omega, k)d\omega = \frac{d\omega}{2K(k)\sqrt{\omega(1-\omega)(1-k^2\omega)}} \quad (25)$$

via $h^{-1}(\omega) = \frac{1}{K(k)}\text{sn}^{-1}(\sqrt{\omega}, k)$, where $\text{sn}(\omega, k)$ is the inverse function of the elliptic integral with modulus k ($|k| < 1$) and $K(k)$ is the complete elliptic integral, each of which is given respectively as

$$\omega = \int_0^{\text{sn}(\omega, k)} \frac{dv}{\sqrt{(1-v^2)(1-k^2v^2)}}, \quad (26)$$

$$K(k) = \int_0^{\frac{\pi}{2}} \frac{d\theta}{\sqrt{1-k^2\sin^2\theta}}. \quad (27)$$

Transformation $x = \text{sn}^2 u$ gives

$$\left(\frac{dx}{du}\right)^2 = 4x(1-x)(1-k^2x). \quad (28)$$

Let $x_n = \text{sn}^2 u_n$, $u_{n+1} = 2u_n$. Then we get 2-dimensional sequences $\{(x_n, y_n)\}_{n=0}$, given by

$$x_{n+1} = R_2^{\text{sn}^2}(x_n, k) = \frac{4x_n(1-x_n)(1-k^2x_n)}{(1-k^2x_n^2)^2}, \quad (29)$$

$$y_{n+1}^2 = \left(\frac{1}{2} \cdot \frac{dR_2^{\text{sn}^2}(x_n, k)}{du}\right)^2 = 4R_2^{\text{sn}^2}(x_n, k)(1-R_2^{\text{sn}^2}(x_n, k))(1-k^2R_2^{\text{sn}^2}(x_n, k)). \quad (30)$$

(4) Jacobian Elliptic Chebyshev map of degree 2:

Kohda and Fujisaki [8] have recently introduced the *Jacobian elliptic Chebyshev rational map* with modulus k , defined by

$$R_p^{\text{cn}}(\omega, k) = \text{cn}(p \text{cn}^{-1}(\omega, k), k), \quad \omega \in [-1, 1] \quad (31)$$

with its ACI measure

$$f(\omega, k)d\omega = \frac{d\omega}{2K(k)\sqrt{(1-\omega^2)\{(1-k^2) + k^2\omega^2\}}} \quad (32)$$

using homeomorphism $h^{-1}(\omega, k) = \frac{\text{cn}^{-1}(\omega, k)}{2K(k)}$ of $N_p(\bar{\omega})$, $p = 2, 3, 4, \dots$, where $\text{cn}(\omega, k)$ is the inverse function of the elliptic integral with modulus k , i.e.,

$$\omega = \int_{\text{cn}(\omega, k)}^1 \frac{dv}{\sqrt{(1-v^2)\{(1-k^2) + k^2v^2\}}}. \quad (33)$$

We know that $R_p^{\text{cn}}(\omega, k)$ satisfies the semi-group property

$$R_r^{\text{cn}}(R_s^{\text{cn}}(\omega, k), k) = R_{rs}^{\text{cn}}(\omega, k) \quad (34)$$

for integers r, s and when $p = 2$

$$R_2^{\text{cn}}(\omega, k) = \frac{1 - 2(1-\omega^2) + k^2(1-\omega^2)^2}{1 - k^2(1-\omega^2)^2} \quad (35)$$

holds. Using the relation $K(0) = \frac{\pi}{2}$, we get

$$R_p^{\text{cn}}(\omega, 0) = T_p(\omega), \quad f(\omega, 0)d\omega = \frac{d\omega}{\pi\sqrt{1-\omega^2}}. \quad (36)$$

Transformation $x = \text{cn} u$ gives

$$\left(\frac{dx}{du}\right)^2 = (1-x^2)(1-k^2+k^2x^2). \quad (37)$$

Let $x_n = \text{cn} u_n$, $u_{n+1} = 2u_n$. Then we get 2-dimensional sequences $\{(x_n, y_n)\}_{n=0}$, defined as

$$x_{n+1} = R_2^{\text{cn}}(x_n, k) = \frac{2x_n^2 - 1 + k^2(1-x_n^2)^2}{1 - k^2(1-x_n^2)^2}, \quad (38)$$

$$y_{n+1}^2 = \left(\frac{1}{2} \cdot \frac{dR_2^{\text{cn}}(x_n, k)}{du}\right)^2 = (1 - (R_2^{\text{cn}}(x_n, k))^2) (1 - k^2 + k^2(R_2^{\text{cn}}(x_n, k))^2). \quad (39)$$

IV. MEASURE ON JACOBIAN ELLIPTIC CURVE

Addition formula for cn function gives [8]

$$R_{p+1}^{\text{cn}}(\omega, k) = \frac{2\omega R_p^{\text{cn}}(\omega, k)}{1 - k^2(1-\omega^2)\{1 - R_p^{\text{cn}}(\omega, k)^2\}} + R_{p-1}^{\text{cn}}(\omega, k) = 0, \quad p = 1, 2, \dots \quad (40)$$

$$\text{with } R_0^{\text{cn}}(\omega, k) = 1, \quad R_1^{\text{cn}}(\omega, k) = \omega. \quad (41)$$

Similarly, $R_p^{\text{cn}}(x_n, k)$ satisfies the Abelian differential equation

$$\left(\frac{1}{p} \cdot \frac{dR_p^{\text{cn}}(x_n, k)}{du}\right)^2 = (1 - (R_p^{\text{cn}}(x_n, k))^2) (1 - k^2 + k^2(R_p^{\text{cn}}(x_n, k))^2). \quad (42)$$

As reported in previous study [9], $R_2^{cn}(x_n, k)$ has a *stable* invariant curve, written by $Y^2 = (1 - X^2)(1 - k^2 + k^2 X^2)$. The adjective *stable* means the curve behaves as an *attractive* curve as shown in Fig.1(a). x_{n+1} is given as eq.(38). On the other hand, eq.(39) gives calculation of y_{n+1}^2 , defined as

$$y_{n+1} = \begin{cases} -\pi(x_{n+1}), \\ \text{for } 0 < 2u_n \pmod{4K(k)} < 2K(k), \\ \pi(x_{n+1}), \text{ otherwise,} \end{cases} \quad (43)$$

$$\pi(x_{n+1}) = \sqrt{(1 - x_{n+1}^2)(1 - k^2 + k^2 x_{n+1}^2)}. \quad (44)$$

Observed measure of real-valued orbits, generated by 2-d map $(x_{n+1}, y_{n+1}) = (R_2^{cn}(x_n, k), \frac{1}{2} \cdot \frac{dR_2^{cn}(x_n, k)}{du})$, as shown in Fig.1(b) supports that there exists an ACI measure on the curve. Figs.2 (a) and 2(b) show its marginal distributions of y and x , respectively given by $\mu_X = \int_{-1}^1 f(x, y) dy$ and $\mu_Y = \int_{-1}^1 f(x, y) dx$. In these figures, their theoretical distributions are also depicted. These are given by integrand of elliptic integral for inverse function $(\text{cn } u)^{-1}$, defined as eq.(33) and one for inverse function $(\frac{d \text{cn } u}{du})^{-1} = -(\text{sn } u \text{ dn } u)^{-1}$, defined as

$$\omega = \begin{cases} \int_0^{-\text{sn}(u,k) \text{ dn}(u,k)} \frac{\sqrt{2k}}{\sqrt{(2k^2 - 1 + \sqrt{1 - 4k^2 t^2})(1 - 4k^2 t^2)}} dt & (k < \sqrt{\frac{1}{2}}) \\ \int_0^{-\text{sn}(u,k) \text{ dn}(u,k)} \frac{\sqrt{2k}}{\sqrt{(2k^2 - 1 + \sqrt{1 - 4k^2 t^2})(1 - 4k^2 t^2)}} dt \\ + \int_0^{-\text{sn}(u,k) \text{ dn}(u,k)} \frac{\sqrt{2k}}{\sqrt{(2k^2 - 1 - \sqrt{1 - 4k^2 t^2})(1 - 4k^2 t^2)}} dt & (k > \sqrt{\frac{1}{2}}) \end{cases} \quad (45)$$

respectively. This implies μ_Y is given by integrands of eq.(45), whereas μ_X is given by integrand by eq.(33). Namely, inverse function of $-\text{sn } u \text{ dn } u$ is also representable in a kind of elliptic functions in real numbers. On the other hand, distribution of the u -axis along the invariant curve, denoted by μ_u , should be uniform as shown in Fig.2(c), which is identical to the uniform ACI measure of $N_2(\bar{u})$, defined as $f(\bar{u})d\bar{u} = d\bar{u}$ because $\text{cn } u$ is written by $\text{cn } u = \cos \theta = \cos \text{am}(u, k)$, where $\text{am}(u, k)$ is Jacobi's amplitude function, defined as

$$u = \int_0^\theta \frac{d\theta}{\sqrt{1 - k^2 \sin^2 \theta}}, \quad \theta = \text{am}(u, k). \quad (46)$$

V. CONCLUDING REMARKS

Jacobian Chebyshev rational map has been shown to satisfy Abelian differential equation. Real-valued

²Another expression for (x_{n+1}, y_{n+1}) has been given in reference [9].

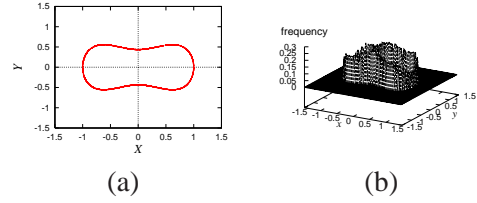


Fig. 1. (a) Stable invariant curve and (b) its joint distribution of 2-dim. map $(R_2^{cn}(x_n, 0.9), \frac{1}{2} \cdot \frac{dR_2^{cn}(x_n, 0.9)}{du})$.

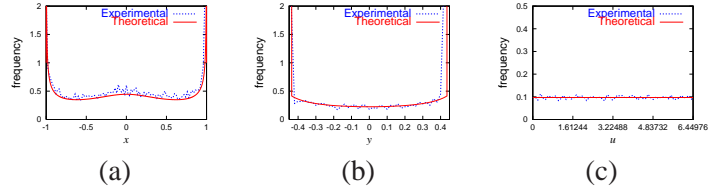


Fig. 2. Marginal distributions (a) μ_X and (b) μ_Y and (c) distribution μ_u along the invariant curve of 2-dim. map $(R_2^{cn}(x_n, 0.9), \frac{1}{2} \cdot \frac{dR_2^{cn}(x_n, 0.9)}{du})$.

orbits on Jacobian elliptic curve have been shown to produce a sequence of 2-dimensional i.i.d. BRVs.

REFERENCES

- [1] S. M. Ulam and J. Von Neumann, "On combination of stochastic and deterministic processes", *Bull. Math. Soc.*, **53**, p.1120, 1947.
- [2] T. Kohda and A. Tsuneda, "Statistics of Chaotic Binary Sequences", *IEEE Trans. Information Theory*, Vol.43, No.1, pp.104–112, 1997.
- [3] T. Kohda, "Information Sources using chaotic dynamics", *Proc. IEEE*, **90**, no.5, 641–661, 2002.
- [4] T. Stojanovski and L. Kocarev, "Chaos based random number generators PartI: Analysis", *IEEE Trans, Circuits Syst.I*, vol.43, no.3, pp.281-288, 2001.
- [5] D. V. Sarwate and M. B. Pursley, "Crosscorrelation properties of pseudorandom and related sequences", *Proc. IEEE*, **68**, no.3, 593–619, 1980.
- [6] C. J. Siegel, "*Topics in Complex Function Theory volume 1–Elliptic functions and uniformization Theory*", John Wiley & Sons, 1969.
- [7] N. I. Akheizer, "*Elements of the Theory of Elliptic Functions*", Translations of Mathematical Monographs, vol.79, American Mathematical Society, 1990.
- [8] T. Kohda and H. Fujisaki, "Jacobian Elliptic Chebyshev Rational Maps", *Physica D*, **148**, pp.242-254, 2001.
- [9] T. Kohda, A. Katoh, Y. Hattori and T.Yoshimura, "2-d dynamics of Jacobian Elliptic Chebyshev rational maps", *Proceedings of the 11th workshop on Nonlinear Dynamics of Electronic System*, pp.129–132, 2003.
- [10] S. Grossmann and S. Thomae, "Invariant distributions and stationary correlation functions of one-dimensional discrete processes", *Z. Naturforsch.*, **32a**, 1353–1363, 1977.
- [11] A. Lasota and M. C. Mackey, "*Chaos, Fractals and Noise*", Springer-Verlag, 1994.
- [12] R. L. Adler and T. J. Rivlin, "Ergodic and mixing properties of Chebyshev polynomials", *Proc. Amer. Math. Soc.*, **15**, 794, 1964.
- [13] S. Katsura, W. Fukuda, "Exactly Solvable Models Showing Chaotic Behaviour", *Physica A*, **130**, pp.597-605, 1985.

**NUMERICAL EXPERIMENTS WITH GROUND ON AED THEORY:
DYNAMIC INVESTIGATION OF ENERGETIC PROCESSES
IN DISORDERED SYSTEMS**

A. Konash¹, P. Buka¹, S. Bagnich²

¹ Institute of Mathematics and Cibernetics, Department of Numerical Simulations
Mensk, Belarus, 220064, P.O. Box 48

e-mail: tum@tut.by, konash@uni-rostock.de

² Institute of Molecular and Atomic Physics,
Mensk, Belarus

Abstract—*In this work we report about our achievements in numerical investigation of energetic processes (migration, merging, fusion, trapping) in systems with complicated structure and defined energetic disorder. The S^l branch of AED theory (hierarchical multilevel system theory) was used for mathematical definition of the task, computer realizations for 1D and 2D cases were done in object-oriented technique of programming language Delphi and results were compared with real experiments. The simulation allows us to investigate the processes in dynamics (in time) and interactively control them by operator. Constructed mathematical definition allows to extend the simulation for 3D case and can be modified for requested practical tasks.*

I. PICTURE OF THE PROBLEM

Novel methods of numerical investigations are strongly required nowadays. And we have applied multilevel hierarchical system theory AED (S^l branch [1]) for investigation of the energetic processes in systems with complex structure. This is an important task due to the demand in newel techniques for signal transfer and processing, energy collection and storage, design of opto-electronic devices. Up to now wide range of experimental works (see, for example, results of our group [2-5]) leads to understanding of complexity and mutual influence of dynamic processes inside of the systems. New suggestions about physical base of the processes require advanced computer simulations to prove and clarify them. To carry out these tasks the special mathematical definitions should be used to provide sufficiently powerful ground for number imitations. And in ideal case, the simulation should be useful (can be applied) for tasks of learning and for practical tasks of manufacture. With this reasons we have applied hierarchical multilevel system the-

ory AED for mathematical definition of the energetic processes in disordered system, and realized (animated) them with digital simulation by object-oriented technique of the language Delphi under Windows

AED THEORY.

Up to now the AED theory has wide range of applications for actual tasks of programming [6], networks [7-9], demography [10], economics [11], biology [12, 13], physics [14, 15, 16] etc. The theory was developed by Novikava at 90th years and has origin in general system theory proposed by Takahara & Mesarovic (for details see [17]). It has two variants S^l and A^l. In this article we deal with S^l and present short introduction to the theory and way of definition for our task (an investigation of energy condition inside of the sample with time) in its symbols.

In the AED theory each process and system should be defined by the same set of features: level, coordinator, structure, lows and condition. Below the short introduction to the mathematics is presented, where the systems are denoted by \mathcal{S} and l is the index of level for the systems.

The system in the theory S^ℓ is described by following symbol construction:

$$S^\ell \leftrightarrow \{\omega, S_0, \sigma\}^\ell$$

ω^ℓ - aggregated dynamical realization of the units and acts (condition), σ^ℓ - construction of the level, S_0^ℓ - co-ordinator for the level, l - index of the level $l \in L^s$.

Farther, $\omega^\ell \leftrightarrow \{\tilde{\omega}, S_0\}^\ell$, $\sigma^\ell \leftrightarrow \{S_0, \tilde{\omega}\}^\ell$, where $\tilde{\omega}^\ell$ and

$\tilde{\sigma}^\ell$ are connected by coordinator S_0^ℓ and contain the dynamical realizations and constructions of unit (object) ${}_o S^\ell$, its environment ${}_\varepsilon S^\ell$ (other units of its level), mutual acts (processes) ${}_{o\pi} S^\ell$ of ${}_o S^\ell$ in ${}_\varepsilon S^\ell$ with acts ${}_{\pi\varepsilon} S^\ell$ of ${}_\varepsilon S^\ell$ and ${}_o S^\ell$:

$$\{ {}_o S, {}_{o\pi} S \} \leftrightarrow S^{\ell \pm 0}, \{ {}_{\pi\varepsilon} S, {}_\varepsilon S \} \leftrightarrow S^{\ell \pm \tau};$$

Each sample of $\tilde{\omega}^\ell$ contains own realization of the dynamical systems

$${}_k \omega^\ell \leftrightarrow {}_k (\bar{\rho}, \bar{\varphi})^\ell, k \in {}_k L \leftrightarrow \{ o, o\pi, \pi\varepsilon, \varepsilon \},$$

where ${}_\omega \gamma^\ell$ - low of connections for ω^ℓ with other units and acts inside and outside of the level, and the construction of ${}_\omega \gamma^\ell$ connects the details of the samples ${}^k \omega^\ell$ (states ${}^k C^\ell$, inputs ${}^k X^\ell$ and outputs ${}^k Y^\ell$):

$${}_\omega \gamma^\ell \leftrightarrow \{ {}^k \{ X, C, Y \} : k \in {}_k L \}^\ell.$$

The dynamical realization of the system ${}^k (\bar{\rho}, \bar{\varphi})^\ell$ is described by set of dynamical functions:

$${}^k \bar{\rho}^\ell = {}^k \{ \rho_i : C_i \times X_i \rightarrow Y_i \ \& \ t \in T \}^\ell$$

$${}^k \bar{\varphi}^\ell = {}^k \{ \varphi_{i^\circ} : C_i \times X_{i^\circ} \rightarrow C_{i^\circ} \ \& \ t, t^\circ \in T \ \& \ t^\circ > t \}^\ell$$

The network of connections of ${}^k C^\ell$, ${}^k X^\ell$, ${}^k Y^\ell$ is described by Table 1.

Table 1.

${}_\omega \gamma^\ell$	States	Inputs	Outputs
${}_o S^\ell$	${}_o C^\ell$	${}_o X^\ell \leftrightarrow X^{\ell \leftarrow (\ell \pm \tau)}$	${}_o Y^\ell \leftrightarrow {}_o C^\ell$
${}_{o\pi} S^\ell$	${}_{o\pi} C^\ell \leftrightarrow {}_o X^\ell$	${}_{o\pi} X^\ell \leftrightarrow {}_o C^\ell$	${}_{o\pi} Y^\ell \leftrightarrow Y^{\ell \rightarrow (\ell \pm \tau)}$
${}_{\pi\varepsilon} S^\ell$	${}_{\pi\varepsilon} C^\ell \leftrightarrow {}_\varepsilon X^\ell$	${}_{\pi\varepsilon} X^\ell \leftrightarrow {}_\varepsilon C^\ell$	${}_{\pi\varepsilon} Y^\ell \leftrightarrow \{ Y^{\ell \pm \tau}, Y^{(\ell \pm \tau) \rightarrow (\ell \pm \tau)} \}$
${}_\varepsilon S^\ell$	${}_\varepsilon C^\ell$	${}_\varepsilon X^\ell \leftrightarrow \{ X^{\ell \leftarrow (\ell \pm \tau)}, X^{(\ell \pm \tau) \leftarrow (\ell \pm \tau)} \}$	${}_\varepsilon Y^\ell \leftrightarrow {}_\varepsilon C^\ell$

Due to the connections in ${}_\omega \gamma^\ell$ of all details of ω^ℓ is restored by its other details with becoming uncertainty.

The co-ordinator is described in the same way:

$$S_0^\ell \leftrightarrow \{ \omega, S_0, \sigma \}_0^\ell,$$

that is S_0^ℓ has own aggregated dynamical realization ω_0^ℓ and the construction σ_0^ℓ ; the availability of S_{00}^ℓ (the connection with higher levels) allows to account

and to change S_0^ℓ by its own activity.

III. ALGORITHM FOR THE TASK DEFINITION.

Below is principal schema for definition of the electronic (energetic) processes in the symbols of the AED theory (definition of levels, units and processes). The main level $\mathbf{I0}$ contains the investigated sample S_0 and its environment (laser S_{0-1} and receiver S_{0+1}). They are connected by laws $\{S_{0-1}, \gamma^{S_0}\}^{\mathbf{I0}}$, and $\{S_0, \gamma^{S_{0+1}}\}^{\mathbf{I0}}$, which define acts (motion, transmission) for input and for output signals. Internal level for S_0 is presented by subsystems $\{S_{0int}\}_i$ (domains of molecules of the sample) and is denoted as $\mathbf{I0}_{int}$ (index i allows to define place of the subsystems in S_0). In its turn each from subsystems $\{S_{0int}\}_i$ has own structure - set of molecules $\{\{S_{0int}\}_i\}_j \leftrightarrow \{Mol_i\}_j$, where j is number of molecule. The molecule in our definition has no structure (structure is undefined) but has condition $C_{S_{0int}_i_j} \leftrightarrow \{Type \{trap, ordinary\}, State \{E_{S_0}, E_{T1}, E_{S1}\}\}$. Inside of the domain $(S_{0int})_i$ energetic disorder for molecules is defined by Gaussian distribution $\{G_{mol}\}_i \leftrightarrow \{\{sigma, E_{T1_average}, E_{T1_max}, E_{T1_min}, dE_{T1}\}_i\}$. And energetic disorder of the domains $\{E_{T1_average}\}_i$ is defined by another Gaussian $G_{dom} \leftrightarrow \{\{sigma, E_{T1_average}, E_{T1_max}, E_{T1_min}, dE_{T1}\}\}$. In general features $\{G_{mol}\}_i$ and G_{dom} are not the same and are varied in our imitation to clarify influence of energy disorder. Beside of the energetic disorder the structure of the systems may be change. The sample S_0 has structure $\mathbf{sigma}_{S_0}^{1int} \leftrightarrow \{\text{dimension, shape, domain interconnection (type of lattice), linear size in domains}\}$. The structure of the domains $\{\mathbf{sigma}_{S_{0int}_i}\} \leftrightarrow \{\text{dimension, shape, bonds between molecules (type of lattice of molecules), linear size in molecules}\}_i$ does not depend on i and is a constant in the simulation (in principle may be varied). In real experiments parameters of *Gaussians* and size of domains reflect way of the sample preparations (fast or slow cooling, for example). And by variation of linear size of S_0 influence of space restriction should be investigated (important for nano-technologies).

By continue in such way the process is defined

mathematically exactly. And the next step is number realization of the definition. One of the most important things is correspondence in the system theory between mathematical definition and number simulation. **S0**, each element of the mathematical definition is realized by certain programming code (as object, for example). It makes the programming very clear for understanding and allows us to advance the simulation with advance of mathematical definition without rebuilding of whole program.

In our simulation we set up **1.** the linear sizes and structure for **S0** and **S0int_i** (lattice, linear size of **S0** and linear size of **S0int_i**), **2.** the energetic disorder **G_{dom}** and **G_{mol.}**, **3.** the intensity of input light (concentration of excitons at $t=0$), **4.** the concentration of traps, **5.** the temperature (influence on *activity* of the excitons), **6.** the number of realizations for the sample energetic disorder, **7.** the number of excitations of the realization. As output data we fixed quantity of excited states **E_{TI}** of molecules and events of energy fusion at each step of time. We have shown, that all of these parameters depend on features of parameters **1-5** with good correspondence by experimental ones (experimental investigation of our group [2-5]). Nevertheless, main achievements is successful application of the theory AED that makes possible dynamical monitoring of the system's conditions on each level, interactive control under processes and fast calculation with presentation of data with real time animation. That allows us to make preliminary decision about actuality of the theory in modern research of complex systems by digital (computer tools).

IV. CONCLUSION

As conclusion we want to emphasize actuality of application of the AED theory for mathematical definition of complex dynamic tasks. It allows to provide actual number investigations of complex phenomena by imitations of the processes with ability of farther developing for required tasks (engineering, learning, fundamental science). At the end we have to note about insufficiently wide range of practical application of the theory and strong demand in finding out advantages and restrictions of application of the theory for modern aims of learning (science, study and teaching) and goals of production (numerical design and testing), what re-

quires using of the theory for new tasks in various applications.

V. REMARK.

Work under imitation of one of the authors (Aliaksei Konash) was funded by INTAS grant (YSF2002-385).

REFERENCES

- [1] S. Novikava, N. Karcianas, S.Gancharova, P. Buka Mathematical construction in AED theory, Proceedings of IFAC/IFORS/IMACS Symposium on Large Scale Systems, LSS98, Paatrac, Grees, 1998
- [2] Bagnich S.A., Konash A.V. Kinetics of triplet-triplet annihilation in disordered organic solids on short time scale. // Chem. Phys.- 2001.-V. 263, N 1. - pp. 101-110.
- [3] Bagnich S.A., Konash A.V. Kinetics of the decay of prolonged luminescence of disordered chrysene under the conditions of nonequilibrium transfer of energy. // J. Appl. Spectrosc. -2001. V. 68, N 3. pp.439-446.
- [4] Bagnich S.A., Konash A.V. Annihilation kinetics for triplet excitations in organic glasses. // Opt. Spectrosc.-2002. V. 92, N 4. pp.505-511.
- [5] Bagnich S.A., Konash A.V. Kinetics of triplet-triplet annihilation in organic glasses. // J. Fluor. -2002. V. 12, N 2. pp.273-278.
- [6] Novikava S., Miatliuk K., Ananich G., Mazanik L., Gancharova S., Galavenchik I., Suponitsky W. The Theoretical Model and the Application of Aed-processor. The International Symposium on Neural Networks and Neural Computing, NEURONET'90, Prague, pp. 259-261.(Reprinted by World Scientific Publishing Co., under the title "Theoretical Aspects of Neurocomputing", Vol.1, Singapore, 1991).
- [7] S.Novikava, K.Miatliuk, S.Gancharova, W.Kaliada, A.Ivanov, S.Kritsky, A.Demyanenko, A.Zhybul. Aed Theory and its Realizations by Hierarchical Knowledge Networks. Preprints of the IFAC Conference on Supplementary Ways for Improving International Stability - SWIIS'95, Vienna, Austria, 1995, p.99-106.
- [8] S.Novikava, K.Miatliuk, S.Gancharova, A.Ivanow, A.Zhybul, A.Danichaw, P.Buka, V.Siageichick. Aed Theory and Hierarchical Knowledge Networks. Proceedings of the Annual Conference of ICIMS-NOE (E.P.9251) on ASI'96 in Life Cycle Approaches to Production Systems: Management, Control, Supervision. Toulouse, France, 1996, p.377-386.
- [9] S.Novikava, S.Gancharova, A.Burawkin, S.Daronin, P.Buka, A.Ivanow, A.Danichaw, A.Demianenko, M.Maroz, A.Michalevich, A.Zagaradnik. Mathematical

Defining of Sway Networks of State and States Unions. Preprints of Eleventh International Conference on Mathematical and Computer Modeling and Scientific Computing. Washington, DC, USA. 1997. p.150.

[10] W.Nowik, V.Barkalin, W.Zianevech, S.Gancharova, P.Buka, K.Miatliuk, A.Astrowskaya, A.Bahutski, Demographic Units in Hierarchical Coordinates: Construction, Activity and Goals, Preprints of the IFAC Conference on Supplementary Ways for Increasing of International Stability - SWIIS'95, SWIIS'98, Sinaia, Romania, 1998.

[11] P.Groumpos, S. Novikava, S. Gancharova, A.Zhybul, V. Siarheichyk, K.Miatliuk,. Design&Creating of New Engineering Units in Reconstruction Regions. Proceedings of the Annual Conference of ICIMS-NOE (E.P.9251) on ASI'97 in Life Cycle Approaches

[12] Novikava S.I., Miatliuk K.N., Gancharova S.A.,Ananich G.A., Novik V.A., Koleda V.V., Kavalyov V.A., Boika T.N. Aed Technology for Ecological, Social and Engineering Systems Coordination. Proceedings of Eighth International Symposium on Modular Information Computer Systems and Networks, ICS-NET'91, Dubna, pp. 145-152.

[13] V.Kaliada, V.Rabeka, Iu.Kaminski, E.Kaminskaia. Oncological Defense Maintenance in Dynamic Multilevel Environment. IXth International Conference on Mathematical and Computer Modelling, ICMCM'93, Berkeley, California, USA, p. 128.

[14] Bagnich S. and Konash A. Computation Study of the Percolation Phenomena in Inhomogeneous Two- and Three- Dimensional systems. J. Phys. A: Math. Gen.36 (2003) 1-13,

[15] Bagnich S. and Konash A Percolation processes in heterogeneous two-dimensional space Phys. Solid State 42 (2002) 1775.

[16] Pavel Buka, The Investigation of Photoluminescence in Low-Dimensional Materials with Aed-Processor. The Eleventh International Conference on Superlattices, Microstructures and Microdevices. Book of Abstracts. Hurghada (Red Sea), Egipt, July 27- August 1, 1998

[17] M.D. Mesarovic and Yasushiko Takahara General System Theory: Mathematical Foundations, Academic Press, New York San Francisco London, 1975

RICH SYNCHRONIZATION OF SIMPLE SPIKING OSCILLATORS

Yoshio Kon'no, Toshimichi Saito and Hiroyuki Torikai

EECE Dept., HOSEI University, Koganei, Tokyo, 184-8584 Japan

e-mail: tsaito@k.hosei.ac.jp

WWW: <http://www.nonlinear.k.hosei.ac.jp/>

Abstract—Applying periodic input, spiking oscillators output various pulse-trains and exhibit rich synchronous phenomena. This paper studies the phenomena using two simple examples. In the first example, the input is a sawtooth base signal and the frequency versus parameter characteristics of the synchronization is the complete devil's staircase. In the second example, a pulse-train input is applied via a refractory threshold and the characteristics of the synchronization is an interesting incomplete devil's staircase. These phenomena can be analyzed theoretically and typical phenomena can be confirmed experimentally.

I. INTRODUCTION

Spiking oscillators output pulse-trains based on the integrate-and-fire dynamics and can exhibit rich synchronous phenomena [1] [2]. Analysis of the phenomena is important not only as fundamental study but also for application to pulse-coupled artificial neural networks (ab. PCNN [1]-[7]). In the PCNN, variety of synchronous patterns relates to variety of information processing functions and may be developed into flexible applications including image segmentation and pulse-based communication [5] [8]. However, theoretical and systematic analysis of the synchronous phenomena is still an interesting problem.

This paper studies the problem using two examples of simple spiking oscillators which output various pulse-trains [2] [4]. Our previous work [2] has discussed that the spiking oscillators can be analyzed theoretically and systematically using pulse-position maps (ab. PPmaps), however, concrete analysis has not been sufficient. The first circuit has a periodic sawtooth base signal and outputs a variety of chaotic and periodic pulse-trains governed by piecewise linear PPmap. In the periodic phase, the frequency versus parameter characteristics of the synchronization is the complete devil's staircase corresponding to all rational numbers [9] [10]. The second circuit has a refractory threshold via which a periodic pulse-train is

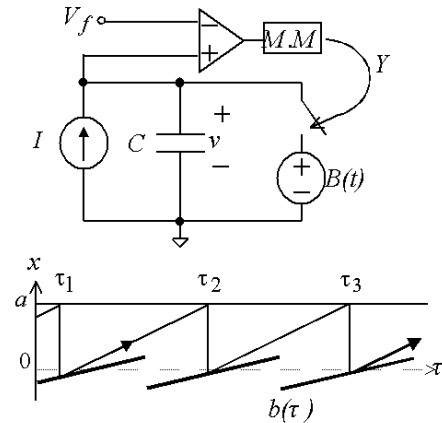


Fig. 1. Spiking oscillator with sawtooth base

applied. In this case the oscillator outputs various periodic pulse-trains and the frequency versus parameter characteristics is an incomplete devil's staircase having an interesting structure [11]. The PPmap is simplified into a circle map with a trapping window that has rich super-stable periodic dynamics. Presenting a simple test circuit, typical phenomena can be confirmed experimentally. It should be noted that the complete and incomplete devil's staircases relate deeply to analysis and improvement of A/D converters [12] [13].

II. THE FIRST SPIKING OSCILLATOR

Fig. 1 shows the first circuit. In the figure V_f is a constant firing threshold and $B(t)$ is sawtooth base signal with period T : $B(t) = K(t - 0.5T)$ for $0 \leq t < T$ and $B(t + T) = B(t)$. $B(t)$ has no dc component and $B(t) < V_f$. The capacitor voltage v increases by integrating current I . If v reaches V_f , the comparator triggers the monostable multivibrator to output a pulse signal Y . The output Y closes the switch S and v is reset to the base $B(t)$ instantaneously. Repeating this integrate-and-fire dynamics, the oscillator outputs a pulse-train. The dynamics is

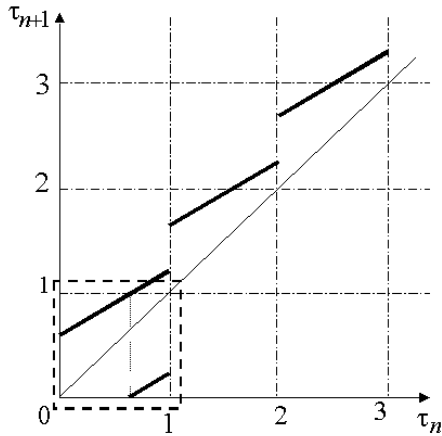


Fig. 2. Pulse position map for the first circuit

described by Equation (1)

$$\begin{cases} C \frac{dv}{dt} = I & \text{for } v < V_f \\ v(t) = B(t) & \text{if } v(t_-) \geq V_f \end{cases} \quad (1)$$

$$Y(t) = \begin{cases} V_{DD} & \text{if } v(t_-) = V_f \\ V_{SS} & \text{otherwise} \end{cases}$$

where V_{DD} and V_{SS} are high and low output levels of the monstable multivibrator, respectively. Using the following dimensionless variables and parameters,

$$\begin{aligned} \tau = \frac{t}{T} \geq 0, \quad x = \frac{Cv}{TI}, \quad a = \frac{CV_f}{TI}, \quad k = \frac{CK}{TI} \\ y = \frac{Y - V_{SS}}{V_{DD} - V_{SS}}, \quad b(\tau) = \frac{C}{TI} B(T\tau), \end{aligned} \quad (2)$$

Equation (1) is transformed into Equation (3)

$$\begin{cases} \frac{dx}{d\tau} = 1 & \text{for } x < a \\ x(\tau) = b(\tau) & \text{if } x(\tau_-) \geq a \end{cases} \quad (3)$$

$$y(\tau) = \begin{cases} 1 & \text{if } x(\tau_-) = a \\ 0 & \text{otherwise,} \end{cases}$$

where $b(\tau) = k(\tau - 0.5)$ for $0 \leq \tau < 1$ and $b(\tau + 1) = b(\tau)$. It should be noted that normalized equation has two parameters a and k and $|0.5k| < a$ is satisfied to guarantee $b(\tau) < a$. For the analysis, we introduce the pulse position map (ab. PPmap). Let τ_n be n -th pulse position at which the oscillator fires and outputs n -th pulse signal as shown in Fig. 1. The pulse-train is governed by the following PPmap.

$$\begin{aligned} \tau_{n+1} &= f_1(\tau_n) \equiv \tau_n - b(\tau_n) + a \\ &= (1 - k)\tau_n + 0.5k + a + \text{INT}(\tau_n), \end{aligned} \quad (4)$$

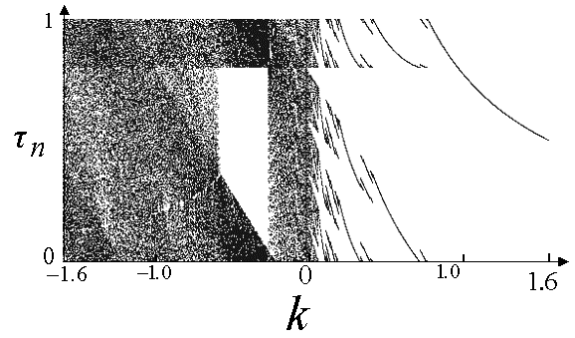


Fig. 3. bifurcation diagram ($S \equiv 0.5k + a = 0.8$).

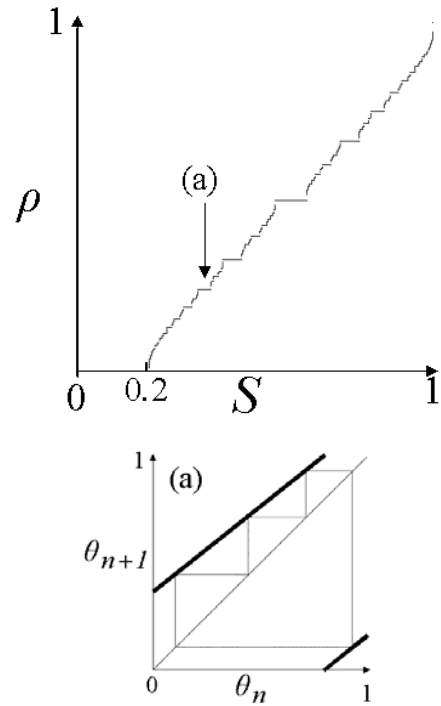


Fig. 4. Devil's staircase and typical return map ($1 - k = 0.8, S \equiv 0.5k + a$). (a) $S = 0.36$

where $\text{INT}(\tau_n)$ denotes the integer part of τ_n . An example of the PPmap is shown in Fig. 2. It goes without saying that $b(\tau) < a$ guarantees $f_1(\tau) > \tau$. For convenience we reduce the PPmap into the return map F_1 from $I = (0, 1]$ to itself:

$$\theta_n = F_1(\theta_n) \equiv f_1(\theta_n) \text{ mod } 1, \quad (5)$$

where $\theta_n = \tau_n \text{ mod } 1$. As parameters vary, this system exhibits rich dynamics as suggested in Fig. 3. Using a simple test circuit presented in [4], typical phenomena can be confirmed experimentally. As discussed in [2], the pulse-train is chaotic for $|1 - k| > 1$ and is periodic for $|1 - k| < 1$. For simplicity, we

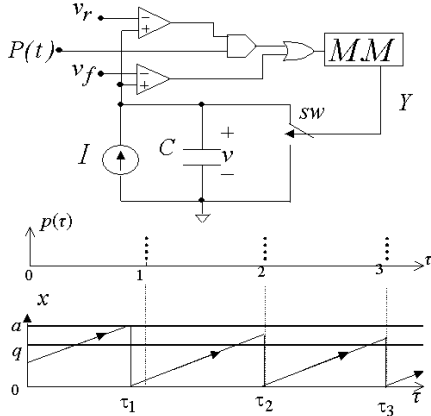


Fig. 5. Spiking oscillator with pulse-train inputs

focus on the case

$$0 < 1 - k < 1, 0.5k + a < 1, 0.5k < a.$$

In this case, the system exhibits periodic phenomena only. In order to characterize the phenomena, we introduce an encoding ω and a frequency ratio ρ :

$$\omega(\theta_n) = \begin{cases} 0, & \text{for } 0 \leq \theta_n < \frac{1-S}{1-k}, \\ 1, & \text{for } \frac{1-S}{1-k} \leq \theta_n < 1, \end{cases} \quad (6)$$

$$\rho = \frac{1}{M} \sum_{n=1}^M \omega(\theta_n) \quad (7)$$

where $S \equiv 0.5k + a$ and M is the period of the orbit: $\theta_m = \theta_0$ and $\theta_m \neq \theta_l$ for $0 < l < m$. Fig.4 shows ρ versus S characteristics and a typical return map. This characteristics is known as the devil's staircase and corresponds to all the rational numbers [10].

III. THE SECOND SPIKING OSCILLATOR

Fig. 5 shows the second circuit where $P(t)$ is a periodic pulse-train input with period T : $P(t) = V_{DD}$ at $t = mT$ and $P(t) = V_{SS}$ for $t \neq mT$ where m is a positive integer. If $P(t)$ does not exist, the circuit dynamics is the same as the first circuit with $B(t) = 0$ and is described by Equation (1) with $B(t) = 0$. In this case, the circuit fires and v is reset to 0 if v reaches V_t . We refer to this resetting as self-firing (ab. SFR). Then the input $P(t)$ is applied via refractory threshold V_r and resets v as shown in Fig. 5:

$$v(t_+) = 0 \text{ if } P(t) = V_{DD} \text{ and } V_r < v(t). \quad (8)$$

We refer to this resetting as compulsory-firing (ab. CFR). Using the following normalization with (2):

$$q = \frac{CV_r}{TI}, p(\tau) = \frac{P(T\tau) - V_{SS}}{V_{DD} - V_{SS}}, \quad (9)$$

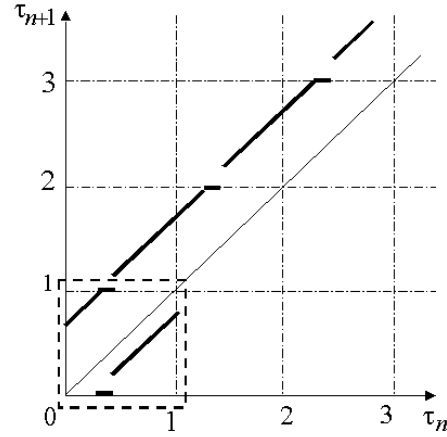


Fig. 6. Pulse position map for the second circuit

we obtain the following normalized equation:

$$x(\tau) = 0 \quad \text{if } x(\tau_-) \geq a \text{ (SFR)}$$

$$x(\tau_+) = 0 \quad \text{if } p(\tau) = 1 \text{ and } q < x(\tau) \text{ (CFR)}$$

$$\frac{dx}{d\tau} = 1 \quad \text{otherwise,} \quad (10)$$

where $p(\tau) = 1$ at $\tau = m$, $p(\tau) = 0$ for $\tau \neq m$ and m is a positive integer. It should be noted that this this normalized equation has two parameters a and q . For simplicity, we focus on the case

$$0 < q < a < 1.$$

In this case the PPmap f_2 and the return map F_2 are given by Equations (11) and (12), respectively.

$$\begin{aligned} \tau_{n+1} &= f_2(\tau_n) \\ &= \begin{cases} m, & \text{for } m - a \leq \tau_n < m - q \\ \tau_n + a, & \text{otherwise,} \end{cases} \end{aligned} \quad (11)$$

$$\begin{aligned} \theta_n &= F_2(\theta_n) = f_2(\theta_n) \bmod 1 \\ &= \begin{cases} \theta_{n+1} + a & \text{for } 0 \leq \theta_n < 1 - a \\ 0 & \text{for } 1 - a \leq \theta_n < 1 - q \\ \theta_n + a - 1 & \text{for } 1 - q \leq \theta_n < 1, \end{cases} \end{aligned} \quad (12)$$

where m is a positive integer and $\theta_n = \tau_n \bmod 1$. Shape of the PPmap is shown in Fig. 6. The return map is the rotation having window with width $a - q$. Since the map is flat on the window, this map exhibits super-stable periodic orbit for almost all initial values. Fig. 7 shows a laboratory measurement corresponding to the periodic orbit. In a likewise manner as Section

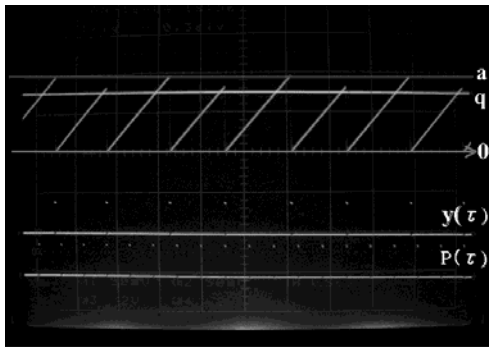


Fig. 7. Laboratory measurement of typical synchronous phenomena, horizontal= $t[0.5s/div.]$ and vertical= $v[0.5v/div.]$. ($a = 0.4, q = 0.3$).

II, we introduce the encoding:

$$\omega(\theta_n) = \begin{cases} 0, & \text{for } 0 \leq \theta_n < 1 - a, \\ 1, & \text{for } 1 - a \leq \theta_n < 1. \end{cases} \quad (13)$$

Substituting this $\omega(\theta_n)$ into Equation (7) we obtain the frequency ratio ρ . Fig.8 shows ρ versus a characteristics with typical return maps. This interesting staircase is different from the devil's staircase in Fig.4. The devil's staircase is continuous function and corresponds to all the rational numbers, however, this staircase is not continuous and corresponds to a subset of rational numbers. The density of the subset depends of the window width $a - q$. Theoretical analysis of this incomplete devil's staircase is in progress.

IV. CONCLUSIONS

We have considered periodic synchronization of two spiking oscillators and have clarified that they exhibit rich synchronous phenomena characterized by complete and incomplete devil's staircases. Our results will be developed into analysis of synchronous phenomena of artificial pulse-coupled neural networks based on the spiking oscillators and its applications including A/D conversion. The authors wish to thank M. Shimazaki, R. Furumachi and H. Hamanaka for their helpful advises.

REFERENCES

[1] R. Perez, R. and Glass, L. Bistability, period doubling bifurcations and chaos in a periodically forced oscillator, Phys. Lett. A, vol.90 no.9, pp.441-443, 1982.
 [2] T. Saito and H. Torikai, Return map modulation in nonautonomous relaxation oscillator, Controlling chaos and bifurcations in engineering systems, pp. 603-624, CRC press, ed. G.Chen, 1999

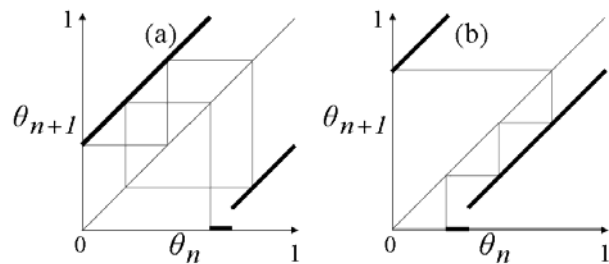
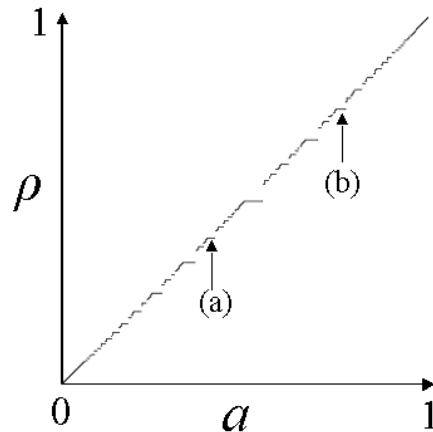


Fig. 8. Incomplete devil's stair case and related return maps, (a) $a = 0.4, q = 0.3$, (b) $a = 0.75, q = 0.65$.

[3] G. Lee and N. H. Farhat, The bifurcating neural network 2, Neural Networks, 15, pp.69-84, 2002.
 [4] H. Torikai, M. Shimazaki and T.Saito, Master-slave synchronization of pulse-coupled bifurcating neurons, IEICE Trans. Fundamentals, E86-A, to appear.
 [5] R.E.Mirollo and S.H.Strogatz, Synchronization of pulse-coupled biological oscillators, SIAM J. Appl. Math., vol.50, pp.1645-1662, 1990.
 [6] S. R. Campbell, D. L. Wang and C. Jayaprakash, Synchrony and desynchrony in integrate-and-fire oscillators, Neural computation, 11, pp.1595-1619, 1999.
 [7] E.M. Izhikevich, Weakly Pulse-coupled oscillators, FM Interactions, Synchronization, and oscillatory associative memory, IEEE Trans. NN, 10, 3, 508-526, 1999.
 [8] M. Sushchik, N. Rulkov, L. Larson, L. Tsimring, H. Abarbanel, K. Yao and A. Volkovskii, Chaotic pulse position modulation: a robust method of communicating with chaos, IEEE Comm. Lett., 4(4), 128-130, 2000
 [9] T.Saito, A chaos generator based on a quasi-harmonic oscillator, IEEE Trans. Circuits Syst., 32, 4, pp.320-331, 1985
 [10] E.Ott, Chaos in Dynamical Systems, Cambridge Univ. Press, 1993.
 [11] T. Allen, Complicated, but rational, phase-locing responses of a simple time-base oscillators, IEEE Trans. Circuits Syst., 30, 9, pp. 627-632, 1983
 [12] O. Feely and L.O. Chua, The effect of integration leak in Σ - Δ modulation, IEEE Trans. Circuits Syst., 38, pp. 1293-1305, Nov. 1991.
 [13] T. Saito and H. Imamura, Analysis of a simple A/D converter with a trapping window, in Proc. IEEE Int. Symp. Circuits & Systems, III, May 2003, pp. 626-629.

CASCADED RETURN MAP MODELS A NONPERIODICALLY CLOCKED CPM BOOST CONVERTER

J. Krupar and W. Schwarz

Fakultät Elektrotechnik und Informationstechnik,
TU-Dresden,
Dresden, Germany

e-mail: krupar@iee.et.tu-dresden.de, schwarz@iee1.et.tu-dresden.de

WWW: http://www.iee.et.tu-dresden.de/iee/ge/

Abstract—*In this paper we model the behaviour of a nonperiodically clocked CPM boost converter. The behaviour can not be modeled by one-dimensional maps. We propose a cascaded map model of a coupled hybrid system. The system consists of a chaos clock generator driving a CPM boost converter. The model is used to apply statistical analysis and for EMI consideration.*

I. INTRODUCTION

The current programmed mode (CPM) boost converter is a standard device in electronic power supply devices. Under certain conditions it exhibits chaotic behaviour, [1], [2]. Some applications use this mode for the better EMI performance [2], [3]. However due to the spectral peak at the clock frequency further improvement is desirable. In the paper we use a separate chaotic clock generator for this purpose. For the analysis of each part separately efficient one-dimensional embedded map models and a variety of tools exist, [1], [2], [4], [5], [6], [7].

When both parts are coupled conventional modelling by a one-dimensional map is not possible. Therefore we introduce a cascaded map model which we convert into a higher-dimensional one. This model allows to efficiently apply statistical analysis to the system and to consider its EMI.

The paper is organised as follows: In section II we summarize one-dimensional maps of the CPM boost converter. In section III we propose the coupled system and enhance the embedded map model by cascading two one-dimensional maps. We develop the model into a higher-dimensional map in section IV. This model we use to apply statistical analysis and to study the EMI behaviour of the system using different clock generators. Section V draws conclusions.

II. ONE-DIMENSIONAL MAP OF THE CONVERTER

Fig. 1 depicts the scheme of the CPM boost converter. In most application C_L is large enough to keep

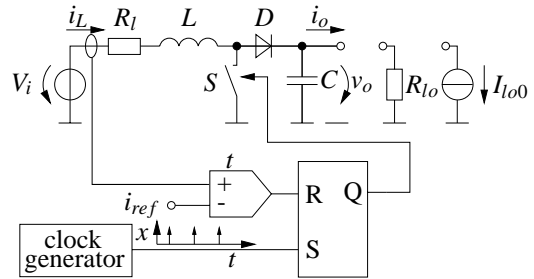


Fig. 1. CPM boost converter scheme.

v_o at a nearly constant level at normal operation. Then the converter current $i_L(t)$ is nearly piecewise linear in time, see Fig. 2. At periodic clock i_L can be described by the a-switching map (switching event-driven)

$$i_{k+1} = i_{ref} - c_2 T + c_2 \left(\frac{i_{ref} - i_k}{c_1} \text{mod} T \right) \quad (1)$$

see [1], [2], [3], [8]. Another description is possible by the so-called stroboscopic map

$$i(i_{L,n}) = \begin{cases} i_{L,n} + c_1 T & T c_1 < i_{ref} - i_{L,n} \\ i_{ref} - c_2 a & T c_1 \geq i_{ref} - i_{L,n} \end{cases} \quad (2)$$

$$a = \begin{cases} T - \frac{i_{ref} - i_{L,n}}{c_1} & T c_1 \geq i_{ref} - i_{L,n} \end{cases}$$

which determines i_L at each clock pulse, [1]. This map will be used in the sequel.

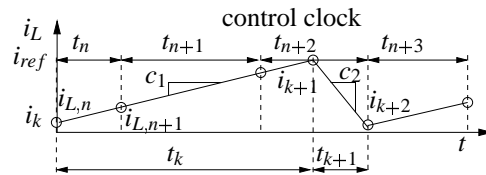


Fig. 2. One-dimensional CPM DC-DC converter maps.

III. CASCADED MAP

Fig. 3 depicts the system corresponding to the chaotically clocked CPM DC-DC converter. The embedded map of the clock generator is g . The map g_{DC}

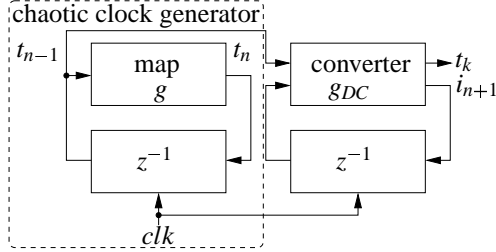


Fig. 3. Cascaded map model.

determines the sequence of converter currents $i_{L,n}$ at the clock events (Fig. 2) and the switching times t_k . It has the form

$$g_{DC} = \begin{pmatrix} i_{L,n+1} \\ k \\ t_k \\ t_{k+1} \end{pmatrix} = \begin{pmatrix} i(i_{L,n}, t_n) \\ k(i_{L,n}, t_n) \\ a \\ \frac{c_2}{c_1} a \end{pmatrix} \quad (3)$$

with

$$\begin{aligned} i(i_{L,n}, t_n) &= \begin{cases} i_{L,n} + c_1 t_n & t_n c_1 < i_{ref} - i_{L,n} \\ i_{ref} - c_2 a & t_n c_1 \geq i_{ref} - i_{L,n} \end{cases} \\ a &= \begin{cases} \{ \} & t_n c_1 < i_{ref} - i_{L,n} \\ t_n - \frac{i_{ref} - i_{L,n}}{c_1} & t_n c_1 \geq i_{ref} - i_{L,n} \end{cases} \\ k(i_{L,n}, t_n) &= \begin{cases} k & t_n c_1 < i_{ref} - i_{L,n} \\ k + 2 & t_n c_1 \geq i_{ref} - i_{L,n} \end{cases} \end{aligned} \quad (4)$$

Note the map g_{DC} returns switching times only at those clock events which cause the converter to switch off during the next cycle. At the other clock events there is no switching and the map gives no t_k , t_{k+1} output.

Analysis of this model is possible by a two-step approach:

1. Generation of the control clock vector t_n
2. Analysis of g_{DC} by using t_n as input

Alternatively the two maps can be combined to a higher-dimensional map as shown in the sequel.

IV. HIGHER-DIMENSIONAL MAP

As g and g_{DC} are driven by the same events the two maps can be combined. Fig. 4 shows the combined model. It is described by the following five-

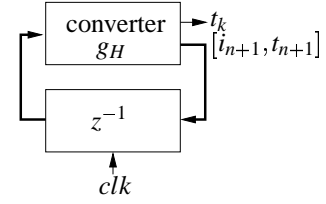


Fig. 4. Higher-dimensional model.

dimensional map

$$\begin{pmatrix} t_{n+1} \\ i_{L,n+1} \\ k \\ t_k \\ t_{k+1} \end{pmatrix} = \begin{pmatrix} g(t_n) \\ i(i_{L,n}, t_n) \\ k(i_{L,n}, t_n) \\ a \\ \frac{c_2}{c_1} a \end{pmatrix} \quad (5)$$

where $g(t_n)$ is the map of the chaotic clock generator. i, k and a correspond to Eq. (4). This map is now used for system analysis.

A. Statistical Analysis

At the moment, analysis showed here is done numerically. But we will derive some approximative expressions from the observed behaviour of the coupled system. To design the input circuit the mean current ripple $\overline{i_{pp}}$ is required. To calculate $\overline{i_{pp}}$ the density of the inductor current i_k at the converters switch-on events is required. It is obtained numerically from the map, Eq. (5). The converter parameters are:

- $V_{in} = 10 \text{ V}$ $\alpha = \left| \frac{c_2}{c_1} \right| = 2$
- $\bar{f} = 100 \text{ kHz}$ $\frac{\Delta f}{\bar{f}} = \pm 10 \%$

First we apply triangular periodic FM (PFM). The map g in this case is

$$\begin{aligned} t_{n+1} &= \begin{cases} t_n + \Psi_1(t_n) & z_n = 1 \\ t_n - \Psi_2(t_n) & z_n = 0 \end{cases} \\ z_{n+1} &= \begin{cases} z_n & t_{min} < t_n < t_{max} \\ \bar{z}_n & \text{else} \end{cases} \\ \Psi_1(t_n) &= \frac{ct_n^3}{1 - ct_n^2} \\ \Psi_2(t_n) &= \frac{ct_n^3}{1 + ct_n^2} \end{aligned} \quad (6)$$

In the chaotic cases we change the clock period every m cycles chaotically. For the $m - 1$ cycles in between it remains constant. The map g then reads as

$$\begin{aligned} t_n &= \frac{1}{\bar{f} + \Delta f(x_n - \frac{1}{2})} \\ x_{n+1} &= \gamma(x_n) \end{aligned} \quad (7)$$

$\gamma(x_n)$ is the bernoulli map or the tent map. Fig. 5 depicts the PDF if i_k (initial current for the switch-on

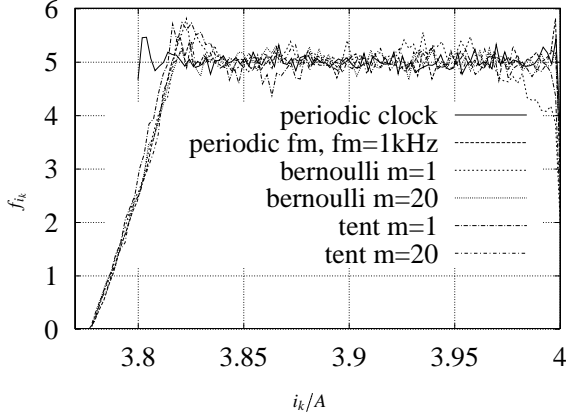


Fig. 5. Density of the start current, $\alpha \approx 2$.

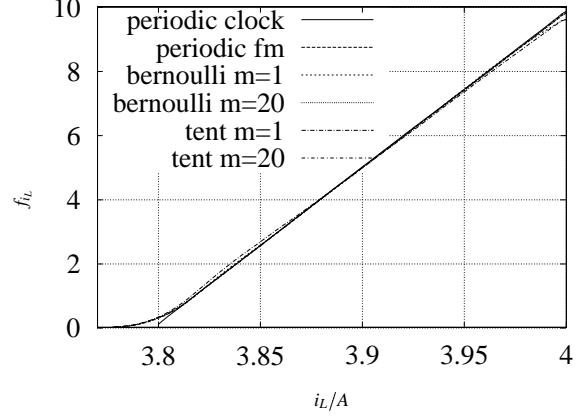


Fig. 6. Converter current density, $\alpha \approx 2$.

phase) for the cases indicated. For integer α it can be approximated by the following function

$$f_{i_k}(x) = \begin{cases} 0 & i \leq i_a \\ \frac{c_2}{N}(t_{max} - t_{min})(i - i_a) & i_a < i < i_b \\ \frac{1}{N} & i_b \leq i \leq i_{ref} \\ 0 & i > i_{ref} \end{cases} \quad (8)$$

with

$$\begin{aligned} i_a &= i_{ref} - c_2 t_{max} \\ i_b &= i_{ref} - c_2 t_{min} \\ N &= \int_{i_a}^{i_{ref}} f_{i_k}(y) dy \end{aligned} \quad (9)$$

From Eq. 8 the mean value $m_1(f_{i_n})$ and the mean current ripple

$$\bar{i}_{pp} = i_{ref} - m_1(f_{i_k}) \quad (10)$$

can be calculated. The estimation f_{i_n} very good fits with simulation results of slow modulation ($m \geq 10$). For decreasing m we obtain an increased error, see cases bernoulli and tent at $m = 1$, Fig. 5 due to the influence of the clock generators dynamics on the converter dynamics.

It can be shown that the PDF of the inductor current is the normalised integral of the PDF of i_n , i.e.

$$f_{i_l}(x) = \frac{1}{N_i} \int_{i_{ref} - c_2 t_{max}}^x f_{i_n}(y) dy \quad x \leq i_{ref} \quad (11)$$

with

$$N_i = \int_{i_{ref} - c_2 t_{max}}^{i_{ref}} f_{i_l}(y) dy \quad (12)$$

Fig. 6 depicts the converter current density using the different clock processes. For the case of periodic clock and integer α an exact analytical expression can be derived too, see [5].

At non-integer α values the PDF is more complicated. Figs. 7 and 8 depict the numerically obtained

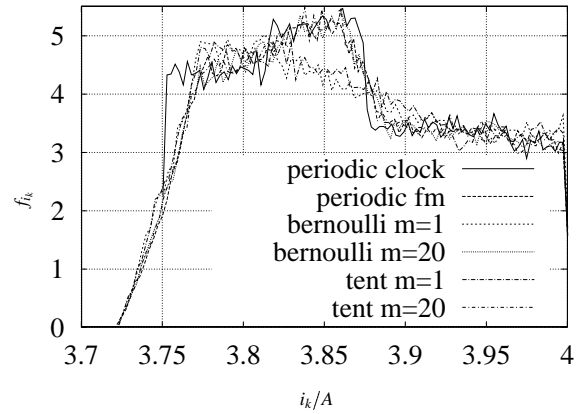


Fig. 7. Converter start current density, $\alpha \approx 2.5$.

results for $\alpha \approx 2.5$. Nevertheless the differences do not show up so strictly in the converter current density.

B. PDS and EMI Consideration

Now the PDS of $i_L(t)$ is calculated using the method shown in [8]. Therefore the converter time series is calculated using Eq. (5). Fig. 9 shows the result for periodic clock and PFM using $\frac{f_m}{f} = \frac{1}{100}$. The PDS using bernoulli map clock generator is depicted in Fig. 10. Fig. 11 shows the for the tent map clock generator.

The PDS consists of a basic wideband part determined by the converter dynamics and a spiky part resulting from the clock. From Figs. 9 to 11 it can be clearly seen that the FM of 10 % takes no significant influence on the converter dynamics. This may give

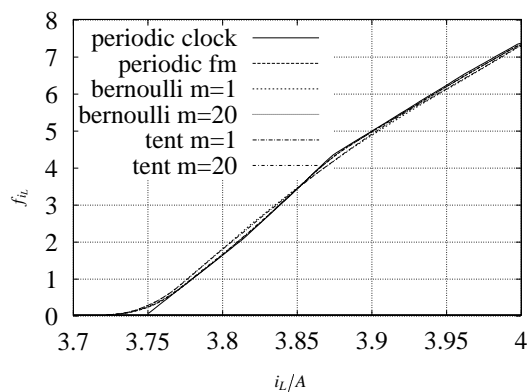


Fig. 8. Converter current density, $\alpha \approx 2.5$.

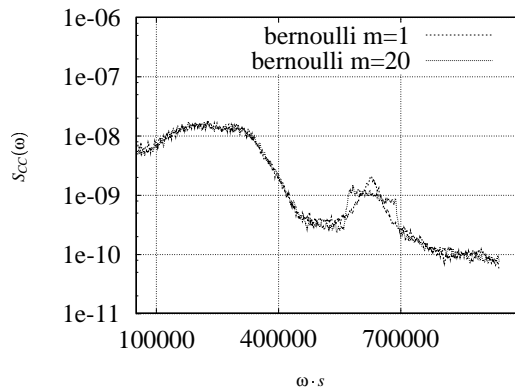


Fig. 10. Cpm boost converter pds.

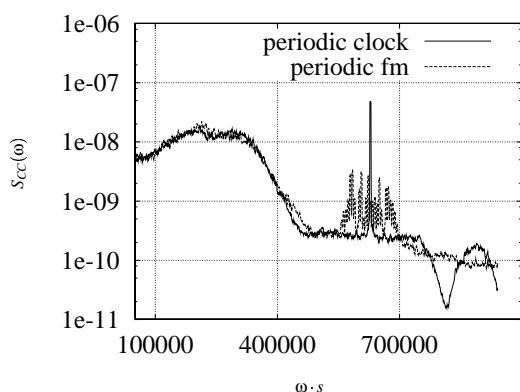


Fig. 9. Cpm boost converter pds.

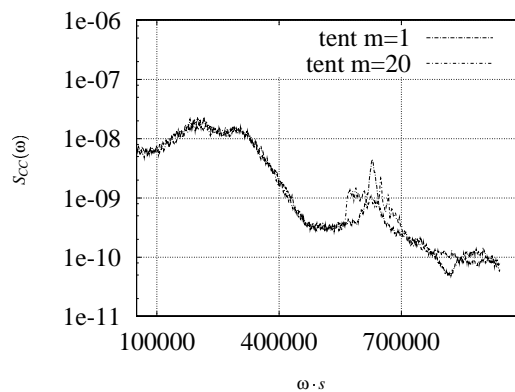


Fig. 11. Cpm boost converter pds.

rise for separate analysis of the two processes.

In these examples chaotic clocking of the converter using bernoulli map and $m = 20$ achieved the best EMI performance and should be preferred.

V. CONCLUSIONS

In the paper we derived coupled and higher-dimensional models for the chaotically clocked CPM boost converter. Using these models efficient statistical analysis, similar to that of one-dimensional systems has been carried out. In the proposed case approximation of the system behaviour by separate analysis of the maps was possible. Approximative analytic expressions have been provided for special cases. However more exact analysis at the moment is possible numerically only. A more extended analysis is subject to further research.

A. References

REFERENCES

[1] M. Bernardo, F. Garofalo, L. Glielmo, and F. Vasca, "Switching, bifurcations, and chaos in dc/dc converters," *IEEE Trans-*

actions on Circuits and Systems-I, vol. 45, no. 2, pp. 133–141, February 1998.

[2] O. Woywode, J. Weber, H. Güldner, A. L. Baranovski, and W. Schwarz, "Statistical analysis of chaotic dc-dc converters," in *Proc. EAIT'01*, Kharagpur, India, December 2001.

[3] O. Woywode, H. Güldner, A. L. Baranovski, and W. Schwarz, "Design rules for aperiodic boost converters," in *PCIM 2000*, Nürnberg, Germany, June 2000, pp. 485–489.

[4] J. Krupar and W. Schwarz, "Discrete time and continuous time modelling of a dc-dc converter – a comparison," in *Proc. NDES'02*, Scuol, Switzerland, May 2003, pp. 145–148.

[5] J. Krupar, A. Mögel, and W. Schwarz, "Analysis of hybrid systems by means of embedded return maps," in *Proc. IS-CAS'04*, Vancouver, Canada, May 2004.

[6] H. Torikai T. Saito and W. Schwarz, "Switched dynamical systems with double periodic inputs: An analysis tool and its application to the buck-boost converter," *IEEE Transactions on Circuits and Systems-I*, vol. 47, no. 7, pp. 1038–1046, July 2000.

[7] A. L. Baranovski and W. Schwarz, "On spectral analysis of impulse process," in *Proc. NDES'02*, Izmir, Turkey, June 2002, pp. 37–40.

[8] J. Krupar and W. Schwarz, "Spread spectrum clock generation – chaotic and periodic modulation schemes," in *Proc. ECCTD'03*, Krakow, Poland, September 2003, pp. 235–238.

[9] W. C. Y. Chan and C. K. Tse, "Study of bifurcations in current-programmed boost converters: From quasi-periodicity to period-doubling," *IEEE Transactions on Cir-*

cuits and Systems-I, vol. 44, no. 12, pp. 1129–1142, December 1997.

NON-AUTHORIZED ACCESS TO THE CHAOTIC COMMUNICATION CHANNEL BASED ON THE PARTIAL APPROACH TO THE INVERSE PROBLEM OF NON-LINEAR DYNAMICS

V. N. Kuleshov, M. V. Tomashevskaya

Moscow Power Engineering Institute (Technical University), Radio Engineering Faculty
 Department of Generation of Oscillations and Signals
 14 Krasnokazarmennaya str., Moscow 111250, Russia; tel. +7(095)362-7624;
 e-mail: m-tomash@yandex.ru

Abstract—*This work is devoted to partial approach to solution of inverse problem of chaotic dynamics as follows to logistic map parameter and initial condition reconstruction from the communication channel chaotic signal in the presence of noise.*

I. INTRODUCTION

In the process of development of information transmission systems using chaotic carrier one has to deal with two fundamental problems of chaotic dynamics: a direct problem and an inverse one. A direct problem solution is necessary when one builds a chaotic carrier generator and analyses an influence of the generator parameters and initial conditions on basic characteristics of chaotic oscillations. It is important to choose a method of modulation and a method of demodulation in an authorized receiver [1]. An inverse problem has to be solved when one builds a non-authorized receiver that has to determine a structure, parameters and method of modulation of chaotic carrier generator to be able to extract an information from chaotic signal in the presence of the channel noise [1,2].

A general approach to the inverse problem solution for the case of one-dimensional time series observation is presented in the paper [3]. In many cases one has some information about chaotic carrier generator that gives an opportunity to reduce a general inverse problem solution to the problem of determination of several parameters and initial values that define a chaotic carrier generator operation with accuracy that is sufficient for practical application. The aim of this paper is to develop an approach to solution of such simplified inverse problem. This approach is illustrated by particular example of chaotic generator of one-dimensional time series using a logistic map.

II. PROBLEM FORMULATION

Let us consider a discrete dynamical system described by equation of one-dimensional map:

$$x(k+1) = F [\lambda_1, \lambda_2, \dots, x(k)] . \quad (1)$$

To simplify the problem we consider a one-parameter map:

$$x(k+1) = F [\lambda, x(k)] . \quad (2)$$

Let us suppose that $F [\lambda, x(k)] = \lambda x(k)(1-x(k))$. This particular example of the map (2) is famous as a logistic map [4]:

$$x(k+1) = \lambda x(k)(1 - x(k)) . \quad (3)$$

It is famous that the map (3) in a case of $\lambda=3.9$ and $x(0)=0.1$ generates a numeric sequence that presents discrete time chaotic oscillation.

This chaotic oscillation can be modulated by its initial values commutation in the clock time moments mL , $m=1,2,\dots$ [2]. If we choose two different initial values, providing two non-correlated in the interval $0 \leq k \leq L$ chaotic sequences $x_0(k)$ and $x_1(k)$ we generate chaotic oscillations containing a binary information signal $a(m)$:

$$a(m) = \begin{cases} 1, & m=1, 2, \dots \\ 0, & \dots \end{cases} .$$

This signal is generated according to the next rule: $x_s\{k, a(m)\} = x_0(k-mL)$ if $mL < k \leq (m+1)L$ and $a(m) = 0$, and $x_s\{k, a(m)\} = x_1(k-mL)$ if $mL < k \leq (m+1)L$ and $a(m) = 1$.

Two different initial values can correspond to the values of the same sequence having time shift q ; so that $x_1(k)=x_0(k+q)$.

The received signal in the presence of additive Gaussian noise $n(k)$ can be presented in the form:

$$y(k) = x(k) + n(k) . \quad (4)$$

Let's assume that receiving the sequence (4) we know that the carrier is generated by logistic map (3) but parameter λ and initial conditions $x_0(0)$ and $x_1(0)$ have to be determined to demodulate the signal (4), using methods, described in [1]. We suppose also that we know positions of clock time moments. By comparisons to the case considered in [1,2], in this case we have to determine not only initial values, but the map parameter λ also.

III. THE MAP PARAMETER DETERMINATION

To find the parameter λ from the sequence (4) we construct the map function diagram as dependence $y(k+1)$ on $y(k)$. In a case of noise absence and constant parameter λ each point of this dependence belongs to the curve $x(k+1)=F[\lambda, x(k)]$. It follows from (2) and it is illustrated by Fig. 1,a that was obtained from the sequence $x(k)$. Addition of the noise leads to random deflection of the points $[y(k),y(k+1)]$ from the curve $y(k+1)=F[\lambda, y(k)]$. It is illustrated by Fig. 1,b where signal-to-noise ratio consists $\sigma_c/\sigma_n = 3$. The values σ_c and σ_n are determined by formulae:

$$\left\{ \begin{array}{l} \sigma_c^2(k) = \frac{1}{N} \sum_{k=0}^N [x(k) - M_x]^2 \\ M_x = \frac{1}{N} \sum_{k=0}^N x(k) \\ \sigma_n^2(k) = \frac{1}{N} \sum_{k=0}^N [n(k) - M_n]^2 \\ M_n = \frac{1}{N} \sum_{k=0}^N n(k) = 0 \end{array} \right. \quad (5)$$

An estimation of λ based on the non-modulated sequence $y(k)=x(k)+n(k)$ and providing minimum of mean-square error of the estimation can be obtained as follows in [5]. One has to find an estimation $\tilde{\lambda}(k)$ from each of the N equations:

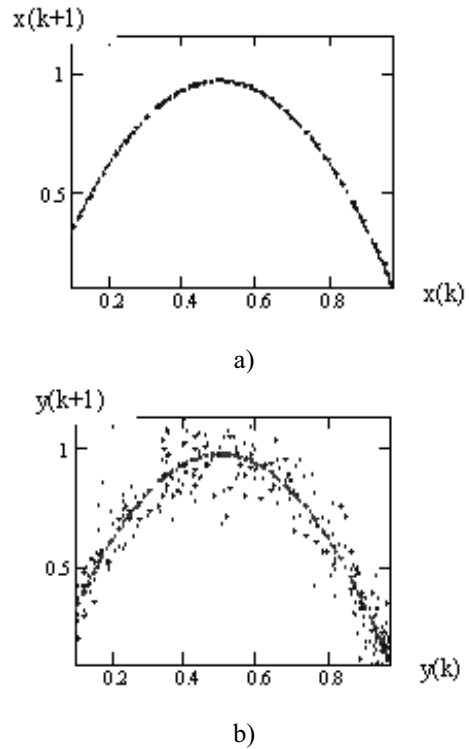


Fig. 1. Map function diagram for logistic map: (a) without noise, (b) in the presence of additive noise

$$F[\tilde{\lambda}(k), y(k)] - y(k+1) = 0, \quad k=0, 1 \dots N, \quad (6)$$

and take their average value.

In the case of logistic map we have from (6)

$$\tilde{\lambda}(k) y(k) (1 - y(k)) - y(k+1) = 0, \quad k=0, 1 \dots N, \quad (7)$$

and an estimation $\tilde{\lambda}(N)$ can be found from the next formula:

$$\tilde{\lambda}(N) = \frac{\sum_{k=0}^N y(k+1)}{\sum_{k=0}^N y(k)[1 - y(k)]} . \quad (8)$$

The dependence $\tilde{\lambda}(N)$ for the case $\sigma_c/\sigma_n=10$ is shown in the Fig. 2,a. One can see that this estimation approaches to the exact value $\lambda=3.9$ when $N \rightarrow \infty$.

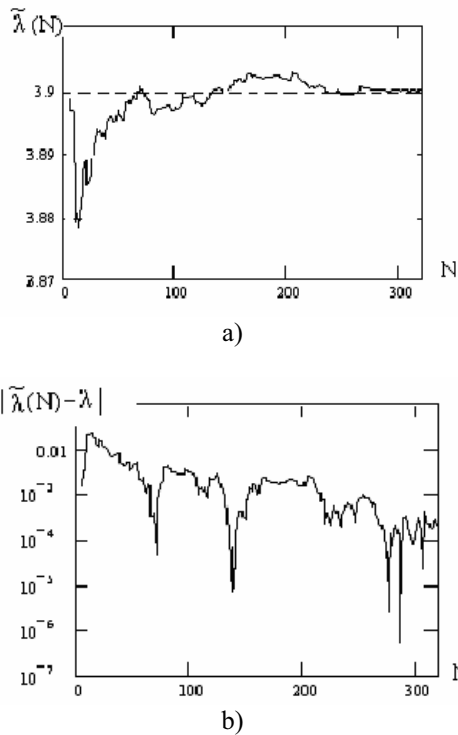


Fig. 2. Map parameter refinement at data accumulation

In the Fig. 2,b a dependence of module of difference between estimation and exact value $|\tilde{\lambda}(N) - \lambda|$ is presented. One can see that an error of $\tilde{\lambda}(N)$ estimation is significantly less than σ_s/σ_n . In the Fig. 3 the dependence of $|\tilde{\lambda}(N) - \lambda|$ at the end of interval $N=300$ versus signal-to-noise ratio σ_s/σ_n is shown.

On can see that if one uses such small values of N an accuracy of λ determination becomes unsatisfactory when signal-to-noise ratio is smaller than 10.

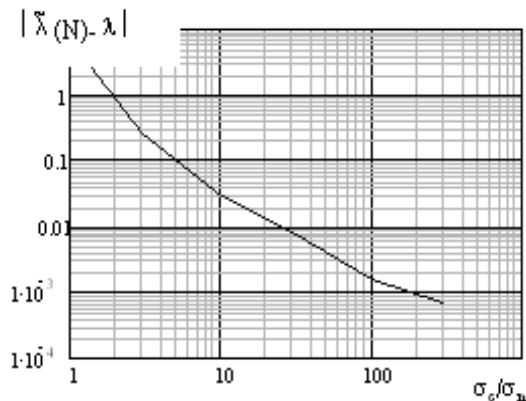


Fig. 3. Parameter dispersion dependence versus signal-to-noise ratio

If one uses modulation by initial values commutation at the clock time moments all points of map function diagram except the ones corresponding to elementary signals commutation moments. Consequently, an accumulation of partial sums $\sum_{k=0}^N y(k)[1 - y(k)]$ and $\sum_{k=0}^N y(k+1)$ for parameter λ estimation has to be carried out with elimination of $y(k)$ corresponding to clock time moments mL .

IV. INITIAL VALUES ESTIMATION

An algorithm for initial values estimation with already given values of parameter λ is given in [2]. This algorithm is based on sequential application of optimal nonlinear filtering and inverse interpolation algorithms. Obviously because the parameter estimation $\tilde{\lambda}$ has a limited accuracy the accuracy of initial value estimation will be limited too. In Fig. 4 the dependence of accuracy of initial values estimation on parameter estimation error is shown. One can see that accuracy of initial condition restoration result less by the order of value by comparison to parameter estimation accuracy.

It is known [4] that two chaotic sequences with parameters or initial values having small difference will missing with

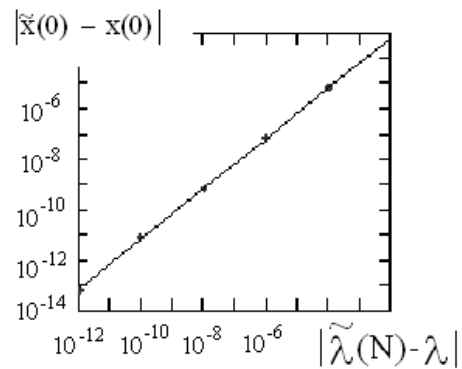


Fig. 4. Connection between parameter and initial values errors

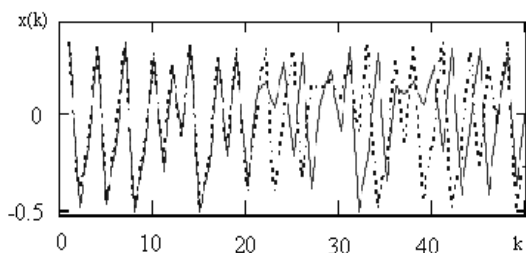


Fig. 5. Divergence of two chaotic sequences with parameter (initial condition) difference ($\Delta=10^{-4}$)

current of time (Fig. 5). Duration of time interval during which the divergence between two chaotic sequences will not exceed a defined threshold ϵ is defined by divergence of parameter or initial condition values. Therefore with parameter and initial condition accuracy refinement the efficacy of chaotic signal treatment increases (Fig. 6). The duration of effective data accumulation interval K increase too with decrease of parameter or initial conditions reconstruction error (Fig. 7).

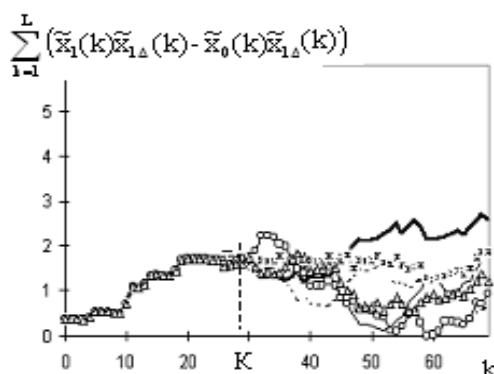


Fig. 6. Restriction of integrator output voltage in correlation non-authorized receiver in conditions of parameter or initial conditions reconstruction error

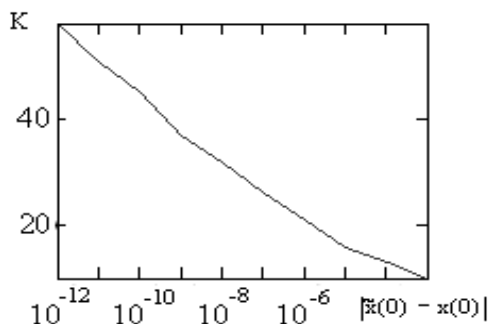


Fig. 7. The voltage accumulation window size dependence versus initial condition error

In the practice the parameter restoration accuracy refinement by data accumulation time increasing in the correspondence with Fig. 2.

V. CONCLUSION

Thus, in relation to this topic, it is possible to propose the simple algorithms for parameter and initial condition restoration. We are investigated an example of derivation and use this algorithm for parameter and initial condition restoration in the simplest one-dimensional one-parameter logistic map. We estimate also the possible accuracy of parameter and initial condition restoration for received chaotic signal with initial conditions modulation with account of additive noise. The achieved parameter and initial conditions restoration accuracy in the case of additive Gaussian noise presence is estimated.

REFERENCES

[1] Kapranov M.V., Kuleshov V.N., and al. Features of Communication Systems with Manipulation of Parameters and Initial Conditions of Chaotic Oscillators. In *Telecommunications and Radio Engineering*, pp. 48-60, №11, 2000.

[2] Kuleshov V.N., Larionova M.V., Udalov N.N. Connection Between a Problem of Non-Authorized Receiving of the Signal With Chaotic Carrier and Inverse Problem of Chaotic Dynamics. In *Proc. of 3-th Int. Symp. "AFC&SG '2000"*, pp. 150-155, St.-Petersburg, Russia, 2000.

[3] Anosov O.L., Butkovskii O.Ya., Kravtsov Yu.A., and al. Dynamic Equation Reconstruction from the Observed One-Dimensional Time Series. In *book: Dynamical Systems and Chaos* (Y.Aizawa, S.Saito, K.Shiraiwa, Eds.), pp. 378-380, World Scientific, Singapore, Vol.2, 1994.

[4] G. Schuster. Determining chaos. Introduction. – Moscow, Mir Publishers, 1989.

[5] I. N. Bronshtein, K.A. Semendyaev. Guide to mathematician. Education 13. – Moscow, Nauka Publishers, 1986.

TWO-STAGE IMPULSIVE CONTROL FOR THE SYNCHRONIZATION OF CHAOTIC SYSTEMS

K. Li^{1*}, Y. C. Soh² and Z. G. Li²

¹Temasek Laboratories,

National University of Singapore, Singapore

²School of Electrical and Electronic Engineering

Nanyang Technological University, Singapore

*e-mail: tsllk@nus.edu.sg

Abstract—In this paper, we examine the stabilization and synchronization of a class of chaotic systems with impulsive control. In particular, we propose a two-stage impulsive control strategy to achieve quick synchronization and to improve the efficiency of bandwidth utilization. The results obtained in this paper can be very useful in applications such as chaotic secure communications and chaotic spread spectrum communications that are based on this class of chaotic systems.

I. Introduction

The synchronization of two chaotic systems is one of the fundamental problems for chaotic secure communication systems and chaotic spread spectrum communications. The chaotic systems can be time-discontinuously synchronized, in which impulsive control method is attractive because it allows the stabilization of a chaotic system by using only small control impulses [1], [2], [3], [4]. It can increase the efficiency of bandwidth usage. Although impulsive chaotic synchronization has been widely studied, the existing results are still very conservative. We shall relax the synchronization condition for a class of chaotic systems.

To evaluate different impulsive synchronization methods, there are two performance indices: the time required to synchronize and the length of the impulsive interval after two systems are synchronized. The two performance indices contradict each other and depend on the choice of a design parameter. To obtain a tradeoff between them, an intermediate value is usually chosen [3],[4]. A simple two stage synchronization strategy is proposed in [5] for Chua's circuit. In this paper, we shall improve on the strategy for a class of chaotic systems. It involves an adaptation of the switching instant which is determined by the local in-

formation of the state variables.

The rest of this paper is organized as follows. In the following section, the synchronization of a class of chaotic systems is considered. A two-stage impulsive control strategy is provided in Section 3. Section 4 provides a numerical example to illustrate the efficiency of the proposed results. Finally, some concluding remarks are presented in section 5.

II. Synchronization of a Class of Chaotic Systems

Consider the synchronization of the following class of chaotic systems:

$$\dot{X}(t) = AX(t) + \psi(X(t)) \quad (1)$$

where $X(t) \in R^3$ is the vector of the state variables and $X(t)$ is globally bounded, $A \in R^{3 \times 3}$ is a constant matrix, and $\psi : R^3 \rightarrow R^3$ is a nonlinear function that gives rise to chaotic dynamics. In the synchronization configuration, the driving system is given by (1), whereas the driven system is given by

$$\dot{\tilde{X}} = A\tilde{X}(t) + \psi(\tilde{X}(t)) \quad (2)$$

where \tilde{X} is the vector of the state variables of the driven system and A and ψ are the same as in (1). We consider the class of chaotic systems that satisfies the following inequality:

$$\begin{aligned} & 2e^T(\psi(X(t)) - \psi(\tilde{X}(t))) \\ & \leq e^T(h(X(t)) + h^T(X(t)))e \end{aligned} \quad (3)$$

where $e = X(t) - \tilde{X}(t)$ is the synchronization error vector, $h : R^3 \rightarrow R^3 \times R^3$ with each element of h a bounded function of $X(t)$.

Since each element of h is a bounded function of $X(t)$, and $X(t)$ is globally bounded, h is thus

globally bounded. That is,

$$|h(X)| \leq \begin{pmatrix} H_{11} & H_{12} & H_{13} \\ H_{21} & H_{22} & H_{23} \\ H_{31} & H_{32} & H_{33} \end{pmatrix} = H \quad (4)$$

where H_{ij} is the upper bound of $h_{ij}(X)$ and the matrix inequality is defined element-wise.

Three typical examples of this class of chaotic systems are Lorenz system, Chua's circuit and Chen's equation.

In the following, we shall derive a sufficient condition for the impulsive synchronization of the driving and the driven systems.

In an impulsive synchronization configuration, at discrete instants $\tau_i (i = 1, 2, \dots)$, the state variables of the driving system are transmitted to the driven system and the state variables of the driven system are then subject to jumps at these instants. In this sense, the driven system is modeled by the following impulsive equations:

$$\begin{cases} \dot{\tilde{X}} = A\tilde{X} + \psi(\tilde{X}); & t \neq \tau_i \\ \Delta\tilde{X}|_{t=\tau_i} = -Be; & i = 1, 2, \dots \end{cases} \quad (5)$$

where B is a 3×3 symmetric matrix satisfying $\rho(I + B) < 1$ and e is defined in (3), $\tau_k (k = 1, 2, \dots)$ are time varying and satisfy [3], [4]

$$\tau_{2i+1} - \tau_{2i} \leq \epsilon_1(\tau_{2i} - \tau_{2i-1}) \quad (6)$$

where $\epsilon_1 < 1$ is a given positive constant. Denote

$$\Delta_1 = \sup\{\tau_{2i} - \tau_{2i-1}\} < \infty \quad (7)$$

$$\Delta_2 = \sup\{\tau_{2i+1} - \tau_{2i}\} < \infty \quad (8)$$

as the bounds for the impulsive intervals.

Let $\Psi(X, \tilde{X}) = \psi(X) - \psi(\tilde{X})$. The error system of the impulsive synchronization is then given by

$$\begin{cases} \dot{e} = Ae + \Psi(X, \tilde{X}); & t \neq \tau_i \\ \Delta e|_{t=\tau_i} = Be; & i = 1, 2, \dots \end{cases} \quad (9)$$

We can obtain the following result.

Theorem 1: The impulsive synchronization of two chaotic systems, with the error system given by (9), is asymptotically stable if

$$\begin{aligned} 0 &\leq \lambda_{max}((A + H)^T + (A + H)) \quad (10) \\ &\leq -\frac{2}{(1 + \epsilon_1)\Delta_1} \ln(\xi d_1) \end{aligned}$$

where $\xi > 1$, $d_1 = \rho^2(I + B) < 1$, and $\xi d_1 < 1$. H is the upper bound of h as defined in (4). $\lambda_{max}(a)$ denotes the largest eigenvalue of a .

Proof: Choose the Lyapunov function as $V(e) = e^T e$. When $t \neq \tau_i$,

$$\begin{aligned} \dot{V}(e) &= e^T(A^T + A)e + \Psi^T(X, \tilde{X})e + e^T\Psi(X, \tilde{X}) \\ &\leq e^T(A^T + A)e + e^T(h(X) + h^T(X))e \\ &\leq \lambda_{max}((A + H)^T + (A + H))V(e) \quad (11) \end{aligned}$$

We can obtain the following comparison system:

$$\begin{cases} \dot{w}(t) = \lambda_{max}((A + H)^T + (A + H))w(t); & t \neq \tau_k \\ w(\tau_k^+) = d_1 w(\tau_k) \\ w(\tau_0^+) = w_0 \geq 0 \end{cases} \quad (12)$$

Similar to the proof of Theorem 2 in [3], when $t = \tau_i$, we know that

$$w(\tau_{2k+1}) \leq e^{-2\ln(\xi d_1)/(1+\epsilon_1)} w(\tau_{2k}^+) \quad (13)$$

$$w(\tau_{2k+2}) \leq e^{-2\epsilon_1 \ln(\xi d_1)/(1+\epsilon_1)} w(\tau_{2k+1}^+) \quad (14)$$

where τ_i^+ is the time instant just after τ_i .

It follows that

$$w(\tau_{2k+2}^+) \leq \frac{1}{\xi^2} w(\tau_{2k}^+) \quad (15)$$

It can be easily shown that the comparison system (12) is asymptotically stable if inequality (10) holds. It follows from Theorem 1 in [4] that the impulsive synchronization of two chaotic systems, with the error system given by (9), is asymptotically stable. ■

To achieve the synchronization of the chaotic systems defined in (9), the impulsive interval bound can be chosen as

$$\Delta_1(\xi) = -\frac{2\ln(\xi d_1)}{(1 + \epsilon_1)\lambda_{max}((A + H)^T + (A + H))} \quad (16)$$

III. Two-Stage Impulsive Control

We have the following two observations from (15) and (16):

a) With a larger ξ , less time is required to synchronization while the bound of impulsive intervals is smaller.

b) With a smaller ξ , more time is required to synchronization while the bound of impulsive intervals is larger.

We shall combine the advantage of the two choices of ξ to design a two-stage impulsive control strategy. In the first stage with a large ξ_1 , for any given $\eta > 0$, we have

$$\|e(\tau_{2k})\| < \eta \quad (17)$$

when $k > \log_{1/\xi_1^2}(\eta^2/M_0)$, where $M_0 = \|e(t_0)\|^2$.

Define a function as follows:

$$\varpi(\xi_2) = e^{\lambda_{max}((A+H)^T + (A+H))\Delta_1(\xi_2)} \quad (18)$$

It can be easily shown that

$$V(e(t)) \leq \varpi(\xi_2)V(e(\tau_{2k-1})) ; \tau_{2k} \leq t \leq \tau_{2k+2} \quad (19)$$

We then have the result that with a small ξ_2 in the second stage, for any $\eta > 0$, there is

$$\|e(t)\| < \eta \quad (20)$$

when $t > \tau_{2\tilde{k}}$. The time instant at which the system is switched from stage 1 to stage 2 is $\tau_{2\tilde{k}}$ where \tilde{k} is defined as follows:

$$\tilde{k} = \log_{1/\xi_1^2}\left(\frac{\eta^2}{M_0\varpi(\xi_2)}\right) \quad (21)$$

It is clear that the major objective in the second stage is to obtain a larger bound of impulsive intervals. We shall provide a method which involves an adaptation of the switching instant to yield a larger bound. This is achieved by using the local maximum values of the state variable.

Set the default values of $\tau_{2\tilde{k}+1}$ and $\tau_{2\tilde{k}+2}$ as $\tau_{2\tilde{k}} + \Delta_1(\xi_2)$ and $\tau_{2\tilde{k}} + (1 + \epsilon_1)\Delta_1(\xi_2)$, respectively. The final values of $\tau_{2\tilde{k}+1}$ and $\tau_{2\tilde{k}+2}$ are given via the following two steps.

Step 1 Compute the final value of $\tau_{2\tilde{k}+1}$.

At the time instant $(\tau_{2\tilde{k}} + \Delta_1(\xi_2))$, the maximum values of $h(X)$ is obtained as follows:

$$|h(X)| \leq H(\tilde{k}) \quad (22)$$

where $H(\tilde{k})$ is the maximum value of $h(X(t))$ within the interval $[\tau_{2\tilde{k}}, \tau_{2\tilde{k}} + \Delta_1(\xi_2)]$. Then the following is true:

$$\begin{aligned} &\lambda_{max}((A + H(\tilde{k}))^T + (A + H(\tilde{k}))) \\ &\leq \lambda_{max}((A + H)^T + (A + H)) \end{aligned} \quad (23)$$

We can therefore compute an upper bound as

$$\tilde{\Delta}_1(\xi_2) = \frac{-2\ln(\xi_2 d_1)}{(1 + \epsilon_1)\lambda_{max}((A + H(\tilde{k}))^T + (A + H(\tilde{k})))} \quad (24)$$

Clearly, $\tilde{\Delta}_1(\xi_2) \geq \Delta_1(\xi_2)$.

Step 2 Compute the final value of $\tau_{2\tilde{k}+2}$.

This step is similar to step 1.

With the adaptive strategy, we can expect to get larger impulsive interval bounds once the systems are synchronized.

IV. Numerical Example

We now use a numerical example to illustrate the effectiveness of the results derived in this paper.

By studying the case of the Chen's equation, which is given by [6]:

$$\begin{cases} \dot{x} = a(y - x) \\ \dot{y} = (c - a)x + cy - xz \\ \dot{z} = xy - bz \end{cases} \quad (25)$$

where a, b and c are the parameters of the Chen's equation.

Let $X^T = [x, y, z]$, then we can rewrite (25) into the form of (1), where $A = [-a \ a \ 0; \ c - a \ c \ 0; \ 0 \ 0 \ -b]$, $\psi(X) = [0 \ -xz \ xy]^T$, and $h(X) = [0 \ -z \ y; \ 0 \ 0 \ 0; \ 0 \ 0 \ 0]$.

Choose the impulsive controller matrix B as

$$B = \text{diag}(l_1, \ l_2, \ l_3) \quad (26)$$

It follows from Theorem 1 that $d_1 = \rho^2(I + B) < 1$ should be satisfied, which implies that $-2 < l_i < 0$, ($i = 1, 2, 3$). It is easy to see that $d_1 = \max_{i=1,2,3}(l_i + 1)^2 = (l + 1)^2$, say, with $-2 < l < 0$

Assuming that M_y and M_z are the upper bounds of the state y and z , respectively. We have $H = [0 \ M_z \ M_y; \ 0 \ 0 \ 0; \ 0 \ 0 \ 0]$.

Let q denote the largest eigenvalue of $(A + A^T)$, we then have the following result:

$$\begin{aligned} &\lambda_{max}((A + H)^T + (A + H)) \\ &\leq \lambda_{max}(A^T + A) + \lambda_{max}(H^T + H) \\ &= q + \sqrt{M_y M_z + M_y^2} \end{aligned} \quad (27)$$

Figure 1 shows the stable region for different value of ξ under our improved condition. The entire region below the curve corresponding to $\xi = 1$ is the estimated stable region. When $\xi \rightarrow \infty$, the stable region shrinks to a line $l = -1$.

If we use the method in [3], the sufficient condition given for the impulsive synchronization of two Chen's equations is

$$0 \leq q + \sqrt{M_y M_z + M_y^2} \leq -\frac{2}{(1 + \epsilon_1)\Delta_1} \ln(\xi d_1) \quad (28)$$

Clearly, our result is less conservative than that derived in [3].

Consider the Chen's equation with the parameters: $a = 35, b = 3, c = 28$, the upper bound

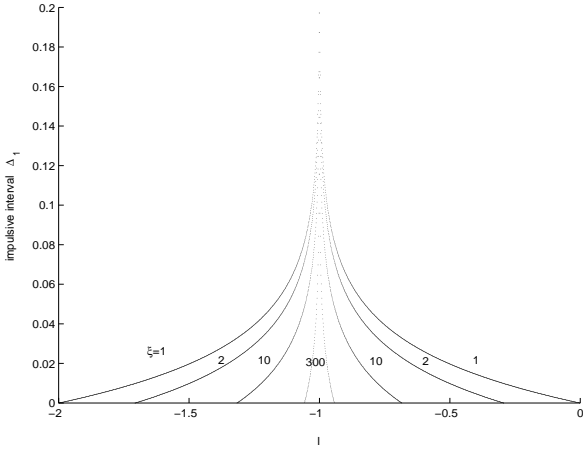


Fig. 1. Estimate of boundaries of stable region, for different value of ξ , under our improved condition.

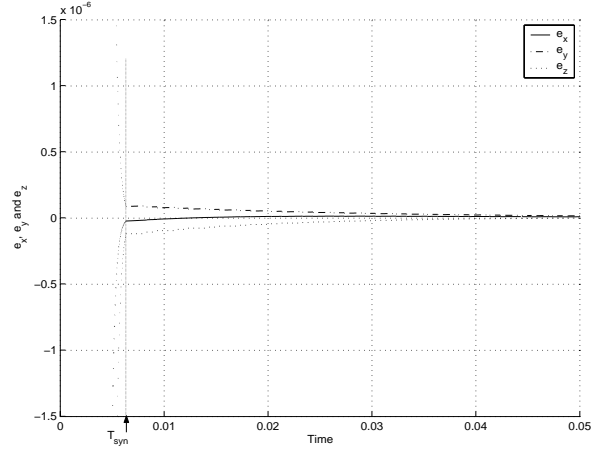


Fig. 2. The synchronization errors of the Chen's equation.

of the state variables are $M_x = 40$, $M_y = 40$, and $M_z = 65$. Then, we have the maximum $M_0 = 7425$. Choose the impulsive controller parameters as $l_1 = l_2 = l_3 = -0.1$, with $\epsilon_1 = 0.5$ and $\xi = 1.05$. It is easy to show that $d_1 = 0.81$ and $\lambda_{max}((A+H)^T + (A+H)) = 108.5509$. The upper bounds of the impulsive interval are $\Delta_1 = 0.002s$ and $\Delta_2 = 0.001s$.

In the two-stage synchronization, we choose $\xi_1 = 1.23$ and $\xi_2 = 1.01$. Then, the upper bounds of the impulsive intervals in the two stage are $\Delta_1(1.23) = 4.5 \times 10^{-5}s$, $\Delta_1(1.01) = 2.5 \times 10^{-3}s$, respectively.

For $\eta = 10^{-6}$, \tilde{k} is given as $\tilde{k} = \log_{1/\xi_1^2}(\frac{\eta^2}{M_0 \varpi(\xi_2)}) = 90$. The time necessary to synchronize the two Chen's systems is then computed as $90 * 1.5 * 4.5 * 10^{-5} (= 0.0061)$. If we use the local values of z and y , we can compute the upper bound of the impulsive time intervals in the second stage as $\tilde{\Delta}_1(1.01) = 4.1 \times 10^{-3}$. It is larger than $\Delta_1(1.01) = 2.5 \times 10^{-3}$. The experimental result is illustrated in Figure 2.

However, if we choose a fixed ξ as 1.05, \tilde{k} is then computed by $\tilde{k} = \log_{1/\xi_1^2}(\frac{\eta^2}{M_0}) = 422$. The time necessary to synchronize the two Chen's systems is then computed as $422 * 1.5 * 0.002 (= 1.266)$ while the upper bound of the impulsive intervals is given by 0.002.

Clearly, our two-stage impulsive control strategy can be used to reduce the time necessary to synchronize the two Chen's systems and at the same time increase the bound of the impulsive interval after the two systems are synchronized.

V. Conclusion

In this paper, we have provided a less conservative condition for the synchronization of a class of chaotic systems and used to develop a two-stage impulsive control strategy to synchronize the class of chaotic systems. With our method, the time necessary to synchronize two chaotic systems is minimized while the bounds of the impulsive intervals are maximized. Our result can be used to improve the transmission efficiency of the chaotic secure communication systems based on chaotic systems because of the less frequent need to transmit the synchronization impulses.

References

- [1] T. Yang and L. O. Chua. Impulsive stabilization for control and synchronization of chaotic systems: theory and application to secure communication. In *IEEE Transactions on Circuits and Systems Part I: Fundamental Theory and Applications*, vol. 44, pp.976–988, 1997.
- [2] T. Yang. Chaotic secure communication systems: history and new results. In *Telecommunications Review*, vol. 9, no. 4, pp. 597-634, 1999.
- [3] W. X. Xie, C.Y. Wen, and Z. G. Li. Impulsive control for the stabilization and synchronization of Lorenz systems. In *Physics Letters A*, vol. 275, pp. 67–72, October 2000.
- [4] Z. G. Li, C. Y. Wen, and Y. C. Soh. Analysis and design of impulsive control systems. In *IEEE Transactions on Automatic Control*, vol. 46, pp.894–897, July 2001.
- [5] K. Li, Y. C. Soh, and Z. G. Li. Chaotic cryptosystem with high sensitivity to parameter mismatch. In *IEEE Transactions on Circuit and System I: fundamental Theory and Applications*, vol. 50, pp. 579-583, April 2003.
- [6] Z.H. Guan, R.Q. Liao, F. Zhou, and H. O. Wang. On impulsive control and its application to Chen's chaotic systems. In *Int. J. of Bifurcation and Chaos*, vol. 12, pp. 1191-1197, 2002.

ON THE MECHANISMS BEHIND CHAOS

Erik Lindberg, IEEE Lifemember

Ørsted•DTU Department,
348 Technical University of Denmark,
Ørsted's Plads, Kgs. Lyngby, DK2800, Denmark
e-mail: el@oersted.dtu.dk
WWW: <http://www.oersted.dtu.dk/~el/>

Abstract— *Chaotic systems are observed everywhere. Electronic circuit analogues based on the differential equations of the models for the chaotic systems are often used to study the nature of chaotic systems. This tutorial is an attempt to classify electronic chaotic oscillators according to the mechanism behind the chaotic behaviour; e.g. one group is based on the sudden interrupt of inductive currents another group is based on the sudden parallel coupling of capacitors with different voltages and a third group may be based on multiplication of signals. An example of chaos based on "disturbance of integration" is discussed in details.*

I. INTRODUCTION

Radio amateurs and electronic engineers have observed chaotic performance of electronic circuits since the invention of the triode amplifier by Lee de Forest in 1906. The phenomena observed were called noise, nonlinear distortion, parasitic oscillations, intermittent operation, asynchronous hetero-periodic excitation etc. It was considered unwanted and impossible to investigate analytically. Edwin H. Armstrong (1890-1954) invented the regenerative circuit for HF oscillations in 1912 (superheterodyne 1918, FM 1937). He possibly observed chaos [1], [2]. Balthasar van der Pol (1889-1959) reports about chaos as "an irregular noise" [3], [4], [5], [6]. Within the last 30 years we have been able to study the nonlinear distortion phenomena by means of computer simulation and to some extent by means of analytical investigation. The concept of chaotic oscillators has been defined by means of a large number of examples. Very little has been reported concerning classification of chaotic oscillators or procedures for design of chaotic oscillators with prescribed attributes.

II. MECHANISMS BEHIND CHAOS

All electrical and electronic engineers know that you should not try to interrupt the current in a coil

or short circuit the voltage of a capacitor in no time. If you try to do this you may expect nasty behavior of your circuit. Apparently the kernel of all chaotic oscillators is an oscillator of some kind [7]. If you disturb the performance of the oscillator by adding some nasty circuit composite with *local activity and memory* [8], [9], you may create chaos. *Chaos sets in when the circuit drifts out of synchronization*, i.e. if you couple two circuits which are not in harmony you may create chaos.

If you take a look at the many proposed implementations of chaotic oscillators [10], [11], [12], [13], you will find that most of them may be classified according to the following list of "mechanisms":

A: Implementation of an analogue computer model for a set of differential equations with chaotic performance e.g. the Lorenz equations [14], [15]. The mechanism behind chaos in many of these circuits is the multiplication of two signals. If one of the signals is close to zero the sign of the signal becomes sensitive and the result of the multiplication may change drastically in almost no time.

B: By means of an "ideal switch" do the following:

B1: Interrupt the current in a coil. This is a well-known nasty operation in electrical circuits which may give rise to sparks and radiation of energy.

B2: Short-circuit a capacitor with charge. Note that this well-known nasty operation is the dual of B1 above.

B3: Connect in parallel two capacitors having different voltages. It is a nasty operation to distribute the charge between the two capacitors in no time.

B4: Connect in series two coils having different currents. Note that this well-known nasty operation is the dual of B3 above.

C: Introducing some kind of hysteresis may give rise to chaos [16], [17].

D: Introducing a circuit composite of a nonlinear conductive component with a variable negative slope characteristic in parallel with a capacitor may create a small signal Thevenin/Norton current source which try to charge the capacitor in a kind of “switching mode”, *Chua’s Diode* [18], [19]. This mechanism seems to be behind all the “Double Scroll” [20] and “Multi Scroll” oscillators [21], [22], [23].

E: Introduce a circuit composite based on *disturbance of integration*. In [24] an ideal sinusoidal oscillator *VS* is loaded with a RC series circuit in connection with the collector of a transistor with grounded emitter, fig. 1. The base of the transistor is loaded

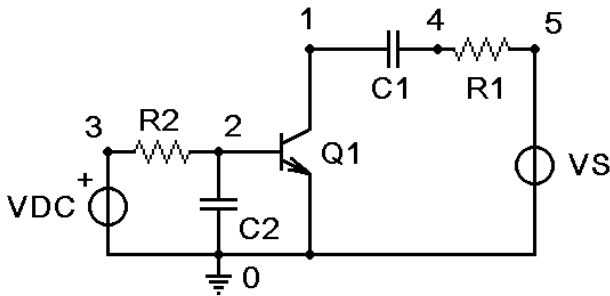


Fig. 1. Oscillator *VS* with an active *RC* load composite. $R2 = 1M\Omega$, $C2 = 680pF$, $C1 = 4.7nF$, $R1 = 1k\Omega$, $VS = 12V/10kHz$, $Q1 = BC107$.

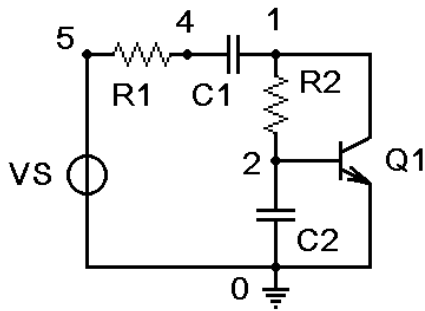


Fig. 2. Oscillator *VS* with an active *RC* load composite. $VS = 10V/3kHz$, $R1 = 1k\Omega$, $C1 = 4.7nF$, $R2 = 994k\Omega$, $C2 = 1.1nF$, $Q1 = 2N2222A$.

with a grounded capacitor *C2* which is charged by a constant dc voltage source *VDC* in series with a large resistor i.e. integration of an almost constant dc current source. The time constant of the charging of *C2* (0.68ms) is large compared with the period of *VS* (0.10ms). When the transistor “goes ON” the integration of the current is disturbed. The two independent

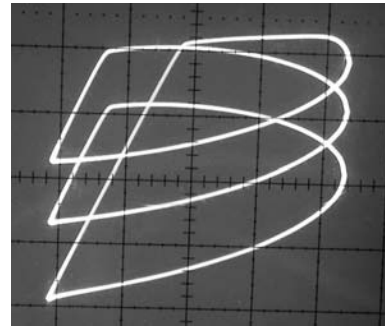


Fig. 3. Measured limit cycle (fig.2). $VS : 10V/3kHz$. $y: V(2) = V(C2)$, 0.5V/div, $x: V(5) = V(VS)$, 2.0V/div

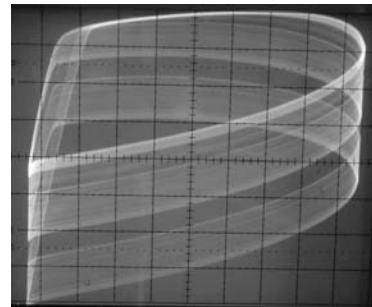


Fig. 4. Measured chaotic attractor (fig.2). $VS : 10V/10kHz$. $y: V(2) = V(C2)$, 0.5V/div, $x: V(5) = V(VS)$, 2.0V/div

sources *VDC* and *VS* are “fighting” concerning the charging of the capacitor. In the following a modified version of this circuit is investigated.

F: Other implementations e.g. based on nonlinear coils and/or capacitors.

III. CHAOS BASED ON DISTURBANCE OF INTEGRATION

Figure 2 shows an ideal sinusoidal oscillator *VS* loaded with an active *RC* composite. Figures 3 and 4 show measurements on the circuit. By varying the frequency (or the amplitude) of the oscillator limit cycle and chaotic behaviour is easily found. In order to study the mechanism PSpice simulations have been made. Chaotic behaviour is easily found, fig. 5. Apparently it is very difficult to find limit cycle behaviour by means of simulation because it is very time consuming to vary the frequency by fractions of a Hz (or the amplitude by fractions of a volt).

If you neglect the transistor *Q1* then the time constant for the passive load of *VS* becomes $\tau = RC = (R_1 + R_2)((C_1 C_2)/(C_1 + C_2)) = 0.886922ms$.

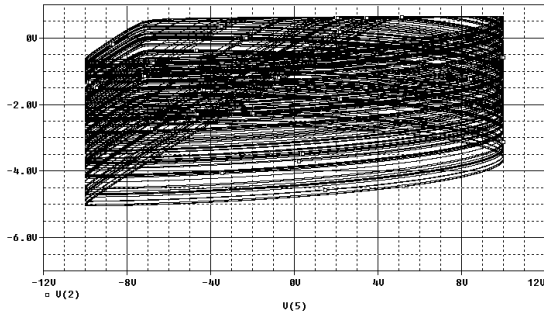


Fig. 5. Calculated chaotic attractor. $VS : 10V/3kHz$.
 $y: V(2) = V(C2)$, $x: V(5) = V(VS)$

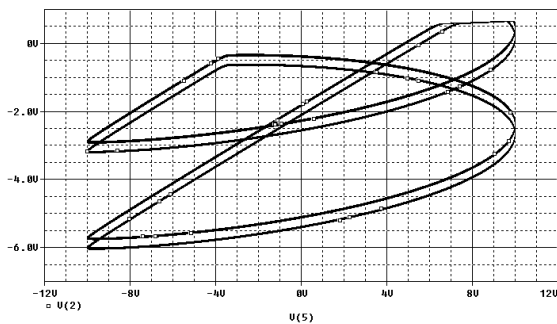


Fig. 6. Calculated limit cycle. $VS : 10V/1.12749433kHz$.
 $y: V(2) = V(C2)$, $x: V(5) = V(VS)$

By choosing a frequency with a period equal to the time constant limit cycle behaviour is found (bifurcation, fig. 6). Figures 7 and 8 show collector voltage and base voltage of the transistor for different models. Figure 9 shows the spectrum. It is seen (fig.7) that the curves are more smooth when the complete PSpice model is used and the circuit is of order 8. The transistor model used in fig.8 is build from two diodes (DBC, DBE) and two current controlled current sources (IAF, IAR). The base-emitter diode DBE and the reverse current source $IAR = AR * I(DBC)$ are in parallel with $C2$. The base-collector diode DBC and the forward current source $IAF = AF * I(DBE)$ are in parallel with $R2$. It is obvious that $C2$ integrates IAR and DBE and IAF try to disturb this integration. If you simplify the transistor model by removing either the two reverse components (DBC and IAR) or the two forward components (DBE and IAF) chaos will not occur, fig.10, 11.

Calculation of Lyapunov exponents must be done in the future.

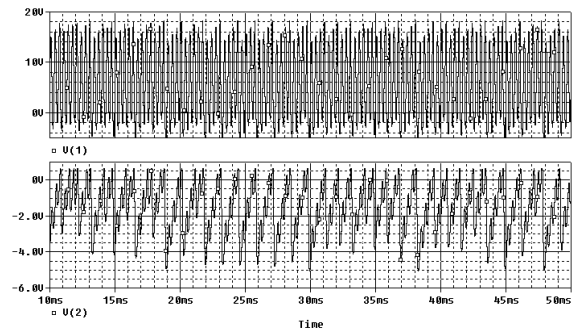


Fig. 7. Collector voltage $V(1)$ and base voltage $V(2)$ as functions of time. $VS : 10V/3kHz$.
 Transistor $Q1 : 2N2222A$

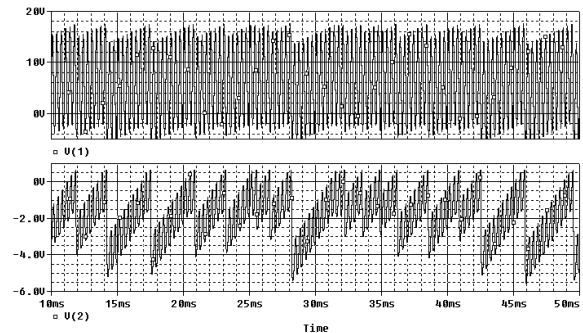


Fig. 8. Collector voltage $V(1)$ and base voltage $V(2)$ as functions of time. $VS : 10V/3kHz$. Transistor $Q1 : Ebers-Moll Injection model with no memory$.
 $AF = 0.997260274$, $AR = 0.5$,
 Diodes: $IS = 14.34e - 15$, $RS = 1$

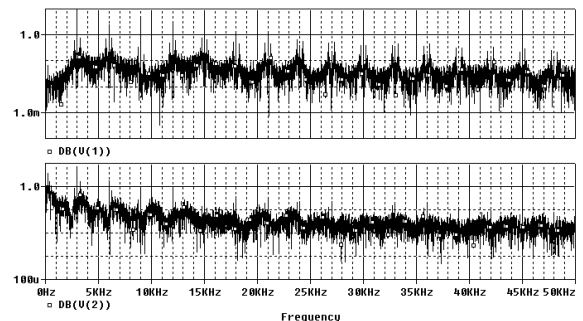


Fig. 9. Spectrum: Collector voltage $V(1)$ dB and base voltage $V(2)$ dB. $VS : 10V/3kHz$. Transistor $Q1 : Ebers-Moll Injection model with no memory$.
 $AF = 0.997260274$, $AR = 0.5$,
 Diodes: $IS = 14.34e - 15$, $RS = 1$

IV. CONCLUSION

An attempt to classify chaotic oscillators according to the mechanisms behind chaos is made. The mechanism "Chaos based on disturbance of integration" is studied in details.

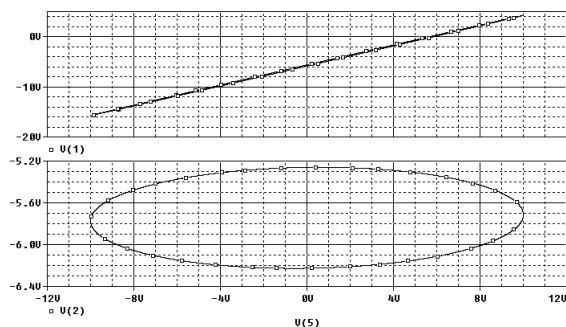


Fig. 10. Collector voltage $V(1)$ and base voltage $V(2)$ as functions of $V(5)$. $VS : 10V/3kHz$. Transistor $Q1$: Ebers-Moll Injection model with no memory. $AF = 0.997260274$, $AR = 0$, DBC removed, Diode $DBE : IS = 14.34e - 15$, $RS = 1$

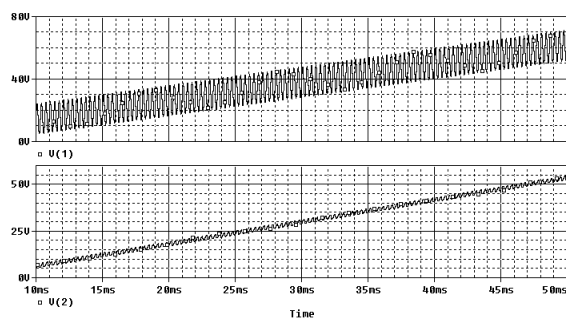


Fig. 11. Collector voltage $V(1)$ and base voltage $V(2)$ as functions of time. $VS : 10V/3kHz$. Transistor $Q1$: Ebers-Moll Injection model with no memory. $AF = 0$, $AR = 0.5$, DBE removed, Diode $DBC : IS = 14.34e - 15$, $RS = 1$

REFERENCES

[1] E. H. Armstrong, "Some recent developments of regenerative circuits," *Proc. Inst. Radio Eng.*, Vol. 10, No. 8, pp. 244-260, 1922.
 [2] D. M. W. Leenaerts, "Chaotic behaviour in super regenerative detectors", *IEEE Trans. on Circuits and Systems - I*, Vol. 43, No. 3, pp. 169-176, March 1996.
 [3] B. van der Pol and J. Van der Mark, "Frequency demultiplication," *Nature, London*, Vol. 120, No. 3019, pp. 363-364, September 10, 1927. Also reprinted in [4] and [5].
 [4] H. Bremmer and C. J. Bouwkamp (Eds.), *Balthasar van der Pol - Selected Scientific Papers*, Vol. I-II, North-Holland Pub. Co. pp. 391-393, 1960.
 [5] T. Kapitaniak (Ed.), *Chaotic Oscillators - Theory and Applications*, pp. 4-5, World Scientific 1992.

[6] M. P. Kennedy and L. O. Chua, "Van der Pol and chaos", *IEEE Trans. on Circuits and Systems*, Vol. CAS-33, No. 10, pp. 974-980, October 1986.
 [7] A. E. Elwakil and M. P. Kennedy, "Design Methodology for Autonomous Chaotic Oscillators", pp. 23-49 in [10].
 [8] L. O. Chua, "CNN: A paradigm for complexity", Chapter 13 in [9], pp. 529-837 (local activity, pp. 793-826), 1999.
 [9] J. L. Huertas, W.-K. Chen and R. N. Madan (Eds.), *Visions of Nonlinear Science in the 21st Century*, World Scientific, 1999.
 [10] Guanrong Chen and Tetsushi Ueta (editors): *Chaos in Circuits and Systems*, World Scientific Series on Nonlinear Science, Series B, Vol. 11, (p. 630), 2002.
 [11] M. Lakshmanan and K. Murali, *Chaos in Nonlinear Oscillators - Controlling and Synchronization*, pp. 1-325, World Scientific 1996.
 [12] M. J. Ogorzalek, *Chaos and Complexity in Nonlinear Electronic Circuits*, pp. 1-276, World Scientific 1997.
 [13] A. Tamasevicius, "Analog Techniques for Modelling, Control and Synchronization of Dynamical Chaos," *Habilitation Thesis, Physical Sciences, Physics (02P)*, Semiconductor Physics Institute, Vilnius, pp. 1-99, Lithuania, June 1999.
 [14] R. Tokunaga, M. Komuro, T. Matsumoto and L. O. Chua, "LORENZ ATTRACTOR from an electrical circuit with uncoupled continuous piecewise-linear resistor", *Int. J. of Circuit Theory and Applications*, Vol. 17, pp. 71-85, 1989.
 [15] J. C. Sprott, "Simple chaotic systems and circuits", *Am. J. Phys.*, Vol. 68, No. 8, August 2000, pp. 758-763.
 [16] E. Lindberg, A. Tamasevicius, A. Cenys, G. Mykolaitis and A. Namajunas, "Hyperchaos via χ -diode", in *Proceedings NDES'98 - the 6th International Specialist Workshop on Nonlinear Dynamics of Electronic Systems*, pp. 125-128, Budapest, July 1998.
 [17] F. Bizzarri and M. Storage, "RC op-amp implementation of hysteresis chaotic oscillator", *Electronics Letters*, Vol. 37, No. 4, pp. 209-211, February 2001.
 [18] E. Lindberg, "A simple explanation of the physical behaviour of Chua's circuit" or "A route to the hearts of Chua's circuit", in A. C. Davies and W. Schwarz (Eds.), *Nonlinear Dynamics of Electronic Systems*, (Proceedings of the Workshop NDES'93, Dresden, July, 1993), pp. 80-88, World Scientific 1994.
 [19] R. N. Madan (Ed.), *Chua's Circuit - A Paradigm for Chaos*, World Scientific 1993.
 [20] L. O. Chua, M. Komuro and T. Matsumoto, "The double scroll family: parts I and II", *IEEE Trans. on Circuits and Systems*, Vol. CAS-33, No. 11, pp. 1072-1118, November 1986.
 [21] G. Chen, "Control and synchronization of chaotic systems (a bibliography)", ECE Dep. Univ. of Huston, Texas, USA, 1997. website: <ftp://ftp.egr.uh.edu/pub/TeX/chaos.tex>
 [22] J. Suykens and J. Vandewalle, "Quasilinear approach to nonlinear systems and the design of n-double scroll (n = 1,2,3,4, ...)", *IEE Proceedings-G*, Vol. 138, No. 5, pp. 595-603, October 1991.
 [23] K. S. Tang, G. Q. Zhong, G. R. Chen and K. F. Man, "Generation of n-scroll attractors via sine function", *IEEE Trans. on Circuits and Systems*, 2001, accepted.
 [24] K. Hoh, T. Irita, T. Tsujita and M. Fujishima, "Generation of Chaos with Simple Sets of Semiconductor Devices", *Proceedings - 1998 Second International Conference on Knowledge-Based Intelligent Electronic Systems*, (Editors: L.C. Jain and R.K. Jain), Adelaide, Australia, 21-23 April 1998.

GENERAL MECHANISM FOR SUPPRESSION OF HOMOCLINIC CHAOS

Aleksander Loskutov and Arsen Janoev

Physics Faculty,
 Moscow State University,
 Moscow, Russia

e-mail: loskutoc@moldyn.phys.msu.ru

WWW: http://chaos.phys.msu.ru

Abstract— *On the basis of the Melnikov method which is a standard tool for the investigation of the chaos onset in the separatrix neighbourhood, the possibility of the stabilization of the behaviour of dynamical systems is studied. An explicit form of external perturbations leading to the chaos suppression phenomenon is obtained. Analytical results are implemented by the numerical analysis of the Duffing–Holmes system.*

I. INTRODUCTION

We apply the Melnikov method [1], which gives a sufficient criterion of the chaos existence, to the analysis of the behaviour of dynamical systems. Such an approach can give us an analytical form of the perturbations which leads to the chaos suppression phenomenon.

Let us consider a two-dimensional system having a unique saddle point:

$$\dot{x} = f_0(x) + \varepsilon f_1(x, t), \quad (1)$$

where $x = (x_1, x_2)$ and f_1 is a T -periodic function. Suppose that the unperturbed system ($\varepsilon = 0$) has a separatrix loop, so that $\lim_{t \rightarrow \pm\infty} x_0(t) = X_0$. In the presence of perturbations ($\varepsilon \neq 0$), the separatrix loop is destroyed. Thus, we have three different cases: separatrix either not intersects another one (so that one of them can completely envelop the other separatrix), or they intersect each other in an infinite number of homoclinic points forming a separatrix splitting. Chaotic motion appears only in the last case.

The Melnikov method consists in the evaluating by the perturbation theory the distance $D(t_0)$ between stable x^s and unstable x^u manifolds at time t_0 measured along the homoclinic trajectory. Chaos appears only if $D(t_0)$ changes its sign for some t_0 . Obviously, such a situation takes place if the separatrices are splitting.

To calculate D it is sufficient to find solutions in x^s and x^u up to the first-order perturbation theory in the

smallness parameter ε . So, let us write

$$x^{s,u}(t, t_0) = x_0(t - t_0) + \varepsilon x_1^{s,u}(t, t_0), \quad (2)$$

where x_0 is a separatrix loop in the unperturbed system. Thus, substituting (2) to (1) in the first order we get:

$$\frac{dx_1^{s,u}}{dt} = M(x_0)x_1^{s,u} + \varepsilon f_1(x_0(t - t_0), t), \quad (3)$$

where $M(x_0)$ is the Jacobi matrix of f_0 taken in the unperturbed trajectory $x_0(t - t_0)$.

To obtain the intersection condition we should find the solution of (3) for x^s at $t > t_0$ and for x^u at $t < t_0$ such that $\lim_{t \rightarrow \infty} x^s = \lim_{t \rightarrow -\infty} x^u = X_p$, where X_p is the position of the hyperbolic point after perturbation. These solutions differ from each other by a vector ($\varepsilon = 1$) $d(t, t_0) = x^s(t, t_0) - x^u(t, t_0) = x_1^s(t, t_0) - x_1^u(t, t_0)$.

The Melnikov distance $D(t, t_0)$ is defined as the projection of d on a normal N :

$$D(t, t_0) = N d. \quad (4)$$

Using (1) (for $\varepsilon = 0$) we can define the normal vector as

$$N(t, t_0) = \begin{pmatrix} -f_{02}(x_0) \\ f_{01}(x_0) \end{pmatrix}.$$

Introducing operation $x \wedge y = x_1 y_2 - x_2 y_1$, the expression (4) can be rewritten as follows: $D(t, t_0) = f_0 d$. To find an explicit form of D , let us note that

$$D = D^s - D^u, \quad (5)$$

where $D^{s,u}(t, t_0) = f_0 \wedge x_1^{s,u}$. Now, differentiate D^s with respect to time, we find

$$\dot{D}^s = \dot{f}_0 \wedge x_1^s + f_0 \wedge \dot{x}_1^s = (M(x_0)\dot{x}_0) \wedge x_1^s + f_0 \wedge \dot{x}_1^s.$$

Thus, from (3) we have $\dot{D}^s = \dot{f}_0 x_1^s + f_0 \dot{x}_1^s = (M(x_0)f_0)x_1^s + f_0(M(x_0)x_1^s) + f_0 f_1$, or

$$\begin{aligned} \dot{D}^s &= \text{Sp}M(x_0)f_0 \wedge x_1^s + f_0 \wedge f_1 = \\ &= \text{Sp}M(x_0)D^s + f_0 \wedge f_1, \end{aligned} \quad (6)$$

where we take into account that $\dot{x}_0 = f_0$ and $\text{Sp}M = \text{div} f_0$.

Consider a case, when the unperturbed system is a Hamiltonian one, i.e. $\text{Sp}M = 0$. Integrating (6) in the interval $[t_0, \infty)$ and taking into account the asymptotics $D^s(\infty, t_0) = f_0(X_0) \wedge x_1^s = 0$, we arrive at the following:

$$D^s(t, t_0) = - \int_{t_0}^{+\infty} f_0 \wedge f_1 dt. \quad (7)$$

Similarly, for D^u we get

$$D^u(t, t_0) = \int_{-\infty}^{t_0} f_0 \wedge f_1 dt. \quad (8)$$

Finally, substituting (7) and (8) to (5) we have:

$$D(t, t_0) = - \int_{-\infty}^{\infty} f_0 \wedge f_1 dt. \quad (9)$$

The given dependence $D(t, t_0)$ defines the character of the motion in the original system. If $D(t_0)$ changes its sign then separatrices intersect each other and dynamics in this area is chaotic.

II. FUNCTION OF STABILIZATION

In this part we find an analytical form of the perturbations at which the Melnikov distance D does not change sign.

Consider the following equation

$$\begin{aligned} \dot{x} &= P(x, y), \\ \dot{y} &= Q(x, y) + \varepsilon[f(\omega, t) + \alpha F(x, y)], \end{aligned}$$

where $f(\omega, t)$ is a periodic perturbation and $P(x, y)$, $Q(x, y)$, $F(x, y)$ are some smooth functions. For this equation the Melnikov distance (see Eq.(9)) is:

$$\begin{aligned} D(t, t_0) &= - \int_{-\infty}^{\infty} y_0(t - t_0) [f(\omega, t) + \\ &+ \alpha F(x_0, y_0)] dt \equiv I[g(\omega, \alpha)], \end{aligned}$$

where $y_0(t) = \dot{x}_0(t)$.

To suppress chaos we should get a function of stabilization: $f^*(\omega, t)$. Thus, consider the inverse problem.

Suppose $D(t, t_0) \in [s_1, s_2]$. After the stabilizing perturbation $f^*(\omega, t)$ for the corresponding Melnikov function $D^*(t, t_0)$ we have: $D^*(t, t_0) > s_2$ or

$D^*(t, t_0) < s_1$. Then $I[g(\omega)] + I[g^*(\omega)] > s_2$,

where $I[g^*(\omega)] = - \int_{-\infty}^{+\infty} y_0(t - t_0) f^*(\omega, t) dt$. It is obvious that $I[g(\omega)] + I[g^*(\omega)] = s_2 + \chi = \text{const}$, where $\chi, s_2 \in \mathbf{R}^+$. Therefore, $I[g^*(\omega)] = \text{const} - I[g(\omega)]$. On the other hand,

$$I[g^*(\omega)] = - \int_{-\infty}^{\infty} y_0(t - t_0) f^*(\omega, t) dt.$$

Suppose that $f^*(\omega, t) = \text{Re}\{e^{-i\omega t} A(t)\}$. In this case, omitting the intermediate expressions, we finally get:

$$\begin{aligned} f^*(\omega, t) &= \text{Re} \left[\frac{e^{-i\omega t}}{y_0(t - t_0)} \times \right. \\ &\quad \left. \times \int_{-\infty}^{\infty} (I[g(\omega)] - \text{const}) e^{i\omega t} d\omega \right]. \end{aligned}$$

For systems for which it is possible to make an additional shift from the critical value of the Melnikov function $D(t, t_0)$, the external stabilizing perturbation has the form [2]:

$$f^*(\omega, t) = - \frac{4\pi a \delta(t)}{y_0(t - t_0)} \cos(\omega t),$$

where $\delta(t)$ is a Dirac delta-function.

III. DUFFING OSCILLATOR

Let us apply the obtained results to the known Duffing equation. We have chosen this equation by the reason that it has a sufficiently reach dynamics, and this system admits analytical investigations.

The Duffing equation with damping and parametric perturbation of the cubic term can be written as follows:

$$\ddot{x} - x + \beta [1 + \eta \cos(\Omega t)] x^3 = \varepsilon [\gamma \cos(\omega t) - \alpha \dot{x}], \quad (10)$$

where η and Ω are the amplitude and the frequency of the perturbation, respectively, $\eta \ll 1$. Chaos in a neighbourhood of the separatrix does not take place (i.e. $D(t, t_0)$ does not change sign, in our case $D(t, t_0) < 0$) if (see [3], [4])

$$\begin{aligned} \frac{6\beta d \sinh(\pi\Omega/2)}{\pi(\Omega^4 + 4\Omega^2)} &= \eta_{min} < \eta \leq \\ &\leq \eta_{max} = \frac{1}{p^2} \frac{6\sqrt{2}\beta\gamma\omega \sinh(\pi\Omega/2)}{(\Omega^4 + 4\Omega^2) \cosh(\pi\omega/2)}, \end{aligned}$$

where p is an integer. In our analysis, we use the left-hand side of this inequality. Consideration of the second case can be carried out by the same manner.

The threshold value of the Melnikov distance is

$$D_c(t, t_0) = \frac{2\sqrt{2}}{\sqrt{\beta}} \frac{\pi\gamma\omega}{\cosh\left(\frac{\pi\omega}{2}\right)} \sin(\omega t_0) + \frac{4\alpha}{3\beta} - d \sin(\Omega t_0).$$

Thus, for $D(t, t_0)$, $D_{out}(t, t_0) < D_c(t, t_0)$, we have:

$$D_{out}(t, t_0) = \frac{2\sqrt{2}}{\sqrt{\beta}} \frac{\pi\gamma\omega}{\cosh\left(\frac{\pi\omega}{2}\right)} \sin(\omega t_0) + \frac{4\alpha}{3\beta} - d \sin(\Omega t_0) - a,$$

where $a > 0$ is a constant.

Let us introduce a stabilizing perturbation in the form: $f^*(\Omega, t) = \text{Re}\{A(t)e^{-i\Omega t}\}$. Then the additive component of the Melnikov distance corresponding to this perturbation function is

$$D_f(t, t_0) = - \int_{-\infty}^{+\infty} A(t) v_0(t - t_0) e^{-i\Omega t} dt,$$

where $v_0(t) = -\sqrt{2} \sinh(t) / [\sqrt{\beta} \cosh^2(t)]$. Thus, the total Melnikov distance $D'(t, t_0) = D_f(t, t_0) + D_{out}(t, t_0) > D_c(t, t_0)$ is written as follows:

$$D'(t, t_0) = - \int_{-\infty}^{+\infty} A(t) v_0(t - t_0) e^{-i\Omega t} dt + \frac{2\sqrt{2}}{\sqrt{\beta}} \frac{\pi\gamma\omega}{\cosh\left(\frac{\pi\omega}{2}\right)} \sin(\omega t_0) + \frac{4\alpha}{3\beta} - d \sin(\Omega t_0) - a.$$

To complete our analysis it is necessary to obtain $A(t)$. From the expression of D_{out} we have:

$$D'(t, t_0) = \frac{2\sqrt{2}}{\sqrt{\beta}} \frac{\pi\gamma\omega}{\cosh\left(\frac{\pi\omega}{2}\right)} \sin(\omega t_0) + \frac{4\alpha}{3\beta} - d \sin(\Omega t_0) + a.$$

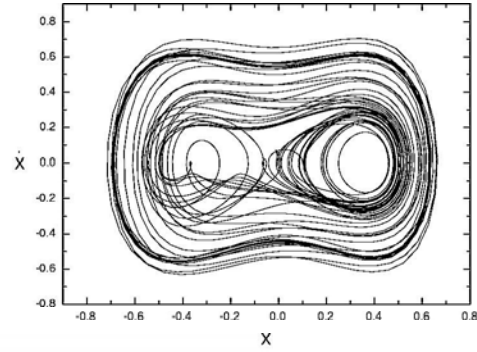


Fig. 1. Phase portrait of the Duffing system (10) for $\alpha = 0.145$, $\beta = 8$, $\eta = 0.01$, $\gamma = 0.14$, $\Omega = \omega = 1.1$ (chaos).

Therefore,

$$- \int_{-\infty}^{+\infty} A(t) v_0(t - t_0) e^{-i\Omega t} dt = 2a.$$

Hence, the inverse Fourier transformation yields

$$A(t) = - \frac{2a}{v_0(t - t_0)} \int_{-\infty}^{+\infty} e^{i\Omega t} d\Omega.$$

Thus, the final expression for the external stabilizing perturbation has the following form:

$$f^*(\Omega, t) = \frac{-4\pi a \delta(t) \cos(\Omega t)}{v(t - t_0)}, \quad (11)$$

where δ is a Dirac delta-function.

IV. NUMERICAL ANALYSIS

We have performed computer simulations of the Duffing equation (10) with the following parameters: $\alpha = 0.145$, $\beta = 8$, $\eta = 0.01$, $\gamma = 0.14$, $\Omega = \omega = 1.1$. It is known that these values corresponds to the chaotic motion in the system (Fig.1).

Let us introduce the stabilizing perturbation $f^*(\Omega, t)$ (see (11)) with $a = 2$. Then we get the chaos suppression phenomenon. The corresponding phase portrait is shown in Fig.2.

Another method of detecting the stabilization of the chaotic motion is to consider the spectral properties of the solution $x(t)$ of the Duffing equation. By the standard Fourier transform we can get the power spectrum:

$$S(\omega) = \lim_{T \rightarrow \infty} \frac{1}{2\pi T} |X(\omega)|^2.$$

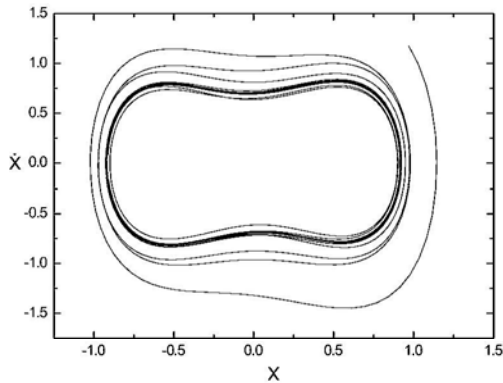


Fig. 2. Phase portrait of the Duffing system (10) with the stabilizing function (11). $\alpha = 0.145$, $\beta = 8$, $\eta = 0.01$, $\gamma = 0.14$, $\Omega = \omega = 1.1$, and $a = 2$ (chaos suppression).

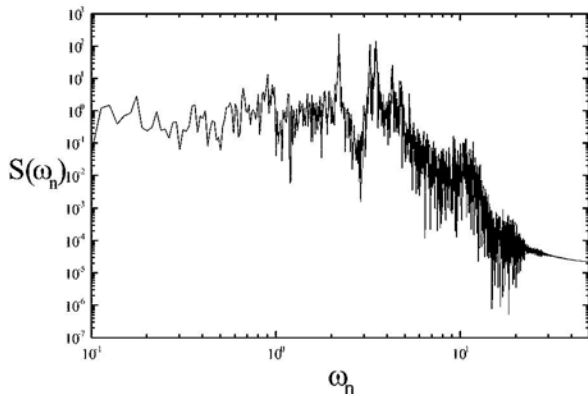


Fig. 3. Power spectrum corresponding to Fig.1.

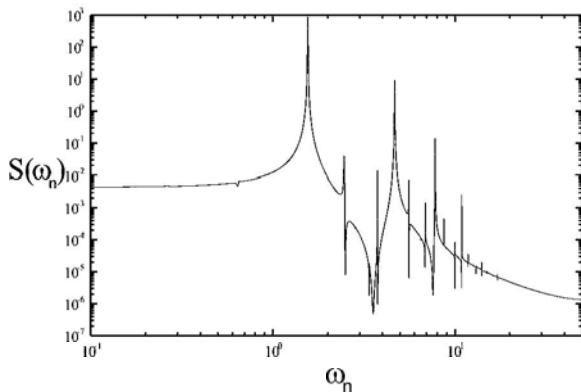


Fig. 4. Power spectrum corresponding to Fig.2.

In Fig.3 and Fig.4 power spectra of the solution $x(t)$ for the Duffing equation (10) are shown. One can clearly see that by means of the stabilizing perturbation (11) it is possible to suppress chaos.

Thus, the numerical analysis is in a fine agreement

with analytical results.

V. CONCLUSION

Analysis of the separatrix splitting is a quite convenience method for investigations of dynamical systems. This is due to the fact that it allows us to get conditions of the integrability and non-integrability. At the same time, now the problem of chaos suppression is mainly considered numerically (see, e.g. [5], [6], [7], [8] and references therein). However, one of the remarkable facts of the study of this phenomenon with the point of view of the analysis of asymptotic trajectories is the possibility of its *analytical* treatment. For systems with a separatrix loop, as a result of perturbation we can find the distance between splitted branches.

In the present paper, on the basis of the Melnikov method we analytically considered the effect of perturbations on a two-dimensional non-autonomous system. In general, we have got an explicit form of the external stabilized perturbations which allows us to suppress chaos. By this reason the obtained results can be applied to the systems and models of various nature in which the separatrix splitting phenomenon is inherent.

REFERENCES

- [1] V. K. Melnikov. Stability of the center at periodic perturbations. *Trans. Moscow Math. Soc.* **12A** pp.1–49, 1963.
- [2] A. Loskutov, A. Janoev. Suppression of chaos in the separatrix neighbourhood. *JETP* **125**, No4, 2004.
- [3] R. Lima, M. Pettini. Suppression of chaos by resonant parametric perturbations. *Phys. Rev. A* **41**, No2, pp.726–733, 1990.
- [4] R. Chacón. Suppression of chaos by selective resonant parametric perturbations. *Phys. Rev. E* **51**, No1, pp.761–764, 1995.
- [5] S. Boccaletti, C. Grebogi, Y.-C. Lai, H. Mancini, D. Maza. The control of chaos: theory and applications. *Phys. Rep.* **329**, pp.103–197, 2000.
- [6] T. Shinbrot, C. Grebogi, E. Ott, J. A. Yorke. Using small perturbations to control chaos. *Nature* **363**, p.411–417, 1993
- [7] E. Ott, M. L. Spano. Controlling chaos. *Physics Today* **48**, No5, pp.34–40, 1995.
- [8] A. Loskutov. Chaos and control in dynamical systems. *Computational Math. and Modeling* **12**, No4, pp.314–352, 2001.

ON THE EXISTENCE OF PERIODIC SOLUTIONS TO THE EQUATION OF A FORCED NONLINEAR OSCILLATOR

O. Makarenkov

Department of mathematics,
Voronezh State University,
Voronezh, Russia
e-mail: omakarenkov@kma.vsu.ru

February 16, 2004

Abstract—*In this paper we provide a topological prove of the periodic solutions existence result of the classical averaging principle, which permit us to obtain an explicit estimation for the small parameter. By using this result we provide a condition for the nonlinearity parameters in a forced nonlinear oscillator to guarantee the existence of periodic solutions.*

I. INTRODUCTION

Since Van der Pol an averaging principle is one of most relevant mathematical tools to investigate a periodic processes in a forced oscillator with small nonlinearity. Indeed, the mathematical model of such oscillator near resonance is the following second order differential equation (see [1])

$$\ddot{x} + w^2x = \mu f(x, \dot{x}) + \mu E \sin wt, \quad (1)$$

where w is a natural frequency of the oscillator, $f : \mathbb{R} \times \mathbb{R} \rightarrow \mathbb{R}$ is a continuously differentiable nonlinear function which describes a nonlinearity (nonlinear resistance, saturable-core inductance or other) and $\mu > 0$ is a small parameter. By the change of variables

$$\begin{aligned} y_1(t) &= x(t) \cos wt - \dot{x}(t) \sin wt, \\ y_2(t) &= x(t) \sin wt + \dot{x}(t) \cos wt. \end{aligned} \quad (2)$$

the equation (1) can be rewritten in the form

$$\dot{y} = \mu F(t, y), \quad (3)$$

where $F : \mathbb{R} \times \mathbb{R}^2 \rightarrow \mathbb{R}^2$ is continuously differentiable and $2\pi/w$ -periodic with respect to the first variable function. It is called averaging principle the following famous result on existence of periodic solutions to

the system (3) (see [2], [3], [4]) and so to the system (1).

Theorem 1. *Let a point $\xi_0 \in \mathbb{R}^2$ such that*

$$F_0(\xi_0) = 0 \quad (4)$$

and

$$0 \notin \text{Re}(\sigma(F_0(\xi_0))), \quad (5)$$

where

$$F_0(\xi) = \int_0^T F(\tau, \xi) d\tau.$$

Then for $0 < \mu < \mu_0$, where μ_0 is a sufficiently small number, the system (3) has a T -periodic solution y_μ satisfying

$$y_\mu(t) \rightarrow \xi_0 \text{ as } \mu \rightarrow 0 \quad (6)$$

uniformly with respect to $t \in [0, T]$.

By using the last result it were obtained many interesting phenomenons in a forced nonlinear oscillator, in particular, the effect of frequency entrainment (see [4] and [1]). But as it was observed in [5] for lack of explicit value of ε_0 the application of averaging principle to a practical problems leads sometimes to mistakes. Some papers are devoted to this problem (see, for example, [6]), but for the best knowledge of the author there is no a common approach to evaluate ε_0 .

In the past few years, several contributions have been made toward a topological approach in averaging principle. For example, in [7] such approach permits the author to deal with the case when (5) is not satisfied, in [8] by topological technic the authors eliminate the differentiability assumption on the function F . A topological proof of an averaging method is provided also

in [9] for a class of the systems of differential equations. A topological generalizations of some Poincaré-Malkin theorems on small parameter method (see [2]) are given in [10] and [11]. By means of topological approach we will obtain the explicit value of ε_0 in the present paper.

The paper is organized as following. In the next section we provide our averaging approach, which coincide with the theorem 1 of this section, but contain an explicit estimation for the parameter ε . In the section 3 we apply our result to the equation (1) describes a valve oscillator with a polinomial dynamic characteristic of valve.

II. THE EXPLICIT FORMULA FOR THE CONSTANT ε_0

For a bounded set $U \subset \mathbb{R}^2$ introduce the constants

$$\begin{aligned} M_U &= \max_{t \in [0, T], \xi \in \bar{U}} \|F(t, \xi)\|, \\ M_U &= \max_{t \in [0, T], \xi \in \bar{U}} \|F_\xi(t, \xi)\|, \\ K_U &= \min_{\xi \in \partial U} \|F_0(\xi)\|. \end{aligned}$$

Theorem 2. Let the point $\xi_0 \in \mathbb{R}^2$ satisfying the conditions (4) and (5) of the theorem 1. Consider an open bounded set $U \subset \mathbb{R}^2$ contained the point ξ_0 and such that the map F_0 doesn't vanish on the set $U \setminus \{\xi_0\}$. Then for

$$0 < \mu < \frac{2K_U}{T^2 M_U M_U} \tag{7}$$

the system (3) has a T -periodic solution y_μ satisfying (6) uniformly with respect to $t \in [0, T]$.

Proof. Let us show that by the condition (7) the compact vector field

$$(F_\mu x)(t) = x(t) - x(T) - \mu \int_0^t f(\tau, x(\tau)) d\tau,$$

linearly homotopic (for all topological notions of this proof see, for example, [12]) to the field

$$(F_{0,\mu} x)(t) = x(t) - x(T) - \mu \int_0^T f(\tau, x(\tau)) d\tau$$

on the boundary of the set

$$W = \{x : x \in C_T, x(t) \in U, t \in [0, T]\},$$

where we denoted by C_T the space of all continuous functions acting from $[0, T]$ to \mathbb{R}^2 . Assume contrary, therefore there exist $\mu > 0$ satisfying (7) and $x_\mu \in \partial W$ such that

$$\begin{aligned} x_\mu(t) &= x_\mu(T) + \lambda \mu \int_0^t f(\tau, x_\mu(\tau)) d\tau + \\ &+ (1 - \lambda) \mu \int_0^T f(\tau, x_\mu(\tau)) d\tau, \end{aligned} \tag{8}$$

where $\lambda \in [0, 1]$. Since $x_\mu \in \partial W$ there exists $t_\mu \in [0, T]$ satisfying $x_\mu(t_\mu) \in \partial U$. We have

$$\begin{aligned} &\left\| \int_{t_\mu - \frac{T}{2}}^{t_\mu + \frac{T}{2}} f(\tau, x_\mu(\tau)) d\tau - \int_{t_\mu - \frac{T}{2}}^{t_\mu + \frac{T}{2}} f(\tau, \zeta_\mu) d\tau \right\| \leq \\ &\leq \max \left\{ \max_{t \in I_{1,\mu}} \|f(t, x_\mu(t)) - f(t, \zeta_\mu)\|, \right. \\ &\quad \left. \max_{t \in I_{2,\mu}} \|f(t, x_\mu(t)) - f(t, \zeta_\mu)\| \right\} \cdot T \leq \\ &\leq \frac{\mu T^2 M'_U M_U}{2} < K_U, \end{aligned} \tag{9}$$

where $\zeta_\mu = x_\mu(t_\mu)$, $I_{1,\mu} = [t_\mu - \frac{T}{2}, t_\mu]$

and $I_{2,\mu} = [t_\mu, t_\mu + \frac{T}{2}]$.

But, from (8) with $t = T$ we have

$$\int_0^T f(\tau, x_\mu(\tau)) d\tau = 0,$$

and so

$$\int_{t_\mu - \frac{T}{2}}^{t_\mu + \frac{T}{2}} f(\tau, x_\mu(\tau)) d\tau = 0.$$

Therefore from (9) we obtain

$$\left\| \int_{t_\mu - \frac{T}{2}}^{t_\mu + \frac{T}{2}} f(\tau, \zeta_\mu) d\tau \right\| < K_U,$$

and so

$$\left\| \int_0^T f(\tau, \zeta_\mu) d\tau \right\| < K_U,$$

which contradict the definition of K_U . So, by the condition (7)

$$\deg_{C_T}(F_\mu, W) = \deg_{C_T}(F_{0,\mu}, W).$$

By a coincidence degree theorem (see, for example, theorem 27.1 from [12])

$$\deg_{C_T}(F_{0,\mu}, W) = \deg_{\mathbb{R}^n}(F_{0,\mu}, U)$$

and since the fields $F_{0,\mu}$, $F_{0,1}$, are linearly homotopic on ∂U we have

$$\deg_{\mathbb{R}^n}(F_{0,\mu}, U) = \deg_{\mathbb{R}^n}(F_{0,1}, U).$$

From the last three equalities we obtain

$$\deg_{C_T}(F_\mu, W) = \deg_{\mathbb{R}^n}(F_{0,1}, U).$$

But by the conditions (4) and (5) $\deg_{\mathbb{R}^n}(F_{0,1}, U) \neq 0$ and so by a property of topological degree we obtain that the field $F_{0,\mu}$ has at least one zero point belonging to the set W for any μ satisfying (7).

III. APPLICATION TO THE SYSTEM (1)

In this section we apply the theorem 2 to the equation (1) in the case

$$f(x, \dot{x}) = hx - (\delta - \gamma x + Kx^2) \dot{x},$$

which correspond to a valve oscillator with a polinomial dynamic characteristic of valve and where it is denoted by h a derangement of the frequency of an external force from the natural frequency of the oscillator (see [1], [4]).

It is known that the system (1) of this form may have more than one periodic solutions, but to illustrate our approach we restrict ourself by only the existence of

periodic solutions which tends to 0 as $\mu \rightarrow 0$. Also to simplicity we consider $w = 1$.

We can prove the following result.

Theorem 3. *Let $r > 0$ such, that*

$$r\sqrt{(Kr^2 + 4\delta)^2 + 16h^2} - 4E > 0. \quad (10)$$

Then for

$$0 < \mu < \frac{\left(r\sqrt{(Kr^2 + 4\delta)^2 + 16h^2} - 4E\right)^2}{(24Kr^2 + 8\gamma r + h + \delta)} \cdot \frac{1}{2(8Kr^3 + 4\gamma r^2 + 2(h + \delta)r + E)} \quad (11)$$

the equation (1) has a 2π -periodic solution inside the ball of the radius r .

Proof. Denote by B_r the inward of the ball of the radius r . After the change of variables (2) and reduction of equation (1) to the standart form (3) we find the following values:

$$M_{B_r} \leq \sqrt{2} (8Kr^3 + 4\gamma r^2 + 2(h + \delta)r + E),$$

$$M_{B_r} \leq \sqrt{2} (24Kr^2 + 8\gamma r + h + \delta),$$

while for f_0 we have the following expression

$$F_0(\xi) = \frac{\pi}{4} \begin{pmatrix} -K\xi_1(\xi_1^2 + \xi_2^2) - 4\delta\xi_1 - 4h\xi_2 - 4E \\ -K\xi_2(\xi_1^2 + \xi_2^2) - 4\delta\xi_2 + 4h\xi_1 \end{pmatrix}.$$

It is easy to verify that if for any $\phi \in [0, 2\pi]$

$$-Kr^3 \cos \phi - 4\delta r \cos \phi - 4hr \sin \phi > 4E$$

then the conditions (4) and (5) hold. Observe, that the last condition coincide with (10). Finally, we obtain the following estimation for K_{B_r} :

$$K_{B_r} = \left(r\sqrt{(Kr^2 + 4\delta)^2 + 16h^2} - 4E\right)^2.$$

To finish the proof of this theorem it is now enough to apply the theorem 2 with $U = B_r$.

In the last theorem we considered the point $\xi=0$ satisfying (4) for simplicity. It easy to see that with the same reasons the theorem 2 can be applied to any another point ξ satisfying (4).

This work is partially supported by Russian Foundation for Basic Research grants 02-01-00189, 02-01-00307 and by U.S.CRDF – RF Ministry of Education grant VZ-010.

References

[1] J. J. Stoker. *Nonlinear Vibrations. Interscience Publishers*, New York, 1950.

[2] I. G. Malkin. Some problems of the theory of nonlinear oscillations. *M.: Gostechizdat*, 1956 (In Russian).

[3] N. N. Bogolyubov and Yu.A. Mitropol'skii. *Asymptotic methods in the theory of non-linear oscillations*. Moscow, Fizmatgiz, 1963 (In Russian).

[4] A. A. Andronov and S. E. Chaikin. *Theory of Oscillations. Princeton University Press*, Princeton, NJ, 1949.

[5] N. N. Bautin. A behaviour of dynamical systems near the boundaries of a stability regions. *L.: Gostechizdat*, 1949 (In Russian).

[6] Yu. A. Riabov. On estimations of applicability region of small parameter method in the problems of nonlinear oscillations. *In book of Proceedings of International Symposium on Nonlinear Oscillations*, Vol. II, Kiev: AN USSR, 1963 (In Russian).

[7] M. I. Kamenskii. On a modification of averaging principle for degenerated equations. *Doklady Akademii Nauk*, Vol. 347, N 2, 1996, pp. 151-153.

[8] A. Buica and J. Llibre. Averaging methods for finding periodic orbits via Brouwer degree. To appear in *Bull. Sci. Math*.

[9] V. V. Strygin. The averaging principle for the equations with a heredity, *Ukrainian math. journal*, Vol. 22, N 4, 1970, pp. 503-513.

[10] M. I. Kamenskii, O. Yu. Makarenkov and P. Nistri. A new approach in the theory of ordinary differential equations with small parameter. *Doklady Akademii Nauk*, Vol. 388, 2003, pp. 439-442.

[11] M. Kamenskii, O. Yu. Makarenkov and P. Nistri. Small parameter perturbations of nonlinear periodic systems. *Nonlinearity*, 17, 2004, 193-205, to appear. (Available in electronic form).

[12] M. A. Krasnoselski and P. P. Zabreyko. *Geometrical Methods of Nonlinear Analysis. Berlin: Springer*, 1984.

SYNCHRONIZABILITY OF POWER-LAW AND FRACTALLY COUPLED DYNAMICAL NETWORKS

Máté Maródi

DFG Research Center, Institute of Mathematics WE1
 Free University,
 Berlin, Germany
 e-mail: marodi@math.fu-berlin.de
 WWW: <http://dynamics.mi.fu-berlin.de/>

Abstract—*Systems of coupled dynamical networks are studied from the point of view of synchronizability. Power-law and fractally coupled networks are introduced through a parameter which describes the spatial decay of interaction. The spectral properties are compared, and a critical value of the relevant parameter is identified, below which increasing the system size increases synchronizability. It is found by numerical computations that for fractally coupled networks this critical value is strictly higher than for power-law coupled systems.*

I. INTRODUCTION

Networks of coupled dynamical units have received much attention recently. These systems play an important role in many fields of life, including biology, neuroscience, communication technology, solid state physics. Especially interesting is the effect of the network structure on the system dynamics [1].

Amongst the many dynamical features, synchronization is of particular interest. The synchronization of interacting systems may give insight to the behavior of several interesting and essential phenomena (see, for example [2], [3]). Recently general methods have been developed for studying the collective synchronization of networks of coupled dynamical systems [4], [5]. These methods induced the investigation of different coupling topologies, including small-world [6], [7] or scale-free networks [8].

In this contribution we compare the synchronizability of two network models which try to capture the phenomena that occurs in real-world networks: the connection is “weaker” between nodes that are “more separated”. In Sec. II we review the methods for synchronization stability and in the next Section we introduce power-law and fractally coupled networks. Spectral properties related to synchronizability are studied in Sec. IV and consequences regarding synchronization are discussed.

II. BACKGROUND

In the following we outline the techniques developed recently for synchronization stability (see, e.g. [4], [5]). Let us consider a system of N coupled oscillators. The dynamics of each uncoupled node is identical:

$$\dot{\mathbf{x}}_i = \mathbf{f}(\mathbf{x}_i),$$

where $\mathbf{x}_i \in \mathbb{R}^m$ ($i = 1, \dots, N$) is the state variable. The coupled system is assumed to be in the form:

$$\dot{\mathbf{x}}_i = \mathbf{f}(\mathbf{x}_i) - K \sum_j A_{ij} \mathbf{H} \mathbf{x}_j, \quad (1)$$

where $K > 0$ is the universal coupling strength, and the coupling structure is included in the interaction matrix \mathbf{A} , which contains information about the - possibly weighted - coupling graph. The matrix \mathbf{H} defines which components of the state variables are involved in the interaction, and is assumed to be diagonal, with H_{ii} being either 0 or 1. We also assume, that \mathbf{A} has 0 row-sums, with non-positive off-diagonal elements:

$$A_{ij} \leq 0 \quad i \neq j, \quad (2a)$$

$$A_{ii} = - \sum_{j=i} A_{ij}. \quad (2b)$$

This property arises naturally for diffusively coupled systems. In this case \mathbf{A} can be considered as the Laplacian of the coupling graph.

The system is called synchronized if

$$\mathbf{s}(t) = \mathbf{x}_1(t) = \mathbf{x}_2(t) = \dots = \mathbf{x}_N(t),$$

which defines the invariant synchronization manifold. Linear perturbation theory around this solution leads to a variational equation, which can be block diagonalized, since the uncoupled dynamics is the same for every node. This uncouples the variational equation into mutually transverse blocks:

$$\dot{\xi}_j = (\mathbf{Df}(\mathbf{s}) - K \lambda_j \mathbf{H}) \xi_j, \quad (3)$$

where λ_j is the j -th eigenvalue of \mathbf{A} . Thus, the problem of stability is separated into two parts: the stability problem of the variational equation parametrized by λ , and a spectral problem. The first depends only on the given node dynamics (and the synchronized solution), while the second depends on the coupling network structure.

We denote the ordered eigenvalues by $\lambda_1 \leq \lambda_2 \leq \dots \leq \lambda_N$. Since \mathbf{A} has 0 row-sums, we always have an eigenvalue $\lambda_1 = 0$, which corresponds to the motion along the synchronization manifold. If the network is connected, then all other eigenvalues are strictly positive. For a large class of systems and parameter ranges the spectral problem reduces to the determination of λ_2 [4], which we identify in the following with *synchronizability*. In particular, in [4] the authors showed that for symmetric diagonal coupling synchronization is asymptotically stable if

$$\lambda_2 \geq T/K. \tag{4}$$

Here $T > 0$ is chosen in a way that the self-feedback uncoupled node is stable, where T denotes the feedback strength.

III. THE TWO MODELS

Usual network models (e.g. small-world, scale free, etc.) are expressed only in graph theoretical terms, i.e. in terms of the sets of vertices and edges. However the modeling of real world phenomena sometimes requires additional assumptions. Both models discussed here are intended to capture the rather widespread phenomenon, where “wider separation” means “weaker” interaction in some sense.

First we define distance, which assumes the existence of an embedding metric space where the distance between two vertices is independent of the graph structure. This metric space corresponds to usual physical space or it can include abstract spaces as well. For simplicity, in the following we assume that vertices are located on a 1-dimensional grid with periodic boundary conditions. Distance is the usual Euclidean distance and the unit is equal to the grid spacing.

The difference between the two models is in the way they contain the “weakness” property.

A. Power-law coupling

First, consider a network where all elements are connected to each other, but the strength of the coupling decays in space according to some power α of the distance. Thus the off-diagonal elements of the

coupling matrix \mathbf{A}^p are:

$$A_{k\ell}^p = -\frac{1}{r_{k\ell}^\alpha} \quad \text{for } k \neq \ell$$

where $r_{k\ell} = \min_n \mathbb{Z} |k - \ell + nN|$ is the distance between two sites, and $\alpha \geq 0$. The diagonal elements satisfy condition (2b). Clearly, \mathbf{A}^p is symmetric. We call this arrangement *power-law coupling*.

This setup might be applied to model systems where the interaction is via some spatially decaying physical intensity or some rapidly diffusing chemical substance. Recent developments connected to this model can be found in [9], [10], [11].

B. Fractal coupling

Fractally coupled networks were introduced in [12] to describe certain collective neural phenomena in networks where the dendritic branching shows fractal properties. Similar networks can be used to model magnetic properties of linear polymer chains [13], [14]. Here all the existing connections are equally weighted, but the *probability* that two nodes are connected decays in space according to a power-law of the distance, i.e. for $A_{k\ell}^f, \ell > k$ we have:

$$A_{k\ell}^f = \begin{cases} -1 & \text{with probability } p = \frac{1}{r_{k\ell}^\alpha} \\ 0 & \text{with probability } q = 1 - p \end{cases}$$

We require that $A_{k\ell}^f = A_{\ell k}^f$, and also condition (2b) should be satisfied. This defines a one-parameter family of graph ensembles, which we call the *fractally coupled* model.

C. A first comparison

In graph theoretical terms one can say that power-law coupled networks are complete weighted graphs, while fractally coupled networks are non-complete, and all the edges have the same weight. In spite of this, it is clear that the two models are similar in many ways. In particular

$$A_{k\ell}^p = \langle A_{k\ell}^f \rangle,$$

i.e. the expectation value of the elements of the Laplacian matrix of the fractally coupled network is equal to the corresponding element of the Laplacian of the power-law model. However, this equivalence does not guarantee the dynamical similarity, since (as it was indicated in Sec. II) it is determined by the spectral properties. Clearly, from the above equivalence does not follow a similar relation for the spectra.

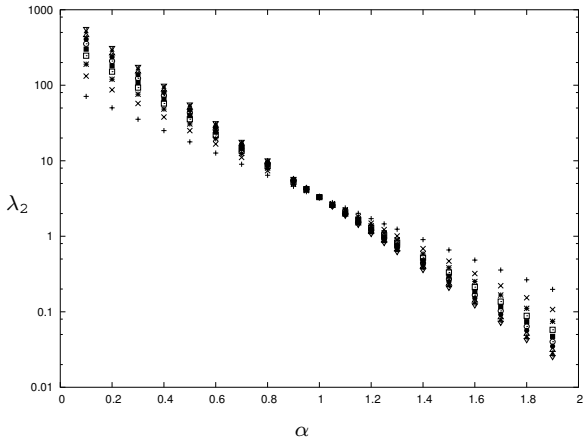


Fig. 1. The second eigenvalue λ_2 as a function of parameter α for the power-law coupled model for different N (from $N = 1001$ (down triangles) to $N = 101$ (pluses), with steps of 100).

For the two limiting cases of the values of α the two models coincide. For $\alpha = 0$ we obtain the globally uniformly coupled model, while for $\alpha \rightarrow \infty$ the nearest neighbor coupling is retrieved. These two cases are amongst the most frequently studied connection schemes.

IV. SPECTRAL PROPERTIES

As we briefly discussed it in Sec. II, the stability of a given network of identical dynamical units depends on the spectral properties of the coupling matrix \mathbf{A} . Note that here $\lambda_2 = \lambda_2(\alpha, N)$, i.e. in general, synchronizability depends on both the parameter and the size. We will be mainly interested in the behavior as the size is increased for given α .

First let us consider the two limiting cases where the two models coincide. For $\alpha = 0$ the spectrum of \mathbf{A} is

$$\lambda_1 = 0, \quad \lambda_j = N, \quad j = 2, \dots, N.$$

In the nearest neighbor coupled case ($\alpha \rightarrow \infty$) the first non-zero eigenvalue is

$$\lambda_2 = 4 \sin^2 \left(\frac{\pi}{N} \right).$$

From these well known results one can conclude that for fixed coupling strength K the increase in system size increases (decreases) synchronizability for globally (nearest neighbor) coupled networks. As α defines a continuous transitions between the two extremes, one can expect that there exists a critical value α_c where this change occurs.

For the power-law coupled model the coupling Laplacian is circulant and the spectrum can be calcu-

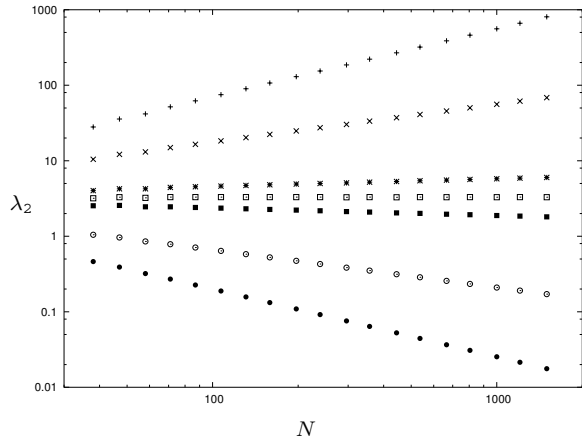


Fig. 2. The second eigenvalue λ_2 as a function of N for the power-law coupled model for selected α values (from top to bottom: $\alpha = 0.1, 0.5, 0.9, 1.0, 1.1, 1.5,$ and 1.9).

lated analytically via Fourier-representations. Assuming N is odd, for the second eigenvalue we get:

$$\lambda_2 = 4 \sum_{k=1}^{(N-1)/2} \frac{\sin^2 \left(\pi \frac{k}{N} \right)}{k^\alpha}.$$

The values of λ_2 as a function of α are plotted in Fig. 1 for different sizes. Note, that for $\alpha < 1$ relation $N_1 < N_2$ implies $\lambda_2(N_1) < \lambda_2(N_2)$, while for $\alpha > 1$ the opposite holds.

It can be seen that for $N \rightarrow \infty$ and fixed $\alpha > 1$ $\lambda_2 \rightarrow 0$. Also, for $\alpha < 1$, λ_2 diverges. The second eigenvalue λ_2 behaves like $\lambda_2 \sim N^{\beta(\alpha)}$ (see Fig. 2), with $\beta(\alpha) \approx 1 - \alpha$ around $\alpha = 1$, and $\beta(\alpha)$ monotone increasing. This implies a change in the behavior of large systems: for $\alpha > 1$ increasing the size will result larger sensitivity to small perturbations, while for $\alpha < 1$, the system becomes more stable, its synchronizability improves.

Now let us consider the fractally coupled network. Clearly, fractally coupled graphs defined in Sec. III are connected for every $\alpha \geq 0$, thus $\lambda_2 > 0$. There is no known analytical method to determine the spectra of such graphs, thus we investigate them numerically. Because of randomness, averaged quantities are studied. Results for $\langle \lambda_2 \rangle$ as a function of the parameter α can be seen in Fig. 3. One can observe a similar transition phenomenon as for power-law coupling, but apparently the crossing point is shifted to $\alpha > 1$ (see inset in Fig. 3). Note also, that it seems that α_c is independent of the system size N .

The location of the transition point can be further investigated by studying the behavior of $\langle \lambda_2 \rangle$ for fixed α as the size is increased. Numerical results are plotted in Fig. 4. From the figure it can be seen that we

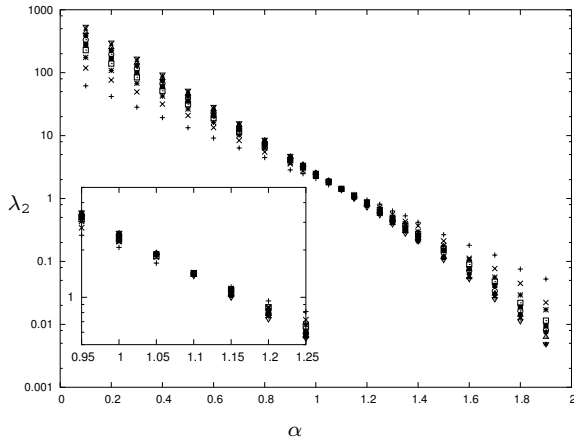


Fig. 3. The average second eigenvalue $\langle \lambda_2 \rangle$ as a function of parameter α for the fractally coupled model for different N (from $N = 1001$ (down triangles) to $N = 101$ (pluses), with steps of 100). Each point represents an average over 25 realizations of the model. Inset: region around α_c .

can assume that the large N behavior can be approximated as $\langle \lambda_2 \rangle \sim N^{\beta(\alpha)}$. The critical value α_c of the crossing point can be determined from $\beta(\alpha_c) = 0$, which gives $\alpha_c \approx 1.1 > 1$. This value is in agreement with the results in [12], where the authors located the transition to the range $1 < \alpha_c < 2$. Below the critical α value larger N results in improved synchronizability, while for $\alpha > \alpha_c$ one needs to increase K to maintain an originally synchronized state.

Finally we remark, that the results above can be checked by direct investigation of given dynamical systems. For example, using condition (4) boundaries of the synchronization region in the (α, N) space can be determined and compared to actual results from direct (numerical) solutions of system (1).

ACKNOWLEDGMENTS

This research has been supported by the DFG Research Center “Mathematics for key technologies” (FZT 86) in Berlin. The author is grateful to Stefan Liebscher and Bernold Fiedler for helpful discussions and suggestions to the manuscript.

REFERENCES

[1] S. H. Strogatz. Exploring complex networks. *Nature (London)*, 410:268–276, 2001.
 [2] Y. Kuramoto. *Chemical Oscillations, Waves, and Turbulence*. Springer, Berlin, 1984.
 [3] A. Pikovsky, M. Rosenblum, and J. Kurths. *Synchronization - A Universal Concept in Nonlinear Sciences*. Cambridge University Press, 2001.
 [4] C. W. Wu and L. O. Chua. Synchronization in an Array of Linearly Coupled Dynamical Systems. *IEEE Trans. Circuits Syst. I*, 42(8):430–447, 1995.

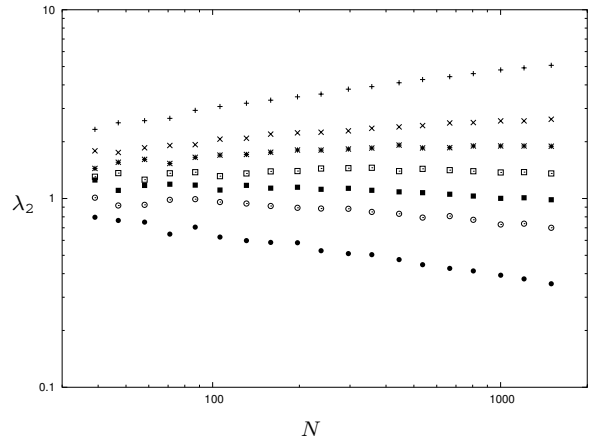


Fig. 4. The average second eigenvalue $\langle \lambda_2 \rangle$ as a function of N for the fractally coupled model for selected α values (from top to bottom: $\alpha = 0.9, 1.0, 1.05, 1.1, 1.15, 1.2, 1.3$). Each point represents an average over 25 realizations of the model.

[5] L. M. Pecora and Th. L. Carroll. Master Stability Functions for Synchronized Coupled Systems. *Phys. Rev. Lett.*, 80(10):2109–2112, 1998.
 [6] M. Barahona and L. M. Pecora. Synchronization in Small-World Systems. *Phys. Rev. Lett.*, 89:054101, 2002.
 [7] X. F. Wang and G. Chen. Synchronization in Small-World Dynamical Networks. *Int. J. Bifurcation Chaos*, 12(1):187–192, 2002.
 [8] X. F. Wang and G. Chen. Synchronization in Scale-Free Dynamical Networks: Robustness and Fragility. *IEEE Trans. Circuits Syst. I*, 49(1):54–62, 2002.
 [9] J. L. Rogers and L. T. Wille. Phase transitions in nonlinear oscillator chains. *Phys. Rev. E*, 54(3):R2193–R2196, 1996.
 [10] C. Anteneodo, S. E. de S. Pinto, A. M. Batista, and R. L. Viana. Analytical results for coupled-map lattices with long-range interactions. *Phys. Rev. E*, 68:045202(R), 2003.
 [11] M. Maródi, F. d’Ovidio, and T. Vicsek. Synchronization of oscillators with long range interaction: Phase transition and anomalous finite size effects. *Phys. Rev. E*, 66:011109, 2002.
 [12] S. Raghavachari and J. A. Glazier. Spatially Coherent States in Fractally Coupled Map Lattices. *Phys. Rev. Lett.*, 74(16):3297–3300, 1995.
 [13] S. Jespersen and A. Blumen. Small-world networks: Links with long-tailed distributions. *Phys. Rev. E*, 62(5):6270–6274, 2000.
 [14] P. Sen and B. K. Chakrabarti. Small-world phenomena and the statistics of linear polymers. *J. Phys. A: Math. Gen.*, 34:7749–7755, 2001.

EXCITATION-RESHAPING-INDUCED CHAOTIC ESCAPE FROM A POTENTIAL WELL

J. A. Martínez^a and R. Chacón^b

^a Departamento de Ingeniería Eléctrica, Electrónica y Automática, Escuela Politécnica Superior, Universidad de Castilla-La Mancha, E-02071 Albacete, Spain

e-mail: martinez@iele-ab.uclm.es

^b Departamento de Electrónica e Ingeniería Electromecánica, Escuela de Ingenierías Industriales, Universidad de Extremadura, Apartado Postal 382, E-06071 Badajoz, Spain

e-mail: rchacon@unex.es

Abstract—*The chaotic escape of a damped oscillator excited by a periodic string of symmetric pulses of finite width and amplitude from a cubic potential well that typically models a metastable system close to a fold is investigated. Analytical (Melnikov analysis) and numerical results show that chaotic escapes are typically induced over a wide range of parameters by hump-doubling of an external excitation which is initially formed by a periodic string of single-humped symmetric pulses. The analysis reveals that the chaotic escape threshold amplitude when altering solely the pulse shape presents a minimum as a single-humped pulse transforms into a double-humped pulse, the remaining parameters being held constant.*

I. INTRODUCTION

Escape from a potential well is an ubiquitous phenomenon in nature. Instances are known in astrophysics [1], chemistry [2], hydrodynamics [3], quantum optics [4], etc., where complex escape phenomena can often be well described by a low-dimensional system of differential equations. In most cases, escape is induced by a *harmonic* (external or parametric) excitation added to the model system [5]-[7], so that, before escape, chaotic transients of unpredictable duration (due to the fractal character of the basin boundary) are usually observed. However, real-world excitations exhibit a great diversity of waveforms as well as many complex transitions from one to another as the system's parameters change. In general, to consider periodic excitations with arbitrary waveform implies extending the amplitude-period parameter space to include the parameters, s_i , that control the excitation waveform. In physical terms this means that, for fixed period and amplitude, the parameters s_i are responsible for the temporal rate at which energy is transferred from the excitation mechanism to the system. Since the choice of a specific mathematical function to model a given real-world excitation

determines, to a great extent, which range of phenomena it could suitably characterize, one would like to use an excitation function which generates a great diversity of waveforms with few parameters s_i . In this regard, the Jacobian elliptic functions (JEF) [8] appear to be suitable candidates fulfilling the aforementioned requirement, since their shapes can be controlled by a single parameter: the elliptic parameter m . This choice is quite natural since the solutions of the most universal nonlinear integrable oscillators (such as the pendulum, and Helmholtz's and Duffing's oscillators) [9] are given in terms of JEF's. With the help of JEF's, there has recently been undertaken the study of excitation-reshaping-induced transitions in a broad class of damped nonautonomous systems [10]-[13]. In particular, some order↔chaos routes have been found to be especially rich when altering solely the width of a *single*-humped periodic excitation [12]-[13].

In this present work we study the chaotic escape of the following universal model

$$\ddot{x} = -x + \beta x^2 - \delta \dot{x} + \gamma N(m) \operatorname{sn}[\Phi(t); m] \operatorname{dn}[\Phi(t); m], \quad (1)$$

when only the excitation shape is varied from *single*-humped to *double*-humped. Here, $\Phi(t) \equiv 4K(m)t/T$, $\operatorname{sn}(u; m)$ and $\operatorname{dn}(u; m)$ are JEF's of parameter m ($K(m)$ is the complete elliptic integral of the first kind), and $N(m)$ is a normalization function (Boltzmann form), $N(m) \equiv \left\{ a + b [1 + \exp((m-c)/d)]^{-1} \right\}^{-1}$, with $a \equiv 0.43932$, $b \equiv 0.69796$, $c \equiv 0.3727$, $d \equiv 0.26883$, which is introduced for the excitation function to have the same amplitude, γ , and period, T , for any waveform (i.e., $\forall m, m \in [0, 1]$). The excitation function $F(t; m, T) \equiv N(m) \operatorname{sn}[\Phi(t); m] \operatorname{dn}[\Phi(t); m]$ is used as an example to illustrate the chaotic escape induced by hump-doubling. This new mechanism of enhancement of chaotic escape could be relevant in

excitable systems (such as neurons and other types of cells as well as some chemical reactions) to increase the firing rates without changing the amplitude and period of the stimulus. When $m = 0$, then $F(t; m = 0, T) = \sin(2\pi t/T)$, i.e., one recovers the previously studied case of a single-humped (harmonic) excitation [3]. This is relevant to comparing the structural stability of the universal escape model when solely the excitation shape is varied from a single-humped shape to a double-humped shape. Since $\text{dn}[4K(m)t/T; m]$ represents a periodic string of asymmetric pulses, whose effective width decreases as m increases from $m = 0$, in the limiting value $m = 1$ the excitation function $F(t; m, T)$ vanishes except on a set of instants that has Lebesgue measure zero, i.e., one recovers the purely damped system.

The rest of the paper is organized as follows. In Sec. II we derive analytical results based on a Melnikov analysis (MA) concerning the threshold of chaotic escape in the parameter space (β, m, T) . In Sec. III we present numerical evidence supporting the theoretical predictions from previous section. Finally, Sec. IV gives a brief summary of the findings.

II. THEORETICAL APPROACH

To obtain an estimate for the threshold of chaotic escape in the parameter space (β, m, T) , we apply MA [14]-[15] to our universal model for the case of weak damping and excitation ($0 < \delta, \gamma \ll 1$). As is well known, MA predictions for the appearance of chaos are both limited (only valid for orbits starting at points sufficiently near the separatrix of the underlying conservative system) and approximate (the MA is a perturbative method). (For a general background, see for example [15].) It is worth mentioning that the criterion for a homoclinic tangency (accurately predicted by MA) in diverse systems [16] is coincident with the change from a smooth to an irregular, fractal-looking basin boundary [17]. These results connect MA predictions with those concerning the erosion of the basin boundary. The application of MA to Eq. (1) involves calculating the Melnikov function,

$$M(t_0) = -\delta \int_{-\infty}^{\infty} \dot{x}_0^2(t) dt + \gamma \int_{-\infty}^{\infty} \dot{x}_0(t) F(t + t_0; m, T) dt, \quad (2)$$

where $x_0(t) = 1 - 3[1 + \cosh(t)]^{-1}$, $\dot{x}_0(t) = 3 \sinh(t)[1 + \cosh(t)]^{-2}$ is the separatrix of the underlying conservative system ($\delta = \gamma = 0$) in parametric form. Substituting $x_0(t), \dot{x}_0(t)$ into (2), after some

algebraic manipulation we obtain

$$M(t_0) = -D - A \sum_{n=0}^{\infty} a_n(m) p_n(T) \cos(\Omega_n t_0), \quad (3)$$

with

$$D \equiv \frac{6\delta}{5\beta^2}, A \equiv \frac{12\pi^5 \gamma N(m)}{\beta \sqrt{m} K^2(m)}, \Omega_n \equiv \frac{(4n+2)\pi}{T} \quad (4)$$

$$a_n(m) \equiv (2n+1)^3 \operatorname{sech} \left[\frac{(2n+1)\pi K(1-m)}{2K(m)} \right], \quad (5)$$

$$p_n(T) \equiv \frac{1}{T^2} \operatorname{csch} \left[\frac{(4n+2)\pi^2}{T} \right]. \quad (6)$$

If $M(t_0)$ has a simple zero, then a homoclinic bifurcation occurs, signifying the *possibility* of chaotic escape. From Eq. (3) one sees that a homoclinic bifurcation is guaranteed if

$$\frac{\delta}{\gamma} < U(\beta, m, T), \quad (7)$$

where the chaotic threshold function is

$$U(\beta, m, T) \equiv \frac{10\pi^5 \beta N(m)}{\sqrt{m} K^2(m)} \sum_{n=0}^{\infty} a_n(m) p_n(T). \quad (8)$$

From Eq. (8) one readily obtains $U(\beta, m, T \rightarrow 0, \infty) = U(\beta, m \rightarrow 1, T) = 0$, i.e., in such limits chaotic escape is not expected. Also, the threshold function $U(\beta = \text{const}, m, T)$ presents a *maximum* in the $m - T$ plane at $(m = m_{\max}, T = T_{\max})$. A plot of $U(\beta = 1, m, T)$ is shown in Fig. 1.

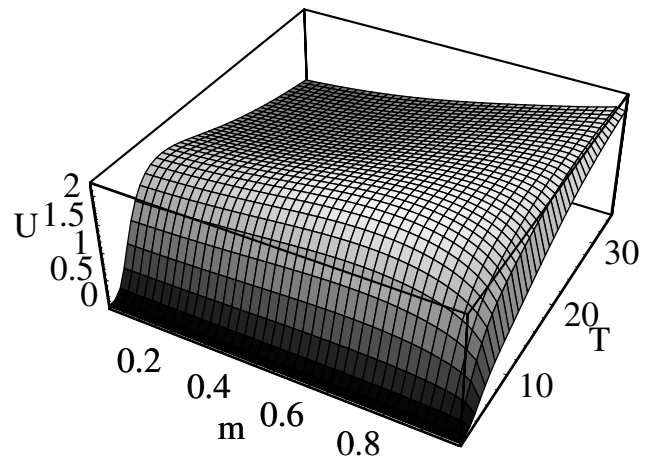


Fig. 1. Threshold function $U(\beta = 1, m, T)$.

Let us consider the chaotic threshold as a function of T , holding β and m constant. Plots of $U(\beta = \text{const}, m = \text{const}, T)$ show that each curve presents a maximum $T_{\max} = T_{\max}(m)$ such that $T_{\max}(m)$ increases from its value at $m = 0$ as $m \rightarrow 1$. We now study the chaotic threshold as a function of m , holding β and T constant. Plots of $U(\beta = \text{const}, m, T = \text{const})$ show that each curve presents a maximum $m_{\max} = m_{\max}(T)$ such that $m_{\max}(T)$ increases as T is increased. Therefore, if one considers fixing the parameters $(\beta, \delta, \gamma, T)$ for the system to lie at a periodic state (i.e., inside the well), then as m is increased a *window* of chaotic escape will appear provided the initial periodic state is sufficiently near the chaotic regime. We should emphasize that, in the context of neurosciences, this reshaping-induced effect represents a new mechanism to control firing rates (see for example [18]).

III. RESHAPING-INDUCED ENHANCEMENT OF THE EROSION OF NONESCAPING BASINS

For the universal escape model (1), the initial conditions will determine, for a fixed set of its parameters, whether the system escapes to an attractor at infinity, or settles into a bounded oscillation. As is well known [3], there can exist a rapid and dramatic erosion of the safe basin (union of the basins of the bounded attractors) due to encroachment by the basin of the attractor at infinity (escaping basin). We shall show in the following how the erosion of the safe basin presents a *maximum* as a single-humped excitation transforms into a double-humped excitation, the remaining parameters being held constant. To generate the basins of attraction numerically, we select a grid of (uniformly distributed) 300×300 starting points in the region of phase space $x(t = 0) \in [-0.7, 1.3]$, $\dot{x}(t = 0) \in [-0.8, 0.7]$. From this grid of initial conditions, each integration is continued until either x exceeds 20, at which point the system is deemed to have escaped (i.e., to the attractor at infinity), or the maximum allowable number of cycles, here 20, is reached. In the case of a single-humped harmonic excitation ($m = 0$), we assume that the system presents a very slight erosion of the nonescaping basin. For the set of parameters considered in Fig. 2 ($\beta = 1, \delta = 0.1, T = 2\pi/0.85$), we calculated the escape probability normalized to that of the case with $m = 0$, $P(m)/P(m = 0)$, versus the shape parameter m for three values of γ (0.071, circles; 0.072, triangles; 0.073, stars). Note that, for the above parameters, the chaotic threshold function presents its

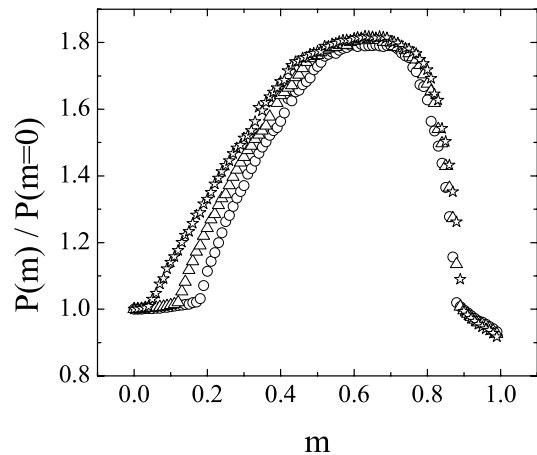


Fig. 2. Normalized probability vs shape parameter.

maxima at $m_{th} \simeq 0.65$ (cf. Eqs. (7) and (8)), which corresponds to the maxima of the normalized escape probability as shown in Fig. 2.

IV. CONCLUSION

In sum, we have shown that chaotic escape from a potential well can be induced over a wide range of parameters by hump-doubling of an external excitation which is initially formed by a periodic string of single-humped symmetric pulses. We should emphasize that the theoretical approach we have discussed as well as the conclusion that chaotic escape can be induced by hump-doubling of an excitation are both general enough to be applied to many other dissipative nonautonomous systems.

REFERENCES

- [1] G. Contopoulos, H. Kandrup, and D. Kaufmann, "Fractal properties of escape from a two-dimensional potential," *Physica D*, vol. 64, p. 310, 1993.
- [2] M. E. Goggin and P. W. Milonni, "Driven Morse oscillator: Classical chaos, quantum theory, and photodissociation," *Phys. Rev. A*, vol. 37, no. 3, pp. 796-806, 1988.
- [3] J. M. T. Thompson, "Chaotic phenomena triggering the escape from a potential well," *Proc. R. Soc. A*, vol. 421, pp. 195-225, 1989.
- [4] R. Chacón and J. I. Cirac, "Chaotic and regular behavior a trapped ion interacting with a laser field," *Phys. Rev. A*, vol. 51, no.6, pp. 4900-4905, 1995.
- [5] J. M. T. Thompson and M. S. Soliman, "Fractal control boundaries of driven oscillators and their relevance to safe engineering design," *Proc. R. Soc. A*, vol. 428, pp. 1-13, 1990.
- [6] A. Riabko et al., "Particle dynamics in quasi-isochronous storage rings," *Phys. Rev. E*, vol. 54, pp. 815-829, 1996.
- [7] R. Chacón and J. A. Martínez, "Inhibition of chaotic escape from a potential well by incommensurate escape-

- suppressing excitations," *Phys. Rev. E*, vol. 65, pp. 036213 (1-7), 2002.
- [8] See, e.g., L. M. Milne-Thomson, "Jacobian Elliptic Functions and Theta Functions," in *Handbook of Mathematical Functions*, New York: Dover, 1972, pp. 567-585.
- [9] H. T. Davis, *Introduction to Nonlinear Differential and Integral Equations*, New York: Dover, 1962.
- [10] R. Chacón and J. Díaz Bejarano, "Routes to suppressing chaos by weak periodic perturbations," *Phys. Rev. Lett.*, vol. 71, no. 19, pp. 3103-3106, 1993.
- [11] A. R. Zeni and J. A. C. Gallas, "Lyapunov exponents for a Duffing oscillator," *Physica D*, vol. 89, pp. 71-82, 1995.
- [12] R. Chacón and A. Martínez García-Hoz, "Bifurcations and chaos in a parametrically damped two-well Duffing oscillator subjected to symmetric periodic pulses," *Phys. Rev. E*, vol. 59, no. 6, pp. 6558-6568, 1999.
- [13] R. Chacón and A. Martínez García-Hoz, "Well-behaved dynamics in a dissipative nonideal periodically kicked rotator," *Phys. Rev. E*, vol. 68, pp. 066217 (1-11), 2003.
- [14] V. K. Melnikov, "On the stability of the center for time periodic perturbations," *Trans. Moscow Math. Soc.*, vol. 12, pp. 1-57, 1963.
- [15] J. Guckenheimer and P. J. Holmes, *Nonlinear Oscillations, Dynamical Systems, and Bifurcations of Vector Fields*, New York: Springer, 1983.
- [16] F. C. Moon and G.-X. Li, "Fractal basin boundaries and homoclinic orbits for periodic motion in a two-well potential," *Phys. Rev. Lett.*, vol. 55, no. 14, pp. 1439-1442, 1985.
- [17] S. W. McDonald et al., "Fractal basin boundaries," *Physica D*, vol. 17, pp. 125-153, 1985.
- [18] J. Rinzel and B. Ermentrout, "Analysis of neural excitability and oscillations." In *Methods in Neuronal Modeling*, Cambridge: The MIT Press, 1999, pp. 251-291.

COUPLED PIECEWISE LINEAR MAPS: FROM COHERENCE TO CLUSTERING

Iryna Matskiv and Yuri Maistrenko

Institute of Mathematics, National Academy of Sciences of Ukraine, Kyiv, Ukraine
 e-mail: matskiv@imath.kiev.ua, maistrenko@imath.kiev.ua

Abstract—For two interacting ensembles of globally coupled one-dimensional piecewise linear maps we find analytically parameter regions for different types of stability of the synchronized state in phase space. We analyse strong (asymptotic) and weak (Milnor) stability of the synchronized set as well as its instability. We find that the stability (instability) regions do not depend on the ensembles size N , and depend only on parameters l and p of the individual skew tent map. In simplest non-trivial case of four coupled maps we obtain stability regions for coherent and two-cluster states. The stability regions appear to be big enough to provide an effective control of coherent and clustered chaotic regimes. Moreover, we identify qualitatively different ways from desynchronization to synchronization, which happen in smooth and piecewise linear models.

I. INTRODUCTION

There is presently a high interest in studying the models which describe collective dynamics of interacting oscillators. Ensembles of globally (mean field) coupled maps

$$x_i^{t+1} = (1 - \varepsilon)f(x_i^t) + \frac{\varepsilon}{N} \sum_{j=1}^N f(x_j^t) \quad (1)$$

have been first suggested and intensively studied by Kaneko [1], [2]. If not all oscillators in the ensemble interact, we get so-called 'fractally' coupled system:

$$x_i^{t+1} = (1 - \varepsilon)f(x_i^t) + \frac{\varepsilon}{A_i} \sum_{j \in \text{conn}} f(x_j^t),$$

where A_i is the number of connections at i th site, and j runs over all sites that are connected to the site i . An interesting example of such kind networks is given by 'small-world' systems, introduced by Watts and Strogatz [3]. It can be interpreted as a mathematical model of many biologic and social networks. Another example is given by neural network with central element, where groups of peripheral elements interact with only one leading element [4].

In the present paper we consider a $2N$ -dimensional system of coupled maps which models the situation when there are two globally coupled Kaneko systems of the mean field type (1), and their elements are pairwise coupled with each others:

$$\begin{aligned} x_i^{t+1} &= \left(1 - \varepsilon - \frac{\delta}{2}\right) f(x_i^t) + \frac{\varepsilon}{N} \sum_{j=1}^N f(x_j^t) + \frac{\delta}{2} f(y_i^t), \\ y_i^{t+1} &= \left(1 - \varepsilon - \frac{\delta}{2}\right) f(y_i^t) + \frac{\varepsilon}{N} \sum_{j=1}^N f(y_j^t) + \frac{\delta}{2} f(x_i^t), \\ & i = 1, \dots, N. \end{aligned} \quad (2)$$

Here $\{x_i^t\}_{i=1}^N$ and $\{y_i^t\}_{i=1}^N$ are N -dimensional state vectors; $t = 0, 1, \dots$ is a discrete time index. $f : \mathbf{R} \rightarrow \mathbf{R}$ is a one-dimensional map.

Model of the form (2), in the case of smooth, logistic map $f = f_a$ was studied in [5], [6]. In the present work, we choose f as a piecewise linear, skew tent map of the form

$$f(x) = f_{l,p}(x) = \begin{cases} lx + 1 - l - \frac{l}{p}, & x \leq 1 + \frac{1}{p}, \\ px - p, & x > 1 + \frac{1}{p}. \end{cases} \quad (3)$$

Piecewise linear maps systems are widely spread in variety of technical, engineering, and electronic applications. Depending on parameters, such systems are characterized by regular or complex chaotic dynamics [7–9]. In many cases piecewise linear dynamics appear to be rather different from smooth ones, especially as for different types of bifurcations and their sequences.

Behavior of $2N$ -dimensional system (2) is controlled by four parameters: $l > 0$ and $p < -1$, which are the coefficients of linear parts of the skew tent map $f = f_{l,p}$, and coupling parameters ε, δ . Model (2) can be interpreted as two groups of interacting oscillators (i.e. neurons), as well as simplest example of 'small-world' network having two groups of elements with strong coupling inside and weaker coupling between the groups.

II. STABILITY OF CHAOTIC SYNCHRONIZING SET

Consider $2N$ -dimensional map F , defined by the system (2). For any N (number of elements in each globally coupled ensemble) Jacobian matrix DF in the point $(x, \dots, x) \in D_{2N}$, where $D_{2N} = \{z \in \mathbf{R}^{2N} | z_1 = \dots = z_{2N}\}$ is the main diagonal of $2N$ -dimensional phase space, has four different eigenvalues:

$$\begin{aligned} \nu_{\parallel}(x) &= f'(x); & \nu_{\perp,1}(x) &= f'(x)(1 - \varepsilon); \\ \nu_{\perp,2}(x) &= f'(x)(1 - \delta); & \nu_{\perp,3}(x) &= f'(x)(1 - \varepsilon - \delta). \end{aligned}$$

Note that $\nu_{\perp,2}(x)$ and $\nu_{\perp,3}(x)$ have multiplicity $N - 1$. Eigenvector v_{\parallel} is directed along the main diagonal D_{2N} , hence its eigenvalue ν_{\parallel} is responsible for 'dispersion' of the trajectories along D_{2N} . Three other eigenvectors are transverse to D_{2N} . Transverse eigenvalues $\nu_{\perp,1}$, $\nu_{\perp,2}$ and $\nu_{\perp,3}$ control attracting (repelling) strength for the trajectories in corresponding transverse directions. So as the eigenvalues do not depend on the system size $2N$, parameter regions for different types of stability do not depend on number of oscillators too.

One-dimensional chaotic set $A_D \subset D_{2N}$ is called *strongly or asymptotically stable* if for any its neighborhood $U(A_D)$ there exists the other neighborhood $V(A_D)$ that for any $x \in V(A_D)$:

- 1) $F^n(x) \in U(A_D)$ for any $n \in \mathbf{Z}^+$;
- 2) $\rho(F^n(x), A_D) \rightarrow 0$ for $n \rightarrow \infty$, $\rho(\cdot, \cdot)$ being distance between a point and a set in \mathbf{R}^{2N} .

One-dimensional set $A_D \subset D_{2N}$ is called *weakly or Milnor stable* if its basin of attraction $B(A_D)$ has a positive Lesbegue measure in \mathbf{R}^{2N} . A_D is called *weakly or Milnor unstable* in the opposite case, i.e. if $mes B(A_D) = 0$.

With change of coupling parameters ε and δ , chaotic synchronizing set A_D typically loses its strong stability through a *riddling bifurcation* [10]. After the riddling bifurcation synchronizing set A_D can still be weakly stable. Note that the strong stability implies weak stability, but not vice versa.

Further change of the coupling parameters can cause loss of weak stability of A_D through *blowout bifurcation* [11]. After blowout bifurcation there still can exist trajectories attracted by synchronizing set A_D , but the Lesbegue measure of their initial points is equal to zero.

Let $Pre(A_D) = \{x \in \mathbf{R}^{2N} | \exists n \in \mathbf{N} : F^n(x) \in A_D\}$ be a set of preimages for A_D . Obviously $Pre(A_D) \subseteq B(A_D)$. Synchronizing set A_D is called *strongly or asymptotically unstable* if $B(A_D) = Pre(A_D)$, which means that A_D attracts only its preimages.

Denote $b_1^{(1)} = 1 - \left(\frac{1}{l^{k-1}|p|}\right)^{1/k}$; $b_2^{(1)} = 1 - \frac{1}{|p|}$;
 $b_1^{(2)} = 1 + \left(\frac{1}{l^{k-1}|p|}\right)^{1/k}$; $b_2^{(2)} = 1 + \frac{1}{|p|}$, and
 $k = \left\lceil 2 - \frac{\ln l + p(l-1)}{\ln l} \right\rceil$, $[\cdot]$ being integer part of a real number.

Statement 1: In the system (2), where individual map $f = f_{l,p}$ has form (3), chaotic synchronizing set $A_D \subset D_{2N}$ is strongly stable, if

$$\begin{aligned} \varepsilon, \delta, (\varepsilon + \delta) &\in (b_1^{(1)}, b_1^{(2)}) \text{ for } l > |p|; \\ \varepsilon, \delta, (\varepsilon + \delta) &\in (b_2^{(1)}, b_2^{(2)}) \text{ for } l < |p|, \end{aligned}$$

and strongly unstable if

$$\begin{aligned} \varepsilon, \delta, (\varepsilon + \delta) &\in \left(-\infty; b_2^{(1)}\right) \cup \left(b_2^{(2)}, +\infty\right) \text{ for } l > |p|; \\ \varepsilon, \delta, (\varepsilon + \delta) &\in \left(-\infty; b_1^{(1)}\right) \cup \left(b_1^{(2)}, +\infty\right) \text{ for } l < |p|. \end{aligned}$$

Consider case where skew tent map $f(x) = f_{l,p}(x)$ has a chaotic interval $I = [0, 1]$. According to the theorem of Lasota and Yorke [12], for the map $f_{l,p}$ there exists a unique probability invariant measure $\mu = \mu_{l,p}$, absolutely continuous with respect to Lesbegue measure. Denote $m = \mu_{l,p}(\{x \in [1 + 1/p; 1]\})$, i.e. $m = \int_{1+1/p}^1 \rho(x) dx$, where $\rho(x)$ is a density function of invariant measure.

Statement 2: For the system (2), chaotic synchronizing set $A_D \subset D_{2N}$ is weakly stable if

$$\varepsilon, \delta, (\varepsilon + \delta) \in \left(1 - \frac{1}{l^{1-m}|p|^m}, 1 + \frac{1}{l^{1-m}|p|^m}\right),$$

and weakly unstable if

$$\begin{aligned} \varepsilon, \delta, (\varepsilon + \delta) &\in \left(-\infty, 1 - \frac{1}{l^{1-m}|p|^m}\right) \cup \\ &\cup \left(1 + \frac{1}{l^{1-m}|p|^m}, +\infty\right). \end{aligned}$$

Invariant measure m can be found in implicit form only in special cases, in particular when trajectory of extreme point $x_0 = 1 - 1/p$ puts, eventually, in the unstable periodic orbit.

Suppose that the parameters l and p are such that the map $f_{l,p}$ is chaotic and its invariant measure m is found, being distributed in the interval $[0, 1]$. Then one can find borders of parameter region for weak stability for synchronizing chaotic set A_D using Statement 2, as well as regions for strong stability and instability from Statement 1.

All stability regions are shown in Figure 1. Triangle colored by dark gray and signed AS is the region of strong (asymptotic) stability of A_D . Region colored by light gray and denoted as MS is the region of

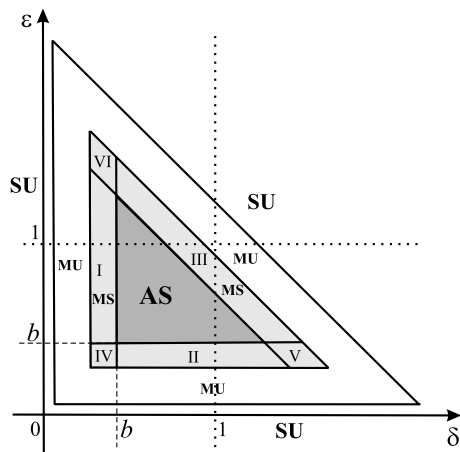


Fig. 1. Parameter regions for different types of stability of set A_D . In the signed regions A_D is: AS- asymptotically stable, MS- Milnor (weakly) stable, MU- Milnor unstable, SU- strongly unstable.

Milnor stability. Lines which bound AS region, divide MS region into six parts, denoted on the figure by numbers from I to VI. In these parameter regions, diagonal still attracts trajectories from a positive Lesbegue measure of initial points.

Synchronizing chaotic set A_D in the main diagonal D_{2N} can lose its stability in three transverse directions which correspond to crossing each of three sides of the stability triangle AS in Fig.1. After loss of the stability, transition to a cluster state takes place. When A_D loses stability entering the region I, transition to the two-cluster state $C_2^{(1)} = \{x_1 = \dots = x_N; y_1 = \dots = y_N\}$ takes place. When entering region II, we get transition to N -cluster state $C_N = \{x_1 = y_1; \dots; x_N = y_N\}$. Finally, when loss of stability happens through the border of the region III, then for even $N = 2n$ it results in two-cluster state $C_2^{(3)} = \{x_1 = \dots = x_n = y_{n+1} = \dots = y_N; x_{n+1} = \dots = x_N = y_1 = \dots = y_N\}$. Coexistence of different types of the two-cluster states is possible in the parameter regions IV, V and VI.

A_D is Milnor unstable in the blank region denoted MU. For the parameter values outside this region MU, A_D is strongly unstable (SU).

To obtain analytically asymptotic stability region AS, it is enough to know value

$$b = \begin{cases} b_1^{(1)}, & l > |p|, \\ b_2^{(1)}, & l < |p|, \end{cases} \text{ which is a left corner point}$$

of AS in Fig. 1. Indeed, as it follows from the Statement 1, strong stability region is bounded by the straight lines $\epsilon = b$, $\delta = b$, and $\epsilon + \delta = 2 - b$. Value of b varies, from 0 to 0.5, with change of coefficients of the single map $f_{l,p}$. $b = 0$ corresponds to the strong

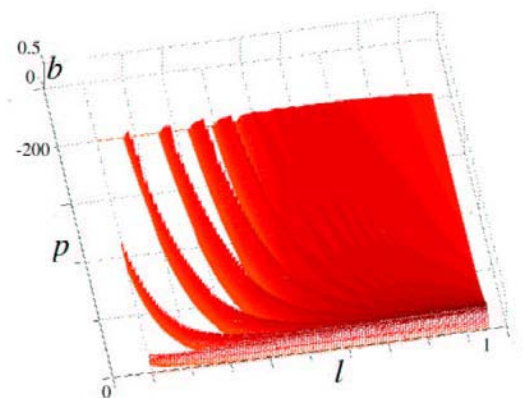


Fig. 2. Variation of the values of b -border of strong stability region of chaotic synchronizing set A_D with change of the coefficients l and p of single skew tent map $f_{l,p}$.

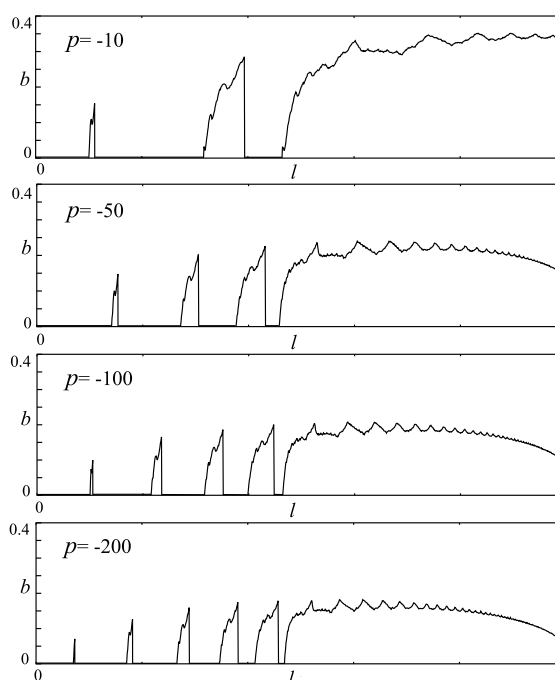


Fig. 3. Variation of b for fixed values of parameter p of single skew tent map. Note in periodic windows of skew tent map b is equal to zero, which means that region of strong stability covers whole unit square $[0, 1] \times [0, 1]$ of the parameter plane.

stability of synchronizing set A_D at all $0 \leq \epsilon, \delta \leq 1$. Figure 2 shows plot of values b versus l and p . Blank regions in the (l, p) -plane correspond to periodic windows of the piecewise linear map $f_{l,p}$. For coefficient pairs (l, p) belonging to these regions diagonal is strongly stable in the whole unit square of (δ, ϵ) -parameter plane. Figure 3 shows variation of b versus l for four fixed values of $p = -10; -50; -100; -200$.

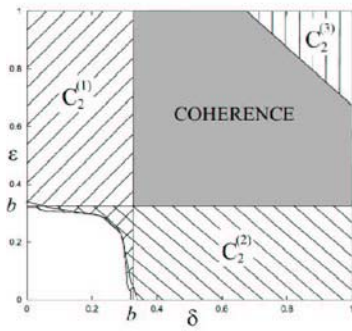


Fig. 4. Stability diagram for the system (2) with $2N = 4$, $l = 0.6$, $p = -10$. Region of stability of the coherent state is shown gray; regions of stability of two-cluster states are denoted by $C_2^{(i)}$, $i = 1, 2, 3$. Note doubly hatched region of coexistence of $C_2^{(1)}$ and $C_2^{(2)}$.

III. EXAMPLE: SYSTEM OF FOUR COUPLED MAPS

As the simplest nontrivial example, consider system (2) with $2N = 4$ coupled skew tent maps. Coupling parameters are supposed to be $0 \leq \epsilon, \delta \leq 1$.

Figure 4 shows stability diagram for the system of four coupled skew tent maps $f_{l,p}$ with coefficients $l = 0.6$, $p = -10$. Region of strong synchronization (coherence) is shown gray. The region is a part of asymptotic stability region AS of the attractor in the main diagonal (see Fig. 1). Stability regions of two-cluster states $C_2^{(1)} = \{x_1 = x_2; y_1 = y_2\}$, $C_2^{(2)} = \{x_1 = y_1; x_2 = y_2\}$ and $C_2^{(3)} = \{x_1 = y_2; x_2 = y_1\}$ are hatched. Coherent state can lose its stability in three transverse directions, which correspond to the transition to a two-cluster state. Stable $C_2^{(1)}$ and $C_2^{(2)}$ clusters coexist in doubly hatched region near left lower corner of the coherence region.

Figure 5 shows another example, here $l = 0.85$, $p = -50$. Note, that the stability region for the coherent state is wider in comparison with the previous case, and for the two-cluster states stability regions are smaller. Moreover, there is no coexistence of two-cluster states $C_2^{(1)}$ and $C_2^{(2)}$.

From obtained stability diagrams we conclude that for small values of coupling parameters ϵ and δ , in blank regions in Fig. 4 and 5 there is no any clustering in the system (2). Then, increasing and varying parameters ϵ and δ , one or even two cluster states $C_2^{(1)}$ or $C_2^{(2)}$ can stabilize, followed by stabilization of coherent state. Moreover, for some values of coefficients l and p , coherent state can be the first to stabilize with grow of coupling parameters.

This type of the synchronization transition is es-

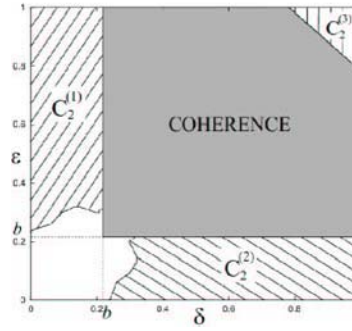


Fig. 5. Stability diagram for the system of four coupled maps with $l = 0.85$, $p = -50$.

entially different from the case of coupled smooth maps $f_a(x) = ax(1 - x)$ [5-6]. In the smooth case, with growing coupling parameters ϵ and δ , two-cluster state $C_2^{(3)}$ is the first to stabilize, only after that we get stabilization of $C_2^{(1)}$ or $C_2^{(2)}$, followed by transition to coherence.

REFERENCES

- [1] K. Kaneko, Clustering, coding, switching, hierarchical ordering, and control in a network of chaotic elements, *Physica D* **41**, 137–172 (1990).
- [2] K. Kaneko, I. Tsuda, Complex systems: chaos and beyond—a constructive approach with applications in life science, Springer Verlag (2000).
- [3] D.J. Watts, S.H. Strogatz, Collective dynamics of 'small-world' networks, *Nature* **393**, 440–442 (1998).
- [4] Y.B. Kazanovich, R.M. Borisyyuk, Dynamics of neural networks with a central element, *Neural Networks* **12**, 441–454 (1999).
- [5] I. Matskiv, Yu. Maistrenko, Synchronization and clustering among two interacting ensembles of globally coupled chaotic oscillators, In *Proc. NDES 2003*, 165–168, Scuol, Switzerland.
- [6] I. Matskiv, Yu. Maistrenko, E. Mosekilde, Synchronization between interacting ensembles of globally coupled chaotic oscillators (to be published).
- [7] Yu. Maistrenko, T. Kapitaniak, Different types of chaos synchronization in two coupled piecewise linear maps, *Phys. Rev. E* **54** (4), 3285–3292 (1996).
- [8] E. Mosekilde, Yu. Maistrenko, D. Postnov, Chaotic Synchronization. Applications to Living Systems, World Scientific (2002).
- [9] M. Hasler, Yu. Maistrenko, An Introduction to the Synchronization of Chaotic Systems: Coupled Skew Tent Maps, *Trans. of Circuits and Systems* **44** (10), 856–866 (1997).
- [10] Y.-C. Lai, C. Grebogi, J.A. Yorke, S.C. Venkataramani, Riddling bifurcation in chaotic dynamical systems, *Phys. Rev. Lett* **77**, 55–58 (1996).
- [11] E. Ott, J.C. Sommer, J.C. Alexander, I. Kan, J.A. Yorke, Scaling behavior of chaotic systems with riddled basins, *Phys. Rev. Lett* **71**, 4134–4137 (1993).
- [12] A. Lasota, J. Yorke, On the existence of invariant measure for piecewise monotonic transformations, *Trans. Am. Math. Soc.* **182**, 481–488 (1973).

CO-MOVEMENTS AND ASYMMETRIC VOLATILITY IN THE PORTUGUESE AND U.S. STOCK MARKETS¹

Rui Menezes

ISCTE - Av das Forças Armadas, 1649-026 Lisboa, Portugal

rui.menezes@iscte.pt

and

Nuno B. Ferreira

ISCTE - Av das Forças Armadas, 1649-026 Lisboa, Portugal

nuno.ferreira@iscte.pt

It has been widely recognised by economists that economic relationships are typically nonlinear. This is so that, for example, Granger and Teräsvirta (1993), inter alia, have dedicated a whole book to the subject of modelling nonlinear economic relationships. Nonlinear relationships are present in many aspects of the economic activity, and particularly so in the context of financial markets. Examples of this include the attitude of investors towards the risk and the process of generating financial variables such as stock returns, dividends, interest rates, and so on. On the other hand, the performance of an economy also presents strong signs of a nonlinear behaviour: e.g. business cycles, production functions, growth rates, unemployment, etc. Although the shape of nonlinearity in these relationships may be rather complex, there are cases where one may admit some sort of linear relationship between the relevant variables within certain regimes. This is the case when one aims to study the co-movements of stock returns volatility and some relevant macroeconomic factors. One obvious question that we may pose in this context is whether the magnitude of positive and negative responses differs for similar positive and negative variations in the predictors, in which case we can say that the underlying variables display asymmetric adjustment. Markets characterised by higher elasticity of supply are likely to show less asymmetry than their counterparts due to increased security of supply. Models of

financial markets have incorporated asymmetry using GARCH-type methodologies. An alternative way to deal with these cases is to use threshold autoregressive (TAR) and momentum threshold autoregressive (M-TAR) models to address the problem of multivariate asymmetry. These methodologies are essential when the asymmetric variables are non-stationary (but not only), because of the low power of unit roots and cointegration tests in such cases. In a non-stationary framework, asymmetric cointegration tests were developed by Enders and Siklos (2001) using a modified error correction model derived from the original EG testing procedure. We apply this methodology to the Portuguese and U.S. stock markets using monthly observations from January 1993 to December 2003.

Keywords

Threshold adjustment, cointegration, stock market volatility.

1 MODELLING VOLATILITY

There are many different ways for measuring the volatility associated with stock market returns. However, since the volatility itself is not directly observed, one needs to find a suitable estimator to

¹ The authors thank to Andreia Dionísio for the valuable comments and suggestions made to earlier drafts of this paper.

measure the risk resultant from changes in stock returns. Stock returns may be measured by $r_t = \ln(P_t/P_{t-1})$, $\forall t, t = 1, \dots, T$, where P_t is the value of the underlying stock index at time t . The series should only reflect the risk of changes in market returns, so one may filter r_t by subtracting from it the series r'_t generated by a non-risky asset. In our case, we considered as r'_t short-run Libor and treasury bill (3 months) rates obtained from the DataStream. The difference between r_t and r'_t is usually termed excess return (R_t).

The volatility of R_t may be estimated on the basis of the absolute deviation from the mean excess return, i.e. $\hat{w}_t = \sqrt{\pi/2} |R_t - \bar{R}|$, $\forall t, t = 1, \dots, T$. Alternatively, a popular measure of volatility of stock returns is based upon the historical standard deviations of the excess return (rolling historical volatility), and is given by

$$\hat{v}_t = \left(\frac{\sum_{p=1}^k (R_{t+1-p} - \bar{R})^2}{k-1} \right)^{\frac{1}{2}} \tag{1}$$

These two measures of volatility will be used in this article to address the issue of asymmetric comovements between stock market volatility and some relevant macroeconomic indicators: (1) dividend yield (dy), (2) earnings price ratio (epr), (3) inflation (cpi), and (4) industrial growth rate (ipi). All macroeconomic variables were found to be I(1). Inflation and industrial growth rates are expressed in terms of the natural logs of the underlying indexes.

2 THRESHOLD ADJUSTMENT

The long-run equilibrium relationship between two time series z_t and x_t can be estimated as a standard regression model $z_t = \alpha + \beta x_t + \mu_t$, where α and β are the estimated parameters, and μ_t is a disturbance term that may be serially correlated. The parameter β gives the magnitude of adjustment of z to variations in x , and is the long-run elasticity of the two variables if they are measured in logs. If $\beta < 1$, then shifts in x are not fully passed onto z .

The second step of the methodology focuses on the OLS estimates of ρ_1 and ρ_2 in the following error correction model:

$$\Delta\mu_t = I_t \rho_1 \mu_{t-1} + (1 - I_t) \rho_2 \mu_{t-1} + \varepsilon_t, \tag{2}$$

where ε_t is a white noise disturbance and the residuals from the long-run equation are used to estimate $\Delta\mu_t$. I_t is the Heaviside indicator function such that

$$I_t = \begin{cases} 1 & \text{if } \xi_{t-1} \geq \tau \\ 0 & \text{if } \xi_{t-1} < \tau \end{cases} \tag{3}$$

If in (3) $\xi_{t-1} = \mu_{t-1}$, then the model specification illustrated in (2) is called the threshold autoregressive (TAR) model. It allows for different coefficients of positive and negative variations. A sufficient condition for the stationarity of μ_t is $-2 < (\rho_1, \rho_2) < 0$. This means that the long-run equation is an attractor such that μ_t can be written as an error correction model similar to that given in (2). If $\rho_1 = \rho_2$ then the adjustment is symmetric, which is a special case of (2) and (3). Expression (2) can also contain lagged values of $\Delta\mu_t$. When μ_{t-1} is above its long-run equilibrium value, the adjustment is $\rho_1 \mu_{t-1}$, and if μ_{t-1} is below its long-run equilibrium value, the adjustment is $\rho_2 \mu_{t-1}$.

If in (3) $\xi_{t-1} = \Delta\mu_{t-1}$, then the model (2) is called the momentum threshold autoregressive (M-TAR) model. The M-TAR model allows the decay to depend on the previous period change in μ_{t-1} . The value of the threshold τ , in our case, will be assumed to be zero in all models.

The TAR model is designed to capture asymmetrically “deep” movements in the series of the deviations from the long-run equilibrium, while the M-TAR model is useful to capture the possibility of asymmetrically “steep” movements in the series [Enders and Granger (1998)]. For example, in the TAR model if $-1 < \rho_1 < \rho_2 < 0$, then the negative phase of μ_t will tend to be more persistent than the positive phase. On the other hand, for the M-TAR model, if for example $|\rho_1| < |\rho_2|$ the model exhibits little decay for positive $\Delta\mu_{t-1}$ but substantial decay for negative $\Delta\mu_{t-1}$. This means that increases tend to persist but decreases tend to revert quickly toward the attractor.

Finally, we can perform a number of statistical tests on the estimated coefficients (and also on the residuals) in order to ascertain the validity of the error correction model outlined in (2), and subsequently if the adjustment is symmetric or not. The relevant tests on the coefficients are $H_0: \rho_1 = 0$ and $H_0: \rho_2 = 0$, for which we obtain the sample values of the t -statistics; and $H_0: \rho_1 = \rho_2 = 0$, for which we obtain the sample values of the F -statistic. The restriction that adjustment is symmetric, i.e. $H_0: \rho_1 = \rho_2$, can also be tested using the usual F -statistic.

If the variables in the long-run equation are stationary, the usual critical values of the t and F distributions can be used to assess the significance level of the underlying tests. However, if these variables are integrated of first order, one can use the critical values reported by Enders and Siklos (2001) to determine whether the null hypothesis of no cointegration can be rejected. If the alternative hypothesis is accepted, it is possible to test for asymmetric adjustment using the standard critical values of the F distribution, since ρ_1 and ρ_2 converge to a multivariate normal distribution [Enders and Granger (1998)].

3 RESULTS

The methodology for assessing asymmetric co-movements between stock market returns volatility and macroeconomic factors was applied to the dataset described earlier. A total of 16 regressions were run for each country analysed (Portugal and US). The resulting residuals were then used to perform the TAR and M-TAR tests of asymmetry. This is however only possible when the residuals of the series are convergent. The results obtained are reported in Table 1 (for Portugal) and Table 2 (for the US).

The estimators of volatility \hat{w}_t and \hat{v}_t were found to be stationary for Portugal on the basis of ADF tests using the Bayesian information criterion for model selection and KPSS tests. Thus, for reasons of consistency, we replaced the original non-stationary macroeconomic variables by their first-difference I(0) counterparts in these models. For the US, however, the estimator \hat{w}_t is I(0) and the estimator \hat{v}_t is I(1). As before, we replaced the original macroeconomic variables by their first-difference counterparts in the models that use \hat{w}_t . With regard to \hat{v}_t , the

first two tests on the estimated values of ρ_1 and ρ_2 are actually cointegration tests.

For both Portugal and the US, the results obtained when \hat{w}_t was used as a measure of volatility show that the null hypothesis that ρ_1 and ρ_2 are zero is rejected at the 1% level or better in all cases (separate and joint tests). The test of the null hypothesis of symmetry, however, was not rejected at significant levels in none case. An error correction model without separation of the positive and negative variations would therefore be a sufficient representation of the process under analysis. Thus, given their triviality, we shall not report the results for the series \hat{w}_t .

Turning now to the results of \hat{v}_t , it can be seen that the null hypothesis that ρ_1 and ρ_2 are jointly equal to zero is rejected at the 1% level or better in all cases for both countries. For the US, the t -max and Φ statistics are reported and were compared to the critical values computed by Enders and Siklos (2001). Rejection of the null hypothesis in this case means that volatility is cointegrated with the macroeconomic variables used in our analysis. However, we found no signs of asymmetric adjustment in any case of the US macroeconomic variables. For Portugal, we found that only ρ_2 is significantly different from zero in the TAR specification, and ρ_1 is significantly different from zero in the M-TAR specification. Locally, however, it seems that the convergence criterion of the model is not violated, although testing the threshold could perhaps add something more on this issue. A general acceptance of the error correction model given by (2), entails testing for asymmetric adjustment using the standard F critical values. The test procedures carried out for Portugal leads to the conclusion that there is no asymmetry in the TAR mechanism but there is asymmetry in the M-TAR mechanism for 3 of the 4 macroeconomic variables.

The 3 cases of asymmetric co-movements in Portugal using \hat{v}_t refer to dividend yields, earnings price ratios, and industrial growth rates. As can be seen, in all cases $|\rho_1| > |\rho_2|$, which means that the model exhibits little decay for negative changes but substantial decay for positive changes in volatility relative to changes in macroeconomic factors. In other words, we may conclude that in the Portuguese stock market, volatility decreases tend to persist but increases tend to revert quickly toward the attractor.

The M-TAR results for the Portuguese stock market volatility suggest that volatility is obtained via an

accumulation of changes in μ_{t-1} above the threshold followed by a sharp drop to the threshold. However, a similar pattern is not observed for changes in μ_{t-1} below the threshold, thus causing asymmetry. That is, volatility departs from its equilibrium level (given by the threshold) relative to the macroeconomic factors and periodically collapses to the threshold, sharply for positive and smoothly for negative changes.

In contrast with the case of the US, the asymmetric results for Portugal may challenge market efficiency according to the efficient market hypothesis. The EMH holds that stock prices adjust rapidly and unbiasedly to new and relevant price sensitive information. Under and over price adjustments relative to its fundamental value are unpredictable so that price changes are independent and random. Given the information provided by the macroeconomic variables, one would then expect that prices adjust rapidly and symmetrically toward the equilibrium level, which is consistent with cointegration (for non-stationary variables) and symmetric adjustment. This behaviour of prices would be transmitted to variables that capture stock returns and the corresponding volatility. Volatility itself would be unpredictable under the EMH. However, predictability is not a sufficient condition for market inefficiency. It is also need to prove that predictability allows for the possibility of generating systematic abnormal gains.

Stock market asymmetry may arise because investors are risk and loss averse. Risk aversion may encourage economic agents to react quickly to bad news while reacting more reluctantly to good news. On the other hand, asymmetries may arise driven by the potential loss in an overvalued stock market. Alternative explanations based on models of structural slumps and booms are also possible [Siklos (2002)]. In our context, the volatility in the Portuguese stock market drops suddenly and periodically toward the attractor when it is substantially above the equilibrium level. Higher volatility induces greater risk and

potentially larger losses, so it may be seen as a sign of bad news to the investor, which prompts him to react quickly to such news, and conversely for lower volatility. For our results, however, we found no evidence of such type of behaviour in the US market.

4 CONCLUSIONS

This paper employs a threshold adjustment methodology to inquire the asymmetric nature of stock market volatility in Portugal and the US. We found no evidence of asymmetric volatility behaviour in the US relative to changes in macroeconomic variables, but evidence of “sharp” movement asymmetry of volatility in some cases of the Portuguese stock market. The results for Portugal do not seem to be consistent with the general efficient market hypothesis.

REFERENCES

- [1] Enders, W. and C.W.J. Granger. “Unit-Root Tests and Asymmetric Adjustment With an Example Using the Term Structure of Interest Rates”. *Journal of Business & Economic Statistics*, Vol. 16, No. 3, pp. 304-311, July 1998.
- [2] Enders, W. and P. Siklos. “Cointegration and Threshold Adjustment”. *Journal of Business & Economic Statistics*, Vol. 19, No. 2, pp. 166-176, April 2001.
- [3] Granger, C.W.J. and T. Teräsvirta. *Modelling Nonlinear Economic Relationships*, New York: Oxford University Press, 1993.
- [4] Siklos, P.L. “Asymmetric Adjustment from Structural Booms and Slumps”. *Economic Letters*, Vol. 77, pp. 329-333, 2002.

Table 1. TAR and M-TAR results for Portugal

Economic factor	ρ_1	ρ_2	$\rho = 0$	$\rho_1 = \rho_2 = 0$		$\rho_1 = \rho_2$	
			t -max	Φ	F	p -value	
TAR							
$\Delta(dy_t)$	-0.093 (0.053)	-0.156 (0.042)	–	8.301	**	0.853	0.357
$\Delta(epr_t)$	-0.080 (0.054)	-0.169 (0.043)	–	8.940	**	1.710	0.193
$\Delta(\ln cpi_t)$	-0.097 (0.052)	-0.135 (0.045)	–	6.281	**	0.305	0.582
$\Delta(\ln ipi_t)$	-0.075 (0.042)	-0.094 (0.035)	–	5.206	**	0.115	0.736
M-TAR							
$\Delta(dy_t)$	-0.201 (0.047)	-0.023 (0.050)	–	9.240	**	6.735	* 0.011
$\Delta(epr_t)$	-0.220 (0.047)	-0.029 (0.052)	–	11.304	**	7.465	** 0.007
$\Delta(\ln cpi_t)$	-0.180 (0.049)	-0.066 (0.045)	–	7.711	**	2.906	0.091
$\Delta(\ln ipi_t)$	-0.190 (0.040)	-0.013 (0.033)	–	11.406	**	11.527	** 0.000

Notes: Dependent variable is $\hat{v}_t \sim I(0)$; * significant at the 5% level; ** significant at the 1% level; asymptotic standard errors are in parentheses.

Table 2. TAR and M-TAR results for the US

Economic factor	ρ_1	ρ_2	$\rho = 0$	$\rho_1 = \rho_2 = 0$		$\rho_1 = \rho_2$	
			t -max	Φ	F	p -value	
TAR							
dy_t	-0.758	-0.639	-3.161	**	37.568	**	0.292 0.590
epr_t	-0.722	-0.509	-2.617	**	34.121	**	0.987 0.322
$\ln cpi_t$	-0.814	-0.599	-3.096	**	39.763	**	0.978 0.325
$\ln ipi_t$	-0.809	-0.635	-3.200	**	40.197	**	0.617 0.434
M-TAR							
dy_t	-0.759	-0.652	-3.490	**	37.209	**	0.263 0.609
epr_t	-0.692	-0.659	-3.492	**	33.150	**	0.024 0.877
$\ln cpi_t$	-0.812	-0.592	-2.952	**	39.430	**	0.978 0.325
$\ln ipi_t$	-0.805	-0.656	-3.355	**	39.769	**	0.468 0.495

Notes: Dependent variable is $\hat{v}_t \sim I(1)$; ** significant at the 1% level; critical values for t -max in the TAR and M-TAR models are -2.55 and -2.47 (1%); critical values for Φ in the TAR and M-TAR models are, respectively, 9.27 and 9.14 (1%).

PERFORMANCES OF UNKNOWN INPUT OBSERVERS FOR CHAOTIC LPV MAPS IN A STOCHASTIC CONTEXT

G. Millérioux and J. Daafouz

Centre de Recherche en Automatique de Nancy (CRAN),

Université Henri Poincaré Nancy 1, Institut National de Polytechnique de Lorraine

e-mail: millerioux@esstin.uhp-nancy.fr, jdaafouz@ensem.inpl-nancy.fr

WWW: http://www.cran.uhp-nancy.fr

Abstract

Jointly modeling chaotic maps as LPV systems and using Unknown Input Observers for retrieving the information in a secure communication scheme has previously been motivated in a deterministic context [1]. In this paper, some new theoretical results from a control theory point of view, concerning the design in a stochastic and so more realistic context of Unknown Input Observers for chaotic LPV systems is provided. The design of such observers is expressed in terms of the resolution of a finite set of Matrix Inequalities constraints and guarantees some prescribed performances on the state reconstruction error.

I. INTRODUCTION

The well-known practical interest of chaos synchronization lies in the potential applications in communications and more specifically in the possibilities of encoding or masking messages by embedding the information into the dynamics of a chaotic system. The information to be masked plays the role of an external input for the dynamical system and is not transmitted to the receiver. Hence, the receiver system must be designed such that the information can be unmasked, given the only available output data consisting of a function of the state vector. In [1], a brief survey of the main approaches proposed in the literature is given. Then, a novel approach based on Unknown Input Observer (UIO) for a noise-free context is proposed.

In a deterministic context, Unknown Input Observers have been largely investigated for linear systems [2][3][4][5]. On the other hand, in a stochastic context, there does not exist a lot of results. For time-invariant systems, we can mention the works of [6] while for linear time-varying systems, the reader can refer to [7], but none of those classes of systems can exhibit chaotic behaviors and so have no interest for chaos-based communications purposes.

The aim of this paper is to state some new results concerning the design of Unknown Input Observers

for Linear Parameter Varying Systems in a stochastic context. The interest of LPV systems lies in the fact that a large amount of chaotic systems enter this class. Furthermore, the UIO design guaranteeing some prescribed performances can be carried out in a tractable way by solving Matrix Inequalities.

Notation : $(\bullet)^T$ stands for the symmetric block of a positive definite matrix, $\mathbf{0}$ and $\mathbf{1}$ stand for the zero and the identity matrix of appropriate size.

$$\|x_k\| = \sqrt{x_k^T x_k}, \|x\|_\infty = \sup_{k \geq 0} \|x_k\| \text{ and } \|x\|_2 = \sqrt{\sum_{k=0}^\infty x_k^T x_k}.$$

II. UNKNOWN INPUT OBSERVERS FOR LPV SYSTEMS

Consider the general state space realization of LPV discrete-time systems in a noisy context.

$$\begin{cases} x_{k+1} &= A(\rho_k)x_k + Bu_k + Ev_k \\ y_k &= Cx_k + Dv_k \end{cases} \quad (1)$$

where $x_k \in \mathbb{R}^n$, $y_k \in \mathbb{R}^m$, $A \in \mathbb{R}^{n \times n}$, $B \in \mathbb{R}^{n \times r}$, $C \in \mathbb{R}^{m \times n}$, $D \in \mathbb{R}^{m \times r}$. $u_k \in \mathbb{R}^r$ is the input, $v_k \in \mathbb{R}^l$ is the disturbance acting on the dynamics through E and acting on the measurement through D . A is of class C^1 with respect to the entries of a L -dimensional time-varying parameter vector $\rho_k = (\rho_k^1, \dots, \rho_k^L)^T$. In [8], it has been shown that a lot of chaotic maps can be modeled by LPV discrete-time systems with ρ_k being a function of the state vector x_k . Since x_k evolves chaotically, ρ_k is bounded in a hypercube Θ . As a result, A lies in a compact set which can always be embedded in a polytope, that is :

$$A(\rho_k) = \sum_{i=1}^N \xi_k^i(\rho_k) A_i \quad (2)$$

where the A_i 's correspond to the vertices of the convex hull $\text{Co}\{A_1, \dots, A_N\}$. The ξ_k 's belong to the compact set $\mathcal{S} = \{\mu_k \in \mathbb{R}^N, \mu_k = (\mu_k^1, \dots, \mu_k^N)^T, \mu_k^i \geq 0 \forall i \text{ and } \sum_{i=1}^N \mu_k^i = 1\}$ and

they can always be expressed as functions of class C^1 with respect to the ρ_k 's. The advantage of such a decomposition lies in the fact that the design problems turn into the resolution of a finite set of constraints involving only the vertices of the convex hull.

For secure communication purposes, u_k plays the role of the information to be masked and acts as an unknown input. y_k is the signal transmitted to the receiver. The structure of the required Unknown Input Observers for the recovering of u_k is reminded from [1].

$$\hat{x}_{k+1} = (PA(\rho_k) - L(\rho_k)C)\hat{x}_k + L(\rho_k)y_k + Qy_{k+1} \quad (3)$$

with $P = \mathbf{1}_n - QC$ and $L(\rho_k) = \sum_{i=1}^N \xi_k^i(\rho_k)L_i$. The gains Q and L_i 's ($i = 1, \dots, N$) are unknown matrices to be computed.

From (1) and (3), it is straightforward to show that the state reconstruction error $\epsilon_k \triangleq x_k - \hat{x}_k$ is governed by :

$$\epsilon_{k+1} = \mathcal{A}(\rho_k)\epsilon_k + PBu_k + \mathcal{B}(\rho_k)v_k - QDv_{k+1} \quad (4)$$

with $\mathcal{A}(\rho_k) = \sum_{i=1}^N \xi_k^i(PA_i - L_iC)$ and $\mathcal{B}(\rho_k) = \sum_{i=1}^N \xi_k^i(PE - L_iD)$.

Before dealing with the performances on the state reconstruction when disturbances act on the system, it is necessary to remind how the global stability of the null solution of (4) can be guaranteed when $v_k = 0$. Some details can be found in [1].

Theorem 1. *The global stability of the null solution of (4) with $v_k = 0$ is ensured if*

- i) $\text{rank}(CB) = \text{rank}(B) = r$,
- ii) *there exist symmetric matrices P_i , matrices F_i and G_i such that, $\forall(i, j) \in \{1, \dots, N\} \times \{1, \dots, N\}$, the following set of Linear Matrix Inequalities is feasible.*

$$\begin{bmatrix} P_i & (\bullet)^T \\ G_iPA_i - F_iC & G_i^T + G_i - P_j \end{bmatrix} > 0 \quad (5)$$

The time-varying gain is given by $L(\rho_k) = \sum_{i=1}^N \xi_k^i L_i$ with $L_i = G_i^{-1}F_i$.

Proof: On one hand, according to the definition of P , the equality $PB = 0$ entails that Q must be subject to

$$B = QCB \quad (6)$$

and i) ensures the existence of the solution Q of (6). Its general expression is :

$$Q = B(CB)^\dagger + Y(\mathbf{1}_m - (CB)(CB)^\dagger) \quad (7)$$

with Y an arbitrary matrix. Then, whenever Q satisfies (7), $PB = 0$ and so (4) turns into an input independent dynamics :

$$\epsilon_{k+1} = \mathcal{A}(\rho_k)\epsilon_k + \mathcal{B}(\rho_k)v_k - QDv_{k+1} \quad (8)$$

On the other hand, the proof follows a reasoning similar to the one carried out in [9]. All the relations are valid $\forall(i, j) \in \{1, \dots, N\} \times \{1, \dots, N\}$.

a) Since P_j is strictly positive, one has :

$$G_iP_j^{-1}G_i^T \geq G_i + G_i^T - P_j$$

b) Substitute F_i by G_iL_i in (5) and take into account the inequality above yields :

$$\begin{bmatrix} P_i & (\bullet)^T \\ G_i(PA_i - L_iC) & G_iP_j^{-1}G_i^T \end{bmatrix} > 0 \quad (9)$$

which is equivalent to

$$\mathbb{H} \cdot \begin{bmatrix} P_i & (\bullet)^T \\ P_j(PA_i - L_iC) & P_j \end{bmatrix} \cdot \mathbb{H}^T \quad (10)$$

with

$$\mathbb{H} = \begin{bmatrix} \mathbf{1} & \mathbf{0} \\ \mathbf{0} & G_iP_j^{-1} \end{bmatrix}$$

and so to

$$\begin{bmatrix} P_i & (\bullet)^T \\ P_j(PA_i - L_iC) & P_j \end{bmatrix} > 0 \quad (11)$$

since G_i and P_j are full rank matrices.

c) For each $i = 1, \dots, N$, multiply the corresponding $j = 1, \dots, N$ inequalities (11) by ξ_{k+1}^j and sum. Then, multiply the resulting $i = 1, \dots, N$ inequalities by ξ_k^i and sum again. We obtain :

$$\begin{bmatrix} \mathcal{P}_k & (\bullet)^T \\ \mathcal{P}_{k+1}\mathcal{A} & \mathcal{P}_{k+1} \end{bmatrix} > 0 \quad (12)$$

with $\mathcal{P}_k = \sum_{i=1}^N \xi_k^i P_i$ and $\mathcal{P}_{k+1} = \sum_{i=1}^N \xi_{k+1}^i P_i$. Applying the Schur complement formula gives :

$$\mathcal{A}^T \mathcal{P}_{k+1} \mathcal{A} - \mathcal{P}_k < 0 \quad \forall k \quad (13)$$

It is shown in [9] that $V : \mathbb{R}^n \rightarrow \mathbb{R}^+$, a function defined by $V(z_k, \xi_k) = z_k^T \mathcal{P}_k z_k$ with $\mathcal{P}_k = \sum_{i=1}^N \xi_k^i P_i$ and $\xi_k \in \mathcal{S}$ acts as a Lyapunov function for (4) when $v_k = 0$ and ensures the poly-quadratic stability of (4) which is sufficient to global asymptotical stability. This completes the proof.

In the forthcoming sections, the case $v_k \neq 0$, that is the stochastic context, is considered and constitutes the main result of the paper.

III. OBSERVER DESIGN WITH PRESCRIBED
PERFORMANCES

A. Bounded \mathcal{L}_2 gain

We define the upper bound denoted σ of the \mathcal{L}_2 gain as a scalar verifying :

$$\sup_{\|\bar{v}\|_2 \neq 0} \frac{\|z\|_2}{\|\bar{v}\|_2} < \sigma \quad (14)$$

where $z_k = \tilde{C}\epsilon_k$, $\bar{v}_k = [v_k^T \ v_{k+1}^T]^T$.

Theorem 2. *The \mathcal{L}_2 gain corresponding to (4) with $v_k \neq 0$ is less than σ if*

- i) $\text{rank}(CB) = \text{rank}(B) = r$,
- ii) *there exist symmetric matrices P_i , matrices F_i and G_i such that $\forall (i, j) \in \{1, \dots, N\} \times \{1, \dots, N\}$, the set (21) of Linear Matrix Inequalities is feasible.*

The time-varying gain is given by $L(\rho_k) = \sum_{i=1}^N \xi_k^i L_i$ with $L_i = G_i^{-1} F_i$.

Proof : For the same reason motivated in the proof of Theorem 1, condition i) ensures the existence of a matrix Q such that $PB = 0$ holds and turns (4) into an input independent dynamics. Besides, define the matrices

$$\mathbb{G}_i = \begin{bmatrix} G_i & \mathbf{0} & \mathbf{0} \\ \mathbf{0} & \sigma \mathbf{1} & \mathbf{0} \\ \mathbf{0} & \mathbf{0} & \sigma \mathbf{1} \end{bmatrix}, \quad \mathbb{P}_i = \begin{bmatrix} P_i & \mathbf{0} & \mathbf{0} \\ \mathbf{0} & \sigma \mathbf{1} & \mathbf{0} \\ \mathbf{0} & \mathbf{0} & \sigma \mathbf{1} \end{bmatrix}$$

and

$$\mathbb{M}_i = \begin{bmatrix} PA_i - L_i C_i & PE - L_i D & -QD \\ \sigma^{-1} \tilde{C} & \mathbf{0} & \mathbf{0} \\ \mathbf{0} & \mathbf{0} & \mathbf{0} \end{bmatrix}$$

(21) can be rewritten :

$$\begin{bmatrix} \mathbb{P}_i & (\bullet)^T \\ \mathbb{G}_i \mathbb{M}_i^T & \mathbb{G}_i + \mathbb{G}_i^T - \mathbb{P}_j \end{bmatrix} > \mathbf{0} \quad (15)$$

$$\begin{bmatrix} P_i & (\bullet)^T & (\bullet)^T & (\bullet)^T & (\bullet)^T & (\bullet)^T \\ \mathbf{0} & \sigma \mathbf{1} & (\bullet)^T & (\bullet)^T & (\bullet)^T & (\bullet)^T \\ \mathbf{0} & \mathbf{0} & \sigma \mathbf{1} & (\bullet)^T & (\bullet)^T & (\bullet)^T \\ G_i PA_i - F_i C & G_i PE - F_i D & -G_i QD & G_i + G_i^T - P_j & (\bullet)^T & (\bullet)^T \\ \tilde{C} & \mathbf{0} & \mathbf{0} & \mathbf{0} & \sigma \mathbf{1} & (\bullet)^T \\ \mathbf{0} & \mathbf{0} & \mathbf{0} & \mathbf{0} & \mathbf{0} & \sigma \mathbf{1} \end{bmatrix} > \mathbf{0} \quad (21)$$

$$\begin{bmatrix} A^T \mathcal{P}_{k+1} A - \mathcal{P}_k + \sigma^{-1} \tilde{C}^T \tilde{C} & (\bullet)^T & (\bullet)^T \\ \mathcal{B}^T \mathcal{P}_{k+1} A & \mathcal{B}^T \mathcal{P}_{k+1} B - \sigma \mathbf{1} & (\bullet)^T \\ -(QD)^T \mathcal{P}_{k+1} A & -(QD)^T \mathcal{P}_{k+1} B & (QD)^T \mathcal{P}_{k+1} (QD) - \sigma \mathbf{1} \end{bmatrix} > \mathbf{0} \quad (22)$$

Following the same three steps a) to c) as in the proof of Theorem 1, feasibility of (15) implies that

$$\mathbb{M}^T \mathbb{P}_{k+1} \mathbb{M} - \mathbb{P}_k < \mathbf{0} \quad (16)$$

with

$$\mathbb{P}_k = \begin{bmatrix} \mathcal{P}_k & \mathbf{0} & \mathbf{0} \\ \mathbf{0} & \sigma \mathbf{1} & \mathbf{0} \\ \mathbf{0} & \mathbf{0} & \sigma \mathbf{1} \end{bmatrix}, \quad \mathbb{P}_{k+1} = \begin{bmatrix} \mathcal{P}_{k+1} & \mathbf{0} & \mathbf{0} \\ \mathbf{0} & \sigma \mathbf{1} & \mathbf{0} \\ \mathbf{0} & \mathbf{0} & \sigma \mathbf{1} \end{bmatrix}$$

and

$$\mathbb{M} = \begin{bmatrix} \mathcal{A} & \mathcal{B} & -QD \\ \sigma^{-1} \mathbf{1} & \mathbf{0} & \mathbf{0} \\ \mathbf{0} & \mathbf{0} & \mathbf{0} \end{bmatrix}$$

Equation (16) can be rewritten like (22). Then, multiply left and right respectively by $[\epsilon_k \ \bar{v}_k]$ and its transpose gives :

$$V(\epsilon_{k+1}, \xi_{k+1}) - V(\epsilon_k, \xi_k) + \sigma^{-1} (\tilde{C}\epsilon_k)^T (\tilde{C}\epsilon_k) - \sigma \bar{v}_k^T \bar{v}_k < 0 \quad (17)$$

Consider (17) from $k = 0$ to N and sum leads to:

$$V(\epsilon_{N+1}, \xi_{N+1}) + \sigma^{-1} \sum_{k=0}^N (\tilde{C}\epsilon_k)^T (\tilde{C}\epsilon_k) - \sigma \sum_{k=0}^N \bar{v}_k^T \bar{v}_k < 0 \quad (18)$$

Yet, $V(\epsilon_{N+1}, \xi_{N+1}) = \epsilon_{N+1}^T \mathcal{P}_k \epsilon_{N+1} > 0$. Hence :

$$\sigma^{-1} \sum_{k=0}^N (\tilde{C}\epsilon_k)^T (\tilde{C}\epsilon_k) < \sigma \sum_{k=0}^N \bar{v}_k^T \bar{v}_k \quad (19)$$

When N tends toward infinity, this relation is equivalent to (14). This completes the proof.

B. Peak-to-peak gain

Let ν be the upper bound of the peak-to-peak gain defined as the ratio between $\|\epsilon\|_\infty$ and $\|\bar{v}\|_\infty$

$$\sup_{0 < \|\bar{v}\|_\infty < \infty} \frac{\|\epsilon\|_\infty}{\|\bar{v}\|_\infty} < \nu \quad (20)$$

Theorem 3. *The peak-to-peak gain corresponding to (4) with $v_k \neq 0$ is less than $\nu > 0$ if*

- i) $\text{rank}(CB) = \text{rank}(B) = r$,
- ii) *there exist symmetric positive definite matrices P_i , matrices G_i , scalars $\lambda \in]0, 1[$, $\mu > 0$ such that, $\forall (i, j) \in \{1, \dots, N\} \times \{1, \dots, N\}$, the Matrix Inequalities (29) are fulfilled.*

The time-varying gain is given by $L(\rho_k) = \sum_{i=1}^N \xi_k^i L_i$ with $L_i = G_i^{-1} F_i$.

Proof: For the same reason motivated in the proof of Theorem 1, condition i) turns (4) into an input independent dynamics. On one hand, again, considering the first inequality of (29) and following the same steps from a) to c) as in the proof of Theorem 1 yields :

$$\begin{bmatrix} (1 - \lambda) \cdot \mathcal{P}_k & (\bullet)^T & (\bullet)^T & (\bullet)^T \\ \mathbf{0} & \mu \mathbf{1} & (\bullet)^T & (\bullet)^T \\ \mathbf{0} & \mathbf{0} & \mu \mathbf{1} & (\bullet)^T \\ \mathcal{P}_{k+1} \mathcal{A} & \mathcal{P}_{k+1} \mathcal{B} & -\mathcal{P}_{k+1} \mathcal{Q} \mathcal{D} & \mathcal{P}_{k+1} \end{bmatrix} > 0 \quad (23)$$

Applying the Schur complement formula and some basic manipulations yields (30). Then, multiply (30) left and right respectively by $[\epsilon_k \ \bar{v}_k]$ and its transpose, entails that :

$$V(\epsilon_{k+1}, \xi_{k+1}) < (1 - \lambda)V(\epsilon_k, \xi_k) + \mu \|\bar{v}_k\|^2 \quad \forall k \quad (24)$$

Applying the Gronwall-lemma in the discrete case gives :

$$V(\epsilon_k, \xi_k) < \frac{\mu}{\lambda} \|\bar{v}\|_\infty^2 \quad \forall k \quad (25)$$

On the other hand, multiplying the second inequality of (29) by ξ_k^i and sum from $i = 1$ to N gives :

$$\begin{bmatrix} \lambda \mathcal{P}_k - \frac{1}{\nu} \mathbf{1} & \mathbf{0} \\ \mathbf{0} & (\nu - \mu) \mathbf{1} \end{bmatrix} > 0 \quad (26)$$

Besides, multiply (26) left and right respectively by $[\epsilon_k \ \bar{v}_k]$ and its transpose leads to :

$$\frac{1}{\nu} \|\epsilon_k\|^2 < \lambda V(\epsilon_k, \xi_k) + (\nu - \mu) \|v_k\|^2 \quad \forall k \quad (27)$$

Finally, combining (25) and (27) and taking into account that $\nu - \mu > 0$ from the second inequality of (29) leads to :

$$\|\epsilon\|_\infty^2 < \nu^2 \|v\|_\infty^2 \quad (28)$$

And yet, (28) is equivalent to (20).

Remark

Note that the Matrix Inequalities corresponding to the peak-to-peak performances are not linear unlike the ones related to the \mathcal{L}_2 gain. They involve a product of two unknowns, say λ and P_i , and a nonlinear dependence on ν which prevents the convexity.

REFERENCES

- [1] G. Millerioux and J. Daafouz. Unknown input observers for message-embedded chaos synchronization of switched discrete-time systems. *International Journal of Bifurcation and Chaos*, 2004. accepted for publication.
- [2] M. Darouach, M. Zazadinski, and S. J. Xu. Full-order observers for linear systems with unknown inputs. *IEEE Trans. on Automatic Control*, 39(3):606–609, March 1994.
- [3] S-K. Chang, W-T. You, and P-L. Hsu. Design of general structured observers for linear systems with unknown inputs. *J. Franklin Inst.*, 334(2):213–232, 1997.
- [4] F. Yang and R. W. Wilde. Observers for linear systems with unknown inputs. *IEEE Trans. on Automatic Control*, 33(7):677–681, July 1988.
- [5] Y. Guan and M. Saif. A novel approach to the design of unknown input observers. *IEEE Trans. on Automatic Control*, 36(5):632–635, May 1991.
- [6] Nikoukhah R. Innovations generation in the presence of unknown inputs: application to robust failure detection. *Automatica*, 30:1851–1867, 1994.
- [7] M. Darouach, M. Zazadinski, and M. Boutayeb. Extension to minimum variance estimation for systems with unknown inputs. *Automatica*, 39:867–876, 2003.
- [8] G. Millerioux and J. Daafouz. Polytopic observer for global synchronization of systems with output measurable nonlinearities. *International Journal of Bifurcation and Chaos*, 13(3):703–712, March 2003.
- [9] J. Daafouz and J. Bernussou. Parameter dependent lyapunov functions for discrete time systems with time varying parametric uncertainties. *Systems and Control Letters*, 43:355–359, 2001.

$$\begin{bmatrix} (1 - \lambda) \cdot P_i & (\bullet)^T & (\bullet)^T & (\bullet)^T \\ \mathbf{0} & \mu \mathbf{1} & (\bullet)^T & (\bullet)^T \\ \mathbf{0} & \mathbf{0} & \mu \mathbf{1} & (\bullet)^T \\ G_i P A_i - F_i C & G_i P E - F_i D & -G_i Q D & G_i + G_i^T - P_j \end{bmatrix} > 0, \quad \begin{bmatrix} \lambda P_i - \frac{1}{\nu} \mathbf{1} & (\bullet)^T \\ \mathbf{0} & (\nu - \mu) \mathbf{1} \end{bmatrix} > 0 \quad (29)$$

$$\begin{bmatrix} \mathcal{A}^T \mathcal{P}_{k+1} \mathcal{A} - (1 - \lambda) \mathcal{P}_k & (\bullet)^T & (\bullet)^T \\ \mathcal{B}^T \mathcal{P}_{k+1} \mathcal{A} & -\mu \mathbf{1} + \mathcal{B}^T \mathcal{P}_{k+1} \mathcal{B} & (\bullet)^T \\ -(\mathcal{Q} \mathcal{D})^T \mathcal{P}_{k+1} \mathcal{A} & -(\mathcal{Q} \mathcal{D})^T \mathcal{P}_{k+1} \mathcal{B} & -\mu \mathbf{1} + (\mathcal{Q} \mathcal{D})^T \mathcal{P}_{k+1} \mathcal{Q} \mathcal{D} \end{bmatrix} < 0 \quad (30)$$

QUANTITATIVE METHODS FOR THE CHARACTERIZATION OF COMPLEX SURFACE STRUCTURES

Alejandro Mora, Maria Haase

Institute for Computer Applications (ICA II),
University of Stuttgart,
Stuttgart, Germany

e-mail: ica2am@csv.ica.uni-stuttgart.de, mh@ica.uni-stuttgart.de

Abstract—*Attempting to model the processes resulting in complex pattern formation and small-scale roughness of surfaces and to compare with experimental measurements calls for numerical methods which allow a quantitative characterization being as complete as possible. New methods incorporating wavelets and stochastic approaches based on the theory of Markov processes allow a stepwise characterization of increasing completeness and unambiguity. In this paper we demonstrate the underlying numerical approaches taking electropolished and laser-jet etched surfaces for demonstration.*

I. INTRODUCTION

The development of new technologies like high-precision microstructuring of metals calls for numerical methods which allow a characterization of the topography and a stochastic description of the surface roughness [1]. The aim is not only to classify different surface structures but also to ensure that model descriptions do not contradict the measured data. Since the nineteen-eighties surface roughness has predominantly been analyzed on the basis of self- or multifractal properties and has thus been described within the framework of fractal dimensions or multifractal spectra. However, many surfaces although sharing the same multifractal properties and thus having the same 2-point correlations, might still differ in their N-point correlations [2]. Here, we present a number of numerical approaches which allow a description of increasing completeness. These include in addition to classical spectral methods more recently developed wavelet approaches which allow to determine characteristic length scales and provide robust methods for the calculation of multifractal spectra. In order to incorporate the complete stochastic information in the description a new method based on the theory of Markov processes is applied [2], [3].

The paper is organized as follows. In section 2, we analyze the characteristic wavelengths and scaling

regions for two exemplary surface profiles, an electropolished brass sheet and a laser-jet etched steel surface. In contrast to the classical Fourier techniques, the continuous wavelet transform (CWT) allows a space-scale resolution of the surface profile. After a brief review of the wavelet transform modulus maxima (WTMM) method [4], [5], the multifractal spectra for the electropolished surface are estimated in section 3. As can be seen from the power spectra, two processes are interacting leading to different multifractal behaviour on different scales. Section 4 deals with the evolution of the probability density functions (pdf) of surface height increments for varying scales and gives a short introduction into the recently developed stochastic approach, which is used for a complete stochastic characterization of the profiles [2], [3]. Finally, section 5 presents our conclusions and perspectives of further investigations.

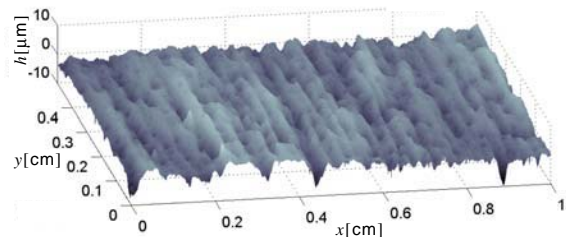


Fig. 1. Laser scan of the height profile of a brass surface electropolished in Methanol-electrolyte.

II. CHARACTERISTIC LENGTH SCALES AND SCALING PROPERTIES

Figure 1 shows a laser-profilometer scan of a surface which is obtained by electropolishing a brass sheet in a electrolyte solution containing Methanol (fig. 1a) [6], [7]. Electropolishing was performed in the transpassive region with vertically arranged electrodes, the workpiece acting as an anode. The sur-

face structure is a result of two competing processes, namely the dissolution of metal leading to a falling film of spent electrolyte containing dissolved metal and the hydrolysis of water, where oxygen is formed at the anode causing gas bubbles to rise forming an unwanted pattern of so-called gas lines [6]. Characteristic length scales can easily be obtained by classical Fourier methods. For the spectrum transversal to the gas lines (fig. 2a), two regions with different decay can be seen, indicating the interplay of two different processes. We estimate the bandwidth of scales introduced by the gaslines from the ratio the power spectral density of ensemble averages transversal and parallel to the gas lines (fig. 2b).

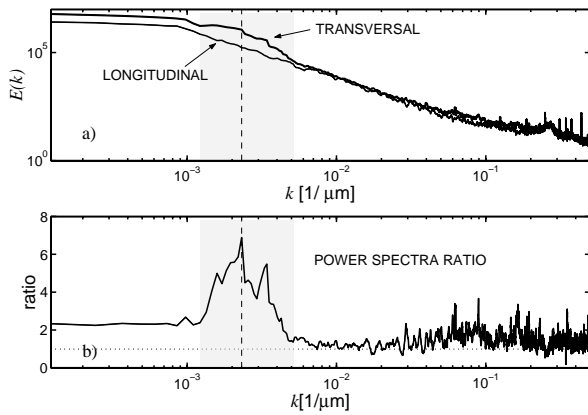


Fig. 2. a) Power spectra of ensemble averages transversal and parallel to gas lines for electropolished brass sheet, b) Ratio of power spectral densities measures the anisotropy of the surface.

Figure 3a shows a scanning electron microscope (SEM) image of a kerf in a steel sheet structured by a recently developed laser-jet assisted wet etching process [8]. In fig.3b the average profile in the bottom of the kerf is shown together with the power spectral density displaying a sharp peak for a wavelength of $40\mu\text{m}$ (fig. 3c). In order to resolve the profile in space and scale, we apply a continuous wavelet transform (CWT) to the profile

$$Wf(a, b) = \frac{1}{a} \int_{-\infty}^{+\infty} f(x) \overline{\psi}\left(\frac{x-b}{a}\right) dx, \quad (1)$$

where $a, b \in \mathbf{R}$, $a > 0$. The CWT decomposes the function $f(x) \in L^2(\mathbf{R})$ hierarchically in terms of elementary components $\psi\left(\frac{x-b}{a}\right)$ which are obtained from a single *mother wavelet* $\psi(x)$ by dilations and translations. Here, $\overline{\psi}(x)$ denotes the complex conjugate of $\psi(x)$, a the scale and b the shift parameter. A

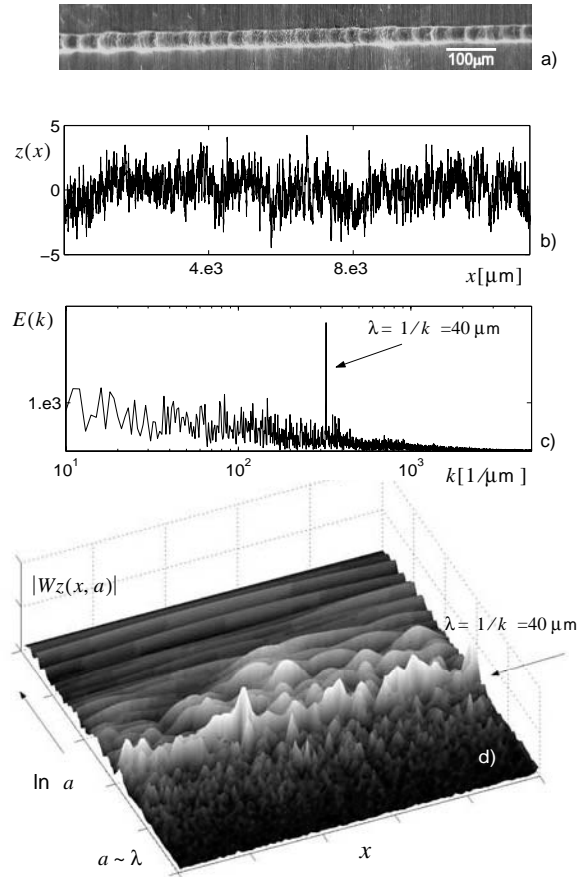


Fig. 3. a) SEM micrograph of a kerf obtained by laser-jet etching, b) Average profile in the bottom of the kerf, c) Power spectral density $E(k)$, d) Wavelet transform (Morlet wavelet, $\omega_0 = 25$).

unique reconstruction of the function $f(x)$ is ensured if $\psi(x) \in L^1(\mathbf{R})$ has zero mean.

Figure 3d shows the CWT using a Morlet-type progressive wavelet: $\psi(x) = \frac{d^2}{dx^2} \left(e^{-x^2/2} e^{i\omega_0 x} \right)$. At a scale corresponding to $\lambda = 40\mu\text{m}$, a dominant band can be seen displaying a strong variation of the wavelet coefficients of the ripple structure.

III. MULTIFRACTAL ANALYSIS USING WAVELET TECHNIQUES

The power spectral density $E(k)$ gives only limited information about the mono- or multifractal properties of the surface roughness. It only allows to estimate a *global* Hölder exponent h via the relation $E(k) \sim k^{-1-2h}$. Local fluctuations in the degree of roughness call for a location-dependent Hölder exponent $h(x)$. In turbulence, the standard way to extract the multiscaling properties of a function $f(x)$ is to study the scaling behaviour of the structure functions

$S_q(r) = \langle \delta f_r^q \rangle \sim r^{\zeta_q}$ of order q of the increments $\delta f_r = f(x + r/2) - f(x - r/2)$. Multifractal behaviour leads to a nonlinear scaling exponent ζ_q . The spectrum $D(h)$ of Hölder exponents is obtained by Legendre transforming the exponents ζ_q leading to [9] $D(h) = \min_q(qh - \zeta_q + 1)$. A severe drawback of this method is, that one has only access to Hölder exponents $0 < h < 1$, i.e. singularities in the derivatives of the function can not be identified. In addition, negative moments $q < 0$ lead to divergencies.

These limitations can be circumvented using the wavelet framework [4]. Choosing derivatives of the Gaussian function as wavelets in eq.1, $\psi_0(x) = e^{-x^2/2}$, $\psi_n(x) = \frac{d}{dx}\psi_{n-1}(x)$ with $n \in \mathbf{N}$, $n \geq 1$, and assuming a cusp singularity with Hölder exponent $h(x_0) \in (n, n + 1)$ at x_0 , the CWT scales like

$$|W_\psi f(a, x_0)| \sim a^{h(x_0)}, \quad a \rightarrow 0^+, \quad (2)$$

provided the analyzing wavelet chosen has $n_\psi > h(x_0)$ vanishing moments. In contrast, if one chooses a wavelet with $n_\psi < h(x_0)$, the CWT scales with an exponent n_ψ . It can be shown, that this scaling behaviour is also valid along the maxima lines of the modulus of the CWT, which point to the singularities [4]. The so-called wavelet transform modulus maxima (WTMM) method [4], [5] is a generalization of the classical multifractal formalism [9], [10], [11] and allows a robust estimation of the full spectrum of singularities. A partition function $Z(q, a)$ is defined

$$Z(q, a) = \sum_{b_i \in \text{max.lines}} \left(\sup_{a' \leq a} |W_\psi f(a', b_i)| \right)^q \quad (3)$$

containing the q th moments of the contributions of $|W_\psi f|$ along the maximal lines, where the supremum in eq. (3) is related to a Hausdorff-like covering with scale-adapted wavelets removing divergencies due to negative order moments [4]. From the power-law behaviour of the partition function (cf. eq.1), $Z(q, a) \sim a^{\tau(q)}$, $a \rightarrow 0^+$, the whole spectrum of Hölder exponents $D(h)$ is obtained by Legendre transforming the scaling exponents $\tau(q)$: $D(h) = \min_q(qh - \tau(q))$. Fig. 4 shows the spectra of Hölder exponents for the electropolished surface. An ensemble of five profiles transversal to the direction of the gas lines containing 12800 maxima lines is used for the calculation of the partition function $Z(q, a)$. According to the observation of two different scaling regions in the transversal power spectrum (fig. 2a), two regions with different power law behaviour occur, which lead to different distributions of the corresponding Hölder exponents.

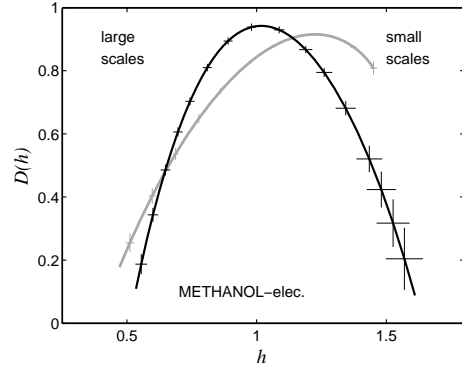


Fig. 4. Spectra of Hölder exponents $D(h)$ for different scaling regions.

IV. STOCHASTIC APPROACH BASED ON THE THEORY OF MARKOV PROCESSES

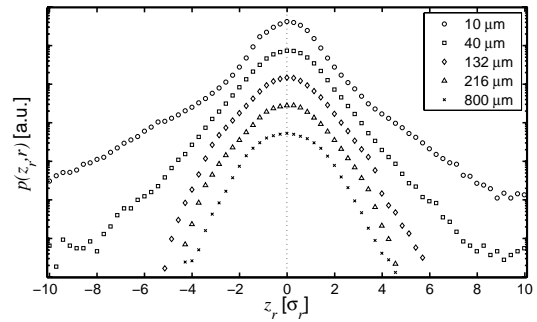


Fig. 5. Probability density functions for electropolished surface.

From a stochastic point of view, the multifractal characterization is still incomplete, since only 2-point correlations are involved in this formulation. The height increment $z_r(x) = z(x + r/2) - z(x - r/2)$ of the surface profile $z(x)$ can be considered as a stochastic variable in the length scale r [2]. Fig. 5 displays the evolution of pdfs of z_r as r is varied. The distributions are normalized to their respective standard deviations σ_r and shifted in vertical direction for clarity. For small scales the shapes of the curves deviate strongly from Gaussian distributions indicating pronounced intermittency effects.

In a series of papers a new approach for the stochastic analysis has been proposed which allows to extract the explicit form of the underlying stochastic process directly from experimentally measured data without making any assumptions, provided the process is Markovian [2], [3]. The aim is to describe the evolution of the conditional probability density functions as r is varied, where the conditional pdf $p(z_1, r_1 | z_2, r_2)$ describes the probability for finding the increment z_1 on scale r_1 provided that the increment z_2 is given on

scale r_2 . A stochastic process is Markovian, if the conditional probability densities fulfill the relations

$$p(z_1, r_1 | z_2, r_2; \dots; z_n, r_n) = p(z_1, r_1 | z_2, r_2), \quad (4)$$

where $r_1 < r_2 < \dots < r_n$. In this case, the conditional pdf satisfies a master equation. Expanding the distribution function into a Taylor series, the evolution equation can be written as [3]

$$\begin{aligned} -r \frac{\partial}{\partial r} p(z_r, r | z_0, r_0) &= \\ &= \sum_{k=1}^{\infty} \left(-\frac{\partial}{\partial z_r} \right)^k D_k(z_r, r) p(z_r, r | z_0, r_0) \end{aligned} \quad (5)$$

where the so-called Kramers-Moyal coefficients $D_k(z_r, r) = \lim_{\Delta r \rightarrow 0} M_k(z_r, r, \Delta r)$ can be directly estimated from experimental data:

$$\begin{aligned} M_k(z_r, r, \Delta r) &= \\ &= \frac{r}{k! \Delta r} \int_{-\infty}^{\infty} (\tilde{z} - z_r)^k p(\tilde{z}, r - \Delta r | z_r, r) d\tilde{z}. \end{aligned} \quad (6)$$

Fig. 6 shows a test of Markov properties of the electropolished surface data. In Fig. 6a, the contour plots of $p(z_1, r_1 | z_2, r_2; z_3, r_3)$ (black lines) and $p(z_1, r_1 | z_2, r_2)$ (grey lines) are shown in units of the standard deviation σ of the z -data. The good correspondence over several orders of magnitude is corroborated by two cuts for $z_2 = \pm\sigma/2$ displayed in figs. 6b,c indicating the validity of the necessary condition eq. (4). However, choosing different scale increments, for example $r_1 = 52 \mu\text{m}$, $r_2 = 60 \mu\text{m}$, $r_3 = 68 \mu\text{m}$, the two sets of contour lines strongly deviate from each other. The minimal increment r_{Markov} , for which Markovian properties hold, is the so-called Markov length.

In the Markovian range, drift and diffusion coefficients D_1, D_2 can be estimated directly from the measured data without making any assumption for the underlying process. If D_4 is small as compared to D_1 and D_2 , the evolution of conditional probabilities can be described by a Fokker-Planck equation.

V. CONCLUSIONS

We presented various numerical techniques including wavelet analysis and stochastic methods for a characterization of complex surface structures. The multifractal scaling behaviour is contained in the singularity spectra $D(h)$ which are estimated using the WTMM method. If Markov properties can be verified, a complete stochastic description of the surface is given by a Fokker-Planck equation (for D_4 negligible), which describes the evolution of conditional

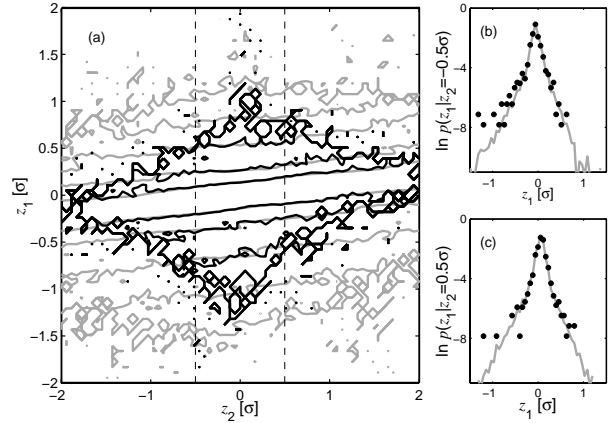


Fig. 6. a) Contour lines of the conditional pdfs $p(z_1, r_1 | z_2, r_2)$ (grey lines) and $p(z_1, r_1 | z_2, r_2; z_3 = 0, r_3)$ (black lines) for $r_1 = 10 \mu\text{m}$, $r_2 = 108 \mu\text{m}$, $r_3 = 216 \mu\text{m}$, b), c) Cuts through the conditional pdfs for $z_2 = \pm\sigma/2$.

pdfs over scales. The corresponding Langevin equation would open the possibility for a direct synthesis of surface profiles [12]. In addition, dynamical and measurement noise and even their magnitude can be extracted from experimental data [13].

REFERENCES

- [1] A.-L. Barabási, H.E. Stanley, *Fractal concepts in surface growth*, Cambridge University Press (1995), T.Vicsek, *Fractal Growth Phenomena*, World Scientific (1992).
- [2] M. Wächter, F. Riess, H. Kantz, J. Peinke, *Europhys. Lett.* **64**, 579–585 (2003). M. Wächter, F. Riess, J. Peinke, *Stochastic analysis of different rough surfaces preprint* (2004).
- [3] R. Friedrich, J. Peinke, *Physica D* **102**, 147–155 (1997), H. Risken, *The Fokker-Planck Equation*, Springer Berlin (1996).
- [4] J.F. Muzy, E. Bacry and A. Arnéodo, *Int. J. Bif. Chaos* **4**, 245–302 (1994).
- [5] M. Haase, B. Lehle, in: *Fractals and Beyond*, (M.M.Novak ed.), World Scientific, Singapore 241–250 (1998).
- [6] C. Gerlach, *PhD thesis*, University of Bremen (2002).
- [7] A. Mora, C. Gerlach, T. Rabbow, P.J. Plath, M. Haase, in: *Nonlinear Dynamics of Production Systems*, (G. Radons, R. Neugebauer eds.) Wiley-VCH, Weinheim (2003).
- [8] T. Rabbow, data of laser-jet etched surfaces (IAPC, Bremen).
- [9] U. Frisch, G. Parisi, in *Turbulence and Predictability in Geophysical Fluid Dynamics and Climate Dynamics*, (M.Ghil et al. eds.) North Holland, Amsterdam, 71–88 (1985).
- [10] T.C. Halsey, M.H. Jensen, L.P. Kadanoff, I. Procaccia and B.I. Shraiman, *Phys. Rev. A* **33**, 1141–1151 (1986).
- [11] J. Argyris, G. Faust and M. Haase, *An Exploration of Chaos*, North-Holland, Amsterdam (1994).
- [12] J. Gradišek, S. Siegert, R. Friedrich, I. Grabec, *Phys. Rev. E* **62**, 3146–3155 (2000), M. Siefert, J. Peinke, *preprint* (2003), G.R. Jafari, S.M. Fazeli, F. Ghasemi, S.M. Vaez Al-laei, M. Reza Rahimi Tabar, A. Iraj zad, G. Kavei, *Phys. Rev. Lett.* **91**, 226101 (2003).
- [13] M. Siefert, A. Kittel, R. Friedrich, J. Peinke, *Europhys. Lett.* **61**, 466–472 (2003).

Image processing with a Cellular Nonlinear Network

S. Morfu, P. Marquié, J.M. Bilbault

Laboratoire d'Electronique, Informatique et Image (LE2i)
 UMR C.N.R.S 5158, Aile des Sciences de l'Ingénieur,
 BP 47870,21078 Dijon Cedex, France
 e-mail: smorfu@u-bourgogne.fr
 WWW: http://www.le2i.com

Abstract—*In this paper, a contrast enhancement realized with a lattice of uncoupled nonlinear oscillators is proposed. We show theoretically and numerically that the gray scale picture contrast is strongly enhanced even if this one is initially very weak. An image inversion can be also obtained in real time with the same Cellular Nonlinear Network (C.N.N.) without reconfiguration of the network. A possible electronic implementation of this C.N.N. is finally discussed.*

I. INTRODUCTION

Since the past ten years, a growing interest has been devoted to nonlinear systems for signal processing purposes. Indeed, unlike linear processing, nonlinear processes present an additional dimension lying in the signal amplitude, which gives rise to new properties not shared by linear systems. Noise filtering using nonlinear dissipative lattices [1], image processing with nonlinear networks [2], [3], [4], [5], [6], are few examples where nonlinear systems provide efficient tools in signal or image processing fields.

It is important to note that both linear and nonlinear image processing tasks can be performed in good conditions only if the image to process is sufficiently contrasted.

The aim of this paper is to propose a Cellular Nonlinear Network (C.N.N.), built with uncoupled oscillators, which allows a contrast enhancement and video inversion in real time.

First, using the mechanical analogy of a particle experiencing a double well potential, we investigate the oscillators dynamic. Then, we show theoretically and numerically that two particles (or oscillators) with a slightly different initial condition can present a maximum, a minimum or a null difference of amplitude. In sect. III, we use the previous oscillators properties to enhance the contrast of the image represented in figure 1.

An image inversion can be also realized for two very

close but different processing times without reconfiguration of the oscillators network. In section IV, an electronic design of the lattice is finally proposed in order to incite electronic engineers and real time image processing specialists to include this solution to their problems.

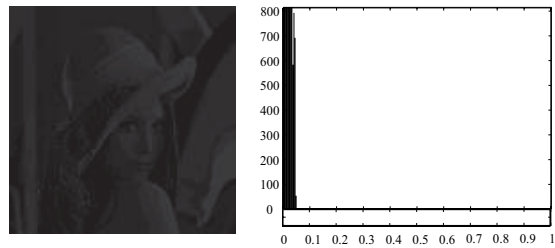


Fig. 1. Weak contrasted picture of Lena and its histogram.

II. THEORETICAL STUDY

The aim of this section is to present the oscillators properties which will allow to perform different image processing tasks. The normalized equation describing the motion of a harmonical particle submitted to a nonlinear force $f(x) = -\omega_0^2 x (x^2 - \alpha^2)$ deriving from the double potential of figure (2) is given by

$$\frac{d^2x}{dt^2} = -\omega_0^2 x (x^2 - \alpha^2). \quad (1)$$

Solutions of eq.(1) for a zero initial velocity are given by the Jacobian elliptic functions of the form:

$$x(t) = A \operatorname{cn}(\omega t, k), \quad (2)$$

where A is the oscillation amplitude. Moreover the pulsation ω and the modulus $0 \leq k \leq 1$ of the Jacobian elliptic function cn are given by

$$\omega = \omega_0 \sqrt{A^2 - \alpha^2} \text{ and } k = \frac{1}{2} \frac{A^2}{A^2 - \alpha^2}. \quad (3)$$

The pulsation ω and the modulus k appear then as two parameters driven by the amplitude of the solution A .

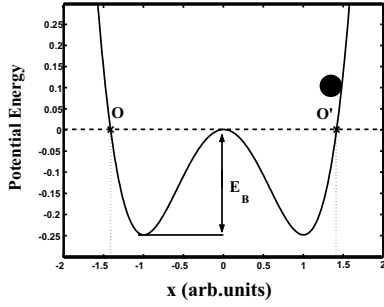


Fig. 2. Double well potential represented for $\alpha = 1$, in which a particle (\bullet symbol) evolves from an arbitrary initial position $x > \alpha\sqrt{2}$, that is with an initial potential energy above the barrier E_B and with a zero initial velocity.

Let us consider now two independent oscillators described by (1), with a very close amplitude initial condition, and starting at the even time. The initial amplitude of the oscillators O_1 and O_2 will be noted $A_{+\varepsilon}$, $A_{-\varepsilon}$ respectively and their respective displacement x_1 , x_2 . The two corresponding pulsations and modula, are given by

$$\begin{aligned}\omega_{-\varepsilon} &= \omega_0 \sqrt{(A - \varepsilon)^2 - \alpha^2} \\ \omega_{+\varepsilon} &= \omega_0 \sqrt{(A + \varepsilon)^2 - \alpha^2}\end{aligned}\quad (4)$$

$$\begin{aligned}k_{-\varepsilon} &= \frac{1}{2} \frac{(A - \varepsilon)^2}{(A - \varepsilon)^2 - \alpha^2} \\ k_{+\varepsilon} &= \frac{1}{2} \frac{(A + \varepsilon)^2}{(A + \varepsilon)^2 - \alpha^2}.\end{aligned}\quad (5)$$

In order to illustrate the oscillators properties, we have represented Fig. 3.(a) and 3.(b) respectively, the position-time dependence of the two oscillators O_1 and O_2 , and their relative difference δ in the case $\alpha = 1$, $\varepsilon = 10^{-1}$, $\omega_0 = 1$ and $A = 2.5$. The temporal evolution of the oscillators (figure 3.a) reveals a periodic behaviour in their phase difference and the possibility for the two oscillators to be very quickly in phase opposition at an optimum time $t = t_{opt} = 16.1$. As a result, the displacement difference δ , represented figure 3.b, reaches a maximum in absolute value equal to $\delta = 2A = 5$ at the optimum time $t = t_{opt}$. This phase opposition, which corresponds to $x_1 = A + \varepsilon = 2.5 + 0.1 = 2.6$ and $x_2 = -A + \varepsilon = -2.5 + 0.1 = -2.4$, allows to realize a strong amplitude contrast enhancement of the weak initial amplitude difference $2\varepsilon = 0.2$. This property will allow in the following section to realize an image contrast enhancement.

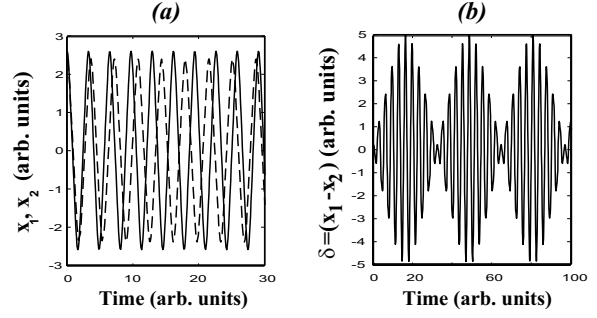


Fig. 3. (a) Displacement x_1 (continuous line) and x_2 (dashed line) versus time of the two oscillators O_1 and O_2 respectively. (b) Displacement difference or contrast amplitude $\delta = x_1 - x_2$ of the two oscillators versus time. Parameters are $A = 2.5$, $\alpha = 1$, $\omega_0 = 1$ and $\varepsilon = 10^{-1}$. The maximum $\delta = 5$ is reached at $t = t_{opt} = 16.1$.

III. IMAGE PROCESSING

Considering each pixel of an image as an oscillator with the properties of the previous section, we propose here two image processing tools.

In order to describe the pixels dynamics between the range $[0; 1]$ (since the standard coding of images defines a white level for $X = 1$, and a black level for $X = 0$, the others gray levels being included between these two values), we consider the following system of equations

$$\begin{aligned}\frac{d^2 X_{i,j}}{dt^2} &= -\left(2X_{i,j} - \frac{1}{2}\right) \times \left(2X_{i,j} - \frac{3}{2}\right) \\ &\times \left(2X_{i,j} - 1\right) \text{ with } i = 1, 2, \dots, N, j = 1, 2, \dots, M,\end{aligned}\quad (6)$$

where $X_{i,j}$ is the gray level of the pixel repered by the indexes i, j , $N \times M$ being the image size.

This equation describes a network of $N \times M$ uncoupled harmonical particles. Initially, each particle has a zero velocity and its initial position corresponds to the gray level $X_{i,j}(t = 0) = X_{i,j}^0$ of the pixel number i, j of the image to process (image of Fig. 1).

As seen in the previous section, the gray level $X_{i,j}$ of each pixel will evolve versus time with the same behavior depicted by figure 3.(a).

Especially, if i_0, j_0 , and i_1, j_1 are the respective indexes of the pixels corresponding to the minimum and maximum gray levels of the initial image, then their difference $\Delta(t) = X_{i_1, j_1}(t) - X_{i_0, j_0}(t)$ characterizes at $t = 0$ the weak contrast of the image to process. For the considered pixels i_0, j_0 , and i_1, j_1 , this difference - called Differential Contrast in the whole article - will follow the same behavior depicted in figure 3.(b)., with the possibility to maximize this quantity

for a given processing time t .

Setting $X_{i,j} = (x + 1)/2$, eq. (6) can be normalized under the form of eq. (1) with $\alpha = 0.5$ and $\omega_0 = \sqrt{2}$. Writing the initial gray level of the pixel number i, j under the form $X_{i,j}^0 = (1 + A)/2$, the solution of (6) can be straightforwardly deduced from eqs. (2) and (3) as

$$X_{i,j}(t) = \frac{1}{2} \left[1 + (2X_{i,j}^0 - 1)c_n(\omega_{i,j}t, k_{i,j}) \right], \quad (7)$$

where the pulsation of the Jacobian elliptic function is

$$\omega_{i,j} = \omega_0 \sqrt{(2X_{i,j}^0 - 1)^2 - \alpha^2}, \quad (8)$$

and its modulus

$$k_{i,j} = \frac{1}{2} \frac{(2X_{i,j}^0 - 1)^2}{(2X_{i,j}^0 - 1)^2 - \alpha^2}, \quad (9)$$

in the specific case $\alpha = 0.5$, $\omega_0 = \sqrt{2}$. An explicit expression of the Differential Contrast is then available with equation (7).

For the image of figure 1, since $X_{i_1,j_1}^0 = 0.05$ and $X_{i_0,j_0}^0 = 0$, the initial Differential Contrast is $\Delta(t = 0) = 0.05$. Figure 4. shows that starting from its initial weak value, the Differential Contrast $\Delta(t)$ periodically decreases and increases revealing the possibility to realize a contrast enhancement.

Indeed, the Differential Contrast can be nul - for $t = 3.74$ and $t = 7.31$ for instance - or it can reach local minima-namely for $t = 2.87$ and $t = 16.33$ - else it can also achieve local maxima - for $t = 6.24$, $t = 12.82$, to cite but a few. The maximum value of the Differential Contrast is obtained at $t_{opt} = 19.91$ and is in good agreement with the theoretical section

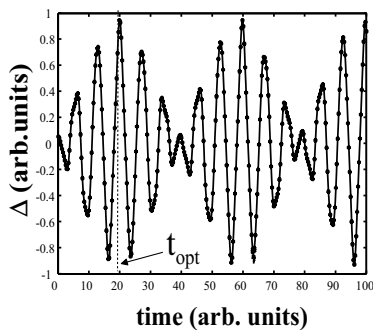


Fig. 4. Differential Contrast $\Delta(t)$ defined as the oscillation difference between the maximum and minimum of the initial image. Solid line: from the theoretical expression (7). \bullet : numerical simulation of (6) using a fourth order Runge-Kutta algorithm with integrating time step 10^{-3} . Parameters: $X_{i_0,j_0}^0 = 0$, $X_{i_1,j_1}^0 = 0.05$, that is $\Delta(t = 0) = 0.05$.

$$\Pi \Delta(t_{opt} = 19.91) = 0.95.$$

Therefore, the image goes through contrast minimum defined by the zeros of the Differential Contrast $\Delta(t)$ (for $t = 3.74$ and $t = 7.31$), as represented in figure 5.(b). and 5.(d).

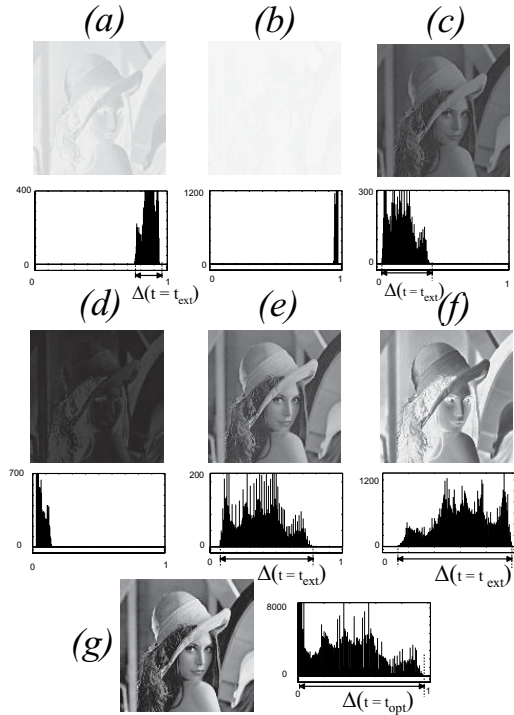


Fig. 5. Images and their histogram for different processing times. Parameters (a) : $t = 2.87$, (b) : $t = 3.74$, (c) : $t = 6.24$, (d) : $t = 7.31$, (e) : $t = 12.82$, (f) : $t = 16.33$, (g) : $t = 19.91$. (b) and (d) represent local minima of contrast provided by the zeros of Δ . (c), (e) and (g), corresponding to contrast enhancements, are obtained with the local maxima of Δ whereas the minima of Δ , images (a) and (f), allow a contrast enhancement with image inversion.

On the other hand, the local maxima of Δ correspond to contrast enhancements of the initial picture with a growing quality versus the processing time (figure 5.(c) 5.(e) and 5.(g) for $t = 6.24$, $t = 12.82$ and $t = 19.91$ respectively). A contrast optimum for a processing time $t_{opt} = 19.91$ is then reached (figure 5.(g)) as predicted by figure 4. (dotted lines).

The local minima, achieved namely for processing times $t = 2.87$ and $t = 16.33$, give also good contrast enhancements (figure 5.(a) and 5.(f)). However, the resulting images are inverted since the minima of the Differential Contrast are negative (see figure 4.). In fact, the pixel corresponding to the maximum gray level of the initial image becomes the minimum of the processed image and vice versa. This is the main property of this *C.N.N.*: at two closely different pro-

cessing times, it is possible, without reconfiguration of the oscillators network, to obtain a contrast enhancement with or without image inversion (fig 5.(f) for $t = 16.33$ and 5.(g) for $t = 19.91$).

Moreover, for a given processing time t_{ext} corresponding to a local extremum of $\Delta(t)$, $|\Delta(t_{ext})|$ represents the range of gray level of the resulting image. For instance, since for $t = 19.91$ the Differential Contrast predicted by figure 4 is $\Delta(19.91) = 0.95$, the image histogram of figure 5.(g) extends over 0.95 gray levels.

Note that the histogram of each resulting image shows clearly the oscillators network dynamic. Indeed, from an histogram corresponding to a weak contrasted image (figure 1), the histogram evolution versus time reveals that the range of gray levels periodically increases (figures 5.(a),(c),(e)) and decreases (figures 5.(b) and 5.(d)), conveying that the picture goes periodically from a weak contrasted situation to a higher contrasted one.

IV. ELECTRONIC IMPLEMENTATION

In this last section, we present an analog electrical lattice based on the properties of (6), which realizes in real time a contrast enhancement of an image loaded at the node of this lattice. This Cellular Nonlinear Network (C.N.N.) is constructed with $N \times M$ uncoupled elementary cells. Each elementary cell, represented in Fig. 6, consists of a basic operational amplifier circuit in parallel with a nonlinear resistor R_{NL} , whose current voltage characteristic obeys to the following cubic law (see ref. [7] for the electronic realization of this resistor):

$$I_{NL}(U) = \frac{-1}{R_0 V^2} \left(2U - \frac{1}{2} \right) \times \left(2U - \frac{3}{2} \right) \left(2U - 1 \right) \quad (10)$$

R_0 is a linear resistor while V is a weighting coefficient analog to a voltage. According to the notation of Fig. 6, and provided that the operational amplifier works in linear regime, we obtain

$$C \frac{dU_1}{dt} = -I_{NL}(U_{i,j}) \text{ and } \frac{U_1}{R} = -C \frac{dU_{i,j}}{dt}. \quad (11)$$

Therefore, the differential equation describing the evolution of the Voltage $U_{i,j}$ at the node number i, j of the C.N.N. writes:

$$\frac{d^2 U_{i,j}}{dt^2} = \frac{-1}{RC^2 R_0 V^2} \left(2U_{i,j} - \frac{1}{2} \right) \left(2U_{i,j} - \frac{3}{2} \right) \times \left(2U_{i,j} - 1 \right). \quad (12)$$

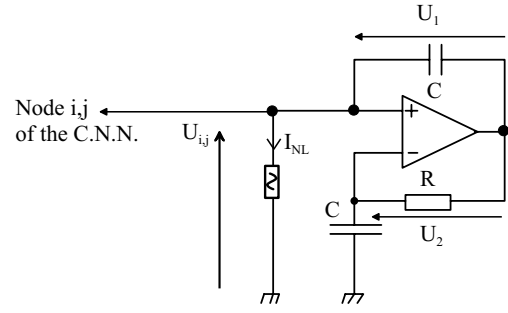


Fig. 6. Sketch of an electronic elementary cell of the C.N.N.. R_{NL} is a nonlinear resistor with a cubic current voltage characteristic, whereas C and R are linear components. The operational amplifier is supposed to work in linear regime, involving $U_1 = U_2$.

Eq. (12) appears as an analog simulation of equation (6) with a scale factor on the nonlinearity $\beta = \frac{1}{R_0 RC^2 V^2}$. Therefore, the experimental processing time to obtain the best contrast enhancement can then be adjusted with R, R_0, C or V to match real time processing constraints.

V. CONCLUSION

Considering uncoupled nonlinear oscillators, we have presented a Cellular Nonlinear Network which offer the advantage to perform two basic image processing tasks (contrast enhancement and image inversion) at two closely different times without needing a network reconfiguration. Moreover, an electronic implementation of this C.N.N. is proposed to realize real time image processing.

On the other hand, one might think that coupling oscillators with linear or nonlinear couplings could allow the extraction of interest region, which is also a current task performed in image processing. Therefore, this C.N.N. constitutes a framework for further investigations in nonlinear image processing.

REFERENCES

- [1] P. Marquié, S. Binczak, J.C. Comte and J.M. Bilbault, *Phys. Rev. E*, **57** (1998) 6075.
- [2] L.O. Chua, *A Paradigm for Complexity*, (World Scientific) (1998).
- [3] A. Adamatzky, B. de Lacy Costello, N. M. Ratcliffe, *Phys. Lett. A*, **297** (2002) 344
- [4] N.G. Rambidi, K.E. Shamayaev, G. YU Peshkov, *Phys. Lett. A*, **298** (2002) 375.
- [5] N.G. Rambidi and D. Yakovenchuk *Phys. Rev. E*, **63** (2001) 026607.
- [6] S. Morfu, J.C. Comte *Int. J. of Bifurcation and Chaos*, **14** (2004).
- [7] J.C. Comte and P. Marquié, *Int. J. of Bifurcation and Chaos*, **12** (2002) 447.

SCHEMES OF POLYNOMIAL EQUATIONS THAT CHARACTERIZE THE VARIATIONAL BEHAVIOUR

F.L. Neerhoff and P. van der Kloet

Dept. of Electrical Engineering
Delft University of Technology
Mekelweg 4, 2628 CD Delft, The Netherlands
e-mail: F.L.Neerhoff@ewi.tudelft.nl; P.vanderKloet@ewi.tudelft.nl

Abstract — *The variational equations of nonlinear dynamical systems are addressed. It is shown that their dynamics is fully characterized by a set of polynomials of decreasing order.*

I. INTRODUCTION

As is well known, small variations around a solution trajectory of general dynamical systems satisfy a linear time-varying (LTV) equation [1]. On their turn, the modal solutions of LTV equations are fully characterized by the earlier introduced dynamical eigenvalues [2].

In this paper, it is shown that the dynamical eigenvalues satisfy a scheme of polynomial equations of decreasing order. The time-dependent coefficients of each polynomial equations incorporate a dynamical eigenvalue solution of a lower order polynomial.

At first glance this seems to be in contradiction with the theory of linear time-invariant (LTI) systems with precisely one characteristic equation for the complete eigenspectrum.

However, in Section 2 it will be shown that also for LTI systems there is a set of characteristic equations corresponding to the set of eigenvalues.

It is derived with respect to single-input single-output (SISO) systems. In Section 3, the state space approach for time-varying systems is used in order to obtain the dynamic eigenvalues and the corresponding characteristic equations. The results are in agreement with LTI systems. It is demonstrated that the set of characteristic equations for LTV systems cannot be reduced to one and the same characteristic equation. As a consequence, our results are generalizations of the work of Kamen [3] and Zhu [4], respectively.

Finally, it is shown how the Cauchy-Floquet decomposition can be obtained without using the state space approach.

II. SCHEME OF CHARACTERISTIC EQUATIONS FOR LTI-SYSTEMS

Assume that the homogeneous input-output relation for SISO-LTI-systems is given by

$$a_0 D^n x + a_1 D^{n-1} x + \dots + a_{n-1} D x + a_n x = 0, \quad (1)$$

where $D = d/dt$ and a_0, a_1, \dots, a_n are constant coefficients, respectively. Relation (1) will be normalized by setting

$$a_0 = 1. \quad (2)$$

In (1) we write, for each time derivative

$$D^k x = D^{k-1} [D - \lambda] x + \lambda D^{k-1} x. \quad (3)$$

Then, the input-output equation (1) can be rewritten as

$$\sum_{i=0}^{n-1} \alpha_i D^{n-1-i} [D - \lambda] x + \left(\sum_{i=0}^n a_i \lambda^{n-i} \right) x = 0, \quad (4)$$

in which

$$\alpha_i = \sum_{j=0}^i a_j \lambda^{i-j} \quad (i = 0, 1, \dots, n-1). \quad (5)$$

Equation (4) shows that a modal solution of the form

$$x = \exp(\lambda t) \quad (6)$$

satisfies (1) if and only if eigenvalue λ is a solution of the polynomial equation

$$\sum_{i=0}^n a_i \lambda^{n-i} = 0, \quad (7)$$

which at this place is called the *first characteristic equation*. Note that in view of (7) it follows that $\alpha_n = 0$. In a further expansion, equation (4) can

be written as

$$\sum_{i=0}^{n-2} \beta_i D^{n-2-i} [D - \mu][D - \lambda]x + \left(\sum_{i=0}^{n-1} \alpha_i \mu^{n-1-i} \right) [D - \lambda]x + \left(\sum_{i=0}^n a_i \lambda^{n-i} \right) x = 0 \quad (8)$$

in which

$$\beta_i = \sum_{j=0}^i \alpha_j \mu^{i-j} \quad (i = 0, 1, \dots, n-1). \quad (9)$$

Now, equation (8) shows that the modal solution

$$x = \exp(\mu t) \quad (10)$$

satisfies the LTI input-output equation (1) if and only if

$$\left(\sum_{i=0}^{n-1} \alpha_i \mu^{n-1-i} \right) [\mu - \lambda] + \sum_{i=0}^n a_i \lambda^{n-i} = 0. \quad (11)$$

Next, if (6) is a solution of (1), equation (11) reduces in view of (7) to a so-called *second characteristic equation*

$$\sum_{i=0}^{n-1} \alpha_i \mu^{n-1-i} = 0. \quad (12)$$

Moreover, the solution (11) yields by substituting of (5) for α_i

$$\begin{aligned} & \left(\sum_{i=0}^{n-1} \alpha_i \mu^{n-1-i} \right) [\mu - \lambda] + \sum_{i=0}^n a_i \lambda^{n-i} = \\ & = \sum_{i=0}^n a_i \lambda^{n-i} - \sum_{i=0}^{n-1} a_j \lambda^{n-j} + \left(\sum_{j=0}^0 a_j \lambda^{0-j} \right) \mu^n + \\ & + \left(\sum_{j=0}^1 a_j \lambda^{1-j} - \sum_{j=0}^0 a_j \lambda^{1-j} \right) \mu^{n-1} + \dots \\ & \dots + \left(\sum_{j=0}^{n-1} a_j \lambda^{n-1-j} - \sum_{j=0}^{n-1} a_j \lambda^{n-1-j} \right) \mu^1 = \\ & a_0 \mu^n + a_1 \mu^{n-1} + \dots + a_{n-1} \mu^1 + a_n. \quad (13) \end{aligned}$$

Thus, for LTI systems the second characteristic equation is observed to be equivalent to the first characteristic equation.

From another point of view, equation (7) gives an

algebraic polynomial of degree n , while (12) yields an algebraic polynomial of degree $n - 1$.

Furthermore, relation (5) directly implies for $(i = 1, 2, \dots, n - 1)$

$$\lambda \alpha_{n-i} = -a_{n-i+1} + \alpha_{n-i+1} \quad (14)$$

and for $i = 0$

$$a_0 \lambda = -a_1 + \alpha_1 \quad \text{with} \quad a_0 = 1. \quad (15)$$

Now, if λ is eliminated from (14) and (15), we obtain for $i = 1, 2, \dots, n - 1$

$$(\alpha_1 - a_1) \alpha_{n-i} - \alpha_{n-i+1} + a_{n-i+1} = 0. \quad (16)$$

Next, we introduce the row vectors

$$\left. \begin{aligned} \mathbf{\alpha}^T &= [\alpha_{n-1}, \dots, \alpha_1] \\ \mathbf{a}^T &= [a_n, \dots, a_2] \\ \mathbf{e}_{n-1}^T &= [0, \dots, 0, 1] \end{aligned} \right\} \quad (17)$$

in which T stands for the transpose and the shift-matrix

$$\mathbf{I}_{n-1}^+ = \begin{bmatrix} 0 & 1 & \dots & 0 \\ \vdots & \ddots & \ddots & \vdots \\ \vdots & & \ddots & 1 \\ 0 & \dots & \dots & 0 \end{bmatrix}. \quad (18)$$

As a consequence, (16) can be written as the vector algebraic Riccati equation [5]

$$\mathbf{\alpha}^T \mathbf{e}_{n-1} \mathbf{\alpha}^T - a_1 \mathbf{\alpha}^T - \mathbf{\alpha}^T \mathbf{I}_{n-1}^+ + \mathbf{a}^T = \mathbf{0}^T. \quad (19)$$

In the same way, the characteristic equation (12) together with (9) induces a second algebraic Riccati equation, namely

$$\mathbf{\beta}^T \mathbf{e}_{n-2} \mathbf{\beta}^T - b_1 \mathbf{\beta}^T - \mathbf{\beta}^T \mathbf{I}_{n-2}^+ + \mathbf{b}^T = \mathbf{0}^T \quad (20)$$

with

$$\mathbf{\beta}^T = [\beta_{n-2}, \dots, \beta_1], \quad \mathbf{b}^T = [\alpha_{n-1}, \dots, \alpha_2], \quad \mathbf{b}_1 = \alpha_1. \quad (21)$$

This process can be continued $(n - 1)$ times. The final result is that the original input-output equation (1) is replaced by

$$\begin{aligned} & [D - \lambda_1][\dots][D - \lambda_n]x + \sum_{i=0}^1 \alpha_i^{(n-1)} \lambda_1^{1-i} [D - \lambda_2][\dots] \\ & \times [D - \lambda_n]x + \sum_{i=0}^2 \alpha_i^{(n-2)} \lambda_2^{2-i} [D - \lambda_3][\dots][D - \lambda_n]x + \\ & \dots + \sum_{i=0}^{n-1} \alpha_i^{(1)} \lambda_{n-1}^{n-1-i} [D - \lambda_n]x + \sum_{i=0}^n \alpha_i^{(0)} \lambda_n^{n-i} x = 0. \quad (22) \end{aligned}$$

It is concluded that the original differential polynomial with constant coefficients in (1) is *factorized from the right* with the eigenvalues $\lambda_n, \lambda_{n-1}, \dots, \lambda_1$. The coefficients $\alpha_i^{(j)}$ ($j = 0, 1, \dots, n-1$) are obtained as

$$\alpha_i^{(0)} = a_i \quad (i = 0, 1, \dots, n), \quad (23)$$

$$\alpha_i^{(j)} = \sum_{k=0}^i \alpha_k^{(j-1)} \lambda_j^{n+1-j} \text{ for } \begin{cases} (i = 0, 1, \dots, n-j) \\ (j = 1, 2, \dots, n-1), \end{cases} \quad (24)$$

with

$$\alpha_0^{(j)} = 1. \quad (25)$$

The elimination of the eigenvalues λ_j from (24) with $i = 1$ leads to

$$\alpha_1^{(j)} = \alpha_1^{(j-1)} + \lambda_j \quad (26)$$

which on its turn yields on account of (25) a set algebraic Riccati equations a for lower dimension.

III. SCHEME OF CHARACTERISTIC EQUATIONS FOR LTV-SYSTEMS

In the preceding section a scheme of characteristic equations for a LTI system has been derived. In it, each equation corresponds to a single algebraic Riccati equation. In this section the reverse problem will be considered: the Riccati equation will be obtained directly from the differential equation, and afterwards the characteristic equation from the Riccati equation (compare [6]). For that purpose, the input-output equation (1) is rewritten in the state space description

$$\dot{\mathbf{x}} = \begin{bmatrix} \mathbf{I}_{n-1}^+ & \mathbf{e}_{n-1} \\ -\mathbf{a}^T & -a_1 \end{bmatrix} \mathbf{x}, \quad (27)$$

where the dot stands for a differentiation with respect to the time t . This equation will be transformed to a second state space description according to the transformation

$$\mathbf{x} = \begin{bmatrix} \mathbf{I}_{n-1} & \mathbf{0} \\ \mathbf{p}^T & 1 \end{bmatrix} \mathbf{y}, \quad (28)$$

in which

$$\mathbf{p}^T = [p_1, \dots, p_{n-1}]. \quad (29)$$

The result of this transformation can be stated as

$$\dot{\mathbf{y}} = \begin{bmatrix} \mathbf{I}_{n-1}^+ + \mathbf{e}_{n-1} \mathbf{p}^T & \mathbf{e}_{n-1} \\ \mathbf{0}^T & \tilde{\lambda}_n \end{bmatrix} \mathbf{y}, \quad (30)$$

where

$$\tilde{\lambda}_n = -a_1 - p_{n-1} \quad (31)$$

and \mathbf{p}^T satisfies the vector Riccati differential equation

$$\dot{\mathbf{p}}^T = -\mathbf{p}^T \mathbf{I}_{n-1}^+ - \mathbf{a}^T + \tilde{\lambda}_n \mathbf{p}^T. \quad (32)$$

It may be clear that in (28) we have assumed that the vector \mathbf{p} is a function of time, thus $\mathbf{p}^T = \mathbf{p}^T(t)$. This allows a generalization to LTV systems.

If \mathbf{p}^T is assumed to be a constant, then the left-hand side of (32) reduces to zero and we have an algebraic Riccati equation. In that case, (30) shows that $\tilde{\lambda}_n$ is a classical eigenvalue of system given by (30) and thus of system (27). As a consequence, $\tilde{\lambda}_n$ is an eigenvalue of the original system, given by (1).

Next, we have to show that $\tilde{\lambda}_n = \tilde{\lambda}_n(t)$ satisfies a characteristic equation. For that purpose (32) is rewritten as

$$-p_i + \tilde{\lambda}_n p_{i+1} = a_{n-i} + \dot{p}_{i+1} \quad (i = 0, 1, \dots, n-2) \quad (33)$$

with $p_0 = 0$. If the equations in (33) are multiplied by $\tilde{\lambda}_n^i$ and subsequently added together, we obtain

$$\tilde{\lambda}_n^{n-1} p_{n-1} = \sum_{i=2}^n (a_i + \dot{p}_{n-i+1}) \tilde{\lambda}_n^{n-i}. \quad (34)$$

Elimination of p_{n-1} from (33) with the aid of (31) yields

$$\sum_{i=1}^n \bar{a}_i \tilde{\lambda}_n^{n-i} = 0, \quad (35)$$

in which the modified polynomial time-dependent coefficients $\bar{a}_i = \bar{a}_i(t)$ are given by

$$\bar{a}_i = a_i + \dot{p}_{n-i+1}, \quad (36)$$

with $p_n = 0$. Thus for LTI systems, where \mathbf{p}^T is a constant vector ($\dot{p}_{n-i+1} = 0$), equation (35) equals indeed the classical characteristic equation with $\tilde{\lambda}_n$ an eigenvalue of the input-output equation (1).

Next, we show

$$\tilde{\lambda}_n = \lambda_1. \quad (37)$$

To that aim, we remark that (30) yields

$$\left. \begin{aligned} \dot{y}_i &= y_{i+1} \quad (i = 1, 2, \dots, n-2) \\ \dot{y}_{n-1} &= p_1 y_1 + \dots + p_{n-1} y_{n-1} + y_n \\ \dot{y}_n &= \tilde{\lambda}_n y_n \end{aligned} \right\}. \quad (38)$$

As a consequence, we have

$$\left. \begin{aligned} D^{n-1}y_1 - p_{n-1}D^{n-2}y_1 - \dots \\ \dots - p_2Dy_1 - p_1y_1 = y_n \\ \dot{y}_n = \tilde{\lambda}_ny_n \end{aligned} \right\} . \quad (39)$$

Hence, y_n has the modal form [7]

$$y_n(t) = C \exp\left[\int \tilde{\lambda}(\tau) d\tau\right], \quad (40)$$

with C a constant. In addition, we have

$$[D - \tilde{\lambda}_n](D^{n-1} - p_{n-1}D^{n-2} - \dots - p_2D - p_1)y_1 = 0. \quad (41)$$

It is observed that the original differential polynomial in (1) will be *factorized from the left* this time. Since the transformation (28) implies

$$y_1 = x_1 = x, \quad (42)$$

equation (41) directly results into the identity (37).

It should be remarked, again, that (41) remains valid if the coefficients a_i are functions of time. To show this directly without the use of any state space description, write

$$D^n x = [D - \tilde{\lambda}_n]D^{n-1}x + \tilde{\lambda}_n D^{n-1}x \quad (43)$$

and substitute (31), resulting into

$$D^n x = [D - \tilde{\lambda}_n]D^{n-1}x - (a_1 + p_{n-1})D^{n-1}x. \quad (44)$$

As a consequence, we obtain

$$D^n x + a_1 D^{n-1}x = [D - \tilde{\lambda}_n]D^{n-1}x - p_{n-1}D^{n-1}x. \quad (45)$$

Next in (45) we apply

$$\begin{aligned} p_{n-1}D^{n-1}x &= D(p_{n-1}D^{n-2}x) - \dot{p}_{n-1}D^{n-2}x = \\ [D - \tilde{\lambda}_n]p_{n-1}D^{n-2}x &+ (\tilde{\lambda}_n p_{n-1} - \dot{p}_{n-1})D^{n-2}x \end{aligned} \quad (46)$$

and subsequently use the expression (33) for $i = n - 2$. This yields

$$\begin{aligned} D^n x + a_1 D^{n-1}x + a_2 D^{n-2}x &= \\ [D - \tilde{\lambda}_n](D^{n-1}x - p_{n-1}D^{n-2}x) &- p_{n-2}D^{n-2}x. \end{aligned} \quad (47)$$

By repetition of the above arguments we get

$$\begin{aligned} D^n x + a_1 D^{n-1}x + a_2 D^{n-2}x + \dots + a_{n-1}Dx &= \\ [D - \tilde{\lambda}_n](D^{n-1}x - p_{n-1}D^{n-2}x - \dots - p_2Dx) &- p_1Dx. \end{aligned} \quad (48)$$

Finally, with

$$p_1Dx = [D - \tilde{\lambda}_n]p_1x + a_nx, \quad (49)$$

we arrive at

$$\begin{aligned} D^n x + a_1 D^{n-1}x + a_2 D^{n-2}x + \dots + a_{n-1}Dx + a_nx &= \\ [D - \tilde{\lambda}_n](D^{n-1}x - p_{n-1}D^{n-2}x - \dots - p_2Dx - p_1x). \end{aligned} \quad (50)$$

It is clear that this process can be continued until the Cauchy-Floquet decomposition is obtained.

IV. CONCLUSIONS

In this paper, it is argued that for linear time-invariant (LTI) as well as for time-varying (LTV) systems each term of the Cauchy-Floquet factorization of the differential operator induces a characteristic polynomial and a set of coupled Riccati equations. For a n -th order system, the first right placed factor gives a n -th order characteristic polynomial and $n - 1$ coupled algebraic Riccati equations, with $n - 1$ solutions. For constant systems, these $n - 1$ solutions are the coefficients in the remaining differential polynomial. For LTV-systems, the vector algebraic Riccati equation is replaced by a vector differential Riccati equation, resulting in modified time dependent coefficients of the polynomials.

REFERENCES

- [1] Minorsky, N., *Nonlinear Oscillations*, R.E. Krieger Publ. Comp., Inc., USA, Chapt. 5, 1987.
- [2] Van der Kloet, P., *Modal Solutions for Linear Time Varying Systems*, Doctor of Science Thesis, 2002, Techn. Univ. Delft, The Netherlands.
- [3] Kamen E.W., *The Poles and Zeros of a Linear Time-varying System*, *Lin. Algebra and its Appl.*, Vol. 98, 1988, pp. 263-289.
- [4] Zhu J., *PD-Spectral Theory for Multivariable Linear Time-varying Systems*, Proc. 36th Conf. on Decis. and Control, San Diego, California USA, Dec. 1997, pp. 3908-3913.
- [5] Bittanti S., Laub A.J. and Willems J. C (Eds), *The Riccati Equation*, Springer-Verlag, 1991.
- [6] Kloet P. van der and Neerhoff F.L., *The Riccati Equation as Characteristic Equation for General Linear Dynamic Systems*, Proc. NOLTA'01, Miyagi, Japan, 28 Oct - 1 Nov., 2001, Vol. 2, pp. 425-428.
- [7] Pol B. van der, *The Fundamental Principles of Frequency Modulation*, *Journ. IEE*, Vol. 93, Part III, No. 23, May, 1946, pp. 153-158.

Identification of Bifurcation Parameters in Boost PFC Circuit

Mohamed Orabi and Tamotsu Ninomiya

Dept. of EESE, Kyushu University,
Fukuoka 812-8581, Japan
e-mail: orabi@ees.kyushu-u.ac.jp

Abstract—*The classical PFC design is based on stable periodic orbit which has desired characteristics. In this paper, the main bifurcations, which may undergo this orbit, when the parameters of the circuit change, are described. Also, the regions of instability phenomena of the PFC converter are delimited, which is of practical interest for engineering design. Beside, a prototype design of the PFC circuit is introduced to detect these instability experimentally. Results show a good agreement between the analysis and experiment.*

I. INTRODUCTION

Electronic equipment typically has the problem that a diode bridge-capacitor rectifier at the front end of the power circuit results in distorted input current waveform with high crest factor and harmonic content. Such a problem has prompted the development of Power Factor Correction (PFC) converter. PFC can be modelled in many approaches. From them, boost PFC with average current mode control approach is the common and most attractive. It has the advantage of improved noise, less total harmonic distortion and easy to shape sinusoidal waveform [1]. Many researchers have worked to investigate and to analysis the dynamic behavior of PFC. Most of them have introduced some assumptions, which have reduced the non-linear system to a linear system. The output voltage has been considered as constant employing the assumption of a very large capacitance in the output of the pre-regulator PFC stage. Therefore, the feedback signal has became time-invariant. Also, the time-varying input voltage has been replaced by its root-mean-square (rms) value, neglecting the effect of its time varying. Under these assumptions, small-signal equivalent circuits have been introduced. Stability problems have been studied on the basis of the linear system [2]-[3]. Also, there was no explanation for the instability waveforms and their frequencies on these linear models. Then, the price that must be paid is the inaccurate results and the disappearance for non-linear phenomena that can be found in practical sys-

tems. Thus, it is very essential to investigate the PFC converter from a nonlinear point of view and without any assumptions or limitation.

Recently the discussion of nonlinear analysis of PFC converter is highlighted. In [4] fast scale instability is detected in PFC converter, which has a slight effect on the power factor values. On the other hand, the authors have detected and introduced new low-frequency instabilities in the boost PFC converter [5]-[6]. These instability broke the converter operation, where the power factor is moved from a near unity to 0.5.

Boost PFC converter uses more complex circuitry in control than simpler cases which most commonly are analyzed from the nonlinear and bifurcation point of view in the literature [7]-[8]. Hence, the input voltage is a time varying, it is obvious that it is very difficult to deal with a complete bifurcation analysis. In this issue, our aim is to provide a clear design procedure to identify and diagnose the instability phenomena. Through these investigation, the difference between the unstable phenomena and input current distortion is made clear.

II. SYSTEM DESCRIPTION

Boost PFC circuit consists of a main power circuit and a control circuit. The main feature of this system is the output bulk capacitance and using multiplier and two control loops, feedback and feed-forward, in control circuit. That assures the non-linearity of the PFC converter. The main power circuit is constructed of full diode bridge circuit follows by dc/dc boost converter. The control circuit is the known used UC-3854A that operates at average current mode control [9]. Fig. 1 shows the detailed circuit of the boost PFC converter with average-current-mode control. The basic circuit of the converter consists of inductor L , diode D , switch Q and capacitor C connected in parallel to load R . The switch Q and the diode D are always in complementary operating states during the continuous-conduction-mode CCM operation. Essentially, it is a typical current-programmed boost converter, with the inductor current i_L chosen as

the programming variable and the programming template I_{ref} being the input voltage waveform. Obviously the average input current is programmed to track the input voltage, and hence the power factor is kept near unity. In addition, a feedback loop comprising a first-order filter serves to control the output voltage v_c . In breve, this done by adjusting the amplitude of the reference current I_{ref} , which is tracking the shape of the input voltage waveform v_{in} . The nonlinear model of the boost PFC converter has been proved though the average-state-space equation without averaging through the main frequency. It is constructed from two equations, one for the main power circuit and the second for the feedback loop [6]. These equations are(no description for these equation because of the limited space):

$$v_c \frac{dv_c}{dt} + \frac{v_c^2}{CR} = \frac{1}{K_1}(1 - \cos 2\omega t)(v_{vea}(t) - 1.5) - \frac{\omega L}{K_1^2 V^2} \sin(2\omega t)(v_{vea}(t) - 1.5)^2 - \frac{L}{K_1^2 V^2}(1 - \cos 2\omega t)(v_{vea}(t) - 1.5)$$

$$\tau \frac{dv_{vea}(t)}{dt} + v_{vea}(t) = V_{ref} + G_{fb}(K_f V_{ref} - v_c(t))$$

where $K_f = \frac{R_{vd} + R_{vi}}{R_{vd}}$, $G_{fb} = \frac{R_{vf}}{R_{vi}}$, and $\tau = R_{vf}C_{vf}$

v_{vea} , V_{ref} , K_{f1} , G_{fb1} , τ_1 , C_{vf} , R_{vf} , K_1 and R_{vd} & R_{vi} are feedback voltage,reference voltage, a constant, feedback gain, feedback gain time constant, feedback capacitor, feedback resistor, constant, and feedback divider resistors of the PFC boost converter, respectively.

From the nonlinear model (1),(2), There are six parametric, which can be varied (R , C , G_{fb} , τ , V , and ω) and three state variables v_c , i_L , v_{vea} . The inductor L has a relation to the fast current control loop with the switching frequency only. The fact that the input voltage of the PFC v_g is a time varying makes the system more complex and difficult to deal with a complete bifurcation analysis. Therefore, in this issue, an attempt to give a general outstanding about the stability condition and their borderline using this nonlinear PFC model.

III. A PROTOTYPE OF BOOST CONVERTER

A prototype of PFC boost converter using UC 3854A for average-current-mode control [9] is constructed in Lab to test the circuit stability under the

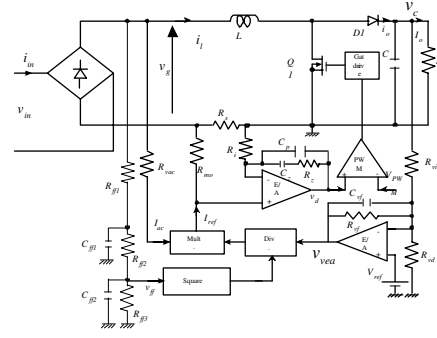


Fig. 1. Boost PFC converter with average-current-mode control circuit diagram.

parameters variation. The tested circuit are 100 kHz switching frequency, 100 Watt, 70-120 input voltage and 180 output voltage. The inductor L is chosen to be equal $700\mu\text{H}$ to achieve continuous-conduction-mode CCM operation. Operating conditions have been chosen as: output capacitor ranges are 22/47/60/100 μF , feedback capacitor ranges are 22/47/60/100 nF, feedback resistor ranges are 100/183/260 Kohm.

It is cleared that there are six parameters (R , V , ω , C , C_{vf} , R_{vf}) controls the system bifurcation. The first three parameters (R , V , and ω) are given data for every converter, and so the design must satisfy their ranges. The next three parameters (C , C_{vf} , R_{vf}) are the design parameters to make the converter stable. A lot of detailed experimental examples are investigated, but only two example is reported here for the limited space. One stable PFC operation point is explained as shown in Fig.2. The input current, i_{in} is periodically, sinusoidal, and in phase with input voltage, v_{in} . In this case, the test parameters have been 100 V input voltage, 60 Hz, 50% load, output capacitance, $C = 47\mu\text{F}$, 183 Kohm feedback resistor (0.31 feedback gain), and feedback capacitance, $C_{vf} = 100\text{ nF}$. The output voltage ripple, Δv_c is periodic with double frequency of the input line voltage. This is the features of stable operation. Then, for the same choosing parameters in Fig.2, stable operation, the circuit is examined with taking the feedback capacitor parametric in consideration. Figure 3 shows the unstable period doubling bifurcation as the feedback capacitor C_{vf} parametric decreased to 47nF. Period doubling bifurcation has the features of double period (half frequency ω) of that in the stable case for the output voltage. Moreover, another instability kind is detected in the system, which is chaotic instability. It is detected for the same parameters in Fig. 3 with 10% load. Chaotic phenomena appear clearly with non-repeating waveforms as shown in Fig.4.

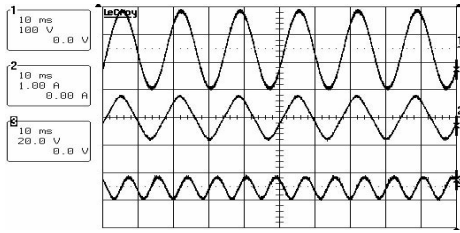


Fig. 2. stable operation of boost PFC converter.

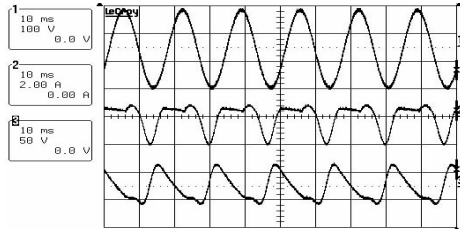


Fig. 3. Period doubling bifurcation operation of same PFC converter operating condition shown in Fig. 2 as the feedback capacitor parametric is decreased to 47 nF.

Therefore, it is important to clarify the whole PFC converter dynamics behavior and its stability borderlines in the parameter space. Testing all other operating points clears that instability phenomena appears as period doubling bifurcation at first and moves finally to chaotic instability with more change in the control bifurcation parameter.

IV. NUMERICAL ANALYSIS AND BIFURCATION MAPS

To help visualize the above results and prove the experiment observation, the nonlinear PFC model is used to plot a few indicative boundary surfaces and curves. Our purpose is to highlight the regions in the parameter space where normal operation is expected. The output voltage v_c is chosen as the judgment signal for the PFC converter stability. As reported in the above section from the experimental results and explained in Fig. 5 that stable operation has output voltage periodic at twice line frequency 2ω . However, period doubling bifurcation has output voltage periodic at line frequency. Also, the output voltage is non-repeating points in chaotic operation case. Therefore, sampling this output voltage every half line period (double line frequency) 2ω provides fixed points every half line period and so on a fixed surface is obtained in stable operation. Period doubling bifurcation gives two different fixed points at every half line period, which provides two different surfaces. Chaotic instability appears as non-repeating two different points every half line period, which can not provide any surface and gives different points only. Beside, high dis-

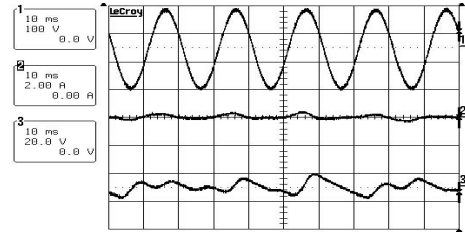


Fig. 4. Chaotic operation of boost PFC converter of same PFC converter operating condition shown in Fig. 3 as the feedback load parametric is decreased to 10%.

1-input voltage 2- input current 3- output ripple voltage

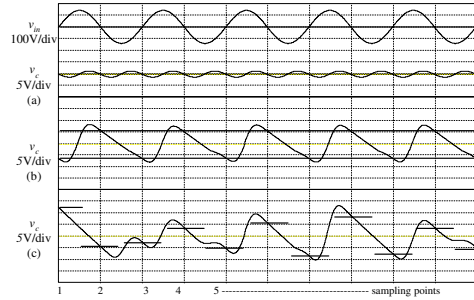


Fig. 5. The sampled output voltage at different cases and what it give in the bifurcation maps. (a) stable operation, region-1, appears as one fixed line. (b) period doubling bifurcation, region-2, appears as two fixed lines. (c) chaos instability, region-3, appears as multi different points.

torted area means a high output ripple values giving a lower output voltages surface than regular output surface values in stable case as shown in Fig. 6. That clears the difference between the instability and high distorted input current cases, which can be explained from linear models, that occurs because of high output ripple. As reported in this figure, as the operation move to region-4, the output voltage values become lower due to the higher output ripple, that results in a lower voltage surface.

Therefore, the bifurcation surface can be represented as:

$$v_c = f(R, V, \omega) + g(C, G_{fb}, \tau) \quad (4)$$

Moreover, choosing the output capacitor voltage v_c as a stability signal provides more information about the PFC converter dynamics, such as its power factor values and output voltage regulation. This can be cleared from the following bifurcation maps. The values of the sampling output voltage $V_{c,s}$ have its influence corresponding to the DC and AC values of the output voltage as shown in Fig. 5 and Fig. 6 for all different possible cases. The DC values are mainly depending on the output load R and the feedback DC gain G_{fb} parametric. Also, the AC values are mainly

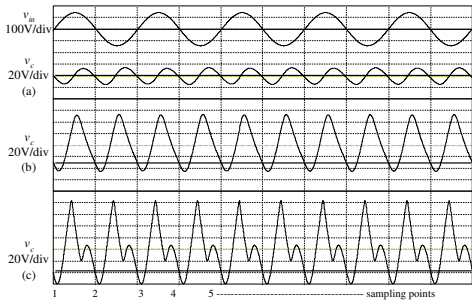


Fig. 6. The sampled output voltage at different cases and what it give in the bifurcation maps. (a) stable operation, region-1, appears as one fixed line. (b) high distorted area, region-4, appears as one lower voltage fixed line. (c) high distorted area, region-4, appears as one more lower voltage fixed line.

depending on output capacitor C parametric. Fixing one parametric and changing the other to establish the bifurcation maps, gives the understanding of the stability and the converter dynamics.

2-D bifurcation diagram is introduced in Fig. 7 for the same tested example. The stability judgment taken from the color difference. In these maps, yellow color indicates higher values of the sampled output voltage. Beside, lower output voltage has been indicated with a red color. Therefore, stable areas can be appears as clean and one color surface. Interpreting more colors in same surface means unstable operation. Clean surface with red color express the low output voltage, which means high output ripple result in a high distorted area as explained before in Fig. 6, unused area. Using this method, the borderline between stable and unstable regions can be made clear. This can be understood easy from Figs. 7(a) and 7(b) for different loads. Moreover, the converter power factor information can be provided from the same maps. Higher output ripple, lower sampled voltage surfaces, gives larger phase shift between the output voltage (and so the input current, where establish the reference current)and the input voltage. This results in a lower power factor. Then, yellow colors indicates high power factor and vise versa. Also, the changing from region-1 to region-4 occurs gradually as shown in the maps by graduate colors between yellow and red. On the other hand, moving from stable to unstable operation occurs suddenly. This clear any misunderstanding between moving from region-1 to region-4 or to other instability regions, region-2 and region-3.

Second, for varying the DC voltage parametric which is controlled mainly through the feedback gain and fixing the AC parametric, Fig. 8 is constructed.

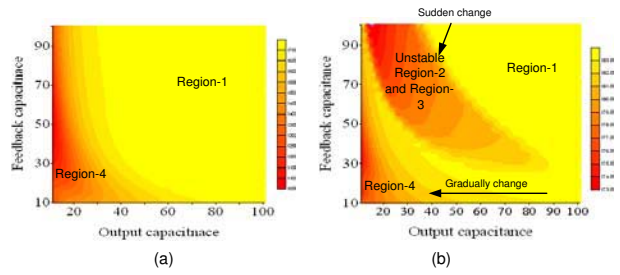


Fig. 7. 2-D bifurcation diagram between the output capacitor C (horizontal) and the feedback capacitor C_{vf} (vertical)at (a) full load and (b) 10% load.

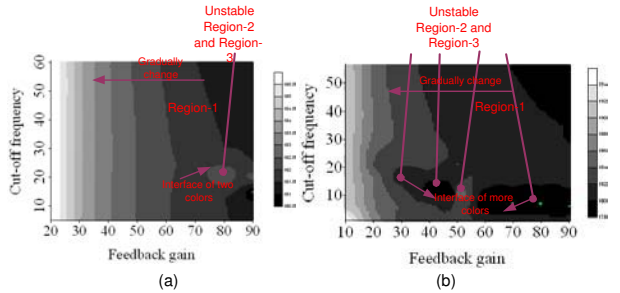


Fig. 8. 2-D bifurcation diagram between the DC feedback gain G_{fb} (horizontal) and the feedback cut-off frequency (vertical)at (a) $C=220\mu\text{F}$ and (b) $C=60\mu\text{F}$.

These maps explain another example for boost PFC converter with the tested parameters 100V, 50 Hz, 10%load (10 W). In this Figure, the feedback parametric effect on the system stability is explained to give guidelines for the feedback design. Fig.8(a) shows the 2-D bifurcation diagram at $C= 220\mu\text{F}$. It is cleared that small instability area appears at higher feedback DC gain. On the other hand, a larger unstable area appears at $C= 60\mu\text{F}$ as shown in Fig. 8(b). In these maps, stable operation, region-1, is indicated as a black color, where a clean surface is obtained. Therefore, unstable regions appear as an interface between the black and weight color together as shown in the maps. Moreover, higher Dc feedback gain means more regulated output voltage and so lower sampled output voltage (black color) means regulated system . Therefore, wight color indicates less regulation system. It is cleared that higher DC gain force the system to be unstable especially at lower output capacitor. Higher cut-off frequency increases the distortion in the system and so not good for practical design.

Generally the aim of these bifurcation maps is to provide an indication about system stability in the parameters space and shows the borderlines between stable and unstable operation. The details of the classification of each unstable area is not as of the interest here in this issue. If this needed another map can be introduced to shows every instable region and its spec-

ified area as will be done as a future work.

V. CONCLUSION

PFC converter has been studied as a nonlinear model. Three-dimensional and two-dimension bifurcation diagram are introduced to discuss the stability problems for boost PFC converter from the bifurcation view point. The instability area can be delimited using these bifurcation maps and it is clearly how to choose the circuit parameters that assures stability at all conditions. Moreover, these bifurcation maps give an indication about converter performance such as its input power factor values and output regulation.

REFERENCES

- [1] L. H. Dixon. High power factor preregulator for off-line power supplies. In *Unitrode Power Supply Design Seminar Manual*, SEM. 600, 1988.
- [2] R. Ridley. Average small-signal analysis of boost power factor correction circuit. In *Proc. VPEC seminar'89*, pp.108–120, 1989.
- [3] James P. Noon and D. Dalal. Practical design issues for PFC circuits. In *Proc. APEC'97*, pp.51–58, Georgia, USA, 1997.
- [4] C.K. Tse, O. Dranga, and H.H.C. Iu. Bifurcation analysis of a power-factor-correction boost converter: Uncovering fast-scale instability. In *Proc. ISCAS'03*, pp. III-312–315, Bangkok, Thailand, 2003.
- [5] M. Orabi, C. Jin, and T. Ninomiya. New formulation for the stability analysis of power factor correction converters. In *Proc. CIEP'02*, pp.33–38, Mexico, 2002.
- [6] M. Orabi, T. Ninomiya. Nonlinear dynamics in Power-Factor-Correction converter. In *IEEE-Trans. on IE*, Vol 50, No.6, Dec. 2003 pp.1116–1125.
- [7] Chi K. Tse. Recent developments in the study of nonlinear phenomena in power electronics circuits. In IEEE CAS newsletter, pp.14–48, March issue 2000.
- [8] E. Toribio, A. El Aroudi, G. Olivar, and L. Benadero. Numerical and experimental study of the region of period-one operation of a PWM boost converter. In *IEEE Trans. PE*, Vol. 15, No. 6, Nov. 2000, pp. 1163–1171.
- [9] P. C. Todd. UC3854 Controlled Power Factor Correction Circuit Design. In *Unitrode Application Note'97*, U-135, pp. 3-289 - 3-287.

ON THE START-UP BEHAVIOR OF SINGULARLY PERTURBED HARMONIC OSCILLATORS

M. Prochaska and W. Mathis

Institute of Electromagnetic Theory and Microwave Technique,
 University Hannover,
 Hannover, Germany
 e-mail: prochaska@tet.uni-hannover.de
 WWW:http://www.tet.uni-hannover.de

Abstract—*In this paper we present an analytic methodology for the analysis of harmonic oscillators. By this we combine geometric methods with the theory of singularly perturbed systems, which we use as tool for reduced order modeling. Through this we get a model for the start-up behavior of sinusoidal oscillators. Furthermore, we demonstrate our technique by means of the Clapp Oscillator.*

I. INTRODUCTION

Circuits like the Wien-Bridge, Hartley or Colpitts Oscillator are nonlinear networks since a nonlinear gain element is necessary to compensate the damping as well as for the stabilization of the amplitude. Oscillators are often modeled by linearized equations. It seems to be the main restriction of the linearization that the amplitude is not computable. However, the difference between a nonlinear oscillatory circuit and its linearization is more fundamental. The nonlinearity of an oscillator is an integral part of its functionality [13]. Moreover, by means of the nonlinear model an approximate amplitude of the oscillation can be calculated.

Oscillators are often modeled using a nonlinear dynamic system $\dot{\mathbf{x}} = \mathbf{f}(\mathbf{x})$, where $\mathbf{f}: \mathbb{R}^n \rightarrow \mathbb{R}^n$ and $\mathbf{x} \in \mathbb{R}^n$. The vector \mathbf{x} corresponds to time depending currents or voltages of the circuit while \mathbf{f} is a nonlinear vector field containing the influence of the gain element. A decomposition of \mathbf{f} gives

$$\begin{aligned} \dot{\mathbf{x}} &= \mathbf{A}\mathbf{x} + \tilde{\mathbf{f}}(\mathbf{x}) \\ &= \mathbf{A}\mathbf{x} + \mathbf{f}_2(\mathbf{x}) + \mathbf{f}_3(\mathbf{x}) + \dots + \mathbf{f}_{m-1}(\mathbf{x}) + O(m) \end{aligned}, \quad (1)$$

where $\mathbf{A} \in \mathbb{R}^{n \times n}$ is the Jacobian matrix $D_{\mathbf{x}}\mathbf{f}(\mathbf{0})$ evaluated at the equilibrium point and the fields $\mathbf{f}_k(\mathbf{x})$ contain the nonlinear terms in the Taylor expansion of \mathbf{f} of precise order k . It is well-known that (1) is locally stable if \mathbf{A} has only eigenvalues λ_i , $i=1..n$, with $\text{Re}(\lambda_i) < 0$ and unstable for $\text{Re}(\lambda_j) > 0$, $j \in [1, n]$. In that case a system is called hyperbolic. It is an also well-establish condition for a steady state oscillation that a system has a pair of conjugate complex eigen-

values with vanishing real parts - related criteria were presented by Barkhausen and Nyquist [17]. In this case the circuit is called non-hyperbolic. Since the Hartman Grobman Theorem tells us that if a system is hyperbolic, i.e. there exist no pure imaginary eigenvalues, a nonlinear system will possess the same behavior as its linearization. Otherwise we cannot neglect the nonlinearity.

A planar nonlinear dynamical system has primary two different types of solutions: Equilibrium points and periodic solutions. The relationship between these solutions is given by the Andronov Hopf Theorem. Originally this theorem was proved by Andronov in 1935 for the analysis of tube oscillators [14]. In this context we consider a dynamic system, which additionally depends on the parameter μ :

$$\dot{\mathbf{x}} = \mathbf{f}(\mathbf{x}, \mu) \quad (2)$$

Let $\mathbf{f}(\mathbf{x}, \mu)$ be a C^3 vector field such that $\mathbf{f}(\mathbf{0}, 0) = \mathbf{0}$ and $D_{\mathbf{x}}\mathbf{f}(\mathbf{0}, 0)$ has a pair of imaginary eigenvalues $\lambda_{\pm}(\mu=0) = \pm j\omega$. A so-called Hopf Bifurcation occurs when a pair of eigenvalues crosses the imaginary axis. The main conclusion of the Andronov Hopf Theorem is the condition that an asymptotic stable equilibrium is necessary for a stable limit cycle. Thus the Andronov-Hopf theorem is the basis for the operating mode of oscillators. For further information see [2], [7] and [16].

In the following we present qualitative methods in order to analyze the stability of the equilibrium point and show techniques which are useful to calculate the amplitude. Since it is difficult to apply symbolic methods for high dimensional systems we also show that the presence of singularities can be an useful tool for an analytic reduction of the dimension of Harmonic Oscillators. This point of view is different to that of Abed [1], who also introduced singular perturbed harmonic oscillators. While in [1] is shown how to neglect parasitic elements in a van der Pol Oscillator, we demonstrate that a singularity, which also can be an important design part of a high dimensional oscillatory circuit, is usable for reduced order modeling. Thus, we model the start-up behavior of sinusoidal oscillators, which is described in

[15], [20] and [21]. Through this, we are able to analyze high dimensional oscillators like the 4th Order Clapp Oscillator.

II. STABILITY

In order to analyze the stability of the equilibrium point Normal Form Transformations are powerful methods. We consider a nonlinear vector field locally in a neighborhood of equilibrium and try to simplify the linear and nonlinear parts. The initial point for our analysis is (1). The matrix \mathbf{A} possesses the eigenvalues $\lambda_1, \lambda_2, \dots, \lambda_n$. The idea is to choose a coordinate transformation so as to simplify the terms of the vector field. In order to simplify the linear part of the field $\mathbf{f}(\mathbf{x})$, we use the Jordan Form Theorem:

$$\dot{\mathbf{y}} = \mathbf{J}\mathbf{y} + \mathbf{T}^{-1}\tilde{\mathbf{f}}(\mathbf{T}\mathbf{y}), \quad (3)$$

with $\mathbf{J}=\mathbf{T}^{-1}\mathbf{A}\mathbf{T}$ and $\mathbf{x}=\mathbf{T}\mathbf{y}$. The invertible transformation \mathbf{T} , which diagonalizes \mathbf{A} or at least puts it into Jordan Form, consists mostly of the eigenvectors of \mathbf{A} . Since \mathbf{A} is diagonalizable, the qualitative behavior is identical to that of a diagonal matrix with the eigenvalues $\lambda_1, \lambda_2, \dots, \lambda_n$.

In order to simplify the nonlinear terms in (1) we try to find a sequence of coordinate transformations $\mathbf{x}=\mathbf{y}+\mathbf{h}_k(\mathbf{y})$ which remove terms of increasing degree from the Taylor series. This equation is a so called near identity transformation. The terms which cannot be eliminated are called resonant terms. A dynamic system which has an equilibrium with eigenvalues $\pm j\omega$ can be expressed in the so called Poincare Normal Form

$$\dot{\mathbf{y}} = \begin{bmatrix} 0 & \omega \\ -\omega & 0 \end{bmatrix} \mathbf{y} + \sum_{i=1}^{\infty} (y_1^2 + y_2^2)^i \begin{bmatrix} a_i & b_i \\ -b_i & a_i \end{bmatrix} \begin{bmatrix} y_1 \\ y_2 \end{bmatrix}, \quad (4)$$

where the coefficients a_i and b_i are 0 for even i . The reader should note that the equilibrium is asymptotically stable, if $a_1 < 0$. So the Poincare Normal Form is a primary key for fulfilling the Andronov Hopf Theorem. How to perform this method in detail is described in [3], [4] and [11].

II. SINGULARITIES

Since (4) is a two-dimensional system a model order reduction for high dimensional systems is necessary, wherefore the Center Manifold Theorem is often used [5], [19]. However, to apply this method the eigenvalues have to be calculated. This leads to a numerical computation, if the dimension of the system is greater than four. We find a remedy if the oscillatory system has singularities, which can be used to apply a reduced order modeling by means of

the Theory of Singularly Perturbed Systems [6]. The initial point is a system $\dot{\mathbf{x}}=\mathbf{f}(\mathbf{x})$ where \mathbf{x} is an n -vector. To reduce the number of differential equations the quasi-steady state assumption (QSSA) is common practice. Therefore, first we have to detect the singularity δ which transfers our system into

$$\begin{aligned} \dot{\mathbf{y}} &= \mathbf{f}(\mathbf{y}, \mathbf{z}, \delta) \\ \delta \dot{\mathbf{z}} &= \mathbf{g}(\mathbf{y}, \mathbf{z}, \delta) \end{aligned} \quad (5)$$

where $\mathbf{y} \in \mathbb{R}^m$, $\mathbf{z} \in \mathbb{R}^l$ and $m+l=n$. Under some additional conditions, (5) represents a dynamic system on a constrained manifold [6],[9]. Under the assumption that the Jacobian $D_{\mathbf{z}}\mathbf{g}(\mathbf{y}, \mathbf{z}, 0)$ is invertible on a solution $\mathbf{g}(\mathbf{y}, \mathbf{z}, 0)=\mathbf{0}$, the vector \mathbf{y} represents the fast variables near the solution for small δ . For $\delta=0$ we get

$$\begin{aligned} \dot{\mathbf{y}} &= \mathbf{f}(\mathbf{y}, \mathbf{z}, 0) \\ \mathbf{0} &= \mathbf{g}(\mathbf{y}, \mathbf{z}, 0) \end{aligned} \quad (6)$$

which is called the degenerate system to (5). Now we can rewrite (5) in the form

$$\dot{\mathbf{y}} = \mathbf{f}(\mathbf{y}, \varphi(\mathbf{z}), 0), \quad (7)$$

where $\mathbf{z}=\varphi(\mathbf{y})$ and $\mathbf{g}(\mathbf{y}, \varphi(\mathbf{z}))=0$. Thus (7) represents the steady state oscillation, while the so-called fast system in the fast time scale $\tau=t/\varepsilon$ represents the start-up behavior for ε small.

If the reduced system (7) is not equivalent to the two dimensional center manifold, another reduction to the center manifold is necessary. However, because of the QSSA we have in that case to reduce (7), which possesses a lower dimension as (2). Typically, systems like (5) are used for the modeling of relaxation oscillators. But it is also possible to reduce harmonic oscillators [1], since the Andronov Hopf Theorem is also valid for singularly perturbed Harmonic Oscillators [23].

III. AMPLITUDE

In order to calculate an approximate amplitude the initial point is (2), which depends additionally on μ . That is why the Center Manifold Theorem has to be modified. We consider the system (2), where $\mathbf{f} \in C_{x,\lambda}^{1,0}$ and $\mathbf{f}(\mathbf{0}, \lambda)=0 \forall \lambda$. If we assume that the Jacobian $D\mathbf{f}_x(\mathbf{0}, 0)$ possesses $k > 2$ eigenvalues with vanishing real parts, then there exists a k -dimensional integral manifold in a sufficient small neighborhood of $\mathbf{x}=\mathbf{0}$ and for small $|\lambda|$. Similar to the center manifold we can express the system which is perturbed by μ in the form

$$\dot{\mathbf{x}}_c = \mathbf{J}_c(\mu)\mathbf{x}_c + \mathbf{f}(\mathbf{x}_c, \mathbf{x}_s, \mu), \quad (8)$$

where \mathbf{J}_c possesses a pair of conjugate complex

eigenvalues. A detailed description provides [22].
 In order to calculate the amplitude of a sinusoidal oscillator it is suitable to transform the reduced system to polar coordinates:

$$\begin{bmatrix} \dot{\Theta} \\ \dot{r} \end{bmatrix} = \begin{bmatrix} \omega \\ 0 \end{bmatrix} + \mathbf{f}_{PC}(\Theta, r) \quad (9)$$

Since the equation $\dot{r}=0$ is mostly a function of Θ , i.e. both equations of (9) are coupled; we cannot calculate the amplitude directly. To produce a relief we use an average technique – a perturbation method. Our approach of Lie series averaging is based upon the results from [8] and [12]. Like the normal form transformation, averaging uses a near identity transformation to simplify the given system. The transformation is to be chosen to transform the original system into the so called averaged system. By means of this method it is our goal to eliminate the action of Θ in the second equation of the system (9). The method hinges on the identification of a small parameter ε which marks the perturbation. In Cartesian coordinates we get for $\mu=0$

$$\dot{\mathbf{y}} = \begin{bmatrix} 0 & \omega \\ -\omega & 0 \end{bmatrix} \mathbf{y} + \varepsilon \mathbf{f}_s(\mathbf{y}) = \mathbf{J} \mathbf{y} + \varepsilon \mathbf{f}_s(\mathbf{y}) \quad (10)$$

In polar coordinates we can write the following system, where mostly both equations are coupled

$$\begin{bmatrix} \dot{\Theta} \\ \dot{r} \end{bmatrix} = \begin{bmatrix} \omega \\ 0 \end{bmatrix} + \varepsilon \begin{bmatrix} \mathbf{R}(\Theta, r) \\ \mathbf{T}(\Theta, r) \end{bmatrix} \quad (11)$$

By using a suitable transformation we find the averaged system

$$\begin{bmatrix} \dot{\bar{\Theta}} \\ \dot{\bar{r}} \end{bmatrix} = \begin{bmatrix} \omega \\ 0 \end{bmatrix} + \varepsilon \begin{bmatrix} \bar{\mathbf{R}}(\bar{r}) \\ \bar{\mathbf{T}}(\bar{r}) \end{bmatrix} \quad (12)$$

Here we have assumed that already one averaging gives a usable result. But sometimes a sequence of coordinate transformations is necessary. Especially in this case our approach which is based upon Lie series is advantageous [12].

IV. CASE STUDY

The methods which are previously listed have been implemented with MATLAB - especially using the symbolic toolbox. By means of these routines we have analyzed the so-called Clapp Oscillator (Fig. 1).

The Clapp Circuit is a member of Colpitts, Clapp and Pierce Oscillator Family [18], so that this circuit is just an example. Our methodology – especially the

reduced order modeling by means of singular perturbations - is also applicable to other sinusoidal Oscillators like the crystal based Pierce Oscillators.

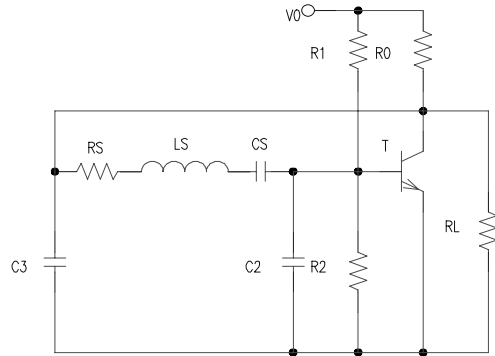


Fig. 1 The Clapp Oscillator

We model the collector-emitter current i_C of the Transistor T for $i_B \approx 0$ by

$$i_C = I_S \left(e^{\frac{v_{BE}}{V_T}} - 1 \right) = k_1 + k_2 v_{BE} + k_3 v_{BE}^3 \quad (13)$$

The model of this circuit is given by

$$\begin{aligned} C_1 \dot{v}_{C1} &= -\frac{R_0 + R_L}{R_0 R_L} v_{C1} - k_2 v_{C2} - i_s - k_3 v_{C2}^3 - k_1 - \frac{V_0}{R_1} \\ C_2 \dot{v}_{C2} &= -\frac{R_1 + R_2}{R_1 R_2} v_{C2} + i_s + \frac{V_0}{R_1} \\ C_s \dot{v}_s &= i_s \\ L_s \dot{i}_s &= v_{C1} - v_{C2} - v_{C3} - R_s i_s \end{aligned} \quad (14)$$

Typically, analog designers choose $C_s \ll C_1, C_2$. In order to transform (14) into a singular perturbed system, time scale modeling is a promising technique [9]. A systematic approach to identify adequate time scales is presented in [10] and [11]. If we choose $\tau = (LC)^{1/2} t = \omega_1 t$ as a capable unit for the time and $C_1 = C_2 = C$ we get

$$\begin{aligned} y_1 &= \frac{\sqrt{CL_s^3}}{\omega_1} y_2 \\ \dot{y}_2 &= \sqrt{\frac{L}{C}} (-y_1 - R_s y_2 + z_1 - z_2) \\ \sqrt{\frac{C_s}{C}} \dot{z}_1 &= -\frac{\omega_1}{RC} z_1 - \frac{\omega_1 C_2}{C} z_2 - \frac{\omega_1}{C} y_2 - \frac{\omega_1 C_3}{C} z_2^3 \\ \sqrt{\frac{C_s}{C}} \dot{z}_2 &= -\frac{\omega_1}{RC} z_2 + \omega_1 y_2 \end{aligned} \quad (15)$$

where

$$R = \frac{R_0 R_L}{R_0 + R_L} = \frac{R_1 R_2}{R_1 + R_2} \quad (16)$$

Because of the Andronov Hopf Theorem the equilibrium of the model must be located at the origin. This is guaranteed by a coordinate transformation, where c_2 und c_3 are the modified coefficients of the nonlinearity. For presentation we neglect quadratic terms. If we choose $\delta = \sqrt{C_s/C} \ll 1$ as the perturbation parameter and under the QSSA we get for $\delta=0$ the reduced system, which is for a suitable choice of the coefficient c_2 equal to the center manifold. With $R_S = \mu^* \cdot 2R/L\mu$, $c = c_3 R^3/L$ and μ small, we get directly the integral manifold of the reduced system in the original time scale

$$\dot{\mathbf{y}} = \begin{bmatrix} \mu & 1 \\ -1 & \mu \end{bmatrix} \mathbf{y} + \begin{bmatrix} 0 \\ -cy_2^3 \end{bmatrix}, \quad (17)$$

where we choose $L_S = C_S = R = 1$. $\mu^* > 0$ is an arbitrary value and μ the bifurcation parameter. For $\mu=0$ we get the following Poincare Normal Form:

$$\dot{\mathbf{y}} = \begin{bmatrix} 0 & 1 \\ -1 & 0 \end{bmatrix} \mathbf{y} + (y_1^2 + y_2^2) \begin{bmatrix} -\frac{3}{8} & 0 \\ 0 & -\frac{3}{8} \end{bmatrix} \begin{bmatrix} y_1 \\ y_2 \end{bmatrix} c + \dots (18)$$

We get the so-called Poincare Coefficient $a_1 = -3/8c$. For $c > 0$ the equilibrium is asymptotic stable and so there exists a variation of circuit parameter c which generates the birth of a limit cycle. In order to predict the amplitude of the limit cycle we have to identify and mark the perturbation of the linear oscillator by means of the parameter ε . Then we can transform (17) to polar coordinates:

$$\begin{bmatrix} \dot{\Theta} \\ \dot{r} \end{bmatrix} = \begin{bmatrix} 1 \\ 0 \end{bmatrix} + \varepsilon \begin{bmatrix} r^2 \sin \Theta \cos \Theta \\ r\mu + \mu \cos^2 \Theta + \dots \end{bmatrix} \quad (19)$$

Since both equations of (19) are coupled averaging is necessary. We calculate

$$\begin{bmatrix} \dot{\bar{\Theta}} \\ \dot{\bar{r}} \end{bmatrix} = \begin{bmatrix} 1 \\ \varepsilon \bar{r} \mu - \varepsilon \frac{3}{8} c \bar{r}^3 \end{bmatrix}, \quad (20)$$

where already one averaging removes the terms depending on Θ . The roots of $\dot{\bar{r}} = 0$ are

$$\bar{r}_1 = 0, \bar{r}_2 = \pm \sqrt{\frac{8\mu}{3c}} \quad (21)$$

The value \bar{r}_1 defines the averaged amplitude for an unstable equilibrium. If the Andronov Hopf Theorem is fulfilled, the Clapp Oscillator has the amplitude $|\bar{r}_2|$.

V. CONCLUSION

In this work we have presented a dynamic systems approach for analyzing nearly sinusoidal oscillators by using geometrical methods. It turns out that geometric methods are powerful tools for investigations of nonlinear oscillators and singularities are useful properties of Harmonic Oscillators for reduced order modeling and the modeling of the start-up behavior.

REFERENCES

- [1] Abed, E.H., Singularly Perturbed Hopf Bifurcation, IEEE-CAS 32 (1985), 1270-1280
- [2] Andronov, A.A.; A.A. Vitt; S.E. Khaikin, Theory of Oscillators, Dover Publications, New York 1966
- [3] Arnold, V.I., Geometrical Methods in the Theory of Ordinary Differential Equations, Springer Verlag 1983
- [4] Ashkenazi, M.; S. Chow, Normal Forms near Critical Points for Differential Equations and Maps, IEEE-CAS 35 (1988), 850-872
- [5] Carr, J. Applications of Centre Manifold Theory, Springer Verlag 1981
- [6] Fenichel, F., Geometric Singular Perturbation Theory for Ordinary Differential Equations, J. Diff. Equ., 31, 1979, 53-98
- [7] Guckenheimer, J.; P. Holmes, Dynamical Systems and Bifurcation of Vector Fields, Springer Verlag New York 1983
- [8] Kirchgraber, U.; E. Stiefel, Methoden der analytischen Störungsrechnung und ihre Anwendungen (German), Teubner Verlag Stuttgart 1978
- [9] Kokotovic K., H. K. Khali, J.O'Reilly, Singular Perturbation Methods in Control, SIAM, 1999
- [10] Mathis, W., L. O. Chua, Applications of Dimensional Analysis to Network Theory, Proc. Of the 10th European Conference on Circuit Theory, 1991
- [11] Mathis, W., Transformation and Equivalence; in: The Circuits and Filters Handbook, Ed. W.K.Chen, CRC Press Boca Raton 1995
- [12] Mathis, W.; G. Wettlaufer, Lie Series Averaging and Computer Algebra, Proc. IEEE 31st Midwest Symp. CAS St.Louis, 664-667
- [13] Mathis, W., Nonlinear electronic circuits – An overview, Proc. 7th. MIXDES 2000, Gdynia, Poland
- [14] Mathis, W., Historical Remarks of the History of Electrical Oscillators, In: Proc. MTNS-98 Symposium, July 1998, IL POLIGRAFO, Padova 1998, 309-312
- [15] Mathis, W., An Efficient Method for the Transient Analysis of Weakly Damped Crystal Oscillators, In: Proc. MTNS-98 Symposium, July 1998, IL POLIGRAFO, Padova 1998,
- [16] Mees, A.I., L.O. Chua, The Hopf Bifurcation and its Application to nonlinear Oscillations in Circuits and Systems. IEEE Trans. Circuits and Systems, vol. 26, 1979, 235-254
- [17] Milman J., A. Grabel, Microelectronics, 2nd ed. Singapore, McGraw-Hill, 1995
- [18] Parzen, B. Design of Crystal and Other Harmonic Oscillators, Wiley & Sons, 1983
- [19] Prochaska, M., W.Mathis, Symbolic Analysis Methodes for Harmonic Oscillators, Proc. 12th International Symposium on Theoretical Electrical Engineering, Warsaw 2003
- [20] Rusznyak, A., Start-Up Time of CMOS Oscillators, IEEE Transactions on Circuit and Systems, 34 (3), 259-268
- [21] Schmidt-Kreusel, C., Rechnergestützte Analyse von Quarzoszillatoren (German), Dissertation, University of Wuppertal, 1997
- [22] Schneider, K.R., On the Application of Integral Manifolds to Hopf Bifurcation, Math. Nachr. 97 (1980), 313-323
- [23] Schneider, K.R., Hopf Bifurcation of Singularly Perturbed Autonomous Differential Systems, Math. Nachr. (1983), 5-18

RECONSTRUCTION OF DRIVEN AND COUPLED TIME-DELAY SYSTEMS FROM TIME SERIES

M. D. Prokhorov, A. S. Karavaev and V. I. Ponomarenko

Saratov Branch of the Institute of RadioEngineering and Electronics
of Russian Academy of Sciences,
Zelyonaya str., 38, Saratov, 410019, Russia
e-mail: sbire@sgu.ru

Abstract – *We propose a method that allows one to estimate the parameters of driven time-delay systems and coupled time-delay systems from time series. The method can be successfully applied to short time series under sufficiently high levels of noise.*

I. INTRODUCTION

The problem of recovery of nonlinear dynamical models of time-delay systems from time series has received much attention in recent years [1–7]. The importance of this problem research is determined by the fact that time-delay systems are wide spread in nature. The behavior of such systems is affected not only by the present state, but also by past states. These systems are usually modeled by delay-differential equations. Such models are successfully used in many scientific disciplines, like physics, physiology, biology, economic, and cognitive sciences. However, the reconstruction of model equations of time-delay systems from time series has not been practically considered for the cases when these systems are coupled to each other or affected by the systems without delay. At the same time such situation is typical for many important applications. In this paper we extend the methods recently proposed by us for the estimation of the parameters of time-delay systems from chaotic time series [5, 6] to the cases of driven and two coupled time-delay systems.

We consider a delayed nonlinear feedback system X described by the following first-order delay-differential equation

$$\varepsilon_1 \dot{x}(t) = -x(t) + f_1(x(t - \tau_1)), \quad (1)$$

where $x(t)$ is the system state at time t , function f defines nonlocal correlations in time, τ_1 is the delay time, and parameter ε_1 characterizes the inertial properties of the system. In general case Eq. (1) is a mathematical model of an oscillating system composed of a ring with three ideal elements: nonlinear, inertial, and delay ones. In Fig. 1 these elements are denoted respectively as f_1 , ε_1 , and τ_1 . Let us consider

the case when the system X is driven by a system Y . The system Y variable can be injected into the ring system X at different input points indicated in Fig. 1 by the numerals I-III. Depending on the point of the signal $y(t)$ input the system X dynamics is described by one of the following equations

$$\text{I: } \varepsilon_1 \dot{x}(t) = -x(t) + f_1(x(t - \tau_1) + k_1 y(t - \tau_1)), \quad (2)$$

$$\text{II: } \varepsilon_1 \dot{x}(t) = -x(t) + f_1(x(t - \tau_1) + k_1 y(t)), \quad (3)$$

$$\text{III: } \varepsilon_1 \dot{x}(t) = -x(t) + f_1(x(t - \tau_1)) + k_1 y(t), \quad (4)$$

where k_1 is the coupling coefficient characterizing the system Y action at the system X .

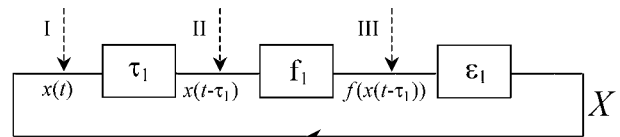


Figure 1. Block diagram of a time-delay system X .

We propose a method that allows one to reconstruct the time-delay system X from the time series of systems X and Y and to define the type of coupling (to distinguish the situations described by Eqs. (2)–(4)) and its strength.

II. METHOD DESCRIPTION

To recover the delay time τ_1 from the temporal realization $x(t)$ we exploit the method proposed recently in [5], where we have shown that there are practically no extrema separated in time by τ_1 in the time series of time-delay system (1). Then, for τ_1 definition one has to determine the extrema in the time series and after that to define for different values of time τ the number N of pairs of extrema separated in time by τ and to construct the $N(\tau)$ plot. If N is normalized to the total number of extrema, then for sufficiently large extrema number it can be used as an estimation of probability to find a pair of extrema in the time series, separated by the interval τ .

The absolute minimum of $N(\tau)$ is observed at the delay time τ_1 . We show that this method of the delay time estimation can be successfully applied in the case when the system X is affected by the system Y . The method is still efficient for sufficiently high levels of the Y action at X , if this action is not followed by the appearance of a great number of additional extrema in the time series of X .

To recover the parameter ε_1 , the nonlinear function f_1 and the coupling coefficient k_1 we propose a method using time series of both variables $x(t)$ and $y(t)$. Let us assume first that the type of action of Y at X is known a priori, i.e., we know the structure of equation governing the dynamics of driven time-delay system. As an example, we consider the case I described by Eq. (2), when $y(t)$ is injected into the system X after the inertial element. Then, it is possible to reconstruct the nonlinear function by plotting in a plane a set of points with coordinates $(x(t-\tau_1)+k_1y(t-\tau_1), \varepsilon_1\dot{x}(t)+x(t))$. According to Eq. (2), the constructed set of points reproduces the function f_1 . Since the parameters ε_1 and k_1 are a priori unknown, one needs to plot $\varepsilon\dot{x}(t)+x(t)$ versus $x(t-\tau_1)+ky(t-\tau_1)$ under variation of ε and k , searching for a single-valued dependence in the plane $(x(t-\tau_1)+ky(t-\tau_1), \varepsilon\dot{x}(t)+x(t))$, which is possible only for $\varepsilon=\varepsilon_1, k=k_1$. As a quantitative criterion of single-valuedness in searching for ε_1 and k_1 we use the minimal length of a line $L(\varepsilon, k)$, connecting all points ordered with respect to the abscissa in the mentioned plane. The minimum of $L(\varepsilon, k)$ is observed at $\varepsilon=\varepsilon_1, k=k_1$. The set of points constructed for the defined ε_1 and k_1 in the plane $(x(t-\tau_1)+k_1y(t-\tau_1), \varepsilon_1\dot{x}(t)+x(t))$ reproduces the nonlinear function, which can be approximated if necessary. The proposed technique uses all points of the time series. It allows one to estimate the parameters ε_1 and k_1 and to reconstruct the nonlinear function from short time series even in the regimes of weakly developed chaos.

Similarly it is possible to recover the nonlinear function and the parameters ε_1 and k_1 for the systems (3) and (4) by plotting $\varepsilon\dot{x}(t)+x(t)$ versus $x(t-\tau_1)+ky(t)$ and $\varepsilon\dot{x}(t)+x(t)-ky(t)$ versus $x(t-\tau_1)$, respectively, under variation of ε and k . If we do not know a priori the point at which the system Y variable is injected into the system X we have to reconstruct each of the model equation (2)–(4). The single-valuedness of the recovered nonlinear

function can be achieved only in the case of true choice of model structure. Thus, the method allows one to estimate the parameters of driven time-delay system from time series and to define the structure of model equation. If the system Y is also a time-delay system, then we have the case of two coupled time-delay systems and the method is able to reconstruct both of them.

III. METHOD APPLICATION

To verify the method we consider the case when the system X is described by the Mackey-Glass equation

$$\dot{x}(t) = -bx(t) + \frac{ax(t-\tau_1)}{1+x^c(t-\tau_1)} \quad (5)$$

and the driving signal of the system Y is harmonic or a chaotic one. Eq. (5) can be converted to Eq. (1) with $\varepsilon_1 = 1/b$ and

$$f_1(x(t-\tau_1)) = \frac{ax(t-\tau_1)}{b(1+x^c(t-\tau_1))}. \quad (6)$$

Figure 2 illustrates the results of reconstruction of the Mackey-Glass system X at $a=0.2, b=0.1, c=10, \tau_1=300$ driven by the harmonic signal $y(t) = A\sin\omega t$ with the amplitude $A=1$ and the period $T = 2\pi/\omega = 130$. The driving signal is injected into the system X at the point I with a coupling coefficient $k_1=0.1$. To construct the $N(\tau)$ plot, Fig. 2(a), we use 5000 points of the realization $x(t)$. The derivative $\dot{x}(t)$ is estimated from the time series by applying a local parabolic approximation. The location of the absolute minimum of $N(\tau)$ allows us to estimate the delay time accurately, $\tau_1=300$.

Assuming that the point of the driving signal injection is unknown we reconstruct each of the model equation (2)–(4). Figures 2(b)–(d) illustrate the results of the nonlinear function recovery for the choice of model equation in the form of Eqs. (2)–(4), respectively, with the parameters ε and k corresponding to the minimal length of the line $L(\varepsilon, k)$. To construct these plots we use only 1000 points of $x(t)$ and $y(t)$ realizations. Searching for $L_{min}(\varepsilon, k)$ we set the step of ε variation equal to 0.1 ($\varepsilon_1 = 1/b = 10$) and the set of k_1 variation equal to 0.01. For the case of model reconstruction in the form of Eq. (2) the minimal value of $L(\varepsilon, k)$ normalized to the number of points is $L_{min}(\varepsilon, k) = L(10.1, 0.10) = 0.007$. Reconstructing a model in the form of Eqs. (3) and (4) we obtain $L_{min}(\varepsilon, k) = L(7.4, -0.05) = 0.153$ and $L_{min}(\varepsilon, k) = L(7.3, 0.06) = 0.147$, respectively. Only one of the

three plots (Fig. 2(b)) demonstrates a practically single-valued curve with $L_{min}(\varepsilon, k)$ significantly smaller than in the two other cases. This result indicates that the model equation has the form of Eq. (2) and the parameters ε_1 and k_1 of this equation are recovered with a good accuracy.

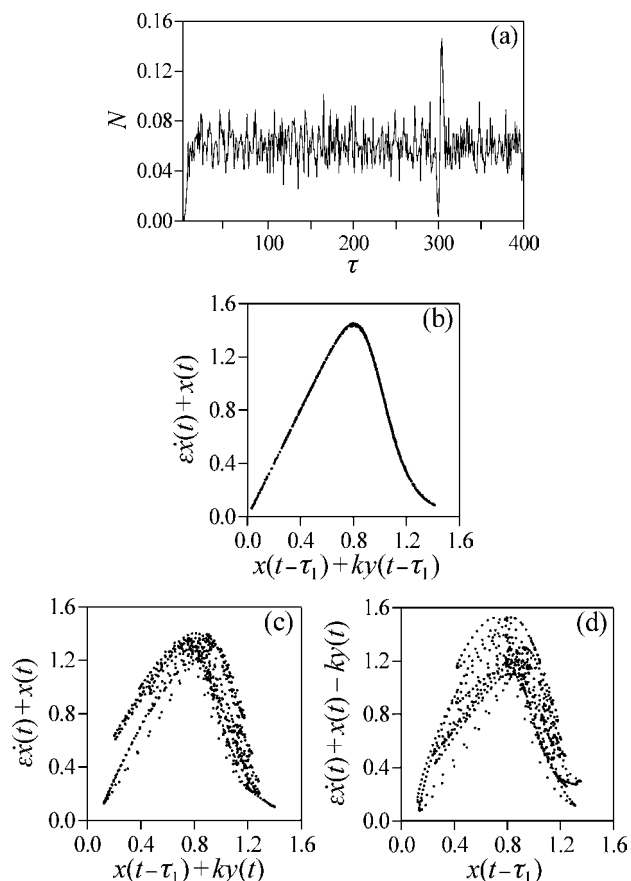


Figure 2. Reconstruction of the harmonically driven Mackey-Glass system. (a) Number N of pairs of extrema in a realization of the system X separated in time by τ , as a function of τ . $N(\tau)$ is normalized to the total number of extrema in time series; $N_{min}(\tau) = N(300)$. (b)–(d) Results of nonlinear function reconstruction for the choice of model equation in the form of Eqs. (2)–(4), respectively, with the recovered parameters $\varepsilon = 10.1$, $k = 0.10$ (b), $\varepsilon = 7.4$, $k = -0.05$ (c), $\varepsilon = 7.3$, $k = 0.06$ (d).

To investigate the robustness of the method to additional noise we analyze the data corrupted with noise. The method is more critical to the presence of noise in the time-delay system. It is still efficient if the level of noise in the system X is about 10% or less. The level of noise in the system Y can be several times higher.

We consider also the case when the time-delay system X is affected by the system Y that is also a time-delay system of form (1). Time-delay systems

X and Y can be coupled by different ways and this coupling can be unidirectional as well as bidirectional. Let us examine a more general case of mutually coupled time-delay systems. As an example, we consider the coupled systems presented in Fig. 3. For this type of coupling (type III in our classification) the coupled time-delay systems are described by the following equations

$$\begin{aligned} \varepsilon_1 \dot{x}(t) &= -x(t) + f_1(x(t-\tau_1)) + k_1 y(t), \\ \varepsilon_2 \dot{y}(t) &= -y(t) + f_2(y(t-\tau_2)) + k_2 x(t). \end{aligned} \quad (7)$$

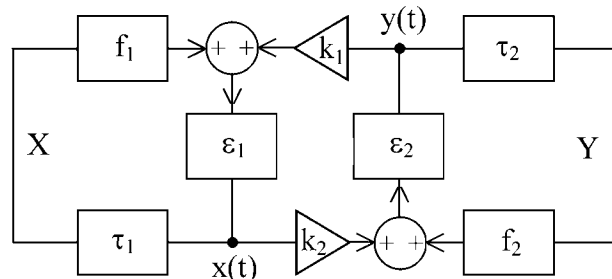


Figure 3. Block diagram of two coupled time-delay systems X and Y .

Figure 4 illustrates the results of reconstruction of the Mackey-Glass system X at $a=0.2$, $b=0.1$, $c=10$, $\tau_1=300$ coupled with another Mackey-Glass system Y at the same values of a , b , c and $\tau_2=400$. The coupling coefficients $k_1=k_2=0.1$. The both systems X and Y are affected by zero-mean Gaussian white noise with a standard deviation of 10% of the standard deviation of the data without noise.

In spite of the noise presence the location of the absolute minimum of $N(\tau)$ (Fig. 4(a)) allows one to estimate the delay time, and the minimum of $L(\varepsilon, k)$ (Fig. 4(b)) to recover the parameters ε_1 and k_1 . To construct the $L(\varepsilon, k)$ we use 2000 points of $x(t)$ and $y(t)$ realizations. The step of ε variation is set 0.1 and the step of k variation is equal to 0.01. The presence of noise results in the deterioration of quality of the nonlinear function recovery (Fig. 4(c)). If the type of coupling is a priori unknown one has to recover all the three forms ((2), (3) and (4)) of the system X model equation and to choose from them the model demonstrating the minimal value of $L_{min}(\varepsilon, k)$. For the true choice of model structure in the form of Eq. (4) we obtain $L_{min}(\varepsilon, k) = L(10.0, 0.10) = 0.026$. Reconstructing the system X in the form of Eqs. (2) and (3) we obtain $L_{min}(\varepsilon, k) = L(10.1, 0.01) = 0.042$ and $L_{min}(\varepsilon, k) = L(10.0, -0.02) = 0.039$, respectively.

The parameters τ_2 and ε_2 , the nonlinear function f_2 of the system Y and the coupling coefficient k_2 can be recovered in a similar way. The values of the re-

covered coupling coefficients k_1 and k_2 allow one to characterize the strength of coupling between X and Y . For the considered values of the system X and Y parameters the method allows us to define the type of the model equations and to reconstruct the systems X and Y for $0.01 \leq |k_{1,2}| \leq 0.5$. The proposed technique has several advantages in comparison with the other methods of detection of coupling between the systems from the time series [8, 9]. In contrast to the directionality indices [9] our method can be applied to the synchronized systems and defines not only the direction but also the value of coupling even in the case of coupling of different systems.

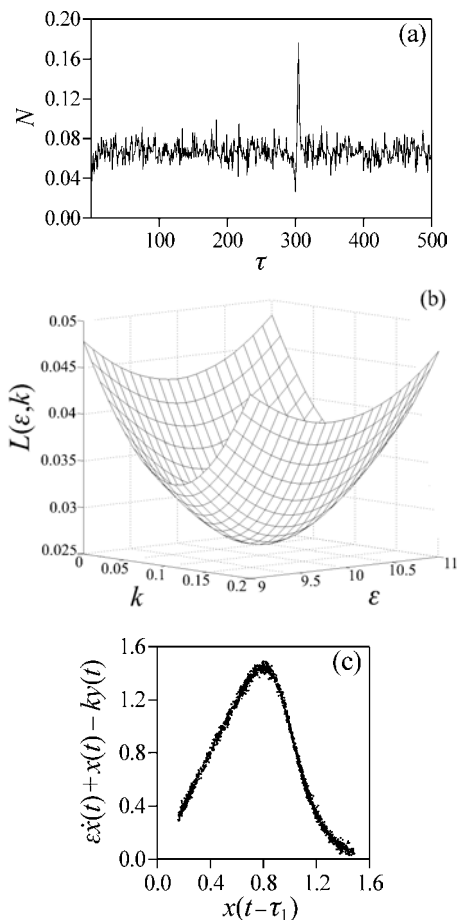


Figure 4. Reconstruction of the Mackey-Glass system X coupled with another Mackey-Glass system in the presence of noise. (a) Number N of pairs of extrema in a realization of the system X separated in time by τ , as a function of τ . $N(\tau)$ is normalized to the total number of extrema in time series; $N_{\min}(\tau) = N(300)$. (b) Length L of a line connecting points ordered with respect to abscissa value in the plane $(x(t - \tau_1), \epsilon \dot{x}(t) + x(t) - ky(t))$ as a function of ϵ and k . $L(\epsilon, k)$ is normalized to the number of points; $L_{\min}(\epsilon, k) = L(10.0, 0.10) = 0.026$. (c) The recovered nonlinear function f_1 at $\epsilon = 10$, $k = 0.1$.

IV. CONCLUSION

We have proposed the method for reconstruction of driven time-delay systems from time series. Different variants of the external signal injection into the time-delay system are considered. The method can be used for the analysis of two unidirectionally or bidirectionally coupled time-delay systems. It allows one to reconstruct both time-delay systems from their time series and to define the coupling coefficients between them. The method can be successfully applied to short time series under sufficiently high levels of noise.

This work was supported by the Russian Foundation for Basic Research, Grant No. 03-02-17593, and U.S. Civilian Research Development Foundation for the Independent States of the Former Soviet Union, Award No. REC-006.

REFERENCES

- [1] M. J. Bünner, M. Popp, Th. Meyer, A. Kittel, J. Parisi. Tool to recover scalar time-delay systems from experimental time series. *Phys. Rev. E*, V. 54, pp. 3082–3085, 1996.
- [2] H. Voss, J. Kurths. Reconstruction of non-linear time delay models from data by the use of optimal transformations. *Phys. Lett. A*, V. 234, pp. 336–344, 1997.
- [3] R. Hegger, M. J. Bünner, H. Kantz. Identifying and modeling delay feedback systems. *Phys. Rev. Lett.*, V. 81, pp. 558–561, 1998.
- [4] M. J. Bünner, M. Ciofini, A. Giaquinta, R. Hegger, H. Kantz, R. Meucci, A. Politi. Reconstruction of systems with delayed feedback: (I) Theory. *Eur. Phys. J. D*, V. 10, pp. 165–176, 2000.
- [5] B. P. Bezruchko, A. S. Karavaev, V. I. Ponomarenko, M. D. Prokhorov. Reconstruction of time-delay systems from chaotic time series. *Phys. Rev. E*, V. 64, 056216, 2001.
- [6] V. I. Ponomarenko, M. D. Prokhorov. Extracting information masked by the chaotic signal of a time-delay system. *Phys. Rev. E*, V.66, 026215, 2002.
- [7] V. S. Udaltsov, J.-P. Goedgebuer, L. Larger, J.-B. Cuenot, P. Levy, W. T. Rhodes. Cracking chaos-based encryption systems ruled by nonlinear time delay differential equations. *Phys. Lett. A*, V. 308, pp. 54–60, 2003.
- [8] M. G. Rosenblum, A. S. Pikovsky. Detecting direction of coupling in interacting oscillators. *Phys. Rev. E*, V. 64, 045202, 2001.
- [9] M. G. Rosenblum, L. Cimponeriu, A. Bezerianos, A. Patzak, R. Mrowka. Identification of coupling direction: Application to cardiorespiratory interaction. *Phys. Rev. E*, V. 65, 041909, 2002.

Conductance and noncommutative dynamical systems

C. Correia Ramos, N. Martins, J. Sousa Ramos

Departamento de Matemática, Universidade de Évora

Rua Romão Ramalho, 59, 7000-671 Évora, Portugal

e-mail: ccr@uevora.pt

Departamento de Matemática, Instituto Superior Técnico

Av. Rovisco Pais 1, 1049-001 Lisboa, Portugal

e-mail: nmartins@math.ist.utl.pt

Departamento de Matemática, Instituto Superior Técnico

Av. Rovisco Pais 1, 1049-001 Lisboa, Portugal

e-mail: sramos@math.ist.utl.pt

Abstract— *In this work we introduce a noncommutative conductance in the context of Cuntz-Krieger C^* -algebras. We study the relation of this conductance with the KMS state for the Cuntz-Krieger algebra.*

in section IV we show how is possible, in the context of Cuntz-Krieger algebras, to define and extend conductance for an infinite graph, choosing an appropriate measure, which is associated to a KMS state for the Cuntz-Krieger algebra.

I. INTRODUCTION

In this work we are interested to study conductance in the context of dynamical systems and C^* -algebras. In a similar way to the concept of entropy which appeared in thermodynamics and has been sucessively generalized in areas such as statistical physics, dynamical systems and C^* -algebras, always related with the complexity of a given system, conductance appeared also in physics, in electric circuits, and now appears in graph theory, random walks, knot theory, related with mixing, or convergence of the system to an equilibrium state, see for example [2], [13], [10], [8]. In [6] is studied the connection of the conductance from graph theory with Markov subshifts, in particular with the second eigenvalue of the Markov matrix. This allows to distinguish systems with the same entropy, see also [12]. Our approach is based on a noncommutative version of a topological Markov subshift, a Cuntz-Krieger algebra. It is interesting to note that conductance, in the physical sense, also appears as a topological invariant, more precisely as a Fredholm index, in the quantum Hall effect, which is related with the irrational rotation algebra.

This article is organized as follows. In the second section we introduce some definitions and notation concerning Markov subshifts and graphs associated to it. In section III we present Cuntz-Krieger algebras and show how is possible to determine the isoperimetric number of a graph (also called conductance in some contexts, see [7]), using a realization of the algebra in a Fock space associated to the graph. Finally

II. DEFINITIONS

Consider a Markov subshift $\Sigma_A = (\Sigma_A^*, \sigma)$, where $\Sigma_A^* = \cup_{k=1}^{\infty} \Sigma_A^k$, and Σ_A^k is the space of admissible symbolic sequences of size k in the alphabet $\Sigma = \{1, 2, \dots, n\}$. The admissibility of a sequence is determined by the Markov matrix $A = (a_{ij})_{i,j=1}^n$ in the usual way, i.e., ij occurs if and only if $a_{ij} = 1$.

The directed graph G associated to the subshift is defined by (Σ_0, Σ_1) where Σ_0 is the vertex set equal to Σ and Σ_1 denote the edge set. The edges are formed by the oriented pairs (ij) such that $a_{ij} = 1$. By this definition the Markov matrix is the adjacency matrix of the graph G .

Define the vector space $C_0(G)$ generated by $(v_i : i \in \Sigma_0)$ and $C_1(G)$ the vector space generated by $(e_{ij} : (ij) \in \Sigma_1)$. We will consider the matrices acting on the left on vectors in $C_0(G)$ or $C_1(G)$, to have the interpretation of a_{ij} as the transition between the vector v_i to the vector v_j .

Other type of matrices, incidence matrices, can be defined, which relates vertices and edges in the graph. We define two types of incidence matrices: Let ∂^- be the matrix defined by $v_i \cdot \partial^- = \sum_{j \in \Sigma_0} e_{ij}$ and ∂^+ the matrix defined by $v_j \cdot \partial^+ = \sum_{(ij) \in \Sigma_1} e_{ij}$. The matrix ∂^- correspond to the incident edges going out of the vertices, and ∂^+ correspond to the incident edges going into the vertices (these matrices are the linear maps version of the sometimes called range map and source map of the graph). The usual incidence matrix is simply $\partial = \partial^+ - \partial^-$, apart from the loops.

The importance of distinguish two incidence matri-

ces is that the Markov matrix, i.e., adjacency matrix of the graph, is given by $\partial^- \cdot \partial^{+*}$. Furthermore, the matrix $\partial^{+*} \partial^-$ represents an adjacency matrix for a graph obtained considering the edges as the vertices. Consider the basis vector v_i (which corresponds to the vertex i). By definition $v_i \cdot \partial^- = \sum_{j \in \Sigma_0} e_{ij} = \sum_{j \in \Sigma_0} a_{ij} e_{ij}$. Now as $e_{ij} \cdot \partial^{+*} = v_j$ we have that $\partial^- \cdot \partial^{+*} = A = (a_{ij})$.

III. CUNTZ-KRIEGER ALGEBRAS

Cuntz-Krieger algebras are related with topological Markov chains, or Markov subshifts, since its appearance[1]. The Cuntz-Krieger algebra O_A , associated to a Markov subshift Σ_A , characterized by Markov matrix $A = (a_{ij})_{i,j=1,\dots,n}$, is the universal C^* - algebra generated by the partial isometries s_i , $i = 1, \dots, n$, satisfying the following relations

$$\sum_i s_i s_i^* = 1, \quad s_i^* s_i = \sum_j a_{ij} s_j s_j^*.$$

Now let us consider the Fock space, H_A , associated with the Markov subshift, see [4], [11], [3]. It is possible to give a realization of the algebra O_A as a concrete subalgebra of $B(H_A)$, the algebra of bounded linear operators in H_A . We will see that this realization is interesting from the graph theory point of view. Consider (v_1, v_2, \dots, v_n) an orthonormal basis of the n -dimensional Hilbert space $H_1 \cong \mathbb{C}^\times$. Define the sequence of finite Hilbert spaces H_k , each generated by the orthonormal basis $(v_\xi : \xi \in \Sigma_A^k)$. The Fock space associated to the subshift Σ_A is defined as $H_A := \mathbb{C} v_0 \oplus_{k=1}^\infty H_k$ (v_0 is the usually called vacuum vector).

Now consider the partial isometries acting on H_A as creation operators $T_i v_{\xi_1 \dots \xi_k} = a_{i \xi_1} v_{i \xi_1 \dots \xi_k}$, for $i \in \Sigma$. Let T_A be the C^* - algebra generated by T_i . These partial isometries satisfies $\sum_{i=1}^n T_i T_i^* = 1 - p_0$ where p_0 is the projection on the subspace $\mathbb{C} v_0$. The ideal generated by the projection p_0 is the C^* algebra of compact operators K , so the quotient $T_A/K(F)$ is a C^* - algebra which turns out to be isomorphic to O_A . The image of T_i under the canonical projection is S_i which will satisfy the Cuntz-Krieger relations

$$\sum_{i=1}^n S_i S_i^* = 1 \quad \text{and} \quad S_i^* S_i = \sum_{j=1}^n a_{ij} S_j S_j^*$$

The interest of this particular realization of Cuntz-Krieger algebra, concerning graph aspects of the subshift, is the following: first note that the vector space H_1 is isomorphic to the space $C_0(G)$ introduced above. Next consider the sequence of graphs $G_k =$

(Σ_0^k, Σ_1^k) such that the vertex set Σ_0^k is the set of admissible sequences of size k (we identify Σ_0^k with Σ^k) and Σ_1^k the set of edges. An edge occur connecting a vertex labeled with $\xi_1 \dots \xi_k$ with the vertex labeled with $\eta_1 \dots \eta_k$ if and only if $\xi_2 = \eta_1, \dots, \xi_k = \eta_{k-1}$ and $a_{\xi_1 \eta_k} = 1$. So we can label the edge that connects the vertices $\xi_1 \dots \xi_k$ and $\xi_2 \dots \xi_k \eta_k$ with the sequence of size $k+1$, $\xi_1 \dots \xi_k \eta_k$. The consequence is that Σ_0^{k+1} is naturally identified with Σ_1^k . The graph G_k can be considered as the graph of the paths of size k in G_1 .

Each vector space H_k is isomorphic to $C_0(G_k)$, so the Fock space presented previously is isomorphic to $\mathbb{C} v_0 \oplus_{k=1}^\infty C_0(G_k)$. With the identification $\Sigma_0^{k+1} \rightarrow \Sigma_1^k$ we have that H_{k+1} is isomorphic to $C_1(G_k)$ which will be useful as we will see.

Any operator T acting on H_A has a block structure $T = \oplus_{k=0}^\infty T_k$, such that the domain of T_k is H_k . In particular the partial isometries $S_i = \oplus_{k=0}^\infty S_{k,i}$, where $S_{k,i} : H_k \rightarrow H_{k+1}$ will be (assuming action on the left) matrices of dimension $n^k \times n^{k+1}$, and the projections $p_i = S_i S_i^* = \oplus_{k=0}^\infty p_{k,i}$, where $p_{k,i} = S_{k,i} S_{k,i}^*$ are matrices of dimension n^k . Each graph G_k has adjacency matrix denoted by A_k and incidence matrices $\partial_k^-, \partial_k^+$, which satisfy the following relations, $A_k = \partial_k^- \cdot \partial_k^{+*}$ and $A_{k+1} = \partial_k^{+*} \partial_k^-$.

Aspects of a graph G concerning subsets of vertices can be put in C^* - algebraic formulation considering instead of subsets of vertices projections of the type $p_{1,i} = S_{1,i} S_{1,i}^*$, i.e., projections in H_1 . Furthermore, a consequence of the isomorphism $H_2 \simeq C_1(G)$ is that aspects of the graph G concerning subsets of edges can be put in C^* - algebraic formulation considering instead of subsets of edges projections $p_{2,i,j} = S_{2,i,j} S_{2,i,j}^* = S_{1,i} S_{1,j} S_{1,i}^* S_{1,j}^*$.

To give a vertex subset S or to give a projection p in H_1 is the same and we have $|S| = Tr(p)$. The same for subsets of edges and projections in H_2 .

Other consequence of the isomorphism $C_1(G_1) \simeq H_2$ is that the incidence matrices $\partial_k^-, \partial_k^+$ can be given in terms of the $S_{k,\xi}$ matrices. In fact $\partial_k^- = \sum_{\xi \in \Sigma_0^k} S_{k,\xi}$, and $\partial_k^+ = \sum_{\xi \in \Sigma_0^k} J_k S_{k,\xi} J_{k+1}$, where J_k is a permutation matrix such that $v_{\xi_1 \xi_2 \dots \xi_k} \cdot J_k = v_{i \xi_k \dots \xi_2 \xi_1}$.

Consider a subset S of Σ_0 . The isoperimetric number $i(S)$, which is related to conductance, see [7], associated to this subset S of vertices is defined by the number of edges with one vertex in S and the other in $\Sigma_0 - S$ divided by the number of vertices in S . The isoperimetric number associated to the graph is the minimum of $i(S)$ over the vertex subsets S such that $|S| \leq |\Sigma_0|/2$. This number associated to the

graph can be presented in an algebraic way. In fact we can extend the isoperimetric number to the graph sequence G_k . We have, for a projection p in H_k ,

$$i_k(p) = \frac{1}{Tr(p)} Tr \begin{pmatrix} \partial_k^- p \partial_k^- + \partial_k^+ p \partial_k^+ - \\ -2 \partial_k^- p \partial_k^- \cdot \partial_k^+ p \partial_k^+ \end{pmatrix}$$

$$i_k = \min_p \phi_k(p)$$

over all projections in $H_k \simeq C_0(G_k)$.

Consider S as the range of the projection p . The diagonal entries of $\partial_k^- p \partial_k^-$ correspond to the edges that go out of S . On the other hand the diagonal entries of $\partial_k^+ p \partial_k^+$ correspond to the edges that go in S . The diagonal entries of $(\partial_k^- p \partial_k^-) \cdot (\partial_k^+ p \partial_k^+)$ correspond to the edges that go out and go in S . So the trace of the matrix $\partial_k^- p \partial_k^- - 2 (\partial_k^- p \partial_k^-) \cdot (\partial_k^+ p \partial_k^+) + \partial_k^+ p \partial_k^+$ is the number of edges that connects S and its complementary vertex set $\Sigma_0 - S$.

IV. RANDOM WALKS

In this section we will consider random walks on a graph arising from a given Markov subshift. Suppose that is given a Markov subshift $\Sigma_A = (\Sigma_A^*, \sigma)$. Associated to it is a graph $G_1 = (\Sigma_0, \Sigma_1)$ and there is a Cuntz-Krieger C^* -algebra O_A , as we saw previously. Instead of the interpretation given in last section with the realization of O_A as an subalgebra of $B(H_A)$ for the Fock space H_A , we will give a different interpretation associated to a different kind of realization of the Cuntz-Krieger algebra. We will consider instead of H_A the inductive limit space $H_\infty = \lim_{k \rightarrow \infty} H_k$, where H_k are defined as in last section, with the difference that we have the inclusion $H_k \subset H_{k+1}$, given by the following: any vector v_ξ in H_k satisfies $v_\xi = \sum_{i \in \Sigma_0} v_{\xi i}$, for every $v_{\xi i}$ in H_{k+1} , i.e., the inclusion map is the incidence matrix ∂_k^- . The projections $p_{k,i}$ as well as the operators $S_{k,i}$, A_k and M_k defined in H_k will correspond to operators p_i , S_i , A_i , M_i in H_∞ , via the inclusion map.

Set $u_{L,k}$ and $u_{R,k}$ the left and right Perron eigenvectors of A_k . Define the diagonal matrix $U_k = \text{diag}(u_{R,k})$. The probabilistic matrix $M_k = \frac{1}{\beta} U_k^{-1} A_k U_k$, will define a random walk in the graph G_k . The left Perron eigenvector of M_k , denoted by μ_k , correspond to the invariant equilibrium state, and is the one associated to maximum entropy measure, or Parry measure, see [14],[9]. We will have μ , eigenvector of M , as the inductive limit of μ_k .

As we saw last section the graph G_k can be seen as the graph of the paths of size k on G_1 . In the limit

we get an infinite graph G_∞ . Reversing the perspective, each G_k can be seen as a coarse-grained graph associated to G_∞ . A vertex $i \in \Sigma_0$ will represent the class of vertices in G_∞ such the label start with the symbol i , in other words, is the class of paths starting in that precise vertex. The weight, arising from the Perron eigenvector μ , on a vertex will correspond to the density of vertices.

In terms of the Cuntz-Krieger algebra the eigenvector μ induces a state τ on the algebra which will correspond to the KMS - state at inverse temperature β considered in theorem 18.5 in [5], where β is the topological entropy of the subshift. This state applied to projections p_i will give $\tau(p_i) = \mu_{1,i}$. For a general projection p_ξ , we get $\tau(p_{\xi_1 \dots \xi_k}) = \mu_{k-1, \xi_1 \dots \xi_k}$. Note that we have $\sum_{i \in \Sigma} \tau(p_{\xi_1 \dots \xi_k i}) = \tau(p_{\xi_1 \dots \xi_k})$. The projections $p_{\xi_1 \dots \xi_k}$ in the algebra correspond to the classes of vertices the class labeled by $\xi_1 \dots \xi_k$, and the value $\tau(p_{\xi_1 \dots \xi_k})$ correspond to the density of the vertices in that particular class.

The conductance for a random walk, see for example [13], [8], with probability transition matrix $W = (w_{ij})$, and with invariant measure u is given by

$$\phi(S) = \frac{\sum_{i \in S, j \notin S} u_i w_{ij}}{\sum_{i \in S} u_i}$$

and

$$\phi = \min_{S: \sum_{i \in S} u_i \leq 1/2} \phi(S).$$

The next result allow us to define conductance for a Cuntz-Krieger C^* -algebra and at the same time to extend the notion to the infinite graph G_∞ . First we define a noncommutative conductance associated to a projection of O_A . Consider D the operator such that $D = \lim_{k \rightarrow \infty} D_k$, where $D_k = (d_{k, \xi \eta})$, $d_{k, \xi \eta}^2 = M_{k, \xi \eta}$.

Definition 1: The conductance associated to a projection p_ξ is given by

$$\phi(p_\xi) = \frac{\tau(p_\xi D(1 - p_\xi) D^*)}{\tau(p_\xi)}.$$

(Note that $1 - p_\xi$ correspond to the projection on the complementary vertex set relatively to the range of p_ξ).

Then we have the following result

Theorem 1: The conductance for any coarse grained G_k , is

$$\phi = \min_{p: \tau(p) < 1/2} \phi(p).$$

in particular the conductance for the infinite graph G_∞ is ϕ .

The conductance for the infinite graph is a finite number because of the inequality that relates the conductance of a random walk and the second eigenvalue λ_2 of the probability transition matrix M (the first is 1). This inequality is $1 - 2\phi \leq \lambda_2$, see . As the second eigenvalue is the same for every matrices M_k then λ_2 is also the second eigenvalue for M . So the conductance of the graphs G_k must be bounded by $(\lambda_2 - 1) / 2$.

In future work we pretend to see if this conductance appears also in the context of an index theorem, in a similar way as the Hall conductance in quantum Hall effect.

REFERENCES

- [1] J. Cuntz, W. Krieger, *A class of C^* -algebras and topological Markov chains*, Invent. Math. 56 (1980), 251-268.
- [2] B. Bollobás, *Modern Graph Theory. Graduate Texts in Mathematics*, 184, Springer, 1998.
- [3] M. Enomoto, M. Fujii, Y. Watatani, *Tensor algebra on the sub-Fock space associated with O_A* , Math. Japan, 26 (1981), no 2, 171-177.
- [4] D. Evans, *Gauge actions on O_A* , J. Operator Theory 7, (1982), 79-100.
- [5] R. Exel, M. Laca, *Partial dynamical systems and the KMS condition*. Comm. Math. Phys. 232 (2003), no. 2, 223–277.
- [6] S. Fernandes, J. Sousa Ramos, *Conductance: from electrical networks, through graphs, to dynamical systems*, NDES 2004.
- [7] C. Godsil, G. Royle, *Algebraic Graph theory*, Springer Verlag, 2000.
- [8] V. Guruswami, *Rapidly Mixing Markov Chains: A comparison of Techniques*, (survey). Preprint.
- [9] L. Rocha, J. Sousa Ramos, *Computing conditionally invariant measures and escape rate*. MPS, Pure Math./ 0303010, 2003.
- [10] J. Goldman, P. Kauffman, *Knots, Tangles and Electrical Networks*, Advances in Applied Mathematics 14, 267-306, 1993.
- [11] K. Matsumoto, *On C^* -algebras associated with subshifts*. Internat. J. Math. 8 (1997), no. 3, 357–374.
- [12] R. Severino, A. Sharkovsky, J. Sousa Ramos, S. Vinagre, *Topological invariants in an idealized time-delayed Chua's circuit*, NDES 2004.
- [13] A. Sinclair, *Improved bounds for mixing rates of Markov chains and multicommodity flow*. Combin. Probab. Comput. 1 (1992), no. 4, 351–370
- [14] P. Walters, *An Introduction to Ergodic Theory, Graduate Texts in Mathematics*, 79, Springer, 1982.

ANTI-PHASE TO IN-PHASE SYNCHRONIZATION IN COUPLED CHUA'S OSCILLATORS

Prodyot Kumar Roy¹, Syamal Kumar Dana²

¹Department of Physics, Presidency College, Kolkata 700073, India
e-mail pkpresi@yahoo.co.in and pkpresi@vsnl.net

²Instrument Division, Indian Institute of Chemical Biology, Kolkata 700032, India
e-mail: skdana@iicb.res.in and sdana_ecs@yaho.com

Abstract—Experimental observations on the effect of coupling on synchronization of two mutually coupled nonidentical Chua's oscillators are presented. We observe that in the very weak coupling region the coupled oscillators gradually move from nonsynchrony to out-of-phase and then to antiphase synchronization with coupling. With further increase of the coupling strength, coexisting antiphase and in-phase states are found in the intermediate range. For strong coupling, stable in-phase synchronization is observed.

I. INTRODUCTION

The studies on synchronization of interacting oscillators are of fundamental importance in many areas of nonlinear dynamics [1-3]. Since 1990 [4] many researchers concentrated on synchronization of chaotic systems [5-6] with evidences of different types of correlation between similar variables of interacting oscillators. Of this phase synchronization (PS) [7] is ubiquitous in nature and found to play important roles in many weakly interacting living systems [8]. Biological examples include cardio-respiratory rhythm [9-10], neural oscillator [11] and cognitive behavior [12]. Many physical systems [13] and electronic circuit [14] also show PS for weaker coupling. Coupling suppresses the natural frequency mismatch in oscillators and they adjust their frequencies to a common locking frequency during PS although the amplitudes are weakly correlated.

In case of PS, two coupled oscillators develop a $n:m$ phase locking relation above a critical coupling when the instantaneous phase difference remain bounded, $|\phi_n - \phi_m| < \text{constant}$ (n, m are integers). In simplest case of 1:1 phase locking, $|\phi_1 - \phi_2| < \text{constant}$, which is defined as in-phase synchrony. Other phase locking relations as antiphase with $|\phi_1 - \phi_2| = \pi$ and out-of-phase synchronization with $0 < |\phi_1 - \phi_2| < \pi$ are observed in

many systems [15-17]. Antiphase and out-of-phase states lie on the synchronization manifold transverse to the in-phase manifold.

Similar systems in nature have parameter mismatch, which induces variations in the natural frequency of individual oscillators. The difference in natural frequency is defined as frequency disorder. A common notion is that coupling induces a monotonic decrease in the frequency disorder and it disappears above a critical coupling. A mark departure from this notion denoted as *anomalous phase synchronization* has been observed recently in Foodweb model [18] where an initial increase in frequency disorder with coupling has been observed before following the usual transition to in-phase synchrony. Experimental evidence of such anomalous transition to both in-phase and antiphase synchrony has been found in coupled Chua's circuit [19] for separate set of parameters.

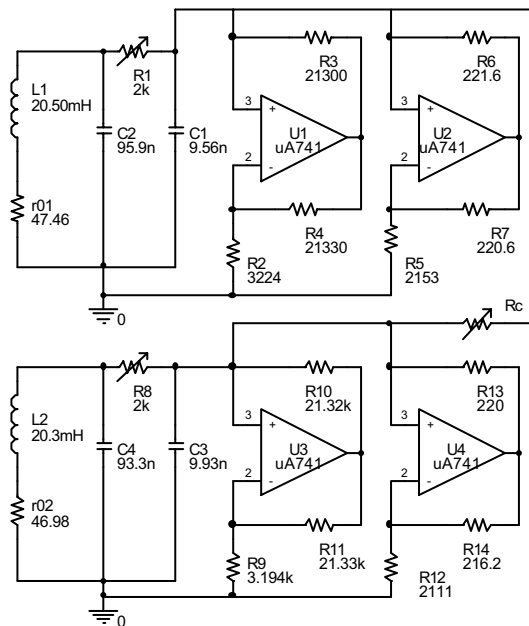


Fig.1. Coupled Chua's Oscillator

Most recent observations on spatio-temporal synchronization of recurrent childhood epidemics [15] show transition from antiphase to in-phase synchronization at a critical coupling while both in-phase and antiphase synchronization co-exist for intermediate coupling. Such in-phase and antiphase synchronization is quite prevalent in neural oscillations like gamma-beta rhythm [16] and in brain function [17]. Different bifurcation phenomena in transition from antiphase to in-phase synchronization has been elaborated in coupled limit cycle neural oscillators [20], nevertheless a complete understanding of the mechanism of this transition with a turbulent phase for intermediate coupling is yet to be made. Similar turbulent phase has been observed in distributed parametric oscillators [21].

II. EXPERIMENTAL CIRCUIT

Experimental circuit is shown Fig.1 where each oscillator consists of linear inductor $L_{1,2}$, capacitors $C_{1,3}$, $C_{2,4}$, resistor $R_{1,2}$ and one nonlinear resistance. The nonlinear resistance is approximated [22] by a piecewise linear function, which is designed by using two Op-amps (uA741). The governing equations of the coupled circuit are

$$\begin{aligned} \frac{dV_{C_{1,3}}}{dt} &= \frac{1}{R_{1,8}C_{1,3}}[(V_{C_{2,4}} - V_{C_{1,3}}) - R_{1,8}f(V_{C_{1,3}})] \\ &\quad + \frac{1}{C_{1,3}R_C}(V_{C_{3,1}} - V_{C_{3,1}}) \\ \frac{dV_{C_{2,4}}}{dt} &= \frac{1}{R_{1,8}C_{2,4}}(V_{C_{1,3}} - V_{C_{2,4}} + R_{1,8}I_{L_{1,2}}) \\ \frac{dI_{L_{1,2}}}{dt} &= \frac{1}{L_{1,2}}(-V_{C_{2,4}} - r_{01,02}I_{L_{1,2}}) \end{aligned} \quad (1)$$

where the piecewise linear function is

$$f(V_{C_{1,3}}) = \begin{cases} b_{1,2}V_{C_{1,3}} + (b_{1,2} - a_{1,2}) & \text{if } V_{C_{1,3}} < -1 \\ a_{1,2}V_{C_{1,3}} & \text{if } -1 \leq V_{C_{1,3}} \leq 1 \\ b_{1,2}V_{C_{1,3}} + (a_{1,2} - b_{1,2}) & \text{if } V_{C_{1,3}} > 1 \end{cases} \quad (2)$$

The measured voltages $V_{C_{1,3}}, V_{C_{2,4}}$ at corresponding capacitor nodes and the inductor current $I_{L_{1,2}}$ are the state variables. The coupling resistance R_c determines the strength of coupling. The slopes $a_{1,2}$ and $b_{1,2}$ of the piecewise linear function are given by

$$a_{1,2} = [-\frac{1}{R_{2,9}} - \frac{1}{R_{5,12}}]R_{1,8}; \quad b_{1,2} = [\frac{1}{R_{4,7}} - \frac{1}{R_{5,12}}]R_{1,8} \quad (3)$$

All the circuit components have mismatches since no two similar off-the-shelf components are

found identical as inevitable in nature. So we started with two nonidentical Chua's oscillators, where the parameter mismatch induces a natural frequency disorder between the two uncoupled oscillators. All components remain fixed throughout this paper except $R_{1,8}$, which is varied to obtain different oscillatory states, periodic to chaotic. The voltages $V_{C_{1,3}}, V_{C_{2,4}}$ at capacitor nodes $C_{1,3}$, $C_{2,4}$ are measured for different coupling resistance R_c using a digital oscilloscope with sampling rate of $40\mu s$. The instantaneous phases $\phi(t)$ of the state variables are determined using Hilbert transform on the measured scalar signals and the mean frequencies $\Omega_i(\epsilon)$ of the coupled oscillators are estimated as mean rate of change of $\phi(t)$. A simple index of relative phase, $\Delta\Omega = 2(\Omega_1 + \Omega_2)/(\Omega_1 - \Omega_2)$ is taken as a measure [8] of synchronization, which is the frequency difference as percentage of mean frequencies of the coupled oscillators $\Omega_i(\epsilon)$ ($i=1,2$). Zero difference in mean frequency ($\Delta\Omega=0$) between the oscillators indicates phase synchronization.

III. RESULTS

We find that the weakly coupled oscillators move from nonsynchrony to out-of-phase above a coupling threshold and then gradually move to antiphase synchronization with coupling. With further increase in coupling above another threshold, the coupled oscillators show desynchronization bursts over a range of coupling strength until they stabilize to in-phase synchronization above a strong coupling. The coupled limit cycle oscillators ($R_1=1552\Omega$, $R_2=1447\Omega$) show stable out-of-phase and antiphase above a coupling strength $\epsilon \geq \epsilon_{C1} \approx 5.952 \times 10^{-6}$ as shown in Fig.2(a). The time series of out-of-phase and antiphase are shown in Fig.3. Onset of desynchronization starts at a critical coupling $\epsilon \geq \epsilon_{C2} (\approx 1.26610^{-5})$ when the frequency disorder ($\Delta\Omega$) suddenly jumps high and fluctuates over a range of intermediate coupling strength. With strong coupling, $\Delta\Omega$ decreases and finally disappears at a large coupling threshold ($\epsilon \geq \epsilon_{C3} \approx 5.952 \times 10^{-5}$).

We note that the frequencies in Fig.2(b) of the individual oscillators rotate at a common frequency for $\epsilon > \epsilon_{C1}$ although the oscillators remain in either out-of-phase or antiphase. However, individual frequencies increase monotonically until desynchronization starts. At the onset of desynchronization at $\epsilon \geq \epsilon_{C2}$ the frequencies of individual oscillators bifurcate again. It is found that

the oscillator with higher frequency is less sensitive to coupling as indicated by its slower rate of change than that of the oscillator of lower frequency. This behavior has similarity with the dephasing effect [23] observed in weakly coupled neural oscillators. Alternate cycles of in-phase and antiphase states are observed during the desynchronization bursts in the intermediate coupling range as shown in the time series in Fig.4. $\Delta\Omega$ starts decreasing once again at intermediate coupling and accordingly, the individual frequencies also start coming closer and finally converge at stronger coupling above a coupling $\epsilon \geq \epsilon_{C3}$ in the in-phase regime as shown in Figs.2(a) and 2(b).

All three coupling thresholds shift with natural frequency mismatch ($\Delta\omega$) of the uncoupled oscillators, which actually depends upon the parameter set of individual oscillators. The two parameter bifurcation of frequency mismatch ($\Delta\omega$) and coupling (ϵ) is shown in Fig.5 for three different regions. The bifurcation diagram is obtained from numerical results closely matching with the behaviors of experimental circuit. It shows striking similarities with the behaviours of simple phase oscillator model as discussed in Ref.24.

III. CONCLUSION

Antiphase, out-of-phase and in-phase regimes are observed in two Chua's oscillators coupled diffusively by one variable. Bifurcation of parameter mismatch and coupling is obtained numerically. Interesting features of coexisting in-phase and antiphase states are observed for intermediate range of coupling in the turbulent phase.

ACKNOWLEDGEMENTS

This work is partly supported by BRNS/DAE under Grant no.2000/34/13/BRNS. Authors like to thank S.Chakraborty for discussions.

REFERENCES

[1] A.T.Winfrey, *The Geometry of Biological Time*, Springer, New York, 1980.
 [2] I. I. Blekhnman, *Synchronization in science and technology*, Nauka, ASME Press, New York, 1988.
 [3] A. Pikovsky, M.Rosenblum, M.Zaks, J.Kurths, *Synchronization-A Unified Approach to Nonlinear science*, Cambridge University Press, Cambridge, 2001.

[4] L.M. Pecora, T.L.Carroll, Synchronizing chaotic circuits, *Phy.Rev.Lett.* **64**, 82, 1990.
 [5] S. Boccaletti, J.Kurths, G.Osipov, D.L.Valladares, C.S. Zhou, *Phy.Rep.* **366**, 1, 2002.
 [6] V.S.Anischenko and T.E.vadivasova, Synchronization of self-oscillations and noise-induced oscillations, *Radiotekhnika i Elektronika* **47**, (2) 133, 2002
 [7] M.G.Rosenblum *et al.*, *Phy.Rev.Lett.* **76**, 1804-1807, 1996.
 [8] B.Blasius, A.Huppert, L.Stone, *Nature(London)* **399**, 354-359, 1999.
 [9] P. Tass, M.G.Rosenblum, J.Wuelle, J.Kurths, A.S.Pikovsky, J.Volkman, A.Schnitzler, H.-J.Freund, *Phy.Rev.Lett.*, **81**, 3291-3294, 1998.
 [10] C. Schäfer, M.G.Rosenblum, J.Kurths, H.-H. Abel, *Nature (London)* **392**, 239-240, 1998;
 [11] V.Makarenko, R.Llinás, Experimentally determined chaotic phase synchronization in a neuronal system, *Proc. Nat. Acad. Sci.* **95**, 15747 (1998)
 [12] J.Bhattacharyya, H.Petsche, Enhanced phase synchrony in electroencephalograph gamma band in the musicians, *Phys. Rev.E*, **64**, 012901, 2002
 [13] S.Boccaletti, E.Allaria, R.Meucci, F.T.Arecchi, Experimental characterization of the transition to phase synchronization of chaotic CO₂ laser systems, *Phy.Rev.Lett.*, **89** (19), 194101, 2002
 [14] P.K.Roy, S. Chakraborty, S.K.Dana, *Chaos* **13** (1), 342-355, 2003.
 [15] D.He, L.Stone, Spatio-temporal synchronization of recurrent epidemics, *Proc. R. Soc. Lond.* **B 270**, 1519-1526 (2003)
 [16] N. Kopell, G.B.Ermentrout, M.A.Whittington, R.D.Traub, *Poc.Nat.Aacd. Sci.*, **97** (4), 1867 (2000)
 [17] A.Meyer-Lindenberg, U.Ziemann, G.Hajak, L.Cohen, K.F.Berman, *Poc.Nat.Aacd. Sci.*, **99** (17), 10948 (2002)
 [18] B.Blasius, E.Montbriá, J.Kurths, Anomalous phase synchronization in populations of nonidentical oscillators, *Phy.Rev. E* **67**, 035204 (R), 2003
 [19] S.K.Dana, B.Blasius, J.Kurths, Experimental observation on anomalous phase synchronization in coupled Chua's oscillators (unpublished)
 [20] D.E.Potsnov, S.K.Han, O.V.Sosnovtseva, C.S.Kim, *J. Diff. Eq. Dynamical Syst.* **10**, 115 (2002);
 [21] T.V.Dmitrieva, N.M.Ryskin, Spatio-temporal chaotic dynamics of distributed parametric oscillators, *Proc. 11th NDES, Switzerland*, pp.77-80, 2003.
 [22] M.P.Kennedy, Three steps to chaos- Part II: A Chua's circuit primer, *IEEE Trans.Cir. Syst.-I* **40**, (10), 657 (1993)
 [23] S.K.Han, C.Kurrer, Y.Kuramoto, H.Kook, Dephasing and bursting in coupled neural oscillators, *Phy. Rev. Lett.*, **75**, pp.3190-3193, 1995
 [24] O. Popovych, V. Krachkovskiy and P.A. Tass *Desynchronization transitions in coupled phase oscillator systems with delay*, *Proc 11th NDES*, pp.197-200, 2003

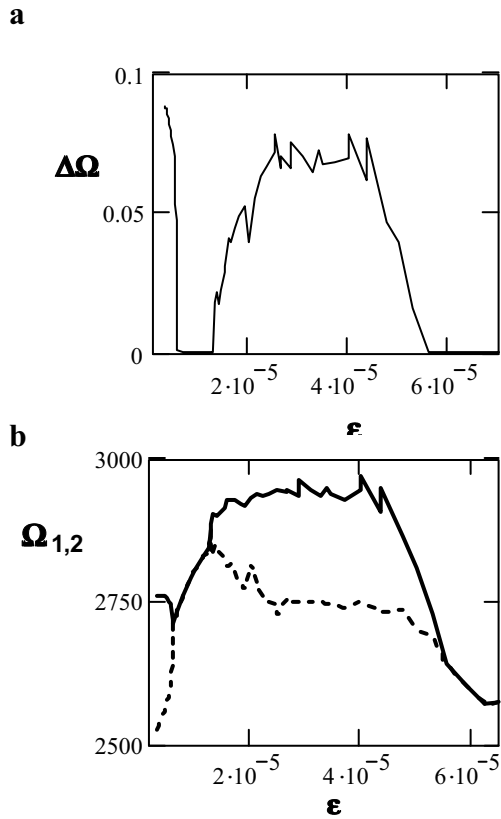


Fig.2. Antiphase, out-of phase and in-phase: $\Delta\Omega$ and individual frequencies Ω_i (dashed and bold lines) with coupling are plotted in (a) and (b) respectively. $R_1=1552\Omega$, $R_2=1447\Omega$

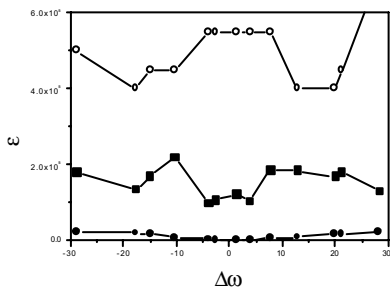


Fig.5. Two parameter bifurcation of ϵ and $\Delta\omega$: Open circle for in-phase, bold square for antiphase and solid circle for out-of-phase thresholds.

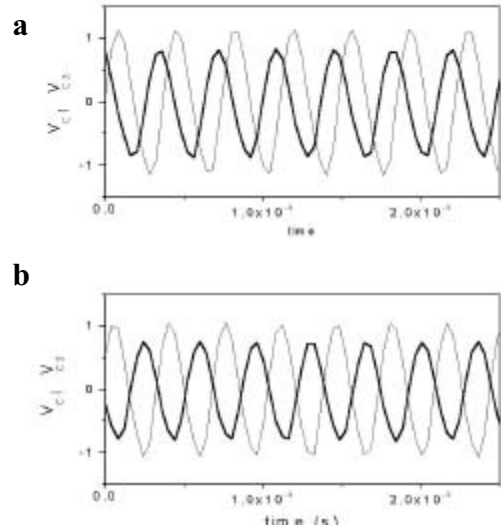


Fig.3. Time series of V_{C1} (light line), V_{C3} (bold line) for parameters: $R_1=1552\Omega$, $R_2=1447\Omega$ (a) out-of-phase, $R_C=168k\Omega$ (b) antiphase, $R_C=79k\Omega$.

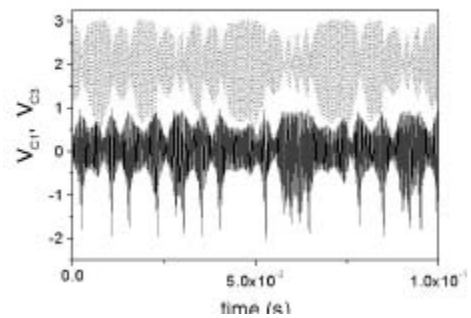


Fig.4. Time series of V_{C1} , V_{C3} for intermediate coupling $R_C= 30.5k\Omega$ [and $R_1=1552\Omega$, $R_2=1447\Omega$].

LIMIT CYCLES IN AUTONOMOUS TWO-DIMENSIONAL FIRST ORDER RECURSIVE DIGITAL FILTERS WITH NONLINEAR ADDER WITHOUT QUANTIZATION

Rudykh D.V., Lebedev M.V., Priorov A.L.

Chair of Dynamics of Electronic Systems, Department of Physics,
Yaroslavl State University,
Sovetskaya 14, Yaroslavl, 150000, Russian Federation
e-mail: dcslab@uniyar.ac.ru

Abstract - *Limit cycles in the two-dimensional first order recursive digital filter with saturation nonlinearity are investigated. Areas, in which concrete types of two-dimensional limit cycles in space of coefficients of the filter can exist, are received. Bifurcation diagram of two-dimensional first order recursive digital filters is analyzed.*

I. INTRODUCTION

Nonlinear problems in digital filters can be divided into three main classes [1]:

- 1) research of processes in the systems with the linear adder and quantization;
- 2) research of processes in the systems with the nonlinear adder and quantization;
- 3) research of processes in the systems with the nonlinear adder without quantization.

The problems connected with the research of the first class for two-dimensional systems are in an initial stage, though similar one-dimensional problems are well studied. The majority of works is dedicated to the analysis of one-dimensional nonlinear systems with the use of statistical approach [2]. With its help it is possible to determine an average level of noise of quantization on an output of nonlinear system and its capacity. The disadvantage of the statistical approach is the certain rigidity of initial requirements for its application that is not always carried out in practice.

Systems with the nonlinear adder and quantization typically have two-dimensional limit cycles on their output. Considering this, the research of the given class of systems is conducted using the determined approach, thus allowing us to find areas of existence and parameters of two-dimensional limit cycles. The

definitions of two-dimensional limit cycles are given in [3]. Necessary and sufficient conditions for appearance of confluent limit cycles in first order filters with three quantizers and necessary conditions for appearance of diagonal limit cycles in the special case of first order equation are found in [4].

Theorems, reflecting some general properties of two-dimensional first order digital filters with two nonzero coefficients and with one quantizer, working on a principle of a roundoff are proved in [5]. For a case of three-level quantization, areas of existence of two-dimensional limit cycles in space of coefficients of the filter are found in [6]. Also such parameters of cycles as an amplitude and a period are determined there.

In the works dedicated to research of systems with the nonlinear adder without quantization, conditions of stability in state-space are considered. Sufficient conditions of stability of Fornasini-Marchesini state-space model are found in [7]. Sufficient conditions of asymptotic stability of the nonlinear two-dimensional filter are also considered there. Lyapunov second method for a determination of sufficient conditions of global asymptotic stability of two-dimensional filter state-space model is used in [8]. Observance of conditions of stability guarantees the absence of limit cycles on an output of the filter. During solution of the given class of problems not much attention is usually paid to areas of existence of two-dimensional limit cycles and their analysis.

Practical interest represents detection of various cycles, which can exist in autonomous system with the nonlinear adder without quantization and areas of their existence in the coefficients space.

The problems connected with studying conditions of existence of limit cycles with the different periods as a result of the adders nonlinearity and with an estimation of their amplitude taking into account the effects of quantization, can be solved with the help of the determined approach [9, 10]. The essence of the approach consists in splitting a range of definition of function of nonlinearity into zones with various values. Then, consistently analyzing possible transitions of system on these zones, restrictions on the parameters of the system corresponding to certain movements are determined. As a result all space of parameters of system can be split into areas with various types of movements. In addition it is necessary to consider function of nonlinearity of the adder in an explicit form.

II. MODEL FORMULATIONS

Let's consider the autonomous two-dimensional first order recursive digital filter with the account of only nonlinearity of the adder. Such model is correct in case when the number of levels of quantization of arithmetic operations is sufficiently large, i.e. effects of quantization do not affect work of the filter.

In this work the two-dimensional first order recursive digital filter, described by the following nonlinear difference equation is considered:

$$y(n, m) = f(b_{10}y(n-1, m) + b_{01}y(n, m-1) + b_{11}y(n-1, m-1)), \tag{1}$$

where b_{10} , b_{01} , b_{11} - coefficients of the filter, and function $f(\cdot)$ - is the characteristic of the adder. In practice commonly the following characteristic of the adder with saturation (Fig. 1) is used

$$f(\varphi) = \begin{cases} \varphi, & \text{for } |\varphi| < 1, \\ \text{sign}(\varphi), & \text{for } |\varphi| \geq 1 \end{cases} \tag{2}$$

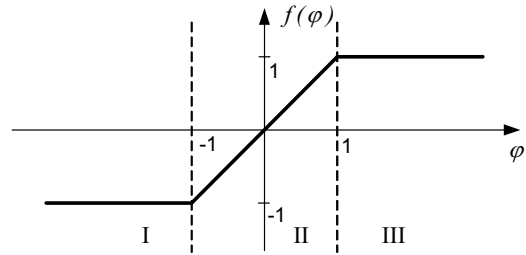


Fig. 1. Saturation nonlinearity

Initial conditions are set as follows:

$$\begin{cases} y(n, -1) = y(-1, m) = 1, & \text{for } n = m = -1, \\ y(-1, m) = y(n, -1) = 0, & \text{for } m > -1, n > -1. \end{cases} \tag{3}$$

III. MAIN RESULTS

The area of a linear mode of the filter is defined by the inequality:

$$|b_{10}| + |b_{01}| + |b_{11}| < 1.$$

According to the method of research, the characteristic of the adder is divided into three zones (Fig. 1).

Let's consider behavior of system (1) for $n \rightarrow \infty$. Taking the initial conditions (3) into account, we have:

$$\begin{aligned} y(0, 0) &= f(b_{11}y(-1, -1)) = f(b_{11}), \\ y(1, 0) &= f(b_{10}y(0, 0)) = f(b_{10}b_{11}), \\ y(2, 0) &= f(b_{10}y(1, 0)) = f(b_{10}^2 b_{11}), \\ &\dots \\ y(n, 0) &= f(b_{10}y(n-1, 0)) = f(b_{10}^n b_{11}). \end{aligned}$$

Thus, for a case $|b_{10}| > 1$, beginning with some $n_1 > N$, the mode $y(n, 0) = 1$ is established, and in case that $b_{10} < -1$ sequence is alternating in sign. From Fig. 1 it is visible, that transition from a zone II of function of nonlinearity is carried out when the module of function argument (2) achieves 1. The value of transient time N can be found using the following expression

$$|b_{10}^N b_{11}| = 1$$

$$N = \text{mod}(1 - \log_{|b_{10}|} |b_{11}|).$$

Applying the formula of transformation of logarithms we derive the final formula of calculation of the transient time $y(n,0)$ receive

$$N = \text{mod}(1 - \frac{\ln|b_{11}|}{\ln|b_{10}|}).$$

If $|b_{10}| < 1$, then $y(n,0) \rightarrow 0$ and periodic movements are impossible. Let's consider the following iteration on an axis m

$$y(n,1) = f(b_{10}y(n-1,1) + b_{01}y(n,0) + b_{11}y(n-1,0)).$$

For prescribed value $b_{10} > 1$

$$y(n,1) = f(b_{10}y(n-1,1) \pm (b_{01} + b_{11}));$$

for the case $b_{10} < -1$

$$y(n,1) = f(b_{10}y(n-1,1) \pm (b_{01} - b_{11})),$$

i.e. since the $N_l > N$, the sequence $y(n,1)$ becomes periodic with the period 1 or 2 and amplitude $|y(n,1)| = 1$. Arguing in the same way for a case $m = 2, 3, \dots, \infty$, we have received, that for given $m = \text{const}$ sequence $y(n,m)$ is periodic with the period which is not exceeding 2, and amplitude $|y(n,m)| = 1$. Character of oscillations is similar for $m \rightarrow \infty, n = \text{const}$. Thus, existence of diagonal limit cycles with the various periods is possible in the system. It is determined, that the basic types of the periods are (1,1), (1,2), (2,1), (2,2). Thus, the amplitude of cycles is equal to 1, and the values $y(n,m)$ belonging to a cycle, are in zones I and-or III (according to Fig. 1).

At Fig. 2 the bifurcation diagram is given and possible kinds of 2-D limit cycles on a plane (b_{10}, b_{01}) for $-1 < b_{11} < 1$ are represented. It is necessary to note, that values of sequence $y(n,m)$ in a cycle of

period (1,1) for the case $-1 < b_{11} < 0$ belong to zone I, and for $0 < b_{11} < 1$ - to a zone III.

Further, row and column limit cycles of the various periods can exist in some zones. For a case when the coefficient b_{11} changes in limits from -1 up to 0, column cycles appear in areas with the periods (1,1) along an axis m and (2,2) along an axis m . If the coefficient b_{11} belongs to an interval from 0 to 1, column cycles appear in areas with the periods (1,2) along an axis m and (2,1) along an axis m .

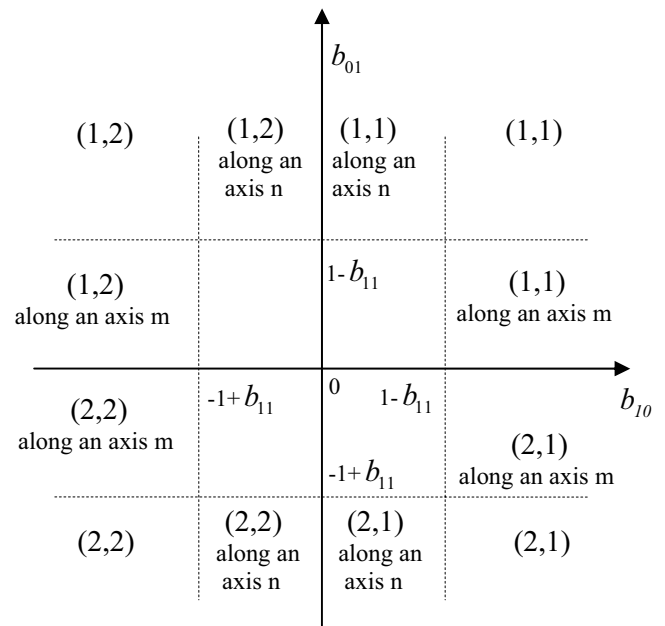


Fig. 2. Bifurcation diagram for a case $-1 < b_{11} < 1$

In the cube in coefficients space $|b_{10}| < 1, |b_{01}| < 1, |b_{11}| < 1$ there can exist two kinds of movements essentially differing in character. In the tetrahedron of stability, movements arise in a zone II, then gradually fade and converge to zero. In the rest of space of a cube outside a tetrahedron of stability can exist some periodic movements with sector character, and their kind is defined by areas, adjacent with given. The example of such sector periodic movements is represented at Fig. 3. There black color designates values $y(n,m) = -1$ (zone I), white color - values $y(n,m) = 1$ (zone III), and gradations of grey

correspond to values $y(n, m) \in (-1, 1)$, belonging to a zone II.

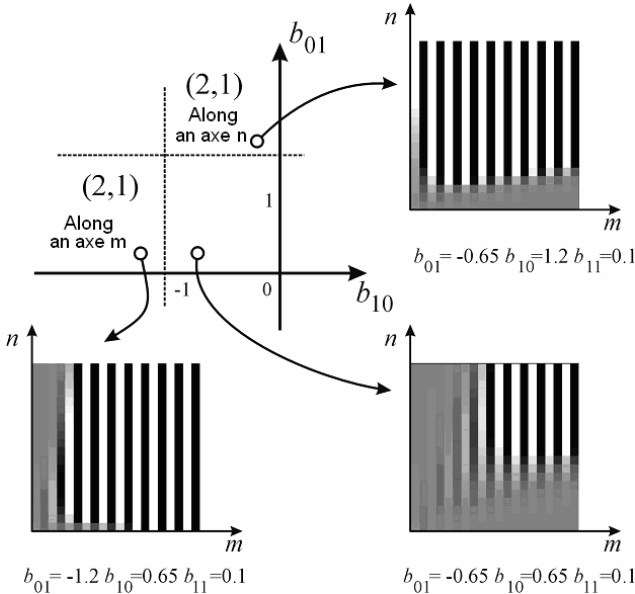


Fig. 3. An example of movements in areas for $0 < b_{11} < 1$

Existence of row limit cycles is probable in areas with the periods (1,1) and (2,2) along an axis n for $-1 < b_{11} < 0$ and in areas with the periods (1,2) and (2,1) along an axis n for $0 < b_{11} < 1$.

IV. CONCLUSIONS

The opportunity of existence of various types of limit cycles in the two-dimensional first order recursive digital filter with saturation nonlinearity is investigated. Areas, in which concrete types of 2-D limit cycles can exist, are received in coefficients space of the filter. Results are shown in the convenient graphic form. Knowledge of 2-D limit cycles peculiarities can help to avoid some undesirable effects connected with it.

V. ACKNOWLEDGMENTS

Work is executed under financial support of Russia Foundation of Basic Research (grant 02-02-17500) and Ministry of Education of Russia (grant A03-2.9-574).

REFERENCES

[1] M. J. Ogorzalek, "Complex behavior in digital filters," *In Int. J. Bifurcation and Chaos* 2, pp. 11-29, 1992.

[2] L. B. Jackson, "Roundoff noise analysis for fixed-point digital filters realized in cascade and parallel form," *IEEE. Trans. Audio Electroacoustics*, vol. AU-18, no. 2, pp. 107-122, 1970.

[3] T. Chang, "Limit cycles in two-dimensional first order digital filter," *IEEE. Trans. Circuits and Syst.*, vol. CAS-24, pp. 15-19, Jan. 1977.

[4] G. A. Maria and M. M. Fahmi, "Limit cycles oscillations in first order two-dimensional digital filters," *IEEE Trans. Circuits and Syst.*, vol. CAS-22, pp. 246-251, Mar. 1975.

[5] T. Bose and D. P. Brown, "Limit cycles in first-order two-dimensional digital filters," *Proc. IEEE Southeastcon*, pp. 371-375, 1989.

[6] D.V. Rudyh, M.V. Lebedev, V.V. Kryashchev, and A.L. Priorov, "Investigation of the two-dimensional first order recursive digital filters with saturation nonlinearity," *Proc. of the 11-th Workshop on "Nonlinear Dynamics of Electronic Systems" (NDES'2003)*, Switzerland, pp. 213-216, 2003.

[7] T. Bose and D. A. Rautman, "Two's compliment quantizations in two-dimensional state-space digital filters," *Proc. IEEE Transactions on signal processing*, vol. 40, no. 10, pp. 2589-2592, Oct. 1992.

[8] D. Liu and A. N. Mitchel, "Stability analysis of state-space realizations for two-dimensional filters with overflow nonlinearities," *Proc. IEEE Trans. Circuits and Syst. I*, vol. 41, no. 2, pp. 127-137, Feb. 1994.

[9] A. A. Sudakov, A. A. Elagin and A. L. Priorov, "Quantization effects in 2-D first-order recursive digital filters," *In Proc. DSPA*, Moscow, vol. 3, pp. 628-629, Sep. 1999.

[10] A. Elagin and A. Priorov, "Quantisation effects in 2-d first order recursive digital filters," *Proc. of the 2000 Internat. Symposium of Nonlinear Theory and its Applications*, Dresden, vol. 1, pp. 185-188, 2000.

COMPLEX DYNAMICS OF A TWO-CAVITY KLYSTRON OSCILLATOR WITH DELAYED FEEDBACK

N.M. Ryskin, A.M. Shigaev

Saratov State University, Russia

E-mails: RyskinNM@info.sgu.ru, Andrew_M_Shigaev@gmx.net

A model of klystron oscillator with delayed feedback is studied in details in a wide range of bifurcation parameters. Due to an infinite-dimensional nature of the system its dynamics is found to be very complex and including a lot of peculiarities that are met among finite-dimensional systems. Presented results help to find the common features specific for distributed systems with delayed feedback and may also have practical implementation.

I INTRODUCTION

One of the topical problems of contemporary radio physics and electronics is a study of complex nonlinear behavior and chaos in RF-oscillators based on interaction between electron beam and electromagnetic fields. An interest in this field is twofold. On the one hand it corresponds to study of extraneous unstabilities in order to avoid them, on the other — to the need of powerful HF-generators capable of producing wide-spectrum radiation that can be achieved in chaotic oscillation regimes. Such devices have applications in design of linear accelerators of charged particles, noise radars [1], microwave plasma heating, etc. Delayed feedback generators based on multiple cavity klystrons appear to be very prospective for these purposes due to their high power and efficiency. However the dynamics of such systems is still practically unexplored.

Mathematical model of delayed-feedback two-cavity klystron oscillator was developed in [2] and basic peculiarities of its dynamics were studied. Qualitative agreement with experimental results was also shown. Dynamics was studied in the particular case of the center of oscillation zone whereas it appears to be most interesting nearby the edges. Complete bifurcation pattern of the system in the whole parameter space is a topic of the research underlying this work.

Following our previous work [2], a model of the two-cavity klystron oscillator is studied. It is described by the system of delayed differential equations:

$$\begin{aligned} \frac{dF_1}{d\tau} + \gamma_1 F_1 &= \gamma_1 F_2, \\ \frac{dF_2}{d\tau} + \gamma_2 F_2 &= 2\alpha e^{i\psi} J_1(|F_1(\tau-1)|) \frac{F_1(\tau-1)}{|F_1(\tau-1)|}. \end{aligned} \quad (1)$$

Here $F_{1,2}$ are slow varying envelopes of oscillations in the input and output cavities, respectively, α is the excitation parameter proportional to the beam current and the feedback ratio, $\gamma_{1,2}$ are the dissipation parameters of the cavities, ψ is a signal phase shift during delay time (that is normalized to unity), and J_1 is the Bessel function of the 1st order.

In the following we consider $\gamma_1 = \gamma_2 = \gamma$.

II SELF-EXCITATION CONDITIONS, STATIONARY REGIMES AND THEIR STABILITY

Linearizing the studied system and considering $F_{1,2} \sim e^{p\tau}$ we derive a characteristic equation

$$(p + \gamma)^2 = -i\alpha\gamma e^{-(p+i\psi)} \quad (2)$$

Taking into account that p is purely imaginary on the stability threshold, $p = i\omega$, where ω — oscillation frequency, we obtain equations for eigenfrequencies

$$\frac{2\omega\gamma}{\gamma^2 - \omega^2} = -\text{tg}\left(\omega + \psi + \frac{\pi}{2}\right) \quad (3)$$

and stability threshold of n^{th} eigenmode

$$\alpha_{st} = \frac{\gamma^2 + \omega_n^2}{\gamma}. \quad (4)$$

An example of graphical solution of (3) in case of high quality factors of resonators, namely $\gamma < \pi/2$, is shown on Fig. 1.

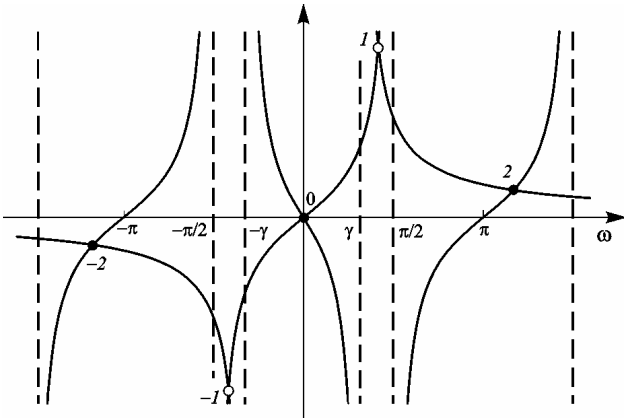


Fig. 1. An example of solution of (3)

It can be shown that eigenfrequencies with even numbers correspond to eigenmodes of the system that can be excited on basis of small fluctuations whereas odd numbers denote self-oscillation modes that can be excited basing on violent eigenmode oscillations. We denote latter eigenfrequencies as self-modulation modes. One can reveal from (4) an existence of the so-called oscillation zones — a pattern on the parameters plane depicted on Fig. 2.

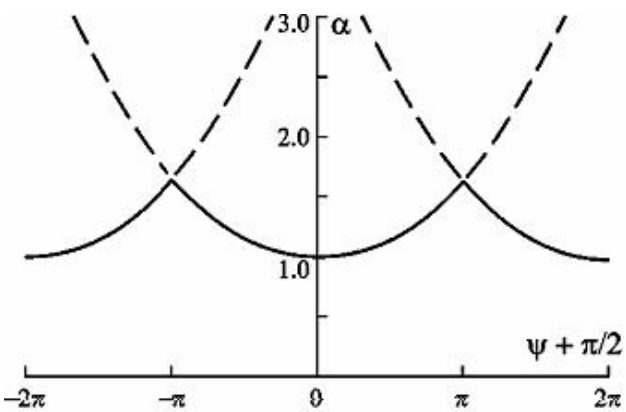


Fig. 2. Self-excitation threshold at $\gamma = 1.0$

Self-excitation occurs at lower bifurcation parameter (α) value at the center of a zone and is impeded at its edges.

Farther, let us consider an important case of generation of the signal with certain frequency, phase and amplitude. Following conventional terminology we call such a regime stationary. In this case

$$F_{1,2} = F_{1,2}^{(0)} e^{i\omega t}, \quad (5)$$

where $F_{1,2}^{(0)}$ are constant. Inserting (5) into (1) we derive an equation for amplitude of stationary generation

$$(\omega^2 + \gamma^2) F_0 = 2\alpha\gamma J_1(F_0). \quad (6)$$

So long as $\omega = 0$ at the center of oscillation zone, we obtain an equation for an amplitude of stationary generation at a given eigenmode

$$\gamma F_0 = 2\alpha J_1(F_0). \quad (7)$$

Graphical solution of this equation is presented at Fig. 3. It can be shown that solutions marked as S_n are always aperiodically unstable, whereas P_n can become unstable only at certain bifurcation parameters values. Analysis of stability conditions shows that P_n is stable at low α . Increase of α leads to the loss of stability and soft inception of a limit cycle in vicinity of P_n that corresponds to excitation of self-modulation mode. The origin of the instability is an amplitude nonlinearity of the device, i.e. a driving curve (output power vs. input power) must exhibit a branch with sufficiently high negative slope. Following [3] this is called an amplitude mechanism of self-modulation.

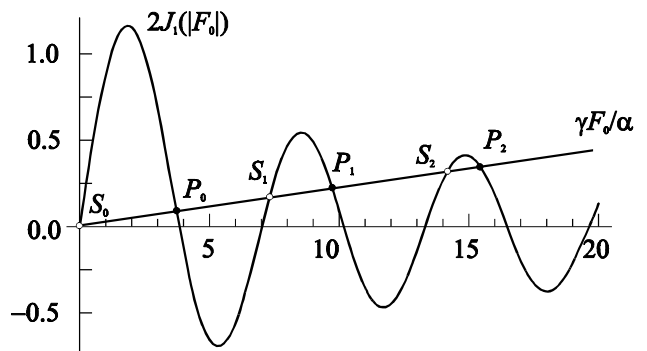


Fig. 3. Graphical solution of (7)

The number of stable solutions P_n increases with the increase of α that lead to multistability.

All the results derived in theoretical analysis were verified numerically.

III NUMERICAL SIMULATION

Simulation of non-stationary processes reveals existence of a variety of limit cycles of different shapes corresponding to regimes of periodical self-modulation. The studied system demonstrates continuous complication of shapes of limit cycles and hard transitions between them. The latter is attended with a hopping of frequency of self-modulation. At $\gamma \ll 1$ transitions between cycles are soft while at larger γ hard transitions are dominating.

As it was predicted by theoretical analysis, multistability between different stationary regimes is

observed at large α . This effect is illustrated by bifurcation diagrams (maxima of output signal versus α) shown on Fig. 4.

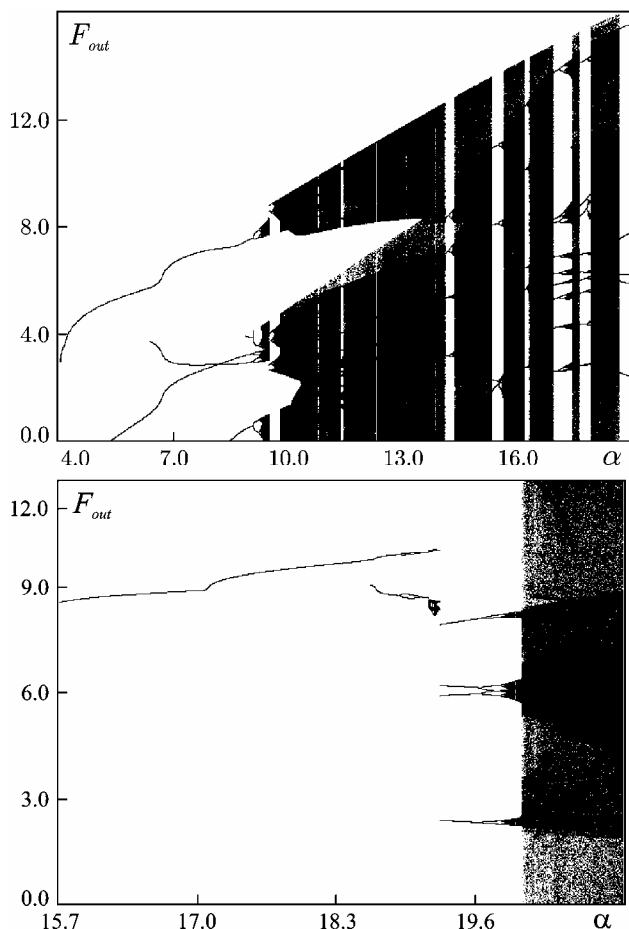


Fig. 4. Bifurcation diagrams at $\gamma = 1.0, \psi = 0.0$.

Transitions to chaos with the increase of α were studied numerically in details. When ψ lies near the center of oscillation zone the Feigenbaum scenario takes place (see Fig. 4). An example of chaotic attractor exhibited by the system at $\gamma = 1.0, \psi = 0$ and $\alpha = 12.875$ is shown on Fig. 5.

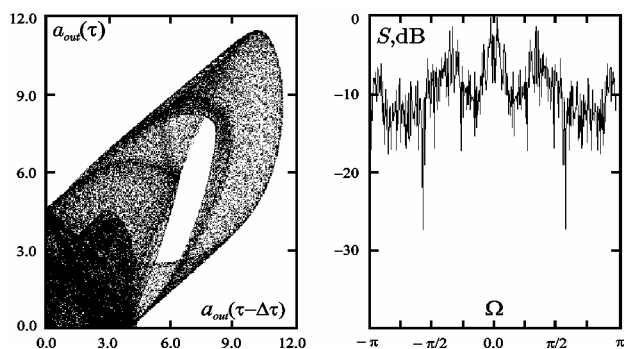


Fig. 5. Phase portrait and spectrum of output signal. $\gamma = 1.0, \psi = 0, \alpha = 12.875$

Much more complicated dynamics is exhibited by the system at the edges of oscillation zones. Depending on initial conditions one of two neighboring eigenmodes could be excited. Each of these modes exhibit own route to chaos.

Farther, let us consider the case of ψ lying close to π so that two adjacent eigenmodes with $n=0$ and $n=2$ can be excited. Parameter plane shown on Fig. 6 gives a notion of dynamic in this case. Firm lines correspond to dynamics on the mode with $n=0$ whereas dashed lines correspond to $n=2$. Since the mode with $n=0$ is fundamental (has a lower threshold of self-excitation) on the left side of a figure and the mode with $n=2$ — on the right and they are symmetric in that sense, the figure itself is also symmetric — mirroring firm lines with respect to $\psi = \pi$ yields dashed lines.

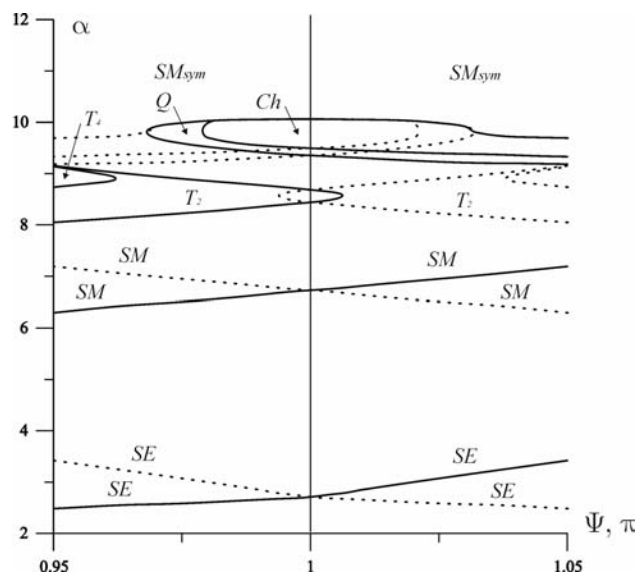


Fig. 6. Parameter plane near the edge of oscillation zones

SE denotes self-excitation, *SM* — self-modulation, T_2 (T_4) — self-modulation with doubled (quadrupled) period, *Q* — quasi-periodicity, *SM_{sym}* — self-modulation with symmetric limit cycle, *Ch* — chaos.

Dynamics of the system on fundamental mode is as follows. Increase of α far above the threshold of self-modulation leads to cascade of period-doublings. But near the edge the cascade can not develop and the system undergoes several bifurcations that are reverse to period-doubling. Further increase of α at $\psi \in [0.97; 1]$ leads to the rise of quasi-periodic motion with subsequent transition via Ruelle-Takens scenario. Increase of α with dynamics based on non-fundamental mode

always leads to quasi-periodicity and transition to chaos via Ruelle-Takens scenario.

An important bifurcation that is met in dynamics of system (1) is marked by the upper line on Fig. 6. This line is common for both adjacent modes and corresponds to transition to a limit cycle of specific shape that is shown on Fig. 7. Spectrum of this limit cycle is symmetric with respect to zero-frequency and has its maxima at frequencies of two adjacent eigenmodes. We call this limit cycle “symmetric” since it expresses symmetry of generator’s eigenmodes near the edge of oscillation zones. A distinctive feature of dynamics on this cycle is that it is based equally on both eigenmodes.

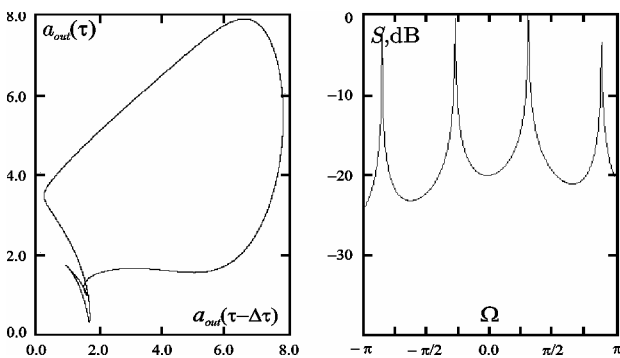


Fig. 7. Phase portrait and spectrum of symmetric limit cycle. $\gamma = 1$, $\psi = 0.95$, $\alpha = 9.875$

An increase of α after transition to symmetric cycle leads to a cascade of period-doubling on its base and transition to chaos via Feugenbaum scenario.

CONCLUSION

Two-cavity klystron oscillator with delayed feedback appears to be relatively simple and very practical object of experimental study of chaotic oscillations in HF range. This device is a typical representative of distributed self-oscillating system with delayed feedback and exhibits numerous peculiarities of complex dynamics incidental to this class of systems. We believe that it will take its stand among reference models of HF-electronics exhibiting complex dynamics such as TWT and BWO.

ACKNOWLEDGEMENTS

This work was supported by the USA Civilian Research and Development Foundation (Award No. REC-006), by the Program “Universities of

Russia — Basic Researches” (Grant No. 01.01.49) and by the Russian Foundation for Basic Research (Grant 03-02-16269).

REFERENCES

- [1] Lukin K.A. The Principles of Noise Radar Technology in Proc. NRTW’02, pp.13-22, Yalta, Crimea, Ukraine 2002
- [2] B.S. Dmitriev, Y.D. Zharkov, N.M. Ryskin, A.M. Shigaev. Journ. Comm. Technol. Electron., Vol. 46, No. 5, pp.561-566, 2001.
- [3] Yu.P. Bliokh, M.G. Liubarskii, V.O. Podobinskii, Ya.B. Fainberg. Plasma Phys. Rep., Vol. 20, No.8, pp.648-658, 1994
- [4] B.S. Dmitriev, D.V. Klokov, N.M. Ryskin, A.M. Shigaev, Yu.D. Zharkov. In Proc. 3rd IEEE IVEC’02, pp.266-267, Monterey, CA, USA, 2002.
- [5] N.M. Ryskin, A.M. Shigaev in Proc. NDES’03, pp. 217-220, May 18-22, Scuol/Schuls, Switzerland.

D/A CONVERTERS AND ITERATED FUNCTION SYSTEMS

Toshimichi Saito, Junya Shimakawa and Hiroyuki Torikai

EECE Dept., HOSEI Univ., Koganei, Tokyo, 184-8584 Japan

e-mail: tsaito@k.hosei.ac.jp

<http://www.nonlinear.k.hosei.ac.jp/>

Abstract—*This paper studies cyclic D/A converters (DACs) as an application of iterated function systems (IFSs) consisting of contractive maps. Operation of basic DACs is described in terms of IFSs and two examples for binary and Gray decodings are introduced. The DACs are compared with an IFS for analysis of DNA structures. We then present a simple implementation circuit of the DAC for Gray decoding. The circuit is based on intermittently coupled switched capacitors.*

I. INTRODUCTION

Cyclic A/D converters (ADCs) and D/A converters (DACs) are indispensable tools in various signal processing systems. There exist various ADC architectures including binary-coding-based ADCs, Gray-coding-based ADCs and their analogues [1]-[3]. The architectures of DACs are usually based on inverse operation of the ADCs. In order to realize these data conversion systems, switched-capacitor-based implementation has been studied intensively [1] [4] [5]. On the other hand, iterated function systems (IFSs [7]) have been studied as interesting dynamical systems with rich phenomena. Although the IFSs include wide class of dynamical systems, this paper focuses on IFSs consisting of contractive mappings such as Sierpinski triangle generators. Applications of the IFSs include DNA sequence analysis, image information compression and encryption [7]-[9].

This paper discusses cyclic DAC as an application of the IFSs. First, as a preparation, we introduce basic cyclic ADCs in terms of 1D maps [10]. Two basic ADC examples for binary and Gray codings [1]-[3] are shown. Cyclic DACs are inverse systems of the ADCs. Second, we describe operation of the cyclic DACs in terms of IFSs. Among many applications of the IFSs, we introduce chaos game representation (CGR [8]) for analysis of DNA structures. We then compare the CGR with the DACs and discuss the differences. Third, a novel simple implementation cir-

cuit of the DAC for Gray-decoding is presented. The circuit is based on intermittently coupled switched capacitors (ICC [11]).

It should be noted that Refs. [1]-[6] discuss cyclic ADCs and DACs, however, the Refs do not cite IFSs. This paper discusses relationship between the DACs and IFSs. The discussion is important to develop efficient DACs and to introduce new researchers to the nonlinear field.

II. ADCS AND CHAOS

As a preparation to consider the DACs, we introduce basic cyclic ADCs in terms of 1D maps [1]. Let us consider ADCs which convert a constant analog input $X \in I \equiv [0, 1]$ to a digital output sequence $\mathbf{y} \equiv \{y(1), \dots, y(l)\}$, $y_i \in \{0, 1\}$, where l is a finite code length. The operation be described by Equation (1).

$$\begin{aligned} x(n+1) &= f(x(n)) = \begin{cases} f_0(x(n)) & \text{for } x(n) \in I_0 \\ f_1(x(n)) & \text{for } x(n) \in I_1 \end{cases} \\ y(n) &= Q(x(n)) = \begin{cases} 0 & \text{for } x(n) \in I_0 \\ 1 & \text{for } x(n) \in I_1 \end{cases} \\ x(1) &= X, \quad 1 \leq n \leq l < \infty, \end{aligned} \quad (1)$$

where n denotes discrete time, the input X is applied as an initial value $x(1)$ and the output is given via one-bit quantizer Q . Also, f_0 and f_1 are expanding affine mappings:

$$f_0 : I_0 \rightarrow I \quad \left| \frac{d}{dx} f_0(x) \right| > 1 \quad \text{for } x \in I_0$$

$$f_1 : I_1 \rightarrow I \quad \left| \frac{d}{dx} f_1(x) \right| > 1 \quad \text{for } x \in I_1$$

where $I = I_0 \cup I_1$ and $I_0 \cap I_1 = \emptyset$. Since f is expanding, the 1-D map f can generate chaos if $l = \infty$ [10]. Although the 1-D map can be a common mathematical model for cyclic ADCs and chaos generators, we should note the following. First, the ADCs operate within finite time ($l < \infty$), and chaos can not be recognized within finite time. Second, in the ADCs, we pay attention to the output sequence \mathbf{y} depending on the initial state X that is an analog input. In

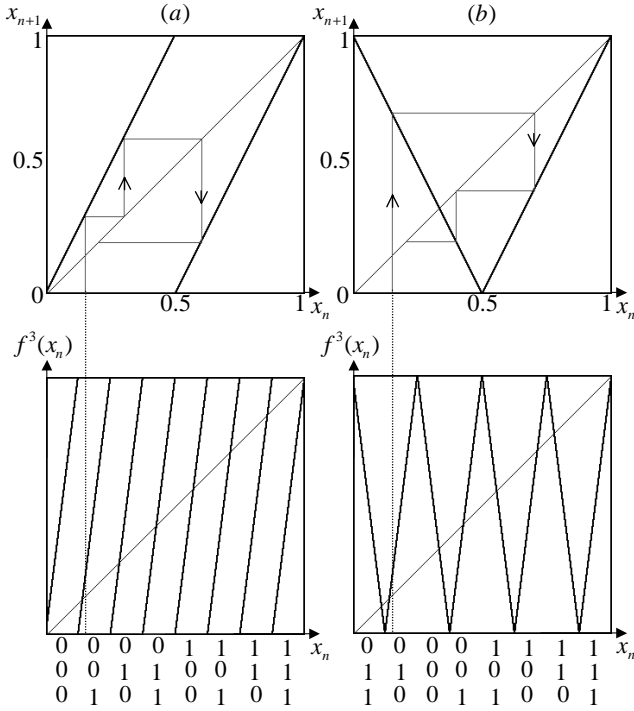


Fig. 1. Cyclic ADCs based on chaotic maps ($x_n \equiv x(n)$). (a) Cut map, (b) Valley map.

the chaos from ergodic theoretical viewpoint, we pay attention to statistic properties of infinite sequence $\{x(n)\}$ which is independent of the initial state [10]. Equation (1) includes the following two typical examples. Fig. 1 (a) shows the first example:

$$x(n+1) = \begin{cases} 2x(n) & \text{for } x(n) \in I_0 \\ 2x(n) - 1 & \text{for } x(n) \in I_1 \end{cases} \quad (2)$$

where $I_0 = [0, 0.5)$ and $I_1 = [0.5, 1]$. This is the cut map [10] and is used as an ADC for binary coding [1]. Fig. 1 (b) shows the second example:

$$x(n+1) = \begin{cases} -2x(n) + 1 & \text{for } x(n) \in I_0 \\ 2x(n) - 1 & \text{for } x(n) \in I_1 \end{cases} \quad (3)$$

where $I_0 = [0, 0.5)$ and $I_1 = [0.5, 1]$. This is the valley map (an analogue of the tent map [10]) and is used as an ADC for Gray coding [3]. The binary and Gray codes for $l = 3$ (code length 3) are shown in the Fig. 1 with the 3-fold compositions of the map.

III. DACS AND CGRS

We have cyclic DACs corresponding to the cyclic ADCs in Section II. Let an ADC of Equation (1) convert an analog value X to a digital sequence \mathbf{y} . In

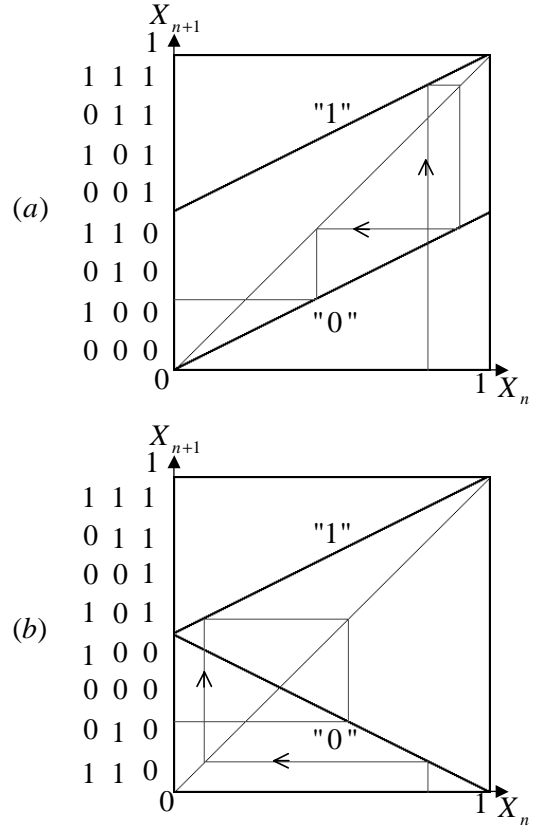


Fig. 2. (a) DAC for binary decoding from $\mathbf{Y} \equiv (1, 0, 0)$, (b) DAC for Gray decoding from $\mathbf{Y} \equiv (0, 1, 0)$.

order to decode \mathbf{y} , the DAC uses the following digital input \mathbf{Y} that is the inverse sequence of \mathbf{y} :

$$\mathbf{Y} \equiv \{Y(1), \dots, Y(l)\} = \{y(l), \dots, y(1)\}$$

where $Y(i) = y(l - i + 1)$. Let $\tilde{X} \in I$ be the output of the DACs. \tilde{X} is often referred to as an estimation of X . The operation of the DAC can be described by

$$X(n+1) = \begin{cases} f_0^{-1}(X(n)) & \text{for } Y(n) = 0 \\ f_1^{-1}(X(n)) & \text{for } Y(n) = 1, \end{cases} \quad (4)$$

where $1 \leq n \leq l < \infty$. If an initial value $X(1)$ and an input \mathbf{Y} are given, Equation (4) is updated and the final value is to be the estimation $\tilde{X} = X(l)$. Since f_0 and f_1 are affine mappings, we can guarantee existence of their inverse mappings $f_0^{-1} : I \rightarrow I_0$ and $f_1^{-1} : I \rightarrow I_1$. It should be noted that f_0^{-1} and f_1^{-1} are contractive since f_0 and f_1 are expanding: Equation (4) is the IFSs consisting of contractive mappings.

Based on Equation (4), we can give two DACs corresponding to two ADCs examples in Equations (2) and (3). If \mathbf{Y} is given by Equation (2) for binary cod-

ing, the decoding is realized by the following DAC.

$$X(n+1) = \begin{cases} \frac{1}{2}(X(n) + 0) & \text{for } Y(n) = 0 \\ \frac{1}{2}(X(n) + 1) & \text{for } Y(n) = 1, \end{cases} \quad (5)$$

where $Y(n) \in \{0, 1\}$. If Y is given by Equation (3) for Gray coding, the decoding is realized by the following DAC.

$$X(n+1) = \begin{cases} \frac{1}{2}(-X(n) + 1) & \text{for } Y(n) = 0 \\ \frac{1}{2}(X(n) + 1) & \text{for } Y(n) = 1, \end{cases} \quad (6)$$

Fig. 2 illustrates these maps with binary and Gray codes. DACs (5) and (6) can provide estimation $\tilde{X} = x(l)$ from Y of binary and Gray codings, respectively. For these two DACs, we have following criterion for the estimation error.

$$|\tilde{X} - X| < 2^{-l} \text{ for any } X(1) \in I. \quad (7)$$

This is an important factor to evaluate performance of the DACs, however, it is hard to give such factor for the generalized cases of Equation (4).

As shown in Section I, the IFSs have rich dynamics and have many applications. Since it is hard to discuss such many applications, we focus on an interesting one: the chaos game representation (CGR [8]) for analysis of DNA sequences. The dynamics of the CGR is two dimensional analogue of Equation (5):

$$\mathbf{X}(n+1) = \frac{1}{2}(\mathbf{X}(n) + \mathbf{Y}(n)) \quad (8)$$

where $\mathbf{X} \equiv (X_1, X_2)$ and $\mathbf{Y} \equiv (Y_1, Y_2)$. \mathbf{Y} can take four values corresponding to four bases of DNA

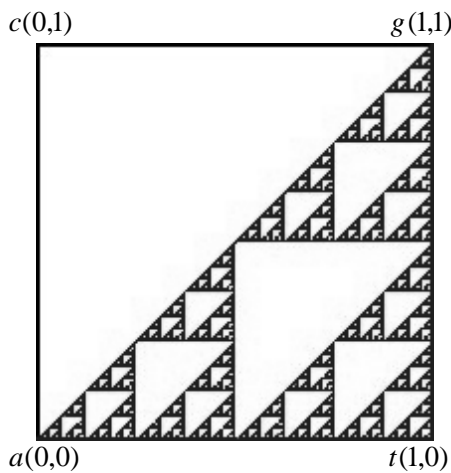


Fig. 3. The result of the chaos game on three points

sequences: $\mathbf{Y} \in \{a, t, c, g\}$, $a \equiv (0, 0)$, $t \equiv (1, 0)$, $c \equiv (0, 1)$ and $g \equiv (1, 1)$. As a DNA sequence is applied to the CGR, the sequence $\{\mathbf{X}(n)\}$ may construct a proper image for any $\mathbf{X}(1) \in I \times I$ that can be used to investigate/classify patterns in the DNA sequence. In addition, if one element of the four bases lacks, e. g., $\mathbf{Y} \in \{a, t, g\}$, the image is to be the Sierpinski triangle as shown in Fig. 3: it corresponds to the chaos game [8]. Although IFS is a common mathematical model for cyclic DACs and CGRs, we should note the contrasts including the following:

1. In the DACs, Y is an encoded digital input. In the CGRs, Y is a DNA sequence data.
2. In the DACs, the output is a point X_l at finite time l . In the CGRs, we pay attention to the limit set $\{X_n\}$ (such as Sierpinski triangle).
3. Requests of DACs researchers include simple and concrete circuit implementation with efficient performances such as high-resolution and low-distortion. Interests of CGRs researchers include generalized system description and classification/recognition of the phenomena.

IV. IMPLEMENTATION

Fig. 4 shows implementation examples of DACs in Equations (5) and (6), where $y \in \{0, E\}$ is an input signal with clock period T . Fig. 4 (a) shows the circuit in [5] that can realize Equation (5) for binary decoding. Fig. 4 (b) shows our circuit in order to realize Equation (6) for Gray decoding. In the circuit, switch S_u is closed only if $y = 0$. If behavior of switches and capacitor voltages are ideal [11], the dynamics is described by the followings.

$$v_1(t) \equiv v_h(n) = \begin{cases} v_3(t) & \text{for } y = E \\ -v_3(t) & \text{for } y = 0 \end{cases} \quad (9)$$

$$v_2(t) = E, \quad v_3(t) = v_1(n-1)$$

$$\text{for } S = \text{on } (nT \leq t < (n+0.5)T)$$

$$v_1(t) = \frac{1}{2}(v_h(n) + E) \equiv v_1(n) = v_2(t) = v_3(t)$$

$$\text{for } S = \text{off } ((n+0.5)T \leq t < (n+1)T) \quad (10)$$

This circuit can realize DAC for Gray decoding, where $v_1(n)$ and y are proportional to $X(n)$ and Y , respectively. Since these circuits correspond to IFSs consisting of contractive maps, the circuits behavior is stable and are suitable for hardware implementation.

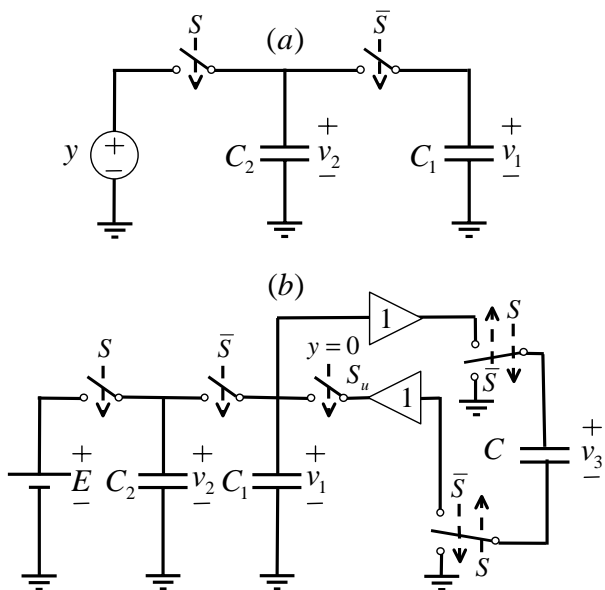


Fig. 4. Implementation examples where $C_1 \doteq C_2$. (a) DAC for binary decoding (cut map), (b) DAC for Gray decoding (valley map). $S = \text{on}$ for $nT \leq t < (n + 0.5)T$ and $S = \text{off}$ for $(n + 0.5)T \leq t < (n + 1)T$, where T is period of clock signal. \bar{S} operates in inverse phase of S .

Fig. 5 shows laboratory measurement by test circuits. In the figure the output y corresponds to 4-bit sequences (0101) and (1010). The circuit in Fig. 4 (b) can realize Gray decoding as shown in Fig. 5 (b): capacitor voltage v_1 enters alternately into two bins corresponding to (0101) and (1010). In a likewise manner, we have confirmed operation of circuit in Fig. 4 (a). Some effective compensation methods for further improvements of the circuits performance can be found in [4] [5].

V. CONCLUSIONS

We have considered cyclic DACs as an application of IFSs and have discussed similarities and differences between DACs and CGRs. A simple implementation circuits of the basic DACs for Gray decoding is also presented. Future problems include the followings.

1. Analysis of encoding/decoding properties for wider class of ADCs/DACs based on IFSs.
2. Extension to higher dimensional systems.
3. Practical circuit implementation.

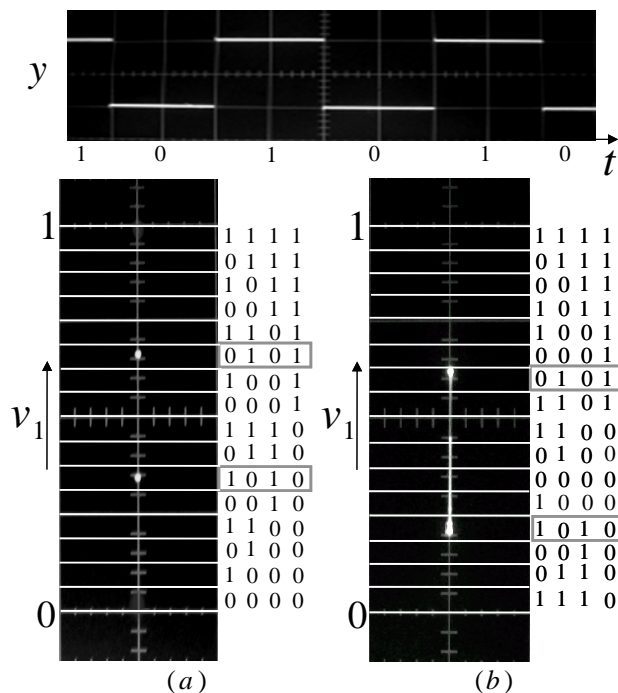


Fig. 5. Laboratory measurements (a) DAC for binary decoding, (b) DAC for Gray decoding.

REFERENCES

- [1] P. G. A. Jespers, Integrated converters, Oxford, 2001.
- [2] S. Signell, B. Jonsson, H. Stenstrom & N. Tan, New A/D converter architectures based on Gray coding, Proc. IEEE/ISCAS, pp. 413-416, 1997.
- [3] L. Chiaburu & S. Signell, An improved binary algorithmic A/D converter architecture, Proc. IEEE/ISCAS, I, pp. 865-868, 2003.
- [4] G. Cauwenberghs, A micropower CMOS algorithmic A/D converter, IEEE Trans. CAS-I, 42, pp. 913-919, 1995.
- [5] L. Weyton & S. Audenaert, Two-capacitor DAC with compensative switching, Electron. Lett. 31, pp.1425-1437, 1995.
- [6] P. Rombouts, L. Weyten, J. Raman & S. Audenaert, Capacitor mismatch compensation for the quasi-passive switched capacitor DAC, IEEE Trans. CAS-I, 45, pp. 68-71, 1998.
- [7] M. F. Barnsley, Fractals everywhere, Springer-Verlag, 1988.
- [8] H. J. Jeffrey, Chaos game representation of gene structure, Nucleic Acids Research, 18, pp. 2163-2170, 1990.
- [9] T. Habutsu, Y. Nishio, I. Sasase and S. Mori, A secret key cryptosystem using a chaotic map, Trans. IEICE, 73, pp. 1041-1044, 1990.
- [10] E. Ott, Chaos in dynamical systems, Cambridge, 1993.
- [11] T. Matsushita, T. Saito & H. Torikai, Basic synchronous phenomena by intermittently coupled capacitors, IEEE Trans. CAS-I, 47, 7, pp. 1105-1109, 2000.

THE TIME-SERIES MODELLING AND CIRCUIT IMPLEMENTATION FROM TIME-FREQUENCY DOMAIN SPECIFICATIONS

F. Acar Savaci*, Nalan Özkurt**

*Electrical and Electronics Eng. Dept.,
Izmir Institute of Technology

e-mail: acarsavaci@iyte.edu.tr

**Electrical and Electronics Eng. Dept.,
Dokuz Eylul University, Izmir, Turkey

e-mail:nalan.ozkurt@eee.deu.edu.tr

Abstract—The synthesis of the nonlinear circuits using the wavelet domain techniques has been accomplished in this study. When the time-frequency domain specifications have been given as the wavelet ridges, the signal with the given ridges has been synthesized. Then, the dynamical wavelet network has been trained for the synthesized signal. The circuit of the wavelet network has been designed and simulated.

I. INTRODUCTION

In this study, a synthesis procedure for the nonlinear circuits with desired time-frequency domain behavior using wavelet domain methods has been proposed [1]. The system includes four main blocks: signals synthesis, system modelling, circuit synthesis and verification which are shown in Figure 1. The signal synthesis block synthesizes the signal with the desired time-frequency domain properties using wavelet ridges method. The system modelling block determines the parameters of the dynamical wavelet network using the time-series synthesized by the first block. In the circuit synthesis block, the wavelet network circuit has been realized with the wavelon circuit proposed. In the verification phase, the wavelet ridges of the output of the wavelet network have been calculated by singular value decomposition based ridge determination method proposed in [2].

II. SIGNAL SYNTHESIS

The signal synthesis block synthesizes the signal with given time-frequency domain specifications as follows:

$$E(t, f) = \begin{cases} E_1(t, f) & t_0 \leq t < t_1 \text{ \& } f_0 \leq f < f_1 \\ \vdots & \\ E_n(t, f) & t_{n-1} \leq t < t_n \text{ \& } f_{n-1} \leq f < f_n \\ 0 & \textit{otherwise} \end{cases} \quad (1)$$

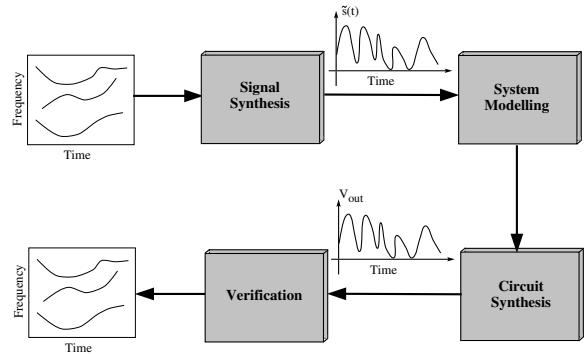


Fig. 1. The block diagram of the system

where $E(t, f)$ represents the energy distribution in the time-frequency plane.

Before introducing the details of these methods, brief explanation about wavelet transform should be given. In continuous wavelet transform (CWT), the signal is projected on a family of zero-mean functions called wavelets, deduced from a mother wavelet by translations and dilations

$$W_s(a, b; \Psi) \triangleq \int_{-\infty}^{\infty} s(t) \Psi_{a,b}^*(t) dt \quad (2)$$

where a and b are the dilation (scale) and translation coefficients, respectively; the scaled and translated wavelet is obtained as

$$\Psi_{a,b}(t) \triangleq \frac{1}{\sqrt{a}} \Psi\left(\frac{t-b}{a}\right), \quad a \in \mathbb{R}^+, \quad b \in \mathbb{R} \quad (3)$$

where $\Psi(\cdot)$ is the mother wavelet and $*$ denotes the complex conjugate. The mother wavelet must satisfy the admissibility condition which implies zero mean as

$$c_\psi = \int_0^\infty |\Psi(\omega)|^2 \frac{d\omega}{\omega} < \infty. \quad (4)$$

as given in [3].

The time-frequency domain specifications have been given as the ridges of the wavelet transforms. The multi-component signal with the instantaneous amplitudes $A_l(t)$ and the instantaneous phases $\phi_l(t)$ can be described by

$$s(t) = \sum_{l=1}^L A_l(t) e^{j\phi_l(t)} \quad (5)$$

where L is the number of the components, then the wavelet transform can be written as

$$W_s(a, b; \Psi) = \frac{1}{2} \sum_{l=1}^L A_l(b) e^{j\phi_l(b)} \hat{\Psi}^*(a\phi'_l(b)) + r(a, b) \quad (6)$$

with $r(a, b) \sim O(|A'_l|, |\phi'_l|)$ where the prime denotes the derivative [4], [5]. Therefore, if the Fourier transform of the mother wavelet “ $\hat{\Psi}(\omega)$ ” is localized near a certain frequency $\omega = \omega_0$, the scalogram is localized around L curves

$$a^l = a^l(b) = \frac{\omega_0}{\phi'_l(b)}, \quad l = 1, \dots, L \quad (7)$$

which are called ridges of the wavelet transform. The values of the scalogram along the ridge construct the transform skeleton or wavelet curve. Thus, the original signal $s(t)$ can be recovered using the skeleton of the transform.

The real part of the signal $s(t)$ given in Eq.(5) can be constructed from the skeleton of the transform using the approximate formula given in Eq.(6) as

$$s_r(b) = 2Re\left\{ \sum_{l=1}^L W_s(a^l(b), b; \Psi) \right\} \quad (8)$$

where L is the number of the ridges [5]. The reconstruction using the transform skeleton is a simple scheme and it produces good approximations. In order to synthesize a signal from the given ridges a code in MATLAB has been written.

III. SYSTEM MODELLING

Any finite energy multivariate function can be approximated by wavelets using the multiresolution approximation property of the wavelet decomposition. In order to approximate arbitrary nonlinear functions the wavelet network which combines feedforward neural networks and wavelet decompositions has been proposed in [6].

When the input-output pairs measured from the system to be modelled is given as

$$\{x(t_k), y(t_k) | y(t_k) = f(x(t_k)) + \varepsilon_k\} \\ k = 1, \dots, K, \quad f(\cdot) : \mathbb{R} \rightarrow \mathbb{R} \quad (9)$$

where ε_k is the measurement noise, the problem is to minimize the mean square error between the actual output and the output of the wavelet network

$$MSE \triangleq \frac{1}{2} E \left\{ (y - f_w(x))^2 \right\} \quad (10)$$

where the output of the wavelet network is defined as

$$f_w(x) = \sum_{i=1}^N w_i \Psi(D_i x - b_i) + c^T x + \bar{f} \quad (11)$$

where N is the number of d -dimensional wavelons, w_i is the wavelet coefficients for each wavelon, $D_i = \text{diag}(d_{11}^i, \dots, d_{mm}^i) \in \mathbb{R}^{d \times d}$ where $d_{jj}^i = 1/a_{ij}$ and a_{ij} is the dilation coefficient, $\Psi(\cdot) : \mathbb{R}^d \rightarrow \mathbb{R}$ is the mother wavelet function, $b_i \in \mathbb{R}^d$ is the translation coefficient vector, $c \in \mathbb{R}^d$ represents the coefficient of the linear term and \bar{f} is the bias term to approximate the functions with nonzero mean.

The wavelet networks have also been used in the identification of the dynamical systems or in the prediction of the future outputs of the systems. Assume that a dynamical system is defined as

$$y(k) = F(x(k)) + \varepsilon_k, \quad F(\cdot) : \mathbb{R}^d \rightarrow \mathbb{R}. \quad (12)$$

According to the Taken's time-delay embedding theorem [7], the multidimensional dynamical structure of the system can be retrieved from single scalar variable observed from the system. Let a vector $x_s \in \mathbb{R}^d$ be constructed from the observations as

$$x_s(k) = [y(k-T) \ y(k-2T) \ \dots \ y(k-dT)] \quad (13)$$

where d is the embedding dimension and T is the embedding delay. Then

$$y(k) = F(x_s(k)) \quad (14)$$

follows the dynamical evolution of the original system. Therefore, the next state of the system is predicted from the previous observations.

The system evolution function F is approximated by some arbitrary set of basis functions for the modelling or identification of the nonlinear dynamical systems [8],[9],[10]. The purpose is to represent Eq.14 with the suitable wavelet network. Since the observations can be expressed as a function of past measurements, the past values are used as inputs and the present values are used as output for the wavelet network to approximate the function $F(\cdot)$. The output of the wavelet network F_w is

$$y(k) = F_w(x_s(k)) = \sum_{i=1}^N w_i \Psi_d(D_i x_s(k) - b_i) + c^T x + \bar{f} \quad (15)$$

IV. CIRCUIT SYNTHESIS

The static and dynamical wavelet networks successfully model the nonlinear systems. The circuit implementation of the wavelet network with Mexican Hat mother wavelet [11] will be introduced in this section.

The Mexican Hat mother wavelet is one of the commonly used real mother wavelet because of its good approximation ability. The mother wavelet is defined as

$$\Psi(x) = (d - \|x\|^2) \exp\left(-\frac{\|x\|^2}{2}\right) \quad \Psi(\cdot) : \mathbb{R}^d \rightarrow \mathbb{R}. \tag{16}$$

where $\|x\|^2 = x^T x$. The circuit implementation of the Mexican Hat mother wavelet has been accomplished using antilog amplifier, operational amplifiers and passive circuit components.

A. The Circuit Implementation of Dynamical Wavelet Network

The wavelet network can be used for modelling the nonlinear dynamical systems. The dynamics given in Eq.(15) has been implemented by the dynamical wavelet network circuit shown in Figure 2.

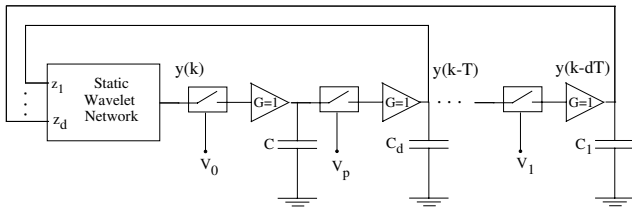


Fig. 2. Dynamical wavelet network circuit.

The capacitances are used as the memory elements which stores the previous outputs of the wavelet network. The voltage controlled switches are controlled by the external pulse generators which are triggered sequentially. Therefore, when the related voltage controlled switch is in ‘‘ON’’ state, the voltage is stored in the capacitance and it is ready as an input to the static wavelet network for the calculation of the next state. The order of the switch control pulses is $V_{cont}, V_{cont_1}, \dots, V_{cont_d}$ for a d -dimensional wavelet network. The switching effects have been filtered out by the low-pass filter.

V. VERIFICATION

In the proposed nonlinear circuit synthesis system the circuit has been designed according to the specifications given in the time-frequency domain. Giving the specific wavelet ridges is one of the proposed

methods for signal synthesis [1] and it is more natural way of determination of the signal properties. When the design process has been completed, the output of the system must be tested to determine whether the proposed circuit satisfies the given conditions. Therefore, the wavelet ridges of the obtained signal should be determined. There are several ridge determination algorithms. although the method proposed in [5] for noisy multicomponent signals are successful in determination of the actual ridges, the proposed method in [2] which is based on the singular value decomposition (SVD) of the scalogram matrix is computationally more effective. In the proposed method the singular value decomposition of the scalogram matrix of the related signal has been obtained. The effects of the Additive White Gaussian Noise (AWGN) is higher on the smaller singular values which correspond to the components of the signal with lower energy levels. Therefore, the effect of the noise is reduced by truncating the lower singular values. The approximated scalogram has been obtained by reconstructing the matrix only by using the larger singular values.

VI. APPLICATION

The time-frequency domain specifications of the desired signal is as following

$$E(t, f) = \begin{cases} 0.2 & 0.2 \leq t < 0.8 \text{ sec} & \text{and} & f = 4Hz \\ 0.3 & 0.2 \leq t < 0.5 \text{ sec} & \text{and} & f = 7Hz \\ 0.2 & 0.4 \leq t < 0.7 \text{ sec} & \text{and} & f = 8Hz \\ 0.1 & 0.3 \leq t < 0.6 \text{ sec} & \text{and} & f = 11Hz \\ 0.2 & 0.5 \leq t < 0.8 \text{ sec} & \text{and} & f = 13Hz \\ 1 & 0.2 \leq t < 0.8 \text{ sec} & \text{and} & f = 15Hz \\ 0 & \text{otherwise} \end{cases} \tag{17}$$

and the desired signal, target time-frequency plane, the synthesized signal and the wavelet transform of the synthesized signal are shown in Figure 3.

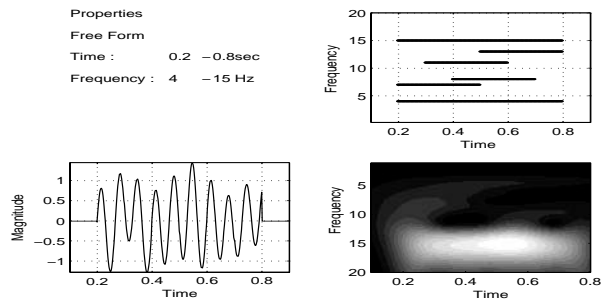


Fig. 3. The synthesized multicomponent aperiodic signal by wavelet ridges method.

In order to train the wavelet network the embedding delay has been chosen as $T = \tau_s$ where the sampling

period is $\tau_s = 0.002sec$ for embedding dimension of $d_e = 3$. Seven wavelons have been used and the network has been trained for 1000 epochs. The obtained mean squared error is $mse = 0.000375857$. The output of the wavelet network in the phase space and in the time domain are shown in Figure 4.

The wavelet network circuit has been simulated in PSpice and the output signal of the circuit is shown in Figure 5. The wavelet ridges of the output signal have been obtained by the SVD-based ridge determination algorithm. The results are shown in Figure 6.

VII. CONCLUSIONS

A nonlinear circuit synthesis method in wavelet domain has been proposed in this paper. When the desired time-frequency domain specifications are given, the values of the parameters of the dynamical wavelet circuit have been determined in three steps: The signal synthesis, the system modelling and the circuit synthesis. As the last step of the procedure, the accuracy of the synthesis has been investigated by the verification block.

REFERENCES

[1] Ozkurt, N., "Synthesis of Nonlinear Circuits in Time-Frequency Domain", Ph.D. Thesis submitted to Dokuz Eylul University, The Graduate School of Natural and Applied Sciences, Turkey, Dec.2003.
 [2] Ozkurt N., Savacı, F.A. "Determination of Wavelet Ridges of Nonstationary Signals by Singular Value Decomposition Method", ECCTD'2003, Krakow, Poland.
 [3] Mallat, S. A Wavelet Tour of Signal Processing, 2nd ed., Academic Press, San Diego, CA, 1999.
 [4] Delprat, N., Escudie, B., Guillemain, P., Kronland-Martinet, R., Tchamitchian, P., Torresani, B. "Asymptotic Wavelet and Gabor Analysis: Extraction of Instantaneous Frequencies", IEEE Trans. on Information Theory, vol.38, no:12, pp:644-664, March 1992.
 [5] Carmona, R.A., Hwang, W.L., Torresani, B. "Multiridge detection and time-frequency reconstruction", IEEE Trans. on Signal Processing, vol.47, pp.480-492,1999.
 [6] Zhang, Q., Benveniste, A. "Wavelet Networks", IEEE Trans. on Neural Networks Vol. 3, No:6, Page(s): 889 -898, November 1992.
 [7] Abarbanel, H.D.I. Analysis of Observed Chaotic Data. Springer,1996.
 [8] Allingham, D., West, M., Mees, A. "Wavelet reconstruction of nonlinear dynamics", Int. Jour. Of Bifurcation and Chaos, Vol.8, No.11, pp.2191-2201, 1998.
 [9] Cao, L., Hong, Y., Fang, H., He, G. "Predicting chaotic time series with wavelet networks", Physica D, Vol. 85, pp.225-238, 1995.
 [10] Zhang, Q. "Using wavelet network in nonparametric estimation", IEEE Trans. on Neural Networks, Vol. 8, pp.227 -236, March 1997.
 [11] Ozkurt, N., Savacı, F.A., Gunduzalp, M., "The Circuit Realization of Mexican Hat Wavelet Function", submitted to AEU Int. Jour. of Electronics and Communications,2004.

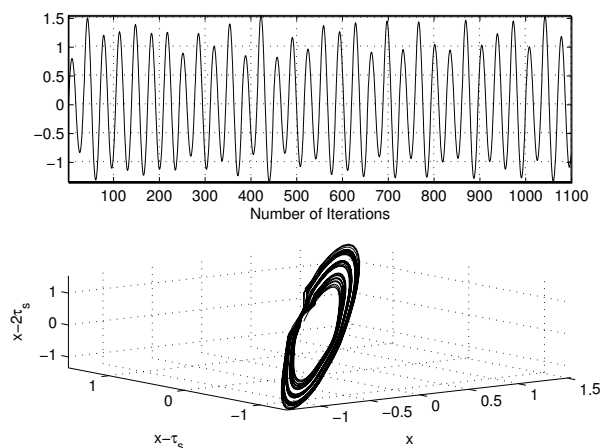


Fig. 4. The embedded multicomponent aperiodic signal in phase space and the output of the wavelet network.

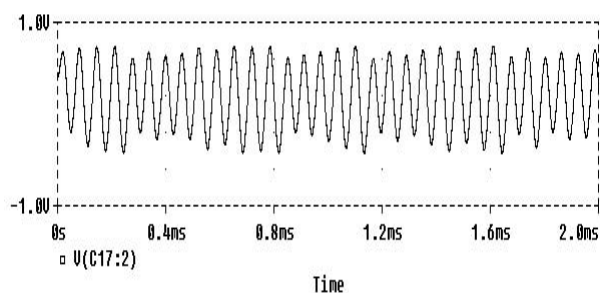


Fig. 5. The output of the circuit for multicomponent aperiodic signal in Spice.

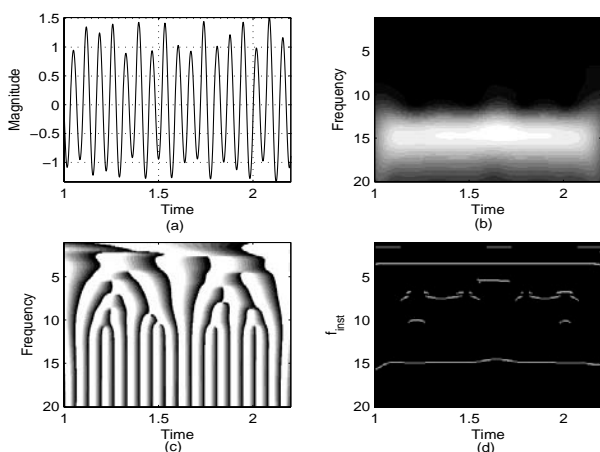


Fig. 6. The wavelet transform and the instantaneous frequency of the output of the wavelet network for multicomponent aperiodic signal.

Collapse and Coexistence of Duck Solution in a Circuit Driven by an Extremely Small Periodic Force

Munehisa Sekikawa[†], Naohiko Inaba[†], Tetsuya Yoshinaga[‡], and Hiroshi Kawakami^{††}

[†]Faculty of Engineering, Utsunomiya University Japan

[‡]School of Medicine, the University of Tokushima Japan

^{††}Faculty of Engineering, the University of Tokushima Japan

Abstract— *The authors study the response of a circuit which generates the duck solution, where an extremely small periodic perturbation is applied. Bifurcation structures of fundamental harmonic entrainment, 1/2 sub-harmonic entrainment and 1/3 sub-harmonic entrainment are analyzed. Period doubling bifurcation is observed even if periodic perturbation is extremely small. This perturbation breaks down the duck solution eventually, and then chaos occurs afterwards. Coexistence of two duck solutions is also observed under the extremely small perturbation.*

I. INTRODUCTION

In a van der Pol oscillator, there are some cases where a limit cycle whose amplitude grows abnormally fast as a control parameter varies[1]. This phenomenon is called “duck solution[2],” because the oscillation trajectory in the phase space looks like a duck. It is also called “lost solution[3], [4],” because this solution behaves as if the oscillation with a medium size amplitude seems not to appear. The duck solution is observed in slow-fast system which contains small parameter ε . It is clarified from the non-standard analysis that the amplitude is changed with the order 1 when the system parameter, which corresponds to direct current term, is varied by the order of $\exp(-1/\varepsilon)$ [2]. The magnitude of $\exp(-1/\varepsilon)$ approximates to 4.5×10^{-5} if $\varepsilon = 0.1$, and moreover, it approximates to 3.7×10^{-44} if $\varepsilon = 0.01$. This phenomenon is called “Singular Hopf bifurcation” in the field of mathematics[5], [6].

Itoh *et al.* carried out detailed laboratory experiment and reported that the duck solution can be observed. However, solutions with various multiple periods and chaos are also observed in their laboratory experiment[3]. Such periodic solution or chaos can not be explained from the second order autonomous equation. Motivated from

such interesting experimental phenomena, the authors believe that it is of great importance to clarify the dynamics which will yield chaos via duck solution breakdown.

In this paper, in order to explain the experimental results carried out by Itoh *et al.*, the authors apply an extremely small periodic force $B \sin \omega \tau$ as perturbation to a van der Pol oscillator. This perturbation corresponds to influence of noise existing in real circuit. The authors make a two-parameter bifurcation diagram by the method presented in Ref. [7]. It is clarified that period doubling bifurcation occurs successively, when the amplitude of small sinusoidal force is about 1/10,000, and chaos occurs. Coexistence of two duck solutions is also observed under the extremely small perturbation.

II. CIRCUIT MODEL AND ITS EQUATION

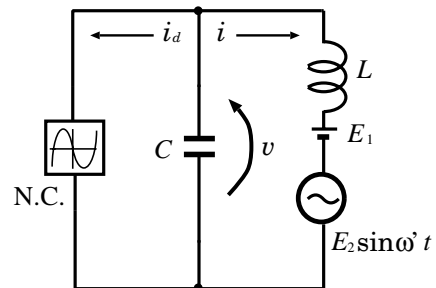


Fig. 1. Circuit diagram.

Figure 1 illustrates circuit model. In this figure, N.C. is a nonlinear negative conductance, and the $v-i$ characteristic of N.C. is represented by the following third order polynomial function:

$$i_d(v) = -g_1 v + g_3 v^3. \tag{1}$$

The normalized governing equation of this oscillator is presented by the following equation:

$$\begin{cases} \varepsilon \dot{x} = y + x(1 - x^2) \\ \dot{y} = -x + (B_0 + B \sin \omega \tau), \end{cases} \tag{2}$$

where parameter B_0 , B , and ε correspond to direct current term, amplitude of an extremely

moosk@every.is.utsunomiya-u.ac.jp

small sinusoidal force, and the capacitor C respectively. C is smaller, then ε is smaller. ε is fixed to 0.1. This assumption is easily realized in laboratory experiment.

III. DUCK SOLUTION, AND CHAOS BY AN EXTREMELY SMALL PERTURBATION

In this section, let us review the behavior of the duck solution in a van der Pol oscillator($B = 0$) briefly. Relaxation oscillation is observed at $B_0 = 0$. The point that satisfies $y + x(1 - x^2) = 0$ and $-x + B_0 = 0$ is an equilibrium point, which is unstable for $|B_0| < 1/\sqrt{3}(= 0.57735\dots)$, and which is stable for $B_0 > 1/\sqrt{3}$ as shown in Fig. 2(d). A remarkable phenomenon is observed when B_0 is chosen slightly smaller than $1/\sqrt{3}$. Hopf bifurcation occurs at $B_0 = 1/\sqrt{3}$. A small amplitude oscillator is observed at $B_0 = 0.5695$ as shown in Fig. 2(c). However, large amplitude oscillation is observed if B_0 is chosen a little smaller than $B_0 = 0.5695$ as shown in Fig. 2(a). It is not easy task to observe the attractor whose amplitude is medium, because medium amplitude oscillation is found at $B_0 = 0.5694$ which is 1/10,000 smaller than $B_0 = 0.5695$ (see Fig. 2(b)) based on the detailed numerical simulations. This phenomenon is called the lost solution or singular Hopf bifurcation and has been studied in detail in the field of mathematics[1], [2], [5]. According to the non-standard analysis, it is known that the am-

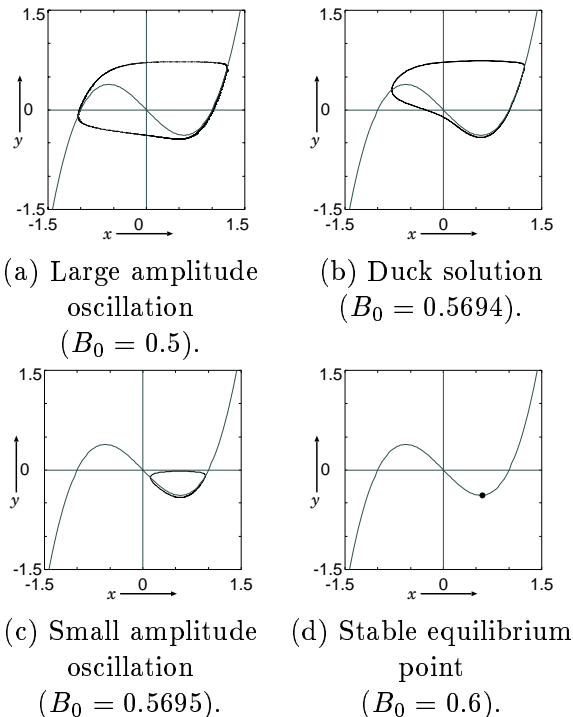


Fig. 2. Attractors ($\varepsilon = 0.1, B = 0$).

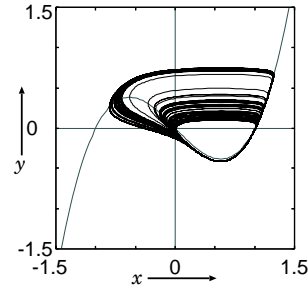


Fig. 3. Chaotic attractor ($\varepsilon = 0.1, B_0 = 0.5694, B = 0.0001, \omega = 3.127$).

plitude of the oscillation changes with the order 1 by changing B_0 with the order of $\exp(-1/\varepsilon)$. Since $\exp(-1/\varepsilon)|_{\varepsilon=0.1} \simeq 4.5 \times 10^{-5}$, this simulation results match the theoretical ones qualitatively. The trajectory of the medium size oscillation looks like a duck as shown in Fig. 2(b). Hence, this phenomenon is also called the duck solution[2]. Characteristic of this attractor is that solution pass by the unstable branch[2].

Itoh *et al.* carried out laboratory experiment and showed that the duck solution was observable[3]. However, chaotic behavior was often observed in the neighborhood of the parameter where the duck solution was observed. To support this experimental result, the authors propose a van der Pol oscillator which is driven by an extremely small periodic perturbation $B \sin \omega \tau$, where $B \ll 1$ is assumed. Let us choose such B_0 that the duck solution appears. That is, B_0 is fixed to 0.5694. This choice of B_0 would be appropriate for taking correspondence with the phenomena, which are observed in laboratory experiment[3]. Chaotic attractor, which is generated by this perturbation, is observed as shown in Fig. 3.

IV. METHOD OF ANALYSIS

The method presented in Ref. [7] is used for the analysis. A summary of the method is presented below. Let the solution of Eq. (2) passing through the initial value $\mathbf{x} = \mathbf{u}_0$ be

$$\mathbf{x}(\tau) = \varphi(\tau, \mathbf{u}_0, \boldsymbol{\lambda}), \tag{3}$$

where $\mathbf{x} = (x, y)^T$, and $\boldsymbol{\lambda} \equiv (\varepsilon, B_0, B, \omega)$ is a parameter. Because, the external force for Eq. (2) is a periodic function of $2\pi/\omega$, the phase plane at $\tau = 0$ and that at $\tau = 2\pi/\omega$ can be considered equivalent. Hence, the following Poincaré map $T_{\boldsymbol{\lambda}}$ can be defined:

$$T_{\boldsymbol{\lambda}} : \mathbb{R}^2 \rightarrow \mathbb{R}^2$$

$$\mathbf{u}_0 \mapsto T_{\boldsymbol{\lambda}}(\mathbf{u}_0) = \varphi(2\pi/\omega, \mathbf{u}_0, \boldsymbol{\lambda}). \tag{4}$$

The periodic solution of continuous dynamic system corresponds to the periodic point of T_{λ} .

If \mathbf{u}_0 is an m -periodic point of T_{λ} , then \mathbf{u}_0 satisfies the following equation:

$$T_{\lambda}^m(\mathbf{u}_0) - \mathbf{u}_0 = 0, \quad (5)$$

where T_{λ}^m is the m -composite map of T_{λ} . The characteristic of the periodic point \mathbf{u}_0 is classified in terms of the root μ of the following characteristic equation:

$$\left| \frac{d}{d\mathbf{u}_0} T_{\lambda}^m(\mathbf{u}_0) - \mu \mathbf{I} \right| = 0. \quad (6)$$

Let the roots of the characteristic equation be μ_1, μ_2 ($|\mu_1| \geq |\mu_2|$). The periodic point is stable when $|\mu_1| < 1$. It is saddle when $|\mu_1| > 1 > |\mu_2|$, and is completely unstable when $|\mu_2| > 1$. Bifurcation occurs when $|\mu| = 1$. According to the analysis of Eq. (2), the following bifurcations are observed.

- Saddle-node bifurcation: This bifurcation occurs when $\mu = 1$. If the parameters are varied in such a way that the bifurcation set is traversed, a saddle point and a stable periodic point may be fused together so that these periodic points become extinct. In the following, this bifurcation parameter set is denoted as G^m , where m means period.
- Period doubling bifurcation: This bifurcation occurs when $\mu = -1$. A stable m -periodic point becomes a saddle point and a stable $2m$ -periodic point is generated on both sides of this saddle point. It is known that period doubling bifurcation occurs successively and thus chaos occurs. In the following, this bifurcation parameter set is denoted as I^m .

These bifurcations obtained by solving simultaneous equations of Eqs. (5) and (6) by Newton's method.

V. TWO-PARAMETER BIFURCATION DIAGRAM

In this section, the bifurcation structure of the driven van der Pol oscillator is rigorously investigated. In the following discussions the parameters ε and B_0 are fixed to 0.1, and 0.5694 respectively. Figure 4 illustrates two-parameter bifurcation diagram. Abscissa represents the angular frequency ω and ordinate is the amplitude B . Figure 5(a), (b), and (c) illustrate two-parameter bifurcation diagram of fundamental harmonic entrainment, 1/2 sub-harmonic entrainment, and 1/3, respectively. These entrainments have similar structure.

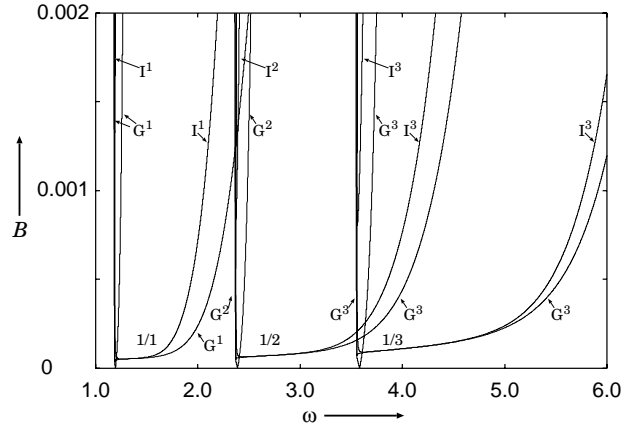


Fig. 4. Two-parameter bifurcation diagram. ($\varepsilon = 0.1, B_0 = 0.5694$)

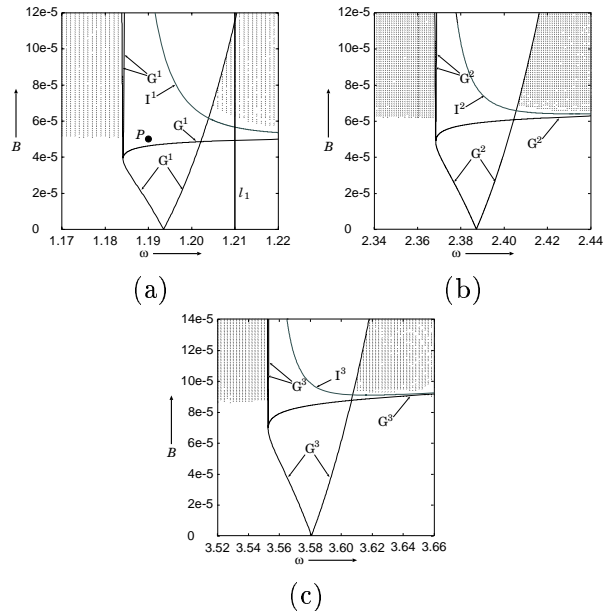


Fig. 5. Two-parameter bifurcation diagram ($\varepsilon = 0.1, B_0 = 0.5694$). (a) Fundamental harmonic entrainment. (b) 1/2 sub-harmonic entrainment. (c) 1/3 sub-harmonic entrainment.

Lyapunov exponent is calculated numerically by Shimada's procedure[8], and chaos generating region is shaded in Fig. 5.

Figure 6 illustrates model of the periodic point manifold. In this figure, we take the scalar function axis (y in Fig. 6) in the direct product for the parameter plane. Here, k_d^m denotes the periodic point[7]. This d-type periodic point indicates that the number of characteristic multiplier is even, for which $\mu < -1$. k indicates the instability dimension and m is the period of the periodic point. The authors trace periodic point, with the result that these entrainments are formed with one periodic point manifold as shown in Fig. 6. At the

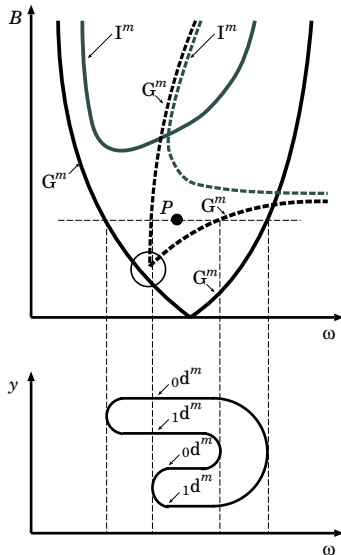


Fig. 6. Model of the periodic point manifold.

point marked with P in Fig. 6, these are two stable periodic points ($0d^m$). Therefore, we can understand that the attractors which correspond to each periodic point coexist. At the point marked with \circ , where saddle node bifurcation curve with broken line makes cusp, broken line is closer to solid line of saddle node bifurcation curve. But, they do not stick together.

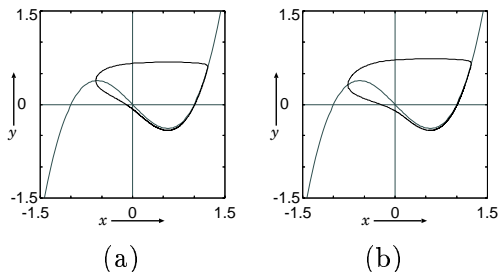


Fig. 7. Coexisting duck solution ($\varepsilon = 0.1, B_0 = 0.5694, B = 5 \times 10^{-5}, \omega = 1.19$).

It was explained that two attractors coexisted at point P in Fig. 6. We can observe those coexisting attractors at point P in Fig. 5(a). Figure 7 illustrates coexisting attractors in fundamental harmonic entrainment. We can see that these attractors look like a “duck.” Coexistence of two duck solutions is observed under the extremely small perturbation. These coexistence of duck solutions is also observed in $1/2$ sub-harmonic entrainment and $1/3$ sub-harmonic entrainment.

Figure 8 illustrates behavior of the largest Lyapunov exponent at the line l_1 in Fig. 5(a). In this figure, we can see that torus occurs in a left part, because the largest Lyapunov exponent is almost zero. When we increase parameter B_0 , pe-

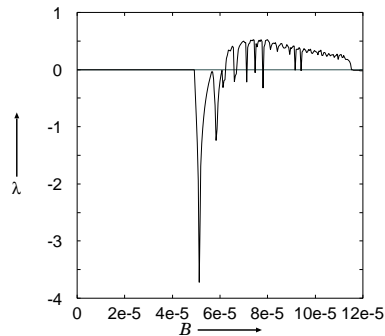


Fig. 8. The maximum Lyapunov exponent ($\varepsilon = 0.1, B_0 = 0.5694, \omega = 1.21$).

riod doubling bifurcation occurs successively and chaos occurs. The duck solution is broken down by this extremely small perturbation. Therefore, chaos will be observed in real laboratory experiment as Itoh *et al.* showed.

VI. CONCLUSION

The authors studied the response of a circuit which generates the duck solution, where an extremely small periodic perturbation is applied. Period doubling bifurcation and chaos are observed by an extremely small periodic perturbation such as $B = 5.5 \times 10^{-5} \sim 9.5 \times 10^{-5} \simeq \exp(-1/\varepsilon)|_{\varepsilon=0.1}$. Coexistence of two duck solutions is also observed under the extremely small perturbation.

REFERENCES

- [1] M. Diener, “The Canard unchained or how fast/slow dynamical systems bifurcate,” *Math. intelligencer*, Vol.6, No.3, pp.38–49, 1984.
- [2] V.I Arnol’d (ed.), “Dynamical systems V,” *Encyclopedia of Mathematical Sciences*, Vol.5, Springer, 1994.
- [3] M. Itoh and R. Tomiyasu, “Experimental Study of the missing solutions ‘Canards,’” *IEICE Trans.*, Vol.E73, No.6, pp.848–854, 1990.
- [4] A. K. Zvonkin and M. A. Shubin, “Non-standard analysis and singular perturbations of ordinary differential equations,” *Russian Math. Surveys*, Vol.39, No.2, pp.69–131, 1984.
- [5] S. M. Baer and T. Erneux, “Singular Hopf bifurcation to relaxation oscillations,” *SIAM J. Appl. Math.*, Vol.46, pp.721–739, 1986.
- [6] B. Braaksma, “Singular Hopf bifurcation in systems with fast and slow variables,” *J. Nonlinear Sci.*, Vol.8, pp.457–490, 1998.
- [7] H. Kawakami, “Bifurcation of periodic responses in forced dynamic nonlinear circuits: computation of bifurcation values of the system parameters,” *IEEE Trans. Circuits Syst.*, vol.CAS-31, pp.248–260, 1984.
- [8] I. Shimada and T. Nagashima, “A numerical approach to ergodic problem of dissipative dynamical systems,” *Progress of Theoretical Physics*, Vol.61, No.6, pp.1605–1615, 1979.

TOPOLOGICAL INVARIANTS IN A MODEL OF A TIME-DELAYED CHUA'S CIRCUIT

R. Severino, A. Sharkovsky, J. Sousa Ramos and S. Vinagre

Departamento de Matemática, Universidade do Minho

Campus de Gualtar, 4710 Braga, Portugal

e-mail: ricardo@math.uminho.pt

Institute of Mathematics, National Academy of Sciences of Ukraine

Tereshchenkivska str., 3, 01601 Kiev, Ukraine

e-mail: asharkov@imath.kiev.ua

Departamento de Matemática, Instituto Superior Técnico

Av. Rovisco Pais 1, 1049-001 Lisboa, Portugal

e-mail: sramos@math.ist.utl.pt

Departamento de Matemática, Universidade de Évora

Rua Romão Ramalho, 59, 7000-671 Évora, Portugal

e-mail: smv@uevora.pt

Abstract—*In the last 30 years, some authors have been studying several classes of boundary value problems (BVP) for partial differential equations (PDE) using the method of reduction to obtain a difference equation with continuous argument which behavior is determined by the iteration of a one-dimensional (1D) map (see, for example, [8], [11], [12], [13], [14] and [16]).*

In this paper we consider the time-delayed Chua's circuit introduced in [10] and [15] which behavior is determined by properties of one-dimensional map, [4], [10], [14] and [15]. To characterize the time evolution of these circuits we can compute the topological entropy and to distinguish systems with equal topological entropy we introduce a second topological invariant.

circuit introduced in [10] and [15], which is an infinite-dimensional generalization of Chua's circuit, obtained by replacing the LC resonant circuit by a lossless transmission line of length l , terminated on its left, $x = 0$, by a short circuit, as shown in Fig. 1.

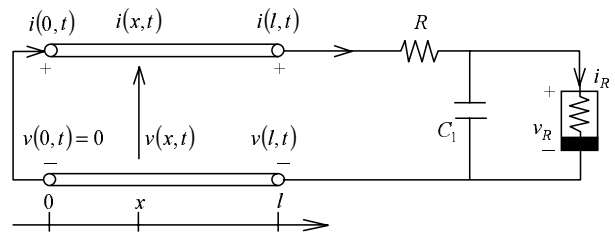


Fig. 1. The time-delayed Chua's circuit.

I. INTRODUCTION

In the last 30 years, some authors have been studying several classes of boundary value problems (BVP) for partial differential equations (PDE) using the method of reduction to obtain a difference equation with continuous argument which behavior is determined by the iteration of a one-dimensional (1D) map (see, for example, [8], [11], [12], [13], [14] and [16]). These classes consist mainly of problems for which the representation of general solution is known.

Thus, the notion of chaos can be taken from discrete dynamical systems: we say that such a PDE system is chaotic if the map that determines its solution exhibits chaos as a discrete dynamical system.

In this paper we consider the time-delayed Chua's

The contents in this paper are organized as follows: in the next section we present the problem following to [10]. In the section 3, we give a brief description of the kneading theory and we apply symbolic dynamical techniques to study the one-dimensional map associated with the difference equation. The properties of this one-dimensional map determine the qualitative behavior of the difference equation with continuous argument. Finally, we introduce a second topological invariant to distinguish systems with equal topological entropy.

With this approach we study the solutions of PDE using the symbolic dynamics, see [9], [17].

II. REDUCTION OF BVP TO DE

Following [10], let the transmission line be defined by the linear partial differential equations

$$\frac{\partial v(x,t)}{\partial x} = -L \frac{\partial i(x,t)}{\partial t}, \quad (1)$$

$$\frac{\partial i(x,t)}{\partial x} = -C \frac{\partial v(x,t)}{\partial t}, \quad (2)$$

where L and C denote the inductance and the capacitance per unit length of the transmission line. The boundary conditions are given respectively at $x = 0$ and $x = l$ by $v(0,t) = 0$ and $i(l,t) = G(v(l,t) - E - Ri(l,t)) + C_1 \partial(v(l,t) - Ri(l,t))/\partial t$, where G is defined by

$$G(u) = \begin{cases} m_0 u & \text{if } |u| \leq 1, \\ m_1 u - (m_1 - m_0) \operatorname{sgn} u & \text{if } |u| \geq 1. \end{cases} \quad (3)$$

The general solutions of equations (1) and (2) are of the form

$$v(x,t) = \alpha \left(t - \frac{x}{\nu} \right) - \alpha \left(t + \frac{x}{\nu} \right), \quad (4)$$

$$i(x,t) = \frac{1}{Z} \left[\alpha \left(t - \frac{x}{\nu} \right) + \alpha \left(t + \frac{x}{\nu} \right) \right], \quad (5)$$

where $\nu = \sqrt{1/LC}$ is the velocity of the incident and reflected waves, $Z = \sqrt{L/C}$ is the characteristic impedance of the transmission line and α is an arbitrary C^1 -smooth function. This boundary value problem is a system of two linear partial differential equations with a nonlinear boundary condition at $x = l$. Substituting (4) and (5) into the boundary condition at $x = l$ with $C_1 = 0$ and introducing the new variables $\tau = t\nu/(2l) - 1/2$ and $\beta(\tau) = \alpha(2l\tau/\nu)$, one obtain the difference equation with continuous argument

$$\beta(\tau + 1) = f(\beta(\tau)). \quad (6)$$

The function f is a piecewise-linear single-valued or multivalued function defined by

$$f(\beta) = A_k \beta - B_k, \quad (7)$$

where $\beta \in I_k$, $k = \pm 1, 0$ and

$$\begin{aligned} A_k &= -1 + q_k, \\ B_k &= \frac{q_k}{2} \left[E + k \left(1 - \frac{m_0}{m_k} \right) \right], \\ q_k &= \frac{2Z}{\frac{1}{m_k} + R + Z}, \\ I_0 &= \left\{ \beta : \left| \beta - \frac{E}{2} \right| \leq |\delta| \right\}, \\ I_{\pm 1} &= \left\{ \beta : \pm \left(\beta - \frac{E}{2} \right) > \delta \right\}, \end{aligned} \quad (8)$$

with $m_{-1} = m_{+1}$ and $\delta = m_0 Z/q_0$.

The initial values of voltage $v(x,0) = v_0(x)$ and current $i(x,0) = i_0(x)$ implies, for the difference equation (6), the following initial conditions

$$\varphi(\tau) = \begin{cases} \frac{v_0(-y) + Zi_0(-y)}{2} & \text{if } -1 \leq \tau < -\frac{1}{2}, \\ \frac{-v_0(y) + Zi_0(y)}{2} & \text{if } -\frac{1}{2} \leq \tau < 0, \end{cases} \quad (9)$$

with $y = l(1 + 2\tau)$.

Thus the time evolution of the time-delayed Chua's circuit with $C_1 = 0$ is governed by a scalar nonlinear difference equation with continuous argument (6) (see [10]). The qualitative behavior of this equation is determined by the properties of the one-dimensional (1D) map

$$\beta \mapsto f(\beta) \quad (10)$$

where f is defined in (7)-(8).

From now on we will write $f_{m_0, m_1, R, Z}$ instead of f for the map in (7) and φ_c instead of φ for the initial function in (9).

III. SYMBOLIC DYNAMICS

Given a bimodal map F in a interval $I = [a, b]$, with $F(a) = a$ and $F(b) = b$, and denote by c_1 and c_2 the turning points. Next, assign the symbols L (left), M (middle) and R (right) to each point x of the subintervals of monotonicity $[a, c_1)$, (c_1, c_2) and $(c_2, b]$, respectively, and the symbols A and B to their turning points c_1 and c_2 . It is called the address of x and it is denoted $ad(x)$. By doing this, we get a correspondence between orbits of points and symbolic sequences of the alphabet $\mathcal{A} = \{L, A, M, B, R\}$, the itinerary by the map F ,

$$it_F(x) = ad(x) ad(F(x)) ad(F^2(x)) \dots$$

The kneading invariant of the map F is the pair of itineraries of the image of each turning point,

$$\mathcal{K}(F) = (it_F(F(c_1)), it_F(F(c_2))).$$

Given a finite symbolic sequence S of $\mathcal{A}^{\mathbb{N}}$, we denote by n_M the frequency of the symbol M in S and we define the M -parity of this sequence, $\rho(S)$, according to whether n_M is even or odd, that is, in the first case we have $\rho(S) = +1$ and in the second $\rho(S) = -1$.

From the order relation $L \prec M \prec R$, inherited from the order of the interval, we introduce an order relation between sequences as follows: given any distinct sequences P and Q of $\mathcal{A}^{\mathbb{N}}$, admitting that

they have a common initial subsequence, i.e., there is a $k \geq 0$ such that $P_1 \dots P_k = Q_1 \dots Q_k$ and $P_{k+1} \neq Q_{k+1}$, we will say that $P \prec Q$ if and only if $P_{k+1} \prec Q_{k+1}$ and $\rho(P_1 \dots P_k) = +1$, or $Q_{k+1} \prec P_{k+1}$ and $\rho(P_1 \dots P_k) = -1$.

Let \mathcal{V} be a vector space of three dimension defined over the rationals having as a basis the formal symbols $\{L, M, R\}$, then to each sequence of symbols $S = S_1 S_2 \dots S_j \dots$ we can associate a sequence $\theta = \theta_0 \dots \theta_j \dots$ of vectors from \mathcal{V} , setting $\theta_j = \prod_{i=0}^{j-1} \epsilon(S_i) S_i$ with $j > 0$, $\theta_0 = S_0$, when $i = 0$, and $\epsilon(L) = -\epsilon(M) = \epsilon(R) = 1$, where to the symbols corresponding to the turning points c_1 and c_2 we associate the vectors $(L + M)/2$ and $(M + R)/2$. Thus $\epsilon(A) = \epsilon(B) = 0$. Choosing then a linear order in the vector space \mathcal{V} in such a way that the base vectors satisfy $L \prec M \prec R$ we are able to order the sequence θ lexicographically, that is, $\theta \prec \bar{\theta}$ iff $\theta_0 = \bar{\theta}_0, \dots, \theta_{j-1} = \bar{\theta}_{j-1}$ and $\theta_j \prec \bar{\theta}_j$ for some integer $j \geq 0$. Finally, introducing t as an undetermined variable and taking θ_j as the coefficients of a formal power series θ (invariant coordinate) we obtain $\theta = \theta_0 + \theta_1 t + \dots = \sum_{j=0}^{\infty} \theta_j t^j$.

In [5] Milnor and Thurston introduced basic invariants called kneading increments, kneading matrix and kneading determinant. The kneading increments are formal power series that measure the discontinuity evaluated at the turning points. For the case of a bimodal map we have two kneading increments defined by

$$\nu_i(t) = \theta_{c_i^+}(t) - \theta_{c_i^-}(t), \quad i = 1, 2, \quad (11)$$

where θ is the invariant coordinate defined previously and $\theta_{c_i^\pm}(t) = \lim_{x \rightarrow c_i^\pm} \theta_x(t)$. After separating the terms associated with the different symbols in (11) we get $\nu_i(t) = N_{i1}(t)L + N_{i2}(t)M + N_{i3}(t)R$ with $i = 1, 2$, and from these we can define the kneading matrix by

$$N(t) = \begin{pmatrix} N_{11}(t) & N_{12}(t) & N_{13}(t) \\ N_{21}(t) & N_{22}(t) & N_{23}(t) \end{pmatrix}.$$

Closely related is the kneading determinant which is defined from the kneading matrix according to the following formula $D(t) = D_1(t)/(1-t) = -D_2(t)/(1+t) = D_3(t)/(1-t)$, where $D_i(t)$ is the determinant obtained by eliminating the i -th column of the kneading matrix.

It is possible to determine the growth number $s(F)$, using this formalism introduced by Milnor and Thurston. Let F be a bimodal map in the interval with kneading invariant $\mathcal{K}(F)$ and $s(F) > 1$. Then,

$s(F)$ is given by the inverse of the smallest zero of the kneading determinant associated to $\mathcal{K}(F)$ and the entropy is given by the logarithm of $s(F)$, (see [5], [6]).

Finally, we introduce a second topological invariant to distinguish systems with equal topological entropy, that is, to distinguish isentropic dynamical systems.

Theorem 1: Let F be a bimodal map, $J = [F(c_2), c_1]$ and $I = [F(c_2), F(c_1)]$. Then the second topological invariant $r(F)$ is a function of the conductance and it is given by

$$r(F) = \lim_{t \rightarrow 1/s} \frac{L(J, t)}{L(I, t)},$$

with the formal power series $L(J, t) = \sum_{n=1}^{\infty} l(f^n) t^{n-1}$,

with the radius of convergence $s = \lim_{n \rightarrow \infty} l(f^n)^{1/n} = 1/t^*$, which verifies $D(t^*) = 0$, where $D(t)$ is the kneading determinant.

Proof: We can conjugate a bimodal map to a piecewise linear map with different slopes and as similar steps like in [7] we can prove the topological invariance of $r(F)$. See Fig. 5 to look in what way we identify $r(F)$ with the conductance. ■

Example 1: To illustrate the previous results, we consider $m_0 = -0.1$, $m_1 = 2.3$, $E = 0.3$, $Z = 5.5$ and $c = 1/R$ between 0.5 and 10.

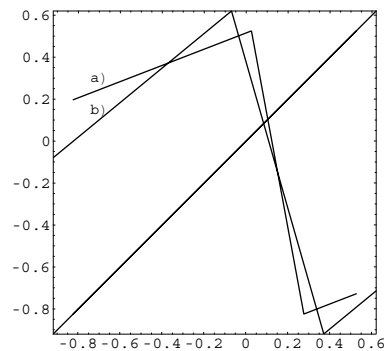


Fig. 2. The graph of the map $f_{m_0, m_1, R, Z}$, with $m_0 = -0.1$, $m_1 = 2.3$, $E = 0.3$, $Z = 5.5$, a) $c = 1/R = 0.5$, b) $c = 1/R = 10$.

Although this system depends on many parameters (m_0, m_1, R, Z and E), the family of bimodal maps depends essentially on two parameters, in what refers to the dynamics, that are functions of the previous ones. This dependence reflects the existence of two topological invariants: the topological entropy and another that is introduced here to distinguish the isen-

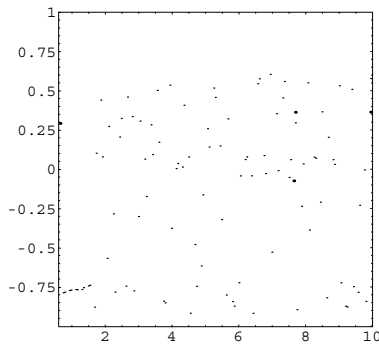


Fig. 3. The bifurcation diagram of the map $f_{m_0, m_1, R, Z}$, with $m_0 = -0.1$, $m_1 = 2.3$, $E = 0.3$, $Z = 5.5$, $c = 1/R \in [0.5, 10]$.

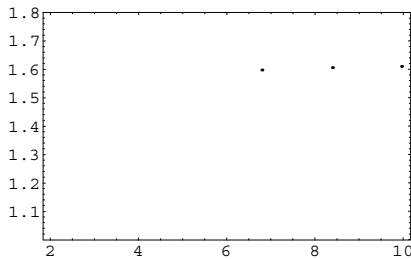


Fig. 4. The graph of the Lyapunov multiplier of the map $f_{m_0, m_1, R, Z}$, with $m_0 = -0.1$, $m_1 = 2.3$, $E = 0.3$, $Z = 5.5$, $c = 1/R \in [2, 10]$.

tropic systems. The calculation of these invariants depends only on the pair of kneading sequences, thus they are topological invariants. We identify this invariant with the conductance, that is, with the inverse of the resistance, see Fig. 5.

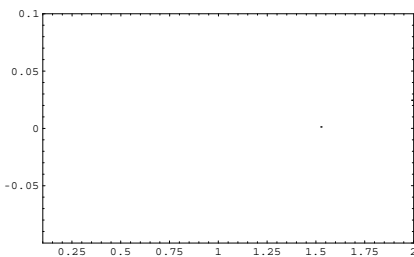


Fig. 5. The graph of the topological invariant $r(f_{m_0, m_1, R, Z})$, with $m_0 = -0.1$, $m_1 = 2.3$, $E = 0.3$, $Z = 5.5$, $R \in [0.1, 2]$.

The complexity of the dynamical behavior of this type of Chua's circuit can be completely determined by two topological invariants which can be explicitly calculated, as we demonstrate in this paper.

In future work, we will study the dependence of

these topological invariants with the variation of the more relevant physical parameters.

REFERENCES

- [1] Chen, G., Hsu, S. B. and Zhou, J., *Nonisotropic spatiotemporal chaotic vibration of the wave equation due to mixing energy transport and van der Pol boundary condition*, Int. J. Bifurcation and Chaos, 12, (2002), n3, 535-559.
- [2] Guckenheimer, J., *Sensitive dependence on initial conditions for one-dimensional maps*, Commun. Math. Phys., 70, (1979), 133-160.
- [3] Lampreia, J. P. and Sousa Ramos, J., *Symbolic dynamics of bimodal maps*, Port. Math. (N.S.), 54, Fasc.1, (1997), 1-18.
- [4] Maistrenko, Yu. L., Maistrenko, V. L., Vikul, S. I. and Chua, L. O., *Bifurcations of attracting cycles from time-delayed Chua's circuit*, Int. J. Bifurcation and Chaos, 5, (1995), n3, 653-671.
- [5] Milnor, J. and Thurston, W., *On Iterated Maps of the Interval*, in: J. C. Alexander (ed.) *Proceedings Univ. Maryland 1986-1987*. Lect. Notes in Math. 1342, 465-563, Springer-Verlag, Berlin-New York, 1988.
- [6] Misiurewicz, M. and Szlenk, W., *Entropy of piecewise monotone mappings*, Studia Math., 67, (1980), 45-63.
- [7] Ramos, C., Martins, N., Severino, R. and Sousa Ramos, J., *Noncommutative topological dynamics*, (2003), submitted.
- [8] Romanenko, E. Yu. and Sharkovsky, A. N., *From boundary value problems to difference equations: a method of investigation of chaotic vibrations*, Int. J. Bifurcation and Chaos, 9, (1999), n7, 1285-1306.
- [9] Severino, R., Sharkovsky, A. N., Sousa Ramos, J. and Vinagre, S., *Symbolic dynamics in boundary value problems*, Grazer Math. Ber., 346, (2004), 393-402.
- [10] Sharkovsky, A. N., *Ideal turbulence in an idealized time-delayed Chua's circuit*, Int. J. Bifurcation and Chaos, 4, (1994), n5, 303-309.
- [11] Sharkovsky, A. N., *Universal phenomena in some infinite-dimensional dynamical systems*, Int. J. Bifurcation and Chaos, 5, (1995), n5, 1419-1425.
- [12] Sharkovsky, A. N., *Iteration of continuous functions and dynamics of solutions for some boundary value problems*, Annales Mathematicae Silesianae, 13, (1999), 243-255.
- [13] Sharkovsky, A. N., *Difference equations and boundary value problems*, in "New Progress in Difference Equations", Proceedings of the ICDEA'2001, Taylor & Francis, (2003), 3-22.
- [14] Sharkovsky, A. N., Deregél, Ph. and Chua, L. O., *Dry turbulence and period-adding phenomena from 1-D map with time delayed*, Int. J. Bifurcation and Chaos, 5, (1995), n5, 1283-1302.
- [15] Sharkovsky, A. N., Maistrenko, Yu. L., Deregél, Ph. and Chua, L. O., *Dry turbulence from a time delayed Chua's circuit*, J. Circuits, Systems and Computers, 3, (1993), n2, 645-668.
- [16] Sharkovsky, A. N., Maistrenko, Yu. L. and Romanenko, E. Yu., *Difference Equations and Their Applications*, Kluwer Academic Publishers, 1993.
- [17] Vinagre, S. and Sousa Ramos, J., *Symbolic dynamics generated by an idealized time-delayed Chua's circuit*, (2003), to appear in Proceedings of the ICDEA'2003.

FRACTAL ANALYSIS OF X-RAY CHEST IMAGES

Maciej H. Słomczyński, Bożena Świdzińska

Institute of Electronic Systems

Faculty of Electronics and Information Technology,

Warsaw University of Technology,

Nowowiejska 15/19, Warsaw, Poland

e-mail: mslomczy@elka.pw.edu.pl, bswid@ise.pw.edu.pl

Abstract—*Fractal dimension as a parameter describing the structure of an object seems useful in medical images processing [5]. We examine X-ray images of lungs. For that case, a special algorithm is designed and the value of fractal dimension is calculated. Its certain values allow one to suspect pathology.*

I. INTRODUCTION

Before the development of fractal geometry, complex biological structures have only been described in terms of idealized Euclidean geometry models. The results used to occur incomplete because the true complexity of the subject could not be modelled properly. The fractal geometry proves more effective when complex or irregular natural shapes are concerned. Application of this geometry is necessary because self-similarity can often be observed in natural objects, as the structure of many plants or animal organs may witness (e.g., the branched structure of blood vessels in lungs). Thus, it is reasonable to treat images as fractal structures and calculate their fractal dimensions [8]. Fractal dimension is one of the most important parameters describing fractals, as well as natural objects. Artificial, man-made objects have integer dimensions, while natural ones are characterized by non-integer (fractional) dimension. It turns out to be a good measure of how rapidly the texture changes. The more rapid the changes, the higher the fractal dimension.

There are a variety of different definitions of dimension: topological dimension, Hausdorff dimension, box dimension, correlation dimension, and others [1],[9]. The box counting method is the most popular fractal dimension method. It is used mainly for binary images. For our purpose, the exact value of fractal dimension is not crucial. What is really important is the monotonic behavior of the algorithm in the whole range of values that can be achieved.

Until now, research has been focused on application of fractal analysis to medical cases, such as trabecular

bones [4], retinal vessels [7][2], renal arteries, mammographic patterns, EEG, ECG signals [3].

This paper presents some results of fractal analysis supporting the diagnosis of X-ray images of lungs. We have analyzed 8-bit greyscale images in various resolutions.

II. FRACTAL DIMENSION METHODS

A. Numerical problems

There are some numerical problems common for all algorithms. They are connected with reliability of results and efficiency of the applied methods.

- We have tested efficiency and accuracy of the numerical methods in the following way. Basing on two-dimensional Weierstrass-Mandelbrot functions, we have constructed surfaces whose dimension had been assumed before. 1D Weierstrass-Mandelbrot functions are given by the formula:

$$W_H(t) = \sum_{i=0}^M \lambda^{-iH} \cos(2\pi\lambda^i t), \quad 0 < H < 1 \quad (1)$$

where $\lambda = 5$, $M = 26$. The fractal dimension is equal to $d = 2 - H$.

- Practically, fractal dimension can only be roughly estimated in finite range of scales. It is confusing that different methods vary in results they give. Fortunately, for all tested algorithms the higher theoretical fractal dimension is, the higher numerical value is obtained. We have only been interested in segmentation of the image into parts with the same fractal dimension, so the exact value of the local fractal dimension has been unimportant.

We had also to solve other problems:

- Noise sensitivity for some types of noise, e.g., salt and pepper, so the filtering methods are recommended at the very beginning, otherwise we can obtain the fractal dimension of a noise, not of the proper image.
- Proper size of analyzed blocks.
- Normalization of the data.
- Influence of the finite resolution of real data on the accuracy of results.

All fractal dimension algorithms use the linear regression method to compute the closest line parameters. Fractal dimension is obtained from the slope of the line. The method must be applied carefully because the results are always obtained but sometimes they are senseless. It is connected with the fact that the plot can be nonlinear. It means that the object is not self-similar in the tested range, so it is not a fractal. Calculation of the variance of data points from the linear regression line is recommended. The large value of the variance weakens the results.

B. Box counting method

The box counting method is the most popular fractal dimension method. It is mainly used for binary images.

Def. For $F \subset R^n$, let $N_\varepsilon(F)$ denote the smallest number of squares with the side ε that can cover F . The box dimension d of the set F is given by the formula:

$$d = \lim_{\varepsilon \rightarrow 0} \frac{N_\varepsilon(F)}{-\log \varepsilon} \quad (2)$$

if the above limit exists. Unfortunately, the algorithm based on (2) in its simplest version is inefficient due to slow and very often non-monotone convergence.

The method has many parameters to be optimized; for example, we must choice:

- proper minimum and maximum sizes of mesh squares,
- an orientation and emplacement of the mesh over the image.

The wrong choice of one of these parameters may rapidly decrease accuracy of the results. It is recommended to convert grey-scale images into binary images, so we must define a binary threshold. Of course, for different threshold values the results differ. In some algorithms squares are divided into three groups: squares with only black points, those with only white, and those with white and black points.

C. Epsilon Blanket method

This method can be applied for digitized signals and grey-scale images. We will present the method for a 2D image G . Let us assign a grey level value $g(i, j)$ to the pixel (i, j) . The measurement scales into x and y directions are identical, the scale unit being a pixel. We perform iterative calculations to get two blanket surfaces $u_n(i, j)$ — the upper one, and $b_n(i, j)$ — the bottom one.

- At the beginning, we set

$$u_0(i, j) = b_0(i, j) = g(i, j) \quad (3)$$

- In the n th step we obtain:

$$u_n(i, j) = \max[u_{n-1}(i, j) + 1, \max_{\|(m,l)-(i,j)\|_1} u_{n-1}(m, l)] \quad (4)$$

$$b_n(i, j) = \min[b_{n-1}(i, j) - 1, \min_{\|(m,l)-(i,j)\|_1} b_{n-1}(m, l)] \quad (5)$$

- Then the volume of the blanket is evaluated

$$v_n = \sum_{i,j} (u_n(i, j) - b_n(i, j)) \quad (6)$$

- The surface area is finally computed from

$$A(n) = \frac{v_n - v_{n-1}}{2} \quad (7)$$

- It can be shown that the value of A depends on fractal dimension $A(n) = cn^{2-d}$
- Finally, we apply the linear regression method to the plot of $\log(A(n))$ versus $\log(n)$.

The main features of the algorithm are the following:

- the algorithm is relatively fast;
- the successive iterations are connected with changes in resolutions;
- sometimes the value of d lies outside the proper interval $[2, 3]$, it occurs for objects with non-fractal structure;
- the maximal proper number n of the iterations strictly depends on the range of the data;
- we can notice that after a finite number of iterations, the value A is constant: the blanket is too thick.

III. MEDICAL DATA

Chest X-ray is the most commonly performed diagnostic X-ray examination. Approximately half of all X-rays obtained in medical institutions are chest images. They are used for lungs, heart, and chest wall diagnosis purpose. Pneumonia, heart failure, emphysema, lung cancer and other medical cases are customarily discovered on the bases of such images.

This paper presents some results of fractal analysis supporting the diagnosis of X-ray images of lungs. We have analyzed 8-bit greyscale images in various resolutions. We examine 2 diseases: tuberculosis and cancer.

IV. DESCRIPTION OF THE DISEASES

A. Tuberculosis (TB)

The chest X-ray is useful for TB diagnosis because about 85% of TB patients have pulmonary TB. Usually, patients with TB in the lungs have abnormal chest

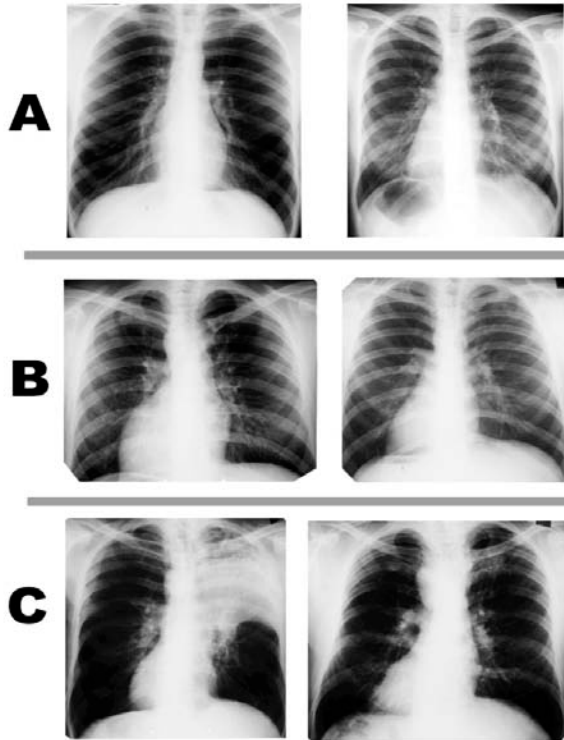


Fig. 1. A — X-ray of healthy chests, B — X-ray of chests with tuberculosis, C — X-ray of chests with cancer

X-rays (Fig.1B). It may reveal infiltrates (collections of fluid and cells in the tissues of the lung) or cavities (hollow spaces within the lung that may contain many tubercle bacilli).

B. Cancer

Cancer of a lung is the most common malignant tumour. When the patient is suspected to suffer from that, usually X-ray photography of their chest is made first. In the image, the light areas that appear as subtle branches extending from the center into the lungs are cancerous (Fig.1C).

V. FRACTAL ANALYSIS

The analysis consists of two steps. In the first step, local fractal dimension is calculated and the output images are subject to further analysis. In the second step the global fractal dimension is obtained.

A. Step I — local fractal dimension

- The image is divided into square blocks. For each block, the value of the local fractal dimension is calculated using blanket method [1].
- Fractal dimension values from the interval [2, 3] are transformed into grey-scale values from the interval

[0, 255]. The greater fractal dimension is, the brighter colour is assigned.

In this way, we obtain what can be called “dimension image” — an image where the colour of each pixel is calculated basing on the local fractal dimension of its surrounding, i.e., the block. The algorithm makes changes of texture in the original image more visible (Fig.2).

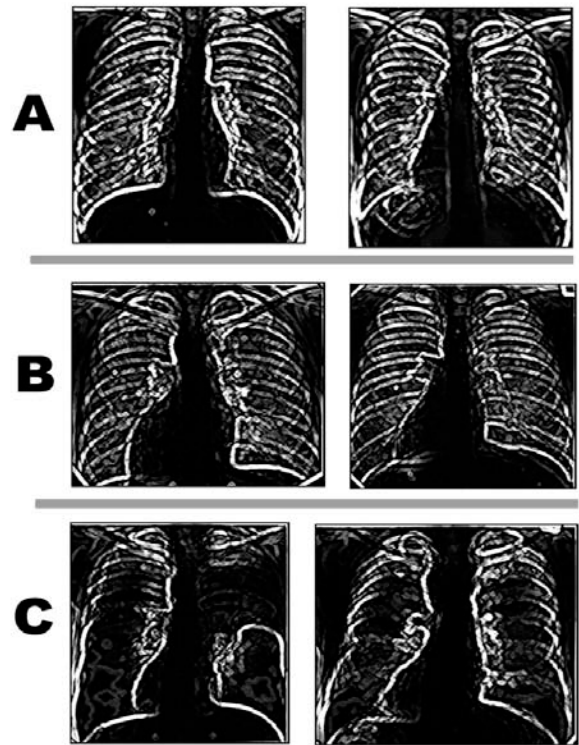


Fig. 2. Dimension images

B. Step II — global fractal dimension algorithm

In step II, the box counting method [1], recommended for binary images, is applied.

- Dimension images are transformed into 256 1-bit images with the threshold method (Fig.3). The threshold values are from the interval [0, 255].
- The box counting method is applied to the images and fractal dimension is calculated.

In Fig.4, black and gray lines correspond to healthy lungs, blue and green lines are obtained for cancer, while red and violet lines — tuberculosis.

VI. CONCLUSIONS

- Fractal dimension analysis of medical images may support diagnosis of pathological changes.
- The results of fractal dimension calculation require interpretation. Pathologies are suggested by abnormal

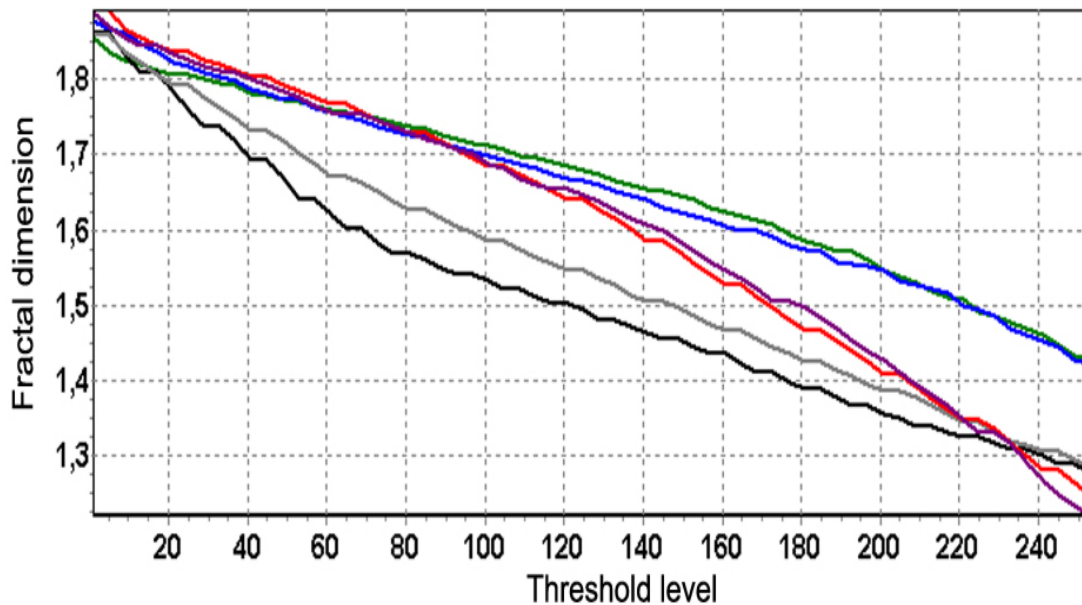


Fig. 4. Fractal dimension — function of threshold level for chest images

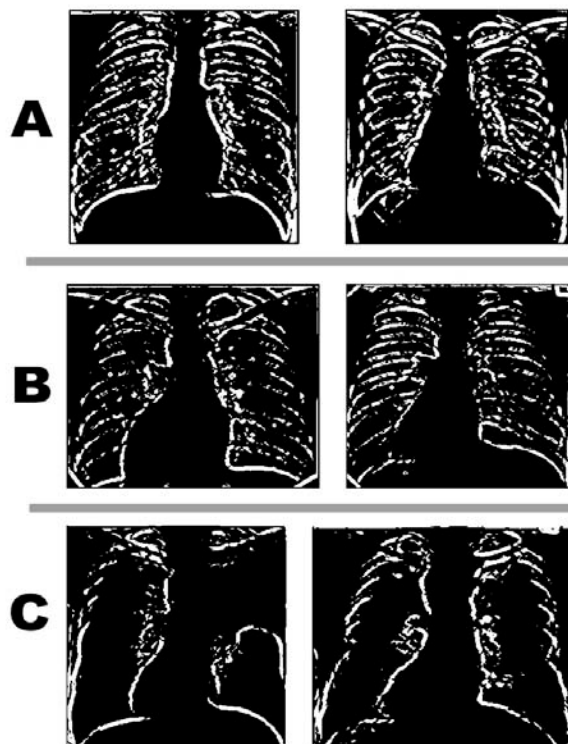


Fig. 3. Threshold images

values of fractal dimension.

- Automatic fractal-based analysis is capable of recognizing features that are beyond the range of human-eye perception.

At present, further developments of the methods are under way, as well as research on other medical cases.

REFERENCES

- [1] R. Esteller: "A Comparison of Waveform Fractal Dimension Algorithms", IEEE Transactions on CAS, vol. 48, No.2, Febr. pp. 177-183, 2001.
- [2] M.H. Słomczyński, B. Świdzińska: "Fractal-Adided Analysis of Eyeground Images", Proc. of ECCTD Conference, 12-15.9.2003, Krakow.
- [3] M.H. Słomczyński, B. Świdzińska: "Application of fractals in monitoring of the electrocardiogram", Proc. of NDES'03, pp. 249-252, Scuol, Switzerland, 2003.
- [4] M.H. Słomczyński, B. Świdzińska: "Application of fractal analysis in diagnosing medical images", Proc. of Czech-Hungarian-Polish Workshop, pp. 112-117, Warsaw.
- [5] H.M. Hastings, G. Sugihara: "Fractals — A user's guide for the natural sciences", Oxford Science Publications, 1993.
- [6] G.A. Losa, D. Merlini, E.R. Weibel, T.F. Nonnenmacher [eds.]: "Fractals in Biology and Medicine", vol. 2. Birkhauser, 1998: pp. 326-334.
- [7] M.A. Mainster: "The Fractal Properties of Retinal Vessels: Embryological and Clinical Implications", Eye, 1990, vol. 4, pp. 235-241.
- [8] B.B. Mandelbrot: The Fractal Geometry of Nature, Freeman, 1982.
- [9] B. Świdzińska: "Fractal Dimension Algorithms — a Critical Study", Proc. of Polish-Czech-Hungarian Workskop on CAS, 12-15.9.2002, Warsaw.

Sympatric speciation in an age-structured population living on a lattice

A.O. Sousa,

Institute for Computer Applications 1 (ICA1), University of Stuttgart,
Pfaffenwaldring 27, 70569 Stuttgart, Germany
email: sousa@ica1.uni-stuttgart.de

Abstract—*A square lattice is introduced into the Penna model for biological aging in order to study the evolution of diploid sexual populations under certain conditions when one single locus in the individual's genome is considered as identifier of species. The simulation results show, after several generations, the flourishing and coexistence of two separate species in the same environment, i.e., one original species splits up into two on the same territory (sympatric speciation). As well, the mortalities obtained are in a good agreement with the Gompertz law of exponential increase of mortality with age.*

I. INTRODUCTION

The understanding of species formation - groups of actually or potentially inter-breeding populations, which are reproductively isolated from other such groups - is still a fundamental problem in biology [1]. Speciation usually occurs when a pre-existing population is divided into two or more smaller populations by a geographical barrier, like an island, river, isolated valley, or mountain range. Once reproductively isolated by the barrier, the gene pools in the two populations can diverge due to natural selection, genetic drift, or gene flow, and if they sufficiently diverge, then the inter-breeding between the populations will not occur if the barrier is removed. As a result, new species have been formed.

In spite of theoretical difficulties to show convincingly how speciation might occur without physical separation [2], there is an increasing evidence for the process of sympatric speciation, in which the origin of two or more species from a single ancestral one occurs without geographical isolation [3]. The most straightforward scenario for sympatric speciation requires disruptive selection favoring two substantially different phenotypes, followed by the elimination of all intermediate phenotypes. In sexual populations, the stumbling block preventing sympatric speciation is that mating between divergent ecotypes constantly scrambles gene combinations, creating organisms with intermediate phenotypes. However, this mixing can be prevented if there is assortative [4] in-

stead of random mating, i.e., mating of individuals that are phenotypically similar. It can be based on ecologically important traits such as body size (as in stickle-backs) [5] or on marker traits that co-vary with ecological traits (such as coloration or breeding behavior in cichlids)[6].

The present paper reports on an attempt to address the challenging problem of sympatric speciation using the widespread Penna bit-string model [7], [8] for age-structured populations, which is based on the mutation accumulation theory for biological aging. It has successfully reproduced many different characteristics of living species, as the catastrophic senescence of pacific salmon [9], the inheritance of longevity [10] and the evolutionary advantages of sexual reproduction [11], as well as a particular case of sympatric speciation [12].

II. THE MODEL

Each individual of the population is represented by a "chronological genome", which consists of two bit-strings of 32 bits (32 loci or positions) each, that are read in parallel. One string contains the genetic information inherited from the mother and the other, from the father. Each position of the bit-strings is associated to a period of the individual's life, which means that each individual can live at most for 32 periods ("years"). Each step of the simulation corresponds to reading one new position of all individuals' genomes. Genetic defects are represented by bits 1. If an individual has two bits 1 at the i -th position of both bit-strings (homozygote), it will start to suffer the effects of a genetic disease at its i -th year of life. If the individual is homozygous with two bits zero, no disease appears in that age. If the individual is heterozygous in that position, it will become sick only if that locus is one for which the harmful allele is dominant. The dominant loci are randomly chosen at the beginning of the simulation and remain fixed. If the current number of accumulated diseases reaches a threshold T , the individual dies.

If a female succeeds in surviving until the minimum reproduction age R , it generates b offspring every year

until death. The female randomly chooses a male to mate, the age of which must also be greater or equal to R . The offspring's genome is constructed from the parent's ones; first the strings of the mother are randomly crossed, and a female gamete is produced. M_m deleterious mutations are then randomly introduced. The same process occurs with the father's genome (with M_f mutations), and the union of the two remaining gametes form the new genome. This procedure is repeated for each of the b offspring. The sex of the baby is randomly chosen, each one with probability 50%.

The description given above corresponds to the original sexual version of the Penna model [13], in which at every time step each individual of the population, independently of its age or current number of accumulated diseases, can be killed with a probability $V_t = 1 - N_t/N_{\max}$; N_{\max} is the maximum population size (the carrying capacity of the environment) and N_t is the current population size. This random time-dependent death, well known as the Verhulst factor, is introduced in order to avoid the unlimited growth of the population and to take into account the dispute for food and space. Since there seems to be no biological justification for considering random deaths in real populations, as well as a controversial importance of its role in the Penna model [14], in our simulations we do not consider random deaths. Instead, we adopt a simple lattice dynamics which also avoids the exponential increase of the population. The details will be presented in the next subsection.

A. Speciation model on a lattice

In the present case each individual lives on a given site (i, j) of a square lattice and, at every time-step, has a probability p_w to move to the neighboring site that presents the smallest occupation, if this occupation is also smaller or equal to that of the current individual's site. We start the simulations randomly distributing one individual per site on a diluted square lattice. That is, if an already occupied site is chosen for a new individual, the choice is disregarded and another random site is picked out.

At any bit position a diploid individual can have $n = 0, 1$ or 2 bits set. The process of sympatric speciation is now attempted by defining one single bit position, which we take as position 11, as an identifier of the species. Mating occurs only among individuals of the same species (same value of n at position 11), which means that this locus also defines the mating preferences. Each able female (with age $\geq R$) with

n such bits randomly selects a neighboring able male with the same n value to breed. If she succeeds, she generates b offspring. Then she chooses at random, again among its four neighboring sites, a place to put each baby, according to the rules below. The newborn dies if it is not possible to find a site respecting these rules:

- 1) the selected site occupation must be ≤ 1 ;
- 2) If the newborn has $n = 0$, then it can occupy an empty site or a site already occupied by a single individual with $n = 2$;
- 3) If the newborn has $n = 2$, then it can occupy an empty site or a site already occupied by a single individual with $n = 0$;
- 4) If the newborn has $n = 1$, it can occupy only an empty site.

Rules 2 and 3 mean that the $n = 0$ and the $n = 2$ populations can share the same habitat, that is, they do not dispute for the same food resources. Rule 4 means that the $n = 1$ population feeds at both niches, competing with the other two. These rules replace the random killing Verhulst factor pointed out in the previous section.

We start our simulations only with $n = 0$ individuals. Due to the randomness of mutations and crossover, the offspring does not necessarily have the same n value of the parents. In our model it is exactly this randomness which allows the emergence of new species out of the original one. These populations co-exist in a stable equilibrium but without cross-mating.

III. SIMULATION RESULTS

The simulation starts with N_0 individuals, half males and half females, and runs for a pre-specified number of time steps, at the end of which averages are taken over the population(s). The general parameters of the simulations are:

- Minimum age of reproduction $R = 8$;
- Birth rate $b = 3$;
- Mutation rate $M = 1$ per bit-string (or gamete);
- Maximum number of genetic diseases $T = 5$;
- Probability to walk $p_w = 1.0$.

Fig. 1 shows how the new species N_2 emerges, within about a hundred iterations, from the original species N_0 . The intermediate population N_1 is only about 0.50% of the total population. Since the rule for an individual to move on the lattice depends only on the existence of a site with an occupation smaller or equal to that of the current individual's site and is completely non-related to the individual species, the different species may bunch together at

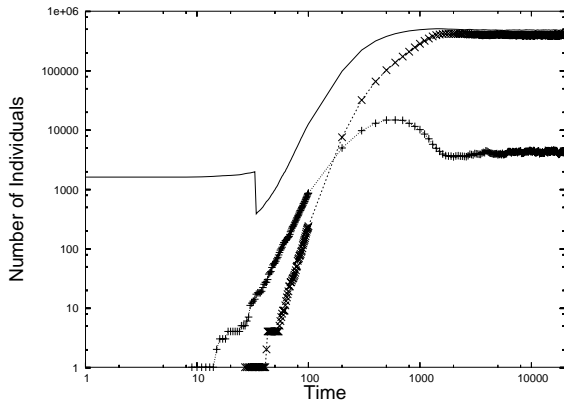


Fig. 1. Time evolution of N_0 (line, original species), N_1 (+, mixed genomes) and N_2 (x, new species), for one diploid sexual population simulated on a $L \times L$ square lattice with $L = 800$ and $N_o = 1600$ individuals.

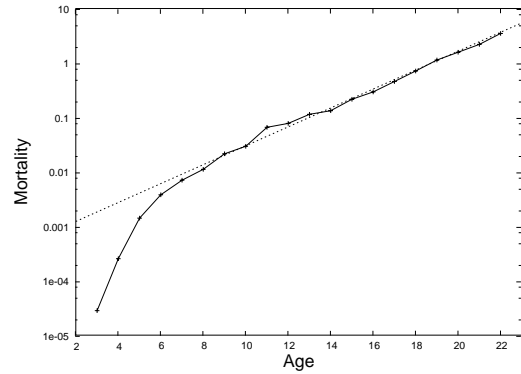


Fig. 2. Mortality as a function of age averaged over 20 diploid sexual populations simulated on a square lattice with $L = 200$ and $N_o = 800$ individuals. The dashed line corresponds to the fit $q(\text{age}) = 0.00055 \exp(0.4 * \text{age})$ in this semilogarithmic plot.

the same site of the lattice. Then, due to the reproduction rules quoted above, after several generations we obtain a great predominance of the two non-competing species N_0 and N_2 living at the same geographic position (sympatric speciation). Our results with $N_o = 1600$ are confirmed by larger simulations with $N_o = 100000$, and also by larger simulations with 10^6 time steps.

It must be remarked that the assumptions we make concerning mating choice and conditions for a newborn to survive were adopted in order to capture some features of field observations and laboratory experiments of species which seems to speciate via disruptive selection on habitat/food preferences and assortative mating.

For instance, in a series of papers Rice and Salt [15] presented experimental evidence for the possibility of sympatric speciation in *Drosophila melanogaster*. They started from the premise that whenever organisms sort themselves into the environment first and then mate locally, individuals with the same habitat preferences will necessarily mate assortatively. Others examples of sympatric speciation can be found for canids [16], lizards [17] and pandas [18]. In this latter example, the Giant Panda (*Ailuropoda melanoleuca*) and the Red Panda (*Ailurus fulgens*) are vegetarian carnivores that specialize in eating bamboo in Sichuan Province, China. The two species share the same habitats and bamboo plants. Both pandas feed on the same species of bamboo, but specialize in eating different parts of the bamboo plant. The Giant Panda feeds more frequently on bamboo stems, while the Red Panda feeds more frequently on bamboo leaves [18]. In our simulation, disruptive selection explicitly

arises from competition for a single resource (a potentially more common ecological situation). In this way, we may imagine, for instance, that the original population $n = 0$ is vegetarian, and the second population $n = 2$ emerging out of it consists of carnivore (thus, there is no competition between the two different populations). However, since the individuals with $n = 1$ feed from the same resources of both populations ($n = 0$ and $n = 2$), this competition for food reduces its abundance in the system and, combined with assortative mating, leads to evolutionary branching.

The situation that better fits our simulations occurs in the Australian Fogg Dam Nature Reserve, where data have been collected [19] from three different snake species: water pythons (*Liasis fuscus*, *Pythonidae*), keelbacks (*Tropidonophis mairii*, *Colubridae*) and slatey-grey snakes (*Stegonotus cucullatus*, *Colubridae*). All are non-venous, oviparous and active foragers, but they differ considerably in body sizes and dietary habits. Water pythons feed almost exclusively on a single species of native rodent; keelbacks feed primarily on frogs and slatey-grey snakes have extremely broad diets (reptile eggs, frogs, small mammals and lizards). According to Ref.[19], the population of slatey-grey snakes is smaller than the other two during the whole year. Particularly from April to May (when neither the rats nor the frogs are in their peaks of abundance), the water python and the keelbacks populations are almost of the same size while the slatey-grey snakes population size is around 1/7 of this value.

As a final study, we examine our populations mortalities. In 1825, based on observed death and population records of people in England, Sweden, and

France between ages 20 and 60 in the nineteenth century, the British actuary Benjamin Gompertz derived a simple formula describing the exponential increase in death rates between sexual maturity and extreme old ages [20]. This formula, $q(\text{age}) = a \times \exp(b \times \text{age})$, is commonly referred to as the Gompertz's law of mortality. As Fig. 2 shows, our results for the mortality above the minimum reproduction age $R = 8$, are in a good agreement with the Gompertz law.

In conclusion, the results presented here are based on a very simple assumption that a single locus in the individual's genome identifies its species. Despite this simplicity, they clearly show the emergence of sympatric speciation in diploid sexual age-structured populations of individuals that are distributed on a square lattice. The non-random mating depends on the number of alleles 1 at this single locus and the probability to find a place for a newborn is related to the competition between the species for food resources. The results also present a good agreement with the Gompertz law of mortality.

I would like to thank Dietrich Stauffer and S. Moss de Oliveira for very important discussions and a critical reading of the manuscript. This work was supported by a grant from Alexander von Humboldt Foundation.

REFERENCES

[1] A.S. Kondrashov and M. Shpak, Proc. R. Soc. Lond. B **265**, 2273 (1998); A.S. Kondrashov and F.A. Kondrashov, Nature **400**, 351 (1999); U. Dieckmann and M. Doebeli, Nature **400**, 354 (1999); G.S. van Doorn, A.J. Noest and P. Hogeweg, Proc. R. Soc. Lond. B **265**, 1915 (1998).

[2] E. Mayr, *Animal Species and Evolution* (Harvard Univ. Press, Harvard, 1963).

[3] T. Tregenza and R.K. Butlin, Nature **400**, 311 (1999).

[4] M. Kirkpatrick, Nature **408**, 298 (2000).

[5] H.D. Rundle, L. Nagel, J.W. Boughman and D. Schluter, Science, **287**, 306 (2000).

[6] A.B. Wilson, K. Noack-Kunmann and A. Meyer, Proc. R. Soc. Lond. B **267**, 2133 (2000).

[7] T.J.P. Penna, J. Stat. Phys. **78**, 1629 (1995).

[8] J.B. Coe, Y. Mao and M.E. Cates, Phys. Rev. Lett. **89**, 288103 (2002); J.B. Coe and Y. Mao, Phys. Rev. E **67**, 061909 (2003).

[9] T.J.P. Penna, S.M. de Oliveira and D. Stauffer, Phys. Rev. E **52**, R3309 (1995).

[10] P.M.C. de Oliveira, S. Moss de Oliveira, A.T. Bernardes, D. Stauffer, Lancet **352**, 911 (1998).

[11] A.O. Sousa, S. Moss de Oliveira and J.S. Sa Martins, Phys. Rev. E **67** 032903 (2003); J.S. Sa Martins, Phys. Rev. E **61** 2212 (2000).

[12] J.S. Sa Martins, S. Moss de Oliveira, G.A. de Medeiros, Phys. Rev. E **64**, 021906 (2001); K. Luz-Burgoa, S. Moss de Oliveira, J.S. Sa Martins, D. Stauffer and A.O. Sousa, Braz. J. Phys. **33**, 1 (2003).

[13] S. Moss de Oliveira, P.M.C. de Oliveira and D. Stauffer,

Evolution, Money, War and Computers (Teubner, Leipzig and Stuttgart, 1999).

[14] S. Cebrat, Physica A **273**, 169 (1999); J.S. Sa Martins and S. Cebrat, Theor. Biosc. **119**, 156 (2000).

[15] W.R. Rice, Evolution **39**, 645 (1985); W.R. Rice and G. W. Salt, American Naturalist. **129**, 911 (1988); W.R. Rice and G. W. Salt, Evolution **44**, 1140 (1990).

[16] B.L. Cypher, Trans. Illinois State Acad. Science **86** 3, 139 (1999); R.K. Wayne, B. Van Valkenburgh, P.W. Kat, T.K. Fuller, W.E. Johnson and S.J. O'Brien, J. Heredity **80**, 447 (1989).

[17] E.R. Pianka *Evolutionary Ecology* (Addison-Wesley-Longman, San Francisco, 2000); E.R. Pianka and L.J. Vitt, *Lizards: Windows to the Evolution of Diversity* (University of California Press, California, 2003).

[18] F. Wei, Z. Feng, Z. Wang and J. Hu (2000), J. Mammalogy **81**, 448 (2000); F. Wei, Z. Feng and M. Li, Mammalia **63**, 417 (1999); K.G. Johnson, G.B. Schaller and J. Hu, J. Mammalogy **69**, 552 (1988).

[19] G.P. Brown, R. Shine and T. Madsen, J. of Tropical Ecology **18**, 549 (2002).

[20] B. Gompertz, Philos. Trans.R. Soc. London **110**, 214 (1825); B. Gompertz, Journal of the Institute of Actuaries **16**, 329 (1872).

Complexity measures for nonlinear electronic systems: Comment on the Shiner-Davison-Landsberg measure

R. Stoop^{1,3}, N. Stoop^{2,3}, A. Kern¹ and W.-H. Steeb³

¹ Institute of Neuroinformatics, Swiss Federal Institute of Technology Zürich

² Physics Department, Swiss Federal Institute of Technology Zürich

³ International School of Scientific Computing, Johannesburg, South Africa

e-mail: ruedi@ini.phys.ethz.ch

WWW: <http://www.stoop.net/group>

Abstract— *The complexity measure from Shiner et al.[1] (henceforth abbreviated as SDL-measure) has recently been the subject of a fierce debate. We discuss the properties and shortcomings of this measure, from the point of view of our recently constructed fundamental, statistical mechanics-based measures of complexity $C_s(\gamma, \beta)$ [2]. We show explicitly, what the shortcomings of the SDL-measure are: It is over-universal, and the implemented temperature dependence is trivial. We, however, also show, how the original SDL-approach can be modified to rule out these points of critique. Results of this modification are shown for the logistic parabola.*

I. INTRODUCTION

The question of complexity measures has continually attracted interest over the last decade, from the theoretical and the experimental points of view [1-21]. The Kolmogorov/Solomonoff algorithmic complexity [3,4,18] has been the most influential concept of complexity. The algorithmic complexity A of an object s expressed in terms of bits, is defined as the length of the shortest program P (in bits) that produces (prints) the object s

$$A(s) = \min_{C,P:C(P)=s} \log(\text{length}(P)), \quad (1)$$

where C is a computer. As there exists a universal computer, called the Turing machine, which is able to simulate any other computer, $A(s)$ is a well-defined quantity.

The problem with this measure is that it violates basic conceptions of complexity. For example, random sequences are assigned the maximal complexity. However, computer-generated random sequences are generally the result of a simple random generator, which, obviously, has a finite algorithmic complexity. Moreover, using an intrinsic notion of complexity, truly random sequences appear no more complex than any pseudo-random sequences, even though the latter have a much shorter description length. In fact,

finding the shortest description length isn't that easy, as there are at least infinitely many programs to be checked. In particular, the product of the algorithmic complexity and the difficulty of finding the right program can be considered an approximation to the perceived, human, notion of complexity. Contrasting a plot of a two-dimensional embedded (pseudo-)random generator output against the output of the two-dimensional circle-standard map, illustrates the dilemma [8]: Whereas the random output is dull and void of structure, the output of the standard map appears as "interesting" and "complex". The reason for this inappropriateness as a natural perception of complexity, can be traced to the fact that the algorithmic complexity has been devised as a measure of the complexity of objects generated by computers, or computer programs. In this context, the world appears to be rational (in the sense of rational numbers), allowing only a countable number of states to be distinguished. The real world as, e.g. generated by analog electronic circuits, however, is based upon real numbers (even when rational numbers are measured), as is any biological or physical system. The reason for this, is that Gödel's Theorem [23] requires small digits in the measurements, due to coupling to the rest of the world, to be unpredictable *per se* (and not as a consequence of chaos theory). Therefore, the need to properly define measures of complexity for natural and physical systems emerges.

II. THE SDL-MEASURE OF COMPLEXITY

One recent approach to define complexity therefore builds on the requirement that the measure should be zero for truly random, as well as completely ordered, objects. Moreover, this complexity measure should be easy to evaluate; it should, in particular, not require hierarchical decomposition of the system. Starting from this position, Shiner, Davison and Landsberg

[1] defined their complexity measure as

$$\Gamma_{\alpha,\beta} = \Delta^\alpha(1 - \Delta)^\beta, \quad (2)$$

where $\Delta = S/S_{max}$, with S being the Boltzmann-Gibbs-Shannon-entropy. They have interpreted Δ as the disorder, and $(1 - \Delta)$ as the order in the system. The rescaling by S_{max} maps measured order / disorder into the unit interval. However, the SDL-measure, as has been pointed out by several authors [21,22], has some important shortcomings. To elucidate the origin of these, and to point out ways to correct them, is the main content of our contribution.

III. A RECENT THERMODYNAMIC-FORMALISM BASED MEASURE OF COMPLEXITY

In order to achieve this, we contrast SDL with our previously proposed measure of complexity [2]. The latter is probably the most general statistical mechanics approach to complexity. For an observer-dependent variable ε , the fluctuation entropy spectrum $S(\varepsilon)$ is derived, using the thermodynamic formalism of dynamical systems [12]. This is achieved by a Legendre transform, applied to the free energy associated with the natural partition sum induced by the temporal evolution of the system. In more detail, the thermodynamic formalism departs from a partition function $Z(n, \beta, \nu)$, where n is the level or depth of the partition and β can be viewed as an inverse temperature. With $Z(n, \beta, \nu)$, a free energy

$$F(\beta) = \lim_{n \rightarrow \infty} \frac{1}{n} \log(Z(n, \beta, \nu)) \quad (3)$$

is associated, where in $F(\beta)$ we suppressed the dependence on the observable. β can be interpreted as an artificial temperature (that has no absolute zero, though). In the absence of phase transitions, an entropy function is obtained by means of the Legendre transform

$$S(\nu) = \nu\beta - F(\beta). \quad (4)$$

Requirements that apply to entropy functions are strict convexity with infinite derivatives at the two end-points of the curve (in the absence of phase transition effects). From the large deviation entropy $S(\varepsilon)$, the complexity measure (for details see [2]) is calculated as

$$C_s(\gamma, \beta) = \varepsilon_0^{2\beta} \frac{\varepsilon_1}{\varepsilon_1 - \kappa} \int_{Supp(\tilde{S})} (\tilde{S}(\tilde{\varepsilon})/\tilde{\varepsilon})^\gamma d\tilde{\varepsilon}. \quad (5)$$

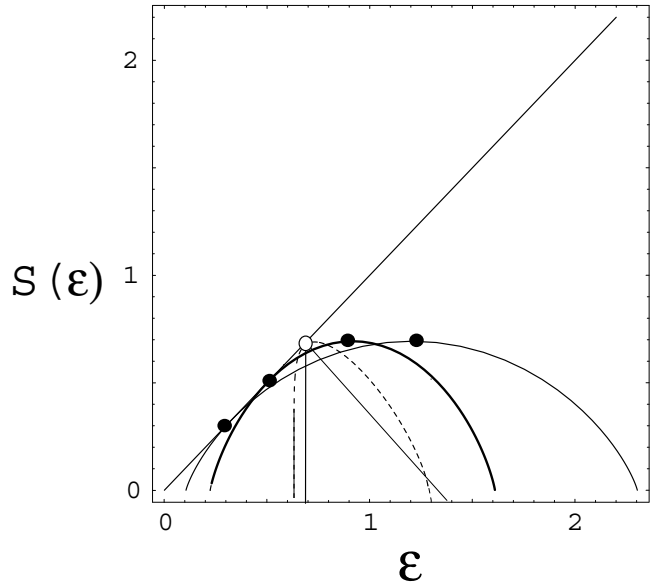


Fig. 1. Fluctuation spectrum of different maps and specific entropy measures S_I and S_{max} , respectively. Thick full lines, filled dots: Convex entropy functions $S(\varepsilon)$ obtained for two asymmetric tent maps of varying asymmetry. Dashed line, open dot: Numerical approximation of $S(\varepsilon)$ obtained for the fully developed parabola (partition level $n = 12$), which slowly converges towards the triangular function (thin full lines). In this case, S_I and S_{max} coincide. In the presence of first order phase transitions, piecewise linear parts of the graph emerge, as is demonstrated by the parabola.

Here, κ denotes a potential escape rate (which is nonzero only for repellors). The fluctuation spectrum generally has the convex form shown in Fig. 1 for the asymmetric tent maps. In the presence of first-order phase transitions, straight-line parts emerge, as is shown by the example of the fully developed parabola. For the measure, the graph of $S(\varepsilon)$ vs. ε has been rescaled by extracting the topological length scale ε_0 on both axes, which is indicated by the tildes applied to S and ε , respectively, see (5).

In the context of the fluctuation entropy spectrum $S(\varepsilon)$, the SDL-complexity measure obtains a simple interpretation: S in their formula corresponds to the observable measure S_I in the fluctuation spectrum, defined by $S_I(\varepsilon) = \varepsilon$, whereas S_{max} corresponds to the topological entropy (the maximum of $S(\varepsilon)$). Their quantity is therefore proportional to the product of $S_I(S_{max} - S_I)$. Geometrically, this measure therefore amounts to the grey area of Fig. 2.

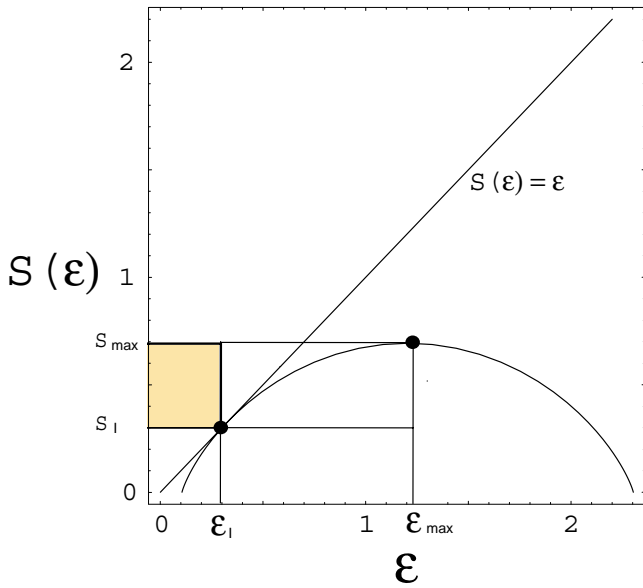


Fig. 2. Geometric meaning of the SDL-complexity measure: The hatched area has the size of $S_I(S_{max} - S_I)$. For the fully developed parabola (see Fig. 1), area zero would be obtained.

IV. PROPERTIES OF THE SDL-MEASURE

By construction, the SDL-measure has the following obvious properties:

- The SDL-measure only depends on two particularly significant points of the fluctuation spectrum: The natural measure S_I and the topological measure S_{max} (the latter sometimes also referred to as the balanced measure). As such, the remaining shape of the fluctuation spectrum $S(\epsilon)$ does not influence the SDL-measure. This leads to an over-universality in the following sense: Dynamical systems that have entirely different properties may be attributed identical complexities. This feature is most dramatically illustrated by hyperbolic maps vs. maps displaying phase-transition phenomena, in particular intermittent maps, that can be made to have identical values of S_I and S_{max} , and hence complexity. Obviously, however, the intermittent maps are much more difficult to predict than hyperbolic ones, yet they are mapped on the identical family of complexity measures $\Gamma_{\alpha,\beta}$. Statistical averaging in terms of the exponents α, β does not add new information if applied to these two points. Therefore, the detailed behavior of the system is not recovered by this approach. Instead, the information contained in the two points of the spectrum is diluted over the infinite real axis.
- For the actual computation, mixing of measures

should be avoided and well-defined measures should be used. This implies that in the application of the complexity calculation for the logistic map $x_{n+1} = ax_n(1 - x_n)$, natural partitions should be used.

- Using the natural partition, zero complexity is obtained, irrespective of the fact that the entropy function extends to the r.h.s. We suspect that the nonzero SDL-complexity $\Gamma_{1,1}$ obtained for the parabola at $a = 4$ is due to the lack of asymptoticity.

V. MODIFICATION OF THE SDL-MEASURE

To obtain measures based on the order-disorder approach originally considered, we propose to remove from the SDL-measure the trivial temperature dependence. This can be achieved in the following way. First, the Stoop-complexity integrand

$$(\tilde{S}(\tilde{\epsilon})/\tilde{\epsilon})^\gamma \tag{6}$$

may be viewed as being related to complexities based upon the product integrand

$$(1 - S(\epsilon)/\epsilon)^\alpha (S(\epsilon)/\epsilon)^\beta. \tag{7}$$

We therefore propose to instead consider an over all possible length scales integrated variant of their measure. The result of this calculation for the logistic map is shown in Fig. 3 for $\alpha = \beta = 1$. Note, however, that for this measure, intermittent length scales do not contribute, something that we would prefer to avoid. As a more promising generalization of our measure, we propose to consider independent exponentiation to the denominator of the integrand instead.

VI. RESULTS

This modification removes the over-universality criticized. A comparison of the SDL-complexity with the one obtained in the proposed way clearly elucidates notable differences between the two results (compare the results shown in Fig. 3 with Fig. 3 of Shiner et al.[1]): Whereas for the first complexity measure we obtain an overall monotonously decreasing function, this is no longer the case with our measure. Moreover, the scaling yielding a nonzero complexity for completely ordered systems (period-doubling cascade cases or period-3 window) look suspicious to us. The results obtained by our computation seem to fit much better the requirements asked for in the definition of a measure of complexity: that it should be zero when either the system is completely ordered or random.

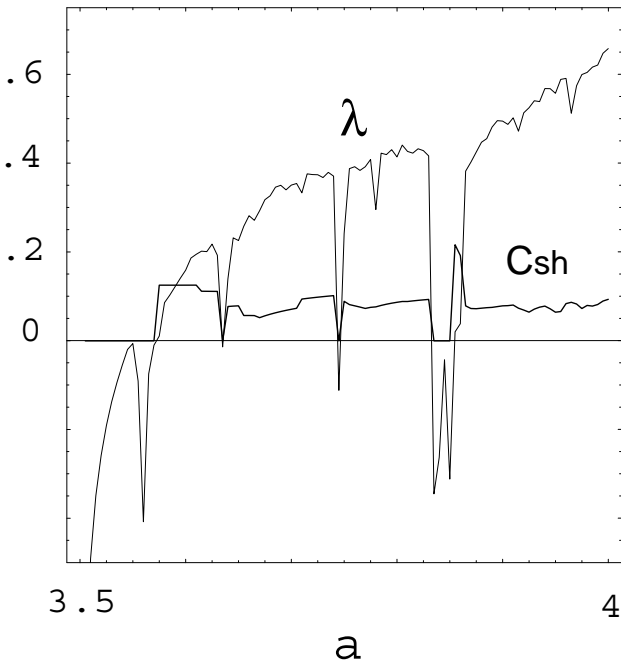


Fig. 3. Modified SDL-complexity C_{sh} and Lyapunov exponent λ for the logistic map, as a function of the order parameter a .

VII. CONCLUSIONS

In this way, the SDL-measure can be modified to invalidate the most pertinent critiques. The non-trivial temperature dependence will remove the over-universality. In particular, the requirements by Binder and Perry [22], that at least some classes of systems known from hierarchical analysis should be discernible, is satisfied: Different dynamical systems will have distinct complexity measure families. In the comment by Crutchfield, Feldmann and Shalizi [21], the authors criticized that any measure of complexity must be tied intrinsically to a process. In our modification, this is now indeed the case. Starting from the fundamental observations of complexity based upon order and disorder, we have arrived at a measure that is no longer subject to the most pertinent critiques, and whose construction is entirely transparent. However, it remains to be seen whether a deeper significance can be attributed to the integrand of Eq. (7), and, connected to this question, how useful the measure could be for practical applications.

R.S. acknowledges original discussions with J.S. Shiner that triggered this work. The work was partially supported by the SNF.

REFERENCES

[1] J.S. Shiner, M. Davison, and P.T. Landsberg. *Phys. Rev. E* **59**, 1459, 1999.
 [2] R. Stoop, N. Stoop, and L.A. Bunimovich. *J. Stat. Phys.* **114**, 1127, 2004.
 [3] C.E. Shannon. *Bell Syst. Tech. J.*, **27**, 379, 1948.
 [4] R.J. Solomonoff. *Rep. ZTB-138*, ZATOR Co., Cambridge, Mass, 1960.
 [5] A.N. Kolmogorov. *Probl. Inf. Theory* **1**, 3, 1965.
 [6] G. Chaitin *J. ACM*, **13**, 547, 1966.
 [7] A. Lempel and J. Ziv. *IEEE Trans. Inf. Theory* **IT-22**, 75 (1976).
 [8] P. Grassberger. *Int. J. Theor. Phys.* **25**, 907, 1986.
 [9] S. Lloyd and H. Pagels. *Ann. Phys. (N.Y.)* **188**, 186, 1988.
 [10] C.H. Bennett. In: *Complexity, Entropy and the Physics of Information*, W.H. Zurek ed. Addison-Wesley, Reading MA, 1990.
 [11] D.W. McShea. *Biol. Philos.* **6**, 303, 1991.
 [12] J. Peinke, J. Parisi, O.E. Roessler, and R. Stoop. *Encounter with Chaos*. Springer, Berlin, 1992.
 [13] J.E. Bates and H.K. Shepard. *Phys. Lett. A* **172**, 416, 1993.
 [14] H. Atmanspacher. *J. Consciousness Studies* **1**, 168, 1994.
 [15] R. Wackerbauer, A. Witt, H. Atmanspacher, J. Kurths, and H. Scheingraber. *Chaos, Solitons and Fractals* **4**, 133, 1994.
 [16] H. Atmanspacher, C. Rth, and G. Wiedemann. *Physica A* **234**, 819, 1997.
 [17] W.-H. Steeb, F. Solms, T.K. Shi and R. Stoop. *Phys. Scr.* **55**, 520, 1997.
 [18] M. Li and P. Vitányi. *An Introduction to Kolmogorov Complexity and its Applications*. Springer, Berlin (1997).
 [19] J.P. Crutchfield and C.R. Shalizi. *Phys. Rev. E* **59**, 275, 1998.
 [20] P.T. Landsberg and J.S. Shiner. *Phys. Lett. A* **245**, 228, 1998.
 [21] J.P. Crutchfield, D.P. Feldman, C.R. Shalizi. *Phys. Rev. E* **62**, 2996, 2000.
 [22] P.-M. Binder and N. Perry. *Phys. Rev. E* **62**, 2998, 2000.
 [23] K. Gödel. In: *Philosophy of Mathematics*, P. Benacerraf and H. Putnam eds. Prentice-Hall, Englewood Cliffs, New Jersey, 1964.

VHF AND UHF CHAOTIC COLPITTS OSCILLATORS

A. Tamaševičius¹, G. Mykolaitis¹, S. Bumeliene¹, A. Baziliauskas², R. Krivickas² and E. Lindberg³

¹ Semiconductor Physics Institute,
A. Goštauto 11, Vilnius, LT-2600, Lithuania
e-mail: tamasev@pfi.lt

WWW:http://www.pfi.lt/index_e

² Department of Signal Processing,
Faculty of Telecommunications and Electronics,
Kaunas University of Technology,
Studentų 50, Kaunas, LT-3031, Lithuania
e-mail: Antanas.Baziliauskas@stud.ktu.lt

WWW:http://www.ktu.lt/en/

³ Ørsted•DTU Department,
348 Technical University of Denmark,
Ørsted's Plads, Kgs. Lyngby, DK-2800, Denmark
e-mail: el@oersted.dtu.dk

WWW:http://www.es.oersted.dtu.dk/~el/

Abstract—*PSpice simulation and experimental results demonstrating chaotic performance of the Colpitts oscillator in the very high frequency (30 to 300 MHz) and the ultrahigh frequency (300 to 1000 MHz) ranges are reported. Period-doubling route to chaos has been detected experimentally confirming dynamical origin of chaotic oscillations.*

I. INTRODUCTION

The classical Colpitts oscillator has been originally designed to generate periodic waveforms. Meanwhile with special sets of the circuit parameters it can exhibit chaotic behaviour as well. The first experiment on chaos in the Colpitts oscillator was carried out at the kHz frequencies [1]. Later the oscillator was investigated in the high frequency (HF: 3 to 30 MHz) range and chaos was demonstrated at the fundamental frequency $f^*=23$ MHz using the 2N2222A [2] also at $f^*=26$ MHz using the 2N3904 [3] bipolar junction transistors (both with approximately the same threshold frequency f_T of 300 MHz). By means of the PSpice simulations chaos was predicted at $f^*=500$ MHz using the Avantek transistor AT41486 with f_T of 3 GHz [2] and at $f^*=1000$ MHz employing the BFG520 with f_T of 9 GHz [3,4]. However these results were not confirmed experimentally as yet.

In this paper we describe chaotic Colpitts oscillator operating in the very high frequency (VHF: 30 to 300 MHz) and the ultrahigh frequency (UHF: 300 to 1000 MHz) ranges.

II. CIRCUITRY

A specific implementation of the Colpitts oscillator is presented in Fig. 1. The Q1-based stage is the intrinsic Colpitts oscillator while the Q2-based one is an emitter follower. The resonance tank combines the inductor L, two series capacitors C1, C2, and the loss resistor R. The C3 is a coupling capacitor. The DC supply voltages and the AC signals are separated by means of the chokes L0 and the blocking capacitors C0. The bias emitter current I_{e0} can be tuned by varying the voltage source V2. The output load is 50 Ω.

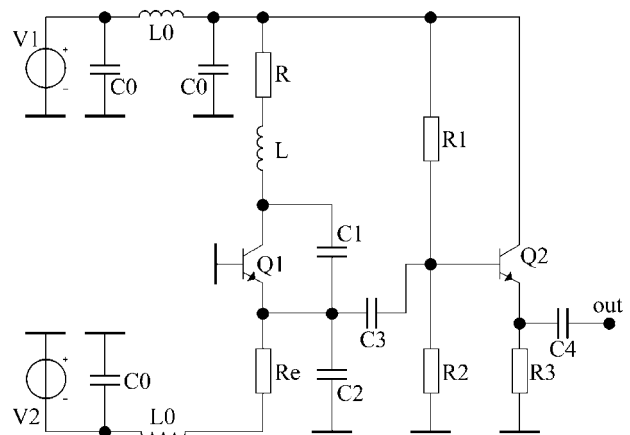


Fig. 1. Circuit diagram of the chaotic Colpitts oscillator.

The values of the tank elements L , C_1 , C_2 depend on the chosen fundamental frequency $2\pi f^* = 1/\sqrt{LC}$, ($C=C_1C_2/(C_1+C_2)$) and are discussed in Section III.

Other circuit elements were the following: $C_3=1$ pF, $C_4=270$ pF, $R_1=5.1$ k Ω , $R_2=3$ k Ω , $R_3=200$ Ω , $R_e=510$ Ω , $L_0=10$ μ H, $C_0=47$ nH. To improve the filtering performance of the L0-C0 networks small additional capacitors of 300 pF were connected in parallel to the main filter capacitors C0. The microwave transistors BFG520 with f_T of 9 GHz were employed in the circuit (Q1 and Q2). All the circuit elements are small-size surface mount devices (SMD). The V_1 was varied from 8 to 9 volts and the V_2 was tuned from 0 to 13 volts (thus the bias current I_{e0} was varied from 0 to 24 mA).

III. SIMULATION RESULTS

Simulations of the circuit in Fig.1 were performed by means of the Electronics Workbench Professional simulator, based on the PSpice software. The Gummel-Poon model of the transistors was employed.

A. Parameters

The values of the tank elements depending on the fundamental frequency f^* are listed in Table 1. Experience shows [1-4] that the loss resistance R should be approximately half of the characteristic tank resistance, $R \approx 0.5 \rho = \sqrt{L/C}$. The specific values of the loss resistor R as well as the supply voltages V_1 and V_2 (thereby I_{e0}) were adjusted empirically to achieve the most complicated behaviour the oscillators (see Table 2). In Table 1 the total inductance L consists of: (1) the inductance L_{ext} controlled by an external SMD inductive element; (2) the parasitic inductance of the loss resistor L_R ; and (3) the parasitic inductance L_{C0} of the filter capacitor C0. So, $L=L_{ext}+L_R+L_{C0}$. The two latter parasitic values are approx. 2 nH each.

Table 1. Tank parameters.

Case	f^* , MHz	L_{ext} , nH	L , nH	C_1/C_2 , pF	C , pF	ρ , Ω
1	500	12	16	10/10	5	56.6
2.1	1000	4	8	5.1/5.1	2.5	56.6
2.2	1000	12	16	2.4/2.4	1.2	115
2.3	1000	—	4	10/10	5	28.3
2.4	2000	12	16	—*/10	0.4	200

*) Parasitic collector-emitter capacitance $C_{CE} \approx 0.35$ pF.

Table 2. Adjustable parameters and results.

Case	f^* , MHz	V_1 , V	I_{e0} , mA	R , Ω	Result
1a	500	8	5.5	27	Period-2, Fig. 2
1b	500	8	20	27	Chaos, Fig. 2,3
2.1a	1000	8	20	27	Period-2, Fig. 4
2.1b	1000	15	20	27	Chaos, Fig. 4
2.2	1000	8	20	56	Period-1, Fig. 5
2.3	1000	8	20	13	Period-4, Fig. 5
2.4a	1600	8	19	78	Period-1, Fig. 6
2.4b	1100	8	19	78/x	Chaos, Fig. 6,7

x) The base of the transistor is grounded via a circuit consisting of a small wiring inductance of 3 nH coupled in series with a wiring loss resistance of 5 Ω .

B. "Pure" cases

At relatively "low" frequencies ($f^*=500$ MHz) chaos can be easily generated at higher bias current I_{e0} of 20 mA (Fig. 2, right and Fig. 3).

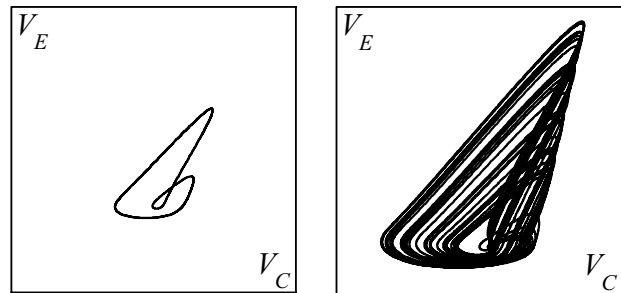


Fig. 2. Simulated phase portraits, emitter voltage V_E versus collector voltage V_C . $f^*=500$ MHz, case 1a, $I_{e0}=5.5$ mA (left), case 1b, $I_{e0}=20$ mA (right).

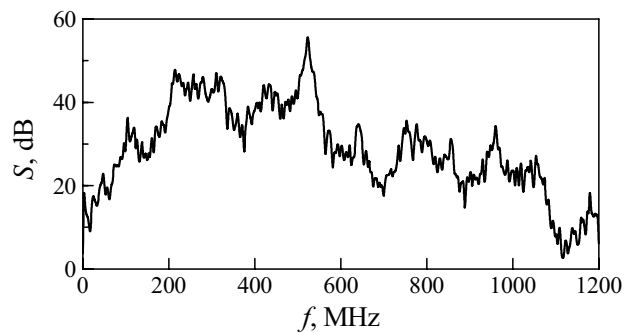


Fig. 3. Simulated power spectrum, case 1b.

To increase the f^* , say by a factor of 2, there are several possibilities to change the tank values: (1) to decrease the both values L and C proportionally (case 2.1); (2) to keep the same value of L and to lower the C by a factor of 4 (case 2.2); (3) to lower L by a factor of 4, but to keep the same C (case 2.3).

In case 2.1 at $V_1=8\text{ V}$ (Fig. 4, left) the most complicated oscillations like period-2 ones are observed. Formally, by increasing the supply voltage V_1 up to 15 V [4] chaos can occur (Fig. 4, right), apparently due to the decrease of the collector-base capacitance. However, this is an impractical supply condition, since 15 V is close to the limiting value for the BFG520 type transistor.

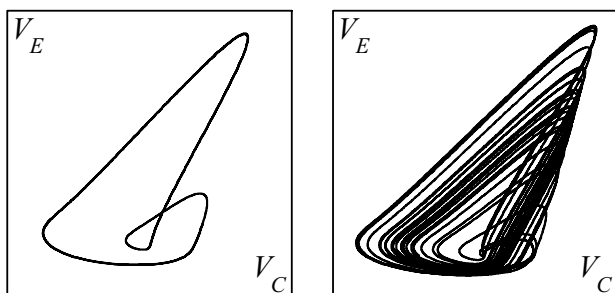


Fig. 4. Simulated phase portraits, emitter voltage V_E versus collector voltage V_C . $f^*=1000\text{ MHz}$, case 2.1a, $V_1=8\text{ V}$ (left), case 2.1b, $V_1=15\text{ V}$ (right).

In case 2.2 with small capacitances of 2.4 pF in the tank only simple period-1 oscillations can be observed (Fig. 5, left). The reason is that at low values of C_1 and C_2 the stronger is the damping influence of the junction capacitances C_{CB} and C_{EB} [3]. Somewhat better result can be obtained in case 2.3 with larger capacitances of 10 pF and lower inductance $L=4\text{ nH}$ (the external inductive element is removed). However, the most complicated oscillations observed in this case are the period-4 ones (Fig. 5, right), i.e. there are no chaotic oscillations. Most probably this is caused by the fact that at low values of L the characteristic resistance of the tank is also low ($\rho=28\ \Omega$). Consequently, the effective loop gain parameter defined as $a=\rho/r$ [3] (here r is the small signal differential resistance of the forward biased emitter-base junction) is insufficient for chaotic oscillations.

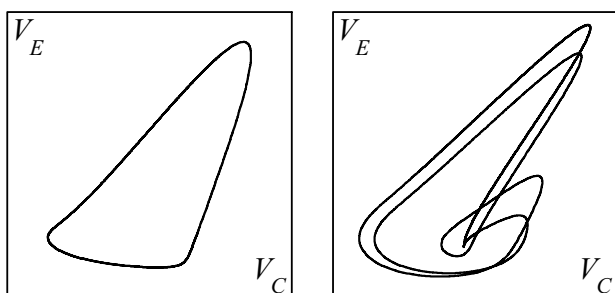


Fig. 5. Simulated phase portraits, emitter voltage V_E versus collector voltage V_C . $f^*=1000\text{ MHz}$, case 2.2, small C (left), case 2.3, small L (right).

C. "Parasitic" cases

Another way to increase the f^* considerably is to remove one of the tank capacitors, say C_1 , and let play the role of the feedback capacitance the C_{CE} (case 2.4). However, the straightforward result is similar to case 2.2 when only simple period-1 oscillations are observed (compare Fig. 5, left and Fig. 6, left).

Along with the parasitic capacitance C_{CE} some other mounting/wiring parasitic elements should be taken into account. For example, nonideal grounding of the base of the transistor should be considered. Indeed, simulations show that even small wiring inductance from the base to ground and small loss resistance appearing due to the skin effect can play an important role, thus giving rise to chaos (Fig. 6, right and Fig. 7). The experimental results presented in Section IV confirm existence of chaos in a circuit with a removed capacitor C_1 .

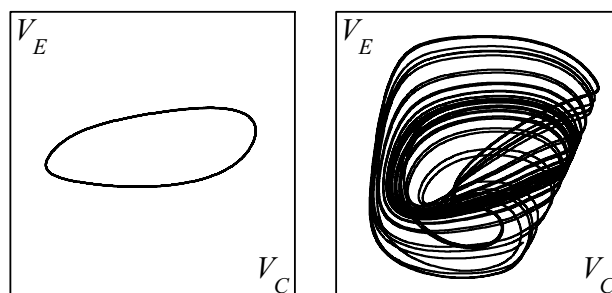


Fig. 6. Simulated phase portraits, emitter voltage V_E versus collector voltage V_C , case 2.4a (left), case 2.4b (right).

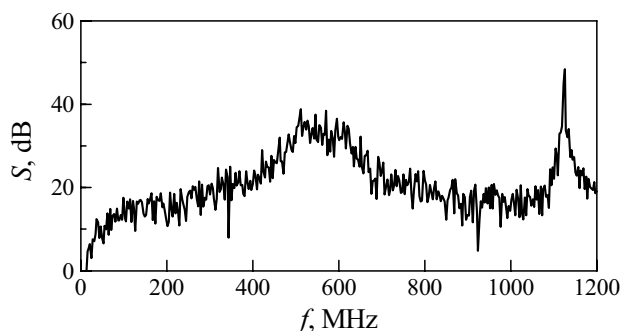


Fig. 7. Simulated power spectrum, case 2.4b.

IV. EXPERIMENTAL RESULTS

A. Bifurcations

The evolution of the output signals with the increase of the emitter bias current I_{e0} is illustrated with the one-dimensional bifurcation diagram in

Fig. 8. The steady state (s) becomes unstable and simple periodic oscillations (period-1) appear in the interval 1.5 to 3.5 mA. With the further increase of I_{e0} the oscillator undergoes the period-doubling bifurcations (period-2, period-4, up to period-32) eventually resulting in chaotic oscillations at approximately 10 mA. This route to chaos is a universal scenario observed in a variety of nonlinear dynamical systems. Meanwhile in the chaotic domain (ch) narrow periodic windows are observed, e.g. period-5 and period-9 ones.

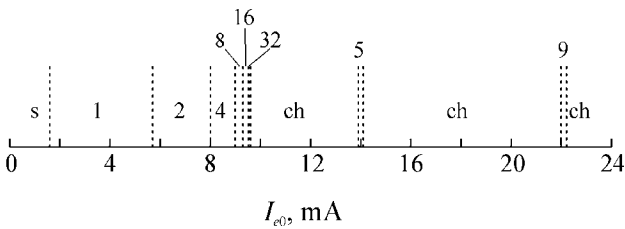


Fig. 8. Bifurcation diagram.
 $C_1=C_2=10$ pF, $R=26$ Ω , $V_1=8.0$ V.

B. Spectra

To characterize the chaotic oscillations the power spectra taken at different fundamental frequencies f^* are presented in Figs. 9,10. In the case of $f^*\approx 1000$ MHz (Fig. 10) the capacitor C_1 is simply removed from the circuit. Thus the parasitic capacitance C_{CE} plays its role. Both spectra taken with spectral resolution of 120 kHz are broadband continuous ones with typical peaks at the fundamental frequency f^* and with local rises at the subharmonics $f^*/2$ (in some cases also at $f^*/4$, $3f^*/4$ and $5f^*/4$). The power spectrum in Fig. 9 covers within the unevenness of approximately 20 dB the VHF range, while the power spectrum in Fig. 10 covers the UHF range.

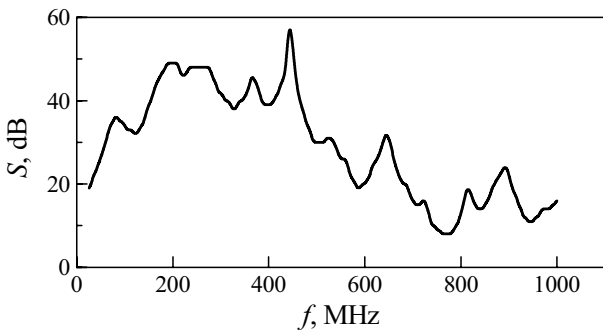


Fig. 9. Experimental power spectrum.
 $C_1=C_2=10$ pF, $R=26$ Ω , $V_1=8.0$ V, $I_{e0}=20$ mA.

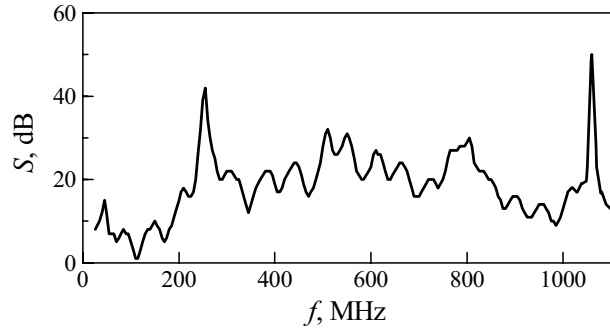


Fig. 10. Experimental power spectrum.
 $C_1=0.4$ pF, $C_2=10$ pF, $R=39$ Ω , $V_1=8.7$ V, $I_{e0}=21$ mA.

V. CONCLUSION

The classical Colpitts oscillator has been demonstrated to generate chaos in the VHF and the UHF ranges both by means of PSpice simulations and experimentally.

ACKNOWLEDGMENT

Part of this work was carried out at University College Dublin and supported by the European Commission under a Marie Curie Fellowship (A. B.).

REFERENCES

- [1] M. P. Kennedy. Chaos in the Colpitts oscillator. *IEEE Trans. Circuits Syst. I*, vol. 41, No. 11, pp. 771-774 (1994).
- [2] C. Wegener and M. P. Kennedy. RF chaotic Colpitts oscillator. In *Proc. NDES'95*, pp. 255-258, Dublin, Ireland, 1995.
- [3] G. Mykolaitis, A. Tamaševičius, S. Bumelienė, G. Lasienė, A. Čenys, A. N. Anagnostopoulos, and E. Lindberg. Towards microwave chaos with two-stage Colpitts oscillator. In *Proc. NDES'2001*, pp. 97-100, Delft, The Netherlands, 2001.
- [4] Tamaševičius, G. Mykolaitis, S. Bumelienė, A. Čenys, A. N. Anagnostopoulos, and E. Lindberg. Two-stage chaotic Colpitts oscillator. *Electron. Lett.*, vol. 37, No. 9, pp. 549-551 (2001).

VARIABILITY OF INTERBURST INTERVALS IN 2D SLOW-FAST MAPS FOR NEURAL RESPONSES

Gouhei Tanaka[†] and Kazuyuki Aihara[‡]

[†] Dept. of Complexity Science and Engineering, University of Tokyo, Tokyo, Japan

[‡] Institute of Industrial Science, University of Tokyo, Tokyo, Japan

e-mail: {gouhei, aihara}@sat.t.u-tokyo.ac.jp

Abstract— *The present paper studies a configuration of 2D slow-fast maps replicating neural bursting activity. We primarily focus on deterministic aspects of the model, where the relation of bifurcations between the fast subsystem and the total system is explained. Secondary a specific family of bursting maps is proposed in order to investigate irregular interburst intervals. Using the notion of relative size of the escape interval, we clarify a cause of the variability of the interval length in the deterministic model.*

I. INTRODUCTION

Statistics of the interspike intervals for spiking neurons (or interburst intervals for bursting neurons) are important for comprehension of the information coding of the biological neural networks [1, 2]. The high variability of responses exhibited by neurons has been pointed out [3] and a number of models have been produced to explain its mechanism [4, 5]. The irregular timing of successive action potentials have been often described stochastically with Poisson processes. On the other hand, the issue has not attracted much attention in the deterministic dynamical neuron models. However, it has not been clarified yet whether the irregular intervals result from the timing variety of the input spikes or the inherent dynamics of the neuron.

Differential equation models exhibiting bursting responses have been intensively studied since the first clarification of slow-fast dynamics in bursting systems by Rinzel [6]. 3D continuous bursting systems have been classified based on the type of bifurcations at the onset and the termination of bursts in fast subsystems [7]. Recently map-based models with analogous slow-fast dynamics have been proposed [8–13]. Classification of bifurcations for emergence and destruction of bursting behavior in the fast subsystem has also been performed [13], though examples for several

types are absent. Most of these studies on map-based models have focused on synchronization of bursts when coupled [8] and bifurcation scenario leading to chaotic bursting behavior [12].

This paper investigates irregular interburst intervals in a family of maps with 2D slow-fast dynamics. First we emphasize deterministic properties of the model in order to understand the role of the fast subsystem. We show that bifurcations of the fast subsystem determine those of the total system. Next proposing a specific family of 2D maps, we examine the mechanism of the irregular bursting behavior in the deterministic model in terms of the relative size of the escape interval. We illustrate changes of the distributions of interburst intervals with variation of one parameter in the proposed model, keeping the minimum interval length which may be regarded as a refractory period.

II. DETERMINISTIC PROPERTIES OF 2D SLOW-FAST MAPS

Let us consider a configuration of 2D slow-fast maps in the form [8]:

$$\begin{aligned} x(t+1) &= f(x(t)) + y(t), \\ y(t+1) &= y(t) - \epsilon(x(t) - \sigma), \end{aligned} \quad (1)$$

where x and y indicate the fast variable representing the membrane potential of the neuron and the slow variable, respectively. The parameter σ denotes the threshold value and the time scale ratio of the two variables, ϵ , is set as a sufficiently small value.

Equation (1), called the total system, is involved in the fast subsystem:

$$x(t+1) = f(x(t)) + p. \quad (2)$$

Here we suppose that the fast subsystem exhibits coexistence of a stable node and a chaotic attracting state in a certain parameter range of p accompanying with a hysteresis. An example of such situation is illustrated in Fig. 1(a). The fixed point

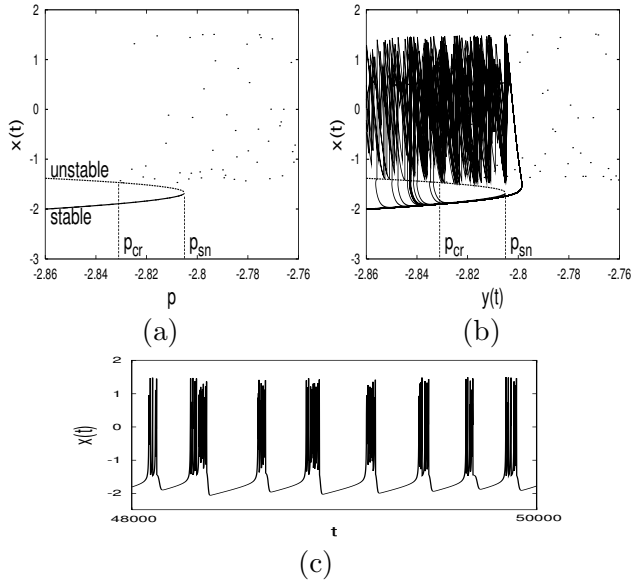


Fig. 1. (a) Attracting states after transition period of the fast subsystem with change of p ($\alpha = 4.3$). The notations p_{cr} and p_{sn} indicate a crisis and a saddle-node bifurcation parameter value, respectively. (b) Trajectory of a bursting response in the total system over the left figure ($\alpha = 4.3$, $\sigma = -1.5$). (c) Corresponding time series.

transits to the chaotic state at the saddle-node bifurcation parameter value $p = p_{sn}$ as p increases, while the chaotic state jumps to the fixed point at the crisis parameter value $p = p_{cr}$ as p decreases.

The function f generating such fast system dynamics enables the total system to exhibit bursting behavior as shown in Fig. 1(b). When $x(t) < \sigma$, the trajectory moves along the stable node of the fast subsystem with increasing $y(t)$ and transits to the bursting state at $y(t) \sim p_{sn}$. Since $y(t)$ decreases if $x(t) > \sigma$, the trajectory moves with decrease of $y(t)$ and finally jumps to the sub-threshold with irregular timing. In Fig. 1(b), the locus of the transition from the chaotic state to the resting state seems to be highly irregular compared with the almost fixed position at the transition to the bursting state. Figure 1(c) shows an example of bursting response. The chaotic fluctuation of the transition points essentially causes the irregularity of interburst intervals as considered in Sec. III. As a result of indefinite iteration of the transition among two states, the bursting behavior continues forever. More detailed analyses of the bursting mechanism through the fast dynamics can be seen in Refs. [8, 10, 11].

Although the total system can often show properties unexpected from the dynamics of the fast

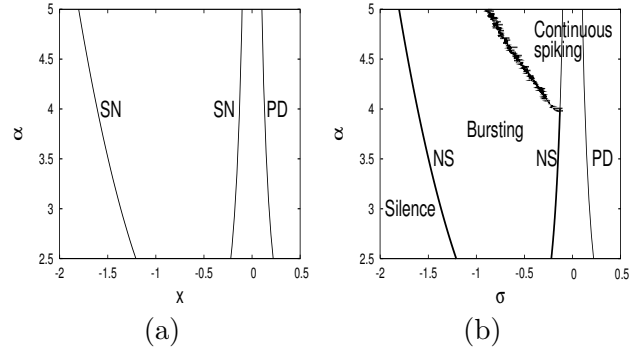


Fig. 2. (a) Bifurcation sets in the fast subsystem. (b) Bifurcation sets in the total system. The Neimark-Sacker bifurcation separates the silence and the bursting region.

subsystem, we can here show that bifurcations of the 1D map are closely related to those of the total system. *If the fast subsystem (2) exhibits a saddle-node bifurcation at $(x, p) = (x_0, p_0)$, then there exists a point $(x, y) = (x_\delta, y_\delta)$ in the neighborhood of the point $(x, y) = (x_0, p_0)$ for any sufficiently small ϵ such that the total system (1) exhibits a Neimark-Sacker bifurcation.* From the assumption,

$$x_0 = f(x_0) + p_0, \quad (3)$$

$$f'(x_0) = 1. \quad (4)$$

Since the fixed point of the total system is given as $(x, y) = (\sigma, \sigma - f(\sigma))$, the Jacobian matrix at the fixed point is described as

$$J = \begin{pmatrix} f'(\sigma) & 1 \\ -\epsilon & 1 \end{pmatrix}, \quad (5)$$

which leads to the characteristic equation:

$$\chi(\mu) = \mu^2 - (f'(\sigma) + 1)\mu + f'(\sigma) + \epsilon = 0.$$

We can take a point $(x, y) = (x_\delta, y_\delta)$ in the neighborhood of (x_0, p_0) such that $f'(\alpha) = 1 - \epsilon$ from Eqs. (3) and (4). Then, the solutions of the characteristic equation are given by a pair of complex conjugate numbers on the unit circle. This means that a Neimark-Sacker bifurcation occurs with $\sigma = x_\delta$, because the bifurcation is not degenerated due to $f'(\sigma) + 1 = 2 - \epsilon \neq 2$.

In the similar way, a period-doubling bifurcation in the fast subsystem implies a period-doubling bifurcation in the total system. We illustrate a corresponding bifurcation sets in both systems with $f(x) = \alpha/(1+x^2)$ in Figs. 2(a) and (b). The Neimark-Sacker bifurcation separates the silence region and the bursting region.

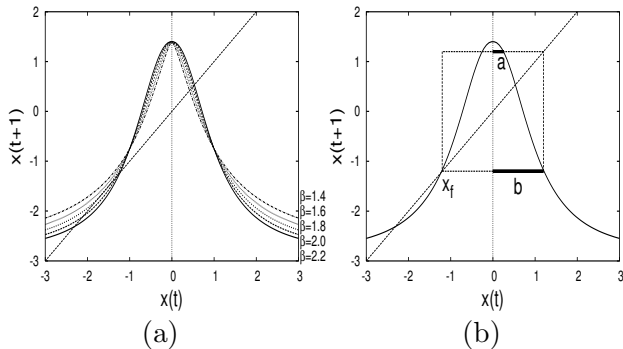


Fig. 3. (a) Return map of the fast subsystem with Eq. (6) for five different values of β ($\alpha = 4.3$, $p = -2.9$). (b) The box size b determined by the unstable node x_f and the escape interval a .

III. IRREGULAR INTERBURST INTERVALS

The two bifurcation points, p_{cr} and p_{sn} , of the fast subsystem are expected to regulate the onset and the termination of the bursts respectively in the total system. In fact, the solution orbit is far from regular motion due to the fluctuation of the transition point from the chaotic state to the sub-threshold state. Thus, in this section, we explore the factors which control the distribution of the irregular interburst intervals.

We use the fast subsystem Eq. (2) and the total system Eq. (1) with the following function:

$$f(x) = \begin{cases} \frac{\alpha}{1+(-x)^\beta} & (x < 0), \\ \frac{\alpha}{1+x^\beta} & (x \geq 0). \end{cases} \quad (6)$$

This function is an even function and takes the maximum value at the origin independent of the value of β . The value of β controls the sharpness of the central peak. The function can be approximated as $f(x) \sim \alpha(1 - x^\beta + x^{2\beta} - \dots)$ near the peak ($x \sim 0$). Thus the peak is more circular for larger β while it is cusp-like for smaller β . When $\beta = 2.0$, this model is equivalent to the map proposed by Rulkov [8]. Examples of the fast subsystem for five different values of β are shown in Fig. 3(a). The bifurcation structure of the fast subsystem with f in Eq. (6) is qualitatively the same as that shown in Fig. 1(a).

Now we assume that a trajectory of the total system exists in the bursting state and $y(t) > p_{cr}$. As the time step goes, $y(t)$ decreases with small variation $\Delta t = \epsilon(x(t) - \sigma)$. When $y(t) > p_{cr}$, the trajectory can not escape from the chaotic state because even the maximum value is mapped into the chaotic region above the unstable node. With further decrease of $y(t)$, a crisis occurs at

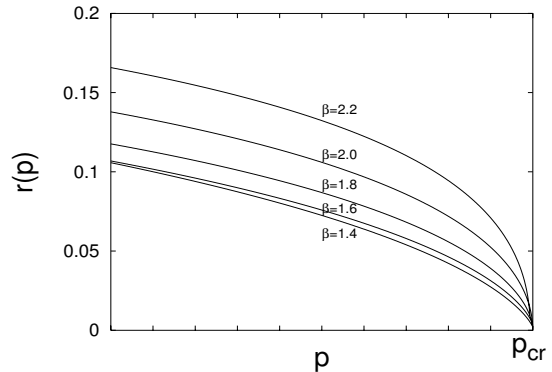


Fig. 4. The relative size of the escape window, $r(p) = a/b$, for the distance from the crisis parameter value p_{cr} .

$y(t) = p_{cr}$. At that time the maximum value is just mapped into the unstable node x_f . Figure 3(b) shows the relation between the second preimage of the unstable node and the peak. That is, it depends on the relation whether the trajectory can escape from the chaotic region or not. When $y(t) < p_{cr}$, the peak is over the box as shown in Fig. 3(b). The relative size of the central interval $[-a, a]$ via which the trajectory can escape for the box size $[-b, b]$ is defined as $r = a/b$.

The probability that a number of uniformly distributed initial points in $[-b, b]$ escape from the chaotic region in the next time is given as r . If r is constant, then the situation is similar to the transient chaos. Therefore, the number of time steps staying in the chaotic region after the crisis corresponds to the mean lifetime staying in the transient chaos. In such static case, if an initial point belongs to the k -th preimages of the escape interval $[-a, a]$, the point remains in the chaotic state for k steps. When a number of initial points are distributed uniformly, the distribution of the mean lifetime is known to be an exponential distribution with the exponent called the escape rate [14].

However, in our case, both of the box size b and the escape interval length a vary with $y(t)$. Thus it is convenient for estimating the relative size r of the escape interval to use the fast subsystem. We numerically calculate r for p . If $p > p_{cr}$, then obviously $r = 0$. Since a and b satisfy the following equations:

$$-b = \frac{\alpha}{1+b^\beta} + p, \quad (7)$$

$$b = \frac{\alpha}{1+a^\beta} + p, \quad (8)$$

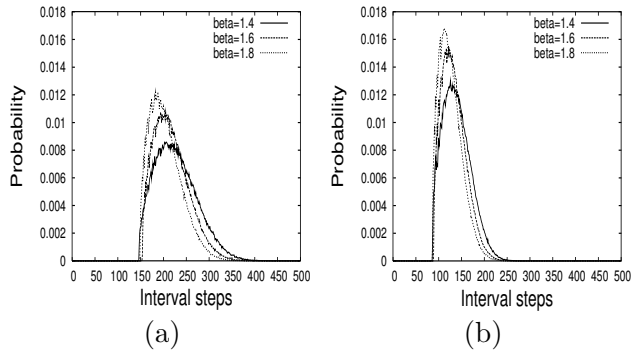


Fig. 5. Histogram of the interburst interval length for $\epsilon = 0.001$ (a) and $\epsilon = 0.002$ (b). In both graphs the distribution changes with the value of β keeping the same minimum interval length.

we obtain

$$r(p) = \left(-\frac{(\alpha + 2p)b^\beta + 2(p + \alpha)}{b^\beta(2pb^\beta + \alpha + 2p)} \right)^{1/\beta}. \quad (9)$$

Therefore, we get the relative size of the escape interval by substituting the numerically computed value of b from Eq. (7) into Eq. (9). As the crisis point is different for different values of β , we illustrate the ratio r for a distance from the crisis point in Fig. 4 for comparison. As the exponent β increases, the differential of $r(p)$ at p_{cr} become larger. This means that the number of time steps until the escape time is shorter for larger value of β . Accordingly the distribution of interburst intervals must reflect the difference of values of β .

Figure 5(a) shows the normalized histogram of the interburst intervals for $\epsilon = 0.001$ and three different β values. We can see that the variance of the distribution increases as the value of β decreases with holding constant minimum interval length. Figure 5(b) shows the same for $\epsilon = 0.002$. Although the minimum length and the average length varies compared with the case of $\epsilon = 0.001$, it is qualitatively invariant how the distribution changes with the value of β .

The distributions are different depending on the relative escape interval size r . Therefore, when the neural bursting behavior is described by the phenomenological model, we can select an appropriate model with the desirable distribution of intervals by adjusting the value of β . On the contrary, ϵ corresponding to the time scale ratio of the fast system and the slow system can be used to control the average of the interval length.

IV. CONCLUSIONS

We have considered a family of 2D slow-fast discrete maps exhibiting neural bursting behavior with irregular interburst intervals. In spite of the deterministic relation between the fast subsystem and the total system, interburst intervals (and burst duration) of the total system are irregular. The notion of relative escape interval size and the comparison with the transient chaos have helped understanding of the unpredictable escape timing from the chaotic attracting state.

REFERENCES

- [1] H. C. Tuckwell. *Introduction to theoretical neurobiology*. Cambridge University Press, 1988.
- [2] P. H. E. Tiesinga and J. V. Jose. Spiking statistics in noisy hippocampal interneurons. *Neurocom p.*, 26-27:299–304, 1999.
- [3] W. R. Softky and C. Koch. The highly irregular firing of cortical cells is inconsistent with temporal integration of random epsps. *J. Neurosci.*, 13(1):334–350, 1993.
- [4] A. N. Burkitt. Interspike interval variability for balanced networks with reversal potentials for large numbers of inputs. *Neurocom p.*, 32-33:313–321, 2000.
- [5] C. Christodoulou and G. Bugmann. Coefficient of variation (cv) vs mean interspike interval (isi) curves: What do they tell us about the brain? *Neurocom puting*, 38-40:1141–1149, 2001.
- [6] J. Rinzel. A formal classification of bursting mechanisms in excitable systems. *Mathematical Topics in Population Biology, Morphogenesis and Neurosciences, Lecture Notes in Biomathematics*, 71 (E. Teramoto and M. Yamaguti, eds., (Springer-Verlag, Berlin)), 1987.
- [7] E. M. Izhikevich. Neural excitability, spiking, and bursting. *Int. J. Bifurcation Chaos Appl. Sci. Eng.*, 10(6):1171–1266, 2000.
- [8] N. F. Rulkov. Regularization of synchronized chaotic bursts. *Phys. Rev. Lett.*, 86(1):183–186, 2001.
- [9] B. Cazelles, M. Courbage, and M. Rabinovich. Anti-phase regularization of coupled chaotic maps modelling bursting neurons. *Europhys. Lett.*, 56(4):504–509, 2001.
- [10] N. F. Rulkov. Modeling of spiking-bursting neural behavior using two-dimensional map. *Phys. Rev. E*, 65:041922, 2002.
- [11] G. de Vries. Bursting as an emergent phenomenon in coupled chaotic maps. *Phys. Rev. E*, 64:051914, 2001.
- [12] A. Shilnikov. Origin of chaos in a two-dimensional map modeling spiking-bursting neural activity. *Int. J. Bifurcation and Chaos*, 13(11):3325–3340, 2003.
- [13] E. M. Izhikevich and F. C. Hoppensteadt. Bursting mappings. *Int. J. Bifurcation and Chaos*, 2004.
- [14] B. Hao. *Experimental study and characterization of chaos*. World Scientific, 1990.

CONTROLLING THE CHAOTIC COLPITTS OSCILLATOR BY ALTERING ITS OSCILLATION ENERGY

V. Tereshko^a, R. Chacón^b and J. Carballar^b

^a School of Computing, University of Paisley, Paisley PA1 2BE, Scotland

^b Departamento de Electrónica e Ingeniería Electromecánica, Escuela de Ingenierías Industriales, Universidad de Extremadura, E-06071 Badajoz, Spain

Abstract—*We further develop the theory of energy-based control of nonlinear oscillators. Controlling the chaotic Colpitts oscillator is considered. The oscillator unstable fixed point and UPOs are stabilized by adjusting the system oscillation energy to levels corresponding to these repellers stable counterparts. The technique does not require knowledge of the system equations and performance of any computation of the control signal, and, hence, can be useful for control and identification of unknown systems.*

I. INTRODUCTION

The chaotic attractors have been observed in several electronic circuits. One of such circuit is the Colpitts oscillator [1–3]. It consists of a bipolar junction transistor (the circuit active nonlinear element) and a resonant L-C circuit. The oscillator is widely used in electronic devices and communication systems.

In this paper, the energy-based control of the chaotic Colpitts oscillator is considered. The technique is based on altering the system oscillation energy [4]. To any type of the system behavior, we put in correspondence the value of the averaged oscillation energy that is an averaged (over the time) compound of the system kinetic and potential energy. The objective is to alter this energy so as to correspond to the desired behavior. This is a general approach that does not depend on particular oscillator equations. Simple feedback depending solely on the output signal is utilized for this purpose. Generally, two strategies of the control are possible. In the first strategy, one simply increases the feedback strength, and, thus, depending on the perturbation phase, increases or decreases the oscillation energy. The strategy does not require knowledge of the system equations and computation of the control signal. It is applicable, hence, for control and identification of unknown systems. In this paper, we follow the above approach. Another strategy is based on goal-oriented control of the desired target when the perturbation strength is calculated for stabilization of an *a priori* chosen orbit.

II. GENERAL APPROACH

Let us consider controlling a general type nonlinear oscillator

$$\ddot{x} + \chi(x, \dot{x}) + \xi(x) = F(t) + g(x, \dot{x}) \quad (1)$$

where $\chi(x, \dot{x})$, $\xi(x)$ and $g(x, \dot{x})$ are dissipative or energy-generating component, restoring force, and control force, respectively. These functions are nonlinear in general case. Also, $\chi(x, \dot{x})$ and $g(x, \dot{x})$ are assumed not contain an additive function of x . $F(t)$ is an external time-dependent driving force.

At $F(t) = 0$ and $g(x, \dot{x}) = 0$, Eq. (1) possesses the equilibriums defined by the equation $\xi(x) = 0$. We assume that at some parameter values, the limit cycle becomes saddle, and a new attractor, say a period-2 cycle, arises. In many well-known example, this scenario leads, through sequence of bifurcations, to the birth of chaotic attractor.

One can define an energy of oscillations as a sum of the “potential” energy and “kinetic” energy

$$E(t) = \int \xi(x) dx + \frac{1}{2} \dot{x}^2 \quad (2)$$

and an averaged over the period T energy

$$\langle E \rangle = \frac{1}{T} \int_0^T \left(\int \xi(x) dx + \frac{1}{2} \dot{x}^2 \right) dt \quad (3)$$

For periodic dynamics T is the oscillation period, and for chaotic one $T \rightarrow \infty$. Each behavior of the oscillator is assigned to the value of the averaged energy (3). If the oscillation amplitude is sufficiently small, the limit cycle oscillations can be approximated as $x \simeq \rho \sin \omega t$, which gives $\langle E \rangle = \frac{1}{2} \rho^2$.

The following control strategy can be proposed. Starting at the lower energy attractor, one stabilizes the higher energy repellers by sequential increasing the averaged oscillation energy. On the contrary, decreasing this energy leads to stabilization of the lower energy repellers.

The change of the energy (2) yields

$$\begin{aligned} \dot{E}(t) &= \xi(x)\dot{x} + \dot{x}\ddot{x} \\ &= (-\chi(x, \dot{x}) + F(t) + g(x, \dot{x}))\dot{x}. \end{aligned} \quad (4)$$

The last term of (4) represents the energy change caused solely by the control. We require that

$$g(x, \dot{x})\dot{x} > 0 \text{ (} < 0 \text{)} \quad (5)$$

for $\forall(x, \dot{x})$. The minimal feedback satisfying (5) is achieved at $g = g(\dot{x})$. Indeed, a simple linear (relative to the velocity) control $g(\dot{x}) \sim \dot{x}$ suffices. However, this type of control as well as nonlinear controls of higher power, say $g(\dot{x}) \sim \dot{x}^3$ can lead to undesirable instabilities in the system. Therefore, the controller dynamics should be described by the bounded functions. In this paper, we consider

$$g(\dot{x}) = kh(\dot{x}) \quad (6)$$

where

$$h(\dot{x}) \begin{cases} > 0 \text{ (} \rightarrow a \text{)}, & \text{if } \dot{x} > 0 \text{ (} \rightarrow \infty \text{)} \\ = 0, & \text{if } \dot{x} = 0 \\ < 0 \text{ (} \rightarrow -a \text{)}, & \text{if } \dot{x} < 0 \text{ (} \rightarrow -\infty \text{)} \end{cases} \quad (7)$$

with $a > 0$ and finite. The $h(\dot{x}) = -h(-\dot{x})$, i.e. it is assumed to be odd. Throughout, we consider $g(\dot{x}) = k \tanh(\beta\dot{x})$ with $0 < \beta \leq \infty$ determining the function slope.

The perturbation (6-7) is specially tuned to control the equilibriums — their positions are not changed by the control as it vanishes at $\dot{x} = 0$. $\dot{E} = 0$ at the equilibriums respectively. The above control does not vanish at the dynamic attractors. Our aim, however, is not stabilization of the UPOs of the unperturbed system existing at given parameter values, but rather shift the system into the region of the desired behavior (say, stable or unstable region if one requires to stabilize or destabilizes the system, respectively). The energy (3) will be changed so as to much the energy of the desired stable orbit or chaotic attractor, respectively.

For small oscillations, one can find their amplitude ρ by substituting $x = \rho \sin \omega t$ to the averaged over the period T energy change and solving the equation

$$\begin{aligned} \langle \dot{E} \rangle &= \frac{1}{T} \int_0^T \dot{E}(t) dt \\ &= \frac{1}{T} \int_0^T (-\chi(x, \dot{x}) + F(t) + g(x, \dot{x}))\dot{x} dt \\ &= 0. \end{aligned} \quad (8)$$

The equation (8) describes a balance of dissipation and supply the energy brought by damping, driving, and control forces. For a general orbit defined by infinite series of periodic modes, the fundamental frequency as well as its harmonics should, in principle, be counted.

In this paper, we simply increase the feedback strength to adjust the oscillation energy to different levels. The above strategy does not require any computation of the control signal and, hence, is applicable for control as well as identification of unknown systems.

Another strategy is based on goal-oriented control of the desired target. It can be applied in cases when the system equations are known or the desired target can be identified (say, UPO extracted from the system time series). The amplitude of system's natural response (i.e. an orbit stable at some parameter values) is derived from the equation

$$\frac{1}{T} \int_0^T (-\chi(x, \dot{x}) + F(t))\dot{x} dt = 0. \quad (9)$$

The equation (9) describes a balance of dissipation and supply of the system intrinsic energy. For free self-sustained oscillations, this balance is supported entirely by the nonlinear damping. To eliminate the natural response distortion imposed by the control, the following condition must be satisfied:

$$\frac{1}{T} \int_0^T (g(x, \dot{x}))\dot{x} dt = 0. \quad (10)$$

For small oscillations, substitution of $g(x, \dot{x}) = k \tanh(\beta\dot{x}) \approx k(\beta\dot{x} - \frac{1}{3}\beta^3\dot{x}^3)$ into (10) yields

$$\beta = \frac{2}{\rho\omega}. \quad (11)$$

The distortion can be minimized, thus, by solely tuning the perturbation shape. If $\rho \ll 1$, β should be sufficiently large so as to preserve the underlying natural response. For an *a priori* chosen small amplitude orbit, find first β from the condition (11) and then, by solving the equation (9), k sufficient for stabilizing this orbit. For an arbitrary amplitude orbit, that generally is a superposition of different periodic modes, one should utilize parameters of the fundamental mode and its harmonics to find β and k .

The control (6-7) does not depend on type of the function $\chi(x, \dot{x})$, $\xi(x)$, and $F(t)$, and, hence, can be applied to linear and nonlinear oscillators, to regular and chaotic dynamics.

The approach can be generalized to the case of coupled oscillator networks [4].

Three-dimensional autonomous dynamical system can be presented in oscillatory form — the oscillator with a dynamically changing feedback. Then, the proposed approach can be applied. Application of the approach to one of such system, the Colpitts oscillator, is considered below.

III. THE COLPITTS OSCILLATOR EXAMPLE

The Colpitts oscillator dynamics can be described by a 3-D autonomous dynamical system [3]:

$$\begin{aligned} \dot{x} &= y - f(x) \\ \dot{y} &= c - x - by - z \\ \varepsilon \dot{z} &= y - d \end{aligned} \quad (12)$$

where the function

$$f(x) = \begin{cases} -a(z + 1), & z < -1, \\ 0, & z \geq -1, \end{cases}$$

the dimensionless variables x and z correspond to circuit's capacitor voltages and the variable y corresponds to circuit's inductor current. a, b, c, d are the dimensionless parameters. This model is equivalent to so-called ideal model of the circuit model [2]. It maintains, however, all essential features exhibited by the real Colpitts oscillator. For $z < -1$, the transistor works in its forward-active region, while for $z \geq -1$, it is cut-off.

Substituting $y = \varepsilon \dot{z} + d$ to the second equation of (13), obtain

$$\begin{aligned} \varepsilon \ddot{z} + \varepsilon b \dot{z} + z &= c - bd - x \\ \dot{x} &= -f(x) + \varepsilon \dot{z} + d \end{aligned} \quad (13)$$

To apply the above approach, one need to add the feedback $g(\dot{x})$ to the first equation of system (13). For the above oscillator, the change of the energy (2) caused by this control yields $\dot{z}g(\dot{z})$. If $g(\dot{z})$ takes the form (6-7), the latter term always provides the increase (decrease) of the oscillation energy for positive (negative) perturbation magnitudes. We, thus, consider $g(\dot{z}) = k \tanh(\beta \dot{z})$. Taking the inverse change of the variables $\dot{z} = \frac{1}{\varepsilon}(y - d)$, obtain the control feedback to be applied to 2-nd equation of the system (13):

$$g(y) = k \tanh\left(\frac{1}{\varepsilon}\beta(y - d)\right). \quad (14)$$

The perturbation (14) is specially tuned to stabilize the fixed point of the system (13). Figure 1 demonstrates

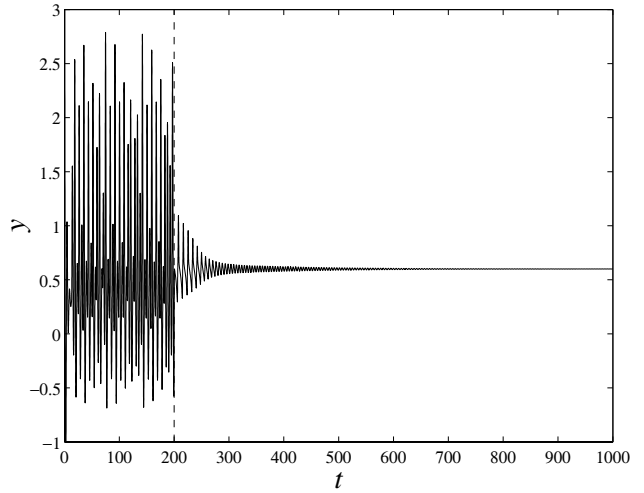


Fig. 1. Dynamics of the state variable y of the oscillator (13) at $\varepsilon = 1, a = 30, b = 0.8, c = 20, d = 0.6, \beta = 10$, and $k = 0 (t < 200); k = -1.6 (t \geq 200)$. Dashed line indicates the time of starting the control.

controlling of this point. k is chosen to be negative, which results in decreasing the averaged oscillation energy. Increasing $|k|$, thus, leads to the oscillation amplitude decrease and, eventually, to suppression of the oscillations.

Note, that stationary point exists only in the forward-active region. Unlike, the (a)periodic orbit trajectories spend most of their times in the cut-off region. Circuit's oscillations are balanced, thus, not around the above stationary point but rather around the total collector voltage equilibrium. The latter is proportional to $x + z$. Let us consider $\varepsilon = 1$ and define $w = x + z$. In the cut-off region, summation of 1-st and 3-rd equations of the system (13) yields $\dot{w} = 2y - d$. Substitution of $y = \frac{1}{2}(\dot{w} + d)$ to 2-nd equation of the system (13) results in the following dynamics of the total collector voltage:

$$\ddot{w} + b\dot{w} + 2w = 2c - bd \quad (15)$$

Applying the perturbation $g(\dot{w})$ satisfying the conditions (6-7) to the oscillator (15) results in the feedback

$$g(y) = k \tanh\left(\beta(y - \frac{d}{2})\right) \quad (16)$$

to be applied to 2-nd equation of the system (13) to control circuit's periodic orbits.

Figures 2 and 3 demonstrate controlling the oscillator periodic orbits. At $k = 0$, the system exhibits chaotic oscillations (Fig. 2(a), grey line). Let us apply the feedback that decreases the oscillation energy. Strengthening its force, one sequentially stabilizes the orbit corresponding to windows in the

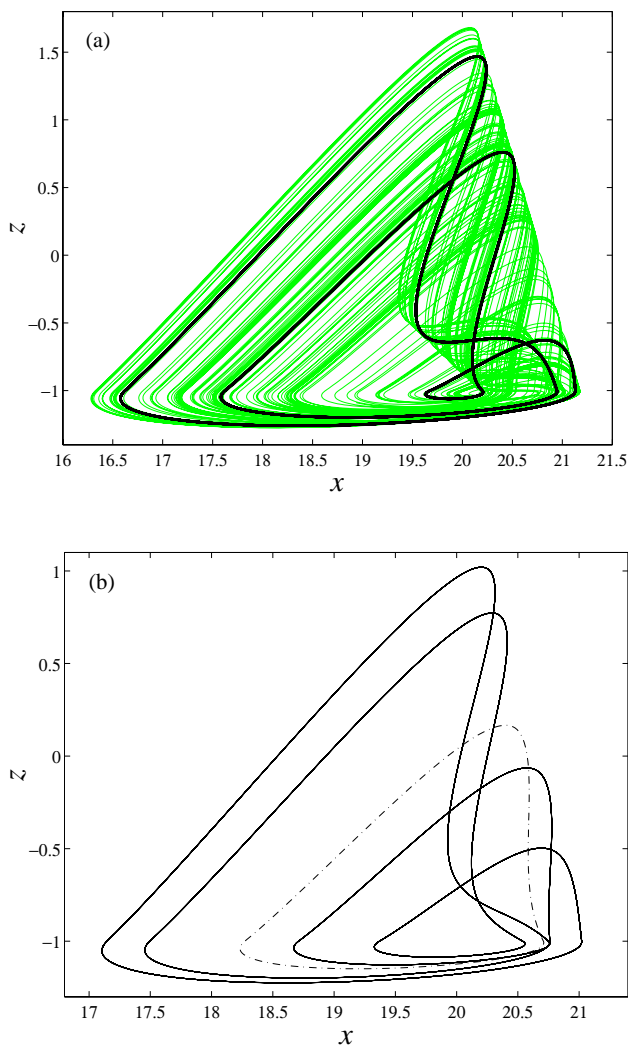


Fig. 2. Phase space of the oscillator (13) at $\varepsilon = 1$, $a = 30$, $b = 0.8$, $c = 20$, $d = 0.6$, $\beta = 10$, and (a): $k = 0$ (grey line); $k = -0.009$ (bold black line); (b): $k = -0.012$ (solid line); $k = -0.24$ (dot-dashed line)

chaotic attractor and the period-doubling orbits in the reverse order. At $k \simeq -0.009$, one obtains the period-3 orbit corresponding to largest window of the chaotic attractor (Fig. 2(a), bold black line). The period-8, -4, -2, and -1 orbits are stabilized at $k \simeq -0.11, -0.12, -0.14, -0.22$ respectively. Figure 2(b) demonstrates stabilized period-4 (solid line) and period-1 (dot-dashed line) orbit respectively.

Increasing the oscillation energy leads to stabilization of orbits corresponding to these energy levels. Figure 3 demonstrates stabilization of so-called 2-pulse orbit.

IV. DISCUSSION AND CONCLUSIONS

The control technique was successfully applied to stabilize the unstable fixed point and UPOs of the Colpitts oscillator. The technique is capable of control-

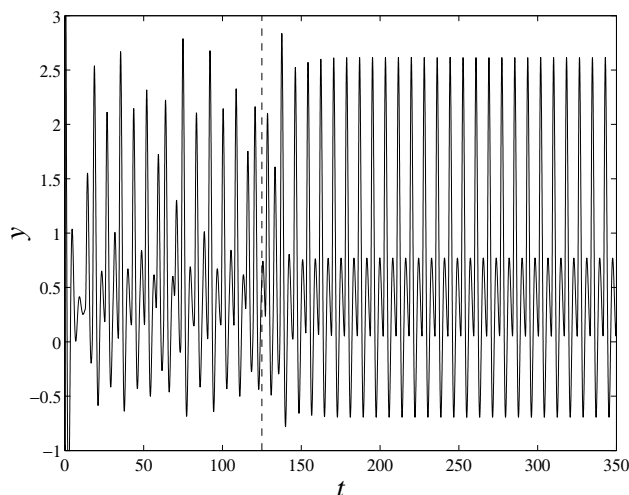


Fig. 3. Dynamics of the state variable y of the oscillator (13) at $\varepsilon = 1$, $a = 30$, $b = 0.8$, $c = 20$, $d = 0.6$, $\beta = 10$, and $k = 0$ ($t < 125$); $k = 0.08$ ($t \geq 125$). Dashed line indicates the time of starting the control.

ling the chaotic repellers too. Indeed, one can convert the equilibrium or periodic dynamics to a chaotic one, or switch the dynamics, say, from the spiral-type chaos to the screw-type one and *vice versa* by simply altering the circuit oscillation energy.

The technique is applicable to controlling coupled oscillators. We considered a chain (ring) of 10 Colpitts oscillators with diffusion-type couplings (with coupled emitters and collectors of the circuit transistor, respectively [3]). Different UPOs were stabilized with a control perturbations applied to only single oscillators.

The approach utilizes simple feedback depending solely on the output signal and, hence, is especially useful when the system parameters are inaccessible or are costly to adjust. The particular type of the perturbation is rather relative — most important, it should comply with the condition (5).

REFERENCES

- [1] M.P. Kennedy. Chaos in the Colpitts Oscillator. *IEEE Trans. Circuits Syst.*, vol. 41, pp. 771-774, 1994.
- [2] O. De Feo, G.M. Maggio and M.P. Kennedy. The Colpitts oscillator: Families of periodic solutions and their bifurcations. *Int. J. Bifurcation and Chaos*, vol. 10, pp. 935-958, 2000.
- [3] A. Baziliauskas, A. Tamaševičius, S. Bumeliene, and E. Lindberg. Synchronization of Chaotic Colpitts Oscillators. In *Scientific Proceedings of Riga Technical University, Ser. 7. Telecommunications and Electronics, 2001*, vol. 1. (*Proc. of the 42nd Int. Conf. of Riga Technical University*), pp. 55-58, 2001.
- [4] V. Tereshko, R. Chacón and V. Preciado. Controlling chaotic oscillators by altering their energy. *Phys. Lett. A*, vol 320, pp. 408-416, 2004.

Spurious Structures in Recurrence Plots Induced by Embedding

M. Thiel, M.C. Romano, J. Kurths

University of Potsdam
 Potsdam, Germany
 email: thiel@agnld.uni-potsdam.de

Abstract— *In this paper we show that delay embedding produces spurious structures in a Recurrence Plot (RP) that are not present in the real attractor. We analyze typical sets of simulated data, such as white noise and data from the chaotic Rössler system to show the relevance of this effect.*

In the second part of the paper we show that the second order Rényi entropy and the correlation dimension are dynamical invariants that can be estimated from Recurrence Plots with arbitrary embedding dimension and delay.

I. INTRODUCTION

Recurrence plots (RPs) visualize the behavior of trajectories in phase space [1]. The recurrence quantification analysis (RQA) then quantifies structures found in RPs to yield objective measures of such patterns and are widely applied [2], [3], [4], [5], [6].

The analytical results concerning structures in RPs presented in [5] were illustrated using systems where all original coordinates are known (i.e. x-,y-,z-coordinates for the Rössler system). However, RPs are usually applied to measured time series. Therefore, we address in this paper the analysis of structures in RPs when the phase space has to be reconstructed from a univariate time series usually based on Takens Theorem [7].

In the first part of the paper we show that spurious correlations induced by embedding can modify considerably the structures that are found in RPs. In the second part we demonstrate that there are quantities that are not only invariant if suitable embedding parameters are used, but also if no embedding is used. This remarkable fact makes RPs an important tool for the analysis of observed time series.

II. RECURRENCE PLOTS AND RECURRENCE QUANTIFICATION ANALYSIS

RPs are a graphical representation of the matrix

$$\mathbf{R}_{\mathbf{i},\mathbf{j}} = \Theta(\varepsilon - \|\tilde{\mathbf{x}}_{\mathbf{i}} - \tilde{\mathbf{x}}_{\mathbf{j}}\|), \quad \mathbf{i},\mathbf{j} = \mathbf{1} \dots \mathbf{N}, \quad (1)$$

where $\tilde{\mathbf{x}}_i \in \mathcal{R}^d$ stands for the point in phase space the system is situated at time i , ε is a predefined threshold and $\Theta(\cdot)$ is the Heaviside function. Then one assigns a “black” dot to the value one to a “white” dot to the value zero. The graphical representation then is called RP.

A homogeneous plot with mainly single points may indicate a mainly stochastic system. Paling away from the main diagonal may indicate a drift i.e. non-stationarity of the time series. Long diagonal lines mean that when the system recurs to a state in phase space, the future development of the system is very similar to the former one for a long time.

In the case of experimental data there is often only one component available. Hence, the embedding dimension d and the delay τ needed for the embedding of the time series

$$\tilde{\mathbf{x}}_i = (x_i, x_{i+\tau}, \dots, x_{i+(d-1)\tau})^T \quad (2)$$

come into play. There are some established methods to determine the embedding parameters [8]. However, the choice of a concrete method is still under debate [9], [10]. The left panel shows the plots for embedding dimension $d = 1$ i.e. no embedding was used. The right panel opposes the same graphics for $d > 1$. These examples make clear that the visual impression that RPs provide can change considerably due to embedding. On the one hand this is expected, as to yield a visualization of the phase space, it has to be reconstructed. On the other hand we will show in the following sections that delay embedding also produces spurious structures that are not present in the real attractor.

III. CORRELATIONS DUE TO EMBEDDING

In this section we compute analytically correlations that are induced by the procedure of embedding. Therefore, we apply the method of embedding to independent Gaussian noise – a test process that has no correlations. The correlations we detect afterwards must hence be due to the

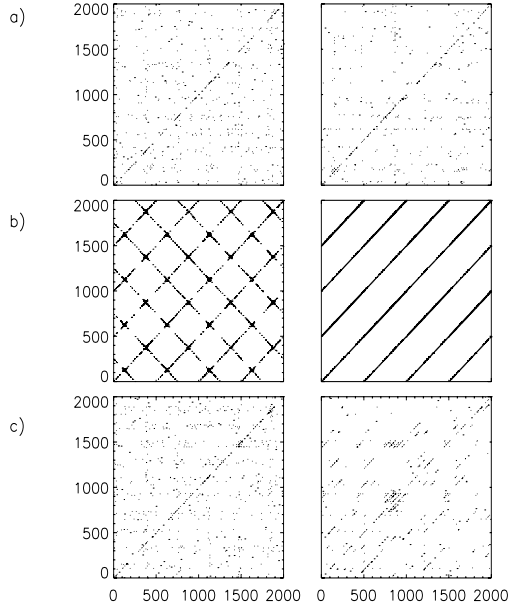


Fig. 1

RPs for uniformly distributed noise (a), the sine function (b) and the Rössler system (c). The left panel shows the plots for $d = 1$. The left panel represents the plots for $d = 14$, $d = 2$ and $d = 3$ from top to bottom. ε is chosen so that the recurrence rate (percentage of black point in the plot) is the same for the embedded and non-embedded time series.

method of embedding.

Using the embedding dimension d and the delay τ , a vector in phase space is given by

$$\vec{\eta}_i = \sum_{m=0}^{d-1} \eta_{i+m\tau} \vec{e}_m, \quad (3)$$

where η_i represents independent Gaussian noise with standard deviation σ and the \vec{e}_m are unit vectors $\vec{e}_m \cdot \vec{e}_n = \delta_{m,n}$. In the RP we have to compute distances of these vectors with respect to some norm: $\Delta_{i,j} = \|\vec{\eta}_i - \vec{\eta}_j\|$. If one moves h steps ahead in time (i.e. on a diagonal in the RP) one finds $\Delta_{i+h,j+h} = \|\vec{\eta}_{i+h} - \vec{\eta}_{j+h}\|$. Next, we could compute the autocorrelation function of $\Delta_{i,j}$. But to further simplify the calculation we compute the autocorrelation function of $\Delta_{i,j}^2$. This gives by using the Euclidean norm

$$C_{\Delta^2}(h, j-i) = \left\langle \left\{ \sum_{m=0}^{d-1} [(\eta_{i+m\tau} - \eta_{j+m\tau})^2] - E \right\} \left\{ \sum_{n=0}^{d-1} [(\eta_{i+h+n\tau} - \eta_{j+h+n\tau})^2] - E \right\} \right\rangle \quad (4)$$

where

$$E = \left\langle \sum_{m=0}^{d-1} (\eta_{i+m\tau} - \eta_{j+m\tau})^2 \right\rangle = 2\sigma^2 d (1 - \delta_{0,j-i})$$

and $\delta_{i,j}$ is the Kronecker delta. $\langle \cdot \rangle$ denotes the expected value. If we further set $p = j - i$ we can evaluate Eqs. (4). Assuming $p > 0$ and $h > 0$ to avoid trivial cases, we find

$$C_{\Delta^2}(h, p) = \sum_{n=0}^{d-1} (d-n) (8\delta_{n\tau, h} + 2\delta_{n\tau, p+h} + \delta_{n\tau, p-h}) \quad (5)$$

This formula shows that there are peaks in the correlation function if h and/or $p + h$ and $p - h$ are equal to one of the first $d - 1$ multiples of τ . These peaks are not present when embedding is not used. These spurious correlations induced by embedding, lead to modified structures in the RP (see Fig. 1 first line, right panel).

In the next section we will investigate numerically the Rössler system as a more paradigmatic chaotic system.

IV. THE RÖSSLER SYSTEM

In this section we compute numerically the correlation of the squared distances using delay coordinates and the original coordinates (x, y, z) for the Rössler system with standard parameters ($a = b = 0.2, c = 5.7$), [11]. Fig. 2 shows results of a simulation for the original coordinates (a) and for the embedded ones using the x-component ((b), with $d = 3$ and $\tau = 8$). Obviously, the correlation structure has changed considerably. The correlation structure for the embedded time series does not reflect characteristic patterns of the Rössler system, but it is mainly influenced by the embedding. In this case the overlaying high frequency is given by the inverse of the delay time $\tau = 8$. This difference in the correlation structure strongly influences the structures in RPs that are computed using on delay embedding. Fig. 2 (c) shows the conditional probability to find a black point h unit time steps after another black point for the embedded Rössler system. Obviously, the form of the curves of Figs. 2 (b) and (c) is qualitatively the same. Our results show that the procedure of delay embedding induces spurious correlations in the data and hence in the RPs. This is also reflected in the RQA measures. Tab. I summarizes the results for four typical RQA measures: the recurrence rate RATE (percentage of black points in the RP), the determinism (number of recurrence points in lines of length $l > l_{\min}$ normalized by the recurrence rate $\text{DET} = \sum_{l=l_{\min}}^{\infty} l P_{\varepsilon}(l) / \text{RATE}$),

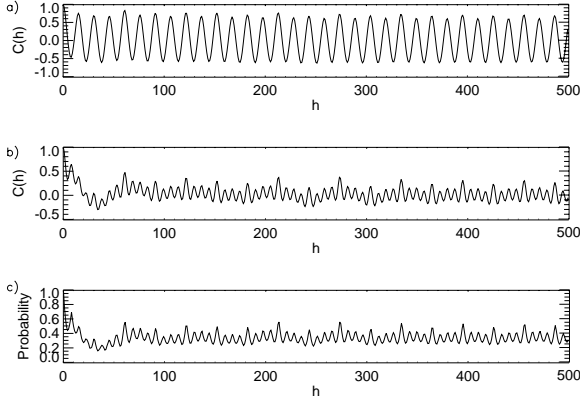


Fig. 2

(a): Autocorrelation function of the squared distances for the real coordinates for $p = 10$. (b): Same for the embedded coordinates $d = 3, \tau = 8$. For the embedding the x-component is used. (c): Probability to find a black point in the RP h points after another one. Same parameters as (b).

embed. param.	DET	RATIO	ENTR
“real coord.”	0.95	96.3	0.0067
$d = 1$	0.04	3.58	0.0670
$d = 3, \tau = 8$	0.72	67.1	0.0169
$d = 3, \tau = 6$	0.83	76.4	0.0142
$d = 3, \tau = 25$	0.50	46.5	0.0288
$d = 6, \tau = 8$	0.75	68.7	0.0129

TABLE I

Comparison of four RQA measures calculated for the Rössler system and for different embedding parameters. In all cases the x-component is used for the embedding.

the ratio ($\text{RATIO} = \frac{\text{DET}}{\text{RATE}}$) and the entropy ($\text{ENTR} = -\sum_l P_\varepsilon(l) \log_2 P_\varepsilon(l)$), where $P_\varepsilon(l)$ is the distribution of diagonals of length l in the RP. To compare all cases we have chosen the threshold ε so that $\text{RATE} \approx 0.01$. The first line of Tab. I summarizes the results for the real coordinates, the rest of the lines for different embedding dimensions. We see, that the measures yield rather different values depending on the embedding parameters. In the next section we introduce measures, that also quantify the structures in RPs but that are invariant with respect to embedding parameters.

V. INDEPENDENCE FROM THE EMBEDDING DIMENSION

In [5], [12] we have shown, that it is possible to estimate the order-2 Rényi entropy [13], [14], [15],

[16] which is defined as

$$K_2 = -\lim_{\tau \rightarrow 0} \lim_{\varepsilon \rightarrow 0} \lim_{l \rightarrow \infty} \frac{1}{l\tau} \ln \sum_{i_1, \dots, i_l} p^2(i_1, \dots, i_l). \quad (6)$$

by means of the cumulative distribution of diagonals in the RP:

$$P_\varepsilon^c(l) \simeq \sum_{i_1, \dots, i_l} p^2(i_1, \dots, i_l) \simeq C_l(\varepsilon) \sim \varepsilon^{D_2} e^{-l\tau K_2}. \quad (7)$$

Therefore, if we represent $\ln(P_\varepsilon^c(l))$ vs. l we obtain a straight line with slope $-\hat{K}_2(\varepsilon)\tau$, where $\hat{K}_2(\varepsilon)$ is an estimator for K_2 .

Next, we treat the case of a reconstructed phase space. To make this clear we write for the cumulative distribution $P_{\varepsilon, \tau}^d$ from now on, where d is the embedding dimension and τ the delay used for the reconstruction. As we have decided to choose the maximum norm in Eq. (1), $P_{\varepsilon, \tau}^d(l)$ is given by

$$P_{\varepsilon, \tau}^d(l) = \frac{\sum_{i, j=1}^N \prod_{m=0}^{l-1} \Theta \left(\varepsilon - \max_{k=0, \dots, d-1} |x_{i+m+k\tau} - x_{j+m+k\tau}| \right)}{N^2} \quad (8)$$

with the embedding dimension d and the delay τ . Obviously,

$$\prod_{m=0}^{l-1} \Theta \left(\varepsilon - \max_{k=0, \dots, d-1} |x_{i+m+k\tau} - x_{j+m+k\tau}| \right) = \Theta \left(\varepsilon - \max_{\substack{m=0, \dots, l-1 \\ k=0, \dots, d-1}} |x_{i+m+k\tau} - x_{j+m+k\tau}| \right) \quad (9)$$

holds. Eq. (9) can be interpreted as testing if the conditions

$$|x_{i+m+k\tau} - x_{j+m+k\tau}| < \varepsilon \quad \forall \quad \begin{matrix} m = 0, \dots, l-1 \\ k = 0, \dots, d-1 \end{matrix} \quad (10)$$

are met. The terms on both sides of Eq. (9) are one if all conditions are simultaneously met and zero otherwise. Hence, $P_{\varepsilon, \tau}^d(l)$ in Eq. (8) can be interpreted as an estimate of the probability that all the conditions Eq. (10) are simultaneously met. Note that Eqs. (10) are a set of $l \cdot d$ conditions that are in general not independent. If for example $m + k\tau = m' + k'\tau$, one of the two conditions

$$\begin{aligned} \varepsilon &> |x_{i+m+k\tau} - x_{j+m+k\tau}| && \text{or} \\ \varepsilon &> |x_{i+m'+k'\tau} - x_{j+m'+k'\tau}| \end{aligned}$$

is redundant. If l is sufficiently large, i.e. $l > \tau$, we can condense the conditions Eqs. (10) and find the $l + (d - 1)\tau$ relations

$$|x_{i+m} - x_{j+m}| < \varepsilon \quad \forall m = 0, \dots, l - 1 + (d - 1)\tau.$$

These conditions have to be met to find a line of at least length $l - 1 + (d - 1)\tau$ if the time series x_i is not embedded. More general one finds

$$P_{\varepsilon, \tau}^d(l) = P_{\varepsilon, \tau}^1(l - 1 + (d - 1)\tau) = P_{\varepsilon, \tau}^1\left(\underbrace{[l \mp \Delta d]}_{l'} - 1 + \underbrace{[d \pm \Delta d]}_{d'} - 1\right) = P_{\varepsilon, \tau}^{d'}(l') \quad (11)$$

provided that $l, l' > \tau$ and $d, d' \geq 1$. Eqs. (11) show that the decay of $P_{\varepsilon, \tau}^d(l)$ is essentially the same for different embedding dimensions and delays. The curve is only shifted to larger l 's if the dimension is decreased. The condition for $P_{\varepsilon, \tau}^d(l) = P_{\varepsilon, \tau}^{d'}(l')$ is $l + (d - 1)\tau = l' + (d' - 1)\tau'$. Thiel et al. have derived an estimator of the correlation dimension \hat{D}_2 (see [5]) from the RP

$$\hat{D}_2(\varepsilon) = \ln\left(\frac{P_{\varepsilon}^c(l)}{P_{\varepsilon + \Delta\varepsilon}^c(l)}\right) \left(\ln\left(\frac{\varepsilon}{\varepsilon + \Delta\varepsilon}\right)\right)^{-1}, \quad (12)$$

where $P_{\varepsilon}^c(l)$ is the cumulative distribution of the real coordinates. Substituting $\ln\left(\frac{P_{\varepsilon_1, \tau}^d(l)}{P_{\varepsilon_2, \tau}^d(l)}\right) = \ln\left(\frac{P_{\varepsilon_1, \tau}^{d'}(l')}{P_{\varepsilon_2, \tau}^{d'}(l')}\right)$ which follows from Eq. (11) in Eq. (12), we see that the estimate D_2 is independent of the choice of the embedding parameters. Our argument shows that at least some of the dynamical invariants, e.g. K_2 and D_2 , can be estimated without any embedding. This is the most important advantage of using RPs in the analysis of measured data.

VI. CONCLUSIONS

In this paper we have shown that delay embedding leads to spurious correlations between the distances of the embedded vectors in phase space and hence change the structures in RPs. These correlations then can lead to an erroneous estimation of characteristics of nonlinear systems that depend on these correlations [9].

We want to stress that these spurious correlations are not due to a wrong choice of the embedding parameters m and τ . It is rather a general problem. As these parameters cannot be unambiguously determined it is in principle possible to choose them so that the results of the RP and the RQA coincide with a priori expectations.

ACKNOWLEDGMENTS

This work was supported by the ‘‘DFG-Schwerpunkt 1114’’ and the ‘‘Internationales Promotionskolleg Computational Neuroscience of Behavioral and Cognitive Dynamics’’.

APPENDIX

REFERENCES

- [1] J.-P. Eckmann, S. O. Kamphorst and D. Ruelle. Recurrence Plots of Dynamical Systems, Eur. Phys. Lett. **4**, pp. 973-977 (1987).
- [2] N. Marwan, J. Kurths. Recurrence Plot Based Measures of Complexity and its Application to Heart Rate Variability Data, Physics Letters A **302** (5-6), pp. 299-307 (2002).
- [3] J. Kurths, U. Schwarz, C.P. Sonett and U. Parlitz. Testing for nonlinearity in radiocarbon data, Nonlinear Processes in Geophysics **1**, pp. 72-75 (1994).
- [4] M. Thiel, M.C. Romano, J. Kurths, R. Meucci, E. Allaria, T. Arcchi. Influence of observational noise in recurrence quantification analysis, Physica D **171** (3), pp. 138-152 (2002).
- [5] M. Thiel, M.C. Romano, J. Kurths, Analytical Description of Recurrence Plots of white noise and chaotic processes, Izv. VUZov- Applied Nonlinear Dynamics **11** (3), pp. (2003)
- [6] C. L. Webber Jr. and J. P. Zbilut. Dynamical assessment of physiological systems and states using recurrence plot strategies, J. Appl. Physiol. **76**, 965-973 (1994).
- [7] F. Takens, *Dynamical Systems and Turbulence*, eds. D. A. Rand and L.-S. Young, Lecture Notes in Mathematics, Vol. 898 (Springer, Berlin, 1980).
- [8] M. B. Kennel, R. Brown and H.D.I. Abarbanel, Phys. Rev. A **45** (6), pp. 3403-3411 (1992).
- [9] P. Grassberger, T. Schreiber and C. Schaffrath. Nonlinear Time Sequence Analysis, Int. J. Bif. Chaos **1** (3), pp. 521-543 (1991).
- [10] J. P. Zbilut and C. L. Webber Jr.. Embeddings and delays as derived from quantification of recurrence plots, Physics Letters A **171**, pp. 199-203 (1992)
- [11] E. Ott. *Chaos in Dynamical Systems*, (Cambridge University Press, 1993)
- [12] M. Thiel, M.C. Romano, J. Kurths, Estimation of Dynamical Invariants without Embedding by Recurrence Plots, Chaos (in press)
- [13] A. Rényi. *Probability theory*, (North-Holland, 1970 (appendix)).
- [14] P. Grassberger. Generalized Dimensions of Strange Attractors, Physics Letters **97** A, pp. 227-230 (1983).
- [15] P. Grassberger and I. Procaccia. Dimensions and entropies of strange attractors from a fluctuating dynamics approach, Physica D **13**, pp. 34-54 (1984).
- [16] P. Grassberger and I. Procaccia. Estimation of the Kolmogorov entropy from a chaotic signal Physical Review A **28**, pp. 2591-2593 (1983).

FRACTAL PROPERTIES OF CHAOTIC DYNAMICAL SYSTEMS IN REVERSE TIME AND ITS APPLICATION FOR DATA ENCRYPTION

A. I. Tomashevskiy, M.V. Kapranov

Moscow Power Engineering Institute (Technical University), Radio Engineering Faculty
 Department of Generation of Oscillations and Signals
 14 Krasnokazarmennaya str., Moscow 111250, Russia; tel. +7(095)362-7624;
 e-mail: alex_tomash@mail.ru

Abstract—*The dynamical process properties of chaotic discrete map in reverse time is considered. The fractal structure of reverse iteration points ordering is investigated. As an application the data encryption algorithm is proposed.*

I. INTRODUCTION

In literature the investigations of secure communication methods with the use of dynamical chaos are well-known and wide-spreading [1]. The majority of approaches proposed are in hiding of the fact of information transmission by means of its *masking* in random-like chaotic signal or other methods [2]. The novel and deeply studied enough theoretical and experimental results have described in a lot of papers, for instance [3,4].

So far relatively new but progressive principle is in active development, that connected with researches of information encryption algorithm based on chaotic properties of nonlinear dynamical systems [5]. By now, there are several of inconsistent opinions about perspectives of this approach. But due to a small number of publications in this direction for the final solution of existing problems, certainly, it's necessary to conduct further goal-directed studies with the help of new ideas and approaches to application of dynamical chaos for data protection.

In given work, as such new idea, it's proposed to use the chaotic processes of the dynamical systems not in "direct", as it's traditionally offered in scientific works, but in "reverse" time. This approach is connected with *inverse problem* of nonlinear dynamics [6], having polymorphism (ambiguous solution) and possessing in general case, exceeding difficulty for research.

This idea is in some relation with several problems of various approaches to solution of inverse problem for dynamical systems and its practical applications, that are investigated in

literature. They are separation of chaotic signals into components from its sum with the noise [7], decoding the information stored in chaotic sequence by *symbolic dynamics* [8], restoration of initial conditions, parameters and nonlinearly of the model from observed chaotic waveform in the presence of noise and other disturbing factors, by means of so called *reverse iteration* [9], the optimization of the most convenient structure of equations and dynamical variables for chaotic waveform simulation [10], error estimation of parameter reconstruction from modulated chaotic signal [11], and etc.

In these works, as a rule, only partial questions of reverse time system applications for *radiophysical* and *telecommunication* problems are considered. At the same time, *reverse dynamics* itself is greatly interesting media for research and has varied properties, that are not enough investigated in literature. For this reason we propose for beginning to pay the attention to some basic theoretical characteristics of chaotic processes in reverse time, but under special practical point of view, and then to consider how that properties can be used in concrete application to information communication system.

The structure of the paper is as following. In Chapter II, a selection of dynamical system as the discrete map is explained and their basic dynamical and statistical characteristics in direct time are discussed. In Chapter III, properties of these systems for *motion in reverse time* are investigated and compared with characteristics obtained in previous Chapter II. There is a small discussion about example application of reverse map complex structure order for information encryption In Chapter IV.

II. BASIC PROPERTIES OF THE MAP IN DIRECT TIME

Let's take as our object of investigation the class of dynamical systems with discrete time t_k in the form

$$x_{k+1}=F(x_k; a), \tag{1}$$

where x_k – state vector of the system in the moment of time $k= t_k/T=0,1,2\dots, T$ – sample period, F – vector map functions, a – vector of constant parameters. State vectors and map functions have the dimension N_x , vector of parameters – N_a . In given paper we consider the simplest example of 1-dimension single-mode map, i.e. $N_x=N_a=1$.

One of the simplest and widely-used types of maps from this class, that providing the chaotic behavior is piecewise-linear map with single maximum (or minimum), that is will-known also as *tent map* (2).

$$x_{k+1} = F(x_k; a) = \begin{cases} x_k/a, & 0 < x_k \leq a, \\ (1-x_k)/(1-a), & a < x_k < 1. \end{cases} \tag{2}$$

In our case we present a modification of *asymmetrical tent map* with fixed maximum, i.e the tent with *top*, that changing along the line of $F(x_k; a)=1$, when varying the parameter, but the *base* of tent is fixed in the definitional domain borders of x_k , i.e. $F(0;a)=F(1;a)=0$ (Fig. 1,a). In this instance we deal with asymmetrical *linear maximum*, that formed by two closing straight line with different tangents, depending on the value of parameter a . Map function becomes symmetrical only in the single situation: $a=0.5$. Exactly the same map was investigated in [12] and was called there as skew tent map.

In this map the band of changing the parameter, corresponding to global stable dynamics, is $a \in (0,1)$; initial condition definitional domain also is the unit interval: $x_k \in (0,1)$.

The reason, why we have selected this type of map function is as followings. The map (2) is *non-compressing* and *non-expanding*, i.e. it converts the unit interval (0,1) into itself. Thereby reverse map also will be non-compressing and non-expanding. This provides the existence of iteration point of reverse map function for all points from definitional domain of the direct map function, and signifies the mutual correspondence of any reverse dynamical process to direct one for all parameter values and initial conditions. While there is no such a correspondence, in general, in compressing or expanding maps.

Let's consider a little bit more in detail some properties and characteristics of our piecewise-linear map. This map generates a dynamical chaos for all

allowed values of parameter, that is confirmed by solid form of bifurcation diagram and positive Lyapunov exponent, when a is changed (Fig. 1,c-d). An example of the chaotic behavior for the fixed parameter is shown in phase plane (Lamerey-Königs diagram) in Fig. 1,a.

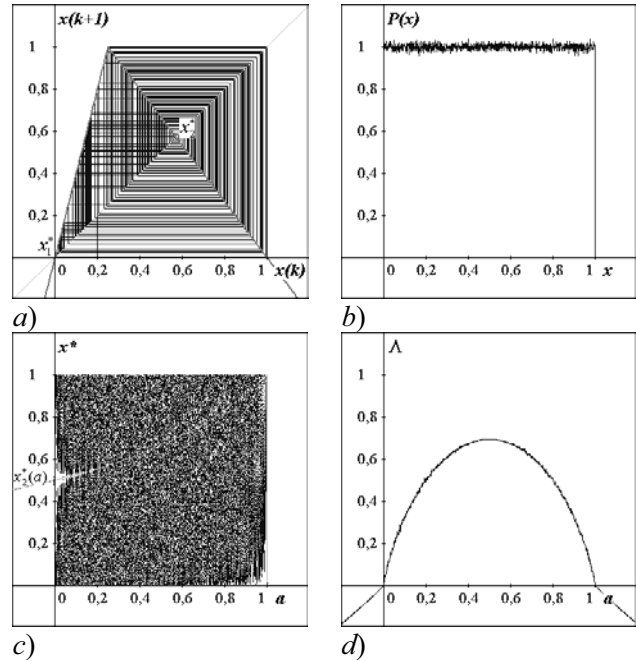


Fig. 1. Characteristics of piecewise-linear map (2): (a) – Lamerey-Königs diagram example; (b)– density of distribution (for (a-b) – $a=0.25$); (c) – bifurcation diagram; (d) – Lyapunov exponent

This is very notable that density of distribution $P(x)$ the chaotic process when increasing of duration of the time sample tends to uniform law for nearly any $a \in (0,1)$ (Fig. 1,b). This is also tracked on bifurcation diagram in Fig. 1,c, on which almost the whole volume of phase space is filled uniformly. As an exception are narrow areas, that are visited by trajectory comparatively less, than all rest space – these areas are concentrated near the fixed points of the system (2). One of them is always in origin $x_1^*=0$, but coordinate of the other point is defined by expression $x_2^*=1/(2-a)$ (this curve is also shown in diagram of Fig. 1,c).

The dependency of Lyapunov exponent on the system parameter, calculated numerically and plotted in Fig. 1,d, can be also derived analytically [12]:

$$\Lambda(a) = -a \ln a - (1-a) \ln(1-a) \tag{3}$$

As you see, $\Lambda(a) > 0$ for any $a \in (0,1)$.

The map presented very suitable from the standpoint of chaos control in secure communication system, since if the parameter is varied slowly the oscillation characteristics practically are not changed, but density of distribution function (consequently mean value, dispersion and etc) is not changed at all.

III. FEATURES OF THE SYSTEM IN REVERSE TIME

The reverse map law in general form is written as following

$$x_k = F^{-1}(x_{k+1}; a), \quad (4)$$

which for 1-dimension system with single maximum has ambiguous functional dependence. In particular, for the map (2)

$$x_k = \begin{cases} F_1^{-1}(x_{k+1}; a) = ax_{k+1}, \\ F_2^{-1}(x_{k+1}; a) = 1 - (1-a)x_{k+1}; \end{cases} \quad (5)$$

Thereby, for every value x_{k+1} we have two preceding values x_k (figuratively expressing, for each "effects" we have two possible "reasons"). Hence, at every n -th step of the motion backwards, where $n \in [0, N]$, ambiguity increases as 2^n . Graphically this phenomenon can be imaged in the manner of *tree of reverse iteration*, Fig. 2, on which all possible trajectories in the time interval $(k-N, k)$, where $k > N$, getting through given value $x_k=0.2$ (the time axis positive direction – on the left)*. All trajectories, starting from manifold $\{x_{k-N}\}$, – values at the right border of the “tree” in Fig. 2 (*top of tree*) – for direct iteration in n steps will reach the value x_k (*base of tree*). As it is shown this process (*branches of tree*) tries to fill the whole volume of source attractor (for direct dynamics) when n increases. However the question appears: what is the structure of top tree manifold?

The density of distribution function $P_{rt}(x)$ of the top tree manifold is presented in Fig. 3. This is quite different distribution as of direct process (compare with Fig. 1,b) and, hence, not the same as of single

* In the paper [7] a calculation of such multiple backward trajectories by means of reverse iteration was used for increasing the separation quality of chaotic process from mixture of a number of signals with noise in communication channel by statistical analysis.

branch of the tree in Fig. 2 (it seems to be also uniform). Only for $a=0.5$ (symmetric map) $P_{rt}(x)$ is the same as $P(x)$. This means that backward process is not *ergodic*, in general case.

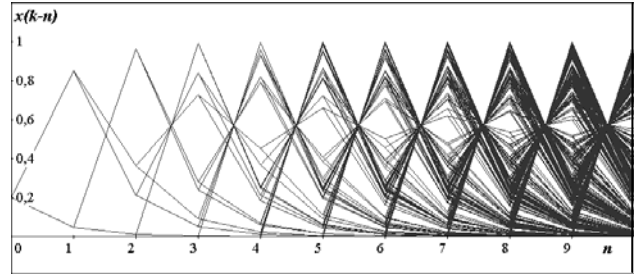


Fig. 2. Tree of reverse iteration; $N=10$, $a=0.25$, $x_k=0.2$

Another difference from the direct process is in the dependence of $P_{rt}(x)$ on the parameter a . So, we see, reverse dynamics generates statistically different process, then direct one.

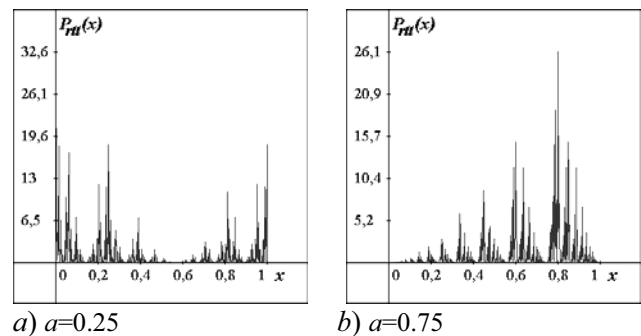


Fig. 3. Density of distribution of top tree manifold; $N=20$, $x_k=0.2$

The characteristics of Fig. 3 already demonstrate self-similar (*fractal*) structure, especially Fig. 3,b. It's interesting to present the top tree as some time waveform, so we could consider the tree of reverse iteration as the generator of complex consequences. But a question arises: how to order this manifold or, in other words, what parameter of ordering we have to choose?

One of the most convenient algorithms is to order in correspondence with branch calculation sequence as the following. If at each n -th reverse time step of tree when calculating x_{k-n} due to (5) we'll give to every value the symbolic digit “0” for calculation via F_1^{-1} , and “1” – for F_2^{-1} , each branch will get the symbolic binary sequence of the length equaled to N (for instance, for most bottom branch of Fig. 2, that

was calculated only via F_1^{-1} , we've got the sequence of "00000..." (N zeros)).

In general case, this sequence can be interpreted as some binary number, where each bit corresponds to any reverse iteration n . Then we could link, for example, the upper bit with $n=N$ (accordingly the lower bit with $n=1$) and convert it into decimal form. In such a manner we obtain the unique number of each branch – "branch index" $i \in [0, 2^{N-1}]$, that we'll use as a parameter of ordering. The dependency of top tree values on the branch index is shown in Fig. 4. This is the fractal structure – each fragment is the similar structure as the whole image. The form of fractal depends on the map parameter a , but not on the x_k and N .

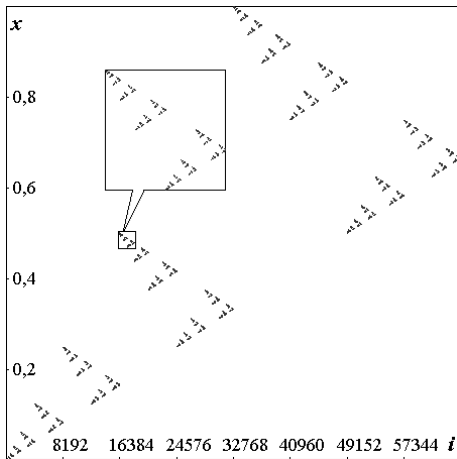


Fig. 4. Fractal top tree structure; $N=16, a=0.5, x_k=0.2$

The ordering principle play the key part in formation of fractal manifold – any other type of ordering leads to different top tree structure.

IV. APPLICATION EXAMPLE

Fractal properties of ordering of iteration points in reverse time is the very interesting result itself from theoretical point of view and could find a lot of its applications. But one of the simplest application it's possible to propose – this is the data encryption algorithm based on reverse maps.

As an input information can be any value $x_{k-n} \in (0, 1)$ – the initial condition for direct map, taken with fixed or varied accuracy N . The output data is the branch index i , that can be calculated during direct iteration as well. Since the index is the unique identity of x_{k-n} , we could always restore

input data by means of reverse iterations only from the index (it's supposed, that a map and its parameter are known). The table of the correspondence is expressed as the fractal structure of Fig. 4.

REFERENCES

- [1] M. Hasler. "Recent Advances In the Transmission of Information Using a Chaotic Signals". *Foreign Radio Electronics. Successes of Modern Radio Electronics*, no. 11, pp. 33-43, 1998.
- [2] U. V. Andreev, A. S. Dmitriev and others. "Strategies of Applying Dynamic Chaos in Communications and Computer Networks. Chaotic Encoder and Channel Encoder". *Foreign Radio Electronics. Successes of Modern Radio Electronics*. no. 11, pp. 4-26., 2000.
- [3] Sato A., Endo T. "Experiments of Secure Communication via Chaotic Synchronization of Phase-Locked Loops". *IEICE Trans. Fundamentals*, vol. E-78-A, № 10, pp. 1286-1290, 1995.
- [4] A. S. Dmitriev, G. A. Kassian, L. V. Kuzmin. "Matched Filtration of Chaotic signals". *In Proc. NDES'03*, pp. 73-76, Scuol, Switzerland, 2003.
- [5] F. Dachsel, W. Schwartz. "Chaos and Cryptography". *IEEE Trans. on Circuits and Systems. I – Fund. Theory and Appl.*, vol. 48, no. 12, pp. 1498-1509, 2001.
- [6] Anosov, O.L. and Butkovskii, O.Ya. "Predictability of Complex Dynamical Systems". Berlin: Springer, 1997, 253 p.
- [7] Y. V. Andreyev, A. S. Dmitriev, E. V. Efremova and A. N. Anagnostopoulos. "Separation of Chaotic Signals Sum Into Components in the Presence of Noise". *IEEE Trans. on Circuits and Systems. I – Fund. Theory and Appl.*, vol. 50, no. 5, pp. 613-618, 2003.
- [8] A. A. Dmitriev. "Perfect Synchronization in Pseudochaotic Systems". *In Proc. NDES'03*, pp. 86-90, Scuol, Switzerland, 2003.
- [9] V. N. Kuleshov, M. V. Larionova. Solution of Inverse Problem of Chaotic Dynamics for One-Dimensional Logistic Map. *In Proc. 100th Anniversary of A.A. Andronov «Progress in Nonlinear Science»*. p. 260. Nizhny Novgorod, Russia, 2001.
- [10] B.P. Bezruchko and D.A. Smirnov. "Constructing nonautonomous differential equations from experimental time series". *Phys. Rev. E*, V. 63. 016207, 2001.
- [11] S. G. Bilchinskaya, O. Ya. Butkovskii, M. V. Kapranov and others. "Signal Reconstruction Errors in Data Transmission via Modulation of the Parameters of Chaotic Sequences". *Journal of Com. Technology and Electronics*, vol. 48, no. 3, pp. 284-292, 2003.
- [12] M. Hasler, Y. L. Maistrenko. "An Introduction to the Synchronization of Chaotic Systems: Coupled Skew Tent Map". *IEEE Trans. on Circuits and Systems. I – Fund. Theory and Appl.*, vol. 44, no. 10, pp. 856-866, 1997.

BIFURCATIONS IN CURRENT COUPLED BVP OSCILLATORS

Shigeki Tsuji, [†], Tetsushi Ueta[‡] and Hiroshi Kawakami[†]

[†] Faculty of Engineering, Tokushima University,
Tokushima, 770-8506 Japan

[‡] Center for Advanced Information Technology,
Tokushima University, Tokushima, 770-8506 Japan

e-mail: {shigeki@is, tetsushi@ait}.tokushima-u.ac.jp

Abstract—*The BVP oscillator is a simple circuit implementation of neuronal dynamics. Lately diffusive coupling structure of neurons is attracting attention since the existence of the gap-junction has been found in the brain. Such coupling is easily realized by linear resistor in the circuit implementation, however, there are not enough investigations about diffusively coupled BVP oscillators, even a couple of two BVP oscillators. We have considered several types of coupling structure between two BVP oscillators, and discussed their dynamical behavior in precedence works. In this paper, we take up a coupling structure called current coupling structure, and study dynamical properties of it by bifurcation theory. As a result, both completely in-phase and anti-phase synchronization stably for coupled identical oscillators.*

I. INTRODUCTION

A circuit equation of Bonhöffer-van der Pol (abbr. BVP) oscillator which is also called FitzHugh-Nagumo model is simplified Hodgkin-Huxley equation. Since a BVP oscillator is a simple electric circuit which consists of some simple elements, many researches have investigated not only about the bifurcation phenomena in single BVP oscillator but also about the various coupled system [1]–[4]. When a linear resistor is used for coupling, it realize a diffusive coupling system. Sine a BVP oscillator has a two interfaces, we have the following four coupling types: voltage-voltage, current-current, voltage-current, and cross voltage-current coupling. Therefore, it is envisaged that various synchronization and asynchronous phenomena, and the chaos oscillation due to bifurcation phenomena are observed by the interactions of initial state of each oscillator and the coupling type although the simple coupling system.

In this paper, we investigate a current coupled BVP oscillators. We consider both coupling systems of identical BVP oscillators and different BVP oscillators, and investigate observed various bifurcation phenomena and chaos oscillation due to changing param-

eter of nonlinear resistor and a linear resistor using for coupling. Then, we show that a current coupled BVP oscillators have various phenomena depending on characteristics of nonlinear resistors although all internal elements of two oscillators are the same. Additionally, when we vary parameters of internal elements, more complicated phenomena are found. We show that a chaotic solution changes between two chaotic solutions in simulation and laboratory experiment.

II. BIFURCATIONS IN SINGLE BVP OSCILLATOR

To analyze bifurcation phenomena in current coupled BVP oscillators, firstly we investigate bifurcation structures in a single BVP oscillator. The circuit equations are described as

$$dv/dt = (-i - g(v))/C, \quad di/dt = (v - ri)/L \quad (1)$$

where the nonlinear negative conductance is modeled by $g(v) = -\alpha \tanh(\beta v)$. From physical measurement of FET, we can determine parameter values $\alpha = 6.0762 \times 10^{-3}$, $\beta = 0.3725$. Hence, we have normalized equations as follows:

$$dx/d\tau = -y + \tanh(\gamma x), \quad dy/d\tau = x - ky. \quad (2)$$

Here, we choose the following transformations:

$$\begin{aligned} \tau &= \frac{1}{\sqrt{LC}}t, & x &= \frac{1}{\alpha} \sqrt{\frac{C}{L}}v, & y &= \frac{1}{\alpha}i, \\ \gamma &= \alpha\beta \sqrt{\frac{L}{C}}, & k &= r \sqrt{\frac{C}{L}}. \end{aligned} \quad (3)$$

We also fix parameters as $L = 10[\text{mH}]$, $C = 0.022[\mu\text{F}]$. Figure 1 shows a bifurcation diagram in γ - k plane. In this bifurcation diagram, h_1 , h_2 and d indicate supercritical Hopf bifurcation, subcritical Hopf bifurcation and pitchfork bifurcation of equilibrium respectively. G and H indicate tangent bifurcation and homoclinic bifurcation of periodic solution. Here, subscript number of these symbols intends to classify the curves of same bifurcation. Figure 1 is divided into six regions by bifurcation curves, and these

regions are topologically classified as follows: Region (a): only a stable equilibrium (origin) exists; Region (b): an unstable equilibrium (origin) and a stable limit cycle exist; Region (c): two unstable equilibria, a saddle (origin) and a stable limit cycle exist; Region (d): two unstable equilibria, a saddle (origin), a stable limit cycle and two unstable limit cycles exist; Region (e): two unstable equilibria, a saddle (origin), a stable limit cycle and an unstable limit cycle exist; Region (f): two unstable equilibria and a saddle (origin) exist. After the following section, coupled system is analyzed based on these topological information.

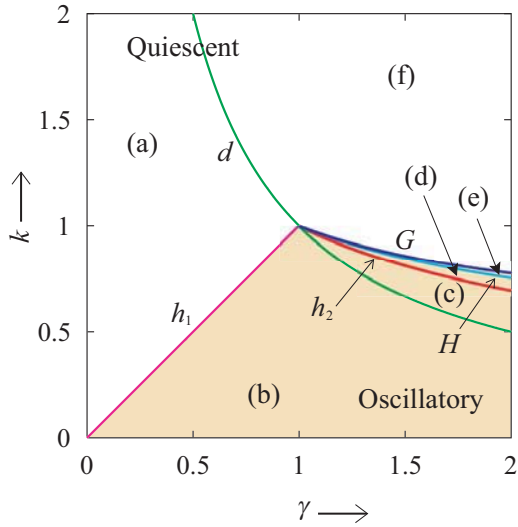


Fig. 1. Bifurcation diagram of equilibria and limit cycles.

III. CURRENT COUPLED BVP OSCILLATORS

We consider the coupled BVP oscillators by a linear resistor with current ports shown as Fig.2. we fix parameters $L = L_1 = L_2$, $C = C_1 = C_2$, and $r = r_1 = r_2$, and then we have normalized equations as follows:

$$\begin{cases} \frac{dx_1}{d\tau} = -y_1 + \tanh(\gamma_1 x_1) \\ \frac{dy_1}{d\tau} = x_1 - ky_1 + \delta k(y_1 - y_2) \\ \frac{dx_2}{d\tau} = -y_2 + \tanh(\gamma_2 x_2) \\ \frac{dy_2}{d\tau} = x_2 - ky_2 + \delta k(y_2 - y_1) \end{cases} \quad (4)$$

Now we choose the same transformations as the previous section, and we set a linear resistor using for coupling to $\delta = Gr/(1 + 2Gr)$. Notice that $\delta \rightarrow 0$ means decoupling of oscillators. We investigate bifurcation phenomena about two cases that a nonlinear

negative conductance value of two BVP oscillators is equal and not equal.

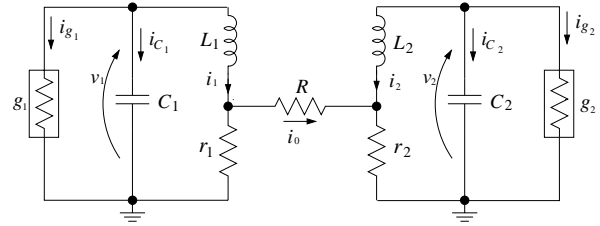


Fig. 2. Current coupled BVP oscillators.

IV. BIFURCATIONS IN γ - δ PLANE

Firstly, we set up nonlinear conductance parameters $\gamma = \gamma_1 = \gamma_2$, and we solve the bifurcation diagram in γ - δ plane as shown Fig.3. h and d indicate Hopf bifurcation and pitchfork bifurcation of equilibrium respectively. In addition, G , I , NS and Pf indicate tangent bifurcation, period-doubling bifurcation, Neimark-Sacker bifurcation and pitchfork bifurcation of periodic solutions respectively. Here, subscript number of these symbols intends to classify the curves of same bifurcation. These curves are converged on some points of $\delta = 0$ line in this figure. In this case, parameter k of each oscillator is fixed to 0.82, i.e., $\delta = 0$ line is corresponding to $k = 0.82$ line in Fig.1. Therefore, to changing parameter γ from $\gamma = 0$, topological structure of each single oscillator changes from (a) to (f) via some bifurcations in Fig.1. Then each intersecting point corresponds to four convergence points in Fig.3, so that four bifurcation curves cross $k = 0.82$ line in Fig.1. However, since it is not solving for homoclinic bifurcations derived from convergence point, five convergence points exist in a normal situation. For these reasons, some bifurcations are generated from five convergence points due to increasing parameter δ .

The state of each oscillator is quiescent state in the lower left side of the region in Fig.3. However, there is only generated oscillation state of anti-phase synchronization as shown Fig.6-(1) via Hopf bifurcation h_1 . Moreover, since other bifurcations which generate the stable limit cycle do not exist, only anti-phase solution exists in the upper side of Fig.3. Hence, when coupling intensity is comparatively strong, anti-phase solution is widely observed in this coupled oscillators compared to voltage coupled oscillators in which in-phase solution is widely observed. there exist various bifurcations of limit cycles in the under side of Fig.3. Figure4 shows enlargement in the under side of Fig.3. Anti-phase solution observed on a point (1) as

shown Fig.6-(1) disappears by Pf . On the other hand, unstable limit cycle generated by h_2 changes stable limit cycle (in-phase solution) via NS_1 . This solution (Fig.6-(2)) is only observed in the region including a point (2). However, in the region including a point (3), anti-phase and in-phase solution are coexistent. In the point (3), anti-phase and quasi-periodic solution are coexistent so that in-phase solution changes to quasi-periodic solution via NS_1 shown Fig.6-(4), but it disappears by tours breakdown instantly. Moreover, chaotic solution is observed in the point (5) such shown Fig.6-(5), although all the parameters of two oscillators are same. In the under side of Fig.4 such that the region (Fig.5) where δ is comparatively small, a solution which changes between two states is observed on the point (6) shown Fig.6-(6) and Fig.7.

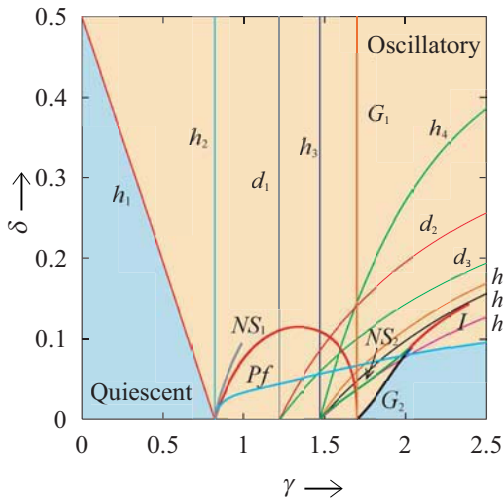


Fig. 3. Bifurcation diagram of equilibria and limit cycles.

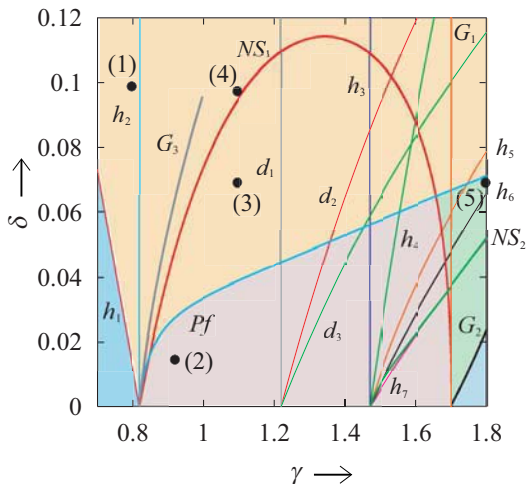


Fig. 4. Bifurcation diagram of equilibria and limit cycles.

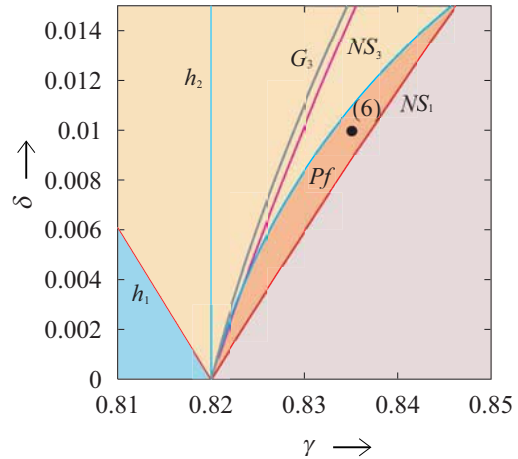
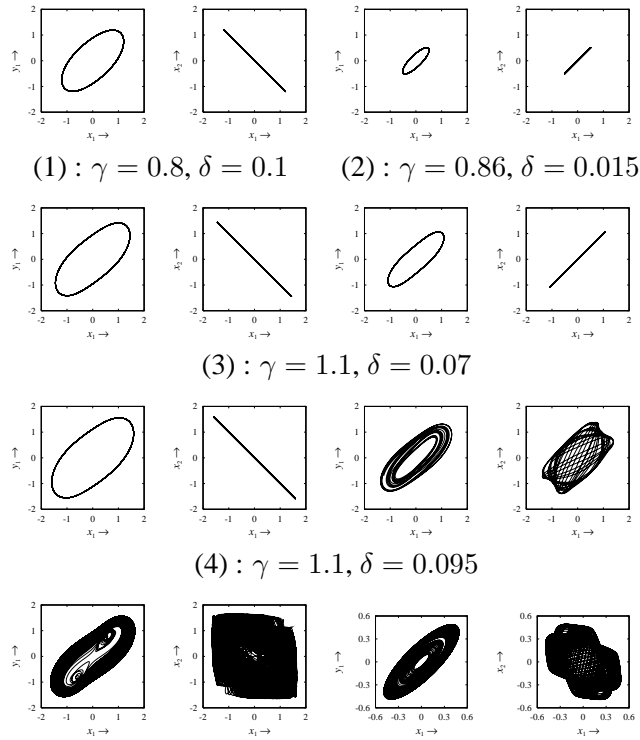


Fig. 5. Bifurcation diagram of equilibria and limit cycles.



(1) : $\gamma = 0.8, \delta = 0.1$ (2) : $\gamma = 0.86, \delta = 0.015$
 (3) : $\gamma = 1.1, \delta = 0.07$
 (4) : $\gamma = 1.1, \delta = 0.095$
 (5) : $\gamma = 1.8, \delta = 0.068$ (6) : $\gamma = 0.835, \delta = 0.01$

Fig. 6. Phase portraits of coupled oscillators in Fig.4.

V. BIFURCATIONS IN γ_2 - δ PLANE

Finally, we fix γ_1 as 0.825, $k = 0.932$. Since the symmetry of each oscillator becomes asymmetrical except for $\gamma_1 = \gamma_2$ generally, more complicated bifurcation structure would be shown compared with a previous cases. We obtain the bifurcation diagram in γ_2 - δ plane as shown Fig.8. Two small stable period-1 solutions (Fig.9-(1)) exist in the point (A) of Fig.8, and a stable equilibrium exists inside each limit cycle. When increasing parameter δ in the direction

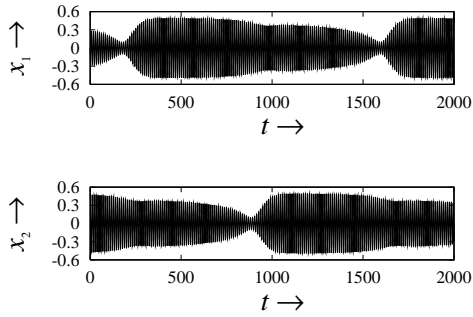


Fig. 7. Wave forms observed in the point (6).

of an arrow from this point, these period-1 solutions change to period-2 solutions (Fig.9-(2)) via period-doubling bifurcation I_1^1 . Moreover, these period-2 solutions change to quasi-periodic solutions (Fig.9-(3)) via NS_1^2 , and thereafter these solutions become single chaotic solutions (Fig.9-(4)) by torus breakdown. These chaotic solutions once disappear, the state of this system changes to two stable equilibrium. However, these stable equilibrium change to unstable via h_1 , and the state of this system shows a big chaotic solution (Fig.9-(5)) changing between single chaotic solutions. this solution can be observed also in a real circuit, and Fig.10 shows that it is in agreement with a simulation result (Fig.9-(5)).

VI. CONCLUSIONS

In this paper, we analyzed a current coupled BVP oscillators about two cases. Firstly, we showed that various phenomena is observed by the values of non-linear resistor and linear resistor using for coupling, although the values of each internal element of two oscillator are the same. Nextly, when each oscillator has different internal nonlinear resistor, we found that the behavior of state switching two single chaotic solutions alternatively shown also by Ref.[4].

REFERENCES

[1] O. Papy and H.Kawakami, *IEICE Trans. Fundamentals*, Vol.E78-A, No. 12, pp.1816–1821, 1995.
 [2] H. Kitajima, Y. Katuta and H. Kawakami, *IEICE Trans. Fundamentals*, Vol. E81-A, No. 3, pp. 476–482, 1998.
 [3] K. Tsumoto, T. Yoshinaga and H. Kawakami, *Physical Review E*, vol.65, No.3, pp.036230,1-9, 2002.
 [4] T. Ueta and H. Kawakami, *Proc. IEEE/ISCAS*, II, pp.544–547, 2002.

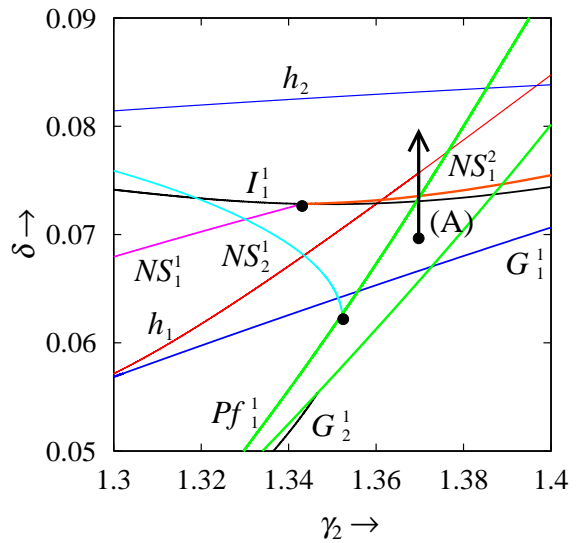


Fig. 8. Bifurcation diagram of equilibria and limit cycles.

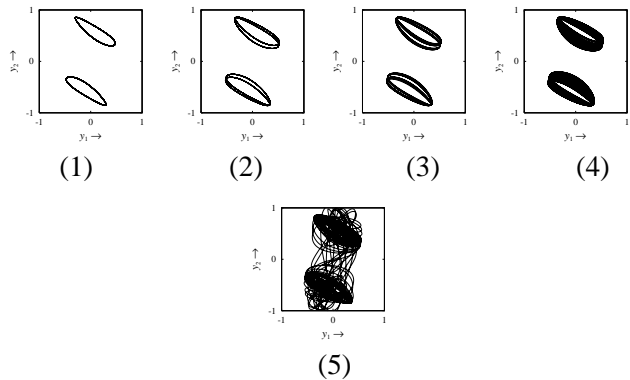


Fig. 9. Phase portraits of coupled oscillators in Fig.8. (1) : $\gamma_2 = 1.37, \delta = 0.07$, (2) : $\delta = 0.0733$, (3) : $\delta = 0.0736$, (4) : $\delta = 0.0739$, (5) : $\delta = 0.076$.

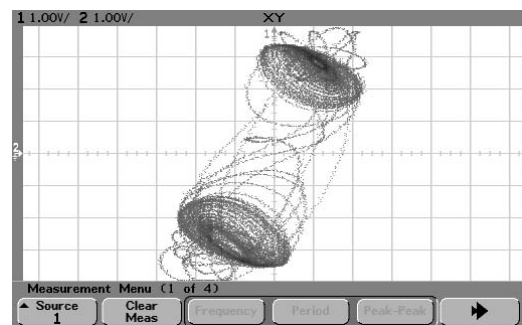


Fig. 10. Laboratory experiment which corresponds to Fig. 9-(5).

An Aspect of Oscillatory Conditions in Linear Systems and Hopf Bifurcations in Nonlinear Systems

T. Ueta and H. Kawakami

Tokushima University, Tokushima, Japan
 e-mail: tetsushi@ait.tokushima-u.ac.jp
 WWW: <http://risa.is.tokushima-u.ac.jp>

Abstract—Hopf bifurcation analysis is very important since both understanding dynamical behavior in a given system, and design of oscillators. In this paper, we show an equivalence among Hopf bifurcation analysis, the phasor method, and Barkhausen criterion experimentally. The phasor method with a virtual source is especially convenient to analyze the oscillator behavior when some linear elements are attached to a conventional oscillator. As an example, the extended BVP oscillator is analyzed by the phasor method. It is clarified that two different frequency oscillations are controlled by a resistor. Bifurcation diagrams and laboratory experiments are shown.

I. INTRODUCTION

In most electrical circuits with smooth nonlinearity, a limit cycle is caused by a super critical Hopf bifurcation of an equilibrium. As the parameter changes, a complex conjugate eigenvalues moves from the left-half plane to the right-half plane in the complex space with Hopf bifurcation. According to this values, a sink changes to a center at the critical parameter value, then it becomes a source. A limit cycle emerges after this bifurcation for typical nonlinear systems such as van der Pol oscillator, Lorenz system, and so on. Generation of oscillatory behavior must be related deeply with destabilization of the linear stability.

However, there are few issues on relationship among linear analysis methods, e.g., oscillator design, feedback control systems, and Hopf bifurcation analysis. In this paper, we present a fundamental oscillator design method by using the phasor method. It is shown that equations induced from the phasor method with a nonzero current assumption is equivalent to equations derived from characteristic equation with a Hopf bifurcation condition. Moreover, we show Barkhausen criterion is also coincident with them.

II. POINTS OF THE ISSUE

A transfer function of the system including feedback is written in the form:

$$G(s) = \frac{A(s)}{1 + A(s)\beta(s)} \quad (1)$$

where, $A(s)$ is a transfer function of the amplifier, and $\beta(s)$ is of the feedback controller. Then several per-

spectives are possible for this transfer function shown as the following:

From control system design perspective:

In common sense of the controller design, the unstable state should be stable, i.e., all real parts of the roots of $1 + A(s)\beta(s) = 0$ must be negative. However, the controller is never considered to make the system be unstable. A negative feedback is widely assumed, and there is no consideration on oscillation from this perspective.

From oscillator design perspective:

then Barkhausen criterion is as follows:

$$\operatorname{Re}[A(j\omega)\beta(j\omega)] = 1, \quad \operatorname{Im}[A(j\omega)\beta(j\omega)] = 0 \quad (2)$$

In some textbooks of electronics, this criterion is explained intuitively, however, they simply ignore the existence of Hopf bifurcations.

From nonlinear analysis perspective:

The super-critical Hopf bifurcation can be considered as a generation of a limit cycle. The bifurcation parameter values might be a clue for understanding the whole dynamical behavior in the given system.

III. HOPF BIFURCATION ANALYSIS

Here we briefly state a typical way of Hopf bifurcation analysis. Suppose a dynamical system is given by: $d\mathbf{x}/dt = \mathbf{f}(\mathbf{x})$, where $\mathbf{x} \in \mathbf{R}$, and \mathbf{f} is C^∞ -class. Assume there is an equilibrium point \mathbf{x}_0 in the state space. Let J be a Jacobian matrix of \mathbf{f} , then the characteristic equation of \mathbf{x}_0 is given by:

$$\chi(\mathbf{x}_0) = \det(J - \mu I) = 0 \quad (3)$$

where, I is an $n \times n$ identity matrix. Hopf bifurcation is occurred when a couple of complex conjugate eigenvalues μ , $\bar{\mu}$ moves from the left half plane to the right half plane with a certain argument. Usually Hopf bifurcation condition are given by substituting $\mu = 0 + j\omega$ into Eq.(3), and it gives a bifurcation set (curve) in a parameter space. In general, after this bifurcation we have a limit cycle, and its angular velocity is ω . Note that the Jacobian matrix contains a first-order term of \mathbf{x}_0 if \mathbf{f} is given by an odd function nonlinearity of \mathbf{x} .

IV. PHASOR METHOD

The phasor method is popular and very useful for calculating or designing alternative current circuits.

It is practically applied to not only elementary circuit theory but advanced circuit technology for a long time. It can be naturally assumed that every electrical engineer knows this method nowadays.

There are two ways how to obtain a Hopf bifurcation condition from linear circuit elements. They are dual:

- insert a virtual voltage source in serial into any cut set of a closed loop linear circuit. To retain a nonzero current in the circuit, the whole impedance Z should be 0 when the virtual voltage source is removed.
- attach a virtual current source to any closed loop linear circuit in parallel. To retain a nonzero voltage in the circuit, the whole admittance Y should be 0 when the virtual current source is removed.

These assumptions directly correspond to Hopf bifurcation conditions. We show this by using some examples in the following sections.

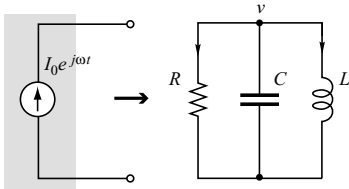


Fig. 1. a virtual alternative current source in an LCR parallel circuit.

We show an illustrative example. Figure 1 shows an LCR parallel circuit with a virtual alternative current source. Suppose that a resistance r is connected to a coil L in serial. The whole impedance of the circuit is given by:

$$Z_1 = (r_1 + j\omega L_1) \parallel \frac{1}{j\omega C} \parallel R \quad (4)$$

More concretely,

$$Z_1 = \frac{R(r_1 + j\omega L_1)}{r_1 + R - \omega^2 RL_1 C + j\omega(L_1 + r_1 RC)} \quad (5)$$

When the current source is connected, the closed circuit equation is as follows:

$$Z_1^{-1}V = YV = I$$

To obtain an autonomous oscillation in this circuit, V should not be zero constantly when the voltage source is removed. Therefore, the admittance should be infinity: $Y = 0$, i.e., the denominator of Eq.(5) should be $0 + j0$. From the real and imaginary parts, we have

$$R + r_1 - \omega^2 RL_1 C = 0 \quad (6)$$

$$\omega(L_1 + Rr_1 C) = 0. \quad (7)$$

Thus,

$$\omega = \sqrt{\frac{R + r_1}{RL_1 C}} \quad (8)$$

$$Rr_1 = -\frac{L_1}{C}. \quad (9)$$

We assume that $L_1 > 0$, $C > 0$, Eq. (9) naturally requires a negative resistance.

If R in Fig.1 is nonlinear, especially, it is given by an odd function nonlinear conductance $g(v)$, the circuit without current source can be regarded as a BVP oscillator. The circuit equation is written in the form:

$$C \frac{dv}{dt} = -g(v) - i, \quad L \frac{di}{dt} = v - ri \quad (10)$$

Usually we try to analyze Hopf bifurcation with the method shown in Sec.III. The Jacobian matrix of the equilibrium point is given by:

$$J = \begin{pmatrix} -\frac{1}{CR} & -\frac{1}{C} \\ \frac{1}{L} & -\frac{r}{L} \end{pmatrix}. \quad (11)$$

where, R is an inverse value of a constant term of $dg(v)/dv$. Then the characteristic equation is as follows:

$$\mu^2 + \left(\frac{1}{CR} + rL \right) \mu + \frac{R+r}{CRL} = 0 \quad (12)$$

By substituting $\mu = 0 + j\omega$ into Eq. (12), finally we have Eq. (8) and (9). Thus it is intuitively shown that both the phasor method with a virtual source and the Hopf bifurcation analysis derive the same Hopf bifurcation condition.

In a linear circuit, such bifurcation gives a critical situation, i.e., after the bifurcation, the state diverges immediately. Thus it is required a global stability in the system. Typically N-shape conductance is chosen, that is, the conductance acts as a positive resistance for large amplitude of v and i .

V. BARKHAUSEN CRITERION

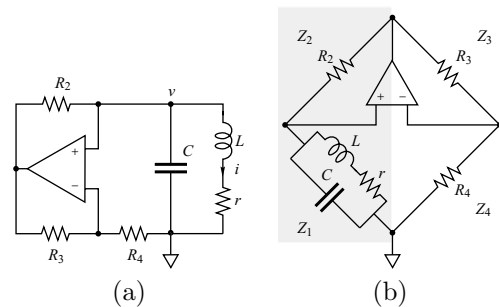


Fig. 2. Two viewpoints of the BVP oscillator with a nonlinear conductor composed by an operational amplifier.

An oscillator is designed by circuit including an amplifier block and a feedback block. In text books explain some points of generating and regulating of oscillation; positive feedback loop for feeding the output back to the input with the same phase, and negative feedback loop for control the amplitude of the oscillation. Barkhausen criterion (2) is instantly induced

from Eq.(1). This condition also gives a critical parameter values of the stability of the closed loop containing linear transfer functions, then this condition is also equivalent to Hopf bifurcation condition.

We show an example. Fig.2 (a) show a BVP oscillator with a nonlinear conductor implemented by an operational amplifier. An LC tank in positive feedback loop creates an oscillation, and divergence of the amplitude is suppressed by the negative feedback loop composed by R_3 and R_4 . The feedback ratio of the positive feedback loop is given as:

$$\beta = \frac{Z_2}{Z_1 + Z_2} = \frac{R_2(1 - \omega^2 LC + j\omega Cr)}{r + R_2 - \omega^2 LC R_2 + j\omega L + j\omega Cr R_2} \quad (13)$$

From the first equation of Eq. (2), we have $A(j\omega) = 1/\beta(j\omega) = 1$, then A is real. From the second equation of Eq. (2), the imaginary part of the denominator of $\beta(j\omega)$ determine the frequency condition. By arranging them, finally we have Eq. (8) and (9).

We also show a bridge formation of the BVP oscillator in Fig. 2 (b). One can see that the equilibrium condition of the bridge corresponds to the characteristic equation, i.e, $Z_1 Z_3 - Z_2 Z_4 = 0$ indicates

$$\chi = \frac{r + j\omega L}{1 - \omega^2 LC + j\omega Cr} \cdot R_3 - R_2 R_4 = 0. \quad (14)$$

If one uses $R = R_3 = R_4$, we have exactly Eq. (8) and (9).

We have seen that the phasor method with a virtual source, Barkhausen criterion and Hopf bifurcation analysis are equivalent each other unless the system is considered in linear region. The relationship among Routh-Hurwitz, Nyquist method and Hopf bifurcation is an interesting topic. We would like to remark here that Hopf bifurcation set is obtained from issues on impedances of the AC circuit theory. Note that there are some special cases that the equilibrium condition can be degenerated. No oscillation is occurred in such cases. Note also that above methods only give critical curves (bifurcation curves), thus the 'oscillatory area' should be confirmed by checking eigenvalues by numerical simulations and so on.

One of merits of the phasor method is convenience of calculation for impedances or admittance. As far as a circuit is composed by linear elements, algebraic calculation is available consistently.

VI. EXTENDED BVP OSCILLATOR

If the whole impedance is known, one can easily investigate influence on parameter values and frequency by the phasor method if a new element is attached into the system. As an application of the phasor method with a virtual source, we now consider modification of the BVP oscillator[1].

The circuit shown in Fig. 3 is obtained by add one more coil to Fig. 1. If R is expressed as a nonlin-

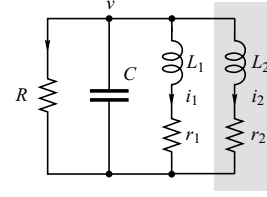


Fig. 3. Extended BVP oscillator—added one more coil into the circuit shown in Fig.1.

ear function, this circuit is called the extended BVP oscillator.

The whole impedance is obtained by utilizing Z_1 which is already calculated as Eq. (5):

$$Z_2 = Z_1 \parallel (r_2 + j\omega L_2) \quad (15)$$

By setting $0 + j0$ for the denominator of Z_2 , we have

$$R(r_1 + r_2) + r_1 r_2 - \omega^2 (r_2 R L_1 C + L_2 (r_1 R C + L_1)) = 0 \quad (16)$$

$$R(L_1 + L_2) + r_1 L_2 + r_2 L_1 + r_1 r_2 R C - \omega^2 R L_1 L_2 C = 0 \quad (17)$$

Then from Eq. (17), the frequency condition is obtained:

$$\omega = \sqrt{\frac{(r_1 + r_2)R + r_1 r_2}{L_1 L_2 + r_2 R C L_1 + r_1 R L_2 C}} \quad (18)$$

By substituting this into Eq. (17), Hopf bifurcation set may be exploited.

Eq.(18) almost equals to the frequency of a limit cycle generated after Hopf bifurcation. Eq. (18) is a function of r_1 and r_2 , in other words, resistors can control frequency of the limit cycle. In the case of $r_2 \rightarrow \infty$,

$$\omega_\infty = \sqrt{\frac{R + r_1}{R L_1 C}}. \quad (19)$$

This coincide with Eq. (8), thereby the system degenerates to the 2nd dimensional BVP system. On the other hand, in the case of $r_2 = 0$,

$$\omega_0 = \sqrt{\frac{R r_1}{L_1 L_2 + R r_1 L_2 C}}, \quad (20)$$

it shows an independent frequency compared with ω_∞ . This result means that different two frequency is obtained by changing a parameter monotonically.

A nonlinear conductance is approximated as $i = g(v) = a \tanh bv$. Assume that $\alpha = L_2/L_1$, $k = r\sqrt{C/L_1}$, $\gamma = ab\sqrt{L_1/C}$. Then the Hopf bifurcation curve is drawn in Fig. 4.

We notice that two different frequencies are obtained by changing only k_2 from Eqs (19) and (20) and this bifurcation diagram. We confirm these results by laboratory experiments. Let us choose parameters for the extended BVP oscillator as: $C = 0.022[\mu F]$, $r_1 = 500[\Omega]$, $L_1 = 10[mH]$, $L_2 = 1[mH]$.

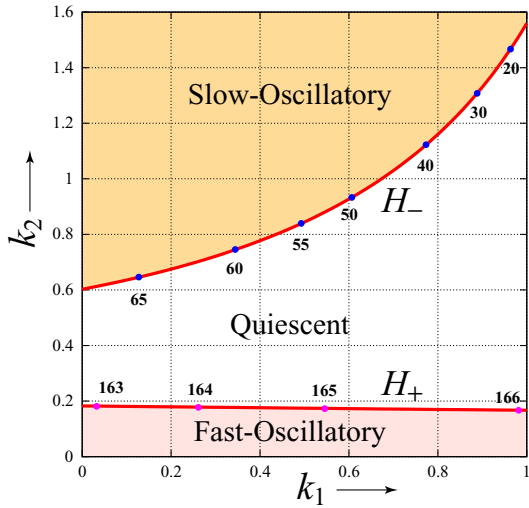


Fig. 4. Hopf bifurcation diagram in k_1 - k_2 plane

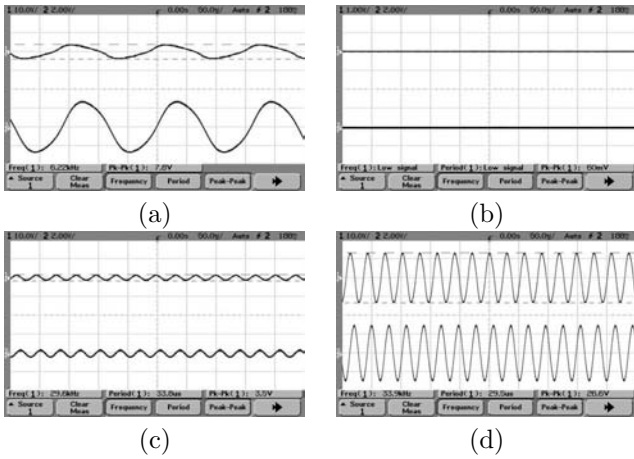


Fig. 5. Measured waves of v and $r_1 \cdot i_1$. (a) $r_2 = 100$ [k Ω], $L_2, r_2, 6$ [kHz]. (b) $r_2 = 400$ [Ω], the oscillation is dead. (c) $r_2 = 100$ [Ω], rebirth an oscillation, 34[kHz]. (d) $r_2 = 0$ [Ω], obtained a large amplitude.

Figure 5 show two frequency oscillations by changing the parameter r_2 . Therefore, we can control the oscillation modes in three-dimensional system with only one parameter.

Finally we show bifurcation phenomenon of Hopf bifurcation curves related with above result. Figure 6 show Hopf bifurcation diagrams with various values of α . One can see merging and separation of bifurcation curves. Even though this phenomenon can not be confirmed with positive values of k_1 and k_2 (equivalently r_1 and r_2), it is very important to investigate this phenomenon in dynamical system point of view.

REFERENCES

[1] K. Yoshikawa et. al, "New strategy of informational processing: Utilization of nonlinear dynamics to chemical sensing," Physica A, Vol. 188, pp. 243-250, June 1992.
 [2] E. Lindberg, "Oscillators — an approach for a better understanding," a tutorial paper, ECCTD'03, Krakow, Poland, September 2003.

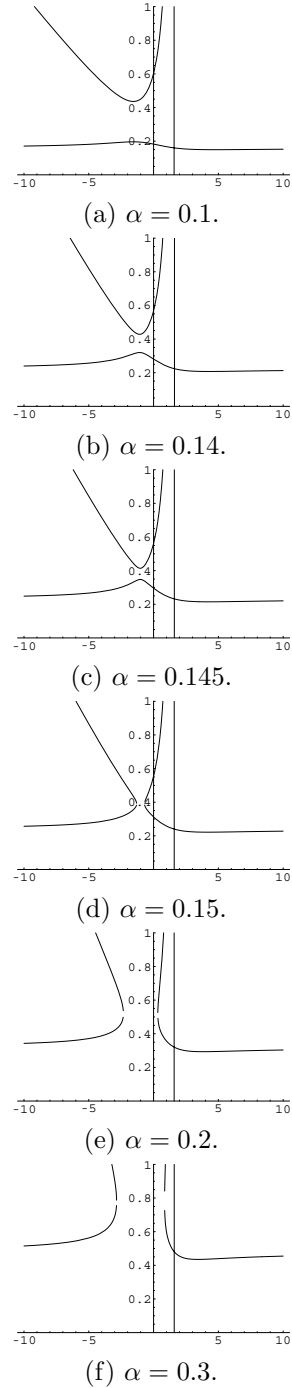


Fig. 6. Bifurcation Hopf bifurcation set in k_1 - k_2 plane. $\gamma = 1.6$.

Floquet Numbers and Dynamic Eigenvalues

P. van der Kloet and F.L. Neerhoff

Dept. of Electrical Engineering
Delft University of Technology

Mekelweg 4, 2628 CD Delft, The Netherlands

e-mail: F.L.Neerhoff@ewi.tudelft.nl; P.vanderKloet@ewi.tudelft.nl

Abstract—*The relation between Floquet numbers and dynamic eigenvalues is derived.*

I. INTRODUCTION

Electronic circuits are nonlinear by nature. Roughly speaking, two different kinds of operation can be distinguished. The first one is described by the behavior of small signals around a fixed operating point, like class A amplifiers. The behavior of small signals can be derived as a set linear algebraic differential equations with constant coefficients. This set of equations is used for stability problems, distortion problems, noise problems and so on. In a mathematical sense, the set of equations is obtained by considering variations around the fixed operating point and hence known as the set of variational equations.

The second kind of operation contains circuits that behave in a time-varying mode of operation, like oscillators. Here also the set of variational equations is identified as a set of linear differential equations. The coefficients, however, are time-dependent. The field of applications is the same as in the first kind of operation: stability problems, distortion problems, noise problems and so on. The time-behavior of the coefficients in the variational equations is derived from the time-behavior of the (time-varying) mode of the circuit. For oscillators, the coefficients of the variational (differential) equations are periodic functions of time. In [1] a representation for the solution of linear time-varying differential equations is derived, either in the form of the fundamental matrix or in the form of a sum of modal solutions. Moreover, it is shown there that these modal solutions reduce to the well-known modal solutions of the exponential type for invariant sets of equations. These modal solutions are characterized for circuits with n dynamical elements as the product of a n -dimensional dynamic eigenvector and an exponential function containing the dynamic eigenvalues. For the subclass of linear time-varying differential equations with periodic coefficients the fundamental solution can also be represented as the product of a pe-

riodic matrix and an exponential matrix containing the Floquet numbers [2]. As a consequence there are two representations for solutions of linear time-varying differential equations with periodic coefficients.

Since the solution is unique, there must be relations between the periodic matrix and Floquet numbers on one hand, and the dynamic eigenvectors and dynamic eigenvalues on the other. It turns out that the Floquet numbers are mean values of the dynamic eigenvalues. As a consequence dynamic eigenvalues contain more detailed information in comparison with the Floquet numbers. They are relevant in general stability problems [3] for nonlinear systems and they might give a theoretical base of moving poles in oscillator problems [4].

The paper is divided in 5 sections. After this introduction, in section 2 is shown how modal solutions can be obtained for second order systems. In section 3 two examples, both with periodic coefficients are discussed. In both examples, the dynamic eigenvalues are collected in a diagonal matrix. This formulation deviates from the Floquet representations in both cases. It is shown in this section how these deviations can be suppressed. In section 4 some remarks with respect to the equivalence Floquet numbers and the mean value of dynamic eigenvalues is discussed. In section 5 some conclusions are formulated.

II. THE RICCATI EQUATION FOR A SECOND ORDER SYSTEM

In this section a second order system is treated. It is shown how a diagonalization process is derived, involving two transformations. Both contain one unknown function. Consider

$$\left. \begin{aligned} \dot{x}_1 &= a_{11}(t)x_1 + a_{12}(t)x_2 \\ \dot{x}_2 &= a_{21}(t)x_1 + a_{22}(t)x_2 \end{aligned} \right\} \Leftrightarrow \dot{\mathbf{x}} = \mathbf{A}\mathbf{x} \quad (1)$$

Apply a first transformation

$$\left. \begin{aligned} x_1 &= y_1 \\ x_2 &= p_1(t)y_1 + y_2 \end{aligned} \right\} \Leftrightarrow \mathbf{x} = \mathbf{P}_1\mathbf{y} \quad (2)$$

If p_1 satisfies

$$\dot{p} = -a_{12}p^2 - (a_{11} - a_{22})p + a_{21} \quad (3)$$

then we get

$$\left. \begin{aligned} \dot{y}_1 &= \lambda_1(t, p_1)y_1 + a_{12}y_2 \\ \dot{y}_2 &= \lambda_2(t, p_1)y_2 \end{aligned} \right\} \Leftrightarrow \dot{\mathbf{y}} = \mathbf{B}_1 \mathbf{y} \quad (4)$$

Here

$$\left. \begin{aligned} \lambda_1(t, p_1) &= a_{11} + a_{12}p_1 \\ \lambda_2(t, p_1) &= a_{22} - a_{12}p_1 \end{aligned} \right\} \quad (5)$$

The functions λ_1 and λ_2 are called the dynamic eigenvalues of (1). Of course λ_1 and λ_2 depend on the chosen solution $p_1(t)$ of the Riccati equation (3), that is on the initial value $p_1(0)$ which generates $p_1(t)$. To show this, transform (4) according to

$$\left. \begin{aligned} y_1 &= y_1^{(1)} \\ y_2 &= v_1 y_1^{(1)} + y_2^{(1)} \end{aligned} \right\} \Leftrightarrow \mathbf{y} = \mathbf{P}_2 \mathbf{y}^{(1)} \quad (6)$$

Remark that the transformation $\mathbf{P}_1 \mathbf{P}_2$ can be written as a single transformation of the same type as \mathbf{P}_1 and \mathbf{P}_2

$$\mathbf{P}_1 \mathbf{P}_2 = \begin{bmatrix} 1 & \\ p_1 + v_1 & 1 \end{bmatrix} \quad (7)$$

If v_1 satisfies

$$\dot{v} = -a_{12}v^2 - (a_{11} - a_{22} + 2p_1 a_{12})v \quad (8)$$

then (4) and (6) yield

$$\left. \begin{aligned} \dot{y}_1^{(1)} &= \lambda_1(t, p_1 + v_1)y_1^{(1)} + a_{12}y_2^{(1)} \\ \dot{y}_2^{(1)} &= \lambda_2(t, p_1 + v_1)y_2^{(1)} \end{aligned} \right\} \Leftrightarrow \dot{\mathbf{y}}^{(1)} = \mathbf{B}_2 \mathbf{y}^{(1)} \quad (9)$$

This suggests that $p_1 + v_1$ is also a solution of the Riccati equation (3). A simple proof confirms the assertion. Moreover it suggests that for our purpose (6) is redundant and is just a change of the initial value. Remark that (8) can easily be solved by changing the dependent variable according to

$$w = v^{-1} \quad (10)$$

so that there results a linear equation

$$\dot{w} = a_{12} + (a_{11} - a_{22} + 2p_1 a_{12})w \quad (11)$$

Next (4) will be forced to a diagonal form using the second transformation

$$\left. \begin{aligned} y_1 &= z_1 + q_1 z_2 \\ y_2 &= z_2 \end{aligned} \right\} \Leftrightarrow \mathbf{y} = \mathbf{Q}_1 \mathbf{z} \quad (12)$$

If q_1 satisfies

$$\dot{q} = \{\lambda_1(t, p_1) - \lambda_2(t, p_1)\}q + a_{12} \quad (13)$$

then

$$\left. \begin{aligned} \dot{z}_1 &= \lambda_1(t, p_1)z_1 \\ \dot{z}_2 &= \lambda_2(t, p_1)z_2 \end{aligned} \right\} \Leftrightarrow \dot{\mathbf{z}} = \begin{bmatrix} \lambda_1 & 0 \\ 0 & \lambda_2 \end{bmatrix} \mathbf{z} \quad (14)$$

Apply next to (14)

$$\left. \begin{aligned} z_1 &= z_1^{(1)} + w_1 z_2^{(1)} \\ z_2 &= z_2^{(1)} \end{aligned} \right\} \Leftrightarrow \mathbf{z} = \mathbf{Q}_2 \mathbf{z}^{(1)} \quad (15)$$

We get (14) back, but now for $z_1^{(1)}$ and $z_2^{(1)}$, if w_1 satisfies

$$\dot{w} = \{\lambda_1(t, p_1) - \lambda_2(t, p_1)\}w \quad (16)$$

Remark that (13) and (16) yield

$$(q+w)' = \{\lambda_1(t, p_1) - \lambda_2(t, p_1)\}(q+w) + a_{12} \quad (17)$$

Or in operator formulation, the product operator

$$\mathbf{Q}_1 \mathbf{Q}_2 = \begin{bmatrix} 1 & q_1 + w_1 \\ 0 & 1 \end{bmatrix} \quad (18)$$

is of the same type as the operators itself. So q_1 can be given any initial value to get an unique solution of (1). We can now state the solution of (1) as

$$\begin{bmatrix} x_1 \\ x_2 \end{bmatrix} = \mathbf{P}_q(t) \begin{bmatrix} e^{\gamma_1(t)} & 0 \\ 0 & e^{\gamma_2(t)} \end{bmatrix} \mathbf{P}_q^{-1}(0) \begin{bmatrix} x_1(0) \\ x_2(0) \end{bmatrix} \quad (19)$$

where

$$\mathbf{P}_q(t) = \begin{bmatrix} 1 & 0 \\ p(t) & 1 \end{bmatrix} \begin{bmatrix} 1 & q(t) \\ 0 & 1 \end{bmatrix} \quad (20)$$

The functions $\gamma_i(t)$ are defined by

$$\gamma_i(t) = \int_0^t \lambda_i(\tau) d\tau \quad (21)$$

III. EXAMPLES

In this section two examples will be presented to illustrate the material of section 2. Both examples concern periodic systems. The first example is a classical one ([5]). Its main purposes are to give an insight in the presented theory and to show the advantages of making choices for the initial values of $p(t)$ and $q(t)$. Moreover, it shows how periodic parts in the dynamic eigenvalues can be treated in order to obtain the Floquet decomposition. For the second example it is also the goal to derive the Floquet decomposition. Here

the matrix in the exponential of this decomposition is not a diagonal one. We show by choosing two initial values for $p(t)$ that the Floquet decomposition is not always obvious.

As first example we have

$$\begin{aligned} \dot{x}_1 &= (-1 + \alpha \cos^2 t)x_1 + (1 - \alpha \sin t \cos t)x_2 \\ \dot{x}_2 &= (-1 - \alpha \sin t \cos t)x_1 + (-1 + \alpha \sin^2 t)x_2 \end{aligned} \quad (22)$$

The system has classical eigenvalues given by

$$\begin{aligned} \det \begin{bmatrix} \lambda + 1 - \alpha \cos^2 t & -1 + \alpha \sin t \cos t \\ 1 + \alpha \sin t \cos t & \lambda + 1 - \alpha \sin^2 t \end{bmatrix} &= 0 \leftrightarrow \\ \leftrightarrow \lambda_{1,2} &= \left(\frac{1}{2}\alpha - 1\right) \pm \sqrt{\frac{1}{4}\alpha^2 - 1} \end{aligned} \quad (23)$$

For $\alpha = 2$ we have $\lambda_{1,2} = 0$. For $\alpha > 2$ one eigenvalue is positive. We will show in due course that this system is unstable for $\alpha > 1$; this is not in line with the suggestions given by the eigenvalues. For $\alpha < 2$ the eigenvalues are complex conjugated with negative real part. Also here a discrepancy in use of eigenvalues. The Riccati equation reads for this example

$$\dot{p} + p^2 + 1 = \alpha[p \cos t + \sin t][p \sin t - \cos t] \quad (24)$$

This has as a solution

$$p_1 = -\tan(t) \quad (25)$$

With $p = p_1 + v_1$, (8), (10) and (11) the general solution of (24) can be obtained as

$$p(t) = \frac{p(0) \cos t - \sin t e^{\alpha t}}{p(0) \sin t + \cos t e^{\alpha t}} \quad (26)$$

Remark that for $p(0) = \infty$ the periodic solution $p_2 = \cot(t)$ is obtained. This solution together with the solution p_1 are the only periodic solutions of (24). All the others are nonperiodic. Moreover, the two solutions $p = -\tan t$ and $p = \cot t$ do not depend on the initial conditions. They serve in some way as equilibrium solutions for the Riccati equations. If $\alpha > 0$ then $p = -\tan t$ can be considered as the stable solution, while for $\alpha < 0$ the solution $p = \cot t$ is stable. We get for (5)

$$\left. \begin{aligned} \lambda_1(t, p_1) &= \alpha - 1 - \tan t \\ \lambda_2(t, p_1) &= -1 + \tan t \end{aligned} \right\} \quad (27)$$

and for (13) we get

$$\dot{q} + (2 \tan t)q - 1 = \alpha[q - \sin t \cos t] \quad (28)$$

It is easy to see that a solution is

$$q_1(t) = \sin t \cos t \quad (29)$$

The general solution of (28) is

$$q(t) = \sin t \cos t + q(0) \cos^2 t e^{\alpha t} \quad (30)$$

which is not periodic unless $q(0) = 0$ is satisfied. With (21) it follows that

$$\left. \begin{aligned} \gamma_1(t) &= (\alpha - 1)t + \ln |\cos t| \\ \gamma_2(t) &= -t + \ln |\cos t|^{-1} \end{aligned} \right\} \quad (31)$$

The next problem is to obtain the Floquet decomposition of (22) and the relation with (27). It is remarked that λ_i ($i = 1, 2$) is periodic, but this will not be true for γ_i ($i = 1, 2$). We state that (14) has for this example the solution

$$\left. \begin{aligned} z_1(t) &= e^{(\alpha-1)t} \cos t \\ z_2(t) &= e^{-t} (\cos t)^{-1} \end{aligned} \right\} \quad (32)$$

In (32) is already build in that we want

$$z_1(0) = z_2(0) = 1 \quad (33)$$

With (25), (29), and (31) we now obtain for (19)

$$\begin{aligned} \begin{bmatrix} x_1 \\ x_2 \end{bmatrix} &= \begin{bmatrix} 1 & \sin t \cos t \\ -\tan t & \cos^2 t \end{bmatrix} \begin{bmatrix} \cos t & 0 \\ 0 & (\cos t)^{-1} \end{bmatrix} \times \\ &\times \begin{bmatrix} e^{(\alpha-1)t} & 0 \\ 0 & e^{-t} \end{bmatrix} \begin{bmatrix} x_1(0) \\ x_2(0) \end{bmatrix} \end{aligned} \quad (34)$$

Thus in the Floquet decomposition

$$\mathbf{x}(t) = \mathbf{F}(t)e^{\mathbf{S}t}\mathbf{x}(0) \quad (35)$$

we have

$$\mathbf{F}(t) = \begin{bmatrix} \cos t & \sin t \\ -\sin t & \cos t \end{bmatrix} \quad \mathbf{S} = \begin{bmatrix} \alpha - 1 & 0 \\ 0 & -1 \end{bmatrix} \quad (36)$$

The second example [5]

$$\left. \begin{aligned} \dot{x}_1 &= -x_1 \\ \dot{x}_2 &= -\cos t x_1 \end{aligned} \right\} \quad (37)$$

serves to show that the outlined procedure does not lead to a Floquet decomposition in a direct way. This depends on the chosen initial values for the Riccati equation. Secondly, this example shows that the matrix in the exponent of the Floquet decomposition is not necessarily diagonal. Here, (37) yields a simplified form of the Riccati equation

$$\dot{p} = p - \cos t \quad (38)$$

with as a general solution

$$p = \frac{1}{2}(\cos t - \sin t) + Ke^t \quad (39)$$

If the initial value $p(0) = 0$ is used, then we find

$$\begin{bmatrix} x_1 \\ x_2 \end{bmatrix} = \begin{bmatrix} 1 & 0 \\ \frac{1}{2}(\cos t - \sin t) - \frac{1}{2}e^t & 1 \end{bmatrix} \begin{bmatrix} e^{-t} & 0 \\ 0 & 1 \end{bmatrix} \times \begin{bmatrix} x_1(0) \\ x_2(0) \end{bmatrix} \quad (40)$$

This is not a Floquet representation. If $p(0) = \frac{1}{2}$, then we have

$$\begin{bmatrix} x_1 \\ x_2 \end{bmatrix} = \begin{bmatrix} 1 & 0 \\ \frac{1}{2}(\cos t - \sin t) & 1 \end{bmatrix} \begin{bmatrix} e^{-t} & 0 \\ 0 & 1 \end{bmatrix} \times \begin{bmatrix} 1 & 0 \\ -\frac{1}{2} & 1 \end{bmatrix} \begin{bmatrix} x_1(0) \\ x_2(0) \end{bmatrix} \quad (41)$$

yielding a periodic part, but now the exponential part causes trouble. Using

$$\begin{bmatrix} 1 & 0 \\ \frac{1}{2} & 1 \end{bmatrix} \begin{bmatrix} e^{-t} & 0 \\ 0 & 1 \end{bmatrix} \begin{bmatrix} 1 & 0 \\ -\frac{1}{2} & 1 \end{bmatrix} = \exp \left\{ \begin{bmatrix} -1 & 0 \\ -\frac{1}{2} & 0 \end{bmatrix} t \right\} \quad (42)$$

it becomes obvious that (41) can be rewritten in the form (35) with

$$\mathbf{F}(t) = \begin{bmatrix} 1 & 0 \\ \frac{1}{2}(\cos t - \sin t) - \frac{1}{2} & 1 \end{bmatrix}, \mathbf{S} = \begin{bmatrix} -1 & 0 \\ -\frac{1}{2} & 0 \end{bmatrix} \quad (43)$$

Note that \mathbf{S} is not diagonal.

IV. THE RELATION BETWEEN FLOQUET NUMBERS AND DYNAMIC EIGENVALUES

In the preceding section, we have shown for two examples, (22) and (37), that their modal solutions can be transformed into their Floquet representations (35), (36) and (43). Both examples show that the mean value of the dynamic eigenvalues equals the Floquet numbers of the differential equation.

To demonstrate this in a more general sense, the modal solution (19) of (1) will be written as

$$\mathbf{x}(t) = \mathbf{P}_q(t) \begin{bmatrix} e^{\gamma_1(t)} & 0 \\ 0 & e^{\gamma_2(t)} \end{bmatrix} \mathbf{P}_q^{-1}(0) \mathbf{x}(0) \quad (44)$$

The solution $p(t)$ in $\mathbf{P}_q(t)$ is assumed to be a periodic solution of (3). In [6] it is indicated when there are periodic solutions $p(t)$. Then also the dynamic eigenvalues $\lambda_1(t)$ and $\lambda_2(t)$ are periodic. With the theory of Fourier series, their integrals $\gamma_1(t)$ and $\gamma_2(t)$ thus have a linear component and a periodic part. Let us write

$$\gamma_i(t) = \{\gamma_i(t) - \bar{\lambda}_i t\} + \{\bar{\lambda}_i t\} \quad (45)$$

where

$$\bar{\lambda}_i = \frac{1}{T} \int_0^T \lambda_i(\tau) d\tau \quad (46)$$

So that

$$\begin{bmatrix} e^{\gamma_1(t)} & 0 \\ 0 & e^{\gamma_2(t)} \end{bmatrix} = \begin{bmatrix} e^{\gamma_1(t) - \bar{\lambda}_1 t} & 0 \\ 0 & e^{\gamma_2(t) - \bar{\lambda}_2 t} \end{bmatrix} \begin{bmatrix} e^{\bar{\lambda}_1 t} & 0 \\ 0 & e^{\bar{\lambda}_2 t} \end{bmatrix} \quad (47)$$

And (19) can be written as (35) with

$$\mathbf{F}(t) = \mathbf{P}_q(t) \begin{bmatrix} e^{\gamma_1(t) - \bar{\lambda}_1 t} & 0 \\ 0 & e^{\gamma_2(t) - \bar{\lambda}_2 t} \end{bmatrix} \mathbf{P}_q^{-1}(0) \quad (48)$$

and

$$\mathbf{S} = \mathbf{P}_q(0) \begin{bmatrix} \bar{\lambda}_1 & 0 \\ 0 & \bar{\lambda}_2 \end{bmatrix} \mathbf{P}_q^{-1}(0) \quad (49)$$

V. CONCLUSIONS

In this paper the Floquet representation for the solution of a periodic differential equation is derived. First the modal solution is obtained which is the sum of number of modes. Each mode is the product of a dynamic eigenvector and an exponential whose argument is the integral of a dynamic eigenvalue.

It is argued that under certain conditions the dynamic eigenvalues are periodic and that the exponentials are the product of an exponential with a periodic argument and a second exponential with a linear argument. It is remarked that the slope of the linear arguments equals the mean value of the dynamic eigenvectors over one period of the coefficients, so this mean value is a Floquet number. Since the dynamic eigenvector is obtained solving a differential equation of Riccati, it is not necessary first to solve the original differential equation in order to obtain the Floquet numbers!

REFERENCES

- [1] Van der Kloet, P., *Modal Solutions for Linear Time Varying Systems*, PhD. Thesis, Delft University of Technology, Delft, The Netherlands, 2002.
- [2] Farkas, M., *Periodic Motions*, Springer Verlag, New York, 1994.
- [3] Jordan, D.W. and P. Smith, *Nonlinear Ordinary Differential Equations*, Oxford University Press, 1999.
- [4] Lindberg, E., *Oscillators, Hysteresis and "Frozen Eigenvalues"*, Proc. NDES 2003, Scuol, Switzerland, May 18-22, 2003, pp. 153-156.
- [5] Rugh, W.J., *Linear System Theory*, Prentice Hall, New Jersey, 1993, ISBN 0-13-555038-6. *Theorie nichtlinearer Netzwerke*, Springer Verlag, Berlin, 1987.
- [6] Bittanti, S., P. Colaneri and G. Guerdabassi, *Periodic Solutions of Periodic Riccati Equations*, IEEE Trans. A.C., Vol. AC-29, No. 7, 1984, pp. 665-667.

SYNCHRONIZATION IN MODELS OF DISCRETE PHASE OSCILLATORS

Anna Vasylenko^{1,2}, Yuri Maistrenko^{2,3} and Martin Hasler¹

¹ Laboratory of Nonlinear Systems, Swiss Federal Institute of Technology,
CH-1015, Lausanne, Switzerland

² Institute of Mathematics, National Academy of Sciences of Ukraine,
3 Tereshchenkivska st, 01601, Kyiv, Ukraine

³ Institute of Medicine, Research Centre Jülich,
52425, Jülich, Germany

Abstract— We investigate the phase synchronization of two and three coupled nonlinear oscillators (or clocks) whose individual dynamics are described by the shift circle maps. We outline the synchronization regions and explore the bifurcations through which the synchronization is achieved and lost.

I. SYNCHRONIZATION IN THE SYSTEM OF TWO COUPLED PHASE OSCILLATORS

A. The model

Let us consider the system of two coupled oscillators, or clocks, of the following form

$$\begin{aligned} x_{n+1} &= x_n + 2\pi\nu_1 + \frac{K}{2} \sin(y_n - x_n), \\ y_{n+1} &= y_n + 2\pi\nu_2 + \frac{K}{2} \sin(x_n - y_n), \end{aligned} \quad (1)$$

where both the variables x and y are calculated modulo 2π . System (1) describes dynamics of two phase oscillators with the corresponding frequencies ν_1 and ν_2 , which are mutually coupled with the sine coupling and K is the coupling strength. The system (1) may be considered as a discrete analog of the continuous-time Kuramoto model [1]:

$$\dot{\psi}_i = \omega_i + \frac{K}{N} \sum_{j=1}^N \sin(\psi_j - \psi_i). \quad (2)$$

The synchronization can be expressed in terms of the difference between the phase variables x_n and y_n . After subtracting the second equation from the first one the following equation for the phase difference $z_n = x_n - y_n$ is obtained:

$$z_{n+1} = z_n + 2\pi(\nu_1 - \nu_2) - K \sin z_n, \quad (3)$$

which is well known Arnol'd sine circle map (3). Therefore synchronization for the system (1) can be clearly achieved, e.g. with the parameter values for which the map has an attracting fixed point $z = \arcsin \frac{2\pi(\nu_1 - \nu_2)}{K}$.

B. Synchronization regions for the discrete-time model

While considering two identical oscillators, i.e. $\nu_1 = \nu_2$, the map (3) has the fixed point $z = 0$ which corresponds to full synchronization in (1): $|x_n - y_n| \rightarrow 0$ as $n \rightarrow \infty$. For the oscillators with different frequencies ν_1 and ν_2 the fixed point is $z \neq 0$, and its stability, if it takes place, means that the oscillators are synchronized but with a nonzero phase difference $|x_n - y_n| \rightarrow z$ as $n \rightarrow \infty$. The map (3) can also exhibit synchronized periodic orbits of higher periods as well as synchronized, when there exist $C > 0$ $|z_n| < C \quad \forall n$.

Figure 1 shows phase-locking regions - so-called Arnol'd tongues of the following rotation numbers $\rho = 0, \frac{1}{3}, \frac{1}{2}, \frac{1}{1}$. Each tongue emanates from a point $(p/q, 0)$ for integer p and q , and corresponds to the existence of stable and unstable periodic orbits of period q and of the rotation number p/q .

For the values of K such that $K \leq 1$ the map (3) is invertible, the Arnol'd tongues do not intersect, and the system can exhibit only periodic or quasiperiodic dynamics. The widest phase-locking region of the rotation number $\rho = 0$ is bounded by the line $K = 2\pi(\nu_1 - \nu_2)$, which is a saddle-node bifurcation line for the stable and unstable fixed points. It is the lower desynchronization line shown in Figure 1. For the parameters values such that $K < 2\pi(\nu_1 - \nu_2)$ no fixed point exists.

Beyond the line $K = 1$ the map (3) becomes non-invertible. With increasing K inside the 0-tongue a period-doubling cascade occurs until the dynamics become chaotic. The synchronization is lost at the other, upper desynchronization line. It is the line where an internal boundary crisis occurs. Beyond this line almost all trajectories do not exhibit zero rotation numbers any more, and consequently, there is no synchronization for these parameter values.

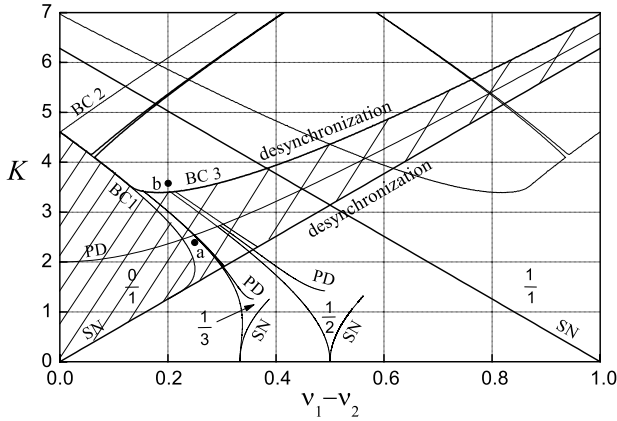


Fig. 1. Regions of the phase synchronization of the system (1) and bifurcation curves for the sine circle map (3): SN - saddle-node, PD - period doubling, BC - boundary crisis; the fractions show the corresponding rotation numbers for the Arnol'd tongues; the points *a* and *b* show the parameter values for the graphs of the map (3) in Fig.2.

The first boundary crisis line BC1 in Fig. 1 corresponds to the situation when the maximum value of the map becomes equal to the value of the unstable fixed point $z^{(u)} + 2\pi$. The second boundary crisis line BC2 represents the analogous situation but for the minimum value which becomes equal $z^{(u)} - 2\pi$. The line BC3 corresponds to the situation when the minimum value reaches the values of the channel appearing after the first boundary crisis. Then, the trajectories come to the unstable fixed point $z^{(u)} + 2\pi$ after the second iteration.

As shown in Fig. 2(a), after the first crisis BC1, depending on initial conditions a trajectory of the map (3) can be attracted to the stable fixed point $z^{(s)}$ or it can make one or more rotations around the circle and eventually, be attracted by z^s . Both these possibilities lead clearly to zero rotation number for the trajectory examined. Furthermore, the trajectory can make infinitely many rotations, i.e. tends to infinity in the corresponding lift from the circle $[0; 2\pi)$ to \mathbf{R}^1 . This behavior can lead to nonzero rotation number and hence, desynchronization. Therefore for the same parameters values beyond BC1-crisis one can observe trajectories with different rotation numbers, which means coexistence of synchronization and desynchronization.

II. DYNAMICS OF THE THREE-DIMENSIONAL SYSTEM

Now let us continue our analysis for the following system of three globally coupled phase oscillators

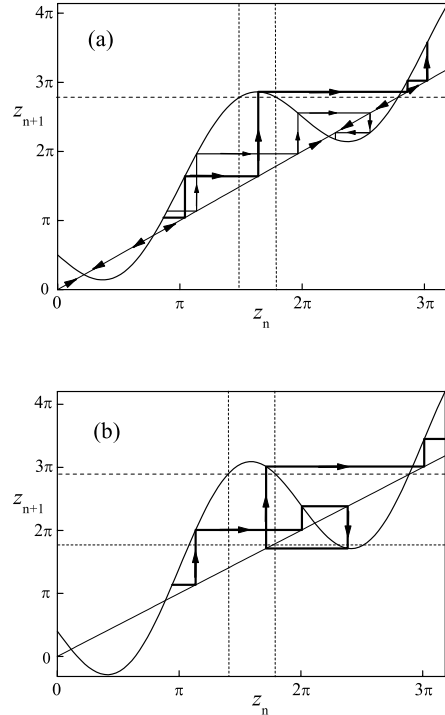


Fig. 2. Appearance of desynchronous orbits in the map (3) beyond the line BC1 (a) and BC1 and BC3 (b). In (a) desynchronous orbits coexist with synchronous ones attracted by the fixed points.

$$\begin{aligned} x_{n+1} &= x_n + 2\pi\nu_1 + \frac{K}{3} [\sin(y_n - x_n) + \sin(z_n - x_n)] \\ y_{n+1} &= y_n + 2\pi\nu_2 + \frac{K}{3} [\sin(x_n - y_n) + \sin(z_n - y_n)] \\ z_{n+1} &= z_n + 2\pi\nu_3 + \frac{K}{3} [\sin(x_n - z_n) + \sin(y_n - z_n)]. \end{aligned} \quad (4)$$

System (4) is a discrete analog of the three-dimensional Kuramoto model (2), and its analysis can be performed following ideology of the paper [2]. After successive subtracting the second and the third equations from the first one our system is reduced to the following two-dimensional system

$$\begin{aligned} u_{n+1} &= u_n + 2\pi\Delta_1 + \frac{K}{3} [-2\sin u_n \\ &\quad + \sin v_n - \sin(u_n + v_n)], \\ v_{n+1} &= v_n + 2\pi\Delta_2 + \frac{K}{3} [-2\sin v_n \\ &\quad + \sin u_n - \sin(u_n + v_n)], \end{aligned} \quad (5)$$

where $u_n = x_n - y_n$, $v_n = z_n - x_n$, $\Delta_1 = \nu_1 - \nu_2$, $\Delta_2 = \nu_3 - \nu_1$.

Let us consider different cases of the system (5).

A. $\Delta_1 = \Delta_2 = 0$

This is a case of three identical phase oscillators, i.e. their frequencies are equal: $\nu_1 = \nu_2 = \nu_3$. The system (5) has six fixed points with corresponding eigenvalues:

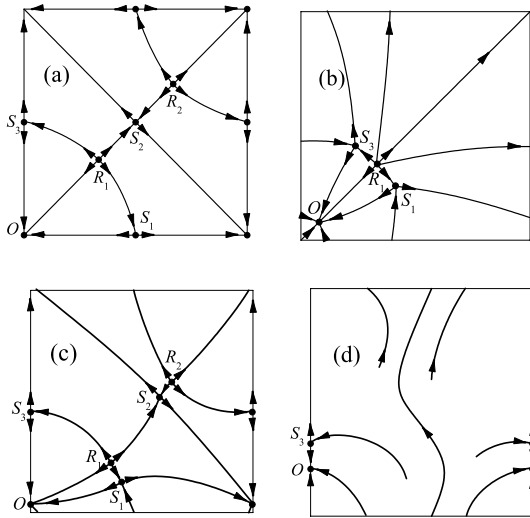


Fig. 3. Phase portraits of the system (5) with (a) $\Delta_1 = \Delta_2 = 0$, (b) $\Delta_1 = \Delta_2 = \Delta > 0$ and Δ and K after the pitchfork bifurcation P $S_1 \& R_1 \& S_3$, (c), (d) $\Delta_1 = 0$, Δ_2 and K before and after the saddle-node bifurcations SN $S_1 \& R_1$ and SN $S_2 \& R_2$.

$O(0, 0)$, $\lambda_1 = \lambda_2 = 1 - K$, which is an attracting node for $K < 2$,

$S_1(\pi, 0)$, $S_2(\pi, \pi)$, $S_3(0, \pi)$, $\lambda_1 = 1 - K/3$, $\lambda_2 = 1 + K$, saddles with $|\lambda_1| < 1$ for $K < 6$ and $\lambda_2 > 1$ for all positive K ,

$R_1(2\pi/3, 2\pi/3)$, $R_2(4\pi/3, 4\pi/3)$, $\lambda_1 = \lambda_2 = 1 + K/2$, repelling nodes for all positive K .

Phase portrait of the system with $\Delta_1 = \Delta_2 = 0$ is schematically presented in the Figure 3(a).

B. $\Delta_1 = \Delta_2 > 0$

Denote $\Delta \stackrel{def}{=} \Delta_1 = \Delta_2$. Then for the system (5) which is defined on the two-dimensional torus $\mathbf{T}^2 = [0, 2\pi) \times [0, 2\pi)$, diagonal $D = \{(u_n, v_n) \in T^2 : u_n = v_n\}$ is an invariant manifold.

In the manifold D the system (5) is reduced to the one-dimensional map:

$$u_{n+1} = u_n + 2\pi\Delta - \frac{K}{3} [\sin(u_n) + \sin(2u_n)] \quad (6)$$

The map has two pairs of fixed points O, R_1 and S_2, R_2 , which are born in saddle-node bifurcations at $K \approx 1.7 \cdot 2\pi\Delta$ and $K \approx 8.1 \cdot 2\pi\Delta$. Figure 4 shows corresponding saddle-node bifurcation lines as well as several major Arnol'd tongues. Both stable fixed points O and S_2 lose their stabilities through period-doubling bifurcations. The bifurcation line for O is denoted as PD in Fig. 4 (for S_2 the bifurcation occurs for $K > 6$). As shown in Fig.4 other Arnol'd tongues

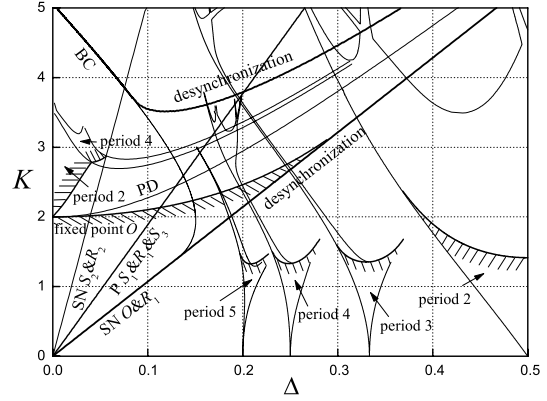


Fig. 4. Regions of the phase synchronization of the system (4) when $\Delta_1 = \Delta_2 = \Delta$ and $u_n = v_n$; the bifurcation curves for the map (6) are denoted as follows: SN $O \& R_1$, SN $S_2 \& R_2$ - saddle-node bifurcations for the corresponding fixed points, BC - boundary crisis; the curves with hachures show where the corresponding transversal Lyapunov exponents change their signs.

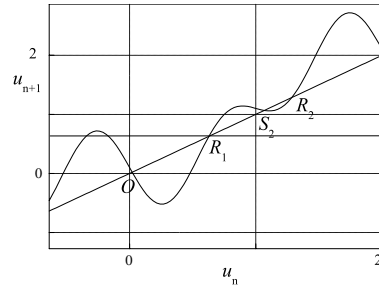


Fig. 5. Graphs of the map (6) with the parameters values $\Delta=0.05$, $K=4.8$.

cross the widest tongue of the rotation number $\rho = 0$ which implies coexistence of the trajectories with different rotation numbers, as was described for the sine circle map, see Section I.B. Fig. 5 shows an example of the graph of the map (6) after the first boundary crisis BC, which nevertheless does not imply desynchronization.

Coming back to the two-dimensional system (5) first, we shall look at the transverse stability of the fixed points O and S_2 or, more general, transverse stability of the invariant manifold D . For any orbit $\{u_n\}_{n=1}$ in the diagonal D the transversal Lyapunov exponent λ is equal to:

$$\lambda = \lim_{N \rightarrow \infty} \frac{1}{N} \sum_{n=1}^N \ln |1 - K \cos u_n|.$$

Transversal Lyapunov exponent λ gives an insight into stability of the periodic orbits or chaotic one-dimensional attractors in the plane. If λ for

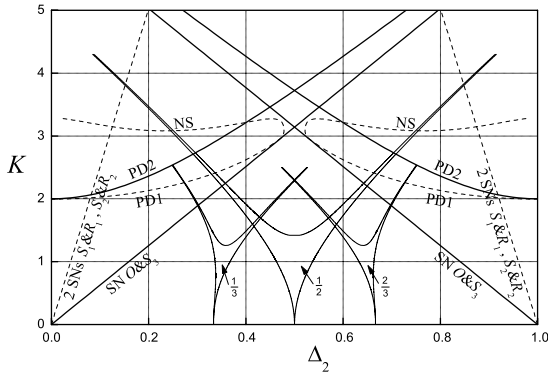


Fig. 6. Regions of the phase synchronization of the system (4) when the difference $\Delta_1 = 0$. The bifurcation lines are denoted as follows: SN - saddle-node, 2 SNs - two simultaneous saddle-node bifurcations, PD1 - transverse period-doubling, PD2 - period-doubling on the manifold V , NS - Naimark-Sacker bifurcations for the period-2 orbit born in the transverse period-doubling bifurcation.

an attractor existing on the diagonal is negative then this attractor attracts almost all trajectories from its two-dimensional neighborhood. In Figure 4, hatched lines separate regions where λ is negative (area with hachures) and positive (the other side).

Figure 4 also shows the line of the transverse pitchfork bifurcation denoted as P S_1 & R_1 & S_3 . In the bifurcation the saddle point R_1 transforms to unstable node giving rise to two saddles S_1 and S_3 . Phase portrait of the system (5) after this bifurcation is shown in Figure 3(b).

C. $\Delta_1 = 0, \Delta_2 \in [0, 1]$

Let us fix the first difference $\Delta_1 = 0$ and consider the parameter plane $(\Delta_2; K)$. In the case, the v_n -axis $V_0 = \{(u_n, v_n) \in T^2 : u_n = 0\}$ is an invariant manifold, and the dynamics in the manifold are governed by the sine circle map (3). Therefore, regions of existence and stability of the fixed point and other periodic orbits inside the manifold coincide with Arnol'd tongues of the sine circle map (3) - some of these regions are shown in Figure 6. Apart from the manifold other attractors exist outside the v_n -axis. As shown in Figure 3(a), in the case $\Delta_1 = \Delta_2 = 0$, there exist 6 fixed points. Four of them S_1, S_2, R_1 and R_2 are located outside the manifold V_0 . We find that with increasing Δ_2 they disappear simultaneously through the saddle-node bifurcations at $K \approx 4 \cdot 2\pi\Delta_2$. Corresponding phase portraits before and after the bifurcations are presented in Fig.3(c,d). With further increase in Δ_2 the fixed points O and S_3 collide and disappear

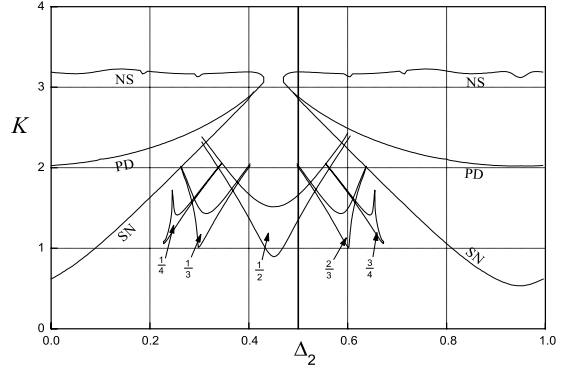


Fig. 7. Regions of the phase synchronization of the system (4) when $\Delta_1 = 0.1$. The bifurcation lines: SN - saddle-node, PD - the first period-doubling, NS - Naimark-Sacker bifurcation for the period-2 orbit born in the first period-doubling bifurcations.

in the saddle-node bifurcation at $K = 2\pi\Delta_2$, and this implies desynchronization of the system.

With increase in the coupling K the stable fixed point O loses its transverse stability through period-doubling bifurcation (PD1 curve in Fig.6) and with more increase in K , the period-2 orbit which was born in the PD1 bifurcation, undergoes Naimark-Sacker bifurcation (NS curve in Fig.6).

D. General case $\Delta_1 \neq \Delta_2$

In Fig.7 several major synchronization regions are depicted in the (Δ_2, K) parameter plane with fixed $\Delta_1 = 0.1$. One can see that their symmetry with respect to the line $\Delta_2 = 0.5$ is lost. Moreover the synchronization regions do not emerge from the points on the Δ_2 -axis and do not have the exact shape of the tongues any more. This means that for small values of $K \leq 0.5$ the system (4) cannot be synchronized. With more increase in Δ_1 the synchronization regions move away from the Δ_2 -axis and become smaller.

III. ACKNOWLEDGEMENTS

A. V. and Yu. M. are grateful for the hospitality of the Laboratory of Nonlinear Systems, Swiss Federal Institute of Technology. A. V. acknowledges the scholarship of the Swiss National Science Foundation.

REFERENCES

[1] Y. Kuramoto, *Chemical Oscillations, Waves and Turbulence* (Springer-Verlag, Berlin, 1984).
 [2] Yu. Maistrenko, O. Popovych, O. Burylko, and P. Tass, *The Mechanism of Desynchronization in the Finite-dimensional Kuramoto Model*, to be published.

APPLICATION OF FRACTAL ANALYSIS IN DETECTION OF BONE STRUCTURE CHANGES

Michał Wróblewski, Bożena Świdzińska

Institute of Electronic Systems,
Faculty of Electronics and Information Technology,
Warsaw University of Technology,
Nowowiejska 15/19, 00-665, Warsaw, Poland,
e-mail: mwroble1@elka.pw.edu.pl, bswid@ise.pw.edu.pl

Abstract—*This paper presents an application of fractal analysis in biomedical signals. The investigation of the X-ray photographs of tibia bone is taken into account. The proposed analysis method is based on the calculation of the fractal dimension as a parameter describing the features of an image texture. Obtained results show that with the aid of fractal analysis it is possible to detect changes in the structure of a bone.*

I. INTRODUCTION

In recent years, there have been numerous reports on possible applications of chaos theory and fractal geometry in natural sciences [1], especially in medicine [2], [3]. Before fractal geometry fully developed natural complex objects had been described using idealized Euclidean geometry models. However, obtained results were insufficient, because complexity of the objects could not be modeled properly.

Fractal geometry seems to be a more effective tool to describe complex and irregular shapes of nature. Consequently, an extensive research on finding applications of fractal geometry in the analysis of biological signals has been conducted. In the range of scientists' interest were for instance, ECG waveforms [4], neoplasms microscope images [3], retina images [5] and brain MR images [6].

This paper presents some results of fractal analysis supporting the diagnosis of Paget's disease of bone. The analysed signals are the X-ray photographs of human tibia bone. The analysis method is based on texture classification with the aid of one of the fractal parameters i.e. fractal dimension.

There is a variety of different definitions of a dimension: the topological dimension, the Hausdorff dimension, the box dimension, the correlation dimension, and others [7]. Therefore, there are many algorithms to estimate the fractal dimension. Selected algorithms, used to perform the analysis, are presented

in the following sections. The fractal dimension is closely connected with our perception of roughness. If a texture is smooth, the fractal dimension takes lower values. And on the contrary if the texture is rougher, the fractal dimension is higher. For a grayscale images the fractal dimension takes values between 2 and 3.

II. PAGET'S DISEASE OF BONE

Paget's disease of bone is a chronic disease in which the bones become enlarged and weakened as a result of a changed, 'chaotic' and brittle bone structure. The disease leads to deformity, fracture, imbalance in calcium metabolism and carries with it an increased risk of cancer. The most commonly affected are the long bones, vertebrae, pelvis, and skull.

III. FRACTAL ANALYSIS METHOD

The original X-ray photographs of tibia bone were digitalized to similar size images of 256 grey levels of intensity. From the digital images to the further processing were selected only 100×100 pixel region of interest (ROI), each containing a different textured part of a tibia bone. Then, to all ROI images the histogram normalization was applied in order to enhance the contrast and to use the full range of grayscale. Finally, the image texture within the ROI was characterized by calculating an image surface fractal dimension. To estimate the fractal dimension three different methods were used: Epsilon – Blanket, Triangular Prism Surface Area and 3-Dimensional Box Counting algorithm. All are to be described below.

A. Epsilon – Blanket algorithm

The idea of the algorithm is based on covering an image surface with a blanket having upper surface u_n and bottom surface b_n [7]. For $n = 0$ they are initialized to the values of the image $u_n = g(i, j) = b_n$, where $g(i, j)$ represents the value of the pixel image at

co-ordinates (i, j) . Starting from $n = 1$ in the n -th step the surfaces of the blanket are obtained from equations:

$$u_n(i, j) = \max \left[u_{n-1}(i, j) + 1, \max_{(k,l) \in \hat{N}(i,j)} u_{n-1}(k, l) \right]$$

$$b_n(i, j) = \min \left[b_{n-1}(i, j) - 1, \min_{(k,l) \in \hat{N}(i,j)} b_{n-1}(k, l) \right]$$

Then the volume of the blanket, enclosed between u_n and b_n , is computed from:

$$V_n = \sum_{i,j} \left[u_n(i, j) - b_n(i, j) \right]$$

and the surface area is defined as:

$$A_n = \frac{V_n - V_{n-1}}{2}$$

The fractal dimension of an image is calculated from the equation:

$$D_{BL} = 2 - d$$

where d is the slope of the linear regression line applied to a graph of $\log(A_n)$ versus $\log(n)$.

B. Triangular Prism Surface Area algorithm

In this method an image is covered with square grid of a side size r [6]. For each grid of a given square side size r a triangular prism is constructed, as shown in Fig. 1. The prism edges are at the square corners A, B, C, D and have values a, b, c, d of corresponding pixels. Similarly, the height of the prism has value p of a pixel P placed at the center of a square. The connections of a, b, c, d and p form four top triangles. The sum of all prism top surfaces gives the entire image surface area $A(r)$. Calculations are repeated for an odd side size r , producing a series of surface areas $A(r)$ at a scale r . Then the double logarithmic plot of $A(r)$ against r is drawn. The slope d of straight line, achieved by the least square regression method, determines the value of the fractal dimension:

$$D_{TPSA} = 2 - d$$

C. 3-Dimensional Box Counting algorithm

The algorithm considers an image as a surface placed above a plane [6]. The distance between the surface and the plane is determined by the value of pixel images. The plane is partitioned into square grids of a side size r . On each grid a column of cubic boxes of size $r \times r \times r$ is built, as shown in Fig. 2. For a

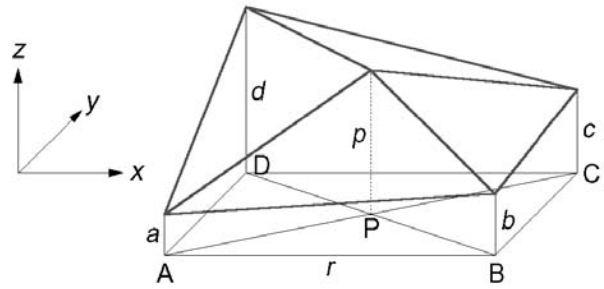


Fig. 1. Triangular Prism Surface Area algorithm

certain column, the number of the highest box, which includes a part of the image, is noted as k . Similarly, l is the number of the lowest box containing a part of the image. The number of boxes N_r containing the whole image is calculated using the equation:

$$N_r = \sum_{\text{each column}} (k - l + 1)$$

Calculation of N_r is repeated for different values of the square grid side size r . Finally, the fractal dimension D_{BC3D} of the image is determined as the value of the slope of the linear regression line applied to a graph of $\log(N_r)$ against $\log(\frac{1}{r})$.

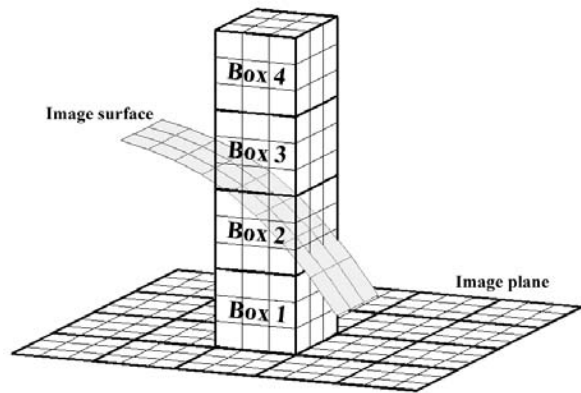


Fig. 2. 3-Dimensional Box Counting algorithm

IV. MEDICAL DATA AND NUMERICAL RESULTS

The analysis method, presented in section III was applied, to several X-ray photographs of tibia bone. Images were diagnosed by specialist physician and depicted both the healthy bone and the bone affected by Paget’s disease. The processed ROI images that correspond to analysed X-ray photographs are shown in Fig. 3 (healthy bone) and Fig. 4 (Paget’s disease of bone).

The results of performed analysis are shown in graphs (Fig. 5) and in Table I.

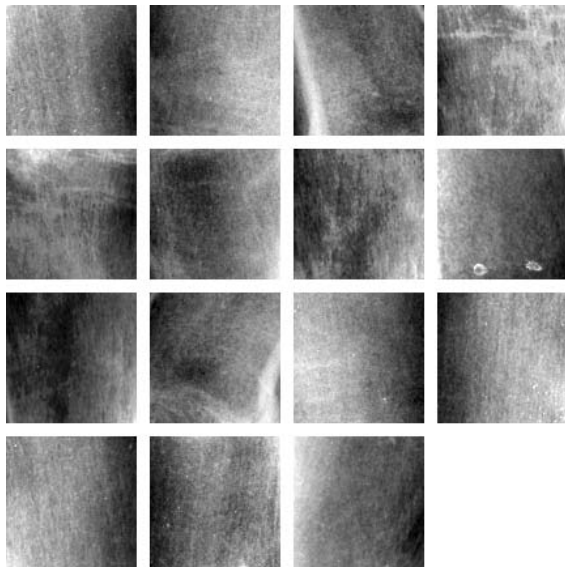


Fig. 3. Analysed ROI images of healthy bone

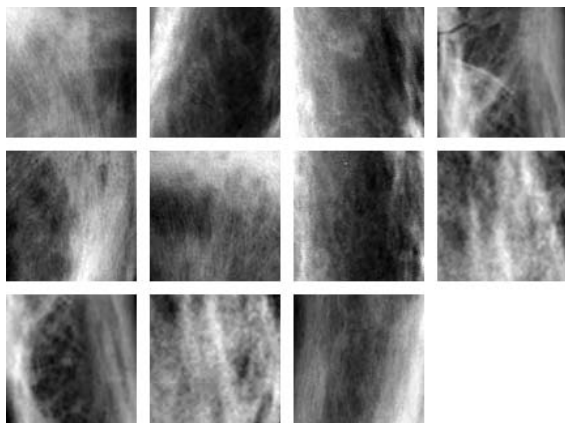


Fig. 4. Analysed ROI images of bone with Paget's disease

The analysis of the results shows that the images of the bone with Paget's disease tend to have lower fractal dimension values than images of a healthy bone. This is particularly visible in the case of the use of Triangular Prism Surface Area algorithm as an estimation of the fractal dimension. The mean of fractal dimension of images with Paget's disease of bone amounts to $D_{TPSA} = 2.2081$ and is significantly lower than the mean of fractal dimension of the healthy bone images which is $D_{TPSA} = 2.5071$. Moreover, these two groups of images can be completely distinguished, because obtained results are separable (compare Fig. 5b and minimal and maximal fractal dimensions in Table I). The 3-Dimensional Box Counting method produces values that can separate these images as well. Although in this case, the difference between the means of fractal dimensions is smaller (means of fractal dimension of Paget's

disease of bone images and healthy bone images are $D_{BC3D} = 2.1207$ and $D_{BC3D} = 2.2678$, respectively). The Epsilon – Blanket algorithm gives slightly different results. The classification can not be performed, because fractal dimension values are too close together (compare Fig. 5a). However, the tendency to get the mean of fractal dimension of bone images with Paget's disease lower than the mean of fractal dimension of healthy bone images is still preserved.

V. CONCLUSIONS

The research has proven that:

- It is possible to monitor changes in the structure of the bone caused by Paget's disease.
- The fractal analysis may be useful as an aid in the diagnosis of skeletal diseases.
- The method of analysis and the algorithm to estimate fractal dimension must be suitable for a particular type of biomedical signal.
- Features of the signal and, consequently, its space-fill ratio carry diagnostically significant information and can be approximated by fractal dimension.
- The fractal analysis is a good supplement to traditional image processing methods.
- The fractal analysis may be useful in other disciplines, especially in those where the differences in image texture occur.

REFERENCES

- [1] B. B. Mandelbrot, "The fractal geometry of nature", Freeman, 1982.
- [2] G. A. Losa, Fractals in pathology: are they really useful?, *Pathol.*, vol. 87, pp. 310-317, 1995.
- [3] W. Kuźniak, J. R. Jabłoński, E. Oczeretko, I. Kasacka, Fractal Dimension in morphology of neoplasmas, *Advances in Cell Biology*, vol. 28, pp. 561-570, 2001.
- [4] M. H. Słomczyński, B. Świdzińska, Application of fractals in monitoring of the electrocardiogram. In *Proc. NDES'03*, pp. 249–252, Scoul, Switzerland, 2003.
- [5] M. H. Słomczyński, B. Świdzińska, Application of fractals analysis in diagnosing medical images. In *Proc. of 24th Czech-Hungarian-Polish Workshop*, pp. 112–117, Warsaw, Poland, 2002.
- [6] K. M. Iftekharuddin, W. Jia, R. Marsh, Fractal analysis of tumor in brain MR images, *Machine Vision and Applications*, vol. 13, pp. 352–362, Springer-Verlag, 2003.
- [7] M. J. Turner, J. M. Blackledge, P. R. Andrews, "Fractal Geometry in Digital Imaging", Academic Press, 1998.

	Epsilon – Blanket		TPSA		3D Box Counting	
	Healthy bone	Paget’s disease	Healthy bone	Paget’s disease	Healthy bone	Paget’s disease
D_{min}	2.4190	2.3231	2.3864	2.1345	2.2279	2.0708
D_{max}	2.6175	2.5206	2.5878	2.3261	2.3097	2.1783
$\mu(D)$	2.5151	2.4303	2.5071	2.2081	2.2678	2.1207
$\sigma(D)$	0.0566	0.0585	0.0636	0.0542	0.0299	0.0348

D_{min} , D_{max} – minimal and maximal value of fractal dimension, $\mu(D)$ – mean of fractal dimension, $\sigma(D)$ – standard deviation of fractal dimension

TABLE I
Results of fractal analysis

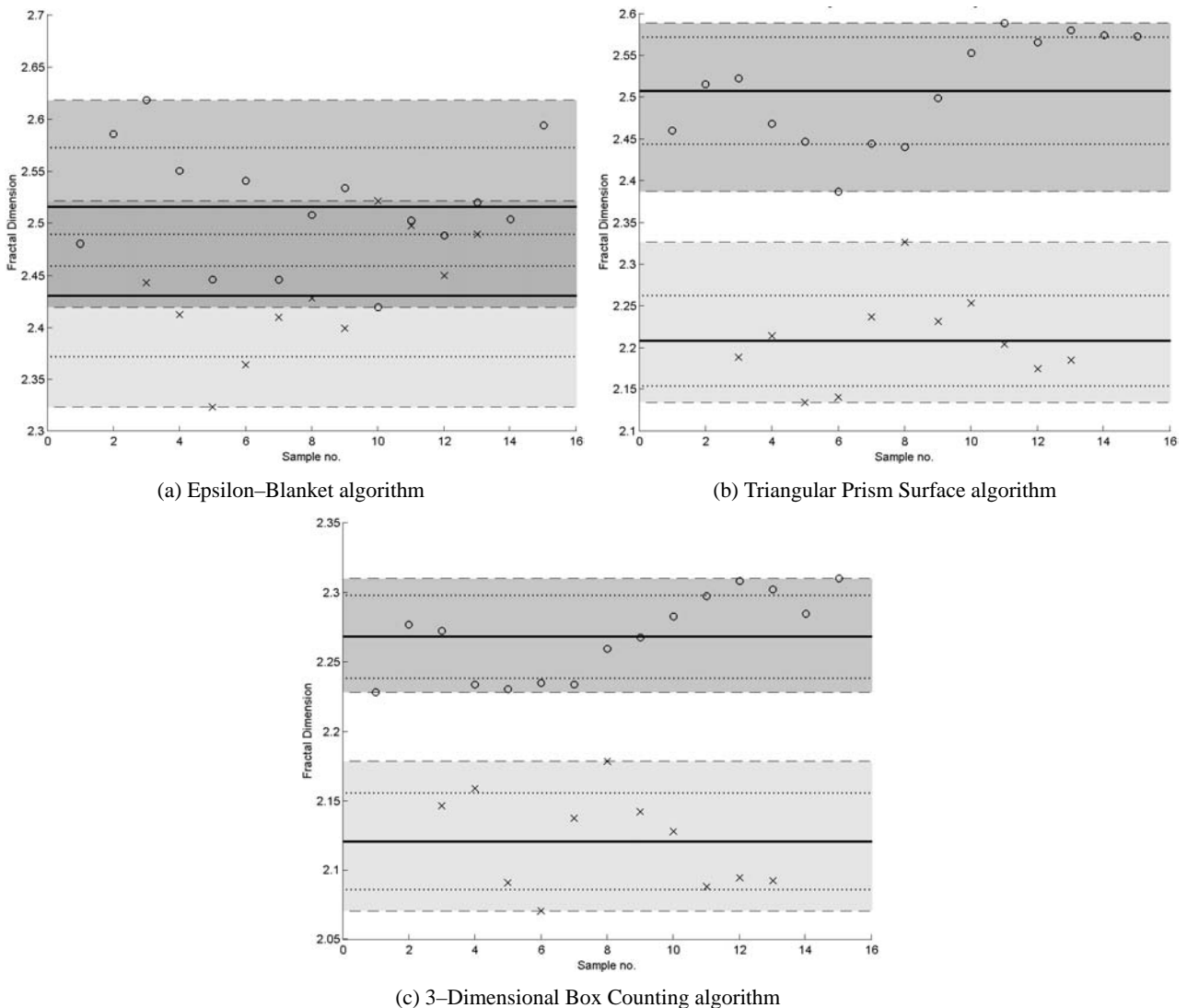


Fig. 5. Results of fractal analysis

circles – healthy bone, *crosses* – Paget’s disease of bone, *solid lines* – $\mu(D)$ value, *dotted lines* – $\mu(D) + \sigma(D)$ and $\mu(D) - \sigma(D)$ values, *dashed lines* – D_{min} and D_{max} values

An Extended Bernoulli Map Driven by Dynamic Thresholding

Kenji Yano and Kiyoshi Tanaka

Faculty of Engineering, Shinshu University,
4-17-1 Wakasato, Nagano, 380-8553 Japan

e-mail: {yano@iplab, ktanaka@gipwc}.shinshu-u.ac.jp

Abstract—An extended Bernoulli map driven by dynamic thresholding is proposed, in which the discontinuous point of Bernoulli map is dynamically changed in every mapping. As the driving option of the discontinuous point, we present a chaotic driving method. We investigate the chaotic behavior in the proposed map and the statistical properties of the dynamics derived from the map.

I. INTRODUCTION

In this paper, we propose an extended Bernoulli map driven by dynamic thresholding, in which the discontinuous point of Bernoulli map [1] is dynamically changed in every mapping. Because the discontinuous point of Bernoulli map is normally fixed to a value in $[0,1)$, the dynamics derived from the map is determined by this parameter as one sequence of orbits from an initial point x_0 . On the other hand, in the proposed extended Bernoulli map the discontinuous point is dynamically altered in every mapping. Thus we can expect to generate a number of different orbits depending on the driving method of discontinuous point even when we use the same initial point.

The proposed map is originated from a study of the chaotic behavior observed in the decoding process of the arithmetic coding [2], [3]. The arithmetic code (codeword) can be considered an initial point of the generalized Bernoulli map, in which the discontinuous point of the map is dynamically changed by the probability of symbols predicted in the context modeling unit. As related studies, Yoshioka et al. [4] have recently proposed a time-variant 1-dimensional return map, in which a periodic input is simply introduced to a nonautonomous manifold piecewise linear circuit. Also, Miki et al. [5] have presented a time-dependent Logistic map, in which a simple periodic time dependent parameter is applied to the amplitude of the map.

In this paper, we present a chaotic driving method as the driving option of the discontinuous point of Bernoulli map. With this option, we can automatically drive the discontinuous point once we specify the mapping parameters and an initial point. In this paper, we first investigate the chaotic behavior in the

proposed map, and then examine the statistical properties of the dynamics derived from the proposed map, such as ergodicity and uniformity of the orbits.

II. PROPOSED MAP

We define an extended Bernoulli map driven by dynamic thresholding $B^* : I = [0, 1) \rightarrow I = [0, 1)$ as

$$B^*(x_k) : x_{k+1} = \begin{cases} \frac{x_k}{\alpha_k} & (0 \leq x_k < \alpha_k) \\ \frac{x_k - \alpha_k}{1 - \alpha_k} & (\alpha_k \leq x_k < 1) \end{cases} \quad (1)$$

$(k = 0, 1, 2, \dots)$

where α_k ($k = 0, 1, 2, \dots$) denotes the value of discontinuous point (threshold) on $I = [0, 1)$. Unlike the original Bernoulli map, we can remarkably increase the possibility to change (control) the dynamics of orbits derived from the map depending on the way of driving α_k .

Among various options we drive $\alpha_k \in I$ by

$$\alpha_{k+1} = A(1 - |1 - 2\alpha_k|^p) \quad (k = 0, 1, \dots) \quad (2)$$

where p and A are mapping parameters, which determine the shape and amplitude of the map, respectively. With this option, we can automatically drive α_k ($k = 1, 2, \dots$) by just specifying (p, A) and an initial discontinuous point α_0 .

Because the orbit x_{k+1} is determined with two parameters, x_k and α_k , the proposed map can be also considered as a 2-dimensional map. From this standpoint, we show the expansion vectors by the map at various points in the 2-dimensional $x_k - \alpha_k$ plane for $p=2.0$ and $A=1.0$ in **Fig. 1**. Each vector is the composite of the expansion ratios of x_k and α_k . From this figure, we can see that the expansion ratio changes depending on the value of discontinuous point α_k even for the same x_k .

III. CHAOTIC BEHAVIOR

First of all, we show the stationary distribution of the orbits of the proposed map when we fix the discontinuous point as $\alpha_k = \alpha$ in **Fig. 2**. In this figure, 2,000 points are depicted as x_k after the initial transition (discarded 10^4 points) for 4,000 kinds of α_k in

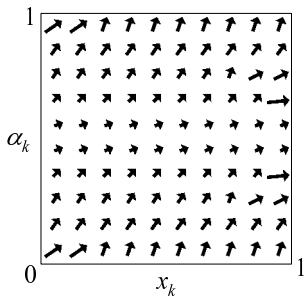


Fig. 1. Expansion vectors in 2-dimensional $x_k - \alpha_k$ plane ($p=2.0, A=1.0$)

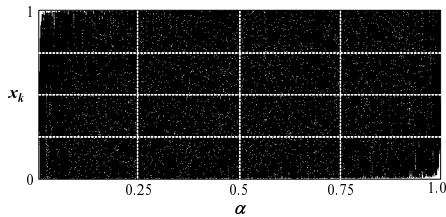


Fig. 2. Stationary distribution of the orbits of the proposed map

$[0, 1)$. From this figure, if we fix α to a value close to the edge regions (0 or 1), it becomes hard for the orbit to visit the opposite edge region. We can say that the orbits tend to transit uniformly over the mapping domain if we drive α around the center of the domain.

Next, we show the bifurcation diagrams for the proposed map when we vary the amplitude parameter A in the range $0 < A \leq 1$ in **Fig. 3**, where we set $\alpha_0 = 0.2$ and $x_0 = 0.2$. The depiction was done with the same manner to **Fig. 2**. Also, we show the bifurcation diagram for the driving map in **Fig. 4**, where the conditions are the same to **Fig. 3**. In the range that the discontinuous point α_k converges to the fixed point 0, the orbits of the proposed map converge to a fixed point. In other words, if α_k does not converge to 0, the orbits by the proposed map behave chaotic spreading in the entire mapping domain. For example, when we set $p=2.0$, the orbits behave chaotic in the range $0.25 \leq A \leq 1.0$. When we set $p = 0.75$, the range producing chaotic orbits becomes narrow $0.628 \leq A \leq 1.0$.

Furthermore, we show the 2-dimensional depiction of bifurcation diagrams as we vary the parameters (p, A) in **Fig. 5**, where the gray tone classifies the orbits into (i) convergence to a fixed point, (ii) several periodic orbits, and (iii) chaotic orbits. In this figure, (p, A) that leads α_k to a fixed point or to periodic orbits occupies a large area of this parameter domain. In this colored region, whatever we choose the initial discontinuous point α_0 , the driving pattern of α_k will become a constant or periodic one. Therefore, if we want to generate the chaotic orbits diversely spread in

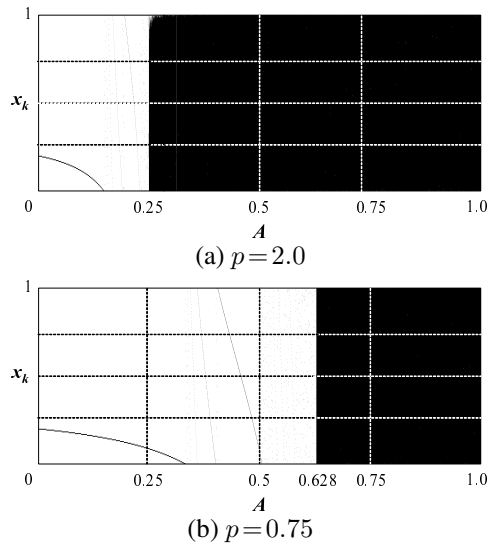


Fig. 3. Bifurcation diagrams of the proposed map

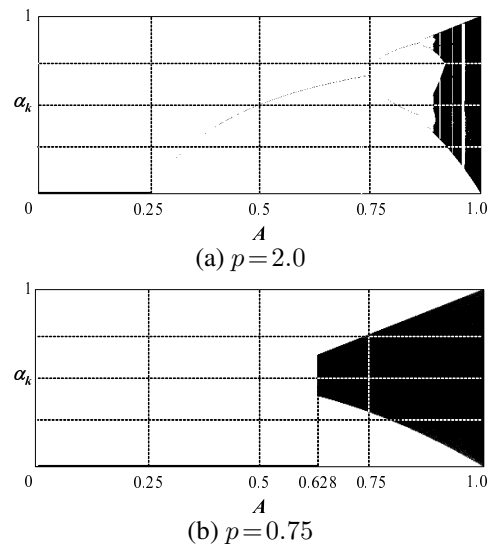


Fig. 4. Bifurcation diagrams of the driving map

the mapping domain, it would be better to use in the white region that the orbits of α_k become chaotic.

Finally, we show the Lyapunov exponent [1] calculated by Shimada and Nagashima's method [7] in **Table I**, when we consider the proposed map as a 2-dimensional map having two variables x_k and α_k . We have two Lyapunov exponents (λ_1, λ_2) , and the bigger one is called the maximum Lyapunov exponent. Similar to [7], we regard λ_1 as the maximum Lyapunov exponent in this paper. If $\lambda_1 > 0$, the proposed map generates chaotic orbits. In this table, we can find a few parameters showing $\lambda_1 = 0$, for example $(p, A) = (0.75, 0.6)$ which do not show chaotic behavior. Also, the parameters showing negative λ_2 , for example $(p, A) = (2.0, 0.8)$ converge the driving map to a fixed point or periodic orbits.

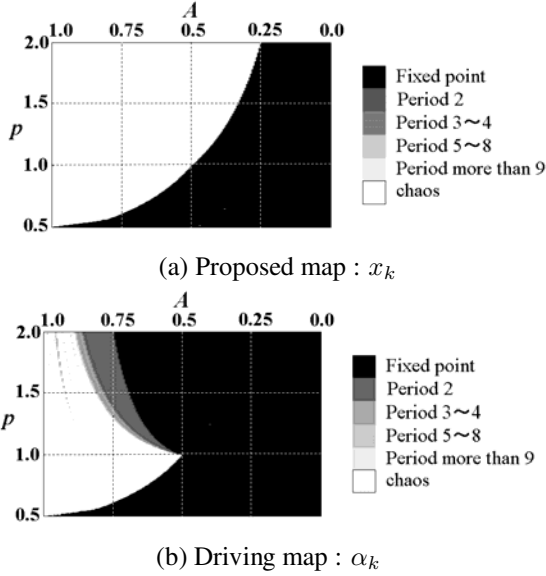


Fig. 5. 2-dimensional bifurcation diagrams for (p, A)

TABLE I

LYAPUNOV EXPONENTS EXPERIMENTALLY OBTAINED

$p \backslash A$	1.0	0.9	0.8	0.7	0.6	0.5
2.00	0.693 0.386	0.538 0.183	0.597 -0.916	0.651 -0.223	0.679 -0.916	0.693 -13.12
1.75	0.693 0.409	0.567 0.348	0.599 -0.351	0.658 -0.103	0.681 -0.659	0.693 -9.842
1.50	0.693 0.435	0.572 0.415	0.608 -0.111	0.660 -0.053	0.684 -0.401	0.693 -6.561
1.25	0.693 0.464	0.575 0.492	0.626 0.299	0.655 -0.018	0.686 -0.130	0.693 -3.281
1.00	0.693 0.500	0.597 0.588	0.643 0.470	0.668 0.336	0.685 0.182	0.611 0.000
0.75	0.689 0.539	0.666 0.614	0.652 0.629	0.676 0.599	0.000 -0.105	0.000 -0.288

upper : λ_1 (maximum exponent), lower : λ_2

IV. STATISTICAL PROPERTIES

A. Ergodicity

For a complex μ -summable function f^* of B^* , we examine if the time average \tilde{f}^* for any initial points $x_0 \in I$ is equal to the spacial average \bar{f}^* [6], i.e.,

$$\tilde{f}^*(x_0) = \bar{f}^*. \tag{3}$$

Since $\mu(I) = 1$, the spacial average is

$$\bar{f}^* = \int_I f^*(x) d\mu, \tag{4}$$

where x is a point on $I = [0, 1)$. In this paper, we choose

$$f^*(x) = \begin{cases} 0, & \left[\frac{i-1}{d}, \frac{i}{d} - \frac{1}{2d} \right) \\ 1, & \left[\frac{i}{d} - \frac{1}{2d}, \frac{i}{d} \right) \end{cases} \quad (i = 1, 2, \dots, d) \tag{5}$$

among possible \tilde{f}^* , where d denotes the number of intervals divided on I . On the other hand, the time

TABLE II

KS-STATISTICS ON ERGODICITY ($d = 2^{10}$)

$p \backslash A$	1.0	0.9	0.8	0.7	0.6	0.5
2.00	0.885 15.77	0.829 0.912	0.766 1.822	0.994 0.925	0.991 1.122	0.843 0.852
1.75	1.116 10.19	0.729 0.796	0.941 1.656	0.758 1.080	0.875 6.585	0.863 0.752
1.50	0.919 5.631	0.786 0.779	0.994 1.108	0.666 0.766	0.853 1.026	0.833 0.915
1.25	0.998 2.529	1.139 0.837	1.132 1.256	0.970 1.026	0.858 0.845	0.894 0.752
1.00	0.779 1.271	0.813 1.018	0.925 0.844	0.821 0.796	1.077 0.760	0.983 0.982
0.75	0.717 0.969	0.893 0.807	0.799 1.015	1.007 0.829	31.62 19.76	31.62 31.62

upper : average of \tilde{f}^* , lower : variance of \tilde{f}^*

average of \tilde{f}^* under a finite times of mapping n is defined as

$$\tilde{f}^*(x_0) = \frac{1}{n} \sum_{k=1}^n f^*(B^{*k}(x_0)), \tag{6}$$

where $f^*(B^{*k}(x_0))$ also follows Eq. (5).

Since $\tilde{f}^* = \frac{1}{2}$, the dynamics of the extended Bernoulli map is considered ergodic if $\tilde{f}^* \approx \frac{1}{2}$ from any initial point $x_0 \in I$. $\tilde{f}^*(x_0)$ theoretically follows a binomial distribution $\mathbf{B}(n, P)$ ($P = \frac{1}{2}$). Here we set the times of mapping $n = 10^3$ and calculate $\tilde{f}^*(x_0)$ by computer simulation. We repeat this operation $N_x = 10^3$ times by changing $x_0 \in I$ to get one statistic for the average and variance of \tilde{f}^* . The former statistic follows a normal distribution and the latter a χ^2 distribution, respectively. **Table II** shows the results by KS(Kolmogorov Smirnov) test [8] for $N_x = 10^3$ pieces of statistics T_l ($l = 1, 2, \dots, N_x$) obtained by changing α_0 . Note that each numerical data in this table is the median among 10 trials of KS test. Here we set $d = 2^{10}$ in Eq. (5). If KS-statistic meets $K_{N_x} \leq 1.358$, the condition on ergodicity is satisfied in case of 5% critical region. From the result, the following observations are relevant: (i) For $p > 1.0$, as we decrease the amplitude A from 1.0, the driving range of α_k ($[A(1 - |1 - 2A|^p), A]$) gradually becomes narrow, periodic, and eventually converges to a fixed point following by the Schwarz's condition. Particularly when A approaches to 0.5, the fixed point also approaches to 0.5, which means the map becomes equivalent to the original Bernoulli map. Thus, the ergodicity generally tends to be satisfied by decreasing A from 1.0 to 0.5. (ii) For $p < 1.0$, as we decrease A from 1.0, the driving range of α_k simply becomes narrow centering around 0.5 by degrees. That makes the characteristic of the map similar to the original Bernoulli map. Thus, as we decrease A from 1.0, the ergodicity generally tends to be satisfied analogous to

TABLE III
KS-STATISTICS ON UNIFORMITY OF ORBITS OVER I

$p \setminus A$	1.0	0.9	0.8	0.7	0.6	0.5
2.00	9.849	0.696	1.703	1.879	1.873	1.910
1.75	8.519	1.037	1.636	1.813	1.676	1.875
1.50	5.616	0.589	1.057	1.484	1.774	1.799
1.25	2.818	0.800	0.786	1.460	1.835	1.744
1.00	1.125	0.930	0.670	0.780	0.796	2.055
0.75	1.111	0.776	0.904	0.708	10.00	10.00

(i). However, for $A \leq 0.6$, the orbits of x_k converges to a fixed point (see **Fig. 3(b)**) since α_k converges to 0 (see **Fig. 4(b)**), and thus the ergodicity is not satisfied. (iii) In case of $A=1.0$, as we decrease p from 2.0, the principal distribution of α_k gradually moves from the edge region (0 or 1) to the center (0.5) of the mapping domain, which improves the KS statistics. From this observation, to satisfy the ergodicity condition, the discontinuous point α_k should be driven around 0.5 avoiding the edge regions. Even periodic orbits or a fixed point showing negative λ_2 are also available as long as the fixed point 0 is avoided. However, in the table, we can find a few particular parameters, for example $(p, A) = (2.0, 0.8)$, which do not follow this observation. This point should be further examined.

B. Uniformity of the Orbits

We examine the uniformity of the orbits in the mapping domain. Here we divide $I = [0, 1)$ into $d = 10^3$ sub-intervals and set the iteration number of mapping to $n = 10^6$. We check the distribution of the orbits from an initial pair (x_0, α_0) if they uniformly visit all sub-intervals by using χ^2 -statistic [8]. We apply KS test for $N_x = 10^2$ pieces of χ^2 statistics T_l ($l = 1, 2, \dots, N_x$) obtained by changing x_0 in the interval $[0, 1)$. Here we set $\alpha_0 = 0.2$ as an initial driving point. The result is shown in **Table III**, where each numerical data is the median among 10 trials of KS test similar to **Table II**. If KS-statistic meets $K_{N_x} \leq 1.340$, the orbits satisfy the condition on uniformity irrelevant to initial point x_0 . From the result, the uniformity (denseness) of the orbits in the mapping domain is explicitly satisfied by using the parameters which make both Lyapunov exponents λ_1 and λ_2 positive in **Table I**. However, in the range of $A = 1.0$ and $p > 1.0$, the uniformity condition is not satisfied similar to the result on ergodicity, because the distribution of α_k inclines to the edge region.

Finally, we classify the parameter regions base on the above observation in **Fig. 6**. In this figure, we denote \bigcirc as the region satisfying both ergodicity and uniformity conditions, \triangle the one only satisfying ergodicity condition, and \times the one which does not satisfy both conditions. From this figure, to satisfy the

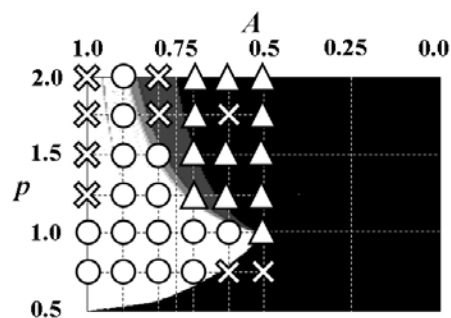


Fig. 6. Classification of mapping parameters

uniformity condition, we should select the parameters in the white region, which lead the orbits of the discontinuous point α_k to chaotic.

V. CONCLUSION

In this paper, we have proposed an extended Bernoulli map driven by dynamic thresholding, in which the discontinuous point of Bernoulli map is dynamically changed in every mapping, and showed the chaotic behavior and its statistical properties on ergodicity and uniformity of the orbits. From the observation of results, we can say that the orbits of the proposed map behave chaotic as long as we avoid the discontinuous point α_k converges to the fixed point 0. Also the orbits satisfy both ergodicity and uniformity conditions if we drive α_k so that the density of α_k increases around the center of the mapping domain.

As future works, we should further investigate on the driving method of α_k and examine its affection to the statistical properties of the orbits. Also, we are planning to increase the dimension of this map, and develop a random number generator using this map.

REFERENCES

- [1] E. Ott, *Chaos in Dynamical Systems*, Cambridge Univ. Press, 1993.
- [2] H. Ishibashi, K. Tanaka, "Data Encryption Scheme with Extended Arithmetic Coding," *Proc. SPIE Mathematics of Data/Image Coding, Compression, and Encryption IV*, vol. 4475, pp.222-233, 2001.
- [3] H. Ishibashi, K. Tanaka, "A Consideration on the Chaotic Dynamics Observed in the Decoding Process of Arithmetic Coding Scheme," *Proc. NOLTA 2001*, pp.355-358, 2001.
- [4] T. Yoshikawa, T. Tsubone and T. Saito, "Time-variant 1-D return map from a simple switched dynamical system," *Proc. ITC-CSCC'01*, pp.1022-1025, 2001.
- [5] T. Miki, J. Kuroiwa, J. Miyao and K. Yamagata, "Response Properties of Logistic Map by Changing System Parameter," *Proc. NOLTA 2001*, pp.115-118, 2001
- [6] V. I. Arnold and A. Avez, *Ergodic problems of classical mechanics*, W. A. Benjamin, 1968.
- [7] I. Shimada and T. Nagashima, "A Numerical Approach to Ergodic Problem of Dissipative Dynamical Systems," *Progress of Theoretical Physics*, vol. 61, pp.1605-1616, 1979.
- [8] D. E. Knuth, *The Art of Computer Programming Vol.II*, Addison-Wesley, 1969.

OPTIMAL MULTI-USER CHAOS-SHIFT-KEYING COMMUNICATION SYSTEMS

Ji Yao

School of Mathematics and Statistics, The University of Birmingham, Birmingham, B15 2TT, UK
 e-mail: yaoji@maths.bham.ac.uk

Abstract—Multi-user CSK communication systems are studied. A statistical approach is developed to calculate the system BER by strictly applying the Central Limit Theorem (CLT). Further discussion, mainly on the autocorrelation coefficients of the chaotic map, is developed to obtain the performance lower bound. The asymptotically optimal maps are used to obtain the optimal performance. This modulation scheme provides a possible choice for multi-access communication.

I. INTRODUCTION

In the single-user chaos waveforms communication systems, the system performance is always not better than corresponding conventional communication system, such as BPSK [1]-[3]. In the chaos shift keying (CSK) system, this performance degradation is mainly due to the non-constant energy per bit, which is termed *estimation problem* [1]. Without further change in the modulation scheme, this estimation problem is always unavoidable. So a question arises: what have we got from *chaos*?

In this letter, a multi-user CSK system is studied, which is possible to over-perform its conventional counterpart. In the conventional multi-access system, it is seldom to send the modulated signal directly. Some multi-access schemes, such as CDMA, TDMA, are usually used to distinguish the useful signal at the receiver. However, in this letter, the directly-send model is studied, which is proved to have a lower bound of single-user BPSK performance. So there may be several users in a system sharing the same frequency, time slot or PN sequences, which double or triple the system capacity.

II. MODELS OF MULTI-USER ANTIPODAL CHAOS-SHIFT-KEYING COMMUNICATION SYSTEMS

In this section, the configuration of multi-user coherent antipodal CSK communication systems are described [4]. The block diagram of this system is plot in Fig. 1.

A. Modulator Scheme

Assuming there are L users within the multi-user antipodal CSK system and that the binary bits are transmitted at time intervals of length T_b . In evaluation of a communication system, the focus is always on the transmission of one bit. So, denote the transmitted data of the l^{th} user by b_l , where $b_l \in \{-1, +1\}$.

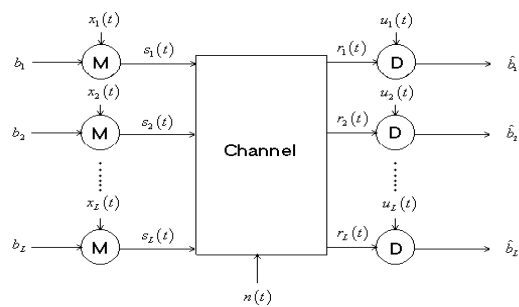


Fig. 1 Block diagram of multi-user antipodal CSK communication system.

A typical bit b_l uses a segment $x_l = \{x_{l,i} | i = 0, 1, \dots, N-1\}$ of N successive values from a chaotic waveform $\{X_l\}$; N is termed the *spreading factor*. These segments are generated by chaotic maps $\tau_l(x)$ for the l^{th} user, that is,

$$x_{l,i+1} = \tau_l(x_{l,i}) \quad i = 0, 1, 2, \dots, N-1 \text{ and } l = 1, 2, \dots, L.$$

The chaotic maps $\tau_l(x)$ may be same for all users, but also may be not. The initial value $x_{l,0}$ is chosen from the natural invariant distribution $\rho_l(x)$ of the map $\tau_l(x)$. The means of $\{X_l\}$ are denoted by $\mu_l = E(X_l)$ and the variance by $\sigma_{X_l}^2$. In the following discussion, it is assumed that $\mu_l = 0$. Because all users have the same average signal energy, it is reasonable to assume that all maps have the same variance, denoted by σ_X^2 .

The output of the chaotic signal generator used by the l^{th} user, denoted by $x_l(t)$, is

$$x_l(t) = \sum_{i=0}^{N-1} x_{l,i} g_{T_c}(t - iT_c), \quad (2.1)$$

where T_c is the time interval between change of $x_{l,i}$, which is always a constant and equals T_b/N .

$g_{T_c}(t)$ is a rectangular pulse of unit amplitude and width T_c , i.e. $g_{T_c}(t) = \begin{cases} 1, & 0 \leq t < T_c \\ 0, & \text{elsewhere} \end{cases}$.

In antipodal CSK, the modulation of bit b_l takes the form as $b_l x_l$. Thus, denoted by $s_l(t)$, the transmitted waveform of the l^{th} user is

$$s_l(t) = b_l \sum_{i=0}^{N-1} x_{l,i} g_{T_c}(t - iT_c). \quad (2.2)$$

B. Channel Model

Additive white Gaussian noisy (AWGN) channel is considered in this letter. Let $n(t)$ be the AWGN with a two-side power spectral density given by

$$S_n(f) = N_0/2.$$

For convenience, we replace $n(t)$ by an equivalent noise source $n'(t)$ [4], given by

$$n'(t) = \sum_{i=0}^{\infty} \varepsilon_i g_{T_c}(t - iT_c), \quad (2.3)$$

where $\{\varepsilon_i\}$ are independent Gaussian random variable with zero mean and variance as $\sigma_n^2 = N_0/2T_c$.

So corrupted by both AWGN and the transmitted waveforms of the other $L-1$ users, which is termed *interference*, the received waveform of the l^{th} user is

$$\begin{aligned} r_l(t) &= s_l(t) + \sum_{k=1 \neq l}^L s_k(t) + n'(t) \\ &= \sum_{i=0}^{N-1} r_{l,i} g_{T_c}(t - iT_c), \end{aligned} \quad (2.4)$$

where $r_{l,i} = b_l x_{l,i} + \sum_{k=1 \neq l}^L b_k x_{k,i} + \varepsilon_{l,i}$. And the per-bit signal noise ratio is $E_b/N_0 = (N\sigma_X^2)/(2\sigma_n^2)$.

C. Demodulator scheme

The coherent communication system is considered in this letter, that is only the user's own reference sequence is known exactly at the receiver. So the reference sequence is $u_l(t) = \sum_{i=0}^{N-1} x_{l,i} g_{T_c}(t - iT_c)$.

The correlation decoder takes the form

$$C(r_l, u_l) = \int_0^{T_b} (r_l(t) - \mu)(u_l(t) - \mu) dt$$

$$= T_c \sum_{i=0}^{N-1} (r_{l,i} - \mu)(u_{l,i} - \mu), \quad (2.5)$$

which calculates the covariance between $r_l(t)$ and $u_l(t)$, and take a sample at time T_b to make demodulation decision. Finally, b_l is estimated by \hat{b}_l as

$$\hat{b}_l = \begin{cases} +1 & \text{if } C(r_l, u_l) \geq 0 \\ -1 & \text{if } C(r_l, u_l) < 0 \end{cases} \quad (2.6)$$

III. STATISTICAL APPROACH TO BER OF MULTI-USER COHERENT ANTIPODAL CSK SYSTEM

The *bit error rates* (BER) of a system is the probability of estimating a bit value -1 or $+1$ given that $+1$ or -1 was transmitted. So the BER of the l^{th} user takes the form

$$BER_l = \frac{1}{2} \left[P(\hat{b}_l = +1 | b_l = -1) + P(\hat{b}_l = -1 | b_l = +1) \right]$$

with the assumption that $P(b_l = -1) = P(b_l = +1) = 1/2$. With (2.4) and (2.6), the BER of the 1st user conditional on $b_1 = +1$ is

$$\begin{aligned} BER_1 | (b_1 = +1) &= P(\hat{b}_1 = -1 | b_1 = +1) \\ &= P \left\{ \sum_{i=0}^{N-1} [\tau_1^{(i)}(X_{1,0})]^2 + \sum_{i=0}^{N-1} [\tau_1^{(i)}(X_{1,0}) \sum_{l=2}^L b_l \tau_l^{(i)}(X_{l,0})] \right. \\ &\quad \left. + \sum_{i=0}^{N-1} [\varepsilon_{1,i} \tau^{(i)}(X_{1,0})] < 0 \right\}, \end{aligned} \quad (3.1)$$

where b_l , $X_{l,0}$ and $\varepsilon_{l,i}$ are random variables as described in Section II. Therefore, to exactly calculate the probability, it will involve an integral with all these variables. However to calculate it statistically, it is reasonable to *strictly* apply Central Limit Theorem (CLT) in (3.1). Because all terms in $\sum_{i=0}^{N-1} [\tau_1^{(i)}(X_{1,0})]^2$ are not independent to each other, it is not qualified to be applied CLT. So the basic idea is to first calculate the BER conditional on $X_{1,0} = x_{1,0}$ and then integrate over all possible $x_{1,0}$.

First, by (3.1), the conditional BER is

$$\begin{aligned} BER_1 | (b_1 = +1, X_{1,0} = x_{1,0}) \\ &= P \left\{ Y(x_{1,0}) < - \sum_{i=0}^{N-1} [\varepsilon_{1,i} \tau_1^{(i)}(x_{1,0})] \right\}, \end{aligned} \quad (3.2)$$

where

$$Y(x_{1,0}) = \sum_{i=0}^{N-1} [\tau_1^{(i)}(x_{1,0}) \sum_{l=2}^L b_l \tau_l^{(i)}(X_{l,0})] + \sum_{i=0}^{N-1} [\varepsilon_{1,i} \tau^{(i)}(x_{1,0})].$$

Because there is

$$\sum_{i=0}^{N-1} \left[\tau_1^{(i)}(x_{1,0}) \sum_{l=2}^L b_l \tau_l^{(i)}(X_{l,0}) \right] = \sum_{l=2}^L b_l \sum_{i=0}^{N-1} \left[\tau_1^{(i)}(x_{1,0}) \tau_l^{(i)}(X_{l,0}) \right]$$

which is composed of $L-1$ independent random variable, $\sum_{i=0}^{N-1} \left[\tau_1^{(i)}(x_{1,0}) \sum_{l=2}^L b_l \tau_l^{(i)}(X_{l,0}) \right]$ can be approximated as a Gaussian random variable.

$\sum_{i=0}^{N-1} \left[\varepsilon_{1,i} \tau_1^{(i)}(x_{1,0}) \right]$ is inherently a Gaussian random variable as $x_{1,0}$ is known. So $Y(x_{1,0})$ can be approximated as a random variable with mean 0 and variance

$$\begin{aligned} \sigma_{Y(x_{1,0})}^2 &\equiv \text{var} \left[Y(x_{1,0}) \right] \\ &= \left[(L-1)\sigma_X^2 + \sigma_n^2 \right] \sum_{i=0}^{N-1} \left[\tau_1^{(i)}(x_{1,0}) \right]^2 \\ &+ 2\sigma_X^2 \sum_{k=1}^{N-1} \left\{ \left[\sum_{l=2}^L \alpha_{l,k} \right] \sum_{i=0}^{N-k-1} \tau_1^{(i)}(x_{1,0}) \tau_1^{(i+k)}(x_{1,0}) \right\}, \end{aligned} \quad (3.3)$$

where $\alpha_{l,k}$ is the k^{th} autocorrelation coefficient of the chaotic map $\tau_l(\cdot)$, i.e.

$$\alpha_{l,k} = \frac{\text{cov}(X, \tau_l^{(k)}(X))}{\sqrt{\text{var}(X) \text{var}[\tau_l^{(k)}(X)]}} = \frac{E[X \tau_l^{(k)}(X)]}{\sigma_X^2}.$$

With this approximation, the conditional BER is

$$\begin{aligned} \text{BER}_1 | (b_1 = +1, X_{1,0} = x_{1,0}) \\ = \Phi \left(- \sum_{i=0}^{N-1} \left[\tau_1^{(i)}(x_{1,0}) \right]^2 / \sigma_{Y(x_{1,0})} \right). \end{aligned} \quad (3.4)$$

Because (3.4) is independent of b_1 , the BER of 1st user is

$$\text{BER}_1 = \int_{X_{1,0}} \Phi \left(- \sum_{i=0}^{N-1} \left[\tau_1^{(i)}(x_{1,0}) \right]^2 / \sigma_{Y(x_{1,0})} \right) \rho_1(x_{1,0}) dx_{1,0}. \quad (3.5)$$

The BER of other users have the same form as (3.5), but may have different value as different map is used to generate the chaos sequence. Usually, (3.5) is calculated by numerical integral. Because the CLT is strictly applied here, it provides almost exact BER in the case of large L , regardless of the spreading factor N .

IV. AUTOCORRELATION COEFFICIENTS AND OPTIMAL MAPS

The optimal problem is to choose the best maps so that the average BER of all users is minimized. In

the results of (3.5), the autocorrelation coefficients $\alpha_{l,k}$ of the chaotic map are involved in the variance of $Y(x_{1,0})$, which make the analysis more complicated. Usually, the larger is the variance of $Y(x_{1,0})$, the larger is the BER. Approximately, the effect of the autocorrelation coefficients can be measured by the expectation of variance of $Y(x_{1,0})$, for example, for the 1st user the measure is

$$\begin{aligned} \sigma_{Y_1}^2 &\equiv E \left[\sigma_{Y(x_{1,0})}^2 \right] = N\sigma_X^2 \left[(L-1)\sigma_X^2 + \sigma_n^2 \right] \\ &+ 2\sigma_X^4 \sum_{k=1}^{N-1} \left\{ (N-k) \alpha_{1,k} \left[\sum_{l=2}^L \alpha_{l,k} \right] \right\}. \end{aligned} \quad (4.1)$$

The chaotic maps that having small $\sigma_{Y_1}^2$ indicates better performance for the 1st user. To consider the overall BER, the average $\sigma_{Y_i}^2$ should be calculated

$$\begin{aligned} \overline{\sigma_Y^2} &\equiv \frac{1}{L} \sum_{l=1}^L \sigma_{Y_l}^2 = LN\sigma_X^2 \left[(L-1)\sigma_X^2 + \sigma_n^2 \right] \\ &+ 2\sigma_X^4 \sum_{k=1}^{N-1} \left\{ (N-k) (A_k^2 - B_k) \right\}, \end{aligned} \quad (4.2)$$

where $A_k = \sum_{l=1}^L \alpha_{l,k}$ and $B_k = \sum_{l=1}^L \alpha_{l,k}^2$.

If all the users use the same chaotic map to generate the chaos sequences, the BER of one user is same as the overall BER. And the variance in (4.1), which is also same for all other users, becomes

$$\sigma_{Y_1}^2 = N\sigma_X^2 \left[\sigma_n^2 + (L-1)\sigma_X^2 \right] + 2(L-1)\sigma_X^4 \sum_{k=1}^{N-1} \left[(N-k) \alpha_k^2 \right]$$

which is minimized when $\alpha_k = 0$. It follows that (3.3) becomes

$$\sigma_{Y(x_{1,0})}^2 = \left[(L-1)\sigma_X^2 + \sigma_n^2 \right] \sum_{i=0}^{N-1} \left[\tau_1^{(i)}(x_{1,0}) \right]^2$$

and the overall BER is

$$\text{BER} = \int_{X_{1,0}} \Phi \left(- \sqrt{\frac{\sum_{i=0}^{N-1} \left[\tau_1^{(i)}(x_{1,0}) \right]^2}{\left[(L-1)\sigma_X^2 + \sigma_n^2 \right]}} \right) \rho_1(x_{1,0}) dx_{1,0},$$

which is similar to the BER of single-user coherent system [3]. So the lower bound of BER is

$$\begin{aligned} \text{BER} &= \Phi \left(- \sqrt{(N\sigma_X^2) / \left[(L-1)\sigma_X^2 + \sigma_n^2 \right]} \right) \\ &= \Phi \left(- \sqrt{N / \left[(L-1) + N / (2E_b/N_0) \right]} \right), \end{aligned} \quad (4.3)$$

and the asymptotically optimal map of the single-user system [5]

$$\tau(x) = \begin{cases} \sqrt{-2x^2 + 1 + i/M} & \sqrt{i/M} < |x| < \sqrt{(2i+1)/2M} \\ -\sqrt{-2x^2 + 1 + (i+1)/M} & \sqrt{(2i+1)/2M} < |x| < \sqrt{(i+1)/M} \end{cases}$$

where M is a positive integer, can also be used in this multi-user system to achieve lower bound performance.

V. SIMULATIONS AND CONCLUSIONS

Simulation BER of the whole system using the asymptotically optimal map with $M=1$ is provided in Fig. 2 and Fig. 3. The BER is plotted against E_b/N_0 in Fig. 2 for fixed $N=10$ and against N in Fig. 3 for fixed $E_b/N_0=10dB$. Analysis BER by (3.5) is also plotted for Chebyshev 3rd-order map and Bernoulli shift map other than the optimal map. The performance lower bound of (4.3) is also provided. A general agreement is shown between the simulation results and the analytical results.

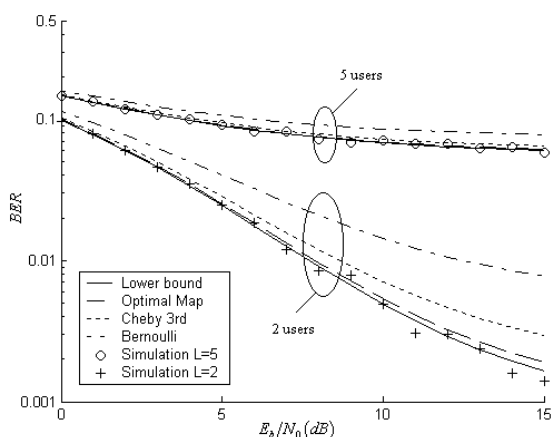


Fig. 2 BER is plotted against E_b/N_0 for $N=10$.

It is known from (4.3) that the lower bound performance is a function of the spreading factor N , as shown in Fig.3, which has the performance limitation $\Phi(-\sqrt{2E_b/N_0})$ for given L and E_b/N_0 when N increase to infinity. This indicates that in theory each user in the multi-user system can achieve the BPSK performance; the interference from other users is compensated by the spreading factors. However there is always some performance degradation due to the limitation of N . If the performance of the multi-user system is k dB poorer than the BPSK system, the required spreading factors is $N \geq 2 \cdot 10^{-(k/10)} / (1 - 10^{-(k/10)}) (L-1) (E_b/N_0)$. For example, if $k=1$, then $N \geq 7.7(L-1)(E_b/N_0)$ and

if $k=3$, then $N \geq 2(L-1)(E_b/N_0)$, both of which are possible to implement.

Another is that the performance lower bound (4.3) is not limited by the number of users in the system. In most conventional multi-user communication system, there is always a ‘BER-floor’, which is limited by the interference from other users. However in this multi-user CSK communication system, the BER is not limited by L . The system BER can achieve any value by increasing N and E_b/N_0 . This is due to the excellent cross-correlation property of the sequence generated by a chaotic map. But if N is fixed, the BER has a limitation of $\Phi(-\sqrt{N/(L-1)})$.

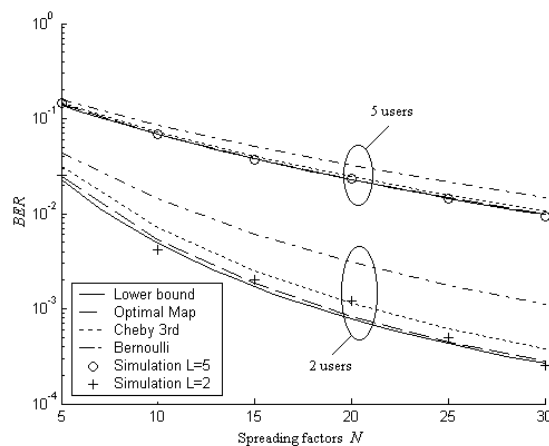


Fig. 3 BER is plotted against N for $E_b/N_0=10dB$.

REFERENCES

- [1] G. Kolumban, M. P. Kennedy, Z. Jako, and G. Kis, “Chaotic communications with correlator receivers: theory and performance limits,” *Proceeding of the IEEE*, vol. 90, No. 5, pp. 711-732, May. 2002.
- [2] A. Abel and W. Schwarz, “Chaos communication-principles, schemes, and system analysis,” *Proceeding of the IEEE*, vol. 90, No. 5, pp. 691-710, May. 2002.
- [3] A. J. Lawrence and G. Ohama, “Exact calculation of bit error rates in communication systems with chaotic modulation,” *IEEE Trans. Circuits Syst. I*, vol. 50, pp. 1391-1400, Nov. 2003.
- [4] W. M. Tam, F. C. M. Lau, C. K. Tse, and M. M. Yip, “An approach to calculating the bit-error rate of a coherent chaos-shift-keying digital communication system under a noisy multiuser,” *IEEE Trans. Circuits Syst. I*, vol. 49, pp. 210-223, Feb. 2002.
- [5] J. Yao, “Optimal chaos shift keying communications with correlation decoding,” to be appear in *Proc. IEEE-ISCAS'2004*, Vancouver, Canada, May 23-26, 2004.

Heart Tissue as a Dynamical System

E.Zhuchkova and A.Loskutov

Physics Faculty,
 Moscow State University,
 Moscow, Russia
 e-mail: zhkatya@polly.phys.msu.ru
 WWW: http://chaos.phys.msu.ru

Abstract—*The heart tissue as a conductive system with interacting excitation sources and a refractory time is considered. The phase locking regions of the developed model are investigated. The existence of the wide areas of the phase lockings confirms the possibility to observe synchronization of nonlinear centers qualitatively corresponding to different cardiac rhythms. The obtained results permit to predict the behaviour of complex biological systems.*

I. INTRODUCTION

As is known, the stability of the cardiac rhythms is vitally important. That is the reason why their analysis attract a considerable scientific interest. Owing to extraordinary complexity of the heart system, many alternative models have been tested. Some of them treat the cardiac tissue as an active conductive system. Then, the cardiac rhythms are described on the basis of the dynamical system theory (see, for example, [1–4] and Refs. therein).

Some disorders of the heart rhythms are induced by the competition of excitation sources and sometimes connected with the appearance of ectopic centers [5–9]. In this case investigation of such pathologies can rely upon the maps representation [3, 9–16].

In the present paper, a general model of two nonlinearly interacting centers based on the circle map is elaborated. The model describes certain types of cardiac arrhythmias (AV-blocks and parasistoles). It occurs to be a universal in the sense that its predictions are not sensitive to the specific form of interactions, i.e. to the phase response curve (PRC). In our analysis, the experimentally obtained PRC is approximated by a certain polynomial function which takes into account the refractory stage of the cardiac tissue.

It should be noted that the refractory stage plays an important role for the normal cardiac functioning. For example, the refractoriness extends almost over the period of the cardiac contraction, protecting the myocardium from premature heartbeats caused by the

external perturbation. The refractoriness provides also the normal sequence of an excitation propagation in the cardiac tissue and the electrical stability of the myocardium.

II. EQUATIONS

Let us consider the system of two nonlinearly interacting pulse oscillators (Fig.1). Suppose that the pulse of the first oscillator with the period T_1 beats at time t_n , and the pulse of the second oscillator (with the period T_2) beats at time τ_n . Then the next moments of the appearance of the impulses are defined as

$$\begin{cases} t_{n+1} = t_n + T_1, \\ \tau_{n+1} = \tau_n + T_2. \end{cases}$$

Now, taking into account that under the influence

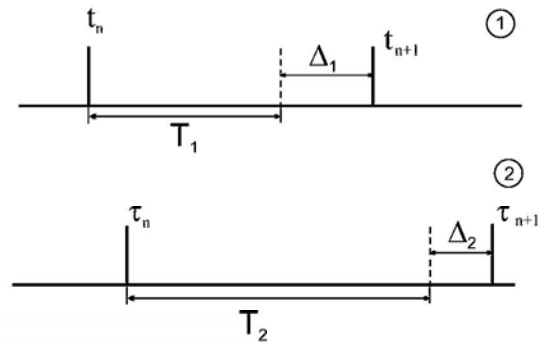


Fig. 1. The model of two interacting sources.

of the second impulse the period of the first oscillator changes by the value of $\Delta_1((\tau_n - t_n)/T_1)$ (where the relation in brackets means that this value depends only on the phase of the second impulse), we get the expression for t_{n+1} : $t_{n+1} = t_n + T_1 + \Delta_1((\tau_n - t_n)/T_1)$. For the further analysis let us consider the case when the pulses of two oscillators strictly alternate each other¹. Then for the second oscillator we obtain: $\tau_{n+1} = \tau_n + T_2 +$

¹The case when the pulses of two oscillators are not intermittent is addressed in [17].

$\Delta_2((t_{n+1} - \tau_n)/T_2)$. Dividing these relations by T_1 one can arrive at the generalized circle map:

$$x_{n+1} = x_n + a + f_2 \left(\frac{1}{a} (1 + f_1(x_n) - x_n) \right) - f_1(x_n) \pmod{1}, \quad (1)$$

where $x_n = \tau_n/T_1 - t_n/T_1$ is the phase difference of the sources, $a = T_2/T_1$, and $\Delta_1/T_1 = f_1$, $\Delta_2/T_1 = f_2$ are phase response curves each of them determines a change in the phase after the action of the stimulus.

As is known from experiments [9], the PRC changes its form depending on the amplitude of the external stimulus. In the simplest case this dependence can be approximated by the multiplicative relation. Then the phase response curves can be written as follows:

$$f_1 = \gamma h(x), \quad f_2 = \varepsilon h(x),$$

where $h(x)$ is a periodic function, $h(x + 1) = h(x)$. Under such assumption, the transformation (1) takes the form:

$$x_{n+1} = x_n + a + \varepsilon h \left(\frac{1}{a} (1 + \gamma h(x_n) - x_n) \right) - \gamma h(x_n) \pmod{1}. \quad (2)$$

In the present paper the circle map (2) with the *polynomial* function $h(x)$ will be addressed. The obtained results are generalization of our previous studies [18, 19].

III. UNIDIRECTIONAL COUPLING OF SOURCES

Let us analyze the situation when permanent inputs act on the nonlinear source, i.e. $f_2(x) \equiv 0$ or $\varepsilon = 0$. As an analytical approximation of the experimental curve, let us consider the following polynomial function:

$$h(x) = Cx^2 \left(\frac{1}{2} - x \right) (1 - x)^2. \quad (3)$$

The normalizing factor C we choose in such a way that the amplitude of $h(x)$ is equal to 1, so that $C = 20\sqrt{5}$. Then taking into account the refractory time δ we can write the map (2) as

$$x_{n+1} = \begin{cases} x_n + a, & 0 \leq x_n \leq \delta, \\ x_n + a - \gamma h \left(\frac{x_n - \delta}{1 - \delta} \right), & \delta < x_n \leq 1, \end{cases} \quad (4)$$

where $h(\cdot)$ is determined by (3). Now let us analyse the dependence of the system dynamics on the refractory time.

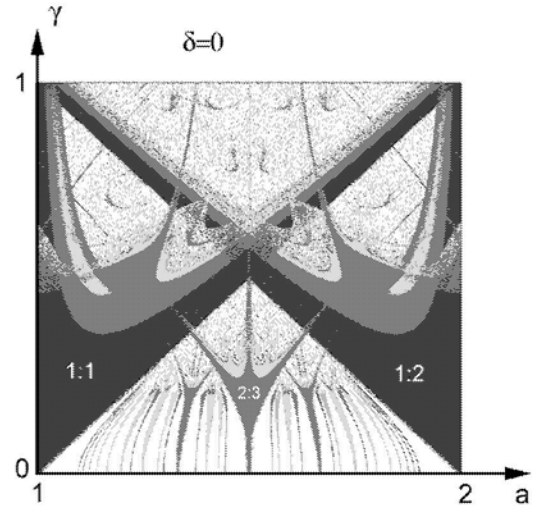


Fig. 2. Phase locking areas of the map (4) at $\delta = 0$.

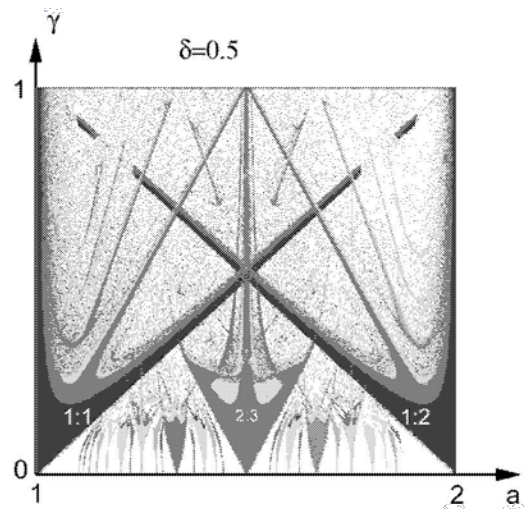


Fig. 3. Phase diagram of the map (4) at $\delta = 0.5$.

We start with the case when the refractory period is trivial, i.e. $\delta = 0$. The phase locking regions in the parametric space (a, γ) obtained by numerical analysis are shown in Fig.2, where $a \in [1, 2]$ is chosen. Different saturation defines the phase locking areas with the multiplicity $N : M$, where N cycles of external stimulus correspond to M cycles of the nonlinear oscillator. One can see that "tales" of the main locking regions are slightly splitted and overlap at large γ . As it follows from the analysis of the system (4) with $\delta = 0.1 - 0.4$, nonvanishing refractory time leads to the extension of the phase locking areas and enhances splitting and overlap of their tales.

The phase locking regions for $\delta = 0.5$ are shown in Fig.3. This phase diagram is *qualitatively* different from Fig.2. The form of the $2 : 3$ phase locking area is stretched and looks like an arrow. At growing the

refractory time, the phase lockings are degenerating into vertical lines. Note that for $\delta = 1$ (i.e. the system does not respond to the external action) there is no dependence on the stimulus amplitude γ .

IV. BIDIRECTIONAL COUPLING OF SOURCES

Assume that the influence of the first oscillator on the second one is small enough, for example, $\varepsilon = 0.1$. The corresponding phase diagram of the map (2) for $\delta = 0.1$ is shown in Fig.4. One can see that the mutual action leads to deformation and splitting in the phase locking areas. Note that even for small values of the amplitude of the second stimulus γ , the main phase locking areas overlap. This means that the system dynamics becomes multistable: Its limiting stage depends on an initial phase difference x_0 . The growth of the refractory time in the model with $\varepsilon = 0.1$ leads to a more deep distortion of the forms of the main tongues and disappearance of the splitting areas.

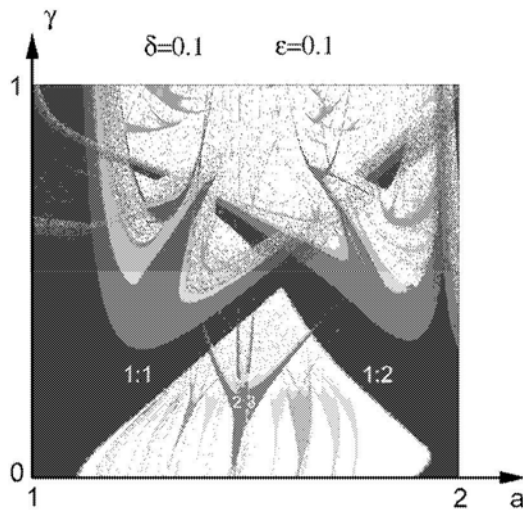


Fig. 4. Phase locking regions of the system (2) with $\delta = 0.1$ and $\varepsilon = 0.1$.

If, however, we increase the influence of the first oscillator up to, e.g $\varepsilon = 0.5$, a very complicated structure with *much more deep* deformation of the main phase locking areas (see Fig.5) will appear. For example, the 1 : 1 area will degenerate into a narrow strip, whereas the 1 : 2 phase locking area will expand due to appearance of long narrow tongues.

The numerical analysis shows that the increase of ε up to approximately 0.5 is accompanied by the expansion of the resonance zones. At the same time, the shape of the phase locking regions becomes more complex, and their location changes. This leads to the complete mixture of zones: Zones of various multiplicity may be found in a small neighborhood of al-

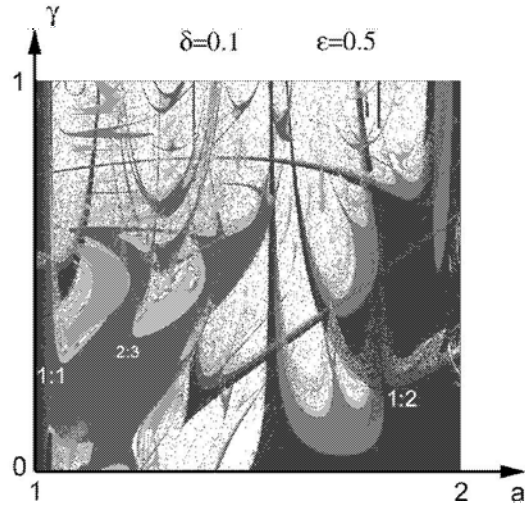


Fig. 5. Phase locking areas of the system (2) with $\delta = 0.1$ and $\varepsilon = 0.5$.

most any point (γ, a) . Nevertheless at any given value of ε self-similarly structures are clearly observed.

Additionally, we have found as the nonlinearity parameter ε further grows, the resonance zones shrink and occupy smaller area. In this case the mixing of the resonance tongues also takes place. Thus, the increase of the interaction of the oscillators causes the mixing of the initially regular structures.

V. APPLICATIONS TO HEART RHYTHM PATHOLOGIES

Let us consider the analogy between the obtained results and pathological states of the cardiac tissue. Using the developed models it is possible, for example, to describe the interaction of the sinus and the ectopic centers, the SA (sinoatrial) and AV (atrioventricular) nodes and impact of an external perturbation on the sinus excitation source.

Consider the types of arrhythmias which one can predict on the basis of our model. If the first pulse oscillator is presented as the SA node and the second one is considered as the AV node, then one can conclude that certain stable phase lockings correspond to the cardiac pathologies which are detected in a clinical practice. In this case among various lockings one can observe the normal sinus rhythm (1 : 1 phase locking). In addition, in the diagrams we can see the classical rhythms of Wenckebach ($N : (N - 1)$ phase lockings) and $N : 1$ AV-blocks.

When the first pulse system is considered as the AV node and the second one is presented as the SA node, we obtain the inverted Wenckebach rhythms (that are similar to the direct rhythms but the roles of ventri-

cles and atria change places) which were recorded for some patients.

The existence of the wide areas of the phase lockings (see Fig.2–5) confirms that it is possible to observe synchronization of two oscillators qualitatively corresponding to some types of cardiac arrhythmias. The phase diagram permits to determine the type of synchronization corresponding to interaction parameters a , γ , ε and δ . Moreover, the phase pictures indicate that as the nonlinearity increases (i.e. at growing γ) the areas with various phase lockings start to overlap. The knowledge of such regions, predicted by the present model, is necessary to operate the biological system dynamics. Removing the system from an undesirable mode of synchronization to an appropriate state by the external action may be of crucial importance for applications. In particular, the knowledge of the multistability areas for the *cardiac tissue* would be helpful to stabilize its behaviour and return the rhythm to the normal functioning.

REFERENCES

- [1] M. Courtemanche, L. Glass, J. Belair, D. Scagliotti, D. Gordon. A circle map in a human heart. *Physica D* **49**, pp. 299–310, 1989.
- [2] A. L. Goldberger. Nonlinear Dynamics, Fractals and Chaos: Applications to Cardiac Electrophysiology. *Ann. Biomed. Eng.* **18**(2), pp. 195–198, 1990.
- [3] G. Bub, L. Glass. Bifurcations in a continuous circle map: A theory for chaotic cardiac arrhythmia. *Int. J. Bifurcation and Chaos* **5**(2), pp. 359–371, 1994.
- [4] L. Glass et al. Predicting the entrainment of reentrant cardiac waves using phase resetting curves. *Phys. Rev. E* **65**, pp. 021908-1–021908-10, 2002.
- [5] L. Schamorth. *The Disorders of the Cardiac Rhythm*. (Blackwell, Oxford), 1980.
- [6] H. J. L. Marriot, M. M. Conover. *Advanced Concepts in Cardiac Arrhythmias*. (C.V. Mosby, St. Louis), 1983.
- [7] D. P. Zipes, J. Jalife. *Cardiac Electrophysiology – from Cell to Bed-Side*. (W.B.Saunders, Philadelphia), 1995, 2nd ed.
- [8] A. T. Winfree. *When Time Breaks Down: The Three-Dimensional Dynamics of Electrochemical Waves and Cardiac Arrhythmias*. (Princeton Univ. Press, Princeton), 1987.
- [9] L. Glass, M. Mackey. *From clocks to chaos: the rhythms of life*. (Princeton Univ. Press, Princeton), 1988.
- [10] G. M. Moe, J. Jalife, W. J. Mueller, B. Moe. A mathematical model for parasistole and its application to clinical arrhythmias. *Circulation* **56**, pp. 968–979, 1977.
- [11] J. Jalife, C. Antzelevitch, G. Moe. The case for modulated parasistole. *Pace* **5**, pp. 911–926, 1982.
- [12] J. Honerkamp. The heart as a system of coupled nonlinear oscillators. *J. Math. Biol.* **18**, pp. 69–88, 1983.
- [13] N. Ikeda, S. Yoshizawa, T. Sato. Difference equation model of ventricular parasystole as an interaction between cardiac pacemakers based on the phase response curve. *J. Theor. Biol.* **103**, pp. 439–465, 1983.
- [14] Y. He, R. Chi, N. He. Lyapunov exponents of the circle map in human hearts. *Phys. Lett. A* **170**, pp. 29–32, 1992.
- [15] G. P. Kremmydas, A. V. Holden, A. Bezerianos, T. Bountis. Representation of sino-atrial node dynamics by circle maps. *Int. J. Bifurcation and Chaos* **6**(10), pp. 1799–1805, 1996.
- [16] P. Ostborn, G. Ohlen, B. Wohlfart. Simulated sinoatrial exit blocks explained by circle map analysis. *J. Theor. Biol.* **211**(3), pp. 219–227, 2001.
- [17] A. Loskutov, S. D. Rybalko, E. A. Zhuchkova. *In preparation*, 2004.
- [18] A. Loskutov. Nonlinear dynamics and cardiac arrhythmia. *Applied Nonlinear Dynamics* **2**(3–4), pp. 14–25 1994 (Russian).
- [19] A. Loskutov, S. D. Rybalko, E. A. Zhuchkova. Dynamics of excitable media with two interacting pacemakers. *Biophysics* **47**(5), pp. 892–901, 2002.

A MODEL FOR THE ‘CHAOTIC’ OSCILLATIONS OF CONGENITAL NYSTAGMUS

Christopher M. Harris* & David L. Berry†

* SensoriMotor Laboratory, Centre for Theoretical and Computational Neuroscience,
University of Plymouth, UK

E-mail: cmharris@plymouth.ac.uk

† Centro de Geofísica de Évora / Departamento de Física, Universidade de Évora, Portugal

E-mail: dberry@uevora.pt

Abstract— *Congenital Nystagmus (CN) is a pathological involuntary oscillation of the eyes with an onset within the first few months of life and with an incidence of about 1:3000. It is a life-long oculomotor disorder that cannot be explained by any underlying neurological abnormality which might compromise adaptive mechanisms. There is no cure, and CN has so far defied explanation in spite of numerous attempts to model the disorder. Preliminary results of an optimal control model are presented here which attempt to show that the distinctive chaotic oscillations of CN are the direct result of the brain trying to produce eye movement trajectories that maximise visual contrast when foveal vision is compromised. This model produces realistic ‘chaotic’ waveforms and correlation dimensions similar to observations. Thus CN may be a biological example of instability as an optimal behaviour.*

waveforms have been observed [2], most are unique to CN and not seen in acquired nystagmus.

The cause of CN is a mystery, but intriguingly, the majority of affected individuals are also born with a detectable congenital visual defect such as oculocutaneous or ocular albinism, aniridia, cone dysfunction, congenital stationary night blindness, cataract, and many more congenital conditions [3]. Seldom does CN have an onset after a few months of age [4]. However, when vision can be restored (e.g., cataract removal), nystagmus persists [5]. Moreover visual deficits with an onset later in life do not precipitate CN-like oscillations. Thus, CN is a developmental anomaly, but why should poor neonatal vision lead to permanently wobbling eyes? We propose that CN is a *normal* adaptive response to maximise visual contrast from an *abnormal* visual system in which central (macular) retinal input is reduced or absent in early infancy – a time of rapid oculomotor development and sensory plasticity.

I. INTRODUCTION

Congenital Nystagmus (CN) is an unusual pathological condition consisting of a life-long spontaneous oscillation of the eyes with an onset around birth. CN is non-progressive with no known neurological ‘lesion’ (unlike acquired nystagmus [1]), and life-expectancy is normal. Usually, affected individuals do not perceive an oscillating visual world (‘oscillopsia’) and may be unaware of their nystagmus, even though retinal images are moving. Eye movement recording has revealed that CN oscillations are usually conjugate and predominantly horizontal. The oscillations usually consist of an alternating sequence of ‘slow’ and ‘fast’ phases (called ‘jerk’ nystagmus). During a slow phase, the eyes drift away from the point of visual regard with a characteristic trajectory in which eye velocity usually increases before a resetting saccade (fast phase) occurs. Occasionally, the waveform may be quasi-sinusoidal with no fast phase (called ‘pendular’ nystagmus). Remarkably, although a variety of

II. MATHEMATICAL MODEL

It is firmly established that retinal ganglion cells (RGCs) have spatial and temporal tuning, with maximal responses for stimuli with a given spatial frequency and a given temporal frequency depending on the size of the receptive field (RF). Thus, RGCs with the small RFs in the fovea are maximally stimulated by stimuli that have high spatial frequencies (fine detail) and with very little motion (although some slight movement is optimal) while the RGCs with large RFs dominate the visual periphery and are maximally responsive to lower spatial frequencies and faster moving stimuli [6]. Normally, there is a huge predominance of RGCs with small RFs in the foveal region, so that overall, contrast is maximised by moderately high spatial frequencies (~4cyc/deg) and almost (but not quite) stationary stimuli [7]. Now, if the retina is deficient in small central RFs through malformation [8] (e.g., foveal

hypoplasia), or cannot use them because of optical abnormalities (e.g., cataract, extreme myopia), then maximal contrast will be achieved not only at lower spatial frequencies, but also by stimuli with some degree of motion [9]. This is borne out in patients with CN, where contrast sensitivity functions are shifted to lower spatial frequencies when gratings are presented vertically (i.e., the spatial frequency is in the direction of the nystagmus) [10]. The fact that nystagmus *improves* sensitivity at low spatial frequencies in the direction of eye movement is a result of the spatiotemporal tuning of the retina. We argue that in a retina without the usual foveal dominance of high spatial frequency responses, this tuning drives oculomotor plasticity towards inducing some kind of image movement by moving the eyes, rather than keeping them still as in normal vision.

To determine the best movement, we couch the problem in terms of optimality and solve for the optimal movement using the calculus of variations. We denote loss of visual contrast as a ‘cost’ to the infant visual system, so that as the image moves away from the fovea, cost will increase as contrast falls. We simplify the total cost over the integration period T by the integral:

$$C = \int_0^T c_1 + c_2 + ay^2(t) + b[\dot{y}(t) - p]^2 dt \quad (1)$$

where y denotes the position of the image relative to the fovea, p denotes the optimal image speed across the fovea and $\dot{y}(t) = dy/dt$ as the speed of the image, and c_1, c_2, a and b are constants. T is the visual integration time. For the abnormal retina p is greater than zero, depending on the degree of foveal degradation.

Using the calculus of variations, the general optimal solution is given by

$$y(t) = Ae^{-t/\tau} + Be^{t/\tau} \quad (2)$$

where A and B are undetermined constants that depend on T, p and any boundary conditions and $\tau = +\sqrt{b/a}$ is a constant.

III. RESULTS

From equation (2), we can see that, for $p > 0$, the optimal strategy is to move the image away from the fovea – a compromise between keeping the image

on the fovea and keeping the image as close to the optimal speed, p . If the image starts at a different position, then there is a different optimal trajectory. Thus there is a set of optimal trajectories for each initial. Thus, it is necessary for the image position to move *away from* or *across* the fovea. It can be seen from equation 2 that as time progresses ($t \gg \tau$) the speed will increase and hence eye position would need to accelerate exponentially, which is one of the unique features of CN. Second, this image movement requires that there is a net change in eye position after time T , which will require resetting. Thus the optimal solution requires epochs or ‘oscillations’ of eye position (which of course we call ‘nystagmus’).

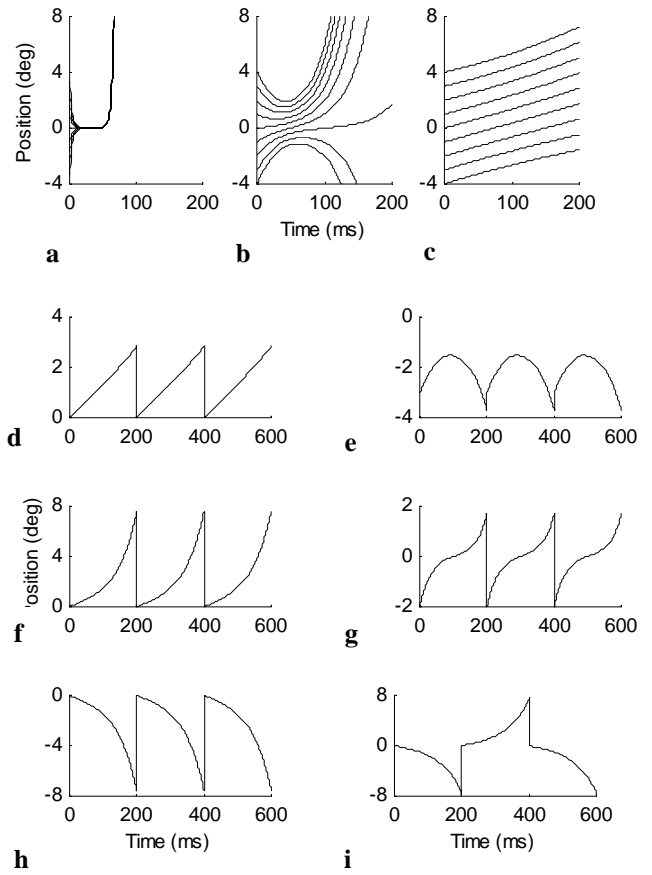


Fig. 1 a-c Variation of image position relative to the fovea for different initial positions (varying from -4 to 4 degrees in one degree steps) with parameters: $T = 0.05$, $p = 13.5$, **a** $\tau = 0.00001$; **b** $\tau = 0.001$; **c** $\tau = 0.1$. **d-g** Typical uni-directional jerk nystagmus sequences with saccadic return phases **d** $\tau = 0.1, x = 0^\circ$; **e** $\tau = 0.005, x = -3^\circ$; **f** $\tau = 0.004, x = 0^\circ$; **g** $\tau = 0.001, x = -2^\circ$; **h** $p = -13.5, \tau = 0.004, x = 0^\circ$; **i** typical bi-directional jerk nystagmus sequence with saccadic return phases $p = -/+13.5, \tau = 0.004, x = 0^\circ$.

Equation (2) captures more than the simple exponential runaway. It describes rich sets of optimal trajectories depending on the parameters, τ , T , and p . We can see that the optimal trajectories described by equation 2 capture most of the observed CN waveforms.

The optimal waveforms in Figure 1 represent ideal epochs, and could not be generated by the human oculomotor system. The human oculomotor system has evolved to service the normal foveate visual system, not to generate CN. Eye movement performance, especially in infancy, will place constraints on how well the ideal epochs can be realised. One important constraint is the oculomotor system can only make abrupt changes in eye velocity via the saccadic system. Thus, to reverse direction abruptly requires small ‘braking’ saccades. Saccades are also the only means for resetting eye position abruptly at the end of an epoch (the fast phase). It is an empirical observation that the timing of fast phases is quite stochastic, with rates no more than 3-4 times per second in adults [11], and in our experience this rate is about halved in young infants. Thus, epochs will usually last longer than the visual integration period, T . Due to the accelerative nature of the optimal trajectories, longer epochs will lead to considerably greater amplitude of movement and higher velocities than the ideal.

It is also well-known that the resetting fast phases have end-point variability, which tends to increase with amplitude [12-14]. This means that the starting position of the *next* epoch is inherently stochastic, which has a profound and complex effect on the optimal trajectory. As shown above (Fig. 1a-c), different starting positions require different optimal trajectories (sensitivity to initial conditions) leading to complex sequences of epochs, where there may even be reversals of slow phase direction. To illustrate this process we generated a sequence of epochs (Fig. 2b) to compare with empirical data taken from a female subject with typical idiopathic congenital nystagmus [15] (Fig. 2a). A dynamical systems analysis, based on the use of delay embedding techniques [16], was subsequently applied to this data. The three-dimensional projection of the reconstructed phase space trajectory shows a similar profile as observed empirically (Fig. 2c,d). The correlation (or ‘fractal’) dimension [17] of the phase space trajectory revealed little or no difference between the empirical data and the simulated data generated by the model. Even though the model contains several random processes, the correlation dimensions were finite and of similar values (empirical data: correla-

tion dimension, $D_2 = 1.404$, model data: correlation dimension, $D_2 = 1.423$) providing confidence in the fidelity of the model.

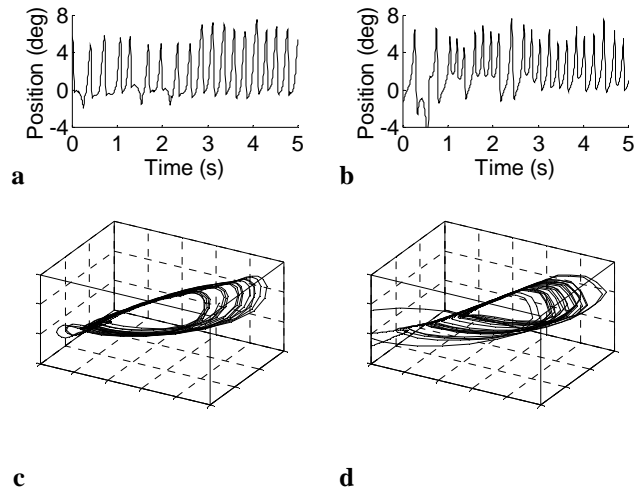


Fig. 2. Comparison of 5 sec sequence of empirical data taken from (a) a female subject with typical idiopathic congenital nystagmus with (b) simulated data generated by the model ($T = 0.05$, $p = 13.5$, $\tau = 0.0025$); (c) and (d) associated three-dimensional projections of the reconstructed phase space trajectories.

IV. DISCUSSION

We have shown that most of the observed CN waveforms are minima depending on the parameters τ and p , which are physiological factors determined by the degree of foveal dysfunction (whether structural or functional). It is not possible for the normal adult oculomotor system to generate CN. Presumably, CN is beyond the adaptive capability of the mature brain, and so we do not see CN emerging in adulthood following acquired loss of foveal function (eg. macular degeneration). On the other hand, infant visuomotor development is remarkably plastic, with rapid oculomotor and sensory development in the first year of life; but how does the immature oculomotor system generate CN?

In the first year of life, the oculomotor system develops the ability to track smoothly a small moving object (smooth pursuit), and as a corollary, to maintain steady eye gaze at an eccentric object. These are crucial for foveate vision. A key requirement is to generate tonic signals to overcome the strong visco-elastic forces that tend to bring the eyes back to primary position, which is achieved by the much-celebrated ‘neural integrator’ (NI) which

mathematically integrates velocity commands to generate the appropriate tonic. In turn this allows the eyes to be driven with the desired velocity independent of eye position, a key oculomotor function. Now, for jerk CN the optimal trajectories do not (and must not) require steady gaze at any eccentricity. Instead each eccentricity must be associated with a specific velocity profile. We argue that this can only be achieved by adapting the NI machinery to 'programme' different velocity-position relationships than those normally seen.

Thus, as the eye moves away from the equilibrium point there will be an ever increasing centripetal force that will eventually reverse eye velocity. This has two effects. First exponential runaway will be gradually slowed and eventually reversed (assuming a quick phase does not intervene) (Fig. 2e). Secondly, attempts to fixate eccentric from the equilibrium point will have large centripetal velocities causing large net movement before a quick phase can be generated. This in turn will lead to large amplitude quick phases with attendant large variability and the pseudo-cyloid waveform would be optimal.

V. CONCLUSION

A simple model has been presented for congenital nystagmus. It implies that the chaotic oscillations are the result of a physiological developmental adaptive process. This is in contrast to the prevailing view that CN is a disease that can be 'cured'. We argue that CN is as adaptive and permanent as normal eye movements are in a normally sighted individual.

REFERENCES

- [1] Leigh, R.J. & Zee, D.S. *The Neurology of Eye Movements*. (OUP, Oxford, 1999).
- [2] Dell'Osso, L.F. & Daroff, R.B. Congenital nystagmus waveforms and foveation strategy. *Doc. Ophthalmol.* **39**(1), 155-182 (1975).
- [3] Casteels, I., Harris C.M., Shawkat, F. & Taylor, D. Nystagmus in infancy. *Br J Ophthalmol.* **76**, 434-7 (1992).
- [4] Gottlob, I. Infantile nystagmus. Development documented by eye movement recordings. *Invest Ophthalmol Vis Sci.* **35**, 3556-60 (1994).
- [5] Ondráček, O. & Lokaj, M. Visual outcome after congenital cataract surgery. Long-term clinical results. *Scripta Medica (Brno).* **76**(2), 95-102 (2003).
- [6] Kelly, D.H. Moving gratings and microsaccades. *J. Opt. Soc. Am. A* **7**, 2237-2244 (1990).
- [7] Virsu, V., Rovamo, J., Laurinen, P. & Näsänen, R. Temporal contrast sensitivity and cortical magnification. *Vision Res.* **22**, 1211-1217 (1982).
- [8] Abadi, R.V. & Pascal, E. Incremental light detection thresholds across the central visual field of human albinos. *Invest. Ophthalmol. Vis. Sci.* **34**, 1683-1690 (1993).
- [9] Loshin, D.S. & Browning, R.A. Contrast sensitivity in albinotic patients. *Am. J. Optom. Physiol. Opt.* **60** 159-166 (1983).
- [10] Burr, D.C. & Ross, J. Contrast sensitivity at high velocities. *Vision Res.* **22**, 479-484 (1982).
- [11] Cheng, M. & Outerbridge, J.S. Inter-saccadic interval analysis of optokinetic nystagmus. *Vision Res.* **14**(11):1053-8 (1974).
- [12] Clamman, P.H. Statistical analysis of motor firing patterns in human skeletal muscle. *Biophysics J.* **9**:1233-1251 (1969).
- [13] Mathews, P.B.C. Relationship of firing intervals of human motor units to the trajectory of post-spike after hyperpolarization and synaptic noise. *J. Physiol.* **492**, 597-628 (1996).
- [14] Harwood, M.R. & Harris, C.M. Time-optimality and the spectral overlap of saccadic eye movements. *Ann. N. Y. Acad. Sci.* **956**: 414-7 (2002).
- [15] Abadi, R.V., Broomhead, D.S., Clement, R.A., Whittle, J.P. & Worfolk, R. Dynamical systems analysis: a new method of analysing congenital nystagmus waveforms. *Exp. Brain Res.* **117**: 355-361 (1997).
- [16] Ott, E., Sauer, T., & Yorke, J.A. *Coping with chaos*. Wiley, New York (1994).
- [17] Theiler, J. Estimating fractal dimension. *J. Opt. Soc. Am.* **7**: 1055-1073 (1990).

Index by Authors

Abel, Markus	55	Cafagna, Donato	107, 111, 115
Aguiar, M.A.M.	154	Caizzone F.	95
Ahnert, K.	55	Carballar, J.	336
Aihara, Kaauyuki	332	Chacón, Ricardo	242, 336
Alves, E. Ivo	59	Chakraborty, S.	126
Ameiniya, Yoóhilhito	71	Chelidze, T.	119
Ananthakrishna, G.	126	Conti, F.	63
Ando, Bruno	178	Cuadros, F.	122
Andriani, P.	63	Curran., Paul	75
Anishchenko, V.S.	67	Daafouz, Jamal	255
Asai, Tetsuya	71	Dana, Syamal Kumar	126, 288
Ascoli, Alon	75	Dionísio, Andreia	130
Baglio, Salvatore	178	Dmitriev, Alexander S.	133, 138
Balestra, Michele	79	Duarte, Jorge	142
Baranorski, Alexander	83	Efremova, Elena	133
Baziliauskas, Antanas	87, 99	Falk, Thomas	146
Berry, David	380	Feely, Orla	75
Bilbault, J.M.	182, 263	Fernandes, Sara	150
Binczak, S.	182	Ferreira, Nuno B.	250
Bryuhanov, Yuriy	91	Fonseca, Alexandre F.	154
Bucolo, M.	95	Fortuna, Luigi	63, 95, 158, 162
Buka, Paval	206	Frasca, Mattia	63, 158
Bulsara, Adi	178	Gabaix., X.	42
Bumeliene, Skaidra	99, 328	Galias, Zbigniew	166
Buononio, Antonio	103	Gopikrishnan, P.	42

Grácio, Clara	170	Kohda,Tohru	202
Grassi, Giuseppe	107, 111, 115	Konash, Aliaksei	206
Graziani, Salvatore	158	Kon'no Yoshio	210
Haase, Maria	259	Krivickas, Romanas	87, 328
Haken, Hermann	3	Krupar, Joerg	214
Harris, C. M.	380	Kuleshov, V.N.	219
Hasler, M.	360	Kurths, J.	17, 340
Hattori, T.	194	Kuzmin., Lev V.	138
Herrmann, Hans J.	9	La Rosa, M.	162
Hevesi, L.	174	Laktushkin, Anton M.	138
Ikebe, Masayuki	71	Lawrance A.J	83
In, Visarath	178	Lebedev, M.V.	292
Inaba, Naohiko	308	Li, K.	223
Jacquir, Sabir	182	Li, Z.G.	223
Janoev, Arsen	231	Lindberg, Eric	99 227, 328
Janósi, L.M.	174	Lo Schiavo, A.	103
Kanazawa. Yusuke	71	Longhini, Patrick	178
Kapranov, M.V.	344	Loskutov, Alexander	231, 376
Karavaev, AS.	280	Lursmanashvili, O.	119
Kasantsev, V.B.	182	Mahnke, Reinhard	206
Katoh, Aya	202	Maistrenko, Yuri	246, 360
Kawakami, Hiroshi	308, 348, 352	Makarenkov, Oleg	235
Kelber, Kristina	186	Malta, Coraci P.	154
Kern, Albert	190, 324	Marodi, Mate	238
Khilinsky Alexander D.	133	Marqui, P.	263
Kho, Andy	178	Martínez, J.A.	242
Kiraly, A.	174	Martins Nuno	284
Kitajima, Hiroyuki	194	Matcharashvili, Teimuraz	119
Kobayashi, Yoshifumi	198	Mathis, Wolfgang	276

Matakwi, Jryna	246	Rizzo, A.	63
Meadows, Brian	178	Romano, M.C.	17, 340
Mendes, Diana A.	130	Rovatti, R.	79
Mendes, Rui Vilela	22	Roy, Prodyot Kuxnar	288
Menezes, Rui	130, 250	Rudykh, Dinitry	292
Millerioux, Gilies	255	Ryskin, N.M.	296
Mora, Alejandro	259	Saito, Toshimidii	198, 210, 300
Morfu, Sa'verio	263	Santi, Stefano	79
Mykolaitis, G.	99, 328	Savaci, F. Acar	304
Nakano, Hidehiro	198	Schwarz, Wolfgang	146, 214
Neerholl; F.L.	267, 356	Sekikawa, Munehisa	308
NeLE, Joe	178	Sergej, Bagmda	206
Nekorkin, V.I.	182	Setti, Giantuca	79
Nicolosi, D.	162	Severino, R.	312
Ninomiya, Tamotan	271	Sharkovsky, A.	34 312
Ogorzalck, Maciej	166	Shigaev, Andrey	296
Okrokvetskikhov, G.A.	67	Shimakawa, Junya	300
Orabi, Mohaiued	271	Sicureila, G	162
Ozkurt, Nalan	304	Silva, Luís	142
Palacios, Antonio	178	Siomczyuski, Maciej H.	316
Parra, M.L.	122	Sou, Y.C.	223
Passiante, G.	63	Sousa, Adriano O.	320
Ponomarenko, V.L.	280	Stanley, H. Eugene	42
Priorov, A.L.	292	Steeb, W.-H.	324
Prochaska, Marcus	276	Stoop, N.	324
Prokhorov, Mikhail	280	Stoop, Ruedi	190, 324
Ramos, Carlos Correia	284	Strelkova, C	67
Ramos, J. Sousa	142, 150, 170, 284, 312	SwidzinRka, Bozena	316, 364
Reddicono, SaIvatore	158	Tanaka, Gouhei	368

Tanaka, Kiyosbi	332
Tamasevicius, Arunas	87, 99, 328
Tereshko, Valery	336
Thiel, Marco	17, 340
Tomarchio, Giuseppina	95
Tomashevskaya, Maria	219
Tomashevskiy, Alexey	344
Torikai, Hiroyuki	210, 300
Tsuji, Shigeki	348
Ueta, Tetsushi	348, 352
Vadivasova, T.E.	67
van der Kloet, P.	267, 356
Vasylenko, Anua	360
Vinagre, S.	312
Wroblewski, Michal	364
Yano, Kenji	368
Yao, Ji	372
Yoshinaga, Tetsuya	308
Zhuchkova., Ekaterina	376